REPORT DOCUMENTATION PAGE

Form Approved

OMB No. 0704-0188

The public reporting burden for this collection of information is estimated to average 1 hour per response, including the time for reviewing instructions, searching existing data sources, gathering and maintaining the data needed, and completing and reviewing the collection of information. Send comments regarding this burden estimate or any other aspect of this collection of information, including suggestions for reducing the burden, to Department of Defense, Washington Headquarters Services, Directorate for Information Operations and Reports (0704-0188), 1215 Jefferson Davis Highway, Suite 1204, Arlington, VA 22202-4302. Respondents should be aware that notwithstanding any other provision of law, no person shall be subject to any penalty for failing to comply with a collection of information if it does not display a currently valid OMB control number.

PLEASE DO NOT RETURN YOUR FORM TO THE ABOVE ADDRESS.

1. REPORT DATE *(DD-MM-YYYY)*	2. REPORT TYPE	3. DATES COVERED *(From - To)*
06-12-2001	Conference Proceedings	13 – 16 Nov 01

4. TITLE AND SUBTITLE

7th Japan International SAMPE Symposium & Exhibition

5a. CONTRACT NUMBER

F6256201M9056

5b. GRANT NUMBER

5c. PROGRAM ELEMENT NUMBER

6. AUTHOR(S)

Conference Committee

5d. PROJECT NUMBER

5e. TASK NUMBER

5f. WORK UNIT NUMBER

7. PERFORMING ORGANIZATION NAME(S) AND ADDRESS(ES)

Nihon University, Department of Production Engineering
1-2-1 Izumi-cho, Narashino
Chiba 275-8575
Japan

8. PERFORMING ORGANIZATION REPORT NUMBER

N/A

9. SPONSORING/MONITORING AGENCY NAME(S) AND ADDRESS(ES)

AOARD
UNIT 45002
APO AP 96337-5002

10. SPONSOR/MONITOR'S ACRONYM(S)

AOARD

11. SPONSOR/MONITOR'S REPORT NUMBER(S)

CSP-011002

12. DISTRIBUTION/AVAILABILITY STATEMENT

Approved for public release; distribution is unlimited.

13. SUPPLEMENTARY NOTES

14. ABSTRACT

The 7th Japan International SAMPE Symposium was held on 13-16 Nov 01 in Tokyo, Japan. 232 papers are included in the proceedings. The conference consisted of 5 satellite workshops and 10 sessions. Satellite workshops included: A. Smart structures and materials/eco-materials, B. Design and Manufacturing of revolutionary light weight aircraft structures, C. Development of low cost composite structures, D. New materials in space vehicles, and E. Composite applications to infrastructure. Sessions included: F. Composite/plastic applications to transportation vehicles, G. Composite applications to sport and leisure goods, H. New trends in polymer composites and their fibers, I. Ceramic matrix composites and carbon/carbon composites, J. Metal matrix composites and related materials, K. Textile composites, L. Interface in composites, M. Modeling and simulation in composite mechanics, N. New trends in damage identification and NDI, and O. Student session.

15. SUBJECT TERMS

Advanced Materials Processing, Composite Materials

16. SECURITY CLASSIFICATION OF:			17. LIMITATION OF ABSTRACT	18. NUMBER OF PAGES	19a. NAME OF RESPONSIBLE PERSON
a. REPORT	b. ABSTRACT	c. THIS PAGE			Thomas D. Kim
U	U	U	UU	1012	19b. TELEPHONE NUMBER *(Include area code)* +81-3-5410-4409

Standard Form 298 (Rev. 8/98)
Prescribed by ANSI Std. Z39.18

INFORMATION AND INNOVATION IN COMPOSITES TECHNOLOGIES

20011213 201

SOCIETY FOR THE ADVANCEMENT OF
MATERIAL AND PROCESS ENGINEERING

Proceedings of the Seventh Japan
International SAMPE Symposium
Tokyo Big Sight, Tokyo, Japan
November 13-16, 2001

by SAMPE JAPAN CHAPTER

INFORMATION AND INNOVATION IN COMPOSITES TECHNOLOGIES

Edited by

T. Ishikawa
S. Sugimoto

Sponsored by
Asian Office of Aerospace Research and Development /
Air Force Office of Scientific Research (AOARD/AFOSR)
Army Research Office – Far East (AROFE)
The Nikkan Kogyo Shimbun (The Business and Technology Daily News), LTD

Additional copies of publication can be obtained from
JAPAN CHAPTER OF SAMPE

JAPAN CHAPTER OF SAMPE
Business Center for Academic Society, Japan
5-16-9 Honkomagome, Bunkyo-ku, Tokyo 113-8622
Tel: +81-(0)3-5814-5801
Fax: +81-(0)3-5814-5820
E-mail: asaiy@bcasj.or.jp

Subsidiary information may be obtained from

SAMPE Japan Information Service Office
Mr. Yoshinori Matsuoka
2-11-23, Zaimokuza, Kamakura 248-0013, Japan
Tel. +81-(0)467-24-2721
Fax. +81-(0)467-24-2735

ISBN4-9900028-7-3

Responsibility for the contents and security clearance of papers
published herein rests solely upon the authors and
not upon SAMPE or any of its members.

All contributions are peer-reviewed by our program committee members.

© 2001 by Society for the Advancement of Material and Process Engineering
All rights reserved

No part of this publication may be reproduced, stored in a retrieval system, or
transmitted in any form or by any means, electronic, mechanical, photocopying,
recording or otherwise, without the prior written permission of the publisher.

The Seventh Japan International SAMPE Symposium Organization

Organizing Committee

Chairman

I. Kimpara	SAMPE Japan Chapter (Chairman), Kanazawa Institute of Technology

Vice-Chairman

T. Tanimoto	Shonan Institute of Technology
A. Hirotani	The Business and Technology Daily News

Symposium Committee

Chairman

T. Ishikawa	National Aerospace Laboratory of Japan(NAL)

Vice-Chairman

H. Fukuda	Science University of Tokyo
Y. Yamaguchi	R&D Institute for Metals and Composites for Future Industries (RIMCOF)
T. Katayama	Doshisha University
K. Sato	Nippon Steel Technoresearch Corp.

Advisory Board Members

N. Igata	Science University of Tokyo
E. Nakata	Composite Engineering Co.
T. Hirai	Formerly of Doshisha University
A. Ohkura	Formerly of Institute of Space and Astronautical Science
N. Ohashi	SAMPE Japan Chapter
T. Kishi	National Institute for Materials Science
Z. Maekawa	Kyoto Institute of Technology
Y. Miyano	Kanazawa Institute of Technology
N. Teranishi	SAMPE Japan Chapter

Symposium Committee Members

H. Asanuma	Chiba University,
G. Ben	Nihon University
H. Hamada	Kyoto Institute of Technology
H. Hatta	Institute of Space and Astronautical Science (ISAS)
K. Kageyama	The University of Tokyo
H. Kawada	Waseda University
H. Kikukawa	Japan Aircraft Development Corporation (JADC)
K. Maruyama	Nagaoka Institute of Technology and Science
N. Mifune	Railway Technical Research Institute
Y. Morino	National Space Development Agency (NASDA)
T. Nishiwaki	ASICS Corp.
Y. Sohda	Nisseki Mitsubishi Oil Co.
N. Takeda	The University of Tokyo

Symposium Secretariat

S. Sugimoto	National Aerospace Laboratory of Japan(NAL)

Program Committee Members

Chairman

T. Ishikawa	National Aerospace Laboratory of Japan(NAL)

Vice-Chairman

S. Sugimoto	National Aerospace Laboratory of Japan(NAL)

Members: All of the Symposium Committee Members

Preface

The Japan Chapter of SAMPE is greatly honored to host the Seventh International SAMPE Symposium and Exhibition, JISSE-7 after the remarkable success in the previous 6 JISSE symposia held in 1989, 1991, 1993, 1995, 1997 and 1999. At this moment, JISSE-7 will be held from November 13 to 16, 2001, at Tokyo Big Sight in the Tokyo Bay downtown area in Tokyo whereas an Exhibition will run from November 13 to 15 at the exhibition halls in Tokyo Big Sight.

The subjects of JISSE-7 cover all areas of advanced materials research and development with a focus on industrial applications. New processing technologies related to low cost structures and futuristic new topics such as nano-technology with a relation to information technology (IT) are of current interest and are expected to develop further in the 21st Century. A total of 234 papers including plenary presentations from all over the world is presented at the symposium. Plenary talks will be given by Dr. James C.I. Chang, Dr. Scott W. Beckwith, Prof. Hiroshi Komiyama, Dr. Darrel R. Tenney, Mr. Jens Hinrichsen, Mr. Hideo Katsumata and Prof. Stephen W. Tsai, highlighting this symposium. Their contribution is hereby acknowledged as well as contribution by other keynote speakers in some sessions. General presentations will be given in 15 sessions including Student Session chaired by Prof. H. Fukuda. Exhibition will provide a general scope of advanced material applications to widespread industries in Japan. The symposium and exhibition was designated to complement each other closely to maximize both benefits.

On behalf of the Symposium Committee, we would like to express our sincere thanks to the Organizing Committee members, Advisory Board members, Exhibition Committee Members, and SAMPE headquarters' staff, whose dedication was the key for the success of this conference. We extend our sincere thanks as well to all speakers and authors, session co-chairs, and participants for making the conference very successful.

We also wish to thank the Asian Office of Aerospace Research and Development/ Air Force Office of Scientific Research (AOARD/AFOSR), Army Research Office-Far East (AROFE), and some foundations for their financial support.

We acknowledge finally Mr. Yoshinori Matsuoka of SAMPE Japan ISO, Dr. Toru Morii and Professor Tosio Tanimoto of Shonan Institute of Technology for their contributions in supporting us for making the conference efficient.

Takashi Ishikawa
Program Committee Chairperson, NAL

Sunao Sugimoto
Program Committee Vice-Chairperson, NAL

Table of Contents

Preface vii

Plenary Presentations

Expanded Horizon in Materials and Processing - Unlimited Frontier - 1
James C.I. Chang

Comparison of Low Cost Composites Manufacturing with Advanced Composites Processing Techniques.....5
Scott W. Beckwith

Structuring Knowledge Project in Nanotechnology Materials Program Launched in Japan 9
Hiroshi Komiyama and Yukio Yamaguchi

Advanced Composites Development for Aerospace Vehicle Applications.....17
Darrel R. Tenney and R. Byron Pipes

A380: Advanced Composite Structures Designed for the Flagship of the 21st Century...23
Jens Hinrichsen

Experience of FRP Strengthening for Historic Structures.....29
Hideo Katsumata and Kozo Kimura

New Examples of Composites Research.....33
Stephen W. Tsai, Akira Kuraishi, Sung-Kyu Ha and Jon Gosse

Satellite Workshops and General Sessions

[In the following, Keynote Speech Titles are indicated by underscored letters.
"N/A" indicates the paper is not available in this conference volume.]

Satellite Workshop A: Smart Structures and Materials/ Eco-materials

Recent Research on Fiber Optic Smart Structure in Italy and Future Trends in Europe 35
A. Paolozzi **(Keynote)**

Smart Materials and Structure at EADS CCR : An Overview.....43
J. Saniger and B. Petitjean **(Keynote)**

Improving the Vibration Damping of CFRP Beam Structures by Use of Piezoelectric Polymer/Ceramic.....47
T. Tanimoto

Cyclic Mechanical Behavior of Composites Based on Shape Memory Polymer 51
Q. –Q. Ni, T. Ohki, N. Ohsako and M. Iwamoto

Source Location in a CFRP Plate with Embedded PZT Sensors 55
R. Oishi, J.-H. Koo, N. Toyama and B. Wang

Effect of Stacking Sequence and Number of Electrodes on Detections of Delaminations of CFRP Using Electric Resistance Change 59
A. Todoroki, Y. Tanaka, Y. Shimamura and H. Kobayashi

Impedance Change Method for Wireless Strain Measurement of Composite Materials...63
A. Todoroki, S. Miyatani and Y. Shimamura

Determination of Internal Conducting Network of CFRP Composites Using Anisotropy of Electrical Conductivity.....67
J. –B. Park, T. Okabe, A. Yoshimura, N. Takeda, M. Xia and W.A. Curtin

Smart Detection of Damage of Composite Structures using Unsupervised Statistical Diagnosis.....71
A. Iwasaki, A. Todoroki, Y. Shimamura and H. Kobayashi

Monitoring Method of Resin Flow and Cure with Electromagnetic Wave Transmission Line Using Carbon Fiber as Conductive Elements.....75
K. Urabe, T. Okabe, H. Tsuda and J. Takatsubo

Process Monitoring and Controlling with Dielectric Sensor for Thermoplastic Composite Vane.....79
K. Yamagishi, S. Kitade, S. Motogi and T. Fukuda

Application of Small-Diameter FBG Sensors for Delamination Detection in CFRP Laminates.....83
S. Takeda, Y. Okabe and N. Takeda

Strain Measurement by the Smart Patch Using FBG Sensors.....87
N. Tanaka, Y. Okabe and N. Takeda

Internal Strain Monitoring of Molded Epoxy Using Embedded EFPI Optical Fiber Sensor during Molding.....91
K. Osaka, T. Kosaka, T. Fukuda, T. Naka, Y. Kurata and H. Miyagawa

Detection of Transverse Cracks in CFRP Quasi-Isotropic Laminates Using Small-Diameter FBG Sensors.....95
T. Mizutani, Y. Okabe and N. Takeda

Development of Smart Braided Composites by Using Fiberoptic Strain Sensors.....99
T. Kosaka, H. Kurimoto, K. Osaka, A. Nakai, T. Osada, H. Hamada and T. Fukuda

High Resistance to Fracture of Optical Fiber Reinforced Plastics.....103
T. Toriyama, Y. Miyazawa and Y. Nishi

Shape Memory Effect of NiMnGa Amorphous Thin Film.....107
K. Akiyama, H. Yabe and Y. Nishi

High Impact Polyethyleneterephthalate-Polyethylene Blockcopolymer from Recovered PET Bottles.....111
T. Fujimaki

Mechanical Properties of Metallic Closed Cellular Materials Containing Organic Material for Smart Structures.....115
S. Kishimoto and N. Shinya

Development of an Aluminum Based Smart Composite with Embedded Oxidized Titanium Fiber 119
H. Asanuma, T. Ishii and G. Hakoda

Spark Plasma Sintering of $Sr_{1.9}Ca_{0.1}NaNb_5O_{15}$ Piezoelectric Ceramics.....123
R.-J. Xie, Y. Akimune, K. Matsuo, T. Sugiyama and N. Hirosaki

Satellite Workshop B: Design and Manufacturing of Revolutionary Light Weight Aircraft Structures

Integrating Research & Development Programs with FAA Certification to Expedite the Introduction of New Technology into Production Aircraft.....129
M. Ashizawa and A. Sato **(Keynote)**

NEDO's R&D Program on Revolutionary Low-Cost and Lightweight Aircraft.....133
Y. Ito

R&D Program of Innovative Structural Technologies 137
A. Yahata and H. Kikukawa

Design, Manufacturing, and Certification Considerations for Modern Integrated Structures **141**
R. Abbott

Development of Affordable Composite Wing Structure **145**
Y. Toi, A. Harada, T. Kamiyama, T. Inoue, K. Amaoka and H. Kikukawa

Innovative Cockpit Structure-Molding Technology of Form Core **149**
T. Ito, T. Sana, Y. Hirose, K. Araya and M. Nishitani

Microstructure and Mechanical Properties in the Friction – Stir - Welded Dissimilar Light Metals **153**
N. Saito, I. Shigematsu and M. Nakamura

Innovative Cockpit Structure - Friction Stir Welding Technology of Al-Alloy **157**
T. Sakanashi, S. Iio, Y. Hirose, K. Araya and K. Kosugi

Structural Development for Innovative Leading Edge of Wing **161**
M. Matoba, S. Ohashi, M. Ochi, M. Motoike and A. Yahata

Large Size Aluminum Precision Sand Casting Technology Development for Aircraft Primary Structures **165**
A. Shibata, M. Nakata, Y. Hirose and Y. Yoshino

On the Tensile Strength of Carbon Fiber Composites out of Various Resin Matrices **169**
Y. Kanatani, Y. Kobayashi, J. Matsui and Z. Maekawa

An Integrated Approach to the Cost-Effective Design of a Composite Aircraft Control Surface (Keynote) **173**
M.-Q. Nguyen, T. –M. Lee and M. L. Scott

Low Cost Composite Design and Manufacturing Options **177**
K. Masugi

Development of Innovative Composite Control Surfaces **181**
A. Harada, S. Maruyama and N. Takizawa

Low Cost Structural Concept for Composite Trailing Edge Flap **185**
Y. Hirose, T. Taki, T. Yamamoto, Y. Mizusaki and T. Fujita

Affordable Composite Fuselage Structure based on Dry Preform/RFI Technology **189**
A. Tanaka and H. Kiriyama

Study of Al Investment Casting for Flight Control System **193**
K. Nakamura, S. Abe and M. Hirahara

Superplastic Forming of Aluminum Sheet with Welded Line **197**
T. Jinishi, T. Naganuma and N. Suzuki

Fatigue Evaluation on Composite Parts of Eurocopter Helicopters 201
H. Bansemir, G. Dreher and S. Emmerling

Methodology for Predicable Damage Growth Design of Aircraft Composite Structures 207
H. Kikukawa

Durability Analysis of Composite Structures Using the Accelerated Testing Methodology 211
A. Kuraishi and S. W. Tsai

Fatigue Life Prediction of CFRP/Metal Bolted Joint under Temperature Condition 215
N. Sekine, M. Nakada, Y. Miyano and S. W. Tsai

Satellite Workshop C: Development of Low Cost Composite Structures

Demonstration of Stitched/Resin Film Infused Composites in Primary Aircraft Wing Structures .....N/A
D. Moon **(Keynote)**

Stitch Parameter Effect on Impact Damage Resistance of a New RTM Composites 219
T. Osada, T. Kamiyama and T. Yoshimura

Low Cost Fabrication of HOPE-X All Composite Prototype Structure.....223
K. Uzawa, K. Nishiwaki, M. Niitsu and T. Kamita

An Overview of EADS Research Activities on Low Cost CFRP Composites 227
D. Guedra-Degeorges and K. Drechsler **(Keynote)**

Development of Thermoplastic Polyimide (PIXA-MT3) Composite 233
Y. Honda, H. Nakamura, T. Kamiyama, H. Tamura, S. Tamai, Y. Endo and Y. Nagao

Study of Automatic Drilling and Fastening for Wing Box.....237
T. Hiroe, T. Osawa, T. Hatakeyama, K. Kosugi and H. Tamura

Current Status and Future Prospects of R&D on Constructions of Design Database for Advanced Composites and Structures in Japan.....241
K. Hirano **(Keynote)**

Establishment of Database of Carbon/Epoxy Material Properties and Design Values on Durability and Environmental Resistance.....245
S. Bandoh, Y. Nakayama, R. Asagumo and T. Yoshimura

Thermal Degradation of CFRP Laminates **251**
T. Naruse and T. Hattori

Folded Honeycomb Core Materials for Automotive and Aerospace Applications **255**
J. Pflug, I. Verpoest and D. Vandepitte

Advanced Pultrusion Process ..... **N/A**
K. Asari

Well-processable Matrix Resins with Less-flammability for Vacuum-assisted Resin Transfer Molding **259**
N. Miyoshi, N. Natsume, I. Endo and H. Kishi

Low Cost Resin Transfer Molding of Carbon Polyimide **263**
H. Mizuno, H. Horizono, Y. Someya, T. Ito and Y. Soeda

Fatigue Strength Evaluation of FRP/Metal Adhesive Joints at Low Temperature **267**
M. Iwasa and T. Hattori

Satellite Workshop D: New Materials in Space Vehicles

Fabrication of a Thin Unlined Reusable Filament Wound Composite Cryogenic Tank... **271**
T. D. Kim **(Keynote)**

Study of CFRP Application to Cryogenic Fuel Tank for RLV **275**
T. Shimoda, Y. Morino, T. Ishikawa, T. Morimoto and S. Cantoni

Damage Evaluation of CFRP Concept Tank in Cryogenic Pressurization **279**
T. Morimoto, T. Ishikawa, T. Yokozeki, Y. Hayashi, T. Shimoda and Y. Morino

Leakage Evaluation of Propellant Tanks by CFRP Laminate Cruciform Specimens under Biaxial Loading **283**
H. Kumazawa T. Aoki and I. Susuki

A Study of Triaxial Woven Fabrics for the Space Inflatable Structure **287**
A. Watanabe, K. Kubomura, Y. Senbokuya and H. Tsunoda

Applying Thermoplastic Composite to Space Inflatable Structure **291**
S. Matsuoka, H. Nakamura, Y. Senbokuya and H. Tsunoda

Research on Applicability of Shape Memory Polymers (SMPs) to Inflatable and Deployable Space Structure **295**
J. Ishizawa, K. Imagawa, J. Yoshikawa, S. Hayashi and N. Miwa

Light Sandwich Panels Utilizing Plastic Foam **299**
K. Imagawa, J. Yoshikawa, J. Ishizawa, H. Mizuno K. Saito and M. Tojo

Development of Super-Lightweight Waveguide for MUSES-C XHGA and Horn Antennas for MUSES-C XMGA.....303
O. Amano, T. Shibata, A. Watanabe and Y. Kamata

Development of Passive Damping Device for Spacecraft Structures.....307
M. Takano, S. Takada, S. Kabashima, T. Ozawa, K. Kojima, H. Seko and I. Masuda

Real Time Spectroscopic Observation of Degradation of Space Use Materials by Space Flyer Unit.....311
T. Yokota, S. Sasaki, M. Ota and H. Yoshida

Development of HOPE-X All-Composite Prototype Structure.....317
M. Niitsu, T. Kamita and K. Uzawa

Structural Testing of a Full-Scale Composite Structure for an Aerospace Vehicle.....321
H. Murayama, T. Kamita and H. Igawa

Low Pressure Plasma Sprayed Yttrium-Silicates for Oxidation Protection of C/C-SiC Composite Structures.....325
T. Ullmann, M. Schmücker, H. Hald, R. Henne and H. Schneider

Erosion Phenomena of High Purity CVD-SiC under High Temperatures.....329
T. Yoshinaka and Y. Morino

Development of C/C Ion Optics for Spacecraft Ion Engine.....333
I. Funaki, K. Goto, H. Kuninaka, Y. Shimizu, K. Nishiyama and K. Toki

Development of Titanium Matrix Composite Rings.....337
T. Yamada, A. Fukushima, C. Fujiwara, M. Hirota, Y. Kawachi and S. Yamamoto

Multiaxial Weibull Analysis of Graphite - from the Launch Failure of M-V-4 Rocket-... 341
E. Sato and J. Onoda

Thermal Characteristics of a High-Thermal-Conductivity Graphite Sheet for Spacecraft Thermal Control.....345
H. Nagano, A. Ohnishi and Y. Nagasaka

Design and Test Results of a Variable Emittance Radiator Device.....349
S. Tachikawa, A. Ohnishi, A. Okamoto, Y. Nakamura, Y. Shimakawa, T. Mori and A. Ochi

Session E: Composite Applications to Infrastructure

JSCE Recommendations for Upgrading of Concrete Structures with Use of Continuous Fiber Sheets.....353
K. Maruyama and T. Ueda **(Keynote)**

Development and Application of Carbon Fiber Composites for Large-span Structures...361
K. Sugizaki **(Keynote)**

Strength Evaluation on Bolt Joints of Pultruded GFRP Members.....363
I. Chou, K. Kamada and T. Kimura

Investigation on the Buckling Strength of the Steel Square Pipe Filled with the Urethane Resin Foam.....367
N. Yamamoto, N. Uno, K. Inose, K. Kamada and T. Kimura

Bending Response of Thick-Walled Laminated Composite Pipes.....371
M. Xia, H. Takayanagi, H. Tsuda, K. Urabe and K. Kemmochi

Dynamic Properties of Laminated Fiber Reinforced Rubber as a Shock Absorber for Bridge Restrainer System.....375
Y. Nishimoto, Y. Kajita, N. Ishikawa, S. Nishikawa and N. Ikoma

Experimental Study on Effects of Resins on Bond Force Transfer of Carbon Fiber Sheet-Concrete Interface.....379
J. Dai, Y. Sato and T. Ueda

Retrofitting RC Beams with Innovative Hybrid Fiber Sheets.....383
Z.-S. Wu, K. Sakamoto, H. Niu and T. Kurokawa

A Sensitivity Analysis for Shear Capacity of RC Member Retrofitted with Continuous Fiber Sheet.....387
A. Kamiharako, T. Shimomura, K. Maruyama and T. Shinbo

Ductility Evaluation of RC Member Retrofitted with Continuous Fiber Sheet.....391
F. Katsuki, K. Maruyama and H. Mutsuyoshi

Strengthening Behavior of Carbon Fiber Sheet Using Flexible Layer.....395
H. Komaki, Y. Sohda, T. Maeda and K. Tsubouchi

Session F: Composite/Plastic Applications to Transportation Vehicles

Crushing Properties of FRP Pipe Bolted Joint to Steel Component - Integrated Crush Experiments -.....399
H. Saito, R. Inai, T. Nakatani, A. Yokoyama and H. Hamada

Numerical Simulation for Crashing Behavior of FRP Tube under Impact Loading.....403
M. Tateishi, A. Yokoyama and H. Hamada

Development of Lightweight and High Stiffness "New KP-Sheet" for Automotive Headliners by Controlling of Glass Fiber Arrangement.....407
Y. Araki, S. Takano, S. Hanatani, M. Ito and H.Kubo

Investigation of Durability and Reasonable Design Method for Elastic Chain.....411
K. Tokubuchi, Y. Nishino and N. Ikoma

Synthesis and Properties of Polyethylene-Clay Hybrids.....415
M. Kato and A. Usuki

Development of New Type High Performance Potassium Titanate for Friction Material Use.....419
H. Konnai and Y. Aso

Advanced Seat Fabrics with Deodorization Function for Vehicles.....423
T. M. Suzuki, K. Fukumoto, N. Sato, Y. Yamada, M. Owaki, M. Mackawa, S. Miura, O. Araki, A. Matsuyama and M. Furuta

Development of the Thermoplastic Elastomer Based on a Waste Rubber.....427
H. Okamoto, K. Fukumori, M. Matsushita, N. Sato, Y. Tanaka, T. Okita, S. Otsuka and Y. Suzuki

Session G: Composite Applications to Sport and Leisure Goods

Designing of CFRP Baseball Bats.....431
T. Nishiwaki **(Keynote)**

Dynamic Response of FRP Structure after Impact.....435
N. Taniguchi and T. Nishiwaki

Prototype of a Finite Element Foot Model 439
T. Asai, T. Nishiwaki and H. Nunome

A Kinetic Comparison Between Dominant and Non-dominant Legs during Soccer Full Kick.....443
H. Nunome, T. Asai, Y. Ikegami and S. Sakurai

The Relationship between the Vertical Movement of Rotational Axis and Swing Speed on the Swing Movement 447
S. Inoue, K. Saitou and R. Sanders

Angular Velocity of Upper Limb and Torso in Baseball Pitches Before and After Ball-Release 451
K. Saitou, S. Inoue, Y. Ohgi, C. Miyaji and S. Takai

Properties of Bioabsorbable Ultra High Strength Poly-L-Lactid (PLLA) Device 455
T. Kawamoto and T. Sugahara

Dynamic Response of a Snowboard Due to Snowboarder's Snowboard Control 459
S. Kawai, H. Otani and T. Sakata

Identification of Equivalent Elastic Parameters for Snowboards 463
K. Hosokawa, S. Ando and T. Sakata

Vibration Properties of Adhesive Structure by Using Polymeric Composites.....467
Y. Tanimoto and Z. Maekawa

Amenity Evaluation of Flooring Structure in Walking Vibration 471
A. Goto and T. Nishiwaki

Eigenfrequency Analysis of HSP.....475
T. Shiomi, T. Nishiwaki and Z. Maekawa

Three-Dimensional Analysis of a New Golf-Swing Robot Model Emulating Skillful Golfers 479
S. Suzuki and Y. Ozaki

New Matrix Resin for High Performance Golf Shafts 483
K. Goto, M. Taguchi and A. Ito

Dynamic Characteristics of Triaxial Woven Fabric Composites for Golf Club Shafts 487
K. Matsumoto, M. Zako and N. Matsumoto

The Designing of Vibration Property for Matrix Hybrid Laminates 491
T. Onita, T. Nishiwaki and Z. Maekawa

Fabrication of Musical Instrument Using General Purposed Material 495
T. Matsubara, T. Nishiwaki and Z. Maekawa

Prediction and Estimation of the Power of Thermoplastic Composite Tennis Racket ...499
Y. Kawazoe

Estimation of the Improvement of the Shock Vibrations at the Wrist Joint Using the Thermoplastic Composite Tennis Racket 503
Y. Kawazoe

Session H: New Trends in Polymer Composites and Their Fibers

New Trends in Polymer Composites and Their Fibers.....N/A
M. E. Tuttle **(Keynote)**

Processing and Properties of Carbon Fiber Reinforced Composites with New Amorphous, Asymmetric, Addition Type Polyimides (Triple A -PI).....507
T. Ogasawara, R. Yokota, Y. Shigenari, K. Miyagawa, H. Ozawa, M. Taguchi and T. Ishikawa

Cyanate Ester Resin Formulations for Aerospace Applications.....511
A. Oshima, H. Ihara, T. Watanabe, M. Shinagawa and H. Onoda

A Low Temperature Cure Material for Large Scale Prototype Model Construction.....515
K. Mitani, S. Hayashi and K. Wakabayashi

Effect of Thermal Cycling and Aging on the Mechanical Properties of Carbon/BMI Composites for the Next-Generation SST Structures.....519
H. Katoh, T. Shimokawa and C. Marais

Strengthening of Short Fiber Reinforced Polyimide Composites in Space Environment 523
Y. Ozawa

Thermal Properties of New Continuous Amorphous Pitch-based Carbon Fiber for Space Applications 527
N. Kiuchi, T. Kihara, T. Matsumoto and G. Ishikawa

Evaluation of the Burst Strength of FW-FRP Composite Pipes with Low-Modulus Carbon Fiber after Impact.....531
S. Wakayama, T. Takekusa, S. Kobayashi, N. Kiuchi and T. Matsumoto

Interply Hybrid Laminates with Improved Flexural Impact Resistance.....535
S. Takemura, H. Ohno and A.S. Kobayashi

Curing Process in SMC Roll Forming - Effects on Characteristics and Formability - ...539
T. Katayama, M. Shinohara, M. Hakotani, G. Kamada and K. Nishi

Comparison of Strength and Damage for Notched FRP Plates Made by Injection Molding with that of Machining.....543
T. Yamamoto and H. Hyakutake

Effect of Thermal Treatment on Mechanical Properties of a Carbon/Epoxy Composite 547
K. Ogi, T. Shiraishi and T. Tokunaga

Electro-Conductive Plastic Compounds Filled with Stainless Steel Micro Fiber 551
K. Yoshino and R. Sakamoto

Silver Coated Carbon Black Epoxy Composites: PTC Effect and Electric Wave Shielding Effectiveness.....555
H. Ohnabe, K. Kamada and F. El-Tantawy

Satellite Workshop I: Ceramic Matrix Composites and Carbon/Carbon Composites

Long-Term Multi-Physics Performance of Functional Ceramic Composite Material Systems.....559
K. Reifsnider, X. Huang and N. Olson **(Keynote)**

Fibre/Matrix Interface Shear Strength Measured *in situ* for SiC/SiC Composites with Different Matrices and Interfaces 565
I.J. Davies, T. Ogasawara and T. Ishikawa (**Keynote**)

High Temperature Behavior of Sintered SiC Fiber-bonded Ceramics 569
S. Kajii, M. Sato, K. Matsunaga, T. Hogami and T. Ishikawa

High Temperature Creep Deformation and Thermal Stability of 3-D Woven Tyranno ZMI Fiber / Si-Ti-C-O Matrix Composite 573
Y. Ohsawa, S. Zhu, T. Ogasawara, T. Ishikawa and Y. Ochi

Distribution of Fibre/Matrix Interface Shear Strength within a Single Fibre Bundle for a 3-D Woven SiC/SiC Composite Tested at 1100℃ in Air 577
I.J. Davies, T. Ogasawara and T. Ishikawa

Shear Modulus of 3-D Woven Ceramic Matrix Composite 581
T. Shiraishi, T. Ogasawara, T. Ishikawa and N. Watanabe

Characterization of Thermal Shock Fracture Behavior in Ceramic Materials by Disk-on-Rod Tests 585
S. Wakayama, K. Nishino and S. Arai

Development Study of Carbon-Carbon Turbine Disk for ATREX Engine 589
K. Goto, H. Hatta, T. Sato and N. Tanatsugu

Ceramic Coatings for Oxidation Protection of C/C Composites 593
T. Aoki, H. Hatta and H. Fukuda

Effect of Interfacial Morphology Formed by Conversion Pretreatment of CVD-SiC Coating on C/C Composites 597
D. Maruyama, H. Hatta and Y. Kogo

Fatigue Behavior of C/C Composite Impregnated with Si 601
H.N. Ko, S. Hanzawa and K. Nakano

The Role of Three Dimensional Reinforcement on Fracture Behavior of Carbon-Carbon Composites 605
M. S. Aly-Hassan, H. Hatta, S. Wakayama, E. Miyazaki, K. Goto and K. Miyagawa

Thermal Shock Damage in Carbon-Carbon Composites 609
Y. Kogo, K. Nakazaki, T. Katagiri and H. Hatta

Compressive Stress Enhancement by EB Treatment of C/C Composite Spring 613
A. Kimura, T. Toriyama, A. Mizutani, K. Oguri, A. Tonegawa and Y. Nishi

Tensile Failure Mechanisms of C/C Composites 617
T. Aoi, H. Hatta and Y. Kogo

Session J: Metal Matrix Composites and Related Materials

Corrosion Mechanisms of Metal-Matrix Composites.....621
L.H. Hihara (**Keynote**)

The Properties of the Titanium Matrix Composites Manufactured by Spray-Winding Techniques.....625
A. Kono, T. Yamada, C. Fujiwara and M. Hirota

Development of Titanium Matrix Composite Rings.....629
T. Yamada, A. Fukushima, C. Fujiwara, M. Hirota, Y. Kawachi and S. Yamamoto

Development of Aluminum MMCs Brake Rotor by Pressure-less Metal Infiltration Process.....633
H. Takahashi, H. Kamii, S. Chonabayashi and T. Inoue

Mechanical Properties and Microstructure of Squeeze Casting $Al_{18}B_4O_{33}$ w/Magnesium Alloy Composites 637
G. Sasaki, M. Yoshida and H. Fukunaga

High Strain Rate Superplasticity of TiN Particulate Reinforced Aluminum Composites 641
T. Imai, L. Zhen and M. Takagi

Application of Intermetallic Compounds Parts by Spark Plasma Sintering Process of Cu-Al Elemental Metal Powders.....645
T. Nakamura, S. Tanaka, K. Hayakawa, H. Imaizumi and H. Kawaguchi

Fabrication of Nickel Based Active Composites.....649
H. Asanuma and G. Hakoda

Development of Active Materials Based on Continuous/Discontinuous SiC Fiber Reinforced Aluminum.....N/A
G. Hakoda and H. Asanuma

Fabrication of TiB_2/Cu Composites by Reaction between Cu, Ti and B.....653
M. Kobashi, S. Yamamoto and N. Kanetake

Surface Modification Technology for TiAl Alloys Using Reactive Plasma Process.....657
M. Inoue, M. Nunogaki and K. Suganuma

Strain Measurements with FBGs Embedded into Cast Metal Alloys.....661
M. A. Caponero, F. Felli and A. Paolozzi

Superconducting Shape Memory Effect (SSME) 665
N. Hagiwara, H. Yabe, T. Suzuki and Y. Nishi

The Evaluation of Mechanical Properties of TiNi/Al Shape Memory Composites by Using Experimental and Finite Element Analysis.....N/A
G. C. Lee, J. H. Lee, D. S. Park and Y. C. Park

Effects of Electron Beam and UV Light Irradiation on Clear Time from Misting for TiO_2 Thin Film.....669
R. Fujii, K. Oguri, M. Tetsuka, A. Tonegawa, H. Uchida and Y. Nishi

Microstructural Changes in an Al-Al3Ti Composite by Equal Channel Angular Extrusion.....673
S. Hosoda and Y. Watanabe

Stress Relaxation Test for Spring Sheet of Tin Coated Cu-Ni-Sn Alloy Applied for Advanced Automobile Connecting Materials.....677
K. Hayashi, K. Gemma, M. Nishihata, T. Kunimine and Y. Nishi

Particle Size Distributions in Al-Al3Ni Functionally Grated Materials Fabricated by a Semisolid Forming.....681
K. Matsuda, Y. Watanabe, K. Yamagiwa and Y. Fukui

High Temperature Mechanical Characterization of Low Activation Materials for Fusion Reactor.....685
S. Uchida, T. Sunamoto, H. Yabe, N. Inoue and Y. Nishi

Satellite Workshop K: Textile Composites

Textile Composites Models: Integration Strategies.....689
I. Verpoest, S. Lomov, E. Belov, R. Parnas and A. Prodromou **(Keynote)**

Cost-Effective Manufacturing Technology for Knitted Fabric Composites 693
K. Nishiyabu **(Keynote)**

Braiding Technologies for Airplane Applications Using RTM Process.....697
T. Uozumi, Y. Iwahori, S. Iwasawa and T. Yamamoto

Mechanical Behaviors of Braids under Tensile Loading.....701
M. Hanada, T. Nishiwaki, H. Hamada, A. Nakai and T. Ishii

Deformation Mechanism of Textile under Uni and Bi-axial Tensile Load.....705
K. Sakakibara, A. Yokoyama and H. Hamada

Strain Distribution in Deep-Drawing of Knitted Fabric Thermoplastic Composites.....709
K. Nishiyabu, N. Takano, M. Zako and R. Fujitsu

Mechanical Properties of Square Braided Fabric 713
T. Ueda, A. Otani, A. Nakai and Y. Fujii

Mechanical Properties of Weft Knitted Fabric Composites 717
S.D. Pandita, G. Huysmans and I. Verpoest

Mechanical Properties of Knitted Fabric Composite with Hybrid Matrix Layer.....721
A. Nakai, A. Otani, T. Ishida and S. Gotoh

Local and Microscopic Analysis of Woven Fabric Composite Material under Bending by Finite Element Mesh Superposition Method 725
N. Takano, M. Zako and T. Okazaki

Non-Constitutive Numerical Modeling for Plain-Weave Fabrics 729
O. Kuwazuru and N. Yoshikawa

Initial Fracture Behavior of Knitted Composites 733
A. Nakai, T. Osada, T. Fukui and M. Inoda

Effect of Processing Conditions on the Mechanical Properties of a 2-D Braided SiC/SiC Composite.....737
A. Ohtani, I.J. Davies, T. Inoue, A. Nakai and H. Hamada

Stitching of 3-Dimensional Preforms for the Production of High Performance Composite Parts.....741
Y.-S. Sun and J. Wittig

Novel Hybrid Textiles for Tough Composites Using Vacuum Inflation.....N/A
P. Hogg

Modeling of Inter-fiber Sliding in Fabric Shaping Process.....745
Y. Arimitsu, S. Takahashi and T.-W. Chou

Fabrication and Mechanical Behavior of Textile Reinforced SMC.....749
A. Nakai and T. Ohkawa

Ironing Assisted Deep-Drawing of Thermoplastics Reinforced with Continuous Carbon Fiber and Characteristics of the Products.....753
T. Machida, T. Okai, K. Yoshimatsu and M. Okada

Information on Pattern Figure in Textiles of Cultural Property.....757
A. Goto, K. Goto, A. Nakai, Z. Maekawa and M. Sato

Interfacial Properties of EB Cured Composite.....761
T. Osada, M. Mizoguchi, A. Nakai and H. Hamada

Investigation of Interfacial Properties Using Compact Tension Tests of Glass Cloth Reinforced Vinylester Composite -Fractographic Approach-.....765
H. Hamada, Y. Fujii, M. Mizoguchi and Y. Koyama

Mechanical Properties of Plain Woven Fabric Composites with Flexible Interphase.....769
S. Kobayashi, T. Osada and A. Nakai

Initial Micro Fracture Behavior of Woven Fabric Composites.....773
T. Osada, T. Shimizu, A. Nakai and H. Hamada

Experimental Characterization of Off-axis Properties of Woven Fabric Composites.....777
H. Hamada, A. Nakai and S. Ogihara

Session L: Interface in Composites

Fundamental Study on Flexural Fatigue Properties in Flexible Printed Circuit Properties of Phenoxy/Epoxy Resin with Mixing Ratio.....781
H. Kawada, K. Nakaya and A. Kobiki

Fatigue Properties of Quasi-Isotropic Alumina-Fiber Reinforced Plastic Laminates.....785
H. Kawada, N. Kobayashi and Y. Koshikiya

Effect of Interphase on Hydrothermal Aging of Glass Fiber Reinforced Unsaturated Polyester Composite.....789
T. Morii and S. Seino

Interfacial Properties of Braided Composites 793
T. Osada, A. Nakai and H. Hamada

Effect of Surface Treatment on Glass Fiber in PP Injection Moldings.....N/A
Y. Kobayashi

Novel Functional Polymer/YBCO Superconductor Ceramic Composites for Thermistor, Electromagnetic Shielding Effectiveness and Electrostatic Charge Dissipation 797
F. El-Tantawy

Excimer Laser Irradiation onto PET Materials.....801
K. Mizoguchi, A. Yamamoto, M. Ishikawa, A. Ohuchi and T. Ohie

Effect of Fiber Sizing Treatment on Mechanical Properties of PE/Epoxy.....805
Y. Higuchi, T. Shimizu, M. Mizoguchi and H. Hamada

Session M: Modeling and Simulation in Composite Mechanics

Influence of Element Size on Damage Growth Simulation Based on FEM.....809
Y. Shimamura, Y. Yamamura, A. Todoroki and H. Kobayashi

Experimental and Analytical Characterization of Microscopic Damage Progress in CFRP Angle-Ply Laminates 813
A. Tanaka, S. Kobayashi, S. Wakayama, Y. Shigenari, K. Miyagawa and S. Suzuki

Analytical Prediction and Experiment of Transverse Lamina Cracking in Multi-directionally Reinforced Symmetric Laminates.....817
S. Abe, K. Kageyama, I. Ohsawa, M. Kanai and T. Kato

Statistical Strength Prediction of CFRP Cross-ply Laminates.....821
J. Noda, T. Okabe, N. Takeda and M. Shimizu

Design and Analysis of Reduced Thickness Solar Panels.....825
S. Hahn and T. Ozaki

Detailed Analysis of the Solar-B SOT Main Mirror Support Structure.....829
H. Ishii and T. Ozaki

Buckling of Composite Structures with Higher-order Shear Deformation.....833
Q. -Q. Ni, J. Xie and Z. Maekawa

Damage Accumulation in Composite Laminates under Quasi-Static Transverse Loading.....837
Y. Aoki and H. Suemasu

A Phenomenological Constitutive Model for Off-Axis Viscoplastic Behavior of Unidirectional CFRP 841
M. Kawai and Y. Masuko

Modeling of Bearing Failure in Bolted Composite Joints.....845
Y. Xiao and T. Ishikawa

Rate Dependence of Linear and Nonlinear Behaviors of Unidirectional CFRP under Off-Axis Loading at High Temperature 849
M. Kawai, Y. Masuko and M. Kohashi

Evaluation of Crack Closure in Epoxy Resin Plates with Embedded SMA Wires by Finite-Element Analysis 853
E. Umezaki and T. Ichikawa

Numerical Prediction of Permeability Tensor for Sheared Woven Fabric by Asymptotic Homogenization Theory.....857
N. Takano, M. Zako and T. Okazaki

A Study of Bridging the Gap between Atomistic and Mesoscopic Simulation for Materials Design.....861
S. Yamamoto and S. Hyodo

Image-Based Modelling of Microstructures of Porous Ceramics to Study the Micro-Macro Coupling Effect.....865
N. Takano, F. Kubo, M. Zako and K. Kimura

Fracture Behavior of Micro Structure in Tibial Plateau under External Loading - The Effect of Aging on the Stress Wave Propagation -.....869
T. Hirai, A. Yokoyama and Y. Watanabe

Satellite Workshop N: New Trends in Damage Identification and NDI

The New Progress and Developing Tendency of NDT for Advanced Composite Materials and Structures.....873
K. Xu **(Keynote)**

Nondestructive Inspection for Metal Matrix Composite.....879
N. Higuchi, M. Uematsu, A. Kohno, T. Yamada, Y. Kawachi and S. Yamamoto

Correlation between Damage and Electrical Resistance Change in Composites with Carbon Particle and Carbon Fiber.....883
D.-Y. Song, Y. Hirata and N. Takeda

Electric Impedance Change Method for Monitoring of Sandwich Plate Damage.....887
A. Todoroki, S. Murase, Y. Shimamura and H. Kobayashi

Ballistic Impact Behavior and Properties of Structural Ceramic Materials.....891
H. Kasano and O. Hasegawa

Acoustic Emission Analysis of Corrosion Resistance of Glass Fiber/Vinylester Composites under Acid Environment.....895
M. Mizoguchi, H. Hamada, T. Morii and Y. Fujii

On the Detection of Fatigue Damage in CFRP by Measuring Poisson's Ratio.....899
S. Bandoh, M. Zako, T. Shiino, T. Kurashiki and K. Matsumura

Adaptive Vibration Control of Composite Beams Using Neural Network Controller.....903
I. Lee, S.-M. Yang, J.-H. Han and S.-H. Youn **(Keynote)**

Delamination Detection Using Curvature Vibration Modes.....907
H. Fukunaga, N. Hu, M. Kameyama and F.-K. Chang

Strain Sensor Output-based Health Monitoring of CFRP Structures by Using Localized Flexibility Method.....911
Y. Aoki and O. –I. Byon (G. Ben)

Delaminated Area Identification of Composite Laminated Beams Based on Resonance and Anti-resonance Frequency Change.....915
T. Inada, Y. Shimamura, A. Todoroki and H. Kobayashi

An Analytical Study of Thermal Conductivity Affecting Thermoelastic Stress Measurement of Laminate Composites.....919
S. Sugimoto, R.E. Rowlands and T. Ishikawa

Session O: Student Session

The Effect of Bundle Size on Tow Impregnation during Liquid Molding Processes.....923
M.E. Foley, S.G. Advani, S.H. McKnight and J.W. Gillespie Jr.

Effect of Orthotropic Electric Resistance on Delamination Detection with Electric Resistance Change Method.....927
A. Todoroki, M. Tanaka, Y. Shimamura and H. Kobayashi

Damage Detection of Bolted Composite Laminates Using Electric Potential Method.....931
Y. Shimamura, S. Mukai, A. Todoroki and H. Kobayashi

Effect of Embedded SMA Foil on Mechanical Properties of CFRP Laminates.....935
A. Kobayashi, S. Ogihara, Y. Shirai and N. Takeda

Mechanical Properties of SMA Fiber/Epoxy Composite.....939
A. Kobayashi, S. Ogihara, T. Uehara and N. Takeda

Development of a High Power Shape Memory Materials Using Hydrogen Storage Alloy Dispersed in Polymer.....943
B. Kim, H. Yabe, H. Uchida and Y. Nishi

Formation of Sensors by Breaking Pre-notched Optical Fiber in Matrix and Their Evaluation .....N/A
K. Kimura and H. Asanuma

Damage Progress Behavior in CFRP Laminates under Thermal Cycle Loading.....947
A. Kobayashi, S. Ogihara, T. Ishiguro and N. Takeda

Evaluation Method for Initial Micro Fracture Behavior in Woven Fabric Composites...951
T. Shimizu, T. Osada, A. Nakai and H. Hamada

Collision Fatigue Life Extension of PZT Irradiated by Sheet Electron Beam.....955
K. Takashina, K. Oguri, A. Tonegawa and Y. Nishi

Machinability of Heat Treated Silicon Powder Compacts.....959
K. Tantikom, K. Sujirote and S. Danchaivichit

Tensile Strength of Carbon Fiber with Different Diameter.....963
A. Hamasaki, Y. Kogo and T. Morimoto

Eccentric Compression Bending Test for CFRP Pipe.....967
H. Fukuda, O. Watanabe, M. Itabashi and A. Wada

Effect of Cyclic Loading on the Monotonic Tensile Behavior of a 3-D Woven Si-Ti-C-O Fiber / Si-Ti-C-O Matrix Composite.....971
T. Gomyou, S. Zhu, Y. Ochi, T. Ogasawara and T. Ishikawa

Damping Capacity of Ti-Ni and Ti-Ni-Cu Alloys Produced by Lamination Process.....975
N. Urahashi, M. Sasaki, D. Imai, Y. Kogo, K. Hishitani and N. Igata

Development of Pultrusion Techniques of Phenol Foam Composite.....979
O. –I. Byon (G. Ben), A. Shoji, T. Takimoto and Y. Aoki

Proceedings of 7th Japan International SAMPE
Symposium & Exhibition, Nov. 13-16, 2001

Expanded Horizon in Materials and Processing - Unlimited Frontier -

James C.I. Chang
Director, Army Research Office

JISSE-7
International Symposium of SAMPE
JAPAN

Expanded Horizons in Materials and Processing
- Unlimited Frontier -

Dr. Jim C.I. Chang
Director, Army Research Office

November 13, 2001

Simple Materials

- Materials Sciences (processing/characterization)
  - X-Ray Diffraction
  - Dislocations
- Mechanics (characterization/design)
  - Slip Plan
  - Plasticity Theory

Composites

- Materials Science
- Mechanics

(processing ⟺ characterization ⟺ design)

- Multi-phase, macro-discontinuity
- Property discontinuity at macro-level
- Pseudo mechanics principals
- But - we have accomplished a lot
- Beginning of Material by Design -- Materials + Mechanics

Functional Graded Materials

- Materials Science
- Mechanics

(processing ⟺ characterization ⟺ design)

- Get rid of macro discontinuity
- Integrated Materials/Mechanics practice
- Design away from inhomogenity and anisotropic
- Simple form - Thermal Barrier Coatings
  Complicated - Composite Systems

Electronics/Smart Systems

- Electronic Device Reliability - Semiconductors
  (processing ⟺ characterization ⟺ design)
  - strain migration
  - electron migration
- Smart Systems: primarily composite systems
  - sensors
  - actuators
  - control
  - processing ⟺ characterization ⟺ design

Learning from Nature

- Biomimetics ⟹ mimicking natural processing
- Bio-inspired ⟹ learning natural processing
- Bio-self assembly ⟹ using natural force to process
- Bio-synthesis ⟹ beyond biosystems, i.e., bio-electro-optics
- Smart systems ⟹ sensors, actuators, control
- New sensors ⟹ olfactory systems

Biomimetic/Bio-inspired
(Abalone Nacre)

- Mechanical Manufactured Silimar System
- Biomimetic/Bio-inspired
  - Lustrin: Modular Elastic Adhesive (Morse, Santa Barbara)
  - Calcium Carbonate Crystals determined by small amount of proteins (Belcher, Texas Austin)

Strategic Targets

To Develop New Tools for Materials Synthesis:

- Discover molecular mechanisms controlling biomineralization
- Adapt these mechanisms to new routes for materials synthesis:
  - Low P, Low T, Neutral pH
  - Environmentally Benign
  - Low Cost
  - Interfacial Control
  - Hierarchical Self-Assembly
- High-Performance Composites Based On:

Abalone Shell:	Microlaminate
Diatoms:	Controlled Porosity Silicates
Sponges:	Silica Networks & Filaments

Energy Dissipation on Cleaved Abalone Nacre

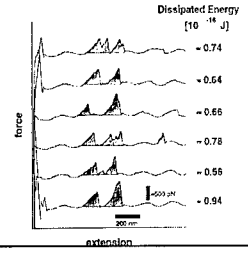

Biomimetic/Bio-inspired

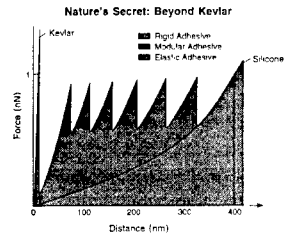

BIO-SELF ASSEMBLY

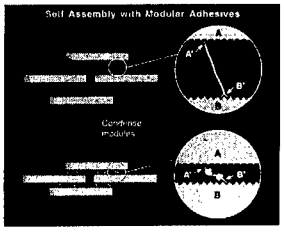

BIO-SELF ASSEMBLY

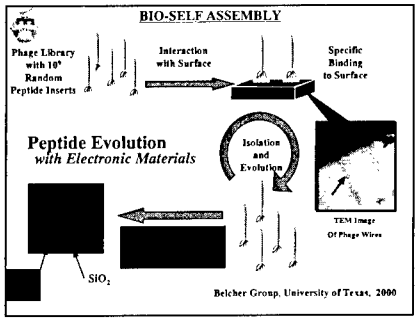

Understanding Olfaction: From Detection to Classification

James Bower *California Institute of Technology*

Objective and Approach

- Establish a new experimental and theoretical base for our understanding of the olfactory system, and apply emerging knowledge of mammalian olfaction to the development of a novel "artificial nose".
- Functional examination at receptor, bulb and cortical levels of the olfactory system, and psychophysical assessment of overall performance. Paralleled in integrated fashion in studies involving the artificial nose.

Research Thrusts

- Molecular and cellular neurobiology of olfactory receptor and pathway function
- Computational neurosciences and modeling of sensory mechanisms in olfaction
- Chemistry of molecular recognition
- Engineered olfactory system analogs

Payoff

- Extend ability to detect trace amounts of specific chemical compounds
- Demining, chemical defense /counter-terrorism/nonproliferation, environmental monitoring, medical diagnostics

Material Systems/Processing Frontier and Nanotechnology

- New Materials
- Microsystems
- MEMS/Smart Structures
- Nanomaterials
  - Strain engineering in electro-optical devices
  - Nanomaterial processing
  - Others

Bulk Metallic Glass Matrix Composites

The Future of Anti-Armor
and
The Future Structural Material?

Advantages

- Performance (density + self-sharpening penetration
- Manufacturing (less volume shrinkage than WHA, DU
- Environmentally friendly (Zr-Nb-Al-Cu-Ni)

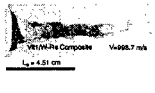

Accomplishments

- Ballistic testing of BMG/tungsten composites demonstrating increased penetrator performance versus WHA
- Fabrication of beryllium-free BMG/tungsten composites
- Initiation of new DARPA effort including penetrator and structural applications
- Synthesis and testing of in-situ Ti-Zr β-phase reinforced BMG composites

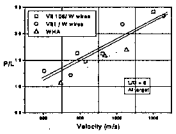

Novel Reinforcement Strategies for Bulk Metallic Glass Matrix Composites (Johnson - California Institute of Technology)

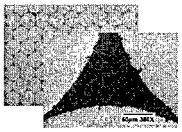

Metallic glass composite reinforced with 80 vol.% tungsten wires

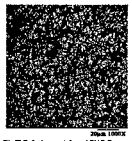

In Situ Ti-Zr β-phase reinforced BMG Composite

Property	Vitreloy-1	β-reinforced Vitreloy-1
Tensile Yield Strength	1.8 GPa	1.3 GPa
Ultimate Tensile Strength	1.8 GPa	1.7 GPa
Plane Strain Fracture Toughness	20-55 MPa-m$^{1/2}$	80 MPa-m$^{1/2}$
Charpy Impact Toughness	80 W/m^2	200-300 W/m^2
Plastic Strain to Failure (tensile)	<0.1%	8-13%
Bend Ductility (3-point bend)	<1%	>70%

Compact Power Sources

ARO program covers full spectrum of power generation

Energy Harvesting	Microturbines	Fuel Cells	AMTEC	TPV
Human Power	Hydrogen	Battery Materials	Methanol	Diesel Fuel

Portable Power Burden for 10 KWhr of Electrical Energy

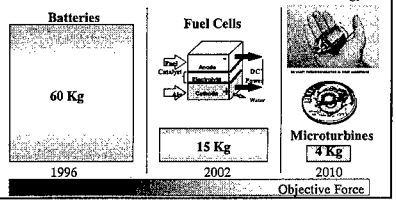

Microturbines

H-Power Fuel Stack (Today)

ARO/DARPA/CECOM Compact Power Program

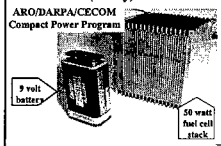

Contractor POC: Dr Art Kaufmann
H-Power Corp, Belleville, NJ

Microturbines (2020)

Payoff

	μturbogen+fuel	BA5590
• Power	50 W	50 W
• Energy	175 W-hr	175 W-hr
• Weight	50 g	1000 g
• Size	50 cc	880 cc

MURI: Dynamics and Control of Smart Structures
Harvard - Boston Univ. - Univ. of Maryland

Micro-deformable mirrors for optics and adaptive optics applications

- ARL-CISD
- China Lake NWC
- Boston Micromachines

Parallel Valve Arrays for Flow Control

Open Closed

Boundary Flow Control and B.U. Smart Wing

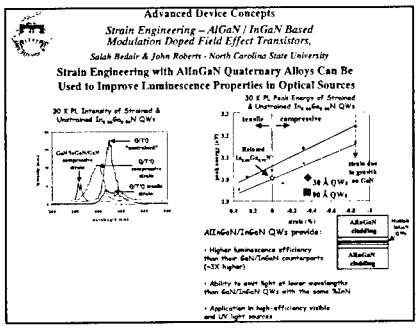

Advanced Device Concepts

Strain Engineering – AlGaN / InGaN Based Modulation Doped Field Effect Transistors,

Salah Bedair & John Roberts - North Carolina State University

Strain Engineering with AlInGaN Quaternary Alloys Can Be Used to Improve Luminescence Properties in Optical Sources

BIOMOLECULAR MATERIALS

- Process control of structure and function
- High tensile strength
- High elasticity/extensibility
- Strength, modulus, elongation increase with loading rates
- Dissipates energy of impact

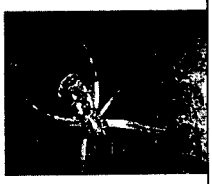

THIN POLYMER FIBERS PRODUCED BY ELECTROSPINNING

(D.H. Reneker, University of Akron)

OBJECTIVE:

Develop electrospinning techniques into a practical method for producing polymer fibers having diameters ranging down to nanometer dimensions

APPROACH:

- Determine electrospinning parameters for common polymers I e , polyacrylonitrile, nylon
- Develop electrospinning parameters for processing unique polymers including spider silk, and mesophase pitch
- Apply electrospinning to processing nonwoven fabrics

BENEFITS:

- Potential for producing high performance nanometer diameter fibers
- A low cost flexible fiber spinning process

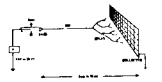

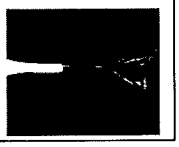

"nano-fibre" Processing

Electrospinning Line for Nanofibre Structures

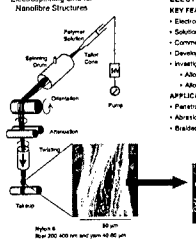

ELECTROSPINNING LINE FOR NANOFIBRE STRUCTURES

KEY FEATURES

- Electrospinning of "nano"-fibres (0.1-0.5 µm dia.)
- Solution or melt spinning demonstrated
- Commercially feasible on industrial scales
- Development of threadlyard spinning techniques
- Investigation of threadlyard properties
  - Allows formation of blends
  - Allows braiding and weaving of large systems

APPLICATIONS

- Penetration resistant micro-denier woven fabrics
- Abrasion/penetration resistant non woven protective clothing
- Braided/woven preforms for helmets and vests

Braiding of Nanofibers

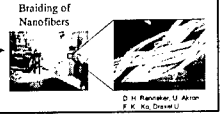

D. H. Reneker, U. Akron
F. K. Ko, Drexel U.

CONCLUSIONS

- Material processing evaluation
  - Material science outgrowth
  - New paradigm
- Miniaturization
- Multifunctional
- Nanotechnology
- Hybrid Biological and Nonbiological Material Systems

Proceedings of 7th Japan International SAMPE
Symposium & Exhibition, Nov. 13-16, 2001

Comparison of Low Cost Composites Manufacturing With Advanced Composites Processing Techniques

Scott W. Beckwith

SAMPE
1161 Parkview Drive, Covina, CA 91724, USA
and
BTG Composites LLC
5108 Germania Place, Murray, UT 84123, USA
E-mail: swbeckwith@aol.com

Abstract

This paper, and the more extended presentation, provides an overview of those manufacturing technologies often considered to be 'low cost' as well as 'low technology'. At the same time, the areas pertaining to 'advanced composites' technology and their 'high technology' counterparts are briefly reviewed. While the advanced composites manufacturing, materials and innovative design have always provided the baseline for technology transfer to FRP (fiber reinforced plastic) composites areas, their influence has constantly impacted the commercial and industrial marketplace. New resins, new processing techniques, new design methods, developments within the nanocomposites scale, and improvements in materials and fabrication costs have all made their contributions to this transfer of technologies [1-3].

Key Words: Advanced Composites, FRP Composites, Nanocomposites, Technology Transfer

Introduction

SAMPE international technical conferences (Europe, Japan, USA) have been an excellent example over the years of documenting materials and processing advances from the time they first enter the research arena until they begin to enter serious usage within specific market places. Aerospace, which represents essentially a very small market for composites, with less than even 5% on a materials weight basis, still plays a dominant role from an entry standpoint. It is from this type of platform that technology is developed and then captured by the commercial and industrial markets.

Sports and recreation, medical, oilfield development and production, ground transportation, wind energy, entertainment, and many other areas have utilized new fiber/resin systems and advanced processing methodology to leapfrog into viable composite products. This paper will examine a few of these materials and processes while discussing the advances in technology transfer seen over the past few years.

Low Cost Composites/FRP Manufacturing Are Not New

Low cost composites and FRP manufacturing technology is not new. There are a number of processes available for producing commercial-grade products using glass-fiber and commercially available resin systems [4,5]. Figure 1 shows underground tanks made by centrifugal casting methods in large diameters. Other low cost methods such as filament winding, contact molding and lamination techniques can also be used.

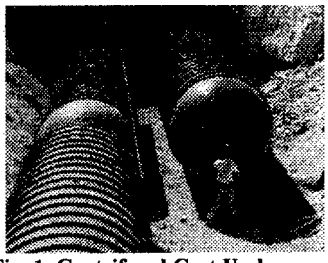

Fig. 1 Centrifugal Cast Underground FRP Composite Storage Tanks

In fact many of these processes have been modified to produce lower cost, production line quantities using the same materials in combination with sand for obtaining stiffness improvements by 'bulking' the EI factor at much lower costs. Figure 2 shows a typical 'continuous' pipe product that rely on low cost materials and mass production filament winding process techniques (like pultrusion).

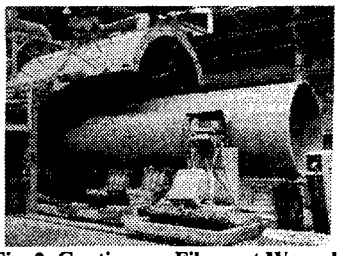

Fig. 2 Continuous Filament Wound FRP Composite Pipe (Drostholm Process)

Advanced Composites Processing is Entering New Territories

Advanced composites processes most likely accelerated with the availability of S-glass fiber in the 1960s, aramid fiber in the 1970s, and, finally carbon and graphite fibers in the 1980s and 1990s [6-8]. Figure 3 is a prime example of a filament wound, prepreg carbon fabric reinforced large diameter solid rocket motor case developed in the 1980s.

Fig. 3 3.7-Meter Carbon Fiber/Epoxy Composite Rocket Motor Case Segment

Automated tape laying, fiber placement technology (derived from filament winding and tape laying), resin infusion methods (RTM, VARTM, SCRIMP™, RFI and others) all saw extensive development in the past 20-30 years. Figure 4 demonstrates the unique aspects of resin transfer molding (RTM) with the cross-section of a propeller blade.

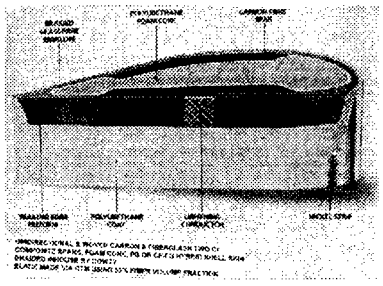

Fig. 4 RTM/VARTM High Performance Composite Aircraft Propeller Blade

Low Cost vs. High Tech: Where Do They Meet and/or Compliment Each Other?

In the two proceeding sections it should be clear that low cost materials, low cost process, high tech materials and high tech processes have been assessed and modified to meet the needs of the various market segments. In fact, many of the manufacturers and material suppliers, because of the rapid changes in the politics associated with the 'Cold War', have repositioned through extensive technology transfer across many market segments.

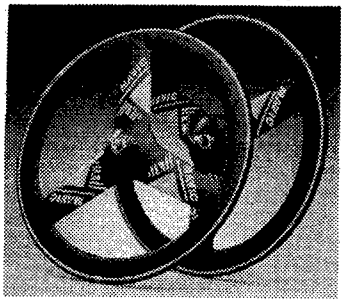

Fig. 5 High Performance Composite RTM/VARTM Racing Bicycle Wheels

Figure 5 is an example of the high performance materials and processing technology applied to sports and recreation products such as racing bicycle wheels. RTM and VARTM processes, and numerous variations of the basic methods, have expanded the applications of materials into the more commercial markets.

Low cost carbon fiber in the form of 'large tow' fiber in the 48K to 140K range have allowed these unique materials to begin entering into the commercial market segment in the oilfield, infrastructure, highway construction, seismic retrofit, CNG/NGV tanks, pultrusion products and several other areas. While the automotive market, with its emphasis on low cost goals and high production rates, is still a tough market to enter at the current time. Entry has been possible primarily through the use of chopped fiber and thermoplastic resin systems except for high performance applications such as drive shafts and CNG tanks.

Stiffness and strength driven commercial and industrial applications are the main market 'pull' for high performance materials and unique processes. Oilfield technology in the form of composite risers, tension leg platforms (TLPs), accumulator bottles, and flexible coiled tubing appear to be the current application areas where carbon fiber materials have considerable potential.

Almost all of the technology developed to date in the 1960-2000 time period has focused on materials development at the macro- and micro-level with significant results. Nanocomposites – the new technology of the 21st Century, is making inroads at a level one order of magnitude below current technology. The materials, processing methods, analysis tools and advanced applications [9] are beginning to become more apparent. 'Smart materials' coupled with 'nanocomposites' technologies are becoming more apparent as we better understand these unique systems.

Summary

The advanced composites and FRP composites areas have continued to growth and feed each other in terms of technology and market needs. New materials, new technology, and ultimately new processing methods are turning to different paths and manufacturing scales. Nanotechnology is an important area of the future that is rapidly being explored. SAMPE Members, and SAMPE Conferences and Symposia, are starting to see the aspects of this new technology show up in the technical programs. The ***SAMPE 2002*** program focus already will include a major portion on nanotechnology by inclusion of a

Nanocomposites Symposium held within the SAMPE 2002 technical program.

References

1. S.W. Beckwith, "Recent Composite Materials and Processing Advances, Market Applications and Current Technology Challenges", Proc. of JISTES-2000 Seminar, Kyoto, Japan, 2000.
2. W. Benjamin and S.W. Beckwith, "Advanced Composites 1998 Market and Technology Review", JEC Composites Workshop, Paris, France, 1998.
3. S.W. Beckwith, "Advanced Composites: Filament Winding, Fiber Placement, Resin Transfer Molding, Infusion Technology, and Aircraft Composite Structures", Advanced Composites Technology Seminars, JEC Composites Workshop, Paris, France, 1997.
4. S.W. Beckwith, "Filament Winding: Tanks, Pressure Vessels, Ducts, Golf Shafts, Paper Rollers and Other Neat Stuff", Composites Fabrication, November/December 2000.
5. S.W. Beckwith, "FRP Pipe – A Look at Manufacturing and Processing Methods", Composites Fabrication, November/December 1999.
6. S.S. Wang, Proc. of 2nd International Conference on Composite Materials for Offshore Operations, CMOO-2, University of Houston, 1999
7. Z.F. Ren et al, "An Insight Into Carbon Nanotube Production", SAMPE Journal, September/October 2001.
8. U. Meier, "State-of-the Practice in Advanced Composite Materials for Structural Engineering in Europe", Proc. of 6th Japan International; SAMPE Symposium, 1999.
9. SAMPE Journal, September/October 2001 focus on Nanotechnology:
   - "Carbon Fiber Composites: Organoclay-Aerospace Epoxy Nanocomposites, Part I"
   - "Resin Matrix Composites: Organoclay-Aerospace Epoxy Nanocomposites, Part II"
   - "An Insight Into Carbon Nanotube Production" [7]

Biography

Scott Beckwith is SAMPE's International Technical Director and Technical Editor for the *SAMPE Journal*, and, president of BTG Composites LLC, an established advanced composites and FRP consultancy in which he has over 35 years experience in composite materials and structures. He received a BS in Aerospace Engineering from Texas A&M University, an MS in Aeronautics from the California Institute of Technology, and a PhD in Materials Engineering from Texas A&M University. He has over 250 publications and presentations in the fields of advanced composites/FRP manufacturing, pressure vessels, damage tolerance, failure analysis and composites nonlinear viscoelastic behavior. He is an advisor to the US Department of Commerce on composites and materials behavior. He has recently been involved in the X-33 Cryogenic Composite LH_2 Tank failure assessment.

Proceedings of 7th Japan International SAMPE
Symposium & Exhibition, Nov. 13-16, 2001

Structuring Knowledge Project in Nanotechnology Materials Program Launched in Japan

Yukio Yamaguchi and Hiroshi Komiyama
Department of Chemical System Engineering, The University of Tokyo
7-3-1 Hongo, Bunkyo-ku, Tokyo, Japan

1. Introduction

Ever since President William J. Clinton declared that we have entered the nano-world on January 21, 2000 at California Institute of Technology, the nanotechnology-related research has become something like a worldwide competition [1], [2]. The potential of nanotechnology is expected to displace major existing technologies, create new industries, and transform archetypal scientific models in the area of energy, environment, communications, computing, medicine, and other materials related areas. Japan is also going to reinforce the development in nanotechnology for materials. This report exhibits the grand design of Structuring Knowledge Project in "Nanotechnology Materials Program [3] (NMP)" planned by Japanese METI (Ministry of Economy and Trade Industry), which will start on fiscal year 2001. Other projects and programs regarding nanotechnology are under planning by MEXT (Ministry of Education, Culture, Sports, Science and Technology).

Nanotechnology requires teams of physicists, chemists, biologists, and engineers to work in concurrent development, because technological innovation and commercialization demands compression of the discovery-invention-development time scales, which requires coordinated work in both basic research and its application development. The Japanese government is trying to connect the research stages with seamless, exploratory research, focused basic research, and technology platform research for industrial development. METI is responsible for the last stage. NMP, a relatively big project, is planned as collaboration between academia, private sectors, and national laboratories. Industries are especially interested in the establishment of a nanotechnology platform for materials, because they want to improve existing processes which sometimes depend on human skills especially for functional materials, and eventually create new products. It is too large an investment for an individual company to develop a nanotechnology platform. The role of government is critical in terms of budget and leadership. Universities also play the key role in making and carrying out plans at improving infrastructure and training young people. The mission of the national labs is mainly to support long-term fundamental research such as materials metrology and improve development. Industries carry out the plans mainly by sending researchers to a center organized by each project, and navigate the direction of the nanotechnology platform by establishing targets to be developed.

2. Nanotechnology Materials Program

One of the objectives of NMP is to establish a nanotechnology materials platform for industry that results in new generalizations in functional materials research and technology for education. The budget of NMP consisting of eight projects is about $35 million per year and will last for 5 years to 7 years. The aims of each project are summarized in Table-1. The role of each project in NMP is shown in Figure-1. The materials to be focused on are metals, ceramics, glasses, and polymers. The particle project mainly focuses on single nano-sized particles utilizing various kinds of materials such as oxides, semiconductors, and metals. The coating project is mainly responsible for interfaces among different materials. The function materials program develops new function through exploratory study. The material metrology project tries to measure nano-related physical characteristics.

Table-1. The aims of each project

Particle Project	·High-rate synthesis for single-nanometer sized particles
	·Surface modification and thin-film preparation for single-nanometer sized particles
	·Performance evaluation of devices utilizing single-nanometer sized particles
	·Systematization of research results
Polymer Project	·Controlling primary structures
	·Controlling three-dimensional structures
	·Controlling surface and interface structures
	·Material molding
	·Material evaluation
	·Development of shared technology platform and systematization of technologies
Glass Project	·Structure control on an atomic or molecular scale
	·Structure control using super fine particles
	·Intelligent structure control
	·Three-dimensional optical circuit materials
	·Systematization of research results
Metal Project	·Controlling the composition of metal materials in the nano-sized level
	·Controlling the structure of metal materials in the nano-sized level
	·Designing metal materials by harnessing computational science
	·System development
Coating Project	·Nano-coating processing utilizing ceramics powder
	·Improvement of functions such as adhesion
	·Performance evaluation
	·Systematization of interfaces between different materials
Function Materials Project	·Fabrication and characterization for functional nanostructured materials
	·Design for optical function nanostructured materials
	·Design for electronic and spinic function nanostructured materials
	·Design for molecular-function nanostructured materials

Material Metrology Project	·Measurement system for determining physical properties of micro-components
	·Measuring nanometer-size pores and holes
	·Measuring surface structures
	·Basic technology for measuring thermophysical properties
Structuring Knowledge Project	·Establishment of a knowledge platform database
	·Development of modeling
	·Development of a basic knowledge platform

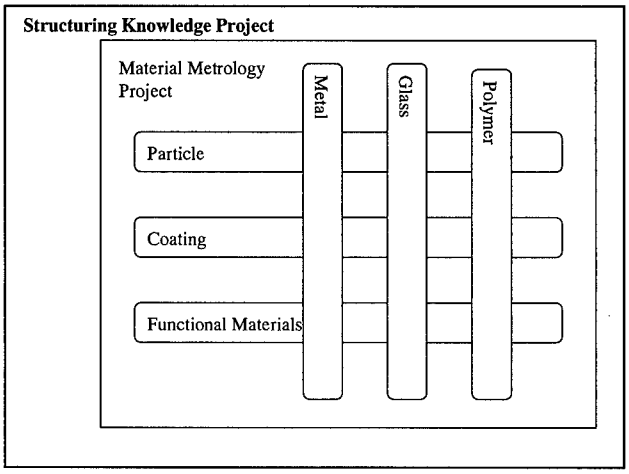

Figure-1. The role of projects in nanotechonology materials program

3. Structuring knowledge project

3.1 Necessity of structuring knowledge

In these decades, human beings have encountered fundamental difficulty due to the gap between the complexity of the problems encountered and the subdivision of our knowledge base. A person finds it difficult to grasp the whole of an issue because only a small aspect of the issue is native to his (her) specific field. This difficulty is a predictable result of the procedure by which human beings create and accumulate knowledge. Knowledge is created from data by defining a domain and finding an order in that domain. We obtain a lot of data, for example, a smaller raindrop falls slower than a

larger one in air, a spear flies further when it is thrown spun, water is liquid, mercury becomes reddish when oxidized, a beam of light travels along a straight line, and so on. Knowledge corresponding to some of these data includes the periodical rule for elements and the Newton's equation of motion, $f=m\alpha$. Knowledge has been written in a book and accumulated in a library. Naturally, the library is our knowledge infrastructure.

The present state is summarized by the fact that, firstly, tremendous volumes of data are left in subdivided fields without being abstracted to yield knowledge, secondly that fields are subdivided into too many pieces, and finally that these subdivided fields are isolated with respect to each other.

Nanotechnology covers a very wide range of knowledge including materials, devices, processes and applications. We need to use the right combination of pieces of the right knowledge to be efficient. The difficulty to do this consists both of the access to the right knowledge and the combination of the pieces of knowledge.

In the light of these considerations, a proposal to solve this difficulty is introduced in the following way. We firstly create knowledge by collecting data in the fields related to nanotechnology, defining sub-domains and finding an order in each domain, secondly make a domain an object having the boundary of which is described explicitly, and finally implement the objects on a network which is accessible from all over the world.

3.2 Structuring knowledge in nanotechnology

Figure-2 shows the basic structure in the knowledge infrastructure in nanotechnology. It consists of process to synthesize nanomaterials, structure that is morphology, function, and application. Process covers physical, chemical, biological, and their combinations. Morphology includes molecular scale to millimeter-scale. A micrometer-sized flock of nanoparticles shows different properties from a well-ordered array of the same nanoparticles [4]. Consequently, we need to control the micrometer-sized morphology of nanomaterials. Even if we succeed in creating a beautifully ordered nanomaterials at micrometer-size, we have not established any procedure to scale them up to millimeter-size. On the other hand, if we succeed to produce a material of millimeter-size, traditional methods based on thermodynamics, hydrodynamics and other established academic disciplines could be used to scale them up even to meter-level. Consequently, 'morphology' covers the molecular-to-millimeter level of structure. Function means properties of a material and performance of a device. Applications of a material are related to processes as well as functions, because the practicability of a material is dependent not only on the functions but also on the process productivity. This basic structure will be detailed as shown in the next section.

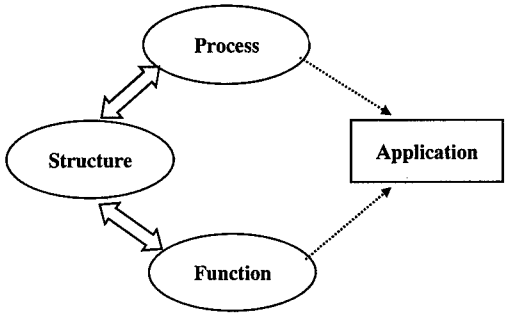

Figure-2. Basic structure in the knowledge infrastructure in nanotechnology

3.3 Example of knowledge creation in the relation of morphology to process [5]

Abnormal growth phenomena, which frequently occur in materials processing, as far as our belief is concerned, zoom up some specific mechanisms among many mechanisms that govern the morphology of particular formation. As many as 700 cases have been collected, some of which are shown in Figure-3. These case studies including the abnormal morphologies and the corresponding understanding of the growth process are data which was not abstracted in subdivided academic domains and could not be used by any others.

Various morphologies including protrusions, voids, fibers, particles, surface roughness, and crystal quality were observed, but most of them could be categorized by six parameters. This means that any morphology could be assigned to a coordinate of a six-axis morphology space. Furthermore, unreported morphologies could be predicted by the coordinates which were not occupied by any of the existing data. This situation is analogous in principle to the relation between the periodical rule and elements.

Any abnormal structure located at a coordinate on the morphology space should be related to a formation process. Logically, it should be linked to a coordinate in the process space. However, another space of process model was defined as a link space to avoid too many one-to-one links between the two spaces. A process model can be effective when combined with parameters, which are stored in a database. Some of the parameters are particularly and specifically important in the morphology formation, including the sticking probability of film-growth species, and others are general in varieties of academic fields, including the diffusion coefficient.

The Information-technology based on knowledge infrastructure of structured knowledge will provide us with an alternative to the present libraries, which will be characterized with easy access to the right knowledge depending on one's basic knowledge and wishes, easy transfer from one knowledge to another, and easy understanding assisted with various new techniques including computer graphics and virtual realities.

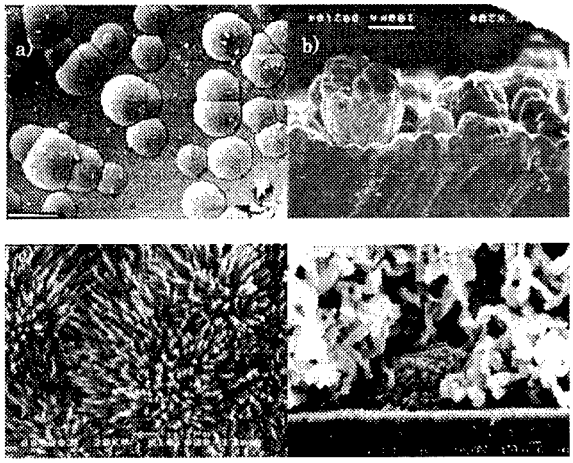

Figures-3. Examples of abnormal growth in material processing.

a) Dome-shaped surface protrusions formed in TiN/AlN composite films deposited by thermal CVD.

b) Dome-shaped surface protrusions formed in SiC films deposited by thermal CVD.

c) Whiskers formed in AlN films deposited by thermal CVD.

d) Noodle like structure formed in Al films deposited by thermal CVD.

3.4 basic concept of structuring knowledge project

The role of structuring knowledge project is summarized as below.

- To develop a database and models from the viewpoint of the process, structure, functional performance and their relations without limiting the scope of materials
- To develop a platform that incorporates the above, thereby structuralizing our knowledge of material technology
- To establish the methodology of inferring a material and process from desired functions by using the platform

The last role is very challenging, and most of materials researchers think that it is not possible. The difficulty lies in the multiple and complex relationships from functions to processes. The key to

overcoming the difficulty is to figure out structures to bridge the processes to functions by defining each space. It is worth-while to make clear the steps as follows with the help of schematically shown Figure-4.

First, the identification of the architecture of the primary database by comprehensively extracting the information items referring to material technology from viewpoint of the processes, structures, and functions involved. The primary database is to store the body of high accurate knowledge on material technology by selecting, collecting, ordering and classifying this knowledge from the literature. Second, the coordinates in the respective spaces for process, structure, and function are calculated using modeling engines developed from the primary database or model experiments done by this project, and results in the secondary database. The problem is to set the axes in each space. For example, super-saturation is an axe for process space. It is very difficult to define the structure space, that is morphology space, but we have a long experience in the field that anomalous growth project already described in 3.3. Third, inferential engines including neural networks are to be developed for deducing the structures from the functions and the processes from the structures. The modeling and inferential engines determine the coordinates in each space and connect the coordinates between spaces, respectively. It is necessary to develop the models in common for NMP such as the nucleation processes, the nucleus coagulation processes, the spinodal decomposition processes, the interface formation processes of nano structures and the self-organization control processes.

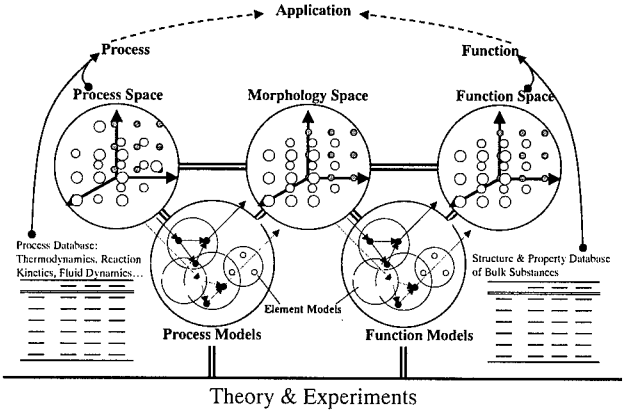

Figure-4 Concept of structuring knowledge pcoject

4. Conclusions

The key issue of Nanotecnology Materials Program is to establish the knowledge infrastructure for nanomaterials and devices. This direction is also stated in NNI program [1]. The thing is how to do and how to collaborate with other countries for the world sustainability in the 21st century. The nano-world comes true soon.

(1) http://www.nano.gov/
(2) http://itri.loyola.edu/nano/IWGN.Research.Directions/
(3) http://www.nedo.go.jp/english/informations/info_index.html
(4) S. Maenosono, E. Ozaki, K. Yoshie, Y. Yamaguchi, 'Non-linear Photoluminescence Behavior Observed in Closed-packed CdSe Nanocrystal Thin Films' accepted by J. Japanese. Applied Physics
(5) Komiyama, H.; Egashira, Y.; Noda S.; Tsuji Y.; Shimada, M.; Matsukata, M.; Ihara, M.; in preparation to be submitted

Figure-1. The role of projects in nanotechonology materials program

Figure-2. Basic structure in the knowledge infrastructure in nanotechnology

Figures-3. Examples of abnormal growth in material processing.

Figure-4. Concept of structuring knowledge peoject

Table-1. The aims of each project

Proceedings of 7th Japan International SAMPE
Symposium & Exhibition, Nov. 13-16, 2001

Advanced Composites Development for Aerospace Applications

Darrel Tenney[1], PhD and R. Byron Pipes[2], PhD, NAE

1: Aerospace Vehicle Systems Technology Program Office, NASA Langley Research Center
E-mail: d.r.tenney@larc.nasa.gov

2: 17th President, Rensselaer Polytechnic Institute
E-mail: rbpipe@wm.edu

Abstract

The evolution of composites applications in aeronautics from 1970 to the present is discussed. The barriers and challenges to economic application and to certification are presented and recommendations for accelerated development are outlined. The potential benefits of emerging technologies to aeronautics and their foundation in composite materials are described and the resulting benefits in vehicle take off gross weight are quantified. Finally, a 21st century vision for aeronautics in which human mobility is increased by an order of magnitude is articulated.

Keywords: Advanced composites, Aeronautics, 21st century vision

Introduction

Advanced composites have emerged as the structural materials of choice for many aerospace applications because of their superior specific strength and stiffness properties. First developed for military aircraft applications, composites now play a significant role in a broad range of current generation military aerospace systems. Commercial transport aviation has also witnessed a significant increase in adoption of composites during the past ten years. And there are currently a large number of general aviation aircraft with significant use of composite materials and structures that anticipate FAA flight certification in the near future.

Yet, there continue to be barriers and challenges to the expanded exploitation of composites technology for primary transport aircraft structures, i.e. wing and fuselage. These include damage tolerance, fuel containment, lightening protection, repair and nondestructive inspection, modeling and failure prediction and cost effective manufacturing. The successful resolution of these issues requires additional research directed at the underlying science through comprehensive programs of research and development. Development of standard engineering practices for exploitation of contemporary composites technology for near term applications can also be expected to benefit new aerospace products under current development.

The future composites technology will provide the platform for the next revolution in aerospace vehicle technology. With recent advances in science and engineering there are new emerging technologies that will likely accelerate the development of aerospace

vehicle design during the next decade including: sensors and devices, intelligent materials and structures, active flow control, reliability-based design and certification, robust manufacturing technology, nanotechnology and biomimetics. Moreover, it is the strategic integration of these technologies that will provide for the next major gains in vehicle performance. Yet the integration of these technologies cannot be achieved with contemporary materials and structures technologies. Therefore, it is essential that significant effort be directed to develop the next generation composites technology.

Current Status

The applications of composite materials in aerospace products are pervasive today, having found their first applications in military aircraft in the early 1970's. The evolution of this important technology has been multifaceted with the initial phase led by the defense industry, significant advances in the commercial aircraft and rotorcraft industries and its most aggressive exploitation in the general aviation industry. Advanced composites can trace its origin to the invention of the boron filament in the United States and the carbon fiber in Japan/United Kingdom in the 1960's. The first production aerospace application was the horizontal stabilizer of the U.S. Navy F-14 in 1970, followed shortly thereafter by applications in the U.S. Air Force F-15 and F-16. During the decade of the 1980's commercial applications were initiated through the NASA ACEE Program. The Boeing 737 horizontal stabilizer was certified in 1982 and applications with composites approaching 10 wt.% were achieved with the Airbus 300 and 310, Boeing 737, 757 and 767, McDonnell-Douglas MD-82, 83 and 87 during the 1980's. The Airbus 320 was first commercial aircraft to exceed the 10% utilization. By 2000, applications approaching 30% weight savings had been achieved by the U.S. Air Force B2 and F-22 and the U.S. Navy V-22. The industry is now poised to develop commercial and military airframes with extensive composite wing, empennage and fuselage applications. The Boeing "Sonic Cruiser" and the 650-seat A380 Airbus will likely be the next examples of the use of composites in future commercial aircraft. Two new business jets with composite sandwich designs in pressurized fuselage have been recently undergone consideration for certification by the FAA. The Raytheon Premier I has been flight certified and the AASI Jetcruzer 500 is well into the process. Propeller-driven aircraft have also incorporated composite materials in their airframes. The PAC USA Lancair LC40-550FG and the Cirrus Design Corp. SR 20 were type certified in 1998 [1]. New rotorcraft vehicles include composites applications in airframe, rotor blades and rotor drive systems (main and tail). The Sikorsky S92 rotorcraft and the Bell Textron BA609 Tiltrotor are two such examples.

Barriers and Challenges: Economics and Certification

Barriers to expanded application to composite materials in aircraft are shared by the defense, commercial and general aviation industries. Manufacturing and non-recurring development costs continue to limit the rate of growth of the field. Current engineering practice is a test-based, building-block approach that is test intensive. Empirical design and process standardization and maintenance technology are also issues of concern. The lack of standardization of material forms and high fidelity, hierarchical design methodologies can result in overly conservative designs that, while providing performance gains and ensuring safety and durability, too often suffer in economy compared to conventional metals technology. Validated progressive failure analyses are also required to predict, without tests, the lifetime performance of composite structures.

Finally, the limited human resources with composites training and experience constrain broader applications [1].

It is also important to point out recent advances that are paving the way to meeting the challenges articulated above. NASA Langley recently successfully tested a full-scale composite wing structure (see Fig. 1) designed to meet the requirements of a 220-passenger commercial transport aircraft [2]. The wing box was 41 feet in length and incorporated advanced graphite fiber textile performs and Kevlar stitching for stringer-skin connections with resin-film-infusion to achieve resin impregnation. These manufacturing innovations by the Boeing Company were focused upon significant manufacturing cost reductions while meeting performance goals. The wing structure sustained 97% of design ultimate load prior to failure through a lower access opening and was, therefore, judged to have successfully met test requirements while providing further insight into refinements necessary for adoption of this new technology.

It should also be noted that the successful design and test of the NASA/Boeing wing structure required an extensive set of material, fabrication and sub-element tests to clarify manufacturability and the preliminary design. Thus, at the end of the 20th century composites technology is found to be largely based in empirical methods with the accompanying limits on economy (See Figure 2). These shortcomings in composites technology will only be overcome with the further developments in the areas described and through new emerging technologies.

Emerging Technologies

There are a number of emerging technologies that will expand the design space in the 21st century air vehicle and provide enhancements in performance, safety and economy. Smart materials and systems technology to control structural and aeroelastic response offer the opportunity to achieve structural and aeroelastic performance and efficiencies not possible with conventional materials and structures technology. Enhanced flutter, gust, buffet and maneuver load behavior can be achieved. Piezoelectric actuators have been successfully employed for active flutter suppression, active gust load alleviation and noise suppression [3]. Shape memory alloys have also been employed to address sonic fatigue and noise suppression issues. Smart structures have been developed to improve aerodynamic performance in such applications as the contoured, hingless flap and aileron with built-in shape memory alloy tendons. Efficiency gains of 8-12% have been achieved for lift, pitching and rolling moments over a broad range in wind tunnel tests [4]. The engine inlet has also been the subject of smart structures development in order to provide for its deformation to achieve optimum configurations for multiple flight conditions.

Synthetic jet actuators for control of flow separation have recently been employed to increase airfoil efficiency. The actuator has the capacity to provide both positive and negative pressure in the flow stream at a small diameter orifice and is thereby termed a "zero-mass flow" device [5]. Jets constructed of two piezoelectric/metal wafer laminates that are actuated by controlling sinusoidal frequency and phase to achieve the desired pressure characteristics. Jet velocities of 60-100 m/second have been achieved in the laboratory and active separation control at Reynold's number up to 40X106 has been demonstrated to delay flow separation under flight conditions [6].

Multidisciplinary design optimization and flight control disciplines have been integrated to utilize localized flow control and distributed shape-change devices to achieve active flight control for tail-less aircraft. The

integration of vehicle configuration, prediction of control moments with computational fluid dynamics, location of shape-change devices, and algorithm for optimum location of devices and simulation of the flight controls, was necessary. In addition, fluidic thrust vectoring, accomplished by deflection of the jet with a secondary air stream, has been examined for additional flight control [7].

Reliability-based design and certification require that new and robust methodologies be developed for high fidelity analysis of composite materials and structures [8]. This approach will replace the empirically based, factor-of-safety design with a design paradigm that features science-based methodology for critical design features. It relates weight, reliability and economics as multiple design merit functions. Process specific imperfections and defects and their impacts on response are considered directly. Progressive failure analyses are carried out with powerful design tools made possible by the integration of advanced modeling methods and scientific understanding. Finally, tailored composite applications based upon biologically inspired concepts to achieve optimum performance are being pursued.

Robust manufacturing technology to insure high performance aerostructures with increased cost-effectiveness has focused on the development of non-prepreg/autoclave systems. The integration of engineered textile preforms, stitching and vacuum-assisted resin transfer molding technology has been shown to provide significant advantages for future aircraft programs. Methods for prediction of manufactured quality, reproducibility and imperfections will be essential.

The field of biological sciences continues to provide new insights into the ways organisms have successfully adapted to their environment over millennia. The integration of materials, structures and aerodynamics simulations with the field of biomimetics provides the framework to develop a link between what nature has learned over time and the need for current aerospace solutions. These efforts require the development of design teams who have representation from the disciplines of biomimetics, materials science, aerostructures, computational fluid dynamics and computer science.

Nanotechnology can also be expected to provide the next generation of revolutionary materials technology for future aero vehicles. Discovered by Iijima [9] the single-walled carbon nanotube possesses extraordinary mechanical, electrical and thermal properties. Early evidence suggests that carbon nanotube/polymer composites will play a significant role in the future aero vehicle systems.

Technology Integration Benefits

The future of aeronautics will significantly benefit from the integration of the numerous advances discussed above and their exploitation will be based in advanced composites as the enabling technology [10]. For military aircraft, smart, flexible structures, synthetic jets, forebody vortex control, advanced control laws, passive porosity, continuous moldline technology and fluidic thrust vectoring will provide for increases in range, improvements in agility and survivability. For commercial transport vehicles, these technologies will provide active shape control, health monitoring, buffet load alleviation, active transition control, thrust vectoring, inlet and nozzle shaping, exterior noise suppression, vibration suppression, active separation control, gust load alleviation and flutter suppression.

Consider the contributions of these technologies for a conventional long haul/high capacity conventional subsonic

transport aircraft. Laminar flow control, design optimization and excrescence drag reduction will yield a reduction of 4.6% in the take off gross weight (TOGW) of the vehicle [11]. Composite wing and tails, composite fuselage, light weight landing gear, advanced metals and aeroelastic tailoring will reduce TOGW by 24.3%. Advances in aero-mechanical propulsion design, hot section, materials and secondary systems can achieve a savings of 13.1%. Finally, in the systems area, relaxed static stability, fly-by-light/power-by-wire, high performance navigation and intelligent flight systems will yield a 9% savings in TOGW. Taken together these advances would yield an aircraft with an overall weight reduction of 51%. Of the total weight reduction, structures technology and composites would account for 48% of the total.

The blended wing body concept to produce a long haul/high capacity subsonic transport aircraft with a capacity of 800 passengers, a range of 8500 nautical miles and a landing requirement of 10,000 feet could achieve a 45.7% weight savings (TOGW) through the incorporation of advanced technology. Laminar flow control, design optimization, and excrescence drag reduction would yield 11.8% savings. Composite wing and fuselage, light weight landing gear and aeroelastic tailoring would reduce weight by 19.1%. In the propulsion arena advances in aero-mechanical design, hot section, materials, secondary systems, boundary layer ingestion would yield 12.2% and in the systems area, fly-by-light/power-by-wire, high performance navigation and intelligent flight systems would reduce weight by 2.6%. Clearly, the technology with the greatest impact on weight remains structures technology and composites for the blended wing body concept vehicle as well as the conventional concept discussed above.

21st Century Vision for Aeronautics Technology

Technology in the Digital Age will revolutionize high-speed mobility of humankind in a manner that will produce a sea change in human prosperity. This change will be not unlike the completion of the intercontinental railroad in the late 1800's or the introduction of the interstate highway system in the in the 1950's in the United States. Today's air mobility of citizens is limited by analog air traffic control systems, the number of trained pilots, the number of full-scale airports and the number and character of aircraft. Future Digital Airspace technology will provide the vehicle with "perfect knowledge" of terrain, geography, weather, vehicle condition, control and navigation through the central digital brain with extraordinary computational power. Embedded sensors and devices will yield smart materials and structures sufficient to achieve performance that allows vehicles to significantly increase performance and land safely on airfields that are insufficient in length for conventional aircraft. This revolution in technology will increase human mobility by an order of magnitude (See Figure 3. However, it is clear that the integration of the necessary technologies will lead to increased complexity of the air transportation system as well as air vehicles. Indeed, as the enhanced capability of the "digital machine" is increased, there will be a significant increase in system complexity such that the technology insertion will appear disruptive. During the next phase, however, increases in capability will result in only a corresponding linear increase in system complexity. It is during this period of technology innovation that the primary benefits described above will be realized.

The primary question to be answered is, "will the benefits in mobility, performance, safety, noise reduction, fuel economy be worth the price required to master complexity of the

multifunctional vehicle and the "open space" air traffic control systems?" One need only examine the benefits of the digital processor in today's society, as described in Moore's Law to answer, yes! Computational power has doubled every eighteen months during the last several decades and it was the mastery of the complexity of modern microelectronics that is responsible for the extraordinary economic growth in much of the world today. Enhanced high-speed air mobility can be expected to produce no less result.

References

1. Ilcewicz, L. and Cheng, L., "Draft Memorandum for National Plan on Safety and Certification Initiatives for Composites Used in Aircraft Products," (2001).
2. Jegley, D.C. and Bush, H.G., AIAA Paper No. 2001-1334-CP, (2001).
3. McGowan, A.R., et al, 5th SPIE International Symposium on Smart Structures and Materials: Industrial and Commercial Applications, Paper 3326-21, San Diego, CA, March (1998).
4. Kudva, J.N., et al, 8th SPIE Annual Symposium: Industrial and Commercial Applications, Paper 4332-48, Newport Beach, CA, March (2001).
5. Chen, F.-J., et al , AIAA Paper 2000-2405, (2000).
6. Seifert, A. and Pack, L., AIAA Paper 2000-2542, (2000).
7. Deere, K.A., AIAA 2000-3598, (2000).
8. Hilburger, M.W. and Starnes, J.H., AIAA-2001-1394, (2001).
9. Iijima, S., Nature, 354, (1991), 56.
10. Tenney, D.R. and Hernandez, G., 21st Congress of the International Council of Aeronautical Sciences, Melbourne, Australia, (1998).
11. McKinley, R.E., "Blended-Wing-Body: Design Challenges for the 21st Century," 2nd Internat. Conf. On Nonlinear Problems in Aviation and Aerospace, April (1998).

Figures

Fig. 1 Boeing – Langley composite wing test

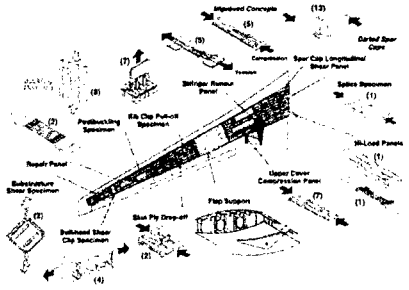

Fig. 2 Building block approach

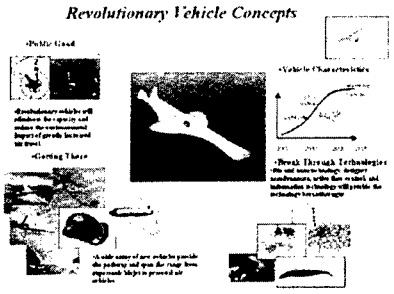

Fig. 3 Revolutionary vehicle concepts.

Proceedings of 7th Japan International SAMPE
Symposium & Exhibition, Nov. 13-16, 2001

A380 - The Flagship For The New Century

Jens Hinrichsen

A380 Engineering, Airbus
1 Rond Point Maurice Bellonte, 31707 Blagnac CEDEX FRANCE
E-Mail: jens.hinrichsen@airbus.fr

Abstract:

Top Level Aircraft Requirements for the down-selection process of advanced technologies for A380 are outlined. The application of composite panels for the un-pressurized fuselage is taken as an example for "best fit" of materials and manufacturing technologies with technology requirements.

Key words: Airbus A380, aircraft structures, material selection, manufacturing technology selection.

Introduction

The A380-family comprises passenger versions with 550 to 650 passengers in mixed-class configuration and a freighter version for up to 150 metric tonnes of payload, [1]. In co-operation with the world's major airports, the aircraft configuration was driven by the target to keep modifications of airport infrastructure at minimum. As a result, wing span and over-all aircraft length had to stay within a so-called 80-by-80m box, Fig. 1. These geometrical constraints, in combination with the selection of a technically feasible fuselage cross section, have delivered an oval cross section with a double-deck cabin configuration, running the full length of the aircraft. The lower deck cargo hold offers full standing height and can accommodate a variety of passenger facilities. Maximum

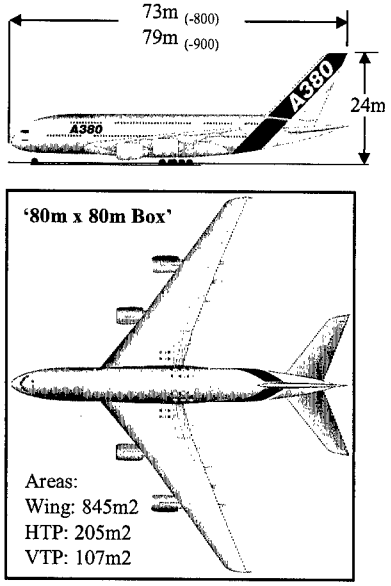

Fig. 1: A380 Outer Dimensions

outer dimensions of the fuselage are about 7.2m width and 8.6m height. This cross section, combined with appropriate floor beam levels, protects the later conversion of a passenger aircraft into a freighter.
Outstanding dimensions of A380 require new approaches, e.g. through panel arrangements with fewer joints and selection of adequate manufacturing technologies. The crucial role that size and complexity of

geometry plays, will be seen from the study results to be presented.

Targets and Requirements

Aircraft performance, costs for aircraft operations and aircraft price are essential parts of the contracts with the customers. As far as the airframe is concerned, the A380 Progamme Management has established targets for weight and manufacturing cost per aircraft section. Also, each of the individual maintenance cost chapters is subject to target costs. Top Level Aircraft Requirements (TLAR) summarize all information, which describe/characterize the product, e.g. maximum take-off and landing weights, altitude, climb and descent rates. Also, design service goals - including inspection intervals - are described in this key-document. Being essential part of the TLAR, Materials and Technology Requirements, [2], combine the selection and preparation of high-performance materials with advanced manufacturing processes and focus on service readiness and maintainability. Full-scale demonstrator programmes support the down-selection process and help to assure that design principles are validated and maturity of manufacturing processes is assured.

The above targets and requirements can be listed in a check list, which will be used for the assessment of CFRP-panels for the un-pressurized fuselage:

Check List:

- Service Readiness
- Maturity of Manufacturing Processes
- Target Weights
- Target Costs

Penel size and number of joints for fuselage shells is another parameter for weight and manufacturing costs, important for all kind of materials: metal, GLARE and composites. The outstanding size of the A380 fuselage, see Fig. 2, needs a new approach compared with smaller aircraft: Material supply and manufacturing processes must allow for the introduction of much longer and wider panels at twice the average thickness compared with smaller aircraft.

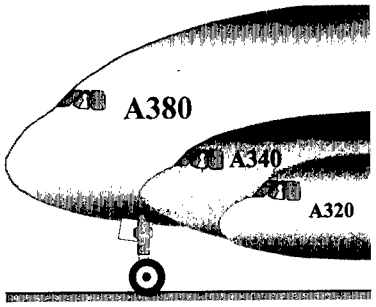

Fig. 2: Size Comparison

Consequently, the assessment has to review different technologies in view of their contribution to this new approach. Finally, application of new materials should also deliver so-called "build-in potentials" for future growth in application and/or increased utilization. All the above targets and requirements will be applied to the selected study on CFRP fuselage panels aft of the rear pressure bulkhead, see Fig. 3.

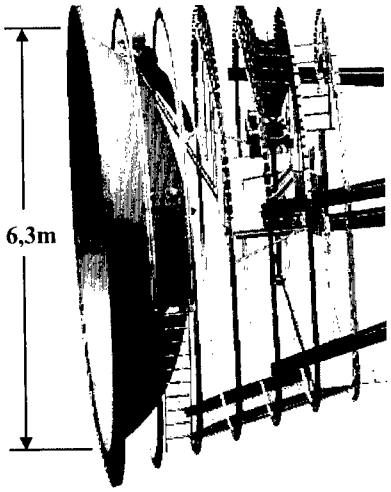

Fig. 3: Aft Pressure Bulkhead

Structural Design for Aft Fuselage

The choice of either aluminium alloys or composite material for panels of the un-pressurized aft-fuselage is in-line with the structural design drivers, Fig. 4.

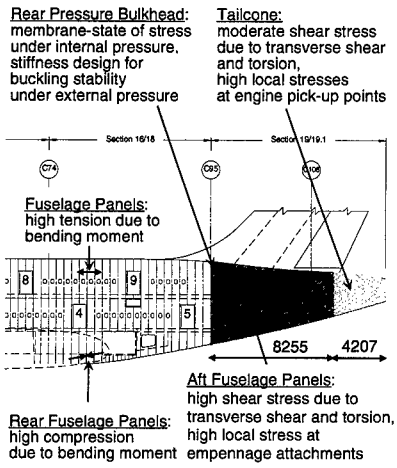

Fig. 4: Drivers for Material Selection

High load introductions from the empennage will require heavy milled metal frames at attachment fittings, as on all other Airbus aircraft. Typical frames can be manufactured using RTM technology. "Design for maintainability" has to take into account repairs after tail-strike events: The panel arrangement and additional frame joints must ease exchange of lower fuselage structure using spare part kits, independent of selection of material and manufacturing processes. Another parameter for the selection process is the complex aerodynamic shape of the aft-fuselage, affecting the number of panels and joints. Requirements from stretch-form operations for strongly double-curved sheet metal skins limit panel sizes and consequently increase the number of panel joints compared with a composite design solution. A complex aft-fuselage shape has also a strong impact on manufacturing process selection for composite panels.

Material Costs

In global terms, material costs cover the price for material to be purchased as well as material overhead cost. The analysis shall identify those material costs, which are associated with the manufacture of 1kg of flying structure, Fig. 5.

The reason for waste of material is manifold: It is obvious that, for example, cutting of pre-forms will result in unusable pieces of pre-impregnated woven fabrics. Also, final trim of edges of the cured lay-up contributes to waste of material.

Other reasons for waste are less obvious and difficult to quantify, because they are linked to the specific way of handling of raw material in an individual factory. Handling can cause damages during storage operations and scrap due to excess time in the refrigerator. Also, raw material of

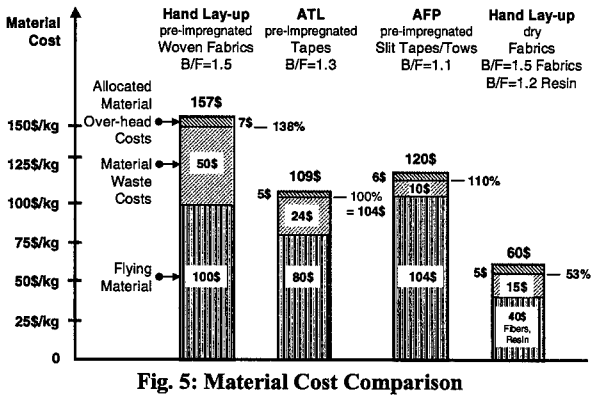

Fig. 5: Material Cost Comparison

unacceptable quality might be sorted out during the manufacturing process and has to be paid by the manufacturer, if these flaws

are not reported and official refusal is not forwarded to the supplier. In order to get a fair comparison of material costs for different manufacturing processes, assumptions have to be made for the percentage of waste, which reflect the material application for very large fuselage panels in combination with state-of-the-art handling of high-value raw material. For other applications, fly-to-buy ratios might be much higher. Allocated Material Over-head Costs in Fig. 5 range at 5% and shall cover all costs linked to purchase activities, acceptance control on delivery and storage. It is recognized that dry fabrics require more costly material handling, but this shall be outbalanced through savings in storage, because a refrigerator is not needed, as for pre-impregnated fibers.

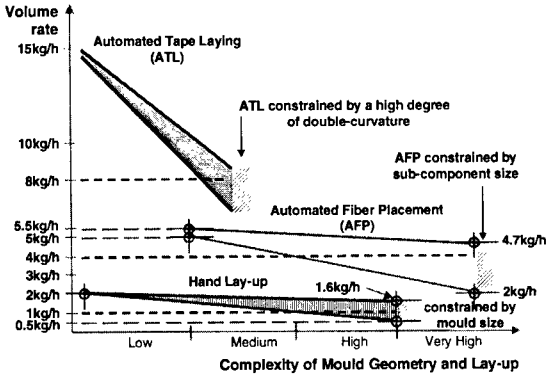

Fig. 6: Process Performance

Manufacturing Process Performance

The search for the most appropriate composite manufacturing process shall be supported by the introduction of a scale that measures the "complexity of mould geometry and lay-up". Fig. 6 displays a linear decrease of lay-up volume rate (kg per hour) versus an increasing degree of complexity, such as double-curvature and size of the mould as well as required optimization of fiber orientation. Simulation of lay-up for different processes revealed that automated tape laying (ATL) is ruled out by the degree of double curvature. Thus, complexity of the panels is beyond the constraint given for ATL in Fig.6. The panel arrangement for the composite solution aims at savings through reduction of number of joints. A split into four huge panels was confirmed to be feasible for both hand lay-up and automated fiber placement (AFP). Access to the female mould for the worker is the type of complexity to be checked for hand lay-up, revealing that the complexity is close to the constraint for this process. Therefore, complexity of such panels was judged to range at "high". AFP is by nature less constrained by the size of the male tool for manufacture of skins. On the other hand, the "wet" skin will be transferred into a female tool for placement of stringers prior to the curing cycle, and stringer positioning requires equivalent accessibility as discussed for hand lay-up. As the "real" performance in terms of lay-up volume is not known, a "best engineering judgement" has to describe a scatter band, which reflects experience with components in existing production lines.

Manufacturing Process Costs

Using the above performances and introducing costs for labour and machine, scatter-bands for "process cost" versus "complexity" can be established, Fig. 7. 500$ per hour are supposed to cover the costs related to the AFP-machine at average utilization, including supervision. Labour cost is introduced at 80$ per hour, including all costs for workforces and the use of shop floor facilities, as far as it is needed to deliver the lay-up. All costs under investigation are re-curring costs and shall cover all efforts linked to the delivery of un-

cured skins for fuselage panels, prepared for positioning stringers on the delivered lay-up in a further process. Materials and

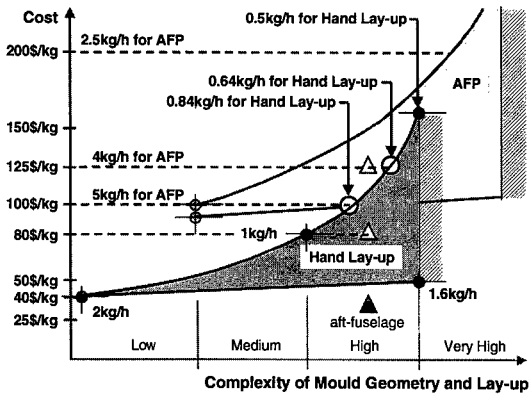

Fig. 7: Process Cost Comparison

manufacturing costs are defined as *re-curring cost per kg flying structure.*

Fig. 7 allows for determination of manufacturing process cost within a scatter-band, once the degree of complexity is fixed. Triangular symbols indicate average values for hand lay-up and AFP, which are chosen for the comparison of costs, Tab.1, except for the Resin Film Infusion (RFI) process, using dry fibers, because hand lay-up of dry fabrics (e.g. non-crimped fabrics) takes more time compared to hand lay-up of pre-impregnated fabrics.

Processes / Volumes	H. Lay-up, imp. Fibers	AFP	H. Lay-up, dry Fibers
Performance	1 kg/h	4 kg/h	0.64 kg/h
Labour per hour	80 $/h		80 $/kg
Labour per kg	**80 $/kg**		**120 $/kg**
Machine per hour		500 $/kg	
Machine per kg		**125 $/kg**	

Tab. 1: Comparison of Process Cost

This is due to the difficulties to place dry fibers with the right accuracy. Also, resin film has to be arranged in-between the fiber layers. Such additional effort is taken into account by using the upper bound for process cost for hand lay-up in Fig. 7.

Costs for Materials and Processes

Costs for materials, Fig. 5, and for processes, Tab. 1, are summarized in Tab. 2.

Total costs are valid for the delivery of *un-cured skins*, as defined previously.

Hand lay-up of prepregs and AFP end up at equal cost, whereas the lay-up for the RFI process apparently allows for savings in the order of 25%, despite the fact that labour costs are 50% higher compared with hand lay-up of prepregs.

Summary: Except for the resin infusion approach, material costs determine half of the cost, which are linked to the delivery of laid-up skins. And, for hand lay-up of woven fabrics, half of these material costs are due to waste. In order to keep manual processes competitive, further efforts have to prioritize waste reductions and to lower material prices.

Process / Source	H. Lay-up, imp. Fibers	AFP	H. Lay-up, dry Fibers
Material	157 $/kg	120 $/kg	60 $/kg
Labour	80 $/kg		120 $/kg
Machine		125 $/kg	
Total	**237 $/kg**	**245 $/kg**	**180 $/kg**

Tab. 2: Material and Process Costs

The above comparison allows for judgement of alternative materials and appropriate manufacturing processes for application of composites. The technology down-selection process requires to complete evaluation on aircraft section level.

Assessment on Aircraft Section Level

The conventional all-metal design with Al2524 panel skins, Al7075 stringers and heavy milled frames out of Al7050, serves as a reference configuration. Introduction of composite materials replaces aluminium panels and sheet metal frames in a first step. Thus, both alternative design solutions share about 36% common metal parts in terms of weight, Fig 8.

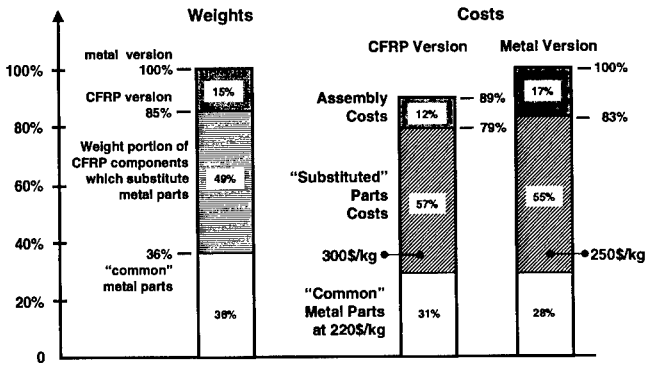

Fig. 8: Weight and Cost Comparison on Aircraft Section Level

Fig. 8 displays cost levels relative to each other in a fair way, rather than claiming absolute cost levels. Costs for metal panels are increased due to a high buy-to-fly ratio resulting from clamp length cut-off after stretch forming. Thus, huge material waste combines with the high price level of advanced aluminium alloys. Complexity of geometry leads to labour-intensive forming/heat-treatment operations and assembly of 16 metal panels. This background delivers the competitive edge for CFRP using either hand lay-up or AFP. Tab. 3 recalls the checklist with targets/requirements. Further to this, build-in potential is identified as a later replacement of heavy milled frames by RTM-parts, when maturity is proven for the size of such parts.

Composite material application saves 15% of the total weight. Weight saving includes the benefit from reducing the number of panels: from 16 aluminium panels down to 4 CFRP panels. This has a huge impact on assembly cost as well, Fig. 8. For the purpose of a rough cost comparison, simple figures have been chosen, such as 300$/kg for CFRP parts substituting metal parts, 220$/kg for common metal parts and 250$/kg for the metal parts which compete with CFRP. Consequently,

Criteria \ Processes	All-Metal	Automated Fiber Placement	Hand Lay-up, Prepregs	Hand Lay-up, dry Fibers	Automated Tape Laying
Feasibility	yes	yes	yes	yes	no
Service Readiness	yes	yes	yes	yes	
Maturity of Manuf. Proc.	yes	yes	yes	no	
Support to Target Weight	no	+++	++		
Support to Target Cost	no	+++	+++		
Support to Size Approach	no	+++	+++		

Tab. 3: Fulfillment of Requirements

References

1. J. Hinrichsen: "Airbus A3XX: Design Features and Structural Technology Review", Galileo Galilei Celebrations, Erice, Italy, 1999.
2. J. Hinrichsen: Proc. of 19th CEAS Conf., 3 (2000).

Proceedings of 7th Japan International SAMPE
Symposium & Exhibition, Nov. 13-16, 2001

Experience of FRP Strengthening for Historic Structures

Hideo Katsumata # and Kozo Kimura#

#: Technical Research Institute, Obayashi Corporation
4-640 Shimo-Kiyoto, Kiyose, Tokyo 204-0011, JAPAN
E-mail: katumata@o-net.obayashi.co.jp

Abstract

Recently, techniques using CFRP are employed for retrofitting of historic structures because these techniques can strengthen such structures while keeping their historic values. This paper describes some Japanese applications of the CFRP techniques, i.e., CFRP jacketing, CFRP gluing, and prestressing with CFRP tendons. They are applied for old concrete columns, wooden building, and brick lighthouse, respectively.

Key Words: CFRP, Prestress, Seismic Retrofitting, Historic Structures.

Introduction

Many Japanese historic buildings need structural retrofitting because of their seismic vulnerability, and so on. However, it is very difficult to simultaneously keep the historic values and gain enough structural improvement. Therefore, recent techniques using CFRP (Carbon Fiber Reinforced Plastic) are widely spread to satisfy such conditions. Since the CFRP techniques enable change of dimensions of structural elements negligibly small, inside and outside appearances of the retrofitted building may not be changed. This paper describes some applications employing the CFRP techniques for various buildings.

Column Jacketing at Osaka Castle

The current Osaka Castle (Photo 1) is used for a museum. The appearance of the building is a Japanese medieval castle, however the structure, constructed with modern technology, is SRC (steel and reinforced concrete). The building age was over 60, and many parts were damaged. The structural evaluation also revealed that the building was not strong against the considerable maximum earthquake. Thus, the building was retrofitted, including structural strengthening. The employed techniques were 1) installing steel plate walls, 2) reinforced concrete jacketing of girders, 3)

Photo 1 Osaka Castle

steel tube jacketing of columns adjacent to the installed steel walls, and 4) CF jacketing of columns. Such columns are supporting floor slabs, therefore, the failure of columns will induce fatal collapse of the building.

The CF jacketing technique is to transversely wrap CFRP on the column surface for making additional closed hoops. The action of the wrapping CFRP is shear reinforcement and confinement of concrete to improve ductility of the columns. The structural design code for the CF jacketing was already established in Japan [1]. Recently, the CF jacketing is widely spread due to low cost and easiness of work.

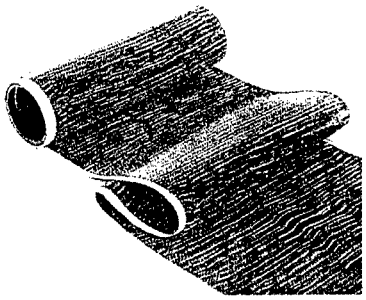

Photo 2 Carbon Fiber Sheet

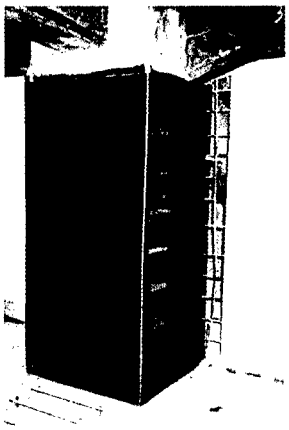

Photo 3 Standard CF Jacketing

At Osaka Castle, a "standard" CF jacketing was applied for short columns. CF sheets (Photo 2), in which CFs are arranged uni-directionally, are placed and glued by hand with impregnating epoxy resin (Photo 3). Cure for FRP fabrication is carried out on site. However, for long columns, a CF strand winding technique [2 and 3] is applied because the winding technique, superior on work speed and quality control, is suitable for large-scaled applications. The CF winding employs a winding machine that winds and supplies CF strands toward the column, impregnating epoxy resin and rotating around the column (Photo 4).

CF Gluing for Wooden Building

There are many old wooden buildings in Japan. Such buildings are retrofitted and used for museums, and so on. Then, a long-term load as well as an earthquake load is an issue to be solved. CFRP is also used for strengthening of bending capacity against the long-term loads.

A CF gluing technique is widely applied for existing reinforced concrete chimneys to improve bending capacity against a severe earthquake [4]. This

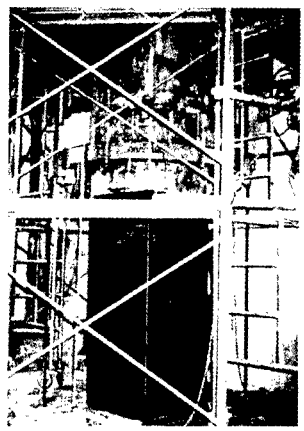

Photo 4 CF Winding

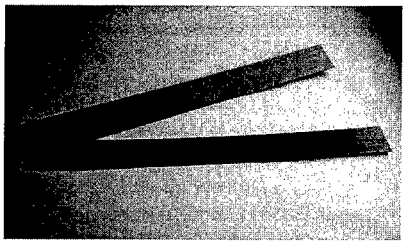

Photo 5 CFRP flat bar

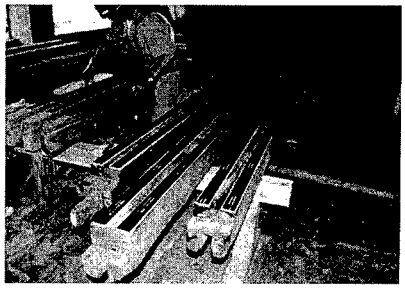

Photo 6 Application of CFRP for Wood

technique is almost similar to the standard CF jacketing, however, CF sheets are placed longitudinally to make the CFRP a resistant element for bending moment. Bending capacity improvement, however, is not always cost-effective due to large number of CF sheets.

Recently, a factory-made CFRP flat bar [5] (Photo 5), which contains large volume of CF, is employed due to reducing construction labor. Since the CFRP flat bars are impregnated and cured, on-site work is to glue with epoxy adhesive of high viscosity. The CF flat bars are applied for bending capacity improvement of several wooden buildings, for example, an old shop building in Hakodate, or an old office building of a mine in Akita. Structural performance of CF-glued wood beam was tested [6].

An usual retrofitting process of a historic wooden building is as follows; 1) decomposition of the building to structural wooden pieces, 2) repaired or retrofit in a factory of the decomposed pieces, and 3) re-composition. In the factory repairing stage, CF flat bars are attached to tensile side of wood beams (Photo 6).

Prestressing at Shiriya-zaki Lighthouse

Shiriya-zaki lighthouse, located in the north end region of Honshu Island, is beautiful brick tower (Photo 7). Constructed in 1877, the lighthouse still contributes on the marine safety. Seismic activity at Shiriya-zaki is low, however, the bending strength of

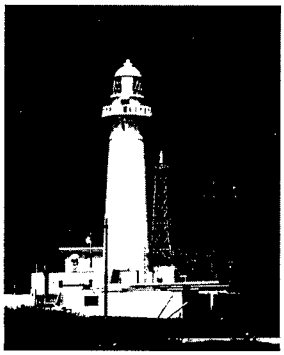

Photo 7 Shiriya-zaki Lighthouse

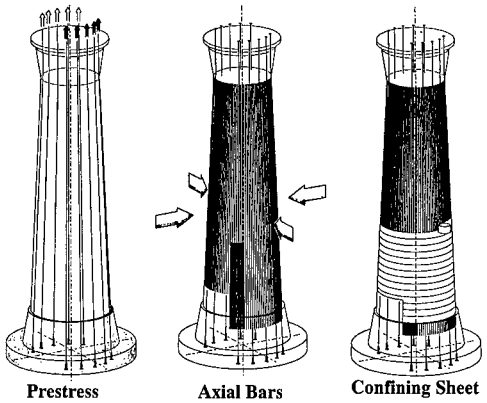

Fig. 1 Retrofitting Techniques for Lighthouse

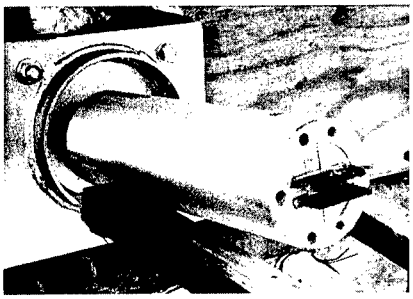

Photo 8 End Tube of CFRP Tendon

the tower was not enough. Retrofit was carried out to satisfy the following criteria; 1) for 10 cm/s^2 earthquake input, service limit state response and 2) for 20 cm/s^2 earthquake input, safety limit state response.

Due to lack of knowledge on bricks, the safety limit was conservatively defined as the compressive elastic limit of brick. For the safety limit strengthening, the CF flat bars were longitudinally glued on the surface of the tower (Fig. 1). The bottom part of the tower was jacketed with reinforced concrete to gain anchorage of the CF flat bars and to improve the strength of the foundation.

The service limit was defined as cracking of brick bed joints. For the service limit strengthening, compressive prestress was applied to the tower by tensioning the CF flat bars longitudinally placed on the tower surface (Fig.1). The ends of the CF flat bar have anchorage stainless tubes. Inserting the CF bar into the tube, expansive material is poured. The chemical expansive pressure can smoothly transfer stress of the CF flat bar to the end tube (Photo 8). At the tensioning end, there are two end tubes on which a thread is curved. At the outside end tube, tension is applied through a connecting PC bar and a jack. The inside end tube is fixed by fastening a nut. Finally, the outside end was cut off.

Concluding Remarks

Inside and outside appearances of the retrofitted building employing the CFRP techniques is almost same while the structural performance is sufficiently improved. Therefore, these techniques are suitable for historic buildings for which historic value should be kept.

Acknowledgment

The authors express their acknowledgement to Toray corp. for providing photographs.

References

1. Japan Building Disaster Prevention Association: Guidelines for Seismic Retrofitting Design and Construction of Existing Reinforced Concrete or Steel Reinforced Concrete Buildings Using Continuous Fiber Composite, (1997) (in Japanese).

2. H. Katsumata, Y. Kobatake and T. Takeda: A Study on Strengthening with Carbon Fiber for Earthquake-Resistant Capacity of Existing Reinforced Concrete Columns, Proc. of 9WCEE (7), 517 (1988).

3. H. Katsumata and Y. Kobatake: Seismic Retrofit with Carbon Fibers for Reinforced Concrete Columns, Proc. of 11WCEE(293) (1996).

4. Y. Kobatake, K. Kimura and H. Katsumata: A Retrofitting Method for Reinforced Concrete Structures Using Carbon Fiber, Development in Civil Engineering 42, Elsevier (1993).

5. K. Kimura, Y. Kobatake, M. Hirata, Y. Tsuchiya: Flexural Behavior on Reinforced Beams with CFRP Laminates by Various Anchorages, Proc. of JCI, 20(1), 527(1998) (in Japanese).

6. J. Onose, M. Kumagai, T. Mizuno and S. Yamada: The Experimental Study on Reinforcing Historical Wooden Structure by Carbonfiber Plastic Board, Memories of the Tohoku Institute of Technology, 197 (2001) (in Japanese).

Proceedings of 7th Japan International SAMPE
Symposium & Exhibition, Nov. 13-16, 2001

NEW EXAMPLES OF COMPOSITES RESEARCH

Stephen W. Tsai, Akira Kuraishi and Sung-Kyu Ha*
Department of Aeronautics & Astronautics
Stanford University

Jon Gosse
Phantom Works
The Boeing Company
Seattle, WA

ABSTRACT

Research topics in micro- and macromechanics of fiber reinforced composites have been evolving during the last 50 years. Like fashion in clothing, emphasis changes from one era to another. Recently a novel mechanics analysis framework was proposed by Gosse in his plenary lecture at ICCM/13 in Beijing. It can be used as a basis for new examples of mechanics research.

In his framework, he provided a powerful computational scheme to analyze the stress and strain distributions and associated failures. This was done on both micro- and macromechanics scales. An effective link between the structural behavior composite components to materials and processing parameters can now be quantitatively established.

While this work is still in its infancy, it already has demonstrated profound implications in design, materials and process selections, and durability in short and long term applications. Research examples derived from this computational intensive framework can be clearly stated. In particular, the framework lays out a natural process where improvements made in research can be integrated in the overall scheme. Immediate impact in design would follow.

In this presentation, challenging research in micromechanics will be described in specific examples. The effects of materials and processing on the strength of unidirectional plies can be defined with improved precision. Proper utilization of such plies is critical in making composite laminates and structural components strong and durable. Such philosophy is not new but with improved accuracy in analysis and materials property data variability in component behavior is significantly reduced.

In component design, ply geometry and material parameters can also be shown in a different light from those derived from treating composites as black aluminum. Failures

On sabbatical leave from Hanyang University, Seoul, South Korea

on micro- and macroscopic scales can be defined with higher predictability not recognized in many current practice.

Examples of practical design problems include bonded and bolted joints, test specimen with free edge stresses, holes in laminates, compression after impact, and other detail design commonly encountered in structures.

Durability is another example of extension of this computational framework. While extensive test data will still be required, a more systematic basis that takes advantage of time-temperature superposition principle can lead to master curves in static, creep and fatigue loading conditions. The utility and confidence of the data will be significantly enhanced. Design for life and durability and accelerated testing can be treated with internal consistency and rationality.

The goals of this computational framework are to reduce empiricism, to increase precision in material characterization and to give composites design and processing a rational tool. With coordinated research tasks that will support this framework, rapid advances can be expected. Composites can finally emerge as a material of the future and can offer reliable service inside and outside the aerospace industry.

Proceedings of 7th Japan International SAMPE
Symposium & Exhibition, Nov. 13-16, 2001

Recent Researches on Fibre Optic Smart Structures in Italy and Future Trends in Europe

Antonio Paolozzi

University of Rome *"La Sapienza"*, Dipartimento Aerospaziale, Via Eudossiana 18
00184 Roma, Italy, Tel. +39 06 44585301, Fax. +39 06 44585670
e-mail: paolozzi@nero.ing.uniroma1.it

Abstract

In this paper recent developments on the embedding of optical fibres into polymeric composites and metal alloys, performed by research groups in Italy will be reviewed. The types of measurements performed with sensorless embedded optical fibres will be outlined. An application related to an intelligent thermal protection system for space vehicles, based on optical fibres will be briefly addressed. Development of sensors for smart manufacturing, the realization of Bragg gratings and relevant interrogation systems will also be considered. Some projects approved by the European union will be also mentioned.

Key Words: Fibre optic smart structures, Embedding, Metallic materials, Structural health monitoring, Smart manufacturing, Bragg gratings.

Introduction

The use of optical fibres in smart structure applications is very attractive because of the well known properties of optical fibers: their capability of carrying information without interfering with the electromagnetic fields, (this is very attractive for an aircraft where communications and avionics are vital), their very low intrusiveness when embedded, the possibility of multiplexing many sensors (Bragg gratings) in one single fibre and their insulation properties (essential when the embedding is performed into metallic materials). The first attempts of embedding optical fibres have been conducted on polymeric composite materials and dates back in the 80's. Remaining for the moment within this particular area and restricting our attention to studies performed in Italy we would like to mention Ref. [1] in which our Department in cooperation with Ferrari Space Division and the Italian National Agency for New Technology, Energy and Environment (ENEA) manufactured many specimen laminates made of Carbon Fibre Reinforced Plastics (CFRP) fabric with different quantities of embedded optical fibres. The material chosen was the one used for both the realization of a small bio lab to be placed inside the International Space Station (ISS) and for Ferrari F1 racing car structure. Traction and interlaminar shear tests were performed at the Ferrari Racing Division. The results have shown negligible effects on the mechanical characteristics even in the case of very high optical fibre/composite volume fraction. Another work [2] was performed in cooperation with ALENIA Aerospazio Equipment & Technologies

Directorate in "L'Aquila". The work consisted in the space qualification of CFRP laminates with embedded optical fibres. All the tests were performed both before and after thermal cycling, i.e., the specimens were exposed cyclically at 160 °C and –180 °C staying for one hour at each temperature. This exposure was necessary to simulate the effect of eclipses on a space structure. The material and polymerisation cycles were the one used for the constellation of satellites called Globalstar. Specifically the prepreg was *HyE 3454-2AH* whose constituents were high modulus carbon fibres and esterocyanate resin. The curing cycle was characterized by a maximum temperature of 177 °C and a pressure of 7 bars. Besides the tests reported in Ref. [1], flatwise, flexural, and pull-out tests were also performed. In spite of the high number of embedded optical fibres used in some specimens the mechanical characteristics of the laminates, both before and after thermal cycling did not show significant variations.

Embedding into Metallic Materials

Telecommunication optical fibres are basically made of silica which have melting point above 1000 °C. Consequently the possibility of embedding them into some metallic materials is in principle possible. Of course not only the survival of the fibre is important but also the optical properties of it need to be considered. Besides some works made by Japanese colleagues (see to mention a few [3,4]) not much can be found in the literature concerning metallic materials with embedded optical fibres. Restricting again our attention to specific works performed in Italy, we can start with Ref. [5] in which an aluminium coated optical fibre was successfully embedded into an aluminium alloy using casting. This work in spite of its simplicity was fundamental to the future development of this field of research since it proved the survival of the fibre, and its unmodified capability of transmitting light. In Fig. 1 is reported a Scanning Electron Microscope (SEM) micrograph of a longitudinal section. It is clear that the contact with the liquid aluminium alloy at about 750 °C did not change the characteristics of the fibre and that the bonding between the silica fibre and the metal alloy was excellent. A further step forward was necessary to verify the measurement capability of the embedded optical fibre. To this end a cooperative effort

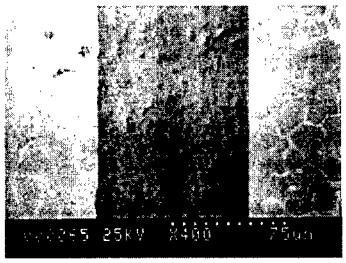

Fig. 1 SEM micrograph of optical fibre embedded into an Al alloy.

between the Aerospace and the Metallurgy Departments of "La Sapienza" University and the ENEA research center in Frascati led to the results described in Refs. [6,7]. In those papers is described a Michelson interferometer (Fig. 2) one arm of which was constituted by an aluminium alloy specimen with an embedded aluminium coated optical fibre. When heated, the speci-

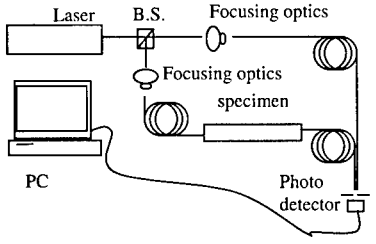

Fig. 2 Michelson interferometer.

men expanded causing a variation in the optical path of the probe arm of the interferometer and consequently a shifting of the fringe pattern. Specifically an expansion of the specimen corresponding to one wavelength (about 0.5 μm) causes a shift of one fringe. By comparing the fringe counting with the temperature obtained by a thermocouple it was possible to establish that the sensitivity of the interferometer was about 0.5 °C/fringe, but above all that the embedding process by casting an aluminium alloy at 750 °C did not spoil the measurement capabilities of the optical fibre. However the fringes obtained by the interferometer were not regular, i.e., they were characterized by several patches each of which with a differently oriented fringe patterns. It was clear, later on, the cause being the core diameter of the optical fibre used. In fact the only aluminium coated optical fibre commercially available were the multi-mode optical fibre with core diameter of 100 μm while the best suited core dimensions for strain measurements are lower than 10 μm. This last consideration led the research group to consider the use of single-mode optical fibre with either acrylate or polyimide coating, the only commercially available at low cost. Differently from the acrylate, the polyimide coating displayed good resistance at the contact with the molten metal but the cracking (i.e., gas formation from the organic material) of tiny portions of the resin, resulted in a poor fibre/metal interface [7]. The only feasible approach was then to remove the coating in the portion of the fibre to be embedded. The elimination of the polyimide is not easily achievable [7] and consequently the best approach was to remove the acrylate coating as shown in Fig. 3. The removal could be performed either mechanically using a stripper or chemically by immerging for few seconds the fibre into dichloromethane (CH_2Cl_2). This approach has been followed for the realization of zinc alloy specimens used for the dynamic tests described in the next section. In Fig. 4. a

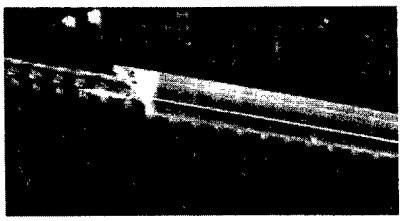

Fig. 3 Optical fibre with partly removed acrylate coating.

SEM micrograph of a longitudinal and a transversal section of a trial specimen is reported. Optimal interface and bonding has

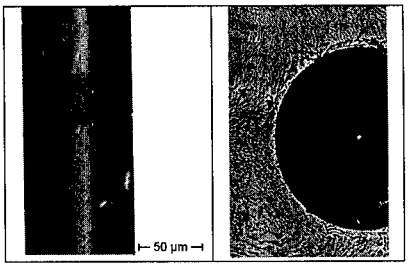

Fig. 4 SEM micrograph of stripped optical fibre embedded into a Zn-Al alloy.

been achieved. Special care has been devoted at the ingress/egress from the specimen. In fact it is well known that those areas are particularly prone to breakage. This weakness is exalted because the protecting coating has to be removed from the fibre. The idea of using cylindrical steel guides in those critical areas is twofold (Fig. 5). Firstly the coating could be maintained in correspondence of the guide because this one prevent the contact with the molten metal. Secondly the guide does not allow

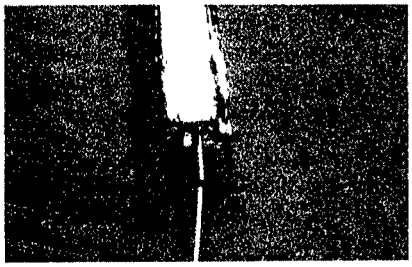

Fig. 5 Detail of cylindrical steel guide and optical fibre.

bending of the fibre right at the ingress and egress from the specimen.

Dynamic Tests Using Embedded Optical Fibres

One of the most important objective of researches concerning fibre optic smart structures is that one of realizing a structural health monitoring system. One way of achieving that is to determine the dynamic characteristics of the structure and following their evolution during service. This approach is studied by many researchers that work out the dynamic characteristics of a structure by using the structural responses gained by accelerometers or scanning laser vibrometers. Usually they try to identify the structures by modal parameters and possibly to pin point damages through the variation of natural frequencies and mode shapes and ultimately even determine the spatial matrices (mass, stiffness and possibly damping matrices). This is a very complex inverse problem that is still far from being completely solved. At the other extreme we have the much simpler problem of determining whether the structure need some inspection or not. In other words instead of trying to identify position and entity of damage one can limit himself to determine if the structure is damaged or not. In Ref. [8] a Zn-Al slender bar with an embedded optical fibre has been inserted into an interferometer similar to that one reported in Fig. 2 and forced to vibrate at given frequencies. The response was observed through the signal of the Photo-detector (PD) sent to a digital oscilloscope. This test was only preliminary to a more significant experiment just conducted and that is described next. In Ref. [9] a broad band test has been performed using the set-up reported in Fig. 6. The cantilever bar is visible in the bottom part of the picture near the impact hammer.

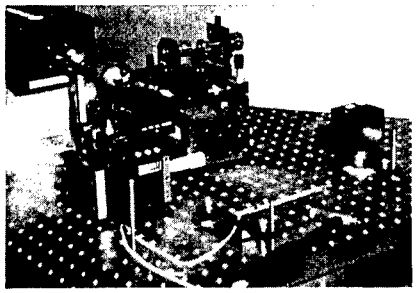

Fig. 6 Setup for Michelson interferometer and broad band test.

The structure is hit with an instrumented impact hammer and consequently, theoretically, excited at all frequencies. In practice, depending on the hardness of the hammer tip mounted, the frequency range of the excitation can be between few hundreds Hz up to 2000 Hz. The vibration of the bar causes a variation of the optical path of the probe arm and ultimately of the amount of light reaching the PD. The signal is then sent to a Fast Fourier Transform (FFT) analyser. In Fig. 7 is reported the Power Spectral Density (PSD) in the range 150-250 Hz obtained by applying a zoom factor to the base band. The curve reported (bottom of figure) is strictly connected to the Frequency Response Function (FRF) of the structure because, as said, the excitation, at least in principle, is a horizontal line in the frequency domain (top of figure).

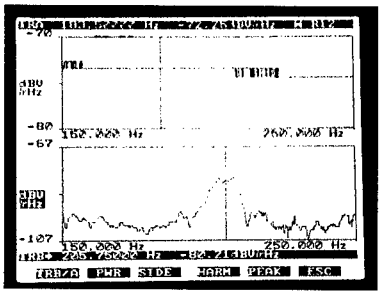

Fig. 7 PSD of hammer excitation (top) and of response by the interferometer (bottom).

The FRF is a good example of a signature of a structure: in fact a damage induce changes in stiffness and/or mass and consequently on the dynamic characteristics represented by the abovementioned FRF. The use of a sensorless optical fibre in conjunction with an interferometer allows, as just shown, acquisition of the global dynamic properties of a structure but is not suitable to perform an experimental modal analysis. To overcome this limitation it is necessary to acquire point measurements. To this end, right at this conference we are presenting another paper in which the static and the dynamic (forced sinusoidal), responses of a Fibre Bragg Grating (FBG) embedded into a Zn-Al bar are measured. This has to be considered a first step before an actual modal analysis could be performed using several sensors multiplexed on different embedded fibres.

High Temperature Applications

Our research group is involved in the study concerning an intelligent thermal protection system for space vehicles [10]. It is known that a significant portion of the launch cost of a reusable launch vehicle is due to the monitoring. The introduction of automated health monitoring systems and in particular of structural health monitoring system could be the key for reducing the cost of access to space. Preliminary tests for embedding optical fibres into a ceramic thermal protection system by the High Velocity Oxy Fuel (HVOF) technique were satisfactory. Particular care was needed to maintain the fibres in place on the aluminium substrate during the deposition process.

Fibre Optic Sensors

An interesting sensor for smart manufacturing applications has been developed by an interdisciplinary group located in Naples and surroundings. The group is constituted by the Departments of Electronic Engineering of the Universities of Naples and Sannio, the Institute of Composite Materials Technology and the Italian Aerospace Research Center. In [11] is proposed the use of an in fibre sensor for refractive index measurements. The refractive index is in fact related to the degree of cure in a thermoset-based composite. Preliminary tests, useful for designing the fibre optic sensor, [12,13] have been conducted on a resin bath by measuring, through a CCD camera, the angle variation of a laser light emerging from the resin, induced by both isothermal and actual curing cycles. The sensor is realized into a step-index single mode fibre. When the infrared (1310nm) light of a laser diode is launched into the embedded fibre, at the interface between the fibre end and the resin there is a reflection which is a function of the two refractive indices (of the fibre core and the resin). The power collected by the PD is therefore related to the degree of cure of the resin. To improve the signal to noise ratio the laser diode is modulated in amplitude while the signal from the PD is analysed by a lock-in amplifier. The integration within the same fibre of a reflectometric sensor and FBGs has been experimented by the same group in Ref. [14]. The use of couples of practically

co-located FBGs could allow the independent measurement of temperature and strain during operation of the structure. The reflected signals are separated by the coupler and processed, for the reflectometer and for the FBGs, according to the synchronous detection just described and with two demodulation techniques respectively (Fig. 8).

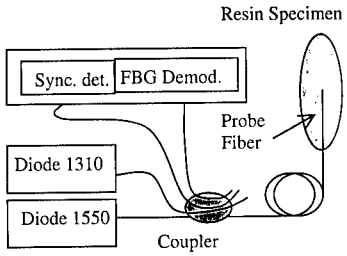

Fig. 8 Optoelectronic set up for FBGs and degree of cure sensor.

The two techniques just mentioned use either a broadband Bragg grating and a narrowband laser source or inversely a narrowband Bragg grating and a broadband (typically 50 nm) source. Both techniques are intensity based, i.e., they convert the wavelength shift into an intensity variation. Another group constituted by the Institute for Research on Mechanical Technology and Automation (RTM) located in Vico Canavese near Turin and the Research Institute on Electromagnetic Waves (IROE) in Firenze are involved in the manufacturing of Bragg gratings to be used for automotive application. In Fig. 9 is reported a windshield instrumented with couples of FBGs (one sensor only in thermal contact to perform temperature compensation). The interrogation system is designed to work at high frequency (few kHz). The group is also working on the manufacturing of FBGs with the phase mask technique exposing the germanium doped optical fibres at the UV

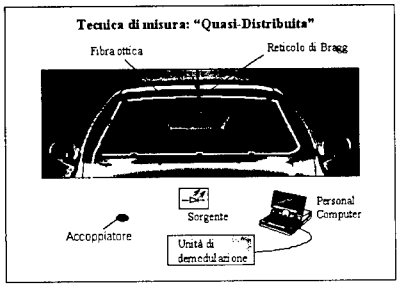

Fig. 9 FBGs used for car windshield health monitoring.

light emitted by an eccimer KrF laser. The fluency were of about 400 mJ/cm^2 per pulse with a repetition rate of 100Hz. In Fig. 10 is reported the experimental set-up for writing the FBGs. An Optical Spectrum Analyser (OSA) observe in real time the transmitted light. By properly pulling the optical fibre during the exposure it is possible to write FBGs with different Bragg wavelength within the same fibre.

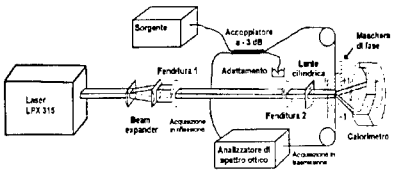

Fig. 10 Set up for FBGs' manufacturing.

European Programs

The interest for smart materials and in particular for structural health monitoring in Europe is witnessed by the regularly organized European conferences on smart structures and materials and by the newly developed conferences such as the First European Workshop on Structural Health Monitoring to be held next year at Cachan near Paris and the first MUltifunction

SEnsors for structural health monitoring in Aerospace Structures (MUSEAS 1) to be held at CIRA in Capua, Italy. As observed in [16] the majority of the papers presented at the conferences mentioned at the beginning of the paragraph were at least partly devoted to fibre optic systems. In Europe the integration between member states is not completely achieved and therefore national programs support researchers in the single states. That is the case of all the Italian research programs presented in this paper which were principally supported by the Italian Ministry of the University and of the Scientific and Technological Research (MURST) and the Italian Space Agency (ASI). However there are collections of projects, that involve the use of fibre optic sensor technology, financed by the European Economic Community (EEC) under various forms. Most of the following information has been retrieved by consulting the COmmunity Research and Development Information Service (CORDIS). In what follows it will be briefly mentioned the more recent European projects that involve fibre optic sensor technology. Starting with the 3rd Framework Program under program BRITE/EURAM 2, we would like to mention the project: FORMS *Distributed strain monitoring on high temperature pipework.* 8 partners (1 of which Italian) were involved. End date was Aug. 1998. The acronym meaning is: Fibre Optics for Remote Monitoring of Structural integrity at elevated temperature insulated Systems. The objective was to use optical fibres to measure the strain because they are capable to withstand the harsh environment typical of pipework in production plants. Furthermore minimal cabling is achievable. Within the 4th Framework Program under program BRITE/EURAM 3 we found the following four projects reported in chronological order:

MONITOR *Monitoring On-line Integrated Technologies for Operational Reliability.* 11 partners (1 of which Italian) were involved. End date: July 1999. The objective is to use on-line monitoring to achieve a reduction in classical inspection of aircrafts of at least 20% within 5 years from completion of the project.

FOSMET (acronym not officially registered on CORDIS database) *Fibre Optic Strain Monitoring at Elevated Temperatures.* 9 partners (1 of which Italian) were involved. End date: Dec. 1999. The objectives is somehow related to those of FORMS. In particular armoured high temperature cabling and methods for sensor attachment to components have been developed.

DAMASCOS *Damage Assessment in Smart Composite Structures.* 6 partners (2 of which Italian) were involved. End date Feb. 2001. The objectives of the project were to perform damage and ageing assessment for large area composite structures. The scattering of ultrasonic waves, induced by damage, are obtained by piezoelectric elements exciting the structure at relatively low frequency (100-500kHz). The sensors can be either optical fibre and/or piezoelectric elements.

AMADEUS *Structures accurate modelling and damage detection in high safety and cost structures.* 6 partners (2 of which Italian) were involved. End date: Aug. 2001. The objective is to realize an autonomous PC based expert system for on site structural health monitoring for structures ranging from highway bridges to spacecraft antennas.

All the above projects have been financed according to contract type CSC (Cost-sharing contracts). Within the 5th Framework program (FP5), that covers the period 1998-2002, has been introduced a new form of contract type called Exploratory award. This is granted to Small and Medium Enterprises (SME) to cover part of the costs of preparing a complete step 2 proposal for submission to one of the Research and Technological Development (RTD) programmes. As examples we have

found in the CORDIS database within the program GROWTH (one of the four thematic programmes of FP5) the following proposals:

Fibre optic cables for temperature monitoring. 2 partners were involved. End date: Apr. 2000. The telecommunication optical fibres are bend sensitive, characterized by graded index and not optimised for sensing. In this program it is proposed to develop specific step index optical fibres and protecting cables with efficient heat transfer towards the optical fibre.

Fibre optic sensors for the monitoring of composites strengthened structures. 2 partners (1 of which Italian). The use of external composite laminates with embedded fibre optic sensors as reinforcement on concrete structures is proposed as opposed to the conventional steel plate.

Another contract type provided by the European community is the RGI (Research Grants – Individual fellowship). The grant is provided under the program TMR (Train and Mobility of Researchers). Within this context and in the field of fibre optic smart structures we have found the following project: *Health and usage monitoring of aerospace structures using optical fibre Bragg grating sensors*. 2 partners involved. End date: June 1999. Among the objectives there are the study of the temperature-strain separation techniques under embedded conditions and the investigation of temperature-strain cross-sensitivity.

Acknowledgments

The author wish to thank Dr. Calabro' of the Italian Aerospace Research Center (CIRA) in Capua, Prof. Cusano of the Department of Electronic Engineering of the Univ. of Naples, Dr. Giordano of the Institute of Composite Materials Technology of Naples, and Dr. Castelli of the Institute for Research on Mechanical Technology and Automation (RTM) for the important information provided, essential for giving a complete picture of the Italian state of the art on fibre optic smart structure applications.

References

1. A. Paolozzi, M.A. Caponero, F. Cassese, M. Leonardi: Proc. of 17th Int. Modal Analysis Conf. (IMAC), 699 (1999).
2. A. Paolozzi, M. Ivagnes, U. Lecci: Proc. of 2nd Int. Workshop on Structural Health Monitoring, 661 (1999).
3. H. Asanuma, K. Ichikawa, T. K. Kishi: J. of Intelligent Material System and Structures, 7, 301 (1996).
4. O. Haga, H. Asanuma, H. Koyama: Advanced Composite Materials, 7(3), 239 (1998).
5. A. Paolozzi, F. Felli, A. Brotzu: Proc. of PACAM VI/DINAME 99, 639 (1999).
6. A. Paolozzi, F. Felli, M.A. Caponero: Proc. of 2nd Int. Workshop on Structural Health Monitoring, 257 (1999).
7. F. Felli, A. Paolozzi, M.A. Caponero: Aluminum Transaction, 2(2), 189 (2000).
8. M.A. Caponero, F. Felli, A. Paolozzi, I. Peroni: SPIE Symposium on Smart Materials, 4234, 152 (2000).
9. A. Paolozzi, F. Felli, Proc. 16th AIDAA Italian Congress, (2001)
10. A. Paolozzi, F. Felli, T. Valente, M.A. Caponero, M. Tului: SPIE Symposium on Smart Material, 4234, 160 (2000).
11. A. Cusano, G. Breglio, M. Giordano, A. Calabro', A. Cutolo, L. Nicolais: J. Opt. A: Pure Appl. Opt., 3, 1 (2001).
12. A. Cusano et al.: Appl. Opt., 37, 1130 (2000).
13. A. Cusano et al.: Sensors Actuators, 84, 270 (2000).
14. A. Cusano et al.: Proc. IEEE/ASME, Int. Conf. on Advanced Intelligent Mechatronics, 401 (2001).
15. R. Falciai, M.A. Forastiere, S. Pelli, G.C. Righini, P. Castelli, P. Giocosa, Proc. Int. Conf. on Fiber Optic & Photonics, 1085 (1998).
16. P.D. Foote, Proc. 2nd Int. Workshop on Structural Health Monitoring, 24 (1999).

Proceedings of 7th Japan International SAMPE
Symposium & Exhibition, Nov. 13-16, 2001

Smart Materials and Structures at EADS Corporate Research Center: An overview

Jordi SANIGER*, Benoît PETITJEAN

* EADS Corporate Research Center
12, rue Pasteur 92152 , Suresnes Cedex -FRANCE
Email:jordi.saniger@eads.net

Abstract

In order to provide the strategic needs for EADS products, the Corporate Research Centre has early developed an activity in the field of Smart Materials and Structures. EADS CCR has developed several technological demonstrators to assess the impact of such technologies on EADS products.

First, the Smart Materials and Structures activity will be briefly described and some of its applications as high accuracy positioning system, development and integration of an active flap actuation system into a full scale rotor blade, development of isolation systems for electronic devices in harsh vibrating environment, or in-flight testing of health monitoring devices and involvement on other programs.

Sensors and actuators integration into real structures will also be introduced, taking into account industrial constraints such as cost, mass, power or compatibility with current manufacturing processes.

Main research priorities will be pointed out to conclude the paper.

Key Words: Smart Materials, composite structures, aerospace applications.

Introduction

Over the last years a considerable development in the field of smart materials and structures has been achieved. The main goal is to obtain a high degree of integration on the functions achieved by a structure.

One of the obvious areas of application is aerospace products, regarding its needs of performance, reliability and weight reduction. The presently developed smart structures are mainly performance or functionality oriented. Thus, the research is carried out on a demonstrator basis for feasibility assessment. Manufacturing and economic impact have also been studied in some particular cases to evaluate the potential benefit of these technologies.

The Multifunctional Structures Laboratory at EADS CCR has been working in the last decade addressing several technological problems on active control of sound and vibration, structural health monitoring and shape control. The different projects have been performed taking into account the industrial requirements and with close cooperation of the different EADS Business Units. In order to fulfill the requirements of the projects, an integrated systems approach in the design of the demonstrators has been followed.

Structural Health Monitoring

Structural health monitoring is a

methodology to cope with the aging of structures or its reliability facing damages produced by accident or under severe environments. Optimization of the maintenance costs and increased safety are the main addressed objectives.

The current projects at the Multifunctional Structures Laboratory addressed the following issues:

- Embedding technologies and methods.
- Damage assessment algorithms.
- Sensor placement methods
- Materials behavior under damage

Two main concepts were investigated for damage assessment: optical fibers and acoustic emission sensors.

SHM based on Fiber Optic Sensors

Optical fiber sensors have been used for damage assessment on composite structures. A demonstrator was manufactured based on bi-refringent fibers. Embedding procedures were studied to establish an appropriate fiber path a carbon fiber composite structure. Different types of fibers were investigated in order to select the most adapted. Strain measures were performed in static and fatigue (0.3% and –0.1%). The concept was based on the damaging of fiber due to an impact and the change on the fiber properties.

Several problems arose while implementing the demonstrator. Connectors were difficult to manufacture due to fiber assembly problems. Also the fiber high price showed that it was too expensive for some applications. The embedding procedure was assessed but the stability of the equipment on an airborne acquisition system was a major issue.

Fig.1 Optical fibers embedded on a representative aerospace structure.

SHM based on Acoustic Emission

Monitoring concepts based on acoustic emission have been studied. Structures emit waves under load produced by an impact or while a crack is developing. This phenomenon known as acoustic emission encompasses different classes of waves travelling through the material. The technique consists in the sensing, acquisition and processing of this data in order to assess the damages on a structure.

The different steps to develop such a system started with a BRITE-EURAM program where an available AE commercial system with its sensors was tested in flight.

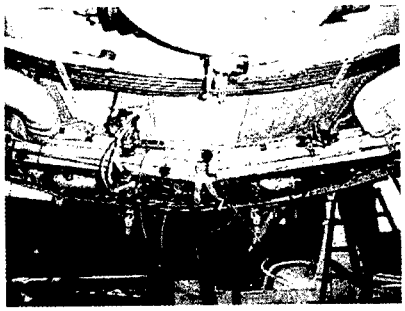

Fig.2 Aircraft aft fuselage with AE sensors (red circular spots)

The research proved that the AE system could detect pulses sent at different flight regimes and could discriminate the background noise due to the different.

This results showed that the AE technique allowed to monitor wide areas on

aircraft structure without altering the structure's configuration. Due to the dynamic character of AE, it is adapted to monitor impact of crack propagation. To optimize the number of sensors necessary for a wide area while ensuring an effective visual inspection of the structure, damage localization procedures must be developed. Classical algorithms and methodologies for damage detection were not adapted as they assumed that the structure was flat and with an isotropic behavior. However, composites structures present usually a high anisotropy. Therefore, a procedure suited to complex structures (e.g. with stiffeners) is necessary in order to develop a system for a real aircraft environment.

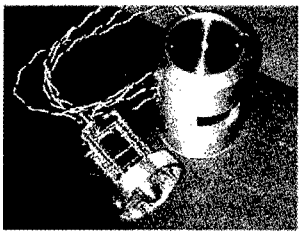

Fig.3 Acoustic Emission impact generator

A cooperation with the RIMCOF Institute of Japan was initiated on this subject. A "learning by experience" system was developed in order to assess the severity and to localize impact on a structure. The procedure was based on the integration of an AE sensors network on a structure. AE stimuli are produced on the structure at some strategic locations to provide a reference behavior. Once the system is on service, it can compare the arrival times of the acoustic wave produced by a real impact to the sensors. The localization is performed with a high degree of accuracy (5% localization error for a CFRP structure of 500 mm length). An electromechanical device was designed and manufactured in order to generate the learning AE waves on the structure.

Active Control of Noise and Vibration

Active Vibration Isolation

One of the major issues in vibration control is the isolation of critical equipment in a harsh environment. The present obsolescence problems on avionics products is a major concern for Air Forces. Research has been conducted in order to provide active systems for vibration isolation of avionics on helicopters. A representative bench was manufactured to test a configuration of four controlled actuators isolating a flexible shelf supporting a dummy avionics rack of 40 kg.

The program is running and an actuator system adapted to the specified requirements for a helicopter has been manufactured. The system is designed to withstand high vibration levels and to reduce acceleration levels from 2.5 g to 0.7 g on the harmonics of the main rotor frequency. Also, shock dimensioning was performed to satisfy crash requirements. Evaluation of the global performances will be carried out by the end of 2001.

Active Rotor - Blade Demonstrator

Reducing the external noise is becoming a major issue for helicopter manufacturers. The idea behind this goal is to reduce or even avoid the blade vortex interaction (BVI), especially during descent and flights over inhabited areas. This can be achieved by changing locally the lift of the blade.

Several strategies to reach this goal were under investigation such as the control of the local incidence of the blade by a direct lift flap.

EADS CCR and EADS Missiles defined, manufactured and tested an electromagnetic actuator system able to answer BVI needs for moving a direct lift flap. The particularity of this actuator is its

ability to apply the required force on the whole stroke range.

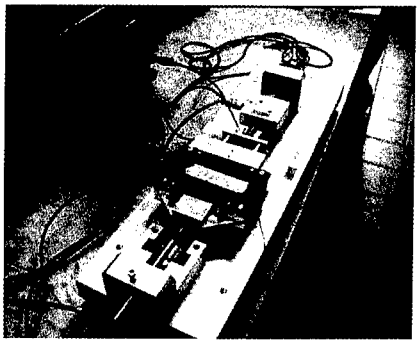

Fig.4 Demonstrator test-bench

The designed flap was integrated on a representative EUROCOPTER DOLPHIN blade section and the actuator system was designed to fit in the available space within the blade. The required stroke and force were achieved over the frequency range of interest.

The system was lab tested on a representative EUROCOPTER test-bed and subjected to realistic mechanical loads. During the static tests a force of 250 N was delivered at 6,5 A, yielding a stroke of ±2 mm and 5° deflection operating at 30 Hz, which suited the specified requirements.

Shape and Position Active Control

Shape and positioning control are critical issues to guarantee a certain behavior under extreme environments. Satellite applications require a high degree of accuracy to ensure their functionally. A study was performed for the positioning of a small reflector on a satellite. A 5 dof. platform demonstrator was manufactured to study the potential of piezoelectric actuators and LVDT sensors to maintain a certain position. The requirements were a precision of 1 µm. The needed voltage was in the order of 35 V for the piezoelectric actuators, for a maximum stroke of 5 µm. The different tested control strategies were PID feedback control, an LQG estimator and an adaptive controller.

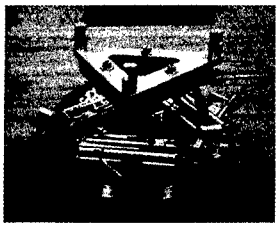

Fig.5 Demonstrator test-bench

Conclusions

EADS is committed to devote a significant research effort on the topic of smart materials and structures. Industrial demonstrators are developed and the main subjects are structural health monitoring, noise and vibration control and shape control. A global system approach allows to include all industrial constraints

References

1. M. Duvernier, L. Reithler, J.Y Guerrero., *"Active Control System for a Rotor Blade Trailing Edge Flap"* SPIE's 7th Annual Smart Structures and Materials. Newport Beach, CA, March 2000.

2. J. Saniger, L. Reithler « Impact assesment and monitoring in composites with acoustic emission sensors : A learning by experience method », Proceedings of smart materials symposium .Tokyo University, December 1999.

3. J. Saniger, L. Reithler: "Structural Health Monitoring Methodology for Aircraft Condition Based Maintenance" SPIE's 8th Annual Smart Structures and Materials. Newport Beach, CA, March 2001

Proceedings of 7th Japan International SAMPE
Symposium & Exhibition, Nov. 13-16, 2001

IMPROVING THE VIBRATION DAMPING OF CFRP BEAM STRUCTURES BY USE OF PIEZOELECTRIC POLYMER/CERAMIC

Toshio Tanimoto
Department of Materials Science & Engineering
Shonan Institute of Technology
Tsujido-Nishikaigan, Fujisawa, Kanagawa 251-8511, Japan
E-mail:tanimoto@mate.shonan-it.ac.jp

ABSTRACT

The optimal design methodology of interleaving and piezoelectric polymer/ceramic for passive vibration damping of CFRP structures is discussed in the present work. An attempt to improve the vibration damping of this material was first performed by introducing polyethylene-based film interlayers between composite plies. It is also shown that the vibration damping of CFRP laminates can be improved passively by use of piezoelectric polymer (PVDF) film interlayers and surface-bonded piezoelectric ceramic PZT sheets. The CFRP beams by use of combined interleaving and surface bonded PZT ceramics is potentially useful for application in structures where light weight and improved vibration damping are desired.

Key Word: CFRP, Vibration Damping, Piezoelectric Materials, Smart Materials

1. INTRODUCTION

Although Carbon fiber-reinforced plastics (CFRP) have a high stiffness and low density, these materials are considered to be unsuitable for low-vibration structures because of their inherent low vibration damping, whose loss factors are 0.001 to 0.005. The authors are interested in two particular methods for improving the vibration damping of CFRP materials: (1) interleaving of visco-elastic plastic films and (2) surface bonded piezoelectric ceramics. The first way improves damping by introducing compliant interlayers between composite plies (Figure 1). The other way is the passive vibration damping of CFRP laminates by use of surface-bonded piezoelectric ceramic PZT sheets (Figure 2). Electrically shunting a piezoelectric ceramics modifies its electrical and mechanical

impedance, and thus leads to a mechanical damping analogous to viscoelastic materials.

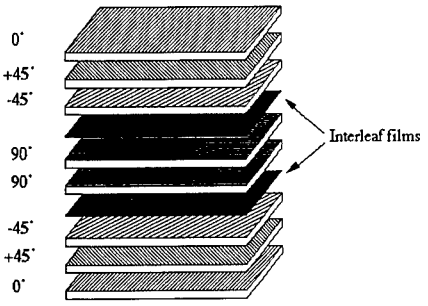

Figure 1 Interleaving concept

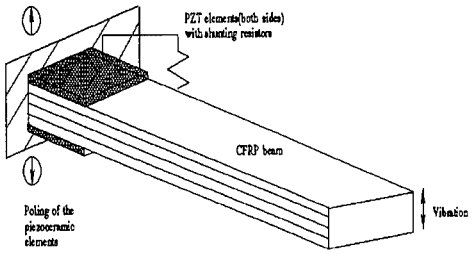

Figure 2 Passive damping by resistively shunted piezoelectric ceramics

The author is also interested in exploring how the interleaved piezoelectric polymer (PVDF) film can work to enhance the vibration damping capability of CFRP beams. From this point of view, this paper deals with the design of damping CFRP beams, by the methods using interleaving of visco-elastic plastic films or piezoelectric polymer (PVDF) film interlayers, and surface bonded piezoelectric ceramics with shunted resistance.

2. SPECIMEN PREPARATION AND EXPERIMENTAL METHOD

Quasi-isotropic [0/±45/90]s and Cross-ply [0°/90°]s cantilever beams were made of T800/2500 unidirectional carbon fiber-reinforced epoxy prepregs (Toray, Japan). The laminates were cured in an autoclave for 3 hours at 130°C and 5bar. The C-82 type piezoelectric ceramic, $PbZrO_3$-$PbTiO_3$ (PZT) elements (Fuji Ceramics) were supplied as sheets measuring 100mm x 15mm x 0.28mm. Cantilever beam tests were carried out on 90mm long and 15mm wide plates, with the surface fiber orientation parallel to the long axis of the beam. The piezoelectric ceramic sheets were cut into the 10mm length and the capacitance of the individual sheets was measured. The piezoelectric ceramics were poled through the thickness. The poling direction of the mounted elements is oriented to the outside of a beam. The outside surface of the piezoelectric ceramic sheets was coasted with a conductive silver paint to form the positive electrodes, and the shunting resistance was connected across these electrodes, as shown by the arrow in Figure 2. The vibration excitation force was applied by means of a magnetic transducer (MM0002; B&K) driving a thin, 0.17 mm steel disk bonded to the beam tip. The beam response was measured using a capacitive transducer (MM0004; B&K). A random, white noise vibration was used as driving signal. The response of the beam for the first four modes was measured at the mid-length and analyzed using a Brüel&Kjær Type 3550 dynamic signal analyzer. The loss factor was determined from the vibration curve decay.

3. EXPERIMENTAL RESULTS AND DISCUSSION

3.1 Passive Damping by Resistively Shunted Piezoelectric Ceramic Sheets

The stiffness of the piezoelectric ceramics, similarly to a viscoelastic material, can be expressed as a frequency dependent modulus and loss factor. The maximum loss factor of a resistively shunted PZT element is [1]:

$$\eta_{max} = \frac{k_{31}^2}{2\sqrt{1-k_{31}^2}} \qquad (1)$$

at a non-dimensional frequency $\rho = RCp(1-k_{31}^2)\omega = \sqrt{1-k_{31}^2}$, where k_{31} is the coupling coefficient, and Cp is the inherent capacitance of the piezoelectric ceramics. For a natural vibration frequency ω, the optimal resistance is thus given by:

$$R_{opt} = \frac{1}{C_p\omega\sqrt{1-k_{31}^2}} \qquad (2)$$

When the piezoceramic is mechanically coupled to the CFRP beam, the optimal resistance is calculated in the same way, but the overall damping is approximated by the average of the CFRP and PZT loss factors weighted by the proportion of strain energy U in them [1]:

$$\eta_{beam} = (\eta_{CFRP}U_{CFRP} + \eta_{PZT}U_{PZT})/(U_{CFRP} + U_{PZT}) \qquad (3)$$

The PZT elements are thus used most effectively in the locations of highest beam curvature [2].

3.2 Interleaving and Resistively Shunted Piezoelectric Ceramics

Four different laminates were prepared for this study. Laminate types, with the **I** showing the location of interleaf, can be distinguished in the following way: (1) $[0°/+45°/-45°/90°]_S$, (2) $[0°/+45°/-45°/\mathbf{I}/90°]_S$, (3) $[0°/+45°/-45°/90°]_S$ with bonded PZT, (4) $[0°/+45°/-45°/\mathbf{I}/90°]_S$ with bonded PZT. The 10mm long PZT sheets were bonded onto the location near the root of CFRP cantilever beams with or without interleaf films (see Figure 2). The cantilever beam vibration tests were performed on these laminates and the first-mode resonant frequency and loss factors were measured and results are summarized in Table 1. Both the interleaving ($[0°/+45°/-45°/\mathbf{I}/90°]_S$) and bonded piezoelectric ceramics ($[0°/+45°/-45°/90°]_S$ with bonded PZT) improved vibration damping in comparison with conventional CFRP laminates ($[0°/+45°/-45°/90°]_S$). In addition to this, by combining the interleaving and surface bonded PZT ceramics ($[0°/+45°/-45°/\mathbf{I}/90°]_S$ with bonded PZT), joint effect of both methods has been achieved for the vibration damping of CFRP laminates. The loss factor of $[0°/+45°/-45°/\mathbf{I}/90°]_S$ with bonded PZT was about 6.3 times higher in the first mode of vibration than that for the conventional laminate, $[0°/+45°/-45°/90°]_S$.

Table 1 Loss factor values for the variaus CFRP beams

Beam description	Loss factor
[0° /+45° /-45° /90°]s	0.00193
[0° /+45° /-45° /**I**/90°]s	0.00302
[0° /+45° /-45° /90°]s with bonded PZT	0.00953
[0° /+45° /-45° /**I**/90°]s with bonded PZT	0.01231

3.3 Passive Damping by Use of Piezoelectric Polymer (PVDF) Film Interlayers and Surface Bonded Piezoelectric Ceramics

In this section, the passive damping by use of piezoelectric polymer (PVDF) film interlayers and surface bonded piezoelectric ceramics is discussed. The PVDF films of 10mm long are incorporated at the interlayers near the root of 70mm long cantilever beam. Four different laminates were prepared for this study. Laminate types, with the **P** showing the location of interleaved PVDF film, can be distinguished in the following way: (1)[0°/90°/90°/0°], (2)[0°/90°/90°/0°] with bonded PZT, (3)[0°/90°/**P**/90°/0°], and (4)[0°/90°/**P**/90°/0°] with bonded PZT. As shown in Figure 3, the interleaved CFRP/PVDF laminate ([0°/90°/**P**/90°/0°]) as well as [0°/90°/90°/0°] with bonded PZT remarkably improved vibration damping in comparison with conventional CFRP laminates, ([0°/90°/90°/0°]).

By combining the interleaving of PVDF films and surface bonded PZT ceramics ([0°/90°/**P**/90°/0°] with bonded PZT), the vibration damping of CFRP laminates were furthermore improved for the higher resonance modes. The loss factor values of cross-ply laminates with piezoelectric polymer/ceramics were higher in every mode of vibration than that for the conventional laminate.

4. CONCLUSIONS

This paper examined the potential of improving the vibration damping of CFRP laminates by the methods using interleaving of visco-elastic plastic films and piezoelectric polymer (PVDF) film interlayers, and surface bonded piezoelectric ceramics. The vibration damping of the CFRP beam was significantly improved at the optimal shunting resistance, which can be predicted theoretically. It was shown that the methods discussed here could be potentially useful for designing low vibration structures with lightweight. This type of beam is suitable for application in structures where lightweight and improved vibration damping are desired, such as low-vibration spacecraft structures [3].

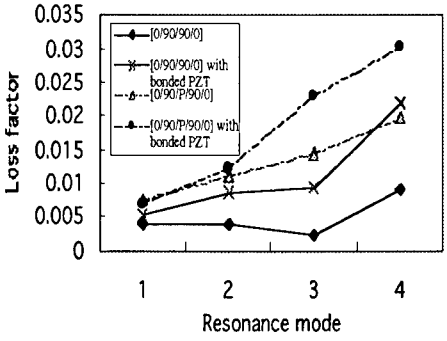

Figure 3 Loss factor vs. resonance mode for various damping CFRP beams

5. REFERENCES

1. N.W. Hagood and A. von Flotow: J.Sound & Vibration 146 (1992) No.2, 185.
2. T. Tanimoto, K. Horiuchi and K. Uchino: Jpn. J.Appl. Phys. 36 (1997) Part 1, No.9B, 6110.
3. T. Tanimoto: Proc. SAMPE 2000 (2000) 645.

Proceedings of 7th Japan International SAMPE
Symposium & Exhibition, Nov. 13-16, 2001

Cyclic Mechanical Behavior of Composites Based on Shape Memory Polymer

Qing-Qing Ni, Takeru Ohki, Norihito Ohsako and Masaharu Iwamoto

Division of Advanced Fibro-Science, Kyoto Institute of Technology,
Matsugasaki, Sakyo-ku, Kyoto 606-8585, Japan
E-mail: nqq@ipc.kit.ac.jp

Abstract

Recently, shape memory polymer as one of functional materials has received much attention and its mechanical properties have been investigated. Shape memory polymer of polyurethane series has the glass transition temperature (Tg) around the room temperature. Based on the large change in modulus of elasticity above and below Tg, the material has excellent shape memory property. In this study, for the wider applications in the field of industry, medical treatment, welfare and daily life, the glass fiber reinforced shape memory polymer was developed. The specimens with different fiber weight fractions, which are SMP bulk, 10wt%, 20wt%, and 30wt%, were prepared, and their mechanical properties were investigated experimentally. Then, the influence of fiber weight fraction on the shape memory polymer was evaluated. It was found that mechanical properties of the shape memory polymer based composites heavily depend on both thermal effects and the fiber weight fraction.

Key words : Shape memory polymer, Fiber weight fraction, Mechanical property

INTRODUCTION

Shape memory materials have received much attention in industries and the other fields, particularly for Shape Memory Alloys (SMAs) that are a group of metallic alloy and exhibit a shape memory effect. On the other hand, Shape Memory Polymers (SMPs) are a group of functional polymer that also has a shape memory effect, i.e., a shape memory polymer deformed at a low temperature will regain its original undeformed shape when heated to a higher temperature. Compared with SMAs, SMPs have the advantages, such as lightweight, large recovery ability, superior processability and lower cost. This means that SMPs may also be used as temperature sensor or actuator.

In the SMPs, the polyurethane series has following advantages: the forming processes for other thermoplastic polymer can still be used; the shape recovery temperature, i.e. Tg, can be set at any value within $\pm$ 50K around the room temperature; there exist the large differences of mechanical properties, optical property and water vapor permeability between temperatures above and below Tg. Based on these advantages, the SMP of polyurethane series will have wider applications in the field of industry, medical treatment, welfare and daily life. However, since the strength of the SMP of the polyurethane bulk is low, the use of the materials is quite limited.

The purpose of this study is to investigate the influence of fiber weight fraction on the mechanical properties of shape memory polymer based composites. The materials developed here were the glass fiber rein-

forced SMP of the polyurethane series with different fiber weight fractions and thermo -mechanical characteristics. The mechanical properties of the GFR-SMP composites with different fiber weight fractions (SMP bulk, 10wt%, 20wt%, 30wt%) were evaluated in static tensile test. Then, for the practical use, cyclic tests were performed at room temperature (Tg-20K) and the mechanical properties of specimens with and/or without thermal treatment after cyclic tests were also investigated.

EXPERIMENTAL WORK

Fabrication of Specimens

For the matrix of developed materials, two series of polyurethane SMPs were used, in which one is of higher elasticity (HE) and the other is of lower elasticity (LE) when the temperature is above Tg. For both materials, Tg was about 318K. As the reinforcement, chopped strand glass fibers with fiber length of 3mm were used. In this manuscript, the results of HE-SMP based composites were related.

The matrix and reinforcements were compounded by the twin screw extruder (LABOTEX-300, produced by JAPAN STEEL WORKS Co., Ltd). Cylinder temperature was 483K and screw rotation was 200rpm. The fiber weight fractions were SMP bulk, 10wt%, 20wt% and 30wt%. Dumbbell type specimens were fabricated by an inline screw type of injection molding machine (Plaster Ti-30F6, produced by TOYO MACHINERY and METAL Co., Ltd.) after enough drying of compounded materials at 353K. The fabricated specimens are non-weld. The processing conditions of cylinder temperature, the mold temperature was, and the injection speed were 483K, 303K and 27.4 cm^3/sec, respectively.

Experimental Procedure

The experimental equipment used in this study was an Instoron Universal Testing Instrument (Type 4466) with a temperature-controlled chamber.

Heating or cooling of specimens was controlled by compressed and heated or cooled air. The temperature was measured by a thermocouple near the specimen.

Tensile test

The static tensile test was performed in the temperature-controlled chamber with cross head speed of 5mm/min. Testing temperature was 298K(Tg-20K).

The strain was calculated by the ratios of the elongation obtained by the cross-head displacement to the span length (60mm) with a maximum of 300%.

Load cycle test

The load cycle test was performed in temperature-controlled chamber between zero and a fixed stress with cross head speed of 5mm/min. For the fixed stress, 50% value of the maximum stress determined by a tensile test was adopted. In order to investigate the influence of cyclic history on mechanical properties, the cyclic loading were interrupted at 20, 40 and 60 cycles and the specimen was removed, and then kept at 338K (Tg+20K) for 1 hour and at 298K (Tg-20K) for 1 hour for thermal treatment. After that, a tensile test was performed for each specimen. As a comparison, the specimens that were kept at 298K (Tg-20K) for 2 hours after cyclic loading were prepared and investigated.

RESULTS AND DISCUSSIONS

Tensile property

In calculation of the experimental data, the engineering stress and strain were used. Figure 1 shows the stress-strain curves for the HE specimen.

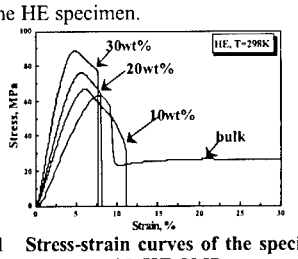

Fig.1 Stress-strain curves of the specimens with HE-SMP

When the temperature was at T=298K(Tg-20K), the 10wt%, 20wt% and 30wt% specimens had small fracture strain, while the bulk specimen was of a upper yielding point and could not fracture within the strain range of 300%. A yielding phenomenon for these specimens was observed due to occurrence and growth of local necking during testing.

Figure 2 shows the relationship between temperature and Young's modulus. Although it is considered that more tests near Tg were necessary, a large change above and below Tg for Young's modulus was thoroughly observed. A key point for shape memory effects of SMPs is how to utilize and control the above variation.

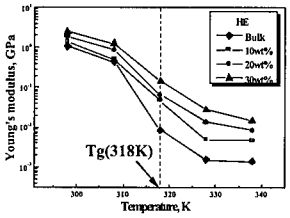

Fig.2 The relationship between temperature and Young's modulus

According to the results of the static tensile test, it was evident that the strength of the developed composites with high fiber weight fraction would increase greatly. They are of high Young's modulus and high yield stress at low temperature, but small resistance against deformation at high temperature. This means that the large change of Young's modulus above and below Tg in the developed SMP composites will exhibit shape memory effects.

Load cycle property

In a similar way to the tensile test, the engineering stress and strain were used in calculation of the experimental data. Figure 3 shows the results of cyclic test interrupted at 40 cycles as the representative stress-strain curves of the HE specimen.

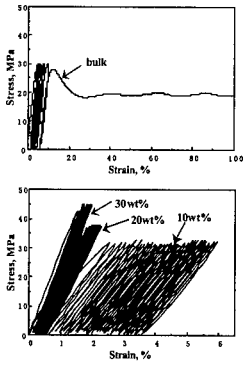

Fig.3 The stress-strain curves of specimens with the HE-SMP interrupted at 40 cycles

The HE bulk specimen yielded before the cycle number reached to the prescribed number of cycles (20, 40, 60 cycles) as shown in Fig.7 (a). In Fig.7 (b), 10wt% specimen indicated large residual strain at each cycle in comparison with 20wt% and 30wt% specimens, so that it is considered that cyclic behavior with 10wt% of fiber weight fraction was influenced greatly by matrix resin. However, 10wt% specimen resisted to 60 cycles and this indicated that the reinforcement worked well for the improvement of the property under cyclic loading. In the 20wt% and 30wt% specimens, although the residual strain had about 0.15% at the first cycle, after that the accumulative strain did not increase at each cycle. In the tests interrupted at 60 cycles, the final residual strain in 20wt% and 30wt% specimens was only about 0.5%.

Figure 4 shows stress-strain curves of the HE specimen after 40 cycles.

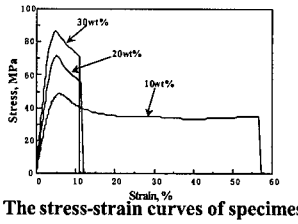

Fig.4 The stress-strain curves of specimes with the HE-SMP after cyclic loading

The HE bulk specimen yielded before number of cycles reach to prescribed number of cycles (20, 40, 60 cycles), so that the stress-strain curve could not be obtained. In the specimen with HE-SMP, fracture strains were slightly larger than those in tensile tests (Fig.2, T=298K). The declines of maximum stress from the specimens without the history of cyclic loading decreased with the increment of fiber weight fraction. Namely, the declines of maximum stress increased with the increment of matrix resin. Accordingly, it is considered that HE-SMP has low resistance to the cyclic loading.

Figure 5 shows stress-strain curves of the HE specimen after 40 cycles and thermal treatment.

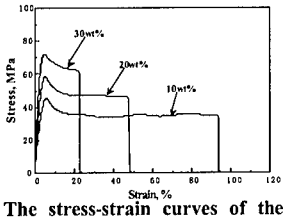

Fig.5 The stress-strain curves of the HE specimen after cyclic loading and thermal treatment

As a result of thermal treatment, the maximum stress in HE specimens with thermal treatment had lower values than without thermal treatment. However, fracture strains remarkably increased in all specimens. These results were also confirmed in the case of the specimens after 20 cycles and 60 cycles with thermal treatment. Fracture strain of 10wt%, 20wt% and 30wt% specimen after cyclic loading were shown in Fig.6.

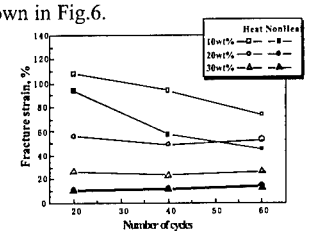

Fig.6 The fracture strain of specimens with HE-SMP after cyclic loading

Fracture strain of specimen with thermal treatment indicated higher value in comparison to specimens without thermal treatment for any fiber weight fraction. Although the maximum stress decreased as a result of thermal treatment, an improvement of resistance to cyclic loading due to reinforcement fiber was observed and the maximum stress increased with increment of fiber weight fraction in the HE specimen. As cited that large recovery ability is one of advantages for shape memory polymer, this means that a certain amount of permissible deformation is necessary. Related to this characteristic, the increment of fracture strain caused by thermal treatment will be important behavior.

CONCLUSION

In this study, the composites based on the SMPs were developed and their mechanical properties and shape memory effects were investigated by the experimental approach. The results obtained are remarked as follows.

The developed specimens were of high tensile strength and it increased with the increment of fiber weight fraction.

It was clear that the improvement of the resistance to cyclic loading for the composites with HE-SMP was obtained due to reinforcement fiber.

REFERENCES

1. H. Tobushi, S. Hayashi and S. Kojima, "Mechanical Properties of Shape Memory Polymer of Polyurethane Series," Transactions of the Japan Society of Mechanical Engineers, A, 57 (1991) 146 (in Japanese).
2. Qing-Qing Ni, Takeru Ohki, Norihito Ohsako and Masaharu Iwamoto, "Thermomechanical Behavior of Smart Composites with Shape Memory Polymer", ICCM-13, China, (2001-6)

Proceedings of 7th Japan International SAMPE
Symposium & Exhibition, Nov. 13-16, 2001

Source Location in a CFRP plate with embedded PZT sensors

Ryutaro Oishi, Ja-Ho Koo, Nobuyuki Toyama, Bo Wang
Smart Structure Research Center (SSRC),
National Institute of Advanced Industrial Science and Technology
1-1-1 Umezono, Tsukuba, Ibaraki, 305-8568, JAPAN
E-mail: r-oishi@aist.go.jp

Abstract

We present a method and the experimental results of estimating two-dimensional AE source locations with 2 sensors. We constructed a CFRP plate of composite material with embedded PZT sensors for health monitoring. The AE source locations in the composite material were estimated from the Lamb S_0/A_0 mode signals detected by the PZT sensors. A wavelet transformation in the frequency-time space provides the arrival times of S_0/A_0 modes from an AE source location without being affected by noise. Using the S_0/A_0 arrival times, it is possible to reduce the number of sensors to 2 for estimating a two-dimensional AE source location in a CFRP plate. Using 2 sensor signals with wavelet, we determined the source location with an accuracy of 1.9 cm.

Key Words: CFRP, composite material, source location, wavelet

Introduction

Acoustic Emission (AE) signal has been widely used for source location and monitoring of a damage in materials. For constructing a health monitoring system of materials such as a CFRP plate, sensors to detect AE signals are mounted on or embedded into a plate. We have constructed a CFRP plate with embedded PZT sensors (smart CFRP plate). The health monitoring plate is expected to be applied to large scale structures, such as airplanes, buildings. In these cases, it is necessary to reduce the number of sensors for the sake of the sensor signal handling and saving the costs for a data acquisition system. We have developed a two-dimensional source location method to reduce the number of sensors [1]. We applied our source location method on the smart CFRP plate. In this article, we report the results of the source location on the smart CFRP plate.

Smart CFRP Plate

We constructed a prototype of smart CFRP plate as illustrated in Fig. 1. The prototype consisted of a cross-ply ($[0°/90°]_{2S}$) CFRP plate, a polyimide sheet and 4 PZT sensors (Fuji Cera Co.), which were bonded with epoxy glue. The size of the smart CFRP plate is 200 mm×145 mm×1.7 mm. On the polyimide sheet, 4 sensors were mounted and conducting wires were printed in order to carry the sensor signals out to the data acquisition equipment.

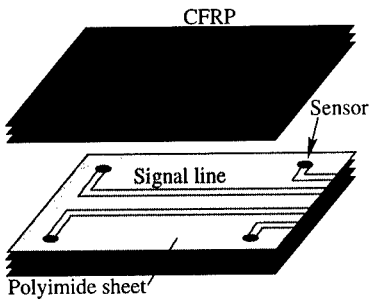

Figure 1: An illustration of a prototype smart CFRP plate. A polyimide sheet is shown as light shaded area, and sensors are shown as small circles on the sheet.

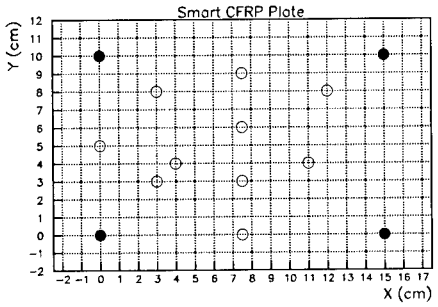

Figure 2: Sensor positions and AE source locations by a pencil lead break are shown as filled and open circles, respectively, on the coordinate system of the smart CFRP plate.

Source Location on the CFRP Plate

We apply two methods to the smart CFRP plate for estimating two-dimensional source location. One is a conventional 4-sensor method by using the arrival time of S_0 mode measured by 4 sensors [2, 3, 4]. The other is a 2-sensor method using the time difference between S_0/A_0 modes measured by 2 sensors, where an wavelet transformation was used for extracting A_0/S_0 mode arrival times. In Fig. 2, we show the coordinate system, the sensor positions (filled circle) and the generated AE source locations (open circle) on the smart CFRP plate. An AE signal was simulated by an impact caused by pressing a pencil lead against the plate until it broke. For checking reproducibility, we repeated to generate an AE signal three times at each position. Figure 3 shows a typical AE signal detected by a PZT sensor and the translated signal by wavelet on the frequency-time space, where the vertical axis (Y) in Fig. 3 -b corresponds to an index of frequency (f) as follows;

$$f = \frac{2^{(1-Y)/4}}{\Delta t}.$$

The outputs of the sensor signals were collected by a LeCroy LC334M digital oscilloscope at a sampling time (Δt) of 0.04 μsec. To estimate an arrival time of an A_0 mode, we selected the wavelet coefficients at 150 kHz. An arrival time of an S_0 mode was determined at a point where the amplitude exceeds a threshold. We measured the velocities of S_0 and A_0 modes in the smart CFRP plate. The velocities were calculated from the arrival time difference between an embedded sensor and an additional AE sensor placed on the smart CFRP plate, which are shown in Fig. 4. As shown in Fig. 4, the angular dependences of the S_0/A_0 mode velocities were parametrized by functions of:

$$\begin{cases} v_S(\theta) &= s_1 + s_2 \times \cos 4\theta + s_3 \times \cos 8\theta, \\ v_A(\theta) &= a_1 + a_2 \times \theta, \end{cases}$$

where θ is an angle with respect to the horizontal axis (X) on the smart CFRP plate, and a_1, a_2, s_1, s_2 and s_3 are parameters.

4-sensor S_0 Method

We applied a conventional source location method to compare accuracy of the source

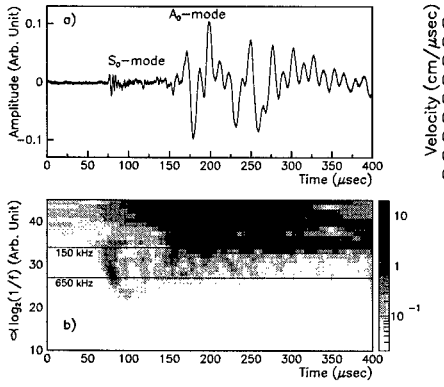

Figure 3: a) A typical AE signal detected by a PZT sensor, b) the translated signal (wavelet coefficients) by wavelet on the frequency-time space, where the vertical axis corresponds to $\log_2$ (1/frequency).

location estimations with our 2-sensor result which will be described in next paragraph. For the estimation, we used the arrival time differences of S_0 modes measured by 4 sensors. We define the average distance between the estimated and the generated AE locations as accuracy of the source location estimation. We obtained an accuracy of 0.8 cm with the conventional method using 4 sensor S_0 signals.

2-sensor S_0/A_0 Method

To reduce the number of sensors to 2, we used the arrival time (t_A) of an A_0 mode as well as that (t_S) of an S_0 mode, which were measured by the 2 sensors at the bottom of Fig. 2. A wavelet transformation was used for determining an A_0 arrival time. An S_0 arrival time was estimated from a time up to a point where an output signal exceeded a threshold, or at the first peak of a wavelet 650 kHz coefficient distribution. In this analysis, we examined

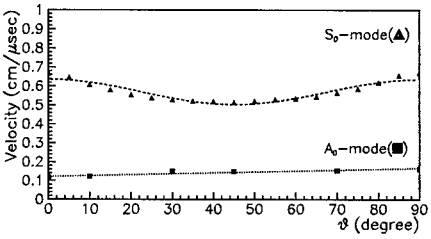

Figure 4: The angular dependences of the S_0 and A_0 mode velocities in the smart CFRP plate are shown with symbols of triangle and square, respectively. The lines represent the parametrized functions of $v_S(\theta)$ and $v_A(\theta)$.

the above two cases for the source location estimations. The arrival time difference ($\Delta t_i = t_S - t_A$) between A_0 and S_0 modes measured by each sensor ($i = 1, 2$) was used to estimate the source location (x,y). By assuming a constant uncertainty on each arrival time measurement, we simultaneously minimize the absolute value of variable:

$$f_i = \frac{L_i - r_s}{v_{S_i}(\theta)} - \frac{L_i - r_s}{v_{A_i}(\theta)} - \Delta t_i,$$

where $L_i = \sqrt{(x - x_i)^2 + (y - y_i)^2}$, (x_i, y_i) is the position of each sensor, r_s(=0.5 cm) is a radius of the sensor, $v_{S_i}(\theta)$ and $v_{A_i}(\theta)$ are the velocities of S_0 and A_0 modes, respectively. In principle, there are two possible locations to minimize the above variables simultaneously, which are actually symmetric with respect to the line including the two sensors. One of the two locations is eliminated by placing the sensors at each corner of the plate. Using the 2-sensor method, we obtained accuracy as 1.9 cm (2.0 cm) by using a threshold (wavelet) for the S_0 arrival time determination. Figure 5 shows a histogram of the average distance between the esti-

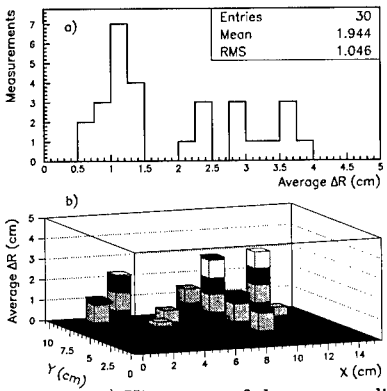

Figure 5: a) Histogram of the average distance between the estimated and the generated AE source locations. b) The average distance at each generated position.

mated and the generated AE source locations, and also shows that at each position. We can see no position dependence of accuracy. The accuracy of the estimated locations dominantly depends on the measured uncertainty of the A_0 arrival times.

Conclusions

We constructed a CFRP plate of composite material with embedded PZT sensors for health monitoring system. Estimating AE source locations on the smart CFRP plate was performed by generating an AE signal of a pencil lead break. Using the arrival times of S_0 modes measured by 4 sensors, we obtained accuracy of 0.8 cm for the estimated locations. To reduce the number of sensors, we placed two sensors on each corner of the smart CFRP plate, and used the arrival time difference between S_0 and A_0 modes. The arrival times of A_0 modes were estimated from the wavelet coefficient distribution at 150 kHz. We obtained accuracy of 1.9 cm (2.0 cm) for the estimated locations by using a threshold (a wavelet coefficient distribution at 650 kHz) for the S_0 arrival time estimations. From the analysis of the prototype smart CFRP plate, we found that it is possible to estimate two-dimensional AE source locations with 2 sensors on the smart CFRP plate.

Acknowledgment

We thank the Smart Structure Research Center staff for their vital contributions. This work was supported by the Japan Science and Technology Corporation (JST).

References

[1] N. Toyama, J.H. Koo, R. Oishi, M. Enoki and T. Kishi, Journal of Material Science Letters, in press.

[2] S. M. Ziola and M. R. Gorman, J. Acoust. Soc. Am. **90** (1991) 2551.

[3] J. H. Koo, B. N. Kim, M. Enoki and T. Kishi, J. Acoustic Emission **15** (1997) 89.

[4] J. H. Koo, N. Toyama, B. K. Jang, J. Takatsubo, Y. Akimune and T. Kishi, Proceedings of the 10th International Conference on Fracture, in press.

[5] H. Jeong and Y. S. Jang, Composite Structures 49 (2000) 443-450.

[6] K. Kinoshita, H. Inoue, M. Hamada and T. Shibuya, J. Appl. Mech. **62** (1995) 841.

[7] H. Suzuki, T. Kinjo, Y. Hayashi and K. Ono, J. Acoustic Emission **14** (1996) 69.

Proceedings of 7th Japan International SAMPE
Symposium & Exhibition, Nov. 13-16, 2001

Effect of Stacking Sequence and Number of Electrodes on Detections of Delaminations of CFRP Using Electric Resistance Change

Akira Todoroki#1, Yuuki Tanaka#2, Yoshinobu Shimamura#1 and Hideo Kobayashi#1

#1: Department of Mechanical Sciences, and Engineering,
Tokyo Institute of Technology
2-12-1 Ohokayama, Meguro, Tokyo 152-8552, JAPAN
E-mail: atodorok@ginza.mes.titech.ac.jp.jp
#2: Graduate student of Tokyo Institute of Technology

Abstract

In the present study, an electric resistance change method is adopted for the identifications of delamination crack location and size of CFRP laminates, and the identifications of delamination cracks is experimentally investigated by using cross ply laminates. Short beam shear tests to create delamination cracks are performed beam-type specimens with multiple electrodes, and electric resistance changes due to the delamination creation are measured. Response surfaces to estimate delamination location and size from electric resistance changes are constructed. In this method, stacking sequence and number of electrodes largely affect reliability of identification of the delamination location and size. In order to estimate these effects, a large number of experiments are performed using three kinds of specimens that have different number of electrodes. Two types of stacking sequences are employed. As a result, the electric resistance change method can be useful for structures monitoring of laminate, and five numbers of electrodes are needed for high reliability.

Key Words: Delamination, Monitor, Electric resistance, Response Surface.

Introduction

Laminated composites have a weak point at delamination resistance. The low resistance causes a delamination crack by a slight impact such as a tool drop. Since the delamination-crack creation is normally delicate problem for a visual inspection, the delamination causes low reliability for a primary structure of laminated composites. Therefore, a health monitoring system to detect the delamination cracks is desired for practical laminated composite structures.

In the present study, an electric resistance change method is employed to identify internal delaminations. The method does not require expensive instruments. The electric-resistance change method owing to the fiber breakage has been adopted by several researches.

Authors have already applied the electric resistance change method to detect an internal delamination crack in the previous paper using beam-type specimens with two electrodes [1]. FEM analyses were also conducted in the previous studies [2,3]. It was shown in the paper [2] that identification of a delamination of a beam

type specimen (estimation of a delamination location and size) is impossible in the case that the only a pair of electric resistance changes are measured using three electrodes mounted on the specimen surface. This is caused by the strong orthotropic electric resistance.

In the present study, identifications of internal delaminations (estimations of delamination size and location) are experimentally attempted by using beam-type cross-ply laminate specimens. Two kinds of the number of electrodes are investigated: four and five. For the four-electrode specimens, two types of electrode spacing are attempted. An interlamina shear test was employed to create a delamination crack in the specimen. Electric-resistance changes between electrodes were measured using a conventional strain-gage amplifier. Response surface methodology is employed as a convenient tool to solve inverse problems to obtain delamination location and size from electric resistance changes.

Specimens and experimental procedures

Specimens

Material used in the present paper is unidirectional graphite/epoxy prepreg. The type of the unidirectional prepreg sheet is A125-Rc33% produced by Shin-Nihon Steel Chemistry Co.. The stacking sequences are $[0_2/90_2]$s and $[(0/90)_2]$s. The thickness is approximately t=1mm. Cure condition is 180°Cx1Mpax2hr . In order to measure electric-resistance changes using a two-probe method, reliable electrodes are indispensable. In order to produce reliable electrodes, rectangle copper foil of 0.02mm thickness is mounted on the prepreg laminates, and these electrodes are co-cured with the laminate. Three types of beam specimens of the width 15mm are made from the laminated plates.

In order to examine the effect of number of electrodes and size of spacing between electrodes, three types of beam

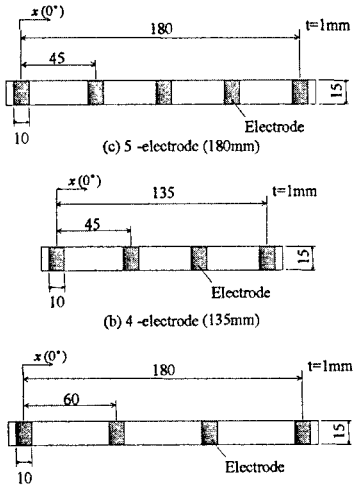

Fig. 1. Specimen configurations

specimens were prepared. These specimen configurations are shown in Fig. 1. For each type of the specimen, multiple electrodes are mounted on a single surface of the specimen in the present study. The reason of placements of all electrodes on the same surface is to simulate of identifications of an invisible internal delamination crack by mounting electrodes just on the inner surface of shell-type structure like aircrafts. For these types, stacking sequence is $[0_2/90_2]$s . Type A specimen has four electrodes of spacing of 60mm, and the length is 180mm. Type B specimen has four electrodes of spacing 45mm, and the length is 135mm. Type C specimen has five electrodes of spacing of 45mm, and the length is 180mm. In order to investigate the effect of stacking sequence, type C specimen is adopted. Two types of stacking sequences were produced for the type C specimens.

Electric circuit

Since electric-resistance change due to a delamination crack creation is very small, the electric-resistance change is measured with a conventional electric resistance bridge circuit. Conventional strain-gage amplifiers are

adopted for measurements of electric resistance change of the specimens.

Experimental method

In order to create a delamination crack in each beam-type specimen, an interlamina shear test is employed. The middle point is loaded from the opposite side where the electrodes are mounted. This is to simulate the placements of electrodes inside of the structures and the impact load that creates a delamination comes from the outside. Since the specimen is a thin laminate, the loading creates a large delamination crack in the 0°-90° interface near the electrodes.

After creating a delamination crack, electric-resistance changes of all segments between electrodes were measured using a conventional strain amplifier. Delamination location and size were measured using an ultrasonic C-scan image. The delamination location is decided at the center point of the delamination crack from the specimen end.

Response surfaces to estimate delamination location and size are created from the measured data.

Experimental results and discussion

The estimation results of delamination locations of the all type are shown in Fig 2. Figure 2 (a) shows the results of the type A specimens. Figure 2 (b) shows the results of type B specimens. Figure 2 (c) shows the results of the type C. For all figures, the ordinates are the estimated delamination locations and the abscissas are the measured delamination locations. Symbols placed on the diagonal lines mean that the response surfaces provide exact estimations.

All of these figures imply that the performances for the estimations of delamination locations are improved as the increase of the number of electrodes. For the cases of type A and (four-electrode), the response surfaces give relatively poor performances. When the number of electrodes is larger than four. The estimations of the response surfaces become excellent.

Effect of the size of spacing between electrodes is shown in the results of type A and B. The type A is the wide-spacing-four-electrode type specimen (60mm), and the type B is

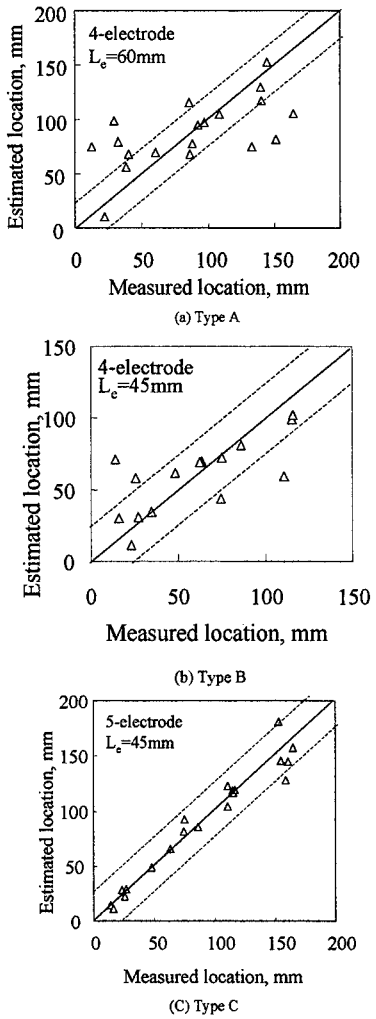

Fig.2 Estimation of delamination

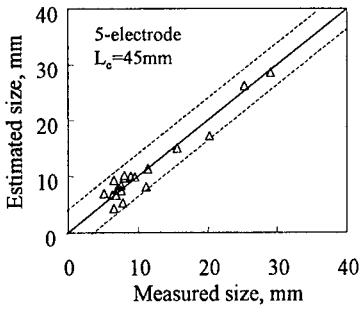

Fig.3 Estimated results of delamination

narrow-spacing-four-electrode type specimens (45mm). Comparing the results of type A with the results of type B, it is clarified that there is little difference in the performance of estimations. Narrow spacing does not cause the increase of the performance of estimations. At least, this tells that the spacing of electrodes is not so significant comparing to the effect of number of electrodes.

For the estimations of delamination sizes, the estimations are very good for all types of the specimens. As a typical example, the case of type C is shown in Fig 3. In this figure, the abscissa is a measured delamination size with ultrasonic C-scan image, and the ordinate is the estimated results of a response surface. The result shows that the estimation of size is not so difficult problem.

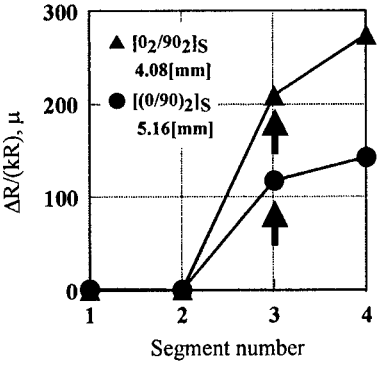

Fig. 4 Typical results of the effect of stacking sequences

Using the type C specimens, two types of stacking sequences are adopted. Typical result of the measured electric resistance change ratio is shown in Fig.4. The abscissa is the segment number and the ordinate is the measured electric resistance change ration of the both type of stacking sequences that have similar delamination crack. As shown in this figure, measured results of $[(0/90)_2]$s is smaller than that of $[0_2/90_2]$s. This is caused by the delamination location in the thickness direction. For the laminates of $[(0/90)_2]$s, the delamination crack locates farer from the surface than the laminates of $[0_2/90_2]$s. The smaller electric resistance change causes smaller estimation reliability for the laminates of $[(0/90)_2]$s.

Conclusions

(1) In order to obtain practically allowable performance of identifications, at least five electrodes are required. Number of electrodes has more significant effect on the identifications than the spacing of electrodes.
(2) Electric-resistance changes due to a delamination creation can be measured with multiple co-cured electrodes mounted on the single surface of a beam type specimen.
(3) Difference of the stacking sequences cause the difference of delamination location in the thickness direction. When the delamination crack is created far from the electrodes, measured electric resistance change ratios become smaller.

References

1. A.Todoroki, Proceedings of the 5th Japan International SAMPE Symposium, 899 (1997).
2. A.Todoroki and H. Suzuki, Applied Mechanics and Engineering,5(1), 283 (2000)
3. A.Todoroki, Compsoite Science and Technoly, (to be published).

Proceedings of 7th Japan International SAMPE
Symposium & Exhibition, Nov. 13-16, 2001

Impedance Change Method for Wireless Strain Measurement of Composite Materials

Akira Todoroki[1], Shintaro Miyatani[2], Yoshinobu Shimamura[1]

1: Department of Mechanical Sciences and Engineering, Tokyo Institute of Technology
2: Graduate Student of Tokyo Institute of Technology
2-12-1 O-okayama, Meguro-ku, Tokyo 152-8552, JAPAN
E-mail: atodorok@ginza.mes.titech.ac.jp

Abstract

Strain monitoring for composite materials in-service is quite effective to improve structural reliability of composite materials. Recently, it is demanded to monitor strain of tire structure in service. Since conventional strain gages have high stiffness and require lead wires, the conventional strain gages are cumbersome for the strain measurement of the tires. Since tires themselves are not expensive, expensive sensors such as MEMS are economically not affordable. That requires a new low cost wireless sensor for tires.

In the present study, impedance change of composite materials due to the deformation by applied strain is measured, and the impedance change is utilized for the frequency generator. By measuring the radio wave change, the strain of the composites can be measured wirelessly. Since the method demands simple oscillator circuits, the total cost of the sensor is very inexpensive, and the circuits themselves can be made compactly.

In the present study, the specification of the method is discussed in detail, and the basic trial experiments of the method are conduced using tire specimens cut from a tire. Steel wires of tire are selected as electrodes and impedance changes due to the applied strain are directly measured. As a result, it is found that the electrodes are stable enough for using to an oscillator. Using a frequency generator circuit and a tuned circuit, the impedance change is wirelessly measured. Finally, the strain is wirelessly monitored.

Key Words: Strain Monitoring, Wireless Monitoring, Impedance Change

Introduction

Strain Monitoring in-service for rotary machines such as helicopter rotors, pumps and tires is a very important technology to improve reliability for actual structures and to improve design technologies of these structures. Recently, MicroElectroMechanical System (MEMS) are attracting remarks for these monitoring. Sensors of MEMS employ processing technologies developed for LSI to produce small size intelligent sensors with data processing unit. These sensors have been applied to monitor composite structures [1-4]. MEMS has, however, a high stiffness substrate made of silicon crystal, and it has high stiffness. It may cause difficulty to measure strain of flexible structures like rubber or plastics and a problem of debonding from structures due to large difference of thermal expansion coefficient. A new wireless sensor that has low stiffness

and is low cost, therefore, is required especially for monitoring tire strain.

For the wireless monitoring, a sensor that utilizes electric capacitance change is the easiest way to use because the electric capacitance change can be easily transferred to frequency change of an oscillator circuit. This type of the sensor, however, has a weak point of stable electric capacitance. If users of the electric-capacitance-change-sensor mount it with polymer adhesive, the adhesive induces the electric capacitance change. Other slight things could have effect on the capacitance change.

In the present study, therefore, a composite material itself that comprises electric conductive wires and electric insulated matrix is selected as an electric-capacitance-change-sensor to measure the strain of the composite material. Since alternating electric current flows inside the composite material, adhesive or other things do not affect the electric capacitance change, and it may provide stable electric capacitance.

The present study shows the concept of the novel method to measure the strain of the composite structure made from electric conductive wires and electric insulated matrix. The method is applied to monitor the static strain of a specimen cut from a steel radial tire. The steel wire is adopted as electrodes to charge the alternating current into the specimen. Using a material testing machine, tension load is applied to the specimen, and the strain is measured by the new method and a conventional strain gage. Conventional analog oscillator circuit is employed to transmit strain data by converting it into frequency change of alternating current. Since the new method does not require expensive equipment, the total cost of the system is significantly low.

Scheme of Wireless Strain Monitoring System

The schematic illustration of the new strain monitoring system for flexible composite materials is shown in Figure 1. The electric capacitance of the material changes due to deformation of the composite structure because spacing between electric conductive fibers changes due to the deformation of the composite materials.

In order to transmit the electric capacitance change wirelessly, an oscillator is employed. The composite structure itself has electric capacitance, and it is connected to the oscillator circuit as a condenser that affects frequency of the alternating current of the oscillator circuit. The electric capacitance change of the specimen causes the frequency change of the oscillation circuit. By measurements of the frequency change of the oscillation circuit with the wireless receiver, we can measure the applied strain of the specimen wirelessly.

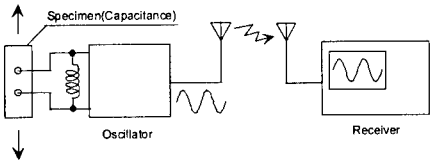

Fig.1 Schematic illustration of wireless Strain monitoring system

Strain Measurement by Impedance Change

Specimen

The configuration of the specimen is shown in Figure 2. The specimen is a commercially available steel radial tire that has polyester fiber carcass. A rectangular specimen (the length is 250mm, width is 32mm and thickness is 5mm) is cut from the tire.

In order to utilize the electric capacitance change by deformation to oscillation circuit, the steel wires of the tire specimen itself are employed as electrodes. Since the specimen is completely covered with rubber, the surface rubber of the two parts of the specimen removed by grinding

the surface, and the lead wires are connected directly to the steel wires with conventional solder. The spacing between the electrodes is approximately 50mm and set to the center of the specimen.

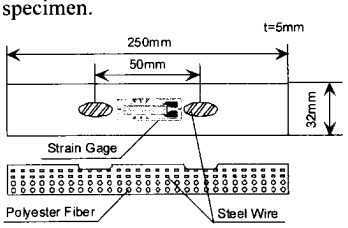

Fig.2 Specimen Configuration

Experimental Apparatus

The oscillator circuit is employed in this study to produce high frequency. This circuit may produce a signal that can oscillate within from 20MHz to 30MHz. In this circuit, the specimen is integrated as one of the serially connected condensers. The distance between electrodes changes with the applied strain causes capacitance change. The frequency of the oscillation circuit changes with the applied strain.

A tensile material testing machine is used to apply strain to the specimen and a strain gage is mounted on the surface of the specimen to measure the strain. In order to keep insulation between the specimen and the testing machine, two sheets of silicon sheet are inserted between the specimen and the jig.

The oscillating frequency can be calculated by the formula as follows.

$$f = \frac{1}{2\pi\sqrt{LC}}$$

where f is oscillating frequency, L is the inductance constant, C is the electric capacitance of the specimen. When the specimen deforms, the frequency f changes because the capacitance C changes as the specimen deforms. The initial capacitance of the tire specimen is 20pF approximately.

Method

Tensile tests were performed to apply tensile deformation to the specimen. During the tests, electric current frequency of the oscillator circuit is measured. The specimen is elongated up to 2mm by displacement between the jigs at the crosshead speed of 0.5mm/min. The output wave was measured by using a digital oscilloscope at the sampling speed of 100MS/s. The frequency of the oscillator circuit is determined by using FFT analysis with 100 times averaging. The measurements were performed at the six stages of the tensile tests; 0mm, 0.1mm, 0.5mm, 1.0mm, 1.5mm and 2.0mm of the displacement between the jigs.

Results and Discussion

In the present study, the initial oscillation frequency is approximately set to 26.5MHz. The typical waveform is shown in Figure 3. The resolution of FFT is 2kHz, and it is judged to be enough for measuring frequency changes.

The measured frequency change with strain change is shown in Figure 4. In this figure, the abscissa is the measured strain and the ordinate is the measured frequencies. This figure shows that the measured frequencies decrease as the increase of measured strain of the specimen. Although there is a hysteresis loop between loading and unloading, this error is supposed to the strain measurement mounted on only one side.

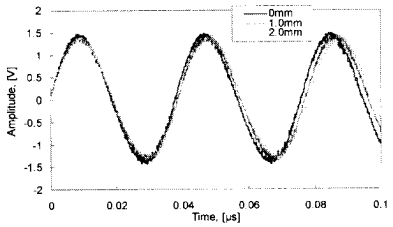

Fig.3 Typical example of acquired waveforms

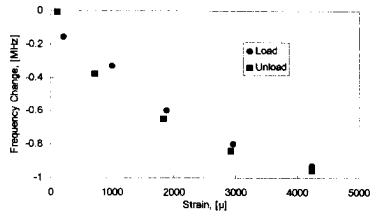

Fig.4 Frequency change with applied strain

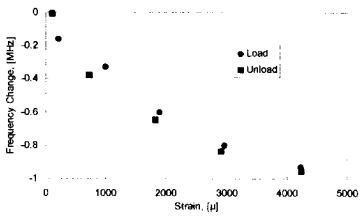

Fig.6 Frequency change with applied strain

Wireless Monitoring

Experimental Apparatus

A wireless strain measurement system is shown in Figure 5. In this system, the oscillating signal transmitted from an antenna can be received in another circuit including a tuned circuit. The specimen and the tensile tests are the same as the cases of the previous wired measurements. The only difference is that the wireless method requires an adjustment of receiving frequency by changing the capacitance of the variable condenser integrated in the tuned circuit.

Results and Discussion

The frequency change with the increase or the decrease of the strain change is shown in Figure 6. This is quite the same as Figure 4. This shows that the new system is quite effective for the wireless strain monitoring.

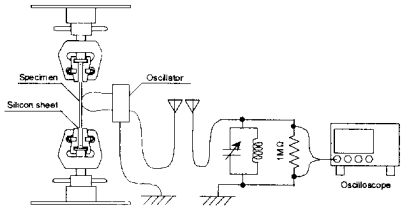

Fig.5 Experimental apparatus

Conclusions

As a low-cost method of strain monitoring for flexible composite materials, a new method was proposed and experimentally confirmed using specimens cut from the commercially available tires. The new strain measurement method employs the oscillator circuit to transmit the electric capacitance change of the specimens. Electrodes were directly mounted to the steel wires of the specimens, and the strain measurements were performed. As a result, this method successfully provides wireless monitoring of the tire structure with a simple electric circuit at very low cost.

References

1. Nadim Maluf, "An Introduction to Microelectromechanical Systems Engineering", Artech House, Inc., (2000)
2. Charles Hautamaki, *Journal of Reinforced Plastics and Composites*, 19(4), pp.268-277, (2000)
3. Vasundara V Varadan, *Smart Mater. Struct.*, 6, pp.745-751, (1997)
4. V K Varadan, *Smart Mater. Struct.*, 9, pp.379-388, (2000)
5. Noritsugu Suzuki, "Design and manufacture of high frequency circuit", (1992), CQ publishing (in Japanese)
6. Noritsugu Suzuki, "Design and manufacture of radio & wireless circuit", (1999), CQ publishing (in Japanese)
7. Naotsugu Mihori, "Science of tire", (1992), Koudansha (in Japanese)

Proceedings of 7th Japan International SAMPE
Symposium & Exhibition, Nov. 13-16, 2001

Determination of Internal Conducting Network of CFRP Composites Using Anisotropy of Electrical Conductivity

J.B. Park#, T. Okabe##, A. Yoshimura#, N. Takeda# and M. Xia###, W.A. Curtin###

#: Graduate School of Frontier Sciences, The University of Tokyo
c/o Komaba Open Laboratory (KOL)
4-6-1 Komaba, Meguro-ku, Tokyo 153-8904, JAPAN
##: SSRC, National Institute of Advanced Industrial Science and Technology
1-1 Umezono 1, Tsukuba 305-8568, JAPAN
###: Division of Engineering, Brown University
Providence, RI 02912-9104, USA
E-mail: jbpark@compmat.rcast.u-tokyo.ac.jp

Abstract

Internal conducting network, which is constructed by contacts between conductive carbon fibers, is very important to predict resistance change in CFRP due to mechanical damage. However, this conducting network depends on the average incline angle of fibers, thus electrical conductivity of unidirectional CFRP shows strong anisotropy characteristics. In this study, we propose a new methodology to determine internal conducting network considering the anisotropy of electrical conductivity. For this purpose, we investigate experimentally the anisotropy characteristics of electrical conductivity in CFRP and apply the DC circuit theory, such as Kirchhoff's rule, to determine the number of contact points. We generate the characteristic curve for unidirectional CFRP and introduce the Monte Carlo simulation. By comparing the simulated and experimental results, the internal conducting network and the contact points density were estimated quantitatively.

Key Words: Electrical Conductivity, Kirchhoff's Rule, Anisotropy

Introduction

As shown by previous studies[1-3], the mechanical damage in CFRP composites can be monitored by measuring the resistance change of CFRP under service condition. This useful property can be well described analytically by Eq.(1), which is composed by introducing the linear relationship between strain and resistance of conductive wires and the Weibull-Poisson statistics for breakage of fiber under mechanical loading[4].

$$\Delta R/R_o = (1+\alpha\varepsilon)/[-(\delta_{cc}/L_o)(E_f\varepsilon/\sigma_o)^m] - 1 \quad (1)$$

where α : gage factor of carbon fiber, ε : applied strain, E_f : Young's modulus of carbon fiber, σ_o and m : the scale and shape parameters of Weibull distribution, δ_{cc} : electrical ineffective length. Especially, δ_{cc}, which means the average value of distance between adjacent contact points between conductive wires, is a very important parameter in predicting resistance change behavior, and indicates that contact situation

and its resulting internal conducting network governs electromechanical characteristics of CFRP.

In present study, the electrical conductive internal network of CFRP composite is investigated using experimental and analytical methods. For this purpose, the anisotropy characteristic of electrical conductivity, which is originated from the internal contact between carbon fibers, is determined experimentally. Based on the experimental anisotropy curve, the contact point distribution is determined statistically by Monte Carlo simulation.

Determination of Anisotropy Curve

Considering the ideal alignment of carbon fibers, it is impossible for unidirectional CFRP have the conducting path across the fiber direction. However, in real situation, the conductive carbon fibers are inclined by some degrees and contacts between fibers exist. Anisotropy characteristic in the electrical conductivity of unidirectional CFRP is due to the these contact points[5]. Therefore, through the investigation of this anisotropy characteristic, the internal contact situation can be estimated quantitatively.

Experimental Procedure

A square type of specimen (80mm × 80mm × 1mm) was manufactured using T700S/2500 prepreg with 60% volume fraction. Table 1 shows the material properties of T700S carbon fiber. To measure the electrical resistance under the same condition at each measurement position, a template as shown in Fig.1 was adopted. For electrode, electrically conductive silver paste was used. Resistance measurement was conducted for the various angles and electrode distances.

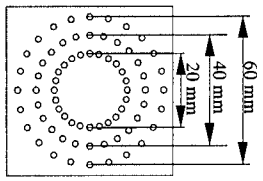

Fig.1 Schematic showing the template used for resistance measurement

Table 1 Material properties of T700S

Gage factor (α)	Resistivity (ρ, $\mu\Omega$m)	Young's modulus (E_f, GPa)
5.14	16.2	230

Experimental results

The measurement results are shown in Fig.2. The resistance changes according to the increase of the angle, which is due to the fact that conducting path depends only on the fiber contact points. Because the resistance value shows linear dependence on the electrode distance, the measurement results of different electrode distances can be integrated by the resistance per unit length. Figure 3 shows the resulting integrated curve

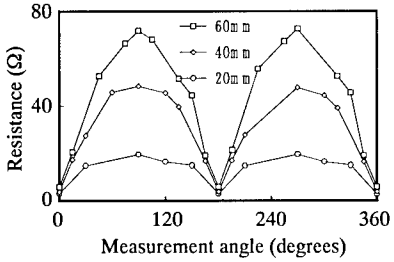

Fig. 2 Resistance measurement results

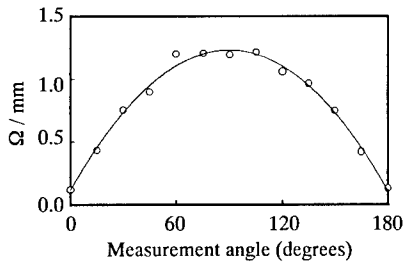

Fig.3 Anisotropy characteristic curve for CFRP (T700S/2500, V_f = 60%)

and we named it the anisotropy characteristic curve for electrical conductivity of CFRP composites. This anisotropy curve provides the key information to evaluate the internal conducting network. Based on this anisotropy characteristic curve, the numerical analysis results are used to estimate the distribution of contact points quantitatively. This is the first main result of this research.

Numerical Analysis

Numerical analysis of the present study consists of two parts. One is the electrical circuit analysis by Kirchhoff's rule[6] and the other is the Monte Carlo simulation for determination of contact points using random number generator. As shown in Fig.4, the unidirectional CFRP was modeled as DC circuit network of conductive wires with the nodes and the randomly distributed contact resistance. We applied the Kirchhoff's rule to this model as shown in Fig.5, and the value of voltage at each node can be expressed as Eq.(2).

$$(V_{i,j-1}-V_{i,j})/R_f + (V_{i,j+1}-V_{i,j})/R_f + (V_{i+1,j}-V_{i,j})/R_{c(i-1,j)}+(V_{i+1,j}-V_{i,j})/R_{c(i,j)} = 0 \quad (2)$$

The contact points assigned randomly by Monte Carlo simulation. At first, we determined the position of contact points and the value of 2.2kΩ was assigned as R_c. For the case of nonexistence of contact point between two nodes, the unrealistic large value of R_c (= ∞) was used to represent the nonconductive state. The specific voltage values were calculated by Successive Over Relaxation (SOR) method[7] as shown in Eq.(3).

$$V_{i,j(new)}=V_{i,j(initial)}+\omega\,(V_{i,j(calculated)} - V_{i,j(initial)}) \quad (3)$$

where ω is the acceleration factor for convergence and we used the value of 1.8. Figure 6 is the calculated results and the tendency of the resistance change for the variation of angle is very similar to the experimental results.

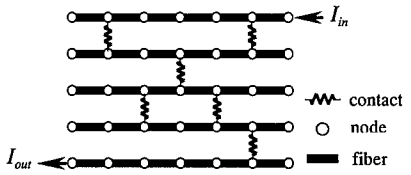

Fig.4 CFRP electrical model for numerical analysis

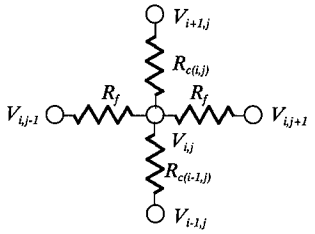

V : voltage
R_f : resistance of carbon fiber
R_c : contact resistance

Fig.5 Characterization of CFRP for application of Kirchhoff's rule

Determination of Internal Contact

Comparison between Numerical and Experimental Results

To determine the internal contact situation, the calculated results were compared to the experimental anisotropy curve. However, as shown in Figs.3 and 6, considerable difference exists between two results. This difference is due to the difference in the specimen size between numerical and experimental works and it is very time consuming work to obtain the numerical solution of the same size of composite to the specimen. Therefore, we introduce a new normalization parameter defined by Eq.(4).

$$R_n = R_\theta / R_{90} \quad (4)$$

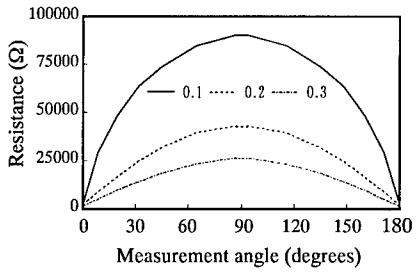

Fig.6 Monte Carlo simulation results for various contact ratio

where R_{90} and R_θ are the resistance at 90° and θ. Figure 7 shows the comparison results using Eq.(4). The anisotropy tendency becomes weaker along with the increase of contact ratio, and this is due to the increase of the conducting path generated by contact points in the transverse direction of conductive wires. At the contact ratio 0.1, the numerical and the experimental results shows good agreement, thus the internal contact situation of unidirectional CFRP with volume fraction of 60% can be characterized by this level of contact ratio. This is the second main result of this research.

Conclusion

Anisotropy characteristic of electrical conductivity in CFRP composites was studied experimentally and numerically. It is shown that the anisotropy curve which is obtained experimentally can be used as important information to evaluate the internal contact situation. In the present study, DC circuit analysis theory, such as Kirchhoff's rule, and Monte Carlo simulation technique were integrated to generate the anisotropy curve numerically. The internal electrically conducting network was estimated quantitatively by comparing the experimental anisotropy curve to the numerical results. At contact ratio of 0.1, two results showed the best coincidence, thus the internal contact situation of unidirectional CFRP with volume fraction of 60% can be characterized by that value.

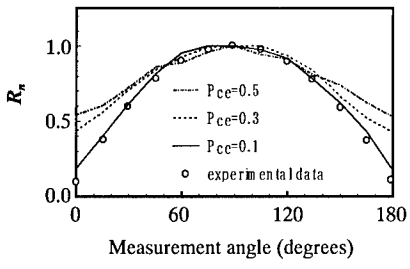

Fig. 7 Comparison between experimental and simulated anisotropy curve

Acknowledgment

The present research was conducted as a part of the 'R & D for Smart Material/Structure System' project within the Academic Institutions Centered Program supported by NEDO (New Energy and Industrial Technology Development Organization), Japan.

References

1. Schulte K, Baron Ch.: Composite Science and Technology, 36, 63 (1989).
2. Muto N, Yanagida H, Nakatsuji T, Sugita M, and Ohtsuka Y.: J. Am. Ceram. Soc., 76, 875 (1992).
3. Abry JC, Bochard S, Chateauminois A, Salvia M, and Giraud G.: Composite Science and Technology, 59, 925 (1999).
4. Park JB, Okabe T, Takeda N, and Curtin WA.: Composites, accepted for publication
5. Carmona F and El Amarti A.: Physical Review B, 35(7), 3284 (1987).
6. Brophy JJ.: *"Basic Electronics for Scientists"*, McGraw-Hill, pp. 9-20.
7. Press WH, Flannery BP, Teukolsky SA, Vetterling WT.: *"Numerical Recipes in C"*, Cambridge University Press (1993).

Proceedings of 7th Japan International SAMPE
Symposium & Exhibition, Nov. 13-16, 2001

Smart Detection of Damage of Composite Structures using Unsupervised Statistical Diagnosis

Atsushi Iwasaki[#1], Akira Todoroki[#2], Yoshinobu Shimamura[#2], Hideo Kobayashi[#2]

#1: Graduate student of Tokyo Institute of Technology,
2-12-1, O-okayama, Meguro-ku, Tokyo 152-8552, Japan
E-mail: aiwasaki@ginza.mes.titech.ac.jp
#2: Mechano-aerospace Engineering, Tokyo Institute of Technology

Abstract

Smart structures for health monitoring are a noticeable technology for civil structures. Most of the structural health monitoring systems adopts parametric method based on modeling or non-parametric method such as artificial neural networks. The former method requires modeling of each structures and latter method requires data for the training. And these modeling and data for the training demands much costs. By the present method, damages are detected by judging statistical difference of data of intact state and present state. This method requires data of non-damaged state and does not require the complicated modeling and a large number of data for training.

As an example, the present study deals monitoring of delamination detections of a composite beam. The damages are detected from the change of strain data measured on the specimen surface by the statistical tools such as Response Surface and F-Statistics. As a result, the new method successfully diagnoses the damage without using modeling and data of damaged state.

Key Words: Smart Structure, Damage Diagnosis, Response Surface, Statistical tool

Introduction

Structural health monitoring system has many sensors mounted on, and evaluates damage state of the entire structure or structural components on real time. In order to prevent serious failures of civil structures such as bridge, gas piping, etc, the structural health monitoring system becomes noticeable technology recently. Especially in Japan, it is very significant to minimize seismic disaster, and to develop a system that diagnoses the condition of civil structure in short time at lower cost is an urgent subject. The present research proposes a new damage diagnostic method for the structural health monitoring at the lowest cost.

Multiple damage diagnostic for structural health monitoring have been proposed, and most of them employs one of parametric methods based on modeling of structure or non-parametric method such as ANN. As a parametric method, a substructural flexibility method [1] and a residual force method [2] are proposed. As a non-parametric method, ANNs [3] and response surface method(RSM) [4] are proposed. The parametric method requires modeling of the each structures and non-parametric method requires a large number of sets of data for training. These structural modeling and sets of data for the

training demands much costs. For existing structures, it is almost impossible to obtain sets of data after damage creation for training of ANN or RSM. This brings significant demand of development of the lower cost diagnostic method. In the present study, therefore, a new low cost statistical diagnostic method for structural damage detection is proposed. By the method, structural damages are detected by statistical tests of similarly of a relationship between measured data of intact state and present state. The new statistical diagnostic method requires sets of data of non-damaged state, and does not require the complicated modeling and a large number of sets of data after damage creations for training ANNs. This causes significant decrease of cost for making a diagnostic system.

As an example of the health monitoring system using the new method, the present method is applied to delamination detection of a composite beam in the present study, and the new damage diagnosis method experimentally investigated here.

Damage Diagnosis Method using comparison of Response Surface

For conventional health monitoring systems, relations between measured sensor data and damage location or size are indispensable to identify damages, or modeling of the entire structure is required to solve the inverse problem for identifications of the damages. The works for obtaining the relations are very time consuming and require high cost for computations and/or experiments. Modeling of the entire structure is the same. The new statistical diagnostic method proposed in the present paper is a low cost simple system. The system does not require the relation between measured sensor data and damages and does not need modeling of the entire structure. This method diagnoses slight change of the relation between the measured sensor data.

Procedure of the new diagnostic method for damage detection is shown in Figure 1. First, a response surface (RS, see next section) is created from the measured sensor data obtained from the initial state. The RS is named the initial response surface. For example, data of a sensor is selected as a response and the data obtained from the adjacent sensors are selected as predictors. Of course, you can select natural frequencies obtained from vibration data instead of using the measured data directly. After the training process, damage monitoring process is started. During the monitoring process, a set of every sensor data is periodically obtained by cycling measurements several times. From the measured set of data, a RS is recreated. The RS is named as recreated response surface here. The two RSs are compared with each other using a statistical similarity test with F-test. When the recreated RS is discriminated from the initial RS, it means that relation between the sensor data is changed, and that can be concluded that something happens in the structure. Of course this does not always means damage initiation, but this can provide a low cost solution for structural health monitoring to decide the necessity of the high cost investigation.

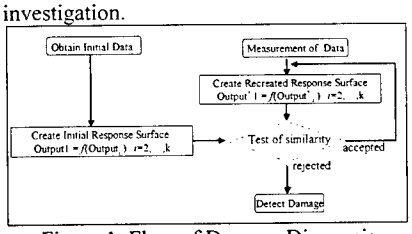

Figure 1. Flow of Damage Diagnosis

Response Surface Methodology

RSM[5] is employed for the process optimization in a quality engineering field. RSM consists of a design of experiments to select the most suitable points for fitting the surfaces effectively and the least-square-method to regress RS. RS is the approximation function that expresses the relationship between a response and predictors. Generally, a RS is represented

with the following formula.

$$y = f(x_1, x_2, \cdots, x_l) + \varepsilon \qquad (1)$$

where x are predictors, y is a response, ε is a regression error and l is a number of predictors. In general, polynomials are used.

For simplification, let us consider the case that a response is approximated by quadratic polynomials of two predictors as followings.

$$y = \beta_0 + \sum_{j=1}^{l} \beta_j x_j + \sum_{j=1}^{l} \beta_{jj} x_j^2 + \sum_{i=1}^{l-1} \sum_{j=i+1}^{l} \beta_{ij} x_i x_j \qquad (2)$$

where β is regression coefficient. If squares or interactions of the predictors ${x_j}^2, x_i x_j$ are replaced by new predictors $x_m (m > l)$, the formula (2) becomes the linear regression model as follows.

$$y = \beta_0 + \sum_{j=1}^{k} \beta_j x_j \qquad (3)$$

where k is number of the predictors after the replacement. In terms of n observations, the equation (3) can be written in matrix form as follows.

$$\mathbf{Y} = \mathbf{X}\boldsymbol{\beta} + \boldsymbol{\varepsilon} \qquad (4)$$

$$\mathbf{X} = \begin{bmatrix} 1 & x_{11} & x_{12} & \cdots & x_{1k} \\ 1 & x_{21} & x_{22} & \cdots & x_{2k} \\ \vdots & \vdots & \vdots & \ddots & \vdots \\ 1 & x_{n1} & x_{n2} & \cdots & x_{nk} \end{bmatrix}, \mathbf{Y} = \begin{Bmatrix} y_1 \\ y_2 \\ \vdots \\ y_n \end{Bmatrix}, \boldsymbol{\beta} = \begin{Bmatrix} \beta_0 \\ \beta_1 \\ \vdots \\ \beta_k \end{Bmatrix}, \boldsymbol{\varepsilon} = \begin{Bmatrix} \varepsilon_1 \\ \varepsilon_2 \\ \vdots \\ \varepsilon_n \end{Bmatrix}$$

Unbiased estimator of $\beta(\mathbf{b})$ is obtained using the least-square-method as follows.

$$\mathbf{b} = (\mathbf{X}^T \mathbf{X})^{-1} \mathbf{X}^T \mathbf{Y} \qquad (5)$$

Similarity Test of Response Surface using F-test

Let us consider, we have two RSs that are created from two different sets of experiments.

$$\mathbf{Y}_i = \mathbf{X}_i \boldsymbol{\beta}_i + \boldsymbol{\varepsilon}_i (i = 1,2) \qquad (6)$$

where the number of experiments for regression are n_1 and n_2 respectively. In order to investigate the similarity of the two RS, a null hypothesis is introduced. The hypothetical definition is shown as follows.

$$H_0 : \ \boldsymbol{\beta}_1 = \boldsymbol{\beta}_2 \qquad (7)$$

Assuming that each error term (ε) is independent and has the same distribution in two sets of experiments. In this case, the F-statistic value F_0 is defined as follows.

$$F_0 = \frac{SSE_0 - SSE_{12}}{SSE_{12}} * \frac{n-2p}{p} \qquad (8)$$

$$n = n_1 + n_2, \ p = k + 1$$

$$SSE_{12} = SSE_1 + SSE_2$$

where SSE represents residual sum of squares of a RS. SSE_0 is a residual sum of squares of the RS created from the entire data $n(=n_1+n_2)$, which regress from all data. This F-statistic value F_0 follows F-distribution of degree of freedom(p, n-$2p$) under the null hypothesis. When both of the RSs are similar with each other F_0 becomes small value. Critical limit for the rejection of the hypothesis H_0 is defined as follows.

$$F_0 > F^{\alpha}{}_{p,n-2p} \qquad (9)$$

where α is significance level. The similarity of RSs is rejected when F_0 is larger than $F^{\alpha}{}_{p,n-2p}$.

Damage Detection of CFRP Beam using Change of Surface Strain Distribution

Specimen for experiment

As mentioned before, the new diagnostic method is applied to delamination monitoring of a CFRP beam, and the effectiveness of the method is experimentally investigated here. Conventional strain gages are employed as sensors in the present study. Specimen configuration of the present study

is shown in Figure 2. The specimen is a CFRP cantilever beam with a thickness of 1.4mm and stacking sequence of the specimen is $[0_2/90_2]_S$.

Three conventional strain gages are mounted on the specimen surface as shown in Figure 2. Gage length of center gage is 10mm and the gage length of the side gages is 2mm.

A delamination crack is created under the center gage with a short beam shear test. Delamination occurs between 0° and 90° plies with matrix cracking in the middle 90°ply that is a trigger of the delamination initiation.

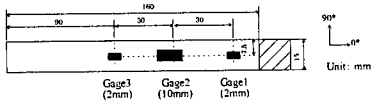

Figure 2. Specimen configuration

Damage detection method

In the present study, strain data of the middle gage #2 is the response, and the strain data of the gage #1 and #3 are predictors. Quadratic polynomials are employed for the creation of the RS. The RSs are approximated as follows.

$$\varepsilon_2 = \beta_0 + \beta_1\varepsilon_1^2 + \beta_2\varepsilon_3^2 + \beta_3\varepsilon_1\varepsilon_3 + \beta_4\varepsilon_1 + \beta_5\varepsilon_3 \quad (10)$$

where represents the strain data of gage #i. Concentrated load is applied to the left edge of the composite beam to obtain large number of sets of strain gage data. A RS of the equation (10) is regressed from the strain data set of 15 experiments.

The critical limit for the similarity test of RS is defined from significant level of 95% confidence probability. In this case, the critical limit is defined as 13.0 from F-test value distribution of intact state structure.

Identification results

Using the significant level of 95%, the performance tests of the diagnostic method are conducted to investigate the effectiveness of the method. Table 1 shows probability of diagnosis. For the in that case (delamination size is zero), the similarity tests of the two RSs passed by the performance of 95%. When the damage is existing to the structure, the similarity of the two RSs is rejected by the performance of 74%. On the basis of the performance results, the new diagnostic method provides high performance at low cost. The new method does not require test of damaged state to defined the limit between the intact state and damaged state.

Table 1. Diagnostic accuracy of detection of delamination

		Estimation	
		Non damaged	Damaged
Experiment	Intact	95.1%	4.9%
	Damaged	26.4%	73.6%

Conclusions

By conducting similarity tests of the two RSs with F-test, the present paper describes the new damage diagnostic method without measurements data of damaged state. As an example of the health monitoring system by this method, the present study deals monitoring of delamination detections of a composite beam. The delaminations are detected from the slight changes of measured strain data mounted on the specimen surface by using the new statistical tools.

References

1.C.A.Felippa, K. C. Park and M. R. Justino Filho. 1998., Computers & Structures, 68-4(1998), p.411-418

2.M.Kameyama, Y.Ogi and H.Fukunaga. 1999, Proc.6th Japan International SAMPE Symposium, (1999), p.987-990.

3.A.C.Okafor, K. Chandrashekhara and Y. P. Jiang. 1996. ,Smart Mater. Struct., 5 (1996) , p.338-347.

4.C.H.Keilers Jr. and F. Chang. 1995. ,J. Intell. Matls. Sys. & Struct. , 6 (1995), p.664-672.

5.R.H.Myers and D.C.Montgomery. 1995., John Wiley & Sons. Inc, (1995)

Proceedings of 7th Japan International SAMPE
Symposium & Exhibition, Nov. 13-16, 2001

Monitoring Method of Resin Flow and Cure with Electromagnetic Wave Transmission Line Using Carbon Fiber as Conductive Elements

Kei Urabe#, Tomonaga Okabe#, Hiroshi Tsuda# and Junji Takatsubo#

#: Smart Structure Research Center,
National Institute of Advanced Industrial Science and Technology
AIST Tsukuba Central 2, 1-1, Umezono 1, Tsukuba, 305-8568 JAPAN
E-mail: urabe-k@aist.go.jp

Abstract

We previously presented a new method for monitoring resin flow and cure with a high-frequency electromagnetic wave transmission line. Here, we propose the use of carbon fiber for conductive elements constructing the transmission line so as to use material reinforcements (i.e., carbon fiber) as sensing probes. The experimental results demonstrated the possibility of carbon fiber as transmission line elements.

Key Words: Curing, Epoxy resin, Carbon fibers, Electromagnetic wave

Introduction

The quality of resin composites strongly depends on the conditions of the manufacturing process. Hence, it is important to develop the "smart manufacturing" technique, in which sensors are embedded in the material and the manufacturing condition is automatically controlled to the best condition [1]. Among several sensing methods for the smart manufacturing, dielectric monitoring has been widely investigated and used [2,3]. In the manufacture of large structures or the resin transfer molding process, it is important to monitor distribution of the properties, discontinuities and/or resin flow. However, in the general dielectric monitoring method, a signal with a relatively low frequency is usually used. Hence, the obtained information is point data, or data integrated over the whole area of the sensor, because of the long wavelength of the signal [4,5]. In contrast, when a transmission line of electromagnetic wave with high-frequency (>100 MHz) is constructed inside the material or structure, the signal propagates as a wave with a wavelength comparable to the typical size of materials or structures. The signal is then expected to provide information on the properties of the material or structure, including their distribution or discontinuity. Therefore, we have recently proposed new cure monitoring techniques with a high-frequency electromagnetic wave transmission line, and have shown the potential as a tool for in-situ monitoring of curing, including information on local distributions or discontinuities, such as resin flow or the existence of air or variation in the cure stage [6,7]. In our previous investigations, the model transmission lines have been constructed with a metal line (diameter 2 mm) and an aluminum box. However, carbon fiber, which is a typical material element of advanced composites, is electrically conductive. Thus, it can be expected that, if the carbon fiber can be used as an element of the transmission line, it

would be possible to avoid a deterioration of material property and an increase in manufacturing cost caused by embedding of sensors. In the present paper, we therefore experimentally investigated the use of carbon fiber as elements of the transmission line.

Experimental

A microstrip line was constructed with a PAN type carbon cloth (Toray Inc. Torayca® Type 6151B, where carbon fiber strand type T300B-1000 is woven in two directions.) as the ground conductor, and a carbon strand pulled out from that type of cloth as the line conductor. Experiments using a thin copper wire of diameter 0.1 mm as the line conductor were also carried out. The experimental setup is shown in Fig. 1. The carbon cloth, 8 cm in width and about 35 cm in length, was placed on the bottom of an acrylic frame. The flange of a receptacle for electromagnetic signals was glued to the center of one end of the cloth using conductive epoxy. The center conductor of the receptacle was connected with one end of the carbon strand using conductive epoxy. When the copper wire was used as a line conductor, it was soldered with the center conductor of the receptacle. The distance between the line conductor (carbon strand or copper wire) and the ground conductor (carbon cloth) was set at 2.5 mm. The receptacle was connected to a digitizing oscilloscope having a time domain plug-in (Agilent Technologies Inc., Model 54750 with 54754). The terminal was short-circuited by connecting the line conductor to the carbon cloth with a conductive adhesive tape at the terminal. The oscilloscope generated a sharp step voltage of 200 mV with 30 ps rise time, and

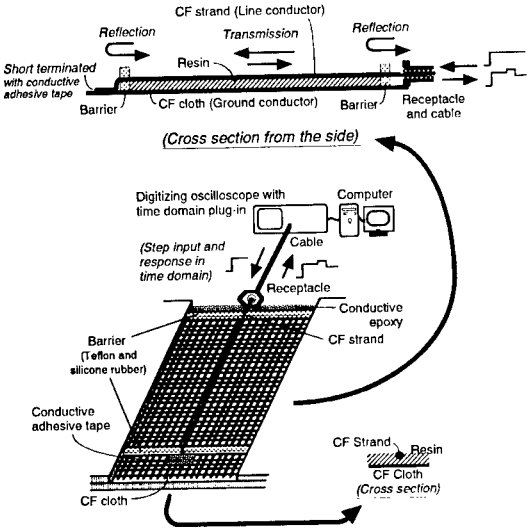

Fig.1 Experimental setup.

voltage change with time at a fixed point inside the oscilloscope was monitored. The monitored signal, that is the "time domain response", provides information on the positions and characteristics of discontinuities of the line, caused by change in the electrical property of the material between the pair of conductors of the line at the boundary as well as change in the shape of the line [7,8]. As the sample, Bisphenol-A type epoxy resin (Epikote®828, Yuka-Shell Epoxy, Inc.), mixed with an equivalent amount of diethylenetriamine was used. It was put in and around the line and cured at room temperature.

Results and Discussion

Figure 2 shows time domain responses for two different conditions, a carbon fiber strand and a copper wire of 0.1 mm diameter, of line conductor of the microstrip line gradually filled with resin from the terminal side. In the response before the line was filled with resin (denoted as "Empty" in each figure), the rise at point

"a" corresponds to reflection at the input of the line, and the drop at point "b" corresponds to reflection at the terminal. Because the impedance of the transmission line was higher than those of both the receptacle at the input and the short-circuited terminal, the voltage response rose at the input and dropped at the terminal [7]. When the line was partly filled with resin from the terminal side, another drop of the response occurred at the resin front, because the impedance of the part of the line filled with resin decreased according to the permittivity and loss factor of the resin. The time between the rise and the first drop in the response, indicated as "Air" for the case of "5 cm filled" in the figure, corresponds to the time for a round trip from input to the resin front. The time between the first drop and the next one can be related to the length of the line filled with resin. When a copper wire was used as the line conductor (Fig. 2 (b)), a similar response as in our previous work, where the transmission line was constructed with metal, was obtained. This means that the carbon cloth works as a ground conductor of the microstrip line in the same way as a metal plate. In contrast, when a carbon fiber strand was used as the line conductor (Fig. 2 (a)), the response showed an exponential increase after the rise at the input. This change in response can be attributed to the higher electrical resistance of the carbon fiber strand compared to the copper wire. Although there was such a difference in the response, the resin flow front was clearly detected even when a carbon fiber strand was used as the line conductor of the microstrip line. However, to obtain a

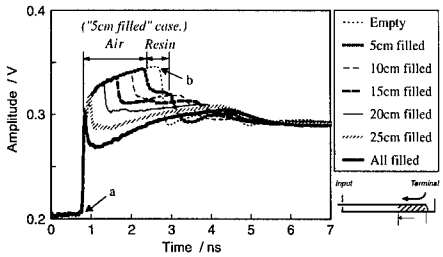

(a) Line conductor: CF strand×1 . (Line length=27cm)

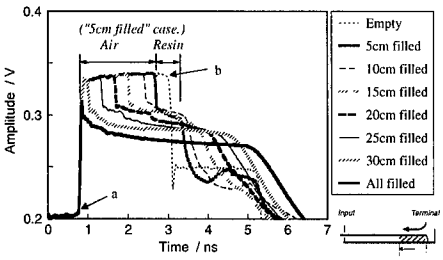

(b) Line conductor: 0.1mmϕ copper. (Line length=31cm)

Fig.2 Time domain response from the microstrip line gradually filled with resin from the terminal side.

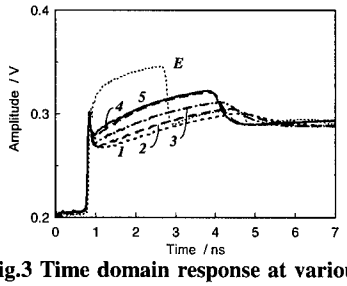

Fig.3 Time domain response at various cure stages. (Line conductor: CF strand×1, Line length=27cm)

***E*: Empty (without resin), *1*: 11min after mixing the curing agent, *2*: 44min after mixing, *3*: 83min after mixing, *4*: 128min after mixing (near peak temperature), *5*: 257 after mixing (after cure).**

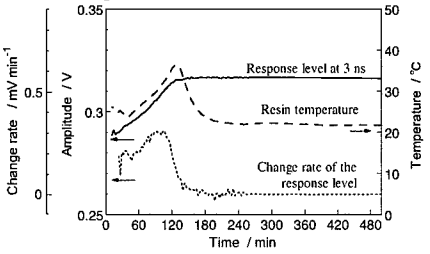

Fig.4 Change in response level at 3 ns with time, during a curing process of the resin, for the sample of Fig.3.

clearer response, it is desirable to use a thin metal wire as the line conductor.

Figure 3 shows the change in the time domain response during the curing of the resin after filling the whole line. A single carbon fiber strand was used as the line conductor in all the data shown hereafter. As curing progressed, the response level gradually increased, and the time between the rise and the drop decreased. This resulted from the decrease in permittivity and the loss factor of the resin with the progress of curing [6]. Taking the level at 3 ns as an index, changes in the level and its time differential with time are plotted in Fig. 4 together with the change in resin temperature. The rise of the level almost ended at the peak temperature, which most likely corresponded to almost the end of the main bridging reaction of the epoxy. This was the same tendency as in our previous works [6,7]. We thus found that progress of cure can be monitored in a similar way even if a carbon fiber is used as the conductive element of a transmission line. An existence of an air part in the resin and a variation in cure stage could also be detected as Figs. 5 and 6. It must be noted that information on the position, along the line, of the air part or the boundary of the cure stage was included in the response.

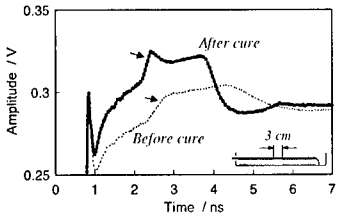

Fig.5 Time domain response when an air part existed in the resin. (Line conductor: CF strand×1, Line length=27cm.)

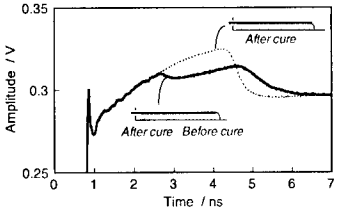

Fig.6 Time domain response when there was a variation in cure stage. (Line conductor: CF strand×1, Line length=31cm.)

Conclusion

We proposed and experimentally investigated the use of carbon fiber as conductive elements for monitoring resin flow and cure with time domain response from a high-frequency electromagnetic wave transmission line filled with resin. Resin flow, progress of cure, existence of air and variation in cure stage were successfully detected together with information on the position along the line. We found that a carbon cloth worked the same way as metal for the ground conductor. When a carbon fiber strand was used as the line conductor, the response was somewhat affected by the higher electric resistance of the carbon. The methodology proposed in the present paper is also applicable to health monitoring with electric conductivity [9], and can give information on the position of damage.

References

1. T. Fukuda and T. Kosaka: Mater. Sci. Res. Int., STP-2, 51(2001).
2. Y. Yamaguchi, M. Yoshida, M. Jinno, S. Sakai, K. Osaka and T. Fukuda: Proc. of 6th Jpn. Int. SAMPE Symp., 1037(1999).
3. K. Nixdorf and G. Busse: Compos. Sci. and Tech., 61, 889(2001).
4. S. D. Shwab, R. L. Levy RL and G.G. Glover: Polym. Compos., 17, 312(1996).
5. S. Motogi, T. Itoh and T. Fukuda: Proc. of 6th Jpn. Int. SAMPE Symp., 1033(1999).
6. K. Urabe, J. Takahashi, H. Tsuda and K. Kemmochi: J. Reinf. Plast. and Compos.,19, 1235(2000).
7. K. Urabe, H. Tsuda, J. Takahashi and K. Kemmochi: Mater. Sci. Res. Int., STP-2, 95(2001).
8. J. C. Freeman: "*Fundamentals of Microwave Transmission Lines*", John Wiley & Sons, New York, 1996, pp.164-202.
9. K. Schulte: Compos. Sci. and Tech., 61, 799(2001).

Proceedings of 7th Japan International SAMPE
Symposium & Exhibition, Nov. 13-16, 2001

Process Monitoring and Controlling with Dielectric Sensor for Thermoplastic Composite Vane

Kenjiro Yamagishi*, Shintaro Kitade*, Shinya Motogi** and Takehito Fukuda**

*: Research Institute, Ishikawajima-Harima Heavy Industries
1, Shin-Nakahara-cho, Isogo-ku, Yokohama, 235-8501, JAPAN
E-mail: kenjirou_yamagishi@ihi.co.jp
**: Department of Intelligent Materials Engineering, Osaka City University
3-3-138, Sugimoto-cho, Sumiyoshi-ku, Osaka, 558-8585, JAPAN

Abstract

Thermoplastic composites have relatively high impact resistance, and are good for the vane of the jet engine that sometimes suffers bird strike damage. Matched-die press molding process is a good process for the vane which has complex airfoil shape. But many laborious test moldings are needed to fix the adequate process parameters. Process monitoring/controlling with in-mold sensor can reduce the number of test moldings. Dielectric properties of PEEK resin in matched-die press molding process are measured. The correlations between melt viscosity, PvT properties and AC conductivity of PEEK are discussed. The inflection point of the temperature-AC conductivity curve agrees with onset of increasing and melt viscosity, and the onset of high shrinkage due to crystallization. The process control diagram utilizing dielectric properties is devised. The laminated CFRP plate is successfully molded by the controlled process. The capability of process monitoring/controlling utilizing the dielectric sensor is confirmed.

Key Words: Thermoplastic composites, Process Monitoring, Process Control, Dielectric sensor.

Introduction

Stator vane of aircraft engine is required to be of light weight and low cost [1]. High temperature thermoplastic CFRP is suitable material for the vane of jet engine, because thermoplastics have higher bird strike impact resistance than thermosets. Matched-die press molding process is good process for the vane, because it has complex airfoil shape, and needs precise molding. Matched-die press molding process enables us to control pressure and temperature more precisely than autoclave forming. But many laborious test moldings are needed to obtain the optimum process parameters for molding of thermoplastic CFRP vane.It is difficult to estimate melt viscosity or volume change of resin in the mold, which is necessary for the process control. The viscosity of the resin in the mold cannot be obtained only by viscosity data from rheometer and temperature from thermocouples because the viscosity changes not only by temperature but also by the cooling speed at the cooling step. The process monitoring and controlling with in-mold sensors can reduce the test moldings. We chose dielectric curing sensor for monitoring the melting/consolidating of the high temperature thermoplastic resin. A high heat resistant dielectric sensor is commercially available for monitoring at the temperature

range over 300 °C.

In this study, dielectric properties of a high temperature thermoplastic resin in matched-die press molding process are measured. The correlations between dielectric properties and viscosity and volume change are discussed. The process control method for high temperature thermoplastic CFRP vane is also discussed.

Experimental

Dielectric Measurement of PEEK

Figure 1 shows the experimental set up of the mold. An interdigitated comb-shape electrode sensor was located at the bottom of the mold cavity, and a thermocouple was built-in under the electrode of the sensor. A round shaped polyimde film(t=20mm) was put upon the electrode of the sensor to prevent adhering to the resin. The dimensions of the mold cavity was 150mm × 150mm × 2mm. Stacked PEEK (Poly-ether-ether-ketone) film (Mitsui-Chemical) was loaded in the mold, and constant pressure was applied by the hot-press. The mold was heated from room temperature to 380 °C at the rate of 2 °C/min, maintained at 380 °C for 30 minutes, and cooled down to 50 °C at the rate of 2 °C/min or 6 °C/min.

Complex dielectric measurements was made using Eumetric 100A (Holometrix -Micromet). The complex dielectric constant (ε*) is expressed as

$$\varepsilon^* = \varepsilon' + i\varepsilon'' \qquad (1)$$

where the real part (ε') is the permittivity that characterizing the capacitive component, and the imaginary part (ε'') is the loss factor characterizing the conductive component. The dielectric loss factor were measured in the process. Time intervals of the dielectric measurement were one minute at heating step and constant step, 20seconds at cooling step. The frequency range of the alternating voltage in the measurement was from 0.5Hz to 5Hz

Demonstration of Process Monitoring/ Controlling for CF/PEEK Composite

Demonstration of process control for CF/PEEK composite was performed using the same mold and the same hot press as that used in the dielectric measurement of PEEK resin. Stacked AS4/PEEK (Cytec-Fiberite) unidirectional carbon fiber prepreg was used for the demonstration. AC conductivity, which is calculated from loss factor, was monitored and applying pressure was controlled according to the monitored AC conductivity and the pressure control diagram that is mentioned later.

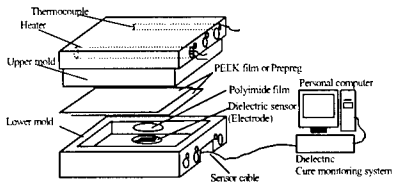

Fig.1 Experimental set up of the mold.

Results and Discussion

Dielectric Measurement of PEEK

The AC conductivity (σ_{AC}) is used to follow curing of thermosets [2]. The AC conductivity is calculated from following equation [3,4],

$$\sigma_{AC} = \varepsilon'' \cdot \omega \cdot \varepsilon_0 \qquad (2)$$

where ε '' is the dielectric loss factor, ε_0 is permittivity of the vacuum (= 8.85×10^{-12} F/m), and ω is the angular frequency. The measured AC conductivity of PEEK increases or decreases as the temperature increases or decreases respectively. Figure 2 shows the AC conductivity at cooling step and dynamic melt viscosity (by rheometer) at equal cooling rate to the dielectric measurement. At about 315 °C at the cooling rate of 2 °C/min or 305 °C of 6 °C/min, the dynamic viscosity significantly increases due to the onset of crystallization, simultaneously with the inflection of AC conductivity. Figure 3 shows correlations between

specific volume and temperature at two cooling rate. The onset temperature of high shrinkage coincides with the inflection temperature of the AC conductivity. Figures 2 and 3 show that the onset temperature of increasing viscosity and decreasing volume shifts lower as the cooling rate increases, and the shifts were monitored by the dielectric sensor. The onset of high shrinkage or increase of viscosity is important and necessary information for process control of thermoplastic composites, and these results show that the information can be monitored by in-mold dielectric sensors even when the cooling rate varies.

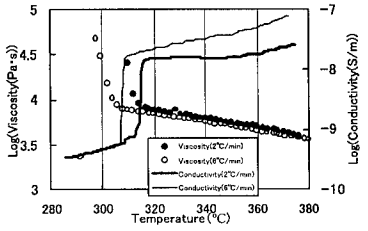

Fig.2 Correlations between AC conductivity and dynamic viscosity of PEEK in the cooling step.

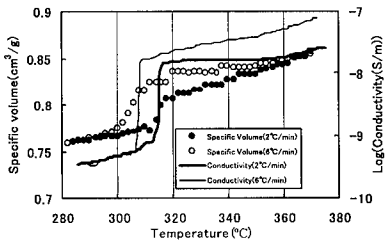

Fig.3 Correlations between AC conductivity and PvT properties of PEEK.

Process control Scheme for Press Molding of Thermoplastic Composites Utilizing Dielectric Sensor

On controlling the process of thermoplastic composites, sudden shrinkage of resin at consolidation point is the most important factor to be considered. We have to apply high pressure at consolidation point to avoid formation of micro void or rough surface in composite vane. The sudden increase of melt viscosity of the resin at the consolidation point is also important for process control. When the viscosity is low, high pressure makes unnecessary flow of the resin that causes misalignment of continuous fiber of the composite vane. On the other hand, when the viscosity is high, low pressure has little effect for the shrinkage.

Figure 4 shows the schematic of the correlations between temperature, AC conductivity, viscosity, and specific volume of PEEK or PEEK composites. Figure 4 also shows the adequate pressure control diagram for PEEK composites based on the correlations. In the heating step, high pressure is not necessary. (Phase I of the diagram) At the maximum temperature, the viscosity of the resin is the lowest in the process. Moderate pressure should be applied to form the desired shape of the composite vane. (PhaseII) At the consolidation point detected by dielectric sensor (point B of the diagram), higher pressure should be applied to prevent void formation due to the sudden shrinkage of the resin. After passing through the consolidation point, we should keep applying high pressure to avoid deformation affected by thermal shrinkage. (PhaseIII) On molding the composite vane, the thickness is not uniform and the shrinkage at consolidation point is not uniform. We also have to control temperature precisely.

Demonstration of Process Monitoring/ Controlling for Composites

Process monitoring/controlling of the press molding was demonstrated according to the diagram. The range of pressure was from 0.22 MPa to 1.33 MPa, and both heating/cooling rates were 2 °C/min. Figure 5 shows an example of AC conductivity monitored at cooling step of the demonstration. Figure 6 shows the CF/PEEK composite plate in the demonstration. The composite plate was successfully molded.

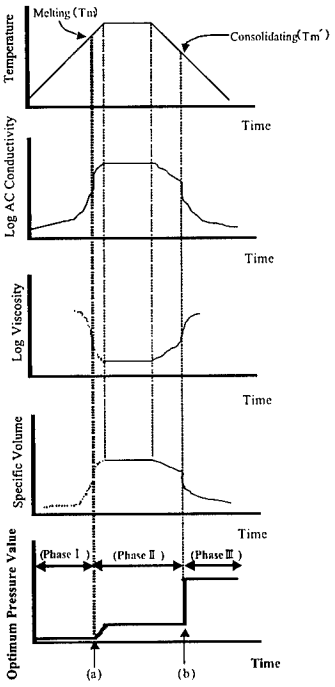

Fig.4 Schematic of the correlations between temperature, AC conductivity, viscosity, volume and optimum pressure.

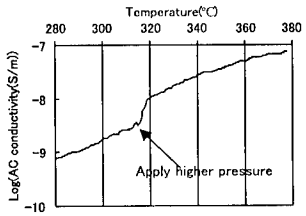

Fig.5 Monitored AC conductivity (1Hz) at pressure control demonstration.

Conclusions

Dielectric properties of PEEK resin in the press forming process were measured. In the cooling step of the process, the inflection point of temperature-AC conductivity curve coincided with sudden increase of viscosity and high shrinkage due to crystallization. The pressure control diagram utilizing the dielectric sensor in the press molding of CF/PEEK was devised, and the demonstration was performed. The capability of the process monitoring/controlling with dielectric sensor was confirmed.

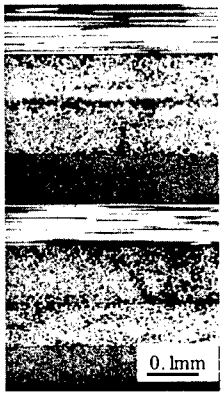

Fig.6 Cross section view of the CF/PEEK composite plate its stacking sequence of (0/45/-45/90)$_{2s}$.

Acknowledgment

This work has been supported by NEDO (New Energy and Industrial Technology Development Organization) and RIMCOF(R& D Institute of Metals and Composites for Future Industries) under "Smart Materials and Structure Systems" project.

References

1. G.E.Gresheim, R.B.Berkley, D.S.Murphy and R.T. Revely: Int. SAMPE Tech.Conf., 28 (1996)
2. W.Sichina, C.L.Marcozzi and P.S.Gill: Int.SAMPE Symp., 35, 1241 (1990)
3. K.Fridrich, C.Vinh-Ting, G.Boiteux, G.Seytre and J.Ulanski: J. of Applied Polymer Science, 65, 2529 (1997)
4. J.M.Gonnet, J. Guillet, A.Ainser, G.Boiteux, R.Fulchiron and G.Seytre: SPIE 4017, 94 (1999)

Proceedings of 7th Japan International SAMPE
Symposium & Exhibition, Nov. 13-16, 2001

Application of Small-Diameter FBG Sensors for Delamination Detection in CFRP Laminates

Shin-ichi Takeda, Yoji Okabe and Nobuo Takeda

Graduate School of Frontier Sciences, The University of Tokyo
c/o Komaba Open Laboratory (KOL), The University of Tokyo
4-6-1 Komaba, Meguro-ku, Tokyo, 153-8904, JAPAN
E-mail: shin-ichi@compmat.rcast.u-tokyo.ac.jp

Abstract

Newly developed small-diameter fiber Bragg grating (FBG) sensors were applied to the detection of the delamination in carbon fiber reinforced plastic (CFRP) cross-ply laminates. The reflection spectra from the FBG sensor were measured at various delamination lengths through four-point bending test. The form of the spectrum was found to change sensitively by the initiation of the delamination and the increase of the delamination length. In order to confirm this change in the spectrum, the spectra were calculated theoretically. Moreover an effective indicator for the prediction of the delamination length was proposed.

Key Words: Fiber-Optic Sensors, Fiber Bragg Grating, Delamination, Health Monitoring.

Introduction

The failure process of CFRP laminates under static or dynamic loadings is known to involve unique microscopic damages, such as matrix cracks and delaminations. Especially, the delamination causes stiffness reduction and often leads to the catastrophic failure. Thus, the delamination detection is very important to evaluate the reliability of CFRP laminates.

In this research, the small-diameter FBG sensors were embedded in CFRP cross-ply laminates. The reflection spectra from this FBG sensor were obtained at various delamination lengths. Then the quantitative evaluation of the delamination was conducted using the change in the reflection spectrum.

Experimental Procedures

Materials

The authors and Hitachi Cable Ltd. have developed small-diameter FBG sensors. Bragg gratings are fabricated in small-diameter optical fibers coated with polyimide layer whose thickness is 6 μm. The core and cladding diameters are 6.5 μm and 40 μm, respectively. The length of grating is 10 mm, and the grating period is about 0.5 μm. The profile of the refractive index modulation was controlled as a Gaussian shape to suppress the side-lobe of the reflection spectrum.

The specimen was CFRP laminates T800H/3631 (Toray Industries, Inc.), in which small-diameter FBG sensors were embedded. The laminate configuration was cross-ply $[90_{10}/0_2]_s$, and the dimensions of test specimen were $140 \times 20 \times 2.7$ mm^3. As shown in Fig. 1, a strip-type delamination grows in four-point bending tests. For the delamination onset from the tip of a transverse crack, a vertical notch was introduced at the mid-span of the

specimen. The transverse crack occurred from the root of the notch and propagated to the 0°/90° interface. In order to examine the effect of the initiation point of a delamination, small-diameter FBG sensors were embedded at two different positions as shown in Fig. 2. The delamination initiated at the center of the FBG sensor in Type A specimens; from the end of the FBG sensor in Type B specimens.

Measurements

Quasi-static load was applied to the specimen with a four-point bending device at room temperature. The loading speed was 0.5 mm/min. The delamination that grew at the 0°/90° interface was observed using a soft X-ray radiography. The optical fiber was illuminated by an amplified spontaneous emission (ASE) light source (Ando Electric Co., Ltd., AQ-6310). After the bending load was decreased to 0 N, the reflection spectrum from the FBG sensor was obtained by using an optical spectrum analyzer (Ando Electric Co., Ltd., AQ-6317).

Analysis of Reflection Spectrum

The spectrum was calculated theoretically for confirmation of the measured spectrum. At first, the strain distribution of the FBG sensor was obtained by FEM analysis with ABAQUS code. The specimen was modeled using 2-D plane strain finite elements. The delamination length used in the FEM analysis was identical with that measured by the experimental observation. Next, the distributions of the grating period and the average refractive index along the FBG sensor were calculated from the strain distribution. Then the reflection spectrum was simulated from the distributions using the couple mode theory and the transfer matrix method. This simulation was conducted with the software "IFO_Gratings" developed by the Optiwave Corporation.

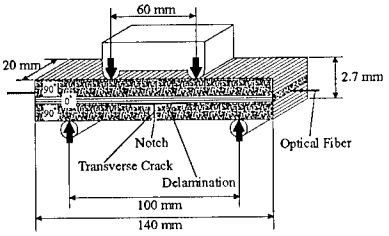

Fig. 1 CFRP laminate with delamination under four-point bending test.

Results and Discussion

Sensor Response to Delamination Growth

Fig. 3 shows the reflection spectra for the Type A test. In this research, the intensity of the reflection spectrum was normalized by the intensity of the highest component. When there was no crack in the specimen, the reflection spectrum had a sharp narrow peak. After a transverse crack occurred in the specimen, the form of the reflection spectrum became broad and had some peaks because of the non-uniform axial strain distribution in the FBG sensor. When a delamination was initiated from the crack tip, the form of the reflection spectrum had one large peak and some low intensity components around it. Then the intensity of these low intensity components decreased with an increase in the delamination length. Since this tendency appeared in both measured and calculated spectra, it was confirmed that these changes in the form of the reflection spectrum were caused by the growth of the delamination.

Fig. 4 shows the reflection spectra for the Type B test. The transverse crack appeared

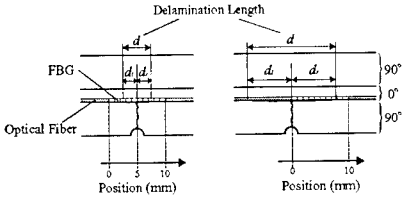

Fig. 2 Embedment of small-diameter FBG sensors at two different positions: (a) Type A and (b) Type B.

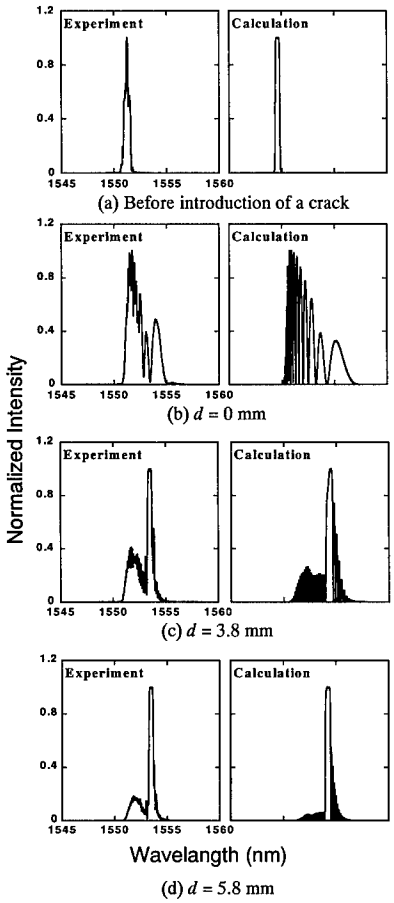

Fig. 3 Reflection spectra in Type A test.

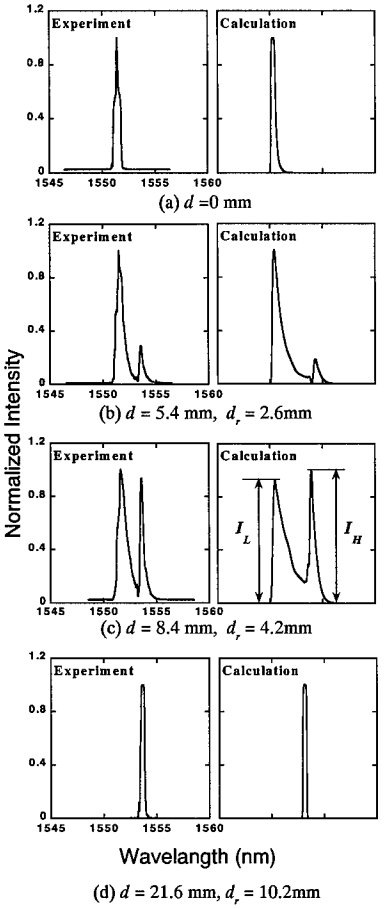

Fig. 4 Reflection spectra in Type B test.

at the end of the FBG sensor, and the transverse crack only affected the strain distribution around the end of the sensor part. Hence the intensity of higher wavelength components increased slightly. After the delamination was initiated from the crack tip, the intensity of the higher wavelength peak increased with an increase of the delamination length in both measured and calculated spectra. The form of the reflection spectrum was found to be sensitive to the delamination length. Especially, the intensities of the two peaks in the spectrum obtained from the Type B test changed depending on the delamination length. Thus, in the following discussion, the change in the intensities of the two peaks was examined based on the theoretical calculation for the result of Fig. 4.

Prediction of Delamination Length

We focused on the axial strain distribution in the FBG sensor that was characterized by two levels of uniform strain as shown in Fig. 5, which were used for the calculation of Fig. 4

(c). The levels I and II are related to the strain at the delaminated area and that at the bonded area, respectively. As the delamination length increases, the region of the uniform strain at the level I will enlarge, and the intensity of higher wavelength peak in the spectrum will increase consistently. In the present study, the intensity ratio of the two peaks, I_H/I_L, was defined as an indicator of delamination length, where I_H and I_L are the intensities of higher and lower wavelength peaks, respectively.

Fig. 6 shows the logarithmic plot of the intensity ratio against the delamination length along the FBG sensor —this length is equal to the value of d_r in the Type B test. The delamination length less than 4.2 mm was well estimated by the value of I_H/I_L. When the delamination length was over 4.2 mm, the increase of I_H/I_L obtained from theoretical calculation became larger than that from the experiment. This difference was caused by the error of delamination length measurement due to the intralaminar delaminations that was observed using a soft X-ray radiography. However, since the intensity ratios obtained from both experiment and calculation increased monotonically with an increase of the delamination length, the intensity ratio of the two peaks was found to be an effective indicator for the prediction of the delamination length.

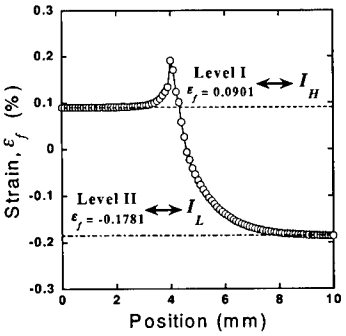

Fig. 5 Strain distribution along grating at Type B test.

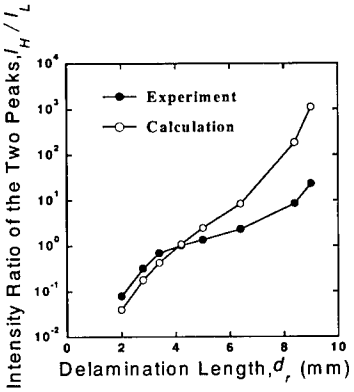

Fig. 6 Intensity ratio of the two peaks against delamination length along grating.

Conclusions

The delamination detection in CFRP cross-ply laminates was performed using an embedded small-diameter FBG sensor. The form of the spectrum changed sensitively, as the delamination length increased. Then, the relationship between the delamination length and the change in the spectrum was clarified by the theoretical calculation. When a delamination was initiated from the outside of the FBG sensor, the intensity ratio in the spectrum was an effective indicator for the prediction of the delamination length. In the delamination growth, if the axial strain distribution in the FBG sensor was characterized by two levels of uniform strain, this indicator could have a potential to be applied to other laminate configurations.

Acknowledgments
This research was conducted as a part of the R&D for Smart Materials Structure System project within the Academic Institutions Centered Program supported by NEDO (New Energy and Industrial Technology Development Organization), Japan.

Proceedings of 7th Japan International SAMPE
Symposium & Exhibition, Nov. 13-16, 2001

Strain Measurement by the Smart Patch Using FBG Sensors

Nobuhira Tanaka#1, Yoji Okabe#2, and Nobuo Takeda#2
#1: Department of Aeronautics and Astronautics, Graduate Student, The University of Tokyo
#2: Graduate School of Frontier Sciences, The University of Tokyo
c/o Komaba Open Laboratory (KOL), The University of Tokyo
4-6-1 Komaba, Meguro-ku, Tokyo, 153-8904, Japan
E-mail: nobu@compmat.rcast.u-tokyo.ac.jp

Abstract

Two devices for strain measurement using FBG sensors were studied. One was the hybrid patch, which included FBG sensors in series. It was experimentally confirmed that the device could measure the strain compensating the change of the temperature simultaneously. The other was the laminate patch. It is theoretically expected that the width of the spectrum increases in proportion to the difference between the strain along the width direction and that along the thickness direction. For the confirmation of this theory, an epoxy plate including an FBG sensor was loaded transversely. It was shown that the width of the spectrum increased in proportion to the transverse strain which caused the difference between the strains along the two directions. The laminate patch uses the spread of the spectrum in order to compensate the temperature change. It was experimentally confirmed that the width changed in accordance with the temperature and the axial strain applied to the patch.

Key Words: Fiber Bragg Grating, Composite, Strain, Temperature

1. Introduction

Although resistive foil strain gauges are widely used for strain measurement, Fiber Bragg grating (FBG) sensors are attracting increasing attention. This is because they have some strong advantages over resistive foil strain gauges, for example, immunity to electromagnetic interference, long lifetime, and simultaneous measurement of the strain at several points [1]. Nowadays, smart patches in which FBG sensors are embedded have been studied for strain measurement.

However, FBG sensors are subject to the influence of temperature. The Bragg wavelength of an FBG sensor depends mainly on strain, but it shifts slightly by the change of temperature. With the change of 1°C, the measured strain has typically an error of 11μ strain.

To achieve higher accuracy, therefore, FBG sensors need temperature compensation. For the simplicity of the device, it is desirable to conduct strain measurement and temperature compensation with a single patch. In this paper, two types of smart patches are introduced. The first one is a "hybrid patch", which consists of CFRP and GFRP connected in series, and the second is a "laminate patch", which is a laminate of CFRP and epoxy.

2. Hybrid Patch

2.1 Principle

A CFRP unidirectional laminate (UD laminate) and a GFRP UD laminate including an FBG sensor in each are connected in series, and its ends are glued to the structure of which the strain should be required (Fig.1). Because of the differences of their Young's moduli and coefficients of thermal expansion (CTEs), the temperature change influences the strains of both materials. Therefore, the strains can be expressed by the following equations.

$$\varepsilon_1^c = \alpha_\varepsilon^c \varepsilon_s + \alpha_T^c \Delta T \quad (1)$$
$$\varepsilon_1^g = \alpha_\varepsilon^g \varepsilon_s + \alpha_T^g \Delta T \quad (2)$$

$$\varepsilon_2^c = \beta_\varepsilon^c \varepsilon_s + \beta_T^c \Delta T \quad (3)$$
$$\varepsilon_2^g = \beta_\varepsilon^g \varepsilon_s + \beta_T^g \Delta T \quad (4)$$

where ε_s is the strain of the structure, ΔT is the temperature change, α and β are constants, suffixes 1, 2, c, and g mean the axial direction, the transverse direction, CFRP, and GFRP, respectively. On the other hand, the shift of the Bragg wavelength $\Delta\lambda$ is expressed by the following equation [2]:

$$\frac{\Delta\lambda}{\lambda_0} = \left(1 - \frac{n_0^2}{2} p_{12}\right)\varepsilon_1 - \frac{n_0^2}{2}(p_{11} + p_{12})\varepsilon_2 + \left\{\frac{1}{n_0}\frac{dn_0}{dt} + \frac{n_0^2}{2}(p_{11} + 2p_{12})\alpha_s\right\}\Delta T \quad (5)$$

where λ_0 is the initial wavelength, n_0 is the refractive index, α_s is the CTE of the optical fiber, and p_{11} and p_{12} are the strain-optic coefficients. From these equations, the shifts of the Bragg wavelengths are expressed with ε_s and ΔT.

$$\begin{pmatrix}\Delta\lambda_c \\ \Delta\lambda_g\end{pmatrix} = K^{-1}\begin{pmatrix}\varepsilon_s \\ \Delta T\end{pmatrix} \quad (6)$$

where K is a constant matrix. By deciding K-matrix, the accurate strain can be calculated from the wavelengths.

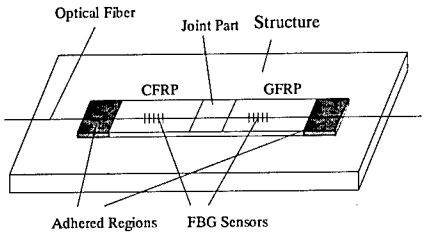

Fig.1 Hybrid patch

2.2 Experiments

The patch size was 11cm×1cm×500μm (4 plies). For the connection of CFRP and GFRP, epoxy adhesive films were inserted. The joint part was 1cm long. Both 1cm regions at the ends of the patch were glued to the stainless plate, which was assumed to be a structural member, by the same adhesive. The dimension of the stainless plate is 20cm×3cm×5mm. The FBG sensors used in this experiment are as follows: λ_0^c =1535.78nm, λ_0^g =1548.53nm, n_0 =1.4575, dn_0/dT =1.2×10^{-5}, α_s =0.5×10^{-6}/°C, p_{11}=0.113, and p_{12}=0.252.

For the symmetry of the specimen, a same patch with no optical fiber was glued on the other surface of the plate. At three different temperatures: 37°C, 55°C, and 73°C, tensile strain was applied to the specimen. The obtained wavelengths were compared with the strain of the structure measured by a resistive foil strain gauge attached to the side of the plate. In the measurement of the strain, a three-wire strain gauge was used for the compensation of the temperature change.

As shown in Fig.2, the relation between the wavelengths and the strain depends on the temperature. However, because of its linearity, it is expected that the relation will be expressed as eqn. (6).

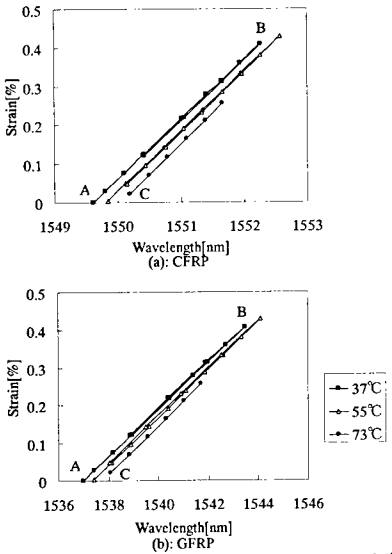

Fig.2 Wavelength shift by the strain and the temperature: (a) FBG sensor in CFRP and (b) in GFRP

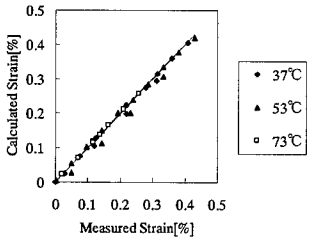

Fig.3 Comparison between the strain calculated from the wavelengths obtained by the hybrid patch and that measured by the strain gauge

2.3 Strain Calculation from the Wavelengths

After K was calculated from the three points of A, B, and C in Fig.2, the strain was calculated from the wavelengths of the FBG sensors. The calculated strains were compared with those measured by the strain gauge in Fig.3. The calculated strains were almost the same as the measured strains. Therefore, it was shown that this patch could measure the strain very accurately in spite of large temperature change.

3. Laminate Patch

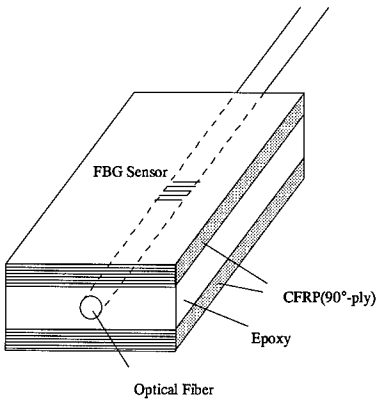

Fig.4 Laminate patch

3.1 Principle

An epoxy plate and two 90° plies of CFRP are laminated and an FBG sensor is embedded in the epoxy-ply as shown in Fig.4. Because of the thermal residual stress, the section of the optical fiber is deformed, which causes birefringence. Hence, the spectrum becomes the coupling of two different spectra. The difference of the two central wavelengths is in proportion to the difference of the strain in the width direction, ε_2, and that in the direction along the thickness, ε_3, as the following equation.

$$\lambda_p - \lambda_q = \frac{n_0^2}{2}(p_{12} - p_{11}) \cdot |\varepsilon_2 - \varepsilon_3| \qquad (7)$$

As the temperature decreases, the thermal residual stress increases, so that the width of the spectrum also increases. Hence, from the width and the central wavelength, both the strain and the temperature are calculated.

3.2 Experiments

The laminate patch consisted of [CFRP 90° / Epoxy / CFRP 90°]. One CFRP laminate was 250μm in thickness, and the epoxy-ply was 500μm in thickness. The FBG sensor was embedded in the center of the epoxy-ply. This patch was cured at 100°C. In order to reveal the influence of the temperature and the strain on the width of the spectrum, following experiments were carried out. The width was defined as a Full Width at Half Maximum (FWHM) and a Full Width at Quarter Maximum (FWQM).

First, an FBG sensor was embedded into epoxy plate, and transverse loading was applied. As a result the width of the spectrum spread as the transverse strain increased (Fig.5). Especially, FWQM increased quite linearly with the strain.

Next, for the investigation of the relation between the temperature and the width, the temperature of the patch was changed without loading. The dimension of the specimen was 9cm×4cm×1mm. Figure 6 shows that the FWQM was linearly decreased as the temperature increased. This result corresponds well with the theory. FWHM also showed the same tendency though the data curve was not smooth because of the side-lobes of the spectrum.

Finally, the laminate patch itself was loaded at 25°C, 38°C, and 58°C. The dimension of the specimen was 15cm×1cm×1mm. As shown in Fig.7, the changes of the data were not linear. The reason may be that the spectrum after embedment was disturbed by the stress concentrations around the voids in the

epoxy-ply.

FWQMs, however, were increased by the strain at all temperatures. This was because Poisson's effect was different between along the width direction and along the thickness direction due to the large stiffness of CFRP. In addition, it was shown that the spectrum at the lower temperature was wider than that at the higher temperature in this experiment. It also corresponded well with Fig.6.

4. Conclusions

In this research, two types of smart patches were developed. It is proved that they can compensate the change of the temperature well, and measure the strain of the structure accurately.

With regard to the hybrid patch, except for a slight error, the strain was measured accurately. To improve the accuracy, adhesive should be carefully selected since the adhesive used in this research did not endure high temperature and high load well.

In the study of the laminate patch, it was shown that the width had a linear relation with the change of the temperature and the axial strain, although it was not smooth. In all experiments, it was found that the changes of the FWQMs were nearer to a linear curve than those of the FWHMs. It is expected that by the use of an FBG sensor with a smooth spectrum, the width will change completely in proportion to the temperature or the strain as Fig.6 shows.

The following two problems should be solved for the numerical analysis of the laminate patch. One is the way to couple two spectra in order to find the relation of the difference of the two central wavelengths and the width. The other is to calculate the strain of the optical fiber transferred from the epoxy-ply.

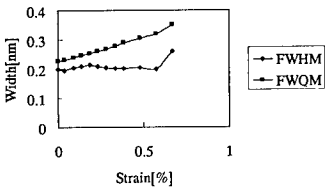

Fig.5 Change of the width of the spectrum by transverse loading

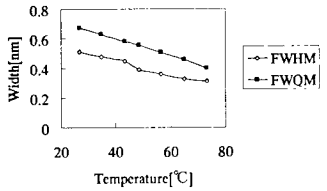

Fig.6 Change of the width of the spectrum by the temperature

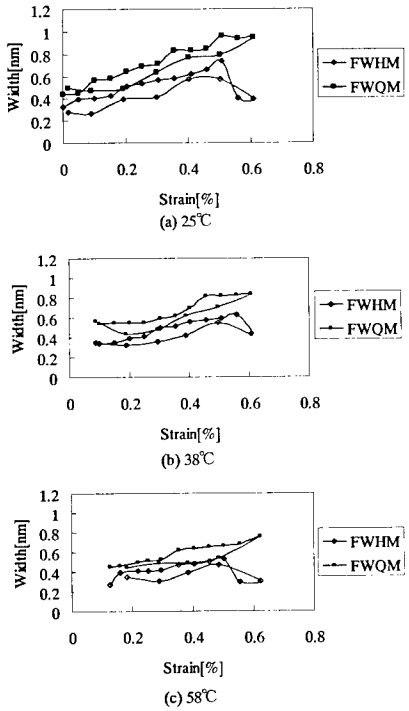

Fig.7 Change of the width by loading: (a) at 25°C, (b) at 38°C, and (c) at 58°C

References

1. N. Takeda and Y. Okabe: Transactions of the Japan Society of Mechanical Engineers-A, 67(655), 378 (2001).
2. Van Steenkiste,R.J. and Springer,G.S.: *"Strain and Temperature Measurement with Fiber Optic Sensors"*, TECHNOMIC Publication, 1997

Proceedings of 7th Japan International SAMPE
Symposium & Exhibition, Nov. 13-16, 2001

Internal Strain Monitoring of Molded Epoxy Using Embedded EFPI Optical Fiber Sensor during Molding

Katsuhiko Osaka*, Tatsuro Kosaka*, Takehito Fukuda*, Tatsuo Naka**,
Yasuyuki Kurata*** and Hiroshi Miyagawa***

*Osaka City University: Sugimoto, Sumiyoshi-ku, Osaka 558-8585, Japan
Katsuhiko Osaka : ohsaka@imat.eng.osaka-cu.ac.jp
**Daihen Corporation: 2-1-11 Tagawa, Yodogawa-ku, Osaka 532-8512, Japan
***Meidensha Corporation: 1-17, Ohsaki 2-Chome Shinagawa-ku, Tokyo 141-8565, Japan

Abstract

In the present study, internal strain monitoring of a molded epoxy using an embedded EFPI optical fiber sensor during molding has been investigated. First, to examine measurement ability of the sensor, experiments on internal strain monitoring of a cubic molded epoxy were performed. In the experiment, two kinds of the EFPI sensors having different stiffness were used. The strain monitoring ability of the sensor was investigated and effects of its stiffness on the sensitivity for strain measurement was also examined. Next, experiments were performed on strain monitoring for an epoxy mold having a cylindrical shape and including a steel cylinder in its center. The sensor was embedded in the location where residual stress should be generated in order to investigate the sensing ability for measurement of the residual stresses. From the results, it was found that the EFPI sensor can monitor the internal strain during molding and has the sensitivity enough to detect the cure shrinkage strain.

Key Words: EFPI Optical Fiber Sensor, Epoxy, Molding, Internal Strain, Monitoring

1.Introduction

The volume of production in resin-molded products including metal parts like as step-up transformers is increasing in recent years. These products have a problem of defects such as clacks generated in the cooling stage after heating and curing of resins during the molding. These defects are caused by residual stress due to the difference between the thermal expansion coefficient of the resins and that of the metals. It is important to decide an optimum molding condition and shape of the embedded metal parts in order to suppress the generation of the residual stresses. For realization of it, a real-time monitoring of internal strains in the molded products is very effective. Some studies on the measurement of the residual stress have been performed. The measuring methods of strains used in them were a photoelastic [1,2] and an electric resistance wire strain gage ones[3-5]. Recently, EFPI optical fiber sensors attract considerable attention as a strain sensor because they have many excellent features. Especially, they are suitable for embedding in the mold because of their very small size.

In the present study, a real-time monitoring of internal strains in the epoxy resin mold using an EFPI optical fiber strain sensor has been investigated. First, the sensitivity of the sensor for measurement of internal strains was examined. Next, internal strains in an epoxy mold including an metal cylinder were measured in the molding process. Based on the results, measuring ability of the EFPI sensor for internal strain monitoring during molding was examined.

2. Sensing Ability of EFPI Sensor

2.1 Experiments

In the measurement of the internal strains of epoxy molds during molding, FTI-buss500 strain measurement system (FISO Technologies, Co. Ltd.) was used. It uses the EFPI optical fiber sensor for strain measurement. In order to examine effects of the sensor stiffness on the measurement sensitivity, two types of the sensor having different stiffness were used. They have the same structure but different diameters in the sensing part. Their outer diameters are 200 μ m and 310 μ m. The internal diameter is the same for the two sensors. The sensor of 200 μ m diameter has a lower stiffness because the thickness of the silica glass tube in the sensing part is thinner. A schematic diagram of the sensing part in the sensor of 310 μ m diameter is shown in Fig.1. In the experiments, to investigate the measurement ability of the EFPI sensor, internal strain monitoring for a cubic mold was performed. The shape and dimensions of the cubic mold are shown in Fig.2. The EFPI sensors and a thermocouple are embedded in the center of the mold. Bisphenol A-based epoxy resins were used for the mold. A curing agent was an alicyclic acid anhydride. A programmable constant temperature oven was used for cure of the epoxy mold. The temperature setting on the oven for the cure is shown in Fig.3. Natural cooling from 150°C to the room temperature was provided for the epoxy mold.

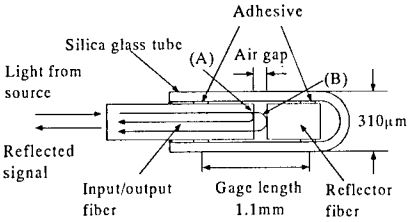

Fig.1 Sensing part of the EFPI optical fiber sensor.

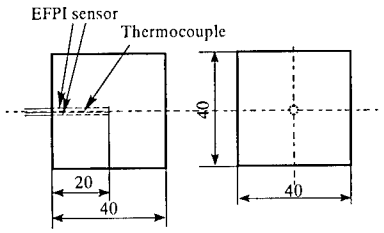

Fig.2 Cubic epoxy mold.

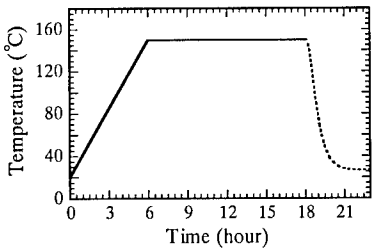

Fig.3 Pattern of the molding temperature.

2.2 Results and Discussions

The measurement results through the use of the EFPI sensors and the thermocouple are shown in Fig.4. The temperature of the molded epoxy is higher than that of the oven at the molding time of about 4 hours(A point). This higher temperature is caused by an exothermic reaction of the cure. After that, the temperature of the mold coincides with that of the oven. The EFPI sensors show almost no strain for about 4 hours. After that, compressive strains are measured, then tensile ones. The timing of this detection of the compressive strains coincides with that of overheating by the exothermic reaction. In the early period in the molding, the EFPI sensors can not detect the strain because the epoxy does not have a stiffness which is enough high to deform the sensing part of the sensor. In the cooling stage, the sensors detect compressive strain caused by the thermal shrinkage. The 200 μ m diameter sensor measures higher compressive strains than 310 μ m diameter one. To compare the strains measured with the two kinds of the EFPI sensors in curing stage in detail, an enlarged view of the strain change is shown in Fig. 5. After a lapse of 4 hours, the compressive strains begin to be detected. Subsequently, the increasing tensile

strains are measured with the temperature. The compressive strains detected with the sensor are thought to be caused by cure shrinkage, because the thermal shrinkage does not occur in this period. The tensile strains measured after the detection of the compressive strains are caused by the thermal expansion of the molded epoxy. After detection of the tensile strains, compressive strains are measured with the sensors despite the temperature being constant. Because no thermal shrinkage occurs in this stage, detection of the compressive strains means that the sensors detect the cure shrinkage. In this curing stage, the 200 μ m diameter sensor detects higher compressive and tensile strains than the 310 μ m diameter one. This fact shows that the sensor with a lower stiffness have a higher sensitivity than that with a higher stiffness. Next, in order to examine the strain change against the temperature, the relations between the strain and the temperature are shown in Fig. 6. In the cooling stage, the total amount of the compressive strain measured with the 200 μ m diameter sensor is higher than that with the 310 μ m diameter one. But the two sensors measure the same amount of the strains under about 100°C. From this result, it is found that the two kinds of sensors have the same sensitivity when the epoxy resins have a higher stiffness than a certain value.

Next, to examine the relation between the stiffness and the measuring sensitivity of the EFPI sensor, FEM analysis was performed. The model used for the strain analysis was an epoxy resin cylinder including the sensor in its center. The results of the calculation are shown in Fig.7. In the figure, the vertical axis shows the ratio of the strain of the sensor to the epoxy resin. The horizontal axis designates the Young's modulus of the epoxy resin. From the result, it is found that the sensor of 200 μ m diameter shows higher sensitivity in the low stiffness area but the two sensors have almost the same sensitivity in the high stiffness area. This analysis result coincides with that of the experiments.

3. Internal Strain Monitoring of Molded Epoxy Including a Metal Inclusion

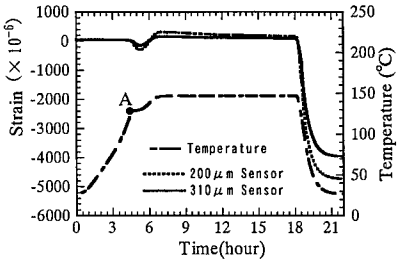

Fig.4 Temperature and strains measured during the molding.

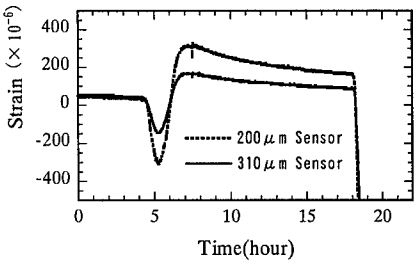

Fig.5 Strains measured with two kinds of EFPI sensors during the molding.

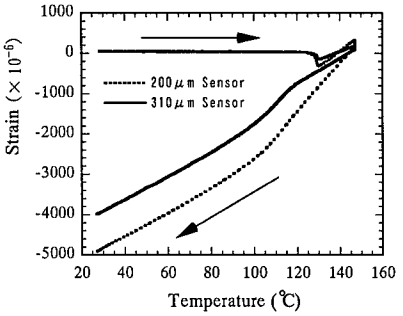

Fig.6 Strains versus temperature in the cubic mold during the molding.

3.1 Experiments

In the experiment, the internal strains of a molded epoxy including a metal cylinder are measured with the embedded EFPI sensor during molding. The experimental setup is

the same with the previous one. Fig.8 shows the mold and the position of the EFPI sensor and the thermocouple. The epoxy mold is a cylinder column and the metal inclusion has a little complex cylindrical shape. The EFPI sensor used in the experiment is that of 230 μ m diameter.

3.2 Results and Discussions

Fig.9 shows the strain measured with the EFPI sensor versus the temperature. Under about 130℃, the sensor does not detect strains like in the experiment of the cubic mold. After detection of the strain, tensile strains are measured due to the thermal expansion, then the compressive ones. In this result, the cure shrinkage is not detected. Both the tensile and compressive strains are small in comparison with those measured in the cubic mold shown in Fig.6. The compressive strains increase linearly with decreasing temperature in contrast to the results of the cubic mold. This results show that the steel cylinder restricts the distortion of the epoxy resin in the area where the sensor is located. Therefore, it is known that the residual stresses arise in the location where the sensor is embedded. Using strain data for the cubic mold, we can calculate the residual stress in the cylindrical mold including the metal inclusion.

4. Conclusions

In the present study, internal strain monitoring of the molded epoxy using the embedded EFPI optical fiber sensor during molding has been investigated. First, the sensitivity of the sensor for measurement of internal strains was examined. Next, internal strains in the epoxy mold including the metal cylinder were measured in the molding process. From the results, the followings were made clear. The EFPI sensor has a good sensitivity for internal strain monitoring enough to detect cure shrinkage of the epoxy resin. The stiffness of the sensing part of the sensor significantly affects its sensitivity for strain monitoring.

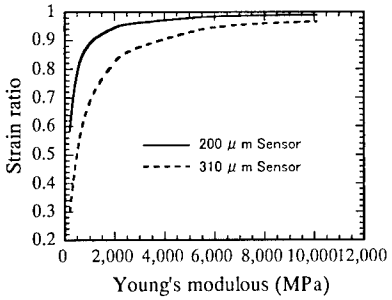

Fig.7 Sensors strains normalized with epoxy one.

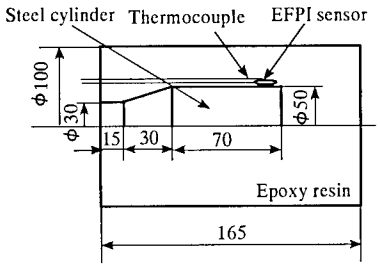

Fig.8 Cylindrical mold including the metal inclusion.

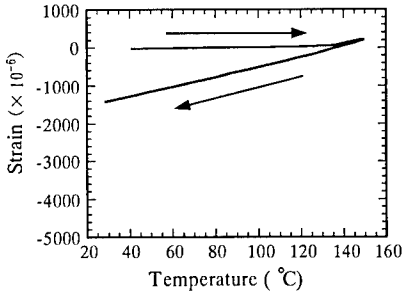

Fig.9 Strains versus temperature in the cylindrical mold during the molding.

References

1. E.G.Koroneos, Colloid and Polym. Sci., 256, 741 (1978)
2. M.Takahashi, S.Koike and M.Koga, Proc. Jpn. Cong. Mat. Res., 26, 215 (1983)
3. R.N.Sampson and J.P.Lesnick, SPE J., 14(8), 33 (1958)
4. A.J.Bush, Mod. Plastics, 35, 143 (1958)
5. A.Hijikata, K.Saho and K.Kataoka, Mech. Behiv. Mat. Proc. Symp., 2, 379 (1974)

Proceedings of 7th Japan International SAMPE
Symposium & Exhibition, Nov. 13-16, 2001

Detection of Transverse Cracks in CFRP Quasi-Isotropic Laminates Using Small-Diameter FBG Sensors

Tadahito Mizutani, Yoji Okabe, and Nobuo Takeda

Graduate School of Frontier Sciences, The University of Tokyo
c/o Komaba Open Laboratory (KOL), The University of Tokyo
4-6-1 Komaba, Meguro-ku, Tokyo, 153-8904, Japan
E-mail: mizu@compmat.rcast.u-tokyo.ac.jp

Abstract

Newly developed small-diameter Fiber Bragg Grating (FBG) sensors, whose cladding was 40 μm in diameter, were embedded in -45° ply on the border of 90° ply in $[45/0/-45/90]_s$ CFRP quasi-isotropic laminates. Then, reflection spectra from the FBG sensors were measured at various tensile stresses. As a result, the reflection spectrum became broad with an increase in the crack density. This change in the form of the spectrum could also be confirmed by the theoretical calculation. Thus, it was found that the small-diameter FBG sensors have a potential to detect the occurrence of transverse cracks through the change in the form of the spectrum, and to evaluate the crack density quantitatively by the spectrum width. Furthermore, a method to identify crack positions in 90° ply was attempted theoretically.

Key Words: CFRP, Transverse Crack, Quasi-Isotropic Laminates, Small-Diameter FBG Sensor, Health Monitoring

Introduction

CFRP composites have a peculiar failure process which involves transverse cracks and delaminations. When transverse cracks occur, the strain distribution in the laminates becomes non-uniform near the crack. Therefore, the monitoring of the change in the strain field could reveal the occurrence of transverse cracks.

Thus, the authors have applied the small-diameter FBG sensors for detecting transverse cracks in 90° ply of $[0_2/90_2]_s$ CFRP cross-ply laminates[1]. In this research, the method to detect transverse cracks in 90° ply was applied to CFRP quasi-isotropic laminates. Furthermore, a method to identify crack positions in 90° ply was attempted theoretically.

Experiments

Materials

Bragg gratings were fabricated to have periodic refractive index changes in the core of the small-diameter optical fibers. The diameters of the polyimide coating, the cladding, and the core of the small-diameter optical fiber are 52μm, 40μm, and 6.5μm, respectively. The profile of the apodization was controlled as a Gaussian shape in order to suppress the side-lobe of the reflection spectrum[2]. These FBG sensors were embedded in CFRP T800H/3631 (Toray Industries, Inc.) quasi-isotropic laminates. The laminate configuration was $[45/0/-45/90]_s$.

The FBG sensor was located in -45° ply on the border of 90° ply as shown in Fig.1 and Fig.2. Since the optical fiber was embedded to be parallel to carbon fibers in -45° ply, it was hardly broken by the stress concentration due to transverse cracks.

Measurements

Quasi-static tensile load was applied to the specimen by a material testing system (Instron Corporation, Load Frame 5582) at room temperature. The loading speed was 0.25mm/min. Tensile strain was measured with the strain gauge attached on a surface of the specimen, and tensile load was measured with a load cell. The small-diameter optical fiber was illuminated by a broadband light source unit (Ando Electric Co., Ltd., AQ6310(155)), and the reflection spectrum was obtained by using an optical spectrum analyzer (Ando Electric Co., Ltd., AQ6317). Transverse cracks that occurred in 90° ply were observed by a replica method.

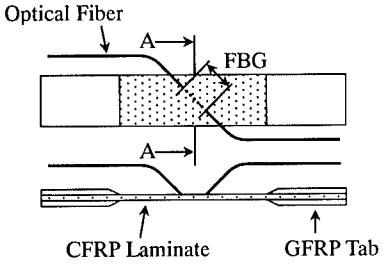

Fig.1 Schematic of a CFRP quasi-isotropic laminate with an embedded small-diameter FBG sensor.

Fig.2 Cross section at A-A in Fig.1.

Experimental Results

Figure 3 shows a transverse crack density ρ in 90° ply measured at various tensile strains ε through the loading/unloading test, and Fig.4 shows the reflection spectra obtained at the data (A)-(E) in Fig.3. While there was no transverse crack, the reflection spectrum kept its shape and the center wavelength shifted corresponding to the strain. After transverse cracks occurred, the spectrum shape was sensitively deformed as the crack density ρ increased.

Analysis

The change in the form of the reflection spectrum was confirmed by theoretical calculation. First, the non-uniform strain distribution in the FBG sensor was calculated using FEM analysis with ABAQUS code. The CFRP laminate was analyzed by a 3D model that included transverse cracks in 90° ply and the FBG sensor in -45° ply. Next, the distributions of the grating period and the average refractive index along the FBG sensor were obtained from the strain distribution in the FBG sensor. Then reflection spectra were calculated from the distributions by the couple mode theory and the transfer matrix method. This calculation was conducted with the software "IFO_Gratings" developed by Optiwave Corp.

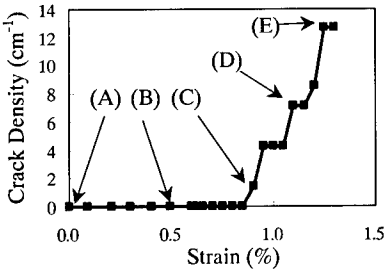

Fig.3 Crack density in 90° ply of the quasi-isotropic laminate measured through loading /unloading test.

tiwave Corp.

Calculated reflection spectra are shown in Fig.5. Similarly, the spectrum shape is deformed in accordance with the occurrence of transverse cracks. Thus, the occurrence of transverse cracks in 90° ply can be detected from the change in the shape of the reflection spectrum.

Discussion

Correlation between Spectrum Width and Crack Density

Spectrum widths were plotted in Fig.6 with the transverse crack density. The spectrum width was defined as Full Width at Quarter Maximum(FWQM) and normalized by the values measured before loading. Although the calculated FWQM has the same tendency to the measured one, these is a difference between those values after transverse cracks occurred. This difference may be caused by the inaccuracy of the strain distribution calculated by FEM analysis and the inexact optical parameters of the small-diameter FBG sensor used for the theoretical calculation. However, Fig.6 shows that there is a similarity between the measured FWQM and the crack density. Thus FWQM could be a good indicator to evaluate the transverse crack density quantitatively.

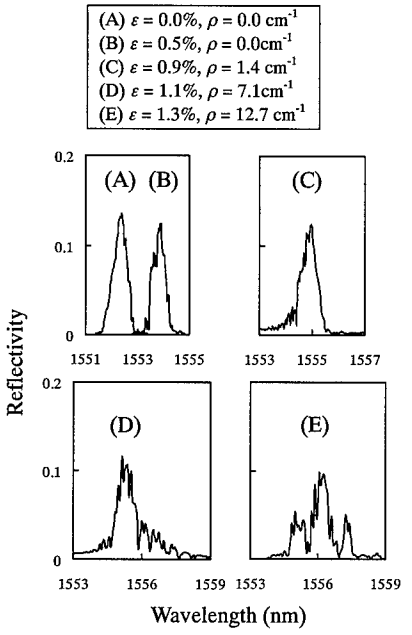

Fig.4 Reflection spectra at each strain ε and crack density ρ. These correspond to the data (A)-(E) in Fig.3.

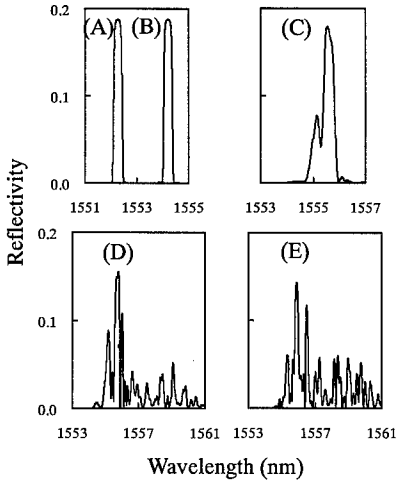

Fig.5 Calculated reflection spectra which correspond to the measured spectra in Fig.4.

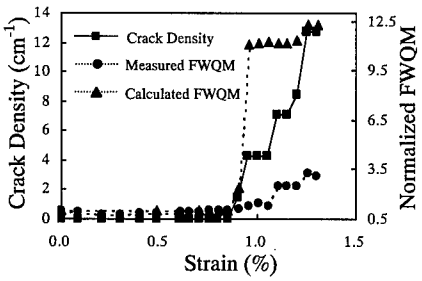

Fig.6 Relationship between crack density and spectrum width.

Crack Position Identification

The damage identification, especially determination of crack positions, would be significant for the practical structural maintenance. In this section, an inverse scattering algorithm[3] was applied to the identification of cracks in CFRP laminates.

This algorithm can reconstruct the distribution of the grating period and the average refractive index along the FBG sensor from the complex reflection spectrum. Since the grating period changes drastically at the positions where transverse cracks occurred, the crack positions could be identified exactly.

In this paper, the complex reflection spectrum was calculated from the strain distribution obtained by FEM analysis, since the experimental setup to measure the complex reflection spectrum was not yet prepared. Then the grating period was reconstructed from this complex reflection spectrum using the inverse scattering algorithm, as shown in Fig.7. The positions of peaks in the grating period correspond to positions of the transverse cracks in 90° ply very well.

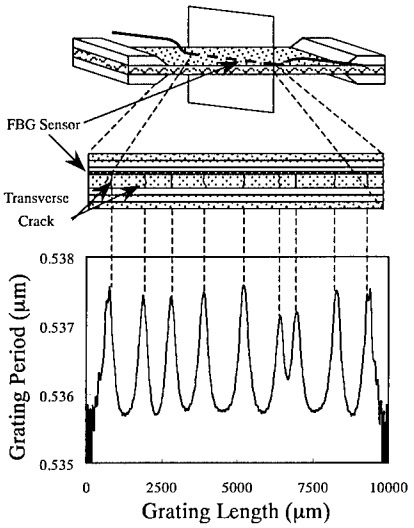

Fig.7 The reconstructed grating period profile using the inverse scattering algorithm.

Conclusions

In this research, newly developed small-diameter FBG sensors were applied to the detection of transverse cracks in CFRP quasi-isotropic laminates.

The reflection spectrum was sensitively deformed as the transverse cracks in 90° ply increased. And the transverse crack density could be predicted quantitatively by the monitoring of the spectrum. These changes were also confirmed theoretically.

Furthermore, it was found theoretically that the positions where transverse cracks occurred could be predicted from the complex reflection spectrum using inverse scattering algorithm.

Acknowledgment

This research was conducted as a part of the "R&D for Smart Materials Structure System" project within the Academic Institutions Centered Program supported by NEDO (New Energy and Industrial Technology Development Organization), Japan.

Reference

1. Y.Okabe, T.Mizutani, S.Yashiro, and N.Takeda: Proc. SPIE, 4328 (in Printing) (2001)

2. K.Satori, K.Fukuchi, K.Kurosawa, A.Hongo, and N.Takeda: Proc. SPIE, 4328 (in Printing) (2001)

3. Ricardo Feced, Michalis N. Aervas, and Miguel A. Muriel: IEEE Journal of Quantum Electronics, 35(8), 1105 (1999).

Proceedings of 7th Japan International SAMPE
Symposium & Exhibition, Nov. 13-16, 2001

Development of Smart Braided Composites by Using Fiberoptic Strain Sensors

Tatsuro Kosaka*, Hideaki, Kurimoto**, Katsuhiko Osaka*, Asami Nakai***,
Toshiko Osada****, Hiroyuki Hamada***, Takehito Fukuda*

*Department of Intelligent Materials Engineering, Osaka City University
Sugimoto 3, Sumiyoshi,Osaka, Japan 558-8585
kosaka@imat.eng.osaka-cu.ac.jp
**Graduate Student, Osaka City University
*** Advanced Fibro-Science, Kyoto Institute of Technology
**** Graduate Student,, Kyoto Institute of Technology

Abstract

This paper describes development of high-functional braided composites using fiberoptic strain sensors. Optical fibers were embedded warpwise in braided composites. Optical power loss measurement and strain monitoring during cure and tensile tests had been conducted. Two types of strain sensors, fiber Bragg grating (FBG) sensors and extrinsic Fabry-Perot interferometric (EFPI) sensors were used for strain measurement in this study. The results of the loss measurement during cure and tensile tests showed that the employed integration design of optical fibers into braided composites was suited for strain measurement. The experimental results of cure monitoring shows that strain behaviors of these sensors were almost same at the cooling stage. From the results of strain monitoring on tensile tests, it was found that both sensors could measure strain correctly up to 0.8 % strain, while the outputs of fiberoptic sensors became different from strain measured by a attached foil gauge over 0.8 % strain. It was thought that damages of fiberoptic sensors and the neighbor affected their strain outputs.

Key Words: Fiber optic sensors, Braided composites, Cure and health monitoring, Strain monitoring

Introduction

In the present paper, smart composites consisting of braided composites and fiberoptic strain sensors have been developed. Although there are many researches on smart composites using fiber reinforced plastic (FRP) laminates, there is no study on braided composites possessing smart functions. However, braided composites have good suitability for integration of fiber-shaped functional components because fiber-shaped components can be integrated straightly into preform as warp. Therefore, functional performance of the integrated functional components can be maximized. Fiberoptic sensors were used as sensing components in this study.

Fiberoptic sensors are powerful sensors for sensing internal state such as strain, stress, temperature and damages. There are many types of fiberoptic sensors for chemical and mechanical sensing. Fiberoptic strain sensors have been proved to have good availability for cure and health monitoring of composite laminates, filament wound (FW) composites and textile composites. Extrinsic Fabry-Perot interferometric (EFPI) sensors and fiber Bragg grating (FBG) sensors are often used for the purpose [1-6]. The present study applied both sensors to internal strain monitoring of braided composites dur-

ing molding and tensile tests. Optical power loss by integration was also investigated for enhancement of the design.

Experiment

Specimen

This study used glass reinforcements (ER11560-F165N, Nippon Electric Glass) and vinylester resin (Ripoxy R-802, Showa Highpolymer) for manufacturing of braided composites. Optical fibers were knitted warpwise in braided preforms before molding. Figure 1 illustrates specimens used in this study. A single-mode optical fiber was embedded with length of *l* for measurement of optical power loss as shown in Fig. 1(a). A fiberoptic sensor was embedded as shown in Fig. 1(b) for internal strain measurement. Figure 1(c) shows the side view of the specimen in Fig. 1(a). These optical fibers were drawn from surface of these specimens. In the molding, optical fibers were drawn through U-grooves of upper steel plate to prevent optical power loss by local bending at egress points as shown in Fig. 2. The resin was cured 80 °C for 5 hours.

Experimental setup

Measurement systems of optical power loss and internal strain are illustrated in Fig. 3. The optical power loss measurement system used an optical loss meter (Anritsu MT9810A) consisting of high-stable 1310nm laser diode (LD) and photo detector (PD) units. The stability of the optical loss meter was about 0.06 dB for 15 hours.

EFPI sensors used in this study have a glass capillary tube of 310 μm diameter to support two mirror-ended fibers. FBG sensors used in this study use single-mode uncoated fiber of 125 μm diameter and they have Bragg grating, which are periodical index variation, in the fiber core. The strain measurement system for FBG and EFPI sensors was composed of a super luminescence diode (SLD), an optical spectrum analyzer (OSA; Anritsu MS9710) and an optical directional coupler. The measured spectra

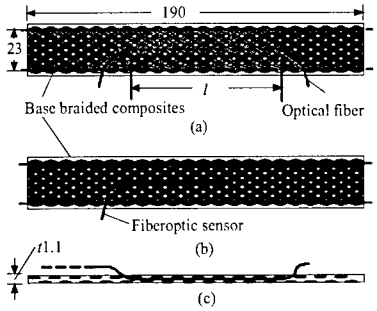

Fig.1 Braided composites specimen with embedded fiberoptic sensor ((a) for optical power loss measurement; (b) for strain measurement; (c) side view of (a); unit : mm)

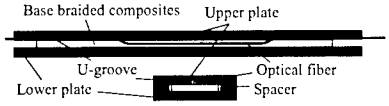

Fig.2 Egress of optical fiber in molding.

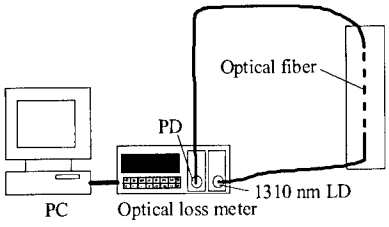

(a) For optical power loss

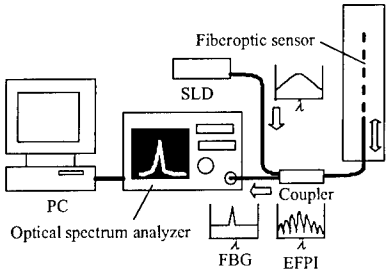

(a) For internal strain measurement

Fig.3 Measurement systems

were sent to PC and then software computed strain from them. The strain output of FBG sensor was obtained from Bragg wavelength shift and temperature variation [7]. Temperature was measued by an attached thermocouple in molding. As for EFPI sensor, the cavity length was obtained by measuring a period of transfer function of the reflected spectrum in wavenumber domain. EFPI sensors used in this study have low temperature sensitivity of about 0.00625×10^{-6}/ °C.

Experimental Results and Discussions

Measurement of optical power loss

Optical power loss was measured during molding and tensile tests. Although the loss increased by 0.7 dB in the molding, the value was so small that it did not affect reliability of fiberoptic sensors. Results of optical power loss measurements during 0.8% tensile tests were shown in Fig. 4 with their different embedded lengths. The results showed there was no strong correlation between embedding length and optical power loss. Therefore, it appears that the stability of optical power is governed mainly by egress configuration of embedded fibers. It means that long optical fibers embedded in braided composites may have good stability. Therefore, it was found that the embedding configuration used in this study was good for using optical fiber sensors.

Measurement of internal strain

Internal strain profiles measured by FBG and EFPI sensors in curing process are plotted against time with temperature in Fig. 5. Both sensors could detect tensile strain at the heating stage and compressive strain at the cooling stage. However, the detected strain in molding by the FBG sensor was different from by the EFPI sensor. It can be considered that difference of stiffness of these sensors affected their strain sensitivity due to low-stiffness resin in curing process. At the cooling stage, both sensors detected almost the same compressive strain as each other.

Figure 6 shows stress-strain curves from an embedded FBG sensor and an attached foil strain gauge during tensile test. It was found that

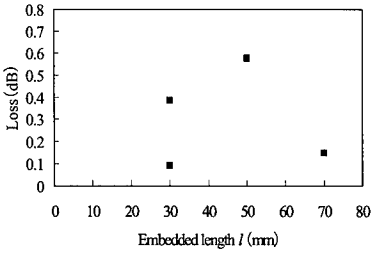

Fig.4 Relation between optical power loss and embedding length of fibers.

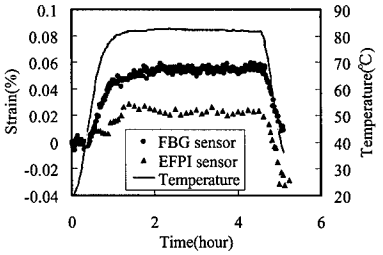

Fig.5 Strain from FBG sensor and EFPI sensor, and temperature vs. time in curing process.

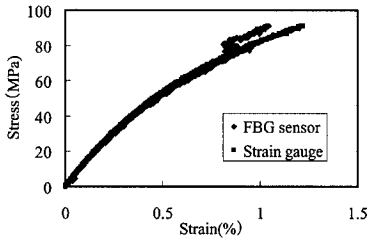

Fig.6 Stress-strain curves from FBG sensor and foil strain gauge on tensile test.

FBG sensors could measure internal strain correctly up to the strain of 0.8 %. At that strain, difference of the curves between FBG sensor and foil strain gauge increased. Since the output of the FBG sensor jumped discontinuously at 0.8% strain, it can be considered that the sensing part was damaged. To investigate behavior of FBG sensors, FBG spectrum, which gives us

information of situation of the sensor itself and the neighbor, was observed during tensile tests. Figure 7 shows spectra from the embedded FBG sensor at various strains. Since the shape of the spectrum changed gradually from single peak to double peaks with increasing of strain, it appears that local strain distribution around FBG sensor affect the reflected spectrum. However, the experimental results proved that the effect of deterioration of the spectrum on the precision of strain sensing was minor. At 0.8% strain, the spectrum shape varied suddenly to multi peaks. Therefore, the jump of strain resulted from damage of FBG sensor itself and the neighbor.

Figure 8 shows stress-strain curves from an embedded EFPI sensor and an attached foil strain gauge during tensile tests. These experimental results show that embedded EFPI sensors in braided composites could measure internal strain over 2.0% strain although the correction of strain was held within 0.8 % strain. The error of strain by EFPI sensor in large strain range was produced by break of the capillary tube. However, the observation of spectrum from EFPI sensor showed good interference, which means that there was no discrepancy of optical axis, until the break. Therefore, it was found that large axial strain affects the precision of strain while the interferometer can be alive in the strain range.

Conclusions

The strain monitoring of braided composites during the cure and the tensile tests had been conducted by using embedded FBG and EFPI sensors. The experimental results of cure monitoring shows that the strain behaviors of these sensors were almost same at the cooling stage. From the results of tensile tests, it was found that both sensors could measure strain correctly up to 0.8 % strain, while the output of fiberoptic sensors showed error in large strain. Therefore, it is concluded that internal strain monitoring of braided composites by fiberoptic strain sensors are a good monitoring method in small strain range, while another method is necessary for the strain monitoring in large strain range.

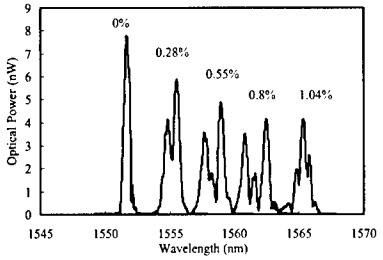

Fig.7 Spectra from FBG sensor on tensile test.

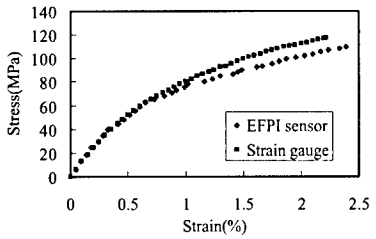

Fig.8 Stress-strain curves from FBG sensor and foil strain gauge on tensile test.

References

1. K. Osaka, T. Kosaka, Y. Asano and T. Fukuda: Proc. 2nd Asian-Australasian Conf. Compos. Mater. (ACCM-2000), Kyongju, Korea, 1117 (2000)
2. T. Kosaka, K. Osaka, M. Sando and T. Fukuda, Proc. 9th US-Japan Conf. Compos. Mater, Mishima, Japan, 151 (2000)
3. T. Kosaka, K. Osaka, Y. Asano and T. Fukuda, Proc. ICCM-13, Beijin, China, (2001)
4. Y. Okabe, S. Yashiro, T. Kosaka and N. Takeda, Smart Mater. Struct., Vol.9, 832 (2000)
5. Y.J. Rao, D.A. Jackson, L. Zhang and I. Bennion, Opt. Lett., Vol.21, 683 (1996)
6. X. Tao, L. Tang, W.C..Du and C.L. Choy, Composites Science and Technology, Vol.60, 657 (2000)
7. Y.J. Rao, Optics and Lasers in Engineering, Vol.31, 297 (1999)

Proceedings of 7th Japan International SAMPE
Symposium & Exhibition, Nov. 13-16, 2001

High resistance to fracture of optical fiber reinforced plastics

Takashi TORIYAMA, Yasuyuki MIYAZAWA and Yoshitake NISHI

Department of Materials Science, Tokai University
1117 Kitakaname, Hiratsuka, Kanagawa, 259-1292 JAPAN
E-mail: am026429@keyaki.cc.u-tokai.ac.jp

Abstract

Using optical fiber which shows high resistance to fracture, fiber reinforced plastics have been developed. Based on composite law, the estimated stress-strain curve was calculated. It was corresponded to the experimental stress-strain curve obtained by tensile test.

Key Words: Optical fiber, Bending test, Tensile test, Health monitoring, Composite

Introduction

Health monitoring sensor is one of recent applications of optical fiber in the engineering fields of aerospace, ship and buildings[1]. Strain sensor to measure optical loss is the simple method [2]. The optical fiber sensor has lately become high transparency and high resistance to fracture. Therefore, the health monitoring provided by optical fiber sensor will be useful for monitoring structural materials for a wide variety of applications. The first step in producing optical fiber composite was filling resin around arranged optical fibers. However, it is easy for the optical fiber composite materials to fracture because of chemical reaction between resin and optical fiber surface. To modify the mechanical properties, optical fiber has been coated by metal [3]. Reaction to polymer matrix could be stopped by metal coating on surface of optical fiber. The optical fiber composites have become toughness. Therefore, the purpose of the present work is to study the enhancement of the resistance to fracture for optical fiber reinforced plastics (OFRP).

Experimental Procedure

The optical fiber (5×10^{-4} m in diameter) was cut into pieces 150 mm in length. Figure 1 shows the schematic drawing of the optical fiber composite sample. Coating on surface of the optical fiber was prepared by spattering process. (model no., VPS-20, Sinku Kiko, Co., Ltd., Yokohama). The distance between samples and spattering target is 60 mm. The target was Au (more than 99.9 %). Spattering time was 5 minutes. The matrix plastics were polyester. The volume fraction of composite sample (150mm x 10mm x 1mm) was 0.22.

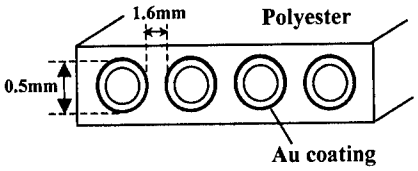

Fig. 1 Schematic drawing of optical fiber composite sample.

To evaluate fracture resistance, bending test and tensile test were performed. The tensile testing apparatus (model no, TMC-AUT-200L, Tokyo Koki, Inc., Kanagawa) was used. The gage length was 30 mm. The strain rate was 50 mm per minutes. The bending test was performed as shown in Figure 2. The gage length of the bending test on measuring strain was 30 mm.

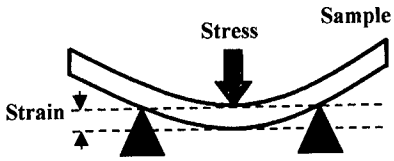

FIG.2 Schematic drawing of bending test.

The strain (ε) was proportional to radius [r_o] of optical fiber cross section and inversely proportional to curvature radius [r_c], as a following equation.

$$\varepsilon = r_o / r_c \qquad (1)$$

Results and discussion

1. Coating on surface of the optical fiber

Figure 3 showed the cross section of the optical fiber composite filled in resin. Metal coating on surface of the optical fiber prevents reaction. The thickness of coating on the surface was about 500 nm.

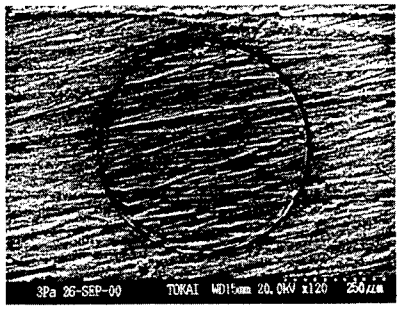

FIG. 3 Cross section of the optical fiber composite filled in resin.

2. Evaluation of fracture resistance

In order to estimate resistance to fracture of optical fiber reinforced plastics, tensile test was performed. Figure 4 shows the stress-strain curve of optical fiber and polyester. The stress value against strain of optical fiber was higher than polyester's value. Optical fiber modulus was two times higher than the polyester's value, and shows high resistance to fracture.

3. The comparison calculated values with experimental stress-strain curve.

The composite, which contains optical fiber of high resistance to fracture, has high fracture stress by the reinforcement. Based on each materials values and composite law, the strength of optical fiber reinforced plastics could be estimated. The stress was expressed by a following equation.

$$\sigma = \frac{NS_{OF}\,\sigma_{OF} + (S_P - NS_{OF})\,\sigma_P}{S_P} \qquad (2)$$

Here, n, S_{OF}, S_P, σ_{OF} and σ_P were number of optical fiber, cross section of optical fiber, cross section of polyester, load stress of optical fiber, and load stress of optical fiber. Based on composite law, the estimated stress-strain curve of OFRP was calculated. The calculated OFRP curve was drowning between optical fiber curve and polyester curve (see Fig.4). To confirm the calculated value, the experimental curve of optical fiber reinforced plastics (OFRP) was obtained. The calculated value corresponded to the experimental stress-strain curve obtained by tensile test (see Fig. 5).

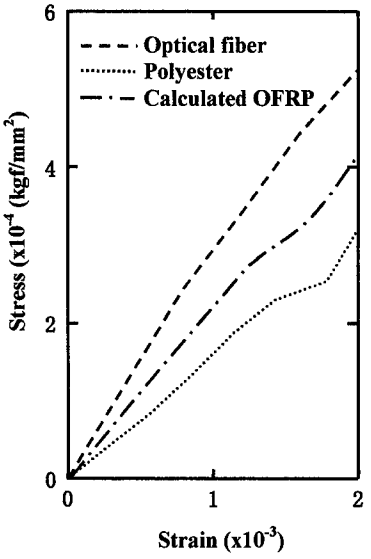

FIG.4 Stress-strain curve of optical fiber and polyester on tensile test.

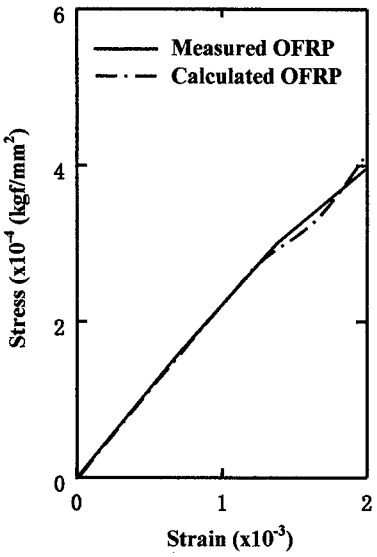

FIG.5 Stress-strain curve of optical fiber composite and calculated value based composite low.

4. Modulus of work hardening

True stress and true strain, as a following equation defines the modulus of work hardening.

$$\sigma = K\varepsilon^n \qquad (3)$$

Here, σ, K, ε, and n were true stress, constant of work hardening, true strain and modulus of work hardening, respectively.

Figure 6 shows the change in logarithmic true stress (Log σ) against logarithmic true strain (Log ε) of optical fiber (OF), polyester and optical fiber reinforced plastics(OFRP). The modulus (n) and constant (**log** K) of work hardening for optical fiber, polyester and OFRP were summarized in Table 1. When logarithmic

true strain (Log ε) is less than 1.8, ***n*** and **log *K*** values of OFRP were approximately equal to those of optical fiber. This showed that the initial work hardening of optical fiber dominated that of OFRP. On the other hand, ***n*** and **log*K*** values of OFRP were approximately equal to those of polyester above 1.8 of Log ε. This was concluded that the work hardening above 1.8 of Log ε f OFRP was dominated by that of polyester.

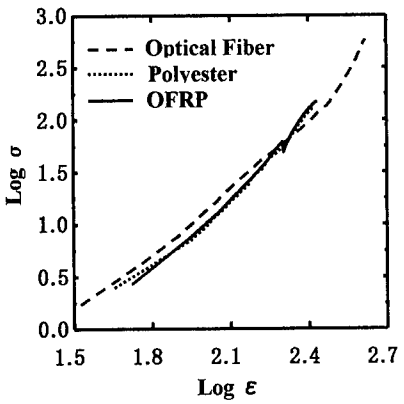

FIG.6 Change in Log σ against Log ε of optical fiber, polyester and OFRP.

Table 1 Modulus (*n*) and constant (log *K*) of work hardening for OF, polyester and OFRP.

	Log K<1.8		1.8<Log K<2.2	
	n	Log K	n	Log K
Optical fiber	0.38	0.2	0.48	0.7
Polyester	0.32	0.4	0.52	0.62
OFRP	0.4	0.42	0.5	0.55

5. High resistance to fracture of optical fiber reinforced plastics.

Figure 7 shows the stress-strain curve of optical fiber and polyester on bending test. The optical fiber reinforced plastics (OFRP) has high deformation resistance. The bending modulus of OFRP was twenty times higher than the polyester's value.

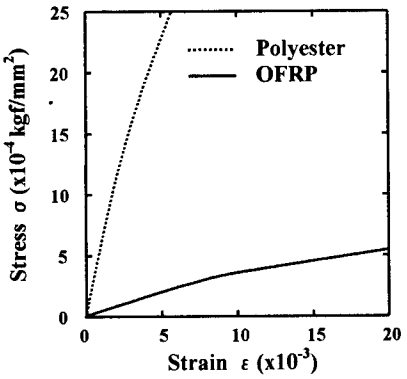

FIG.7 Stress-strain curve of optical fiber and polyester on bending test.

Conclusion

Based on composite law, the calculated stress-strain curve was corresponded to measured value of OFRP.

Reference

[1] H. MURAYAMA, K. KAGEYAMA, I. KIMPARA, A. SHIMADA, H. NARUSE : Journal of Advanced Science, 12 (3), 298 (2000).

[2] H.AOYAMA, H.WATANABE, M.TERAI : The Japan Society of Mechanical Engineering, 64 (628), 43 (1998).

[3] K.EGAWA, S. KIKUTI : Journal of the Japan Society of Mechanical Engineers, 72 (2), 458 (1995).

Proceedings of 7th Japan International SAMPE
Symposium & Exhibition, Nov. 13-16, 2001

Shape memory effect of NiMnGa amorphous thin film

Kazunori AKIYAMA, Hiromasa YABE and Yoshitake NISHI

Department of Materials Science, Tokai University
1117, Kitakaname, Hiratsuka, Kanagawa, 259-1292 JAPAN
E-mail: am026429@keyaki.cc.u-tokai.ac.jp

Abstract

A thermal shape memory effect (TSME) was found for the $Ni_{80}Mn_{10}Ga_{10}$ alloy film prepared by magnetron sputtering process. The $Ni_{80}Mn_{10}Ga_{10}$ film was deposited on poliimide substrate. The structure of the sample was examined by means of XRD. The thermal expanded bending strain induced by thermal shape memory effects increased at elevated temperatures.

Key Words: Shape memory effect, NiMnGa., Thin film.

Introduction

If a metallic glass sample could be heated over the glass transition temperature (T_g) and could be converted to super cooled liquid, the shape memory effects were obtained [1-3]. Sputtering process often forms the amorphous structure. To form the film of the amorphous structure for the thermal shape memory alloy, the magnetron sputtering process has been performed. Various kinds of applications such as micro-actuators for the advanced science and technology can be expected. Furthermore, shape memory glass should be useful for micro-actuator in hard environmental conditions of radiation damage [3]. To confirm the adaptability to shape memory material, we have studied the thermal shape memory effect of $Ni_{80}Mn_{10}Ga_{10}$ metallic glass, because glass transition has often induces reversible shape memory effects. The reversible shape memory metallic glass has been mainly induced by volume change near T_g. It is easy for the glass transition to induce shape memory effect with the large thermal expanded bending. Therefore, the shape changes have been also studied of bimetal constructed by poliimide and $Ni_{80}Mn_{10}Ga_{10}$ amorphous alloy sheets.

Experimental

$Ni_{80}Mn_{10}Ga_{10}$ films were prepared by using RF magnetron sputtering process (see Fig.1). The sputtering conditions were summarized in Table 1. The sputtering was performed under 4.0×10^{-4} Pa total gas pressure with 2.0 Pa of Ar gas partial pressure, sputtering power was 150 W and sputtering time was 14400 s. The NiMnGa films were deposited on poliimide substrate. The sample thickness was about 200 nm. The chemical composition was analyzed by energy dispersion X-ray spectroscopy (EDS: JSM-6301F, JEOL). The NiMnGa film composition was Ni-10at%Mn-10at%Ga. The cross-section morghorgy of the film was observed by field emission scanning electron microscopy (SEM: JSM-6000SeriesJEOL). The structure was analyzed by means of X-ray diffraction (XRD: MRD,Philips.). Figure 2 was schematic diagram of TSME measuring system. The thermal shape memory effect was recorded by CCD-video camera [4-8].

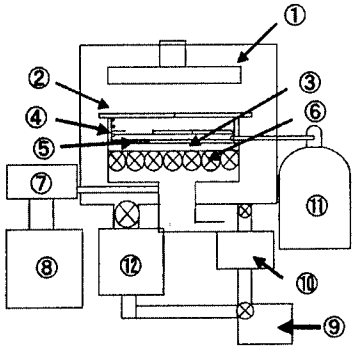

①Substrate ②Shutter
③RF magnetron Gan
④shield ⑤target ⑥Erosion Control
⑦Matching Box ⑧RF Power unit
⑨Rotary Pump ⑩Mechanical Booster Pump
⑪Ar gas ⑫ Turbo Pump

Fig. 1 Schematic diagram of magnetron sputtering apparatus.

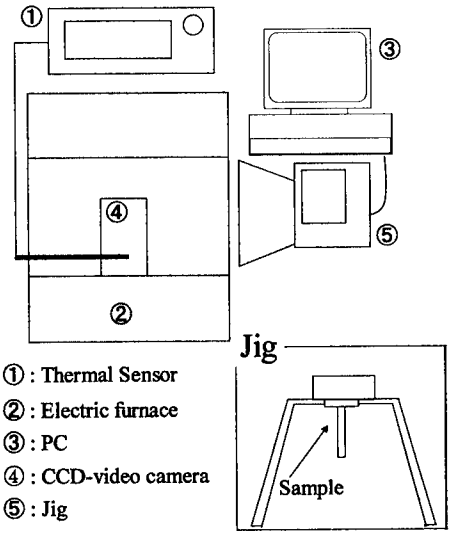

① : Thermal Sensor
② : Electric furnace
③ : PC
④ : CCD-video camera
⑤ : Jig

Fig.2 Schematic diagram of TSME measuring system.

Table 1 Sputtering condition

Total gas Pressure	**4.0×10^{-4} Pa**
Ar gas partial pressure	**2.0 Pa**
Sputtering gas	**Argon**
Sputtering power	**150 W**
Sputtering time	**14400 s**
Back Sputtering time	**180 s**
Pre sputtering time	**600 s**
Substrate	**poliimide**
Substrate temperature	**300±2 K**

Results and discussion

Sample morphology

Figure 3 shows the SEM microphotograph of $Ni_{80}Mn_{10}Ga_{10}$ thin film. The cross-section morphology was a fine texture. Since the fine texture shows the high anisotropy, it could be expected to be high sensitivity for the thermal expanded bending. Fine texture could be obtained of $Ni_{80}Mn_{10}Ga_{10}$ thin film.

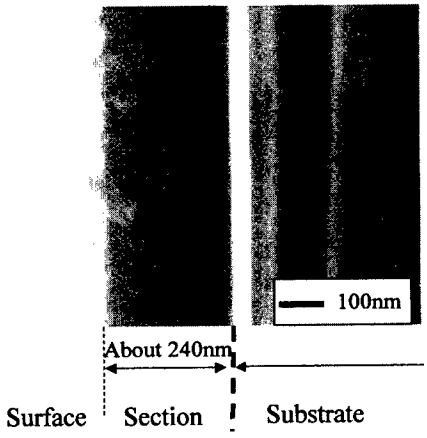

Fig.3 Cross-section SEM microphotograph, $Ni_{80}Mn_{10}Ga_{10}$ thin film is fine texture.

Sample structure

The result of XRD is shown in Figure 4. The sample structure was amorphous. Although SEM microphotograph (Fig.2) was fine texture morphology, shape crystal peak obtained by X-ray diffraction pattern shows amorphous structure.

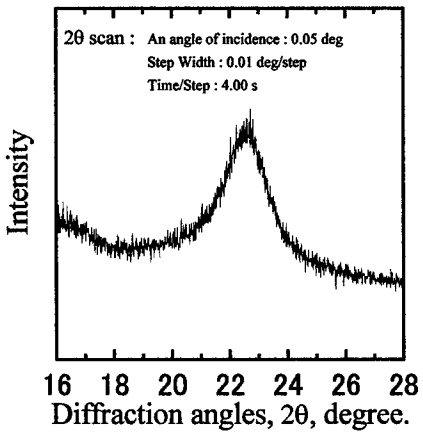

Fig.4 Film surface X-ray diffraction pattern of $Ni_{80}Mn_{10}Ga_{10}$ thin film.

Shape memory effect

Figure 5 (a), (b) and (c) are the photograph which show thermal shape memory effect of $Ni_{80}Mn_{10}Ga_{10}$ thin film deposited on poliimide substrate. The film was bended by residual stress at room temperature, as shown in Fig. 4(a). The straight shape of sample was found in Fig. 4(b) because of relaxation by heating. Namely, the heating caused giant thermal expanded bending. However, the cooled sample (see Fig 4(c)) was reversibly bended.

Figure 6 is also shows the schematic diagram of bending displacement of the thermal expansion. The bending displacement was expressed by Y/X, where X and Y were length values as shown in Fig. 6.

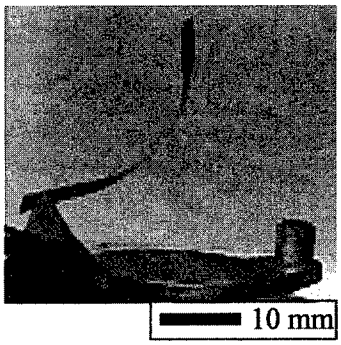

(a) Before heating 300 K.

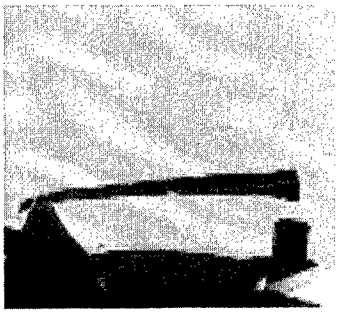

(b) At 473 K

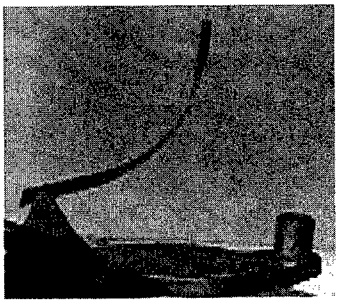

(c) After cooling 300 K

Fig.5 The photographs of thermal shape memory effect induced by thermal expansion of $Ni_{80}Mn_{10}Ga_{10}$ thin film.

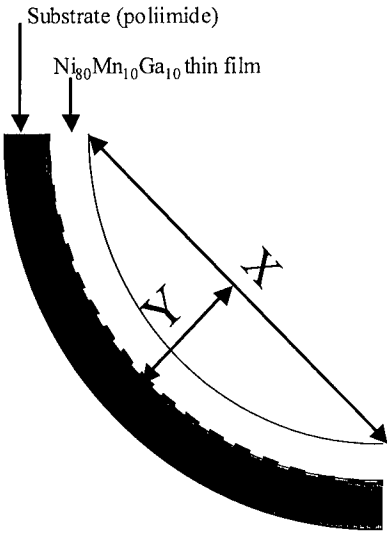

Fig.6 Schematic diagram of the thermal expanded bending.

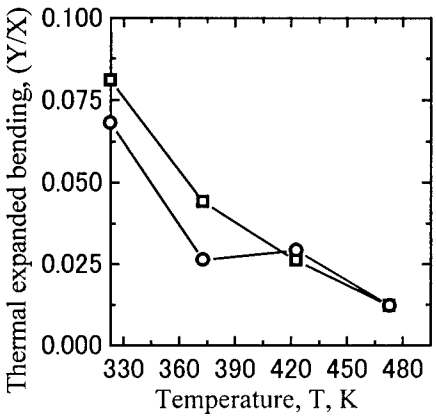

Fig.7 Change in thermal expanded bending displacement, Y/X against temperature (T) of $Ni_{80}Mn_{10}Ga_{10}$ alloy thin film.

Figure 6 shows the change in the thermal expanded bending displacement and temperature from 323K to 473K. The thermal expanded bending displacement was reversible from 423 to 473 K.

Conclusions

Reversible thermal shape memory effects from room temperature to 473 K can be observed for amorphous $Ni_{80}Mn_{10}Ga_{10}$ texture film prepared by magnetron sputtering process.

Acknowledgment

The authors wish to thank Mr.T.Kaneko and Mr.F.Kanazaki, Saginomiya Ltd., for their assistance for the preparation of specimens.

References

1. M.Tetsuka, H.Yabe, K.Oguri, and Y.Nishi : J. Adv. Sci, 1&2 (12), 38 (2000).
2. H.yabe, K.Takashina, M.Tetsuka and Y.Nishi : Proc. of 45th SAMPE symposium SAMPE 2000, 201(2000).
3. K.Takashina, H.Yabe, K.Oguri,Y. Miyazawa and Yoshitake Nishi : I. J. Appl. Ele. and Mech, in press.
4. N.Kishimoto, H.Amekura, K.Kono, and C.G.Lee, J. National : res. Inst. Metals, 258/263, 1908 (1998).
5. T. Nakamura, T. Matsumura, K. Tajima, Y. Miyazawa and Y. Nishi : J.Adv. Sci, 11(1), 34 (1999).
6. T. Matsumura, K. Takashina. and Y. Nishi : Proc. 9th Int. Mat. Sym, 16 (2000).
7. T. Matsumura, T. Nakamura, H.Ishii, K. Tajima, Y. Miyazawa and Y. Nishi : Proc.44th Int. SAMPE Sym, 1961 (1999).
8. T.Matsumura, T.Nakamura, H.Ishii, K.Tajima, K.Oguri and Y.Nishi : Proc. 44th SAMPE symposium SAMPE 1999, 2, 965 (1999)

Proceedings of 7th Japan International SAMPE
Symposium & Exhibition, Nov. 13-16, 2001

High Impact Polyethyleneterephthalate-Polyethylene Blockcopolymer from Recovered PET bottles

Takashi Fujimaki

DJK TECHNO SCIENCE LABORATORIES INC.
1-20, Takada-Higashi 1-chome, Kouhoku-ku, Yokohama 223-0065, Japan
E-mail: djklab@jade.dti.ne.jp.

ABSTRACT

A new PET-PE Blockcopolymer having high molecular weight and high impact strength has been developed by the reactive processing method, which was constructed with raw materials of (1) a lot of recovered PET bottle flakes, (2) considerable amount of polyethylene having carboxylic acid, (3) a small quantity of coupling agent, (4) a very small amount of catalyst and followed by (4) coupling reaction with extruding machines at about 300℃. The Blockcopolymers are white crystalline resin and have good physical and mechanical properties like commodity plastics, especially high impact strength and low brittleness temperature. And their processabilities are excellent in comparison with commercial PET, thus they can greatly contribute to vast usages as plastic moldings and also effective use of recycled resources.

KEY WORDS : PET-PE Blockcopolymer, Reactive Processing Method, High Molecular Weight, Low Melt Flow Rate, High Impact Strength, Low Brittleness Temperature

1. INTRODUCTION

DJK had developed for these ten years to produce a new PET with high molecular weight, low melt flow rate and high melt viscosity from recovered polyethylene terephthalate (PET) bottles or virgin PET as prepolymers by reactive processing method [1]. The New PET was transparent glassy resin and had excellent processability like polyethylene and polypropylene and also physical properties similar to PET, but had poor mechanical properties at the low temperature. A new PET-PE Blockcopolymer(tentatively called High Impact PET or HI PET) having high molecular weight, low melt flow rate, high impact strength and low brittleness temperature has been developed by the similar reactive processing method in cooperation with FTEX Inc. [2].

2. PRODUCTION METHOD

Fig.1 shows coupling reaction mechanism in order to produce PET-PE Blockcopolymer with linear structure from difunctional epoxide and long chain branched structure from trifunctional epoxide which give the polymers extremely high melt viscosity and high swell value. Actually the new PET-PE Blockcopolymer having high molecular weight and high impact strength can be produced by the reactive processing method, which was constructed with raw materials of (1) recovered PET bottle flakes, (2) considerable amount of polyethylene having

carboxylic acid, (3) coupling agent, (4) catalyst and followed by (4) coupling reaction at about 300℃. Catalyst is most important key technology, can achieve to increase high molecular weight within several minutes in comparison with commercial PET by solid phase polymerization method of about ten hours.

PRODUCTION OF HI PET

Table 1 presents small-scale production results(about 2 kg/h) by KURIMOTO: S1 extruder with twin screw of 25mm diameter and mechanical properties of HI PET [2]. Recovered PET bottle flakes having IV 0.73dl/g and MFR(280℃, lord 2.16Kg) 60g/10min was used as prepolymer and ethylene- maleic anhydride- methylacrylate copolymer having MI(190℃, lord 2.16Kg) 8g/10min was used as polyethylene (PE) carboxylated. Ethyleneglycol diglycidyl ether (D) and trimethyrolpropane triglycidyl ether (T) (D/T ratio = 75/25) were used as coupling agents, and alkali metal stearates were used as mixed catalysts. HI PET had extremely low MFR of about 0.3 g/10min in comparison with raw material of PET flakes and PE and also blend of them(Fig.2).

Table 2 presents large scale production results by IKEGAI : PCM-70 extruder with twin screw of 70mm diameter and 3 vacuum vents and brittleness temperature of HI PET thus obtained. Production speeds were about 50-100 kg/h (industrial scale level of about 25-50 ton/month).

3. RESIN PROPERTIES

HI PET contains generally about 17~33 wt.%(20~50phr) of polyethylene unit, has two melting points of about 98 and 250℃ by DSC and is white crystalline resins. For example, Fig.2 shows that tensile strength at break of HI PET reduce rapidly into 15 Mpa with increasing PE content up to 50 wt.% and Izod impact strength of them increase rapidly into 490 J/m with increasing PE content up to 50 wt.%. And also Table 2 shows that brittleness temperature of them can be improved drastically into –15℃ with increasing PE content up to 33 wt.%(50 phr). These basic data indicate that HI PET with PE 17 wt.%(20phr) is similar to polypropylene and HI PET with PE 33 wt.%(50phr) is similar to high-density polyethylene.

4. EXCELLENT PROCESSABILITY

HI PET has highly viscous property and high melts strength due to introduction of long chain branches(LCB) into a high molecular weight molecule. Therefore, it has generally MFR (280℃, 2.16Kg) of 0.1 ~50g/10 min, SWELL (280℃, 2.16Kg) of 50~200% and high melt viscosity(280℃) of over 10,000 Pa • s in comparison with commercial PET with linear structure and MFR of 10~50g/10 min, almost zero% of SWELL and low melt viscosity of about 70 ~ 300Pa • s [1]. These HI PET are excellent proccesabilities in comparison with commercial PET, can be processed by conventional equipments for polyolefins at 260~300℃ into various forms, such as blown bottles, tublar film, extruded T-die sheet, injected mold products and foamed products. Especially HI PET with low brittleness temperature and high impact strength is suitable for packaging material and so can greatly contribute to vast usages as plastic moldings and also effective use of recycled resources.

5. Conclusions

PET-PE Blockcopolymers are still under development and resin and mold products samples are not generally available at this moment. Situation for providing resin samples would be improved in the end of 2001. DJK and FTEX have applied several original patent applications in Japan, U.S.A. and Europe etc.

REFERENCES

1. T. Fujimaki and Y. Urata, Proc. of 6th International SAMPE Symp., 11(1999);
PCT Patent WO98/44019, to the DJK.
[2] Japanese Patent, P2001-122955A(May 8, 2001), to the FTEX and DJK.

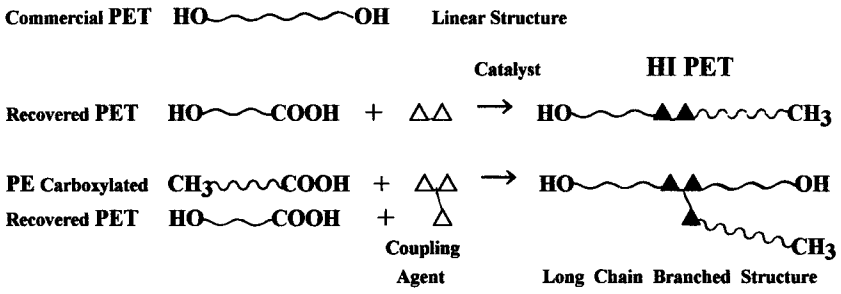

Fig. 1 Production mechanism of high impact PET-PE Blockcopolymer with high molecular weight by coupling reaction

Table 1 Small scale production and mechanical properties of High Impact PET (PET-PE Blockcopolpmer) [2]
Kurimoto : S1 extruder with twin screw of 25mm diameter

Resins Model	Composition (weight) PET / PE /Coupling/Catalyst recovered/ carboxylated /agent	Temp. (℃)	Screw rotation (rpm)	MFR 280℃ (g/10min)	Break Strength (MPa)	Elongation (%)	Izod Impact (J/m)
New PET1	100 / 0 / 0.67 / 0.25	280	82	29	76.5	5.5	34
HI PET 1	100 / 50 / 1 / 0.5	280	82	0.32	29.6	154	137
HI PET 2	100 / 100 / 1 / 0.5	280	82	0.49	14.7	20	>490
HI PET 3	50 / 100 / 1 / 0.5	280	82	0.14	10.5	26	>431
PET recovered	100 / 0 / 0 / 0	280	82	61	60.8	42	29
PE carboxylated	0 / 100 / 0 / 0	280	82	109	14.7	820	>490
Blend of PET recovered /PE carboxylated	100 / 100 / 0 / 0	280	82	93	12.5	14	31

Table 2 Large scale production and mechanical properties of High Impact PET (PET-PE Blockcopolymer)
IKEGAI : PCM-70 extruder with twin screw of 70mm diameter and 3 vents

Resins Model	Composition (weight) PET / PE / Coupling/ Catalyst recovered/ carboxylated /agent/	Temp. (℃)	Screw rotation (rpm)	Pellet yield (Kg)	MFR 280℃ (g/10min)	Brittleness temp. (℃)
New PET 2	100 / 0 / 0.95/ 0.10	280	100	313	2.3	35~70
HI PET 6	100 / 30 / 1.0 / 0.10	280	100	83	9.9	2.0
HI PET 7	100 / 30 / 1.3 / 0.75	280	100	152	2.1	16
HI PET 8	100 / 40 / 1.3 / 0.75	280	100	203	0.63	10
HI PET 9	100 / 50 / 1.3 / 0.75	280	100	160	2.4	- 15

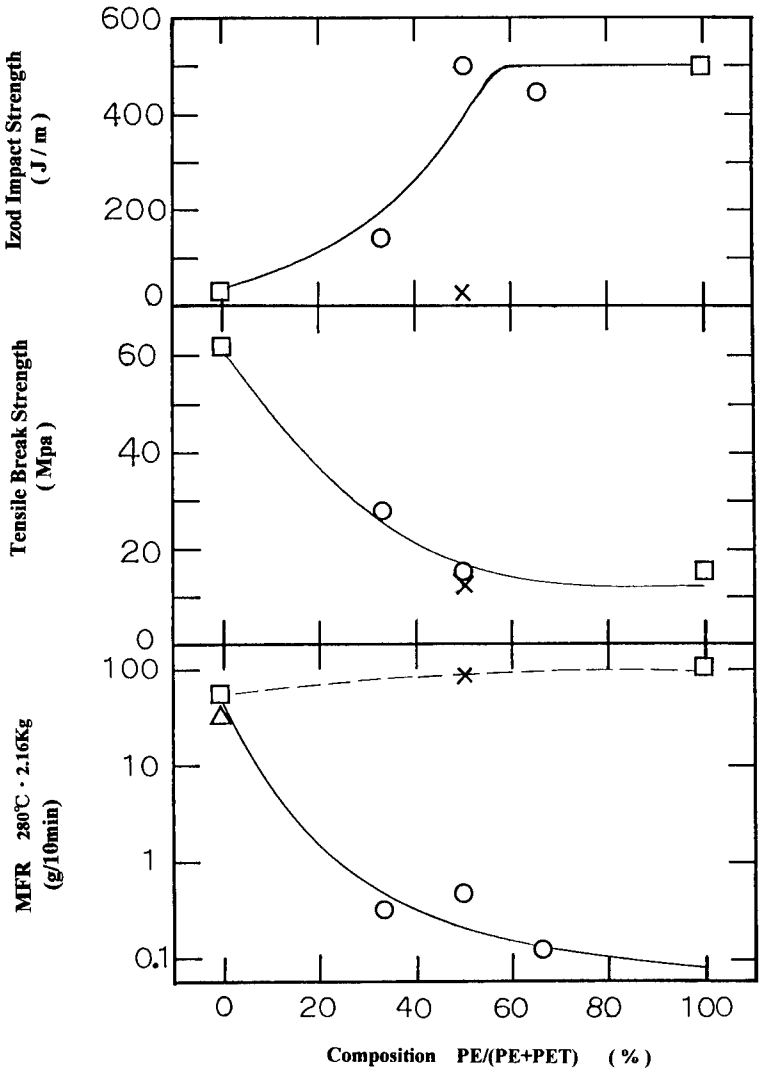

Fig. 2 Relationship between composition of PET/PE and MFR-Break Strength-Izod Impact of PET-PE Blockcopolymer

□ raw materials of PET and PE
△ New PET
○ PET-PE Blockcopolymer
× Blend of PET and PE

Proceedings of 7th Japan International SAMPE
Symposium & Exhibition, Nov. 13-16, 2001

Mechanical Properties of Metallic Closed Cellular Materials Containing Organic Material for Smart Structures

Satoshi KISHIMOTO and Norio SHINYA

Intelligent Materials Research Group, Materials Engineering Laboratory
National Institute for Materials Engineering
1-2-1, Sengen, Tsukuba, Ibaraki, 305-0047 Japan
E-mail:KISHIMOTO.Satoshi@nims.go.jp

Abstract

A metallic closed cellular material containing organic materials has been developed. Powder particles of polymer coated with a nickel-phosphorus alloy layer using electroless plating were pressed into pellets and sintered at high temperature. A metallic closed cellular material containing organic material was then fabricated.

The compressive tests were carried out. This material has the different stress-strain curves among the specimens that have different thickness of the cell walls. And also the results of the compressive tests show that this material has high-energy absorption and Young's modulus of this material depends on the sintering condition. In addition, it seems that this material has a large ultrasonic attenuation coefficient. The obtained results emphasize that this metallic closed cellular material can be utilized as energy absorbing material and passive damping material.

Key Words: Closed Cellular Material, Sintering, Isostatic Pressing, Eenergy Absorbing, Passive Damping.

Introduction

At many current research projects, for smart structures are been developing. Particularly, vibration control systems and energy absorbing systems are required to insure the safety of transport facilities. Therefore, materials for the smart structures are becoming important in terms of vibration control and energy absorbing systems.

Recently, cellular materials are receiving renewed attention as structural and functional materials. Cellular materials have unique thermal, acoustic and energy absorbing properties that can be combined with their structural efficiency[1]. Therefore, many kinds of cellular materials have been tested as damping and energy absorbing materials. Particularly, the closed cellular materials are thought to have many favorable properties and applications. However, there is a lack of technique to produce such fine closed cellular materials except for the gas forming [2-7], the sintering of hollow powder particles [8] and the two-dimensional honeycomb structures [1].

In this study, a new method to produce a metallic closed cellular material containing organic materials has been developed. In addition, the mechanical and ultrasonic properties of this material are measured. The utilities of this material are then discussed.

Conceptual Process

The schematic process flow diagram of the metallic closed cellular material

fabricating process is shown in Fig. 1. The process is as follows: 1) Powdered polymer particles are coated with a metal layer using electroless plating. 2) The powder particles are pressed into pellets (green compacts) by cold isostatic pressing. 3) After sintering at high temperature in a vacuum, the closed cellular material is produced.

Experiments

Preparing the metallic closed cellular material

A thermal plastic polymer, polystyrene, particles of 10μm diameter (Japan Synthetic Rubber Co., Ltd.) was selected for this study. These polystyrene particles were coated with a nickel-phosphorus alloy layer (about 0.19-0.46μm thick) using electroless plating [9]. These particles were pressed into pellets (green compacts) with about 8 mm diameters and about 8 mm long by isostatic pressing at 200MPa and 90°C. After this, these green compacts were sintered for 1 h at 800°C and 850°C in a vacuum.

Characterization

The microstructure of the green compacts before sintering and the cross-sections after sintering were observed using a scanning electron microscope (SEM). To observe the cross-section of this material, the specimen was cut and the cross-section surface was polished using emery paper (#600) and then Al_2O_3 powders. To measure the mechanical properties, compressive tests were performed at room temperature. In addition, ultrasonic measurements were carried out to estimate the attenuation coefficient of this material. The measurement was carried out with a 6.4 mm diameter probe generating a longitudinal wave of 10MHz at room temperatures.

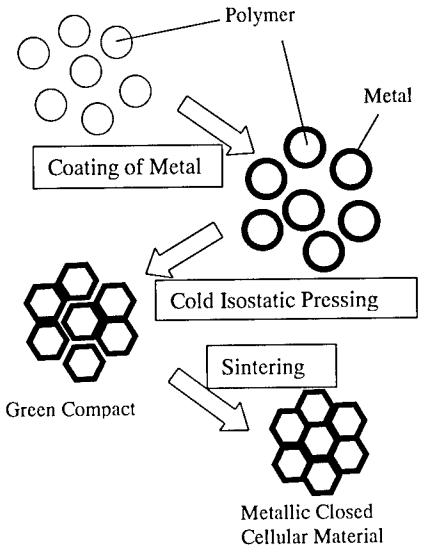

Fig. 1. Flow diagram of metallic closed cellular material fabricating process.

Results

Microstructural observation

Figure 2 shows an SEM image of the green compact after cold isostatic pressing. The polystyrene particles were deformed to polyhedra by isostatic pressing. The surface of the polystyrene particles coated with the nickel-phosphorus alloy exhibited facets. An SEM image of the cross-section of this material after sintering at 850°C is shown in Fig. 3. In this figure, the cell walls of the nickel-phosphorus alloy are observed as bright parts and the material inside the cell walls is observed as the darker parts.

Compressive test

Compressive tests were carried out at room

temperature. A typical example of the compressive test results is shown in Fig. 4 (a) and (b). Figure 4. (a) and (b) show the stress-strain curves of this closed cellular materials that have different thickness of the cell walls sintered at 800℃ and 850℃, respectively. The stress-strain curve shows a linear elastic region, a long plateau where the stress gradually increases and a wavy region where the stress repeatedly decreases and increases. In addition, the plateau stress of this material sintered at 850℃ is higher than that of this material sintered at 800℃.

Ultrasonic measurement

The ultrasonic attenuation was measured at room temperature. The attenuation coefficient (about 2.8 - 4.8 dB/cm) is larger than that of

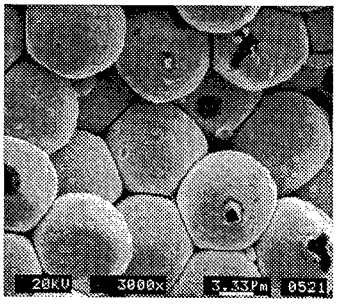

Fig. 2. SEM image of green compact.

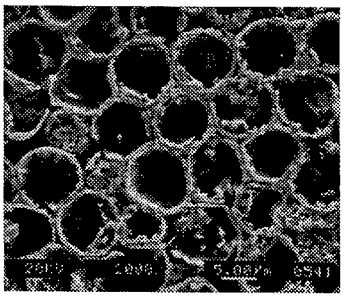

Fig. 3. Cross-section of the metallic closed cellular material after isostatic pressing.

(a)

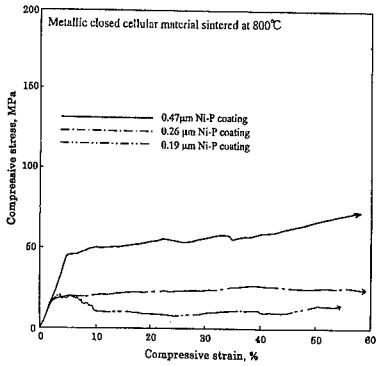

(b)

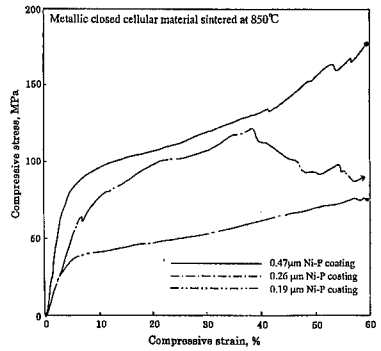

Fig. 4. Compressive stress-strain curve for metallic closed cellular material sintered at 800 °C (a) and 850 °C (b).

metallic materials, but smaller than that of polystyrene (15.2dB/cm).

Discussion

Metallic closed cellular material

A metallic closed cellular material has been developed in this study. The density of this

material is from 1.23 to 2.31g/cm^3 which is smaller than that of an aluminum alloy. As Fig. 2 shows, the polystyrene particles were deformed to polyhedra by isostatic pressing. Also, Fig. 3 shows that cell walls of a nickel-phosphorus alloy are observed as bright parts and the material inside the cell walls is observed as darker parts. The amount of emitted secondary electrons per a primary electron of the organic material is smaller than that of metals. During polishing, only 0.05μm Al_2O_3 powders were used. Therefore, the material inside cell walls is thought to be polystyrene or organic material. This result indicates that the organic material remains inside of the cell walls after heat treatment at 850 ℃ and this metallic closed cellular material including the organic material can be produced using this technique.

Energy absorption

As shown in Figs. 4 (a) and (b), the stress-strain curve has a linear elastic region, a long plateau region and a wavy region. After the linear elastic region, cracks occur in the direction parallel to the stress axis. Comparing Figs. 4 (a) and (b), the plateau stresses of the specimens sintered at are higher than that of the specimens sintered at 800 ℃. As the presence of the plateau in the compressive stress-strain curve is responsible for the high energy absorption. This metallic closed cellular material seems to have a high-energy absorbability. And it seems that this energy absorbability can be controlled by changing the sintering conditions.

Attenuation coefficient

The attenuation coefficient of this material (about 3.8-4.8 dB/cm) is larger than that of metallic materials, but smaller than that of polystyrene (15.2dB/cm). These results suggest that this material can be utilized as a passive damping material.

Conclusion

A closed cellular material containing polystyrene has been developed. This metallic cellular material is very light and has a high energy absorption and a large ultrasonic attenuation coefficient. The obtained results emphasize that the metallic closed cellular material can be utilized as an energy absorbing material and passive damping material.

Reference

1. L.J. Gibson, M.F. Ashby:"Cellular solids Structure and properties", Pergamon press, Oxford, 1988. p.1-41.
2. J.T. Beals, and M.S. Thompson, J. Mater. Sci.,32,3595(1997).
3. N. Chan and K.E. Evans, J. Mater. Sci., 32, 5945(1997).
4. D.J. David, A.P. Phillip and H.N.G. Wadly, "Porous and Cellular Materials for Structural Applications", Materials Research Society, Warrendate, 1998, pp.205-210.
5. Y. Sugiyana, J. Meyer, M.Y. He, H. Bert-Smith, J. Grenstedt, A.G. Evans: Acta Mater. 45(12), 5245(1997).
6. S.K. Maiti, L.J. Gibson, M.F. Ashby: Acta Metall., 32(11):1963(1984).
7. J. Benhart, J. Baumeister: J. Material Sci., 33, 1431(1998)
8. M. Hartmann, R.E. Reindel, R.F. Singer: "Porous and Cellular Materials for Structural Applications", Materials Research Society, Warrendate, 1998. P.211-216.
9. J. Takeshita: J. of the Surface Finishing Society of Japan, 47(11), 896(1996) (in Japanese).

Proceedings of 7th Japan International SAMPE
Symposium & Exhibition, Nov. 13-16, 2001

DEVELOPMENT OF AN ALUMINUM BASED SMART COMPOSITE WITH EMBEDDED OXIDIZED TITANIUM FIBER

H. ASANUMA, T. ISHII and G. HAKODA
Dept. of Electronics & Mechanical Engineering, Chiba University
1-33, Yayoicho, Inage-ku, Chiba-shi, Chiba, 263-8522, Japan

ABSTRACT

This paper describes development of an active and sensitive composite based on a simple metal composite. To realize this material system, continuous titanium fiber was embedded in aluminum matrix together with stainless steel reinforcement fiber, of which surface was oxidized to be insulated from matrix to form a heater and a temperature/strain sensor. It successfully actuated and sensed with the multi-functions of the embedded TiO_2/Ti fiber.

1. INTRODUCTION

The authors have developed a temperature and strain sensor by embedding surface oxidized nickel (NiO/Ni) fiber in aluminum matrix [1]. In this study, one more function as a heater was tried to be added by using titanium fiber because its electrical resistance is much higher than that of nickel.
An active and sensitive material was also tried to be developed based on this material system and embedded with stainless steel fiber as reinforcement.

2. EXPERIMENTAL

Pure aluminum plates of 0.2 and 0.4mm thickness, 30mm width and length were used as matrix. Titanium fiber of 0.15mm diameter and 99.5% purity was used as functional fiber and SUS304 stainless steel fiber was used as reinforcement.

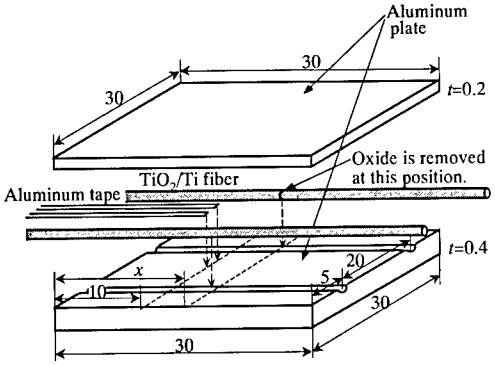

Fig. 1 Fabrication of the TiO_2/Ti fiber embedded aluminum.

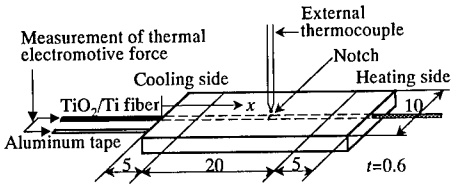

Fig. 2 The specimen for measurement of temperature.

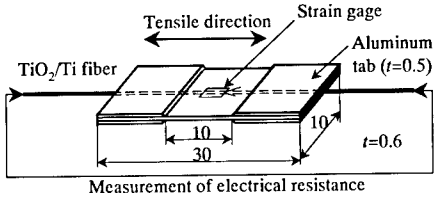

Fig. 3 The specimen for tensile test and measurement of electrical resistance.

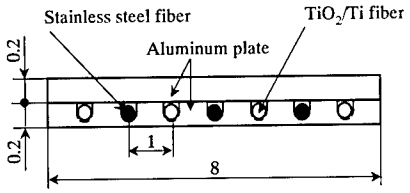

Fig. 4 Cross sections of the materials piled up for hot pressing.

The titanium fiber was oxidized at 1073K and for 1.8ks in air in an electric furnace to obtain TiO_2/Ti fiber. This composite fiber was arranged in the U-grooves made on a 0.4mm thick aluminum plate and they were covered with a 0.2mm thick aluminum plate as shown in Fig. 1. These materials were hot pressed under the condition of 798K, 16.4MPa and 1.8ks in air.

The specimen shown in Fig. 2 was cut out from the hot pressed sample and a temperature gradient was given on it by heating one end of it and cooling the other end, which was measured with a K-type thermocouple. A circumferential notch was already made on the TiO_2/Ti fiber at the middle of it to remove TiO_2 layer and make direct contact between

titanium and aluminum to form a thermocouple at this position. This temperature obtained by the embedded fiber was compared with that obtained with the K-type thermocouple.
Strain measurements were undertaken by using the specimen shown in Fig. 3 under the crosshead speed 1×10^{-4}mm/s of an Instron type tensile test machine.
An active and sensitive composite was tried to be fabricated. As shown in Fig. 4, U-grooves were made on 0.2mm thick aluminum plate and TiO_2/Ti fibers with notches and stainless steel fibers were arranged in them. A specimen of 8mm wide and 30mm long shown in Fig. 5 was cut out from this sample. There are four TiO_2/Ti fibers of which outer side ones were used as heaters and inner side one was used as a temperature or strain sensor. At the beginning, the current value was set at 0.2A and all measurements, that is, curvature measurement, temperature and resistance measurements by the embedded fiber, surface temperature measurement with a K-type thermocouple were made between 0.3 and 0.36ks after the start of heating. After the all measurements were undertaken, the current was increased by 0.2A and the measurements were repeated.

3. RESULTS AND DISCUSSION

3.1 Evaluation of the TiO_2/Ti Fiber The TiO_2/Ti fiber could be embedded in aluminum matrix without fracture of its TiO_2 layer when hot pressed under the condition of 823K and 1.8ks in air, where the thickness of its TiO_2 layer is about 2.5μm.
Thermal electromotive force of the TiO_2/Ti fiber against aluminum monotonously increased with increasing temperature up to about 700K, which proved its possibility as a temperature sensor of this temperature range. Making use of this result, the temperature measured with the embedded TiO_2/Ti fiber was obtained as 373K which coincided well with the temperature 370K on the surface just above the notch obtained with a K-type thermocouple, which means the embedded fiber is working as a temperature sensor at the notched position.
Due to the linear relationship between strain of the tensile specimen and the electrical resistance of the embedded fiber, the fiber is able to work as a strain sensor.
3.2 Evaluation of the active composite In Fig. 6, relation between the curvature and the surface temperature of the active composite is shown. According to this figure, it is clear that the embedded fibers are working as heaters and curvature of the composite increases with increasing temperature.
Relation between temperature obtained by the embedded TiO_2/Ti fiber and surface temperature of the active composite is given in Fig. 7, which shows good coincidence of the temperatures even after deformation of the active composite up to the temperature of about 500K. According to this result, it is clear that curvature of the active composite can be monitored by the temperature measurement with the embedded fiber.
Relation between electrical resistance of the embedded TiO_2/Ti fiber and surface temperature of the active composite was given in Fig. 8. This shows a linear relationship between them, which means that the curvature of the active composite can be monitored by this resistance measurement though it includes the both effects of the temperature increase as well as the decrease of the strain.

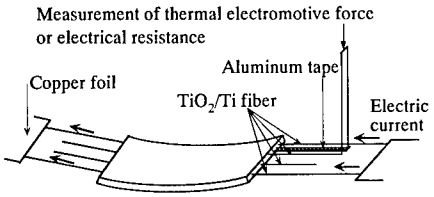

Fig. 5 The active composite with embedded TiO_2/Ti fiber.

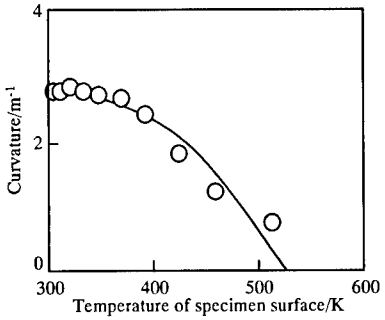

Fig. 6 Effect of temperature on curvature of the active composite.

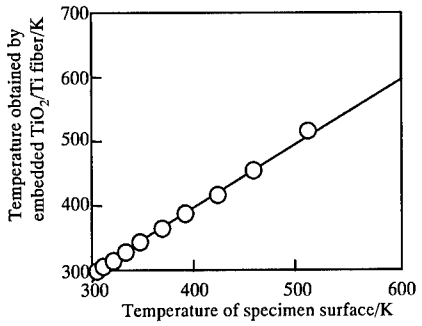

Fig. 7 Relation between temperature measured by embedded TiO_2/Ti fiber and temperature of specimen surface.

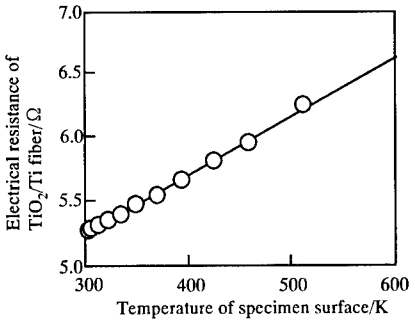

Fig. 8 Relation between electrical resistance measured by embedded TiO_2/Ti fiber and temperature of specimen surface.

4. CONCLUSIONS

The TiO_2/Ti fiber embedded in stainless steel fiber/aluminum active composite worked as a heater as well as a temperature/strain sensor for thermal actuation of the composite and its deformation sensor.

REFERECES

1. H. Asanuma, The Development of Metal-Based Smart Composites, JOM, 52, 21(10), (2000)

Proceedings of 7th Japan International SAMPE
Symposium & Exhibition, Nov. 13-16, 2001

Spark Plasma Sintering of $Sr_{1.9}Ca_{0.1}NaNb_5O_{15}$ Piezoelectric Ceramics

Rong-Jun Xie Yoshio Akimune Kazuo Matsuo Tatsuo Sugiyama Naoto Hirosaki*

Smart Structure Research Center, National Institute of Advanced Science and Technology
Umezono 1-1-1, Tsukuba, Ibaraki 305-8564, JAPAN
E-mail: rj-xie@aist.go.jp
*Advanced Materials Lab, National Institute of Materials Science,
Namiki 1-1, Tsukuba, Ibaraki 305-0044, JAPAN

Abstract

Dense and pore-free $Sr_{1.9}Ca_{0.1}NaNb_5O_{15}$ piezoceramics with the tungsten bronze structure were prepared by spark plasma sintering at 1000 - 1200°C for 5 min in vacuum, followed by annealed at 1000°C for 10 h in air. Fully densified ceramics with density > 99.4% TD could be achieved when sintered above 1050°C, which consisted of uniform grains with 2-6 μm in size. A typical P-E hysteresis loop was observed for the sample sintered at 1200°C, indicating its ferroelectrics. The piezoelectric properties of this sample were shown as follows: T_C = 290°C, $\varepsilon_T/\varepsilon_o$ = 1273, k_{31} = 6.9%, k_{33} = 15.1%, d_{31} = 87.0 PC/N and d_{33} = 39.9 PC/N.

1. Introduction

In recent years, a number of alkali and alkaline-earth niobates, i.e., $Sr_{1-x}Ba_xNb_2O_5$ (SBN), $Sr_2NaNb_5O_{15}$ (SNN), $Ba_{2-x}Sr_xK_{1-y}Na_yNb_5O_{15}$ (BSKNN), $K_3Li_2Nb_5O_{15}$ (KLN), and etc., have been extensively investigated for applications in optoelectronics, utilizing their large electro-optic effects or large non-linear optic effects, as well as for applications in pryoelectric detectors and piezoelectric transducers and actuators [1]. Among these niobates, calcium-modified strontium sodium niobate ($Sr_{2-x}Ca_xNaNb_5O_{15}$, SCNN) is one of the most promising ferroelectric and piezoelectric materials having the tungsten bronze structure (TB) [1, 2]. Unlike strontium barium niobate ($Sr_{1-x}Ba_xNb_5O_{15}$, SBN), very few reports on sintering and properties of SCNN materials are available in the literature. It is hard to fabricate dense SBN ceramics by using conventional sintering techniques, and abnormal grain growth and associated crack formation are widely observed in sintered SBN ceramics [3], which reduce the density and degrade

the properties as well. The same problems are also encountered in SCNN ceramics when the conventional pressureless sintering technique is used.

Spark plasma sintering (SPS) is a recently developed technique that enables ceramics to be fully densified at comparatively low temperatures and in very short times. Recently, Takeuchi *et al.* [4, 5] has successfully prepared dense and fine-grained $BaTiO_3$ and $PbTiO_3$ ferroelectric ceramics using SPS. In the present work, this novel sintering technique, namely spark plasma sintering, was attempted to densify SCNN ceramics, and their electric properties were reported.

2. Experimental Procedures

Synthesis of calcium-modified strontium sodium niobate, $Sr_{1.9}Ca_{0.1}NaNb_5O_{15}$, was conducted using solid-state reaction routes from individual oxide and carbonate powders: $SrCO_3$, Na_2CO_3, $CaCO_3$, Nb_2O_5. The raw materials were weighted in the appropriate molar ratio and ground for 24 h using zirconia balls and ethanol. The powder was dried at 60°C and calcined at 1150°C for 8h in air. The calcined powder was ground again in a mortar and sieved through a 60-mesh screen. The XRD pattern of the calcined powder showed a single phase of SCNN according to JCPDS 34-0429.

The powder of ~ 3g was put into a graphite die with an inner diameter of 15mm, and spark plasma sintering was subsequently carried out using Dr. Sinter (Model SPS-1030, Sumitomo Coal Mining Co., Ltd., Kanagawa, Japan) under a pressure of 35 MPa in vacuum. The sintering temperatures varied from 1000°C to 1200°C, and the heating rate was 300°C/min. After holding for 5 min at the sintering temperature, samples were slowly cooled with a rate of 150°C/h. The spark plasma sintered ceramics were subsequently annealed at 1000°C for 10 h in air to eliminate carbon contamination during sintering. For comparison, conventional sintering of SCNN ceramics was also performed by sintering the powder compacts at 1240°C for 6 h and then at 1300 ~ 1380°C for 25 h in air. The heating and cooling rates were both 100°C/h.

Densities of sintered specimens were measured using the Archimedes method. Theoretical densities of SCNN ceramics were determined from the mass of the constituent ions in the unit cell and lattice parameter data. Microstructural observations of sintered samples were conducted using a scanning electron microscope (SEM, Model S-5000, Hitachi, Japan). The polished specimens for SEM observations were thermally etched at 1200°C for 1 h in air.

The dielectric measurements were made at frequency of 1 kHz on silver-plated pellets using HP4294A LCR meter over a temperature range of 25°C to 360°C. The P-E hysteresis loop was observed by a Sawyer-Tower Circuit at 1 Hz. The poling was conducted by applying an electric field of 30 KV/cm at a temperature of 200°C for

30 min and then cooling to room temperature while maintaining the filed. Piezoelectric properties were determined from the resonant and antiresonant frequencies method.

3. Results and Discussion

3.1 Densification

The density of spark plasma sintered specimens as a function of temperature is given in Fig. 1. For comparison, the density of specimens sintered using conventional method is also included in Fig. 2. As can be seen, the density of spark plasma sintered specimens increases monotonically with increasing sintering temperature, with a sharp increase in the temperature interval: 1000 – 1050°C. The specimen had a density of >99.4% TD when it was sintered at temperature above 1050°C, suggesting that fully densified specimens could be obtained using spark plasma sintering. Interestingly, it only took about 10 min during the whole sintering process (5 min for sintering and 5 min for holding) to achieve such high density. In contrast, the density of specimen sintered using conventional method first increased with increasing temperature, reached a maximum value at 1320°C, and then decreased dramatically as the sintering temperature further increased. The decrease in density was ascribed to the rapid grain growth in specimens sintered at temperature above 1320°C, and thus leading to the formation of giant grains and cracks. Compared with the spark plasma sintered specimens, the conventionally sintered specimens had relatively lower densities, although the latter ones were sintered at higher temperatures and held for longer duration.

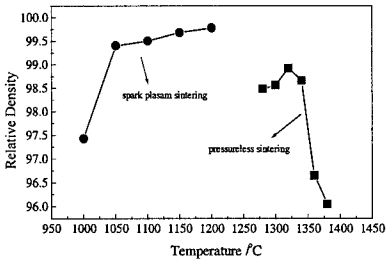

Fig. 1 Density *vs* sintering temperatures

3.2 Microstructural Observations

X-ray diffraction spectra of all sintered products revealed only single phase SCNN. At room temperature, the structure of SCNN appears to be an orthorhombic distortion of that for tetragonal tungsten bronze similar to SNN [1]. Figure 2 shows typical microstructures of conventionally sintered (1320°C, 25 h) and spark plasma sintered (1200°C, 5 min) specimens, respectively. As can be seen in Fig. 2a, the conventionally sintered specimen featured a microstructure consisting of grains having the size in the range of 6 –15 μm. No cracks but pores trapped at the grain boundary during particle coarsening were clearly observed, which were also encountered in other material systems like SBN [3], PBN [6] made by normal sintering method. On the contrary, a smaller and pore-free microstructure developed in the spark plasma sintered

specimen, which was composed of grains having the size of 2 - 6 μm. Furthermore, the SPSed specimen exhibited a narrower grain size distribution than the normally sintered specimen. The fine and uniform grain structure found for SPSed specimens, indicating minimal grain growth during sintering, was believed to result from very rapid consolidation of powder and relatively lower sintering temperature using spark plasma sintering. The similar phenomenon was widely observed in spark plasma sintered $BaTiO_3$, $PbTiO_3$ ceramics [4, 5].

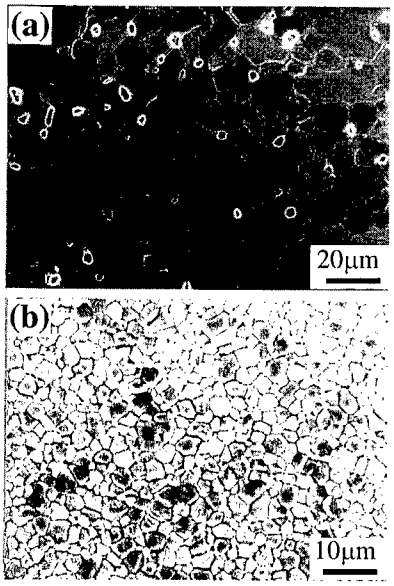

Fig. 2 SEM images of sintered SCNN ceramics: (a) conventionally sintered, (b) spark plasma sintered.

3.3 Electrical Properties

Figure 3 shows the curve of relative permittivity vs temperature for the specimen sintered at 1200°C. The Curie point, i.e., the temperature of the dielectric peak, was about 290°C. Relative permittivities at room temperature and at the Curie point were 1530 and 1273, respectively. A typical ferroelectric P-E hysteresis loop was shown in Fig. 4, giving P_r = 2.94 μC/cm^2 and E_C = 1.04 kV/mm, respectively.

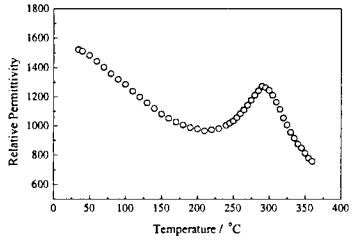

Fig. 3 Permittivity *vs* temperature of the sample sintered at 1200°C

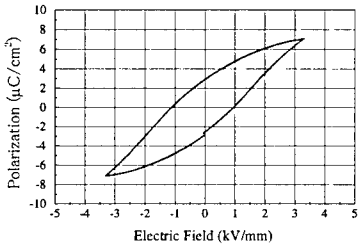

Fig. 4 Typical P-E hysteresis loop of the sample sintered at 1200°C

The electromechanical coupling factors k_{31} and k_{33} of the sample sintered at 1200°C were 6.9% and 15.1%, respectively. The piezoelectric constants d_{31} and d_{33} were calculated to be 87.0 and 39.9 PC/N for the same sample.

4. Conclusions

Spark plasma sintering was applied to fabricate dense SCNN piezoceramics in this work. Fully densified and pore-free SCNN ceramics could be achieved at relatively lower temperature and in a shorter time in comparison to the conventionally sintered ones. The electrical properties of the sample sintered at 1200°C were shown as follows: T_C = 290°C, $\varepsilon_T/\varepsilon_o$ = 1273, k_{31} = 6.9%, k_{33} = 15.1%, d_{31} = 87.0 PC/N and d_{33} = 39.9 PC/N.

Acknowledgement

The authors are grateful to the Japan Science and Technology Corporation for financial support.

References

1. R.R. Neurgaonkar, J.R. Oliver, W.K. Cory, Le. Cross and D. Viehland: Ferroelectrics, 160, 265 (1994).
2. J.R. Oliver, R.R. Neurgaonkar, L.E. Cross: J. Am. Ceram. Soc., 72(2) 202 (1989).
3. H.Y. Lee and R. Freer: J. Appl. Phys., 81(1) 376 (1997).
4. T. Takeuchi, M. Tabuchi, H. Kageyama and Y. Suyama: J. Am. Ceram. Soc., 82(4) 939 (1999).
5. T. Takeuchi, M. Tabuchi, I. Kondoh, N. Tamari and H. Kageyama: J. Am. Ceram. Soc., 83(3) 541 (2000).
6. T. Hiroshima, K. Tanaka and T. Kimura: J. Am. Ceram. Soc., 79(12) 3225 (1996).

Proceedings of 7th Japan International SAMPE
Symposium & Exhibition, Nov. 13-16, 2001

Integrating Research &Development Programs with FAA Certification to Expedite the Introduction of New Technology into Production Aircraft

Moto Ashizawa# and Atuo Sato#

#: Pacific Rim Consilium, LLC
5729 Lakeview Drive NE, Kirkland, Washington 98033
E-mail: MOTOAACE@aol.com and ATUOASEC@aol.com

Abstract

Many Research & Development, (R&D), programs have been initiated since the inception of the aerospace industry with the goal of developing improvements which would eventually be applied to production aircraft. While good results have been obtained from past programs, a relatively small number of them have actually found their way into production aircraft. Many factors are responsible for this including the failure of research program planners to consider the significant impact which Federal Aviation Administration, (FAA), certification rules would have on a production design. The National Aeronautics and Space Administration, (NASA) recognized this problem and surmounted it in their Aircraft Energy Efficiency, (ACEE), program by requiring FAA certification to be obtained concurrently with the design, testing and manufacturing of new components manufactured as a result of the research. These components were then installed on in-service transport aircraft where valuable service history was obtained. NASA's approach was successful and led to the timely, widespread use of composite structure on new commercial aircraft. A similar approach is currently being followed by Japan's New Energy and Industrial Technology Organization, (NEDO) for the development of fuselage structural components. This paper discusses the past history of R & D projects and focuses on current certification procedures and how they can be used to obtain FAA approval for aircraft components developed using new technology.

Introduction

Although numerous R & D programs have been attempted since the inception of the aerospace industry, only a small number of them have achieved the goal of eventually appearing in production aircraft. There are several reasons for this, among which are too high a cost, impractical to introduce into production, insignificant improvement and failure to consider the impact of FAA certification requirements. In this paper, we will concentrate our discussion on this last item and suggest a solution for it which we believe will expedite the implementation of new technology into production aircraft. In a typical R&D environment, FAA Certification is seldom considered. Most, if not all, of the R&D effort is usually expended on technology development. As a result, even the best technology improvements may be uncertifiable or miss their critical timing for introduction into production because they were not ready for FAA Certification. What

must be done to alleviate this problem? One of the best examples in recent aviation history was NASA's ACEE program.

NASA's ACEE Program

The "Oil Crisis" of 1973 resulted in severe shortages of crude oil which, in turn, caused the price of aviation fuel to soar thus spurring NASA into sponsoring its ACEE program [1]. Not only it was necessary to develop new, fuel saving technology but also this technology must be integrated into aircraft production very quickly in order to alleviate the fuel shortage.

NASA sponsored six advance composite programs among three major commercial aircraft companies - Boeing, Lockheed, and McDonnell Douglas. Each company was to develop one secondary s and one primary structural component using advanced composites to reduce weight thus saving fuel. Figure 1 shows the components selected each company.

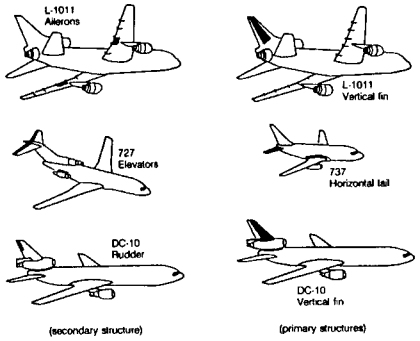

Fig. 1 NASA ACEE Program

The unique requirement of the AACE R&D program was that, in addition to developing new technology, it was necessary to obtain FAA certification, conduct flight tests, and install the composite components on aircraft currently in revenue service for a number of years. The incentive for the airlines to participate was that NASA would pay to replace the composite components with new metal components after the in-service testing was completed.

Some of the composite components performed so satisfactorily in actual service, the airlines requested to keep them in service in lieu of replacement and now, after more than 25 years, ACEE composite components are still flying. The biggest benefit of the ACEE program came when major companies were ready to use composites into new production aircraft. The "Production Aircraft Readiness" was there.

FAA Procedures to Introduce New Technology

Basically, there are six FAA procedures that can be used to introduce a new technology into commercial aircraft, namely, (1) Type Certification, (2) Change to Type Certification, (3) Supplemental Type Certification, (4) Technical Standard Order, (5) Part Manufacturer Approval, and (6) Repair & Alteration.

By far, the best way to introduce a new technology to commercial aircraft is by Type Certification (TC). Whenever a new aircraft is introduced, such as B-777, the type certification procedure is used and many new technologies are introduced at that time. Unfortunately, the number of new aircraft coming out is very few and far between; therefore, the opportunity to introduce a new technology by type certification is extremely limited.

The next best way is when Change to Type Certification (CTC) occurs. This happens when an aircraft manufacturer decides to undertake a major change to type certificated aircraft, such as, introducing stretched or extended range version of B-777. Only the holder of the original Type

Certificate allows the CTC.

Supplemental Type Certificate (STC) is a very powerful FAA procedure that can be used by the companies other than the original type certificate holder. New technology can be introduced to existing aircraft by STC at any time. Many companies use an STC to introduce new technology, new products, and new design concepts.

Technical Standard Order (TSO) is used to certificate those components and equipment that are interchangeable with several different types of aircraft. An example of TSO is item is Auxiliary Power Unit. The TSO certifies that the part complies with certain FARs but does not automatically authorize its installation on any aircraft. It is usually necessary to also have an STC, which installs the part on a specific aircraft.

Part Manufacturer Approval (PMA) is used to certificate replacement parts. Normally the PMA replacement parts are identical to the original parts; however, it is possible to introduce new technology replacement part using this PMA procedure in conjunction with an installation STC.

Although not very commonly used, it is also possible to introduce a new technology during Repair & Alteration procedure. One good recent example was the introduction of "Boron Composite" repairs for damaged metal structures.

Although any of these six FAA procedures can be used to introduce a new technology; however, the most commonly used are TC, CTC, and STC.

During the development of new technology under R&D program, it may not be possible to undertake a full FAA Certification as it was done with NASA ACEE program due to insufficient funding, schedule problems, and/or lack of manpower. Nevertheless, many companies today would like to see that their technologies are FAA Certifiable. In view of this need a "Simulated FAA Certification Program" has been initiated as an integral part of R&D program by Kawasaki Heavy Industries, (KHI), sponsored by the Japan Aircraft Development Corporation, (JADC).

New Technology Program

Under the sponsorship of JADC, KHI has been developing three new technologies which are (1) A Large Thin Precision Casting, (2) Friction Stir Welding, and (3) Composite Sandwich Nose Section some photos of which are shown below:

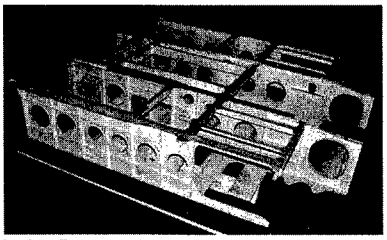

Fig.2 Large Thin Precision Casting [2]

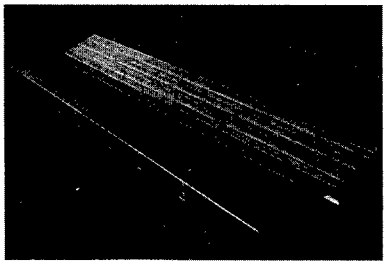

Fig. 3 Stir Friction Welding [2]

Simulated FAA Certification Program

JADC has adopted the "Simulated FAA Certification Program" [3] in order for the results of the R &D activities conducted by

KHI to concurrently meet the FARs.

With this in mind, JADC has invited several FAA Designated Engineering Representatives (DERs) as a consultants to provide KHI with guidance on regulatory procedures. These consultants were not acting as representatives of the FAA during this project and did not approve any data since the program was not an FAA accepted project but rather a simulation of what would be required to obtain FAA certification, i.e., for each project, KHI performed a simulated certification procedure to demonstrate compliance to the applicable FAR.

The first step taken for certification purposes was to write a Certification Plan containing the appropriate certification basis and a complete compliance checklist. The certification plan served as a "road map" for all forthcoming certification activities. The applicant is responsible for showing compliance to the FARs applying to the specific product by submitting type design and substantiating data necessary to demonstrate that the product meets all applicable airworthiness requirements.

Type Design data consists of drawings and specifications; information on dimensions, materials, and processes, and any other data used to describe and substantiate the product including test and analysis reports, etc. As an example, the following documents must be prepared to substantiate an item by testing:

1. The applicant should prepare a test plan which contains as a minimum (a) a clear description of the item to be tested, (b) a list of equipment required and its current calibration status, (c) required conformity inspection information for the test unit and test set up (d) test procedure to accomplish the goal and (e) the applicable FARS for which the test will demonstrate compliance.

Once the test plan and all applicable type design data are approved, the cognizant engineer requests conformity inspections be made to ensure that the product being tested complies with the type design data prior to beginning any test.

2. Conformity and Test Witnessing: A Statement of Conformity can be issued either by the manufacturer or the applicant. Conformity inspections should not be confused with engineering compliance inspection, which is conducted to ensure that an installation and its relationship to other installations comply with the regulations. After the test witness has confirmed that the appropriate conformity inspections have been made and that all appropriate paperwork has been completed, the test may proceed.

3.After the test has been completed, a test report must be prepared which states the results.

Similar convoluted approval steps must be taken for all substantiation documents in each applicable discipline. A short summary of the intent of NEDO-JADC has been presented. This intent has a deep meaning to the aircraft industry.

Acknowledgment

The authors appreciate the support from NEDO, Dr. Kikukawa from JADC and Mr. Hirose from KHI.

References

1. M.C.Y. Niu: "Composite Airframe Structures", Technical Book Company, USA, 1992

2. Y. Hirose, T.Tsujimoto, K.Kosugi, M.Imuta, H. Fukagawa: "Innovative Nose Section of Aircraft by applying Friction Stir Welding (FSW) to an Aluminum Alloy and by using Large Thin Casting of improved Aluminum Alloy", Limat, The 2nd International Conf. on Light Materials for Transportation Systems, Pusan, Korea, to be published.

3. FAA Order 8110.4B "Type Certification"

Proceedings of 7th Japan International SAMPE
Symposium & Exhibition, Nov. 13-16, 2001

NEDO's R&D Program on Revolutionary Low-Cost and Lightweight Aircraft

Yukio Ito

New Energy and Industrial Technology Development Organization(NEDO)
Sunshine 60,29F,1-1,3-Chome Higashiikebukuro, Toshimaku, Tokyo,170-6028, Japan
E-mail:itoyko@nedo.go.jp

Abstract

Innovations for low-cost and lightweight structures are required for new-generation, high-speed transport (aircraft, trains, ships) and other structures (bridges, etc.) to conserve resources and energy and protect the environment. Current structures have a high part count. Application of conventional technologies will have little effect for future lightweight structures. Recent technological developments have given us hints for near-term future structures. This program covers three areas:
(i) New design and manufacturing technologies for co-cured CFRP structures;
(ii) New precision casting and welding technologies for large-size metal structures;
(iii) Integration technologies for innovative light structures.
The goal is to drastically and cost-effectively save weight and reduce the part count of cockpit and wing structures for civil aircraft. Advanced CFRP manufacturing technologies will be developed for parts having complicated forms, large-size structures, and new-type sandwich panels. In addition, advanced technologies such as thin, large-size precision casting, friction stir welding and super-plastic forming will be developed. Integration technologies for fastening technology between CFRP parts and metal alloy parts, 3-dimensional CAD and a structural work station will also be developed. This will contribute to the verification process of the above work for commercial aircraft. This five-year program commenced in summer 1999.

Key Words : Lightweight structures,
Co-cured CFRP structures,
Precision casting, Super plastic forming

1. Introduction

Global economic growth and a high quality of life demands high-speed transportation. On the other hand, calls to save energy and resources and protect the environment are increasing year by year. For these reasons, low cost and lightweight vehicles are urgently required. Nowadays vehicles are complex and have a large part count due to a design consistent with strength and light weight. Application of conventional design methods yields little effects. However, recent advanced manufacturing technology developments such as composite materials, aluminum casting, alloy welding and structural design technologies implies the possibility of innovation for light weight and an extremely small number of parts. Under these circumstances, NEDO started a R&D program in 1999 entitled "Key Technology for Innovative Low-cost and Light Structures" as a five year program. This program is aimed at design and manufacturing technology development for

innovative light aircraft structures using CFRP (carbon fiber reinforced plastic) and program will be used for high-speed trains, ships and other structures that can conserve resources and energy, and for creating simple, reliable and lightweight structures which will induce and create new industrial fields.

2. Outline of the R&D Program

The program covers the following three areas:

① *Design and manufacturing technologies for co-cured CFRP structures*

Structures made of metal have been refined and cultivated for light weight and high strength properties by the "built-up method" (fastening frames, thin skins, etc.). Efforts for light weight have been made by replacing the metal with an aluminum alloy with high specific strength or a composite material but keeping the conventional built-up method. However, it has limitations. By making the best use of the co-curing characteristic of advanced aluminum alloy as excellent materials with specific strength. The achievements of this composite material, a new concept for making and assembling structure components can be introduced. It will then be possible to reduce part count and weight.

② *Precision casting and welding technologies for large-size metal structures*

Conventional large-size metal structures have the disadvantages of a complicated manufacturing process due to high part counts, required reliability levels, weight increases from rivet fastening, and corrosion tendencies at the contact surfaces of two materials.

③ *Integration technologies for innovative light structures*

In order to optimize strength, cost, etc. for a whole structure, it is necessary to develop technology connecting different materials, design technology including apparatus and devices, evaluation know-how for strength and reliability of a whole structure.

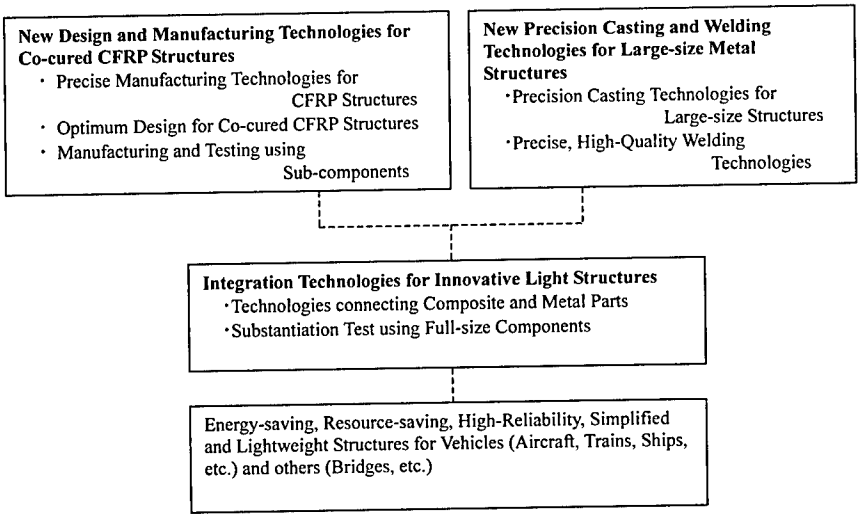

Figure 1. Outline of the R&D Program

3. Verification by Design, Fabrication, Testing for Full-scale Component

By incorporating innovative key technologies, nose and wing structures applicable to a small civil transport will be trial fabricated, strength tests will be performed and design and fabrication issues will be identified and solved. Figure 2 shows the actual full-scale components of this project. The first is the nose structure, and second is the wing box structure.

Design and manufacturing technologies which conform to airworthiness standards set by airworthiness bureaus, such as the FAA, will be established.

As for nose structures, the conventional method requires many parts to build up a multi-frame. Using the innovative method, a CFRP sandwich panel can reduce frames and stringers, and new casting and welding techniques can also reduce part count. For example, the pressurized bulkhead is made by friction stir welding. In the case of nose structures, the objectives are a 10% weight saving and an 80% part count reduction compared with conventional structures.

In the case of wing structures, many parts are necessary to construct a skin-stringer panel and multi-rib wing box. A new concept for making structure composites and assembling them will be introduced by making the best use of the co-curing characteristic of advanced

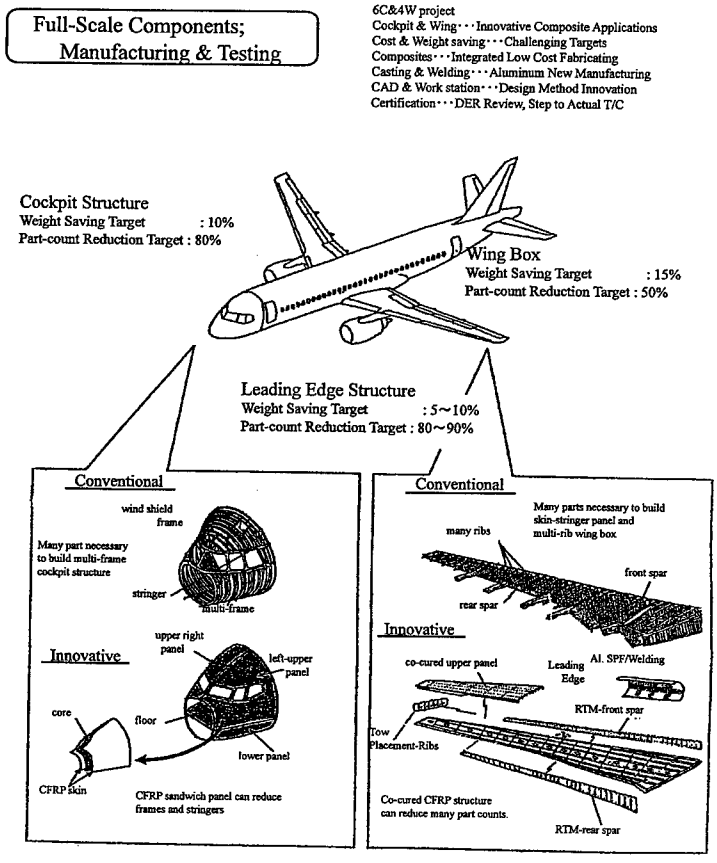

Figure 2 R&D Program of Key Technology for Innovative Structures

composite materials. Some integrated pieces using these materials can reduce part count. In this case, the objectives are a 15% weight saving and 50% part count reduction.

4. Organization of the Project

The New Energy and Industrial Technology Development Organization (NEDO) solicited proposals for participation in an R&D program entitled "Key Technology for Innovative Low-cost and Lightweight Structures" in FY1999. Following a strict and fair assessment of all proposals, NEDO selected Japan Aircraft Development Corporation (JADC) as the contractor. NEDO commenced a five-year program in summer 1999. NEDO's policy is to promote the R&D program efficiently with the participation and cooperation of researchers from industrial, academic and governmental fields. An assessment committee composed of NEDO representatives, researchers in these fields, and knowledgeable academic experts was established to promote the project. Assessments are conducted in a timely and proper way.

6. Conclusion

The targets of this project can be summarized as follows:

(1) Wing structures and a nose will be fabricated incorporating innovative key technologies and assessment tests equivalent to those in actual aircraft development. Design and manufacturing technologies conforming to airworthiness standards established by airworthiness bureaus, such as the FAA, will be established. (2) As for wing structures, the objectives are a 15% weight saving and 50% part count reduction compared with conventional structures.

(3) As for nose structures, the objectives are a 10% weight saving and 80% part count reduction compared with conventional structures.

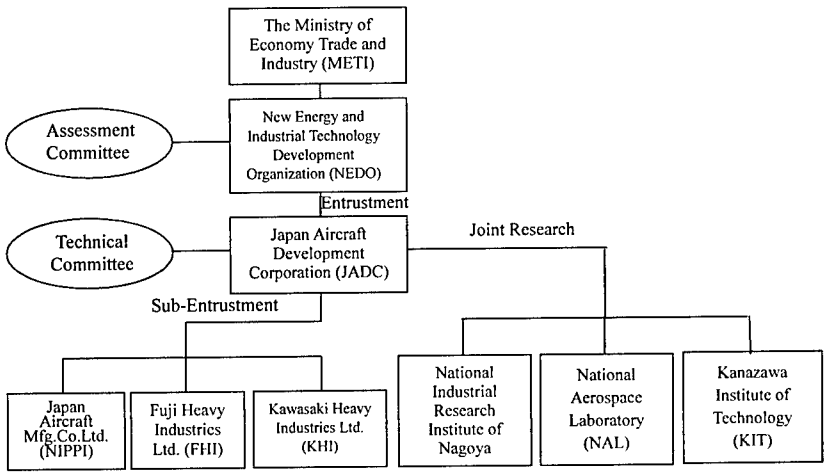

Figure 4 Organization Chart of the R&D Project (FY2001)

Proceedings of 7th Japan International SAMPE
Symposium & Exhibition, Nov. 13-16, 2001

R&D Program of Innovative Structural Technologies

Akikazu Yahata# and Hiroshige Kikukawa#

#: Japan Aircraft Development Corporation
Toranomon Daiichi Bldg.,2-3,Toranomon 1-chome, Minato-ku, Tokyo 105-0001, JAPAN
E-mail: ayahata@jadc.or.jp

Abstract

Demands for lighter structures will increase for transport vehicles from the aspects of economic growth, energy saving, environmental concerns and customer-satisfaction. If we can solve cost-reduction and weight-reduction demands, especially civil aircraft development would be more activated and accelerated. Recent technology developments have given us hints for near-term future structures. Eventually an R&D plan was presented for "key technology for innovative low cost and light structures", approved and commenced in 1999 as a 5-year program. The approach to reduce weight is by applying composite material and new metal related technologies. The target is a 15% and 10% weight-reduction for the wing and nose structures respectively. The efforts were focused on basic design and fundamental technology establishment in the first two year. Based on development building block method, simulated certification process for the wing and nose structures will be performed through DER (Designated Engineering Representative) evaluations.

Key Words : co-cured CFRP structures, light-weight structures, wing structures, nose structures

Introduction

Demands for aircraft transportation systems will steadily increase to more than 200% in the next 20 years according to the forecast of passengers (unit : man-miles). In such circumstances, demands will grow for light and low-cost airframes that are not only cost-effective but also conserve energy. So, development of advanced technology for light structures is continuously necessary in the future. But adopting advanced technologies yields a sharp rise of capital cost for developing a new aircraft with high-performances the airlines demand. On the other hand, discount pressure for aircraft prices by the airlines due to market competition remains as intense as before. As a result, the gap between development cost and the aircraft price becomes gradually bigger. Already new aircraft development using conventional methods is not feasible and the aircraft business became very difficult. In order to overcome the situation, drastic light structure design is needed. The technology to achieve both light-weight and low-cost is needed. If we can find a solution, new development for civil transport will be accelerated. Moreover it is desirable to perform an R&D program so that actual development of a new aircraft does not cost so much. For those reasons, NEDO (New Energy and Industrial Technology Development Organization)'s open-bidding program "R&D of Key Technologies of Design and Manufacturing for Innovative Light Structures" was planned. JADC applied for the program with a proposal document and was nominated as a contractor. Main points of the program are shown in Figure 1.

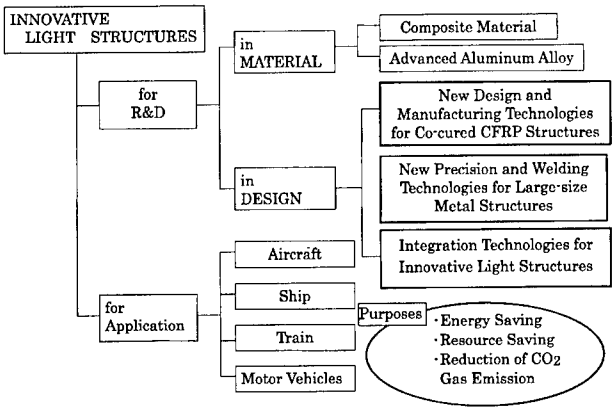

Fig.1. Main Points of the Program

Outline

The structures of an aircraft are dominantly made by the built-up method in which many parts are assembled by rivets and fasteners, so the part count is an extraordinarily a large number. Reducing part-count is the most effective way to reduce costs because it reduces working time for fabrication, assembling and processing. In the program, we selected the wing structure and the nose structure as representative portions since they have a large number of parts and complicated figures. The wing structure is sensitive to strength and has the fuel tank. The nose structure has the pressurized space. The part-count reduction targets are set at 50% and 80%, respectively. Technologies for the program are co-cured CFRP structures, CFRP sandwich panels, VaRTM, large-size, thin precision casting, friction stir welding, super plastic forming and others.

The Clue to Innovative Structures

For part-count-reduction and weight reduction, we are trying to get innovative structures. The positions or clue of the target

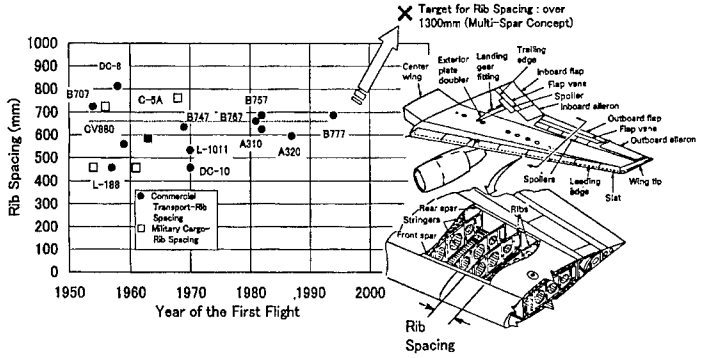

Fig.2. Target of Rib Spacing in Wing Box

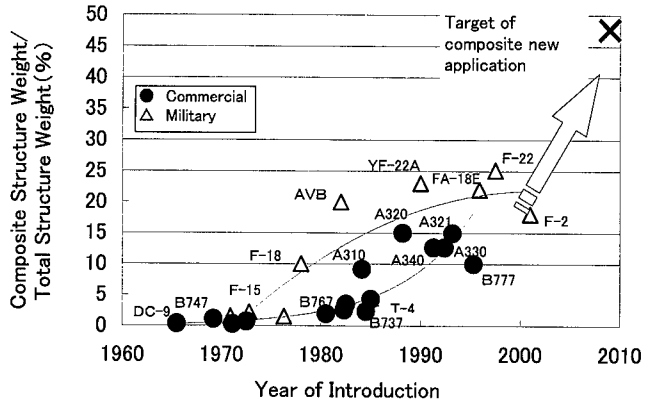

Fig.3. Target of Composite Application for Light Weight

are described below. The spacing of frames and stringers are main parts of the fuselage and wing. Part-count can be reduced when the spacing becomes wide. The historical data show that the spacing of frames and stringers remains constant from B707 (First flight: 1954) to B777 (First flight: 1994). The reasons for constant spacing are because the same material, i.e. aluminum alloys, were used. The most lightweight structure for the wing structures is the co-cured CFRP structure. Fig. 2 shows rib spacing in a wing box. The historical data show that the spacing is scattered 450 to 800mm, but the average is approx. 650mm. The rib spacing has remained nearly constant for forty years. Our efforts were focused on how to combine ribs and stringers directly without numerous clips or other parts stiffening ribs and stringers. In the program, part-count for a wing box will be reduced by using one-piece-oriented composite technologies such as the unique co-bonding process.

The rate of composite material in current aircraft structure occupies about 15% in weight percentage. Applying composite material to nose and wing structures in the program, the rate will increase from about 15% up to about 45% as shown in Fig. 3.

Approaching Methods

The project is a five-year program begun in FY1999. We determined yearly targets, called "Exit Criteria", for the nose, wing, and leading-edge structures. We adopted a method to step up to the next year's entrance through assessing whether the year's target is accomplished or not. Consequently the five-year R&D program schedule was determined. Furthermore we adopted a "Building Block Approach" method. The method is often used for innovative R&D programs in which optimum solution on means, effects etc. are unknown. Using the method we expect a steady technological approach to the goal. In the beginning of the program, we concentrated on steady steps. We intended to perform the same procedures as in the actual development of a new aircraft. We made an execution plan, and considered these important items: (a) a design based on firm procedures, specifications etc.; (b) technical assessment; (c) assessment of a substantiation test by a DER. To assess the design and its validity, we examined the design standards and adopted Japanese Airworthiness Standards Chap.III (Transport Category), FAR Part 25 (the latest revision),

Table 1. Estimated Effect of Energy-Saving

(unit :10^4 kilo liter- crude oil)

		FY 2000	FY 2005	FY 2010	FY 2020
Aircraft		0	2.7	6.9	22.7
Ship		0	1.2	2.4	3.6
Train		0	3.2	6.3	8.4
Motor Vehicles	For Passengers	0	4.2	9.2	16.4
	For Cargo	0	3.4	6.9	10.3
Sum		0	14.7	31.7	61.4

Table 2. Estimated Effect of CO_2 Reduction

(unit : 10^2 kilo ton-CO_2)

		FY 2000	FY 2005	FY 2010	FY 2020
Aircraft		0	0.7	1.7	5.5
Ship		0	0.3	0.7	1
Train		0	0.8	1.7	2.2
Motor Vehicles	For Passengers	0	1	2.2	3.9
	For Cargo	0	0.9	1.8	2.6
Sum		0	3.7	8.1	15.2

Advisory Circulars (AC) and supplemented documents as design rule for a commercial airplane.

Energy-saving and CO_2 Reduction Effects

Here is an estimate of how much energy consumption could be saved if the innovative technologies were developed and the substantiation tests were executed successfully. As a result, 2% of the total energy consumption used for transportation in Japan could be saved 20 years from now as shown on Table 1. At the same time, that contributes approx. 13% of the target for the Kyoto Protocol (reduced CO_2 emission : 1.5 million-ton) as shown on Table 2. We forecast that the needs to adopt such light-structure technologies would surge in high-speed vehicles, especially superexpress railway vehicles, motor vehicles and so on.

Conclusion

The program is aimed at light-structures for energy and cost savings. We will promote key technologies cultivated for a long time to the level where they can be applied to an actual vehicle approximately five years from the start. Furthermore, we are trying to apply the technologies to an airplane in which the requirements for safety, reliability, airworthiness, maintenance are the most rigorous. The introduction of an innovative structural method involves risks for its substantiation. In order to get substantiation, we have made a plan based on legal standards, accumulated characteristic data, full-scale components fabrication and tests. In the future we hope to present these technologies as substantiated and globally competitive. This report is a summary of our two year's result.

The authors wish to thank METI and NEDO representatives for their advice, help and suggestions. We also should like to thank all persons concerned for their contributions and promotion to the program.

Proceedings of 7th Japan International SAMPE
Symposium & Exhibition, Nov. 13-16, 2001

Design, Manufacturing, and Certification Considerations for Modern Integrated Structures

Ric Abbott

Raytheon Engineering Fellow
Raytheon Aircraft Company
Wichita Kansas
E-mail: ric_abbott@rac.ray.com

Abstract

The optimum balance of cost and performance for airframe components is achieved when light weight parts are used and assembly costs are minimized. Material cost, labor content, and assembly cost must be weighed against the effects on vehicle cost, weight, and performance.

Modern manufacturing concepts include machine laid and co-cured composites, resin transfer molded composites, adhesively bonded assemblies, machined aluminum, advanced castings, and various combinations of these.

This presentation describes the design, fabrication, and certification issues with major integrated aerospace structures.

Key Words: Composites, co-cured, integrated structures.

Introduction

Large co-cured or co-bonded structures are the key to producing aerospace composite structures at a reasonable cost. In this context, reasonable cost means equal to, or almost as low as, the cost of riveted aluminum structures.

However, traditional materials such as aluminum and titanium are not to be ignored, even in largely composite structures. Fittings for attachment and load transfer are typically more efficient when designed for metallic materials. Also, there been have tremendous advances in both high speed-machining and precision casting technologies.

We should remember that the lightest possible structure is a semi-monocoque design; that's why riveted metallic airplane structures look like they do. A small weight penalty will be incurred when using machined parts, cast parts, or cored-sandwich structure in place of riveted assemblies of sheet metal and extrusions. However, the cost saving gained by lower part count and reduction in assembly labor hours will more than offset the weight penalty for all except vehicles with the very highest cost of useful load. See table 1

Modern castings have much to offer in the way of reduced part count and reduced labor for subsequent operations. Historical drawbacks such as excess wall thickness, coarse grain structure, and porosity have largely been eliminated in modern casting technology. Materials such as titanium, which present difficulties in machining and in drilling on assembly, can now be cast with acceptable surfaces which may eliminate subsequent machining operations.

Table 1
Capital Cost of Useful load

USER	VEHICLE	USEFUL LOAD kg	COST $ per kg
ARMY	TRUCK	34,500	11
LAWYER	BMW	680	80
NAVY	SPOOK BOAT	18,000	1,000
AIRLINE	B 767-300	73,000	1,300
USAF	C-17	140,000	1,430
CORP	BIZ JET	2,000	2,125
USMC	V-22	14,500	7,000

Single-Cure-Cycle Pressure Cabin

As in many innovative approaches, new challenges have to be met and overcome. In the case of large integral composite parts, such as the one-piece pressure cabin shown in figure 1, the challenges include precision tooling, new process controls, development of quality assurance methods, and related certification issues.

Figure 1
One Piece Pressure cabin

Automated fiber placement is used to reduce labor cost below that of hand layup and possibly below that of riveted metal structures. Sophisticated tooling allows the automated fiber placement to take place on a male tool, and yet facilitates transfer of the part to a female tool for final cure. The mandrel is removed prior to autoclave cure which reduces the thermal mass in the autoclave and puts the mandrel back into the production cycle.

Conformity inspection on the first few articles involved visual inspection of every ply. After validation, software-based self-checking verifies the location and correct tension on every ply and in fact on every tow placed. Laser ply location is employed to identify the locations of each piece of core, adhesive, and reinforcing framework

New specifications were written to qualify the material properties, control the incoming materials, and control the fiber placement and cure process. Material controls and process controls are built into the specifications. Material out time is carefully monitored and process test specimens for process checks are machine laid and cured in exactly the same manner as the cabin itself

Certification issues included validation of the laminate properties; machine layup tolerances; and demonstration of damage tolerance properties. Damage tolerance considerations included: intrinsic manufacturing quality and NDI standards; possible in-service damage; and massive discrete damage from such rare occurrences as lightning strike, engine fire, tire burst, and rotor burst. The end point of all the damage tolerance tests and analyses was inspection methods and intervals published in the maintenance manual. These were designed to maintain safety and economy of operation throughout the airplane life. Further details on certification of integrated structures may found in reference 1.

Fuel Tank Bonded Assembly

For a composite wing fuel tank, there are many benefits of an all-bonded

assembly. Metallic fasteners represent a lightning strike threat in a composite fuel tank, not to mention the cost, weight, and fuel sealing issues which accompany drilling, fastening, inspecting, and sealing the fasteners.

Non conducting materials were used to fabricate internal ribs and baffles and hybrid woven fabric of carbon fiber and aluminum wire was used as the exterior ply in the outside skins. A simple technique was employed to verify the integrity of the internal bonds in the fuel tank. Every tank was sealed, leak checked, and finally subjected to a proof pressure check to the highest pressure expected in service.

A test specimen of the tank was sled tested to demonstrate fuel containment under emergency landing conditions.

Resin Transfer Molded Stabilizer

A horizontal stabilizer development article was fabricated by the resin transfer molding (RTM) technique. This part represents the ultimate in low part count and low labor content. Combined with the high stiffness and low density afforded by carbon fiber materials and the smooth rivet-free aero-surfaces this is a very attractive alternative to traditional manufacturing methods, see figure 2.

The materials used were a combination of dry, 6K, carbon 2D braid and dry 6K, five harness fabric. These were saturated with 3M 520 resin using RTM technique.

The braids were applied to male mandrels to form the internal cells and webs which were then wrapped with plies of fabric to form the external skins. The cure tool was then closed around the dry fiber assembly and the tool placed in a heated press. The tool was vacuum evacuated, and the resin injected until the tool cavities were totally filled; final cure pressure and temperature were then applied.

Again, heavy-duty precision tooling is required to facilitate the lay-up on male mandrels and the in-tool resin saturation and cure at high pressure and high temperature.

Other manufacturing issues included access to internal cavities to install aircraft systems and to affect structural attachments. For this particular part, internal equipment could be installed by cutting a single access opening in the lower skin. Attachments to the rear spar could be accomplished with blind fasteners. The QA issue was how to accomplish inspection of internal webs. NDI of internal webs was possible with the aid of special probes clamped on the end of long supports.

Certification issues centered on qualification of the material properties and control of the process. Material qualification represented some new challenges in that the raw material does not exist in the traditional aerospace format of prepreg fabric or tape. The qualification therefore starts with multi-batch tests of the neat resin. Raw material fiber was already qualified because of use in prepreg materials. So, material property testing was concentrated on specimens cut from panels fabricated by the RTM techniques used in production. The test matrix was similar to that used for lamina properties of prepreg materials except the braid angles were tested at three different angles representing the mean and practical extremes of fiber angles used in production. The test matrix had approximately 33% more test points than a typical prepreg matrix. See reference 2.

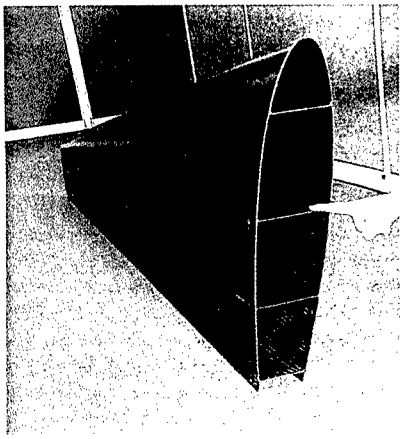

Figure 2
Resin Transfer Molded Stabilizer

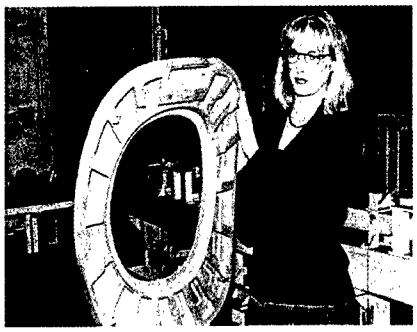

Figure 3
Emergency Exit Casting

Precision castings

In spite of the recent advances in high speed machining of aluminum, precision castings can still contribute to lower cost and in some cases lower weight. Changes in the regulations now permit critical castings to used without the penalty of casting factors requiring increased load capacity above the FAA ultimate load and without testing multiple samples of the casting. It so happens that when castings are used in critical applications, the compression stability requirements on thin webs and the fatigue durability requirements on tension members result in extra static load capacity almost equal to the factors traditionally applied to account for unpredictable grain structure, etc. For example, in a recent study finite element analysis showed a large casting to have 1.38 times the minimum required static strength after design for stability and fatigue compared to a 1.50 factor required in the FAA regulations to avoid multiple tests

The precision casting shown in figure 3 produces an emergency exit frame work without any surface machining and is cheaper and lighter than the equivalent riveted assembly.

References

1. R. Abbott, *Damage Tolerance Evaluation of Composite Honeycomb Structures,* 43rd International SAMPE Symposium, 1998.

2. D. Swain and R. Abbott, *Advanced Manufacturing Techniques using Carbon Fiber Braid and RTM,* 45th International SAMPE Symposium, 2000.

Proceedings of 7th Japan International SAMPE
Symposium & Exhibition, Nov. 13-16, 2001

Development of Affordable Composite Wing Structure

Yasuhiro Toi#, Atsushi Harada#, Takayuki Kamiyama#, Tomohiro Inoue#, Kazuaki Amaoka#, Hiroshige Kikukawa*

#: Fuji Heavy Industries LTD. 1-1-11 Yonan, Utsunomiya, Tochigi ,320-8564, JAPAN
*: Japan Aircraft Development Corporation, 1-2-3 Toranomon, Minato-Ku, Tokyo 105-0001, JAPAN
E-mail: toiy@uae.subaru-fhi.co.jp

Abstract

A wide range of 5-year study to expand the advanced composite application in wing primary structures has started in Japan. Develop and verify the technology to provide the improvement / innovation in parts count and damage tolerance is the aim of this research. The objective of this paper is to introduce the vision of the 5-year research program and the intermediate results of structural concept studies. Structural concepts, materials and process selection for affordable and high performance structures have been discussed. Some producibility element tests have been conducted in parallel with conceptual design studies. Resin Transfer Mold (RTM), Vacuum Assisted RTM (VaRTM) and stiffened co-bond panels with unique RTM stringers have been made with new RTM resin and carbon fiber textiles. Intensive case studies for structural concept have been conducted. Clarification of the design criteria for composite wing, potential to apply affordable material/manufacturing technology, and substantiation methods have been discussed.

Key Words: Composite Wing, Affordable Composite, RTM, VaRTM

Introduction

Advanced composite application to commercial aircraft structures started in the 1970's, to reduce airframe weight and to pursue energy efficiency. Successful technology has been achieved for the secondary structures and control surfaces by continuous researches. It has been expanded to some empennage structures. For the other primary structures, however, the application is stagnated mainly with two issues. The first is damage tolerance capability of laminates and its verification. The second is higher cost than the existing metal structures. Currently, many element technologies have been studied to focus on the affordable composite application. New low cost materials, innovative and affordable processes, and innovative designs to derive the composites benefit effectively. Integrated research to accomplish the innovative composite wing with these element technologies started in Japan in 1999. The program objectives are to develop the technology to achieve 15% lighter weights and 50% less in parts count in comparison with existing aluminum built-up wing structures, and to show high maturity for certification. This research is conducted by Fuji Heavy Industries (FHI),

led by Japan Aircraft Development Corporation (JADC) and funded by New Energy and Industrial Technology Development Organization (NEDO). This paper introduces the outline of the 5-year research and the intermediate results with related FHI in-house researches.

Damage Tolerance Improvement

An initial approach to provide better damage tolerance capability has been considered by resin improvement to tough, and still continuously investigated. Current efforts have been focused to reduce resin cost and development of automated tow placement technology with these resin systems.

Another approach is using Textile preform reinforced by thru-thickness fibers. Resin Transfer Molding (RTM) or Resin Film Infusion (RFI) are combined with textile to accomplish affordable composites. A comparative study with compression after impact (CAI) tests has been conducted to investigate the improvement of damage tolerance performance by simply stitched laminates (see Figure 1). It is important to find out the practical and effective level of stiching density.

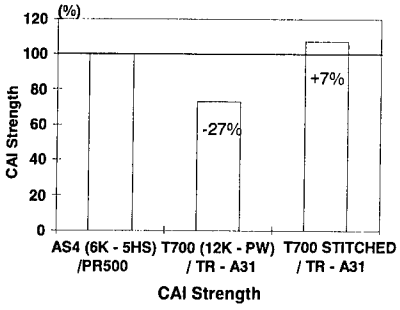

Figure 1 CAI Improvement by Stitching

Simulation of Resin Transfer

In RTM process, one of the most important characteristics is "low viscosity" of the resin and need to provide a proper resin flow. This is especially important to realize large RTM parts. New unique resin is used in this research and analytical simulation supported by basic coupon tests has been conducted.
Darcy's law is selected as the macroscopic resin flow model.

$$\vec{v} = -\frac{[K]}{\mu}\nabla P$$

where μ; Viscosity (dependent on time; t),
$\mu = a3t^3+a2t^2+a1t+a0$
v; Flow Velocity, K; Permeability Tensor,
P; Pressure

K parameter has been obtained through simple coupon tests with the specified condition including textile pattern, temperature and pressure. Verification with simple plate and actual parts are shown in Figure 2. The example actual part is a hat shaped stringer with simple textile preform and fabricated by VaRTM. This simulation provides proper planning to set input/output ports and flow path of the resin for large RTM parts.

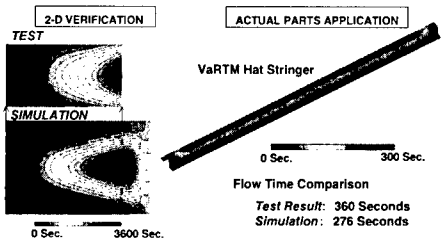

Figure 2 Simulation of RTM/VaRTM Resin Permeation

Unique Hybrid Co-Bonding

The new RTM resin has another feature to accept 2-stage cure process. The parts shape can be fixed at the initial low temperature cure stage. Then, the parts can be handled as free-standing (without complicated shape-constrained jigs) in the second high temperature stage. Unique hybrid co-bonding process has been created with this feature. Prepreg with low cost tough resin can be laminated by automated tow placement. Adhesive films and the first stage cured RTM stringers/spars will be set on the raw skin without complicated support jigs, then cured simultaneously. A good panel quality has been confirmed through the proof of concept tests (Figure 3). The specimens of the bonding surface between the prepreg and the RTM have been cut-out and the strength in Mode-I and II has been checked. The results show the equivalent strength compared to the prepreg co-cure panels. The compressive strength tests with stiffened panel (Figure 4) have been conducted and no-hazardous pre-mature debonding has been found up to design compressive strain level.

Wing Structural Concept Design

Conceptual wing structural design has been continued in parallel with the affordable element studies. Several concepts have been considered in view of cost, weight, risk, maintainability, growth potential and major design concerns listed in Figure 5. Then, the baseline concept shown in Figure 6 has been selected. Structural arrangement looks like the conventional aluminum structure, however, the affordable element technologies make the fabrication flow very simple and high structural efficiency and good accessibility can be maintained. This is a concept of "the right person in the right place".

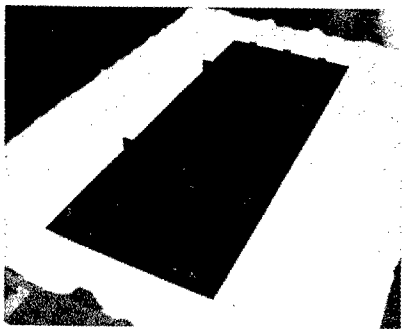

Figure 3 Unique Hybrid Co-Bonding Panel

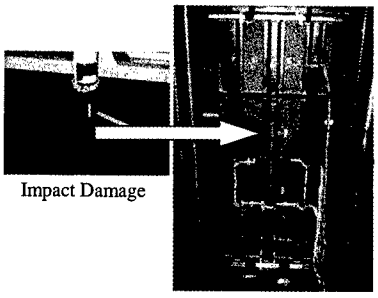

Figure 4 Panel Compression Test

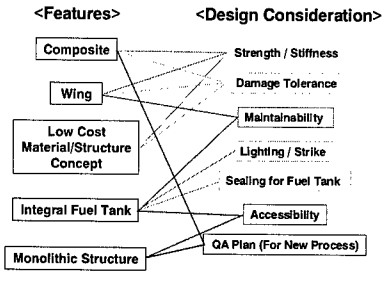

Figure 5 Design Consideration for Composite Wing

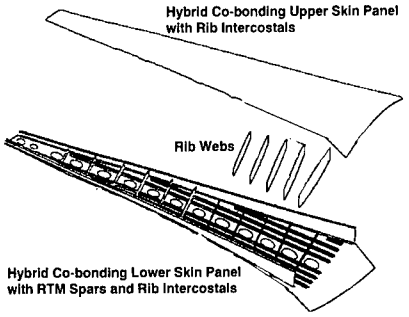

Figure 6 Baseline Structural Concept

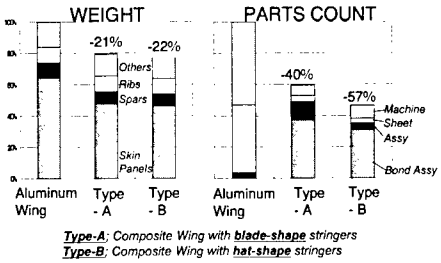

Figure 7 Weight and Cost Comparison

Results of the cost and weight comparison are shown in Figure 7.

Substantiation Plan

The building block approach (Figure 8) will be applied in the structural verification of the real wing development. In this research, the critical portions will be tested by a similar approach to the real structural certification tests of the assumed flight article to show high maturity of the technology. In the initial stage, design requirements and conditions, over all certification plan, and verification test plans have been clarified and reviewed by an experienced person who has the qualification of FAA DER for structural integrity.

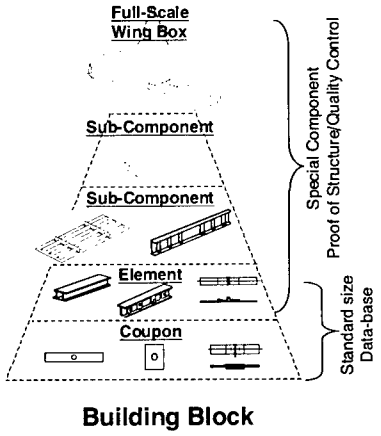

Figure 8 Building Block Verification

Conclusion

The first phase to develop element technology has been almost completed successfully and activities continue to the second phase to demonstrate the structural capability with full-scaled test article towards realizing an affordable composite wing.

Proceedings of 7th Japan International SAMPE
Symposium & Exhibition, Nov. 13-16, 2001

Innovative Cockpit Structure-
Molding Technology of Foam Core

Toshihiko Ito#, T.Sana, Y.Hirose, K.Araya, M.Nishitani

#: Kawasaki Heavy Industries, LTD
1 Kawasaki-cho, Kakamigahara-City, Gifu-pref. 504-8710, JAPAN
E-mail: ito_toshihiko@khi.co.jp

Abstract

The innovative study of applying composite materials to the cockpit structure has been made since 1999 sponsored by the New Energy Industrial Technology Development Organization (NEDO)[1]. This paper presents the molding technology of foam core.
The final objectives of our research and development are to apply Co-cured CFRP sandwich panel with foam core technology to a transport aircraft structure. The structual detail of conventional built-up structure and CFRP sandwich panel is shown in Fig.1.
They leads to the drastic reduction of weight, part count, and assembly cost as compared with the conventional built-up structure. The full scale test of cockpit structure will be performed in the final year for substantiation.
As one of this study, several tests of foam core were conducted to establish the manufacturing process of sandwich panel with foam core.

Key Words: Composite, Foam core, Sandwich Structure, Cock-pit

Introduction

In recent years, the sandwich panel with foam core is applied increasingly for the aerospace structures, besides the application to the Shinkansen[2] and other transport. The reason is that this structure is superior to the conventional honeycomb sandwich panel in the point of high impact resistance, negligible water entrapment, good electrical properties, and high surface quality.
On the other hand, in the manufacturing process of sandwich panel, foam core should be molded prior to the fabrication of sandwich panels. The core is formed by heated and pressured. It is necessary to develop the molding process of foam core with stable quality and high precision and low cost to fabricate the sandwich panel.
Several properties of the foam core have been evaluated to establish the process condition of core-molding.

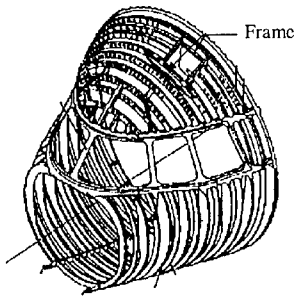

(a) Conventional Built-up structure

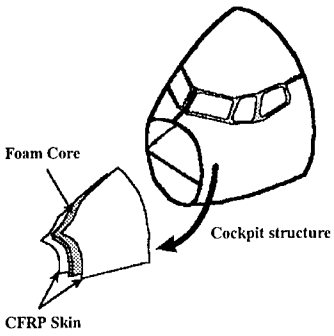

(b) CFRP Sandwich Structure

Fig.1 Structual detail of Conventional Built-up structure and CFRP Sandwich Panel

Experimental And Results

Core Material

Features of the core material, named RFC S-60 by KHI is as follows.

-closed-cell
-thermoplastic foam
-high service temperature

Sandwich panel can be cured with composite skins for at 180℃. Thickness of the core sheet is 35mm constant in all test core.

The process and characteristics of core-molding

Foam core is formed to the required shape by pressed on the mold after heated in heat resources. Following tests were conducted to determine the heating method and the heating temperature condition of foam core. The molded quality is dominated by these parameters.

(1)Heating method of Form Core

The following equipment were evaluated to determine the suitable way of heating the core.

(a)Circulated air oven
(b)Hot-plate
(c)Infrared radiator heater.

Heating temperature of the core was ranging from 200 to 205℃. Measurement points were the top-surface, side-surface, and inside.

As a result, the saturated temperature of top-surface and inside rised to the set temperature in every equipment, but the temperature of side-surface in hot-plate and infrared radiator heater did not go up to the set temperature. It was confirmed that the circulated air oven is suitable equipment for uniform heating.

(2)Heating Temperature Condition of Foam Core

Molding test of the core was conducted to optimize heat temperature condition. The schematic diagrams of core-molding is shown in Fig.2.

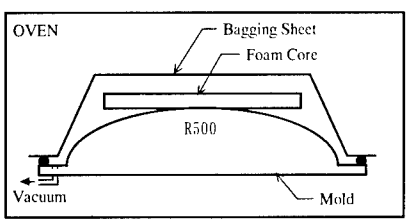

Fig.2 Conventional Core-Molding Method

The six kind of heating temperatures were selected within the range from 215℃ to

190℃. The core size was 500 mmL and 100 mmW, and the molded shape had a single contour of R500 mm. This contour has a meening of the dimension of a minimum contour in the cockpit panel. Vacuum pressure was applied in order to press the core against the mold.
Figure 3 shows the tendency of spring-back and shrinkage of the core thickness after the core was molded by each temperature.

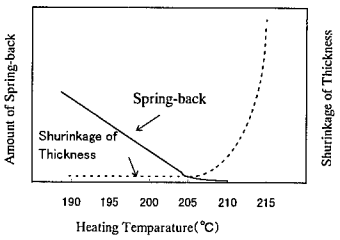

Spring-back was measured by the gap between the molded-core and the mold.

Fig.3 Tendency of spring-back and shrinkage of the molded core

The following result were obtained by molding tests.

(1) Increasing heat temperature, the amount of spring-back decreases, and the core is nearly fitted to the mold when it is higher than 205℃.

(2) Shrinkage is very small at below 205℃, but rapidly increased over 205℃.

Next, an actual size of the core with complex contour from R500mm to R2000mm was molded on the basis of these results corresponding to the cockpit structure. Core size was about 1mL and 1mW. The molded core is shown in Fig.4. The amount of spring-back and the shrinkage of thickness are very small and equivalent to the above result. According to our experience, this quality is practicaly enough to fabricate the sandwich panel.

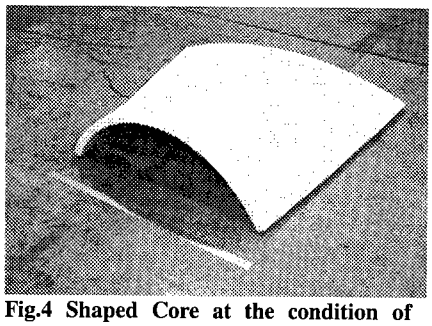

Fig.4 Shaped Core at the condition of optimum heat temperature

Low-cost Molding Method

Foam core should be divided into many pieces for the large scale of parts as the cockpit, and many molds must be needed in every devided pieces.
The core is usually molded in the oven and heat-proof mold is required for the molding temperature. The alternative method of molding is introduced and the concept of the new method is shown in Fig.5.

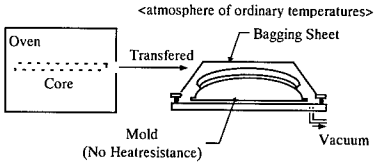

Fig.5 Alternative Core-molding method

In this method, the core is formed on the mold at room temperature after it was heated in the oven. Heat-proof mold is not required, so that mold cost can be reduced. Because molds does not need to set into the oven. Also heating time can be shortened due to avoid heating the mold. So it has a great merit to reduce mold costs and molding time.
Molding tests were conducted with the alternative method. The core size is 500mmL and 500mmW, and the molded cores have a single contour of R500, R1000, R1500,and R2000. The cores were molded while the core temperature was kept from 200℃ to 205℃.

Figure 6 shows the amount of spring-back to each shape after the cores were molded.

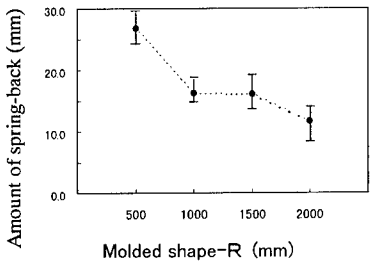

Fig.6 Amount of spring-back vs Molded shape after core molded

Large amout of spring-back occurred in all shapes, and as the contour radius increases, the amount of spring-back decrease. Thickness shrinkage was not always occurred. One of the method to correct the amount of spring-back is adjust the shape of mold in accordance with the core deformation. Fundamental data are obtained through this test.

Conclusions

The following results could be obtained on properties of foam core and process data of the core-molding.

(1) The foundamental heating method and molding process of the core were established, and the contoured core has enough quality for the practical use.

(2)Alternative low cost method for mold the core was established.

The reserch and development of molding the core technology has been performed. The manufacturing process of sandwich panels will be studied at the next step.

Acknowledgment

The authors wish to thank NEDO and JADC for great support and understanding for this study.

References

1) Hirose et al.,Technology Development for Innovative Cockpit Structure of a Transport Aircraft, Presented at Thermec 2000, Las Vegas, USA, Dec. 2000

2) Konishi et al.: Proc. of The 37th Aircraft Symposium,433 (1999)

Proceedings of 7th Japan International SAMPE
Symposium & Exhibition, Nov. 13-16, 2001

Microstructure and Mechanical Properties in the Friction - Stir - Welded Dissimilar Light Metals

Naobumi SAITO#, Ichinori SHIGEMATSU# and Mamoru NAKAMURA#

#National Institute of Advanced Industrial Science and Technology
Institute for Structural and Engineering Materials
1-1 Hirate-cho, Nagoya, Aichi 462-8510, JAPAN
E-mail: Naobumi-saito@aist.go.jp

Abstract

In the last ten years, friction stir welding (FSW) has emerged as a new solid-state joining technique for aluminum alloys. For a design of light-weight aircraft structure, FSW is expected to be an optimum welding process and yield cost benefits over the design and manufacturing root. At the present time, FSW is conducted mainly for the similar materials. However, FSW of dissimilar materials will be required in the near future for the advanced aircraft design.

In the present research, we have tried to apply the FSW technique for dissimilar light metals such as 5083 and 6061 aluminum alloys. Then, we have examined the microstructure and the mechanical properties of the FSWed aluminum alloy joint.

Key Words: Friction Stir Welding, Aluminum Alloy.

Introduction

Friction stir welding (FSW) has emerged as a new solid state joining technique [1], especially for aluminum alloys [2-6]. In this processing, a rotating tool travels down the length of contacting metal plates, and produces a highly plastically deformed zone through the associated stirring action. The localized heating zone is produced by friction between the tool shoulder and the plate top surface, as well as plastic deformation of the material in contact with a tool [1].

At the present time, FSW is conducted mainly for the similar materials. As far as dissimilar welding, few systematic studies aiming at clarifying an effect of material combination and welding conditions on welding property [7-8].

However, FSW of dissimilar materials will be required in the near future for the advanced aircraft design. In the present research, we have tried to apply the FSW technique for dissimilar light metals such as 5083 and 6061 aluminum alloys. Then, we have examined the microstructure and the mechanical properties of the FSWed aluminum alloy joint.

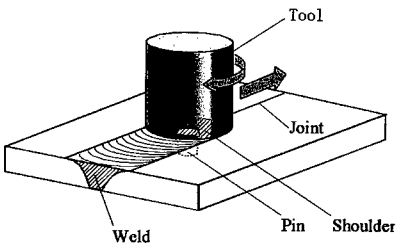

Fig.1 Schematic illustration of friction stir welding.

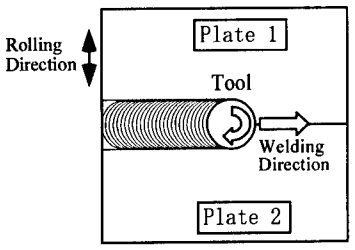

No	Plate 1	Plate 2
No. 1	5083	5083
No. 2	6061	6061
No. 3	6061	5083

Fig.2 Combinations of joining materials.

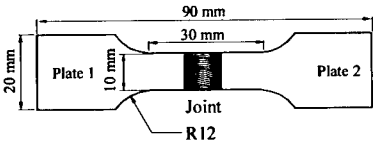

Fig.3 Dimensions of test piece for tensile test.

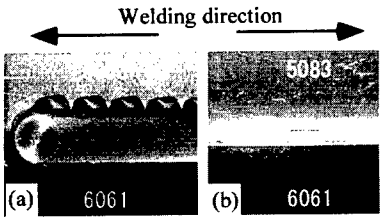

Fig.4 Typical appearance of 5083 and 6061 aluminum alloy joint. (a) top surface (b) root surface

Experimental procedure

3mm thick plates of cold-rolled 5083 (0.4%Si, 0.4%Fe, 0.4%Mn, 4%Mg, balance Al) and 6061-T6 (0.7%Si, 0.7%Fe, 0.1%Mn, 1.0%Mg, 0.4%Cu, 0.1%Cr, balance Al) aluminum alloys were used in this experiment.

Fig.1 shows a schematic illustration of the experimental apparatus. The test piece was fixed onto a steel plate horizontally. Welding direction was perpendicular to the rolled direction of aluminum plates. Diameter of tool's shoulder was 10mm. Diameter of insert pin and height were 3.0mm and 2.8mm respectively. The rotation speeds of tool were 890rpm and 1540rpm. The traverse speeds of the moving table were 118 mm/min and 155 mm/min.

Fig.2 shows combinations of test pieces. Following FSW, microstructures of the samples were observed by optical microscopy. Vickers microhardness profiles were measured on the cross section perpendicular to the welding direction.

Tensile test was performed to evaluate the mechanical property. Fig.3 shows dimensions of a tensile specimen.

Variations of the Vickers hardness by aging were also evaluated.

Results

Fig.4 shows the typical appearances of a welded 5083-6061 specimen. Both at top and root surfaces, surface roughness, i.e., surface quality was excellent. Waving burrs on the top surface were observed on the retreating side.

Fig.5(a) and (b) show the optical microscopic photographs of the cross sections. In Fig.5(c), the lines indicated by A-A' and B-B' show the position corresponding to the photographs of cross section shown in Fig.5(a) and (b), respectively. Since 5083 and 6061 aluminum alloys have difference etching behaviors, the metal flow from two sides was clearly visible in the nugget (friction stirred region). On the upper side, two aluminum alloys were relatively separated. In contrast, complicated layer structure, which consists of two aluminum alloys, was observed on the lower part. The structure was formed by the traverse of the rotating tool and the thread of insert pin.

Fig.6 shows element distribution maps by EPMA. Mg-rich region and Cu-rich

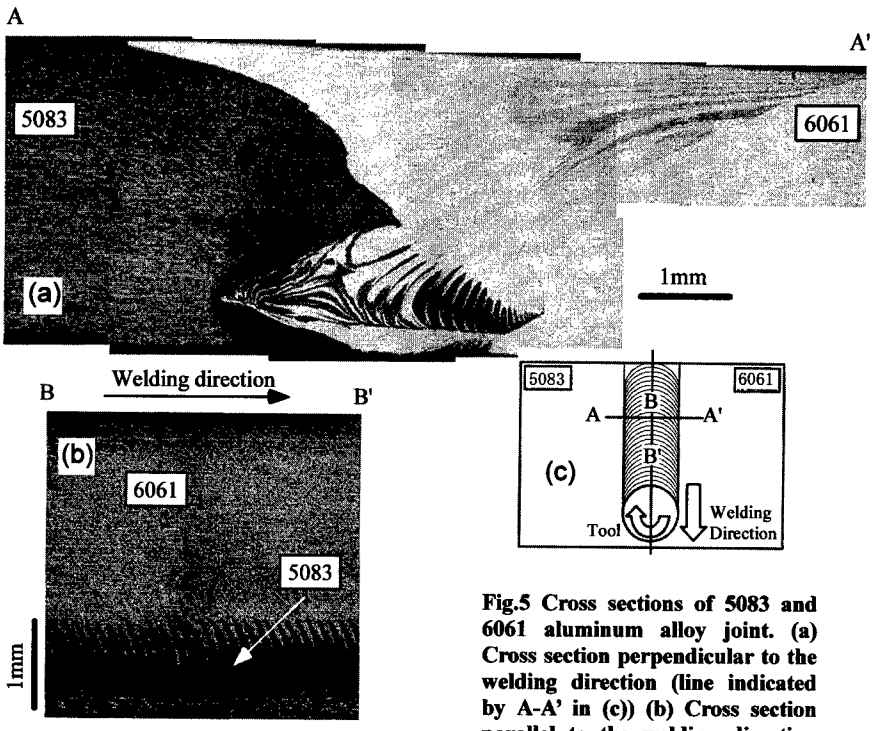

Fig.5 Cross sections of 5083 and 6061 aluminum alloy joint. (a) Cross section perpendicular to the welding direction (line indicated by A-A' in (c)) (b) Cross section parallel to the welding direction (line indicated by B-B' in (c))

region were corresponded to 5038 and 6061 aluminum alloy, respectively. It seemed that the diffusion and chemical reaction did not occurred.

Fig.7 shows hardness distribution at cross sections of specimens. At 5083-5083 joining zone, the hardness was slightly higher than the original value. However, in the 6061-6061 joining zone, the hardness dropped sharply. It is likely that the low hardness is attributed to the re-solution of the precipitates during FSW. Effects of aging on the hardness distributions were also shown in Fig.7. As for the 6061-6061 and 6061-5083 joints, hardness at the interface of the joints increased as the aging time increased.

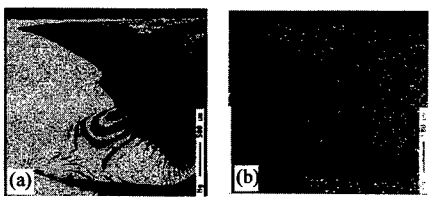

Fig.6 Element distribution map on the cross section of 5083-6061 joint specimen by EPMA. (a) Mg (b) Cu

Table 1 shows the results of tensile test. The strength of 5083-5083 joint was 97% of that of mother material. In contrast, the strength of 6061-6061 joint was 63% of that of mother material. The strength of 5083-6061 joint was almost equal to that of 6061-6061 joint. These results show that tensile strength of the joint is affected by the types of the joint (similar or dissimilar) and the alloys (5083 or 6061).

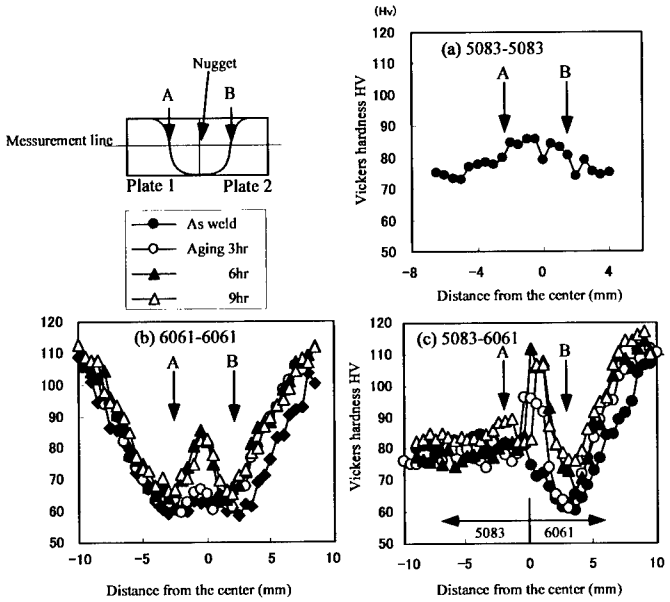

Fig.7 Vickers hardness distribution of as-welded and after aging materials (at 433K in oil bath) in cross section perpendicular to the welding direction,. (a) 5083-5083 joint. (b) 6061-6061 joint (c) 5083-6061 joint.

Conclusion

FSW of the similar materials (5083 and 6061 aluminum alloys) and dissimilar materials (6061/5083) were carried out. Every couple of specimens could be joined successfully. That is, it seems that FSW has the potential for joining dissimilar material such as different types of aluminum alloys. Welding properties, such as the hardness distribution and the tensile strength, were strongly influenced with the material combination.

Table 1 Tensile strength and Elongation of mother material and joint specimens.

Alloy	Strength (MPa)	Elongation (%)
5083	328	24
6061	320	16

Joint	Strength (MPa)	Elongation (%)
5083 - 5083	318	21
6061 - 6061	199	11
6061 - 5083	202	7

References

1.W.M.Thomas, E.D.Nicholas, J.C.Needham, M.G.Murch, P.Templesmith and C.J.Dawes: GB Patent Application No. 9125978.8, Dec. 1991, US Patent No. 5460317, Oct. 1995

2.L.E.Murr, G.Liu and J.C.McClure: J. Mater. Sci. Let., 16, 1801(1997).

3.G.Liu, L.E.Murr, C-S.Niou, J.C.McClure and E.R.Vega:Scripta Mater., 37, 355(1997).

4.C.G.Rhodes, M.W.Mahoney, W.H.Bongel, R.A.Spurling and C.V.Bampton:, Scripta Mater., 36, 69(1997).

5.V.Flores, C.Kennedy, L.E.Murr, D.Brown, S.Pappu, B.M.Nowak and J.C.McClure, Scripta Mater., 38, 703(1998).

6.M.W.Mahoney, C.G.Rhodes, J.G.Flintoff, R.A.Spurling and W.H.Bingel:, Metall. Mater. Trans. A, 29A, 1955(1998).243-1251.

7.Y.Li, L.E.Murr and J.C.McClure:, Mater. Sci. Eng.,A271, 213(1999).

8.Y.Li, L.E.Murr and J.C.McClure:, Scripta Mater., 40, 1041(1999).

Proceedings of 7th Japan International SAMPE
Symposium & Exhibition, Nov. 13-16, 2001

Innovative Cockpit Structure -Friction Stir Welding Technology of Al-alloy

Takafumi Sakanashi#,S.Iio, Y.Hirose, K.Araya, K.Kosugi

#: Kawasaki Heavy Industries, Ltd.
1. Kawasaki-Cho, Kakamigahara City, Gifu-Pref.504-8710 ,JAPAN
E-mail: sakanashi_t@khi.co.jp

Abstract

The Friction Stir Welding (FSW) is a solid state joining process invented by The Welding Institute (TWI). In addition good quality, its unique process allows the welding of 2xxx and 7xxx series aluminum alloys which has been considered unweldable. Traditionally, these alloys have been limited to use only in mechanical-joined structures. FSW offers huge potential for low cost, fastenerless joining of lightweight aircraft structure. The five years research activity that is "technology development for innovative cockpit structure of a transport aircraft" has been started in 1999 sponsored by the New Energy Industrial Technology Development Organization (NEDO)[1]. As one of the new technologies which lead to the cost reduction and the number of parts for the nose structure, we are studying to apply friction stir welding to the forward pressure bulkhead consisting of 7050-T7451 aluminum alloy machined parts. This paper describes the research plan and results of two year.

Key Words: Friction Stir Welding, Aluminum Alloys, Aircraft Structure

Introduction

Five year research activities have started in 1999. This paper describes the research plan and Two year results. The objectives of our research are to apply new technology Friction Stir Welding (FSW) to a transport aircraft structures. The nose structure of an existing twin turbojet was selected as a base line model. It is expected that the application of FSW leads to heavy reduction of weight and part count. In our research activities of two year, we carried out welding test by coupon specimens. From those test results we welded and estimated sub-component of forward pressure bulkhead. Based on these activities, Friction Stir Welding test equipment was introduced and the following results were obtained.

1) Appropriate welding conditions
2) Mechanical properties of welded joints
3) Fabrication and Evaluation of sub-component article of forward pressure bulkhead with FSW.

Through these activities the prospects of engineering viability for the application of Friction Stir Welding were obtained and the next step of our studies will be scheduled to proceed.

Friction stir welding technology

Friction Stir Welding (FSW) is new solid state welding which was developed by TWI in 1991. 2xxx and 7xxx series aluminum alloys can not be welded with conventional welding technologies. Friction Stir Welding technology enables these alloys to be welded due to joining temperature

below their melting point. Schematic process of FSW is shown in Fig.1.Because FSW is solid state welding, it has several benefits as below.

1) FSW can weld Al alloys which can not welded by Fusion welding.
2) FSW joints have better mechanical property than Fusion welding.
3) FSW process is suited to automation, not required special welding technique.

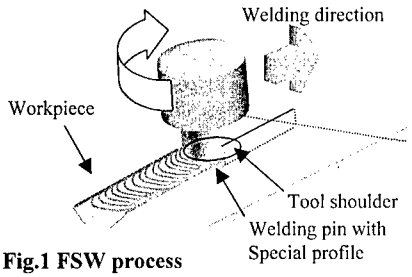

Fig.1 FSW process

Concepts for Forward pressure bulkhead

Conventional forward pressure bulkhead is built up component and has to maintain structural integrity against the damage of bird strike. In this case, casting is not suitable due to its brittle fracture and composite is also unsuited because of open holes for system installations. In order to reduce the part count, application of the FSW is expected to be suitable. Fig.2 shows new concept for pressure bulkhead.

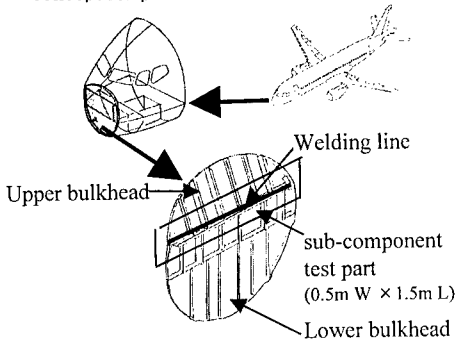

Fig.2 Pressure Bulkhead Structure

Experimental results

Through our study FSW, equipment was introduced and welding conditions and mechanical properties of welded joint were estimated. In order to gain the perspectives of the application of FSW technology, welding conditions should be estimated and mechanical properties of welded portion should be estimated as the step results.

Material characterization test of FSW joints

In the FSW, welding conditions, those are, rotation speed, welding speed the shape of tool which should be decided for 2024 alloy and 7075 alloy respectively through the laboratory tests using these conditions, coupon size welded joint specimens were fabricated and mechanical characterization tests of static strength, fatigue strength, crack propagation and corrosion resistance were conducted.

The following results were obtained through these tests. Static and fatigue test results are shown in Table 1. For crack propagation tests, the crack propagation speed of FSW joints was a little faster than that of base metal. For corrosion resistance tests, it was revealed that 2024 joints have tendency of faster corrosion spread and 7075 joints have tendency of lower spread. Comparing with metal respectively. Through these tests,basic mechanical properties of FSW joints wre obtained. These data can be used for the further improvement of the FSW technology and preliminary design.

	Tensile strength (%)	Fatigue strength (%)
2024	85～93	About 80
7075	68～83	About 60

Base metal is 100%

Table 1 Example of Table

Functional tests of FSW equipment

FSW equipment was introduced to be used in the fabrication of full-scaled article. In last year functional tests of the equipment were conducted in order to verify the compliance with our specifications. The general aspect of the equipment is shown Fig.3. Based on the function tests, it was confirmed that the equipment has enough capability to fabricate full-size sub-component. FSW process is shown in Fig.4.

[FSW equipment Specification]

work table size : 1.6m width x 2m length
control type : 3-axis NC
Max rotational speed : 3,000rpm
Max travel speed : 1m/min.

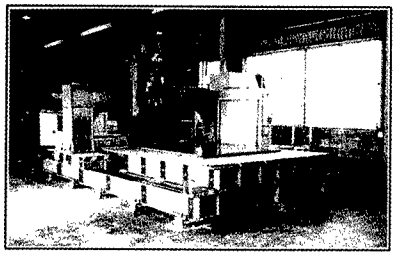

Fig.3 FSW equipment

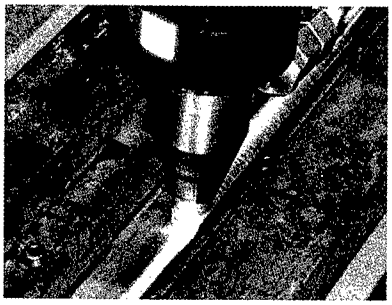

Fig.4 FSW process

Evaluation of sub-component test

appearance of sub-component test article of pressure bulkhead is shown in Fig.5.

After welding Non-Destructive Evaluation (NDE) process (radiographic inspection) were conducted. From the results of NDE, friction stir welds are free of volumetric defects.

Specimens cut from sub-component test article were evaluated. Tension test results of sub-component is shown in Fig.6.[2] FSW joints have 78% tensile strength, 74% yield strength, 64% elongation of base metal (7050-T7451).

The microstructure of cross section of sub-component is shown in Fig.7.

It is investigated stirred metal structure at center of FSW joint. From these results it was confirmed that FSW technology is successfully applied to the sub-component test article.

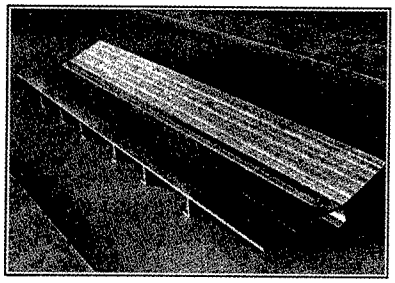

Fig.5 Appearance of sub-component of pressure bulkhead

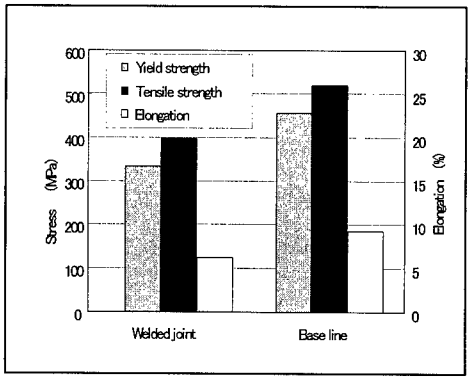

Fig.6 Tensile test (7050-T7451)

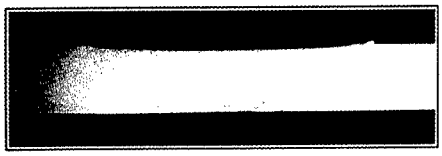

Fig.7 Microstructure of cross section

Conclusions

The bare bone of our research plan was established. Fundamental research and tests of Friction Stir Welding were conducted through these activities, the prospects of the weight reduction by 10% and the part count reduction by 80% were obtained. Based on these results we would liked to proceed with our activities toward the final goal.

Acknowledgment
The author would like to appreciate NEDO and JADC , especially Mr.Itho, Dr.Kikukawa and Mr.Yahata.

References

1. Hirose, Y., Maekawa, S., Imuta, M., Tajima, N., and Kikukawa, H. : Technology Development for Innovative Cockpit Structure of a Transport Aircraft, Presented at Thermec 2000, Las Vegas, USA, Dec. 2000
2. Y.Hirose et al.: Innovative Nose Section of Fuselage Structures applied by Friction Stir Welding of Aluminum Alloy and Large Thin Casting of Improved Aluminum Alloy, Presented at 2nd International Conference on Light Materials for Transportation Systems LiMAT-2001, Pusan, Korea, May, 2001

Proceedings of 7th Japan International SAMPE
Symposium & Exhibition, Nov. 13-16, 2001

Structural Development for Innovative Leading Edge of Wing

M. Matoba[a], S. Ohasi[a] , M. Ochi[a], M.Motoike[a], and A. Yahata[b]

a: Aerospace Div. ,Japan Aircraft Manufacturing ,Ltd.
3175 Showa-machi, Kanazawa-ku, Yokohama, 236-0001,Japan
E-mail: mmatoba@mail.nippi.co.jp
b: Japan Aircraft Development Corporation, Totanomon Daiichi Bidg.,
2-3,Toranomon 1-chome,Moinato-ku,Tokyo,105-0001,Japan
E-mail: ayahata@jadc.or.jp

Abstract

The 5-year research program for cost saving product design and light weight design on wing leading edge structure of commercial airplane begun in FY1999. This paper describes the results of researches in first and second year. A leading edge with new concept has been designed in consideration of bird strike and de-icing etc. The new technologies to be applied the concept are ; · Super plastic forming (SPF) of aluminum(Al.) sheet metal · Integral precision Al. casting · Ultrasonic welding · Magnetic stirring TIG welding. The full scale test of the wing leading edge will be performed in the final year for the sustantiation. In the first and second years, preliminary design and structural manufacturing trials were conducted, and mechanical/ metallurgical properties of the materials and the structural elements were investigated. Experimental design data against the bird strike as the first step of the researches were obtained.

Key Words: Wing Leading Edge, Bird Strike, SPF, Precision Casting

Introduction

Properties of toughness against bird-strike and of anti-icing are required for the structures of a wing leading edge. The structures on conventional airplane are build-up from many sheet metals and machined parts, and assembled using a lot of fasteners. The newly designed leading edge of light-weight and cost-saving in production is required of commercial airplanes to sustain a direct impact of 4 lbs. bird at Vc. A structure of wing leading edge of commercial airplane was approach ed as the one of innovative structure applied cost-saving product design and light l-weight design, i.e. super plastic forming (SPF), integral precision casting and high quality welding. The structural targets of this design is to achieve a 5% weight reduction and a 1/7 part count reduction compared with the conventional ones.

Design Standard

· FAR Part 25, Structure general requirements

- Japanese Airworthiness Standard "Taikyusei Sinsa Yoro" Cap.III (Transport Category)
- FAA AC No: 25.571-1(e) , Bird impact requirements
- FAA AC No: 25-21, Certification of transport airplane structures

Conceptual Prototype for the Innovation leading Edge

The new concept wing leading edge was preliminarily designed with metal processes shown in Fig.1. The structure consists of a front skin panel, a aft support frame and a de-icing tube. The front panel consists of a pair of 5083 super plastic forming (SPF) panels; an outer skin and an inner skin. The inner skin is corrugated to form many small ducts in which hot-air flows for anti-icing, and is expect to absorb bird strike energy by its deformation. SPF process is applied for its forming along with bending of the panel in to a shape of wing section. Before forming, the two skins are lap joined by using ultrasonic spot welding. The aft support frame is made of one piece of D357 Al. alloy precision casting by lost wax method, and has an integrated skin, stiffeners and ribs of minimum 1.5mm thickness for a weight-saving design.

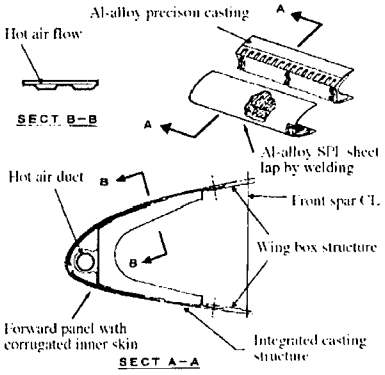

Fig.1 Structure of a wing leading edge

The wing leading edge is installed to CFRP wing box by the Al. alloy wiggle plate and fasteners to release the deflection gap between wing box and leading edge. The skin panels and support frames are separately welded span-wise using magnetic stirring TIG welding . A titanium tube with many small holes is installed in front of the support frame to supply hot air to the duct on the skin panel. The skin panel and support frame are fastened with rivets. The concept of structure is shown in Fig.1.

FEM Analysis

The FEM analysis was performed for the maximum aerodynamic load and the wing deflection. Through this statistical analysis, It was confirmed that the structure had enough strength for the loading. Some parts have an excessive margin of safety because of minimum gauge of casting. A dynamic analysis of bird strike on the wing leading edge was performed using the LSTC/ LS-DYNA950d in the case of a 4lbs bird traveling at velocities of 320 knots. The FEM model consist of 770 nodes, 747 shell elements and 200 beam elements. The model was constrained at points

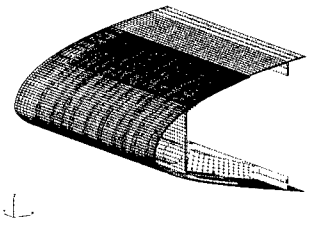

assembled to the wing spar. FEM model is shown in Fig.2.

Fig.2 FEM Model

The result of the analysis is shown in Fig.3 , indicates that bird will penetrate through the leading edge. The design criteria of the leading edge is that no detrimental damage occurs to the forward spar web of the wing structure located behind the leading edge, as fuel leak due to the residual energy of the bird after penetrating the leading edge. Because of capabilities on the present analysis, it would be inappropriate to predict the residual energy and an influence of the damage for the forward spar. However, a qualitative analysis of the thickness and the different materials properties of leading edge revealed many interesting features of the damage extension.

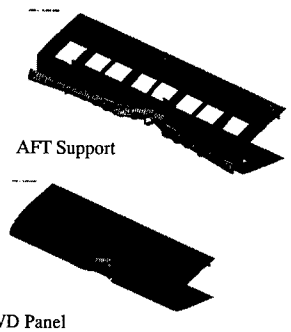

(Case No.0103)

Fig. 3 Analysis result

Fabrication Trials

To verify the design concept and its productivity, the manufacturing and testing 1 m length articles were produced. The inner and outer skins of the front skin panel were lap joined by ultrasonic spot welding before their forming. The ultrasonic welding are solid-state metallurgical bonds, with a smoother surface compared with other welding, it is significant to keep smooth surface on its outer skin. The bonded double blank sheets were press-formed to the shape of the leading edge. And Super-plastic forming(SPF) Argon gas pressure was supplied in the bonded sheets to make many small hot air ducts of the inner skin panel. The aft support frame of leading edge, integrated of skin, stiffeners, ribs etc. were cast by a lost wax method. The master model was made using a rapid prototyping method based CAD data. The forward SPF panel and the aft support casting frame were TIG welded span-wisely with magnetic stirring respectively. After installing anti-icing duct of titanium, the forward panel and the aft support frame were fastened by flash head rivets. Fig.4 shows over view of the wing leading edge.

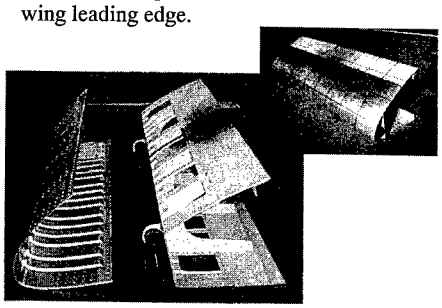

Fig.4 The assemble of test article

Experimental Results

Mechanical and metallurgical properties of the materials processed by SPF, casting and welding were investigated by coupon tests and structural element tests. And the bird strike tests were performed. The bird strike tests consisted of impacting the fabrication trying articles with a 4-lbs bird traveling at a nominal velocity of 320 knots. From the high speed film, the residual velocity of the bird after penetration were measured. The test articles were setup with a 17.5° sweep back angle resulting in an angle of 72.5° between the projectile trajectory and the leading edge. The outer wing skins of test articles were 1.6-mm (0.063-inch) thick 5083 Al. with a 0.8 mm (0.032 inch) thick 5083 Al. inner skin. No.1 test was impacted directly on a rib with an artificial bird. No.2 test was impacted at the middle of rib

space with real bird (chicken). No.3 test was impacted at the middle of rib space with an artificial bird. As a result of these tests, The bird penetrated through the leading edge. The hole was opened in the leading edge with inward buckling of the forward panel. These features of the damages were different from the other respectively, shown in Table 1 and Fig.5.

Table 1 Impact Test Results

Test No. **Bird, Impact Point**	**Bird Velocity/ Residual V.** (knots)	**Damage Hole Dim.** (mm)	**Inward Buckling Length of the For-word Panel** (mm)
0102, **Artificial On the Rib**	331 /189	210W × 185H	380
0101, **Chicken On the middle of Ribs**	317 / ---	120W × 139H	260
0103, **Artificial On the middle of Ribs**	320 /about 256	145W × 190H	300

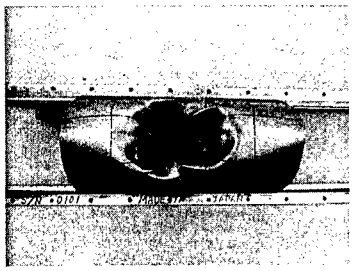

(Test No.0101)

Fig.5 Post impact view of the leading edge

Conclusion

The FEM analysis, fabrication trials and an investigation of the bird strike tests of the wing leading edge structure applied the new technologies has revealed many interesting features and damage characteristics. Especially, the bird strike test results indicate that the small residual energy caused by an extensive deformation of the forward panel is notable in case of impact on the rib. It means to be an effective design of the short rib-spacing and the small ribs. The design and testing of leading edge in next step would be performed in consideration of the compromising with the integrity of the forward spar on possible fuel loss.

The work presented here forms only an initial study and further trials are required to achieve the structural targets.

Acknowledgements

This work was supported under the program: " the Innovative Structural Development for Civil Transport" of New Energy and Industrial Technology Development Organization, and Japan Aircraft Development Corporation. The authors wish to thank Mr.Y.Ito of NEDO, H.Kikukawa and A.Yahata of JADC.

References

1. N.Suzuki,H.Kohzu, S.Tanabe and K. Higasi; "Materials Science Forum" , 1999, pp.304-306

2. J.Wilbeck, Impact Behavior of Low Strength Projectiles, US.AF: Technical report, AFML-TR-77-134,(1977)

3. Metallic Materials and Elements for Aerospace Vehicle Structures, DOD: MIL-HDBK-5G,Vol.1,Chp.3, Nov 1.1994.

4. Damage Tolerance and Fatigue Evaluation of Structure, FAA: Advisory Circular, AC25.571-1C, Apr 29.1998.

5. McClellan AFB: Proc. of 31st International SAMPE Tech. Conf., 832(1986).

Proceedings of 7th Japan International SAMPE
Symposium & Exhibition, Nov. 13-16, 2001

Large Size Aluminum Precision Sand Casting Technology Development for Aircraft Primary Structures

Akinori Shibata#, Mamoru Nakata#
Yasuo Hirose##, Yasuaki Yoshino##

#:Aluminum & Copper Company, Aluminum Cast & Forged Product Group, Kobe Steel, Ltd.
1100,Umedo Daian-cho,Inabe-gun,Mie-Pref.,511-0284,JAPAN
E-mail: a-shibata@kobelco.jp
##:Aerospace Division, Aerospace Group, Kawasaki Heavy Industries,Ltd.,
1 kawasaki-cho, Kakamigahara City, Gifu-Pref., 504-8710,JAPAN
E-mail: hirose_yasuo@khi.co.jp

Abstract

Recent development of casting technology increases the demand of the large integrated casting structure in order to reduce the parts count and structural weight. This paper describes the technical trend of the manufacturing technology and the distortion problem encountered in the application of the integrated casting to the large size and thin wall thickness for the aircraft structural part. As for the reduction of the camber distortion at the thin wall areas, the relation among the camber distortion, wall thickness, reinforcement rib intervals and rib height were confirmed. It was found that the appropriate arrangement of the reinforcement rib improved the local distortion. As for the overall distortion of the pressure floor support structure, it was revealed that the improvement of heat treatment jigs reduces the distortion of the casting.

Key Words: D357, Large Integrated casting Distortion, Reinforcement rib

Introduction

Kobe Steel, Ltd. has conducted to develop the pressure floor support casting structure under the contract of Kawasaki Heavy Industries, Ltd. in 1999 and 2000. This time, measurements of reducing distortion that occurs in the heat treatment process are described experimentally using fundamental data that are applied on the pressure floor casting structure.

R&D Activities and Subjects for Aluminum One-piece Casting Structures

Aluminum one-piece casting structures have been widely used for aircraft structures and engine parts. The strength of conventional aluminum castings, however, has large dispersion, which has prevented their application to primary structures. Recently, the D357 alloy was developed as an alloy for high strength castings and has improved the scattering of the mechanical properties. Fig.1 shows the frequency of scatterings of the tensile strength for D357 alloy, die-forging, extrusion, and plate[1]. The scattering of the strength of D357 alloy is

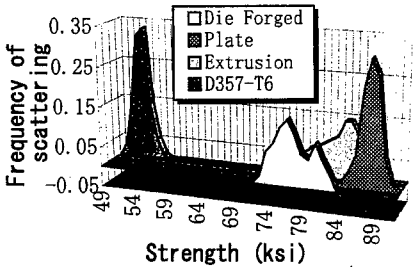

Fig.1 Comparison of Strength Distribution of D357 Alloy

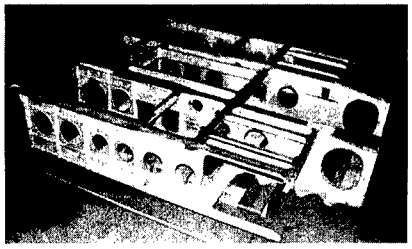

Fig.2 Pressure Support Structure Casting (1850x1520x350.Wall thickness 2.0mm)

small enough compared with those for the forging and the extrusion. Because of the increased reliability of the strength, castings tends to apply the aircraft primary structures.

Kobe Steel have conducted R&D activities for the thin wall one-piece structure casting as follows. In 1987, a development work for a DOOR STRUCTURE using a high strength casting alloy A357 under the contract of The Society of Japanese Aerospace Companies was started as a model work for the application of castings to the aircraft primary structures. In 1996, a development work for the application of the D357 alloy to LEADING EDGE(under the contract of the JADC) was started, and in 1999, a development work under the contract of Kawasaki Heavy Industries, Ltd. for the application of the D357 alloy to

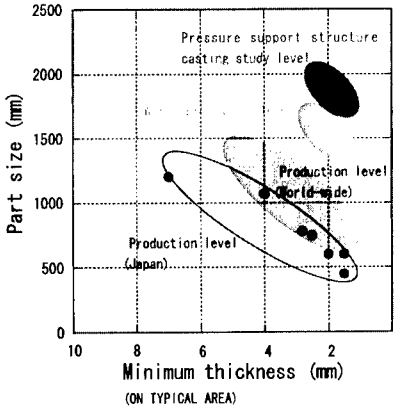

Fig.3 Relations between Casting Size and Wall Thickness

COCKPIT PRESSURE FLOOR SUPPORT STRUCTURE (See Fig.2) was started. In foreign countries, development works for the bulk head were conducted in 1970's.[2] In recent years, R&D activities for large-sized thin wall one-piece castings such as a cabin door of large-sized aircraft have been conducted same as in Japan[3]. Fig.3 indicates the difficulties of casting technology.[4] For example, the fabrication of the larger and thinner casting products require higher level of casting technologies. In this point of view, the fabrication of pressure floor support structure is very challenging. In the fabrication of pressure floor support structure, the distortion during the heat treatment due to thin walls is an important problem to be solved. In the following, the fundamental data relating to the decrease in the distortion generated during the heat treatment of thin wall castings will be presented and the result of the application of these data to the pressure floor support structure will be described.

Experiments to Decrease Heat Treatment Distortion

Method of Model Test to Decrease Camber Distortion

To decrease the camber distortion generated during the heat treatment of aluminum thin wall castings, model tests were carried out. In this test, the thin wall area of the test article was strengthened with reinforcing ribs. Fig.4 shows the photograph of the test article as a thin wall casting model (250 x 200 x 80mm). The test articles are comprised of a thin wall bottom area with the thickness of 2.0 mm and high rigidity side walls with the thickness of 5.0 mm and

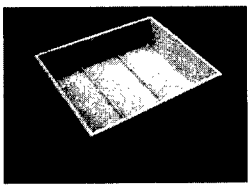

Fig.4 Thin Wall Casting Model

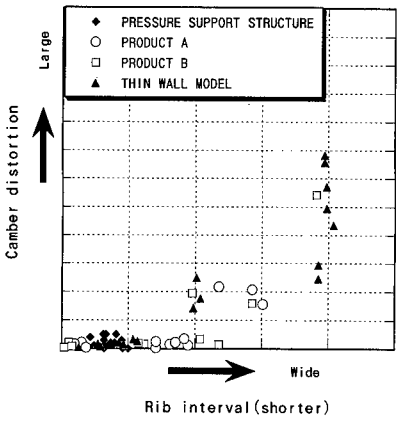

Fig.5 Relations between Rib Interval and Camber Distortion

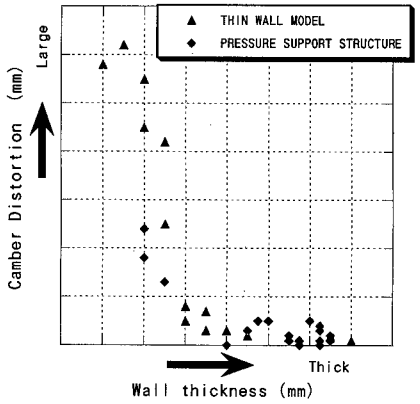

Fig.6 Relations between Wall Thickness and Camber Distortion

the height of 80 mm. In the thin wall bottom area, reinforcement ribs with various intervals were attached. Through this test, the relation between the rib intervals and the camber distortion were obtained. The test results are shown in Fig.5 and Fig.6. The figure 5 indicates that the camber distortions in the area surrounded with ribs and walls increase rapidly over the certain value of the rib interval to thin wall thickness ratio. The figure 6 tells us that the camber distortions decrease rapidly over the certain value of the wall thickness for the constant rib interval. On the basis of these results, reinforcement ribs were applied to the pressure floor support structure. The results are also plotted in Fig.5 and 6. They are similar to the results of model tests. The results mentioned above gave design guidelines of reinforcement ribs to prevent the camber distortion for aluminum thin wall castings.

A Test to Decrease The Overall Distortion of Pressure floor Support Structure

When the pressure floor support structure casting with the size of 1850 x 1520 x 350 mm is heat-treated, not only the camber distortion in the thin wall area but also an overall distortion of the structure is caused. Fig.7 shows the data of its overall distortion. Possible measures to decrease the overall distortion are to fix the component with jigs

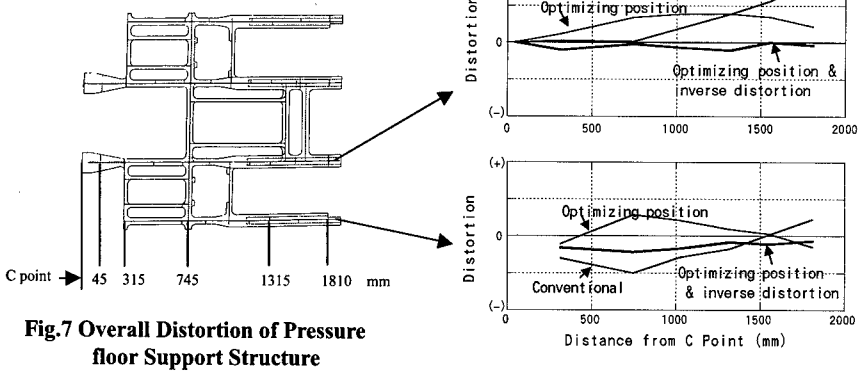

Fig.7 Overall Distortion of Pressure floor Support Structure

during the heat treatment, to find the suitable position of the component during heat treatment and to give the inverse distortion. The latter two measures were estimated in this study. The overall distortion of the structure was measured for the two different positions. One was the normal position and the other was upside down. For the upside down case, the pre-distortion was given with spacers between jigs and the component.
Through these measures, 70% reduction of the overall distortion was achieved.
In order to find the suitable position for the heat treatment, the shape of the component and the cooling rate of the component should be considered.

Application Examples of One Piece Castings

Kobe Steel, using a high strength casting alloy A357, is producing several tens of kinds of one-piece thin wall castings including passenger door parts for commercial aircraft (800 x 400 x 360, wall thickness : 2.8 mm). D357 alloy is applied to air inlet parts for aircraft (1500 x 900 x 400 mm) on a mass scale. D357 alloy makes it possible to produce high strength one-piece castings with more stable quality than that by A357 alloy.
In other countries, using high strength casting alloys such as A357 and D357, large-sized primary structures including door structures, leading edges, and kruger flaps are produced on a mass scale.
The development of D357 alloy is increasing the application of castings to aircraft primary structures. One-piece casting satisfies the requirement for cost reduction and, consequently, the requirement for the cost reduction is also accelerating this tendency.

Conclusion

Although the development of D357 alloy has increased the reliability of casting strength, the distortion of thin wall one-piece castings caused during the heat treatment process has been remaining as an important problem. This problem has been a barrier to the application of one-piece castings to aircraft primary structures. Since it was found in this study that the camber distortion in thin wall area can be decreased, it became possible to propose an appropriate shape of the structure and incorporate it into the design of aircraft castings. Straightening of the camber distortion of the thin wall area during the production process, which has hitherto been impossible, became possible. By introducing pre-distortion, the overall distortion can be decreased to the level of the straight.
Recent tendency of the cost reduction in aircraft industry will accelerate the application of thin wall one-piece castings to aircraft structures. To meet the customer requirement of cost reduction, we would like to continue further technical innovation.

Acknowledgement
The authors would like to express their appreciation for NEDO and JADC, especially Mr. Itoh, Dr. Kikukawa and Mr. Yahata.

References
1.F.Feiertag, "Casting Properties from a Modern Viewpoint",Aeromat'95(1995)
2.James W.Faber : "Metallographic Analysis Techniques Used Furing The Cast Aluminum Structures Technology (Cast) Program", Natl SAMPE Tech. Conf.,768-775(1980).
3.Yasuaki Yoshino, "Recent technology of aluminum alloy castings which enable cost reduction of aircraft structure", JSASS(1998)
4.JADC report : " The Development of Fundamental Design and Manufacturing Technologies for Innovative Light Structure",100(2000)

Proceedings of 7th Japan International SAMPE
Symposium & Exhibition, Nov. 13-16, 2001

On the Tensile Strength of Carbon Fiber Composites out of Various Resin Matrices

Yasuyuki Kanatani[#1], Yoshikazu Kobayashi[#1], Junichi Matsui[#2] and Zenichirou Maekawa[#1]
#1: Advanced Fibro-Science in Graduate School, Kyoto Institute of Technology,
Matsugasaki, Sakyo-ku, Kyoto 606-8585, JAPAN,
E-mail: b5330040@ipc.kit.ac.jp
#2: Venture Labo Co, 1-11-1 Nishishinbashi, Minato-ku, Tokyo 105-0003, JAPAN

Abstract

Utilization of knowledge of CFRP and GFRP to each other is important subject to expand demand for composite materials. As a first step of mutual utilization of the knowledge, axial tensile properties of CFRP out of epoxy, unsaturated polyester, vinylester, and phenolic resins are studied. Tensile load at failure is measured with CFRP single end specimens which are made of Torayca carbon fiber T300B-3k and the said resins. To give a conclusion, the tensile load at failure with CFRP specimens out of four different matrix resin types is in same level. Resin contents and void contents don't have a great influence upon the failure load, but insufficient cure gives poor strength.

Key Words: CFRP, Resin matrix effect, Tensile strength property

Introduction

Light in weight, and high strength and high elastic modulus at axial tension loading are characteristic of CFRP. The forte has adapted aircrafts, spacecraft, sporting goods such as race cars, race yachts, golf clubs, tennis rackets, etc. But a demand has been a little. GFRP has been established production system in the steadily increasing volume and has achieved the results of the world business more than five million metric tons a year for various uses. Utilization of knowledge of CFRP and GFRP to each other is an important subject to expand demand for composite materials. CFRP has been fabricated for the most case out of epoxy resin. On the other hand GFRP has been fabricated out of unsaturated polyester and phenolic resin since its practical use in 1940s. As a first step of mutual utilization of the knowledge, axial tensile properties of CFRP out of epoxy, unsaturated polyester, vinylester and phenolic resins are studied[1)2)].

Experiment

Materials

Carbon fiber Torayca T300B-3k (Toray Industries) Lot No.419081 and four resins given in Table 1 are used.

Procedure

ISO10618-1999 is applied to all the test procedure. T300 single end yarn is impregnated with matrix resin, then squeezed excess resin in order to control resin content and also to avoid forming resin beads on the specimen after cure. Since resin beads on the specimen tend to cause failure inside of the grip at low tensile load, the specimens with beads are discarded by visual inspection. Instron Type 4466 with air actual grips is used for tensile testing. To fasten the

specimen emery cloth, grit 200 or 240, is inserted between the specimen and chuck faces of the grip. Gage length 150mm and crosshead movement speed 1mm/min apply without specially notified. Resin contents and void contents are determined by measuring density of the specimen in ethanol.

Number of test

Number of test, 30, was determined by statistic analysis of 300 measurements for T300-ERL4221/BF_3MEA specimen, which was carried in advance to know the distribution features based on MILHDBK-5C. It is confirmed that 300 individual measurements can be explained as the Normal distribution.

Experimental Results and Discussion

The results are given in Table 1 and Fig.1 to Fig.7. In Table 1 test results on tensile failure loads per single end CFRP specimen for epoxy, unsaturated polyester, vinylester and phenolic resins are given. Two commercial products for each resin are chosen. Average value (N), standard deviation (SD, N) and coefficient of variation (CV, %) are calculated regarding the observed loads conform to the Normal distribution. Those figures are useful to define how many numbers of T300B-3k yarn are needed for CFRP parts to endure a given tension load under, for example, reliability 95% and failure probability 90%. Average failure load of 1B is higher and 4G is lower than the others, and also standard deviation of both 1B and 4G is higher than the others.

Figures 1 to Figure 4 illustrate the distribution of failure loads for CFRP single end specimens out of four resins, two commercial products each. The distribution feature and the range of failure loads of eight CFRP samples present similarity each other. In Figure 1 the distribution for carbon fiber specimen (without resin impregnation and curing) is given as a reference and average value is around 100N.

Figure 5 illustrates the effect of resin mass content of test specimens on the failure load being exemplified by a case of epoxy resin composites. The resin content has no effect on the failure load as far as the strength is represented load/end (N) and not by load/cross sectional area (N/mm^2 or Pa).

Figure 6 illustrates the effect of gage length of the test specimens from 50mm to 250mm. It is evident that the gage length has no relation with the ultimate failure load in contrast with the case of metals. Size effect on the strengths is the point at issue to make use of large structures such as big boats, long bridges or tall building. The effect of length of yarn and number of collimated yarns should be elucidated.

Figure 7 illustrates the effect of cure conditions as an example of vinylester resin 3E. Vinylester resin can polymerize and crosslink even at room temperature to provide apparently composite materials, but it is not yet sufficiently cured. 3E kept at room temperature about 25°C for one day gives fairly lower ultimate tensile failure loads compared to 3E heat treated at 80°C, 2hours after room temperature curing.

References

1)T.T.Chiao, M.A.Hamstad and E.S. Jessop
Tensile properties of an ultrahigh strength graphite fiber in an epoxy matrix
"Composite Reliability" ASTM STP 580, ASTM, 1975, pp.612-620.

2)J.T.Schaffer
Stress rupture of fiber composite materials
18th International SAMPE Technical Conference, October 7-9 1986, p.613-622.

Table 1 names of commercial product used and results of tensile test

Resin		Hardener and catalyst		Number of test	Tensile failure load Ave (N)	S.D (N)	C.V (%)
Epoxy	ERL4221	BF_3MEA	1A	340	377	27.5	7.3
	EPIKOTE827	DICY, DCMU	1B	300	405	33.4	8.2
Unsaturated polyester	POLYMAL6339		2C	28	370	27.4	7.4
	POLYLITE FW-231-C	MEKPO	2D	29	360	30.1	8.4
Vinylester	EPOLAC RF-701	CoNaph	3E	30	368	19.7	5.3
	RIPOXY R-802		3F	30	387	22.8	5.9
Phenolic	SHONOL BRL240		4G	30	351	44.1	12.6
	RESITOP PL-2205		4H	27	380	27.1	7.1

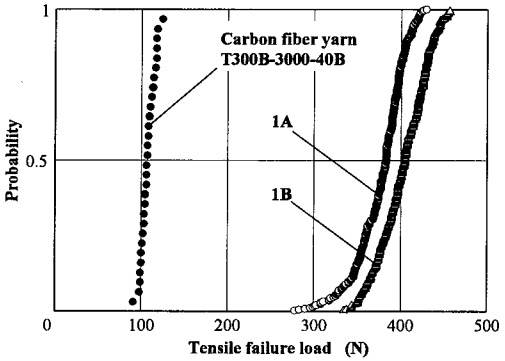

Fig. 1 The distribution of tensile failure load for Carbon Fiber T300 and CFRP out of Epoxy resin

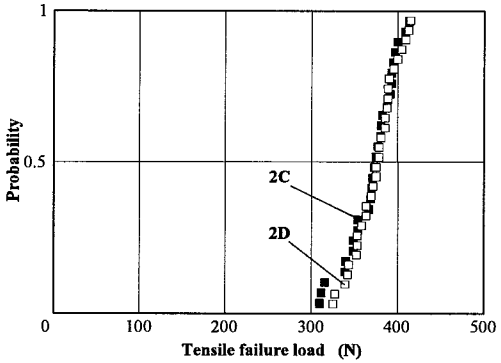

Fig. 2 The distribution of tensile failure load for Carbon Fiber T300 and CFRP out of Unsaturated Polyester resin

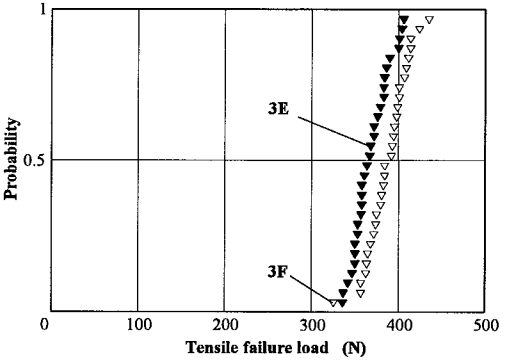

Fig. 3 The distribution of tensile failure load for Carbon Fiber T300 and CFRP out of Vinylester resin

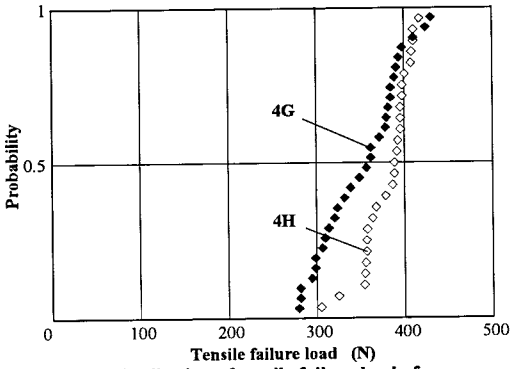

Fig. 4 The distribution of tensile failure load for Carbon Fiber T300 and CFRP out of Phenolic

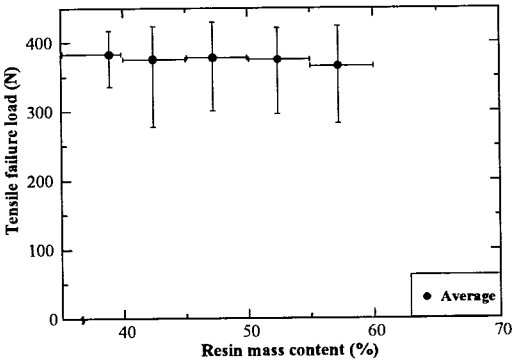

Fig. 5 The relation between tensile failure load and resin mass content of specimen out of 1A resin matrix

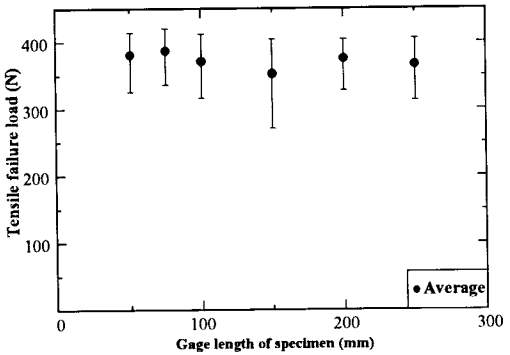

Fig. 6 The relation between tensile failure load and gage length of specimen out of 1A resin matrix

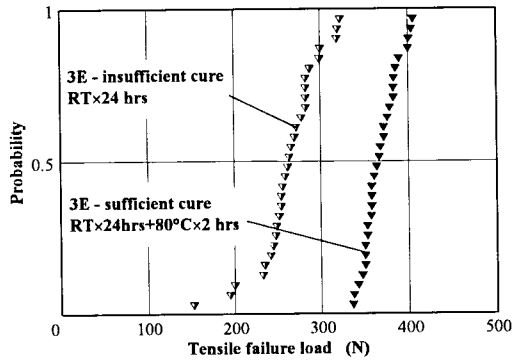

Fig. 7 The distribution of tensile failure load for CFRP out of Vinylester resin - Effect of Cure conditions

Proceedings of 7th Japan International SAMPE
Symposium & Exhibition, Nov. 13-16, 2001

An Integrated Approach to the Cost-Effective Design of a Composite Aircraft Control Surface

Minh Q. Nguyen, Tao-Min Lee and Murray L. Scott

The Sir Lawrence Wackett Centre for Aerospace Design Technology
Department of Aerospace Engineering, Royal Melbourne Institute of Technology
GPO Box 2476V, Melbourne, Victoria, 3001, Australia
E-mail: wackett_centre@rmit.edu.au

Abstract

This paper describes an approach to the integrated design and manufacture of a cost-effective optimised composite aircraft control surface. By broadening the design constraints to consider both production and operational requirements, the result was an improvement to the overall quality of the design and the design process. The application of computer aided engineering tools throughout the design was found to be a powerful approach for the rapid detection, visualisation and rectification of potential structural and manufacturing problems. By employing an integrated approach to structural analysis, manufacturing and computer aided design, the result was the development of an optimised structure that not only met all the stringent design constraints, but also from a manufacturing viewpoint, was highly cost-effective.

Key Words: Design, Manufacture, Cost, Optimisation

Introduction

The process of designing aircraft control surfaces usually involves the meeting of stringent requirements against sometimes competing goals. In order to produce a structure capable of satisfying all the demands imposed on it, there is a need to establish a strong collaborative approach in the early stages of design between the various disciplinary areas of computer aided design (CAD), finite element (FE) analysis, design optimisation and manufacturing. This paper presents such an approach and the associated benefits in pursuing this methodology. Furthermore, it is shown how the implementation of CAD was deemed to be highly important throughout the research and development program, as it enabled the representation of FE and optimisation results, that in turn facilitated the generation of cost-effective manufacturing solutions.

The structure studied was a large civil transport aircraft control surface. Loading conditions were derived from the operational conditions experience by structures of a similar size and function, with the manufacturing concept being a rib and spar dominated co-cured construction. The primary design constraints for this structure included various buckling, slope and strength requirements. To complement this, the structure also needed to satisfy the manufacturing concerns of tooling cost, process development, labour intensity and the risks associated with innovative advanced composite manufacture.

Optimisation and FE Analysis

Design optimisation is of primary importance at both the preliminary design and the detailed design stages. In the early phases of the design process, the level of complexity and configurational possibilities that exist, can often overwhelm the designer's ability to select the most suitable solution in which to initiate detailed analysis. In this light, the implementation of commercial finite element codes such as MSC.Patran/Nastran (Patran/Nastran) and ANSYS (Ansys) have been employed for this study. Ansys was used at the conceptual level, whilst Patran/Nastran enabled detailed analysis and refinement of the structure. The capability of Ansys was found to be particularly powerful in topological optimisation studies, as design variables making up the internal configuration were allowed to vary and their influence studied. Thus design unknowns such as rib or spar population and position, distribution of thickness and mass allocation, and the identification of likely regions of structural failure could be ascertained and evaluated [1,2].

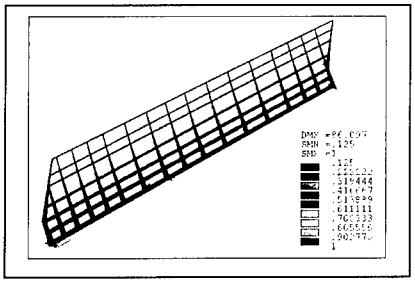

Fig.1 Results of an optimisation routine as performed by Ansys

Once a concept of the initial internal configuration had been decided, it was possible to modify the design variables within Ansys via iterative runs in an attempt to optimise the structure. Figure 1 shows the results for a topology optimisation routine. The initial step prior to conducting the optimisation was to read the outer mould line geometry of the structure and to ensure that operations such as cutting areas, lines etc. could be performed without problems. Aerodynamic loads and wing sympathetic bending conditions were then imposed, after which topology optimisation was undertaken to systematically re-distribute and eliminate material throughout the structure, whilst satisfying all of the imposed loading conditions.

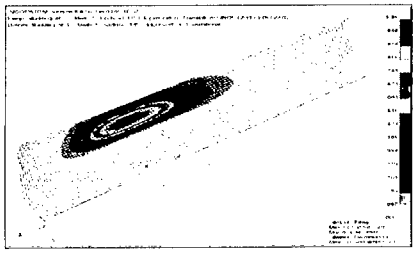

Fig.2 Results of an FE analysis for buckling using Patran/Nastran

After a suitable design configuration was selected, a surface model of the control structure was created. The CAD model was imported into Patran where it was meshed and the loads and constraints applied. A Nastran FE analysis was undertaken to determine the buckling eigenvalues, out-of-plane displacements and failure index under the specified loading conditions using the desired materials.

Computer Aided Design

The CAD software used for the visualisation of the design and manufacturing processes was CATIA. A detailed representation of the FE model within CAD was found to significantly enhance the understanding of the geometric characteristics of the control surface. This in turn enabled implementation of low-cost

manufacturing practices, by enabling manufacturing issues to have an influence on the evolution of the structure. Any manufacturing modifications were implemented into the CAD model; the model was then re-imported into the FE model where it was re-checked to ensure satisfactory structural integrity. This approach allowed the design process to be iterated between the constraints of structural design and manufacturing, employing CAD as the interface between the two disciplines. Termination of this design cycle only occurred when the CAD model was able to represent a component that not only met all load requirements, yet satisfied many of the cost driven manufacturing issues. Figure 3, shows the CAD representation of the final configuration of the control surface.

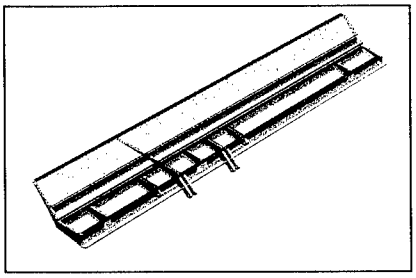

Fig.3 CAD representation after all manufacturing and structural issues were addressed

As the production cost of any part can be shown to be a direct function of its geometric complexity [3], the profiles and geometry of certain members became highly dependent upon the selected manufacturing process. Resin film infusion was the chosen process in which the control surface was to be fabricated; this presented some unique problems that could only be studied using CAD. For instance, the detailed geometric features of the interface and nesting regions between adjacent parts to ascertain the quality of the connections, as well as part internal radii, were extensively studied to ensure manufacturability of individual components and overall construction of the component.

Manufacturing

One of the most important aspects for manufacturing was to determine a solution that would minimise the recurring costs associated with production. Ideally, the most desirable solution would be the construction of the control surface as a single component. However, due to design, assembly and tooling limitations, the realistic option is most likely be a compromise solution between minimising tooling complexity and maximising unitised construction [4].

The use of CAD was employed to achieve this goal, by enabling a virtual presentation of the final control surface configuration. The tooling geometry was then designed directly within the model by filling the empty spaces between the internal members. Since the selected manufacturing process employs co-curing to reduce fastener related costs and mass, after the tooling profile had been obtained, methodologies for tooling assembly, installation and release were defined to generate the most practical and low-cost solution. This then led to a focus on tooling design, which then addressed the specific problems of sealing, location and sizing of bleed holes, elimination of spaces (allowing for resin migration) and the accommodation of tool movement during compaction and cure. In fact, a wide range of potential manufacturing problems and defects were identified and rectified by closely interfacing the CAD and FE models and manufacturing issues, before costly tooling was built.

Discussion of the Design Process

The integration of the design disciplines of optimisation, FE and CAD

modelling with the various manufacturing disciplines at the initial phases of design, was found to be essential in developing an aircraft structure that would be capable of satisfying broad design constraints. The results obtained from the Ansys optimisation routines enabled multiple solutions to be generated, from which the most suitable was selected for further analysis and refinement using Patran/Nastran.

Studies indicated that the optimisation process is very useful at the conceptual level, particularly in gaining insights during the preliminary lay-out design. However, once solutions have been generated, difficulty was noted to lie in the interpretation of the results. At this stage of the design process, the decision to proceed to detailed FE analysis using a selected configuration becomes dependent on the experience and judgement of the designers. Patran/Nastran was employed to analyse the failure conditions of buckling, out-of-plane displacement and material strength. Depending upon the results, adjustments to improve the performance of the structure were implemented, with all changes constantly updated into the CAD model ready for manufacturing assessment and input. The use of CAD proved to be an important communications interface, between the results generated by numerical analysis and the practical demands imposed by manufacturing [5]. In this role, CAD facilitated the representation of manufacturing features in the design model, the use of manufacturing simulations data to assess production, and the inclusion of process information throughout the design stages. The overall result was a structure with excellent structural integrity and highly favourable manufacturing characteristics.

Conclusion

The CAD package, CATIA, was utilised in conjunction with the finite element modelling programs, Patran/Nastran and Ansys, to provide a detailed interface with manufacturing, for the design of an aircraft control surface. Optimisation enabled multiple design solutions to be compared and evaluated to determine the most viable configuration. Difficulty during this phase of the design lay in the interpretation of the results, as it was noted that decisions to proceed to detailed FE analysis became highly dependent upon the experience and judgement of the designers. It was necessary to constantly update the CAD model to represent structural performance changes in the FE model for manufacturing input and evaluation. By being involved within the design cycle, the manufacturing issues can directly influence the design and evolution of the structure.

Acknowledgments

The authors would like to thank their RMIT colleagues, Ms Stephanie Germancheva, Mr Cameron McMahon and Mr Sagar Rajbhandari, and also Mr John Raju and Dr Adrian Rispler from the research and development team at Hawker de Havilland, Bankstown for their support.

References

1. C.D. McMahon, M.L. Scott and S.P. Rajbhandari: Proc. of 13th International Conference on Composite Materials (ICCM-13), Beijing, China, CD-ROM (2001).
2. C.D. McMahon and M.L. Scott: Proc. of 9th Australian International Aerospace Congress (AIAC-9), Canberra, Australia CD-ROM (2001).
3. D. Do, R. Paton, S. John and I. Herszberg: Proc. of 12th International Conference on Composite Materials (ICCM-12), Paris, France, CD-ROM (1999).
4. J. Raju, T. Kanavas, T. Kruckenberg and J. Salmon: CRC-ACS Technical Memorandum, June (1997).
5. M.L. Scott, J.A.S Raju and A.K.H. Cheung: Composites Science and Technology, 58, 199 (1998).

Proceedings of 7th Japan International SAMPE
Symposium & Exhibition, Nov. 13-16, 2001

Low cost composite design and manufacturing options

Masugi Kyoichi#

#: Fuji Heavy Industries Ltd. Aerospace Division Technology Development Center
1-1-11 Yonan, Utsunomiya, Tochigi 320-8564, JAPAN
E-mail: MasugiK@uae.subaru-fhi.co.jp

Abstract

Though the composite materials used to be applied to make the airframe lighter paying some costs, in 90s the composite technology trend toward the affordable structure rapidly. For 2000s, most important key word of the composite technology research and development area will continue to be affordability. However it is always required to make airframe lighter, the detail design conditions and the detail requirements of the airframe vary components by components, parts by parts and the functions that are required. To comply with every requirement and to achieve affordability at the same time, the airframe needs to be optimized to integrate the ample of low cost fabrications and assembly technologies. And also it is important to employ the design that can fully use the characteristic of those technologies. Thus Fuji heavy industries have been conducting research and development of the affordable part fabrication, assembly and design concepts.

Key Words: Affordable, Composite

Introduction

Efforts to employ low cost composite structure had been taken various approaches such as material, fabrication and assembly. The requirements such as cost, weight and function is different among every airframe development program and also the resources are different among each manufacturers. Thus the optimum design should be individual. Several structural concepts for elevator as one of the most popular composite applied structure in commercial aircraft are reviewed here.

Design Considerations

Elevator structure for example study is shown in Fig.1, and appropriate loads are considered the study.

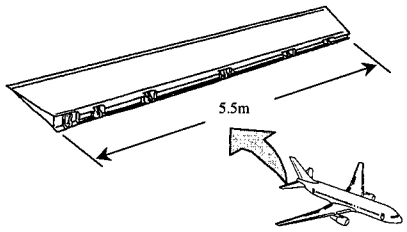

Fig.1 Elevator structure for study

The Structural concepts for elevator are generally classified as Assembled structure or Monolithic structure, and/or sandwich structure or solid structure.

Though the fastener-assembled structure has many advantages in numerous application experiences, reliability in

environment and inspectionability / repairability in operation, on the other hand it is need to be thicken around the joint because of low bearing strength and stress concentration. Since every component in monolithic structure is joined by adhesive or resin without applying holes, reinforcement around the holes are not required. But dedicated equipment may be required for assurance in production and inspection/repair in operation.

Though honeycomb sandwich structure has advantage in weight with its high stiffness compare to solid laminate structure for non-buckle design structures, honeycomb sandwich structure is suffering from water infusion or repair issues. Solid laminate do not have water infusion problem and can be applied easier repair method than sandwich structure, but post buckle design which requires more complicated design and more design data than sandwich structure must be employed to minimize weight.

Low Cost Fabrication Concepts

Several low cost composite fabrication methods, described below, was done applying to following structure concept review in next chapter.

Monolithic RTM part fabrication

Wet process such as RTM process is known as one of keys for low cost composite technologies. Two different approaches will be reviewed here. One is RTM full depth honeycomb sandwich structure technology. RTM process was hardly applied to honeycomb sandwich structure fabrication because of resin infusion into core. To resolve resin infusion problem, core should be sealed in fabrication process before resin injection without spoiling integrity between core and facesheet. The other is RTM solid laminate monolithic box with complex shape preform. The pan shape automatically woven preform can support the spars and skins to co-cure with RTM method.

Honeycomb sandwich Solid laminate

Fig.2 Example of RTM structure concepts

Vacuum secondary Bonding

This technique substitutes non-autoclave secondary bonding process for labor intensive assembly process. Since severe surface treatment is not required, paste adhesive is applied instead of current film adhesive.

Composite automatic riveting

Since fastener joint has numerous experiences, it is still most reliable joining method. But the assembly such as drilling , deburing and fastening is labor intensive process. To save labor, special rivet which has unique shape that does not damage composite during squeezing rivet had been developed for automatic assembly.

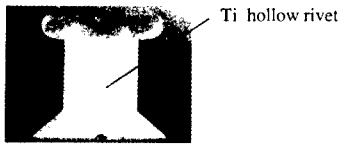

Fig.3 Example of Composite rivet

Comparison of Structural Concepts

Following 4 affordable structural concepts which are applied the technologies described in previous chapter. Characteristic and comparison of conventional honeycomb sandwich structure and 4 optional concepts are shown in Tab.1.

1. Conventional honeycomb sandwich structure (Base line)
2. Full depth RTM honeycomb sandwich structure
3. Multi-rib RTM solid laminate structure
4. Secondly bonded sandwich structure
5. Automatic riveted honeycomb sandwich structure

As Tab.1 shows, concept 1 to 4 can achieve lower cost than conventional honeycomb sandwich structure. Though Tab.1 shows that the concept RTM multi rib solid laminate structure concept achieves the lowest cost and weight, to employ this concept postbuckling design and RTM fabrication ability is required.

Conclusions

4 different affordable structure concepts are reviewed in previous chapter. Each concept has different low cost approaches and structural characteristics. Therefore the results shown in Tab.1 may be different when the different structure is studied. Thus full utilization of ample of technology options and structural concept options that fully utilize those technologies are required to design affordable structure which is fully comply with design requirement and achieve minimum cost at the same time.

Tab.1 Comparison of structural concepts

CONCEPTS	CHARACTERISTIC	TECHNOLOGY	FACILITY	COST	WEIGHT
1.Conventional Honeycomb sandwich concept Hand lay up ribs, spars and skins are assembled with bolts.	Numorous application experiences Water infusion probrem in operation. Poor repareability	Hand Layup part fab.	Autoclave Conventional tool	1	1
2.RTM full depth honeycomb sandwich concept Honeycomb core and facesheet are integrally cured by RTM.	Less part count. Water infusion probrem in operation. Poor repareability	RTM Core Seal	RTM equipment	0.7	1.1
3.RTM multi rib solid raminate concept Solid laminate spars and skins are integrally cured with pan shapd rib by RTM.	Less part count. Good repareability Difficult bond line inspection	RTM Complex shape preform (Pan shape)	RTM equipment	0.7	0.85
4.Secndly bonded concept Integrally cured ribs and skins and spar are secondly bonded.	Less part count. Difficult bond line inspection	Low cost secondly bonding technique Hand Layup part fab.	Oven Conventional tool	0.75	1
5.Rivetted Honeycomb sandwich concept Hand lay up ribs, spars and skins are automatically assembled with rives.	Numorous application experiences Water infusion probrem in operation. Poor repareability	Hand Layup process Composite riveting	Autoclave Conventional tool Riveter	0.85	1

References

1. Research of low cost composite monolithic control surface. 2001.3 Society of Japanese Aerospace Companies Report No.1201
2. Research of low cost composite monolithic control surface. 2000.3 Society of Japanese Aerospace Companies Report No.1201
3. Research of innovative riveting technique for composite structures. 1998.3 Society of Japanese Aerospace Companies Report No.0901
4. Research of innovative riveting technique for composite structures. 1998.3 Society of Japanese Aerospace Companies Report No.0901

Proceedings of 7th Japan International SAMPE
Symposium & Exhibition, Nov. 13-16, 2001

Development of Innovative Composite Control Surfaces

Atsushi Harada#, Seiji Maruyama#, Naoya Takizawa#

#: Fuji Heavy Industries Ltd. Aerospace Division Technology Development Center
1-1-11 Yonan, Utsunomiya , Tochigi , 320-8564, Japan
E-mail: HaradaA@uae.subaru-fhi.co.jp

Abstract

Resent years, the studies and application of the processes to accomplish affordable composite fabrication, such as RTM(Resin Transfer Molding) and RFI(Resin Film Infusion), has been conducted to reduce the raw material usage and the fabrication time.

However, because those affordable manufacturing process has still been applied for the detail parts and/or sub-assembly parts, their high potential of the integration has not been derived enough. There is some affordability still remaining in the assembly sequence.

In this study, integrating the parts at higher degree by using "Box Shaped" textile as the RTM Pre-form and reducing of the fabrication time has been demonstrated. And also the unique fabrication process combining the RTM and the secondary bonding can keep assembly time as low as possible for the control surface fabrication.

Finally over 30% affordable fabrication process has been demonstrated, at the same time weight reduction has been more than 15% to the conventional CFRP honeycomb sandwich construction.

Key Words: RTM, Pre-form

Introduction

To demonstrate higher level structure integration with Resin Transfer Molding(RTM) using 3D box shaped pre-form and the practical low cost use of secondary bonding scheme with new RTM's unique feature, the design and trial fabrication of sub-component structure are conducted for control surface structure of the transport airplane. Fig.1 shows a common existing structure and a new structure using new fabrication method. Span of the structure is about 5m

(a) Conventional elevator structure

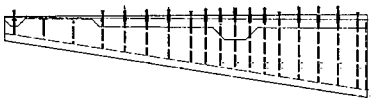

(b) New structure

Fig.1 Target structures

New Fabrication Process

Process Outline

Fig.2 shows process outline.

・Jig Set

Setting the pre-form and/or dry fabric into the RTM tool.

・Resin Transfer Molding

Resin is transfered into the molding jig.

・First stage cure

Heating at low temperature (90 ℃) for the first stage cure.

・Separation/Preparation for secondary bonding

Cured RTM structure is taken out from jig and trimed. RTM parts, cover plate which is molded in the different process and adhesive film are set to the bonding jig which has unique soft mandrel inside then bagged.

・RTM final cure/Secondary bonding

RTM final cure and secondary bonding are conducted simultaneously applying vacuum pressure and heating in the oven.

・Completion

Structure is de-bagged and removed from bonding jig.

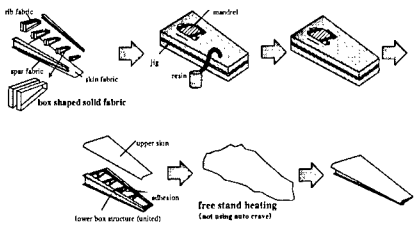

Fig.2 New RTM fabrication process

Merit of the New Process

Assembly cost is reduced by following RTM integrated fabrication. And fabrication processing cost is also reduced using low temperature first stage cure and 3D shaped pre-form. There are other potential cost reduction in the assembly and processing, because secondary bonding and RTM cure are conducted simultaneously. And this structure has solid laminate (non honeycomb) as the design features, it is possible to lighten by the post-buckle design and the invasion of the water into the honeycomb core can bee eliminated.

Process Development

"Box Shaped" textile

To achieve low cost fabrication to simplify the lay up process, RTM 3D Box shaped textile is developed and applied for the ribs. Fig3 is the picture of the trial specimen. Weaving result is good and it is demonstrated that the 3D shaped textile is applicable to the actual airplane part fabrication.

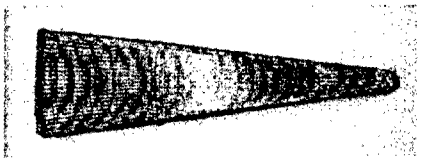

Fig.3 Trial specimen

Strength Validation

・Tensile/Compressive strength of RTM part

Fig.4 shows tensile/compressive strength test results. It is confirmed that both of stitched fabric and plain weave fabric are both good for the design ultimate load

・Bond plane shear strength test

Bond plane shear strength test was conducted considering environmental effect. Fig.5 shows the test results. It is confirmed that bond plane shear strength is strong enough for the design ultimate load with critical environmental condition.

・Delamination strength test

Delamination strength at the rib and skin interface was verified both for bonding and RTM integrated location with simulated damage. The level of impact damage has been

defined by the actual damage detectability test. Fig.6 shows the test results. It is confirmed that delamination strength at rib and skin interface is strong enough for the ultimate load even with the barely detectable damage.

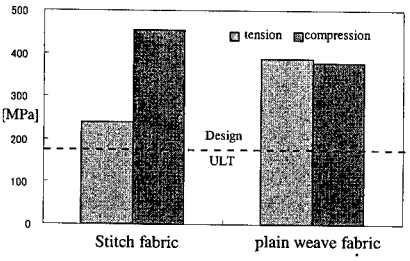

Fig.4 Tensile/compressive strength test

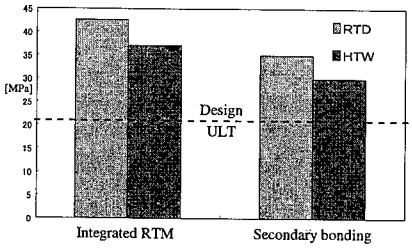

Fig.5 Bond Planer strength test

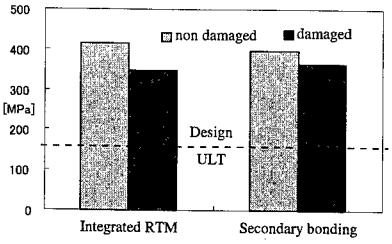

Fig.6 Delamination strength test

Concept Demonstrator

Demonstrator Fabrication

Demonstrator was fabricated by following the sequence described in the Process Outline. Fig.7 shows RTM fabrication jig and Fig.8 shows lower box. Fig9 shows sketch of secondary bonding concept and Fig.10 is the complete part after secondary bonding.

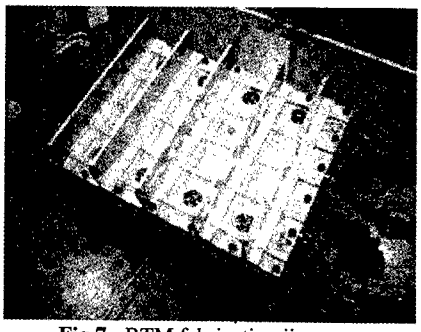

Fig.7 RTM fabrication jig

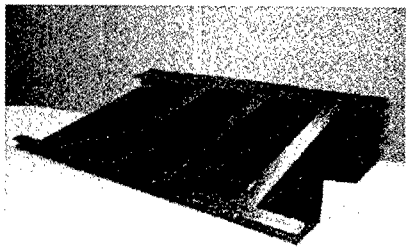

Fig.8 RTM Integrated Lower box

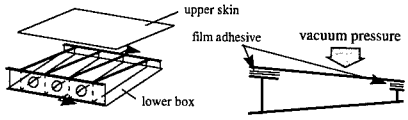

Fig.9 Sketch of secondary bonding

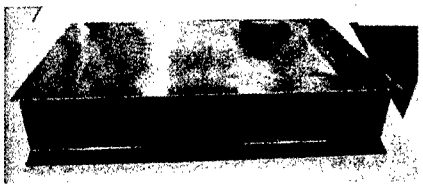

Fig.10 Product after secondary bonding

Evaluation

・External appearance inspection

RTM fabricated part has barely lack of resin and good fabrication results was observed.

・Measurement of Vf

It was confirmed that Vf was varied partially. This is mainly due to the tolerance of RTM jig.

Weight and Cost study

Fig.11 and fig.12 show estimated results of weight and cost for the elevator. As a results of this estimation, 18% of weight reduction and 36 % of cost reduction are expected to the conventional honeycomb structure.

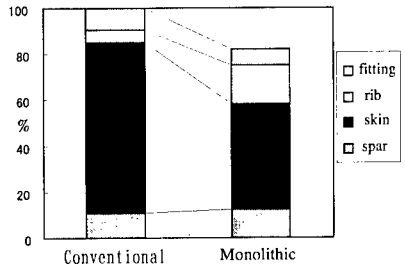

Fig.11 Weight estimation

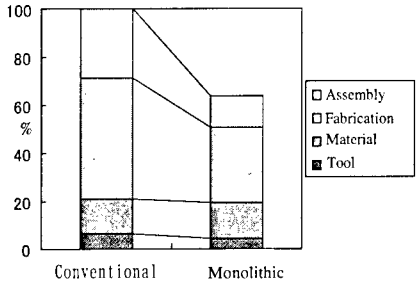

Fig.12 Cost estimation

Conclusion

As the results from demonstrator fabrication, 18% of weight reduction and 36% of cost reduction compared to the conventional structure will be expected.

The grate potential of the unique secondary bonding process with two staged RTM process is well demonstrated.

This technology will be able to apply to the actual aircraft fabrication.

Acknowledgment

This work was performed as a part of the R&D project of 'Advanced Aeronautical Technology Development' in the management of SJAC (Society of Japanese Aerospace Companies).

References

1. Research of low cost composite monolithic control surface. 2001.3 Society of Japanese Aerospace Companies Report No.1201

2. Research of low cost composite monolithic control surface. 2000.3 Society of Japanese Aerospace Companies Report No. 1102

Proceedings of 7th Japan International SAMPE
Symposium & Exhibition, Nov. 13-16, 2001

Low cost structural concept for composite trailing edge flap

Y.Hirose#. T.Taki#,T.Yamamoto#,Y.Mizusaki#,T.Fujita#

#: Kawasaki Heavy Industries, LTD

1.Kawasaki-cho,Kakamihara City, Gifu-Pref. 504-8710,JAPAN
E-mail: hirose_yasuo@khi.co.jp

Abstract

Low cost combined with aircraft-quality fabrication technologies is the key for the wide range application of composite materials in the industry. Two years research activities sponsored by Japan Aircraft Development Company (JADC) resulted in the application of low cost composite materials to the trailing edge flap for the transport category aircraft and its advantages are presented.

Low-cost high-quality structural design concept is introduced supported by manufacturing technologies. Many tests have been conducted to confirm the viability of the new design and manufacturing concept.

This concept was used in the flap design and a full-scale subcomponent test article of the flap box structure was fabricated. An estimated cost reduction of 29% was obtained compared with the conventional hand lay-up method

As for the full-scale subcomponent test, a static strength test was performed to confirm the validity of the new structural design concept supported by new manufacturing technologies.

Key Words: Composite structure, Low cost design, Low cost fabrication, Trailing edge flap

Introduction

A considerable weight reduction can be achieved when new design concept supported by manufacturing technologies is applied to the composite materials. In the past, the high cost associated with the conventional hand lay up fabrication was inevitable. However, some of the difficulties have been successfully overcome through the two years research program undertaken by KHI under the sponsorship of JADC. It is shown below a new design concept and manufacturing technologies through the application on the trailing edge flap of the transport category aircraft. This approach has been supported by the full-scale sub-component test. The results obtained are encouraging for this endeavor undertaken by KHI staff

Composite Flap Structural design

The flap configuration and the design loads used were based on the aerodynamic research on the YSX flap conducted under different project. These data have been used for the present structural design concept

Flap configuration and aerodynamic load

The single slotted outboard flap was selected as a model. To supplement the

existing data, an additional CFD analysis was conducted to establish aerodynamic and actuator loads. The flap plan form is shown in Fig.1.

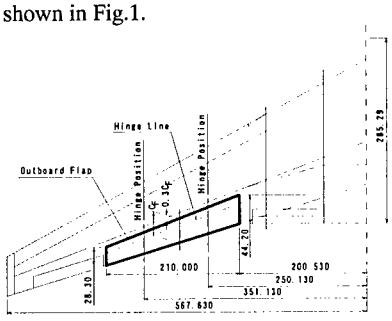

Fig.1 Flap Configuration

Structural concept of flap box component

For the composite box structure, it is commonly used two types of concept: the honeycomb sandwich panel and the solid laminate. Due to an insignificant weight trade between these two types, the solid laminate type concept was selected due to the applicability of the low cost manufacturing process.

The flap design concept is shown in Fig.2

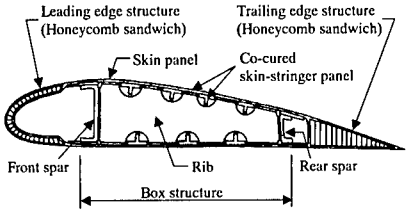

Fig.2 Flap Design Concept

The new lay-up concept for the stiffeners, spars and ribs were introduced for the structural concept.

One is the folding mold method for stiffeners and the other is the hot drape mold method for spars and ribs. In the *folding mold method*, flat lay-up prepregs were folded by the mechanical device to mold the stiffener with various cross sections such as J-shape and T-shape. The concept of the folding method is shown in Fig.3, and has the following sequence of a process flow:

1) The flat lay-up prepregs are set between the upper and lower jigs. 2) The prepregs are pushed by the rod and folded. 3) The rod is pulled out and the prepregs are pressed by the jigs.

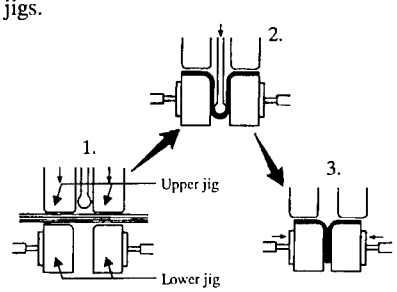

Fig.3 The concept of the folding method

This method is suitable for the low cost fabrication for the long slender parts such as stringers.

In the hot drape method, the flat lay-up prepregs were heated and pressed. The softened prepregs were pressed to the jig in order to mold a complex shape. This method is suitable for the composite parts with relatively large area. The concept of the hot drape method is shown in the Fig.4, and the steps are shown as follows.

1) The flat lay-up prepregs are set on the molding jig. 2) The prepregs are heated by the heater such as an infrared lamp and softened. 3) The softened prepregs are stuck to the molding jig by the vacuum pressure.

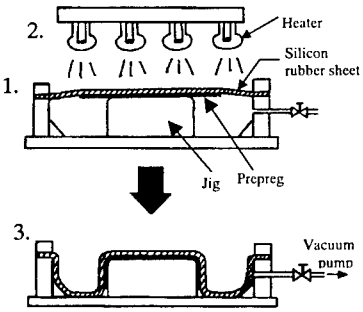

Fig.4 The concept of the hot drape method

Through these new concepts, the cost reduction in the lay-up processes for the complex parts was achieved compared with the hand lay-up method.
Another cost reduction concept in the lay-up process is the introduction of the pultrusion corner fillers instead of the hand made ones, which fill the gap between the skin and stringers.

Flap design

Using the aerodynamic loads, bending, shear and torsional moment diagram were established and internal loads were obtained with the FEM analysis. Using these internal loads, the stress analysis was conducted for the sizing of the flap structure and the design was established. The typical drawing is shown below in Fig.5

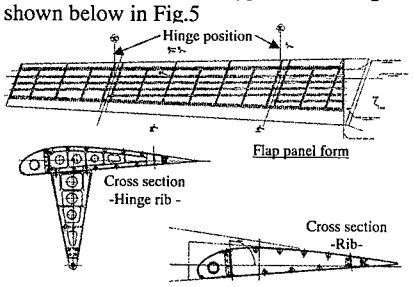

Fig.5 Flap Drawing

Structural element test for stiffeners

In order to confirm the strength of the stiffener made by the folding mold method, the structural element tests were conducted. Test specimens are shown in Fig.6 Tests results are shown in Table.1.

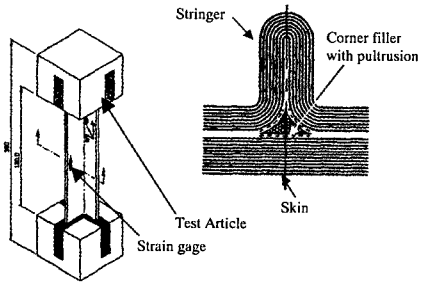

Fig.6 Test specimens

Table.1 Structural Element Test Results

Type of specimens	Failure Load (kN)	Cross sectional area (mm2)	Strength (MPa)	Failure strain (micro strain)	Failure mode
Conventional Lay-up + Prepreg filler	68.8	132.5	519	-10,333	Torsional buckling
Folding mold method + Prepreg filler	68.5	132.2	518	-9,833	Torsional buckling
Folding mold method + Pultrusion filler	70.2	140.5	501	-10,400	Torsional buckling

Note: Average values are shown.

The tests confirmed that the new stiffeners have compressive strength comparable to the conventional ones.

Design and fabrication of the test article

The test article was designed with the constant cross section, 2 hinge points and a length of 2m in order to evaluate the design of the critical cross section. The critical cross section in the structural analysis is the hinge position. The critical loading condition occurs from one actuator malfunction. In this case, the aerodynamic load should also be taken into consideration.

Prior to the full-scale subcomponent test, the FEM analysis of the test article was conducted to assess any unexpected deformation. The FEM analysis result is shown in Fig.7.

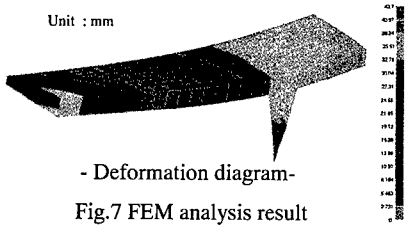

- Deformation diagram-

Fig.7 FEM analysis result

In the fabrication of the test article, low cost manufacturing technologies such as the folding mold method and the hot drape method were applied. The test article is shown in Fig.8.

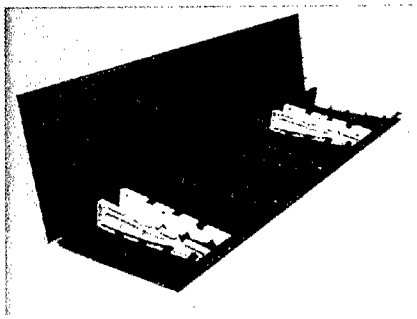

Fig.8 Test article

Full-scale component test

The full-scale component test was conducted in order to show the compliance with the FAR requirements. The comparison of strain distribution with analyses is shown in Fig.9, which shows a good agreement between the test results and analysis.
Through the destructive test, the compliance with FAR requirement of no destruction for three seconds at 150% limit load was confirmed and skin local buckling was occurred at 185% limit load.

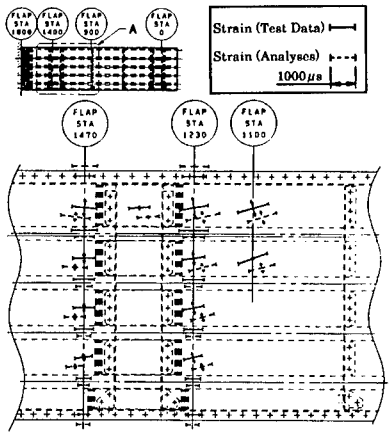

Fig.9 Comparison between analytical and test results

Cost estimation

Based on the design and fabrication data, it has been estimated a cost saving of 29% compared to the conventional process. In this estimation, material and assembly cost are included.

Conclusions

Through these activities, the low cost design concept and the manufacturing process were established. The results of the present research have been applied to ERJ170/190 projects

Acknowledgment

The authors would like to acknowledge their appreciation for the JADC in supporting this program, especially to Mr.M.Hirahara.

References

1.Y.Hirose,S.Bando,H.Masaeda,and N.Tsuda : Proc.of the Third Japan-U.S Conference on Composite Materials,683(1986)

Proceedings of 7th Japan International SAMPE
Symposium & Exhibition, Nov. 13-16, 2001

Affordable Composite Fuselage Structure based on Dry Preform/RFI Technology

Atsumi Tanaka# and Hiroyuki Kiriyama#

#: Nagoya Aerospace Systems, Mitsubishi Heavy Industries, LTD.
10 Oye-cho, Minato-ku, Nagoya, 455-8515, JAPAN
E-mail: hiroyuki_kiriyama@mx.nasw.mhi.co.jp

Abstract

Composite material is one of the most effective solutions for weight reduction of the aircraft. The latest aircraft consist of many composites not only for the secondary structures but also for the primary ones. But we have serious problems, low post-impact strength, low interlaminar strength, and high manufacturing cost etc., for the conventional prepreg type structures. Our researches were funded the Society of Japanese Aerospace Companies (SJAC) during JFY1996-1999 and developed dry preform/Resin Transfer Molding (RFI) technologies. During first two years, we had investigated the stitched dry fabric/RFI, which was expected 26% cost reduction for manufacturing and the high mechanical performance, compression after impact (CAI) and interlaminar strength, compared with the conventional's [1,2]. And following two years, we have investigated higher performance to apply our original 5 axes 3 dimensional weaving preform (5A3D WP)/RFI technologies [3,4].

Key Words: RFI, Stitching, 5A3D, BMI.

Introduction

Many R&D's have been performed for new generation commercial aircraft. We started our researches for the HSCT and had developed more affordable, lighter, and and easier to fabricate for the new commercial aircraft. Through the R&D of the stitched dry fabric/RFI, we had developed basic RFI processes for Bismaleimide (BMI : Cytec 5250-4-RTM) resin and evaluated the basic mechanical properties, shown good CAI and interlaminar strength. As following 5A3D WP/RFI researches, we had developed higher performance for manufacturing of the commercial aircraft through application of our original textile technology. In these researches, we had selected the same resin, 5250-4-RTM, for comparison with previous researches.

Stitched Dry Fabric/RFI

Manufacturing process is shown in Fig.1. In this process we had applied the carbon fiber(CF) dry fabric (MRC:MR50K 8HS) for in-plane lamination. And the laminated dry fabric was stitched with the aramide fiber (Dupont:Kevlar 49). Major assemblies, between skin and stiffeners, were also stitched same material as shown in Fig.2.

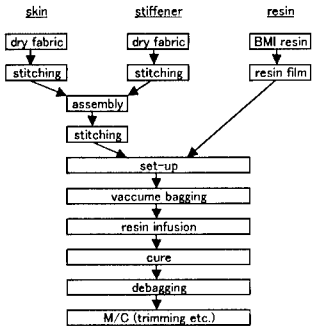

Fig.1 Major Manufacturing Process

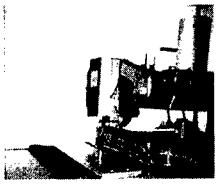

Fig.2 Stitching Process for Assembly

Mechanical Properties

Conventional prepreg stitching had big problem, in-plane strength reduction through the fiber broken by stitching. In our process, in-plane strength reduction by stitching was almost negligible as shown in Table 1. And we had obtained good CAI and interlaminar strength as shown in Table 2.

Table 1 In-plane Properties

	stitching	requirement			Cond	Vf (%)	F (MPa)	E (GPa)	ε (%)	ν
		direction	pitch(mm)	width(mm)						
NHT	×	-	-	-	RTD	55.7	751	55.6	1.35	0.323
					HTD	56.4	790	54.6	1.42	0.290
	○	0	5	5	RTD	55.0	779	54.6	1.43	0.266
			5	10		55.0	761	53.2	1.44	0.298
			10	5		55.4	784	59.4	1.28	0.328
		90	5	10		55.4	796	58.2	1.45	0.301
NHC	×	-	-	-	RTD	55.5	485	49.4	0.95	0.304
					HTD	55.8	522	52.3	1.20	0.342
	○	0	5	5	RTD	55.0	515	51.6	0.98	0.316
			5	10		55.3	521	51.3	1.01	0.325
			10	5		55.3	568	49.8	1.17	0.296
		90	5	10		55.4	579	52.7	1.09	0.312

Note) Cond : Environmental Conditions
Vf : Fiber Volume Fractions
F : Maximum Strength
E : Young's Modulus
ε : Maximum Strain
ν : Poisson's Ratio
Lay-up NHT[+45/0/0/+45]s, NHC[+45/0/0/+45]2s
NHT : Non-Hole Tensile
NHC : Non-Hole Compressive
RTD : Room Temperature Dry (23°C Dry)
HTD : Hot Dry (150°C Dry)

Table 2 Interlaminar Properties

	U (in-lb/in)	Cond	Vf (%)	G (Nm/m2)	F (MPa)	E (GPa)	ε (%)	A (cm2)
DCB	-	RTD	-	3470	-	-	-	-
		HTD	-	2330	-	-	-	-
ENF	-	RTD	55.3	2180	-	-	-	-
		HTD	55.2	2000	-	-	-	-
MMF	-	RTD	57.1	2030	-	-	-	-
		HTD	58.7	1730	-	-	-	-
CAI	1200		55.0	-	272	52.0	0.535	6.76
	1500	HTD	55.3	-	263	51.5	0.519	7.79
	2000		54.8	-	237	49.8	0.470	14.49

Note)
U : Impact Energy Level
Vf : Fiber Volume Fractions
F : Maximum Strength
ε : Maximum Strain
DCB : Double Cantilever Beam
MMF : Mixed Mode Flexture
RTD : Room Temperature Dry (23°C Dry)
HTD : Hot Dry (150°C Dry)
Cond : Environmental Conditions
G : Critical Energy Release Ratio
E : Young's Modulus
A : NDI Indication Area
ENF : End Notch Flexture
CAI : Compression after Impact

Trial Production of Structural Element

Fig.3 shows the representative stiffened panel structural element for aircraft fuselage. Through the trial production of this structural element, we had determined the good RFI process. As the results of visual inspection, non-destructive inspection (NDI) and DI, the structural element had shown good quality.

Fig.3 Stiffened Panel Structural Element

Based on this trial, these RFI process was affordable rather than the conventional ones as shown in Fig.4.

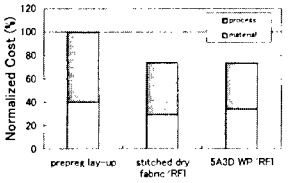

Fig.4 Normalized Cost Estimation

Structural Element Test

After trial production, Structural element tests, such as cut-out coupons and post-buckling shown in Fig.5, were performed. Summary of post-buckling test result is shown in Table 3. That shows good relations with finite element method (FEM) analysis as shown in Fig.6.

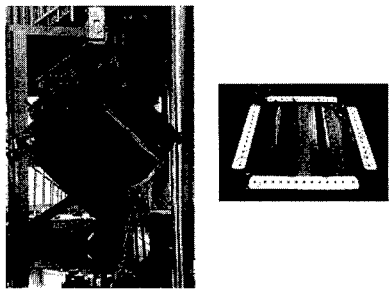

Fig.5 Post Buckling Test of Stiffened Panel Structural Element

Table 3 Summary of Test Result

Load [kN]	Events of the test article
39	Initial buckling
157	Delamination at the edge of C stiffener (shown as No.1)
167	Delamination at the edge of A stiffener (shown as No.2)
206	Delamination at the center of B stiffener (shown as No.3)
235	Growth of delamination
265	Shear Failure at the edge of test article. Separation B and C stiffener from skin.

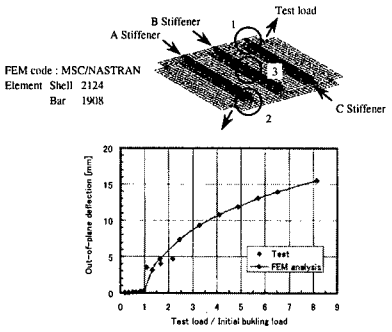

Fig.6 Post Buckling Analysis of Stiffened Panel Structural Element

5A3D WP/RFI

Manufacturing process is shown in Fig.7. In this process we had applied our original 5A3DWP(MRC:MR50K for in-plane fiber, TR40 for Z direction fiber). And the structural parts were consisted of these 5A3D standard thickness panel preforms made by our original weaving machine as shown Fig.8.

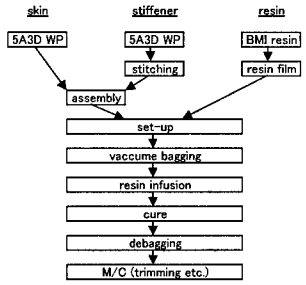

Fig.7 Major Manufacturing Process

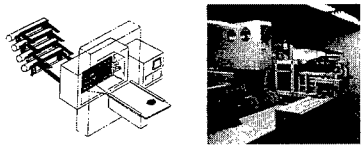

Fig.8 5A3D WP Weaving Machine

Mechanical Properties

Previous stitching researches had shown good performance, but we found problems in performing. That is difficulties for cutting and lay-up of dry fabric. Our 5A3D WP could be resolved that problem and shown better performance for interlaminar strength than stitching. Test results are shown in Table 4.

Table 4 Summary of Test Result

	U (in-lb/in)	D (mm)	W (mm)	F (MPa)	E (GPa)	ε (%)	ν	A (cm2)	
NHT	–	–	–	491	40.9	1.20	0.345	–	
NHC	–	–	–	475	39.0	1.22	0.322	–	
OHT	–	6.35	38.1	402	–	–	–	–	
	–	6.35	25.4	358	–	–	–	–	
	–	40.0	240	249	–	–	–	–	
	–	6.35	38.1	398	–	–	–	–	*1
OHC	–	6.35	38.1	362	–	–	–	–	
CAI	2500	–	–	335	–	0.72	–	6.2	

Note) Environmental Conditions : RTD Vf = 50 % *1 : off-axis
NHT : Non-Hole Tensile U : Impact energy Level ε : Maximum Strain
NHC : Non-Hole Compressive D : Hole Diameter ν : Poisson's Ratio
OHT : Open Hole Tensile W : Specimen Width A : NDI Indication Area
OHC : Open Hole Compressive F : Maximum Strength
CAI : Compression after Impact E : Young's Modulus

Trial Production of Structural Element

Fig.9 shows the representative side panel structural element for aircraft fuselage. As the results of visual inspection, NDI and DI, the structural element had shown good quality.

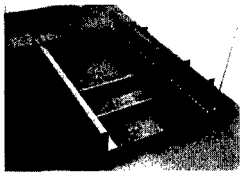

Fig.9 Side Panel Structural Element

Structural Element Test

After trial production, structural element tests, such as cut-out coupons and post-buckling shown in Fig.10, were performed. Summary of post-buckling test result is shown in Table 5. That shows good relations with FEM analysis as shown in Fig.11.

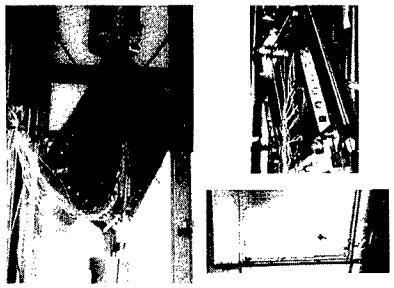

Fig.10 Post Buckling Test of Side Panel Structural Element

Table 5 Summary of Test Result

Load [kN]	Events of the Test Article
40	Initial Buckling
50	Change of Buckling Mode
120	Delamination at the corner of skin Pad-up Area
158	Shear Failure around the minimum thickness area of the skin

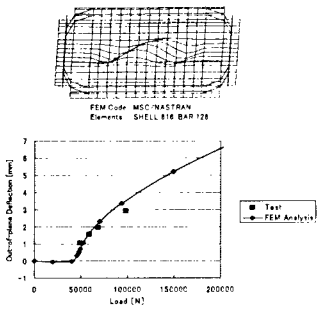

Fig.11 Post Buckling Analysis of Side Panel Structural Element

Conclusions

Through these works, our dry perform/RFI process is expected to apply the future aircraft as the affordable manufacturing technology and higher structural performance.

Acknowledgment

The authors thank SJAC for sponsorship of these works. And the authors also thank Mr.Hirokawa and other Shikibo's personnel for stitching, Mr.Uchida and other Muratec's personnel for 5A3D WP, and our MHI's good colleagues of these works.

References

1. Y.Noumaru, M.Yoshida, S.Sakai, H.Koiwai, A.Tanaka and M.Hasegawa: ISSN 1342-4017, No.0806, Mar.1997.
2. K.Enomoto, M.Yoshida, S.Sakai, T.Nagase, R.Yoshinaga, A.Tanaka and H.Kiriyama: ISSN 1342-4017, No.0902, Mar.1998.
3. K.Enomoto, S.Nishiyama, M.Shinya, Z.Yamaguchi, A.Tanaka, H.Kiriyama, Y.Uchida, T.Yamamoto and H.Takashima: ISSN 1342-4017, No.1003, Mar.1999.
4. M.Yoshida, S.Nishiyama, M.Shinya, T.Onishi, A.Tanaka, T.Muraki, Y.Uchida, T.Yamamoto and H.Takashima : ISSN 1342-4017, No.1101, Mar.2000.

Proceedings of 7th Japan International SAMPE
Symposium & Exhibition, Nov. 13-16, 2001

Study of Al investment Casting for flight control system

○Koichi Nakamura , Shigeki Abe
Mitsubishi Heavy Industries, Ltd
Makoto Hirahara
Japan Aircraft Development Corporation

The investment casting has developed significantly to have high mechanical properties and to decrease defects in casting using high integrity D357 Al alloy. On the other hand, the rapid prototyping techniques can be used in past decade to develop to shorten the certification period component test for the critical structures. A Casting with rapid prototyping is the equal of machining in developing period.

In this study, the investment casting for the flight control system using the rapid prototyping has been developed and evaluated sample casting parts in accordance with the requirements of public specifications. As a result, significant cost reduction can be achieved without the weight increasing or without impact on the casting factor, when replacing machined components or fabricated sheet metal components to apply the investment casting.

1. Introduction

The investment casting technology has developed greatly with these 10 years. With no or even for Al alloy of expensive strength, high toughness aluminum casting (D357), a possibility of substitute structure of a machining part and a sheet metal build-up part of a complicated shape rises and is expected as a valid measure of low getting a cost of civil airplane. On the other hand, Rapid Prototyping develops in these years in order to get a large merit to get shortening development period.

Figure 1 shows the relationship between material strength and a part shape applied to an airplane. Generally sheet metal build-up structure is popular structure in an airplane. Machining from block materials is applied to a high strength part. Machining part has a great merit to shave out as a one part. It is valid as considering forging also as an expensive strength part, if a shape isn't complicated. A casting is good for a complex shape and moderate and less strength part. In these years, Al alloy casting application range in figure 1 is getting increasing as a substitution of a sheet metal build-up structure and / or machining structure.

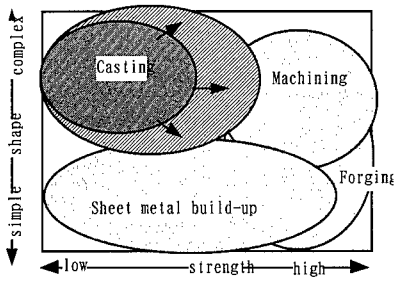

Figure 1 Application map

The investment casting application to a small-sized civil airplane to consider the low cost that it enforces as Japan Aircraft Development Cooperation (JADC) consignment research as an aim a report introduces a summary of research. A trial part took a part to have a strength demanded and produced a berry machine simulation attendant trial body of an operation by way of trial from conventional casting object with a complicated shape especially. With various automatically characteristic acquisition of a new expensive strength Al alloy investment casting object and also small-sized private airplane application of a investment casting part examined it while comparing it with a machining part about weight and cost. There is a line for an examination of a making practicable feasibility of Rapid Prototyping.

2. Requirements for the casting part

We choose the fitting of the flight control system as a trial model for investment casting. This part is not the load member part and is very complex shape.

If this part judged that a case of machine processing is suitable for casting getting an object from that multi-axial machining processing is a necessary complicated shape part. We set up the design requirements as show as table 1 and designed an attendant trial body shape of a thickness while analyzing as a design requirements against a casting object part at first.

Table 1 Design Requirements

	Item	Requirements	Remarks
Stress	Material	Ftu:345Mpa Fty:275Mpa el: 5%	Big elongation
	Casting Factor	1.25	FAR25.621
Shap	Model	Complex	5-axis Machining
	Thickness	1.00mm	Arm portion
	Dimension	+/- 0.3mm	
Weight		< Machining	

3. Manufacturing Process

The process of investment casting with using the rapid prototyping is to use stereo-lithography resign pattern instead of the wax pattern. A rapid prototyping is a method not to need the permanent mold design manufacturing to occupy the majority of the development period and the development cost at lost wax investment casting. However for stereo-lithography resin played with overwhelmingly early, moreover the development risk also is small, though we don't turn toward mass production from that a unit price is expensive compared with a wax pattern. Consequently, Rapid Prototyping is a very charm-like process at brief development. Figure 2 shows the investment casting process that we applied. The manufacturing process of rapid prototyping (see figure 3) can be made by the digital data of 3 dimension CAD drawing and no special jig. The other processes are fundamentally in the same way as lost wax investment casting as shown as figure 4.

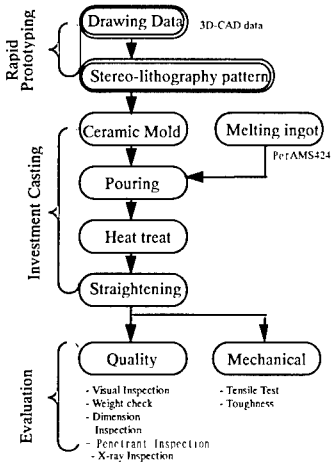

Figure 2 Process Chart

4. Evaluation of sample casting

As non-destruction inspection for quality, X-ray inspection, dimension inspection, and fluorescent penetrate inspection were performed. As a mechanical property evaluation, tensile test, fracture toughness was performed. And we evaluated the relationship with a strength characteristic and a microstructure, especially a width of the 2nd arm to form branch formed of a casting microstructure (Dendrite Arm

Spacing, DAS). Here, and give an overview of a result of a tensile test X line inspection, dimension inspection.

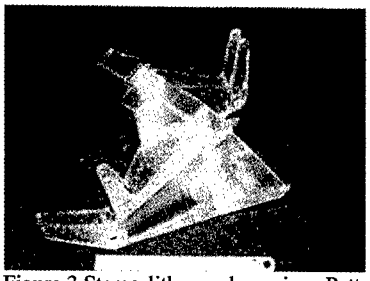

Figure 3 Stereo-lithography resigns Pattern

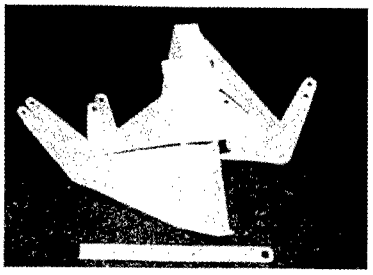

Figure 4 Sample Casting

4.1 Quality Evaluation

We cast the sample casting material standardized AMS 4241 and based on a claim of an object quality claim standardized MIL - STD - 2175 GRADE B, and X-ray inspection. The sample casting is good quality without gas defect, shrinkage, inclusion and any other harmful level defect more than 0.040-in. (1.0-mm) size. Again, at a dimension inspection even though as being contained within a dimension difference +/- 0.5 mm, a casting superficial smoothing also was excellent.

4.2 strength evaluation

Tensile test was based on tensile test standardized ASTM B 557 of Al alloy casting, and enforced a tensile test with normal temperature. We grasped it of a tensile test piece and observed a microstructure. Figure 5 shows ultimate tensile strength, 0.2 % yield strength at an every casting condition for around to arrange it with DAS. A broken line during a figure shows a design requirements, and a solid line shows relationship of D 357 tensile test characteristic and DAS that it requests distinctly. As a tensile test result of this attendant trial body shows it for a diagonal line division, DAS is a few for deviation with a minute grain less than 40 μ m. Even though a harmful needle formed precipitation isn't admitted.

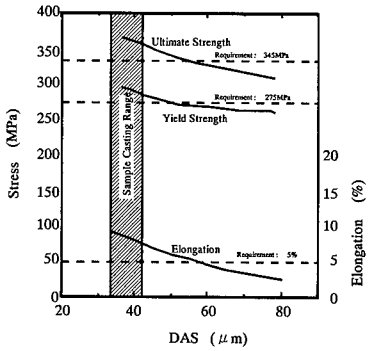

Figure 5 Tensile Properties and DAS

5. Feasibility Study

All results of the quality and the mechanical properties meet the requirements. From a point of view of a cost and weight, we discussed comparison with casting part and machining part as shown as figure 6.

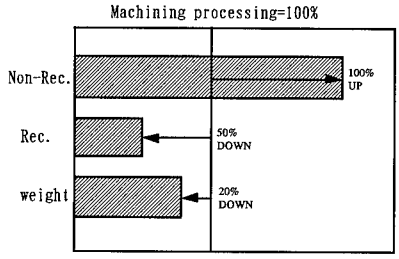

Figure 6 Estimation of Cost and Weight

Development cost of casting part is more expensive than machine processing. But unit cost of casting is lower than machining part. If a production number increases to show it for figure 7, a unit price is estimated that total cost of a cheap investment casting part

gets cheaper than total cost of machine processing. Moreover by an application of Rapid Prototyping regarding Development even though there is the following merit.

In order not to need permanent mold, it is small and is possible for an investment in the early time at Development period.

On the other hand, about that we achieve lightweight getting, the following factor is raised.

Using D357 casting alloy, minimum wall thickness achieved to 1 mm (0.040 in.) with respect to a strength analysis at this attendant trial body shape.

It is possible to manufacture more complex one-piece structure than machine processing. In this model part, a shape of design was very difficult for machining processing, because it need special machining tool to shave narrowly and deeply. As I do the smallest thickness for 1.8 mm (0.070 in.) ~ 2.0 mm (0.080 in.) grade for machining processing. The part weight is heavy only for thickness increase.

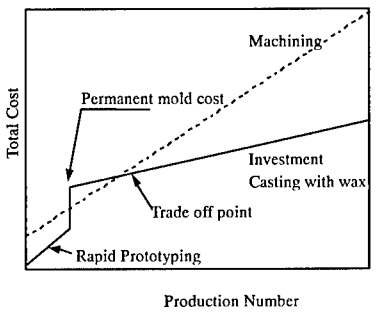

Figure 7 Comparison with Machining

5. Conclusion

We produced a summary operation by way of sample with the investment casting to use rapid prototyping and obtained the following result, result that we examine it comparatively with machine processing.

(1) To manufacture the model part by the investment casting with minimum wall thickness (1.0 mm).

(2) To achieve lightweight getting more than 20 % from machine processing.

(3) Total cost restricted with small number production, even though development cost, as achieving low getting a cost more than 50% from machining processing.

Proceedings of 7th Japan International SAMPE
Symposium & Exhibition, Nov. 13-16, 2001

Superplastic Forming of Aluminum Sheet with Welded Line

Toru Jinishi#, Toshiyuki Naganuma# and Nobuyuki Suzuki#

#: Aerospace Div., Japan Aircraft Mfg. Co., Ltd,
3175 Showa-machi, Kanazawa-ku, Yokohama 236-8540, JAPAN
E-mail: tjinishi@mail.nippi.co.jp

Abstract

Superplastic forming process enables us to produce a monolithic structure with complex shape. This process is usually applied to blow forming, and sometimes problems happen on thickness distribution of formed parts. So, a new method of superplastic forming process has been studied in order to control the thickness distribution by using a tailored blank sheet. Some of fundamental properties of superplastic deformation were observed on a forming experiment using Al5083 sheets with weld lines. The area of weld line in the blank sheet lost property of superplasticity due to remelting and recrystallization to anisotropic grain in microstructure. Therefore, weld area on the blank sheet did not elongate superplastically to the direction parallel with the weld line direction during superplastic forming. On the other hand, an area free from recrystallization was elongated enough on perpendicular direction to the weld line. This method is also expected to be applicable to superplastic forming of a new monolithic structure made from combined materials with different properties.

Key Words: Superplastic forming, Welding, Tailored blank.

Introduction

Superplastic forming (SPF) process is suitable for a fabrication of monolithic structure with complex shape. For this reason, SPF process has been used in some fields, such as aircraft or automobile manufacturing. This process usually uses gas blow forming for sheet metal, and sometimes problems happen on thickness distribution of formed part. As a way to control thickness distribution on formed part, some processes using a blank sheet adjusted with thickness distribution before forming have been researched. There are some papers regarding these processes. One of these processes is an application of blank sheet which made thickness distribution by machining [1]. The other is an application of blank sheet with thickness distribution prepared by SPF as a preforming [2]. These are effective methods to control thickness distribution for some parts. However, these methods cannot control material properties locally on formed part. For example, in automobile industry, tailored blank sheet that is welded different thickness or property steel sheets has been pressed into required shape. The formability of the tailored blank sheet has been reported in some papers [3]. It is expected that the tailored blank sheet can be used on SPF to control thickness distribution. This technique is expected to extend

application of SPF to many portions of structure. However, there are few reports regarding superplastic formability of blank sheet with weld line. So, in this paper, fundamental properties of superplastic deformation are observed and verified on a forming experiment using 5083 SPF aluminum alloy sheets with weld lines.

Experimental Procedures

Material and Forming Die

5083 SPF aluminum alloy was used for a blank sheet. The *m* value of this alloy is 0.5 (nominal). 1.0mm thickness 5083 aluminum alloy sheets were used and butt welded. Test article has been formed into long and narrow container shape that has a rectangle cross section. Fig.1 shows the shape of transverse section. Longitudinal section has trapezoid shape with 45 degrees oblique sides. This article is 400mm long and 50mm width. Since the length is much longer than width, it can be considered as a plane strain forming at the center of this article. So evaluation is made on deformation at the center. The forming die is made of SUS304 stainless steel. The die surface was finished to roughness Ra=1.5μm. The die surface was coated using BN powder lubricant with uniform thickness.

Welding Conditions

Electron beam welding (EBW) was used for fabrication of blank sheet on this study because of narrow bead and heat affected zone. The blank sheet size and locations of weld line were set up as shown in Fig.2 (a) and (b) to verify formability of perpendicular and parallel direction respectively to weld line.

Forming Condition

A press machine with hot platens was used for the experiment. The die is set in the press machine, and heated up and kept at 789K±5K.

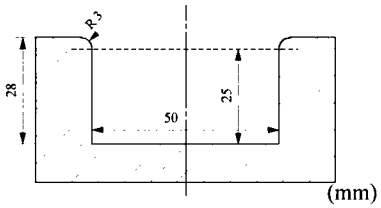

Fig.1 Cross Section of Forming Die

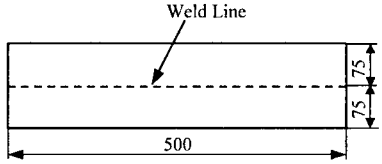

(a) Longitudinal Weld Line for Verifying Formability of Perpendicular Direction to Weld Line

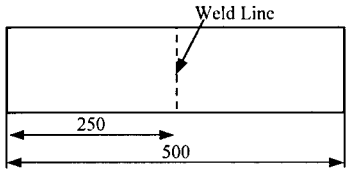

(b) Transversal Weld Line for Verifying Formability of Parallel Direction to Weld Line

Fig.2 Shape and Welding Location of Blank Sheet (mm)

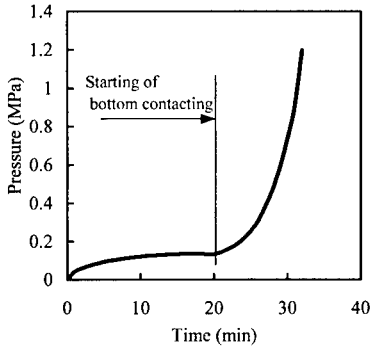

Fig.3 Pressurization Schedule

Argon gas pressurization schedule for the forming was set up, with maximum strain rate of $5 \times 10^{-4} s^{-1}$, calculated using original simulation code [4]. The applied pressurization schedule is shown in Fig.3.

Results and Discussion

Fig.4 shows a cross section of the butt welded blank sheet by EBW before forming. A width of fused metal and heat affected zone was approximately 1.5mm. No reinforcement of weld in thickness was formed, and thickness reduction was very small.

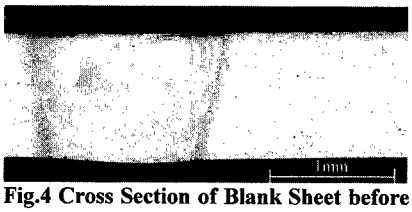

Fig.4 Cross Section of Blank Sheet before Forming

Formability of Perpendicular Direction to Weld Line

Fig.5 shows an article formed using the blank sheet with the longitudinal weld line (Fig.2 (a)). The article is formed almost along the die surface in good condition. This result is similar to an article of a blank sheet without weld line.

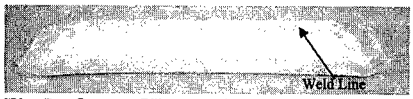

Fig.5 Over View of Formed Article (Longitudinal Weld Line)

Fig.6 shows a cross section at the center of the formed article. The thickness after forming was reduced approximately to 1/2 from the blank sheet before forming. At the center of the bottom, the shape of the weld bead can be seen clearly. A magnified view of this portion is shown in Fig.7. The weld bead was not deformed and the blank sheet around the bead was deformed. The base metal was reduced its thickness to 1/2, and formed fillet radius at the weld bead. Some blowholes in the weld bead are observed, and they kept their round shape after forming. There was no deformation at the weld bead. On the other hand, because of large deformation reducing its thickness to 1/2, some minute cavities were formed in the base metal.

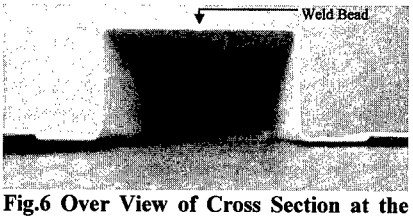

Fig.6 Over View of Cross Section at the Center of Formed Article

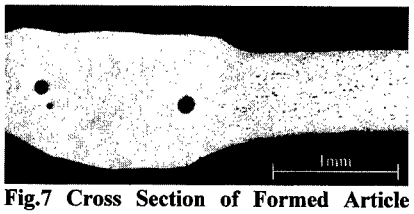

Fig.7 Cross Section of Formed Article (Longitudinal Weld Line)

Formability of Parallel Direction to Weld Line

Fig.8 shows an article formed using the blank sheet with the transversal weld line (Fig.2 (b)). In the latter stage of forming, some small holes were opened through the weld bead, and the forming gas leaked from these holes. So, the forming has not been completed along die surface.

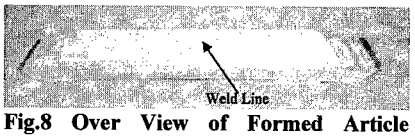

Fig.8 Over View of Formed Article (Transversal Weld Line)

Fig.9 shows the longitudinal cross section at

the bottom of formed article including the weld bead. This photo shows that the thickness on both sides of the weld bead is reduced in the same way as in the article with the longitudinal weld line.

Fig.9 Zoom Up View of Cross Section at the Center of Formed Article

The magnified view of a cross section of the formed article at the weld bead area is shown in Fig.10. Fig.11 shows a plane view at the boundary of the weld bead. Thickness of the base metal was reduced, and forming of fillet radius was the same as in the longitudinal weld line forming. However, some large voids in the weld bead are observed, as shown in Fig.10 and Fig.11. The blowhole that appears in Fig.10 at near center of the weld bead was deformed. It shows that the weld bead was deformed plastically. These voids arose in the weld bead grew and joined each other with the progress of forming. In the latter stage, the forming gas leaked and the forming could not be completed. It is considered that the weld bead does not have property of superplasticity.

Fig.10 Cross Section of Formed Article (Transversal Weld Line)

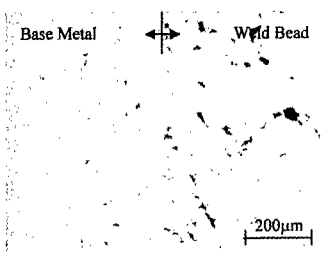

Fig.11 Plane View of Weld Bead

Summary

Fundamental properties of superplastic deformation have been observed and verified on a forming experiment using 5083 superplastic forming aluminum alloy sheets with weld lines. As a result, it has been verified as follows,

(1) Superplasic forming on perpendicular direction to the weld line is completed in good condition, and the influence of the weld line is light.

(2) In the case of superplasic forming to the direction parallel with the weld line, the forming is not completed since voids increase and make holes in the weld bead with the progress of forming.

Acknowledgment
This work was supported by Aerospace Division, Japan Aircraft Mfg. Co., Ltd.

References

1. A. Takahashi, S. Shimizu and T. Tsuzuki: Japan Society for Technology of Plasticity, 31(356), 1128 (1990).
2. N. Suzuki, M. Kohzu, T. Jinishi, S. Tanabe and K. Higashi: Japan Inst. of Light Metals, 51 (1), 14 (2001).
3. K. Ikemoto, H. Sugiura, K. Azuma, K. Arima and T. Takasago: Japan Society for Technology of Plasticity, 32 (370), 1383 (1991)
4. N. Suzuki, M. Kohzu, S. Tanabe and K. Higashi: Materials and Science Forum, 304-306, 777 (1999).

Proceedings of 7th Japan International SAMPE
Symposium & Exhibition, Nov. 13-16, 2001

Fatigue Evaluation on Composite Parts of Eurocopter Helicopters

Dr. Horst BANSEMIR, Gabriele DREHER* and Stefan EMMERLING

EUROCOPTER Deutschland GmbH
81663 München, GERMANY
*86607 Donauwörth, GERMANY
E-mail: stefan.emmerling@eurocopter.com

Abstract

The Helicopter composite structures are designed to meet the latest certification requirements. These also ask for some new specific characteristics concerning structure related safety aspects such as damage tolerance. The development and substantiation of some dynamically loaded composite structures such as the horizontal stabilizer and the rotor blade of the BK117 C-2 and the carbon fenestron drive shaft of the EC135 are presented, taking into account the presence of certain structural defects like impacts or manufacturing flaws. The damage tolerance evaluation has been performed analytically based on test results. The results are an important basis for the definition of inspection and maintenance procedures for the helicopter. Substantiation methods such as flaw tolerance safe life and damage tolerance as described in the FAR 29.571 are used to certify composite structures. In addition the Special Conditions 'Primary Structures Designed with Composite Material' of the LBA (Luftfahrtbundesamt: German Airworthiness Authority) had to be fulfilled. NDT methods are used to detect failure modes such as delaminations and fiber cracks. The results of the substantiation are composite structures with high replacement times or inspection intervals.

Key Words: Fatigue Evaluation, Composite, Eurocopter

Introduction

Beginning with the BO105 helicopter in 1970, and followed a decade later with the BK117, MBB Helicopter Division - now EUROCOPTER Deutsch- land - brought up two innovative products, which both revolutionized the market by advanced design features. Their characteristics included twin engine application, four-bladed hingeless rotor "System Bölkow", redundant system layout, and rear loading capability together with a one-level cabin and compartment floor for unobstructed cabin use. The BK117 was co-developed with Kawasaki Heavy Industries of Japan, who was responsible mainly for design and manufacturing of the center fuselage, main gear box and electrical system as well as fuel tank design.

In the 90's, further improvements such as glass cockpit technology and aerodynamic optimized fuselage shaping, along with the use of composite material and new fabrication methods - not mentioning other design features - led to development of the light twin EC135 [1] as successor to the BO105. As a logical step, the BK117 C-2 (EC145) now follows to satisfy market demands of the new century by taking the best technology available from EC135 and BK117, and providing customers a state-of-the-art technology medium twin helicopter meeting their requirements for present and future operations [2] (Fig. 1).

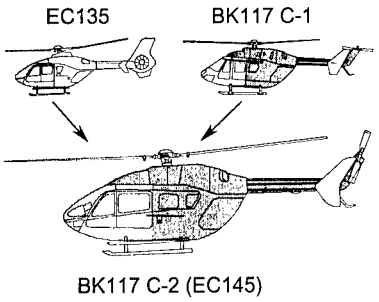

Fig. 1: BK117 C-2 Evolution

BK117 C-2 Horizontal Stabilizer

A good example for a fatigue loaded composite part of the BK117 C-2 fuselage structure is the horizontal stabilizer. It consists of two major parts, the wing box made in carbon fiber composite with a resin system curing at 180°C and the end flag which is a sheet metal design. The wing box carryies the aerodynamic loads coming from the horizontal stabilizer and the end plates and comprises two spars (forward and rear spar) and the leading edge which are carried out in monolithic design and the skin area designed as honeycomb sandwich structure to avoid ribs (Fig. 2).

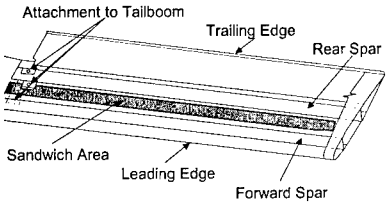

Fig. 2: Horizontal Stabilizer (lh)

The horizontal stabilizer is connected to the tailboom via a metallic fitting riveted on the tailboom structure to which it is attached with two bolts on each side (Fig. 3).

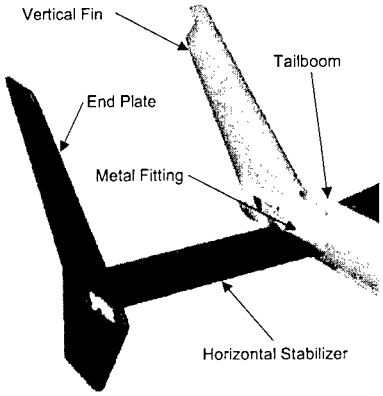

Fig. 3: Installation of BK117 C-2 Horizontal Stabilizer on Tailboom

The fatigue requirements to be fulfilled are given in FAR29.571 and in the „Special Conditions: Primary Structures Designed with Composite Material" which were defined by the authorities. One of the main design goals was to get a structure without any lifetime limitation (unlimited life) and large inspection intervals.

To meet this challenge the horizontal stabilizer is designed as a damage tolerant structure. The two spars allow to consider the design as a multiple load path structure. Allowable manufacturing defects and barely visible impact damages (BVID) which can be realistically expected during operational service are taken into account for the dimensioning of the structure. The maximum size of manufacturing defects to be considered is limited by the NDT techniques applied during the manufacturing process by the quality assurance.

Based on the material data, the structural design and the external loads a detailed FE-model is established (Fig. 4) to determine the internal loads in the structure.

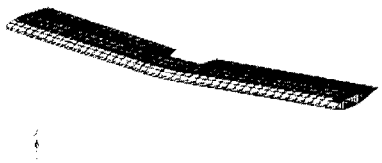

Fig. 4: FE-model of Horizontal Stabilizer

Now for each part of the structure the stress analysis and strength substantiation is carried out. The internal load distribution resulting from the FE-model has been verified by a static limit load test (Fig. 5).The comparison of the theoretical results to the test results showed a good correlation concerning the internal loading distribution and confirmed the analytical results of the strength substantiation.

Fig. 5: Static Limit Load Test

For the fatigue substantiation of these types of defect the „no-growth-approach" is chosen, i.e. the damage may not grow during the complete life of the structure under the occurring loads to such an extent that the structural strength will be reduced below Design Ultimate Load (DUL). To fulfil this requirement a strain limit is applied to the structure as a dimensioning criterion. The strain threshold where a damage begins to grow under fatigue loading has been determined by specific fatigue tests on coupon level carried out with the material used for the horizontal stabilizer. This approach was already verified in previous programs by full scale fatigue tests containing representative manufacturing defects and BVID's.

BK117 C-2 Main Rotor Blade

The BK117 C-2 main rotor blade design (Fig. 6) includes a 150kg thrust increase at comparable power versus BK117 C-1, noise reducing parabolic blade tip shape, leading edge with nickel erosion protection, integration of balancing weights to allow blade interchangeability, and the use of advanced prepreg fabrication methods. A newly developed series of advanced blade airfoils with optimised distribution over the blade radius was applied. The blade planform with negative taper and the twist distribution were based on the experience gained in former research programmes.

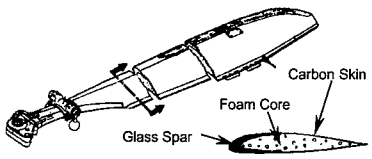

Fig. 6: Main Rotor Blade of BK117 C-2

Experience from the fleet of BO105 and BK117 helicopters led to an investigation on the fatigue damage tolerance of the main rotor blades. The goal of the study was to prove that damages in the fiber loop of the blade root attachment grow with a slow rate [3].

For fatigue testing the blade root is loaded with centrifugal force, torsional moment and flapwise and lead lag bending. During the fatigue test several non destructive inspections of the test specimen were carried out using computer tomography [4]. The crack development as well as the spreading of delaminations were monitored.

Additionally tests on the whirl tower were done to examine the influence of the propagating damage on the behavior of the blade. The damage propagation was simulated by successive cuts with increasing depth into the fiber loop. A clear correspondence between the damage size and main rotor imbalance and lead lag track could be demonstrated. Both of these deviations from normal blade behavior can be measured and provide an indirect detection method for the internal damage. The maximum damage was simulated by cutting 60% of the cross section of the fiber loop (Fig. 7).

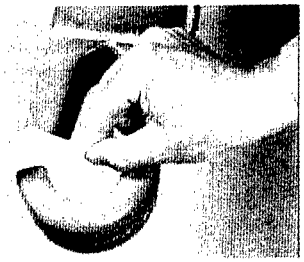

Fig. 7: Maximum simulated Damage on Blade Root

After whirl tower testing the damaged blade was subjected to an test with 1.5 times the limit load without fracture. This proved the residual strength capacity with a clearly detectable damage size.

EC135 Fenestron Drive Shaft

The dynamic performance of subcritical drive shafts running with high speed is highly influenced by their weight and bending stiffness. The use of carbon fiber composite offers the opportunity to create an advantageous relation between weight and bending stiffness. Furthermore the proportion between bending and torsional stiffness can be adjusted to the requirements.

These features helped to improve the fenestron drive train of the EC135. Figure 8 shows the shafting with one long steel shaft and two short shafts being previously made of aluminum and now replaced by carbon composite.

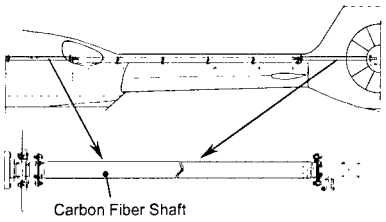

Fig. 8: Carbon Fiber Fenestron Drive Shaft of the EC135

The carbon fiber design of the short drive shafts fulfils the following important requirements:

- damage tolerance
- infinite life
- higher Eigenfrequency (even at slightly higher length)
- less weight
- same cost as aluminum part

For the certification of the shafts the special conditions for fiber composites had to be satisfied. To show the dynamic strength after impact damage tests with shafts impacted at 25 J were carried out. These tests were stopped after the required number of load cycles to demonstrate ultimate strength after dynamic loading with impact/defect. The mean S/N curve is reduced by a factor of 0.75 to account for the required statistical values for the survivability and confidence level. The resulting working S/N curve (Fig. 9) shows dynamic torque load versus number of load cycles and yields unlimited lifetime for the carbon shafts.

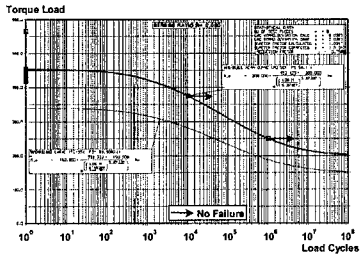

Fig. 9: S/N Curve of the Drive Shaft

Also the sensitivity against manufacturing defects was taken into account. Static tests on specimen with a 25 J impact and with artificial manufacturing defects proved the equivalence of the impact damage and the considered manufacturing defects. To care about the variation of the impacts each tested shaft has three impact locations. Figure 10. shows the shaft after completion of the test.

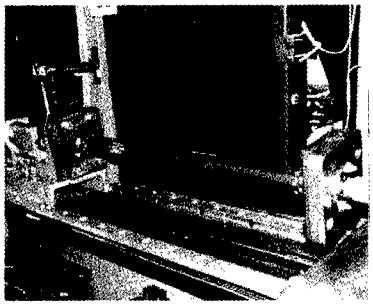

Fig. 10: Drive Shaft after Rupture

Conclusions

Fiber composite structures are increasingly spreading in aeronautic applications since the last decades. For helicopters important improvements were achieved with composite rotor blades leading to simpler concepts, less weight and maintenance effort combined with higher reliability and service life. New developments feature fiber composites also in other components of the dynamic system as well as in the airframe structure and empennage.

Composite parts show a good damage tolerance potential which is important to meet the more and more stringent demands of the certification.

For the customer composite components are highly reliable and cost effective due to high replacement or inspection intervals.

References

[1] C. Zwicker, Configuration and Program Status of EUROCOPTER's New Light Twin Helicopter EC135, 19th ERF, Cernobbio, Sept. 1993

[2] A. Humpert, Design, Development and Flight Testing of the new EUROCOPTER EC145 Medium Twin, 27th European Rotorcraft Forum, September 2001, Moscow

[3] R. Pfaller, H. Bansemir, K. Pfeifer, Entwicklung schadenstoleranter Faserverbundstrukturen für Hubschrauber, DGLR Jahrestagung, 18.-21. September 2000

[4] R. Oster, Computed Tomography as a Nondestructive Test Method for Fiber Main Rotor Blades in Development, Series and Maintenance, 23rd European Rotorcraft Forum, Dresden, Germany, 16-18 September 1997

Proceedings of 7th Japan International SAMPE
Symposium & Exhibition, Nov. 13-16, 2001

Methodology for Predictable Damage Growth Design of Aircraft Composite Structures

Hiroshige Kikukawa#

#Japan Aircraft Development Corporation
Toranomon Daiichi Bldg., 2-3 Toranomon 1-chome, Minato-ku, Tokyo, 105-0001 Japan
E-mail: hkikukawa@jadc.or.jp

Abstract

The discrepancy of DTD methods is existent between composite structures and aluminum structures. The composite structures are currently designed by no-growth concept, whereas the aluminum structures are designed by damage growth concept. In the early stage for application of composite materials, fracture mechanics were not enough to be known to design by damage growth concept. Methodology for predictable damage growth design is presented by founding on the many recent studies.

Key Words: composite structure, damage growth, purpose, methodology

Introduction

The stress threshold of delamination growth at hole edges in composite structures is 40% thru 50% of failure load. This is very high stress level in comparison with that of cracking at notches of aluminum alloy. e.g. 10%. Owing to this superiority, the design method based on no-growth concept has been main policy of long standing in the practice of composite structure design. Historically the damage growth concept was poorly understood, the lack of knowledge led to overdesigned, i.e. overweight.

Purpose of PDGD

The purposes of Predictable Damage Growth Design (PDGD) are
(1) To put the improvement of design allowables into practice through Damage Growth Simulation and Residual Strength Prediction for advanced composite materials application to new aircraft such as Sonic Cruiser (SC).
(2) To realize the weight saving needs for Super Sonic Transport (SST) or Reusable Space Vehicle (SSTO).
(3) To maintain the flight safety of aging aircraft.

Improvement of design allowables

In comparison between CAI(Compression strength After Impact) and OHC(Open Hole Compression strength), CAI<<OHC for brittle resin in the past. However CAI≧ OHC for current tough epoxy resin or tough thermoplastic resin [1]. Design allowable for CAI can be reformed by reflecting the improvement of resin. As the impact damage size of these tough resins is non-visible, damage growth from small defects must be predicted.
Similarly in tension loading, the matrix crack initiation has been delayed from 0.35% strain of brittle resin in the past [2] to 0.70% strain of current tough epoxy resin [3]. The tension allowable can also be reformed and then the increase of matrix crack density must be predicted.

PDGD is effective procedure to predict damage growth from small impact damage and increase of matrix crack density.

Weight saving needs

By the improvement of design allowables mentioned above, much weight saving can be attained. Non-visible CAI design gives about 6% structural weight saving by improving compression allowables from 25% of intact compression strength to 60% in the application to CAI critical parts of wing upper side. Matrix crack tolerant design gives about 14% structural weight saving by improving tension limit allowables from 0.35% strain to 0.70% in the application to tension critical parts of wing lower side, empennage and pressure cabin.

Super sonic transport (SST) or Reusable space vehicle (SSTO) needs 50% weight saving in comparison with conventional aluminum structures. No-growth design gives at most 40% weight saving by the maximum composite application up to 90% structural weight , but can not attain a full need. PDGD based on non visible CAI design and matrix crack tolerant design gives about 10% additional weight saving and then can attain the full need, i.e. 50%.

Flight safety of aging aircraft

The total number of commercial transport aircraft in service at the end of 2000 is about 22,300. Looking on the design life as 20 years, 30% of them (i.e. about 6,400) are over the design life. Airworthiness of aging aircraft must be maintained as long as the aircraft remain in service by keeping enough flight duration through the damage detection and repair. PDGD based on damage growth concept is the most effective procedure to decide detectable damage size and inspection intervals.

Methodology of PDGD

One of main purposes of PDGD is on estimation of Time Before Catastrophic Failure (TBCF). Damages in composite structure are divided into the following four kinds by their sources. (i)Pre-existing damage, (ii)Damage initiation,(iii)Impact damage and(iv)Discrete source damage. Of these damages, PDGD is needed for (i)(ii) and (iii) because of the origin (small defects) of damage growth in service.

Approach

An approach is shown in Fig.1.In the current design based on no-growth concept, residual

Fig.1 Approach to Predictable Damage Growth Design to estimate Time Before Catastrophic Failure

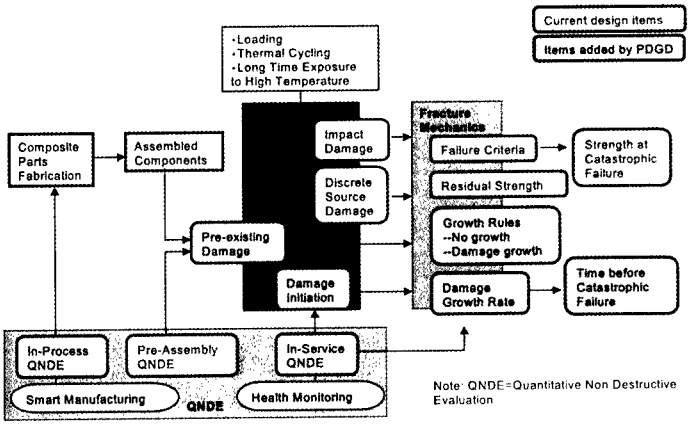

strengths for visible impact damage and discrete source damage are estimated. In PDGD based on damage growth concept, non visible damages such as pre-existing damage, damage initiation and small impact damage are newly defined and then the damage growths from them are predicted.

Pre-existing damage and growth rate

In the process of drilling, edges of hole are subject to very small defects as same as aluminum structures. In case of composite structures pre-existing damages by drilling are chipout, delamination and oversize. The location and size can be defined by hole accept/reject criteria [4] in pre-assembly inspection.

An example of characterization for damage growth rate from hole edge delamination is shown in Fig.2. In this characterization the similar method as crack propagation formula of aluminum alloy, i.e. the function of stress intensity factor, was found to be applicable.

Fig.2 Example of Damage Growth Rate

(1) Damage Location and Size:
Pre-existing damage by drilling

(2) Delamination Growth Rate:
$db/dN = C[\Delta\tau\sqrt{b}]^n$
$\Delta\tau = f(b/D)(\tau_{max} - \tau_{min}) - \tau_{th}$
for T300/#3601
$db/dN = 2.76\times10^{-13}(\Delta\tau\sqrt{b})^{8.01}$
for T500/#3620
$db/dN = 5.42\times10^{-12}(\Delta\tau\sqrt{b})^{6.73}$
for AS4/PEEK
$db/dN = 3.94\times10^{-9}(\Delta\tau\sqrt{b})^{3.98}$

(3) Empirical Factor f(b/D):
$f(b/D) = 1.06 - 0.127(b/D)$

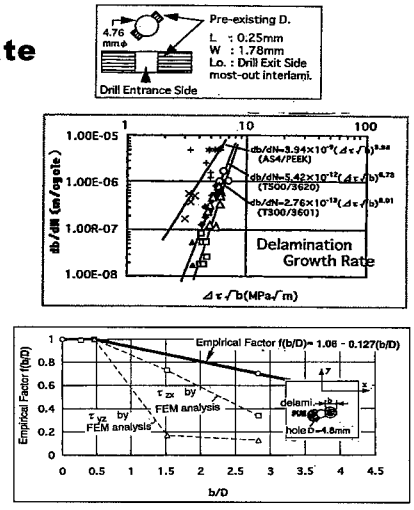

Damage initiation and growth

Some results of recent damage mechanics analyses [5] [6] [7] indicate the capability to predict matrix crack initiation and density growth rate as shown in Fig.3. The matrix crack density growth rate is characterized as a function of energy release rate range.

Impact damage

Prediction of multiple layer delamination growth studied by H.Suemasu (Sophia University), Prediction of growth and residual strength for coexisting transverse cracks and delaminations studied by M.Zako (Osaka University) [8] are interested as a method to characterize the complicated multiple layer damage due to impact.

Other damages

Other damages to be developed for their growth and residual strength are porosity, post impact fatigue (PIF), discrete source damage.

Construction of Methodology

There are many assumptions in fracture mechanics of composite materials and structures. Many and much efforts are necessary to get complete knowledge and to construct the methodology of PDGD through a process started from many assumptions as shown in Fig.4.

FIG.3 Damage Initiation and Growth Characterization of Matrix Cracking by S.Kobayashi,S.Ogihara and N.Takeda

Matrix Crack Initiation

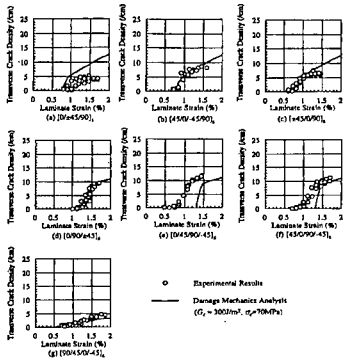

Figure 7. Transverse crack density in 90° plies as a function of laminate strain (experimental results and analytical predictions, σ_T^s = 70 MPa and G_c = 300 J/m²)

Matrix Crack Density Growth Rate

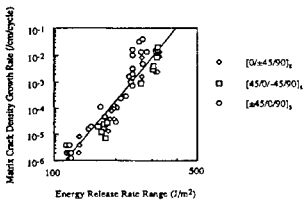

Fig. 11: Matrix crack density growth rate as a function of energy release rate range.

Material:T800H/3900-2

References

Fig.7: S.Kobayashi, S.Ogihara and N.Takeda, Adv. Composite Materials, Vol.9.No.3 pp.241-251 (2000)

Fig.11: S.Kobayashi, S.Ogihara and N.Takeda, Science and Engineering of Composite Materials, Vol.9, No.2,pp.45-54 (2000)

Conclusions

(1)The purposes of PDGD are improvement of design allowables and realization of additional weight saving needs for new aircraft and maintaining flight safety of aging aircraft.

(2)Many current comprehensive studies to characterize the complicated phenomena concerned about fracture mechanics of composite materials lead to the construction of methodology for PDGD.

Fig.4 Effort from many Assumptions to complete Knowledge

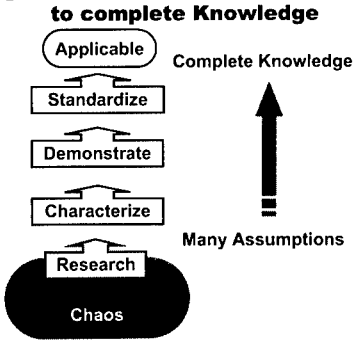

References

1. data presented by T.Ishikawa (NAL),2001
2. N.Takeda, et al. Proceeding of Smart Materials Symposium 2000, RIMCOF, 2000, pp.63-68.
3. data presented by N.Takeda (The university of Tokyo), 2001.
4. Pengra,J.J and Wood,R.E., AIAA 80-0777, 1980, Table II.
5. Kobayashi,S., Ogihara,S., Takeda,N., Adv. Composite Materials, Vol.9, No.3, 2000, pp.241-251.
6. Kobayashi,S., Ogihara,S., Takeda,N., Science and Engineering of Composite Materials, Vol.9, No.2, 2000, pp.45-54.
7. Kageyama,K., An annual report (SST) of RIMCOF, 2001, pp.368-384.
8. Zako,M., An annual report (SST) of RIMCOF, 2001, pp.385-404.

Proceedings of 7th Japan International SAMPE
Symposium & Exhibition, Nov. 13-16, 2001

Durability Analysis of Composite Structures Using the Accelerated Testing Methodology

Akira Kuraishi and Stephen W. Tsai

Department of Aeronautics and Astronautics, Stanford University
496 Lomita Mall, Durand 250, Stanford, CA 94305-4035, USA
akirak@leland.stanford.edu

Abstract

The use of composite materials is increasing steadily in many applications, but not as much in the durability critical applications. One reason is that the durability of composite materials is hard to characterize due to their viscoelastic nature. The Accelerated Testing Methodology is an efficient and systematic method of characterizing the viscoelastic material properties, through series of short-term tests at elevated temperatures. In this paper, we will show the outline of the durability design of composite structures using this methodology. The methodology provides valuable long-term predictions that can be used for the material selection, design guidelines, design optimization, and proof test.

Key Words: Durability, Accelerated Method

Introduction

The use of composite materials is increasing steadily due to their high specific properties and design flexibility. In applications such as certain sporting goods, composite materials have completely replaced conventional materials. On the other hand, the use of composite materials is still very limited in the durability critical applications, such as the commercial aircraft applications. One reason is that the durability of viscoelastic materials, such as composite materials, is hard to characterize.

S-N curve is the most common tool used to study the durability of conventional materials. Based on the assumption that fatigue strength depends on cycles but not on time, the test can be accelerated by applying the cyclic loading at high frequencies. This assumption does not hold for polymeric composite materials, whose stiffness and strength show strong time- and temperature dependence. This time-dependence, which can also be called the rate-dependence, is not observed in conventional metals and is often ignored in most test, analysis, and design methods.

Design of Composite Structures

In the design of a structure, the internal stresses are analyzed and are compared with the design allowables. For composite materials, these design allowables are time- and temperature-dependent, and must be obtained through time-consuming tests. For example, if the service life is 15 years, regular approach calls for 15 years of tests at the same condition. This is not practical, and thus

we resort to accelerated methods such as the Accelerated Testing Methodology (ATM) proposed by Miyano [1]. Using this methodology, long-term material properties can be predicted through series of short-term tests.

Fig.1 shows the outline of a proposed durability design method using the ATM. The long-term predictions can be used as the basis of the material and process selections. They can also be used as the design guidelines to optimize the structure for durability and performance. ATM also provides useful information for the design of a proof test.

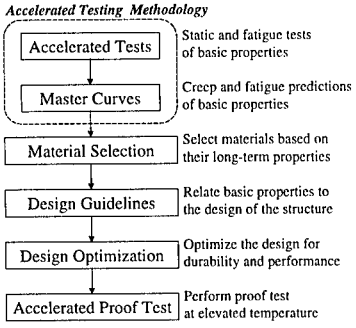

Fig.1 Durability Design Method

Let us set our goal to analyzing the durability of a composite structure subject to either creep or fatigue loading for 15 years at 50°C. For the fatigue loading, we assume 10,000 load cycles in 15 years.

Accelerated Testing Methodology

The Accelerated Testing Methodology is based on the time-temperature superposition principle of polymeric materials, which relates the effect of temperature and the effect of time on the strength and stiffness. In this methodology, elevated temperatures are used to accelerate the mechanical degradations, which occur under loads over long period. Not only are the tests accelerated, but the results are applicable to wide ranges of temperature and time to failure.

Using this as the building block, the methodology predicts the long-term static (constant-strain-rate), creep, and fatigue strengths as shown in Fig.2.

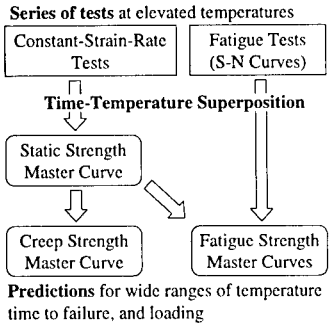

Fig.2 Accelerated Testing Methodology

Using this methodology, valuable database for the durability design can be generated in a relatively short period.

Sample Test Results

Composite materials are highly anisotropic, and their strengths differ greatly according to the directions. The following are some examples from the published test results of the two most important strengths of a composite lamina, namely the longitudinal and transverse tensile strengths.

The longitudinal tensile strength of CFRP was measured by Miyano et al [2] using the carbon fiber strand tension test. Fig.3 shows the test results and the master curve of the static strength. The constant-strain-rate tests were performed for 3 strain rates and 6 temperatures. The

measured static strengths were plotted on logarithm of time to failure as shown to the left. These measurements were contracted into a single master curve using a combination of temperature and time to failure as the horizontal axis. This new parameter is called the reduced time, and can be related to the Arrhenius equation.

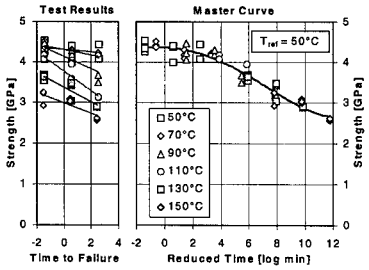

Fig.3 Static Master Curve (CFRP Longitudinal Tension)

Fig.4 shows the master curve of the creep strength calculated from the static master curve above using an equation derived from the cumulative damage law.

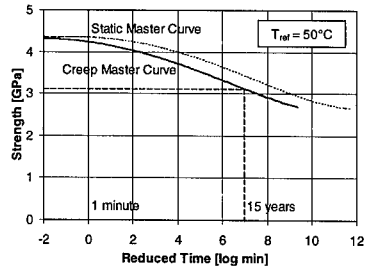

Fig.4 Creep Master Curve (CFRP Longitudinal Tension)

Fig.5 shows the fatigue master curves generated by applying the time-temperature superposition to the S-N curves from the fatigue tests at elevated temperatures. The vertical axis is the applied stress amplitude, the horizontal axis is the reduced time to failure, and the different curves represent different numbers of cycles to failure.

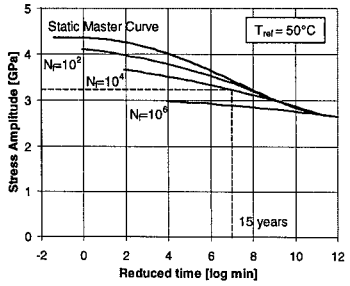

Fig.5 Fatigue Master Curves (CFRP Longitudinal Tension)

The master curves of the transverse tensile strength of CFRP were generated by Miyano et al [3] using the transverse bending test of the CFRP laminate. Fig.6 shows the static, creep, and fatigue master curves of CFRP transverse tensile strength.

Note that the reduction in the transverse strength is more significant than in the longitudinal direction.

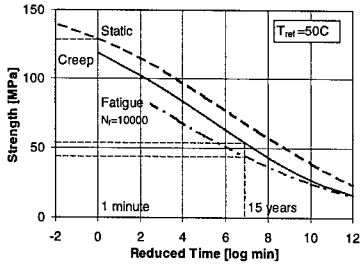

Fig.6 Master Curves (CFRP Transverse Tension)

The maximum allowable stresses in the longitudinal and the transverse directions are summarized in Table 1.

Table 1 Maximum Allowable Stresses

Loading	Static	Creep	Fatigue
	1min	15years	15years 10^4cycles
Longitudinal	4400	3100	3200
Transverse	129	54	45

Stresses in MPa

Typically, the static strength is measured using a constant-strain-rate test with a time to failure of about 1 minute. Compared to this static strength, the creep and fatigue strengths for 15years are about 70% in the longitudinal direction and about 35% in the transverse direction.

Note also that the difference between the allowable stresses at 15 years ($10^{6.9}$minutes) and 60 years ($10^{7.5}$minutes) are very small. This suggests that the typical safety factor of 4 in life may not be sufficient for the safe design.

Durability Design Guidelines

From the results shown above, the following durability design guidelines can be derived.

(1) The longitudinal stress must be designed below 70% of the longitudinal tensile static strength.

(2) The transverse stress must be designed below 35% of the transverse tensile static strength.

(3) The creep loading is more critical for longitudinal stress, and fatigue loading is more critical for transverse stress.

Accelerated Proof Test

The results suggest that a proof test under normal conditions can overestimate the durability of the structure. Using the time-temperature superposition, we find that 15 years of creep loading at 50°C is equivalent to 1 minute of creep loading at 120°C. Therefore, we can perform a creep test for 1 minute at 120°C as the proof test.

Conclusions

The time- and temperature-dependent strength of polymeric composite materials can be predicted by the Accelerated Testing Methodology. The results can be used as the basis of material selection, guidelines for the durability design, and for the proof test.

Future Work

The design allowables can be generated from the master curves with appropriate statistical analysis. This issue is being studied by the authors, but is outside the scope of this paper.

Acknowledgements

We would like to acknowledge the National Science Foundation for the funding of this research, which is performed jointly with Kanazawa Institute of Technology. We would also like to thank Prof. Miyano, Prof. Nakada, and their students for supplying us with the relevant test results shown in this paper.

References

1. Y. Miyano, M. Nakada, and R. Muki: Mechanics of Time-Dependent Materials, 3, 141 (1999)
2. Y. Miyano, M. Nakada, H. Kudo, and R. Muki: J. Composite Materials, 34, 538 (2000)
3. Y. Miyano, M. Nakada, M. K. McMurray, and R. Muki: J. Composite Materials, 31, 619 (1997)

Proceedings of 7th Japan International SAMPE
Symposium & Exhibition, Nov. 13-16, 2001

Fatigue Life Prediction of CFRP/Metal Bolted Joint under Temperature Condition

Naoyuki Sekine*, Masayuki Nakada**, Yasushi Miyano** and Stephen W. Tsai***

*Graduate School, Kanazawa Institute of Technology
7-1 Ohgigaoka, Nonoichi, Ishikawa 921-8501, JAPAN
E-mail: naoyuki@venus.kanazawa-it.ac.jp

**Materials System Research Laboratory, Kanazawa Institute of Technology
3-1 Yatsukaho, Matto, Ishikawa 924-0838, JAPAN

***Department of Aeronautics & Astronautics, Stanford University
Stanford, CA 94305-4035, USA

Abstract

We proposed a prediction method of fatigue failure load for polymer composite structures under an arbitrary frequency, load ratio (minimum load / maximum load), and temperature from the results of constant elongation-rate (CER) test under various temperatures and loading rates, and fatigue tests at a single frequency under various temperatures. Tensile CER and fatigue tests of CFRP/metal bolted joint were conducted for various temperatures and loading rates. The validity of this method was proven for the tensile fatigue failure load for this CFRP/metal bolted joint

Key Words: Life prediction, Bolted joint, Time-temperature dependence, Fatigue

Introduction

The mechanical behavior of polymer resins exhibits time and temperature dependence, called viscoelastic behavior, not only above the glass transition temperature T_g but also below T_g. Thus, it can be presumed that the mechanical behavior of polymer composites also significantly depends on time and temperature. [1-6],

In our previous papers [7], we proposed a prediction method for the fatigue life of polymer composites under an arbitrary frequency, stress ratio, and temperature from the data measured by constant srtain-rate tests at several strain-rates and various temperatures, and fatigue tests at a single frequency and various temperatures. The validity of this method and the hypotheses was confirmed by three-point bending tests of strain-woven CFRP laminates and others.

In this paper, the validity of the prediction method is discussed for the case of the tensile fatigue failure load of CFRP/metal bolted joint.

Prediction Procedure of Fatigue Failure Load

A prediction method for fatigue failure load of composite structures under an arbitrary frequency,

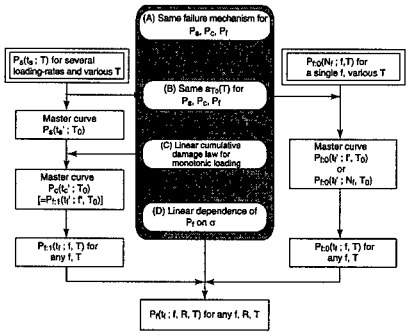

T, T0 : temperature, reference temperature
f, f' : frequency, reduced frequency
tu, tc, tf : time to failure under CER(Constant Elongation Rate), creep and fatigue loadings
tu', tc', tf' : reduced time to failure
aT0(T) : time-temperature shift factor ($a_{T0}(T)=t_u/t_u=t_c/t_c=t_f/t_f'=f'/f$)
R : stress ratio ($R=P_{min}/P_{max}$)
Nf : number of cycles to failure ($N_f=f\cdot t_f$)
Pu, Pc, Pf : CER, creep and fatigue strength
PfO, Pf-1 : σf for R=0 and R=-1

Fig.1 Prediction procedure of fatigue failure load for FRP structures

load ratio, and temperature rests on the four hypotheses; (A) same failure mechanism for CER, creep, and fatigue failure, (B) same time-temperature superposition principle for all failure loads, (C) linear cumulative damage law for monotonic loading, and (D) linear dependence of fatigue failure load upon load ratio. When these hypotheses are met, the fatigue failure load can be determined based on the master curves of CER failure load and fatigue failure load for zero load ratio. The master curve of CER failure load can be constructed from the test results at several elongation-rates for various temperatures. On the other hand, the master curve of fatigue failure load for zero load ratio can be constructed from the test results at a single frequency for various temperatures using the time-temperature superposition principle for the CER failure load. The outline of this method is shown schematically in Fig.1 together with definitions of some notations.

Experimental Procedure

The CFRP/metal bolted joint is constructed from a CFRP pipe, steel rod (C45), and bolt as shown in Fig.2. The CFRP pipe is joined to steel rod by two ¼-20UNC bolt with small washer. The thickness of CFRP pipe is 2.6mm. The fracture of these bolted joints occur at the corner of CFRP pipe at ¼-20UNC bolt.

The tensile CER tests were carried out under various loading rates and temperatures. The loading rates were 0.01, 1 and 100mm/min. The creep tests were carried out under various temperatures. The tensile fatigue tests were carried out under various temperatures at two frequencies f=5 and 0.05Hz. Load ratio R was 0.05. Furthermore, the fatigue tests at f=5Hz and R=0.5 were also conducted under several temperatures.

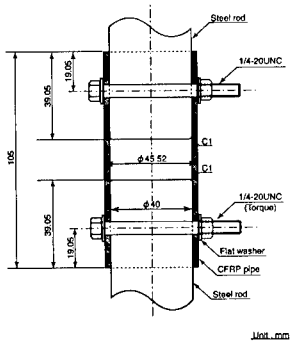

Fig.2 CFRP/metal bolted joint system

Results and Discussion

Master Curve of CER Failure Load

The left side of Fig.3 shows the tensile CER failure load P_s versus time to failure t_s, where t_s is the time period from initial loading to maximum load. The master curve for P_s was constructed by shifting P_s at various constant temperatures along the log scale of t_s so that they overlap on P_s at the reference temperature T_0 or on each other to from a single smooth curve as shown in the right sides of this figure. Since the smooth master curves can be obtained, the time-temperature superposition principle is applicable for P_s.

Time-temperature shift factor $a_{T0}(T)$ is defined by

$$a_{T_0}(T) = \frac{t_s}{t_s'} \tag{1}$$

where t_s' is the reduced time to failure.

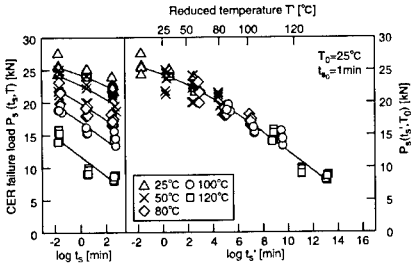

Fig.3 Master curve of CER failure load

The time-temperature shift factors $a_{T0}(T)$ for P_s obtained experimentally in Fig.3 are plotted in Fig.4. These $a_{T0}(T)$ agree with those for the storage modulus of the matrix resin for CFRP indicated by dotted lines, which are described by two Arrhenius' equations with different activation energies ΔH,

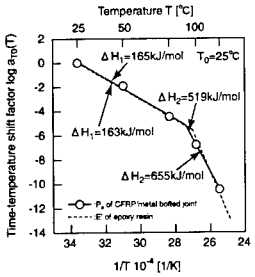

Fig.4 Time-temperature shift factor for CER failure load

$$\log a_{T_0}(T) = \frac{\Delta H}{2.303G}\left(\frac{1}{T} - \frac{1}{T_0}\right) \quad (2)$$

where G is gas constant 8.314×10^{-3}[kJ/mol].

Master Curve of Creep Failure Load

We proposed a prediction method of creep failure load P_c from the master curve of CER failure load using the linear cumulative damage law. Let $t_s(P)$ and $t_c(P)$ be the CER and creep failure times for the load P. Suppose that the material experiences a monotone load history P(t) for $0\le t\le t^*$ where t^* is the failure time under this load history. The linear cumulative damage law states

$$\int_0^{t^*} \frac{dt}{t_c[P(t)]} = 1 \quad (3)$$

Figure 5 displays P_c versus time to failure t_c. The left side shows the experimental data, while right side exhibits the data shifted to T_0=25°C using the shift factors for CER failure load.

The right side of this figure also displays the master curve for predicted P_c in the curve of thick line, which is obtained from the master curve of P_s based on the lines cumulative damage law. The experimental P_c agrees well with the predicted P_c. Therefore, the hypothesis (C) is application to this joint, and it seems that the time-temperature superposition principle for P_s also holds for P_c.

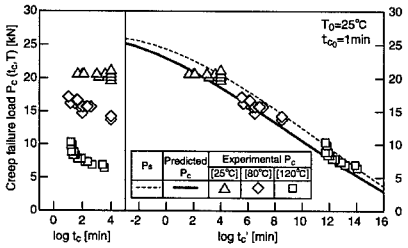

Fig.5 Prediction of creep failure load

Master Curve of Fatigue Failure Load for Zero Load Ratio

We regard the fatigue failure load P_f either as a function of the number of cycles to failure N_f or of the time to failure $t_f=N_f/f$ for a combination of f, R, T and denote them by $P_f(N_f; f, R, T)$ or $P_f(t_f; f, R, T)$. Further, we consider that the CER failure load $P_s(t_f; T)$ is equal to the fatigue failure load at N_f=1/2 and R=0 by choosing t_f=1/(2f). At this point, we introduce special symbols for fatigue failure load at zero and unit load ratios by $P_{f:0}$ and $P_{f:1}$ where the latter corresponds to creep failure load.

Thus, the master curve has the form, $P_{f:0}(t_f'; f', T_0)$. An alternative form of the master curve is possible by suppressing the explicit dependence on frequency in favor of N_f as $P_{f:0}(t_f; N_f, T_0)$. Recall that the master curve of fatigue failure load at N_f= 1/2 reduces to the master curve of CER failure load.

To describe the master curve of P_f, we need the reduced frequency f' in addition to the reduced time to failure tf', each defined by

$$f' = f \cdot a_{T_0}(T),\ t_f' = \frac{t_f}{a_{T_0}(T)} = \frac{N_f}{f'} \quad (4)$$

The $P_{f:0}$ versus N_f ($P_{f:0}$-N_f curve) for FRP joint at f=5Hz and R=0.05 are shown in Fig.6. The $P_{f:0}$ depends remarkably on temperature as well as N_f.

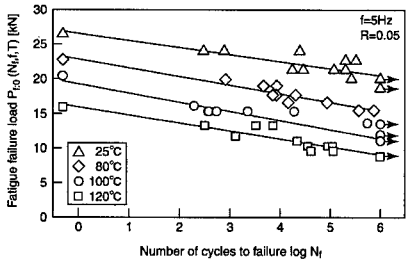

Fig.6 Fatigue failure load versus number of cycles to failure at frequency f=5Hz

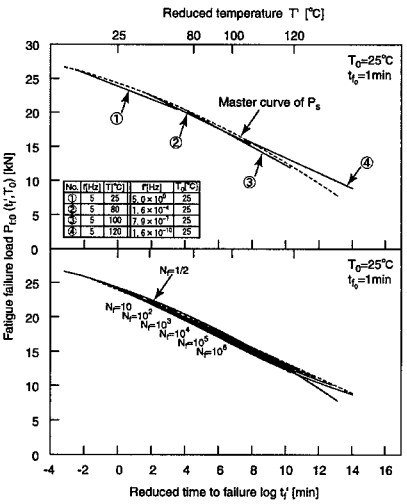

Fig.7 Master curve of fatigue failure load

The upper portion of Fig.7 shows $P_{f:0}$ versus the reduced time to failure t_f'. On the other hand, each point on the master curves of constant reduced frequency represents a number of cycles to failure. Connecting the points of the same N_f with these curves, the master curves of $P_{f:0}$ for constant N_f are constructed as shown in the lower side of Fig.7. This result indicates that the fatigue failure prediction for this joint should be based on time to failure and temperature rather than on cycles to failure.

The $P_{f:0}$-N_f curves of FRP joint at f=0.05Hz and R=0.05 are shown in Fig.8. The solid lines in this figure indicate the predicted $P_{f:0}$-N_f curves at various temperatures obtained from the master curves of $P_{f:0}$ as shown in the lower side of Fig.7. Since the predicted $P_{f:0}$-N_f curves agree with the experimental data, the time-temperature superposition principle for P_s also holds for $P_{f:0}$. Therefore, the hypothesis (B) is valid for this joint.

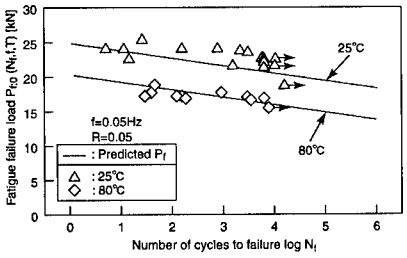

Fig.8 Prediction of fatigue failure load at frequency f=0.05Hz

Prediction of Fatigue Failure Load for Arbitrary Load Ratio

We have the master curve for creep failure load $P_c(t_c'; T_0)$ from which follows the creep failure load at any temperature T. The creep failure load, in turn, may be regarded the fatigue failure load $P_{f:1}(t_f; f, T)$ at unit load ratio and arbitrary frequency f with $t_c = t_f$. Further, from the master curve for fatigue failure load at zero load ratio, we can deduce the fatigue failure load $P_{f:0}(t_f; f, T)$ at zero load ratio for any frequency f and temperature T.

Implementing hypothesis (D), we propose a formula to estimate the fatigue failure load $P_f(t_f; f, R, T)$ at an arbitrary combination of f, R, T by

$$P_f(t_f;f,R,T) = P_{f:1}(t_f;f,T)R + P_{f:0}(t_f;f,T)(1-R) \quad (5)$$

Figure 9 shows experimental data of P_f-t_f for f=5Hz, R=0.5 at various temperatures. The curves of R=0.05 and R=1 respectively represent the least squares fit for experimental data of fatigue test of R=0.05 and R=1. The curves for R=0.5 are calculated from equation (5) on the basis of the curves for R=0.05 and R=1. As can be seen, the predictions correspond well with the experimental data. Therefore, the hypothesis (D) is valid for this joint.

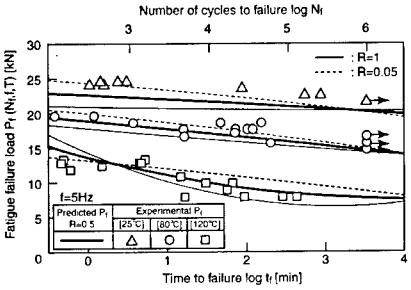

Fig.9 Prediction of fatigue failure load at load ratio R=0.5

Conclusion

We proposed a prediction method of fatigue life for polymer composites and structures under an arbitrary frequency, stress, and temperature from the results of CER and fatigue tests under various temperatures and loading rates. Tensile tests of CFRP/metal bolted joint for CER and fatigue loadings were conducted for various temperatures and loading rates. The validity of this method was proven for the tensile fatigue life for the CFRP/metal bolted joint from these test results. Furthermore, it is found from these experimental results that the fatigue failure load of this joint decreases clearly on time and temperature rather than the number of cycles to failure.

Reference

1. Aboudi, J. and G. Cederbaum, Composite Structures, 12 (1989), p.243.
2. Ha, S.K. and G. S. Springer, J. Composite Materials, 23 (1989), p.1159.
3. Sullivan, J.L., Composite Science and Technology, 39 (1990), p.207.
4. Miyano, Y., M. Kanemitsu, T. Kunio, and H. Kuhn, J. Composite Materials, 20 (1986), p.520.
5. Miyano, Y., M. K. McMurray, J. Enyama, and M. Nakada, J. Composite Materials, 28 (1994),p.1250.
6. Miyano, Y., M. K. McMurray, N. Kitade, M. Nakada, and M. Mohri, Advanced Composite Materials, 4 (1994), p.87.
7. Miyano, Y., M. Nakada, M. K. McMurray, and R. Muki, J. Composite Materials, 31 (1997), p.619.

Proceedings of 7th Japan International SAMPE
Symposium & Exhibition, Nov. 13-16, 2001

Stitch Parameter Effect on Impact Damage Resistance of a New RTM Composites

Tamotsu Osada#, Takayuki Kamiyama#, Tsutomu Yoshimura##

#: Material Research Section, Fuji Heavy Industries LTD.
1-1-11 Yonan, Utsunomiya, Tochigi 320-8564, JAPAN
E-mail: osadat@uae.subaru-fhi.co.jp, kamiyamat@uae.subaru-fhi.co.jp
##: SST project, Japan Aircraft Development Corporation
Daiichi Bldg, 1-2-3 Toranomon, Minato-ku, Tokyo 105-0001, JAPAN
E-mail: tyoshimura@jadc.or.jp

Abstract

This paper presents the effect of stitch parameter (stitch thread size and stitch density) on impact damage resistance of through the thickness stitched composites. The preforms consist of carbon fiber plane weave fabric stitched using two types stitch method with aramid fiber thread (Kevler®) or consist of 3D textile stitched with carbon fiber thread. Test specimens were fabricated from new epoxy resin using RTM process. In order to evaluate impact damage resistance property, compression after impact (CAI) test was performed. As the results of tests, CAI strength was much affected by stitching and stitch parameter. CF stitched specimen shows over 70% higher strain than unstitched specimen at the CAI test. The increase of stitch density contributed the degradation of damage area and the improvement of residual strength. While the increase of stitch thread size was not so effective in residual strength in this case.

Key Words: composite, stitching, impact, compression after impact

Introduction

Carbon fiber-reinforced polymer composites have been used as structural materials for military and commercial aircraft to achieve substantial reductions in the structural weight. However, the use of structural composite has been limited by their high process cost and low impact resistance or otherwise by high material cost of toughened epoxy resin. Nowadays, many studies [1-9] have been conducted to improve these problems by using resin infusion techniques including Resin transfer molding (RTM) and Resin Film infusion (RFI) process and advanced textile techniques including stitching, braiding and 3D textile. We have evaluated a new epoxy resin for structural parts which was developed by TORAY Industries, Inc.. This new resin named TR-A31 is two-parts epoxy resin system for RTM process. This resin can be cured initially at under 100°C and has a low cost processing potential. However, carbon/TR-A31 composite is not enough for CAI property. In order to improve this low damage tolerance property, we have been trying to apply the through the thickness stitching and 3D textile preform as a reinforcement of TR-A31 composite. This study presents the evaluation of the stitch parameter effect on impact damage resistance.

Test Specimen and Procedure

In this study, three types of stitch method were evaluated; Lock stitch, One side stitch and 3D stitched textile. The lock stitched preform and the one side stitch preform were produced from quasi-isotropic layers of 24 plies low crimp plane weave fabric of T700-12K and Kevlar 29 yarn as a stitch thread. The lock stitch was performed by industrial sewing machine with a stitch pitch of 3mm and spacing of 3mm. The one side stitch was performed by typical one side stitch machine [10] with a pitch of 6mm and spacing of 4.4mm. Because this machine can stitch from one side of the preform, it is adaptable to any preform shapes. In order to evaluate the effect of stitch thread size, 400 and 1600 denier stitch thread were evaluated in lock stitch and one side stitch. 3D stitched textile [11] consists of 24 plies T700 multi-axial layers (0°/45°/90°=20.7/58.6/20.7) and carbon-2K z-direction fibers. In order to evaluate the effect of stitch density, two stitch patterns (6x6 mm and 3x3 mm) were evaluated. The salient features of these stitch patterns are shown in Fig.1 and Fig.2.

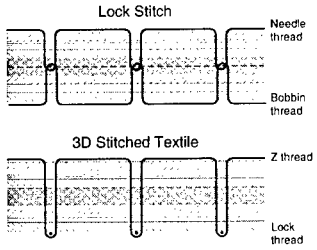

Fig.1 Stitching Patterns

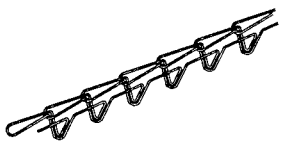

Fig.2 One Side Stitch Pattern [10]

Compression after impact test was conducted as per SACMA SRM 2R-94 at room temperature/dry and 82°C/wet conditions. The wet specimens were conditioned in deionized water at 72°C for just two weeks. The impact energy levels were ranging from 2.22J/mm to 11.1J/mm. The stitch was conducted along the load direction.

Result

Damage Area after Impact

A damage area measurement was conducted by an ultrasonic NDI machine after impact. Result is shown in Table1. Damage area of stitched specimen was clearly smaller than that of unstitch specimen.

Table 1 Damage Area of Impacted Specimen (Impact Energy: 6.7J/mm)

Specimen	Damage Area (mm^2)
Unstitched	1156
LS Kevlar 400d	792
LS Kevlar 1600d	702

LS: Lock Stitch

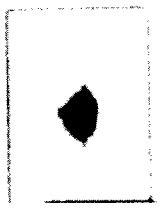

Fig.3 C-Scam Image of Kevlar 1600d stitched specimen after impact (Impact energy: 6.7J/mm)

Fig.3 shows C-Scan image of Kevlar lock stitched specimen. An elliptic shape of which major axis was along the stitch direction was observed at stitched specimen. As the results of cross section observation,

the damage consisted of delaminations between plies together with a number of transverse share cracks which seemed to spread from impacted point. The cracks which were in the stitch thread or along the stitch thread at just around the stitch thread were barely observed in damage area.

Residual Compression Result

CAI test results on RT/dry condition are shown in Table2. Take notice of anisotropy of 3D textile. The Kevlar 1600d stitched specimen showed a highest residual strength. While the 3D textile specimen stitched with carbon fiber thread showed a highest impact resistance property in failure strain. The one side stitched specimen showed reasonable strength corresponded to stitch density.

Table3 shows CAI test results of unstitched, Kevlar 1600d lock stitched and CF 6x6mm stitched specimen on 82°C/wet condition. It appears that the stitch using the CF thread was effective in CAI property on the hot/wet condition.

The failure mode was similar for both stitched and unstitched specimens. According to the inspection of failure edges, the failure seems to be occurred by propagation of gathered transverse shear cracks.

Table 2 CAI Test Result (RTD) (Impact Energy: 6.7J/mm)

Specimen	CAI Strength (MPa)	Failure Strain (x 10^{-6})
Unstitched	203	4400
LS Kevlar 400d	268	5900
LS Kevlar 1600d	301	6790
OSS Kevlar 400d	216	5060
OSS Kevlar 1600d	238	5550
3D CF 6x6 mm	199	5380
3D CF 3x3 mm	270	7720

LS: Lock Stitch (Pitch: 3mm, Space: 3mm)
OSS: One Side Stitch (Pitch: 6mm, Space: 4.4mm)
3D: 3D Stitched Textile

Table 3 CAI Test Result (HTW) (Impact Energy: 6.7J/mm)

Specimen	CAI Strength (MPa)	RTD to HTW Reduction
Unstitched	158	78%
LS Kevlar 1600d	231	77%
3D CF 6x6 mm	167	84%

LS: Lock Stitch , 3D: 3D Stitched Textile

Discussion

Fig.4 shows a influence of stitch density on CAI strength at Kevlar and carbon fiber stitched specimen. It appears that the effectiveness of the stitching on CAI property is correlated with stitch density irrespective of stitch method and thread materials.

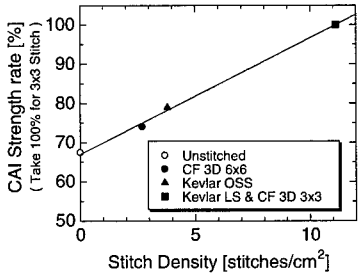

Fig.4 Stitch Density vs. CAI Strength

It was said that the roles of the stitch thread in CAI test were to prevent the delamination at impact and to arrest the crack propagation at residual compression test. The damage area result after impact test shows the delamination prevention effect. On the other hand, the crack arresting effect is shown in the residual compression test results. Fig.5 and Fig.6 show the influence of damage area on residual compression strength of lock stitch and 3D textile specimen respectively. In lock stitch specimen (Fig.5), both 400 and 1600 denier thread did not change in the residual compression strength. In this study case,

stitch thread size had no significant change effect during residual compression test. In 3D textile specimens (Fig.6), 3x3 mm pattern specimen showed clearly higher strength than 6x6 mm pattern.

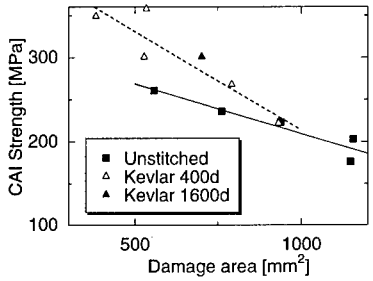

Fig.5 CAI Strength vs. Damage Area for Kevlar Lock Stitched Specimens

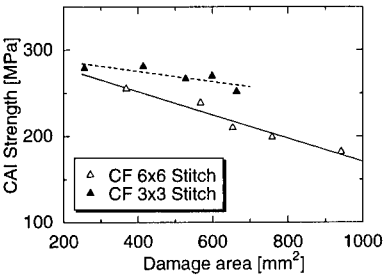

Fig.6 CAI Strength vs. Damage Area for 3D Textile Specimens Stitched with Carbon Fiber

Conclusions

1. The Stitching was much effective in CAI property in some stitch parameter case.
2. Because the damage area of stitched specimen spreads along the stitch direction, the stitch direction is important for parts design.
3. The effectiveness of the stitching on CAI property was correlated with its stitch density irrespective of stitch method and thread materials.
4. The increase of stitch density contributed the degradation of damage area and the arresting of crack propagation. However, in this study case, the increase of stitch thread size did not affect the improvement of crack arresting.

Acknowledgment

Some data of this study were quoted from the part of the Database program of "Database of Carbon / Epoxy Material Properties" under the contract by METI (Ministry of Economy, Trade and Industry). The authors would like to have grateful acknowledgment for permission. The authors also wish to thank ALTIN Nähtechnik in supplying stitched preforms.

References

1. R. M. Pelstring and R. C. Madan: Proc. of 34th Int. SAMPE Symposium, 1519 (1989)
2. M. B. Dow and D. L. Smith: Proc. of 21st Int. SAMPE Tech. Conf., 595 (1989)
3. N. Harris, N. Schinske, R. Krueger and B. Swanson: Proc. of 36th Int. SAMPE Symposium, 521 (1991)
4. K. Dransfield, C. Baillie and Y.-W. Mai: Comp. Sci. and Tech., 50, 305 (1994)
5. W. C. Jackson and M. A. Portanova: Proc. of 28th Int. SAMPE Tech. Conf., 339 (1996)
6. H. B. Dexter: Proc. of Int. SAMPE Tech. Conf., 404(1996)
7. L. K. Jain and Y.-W. Mai: Proc. of ICCM-11, I-25 (1997)
8. B. Qi, I. Herszberg, A. A. Baker and M. K. Bannister: Proc. of ICCM-11, V-149 (1997)
9. I. Herszberg and M. K. Bannister: Proc. of 5th Japan Int. SAMPE Symposium, 697 (1997)
10. J. Wittig and F. Rattay: Proc. of 46th Int. SAMPE Symposium, 2433 (2001)
11. I. Susuki, M. Shinya and Y. Yasui: Proc. of ICCM-11, V-614 (1997)

Proceedings of 7th Japan International SAMPE
Symposium & Exhibition, Nov. 13-16, 2001

Low Cost Fabrication of HOPE-X All Composite Prototype Structure

Kiyoshi Uzawa #1 Kozo Nishiwaki #2 Mayuki Niitsu #2 Toru Kamita #3
Gaku Kimura #1

#1 : GH Craft Ltd.
11-6 Itazuma, Gotenba, Shizuoka 412-0048, JAPAN
E-mail : k-uzawa@ghcraft.com

#2 : Mitsubishi Heavy Industries Ltd.
10, Oye-cho, Minato-ku, Nagoya 455-8515, JAPAN
E-mail : mayuki_niitsu@mx.nasw.mhi.co.jp

#3 : National Space Development Agency of Japan (NASDA)
7-44-1, Jindaiji Higashi-machi, Chofu-shi, Tokyo 182-8522, JAPAN
E-mail : kamita.tooru@nasda.go.jp

Abstract

In the development of HOPE-X, it is strongly required for the ultra short manufacturing term and low cost fabrication. A new access in designing and trial manufacturing has been achieved so that the design is to be the all-composite structure whereas the aluminum skin-stringer-frame structure has been the ordinary.
In order to meet these requirements, the large monocoque parts for minimizing numbers of parts, the non-autoclave curing technique with low temperature resin, and all bonding joint structure were adopted. This paper presents the development of the low cost and high accuracy large lay-up tool, the custom made oven and the affordable structure, which hold the keys to success at these adopted points.

Key Words: reentry vehicle, all-composite, honeycomb sandwich panel, low cost and high accuracy large tool, bonding joint structure, non-autoclave curing technology.

Introduction

HOPE-X is a Japanese experimental reentry vehicle which has been developed by NAL and NASDA. It's about 13m in length, 10m in width. To attain the low-cost, short-time and light weight manufacturing simultaneously, the HOPE-X adopted the all composite honeycomb sandwich panel structure instead of the aluminum skin-stringer-frame structure, and;
(1)Large monocoque parts, the upper fuselage and the lower wing-body that minimized the number of parts.
(2) Non-mechanical fastener and all-bonding structure was required.

In general, larger composite parts and the bonding structure do not lead directly to a low-cost manufacturing.
Larger composite parts need large facilities,

bonding structure requires fabricating complex bonding flanges. And as a result, the lay-up tool must be very accurate.
To settle these problems, the following methods had been used.
1) Low temperature curing prepreg with non-autoclave manufacturing method.
2) Bonding joint with additional wet lay-up.
3) Postcuring the whole body freestanding after all parts were bonded on the final state.
Fig.1 shows the structural concept of HOPE-X.

The low cost and development in a short term is not easily achieved only with the CFRP structure instead of the aluminum structure. The short-term development works on the low cost. The compatibility of the low cost and short-term development is realized by the new structural design and the innovational manufacturing technology aiming the compatibility.

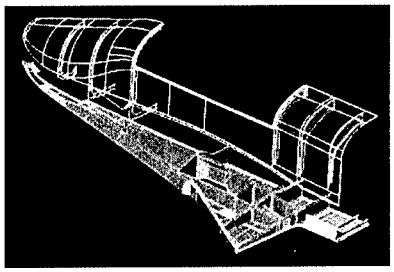

Fig.1 Structural Concept

TOOL

It is intended to reduce the construction cost by lessening the numbers of parts, so that
each parts are unified into the large-sized parts and consequently the tools became large.
"Large" and "high accuracy" are contrary and so on "low cost" and "short term development". As the low temperature curing was adopted, the material cost reduction was attempted by combining the plywood eggcrate structure & strip-planking panel and the FRP face-sheet as the hybrid material. To get the accuracy of the shape, the tools were divided into 15 to 16 pieces, whose module were sized at about 2 meters by 3 meters, and processed with the CNC machine at the mould face in a few millimeter thick. To fix the modules, the steel anglepipe would be used Fixing those modules up on the base directly leveled from the ground, It can get the sufficient accuracy as a whole at the low cost. At this moment, the heat expansion rate of the ground & the steel frame base, and that rate of plywood & FRP tool are not same. The heat expansion of the plywood is small enough to ignore but plywood contracted by the dryness while being kept at 100 deg-C. On the other hand, heat expansion rate of FRP layer itself in the surface of tool is larger than that of the CFRP fuselage panel. As a result, expansion rate balanced the FRP layer combined from glass fiber and carbon fiber, as a hybrid layer, to the plywood's one. This alignment kept the fitness of the fuselage and the tool under 3 times curing of the sandwich panel. And after curing, at the steps of frame set-up, it could be preceded to an assembly jig. It is easy to set the frame, because the cured panel stayed hold on the tool that is leveled.

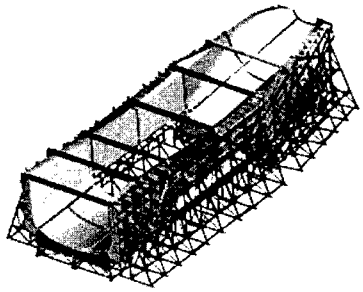

Fig.2 Lay-up Tool of Upper fuselage part

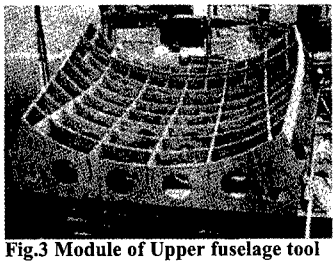

Fig.3 Module of Upper fuselage tool

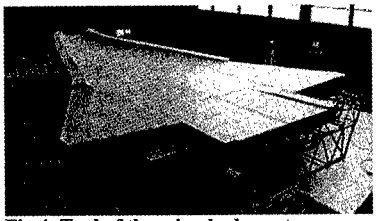

Fig.4 Tool of the wing-body part

Oven

The temporary oven was built for curing, for the lay-up tool was based on the ground. This oven was built up with the heat-resisting form panel on the truss frame of the steel angle pipes. The form panel is the form material of the phoenolic resin, which has the heatproof capacity more than 200 deg-C.

These materials are for the heat-resisting form panel for general construction and very cheap, so the construction cost can be kept low.

The oven was built exclusively to optimize the shape easily for the upper fuselage and for the lower wing-body.

This facility also works as clean room for lay-up, and lower oven was used two times for prepreg curing and post curing.

The hot air heater with the kerosine burner was used for the source of heat, and the additional blowers were settled to improve the heat transmission to the tool and the environment of inside oven.

At the post-curing the electric heaters were settled for supplying enough heat and making up to unify the inner oven temperature.

This oven was a temporally facility, but being optimized to the shapes of the parts to be formed (upper-FUS and lower W/body), its quality could be good with no unevenness of temperature.

As a result, the variation of the material temperature during cure kept within ± 3 deg-C and during post-cure ± 2 deg-C had been realized.

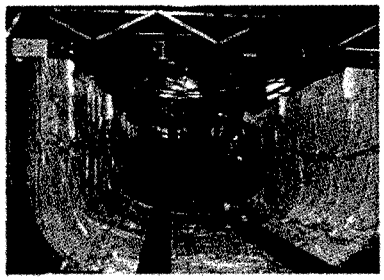

Fig.5 Bagging of upper fuselage part

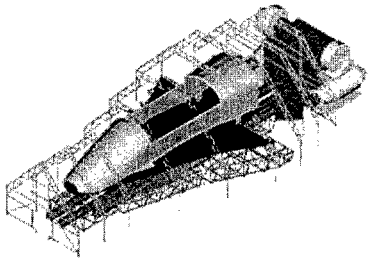

Fig.6 Post-cure with assembled body

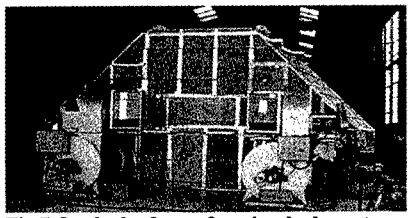

Fig.7 Out look of oven for wing-body part

Frame /Longeron

The Frame/ Longeron / Lay-up tool were made up by proceeding the NC machining directly to the ceramics board. This material was one of plaster boards made from the inorganic xonolite & the grassfiber/resin, developed for the insulation panel in the general construction. It is inexpensive, easy to do machining and has good accuracy with the expansion rate about $6 \times$ E-6. The detailed frame design was promoted parallel with the fabrication of outer structure so that the period shared for tooling was quite short. And the bonding strength required the maximum thickness of adhesion less than 1 millimeter.

Simplifying the flange shape had the important influence to the tool making.

Adding the wet-lay-up had a big effect to the bonding strength between the frame and the outer body and it was up to 50% more than the simple one-side flange.

The effect of using this simple flange reduced the cost to less than half of the frame fabrication even including the tool assembly cost.

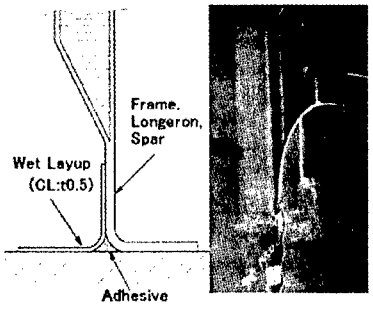

Fig.8 Bonding with additional Wet-lay-up

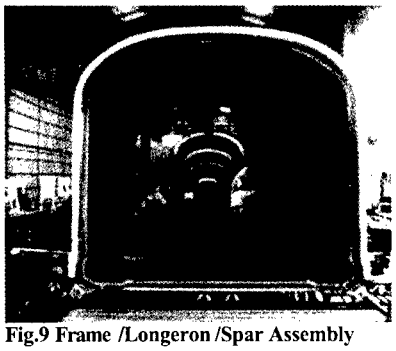

Fig.9 Frame /Longeron /Spar Assembly

Fig.10 All Composite monocoque Structure

CONCLUSIONS

On the HOPE-X prototype construction activity, with the affordable structure and manufacturing planning driving at a low cost, the easy-fabrication was realized without huge facilities.

The period from the structural design to the completion was 15 months, quite short. And the manufacturing cost has been reduced to almost one fifth to the ordinary aluminum structure vehicle and what is more the 20 % weight reduction has been achieved

Acknowledgment

Authors would like to thank design built team (DBT) for this program composed of the engineers from NASDA, NAL, MHI and GH craft.

Proceedings of 7th Japan International SAMPE
Symposium & Exhibition, Nov. 13-16, 2001

An overview of EADS research activities on low cost CFRP composites

Didier Guédra-Degeorges* and Klaus Drechsler#

EADS Corporate Research Centers
* : 12, rue Pasteur 92152 , Suresnes Cedex -FRANCE
Email : didier.guedra-degeorges@eads.net
: 81663 Munich, GERMANY
E-Mail: klaus.drechsler@eads.net

Abstract

Due to the economic pressure, perenniality of the aeronautical composite structures will be ensured if they tend to be as affordable as metallic ones.

Various directions for composite structures cost reduction are possible : the process, the material cost, the part design with function integration, the quality insurance, the maintenance, the material qualification, the certification...

Purpose of this paper is to present an overview of recent researches performed at EADS Corporate Research Centers (CRC) in the field of low cost composites processes and materials. Three main items will be addressed :
-new thermoset prepreg presentations for increased productivity
-integrated resin injection processes with advanced textile architectures
-advanced automated thermoplastic composites

Key words : *low cost , CFRP composites.*

Introduction

Few years ago, when engineers designed new aeronautical structural parts, the driver was mainly technical performance. Today, due to strong competition, cost savings have become a key parameter with regard to manufacturing of aerospace structures. In these conditions, the present high costs of CFRP aircraft components are a handicap to extend their field of applications despite their high mechanical performances. High prices of present composites elements could mainly be attributed to expensive raw materials and time consuming low-automated manufacturing processes. To overcome these problems, various researches are underway in EADS CRC. At the moment, most of aeronautical CFRP components in production used U.D. or fabric prepreg technology with carbon fiber and epoxy resins materials. First part, of this paper will describe investigated ways to reduce costs of this industrial prepreg technology. Second part will be dedicated to alternative emerging technologies that can contribute to extend field of application such as dry textiles techniques with various resin injection possibilities or thermoplastic technology that will be cost effective if running technological developments are successful.

New thermoset prepregs for increased productivity of industrial composite part manufacturing.

Depending on the industrial process used, a first approximation for a carbon fiber epoxy resin prepreg composite component gives about 10% of the final cost for the quality control (NDT), 40% of

the total cost for the material purchasing and 50% of the total cost for the manufacturing task. Consequently, price reduction of raw material is an important parameter for global reduction cost of the component.

Carbon fibers considerations

The most important technical aspect that contributes to reduce the price of the carbon fibers is the increase of the number of mono-filament in the tow. The first example, after a first standardization in 1990's, was the replacement of an equilibrated fabric made from 3K carbon fibers by an equilibrated fabric made from 6K carbon fibers. Then, the price of the fabric was cut down by a factor two. In 2000's, a step forward was achieved with utilization in EADS of 24K carbon fiber for unidirectional tape with acceptable compromise on the mechanical properties.
Since few years Mitsubishi and Toray made developments to propose heavy tow fabrics with a special process that sprayed the heavy tow filaments to be capable to produce fabrics under 400 g/m2. The mechanical properties of such fabrics are under evaluation.
The price reduction has to be confirmed, and also the fact that the mechanical performances (Fig 1) and the processability are not to much affect with these new fabrics.

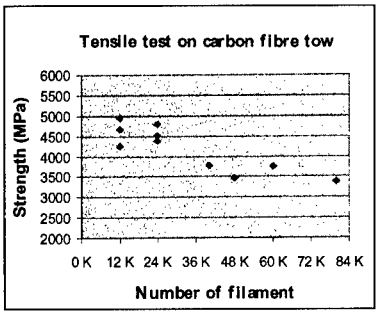

Fig1: Carbon fiber performance versus number of filament of tow.

Autoclave process considerations

From a process aspect, the utilization of an autoclave with high temperature and long time of polymerization is also very expensive.

The high temperature is expensive not only with the energy required to heat the autoclave, but also with the necessity to use specific tooling capable to resist to pressure and deformation at high temperature. The cost of a composite part tool is higher if the complete polymerization needs to be performed at 180°C (classical epoxy cure temperature) compared to 100°C. If Steel tools are absolutely necessary at 180°C, low cost composite or aluminum tools could fulfill the requirement at 100°C.
Based on the previous analysis, resins with low manufacturing temperature have been developed. These materials could be cured in autoclave at temperatures under 100°C. To achieve acceptable glass transition temperature a post curing in an simple oven out of the mold has to be performed at 180°C .This allows use of low cost tools for autoclave phase.
The cost reduction of these low temperature manufacturing materials has to be assess case by case to validate the real cost benefit.

Laying-up considerations

At the beginning of composite utilization, structural parts where made from prepreg by hand lay up. To reduce the cost of manufacturing, automated tape laying up machine have been developed to produce large structural parts with a minimum of human intervention. The main use of automated tape laying machine where to produce flat panels.
With the utilization on the latest development of composite materials for high loaded structural part, the consequence is the increase of the composite thickness. Today composite part could achieve 50 mm of thickness. With conventional prepreg (thickness 140 µm) it takes a lot of time to lay up the part. A

solution is to increase the prepreg thickness. Some first tentative has been made and shows a limit in the pre-preg thickness of about 230 µm when the prepreg is manufactured with conventional processes [1]. To go over 230 µm per ply, prepreg manufacturers have to improve or modify the pre-preg manufacturing technique.

An innovative way has been proposed with the semipreg technology [2] which consist in recovering a thick dry fiber tape with a thick resin film. The impregnation is done during the autoclave phase with special care to eliminate all the air inside the material. This technology could be considered as very closed to the resin film infusion technique, but the advantage is to manipulate only one intermediate product (resin + fiber). This new technology needs some work to be technically validated and also need some economical study to assess the cost reduction that could be achieved.

Integrated resin injection processes with advanced textile architectures

Advanced preforms

An approach to partly overcome economic disadvantages of conventional prepreg technology is the use of textiles techniques associated with various resin injection processes.

Textiles techniques allows the processing of dry fibers to near net shape preforms. EADS CRC has accomplished many investigations on various techniques aiming to develop automated manufacturing processes derived from the garment industry (weaving, braiding, warp knitting, stitching...) to allow processing of high performance fibers. Particularly, a specific Braiding device has been developed to generate 3-dimensionnally shape section with variable fiber orientations during the braiding and continuous changes in profile cross section [3]. Regarding stitching, current studies at EADS CRC focus on the optimization of stitching preforms with respect to improved damage tolerance and automated attachment process using robot (fig 2).

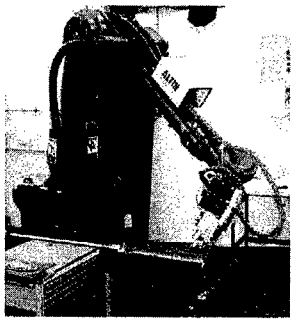

Fig 2 : One-side-stitching robot for preforms assembly

Specific spray aiming to stiffen preform are also under studies in order to facilitate handling and positioning for complex 3D Shape (Fig 3).

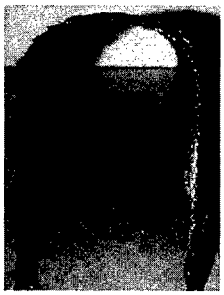

Fig 3 : 3D shaped stiffened preform for handling using specific spray

Integrated Resin injection processes

The resin transfer moulding (RTM), the resin film infusion (RFI) or the liquid resin infusion (LRI) could be considered as low cost manufacturing technologies if the design of the component contributes to eliminate or reduce number of sub elements to assemble compared to a metallic design. To obtain an acceptable cost reduction with these technologies, it is preferable to polymerize the resin with a

self heating mould if the number of parts to produce is high enough. Process simulation is also a key parameter to reduce costs and time to develop a new concept. Modeling contributes to optimize resin injection parameters and mold injection holes. A complete resin injection integrated process including resin permeability measurement device, process simulation , preform and tooling design has been developed in EADS CRC (fig 4). Advanced automated 3D textile preforms associated with resin injection techniques offer also clearly the possibility to extend field of composites applications to complex 3D parts inaccessible with classical prepreg technology.

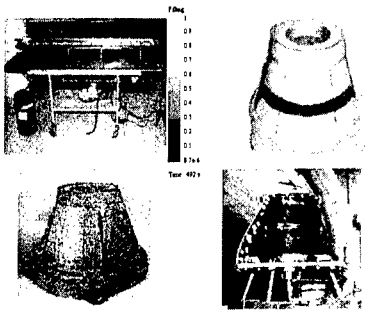

Fig 4: Integrated R.T.M process for an helicopter housing demonstrator

Advanced automated thermoplastic composites

The thermoplastic materials do not need specific storage conditions like refrigeration and they do not have shelf life limitation. As the transformation is reversible, they may be repaired and recycled . Other advantages include damage tolerance resistance [4], solvent resistance, very good behavior to hot wet ageing conditions and comply with current specification concerning fire, smoke and toxicity requirements.

Integrated Stamping process

At the beginning of 90's, a lot of researches have been performed to develop cost effective process like stamping for thermoplastic advanced composites. But it takes more efforts than expected to understand processability of high performance thermoplastics such as C/Peek, C/PPS, C/PEI and to admit that heated tooling were necessary to achieve required quality. The stamping technology with thermoplastic pre-consolidated laminates (made from long fibers prepreg) is nevertheless an interesting innovative process to produce specific parts competitive with sheet forming metallic ones. By the time being, EADS CRC focuses research efforts to establish an integrated stamping process [5] that allows to compute optimized initial flat shape of stamped elements, to control thickness, fiber angle variations and to correct spring back effects (fig 5). The final aim is to reduce non recurrent costs and time to develop thermoplastic sheet forming elements.

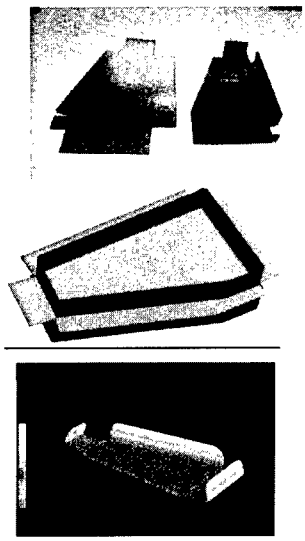

Fig 5: Integrated Thermoplastic stamping process for a rib demonstrator (stamping and spring back simulation)

In situ consolidation thermoplastic tape laying process: a cutting edge technology

The basis of continuous consolidation is to perform both steps simultaneously by laying up the material while heating it at the proper temperature with a gas torch and applying the pressure by mean of a roller (fig 6).

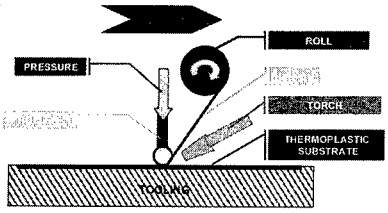

Fig 6: In situ consolidation principle

Due to high potential cost and cycle benefits, a common research project bringing together EADS, Dassault Aviation and Eurocopter has been started few years ago. The industrial objective is to perform a one-phase process by laying up the material directly on the substructure. The tooling is specially designed to be able to integrate stringers and frames; those are previously cut and formed to the final shape from a consolidated plate. The particular properties of thermoplastics enable the welding of the skin to the substructures if sufficient heat and pressure is available while placing the tape [6].
The first manufacturing feasibility test shows that no major problems occurred during the process (fig 7).

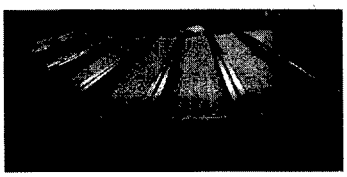

Fig 7 : "In situ consolidation" thermoplastic tape laying process of a fuselage panel demonstrator

Geometrical and ultrasonic controls revealed an encouraging level of quality of the skin and of the welded areas between the stringers and the skin. However further improvement is needed to increase the quality level and optimize the process on a productivity basis.

Conclusion

Due to their high specific mechanical performances, C.F.R.P are still a source of weight savings regarding some metallic parts. Nevertheless, reduction of global costs for composite elements is a condition to increase composites share on aeronautical structures. In order to lower global composite costs, continuous research efforts are performed in EADS CRC in three main directions :
-increase productivity of existing industrial thermoset prepreg manufacturing line,
-assess potential of resin injection processes associated with advanced textiles preforms
-develop cutting edge technology such as advanced automated thermoplastic composite manufacturing

references

1. J. Cinquin : Proc. of NATO RTA Tech. Conf., MP-69-P-01 (2001), Loen, Norway.
2. A. Mills., R. Backhouse : Proc. of 44th International SAMPE symposium. P 2255-2267.(1999)
3. J. Brandt ,K.Drechsler, J.Filsinger : Proc. of NATO RTA Tech. Conf., MP-69-P-17 (2001),Loen, Norway.
4. D.Guedra-Degeorges, M.C. Lafarie-Frénot, F.Touchard- Composites Science and Technology, n°881, pp 15-24, (1996)
5. A. Chéruet, D. Soulat, P. Boisse, E. Soccard, S. Maison-Le Poec : Proc. of the 4th international ESAFORM conference on material forming, A.M. Habraken editor, pp. 115-118 (2001)
6. D.Lang, S.Barre, C.Coiffier-Colas, H.Sibois : Proc. of NATO RTA Tech. Conf., MP-69-P-30 (2001), Loen, Norway.

Proceedings of 7th Japan International SAMPE
Symposium & Exhibition, Nov. 13-16, 2001

Development of Thermoplastic Polyimide (PIXA-MT3) Composite

Yoshiyuki Honda, Hiroyuki Nakamura, Takayuki Kamiyama and Hirobumi Tamura,
Aerospace Division, Fuji Heavy Industries Ltd.,
1-1-11, Yonan, Utsunomiya, Tochigi 320-8564, Japan
E-mail: HondaY@uae.subaru-fhi.co.jp
Shoji Tamai, Material Science Laboratory, Mitsui Chemicals, Inc., 580-32, Nagaura,
Sodegaura, Chiba 299-0265, Japan
Yoshihiro Endo, Research Laboratories, Toho Tenax Co., Ltd., 234 Kamitogari,
Nagaizumi-cho, Santo-gun, Shizuoka 411-8720 , Japan
Yosuke Nagao, Japan Aircraft Development Corporation, 2-3 Toranomon 1-chome,
Minato-ku, Tokyo 105, Japan

Abstract

Thermal resistant, light weight and low cost structure of composite materials are required by future high speed commercial airplane in not only economic aspect but energy saving aspect. Fuji Heavy Industries Ltd. has been continuing development of carbon fiber (IM600) / thermoplastic polyimide (PIXA family) composite material with Mitsui Chemicals Inc (MCI). and Toho Tenax Co., Ltd. (THT)[1]. IM600/PIXA-M composite material is excellent in impact and heat resistance, and has potential of in-situ consolidation which could reduce manufacturing cost significantly. However, it is known that PIXA-M composite has microcracks after solvent exposure such as methyl ethyl ketone (MEK) soaking with strain or thermal cycling. MCI has developed new type of PIXA family resin; PIXA-MT3[2] to reduce and restrain microcrack appearance. Physical properties of PIXA-MT3 neat resin and solvent resistance, thermal cycling resistance, processability including secondary forming of IM600/PIXA-MT3 are evaluated. It is suggested that IM600/PIXA-MT3 has a microcrack resistance and has a good processabillity.

Key Words: Thermoplastic Polyimide, Composite Material

Introduction

MCI has developed a new type of PIXA family thermoplastic polyimide resin; PIXA-MT3[2]. IM600 /PIXA family resin composite material offers possibility of light weight structure and low cost manufacturing for future high speed commercial airplane, because it has a higher CAI strength than toughened epoxy resin composite, and has a possibility of low cost manufacturing by in-situ consolidation. Further, it has thermal stability over 180 °C. However, PIXA family resin (e.g. PIXA-M) composite material has problems for solvent and thermal cycle resistance[3,4]. PIXA-M

composite material has microcracks after MEK soaking with strain or thermal cycle exposure. Physical properties of PIXA-MT3 neat resin and solvent resistance, thermal cycling resistance and processability including secondary forming of IM600/PIXA-MT3 are evaluated.

Experimental

Physical Properties of PIXA-MT3 Neat Resin

PIXA-MT3 neat resin is developed to improve thermal and microcrack resistance. PIXA-MT3 has cross linking in the molecular structures in order to restrain microcrack appearance.

PIXA-MT3 has good melt flow properties which is important for processing of prepreg and laminate. And initial melt viscosity is similar to that of PIXA-M. However, PIXA-MT3 needs to be annealed for cross linking.

Solvent Resistance of PIXA-MT3 Neat Resin

Bending test specimens of PIXA-MT3 neat resin and PIXA-M neat resin are fabricated at 330 °C for 150 minutes. At the beginning, test specimens are loaded with strain of 0.6 % on bending jig. And then, these are soaked in MEK with bending jig.
As the test result, PIXA-MT3 has no microcrack after the soaking for 24 hours. On the other hand, PIXA-M has microcracks after the soaking for 15 minutes.

Processability of IM600/PIXA-MT3 Composite Material

Processability of IM600/PIXA-MT3 composite is demonstrated to decide on a fabrication condition. Quasi-isotropic laminate panel of PIXA-MT3 and IM600 carbon fiber, which is 8 plies and 300 mm by 300 mm, is fabricated to demonstrate processability. Here, unidirectional prepreg of IM600 carbon fiber and PIXA-MT3 is developed by THT. Internal quality of fabricated IM600/PIXA-MT3 is confirmed by ultrasonic testing and cross section observation.

It is confirmed that void free IM600/PIXA-MT3 can be fabricated, under the following condition;

Consolidation condition; dwell temp.: more than 340 °C, dwell time: 10 min., pressure: 988 kPa in vacuum

Annealing condition; dwell temp.: 360 °C, dwell time: 240 min., pressure: more than 588 kPa in vacuum

Further, result of fabrication at 390 °C, 120 min, 981 kPa in vacuum is suggested that consolidation and annealing process are accomplished at the same time.

Solvent Resistance of IM600/PIXA-MT3 composite Material

IM600/PIXA-MT3 composite panel of quasi-isotropic 32 plies is fabricated. At the beginning, fatigue test specimens are made from the panels, and are soaked in MEK for 10 days. The fatigue test specimens are loaded tension-tension fatigue up to 20 x 10^5 cycles at 177 °C. The fatigue condition is as follows; stress ratio: 0.1, frequency: range of 8 to10 Hz. After the fatigue test, tensile test specimens and cross section observational specimens are cut off from the specimens. Tensile test is conducted to evaluate residual strength at room temperature. And microcracks per width in observational specimens are counted after soaking.

Result of solvent resistance test is shown in Figure 1. IM600/PIXA-MT3 has very little microcracks after 20 x 10^5 fatigue cycles even if it is soaked in MEK for 10 days. On the contrary, IM600/PIXA-M has some microcracks after fatigue whether it is

soaked or not. However, the residual tensile strength of IM600/PIXA-M composite is not reduced after microcracking.

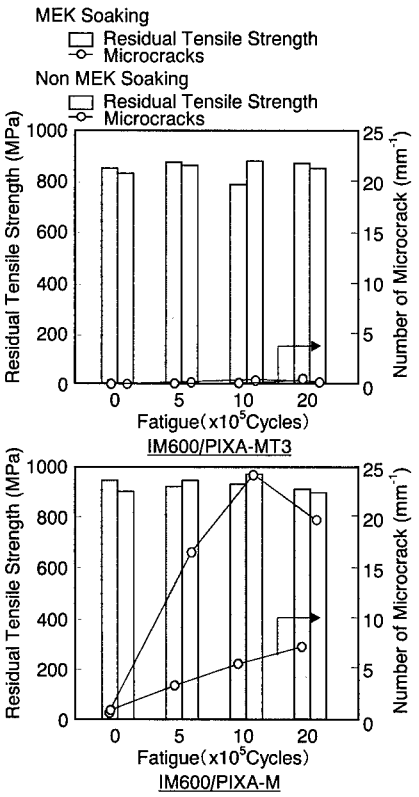

Figure 1. MEK Resistance Test Results

Thermal cycle Resistance of IM600/PIXA-MT3 composite

Open Hole Compression (OHC) and cross section observational test specimens of IM600/PIXA-MT3 which are quasi-isotropic 32 plies are fabricated. At the beginning, both of the test specimens are exposed to thermal cycles between 177 °C and -54 °C. After the thermal cycles, the OHC test is conducted at room temperature. And microcracks per width in observational specimens are counted after exposure.

The result of thermal cycle resistance test is shown in Figure 2. IM600/PIXA-MT3 has no microcrack after 200 cycles exposure. On the other hand, PIXA-M has microcracks after thermal cycles exposure. The microcracks of PIXA-M increased with thermal cycle. And the reduction of OHC strength is not observed for each materials.

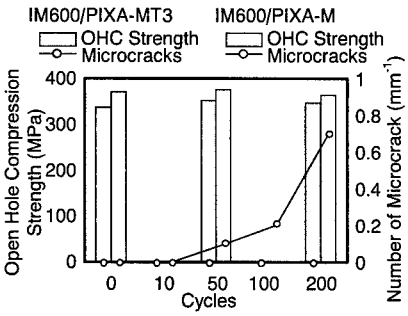

Figure 2. Thermal Cycle Resistance Test Result

Evaluation of Secondary Forming

Processability of IM600/PIXA-MT3 composite is demonstrated to decide on a secondary forming condition for processing of structure. At the beginning, IM600/PIXA-MT3 panels are laminated to quasi-isotropic 24 plies (about 3.2 mm in thickness) and 300 mm in length by 150 mm in width. And then, four panels are processed after consolidation, and one panel is processed after annealing. The consolidation condition is 340 °C in dwell temp., 10 minutes in dwell time, 988 kPa in pressure, under vacuum. And the annealing condition is 360 °C in dwell temp., 240 minutes in dwell time, 988 kPa in pressure under vacuum. In this test, all fabricated panels are pressed

using angle shape jig, which has 92.75 ° in angle and 3 mm in radius, at the temperature range from 300 °C to 400 °C, the pressure range from 294 kPa to 981 kPa for 10 minutes.

Secondary formability of test specimen after consolidation is favorable at over 320 °C and 588 kPa. However, test specimen after annealing has wrinkles at the inner surface of corner. Further, all of panels show spring-in after secondary forming. Cross section of consolidated panel after secondary forming is shown in Figure 3.

Figure 3. Cross Section of Consolidated panel after Secondary Forming (Secondary Forming Condition: 320 °C, 588kPa, 10min.)

Conclusions

1. PIXA-MT3 neat resin which is modified from PIXA-M, has enough solvent resistance.
2. It is confirmed that IM600/PIXA-MT3 shows good solvent and thermal cycle resistance compared with IM600/PIXA-M.
3. It is confirmed that void free IM600/PIXA-MT3 can be fabricated, under the following consolidation;
   Condition; dwell temp.: more than 340 °C, dwell time: 10 min., pressure: 988 kPa in vacuum
   Annealing; dwell temp.: 360 °C, dwell time: 240 min., pressure: more than 588 kPa in vacuum
4. It is confirmed that IM600/PIXA-MT3 after consolidation can be secondary formed under the following condition; temperature: over 300 °C, pressure: over 588 kPa.

Consequently, it has confirmed that IM600/PIXA-MT3 composite has a good characteristics after environmental exposure and has a potential to be applied to the future high speed commercial airplane.

Acknowledgment

This work was performed as a part of the R & D project of "Advanced Composite Materials for Transportations" in the management of RIMCOF (R&D Institute of Metals and Composites for Future Industries) under the contract by METI (Ministry of Economy, Trade and Industry).

References

1. N. Mori, H. Nakamura, K. Umeki, S. Tamai, Y. Endo and H. Tamura, 24th Composite Materials Symposium, 137, (1999)
2. PCT Int.Appl. WO 0008090 (Feb. 17, 2000) S. Tamai, et al (to the Mitsui Chemicals Inc.)
3. A. Sakamoto, M. Noda and Y. Yamaguchi, Proceeding of the 9th US-Japan Conference on Composite Materials, 23 (2000).
4. T. Shimokawa, H. Kato, Y. Hamaguchi, et al, Proceedings of The 36th Aircraft Symposium (1998)

Proceedings of 7th Japan International SAMPE
Symposium & Exhibition, Nov. 13-16, 2001

Study of Automatic Drilling and Fastening for Wing Box

Tomohisa Hiroe#1 Tsuyoshi Osawa#1 Tokuhisa Hatakeyama#1 Kenichi Kosugi# 1 and
Hirobumi Tamura#2

#1: Kawasaki Heavy Industries, Ltd.
1.Kawasaki-Cyo, Kakamigahara City, Gifu-Pref. 504-8710 Japan
E-mail: hiroe_t@khi.co.jp

#2:formerly Japan Aircraft Development Corporation
Toranomon Daiichi Bldg., 2-3, Toranomon 1-Chome, Minato-Ku Tokyo, 105-0001, Japan

Abstract

The widespread use of the CFRP (bismaleimide) and titanium alloy are expected in the future High Speed Transport Aircraft main wing box structure. At the assembly of different parts such as the Ti spar and the CFRP skin, one shot drilling and fastening to the different parts is difficult due to the different drilling characteristics for each material. In order to achieve significant cost reduction comparing to the manual assembly, the suitable drill condition and the fastening process should be established. Based on this conditions, the automatic drilling and fastening system was developed through this research. This system is comprised of two articulated type robots. One robot has drill end-effector and part of fastening function, another has collar fastening function. These end-effectors have capability to drill the stacked parts with in the one shot process. This automatic drilling and fastening process for the stacked parts and its quality were estimated.

Key Words: Automatic, Drilling, Fastening, Robot.

Introduction

CFRP(bismaleimide) and titanium alloy are expected as candidate materials of the main wing box structure for High Speed Transport Aircraft. While the utilization of CFRP are expected as a point of the weight reduction, titanium alloy are also expected for the parts which are acted on high load density like spars or ribs. From the viewpoint of assembly technology, it is very difficult to drill stacked materials by hand drill operation, specially titanium alloy and CFRP combination. The reason of that is each material has its own drilling characteristics and suitable drilling conditions. We did a case study of a wing structure like spars and ribs are made of titanium alloy, and skins are made of CFRP, and tried to drill and fasten by automatic system. Fig.1 shows the example of main wing structure for High Speed Aircraft.

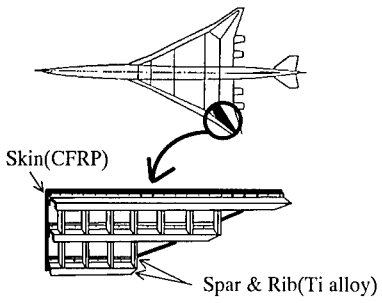

Fig.1 Example of main wing structure for High Speed Aircraft

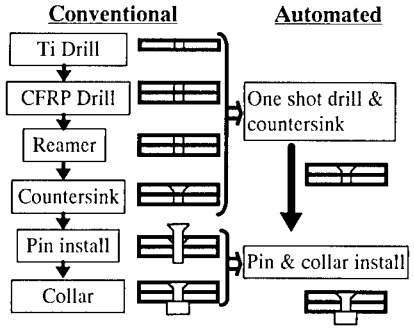

Fig.2 Comparison of the assembling processes

Necessity of automatic drilling and fastening using robot

Fig.2 shows the comparison of the assembly processes between the conventional method and the automated one. Many processes are required in the conventional method , such as drilling titanium alloy and CFRP separately, reaming, and countersinking, to maintain hole quality against the thick CFRP and hard materials like titanium alloy. However, in the automated system, it has more rigid than manual drilling method, and it can change drilling conditions for each materials automatically. So we will be able to drill the stacked parts with one shot process. Furthermore we will be able to reduce assembly time dramatically.

And we adopted articulated type robots for the platform. The equipment cost is lower than the gantry type which is more popular for the automated system, and the articulated type robots have more flexible movement to adapt complex parts.

One shot drilling Technology

Development of special drill

First we examined cutter material, on the view point of material properties of drilling. There are much difference between CFRP and titanium alloy, and the suitable drill material for CFRP is PCD(Poly Crystal Diamond) the wearing speed of the cutter edge is very fast when CFRP is drilled, so the hardest material like PCD is suitable. On the other hand , PCD cutter is easy to chip in the case of titanium alloy. So we selected the carbide material for a one shot drill which are not harder than PCD but has more toughness. Next we examined drill shape. At this study, the drill direction is from CFRP to titanium alloy (Fig.3). But titanium chips damage the CFRP hole quality in one shot drilling operation. So we developed special edge type drill to prevent this problem. The developed drill is shown Fig.4.

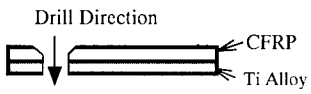

Fig.3 Drill direction of one shot drilling

Fig.4 Original designed drill developed by R&D

Adjustment of drilling conditions

The suitable drilling condition is adjusted to each CFRP and titanium alloy. For example, high speed rotation is suitable for CFRP to reduce delamination and to keep surface smoothness. But for titanium alloy, low speed rotation is suitable to reduce heating caused by drilling operation. The drilling conditions were changed automatically for each CFRP and titanium alloy to do one shot drilling operation.

Development of automatic drilling and fastening system

The outline of developed system is shown in Fig.5. This system is consisted of two articulated type robots. One robot has a drilling and fastener pin installation end-effector and the other has a collar installation end-effector. The functions are as follows.

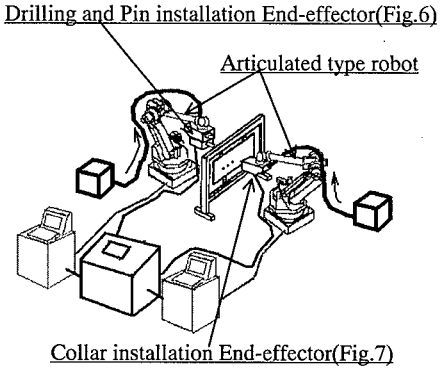

Fig.5 System Outline

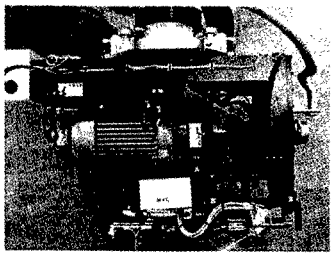

Fig.6 Drilling and Pin installation End-effector

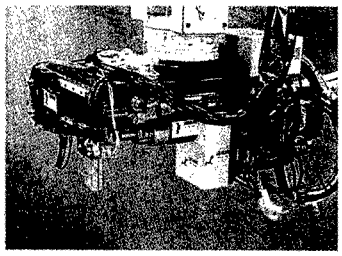

Fig.7 Collar installation End-effector

Automatic drilling function

A drilling end-effector has capability to drill the stacked parts of CFRP and titanium alloy. We used articulated type robots and the rigidity is not so high, so we used drill plate jig to absorb the high thrust power when titanium alloy is drilled. Besides we set up the function to change a drilling condition by each material automatically, and cooling function using cold air.

Automatic fastening function

An operation flow of automatic fastening system is shown Fig.8. A Hi-Lok pin is inserted automatically to the hole by the pin installation end-effector, and a collar is installed by the collar installation end-effector on the other side robot. Clearance of pin fitting condition is required for the stacked parts including CFRP. This system

also has a function to stop rotating a Hi-Lok pin when a collar is inserted and rotated. And the torque is monitored and automatically judged to twist off the collar head during the collar rotation. To keep the fastening quality we adjusted the suitable condition of the pin insertion speed and collar rotation speed. A sample part fastened by this system is shown Fig.9

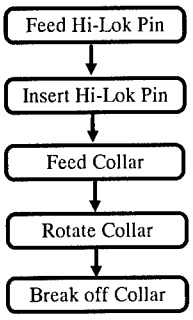

Fig.8 Operation Flow of Automatic Fastening

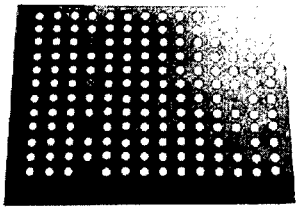

Fig.9 Sample Part

Conclusions

In conclusion, we developed automatic drilling and fastening technology, and accomplished the improvement of the hole quality and reduction of the labor cost. As a result of calculating the manufacturing time compared to the conventional method, it is appeared to reduce about 30%. We will continue this study for the model parts of real airframe and estimate the cost data in detail.

Acknowledgment

This program is a part of Advanced Composite Design & Manufacturing Technology (ACDMT) program funded by Ministry of Economy, Trade and Industry (METI) of Japan via R&D Institute of Metals and Composites for Future Industries (RIMCOF). The authors would like to thank RIMCOF, especially Mr. Y.Yamaguchi and Mr.M.Noda for professional and dedicated support.

References

1. K.Kosugi, H.tamura, S.Maekawa, Y.Hirose, T.Sana and T.Hatakeyama: Low Cost Manufacturing Approach for Composite Outer Wing of SST: Proc. of the 9th United States - Japan Conference on Composite Materials, pp.97-103 (2000)

Proceedings of 7th Japan International SAMPE
Symposium & Exhibition, Nov. 13-16, 2001

Current Status and Future Prospects of R&D on Construction of Design Database for Advanced Composites and Structures in Japan

Kazumi HIRANO

Advanced Materials & Structural Integrity Research Group
National Institute of Advanced Industrial Science and Technology (AIST)
Namiki 1-2, Tsukuba-shi, Ibaraki-ken 305-8564, JAPAN
E-mail:hirano@mel.go.jp

Abstract

It is very important and urgent for development of low cost manufacturing technology of composite materials and structures to construct the design database included guidelines and references to proven engineering practices. In this paper, current R&D activities of preparation and construction of database for advanced composite materials and structures in Japan are first outlined in the field of aeronautics, aerospace and power generator technologies. Secondly, some topics are briefly introduced by focusing on the related R&D projects. Finally, future prospects are addressed for academia, industry and government partnerships.

Key Words: Techno-infrastructure for Composite Materials and Structures, Design Database, Advanced High Temperature Composites

Introduction

Recently, it is very important and urgent to construct not only materials database but also design database included guidelines and references to proven engineering practices for a wide use of advanced composites and structures system. Along with research and development (R&D) on low-cost manufacturing technologies of composite materials and structures, the following feasibility studies have been done on preparing and construction of the design databases for advanced high temperature structural composite materials [1].

- High temperature polymer matrix composites
- Continuous fiber reinforced Ti-alloy matrix composites
- Melt growth composites

First is concerned with the long-term durability performance focused on fatigue behavior and accelerated testing methodologies of the interesting and candidates for next generation supersonic civil transportation. Second is low-cycle fatigue design database for continuous fiber reinforced Ti-alloy matrix composites (TMCs) rotating parts in aircraft engines, such as impellers, disks, integrally bladed rotors or bladed disks, and bladed rings. Third are generally considered to be one of the most interesting and attractive as the ultra-high temperature structural materials.

In this paper, current R&D activities of preparation and construction of database for advanced composite materials and structures in Japan are first outlined in the field of aeronautics, aerospace and power generator technologies. Secondly, some topics are briefly introduced by focusing on the related R&D projects. Finally, future prospects are

discussed for academia, industry and government partnerships.

High Temperature Polymer Matrix Composites (PMCs)

One of critical technological issues for 2nd Generation Supersonic Civil Transport is how to ensure the long-term durability and structural integrity of advanced high temperature polymer matrix composite system. This research has been conducted in a close collaboration with evaluating and predicting long-term durability performance of candidate composite materials and structures in Japan Supersonic Research Program [2,3].

Relatively little information is available on the long-term durability performance of high temperature thermosetting and thermoplastic polymer matrix composites, such as fatigue and creep in comparison with conventional epoxy matrix composites. The following researches have been done in order to finally achieve through long-term and short-term tests under conditions simulating flight profile, development of associated predictive and accelerated test methods, and assessment of durability performances for design. In particular, it is very important for the development of associated predictive and accelerated test methods to investigate in details damage and failure mechanisms.

- Influence of stress ratio and the related fatigue failure mode transition in fully reversed, tension-compression open-hole fatigue behavior
- High temperature open-hole compressive fatigue behavior
- Low-velocity impact damages and post-impact fatigue behavior
- Moisture absorption effects and fatigue damage tolerance behavior
- Residual open-hole tension/compression strength and fatigue behavior after thermal cycle aging
- Thermo-mechanical response under the simulated SST flight cycles and long-term durability analysis and database

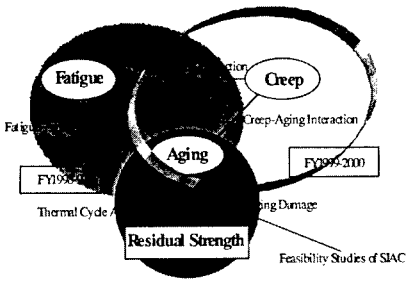

Fig. 1 R&D plan of long-term durability performance for high temperature polymer matrix composites

Ti-alloy Matrix Composites (TMCs)

Continuous fiber reinforced metal matrix composites (MMCs) have been researched and developed because of high specific strength and high temperature capability for the past twenty years and fatigue damage tolerance behavior have also been characterized on the basis of fracture mechanics [4-7]. They have been innovatively applied to various high temperature structural components in the field of acronautics, aerospace and power generation industries. The continuous fiber partially reinforced Ti-alloy matrix composite rotor bladed ring has also been successfully fabricated on the basis of the design requirements as one example was shown in Fig. 2 [8-10]. However, there is the limited number of research for long-term durability performance at practical use temperature ranges in comparison with the static strength characteristics. It is therefore necessary to investigate the elevated temperature fatigue behavior for ensuring structural integrity of MMCs components.

The final goal of this research is to

construct the fatigue damage tolerance design database. It is also necessary to research and develop the materials testing and evaluation method. The research and developed database for SCS-6/SP700 consists of the following data. Typical processing methods, low-cost fabrication method of TMCs bladed rotors and life prediction methods are also included in this database.

- Mechanical properties
- Thermal properties
- Tensile strength at elevated temperature
- Measurements of residual stresses
- High-cycle fatigue behavior
- Low-cycle fatigue behavior
- Thermo-mechanical fatigue behavior
- Thermal cycling test
- Influence of reinforcement fiber ends
- Creep resistance

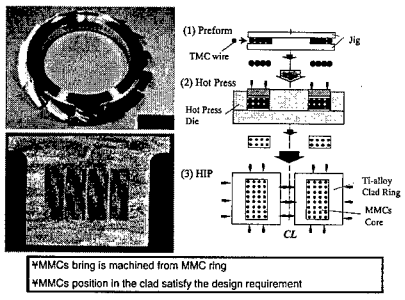

Fig. 2 Schematics of TMCs rotor bladed ring and its fabricating method

Melt Growth Composites (MGCs)

Melt growth composite (MGCs) have many potentialities that the tensile strength is maintained right below the melting point temperature, increases with decreasing of a characteristic dimension of the network microstructure without the reduction of creep resistance and plastically deformed at ultra-high temperature ranges [11]. Also, there is a good productivity of complex structural components as compared with conventional sintered engineering ceramics. Feasibility study has also been done on applying MGCs to ultra-high temperature components for realization of ultra-high efficient 1700°C class non-cooled TBC-free gas turbine system [12]. The MGCs are still now R&D stage and the database also focus on the processing technology. A distinctive feature of this database is to cover crystallographic analysis, solidification analysis and computer simulation techniques of phase diagram.

- Thermal properties
- Chemical properties
- Mechanical properties
  - Elastic modulus
  - Flexural strength
  - Creep resistance
  - Fracture toughness
  - Thermal shock resistance
  - Fatigue strength
  - Environmental effects
  - Measurements of residual stress

Concluding Remarks

Current R&D status of construction of the design database for advanced structural composites in Japan are briefly introduced. It is still more important for the design-by-analysis age to prepare and construct the materials and design databases. The design database has to be prepared for a wide practical use from triangle structural design, manufacturing and applications relationships points of view. The integrated modeling and simulation technologies play an important role as shown in Fig. 3. Academia, industry and governments partnerships have been strongly expected than ever before.

The materials and design databases introduced here are also opened to the public in RIMCOF internet web site.

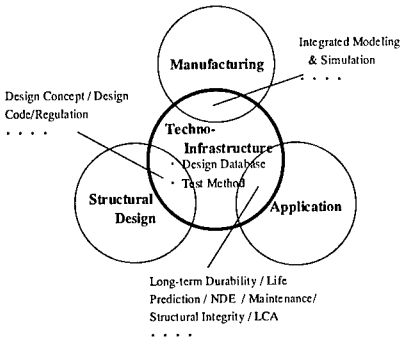

Fig. 3 Schematics of triangle structural design, manufacturing and applications relationships

Acknowledgements

This research projects had been promoted by the former Agency of Industrial Science and Technology, Ministry of International Trade and Industry. The author also highly acknowledged all members of Technical Committee of Research Institute of Metals and Composites for Future Industry (RIMCOF).

References

1. RIMCOF Report, Preparing and Construction of the Design Databases for Advanced High Temperature Structural Composite Materials, (2001-3) (in Japanese)
2. Hirano, K., Strategies for R&D on Construction and Preparation of Design Database for Advanced Composite Materials, *J. of the Japan Society for Composite Materials,* Vol.26, No.1(2000), pp.3-8 (in Japanese)
3. NEDO Report, Studies on Establishment of Long-term Durability Testing and Methodologies for High Temperature Polymer Matrix Composites, March 31, 2000 (in Japanese)
4. Mall, S and Nicholas, T., Titanium Matrix Composites, TECHNOMIC Publishing CO., INC., (1998)
5. Hirano, K., Current R&D Trends of Advanced Metallic and Inorganic Materials and Its Technical Problems, *Trans. JSME (A),* 58-550(1992) pp.817-823 (in Japanese)
6. Hirano, K., R&D Trends of Advanced Metal Matrix Composites and Fracture Mechanics Characterization, *ISIJ International,* 32-12(1992) pp.1357-1367
7. Hirano, K., High Performance Materials for Severe Environments in the Field of Aerospace and Power Generator Technologies in Japan (Invited Lecture), Metal Matrix Composites, *Proc. 9th Int. Conf. on Composite Materials,* 1(1993) pp.87-88
8. Natsumura, T., et al., Component Design of CMC and MMC rotor for Turbine Engine Applications, *SAMPE COMPOSITE '99,* (1999)
9. Yamada, T., Tsuzuku, T, Kawachi, Y. and Yasuhira, K., *Materials and Manufacturing Process,* Vol. 15, No.3 (2000)pp.347-358
10. Fujiwara, C., M. Yoshida, M. Matsuhama and S. Ohama, *Proc. ICCM-10,* Vol. II(1995)pp.687-694
11. Waku, Y. et al., "A Ductile Ceramic Eutectic Composite with High Strength at 1873 K", Nature, Vol. 389, No. 6646, (1997-9), pp.49-52
12. Hirano, K., Suzuki, T. and Sasamoto, A., "Feasibility Studies on Applying In-Situ Single Crystal Oxide Ceramic Eutectic Composites in Non-cooled High Efficient Turbine System", Ceramic Materials and Components for Engines (Eds.: J. G. Heinrich and F. Aldinger), WILEY-VCH, 2000, 543-548.

Proceedings of 7th Japan International SAMPE
Symposium & Exhibition, Nov. 13-16, 2001

Establishment of Database of Carbon/Epoxy material properties and design values on durability and environmental resistance

Shunichi Bandoh#1, Yoshihiro Nakayama, Ryoji Asagumo (Kawasaki Heavy Industries, Ltd.)
Tsutomu Yoshimura (Japan Aircraft Development Corporation)

#1: 1 Kawasaki, Kakamigahara, Gifu 504-8710, Japan (E-mail: bandoh_syunniti@khi.co.jp)

Abstract

A database of durability and environmental resistance of several carbon/epoxy composites and adhesives was established under Japan government-fund. In 2000, we had established a basic database of carbon/epoxy composite and installed in a CD-ROM. In this project, some materials and properties were added further and the database was expanded. The prototype online database system was also studied.

Key Words: Database, Carbon/Epoxy composite, Durability, Environment

1. Introduction

CFRP material have high specific modulus and strength, and good fatigue and corrosion durability. So CFRP is beginning to be used not only in aircraft field but also in building construction field. And use of CFRP is expected to increase in general industry purpose. In these situation, " Establishment of Carbon/Epoxy material properties and design values" project[1)3)] was carried out at " Establish of immediately effective intelligent foundation" project of Ministry of Economy, Trade and Industry to develop the industry of composite materials. Three problems of some revealed problems in that project are paid attention to; (a) Expansion of materials, (b) Expansion of design data (c) Improvement of ease of use. " Establishment of Carbon/Epoxy material properties and design values on durability and environmental resistant" project were carried out[2)]. In this project, research of user friendly database for design was conducted by collecting data on strength, durability, and environmental resistance property of CFRP for low temperature cure and adhesives ,etc expected to be developed in the future.

This report shows that the summary of selected materials for database, various test items in charge of KHI, and database.

2. Material selection for Database

Several CFRP materials showed at table 2-1 are selected for the database according to conditions as follows;

(a) Carbon Fiber : Modulus 235 GPa class fiber that was developed recently and will be major products probably.
(b) Prepreg: Unidirectional prepreg, cloth prepreg, and stitching cloth for RTM.
(c) Supplier : Toray, Toho-Rayon, and Mitsubishi Rayon (Major suppliers in Japan)
(d) Resin : General purpose epoxy, or epoxy for low temperature cure.
(e) Impregnation : 2 method of impregnation (Prepreg, and RTM)

In addition, room temperature cure epoxy adhesive is selected, that is expected to be applied to adhesives of composite structure . Sumitomo 3M DP-460 is selected.

Table 2-1 Materials for database

Material Name	Material Designation	Fiber	Form of Fiber	Name of Supplier	Resin	The way to impregnate	Company in charge
T700UP	P3312G-19	T700GC	Tape	Toray	3900MI	preimpregnated	MHI
T700CP	FF6273H-24K	T700GC	Fabric	Toray	3680	preimpregnated	MHI
T700UR	-	T700GC	Tape	Toray	R9803	RTM	FHI
T700CR	-	T700GC	Fabric	Toray	R9803	RTM	FHI
UT500UP	QU135-197A	UT500	Tape	Toho-Rayon	#135	preimpregnated	KHI
TR30UP	TR830F190SMXY	TR30	Tape	Mitsubishi Rayon	#830	preimpregnated	MHI
TR30UPA	TR850G190SMXX	TR30	Tape	Mitsubishi Rayon	#850	preimpregnated	MHI
T700UPA	P3242G-19	T700	Tape	Toray	3680	preimpregnated	MHI
T700CRA	-	T700GC	Fabric	Toray	TR-A31	RTM	FHI
T700CRA 1	-	T700GC+TR40	Fabric + Stitching (6mm)	Toray	TR-A31	RTM	FHI
T700CRA 2	-	T700GC+TR40	Fabric + Stitching (3mm)	Toray	TR-A31	RTM	FHI
T700CRA 3	-	T700GC +Kevlar	Fabric + Stitching (3mm)	Toray	TR-A31	RTM	FHI

3. Test item and summary

Various kinds of test of Toho-Rayon UT500UP (one of 12 materials showed in table 2-1) were conducted in KHI. Basic material property showed in table 3-1 have been conducted in the previous project.[1)3)]

In the project of this year, durability test and environmental resistance tests were conducted and added to database. Details of each test are described below.

Table 3-1 Basic material property test

Test Item	
Material and coupon properties	Uncured physical properties
	Chemical properties
	Cured physical properties
	Fire resistant property
	Mechanical properties of lamina
	Mechanical properties of laminate
	Fracture toughness properties
Elements properties	Fastener joint property
	Post buckling property of stiffened panel
	CAI property of stiffened panel

Material durability tests

Durability test on cyclic load was conducted to confirm that structure of composite material have enough durability to use it for a long term. 3 items of durability test is performed as follows:

①Basic fatigue property test of general composite laminate

② Fatigue test of principal structure elements of practical composite parts.

③Confirmation test of fatigue property of typical sub-component structure

Details of conducted durability test is showed in table 3-2.

Table 3-2 Durability test item

	Test item	Summary of test	Specimen
Basic fatigue property test of laminate	Fatigue test of open-hole, and non-hole laminate (Tension)	Tension fatigue tests of open-hole and non-hole laminate are conducted to get basic fatigue properties of composite laminate. (R=0.1)	
	Fatigue test of laminate with impact damage (Tension, and compression)	Coupons impacted in advance are loaded cyclically (R=0.1) to get data of fatigue property of damaged laminate. (Tension and compression, 2 energy of impact)	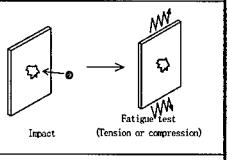
	Fatigue test of delamination	Coupon with artificial delamination (release film inserted) is loaded cyclically (Bending and shear load, R=0.1). The number of load cycle up to first propagation of delamination is measured. (2 variety of energy release rate ratio of mode I and mode II are selected.) (Energy release rate ratio of mode I and mode II are changeable by selecting position of loaded point and specimen loaded point.)	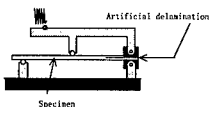
Elements property test	Fatigue test of fastener joint (Tension)	Single or double fastener joint fatigue test is conducted (R=0.1).	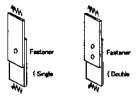
	Fatigue test of corner bending (Tension)	Fatigue test of Specimen for corner bending (L shape) is conducted to get fatigue property of composite corner radius part. (Tension load, R=0.1, 2 thickness specimen)	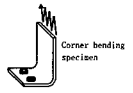
Sub-components	Fatigue test of stiffened panel with local buckling of skin (Compression and shear)	At first static test of stiffened panel is conducted to get preliminary buckling data for fatigue test. Next, fatigue test is conducted (R=0.1). The number of load cycle is measured up to delamination between stiffener base and skin.	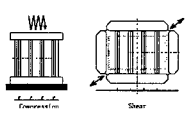

Environmental resistant test

Composite structure is required to keep its strength and stiffness against actual environmental effects. So environmental resistant test of composite is conducted in order to get properties of composite

materials after environmental aging. 4 major environmental factor are collected, which possibly effect resin property of composite, as follows ;

(a) Effect of ultraviolet rays or ozone environment

(b) Chemicals which is possibly into contact with composite structure during aircraft operation.

(c) Thermal cycling which possibly operate composite structure during aircraft operation

(d) Effect of nature environment cycle of sunlight and rain

Details of each test is showed in table 3-3.

Table 3-3 Environmental resistant test

Test item	Summary of test	Environment condition	Test parameter
Ultraviolet rays	Open-hole compression test and observation of edge fracture of specimen are conducted after aging specimens in ultraviolet rays environment to evaluate effects of environment on material strength property.	· Strength of ultraviolet rays 0.3~0.4 W/m^2 · Wavelength 340nm	· Aging time(250/500H) · Painted / No painted
Ozone	Open-hole compression test and observation of edge fracture of specimen are conducted after aging specimens in ozone environment to evaluate effects of environment on material strength property.	Ozone concentration 50±5ppm	· Aging time(250/500H) · Painted / No painted
Chemicals (fuel, solvent)	Open-hole compression test and observation of edge fracture of specimen are conducted after immersing specimens in chemicals to evaluate effects of environment on material strength property.	fuel/solvent/lubricating oil	· Aging time (500/1000H) · Painted / No painted
Thermal cycling	Open-hole compression test and observation of edge fracture of specimen are conducted after thermal cycling of specimens to evaluate effects of thermal cycle on material strength property.	· Temperature : -54~82°C	· Number of cycle (1000/2000 times)
Nature environment cycling	Open-hole compression test and observation of edge fracture of specimen are conducted after nature environment cycling of specimens to evaluate effects of nature environment on material strength property.	· strength of ultraviolet rays 0.3~0.4 W/m^2 · Wavelength 340nm · Temperature 60±3°C · Humidity 50±4%	· Number of cycle (1000/2000 times) · Painted / No painted

There is no reduction of material property of UT500UP on environmental effects in table 3-3. For example, results of ultraviolet rays test is shown in figure3-1. This picture is displayed on database software (CD-ROM) by selecting property type, material type, and environmental condition. There is no reduction of strength and increase of cracks of specimen edge after 500 hours aging under the stratosphere condition (strength of ultraviolet rays0.3~ 0.4W/m^2、wavelength 340nm) . Hence, There is no need to consider reduction of material property in the use under restriction of this test parameter.

As this example is showing, material properties under various kinds of environmental condition are collected in this database. So this database is very effective tool for getting guidance to design structures in the practical environment during operation.

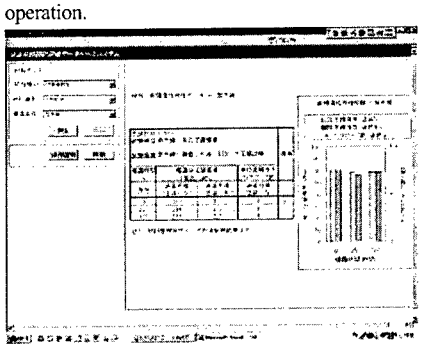

Figure 3-1 Test result of ultraviolet rays aging test (Example of display of database software : material data、UT500UP、ultraviolet)

4. Composition of the whole of database

Composition of the whole of database constructed in this project is showed in figure 4-1. Composition of database of the previous project is used, and durability and environmental resistance data of this year are added to the previous database to make database CD-ROM in this project. In addition, on-line type database , which is usable on the internet web, has been made in this project.

In this database, not only design data and raw data of test results but also another important information for design is mentioned, that is, " explanation" (the way to use database software, condition of design, and so on) and " theoretical explanation" (basic information of composite materials, theoretical explanation, and reference books).

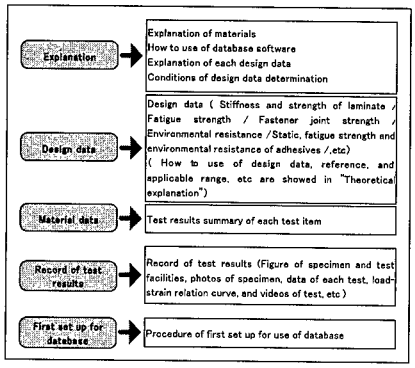

Figure 4-1 Composition of the whole database

5. Conclusions

Useful data of various materials are obtained by cooperation of three private enterprises (KHI, MHI, FHI). And CD-ROM and On-line database could be constructed by cooperation of The Japan research institute and Doshisha University. Increase of use of composite materials in the general industrial world is expected by utilizing this database project results.

Acknowledgment

This study is sponsored by Ministry of Economy, Trade and Industry and Japan Aircraft Development Corporation. We are very thankful to Ministry of Economy, Trade and Industry for giving us opportunity to obtain material data and construct database.

References

(1)Japan Key Technology Center " Report; Establishment of Database of Carbon/Epoxy material properties and design values" , March,2000

(2) Japan Aircraft Development Corporation " Report; Establishment of Database of Carbon/Epoxy material properties and design values on durability and environmental resistance" , March, 2001

(3)K. Masuda, Y. Ichihara et al. " Establishment of Database of Carbon/Epoxy material properties and design values (Part1 Data preparation) (Part2 Database Establishment)" the 38th aircraft symposium ,2000

Proceedings of 7th Japan International SAMPE
Symposium & Exhibition, Nov. 13-16, 2001

Thermal Degradation of CFRP Laminates

Tomohiro Naruse and Toshio Hattori

#: Mechanical Engineering Research Laboratory, Hitachi, Ltd. 502 Kandatsu-machi,
Tsuchiura-shi, Ibaraki, 300-0013, Japan
E-mail: naruse@merl.hitachi.co.jp

Abstract

To confirm the usability of carbon-fiber-reinforced plastic (CFRP) laminates for thermally loaded machines, we investigated the thermal degradation of fatigue strength of CFRP laminates. We evaluated the fatigue strength under interlaminar shear stress of virgin materials and degraded materials. Ot was found that (i) the fatigue strength was reduced with increasing degradation time and temperature and (ii) the reduction ratio of fatigue strength decrease in proportion to the logarithm of degradation time at a certain temperature. We then estimated the relation between temperature and degradation time by fitting the experimental results to the Arrhenius equation. Using this relationship, we predicted the reduction in fatigue strength for CFRP laminates, for example the predicted fatigue strength of CFRP laminates would reduce by 10% (i.e., a fatigue strengh reduction ratio of 0.9) when heated at 40℃ for 9×10^6 hours.

Key Words: FRP, Thermal degradation, Fatigue strength.

Introduction

Since fiber-reinforced plastic (FRP) has high strength but low density compared with steels, FRP laminates are used in pressure vessels, transportation systems, etc. When FRP is used in such structures, it is exposed to a degrading environment, such as high temperature, high humidity, or strong light, as well as mechanical load [1-3]. Such environmental conditions reduce the strength of the FRP. Therefore, It is therefore necessary to develop a degradation acceleration test that can estimate in a comparatively short time, the strength reduction under an actual working environment for the working life of the product.

With the aim of developing this test, we used carbon FRP (CFRP) laminates to study the thermal degradation of fatigue strength. We measured the thermal degradation of fatigue strength under interlaminar shear stress. Fatigue tests were performed on virgin CFRP laminates and several thermally degraded CFRP laminates. We applied the Arrhenius equation to the measured fatigue strength in order to determine the relation between temperature and time. We then used this relation to predict the thermal degradation of fatigue strength of CFRP laminates.

Dimension of test piece and fatigue test method

The test piece configuration for the fatigue test is schematically shown in Fig. 1. The CFRP laminates consist of a type of PAN carbon fiber and epoxy resin, and the laminate configuration comprises quasi-isotropic laminates $[+45/0/-45/90]_{4S}$. The

glass transition temperature, Tg, of the epoxy resin is about 120℃. And the fiber volume fraction of each CFRP laminates—measured by the specific weight method—is approximately 60%.

We used Standard Test Method for Apparent Interlaminar Shear Strength of Composites (ASTM D2344) for the fatigue tests. The ends of the test piece rest on two supports, the load being applied by means of a loading nose directly centered at the midpoint of the test piece. Stress ratio R was 0.01 and loading frequency was 4—10 Hz.

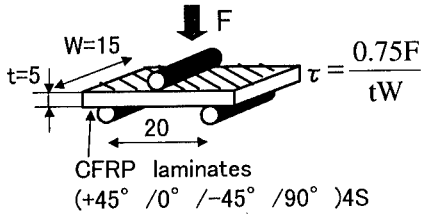

Fig. 1 Dimensions of Test piece for fatigue test

Testing method for thermal degradation of fatigue strength

First, we fatigue-tested CFRP laminates before degradation (virgin rings) at room temperature. Next, to accelerate thermal degradation, some test pieces were heated to some higher temperature. Aging conditions are listed in Table 1. We fatigue-tested the degraded test pieces at room temperature in the same way as the virgin test pieces. Then we evaluated the reduction of fatigue strength of the degraded test pieces.

Table 1 Degradation conditions

Degradation temperature (℃)	Degradation time (hours)
85	200, 1340, 2600, 5200
100	200
115	200, 500, 1340, 2600, 5200

CFRP consists of carbon fiber and a matrix. It is predicted that the material properties of carbon fiber do not degrade much at high temperature. It is therefore conceivable that the thermal degradation of CFRP laminates is caused by the thermal degradation of the matrix. The matrix consists of polymeric materials, so it is assumed that the thermal degradation of such materials is a kind of chemical reaction. According to this assumption, the relationship between degradation time and degradation temperature is given by the Arrhenius equation as [4-6],

$$\ln t = \frac{Ea}{R}\frac{1}{T} + A, \qquad (1)$$

where, T is degradation temperature (absolute temperature), t is degradation time, Ea is activation energy, R is gas constant, and A is a constant representing the reduction ratio of fatigue strength. By extrapolating the linear relationship between ln t and 1/T, it is possible to predict the strength reduction after a specified lifetime.

We also assume that thermal degradation is independent of fatigue behavior under mechanical load. We thus think that the chemical reaction of the matrix is not accelerated by mechanical load. So we evaluated thermal degradation and fatigue strength separately.

Results

The measured fatigue strength of the virgin material at room temperature is shown in Fig. 2. The horizontal axis is the logarithm of the number of cycles to failure and the vertical axis is the stress amplitude calculated by using the equation shown in Fig. 1. The figure shows a linear relation between the logarithm of the number of cycles to failure and stress amplitude in the range of 10^3-10^6 cycles.

The fatigue test results of test pieces degraded under the conditions listed in Table

1 are shown in Figs. 2 and 3. The reduction ratio of fatigue strength, D, is obtained by dividing the fatigue strength of the degraded material by the fatigue strength of the virgin material. The relationship between the D and degradation time, t, at each degradation temperature, T, is shown in Fig. 4. This figure shows that the reduction ratio of fatigue strength, D, reduces in proportion to logarithm of degradation time t. From this graph, the degradation times at a certain reduction ratio can be read off at each degradation temperature, and these times are plotted against temperature in Fig. 5. The horizontal axis is the reciprocal of the degradation temperature and the vertical axis is the degradation time. This figure shows that the degradation time, t, at each reduction ratio (0.95,0.9 or 0.85) is proportional to the reciprocal of degradation temperature, 1/T. We thus consider thermal degradation is not accelerated by mechanical load. And extrapolating these linear relations predicts that the fatigue strength will reduce to a ratio of 0.9 under a working temperature of 40℃ after 9×10^6 hours. It is thus possible to evaluate the degradation of fatigue strength under any temperature and after any time by this acceleration test method.

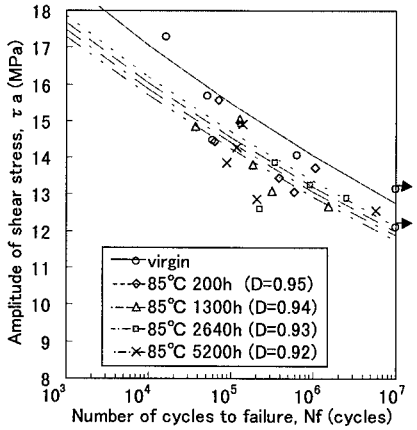

Fig. 2 Fatigue strength after thermal degradation (85℃)

It should be noted that in this study we assumed thermal degradation is not influenced by mechanical load. But it is conceivable that thermal degradation is accelerated by mechanical load. This subject remains for future work.

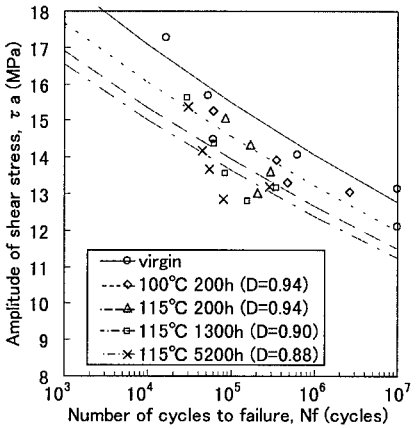

Fig. 3 Fatigue strength after thermal degradations (100℃ and 115℃)

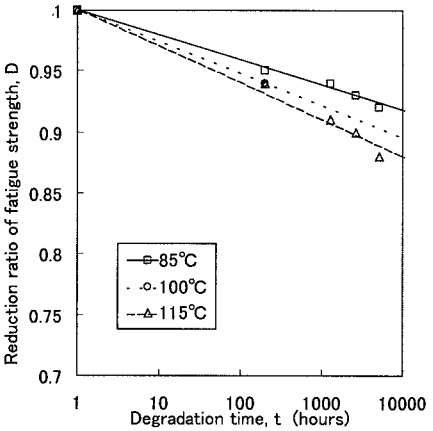

Fig. 4 The reduction ratio of fatigue strength

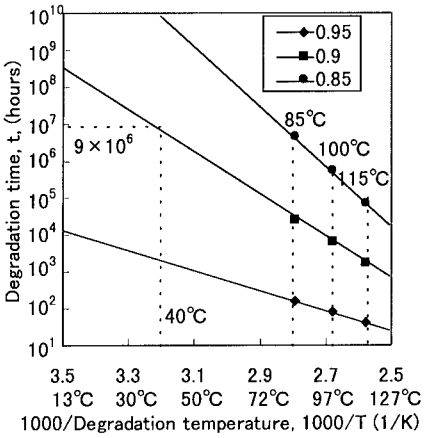

Fig. 5 Prediction chart for fatigue strength reduction by thermal degradation

Summary

We studied the thermal degradation of fatigue strength under interlaminar shear stress of quasi-isotropic CFRP laminates. We fatigue-tested virgin CFRP laminates and several thermally degraded CFRP laminates, and we determined the relation between temperature and time by using the Arrhenius equation. Then we used this relation to predict the thermal degradation in a shorter time (several thousand hours) than working time. The main results of our study can be summarized as follows.

· The reduction ratio of fatigue strength for interlaminar shear stress reduces in proportion to logarithm of degradation time t.

· The predicted fatigue strength of CFRP laminates would reduce by 10% (i.e., a fatigue strength reduction ratio of 0.9) when heated at 40℃ for 9×10^6 hours.

Acknowledgment

This work was supported by a grant from the Research & Development Institute of Metals and Composites for Future Industries (RIMCOF), Japan, on the basis of Application of Advanced Composites for Transportation Systems proposed by the Ministry of Economy, Internal Trade and Industry (METI) of Japan.

References

1. Yeow Y.T, Morns D.H and Brison H.F, Composite Materials: Testing and Design (First Conference) ASTM STP674 (1979), 263-281.
2. Wang A S D and Liu P K, J. Aircraft,5, 208(1971).
3. Nakada M and Miyano Y, ACCM-1, Osaka, 7, 442-1(1998).
4. Ohishi F, Durability of Plastics Material (in Japanese). NIKKAN KOTYO SHINBUN LTD, 1993.
5. Sakamoto A and Hattori T. ICM & M '97, Tokyo, 275 (1997).
6. Miyano Y, Nakada M and Hiroshi K, J. Composite Materials, 34(7), 538 (2000).

Proceedings of 7th Japan International SAMPE
Symposium & Exhibition, Nov. 13-16, 2001

Folded Honeycomb Core Materials for Automotive and Aerospace Applications

Jochen Pflug*, Ignaas Verpoest* and Dirk Vandepitte#

#: Katholieke Universiteit Leuven, Div. PMA, Celestijnenlaan 300 B, 3001 Leuven, Belgium
*: Katholieke Universiteit Leuven, Department of Metallurgy and Materials Engineering, Kasteelpark Arenberg 44, 3001 Leuven, Belgium,
E-mail: Jochen.Pflug@mtm.kuleuven.ac.be

Abstract

Two new cost efficient honeycomb materials and their continuous production processes have been developed at the K.U.Leuven. The materials and production methods enable an automated in-line production of paper and polypropylene (PP) based honeycombs for automotive sandwich panels and parts. Furthermore, the production of honeycombs from high performance thermoplastics, for aircraft interior, may become feasible with folded honeycombs. The production concepts and material combinations for automotive and aerospace sandwich parts are presented.

Key Words: honeycomb, core, sandwich, continuous production

Introduction

Two groups of sandwich core materials can be distinguished, the homogeneous and the structured cores. Homogeneous core materials, especially polyurethane foams, are widely used in the automotive industry. Recently polypropylene foams have become a better recyclable, but more expensive alternative to polyurethane foams. For thermoplastic aircraft interior parts polyetherimide (PEI) foam cores have been considered because of their good fire, smoke and toxicity (FST) properties.

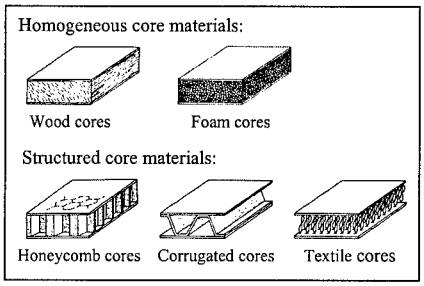

Fig. 1 Homogeneous and structured core materials

Honeycomb core materials are used in aerospace industries since many decades as the preferred core material for buckling and bending sensitive sandwich panels and structures. In automotive applications, except where crash energy absorption is the main function, honeycombs are less often used, due to their high production costs.

The packaging industry, on the other hand, employs already cost efficient all thermoplastic sandwich materials, e.g. extruded double wall panels [2] or sandwich panels with a thermoformed cup-shaped core layer [3, 4] from PP. However, those materials have generally lower mechanical properties compared to a sandwich material with a hexagonal honeycomb core.

Honeycomb Core Production Today

The main reason for the high costs of traditional expanded honeycomb cores is the batch like production process. Honeycomb core production today is labor intensive, discontinuous and not in-line. Most honeycomb cores are adhesive bonded expanded cores [1]. Low cost paper honeycombs are produced with the same process, shown in figure 2. First, glue lines are printed on flat sheets. Second, a stack of many sheets is made and the glue is cured. In the third phase, slices are cut from these blocks. Finally, the sheets are pulled apart, thus expanding into a honeycomb core.

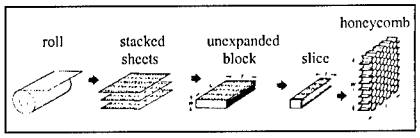

Fig. 2 Expansion production process of conventional honeycombs

For low cost applications the degree of automation has exceeded the level reached in aerospace honeycomb production. However, cell size and core height of these low cost paper honeycombs are usually above 10 mm, because the expansion process step in conventional honeycomb production gets more difficult at lower cell sizes. A second production process for conventional honeycombs is the corrugation process.

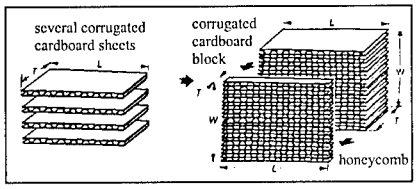

Fig. 3 Manual production of corrugated cardboard honeycomb cores

This process is not so often used and more expensive due to the handling operations required for the production of the block and the more difficult cutting from the block. However, if inexpensive corrugated cardboard sheets are used, a low cost honeycomb core can be produced with the process shown in figure 3. The increasing demand for low cost sandwich core materials and their advantageous mechanical properties have stimulated research activities at the K.U.Leuven to reduce the production costs of honeycomb cores, produced from paper as well as from thermoplastic materials.

Folded Honeycomb Sandwich Cores

In the framework of the European research projects FoldHex-ThermHex-TorHex, cost efficient honeycomb materials and their continuous production processes have been developed at the K.U.Leuven. For the production of those patented, so called "folded" honeycombs, production technology and processes of the packaging industry are used [5, 6]. Within a two year project the feasibility of two core versions has been proven: the TorHex paper honeycomb and the ThermHex thermoplastic honeycomb. These folded honeycombs are produced from one continuous thermoplastic sheet or from corrugated cardboard by successive in-line operations. The current development of cost efficient production machinery is driven by the request for large production capacities for applications like reusable thermoplastic boxes and recyclable cardboard boxes.

TorHex

The TorHex paper honeycomb process uses the corrugated cardboard production technology to a maximum extent. The inner core structure is a honeycomb with sinusoidal corrugated cell walls and folded straight reinforcing cell walls. Figure 4 shows the main geometric parameters as well as a TorHex sample. The reinforcing folded cell walls improve the shear

properties in the machine direction (MD). They can carry the tension forces in this direction and enable a fast transport of the material during production.

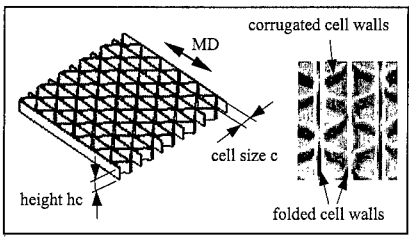

Fig. 4 Main geometric parameters and view onto a TorHex sample

The principle production concept is shown in Figure 5. Compared to the production of single flute corrugated cardboard, the TorHex honeycomb process requires additionally a lengthwise slitting step and a folding/turning process.

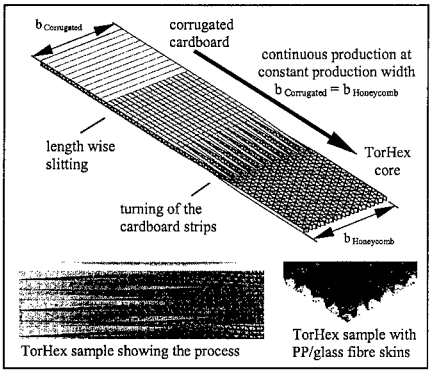

Fig. 5 TorHex paper honeycomb process

It is expected that this process will be not much more expensive than the additional corrugation and gluing steps for a double flute corrugated cardboard.

ThermHex

The ThermHex core, the thermoplastic folded honeycomb version, has hexagonal cells and closed skin strips, which allow a fast and reliable bonding of the skins onto the core without an additional glue layer.

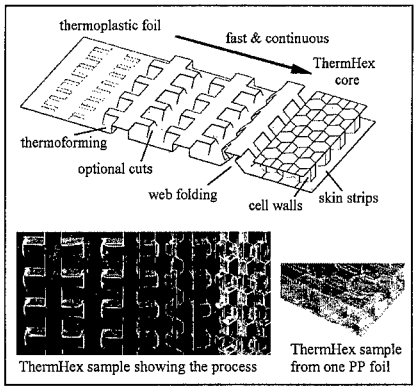

Fig. 6 ThermHex production process for thermoplastic honeycomb

The ThermHex core material can be produced in a continuous process in one production line. All the production steps can be done successively by rotational operations, which should make a core production speed of 10 m/min or more possible. Starting from one endless thermoplastic foil, the production steps are:

1. Forming of half-hexagonal shape by deep drawing or by vacuum thermoforming
2. Folding of the half-hexagonal web to build the honeycomb core
3. Internal bonding of the honeycomb core by thermal fusion
4. Lamination of thermoplastic skins onto the honeycomb core

This concept has proven to be feasible for different types of thermoplastic materials. Thermoplastic folded honeycomb samples have been produced from PP, PET, PC, PA and PEI foils.

Honeycomb Cores in Automotive Parts

In modern automobile design, integrated interior parts such as door trim panels, headliners and package trays have

multiple functions such as structural support, acoustic damping and water/dust barrier. The need to recycle automotive parts initiated developments of monomaterial sandwiches (all PP parts) and automotive interior parts with a high content natural raw materials such as flax, hemp or sisal fibers. Honeycomb sandwich construction can offer the solution to several of these demands. Figure 7 shows a schematic view of potential applications.

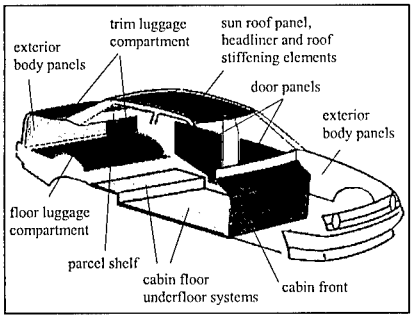

Fig. 7 Potential automotive sandwich applications

Honeycomb Cores in Aircraft Interior

The reduction of the production costs of aircraft interior panels, today made from expanded phenol coated aramide paper honeycombs, is desired.

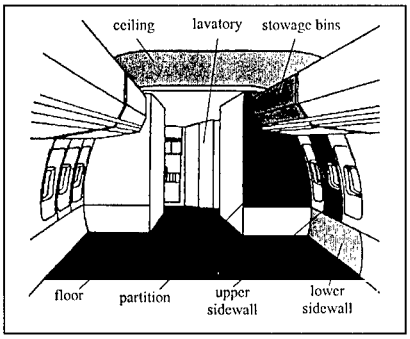

Fig. 8 Potential applications in the aircraft interior

To increase the safety in case of a fire accident, non-flammable high performance thermoplastics (e.g. PEI) could be used. With a PEI-ThermHex core all PEI-sandwich panels could be produced in a cost efficient continuous process. Those panels could be formed to complex curved parts using a hot press.

Conclusions

The folded honeycomb materials and production methods developed at K.U.Leuven offer a cost efficient automated in-line production of honeycombs. The TorHex concept allows the production of low costs paper honeycombs for high volume markets. The ThermHex concept is suitable for the production of cost efficient honeycombs for automotive and aerospace applications as well as for other markets. Additional research on the further processing of honeycomb sandwich panels to complex low cost sandwich parts is required.

Acknowledgment

The authors acknowledge the support of the Flemish Institute for the Promotion of Scientific and Technological Research in Industry (IWT) and the Belgian program on Interuniversity Poles of Attraction initiated by the Belgian State, Prime Minister's Office, Science Policy Programming.

References

1. Bitzer, T. N.: Recent Honeycomb Core Developments Sandwich Construction 3, Southampton ,1995, page 555-563
2. Akylux, Akyplac products technical information, Kaysersberg Packaging S.A., Product information, 1998
3. Pla-Pearl, Kawakamisangyo Co. Ltd. Product information, Nagoya, 1999
4. Con-Pearl, Con-Pearl friedola GmbH, Product information, Thüringen, 2000
5. Pflug, J. and Verpoest, I.: WO 00/32382 ThermHex, PCT patent publication, 2000
6. Pflug, J. and Verpoest, I.: WO 00/58080 TorHex, PCT patent publication, 2000

Proceedings of 7th Japan International SAMPE
Symposium & Exhibition, Nov. 13-16, 2001

Well-processable matrix resins with less-flammability for vacuum-assisted Resin Transfer Molding

Naomi Miyoshi#, Norimitsu Natsume#, Itaru Endo# and Hajime Kishi #

#: Composite Materials Research Laboratories
TORAY Industries, Inc., Ehime Plant
1515, Tsutsui, Masaki-cho, Iyogun, Ehime, 791-3193, JAPAN
E-mail: Naomi_Miyoshi@nts.toray.co.jp

Abstract

Phenolic resin and cyanate ester resin were chosen as the candidate matrix resins in view of less-flammability and processability for vacuum-assisted Resin Transfer Molding (VaRTM).

Less-flammabilities of phenolic resin and cyanate ester resin were quantitatively evaluated by cone caloriemetry, and the relation between heat release rates determined by the cone caloriemetry and the materials combustion test results for rolling stock in Japan was discussed.

Improvements in less-flammability and cure ability of cyanate ester resin were also studied. The heat release rate was decreased with the addition of flame retardants into cyanate ester resin. The cure ability of cyanate ester resin was improved with addition of catalysts. A sandwich-structured composite panel was fabricated using the resin by VaRTM, pre-cured for 1 day at 80 degree C and post-cured for 2 hours at 130 degree C.

Key Words: less-flammability, VaRTM, cyanate ester, railcar

Introduction

Technology for high speed and mass volume of transportation are needed as demand for carrying power of transportation increases. In such situation, the weight reduction of transport is the important subject to make efficient use of energy and resource for transportation. Advanced composite materials, especially polymer matrix composites are preferred materials responding these demands. The issue is to establish the practical and economical technology of fabricating composite structure.

From the above point of view, it is studied for developing fabrication process technology for large scale composite structure that design and analytic technology of composite, rapid cure cycle process, matrix resins for rolling stock structural materials, flow monitoring and evaluation technology for fabricated composite.

In this paper, the selection of candidate matrix resins, the relation between heat release rates determined by the cone calorimeter and the materials combustion test results for rolling stock in Japan are described and discussed for developing matrix resins for rolling stock structural materials. Furthermore, the improvement of less-flammability and cure ability of cyanate ester resin, which is one of the candidate matrix resins, are also described and discussed.

Selection of matrix resins

Five thermosetting resins (epoxy resin, phenolic resin, benzoxazine resin, cyanate ester resin and bismaleimide resin) were evaluated on mechanical properties, heat resistance, processability and less-flammability. These results are shown in Table.1.

Table 1 Resin properties of screened resins

	Mechanical property	Heat Resistance	Fabrication friendly property		Less-flammability
	Elastic modulus (MPa)	10% Weight decrease temperanure (℃)	Weight decrease during cure	Viscosity @ R.T.	Material combustion test for railroad coach (JAPAN)
Epoxy resin	3.4	348	0.0	○	×
Phenolic resin	3.3	460	25.4	○	◎
Benzoxazine resin	5.4	348	7.7	×	---
Cyanate ester resin	3.0	432	0.4	○	○
Bismaleimide resin	4.1	425	4.5	×	---

--- could not evaluated

As the result, phenolic resin and cyanate ester resin were chosen for further study on rolling stock structural materials.

Phenolic resin has good heat resistance and less-flammability that was classified "incombustible" in the materials combustion test for rolling stock in JAPAN[1]. Furthermore, phenolic resin can be cured at low temperature such as 25 degree C.

The fabricated composite by phenolic resin, however, contains much surface pits and internal voids due to water by the condensation reaction, that would deteriorate the mechanical properties. Besides, the pot life and curing time of phenolic resin should be optimized for fabricating the large scale composite structure.

Reduction of contained voids in cured resin and optimization of cure ability is required for phenolic resin.

Cyanate ester resin has good heat resistance, mechanical property and surface smoothness of the fabricated composite, because no low molecular weight compounds are generated during curing. The relatively less-flammability to other resins is also the characteristic of cyanate ester resin. However, the less-flammability should be improved for the application of cyanate ester resin for rolling stock structural material.

High temperature such as 230-250 degree C is needed to cure cyanate ester resin. It is not realistic to prepare the huge and highly heat- resistant mold to fabricate large scale composite such as rolling stock structure from an economical point of view. It is necessary for cynate ester resin to improve cure ability so that the resin can be cured below 100 degree C. This improvement leads big advantage of cost-competitiveness in fabricating composite for VaRTM because hot water is applicable as heat source and FRP or plaster mold can be used.

Improvements of less flammability and cure ability of cyanate ester resin were studied, in this paper.

The determination of quantity of less-flammability for rollig stock structural materials

The material combustion test for rolling stock in JAPAN that classifies less-flammability is qualitative method. The most part of the judgement tends to depend on sense of the referee.

In this study, less-flammability was evaluated by means of cone calorimeter to determine less-flammability qualitatively, quantitatively and objectively. The heat release rate (HRR) is the quantitative parameter obtained by cone calorimetry, that is reflected the easiness of expanding of combustion .

As a result, there was correlation between the judgement of less-flammability of the material combustion test and HRR. The HRR of phenolic resin that was not flammable in the material combustion test was the lowest of the three resins (Fig.1). On the other hand the HRR of epoxy resin that

didn't meet requirement of less-flammability in material combustion test was the highest. It was found that the HRR became lower, judgement in material combustion test showed higher level of less-flammability.

Since less-flammability would be evaluated by means of cone calorimetry, the level of the HRR of phenolic resin was decided as the target in improvement of less-flammability of cyanate ester resin.

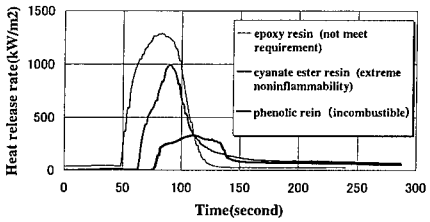

Fig. 1 Evaluation of heat release rate by cone caloriemetry

Improvement of less-flammability of cyanate ester resin

The method of addition of flame retardant contained halogen monomer is widely used in order to improve less-flammability. While combustion of these monomers, however, poisonous gases will be generated. In this research, addition of flame retardants without halogen compounds was chosen to improve of less-flammability of cyanate ester resin. [2]

Several conventional flame retardants without halogen compounds were applied to cyanate ester resin, and less-flammability was evaluated by cone calorimetry. As a result, it was found that an appropriate phosphoric flame retardant enables cyanate ester resin to exhibit almost equivalent HRR of conventional phenolic resin. It also has good processability from the view point of viscosity.

Table 2 HRR and viscosity of modified cynate ester resin

	HRR (kW/m2)	viscosity* (mPa · s)
unmodified	1000	84
Al additive	430	620
Phosphoric additive	440	50
Boric additive	453	78

* @25 degree C

Cyanate ester resin generates more smoke during burning than phenolic resin. The further task of this study would be reduction of quantity of smoke.

Improvement of cure ability of cyanate ester resin

Resin modification with curing catalysts.

Curing catalysts for cyanate ester was searched and applied, referring known literature.[3] The exothermic curves are shown in Fig.2. It was found that the start temperature of exothermic reaction of cyanate ester resin was 100 degree C or less by mixing cyanate ester resin with an appropriate organometalic compound and hydroxy compoud as curing catalyst. In the mean time that of unmodified resin was 210 degree C.

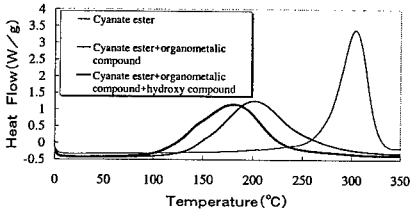

Fig. 2 Exothermic curve of cyanate ester resins

The curing test of the modified resin at 80 degree C was performed. The results are shown in Table.3. It was found that this modified resin had enough mechanical strength and Tg for demolding after

pre-curing for 24 hours at 80 degree C. Furthermore, higher mechanical strength and Tg were obtained by post-curing for 2 hours at 130 degree C.

Table 3 Properties of cured resin

Cure condition	A*	B*
Flexual properties		
Modulus(GPa)	3.8	3.8
Strength(MPa)	30	190
Tg (degree C)	92	167

*: 80℃×24hours

**: 80℃×24hours+130℃×2hours

Model test of fabricating sandwich-structured panel

The fabrication of sandwich-structured panel was examined by VaRTM to indicate the potential of low temperature process using the modified resin. After lamination of preforms and injection of the modified resin, the sandwich-structured composite panel was easily demolded after curing for 24 hours at 80 degree C. The sandwich-structured composite panel post-cured for 2 hours at 130 degree C had good surface quality and had no obvious void and crack.

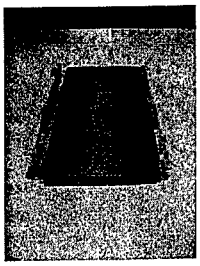

Fig. 3 sandwich-structured composite panel of CF fabric/Cyanate ester resin

Conclusions

Phenolic resin and cyanate ester resin were chosen as candidate matrix resins for further study on rolling stock structural materials.

Modified cyanate ester resin, which exhibits almost equivalent HRR during cure to conventional phenolic resins and has good processability, was developed using an appropriate phosphoric flame retardant.

It was found that cyanate ester resin with an appropriate catalyst could be pre-cured at 80 degree C, which temperature is low enough to apply a low cost composite fabrication, VaRTM.

Acknowledgment

This research and development project on advanced composite materials for transportation has been performed since September, 1998 as a 5-year project, sponsored by the Ministry of Economy, Trade and Industry.

References

1. Japan railway engineers association: Technical report "*Research on fire protection measures for rolling stock*" 1991, pp.24.
2. H. Nishizawa (eds.): "*Flame-retardancy of polymer, the chemistry and practical technology Vol.3*" Taiseisha, Japan, 1992, pp. 62-97.
3. Asahi-KASEI epoxy Co., Ltd.: Technical report

Proceedings of 7th Japan International SAMPE
Symposium & Exhibition, Nov. 13-16, 2001

Low Cost Resin Transfer Molding of Carbon Polyimide

Hiroshi Mizuno, Hideki Horizono
: Nagoya Aerospace Systems, Mitsubishi Heavy Industries, Ltd., Japan
10, Oye-cho, Minato-ku, Nagoya 455-8515, JAPAN
Yoshiaki Someya, Tomohiro Ito, Yoshihiro Soeda
: The Yokohama Rubber Co., Ltd
2-1, Oiwaka, Hiratsuka, Kanagawa 254-8601, Japan
E-mail: someya.y@mta.yrc.co.jp

Abstract

In order to manufacture carbon polyimide at low cost, RTM (Resin Transfer Molding) process of thermosetting polyimide has been studied. To remove methanol and water during cure, tooling attached with micro-porous filter and curing condition have been improved. The improved process has manufactured void free laminate. When transferring polyimide to the tool, it needs high pressure. There occurred the waviness of dry cloth around the transport area. To apply open mesh for the transport area, the dry cloth waviness problem was solved. To establish further cost reduction, closed-RTM process, which is no-vacuum assist and inflatable mandrel, has been studied. It is not necessary to use vacuum pump during transferring polyimide and to use heat press during cure. Then the process has established fifty percent cost reduction compared with prepreg lay-up process.

Key Words: RTM, Polyimide,

1. Introduction

For the prime structure of a future high-speed aircraft, lightweight and high temperature composites would be widely used. Thermosetting polyimide is one candidate matrix of high temperature material, however it generates methanol and water during cure. So it is necessary to remove those condensed materials from the composites during cure, otherwise there would be void, delaminating, or crack in the laminate. Commonly used manufacturing process of thermosetting polyimide is prepreg-autoclave method, but it need high labor cost for material, tool, lay-up, and curing processes. In order to manufacture low cost carbon polyimide parts we selected RTM[1] process. We selected PMR-15[2] as polyimide matrix among several high temperature polymers, because it has been used as industrial parts and this polyimide RTM process will be applicable for another polyimide such as imide oligomer solution, another thermosetting or pseudo-thermoplastic polyimide. It is difficult to manufacture void free composites using conventional RTM[3] process. To remove methanol and water from polyimide, micro-porous filter was used.

This report describes a low cost RTM for matrix which generate condensed material during curing or consolidation and this process would be used not only PMR-15 but imide oligomer, pseudo-thermoplastic polyimide, phenolic resin and so on.

2. Experimental

2.1 Resin: thermosetting polyimide: PMR-15 methanol solution (Yokohama Rubber Co.,) was prepared from three monomer reactants: nadic anhydride monomethyl ester (NE),

4,4'-methylene dianiline (MDA), and 3,3', 4,4'-benzophenone tetracarboxylic anhydride dimethylester (BTDE)

2.2 Fabric: graphite fiber: Intermediate modulus graphite fabric was used in this study; T800H eight harness satin fabric CL6649 (Toray Corp.) Stitch fabric was also evaluated in this study. Its specification is as follows;

Fabric	Eight harness satin 16 ply
Fabric Yarn	T800HB-6K-40B
Stitch Yarn	T900-1K
Size	300mm x 300mm
Stitch Pitch	Pitch: 5mm, Width: 10mm
Stitch Type	Modified Lock Stitch

2.3 Tool: Vacuum assist tool is illustrated in Fig. 1. A micro-porous filter [4] has been prepared from PTFE(Polytetrafluoroethylene) powder. This powder was pressed, and then RTFE filter, which contains small particle size (10-40 micrometer), was prepared. This micro-porous filter was placed in the RTM tool cavity. Methanol and water, which was generating during imidization, removed through the filter by vacuum and imide oligomer remains in graphite fabrics.

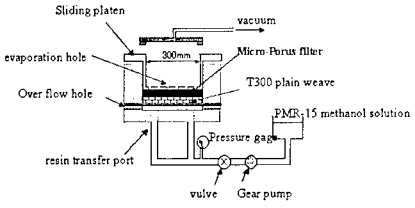

Fig.1 polyimide RTM tool for flat panel

3. Result and Discussion

3.1 Polyimide RTM Process: Micro-porous filter has been suitable to remove methanol and water from a composite, but at 1.4 MPa which is as same pressure as an autoclave process, there remained void in the laminate and its inter laminate shear strength was lower than that of autoclave cure. Several RTM pressure tests were performed and we found that there was no void in a laminates and its inter laminate shear strength was as same or higher value as a laminate manufactured at the pressure higher than 2.7 MPa. Refer fig. 2. At polyimide RTM process needs higher curing pressure than autoclave because of it is high viscosity.

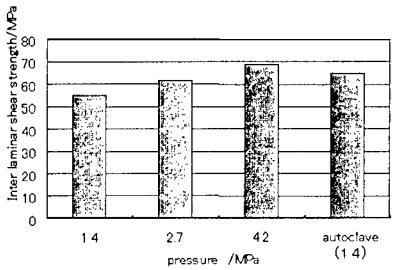

Fig. 2 RTM pressure vs. ILSS

3.2 Thick laminate: 8-ply laminate panel was fabricated for mechanical property tests and 16 ply for thick laminates evaluation. For thick laminate, it is anxious that there was void because of degassing difficulty. At 4.1 MPa of RTM pressure, there was no void in the 16 ply laminates and PMR-15 resin was fully impregnated in the fiber. Refer fig. 3.

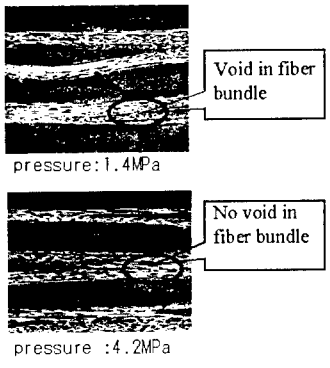

Fig. 3 RTM pressure comparison

3.3 Stitch fabric: 300mm x 300mm x 16 ply

of stitch fabric were evaluated for polyimide RTM process. There was no void in the laminate except around stitch yarn. There are little crack stitch yarn only. Where stitch yarn was inserted, there is some room where polyimide resin content is relatively high compared another area. At relatively resin rich area, there happened to be curing stress and it generates crack in the laminate. Compressive strength of stitch fabric was also evaluated in matrix comparison with PMR-15 and BMI. The compressive strength of both matrix are similar, that is PMR-15: 564MPa and BMI: 572Mpa.

3.4 T-shape frame: There was resin leaking through the tool illustrated fig. 1. T-shape parts shall be pressured both side of top-bottom and sides simultaneously. The tool for PMR-15 needs both function of slide and seal. Then the toll was improved as fig.4. The tool includes tapered block and O-ring.

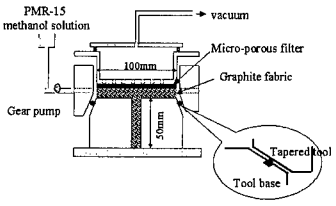

Fig. 4 Tool for T-shape frame

There is "spring-in" at the point of web and fringes. Fig. 5 shows the angle of T-shape, that is 89 degree and the "spring-in" is 1 degree as similar result as epoxy prepreg. This result could be applied to RTM tool design.

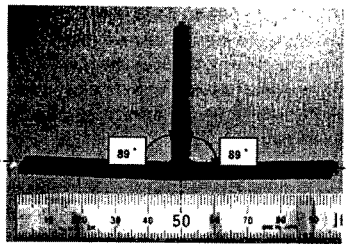

Fig. 5 Spring-In of T-shape frame

3.5 Cylinder: To eliminate resin transfer pump, to simplify the polyimide tool, and not to use autoclave or heat press, PTFE solid mandrel, open-mesh cloth, and micro-porous filter were prepared for the PMR-15 cylinder tool. We named this tool as "closed –RTM" process. PMR-15 methanol solution was transferred by vacuum only during imidization stage the mandrel inflates by heat, imidized by-products were pushed out through micro-porous filter.

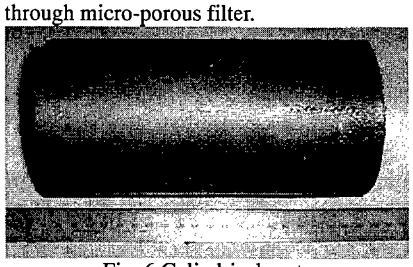

Fig. 6 Cylindrical parts

3.6 Low Cost RTM Evaluation: PMR-15 manufacturing process cost was compared with prepreg lay-up, Pressure RTM and Closed-RTM. Closed-RTM process does not need pressurized-machine, it is established to simplify tool and labor cost of dry fiber setting, resin transferring and lay-up. Further running cost of cure is also reducted. We estimate that approximately fifty percent cost reduction is established as for curing, layup, material and tooling process.

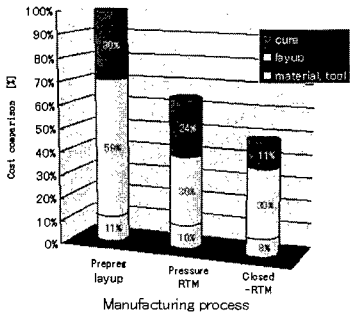

Fig. 7 Cost comparison RTM vs Lay-up

4. Conclusions

Polyimide resin has inherent difficult properties that is 1) gas generation during imidization, 2)high viscosity. These difficulties were solved by the following manufacuring process: 1) through micro-porous filter gas is removed and oligomer can be remained in the composites , 2)open-mesh dry fiber prevent waviness of polyimide composites

By high pressure RTM or Closed-RTM, thick laminates, stitch fabric laminates and cylindrical parts can be manufactured with no void and high mechanical properties.

Low cost polyimide RTM process was evaluated as fifty percent cost reduction compared with autoclave process.

References

1) Krolewski, Suwan: 34th SAMPE Symposium, 329(1989)
2) Serafini, Tito T.;Delvigs,Peter and Lightsey Geroge R.: J. Apply. Polym. Sci., 16, (4), 905(1972)
3) Doug Wilson: High Performance Polymers, 3, (2), 73(1991)
4) Soeda, Yoshihiro, et al., 28th SAMPE Technical Conference, 687(1996)

Proceedings of 7th Japan International SAMPE
Symposium & Exhibition, Nov. 13-16, 2001

Fatigue Strength Evaluation of FRP/Metal Adhesive Joints at Low Temperature

Masaaki Iwasa# and Toshio Hattori#

#: Mechanical Eng. Res. Lab., Hitachi, Ltd.
502 Kandatsu-machi, Tsuchiura, Ibaraki, 300-0013 Japan
E-mail: iwasa@merl.hitachi.co.jp

Abstract

The fatigue strength of two types of FRP/metal adhesive joints at low temperature, a double lap joint and an embedded joint, was evaluated analytically and experimentally. First, the stress singularity parameters of the delamination edges under mechanical and thermal loadings were analyzed by FEM for various delamination lengths. The delamination propagation rate of the double lap joint was measured under mechanical cyclic loadings at room temperature. Using the relationship between the measured propagation rates and the analyzed ranges of stress singularity intensity, we estimated the fatigue strength of the embedded joint, the estimated fatigue strength coincides well with the measured one. Second, we developed an evaluation method that separates the effects of temperature on fatigue strength into the effect of thermal residual stress and the effect of low temperature.

Key Words: Adhesive joints, Fatigue strength, Stress singularity, Thermal stress

1. Introduction

We are now developing cryogenic structures for superconducting magnets such as those used in magnetic resonance imaging (MRI). Since these structures are used at low temperature, fiber reinforced plastics (FRP), which has excellent thermal isolation characteristics and high strength, is often used, for example, in FRP/metal adhesive joints. If these adhesive structures are cooled, thermal residual stresses occur because the difference between the thermal expansion coefficients of FRP and metal is large. It is thus essential to evaluate the mechanical cyclic loadings fatigue strength under thermal residual stresses in order to evaluate the reliability of these cryogenic structures.

Strength evaluation methods for various adhesive joints at room temperature are based on stress analysis.[1]~[3] However, there are few studies on the strength of adhesive joints at low temperature.[4] In particular, to our knowledge, there are no evaluation methods for the fatigue strength of FRP/metal adhesive joints at low temperature. Accordingly, we have studied two types of adhesive joints under different thermal residual stresses at low temperature, and we have developed a fatigue strength evaluation method based on three-dimensional stress analysis and fatigue testing.

2. Stress Analysis and Stress Singularity Analysis

2. 1 Stress singularity parameters

If adhesive structures are loaded, the stress fields near the bonding edge are under stress singularity condition. The stress distribution near the bonding edge can be expressed by two stress singularity parameters, H and λ, given by Eq. (1).[5][6]

$$\sigma = H / r^{\lambda} \qquad (1)$$

where σ: stress (MPa), H: intensity of stress singularity, r: distance from singular point (m), λ: order of stress singularity

These stress singularity parameters also apply to delamination near bonding edge. In this study, delamination propagation from the bonding edge is evaluated by using stress singularity parameters of Eq. (1), and fatigue strength is evaluated from delamination propagation.

2·2 Stress analysis method

The shape and sizes of the tested Alumina-fiber reinforced plastics (Al_2O_3FRP)/stainless steel (SUS304) adhesive joints are shown in Fig. 1. A double lap joint is shown in Fig. 1(a), and an embedded joint is shown in Fig. 1(b). The stress analysis was carried out by using a quarter-cut FEM model considering the symmetry of the adhesive joint and the mechanical anisotropy of the FRP. The adhesive used was 50- μ m-thick epoxy resin. The delamination edge was divided into small meshes and the minimum mesh size was 0.002 mm. A thermal load was applied to cool the adhesive joint from room temperature (293 K) to liquid-nitrogen (LN_2) temperature (77 K). An axial load, producing an average shear stress of 2.9 MPa without delamination, was applied to the Al_2O_3FRP sectional area.

In order to determine the delamination propagation rate, stress analysis in the case of interface delaminations between the Al_2O_3FRP and the adhesive was carried out. Delamination lengths were 1, 5, 10, 15, and 20 mm. The order of the stress singularity at the delamination edge was 0.5, and the intensity of stress singularity was calculated from the FEM stress analysis results by fitting them to Eq. (1).

2.3 Stress analyses results

The normal stress distributions near the delamination edge at the interface between the FRP and the adhesive in the double lap joint under mechanical loading are shown in Fig. 2. The stress distributions can be expressed by the two stress singularity parameters given in Eq. (1). The normal stress at the interface along the line A (see in set Fig. 2) is higher than that along the line B at the side face.

The dependence of the intensity of stress singularity (H) for each delamination length (a) is shown in Fig. 3. The intensity of stress singularity in the double lap joint increases steadily, on the other hand, the intensity of stress singularity in the embedded joint decreases until the delamination length is about 5 mm and becomes constant after that. It is therefore concluded that fatigue strength of the double lap joint is determined by the initiation of delamination, on the contrary, that of the embedded joint is determined by delamination arrest.

Stress analyses of the double lap joint and the embedded joint at a delamination length of 5 mm under thermal loadings were performed (double lap joint : Fig. 4, embedded joint : Fig. 5). It is shown that the thermal stress in the embedded joint is 2.6 times higher than that in the double lap joint.

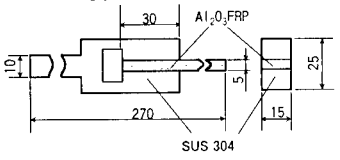

(a) Double lap joint

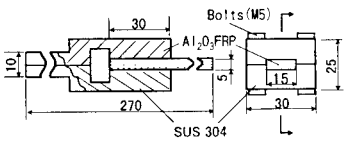

(b) Embedded joint

Fig. 1 Shape and sizes of double lap and embedded joints

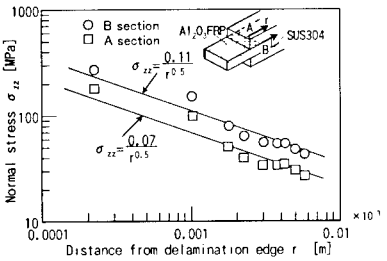

Fig. 2 Stress distributions near delamination edge of double lap joint under mechanical loadings (delamination length : 5 mm)

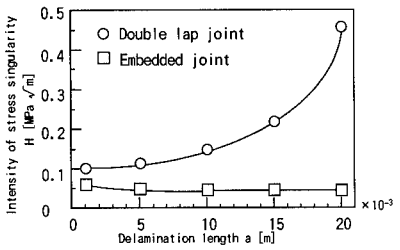

Fig. 3 Intensity of stress singularity for each delamination length (τ n=2.9 MPa)

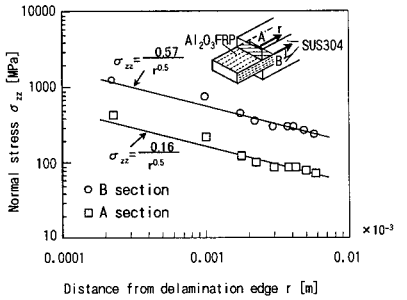

Fig. 4 Stress distributions near delamination edge of double lap joint under thermal loadings (delamination length : 5 mm)

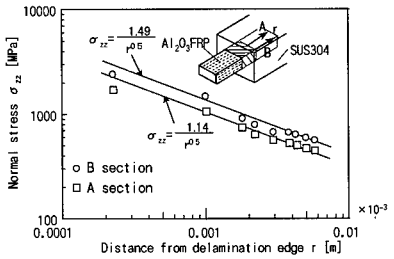

Fig.5 Stress distributions near delamination edge of embedded joint under thermal loadings (delamination length : 5 mm)

3. Fatigue Test

3.1 Fatigue test method

Fatigue tests on Al_2O_3FRP/SUS304 adhesive joints were performed at room temperature and LN_2 temperature (cyclic loadings speed : 5Hz ; sine wave pulsating load (R=0).)

3.2 Fatigue tests results

The fatigue tests results on the two types of adhesive joints are shown in Fig. 6. Shear stress amplitude τ_a was calculated by dividing axial load amplitude by total adherence area. In this figure, the fatigue strength of the embedded joint is higher than that of the double lap joint.

We first observed the delamination propagation behavior of the double lap joints. We measured the delamination length at each fatigue cycle by using crack gauges adhered near the bonding edge. We then calculated the relationship between delamination propagation rate da/dN and the range of normal stress singularity intensity on adhesive face $\triangle$H. The calculated results are shown in Fig. 7. The relationship between da/dN and $\triangle$ H is expressed as a straight line from $\triangle$H of 0.11 to $0.26 MPa\sqrt{m}$ given by the following equation:

$$da/dN = 0.36(\Delta H)^{8.5} \qquad (2)$$

We estimated the fatigue limit of the embedded joint from both the range of stress singularity intensity $\triangle$Hth at the delamination propagation limit of the double lap joint and the intensity of stress singularity in the embedded joint shown in Fig. 3. And this estimated fatigue limit of embedded joint (τ_w) is 3.5 MPa coincides well with the measured τ_w of 3.7 MPa as shown in Fig.6. Figure shows that the fatigue strengths of the embedded joint at LN_2 temperature and room temperature are almost the same. On the other hand, fatigue strength of the double lap joint at LN_2 temperature is higher than that at room temperature.

Figure 8 shows the relationship between the ratio of range of stress singularity intensity under mechanical cyclic loadings ($\triangle$H) and mean stress singularity intensity under thermal loadings or mean loadings (Hm) [X-axis] and range of stress singularity intensity at the delamination propagation limit [Y-axis]. Thermal residual stress singularity intensity of the embedded joint at LN_2 temperature is 13 times higher than the range of stress singularity

intensity of the fatigue limit. Thermal residual stress singularity intensity of the double lap joint at LN_2 temperature is 4 times higher than the range of stress singularity intensity of the fatigue limit. It is thus concluded from the figure that fatigue strength of an adhesive joint depends on adhesive strength dependence on temperature and reduction in adhesive strength due to the existence of thermal residual stresses.

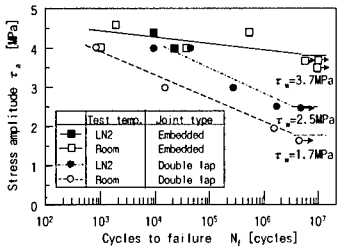

Fig. 6 Results of fatigue tests on adhesive joints (R=0)

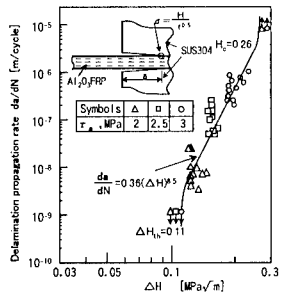

Fig. 7 Relationship between delamination propagation rate and range of stress singularity intensity ΔH (R=0, at room temp.)

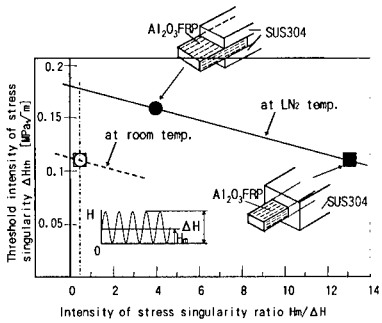

Fig. 8 Thermal stress effect on fatigue strength

4. Conclusions

Stress analyses and fatigue tests on two types of adhesive joints (double lap joint and embedded joint) were performed on Al_2O_3FRP/SUS304 adhesive joints at room temperature and LN_2 temperature. First, the relationship between delamination propagation rate and range of stress singularity intensity was measured by delamination propagation tests on the double lap joints. This relationship enabled us to predict the fatigue limit of the embedded joint at room temperature. And it was found that this prediction agrees well with experimental results. Second, we evaluated the fatigue strength of the adhesive joints at LN_2 temperature by separating the reduction in strength due to the existence of thermal residual stress and the intrinsic increase in adhesive strength at LN_2 temperature.

Acknowledgment

This work was supported in part by a grant from the Research & Development Institute of Metals and Composites for Future Industries (RIMCOF), Japan, on the basis of Application of Advanced Composites for Transportation Systems proposed by the Ministry of Economy, Trade and Industry(METI) of Japan.

References

1. R. Yuuki, T. Ohira, T. Ono, J. Liu and J. Xu: Journal of the Society of Materials Science, 41(467), 1299 (1992).
2. M. Arai and H. Kobayashi: Transactions of the Japan Society of Mechanical Engineers (A), 64(619), 618 (1998).
3. R. Yuuki, N. Chung, H. Ishikawa and S. Nakano: Journal of the Society of Materials Science, 39(443), 1095 (1990).
4. T. Mori, Q. Yu, S. Takehana and M. Shiratori: Transactions of the Japan Society of Mechanical Engineers (A), 56(523), 437 (1990).
5. T. Hattori, S. Sakata, T. Hatuda and G. Murakami: Transactions of the Japan Society of Mechanical Engineers(A), 54(499), 597 (1988).
6. M. Iwasa, H. Aoyama and T. Hattori: Proc . of 7th Composite Material Interface Symposium, O-54-1 (1999).

Proceedings of 7th Japan International SAMPE
Symposium & Exhibition, Nov. 13-16, 2001

Fabrication of a Thin Unlined Reusable Filament Wound Composite Cryogenic Tank

Thomas D. Kim
Air Force Office of Scientific Research
4040 N. Fairfax Drive, Arlington, VA 22203
E-mail: thomas.kim@afosr.af.mil

Abstract

Thin unlined reusable filament wound composite cryogenic tanks were fabricated using EnTec 5-axis filament winder and sand mandrels. These pressure vessels were fabricated with IM7/977-2 graphite/epoxy material. This material was chosen for its resistance to microcracking and low permeability. The layup used was 12 plies of 90°, +33°, -33° symmetrical orientations. The cured tank wall thickness was measured to be 2.13 mm. The weight of the composite tank without the metal boss was 4.08 kg. The tanks were designed to burst at the pressure of 12.41 MPa. The tanks were successfully tested under liquid hydrogen (LH2) and liquid oxygen (LOX).

Key Words: Composite, Cryogenic, Unlined, Permeability

Introduction

Over the past 50 years of space flight, cryogenic fueled propulsion systems have been frequently used to power launch vehicles. The initial use of liquid oxygen as the oxidizer in a bi-propellant system goes back to the Atlas ICBM and launch vehicle. The initial use of liquid hydrogen as a fuel was in the 1960's J2 engine system for Saturn V and the 1970's RL10 engine for the Centaur upper stage. Later developments in the 1980's, including the Space Shuttle, used liquid oxygen (LOX) and liquid hydrogen (LH_2). The cryogenic fluids for all of these propulsion systems were stored in insulated aluminum alloy tanks. The current metallic technology for cryogenic tanks for space launch vehicles has not changed significantly since the days of the multiple stage launch vehicles. The metal tank technology results in a weight increase that seriously limits reusable launch vehicle and extended launch vehicle mission capabilities. In all cryogenic pressure tank applications, either a fiberglass or Kevlar overwrap composite system utilizes metal liners for containment. In the 1990's, mission and system analyses for the reusable vehicles showed that not only are composite cryogenic tanks the technology of choice, but also they are mission enabling. Therefore, it is vital to eliminate the metallic liner and utilize the composite system as both the loads carrying structure and the cryogenic fluid/vapor containment system. Since large cryogenic propulsion tank systems are nominally a low pressure system there is no doubt that advanced composite materials will be structurally sound for this application. The composite materials are now available which could substantially reduce the cryogenic tank to launch vehicle structure mass ratio. The use of composite material will potentially reduce the weight and cost of fabricating the tank by 30% compared to current methods of fabrication.

Technology Development

This program will demonstrate that composite cryogenic tanks will meet the lightweight and low cost requirements and survive robust operability of stringent space environments. To date, there have been only limited successes; all such tanks have leaked at the composite laminates and at the seals. The first critical technology challenge is finding a suitable composite fiber/matrix system that is impermeable and compatible with cryogenic fuel systems. The second challenge is elimination of the metallic or plastic liners. The third challenge is to determine the composite tank manufacturing method that is the lowest cost.

The past composite LH2 tank efforts, such as the Boeing built DC-X tank, were fabricated in two halves using the hand fabrication method.[1] The two halves were later joined by double lap shear. This method can be costly and unreliable for the fabrication of large thin tank structures. The X-33 LH2 tank had proposed to utilize a metallic liner and composite fiber placement method. This method had disadvantage of not having fiber tension during the winding process. The metallic liner increases the weight and causes concern for delamination of liner material during extreme temperature fluctuation. Besides the thermal expansion problem, additional technical concern for the LOX tank involves potential for the chemical reaction and oxidation of the composite matrix system. Advanced composite materials that are compatible with cryogenic fuel and resistant to microcracking when exposed to harsh and cyclic conditions are being explored.

Air Force Research Laboratory (AFRL) had successfully utilized a building block approach to expand existing technology such as that from the NASP program for application to composite cryogenic tanks. A suitable material for the cryogenic applications was identified. The coupon size specimens were fabricated for the material characterization and diffusion testing. Using the NASA supplied san mandrels, two subscale unlined filament wound tanks were simultaneously fabricated and tested to demonstrate fabricability and structural integrity. Upon successful results from the subscale evaluations, AFRL demonstrated the scaleability of the concept by fabricating a 1.17 meter diameter unlined filament wound composite tank.

Material Selection

Selecting an appropriate material is one the most critical aspect for the cryogenic propellant application. The material system must meet several key requirements such as low permeability rate, resistance to oxidation, and resistance to microcracking due to the thermal and mechanical cycling.[2] Thus, the matrix is more critical to meet this stringent conditions. The evaluation of several materials have determined that two toughened epoxy resin systems have shown good characteristics for meeting cryogenic applications: Hexcel Hercules 8552 and Cytec Fiberite's 977-2. The IM7/977-2 carbon fiber/toughened epoxy prepreg material system was chosen due to strength, stiffness advantages and past handling experiences. The material properties were re-evaluated by the University of Dayton Research Institute and were compared to manufacturer's existing data.

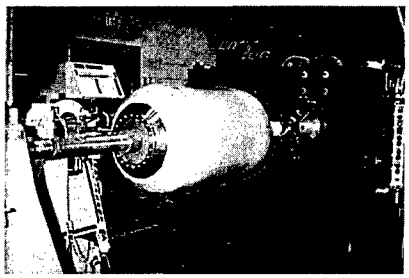

Fig. 1 Sand Mandrel and Filament Winder

Manufacturing Method

Two 45.72 cm diameter by 81.28 cm long sand mandrel made with borosilicate sand and sodium silicate binder were provided by NASA Marshall Space Flight Center. The metallic boss closure fittings were attached on the dome section of the mandrel as shown in Figure 1.

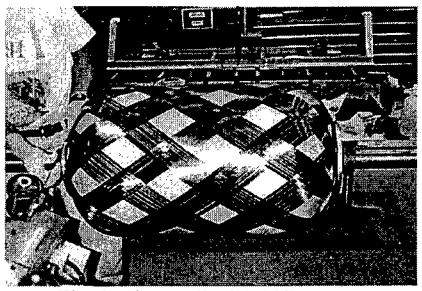

Fig. 2 First Helical (±33°) Layup

EnTec 5-axis filament winder and six spools of tow prepreg were used. Each tow had a bandwidth of 2.29 mm and a thickness of 0.13 mm. Each tow had 22.24 N of fiber tension applied during the winding process. The first two lay ups were ±33° helical patterns as shown in Figure 2. A layer of 2.0 mm thick film resin was added to the helical layers to ensure adequate resin flow and consolidation during the cure cycle. Next three layers of tape prepreg were hand placed on the dome area with overlaps varying from 63.5 mm to 76.2 mm. Additional resin was brushed on to the dome section. Two layers of hoops were then filament wound over the cylindrical section followed by two layers of helical patterns as shown in Figure 3. Then four layers of reinforcements were again hand placed on to the dome area and liberally coated with the resin. The final two helical patterns were filament wound followed by two hoop layers on the cylindrical section. Total of twelve plies were filament wound and seven plies of reinforcements were used on the dome area.

The filament wound composite surfaces at the openings did not have an adequate smoothness to provide an acceptable sealing surface. Therefore, the sealing surface was built up at the tanks openings with additional strips of unidirectional tape, which consisted of 0° 90°, and ±45° orientations and widths varying from 9.65 to 19.06 mm. These four tape strips were placed tangentially onto the sealing surface recess of the aluminum boss mold tooling starting with the narrowest strips and building up to the widest. Slurry of dry chopped fibers and resin was mixed and deposited in the tooling on top of the strips. Enough slurry was added to assure complete filling of the sealing area. The aluminum tools were than attached to the sealing surface of the tank openings using ten 3/8-24 fasteners torque to 22.6 N/m.

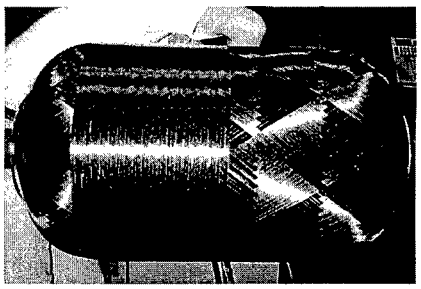

Fig. 3 Hoop Winding Over the Helical

The filament wound tank was vacuumed bagged. The bagging materials consisted of perforated release film (Airtech A-4000), breather cloth (Airweave N-10), and a bagging film (Stretchlon). The part was autoclaved with 177 °C and 5.88 atm cure temperature and pressure. The sand mandrel and the cured composite tank were soaked with warm water for 8 hours. This process dissolves the sand binder and sand was then simply washed out with water spray. The tank was thoroughly air-dried and interface seals were attached at each end of the tank. The polar interface seal consisted of an

external Gortex gasket that was placed between the external fitting and the external tank composite surface. The Gortex seal was installed by bolt clamping pressure of 20.68 MPa and was inelastically compressed to 75%. During the clamping process, the seal is forced to conform to the mating surfaces and closed all potential leak paths. The total weight of the tank with metallic closure and bosses installed was 24.95 kg. The weight without the metal parts was 4.08 kg.

Conclusions

Air Force Research Laboratory has successfully fabricated two 45.72 cm diameter tanks at the Applied Composites Lab. The composite tanks were filament wound on the sand mandrels using the graphite/epoxy (IM7/977-2) material system. The tanks had a total of 12 plies of various layup orientations [±33, 90]. The wall thickness was measured to be 2.11 mm. The dome/tangent areas were build-up using the tape reinforcements. The tanks were autoclave cured. Of the two fabricated tanks, the first tank was tested at the NASA Marshall Space Flight Center for liquid hydrogen permeability as shown in Figure 4.

Fig. 4 Liquid Hydrogen Testing

The second tank was tested by the Boeing Company for liquid oxygen compatibility. Both tanks performed very well with the compatibility and permeability issues without any problems. The propellant tanks of launch vehicles can be made of unlined composite material, which will provide considerable weight reduction. AFRL has since fabricated 1.17 m diameter composite tank and all composite tank weighing 6 Kg. Further weight reduction can be realized by filament winding and E-beam curing method as shown in Figure 5.[3] This method might be ideal for future expendable and reusable launch vehicle systems.

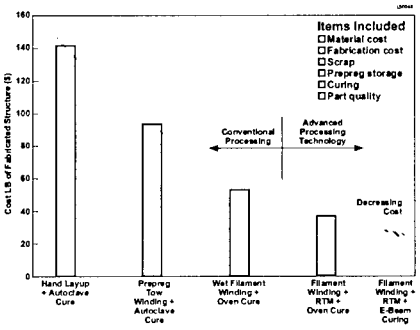

Fig. 5 Comparison of Fabrication Methods

Acknowledgment

This program was performed by the Wilson Composites Group, Inc. under the Air Force Contract #: F29601-95-C-0217. The Wilson Composite Group team for the tank program was Mr. David L. Whitehead, Dr. R. Grover, Dr. R. Adsit, R. Bertolucci, and R. Hagan.

References

1. V. McConnell, "*DC-XA Spacecraft to Fly First Composite Liquid Hydrogen Fuel Tank*," High Performance Composites, 1996.
2. B. Agarwal and L. Broutman, "*Analysis and Performance of Fiber Composites*," John Wiley & Sons, Inc., 1990, pp. 339-354.
3. L. Greszczuk, "*Advanced Composite Isogrid Structures*," USAF Contract No. F29601-95-C-0179, 1996.

Proceedings of 7th Japan International SAMPE
Symposium & Exhibition, Nov. 13-16, 2001

Study of CFRP Application to Cryogenic Fuel Tank for RLV

Takayuki Shimoda,# Yoshiki Morino,# Takashi Ishikawa,## Tetsuya Morimoto,##
and Stefania Cantoni###

#. National Space Development Agency of Japan
2-1-1 Sengen, Tsukuba, Ibaraki, 305-8505, JAPAN
E-mail: shimoda.takayuki@nasda.go.jp

##. National Aerospace Laboratory
6-13-1, Osawa, Mitaka-city, Tokyo 181-0015, JAPAN

###. Italian Aerospace Research Center (CIRA),
Via Maiorise-I81043- Capua, Caserta- ITALY

Abstract

The National Space Development Agency of Japan (NASDA) is conducting a feasibility study of applying CFRP to the cryogenic propellant tank of a reusable vehicle system. As part of the feasibility study we are now conducting a small tank test with 300mm diameter filament winding (FW) tanks. The first phase test of a FW tank was conducted in 1999. The tank surface leaked considerably after being chilled down to LN2 temperature. We analyzed the weak points of the first series of FW tank and are conducting the second phase test in collaboration with Italian Aerospace Research Center (CIRA). The design and manufacturing processes were improved, and the first tank produced in collaboration with CIRA was completed. After performing a helium leak test to obtain background data, we conducted a pressurization test with the first tank. At 0.4Mpa, leakage occurred along the large wrinkles produced in the curing process. After repair, the tank was used for water proof testing at 1.0MPa and strain data was obtained. We then conducted a gas pressure test at 0.6MPa to identify strain data. Finally a 1.5MPa water proof test was conducted.

Key Words: FW, RLV, water proof test

Introduction

Reusable Launch Vehicles (RLVs) are being active researched and developed. The USA is starting several programs to recover from the failure in developing the X-33, and Europe is starting FLTP program as a follow-on to the FESTIP program. Japan is focusing R&D for RLVs on TSTO and is endeavoring to realize the system (see Fig. 1). A lightweight propellant tank will be important in realizing SSTO or TSTO, and advanced materials should be developed to replace aluminum alloy. Our current research purpose is to estimate the possible reduction of weight and to identify technical problems for realizing RLVs. We will present the research status of our feasibility study on CFRP application in this paper, focusing on the filament winding tank test.

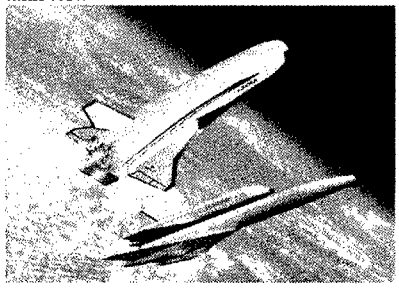

Fig.1 Image of future Japanese RLV

FW tank test

The first tank of the second phase FW tank test was fabricated and used for the pressurization test.

Helium Leakage Test

We conducted a helium leakage test at 0.2MPa internal pressure to obtain background data. We then conducted a pressurization test at 0.2MPa, 0.3MPa and 0.4MPa internal pressure and measured helium leakage. Fig.2 shows the result of the first helium leakage test. Permeability of helium reached around $5.3*10^{-5}Pam^3/sec$.

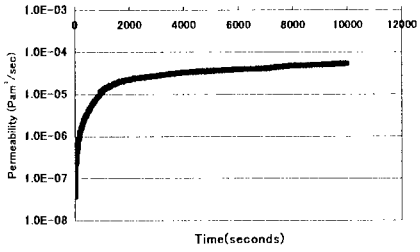

Fig.2 Helium Permeability Background

We then conducted a continuous pressurization test in which we planned to increase the internal pressure from 0.2MPa to 0.5MPa in 0.1MPa steps. Fig.3 shows the result of the pressurization test. It shows that permeability increased with increasing internal pressure from 0.2MPa to 0.3MPa then became constant. When the pressure reached 0.4MPa, the permeability continued increasing and eventually surpassed the limitation of the helium leak detector.

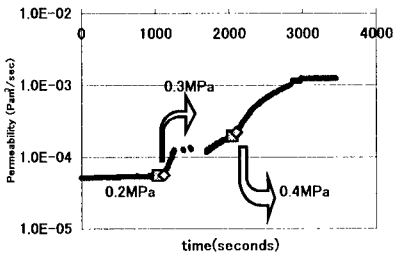

Fig.3 Permeability at Pressurization test

Leak paths seemed to have been created while internal pressure was increasing from 0.3MPa to 0.4MPa. We conducted a snoop test with soap to identify leak points and found several leaks especially along the large wrinkles produced during the cure process (see Fig.4). There were many large wrinkles on one side of the tank and almost no large wrinkles on the other side. We believe that the wrinkles developed because of gravity during the cure process. The tank was cured with the axis horizontal. The fibers of the upper side were under strain, but the fiber of the lower side was not causing large wrinkles. The fibers inside large wrinkles are easy to deform by internal pressure.

Fig.4 Snoop test at Wrinkles

Identified leaks were covered by EA9394 epoxy adhesive before conducting the water proof test with 1.0MPa internal pressure.

Water Proof at 1.0MPa

We conducted a water proof test with 1.0MPa internal pressure and obtained strain data at 18 points on the tank surface. Water pressure was applied by hand pump and many leaks occurred at an internal pressure of 1.0MPa. The internal pressure was kept 1.0MPa for 470 seconds. The strain data and measurement points at one side of the tank with wrinkles are shown in Fig.5 and Fig.6. Fig.5 shows nine strain data points in the hoop direction and one in the axial direction.

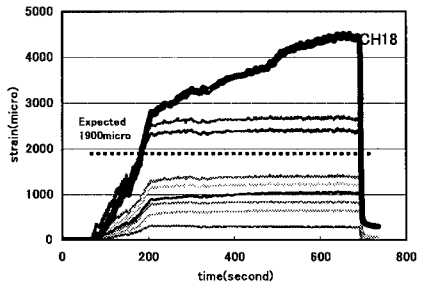

Fig.5 Strain data at 1.0MPa water proof

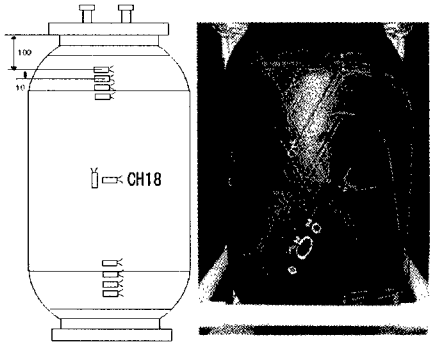

Fig.6 Measurement Points of Strain

Eight strain gauges were put on the transition area from cylinder to dome. These data were obtained in order to identify the complex stress distribution around the border area. The complexity is caused by not only the position of border but also the local fiber direction and the existence of wrinkles. We are analyzing the stress around the border and we took special notice of the data at the center of cylinder-CH18 shown in Fig.6. As you can see in Fig.5, the strain kept increasing while the internal pressure was held at 1.0MPa and other data remained constant. To verify this, we performed a pressurization test with nitrogen gas at 0.6MPa before the water proof test at 1.5MPa.

Helium Leakage after Water Proof

A helium leakage test was conducted before the gas pressurization test. Fig.7 shows the helium leakage after the water proof test at 1.0MPa. The permeability level is the same as the first background data shown in Fig.2. We can say that the healthy part of the tank surface without micro cracks remained tolerant to helium permeability.

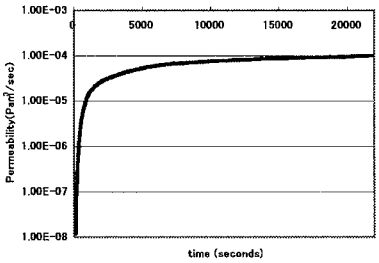

Fig.7 Helium leakage after water proof

Gas pressure test at 0.6MPa

We pressurized the tank with nitrogen gas to 0.6MPa in 0.1MPa steps and obtained strain data. We added the strain gauges mainly on the cylinder after the water proof test and obtained some data at the same points as in the water proof. All the strain gauge points are shown in Fig.8. 16 strain data points were obtained. CH1–CH7 and CH15 are new points for evaluating the hoop direction strain on the cylinder. The other gauges, that is, CH11–CH14 for the hoop on the dome, CH18 and 21 for hoop on cylinder, and CH17 and 20 for the cylinder axis, are at the same position for comparison.

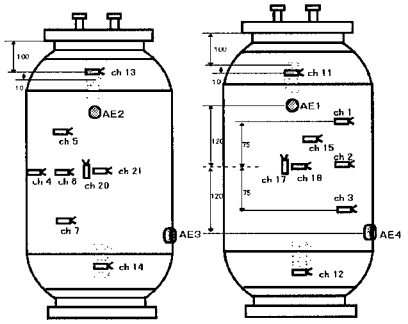

Fig.8 Strain Measurement Points

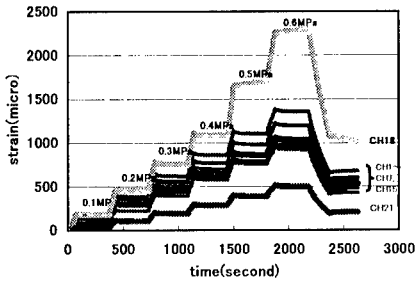

Fig.9 Strain of Hoop Direction

Fig.9 shows the result of hoop strain on the cylinder. The strain at CH18 is much larger than at other points. We can also see the data kept increasing at 0.5 and 0.6MPa internal pressure while pressure kept constant. The CH18 strain gauge is near a large wrinkle that is resin rich. The local strain can be very great and many eventually produce a micro crack.

Water Proof at 1.5MPa

After performing the gas nitrogen pressurization test, we conducted a water proof test up to 1.5MPa. We pressurized the tank to 1.0MPa then we pressure constant for one minute. We next pressurized it to 1.5Mpa, then kept pressure constant for three minutes and then released it. All the strain data were at the same positions as for the gas nitrogen pressure test. Fig.10 compares strain data at the same positions for the three pressurization tests. All the strain data were at 1.0MPa internal pressure. The data for the 0.6MPa gas nitrogen pressure test were converted by being multiplied by 1.0/0.6. There was good agreement for the strain data on the cylinder except CH18. As mentioned before, CH18 is located near a large wrinkle, and the strain was larger than at others points. It seems that a micro crack occurred under strain gauge CH18 during the second water proof test at 1.5MPa and the crack spread. This seems likely because we observed large bubbles in the snoop test after the second water proof. There were major differences at two of four points of the data on the dome (CH11-CH14). At CH11 and 14, the strain data of the first water proof were twice that of the other two tests. This may be related to the complexity of the stress distribution, the cause is still under investing.

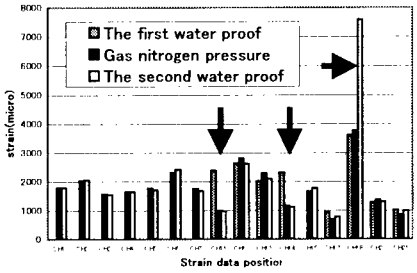

Fig.10 Comparison of Strain Data

Conclusions

Some parts of the tank surface, such as those with large wrinkles were damaged by high internal pressure, but well-produced parts were intact after successfully completing the water proof test. The result is promising regarding healthy parts. A tank with a properly prepared surface should be able to withstand high internal pressure.

References

1. Morimoto, T., Shimoda, T., and Morino, Y., "Cryogenic Test of CFRP Scale Tank for the Future Rocket Plane Propellant," Proceedings The 37th Aircraft Symposium, pp. 541-544, Tokyo, November 1999

2. S. Cantoni, G. Di Vita, G Totaro, Morino, Y., and Morimoto, T.,"Applicability of Filament Winding Method to Fabricate Cryogenic Composite Tanks for Liquid Propulsion," IAF-00-S.3.08

3. S. Cantoni, G. Di Vita, G. Totaro, Morino, Y., Morimoto, T., and Shimoda, T., "Cryogenic Composite Tanks for Liquid Propulsion" 2nd International Symposium Atmospheric Re-entry Vehicles and Systems, 2001, Arcachon

Proceedings of 7th Japan International SAMPE
Symposium & Exhibition, Nov. 13-16, 2001

Damage Evaluation of CFRP Concept Tank in Cryogenic Pressurization

Tetsuya Morimoto, Takashi Ishikawa[1)]

1): National Aerospace Laboratory (NAL), 6-13-1 Ohsawa, Mitaka, Tokyo 182-0015, JAPAN

E-mail: morimoto@nal.go.jp

Tomohiro Yokozeki[2)]

2):The University of Tokyo, Hongo, Bunkyo-ku, Tokyo 113-8656, JAPAN

Yoichi Hayashi[3)]

3): Tokyo Business Service Co. LTD, 6-14-1, Nishi-Shinjuku, Shinjuku-ku, Tokyo 160-0023, JAPAN

Takayuki Shimoda, and Yoshiki Morino[4)]

4): National Space Development Agency of JAPAN (NASDA), 2-1-1 Sengen, Tsukuba, Ibaraki 305-8505, JAPAN

Abstract

The authors present in this study an approach evaluating the damage of tough-epoxy CFRP concept tank, under the internal pressure in cryogenic temperature. Two tanks were prepared so far for the demonstrations with eight-ply UD quasi-isotropic lay-up in two patterns. Each tank was designed as the cylinder of 600mm in the diameter and 1200mm in the length, covered with aluminum flange at an end and with 600mm hemisphere dome of CFRP at the other. The gauge was the central 300mm of the cylinder section of the wall thickness 1.1mm made of IM600/#133 tough epoxy CFRP. The CFRP concept tanks showed no damage under the pressurization in LN2 temperature thus, they were successfully evaluated as the cryogenic CFRP tank. Although there are technical steps remained for the larger structures, the CFRP was found hopeful for the realization of launch vehicle cryogenic propellant tank.

Key Words: Cryogenic Tank, CFRP, Damage Evaluation, Pressurizing Test.

Introduction

Carbon fiber reinforced plastics (CFRP) composite is attractive for the liquid propellant tanks of launch vehicles due to its excellent specific strength[1].

The launch market is known for the aggressive commercial environment that drives the launch vehicles in the directions of increased payload capacity. Thus, demand is steady for lightweight structures with the superior performance of CFRP composites. The CFRP cryogenic tank is thus an indispensable factor to the future launch vehicles being accepted in the market.

The design of a CFRP cryogenic tank requires tough material such as CFRP composites that have been developed with tough-epoxy matrices and high strength carbon fibers.

However, the cryogenic performance of structures with these materials is still in the experimental stage. Although promising data have been reported for specimen strength in cryogenic conditions[2], very few successes have been realized for tank structures[3-5]. In particular, one important technical step for CFRP cryogenic tanks is the damage evaluation, which leads to the knowledge for the prevention of matrix cracking.

The authors present in this study an approach to evaluate the damage of tough-epoxy CFRP concept tanks, under internal pressure at LN_2 temperature. The CFRP tanks were evaluated in the tests and no damage was detected. CFRP composite appears thus, promising for the lightweight pressure vessels such as launch vehicle cryogenic tanks.

Tank Configuration

Following preliminary studies, IM600/#133 tough-epoxy resin containing high strength carbon fiber (Toho Composites Co. Ltd.) was selected as the tank material.

For the LN_2 temperature condition, the operational pressure was set to be 0.98 MPaG with a safety factor of 1.5 for the onset of matrix cracking. Under 0.98 MPaG the maximum strain in the hoop direction at the center of the gauge section was estimated to be 4.5×10^3 μ. Figure 1 shows the schematic diagram of the tank configuration.

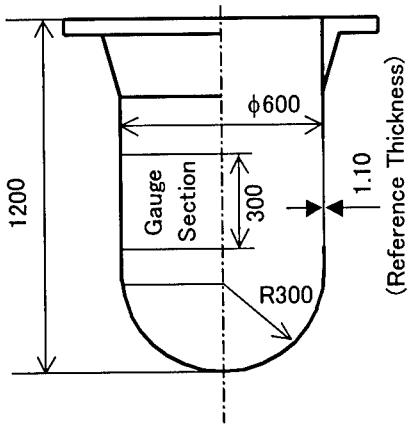

Fig. 1 Configuration of CFRP tank

(Units: mm)

Each tank was designed as a cylinder of 600 mm in the diameter and 1200 mm in the length, covered with an aluminum flange at one end and a 600 mm hemispherical CFRP dome at the other end. The gauge section was the central 300 mm of the cylinder section that possessed a wall reference thickness of 1.10 mm.

Two liner-less tanks were tested so far that have produced by Fuji Heavy Industry Co. Ltd. comprising of an eight-ply UD quasi-isotropic lay-up in two different patterns, Type A $(45/0/-45/90)_S$, and Type B $(45/90/-45/0)_S$.

Experimental

The main objective of this experiment was to assess the presence of matrix cracking in the concept tanks at a pressure of 0.98 MPaG under LN_2 temperature. Thus, He flow measurement and acoustic emission (AE) methods were applied for detecting the onset of microcracking.

Each tank was set inside a vacuum chamber as shown in Fig.2. The vent pipeline was connected to a helium leak detector in order to monitor the through-crack leakage. LN_2 was filled into the tank through the cover and drained using the GHe pressure. GHe does not diffuse into LN_2 and thus through-crack leakage was limited to above the height of the LN_2 surface. Therefore, the surface was monitored whilst the LN_2 was drained in order to detect the position of through-crack leakage.

The experiments were conducted as follows. Each tank was checked by the supplier, Fuji Heavy Industry Co. Ltd. using an ultrasonic method immediately following the production. The tanks were then pressurized to 1 MPa with water and checked for signs of visible damage with the extent of any microcracking checked using helium flow detection at 0.1 MPaG. After the supplier check, each tank was installed into a vacuum chamber following setup for the AE and strain measurements and then covered for the pressurizing tests. The helium permeability was measured at 0.1 MPaG and 0.2 MPaG in order to derive background data prior to the pressurizing and through-crack leakage measurements. So as to confirm any damage being due to the cryogenic temperature, LN_2 was stored without the additional pressure with GHe for about 1 hour then being checked with helium leak at R.T. The tanks that satisfactory passed these tests were then filled with LN_2 and pressurized with GHe up to 0.98 MPaG in step of 0.2 MPaG. Figure 3 illustrates an example of the LN_2 storage process.

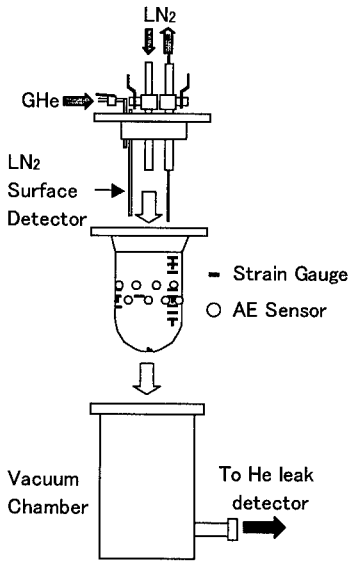

Fig. 2 Schematic diagram of the test configuration

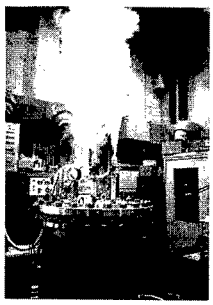

Fig. 3 Photograph of the cryogenic test

Experimental Results

Following the initial LN_2 storage test, tank A and B were filled with LN_2 and pressurized with GHe in order to verify the

absence of through-crack leakage in IM600/#133 at LN_2 temperature and thus, applicable for cryogenic pressure vessels. AE signals were not detected during the test whilst the strain data was within estimated levels of 4.2×10^3 μ at the middle of the gauge section in the hoop direction. Thus, through-crack leakage was believed to be absent in tank A and B during the cryogenic pressurizing tests. In order to confirm the fact, He leak tests were conducted at R.T. condition before and after the cryogenic pressurizing tests. The leakage patterns were consistent with the He permeability data as depicted in Fig.4. Therefore, it was concluded that the tanks were kept intact under conditions of a LN_2 temperature and pressure up to 0.98 MPaG.

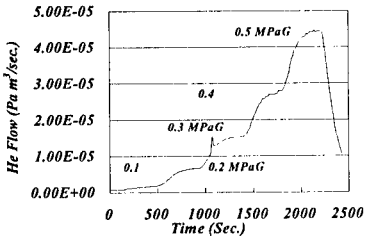

(a) Before the cryogenic pressurizing test

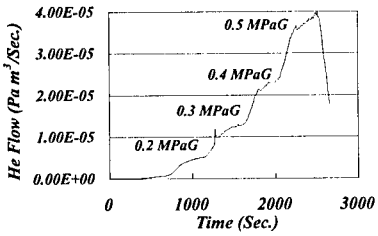

(b) After the cryogenic pressurizing test

Fig. 4 An example of data showing the helium permeability (Type A)

Concluding Remarks

CFRP concept tanks were produced for the damage evaluation tests under internal pressure at a LN_2 temperature.

Two tanks were so far evaluated with GHe in LN_2 temperature up to 0.98 MPaG that have shown no damage in the gauge sections. Therefore, it was concluded that the concept of the CFRP tank structure was successful for the prevention of damage by internal pressure in cryogenic conditions.

Although technical steps remain until the realization of engineering structures, CFRP composite appeared promising for the realization of lightweight pressure vessels such as the cryogenic tanks of future launch vehicles.

References

1. M. J. Robinson, "Composite Cryogenic Propellant Tank Development," AIAA-94-1375-CP

2. Y. Morino, T. Ishikawa, T. Aoki, H. Kumazawa, and Y. Hayasi, "CFRP Material Characterization Testing for the RLV Cryogenic Propellant TANK," AIAA-99-1297

3. M. Yoshida, T. Sudo, M. Nosaka, T. Goto, and M. Yamashita, "Evaluation of CFRP Tank Element Pressurized up to 2 MPa with Liquid Hydrogen," Proceedings of the Annual Meeting and the First Symposium on Propulsion System for Reusable Launch Vehicles, pp. 195-200, Sendai, March 1998

4. T. Morimoto, T. Shimoda, and Y. Morino, "Cryogenic Test of CFRP Scale Tank for the Future Rocket Plane Propellant," Proceedings The 37th Aircraft Symposium, pp. 541-544, Tokyo, November 1999

5. T. Morimoto, T. Shimoda, Y. Morino, Y. Hayashi, T. Yokozeki, and T. Ishikawa, "Pressurizing Test of CFRP Model Tank in Cryogenic Temperature," AIAA 2001-1882, in press

Proceedings of 7th Japan International SAMPE
Symposium & Exhibition, Nov. 13-16, 2001

Leakage Evaluation of Propellant Tanks by CFRP Laminate Cruciform Specimens under Biaxial Loading

Hisashi Kumazawa#, Takahira Aoki& and Ippei Susuki#

#: Structures and Materials Research Center, National Aerospace Laboratory
6-13-1 Ohsawa, Mitaka, Tokyo 181-0015, JAPAN
&: Department of Aeronautics and Astronautics, University of Tokyo
7-3-1 Hongo, Bunkyo-ku, Tokyo 113-8656, JAPAN

Abstract

For evaluating leakage property of carbon fiber reinforced plastics (CFRP) laminates of the propellant tanks for reusable launch rockets (RLV), leak experiments are conducted by means of cruciform specimens. Prior to leak experiment, CFRP laminate specimens have been applied with biaxial load to develop matrix cracks in all layers acting as the leak path, and the matrix cracks in the laminate are observed through the use of ultrasonic C-scan. Then leak rate through the laminate, which is biaxially loaded to simulate the condition of pressurized and loaded tanks, is measured at room temperature. The results from leak experiments indicate that loads and their biaxial ratios have large effects on the leakage property of CFRP laminates.

Key Words: CFRP Laminate, Propellant Leakage, Cryogenic Tanks, Matrix Crack, Biaxial Load Test

Introduction

The next generation reusable launch vehicle has been sought for cost reduction of space transportation. The application of CFRP to liquid hydrogen tanks to reduce the structural weight, which is mainly occupied by propellant tanks, is essential in the realization of the RLV. Recent studies have mentioned that severe thermal strain at cryogenic temperature of liquid hydrogen induces matrix cracks in CFRP composite materials at relatively low loads, and the chain of continuously connected matrix cracks might cause propellant leakage [1- 4].

In this work, leak experiment for cruciform CFRP specimens under biaxial loading has been developed at room temperature. Previous to the leak experiment, cruciform laminates have been biaxially loaded for making matrix cracks in the laminate, which are performing as leakage path. Leak rates through the center portion of the cruciform laminate are measured as function of loads and their biaxial ratios. The results of this study reveal that load and biaxial ratio on the laminate have a great influence on the leakage, and loading conditions due to the internal pressure and structural load have to be considered for evaluating leakage property of CFRP composite tanks.

Leak Experiments

Plane CFRP laminates are subjected to leak experiment instead of CFRP tanks, and the shape of CFRP specimens is cruciform for applying biaxial load as shown

in Fig.1. Material system used in this study is IM600/Q133 and the laminates with the stacking sequences $(0/0/90/90)_S$ were fabricated. The stainless steel cups for measuring leak rates are padded to both surfaces of the cruciform CFRP specimen that is loaded as shown in Fig.2. One of the stainless steel cups is to supply helium gas to the laminate surface, and the other connected to the helium leak detector is used to capture the leaked gas through the laminate. Flow rate of the helium gas through the supplying cup was kept to be low enough to introduce atmospheric pressure into the cup, and the helium leak detector connected to the detection cup draws vacuum inside it. Then pressure difference between both sides of the laminate is held to be atmospheric pressure. CFRP specimens padded these cups are biaxially loaded at room temperature as shown in Fig.3, and leak rates are measured as functions of loads and their biaxial ratios.

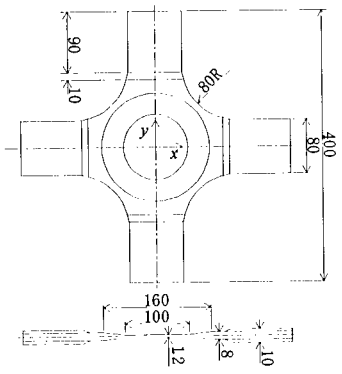

Fig.1 Specimen for Leak Test

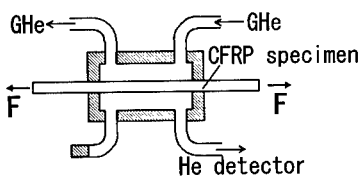

Fig.2 Cross Section of Leak Test

In this study, the leakage through the continuous series of matrix cracks in all layers is measured. If there is any layer with no matrix cracks, leakage through the cracks no longer exists and diffusion is merely measured. Before leak experiments are conducted, the laminate specimen has been applied with biaxial load for initiating matrix cracks, and existence of matrix cracks in the specimen is observed with using Ultrasonic C-scan instead of X-ray photography because penetrant in matrix crack for X-ray photography could affect the measurement of leakage.

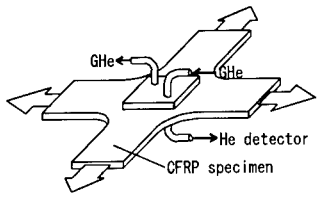

Fig.3 Leak Test through a Biaxial Loaded Laminate

Results and Discussion

Strain on Cruciform Specimen

Leakage is measured in the area of $45mm \times 45mm$ on the center of biaxial specimen as shown in Fig.4. It is important to comprehend strains induced by the biaxial load in the leak test area. Strain gauges are attached on both sides for measuring strains on center portion of biaxial specimen as shown in Fig.4. Figure 5 shows load-strain curve at the two points on IM600/Q133 $(0/0/90/90)_S$ laminate specimen under biaxial load (load ratio $Fx/Fy=1$) at room temperature, and indicates that x and y directional strains at the two points are almost coincident. Axes x and y coincide with 0° and 90° directions, respectively.

Ultrasonic C-scan

The IM600/Q133 $(0/0/90/90)_S$ laminate specimen was subjected to biaxial load to induce matrix cracks as shown in Table 1.

Figure 6 is the result of Ultrasonic C-scan for the damaged laminate, and indicates that matrix cracks exist in both $0°_2$ and $90°_4$ layers of $(0/0/90/90)_S$ laminate. The chain of these matrix cracks can provoke the leakage through the laminate.

Results of Leak Test

Leak rates through IM600/Q133 $(0/0/90/90)_S$ laminate containing matrix cracks as shown in Fig.6, were measured at room temperature. Leak rate through the specimen under uniaxial load (Fy/Fx=0) changed in accordance with the change in applied load Fx as shown in Fig.7. In this study, leak rates are converted to the values under unit volume at atmospheric pressure per second. Increase of leakage in connection with load is supposed to be caused by enlargement of matrix crack opening. Leakage through the laminate was even measured under no mechanical loads, because thermal contraction forces matrix cracks to open.

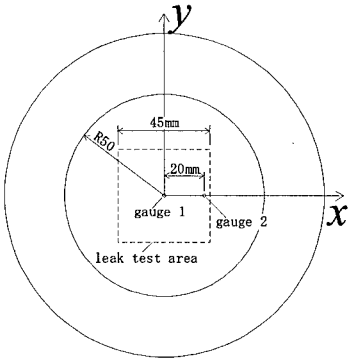

Fig.4 Leak Test Area and Strain Gauges on Central Portion on Cruciform Laminate Specimen

Figure 8 shows measured leak rate through the same specimen under biaxial load (Fy/Fx=1), and reveals that the leak rate is larger than that under uniaxial load (Fy/Fx=0) in Fig.7. This supposedly implies that amount of crack opening displacements under biaxial load (Fy/Fx=1) are larger than those under uniaxial load (Fy/Fx=0), and in consequence resistance of leak path composed of cracks to gas flow becomes relatively lower.

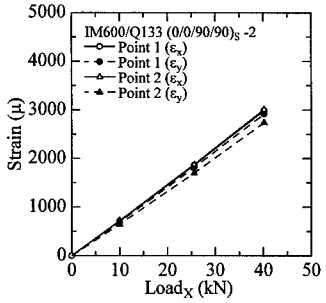

Fig.5 Load-Strain Curve on the Central Portion of IM600/Q133 $(0/0/90/90)_S$ Specimen under Biaxial Loading

Table 1 Applied Biaxial Load to IM600/Q133 $(0/0/90/90)_S$ Specimen

specimen		load
(0/0/90/90)s-1	first	Fx=80kN, Fy=38kN
	second	Fx=26kN, Fy=53kN

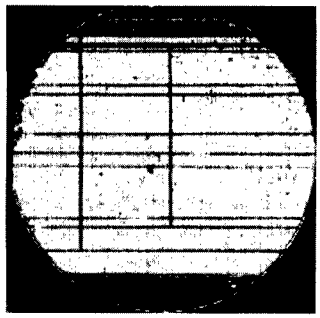

Fig.6 Crack Pattern in Damaged IM600/Q133 $(0/0/90/90)_S$ Specimen

Relationships among leak rate, biaxial load and strain are shown in Figs.9 and 10, which reveal that leak rate correlates closely with not only load levels but also load ratio. In Fig.9, leak rate at the load Fx=25kN with load ratio Fy/Fx=1 ($\varepsilon_x/\varepsilon_x$=1) is largest and

about thrice as large as that without mechanical load. It is significant that strain caused by biaxial loading (*Fy*/*Fx*=1) makes leak rate increase remarkably.

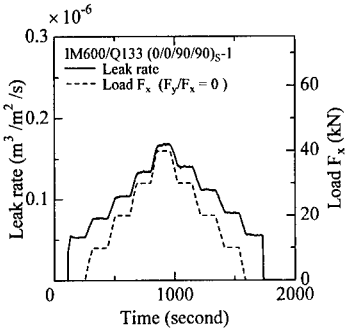

Fig.7 Change of Leak Rate and Uniaxial Load (IM600/Q133 (0/0/90/90)$_S$ Laminate)

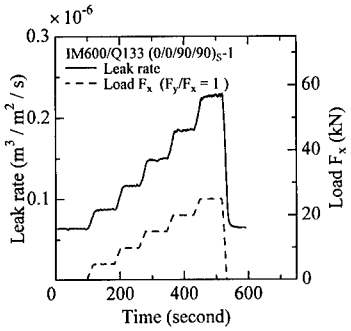

Fig.8 Change of Leak Rate and Biaxial Load (IM600/Q133 (0/0/90/90)$_S$ Laminate)

Conclusions

In this study, leak rate through the CFRP laminate containing matrix cracks in all layers was experimentally measured under biaxial loading. The results of leak experiment indicate that leakage through the laminate occurs even if the laminates are not loaded, and biaxial load and load ratio have a significant impact on the leakage of CFRP laminates.

References

1. T. Aoki, T. Ishikawa, H. Kumazawa and Y. Morino: AIAA paper, AIAA-2000-1605 (2000).
2. Marshall Space Flight Center – NASA: "Final Report of the X-33 Liquid Hydrogen Tank Test Investigation Team", (2000).
3. S. Disdier, J. M. Rey, P. Pailler and A. R. Bunsell: Cryogenics, 38, 135 (1998).
4. H. Kumazawa, T. Aoki, T. Ishikawa and I. Susuki: AIAA paper, AIAA-2001-1217 (2001).

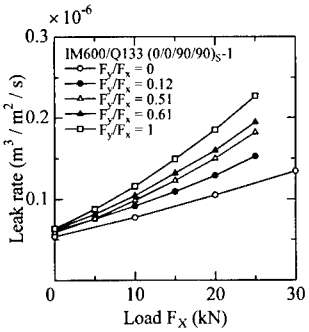

Fig.9 Leak Rate-Load Curve under Biaxial Loading (IM600/Q133 (0/0/90/90)$_S$ Laminate)

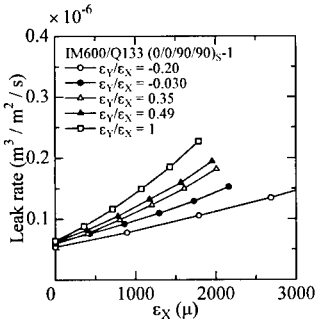

Fig.10 Leak Rate-Strain Curve under Biaxial Loading (IM600/Q133 (0/0/90/90)$_S$ Laminate)

Proceedings of 7th Japan International SAMPE
Symposium & Exhibition, Nov. 13-16, 2001

A Study of Triaxial Woven Fabrics for The Space Inflatable Structure

Akihito Watanabe
Sakase Adtech Corporation, 14-10 Shimoyasuda, Maruoka-cho, Fukui 910-0363, Japan
a-watanabe@sakase.co.jp

Kenji Kubomura
Kanazawa Institute of Technology, 7-1 Ohgigaoka, Nonoichi, Ishikawa 921-8501, Japan
kubomura@neptune.kanazawa-it.ac.jp

Yumi Senbokuya and Hiroaki Tsunoda
NTT Network Innovation Laboratories NTT Corporation, 1-1 Hikarinooka, Yokosuka-shi, Kanagawa 239-0847, Japan
senbok@wslab.ntt.co.jp, tsunoda@wslab.ntt.co.jp

Abstract

A large deployable satellite antenna will be very likely a foldable thin construction and supported by an inflatable structure that can be also folded into a launch vehicle and inflated to be the deployed condition in space. One possible design of the support structure is an inflatable tube made of thin polymeric film wrapped with uncured fiber reinforced polymeric composites, which will be cured in space to maintain the rigidity after inflation.

The potential of using triaxial woven fabrics (TWF) was studied for fabricating the inflatable support structure. For this purpose, a tube of diameter 150 mm and length 2000 mm was fabricated with a 50 μ m polyimide film and one Ply of TWF prepreg. The tube was folded and smoothly inflated without any damage.

Key Words: Carbon Fibers, Composites, Fabrics, Inflatable Structures, Space Structures

Introduction

Through various space activities, the needs for the construction of large space structures have been realized[1]-[3]. An inflatable structure may have potential advantages for the construction of a large space structure in weight and cost. The space inflatable structure can be folded in a small payload area of a launch vehicle and deployed in space by inflation. After the structure is deployed, the deployed shape must be maintained during the lifetime of satellite's mission. One way to maintain the deployed shape is to use uncured polymer reinforced fiber, then cure it after the structure is deployed in space. An appropriate choice of polymeric composites can accommodate enough flexibility for folding and expanding, and it also maintains the rigidity of the expanded shape.

Because of using this construction for a large satellite antenna, we have been investigating the flatness of the planar array antenna formed on the triaxial woven fabrics (TWF) which is stretched by the inflatable

tube placed around the circular planar array antenna[4]. The result of this investigation is promising though premature and warrants the further investigation of the antenna support structures such as the inflatable structure.

In many structures such as aircrafts, and sporting goods, the use of heat cured fiber reinforced polymeric composites has been widespread and can be taken advantage for applying to an inflatable structure. There are some requirements for the materials to be used for the inflatable structures. The materials must be flexible enough to be folded before rigidized, and have long shelf time before heat curing. The materials also have to have enough rigidity and durability in space after heat curing[5]-[6]. The use of polymer composite reinforced with biaxial woven fabrics (BWF) may cause adverse effects on the dimensional reliability after inflation, used as lay-upped structure, due to sliding movement between each ply during folding and expanding[7].

In this paper, the use of TWF is proposed because in-plain isotropy and high bending rigidity of one ply can be obtained by proper weaving, compared with other fiber arrangements which the areal density and fiber properties of the fabrics are the same. Because the TWF can be woven into isotropy and high in-plain bending rigidity, the one ply construction may become possible which ensures the dimensional reliability after inflation and ease of fabricating structural shapes such as Y-shape, T-shape compared with the BWF or Iso Truss[8]. Cylindrical tubes were fabricated with carbon fiber TWF and BWF, and structural rigidities were evaluated. For a further demonstration, the inflatable tubes of diameter of 150 mm and length of 2000 mm was fabricated using the TWF, and its foldability and expandability was evaluated.

Experiment

Cylindrical Tubes

Fiber reinforced polymer composites are used by laying-up on the long cylindrical tubes to obtain proper in-plain and out-of-plain properties. This may cause unexpected dimensional anomalies associated with laying-up of plies such as relative movement of each ply while folding and expanding. For this reason, the cylindrical tubes are fabricated by one ply of either BWF or TWF as shown in Fig. 1 with understanding that one ply construction of the inflatable structure is more manageable for the dimensional stability during deployment. Details of the cylindrical tubes are listed in Table 1. It should be mentioned that the areal densities of the fabrics are the same for proper comparison of the test results. The tubes were compressed and tensioned along the axial direction of the cylindrical tubes, and the displacements of the tubes were measured.

Folding and Expansion

Folding method and the construction of the inflatable tube are shown in Fig. 2. This type of inflatable tube is fabricated and tested for foldability and expandability.

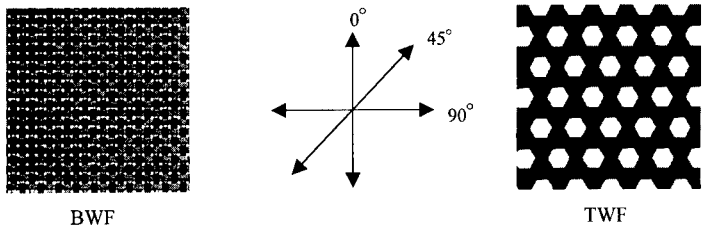

Fig. 1 Directions of BWF and TWF

Table 1 Details of the Cylindrical Tubes

Fabric Style		BWF 0°	BWF 45°	TWF 90°	TWF 0°
Weave		Plain		Basic	
Fiber		T300-3K		T300-6K	
Construction	(Yarns/25mm)	12.50		4.625	
Tube Weight	(g)	17.5		19.2	
Tube Thickness	(mm)	0.28		0.43	
Tube Diameter	(mm)	150			
Tube Length	(mm)	100			
Process		Autoclave			
Condition		160 ℃, 90 min, 0.5 MPa			
Resin Type		Long Shelf Life Epoxy at Room Temperature			

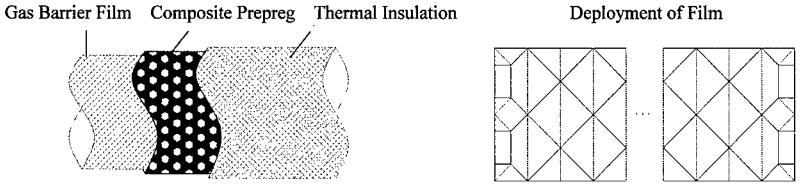

Fig. 2 Folding Method and the Construction of the Inflatable Tube

Results and Discussion

Properties of the Cylindrical Tubes

Figure 3 shows the force applied to the cylindrical tubes to the direction of cylindrical axis. We call it "axial force", and displacements of the cylindrical tubes for both BWF and TWF. The results show that the rigidity of the tube of TWF is larger than that of BWF tube. This difference is caused by the wall thickness of the tubes; 0.28 mm for the BWF and 0.43 mm for the TWF, though they have the same areal density. Further, the rigidity differences between the different directions of the same fabric are more prominent for the BWF: the displacements of BWF tubes are 18.93 mm for the 0 degree direction and 25.81 mm for the 90 degree direction at 1 N of the axial force, and those of TWF tubes are 9.55 mm for the 0 degree direction and 9.08 mm for the 90 degree direction at the same force. It is conceivable that isotropy of any fabric is more manageable than anisotropy for construction of joints or blanches of tubes such as T-shape or Y-shape of an inflatable structure.

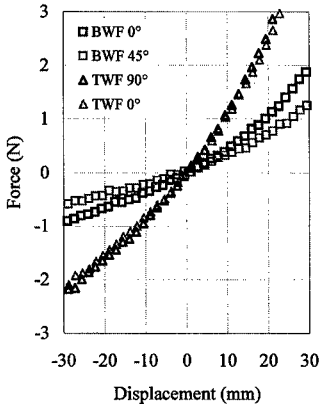

Fig. 3 Force-Displacement Curves for the Cylindrical Tubes

Foldability and Expandability

The inflatable tube was fabricated as shown in Fig. 2 except it does not have a thermal insulation equipment. As shown in Fig. 4, the inflatable tube was first folded in the size of 167 mm x 167 mm x 100 mm, and then expanded to the size of diameter 150 mm and length 2000 mm by inflating the gas barrier film by the compressed air. The folding and expanding of the inflatable tube proceeded very smoothly, and any damage or disorientation of the fiber was not observed in the prepreg. The total weight of the 2000 mm inflatable tube is 390 g.

Fig. 4 Inflation of Inflatable Tube

Conclusions

The displacement under the axial force of the cylindrical tubes fabricated by TWF is much smaller than that of the tube fabricated by BWF. This is because TWF can be woven with a low weaving density resulting in a thicker fabric compared with that of BWF. The thicker fabric with the same areal density and fiber properties results in a larger plate bending rigidity leading to a stiffer cylindrical tube. Further, the TWF possesses less in-plain anisotropy than the BWF.

The inflatable tube fabricated using the TWF prepreg could be inflated smoothly without observing any damage. It should be noted that the expansion of the tube proceeded uniformly in the length-wise because of the new folding method presented in this paper.

References

1. R.E.Freeland, G.D.Bilyeu, G.R.Veal, and M.M.Mikulas: 49th International Astronautical Congress, IAF-98-I.5.01, (1988).
2. M.C.Lou: International Symposium on Space Technology and Science, ISTS 2000-c-21, (2000).
3.E.G.Njoku, Y.Rahmat-Samii, J.Sercel, W.J.Wilson, and M.Moghaddam: IEEE Trans. Geoscience and Remoto Sensing, 37(1), 63(1999).
4. H.Tsunoda and Y.Senbokuya: 42nd AIAA/ASME/ASCE/AHS/ASC Structures, Structural Dynamics, and materials Conf., AIAA-2001-1597, (2001).
5. D.P.Cadogan, S.E.Scarborough: 42nd AIAA/ASME/ASCE/AHS/ASC Structures, Structural Dynamics, and materials Conf., AIAA-2001-1417, (2001).
6. K.Higuchi, M.C.Natori, H.Hatta, and R.Yokota: 20th International Symposium on Space Technology and Science, 96-b-11v, (1996).
7. D.Cadogan and M.Grahne: 49th International Astronautical Congress, IAF-98-I.1.02, (1988).
8. D.K.Darooka and D.W.Jensen: 42nd AIAA/ASME/ASCE/AHS/ASC Structures, Structural Dynamics, and materials Conf., AIAA-2001-1257, (2001).

Proceedings of 7th Japan International SAMPE
Symposium & Exhibition, Nov. 13-16, 2001

Applying Thermoplastic Composite to Space Inflatable Structure

Seiichi Matsuoka#1 and Hiroyuki Nakamura#2

Aerospace Division, Fuji Heavy Industries LTD
1-1-11 Yonan, Utsunomiya-Shi, Tochigi 320-8564, JAPAN
#1:E-mail: matsuokas@uae.subaru-fhi.co.jp
#2:E-mail: nakamurah1@uae.subaru-fhi.co.jp

Yumi Senbokuya#3 and Hiroaki Tsunoda#4

NTT Network Innovation Laboratories, Nippon Telegraph and Telephone Corporation
1-1 Hikarinooka, Yokosuka-Shi, Kanagawa 239-0847, JAPAN
#3:E-mail: senbok@wslab.ntt.co.jp
#4:E-mail: tsunoda@wslab.ntt.co.jp

Abstract

The space inflatable technology is paid attention to realize large aperture spaceborn antenna systems. Over the past years, several studies have been made on an inflatable rigidized structure which used the thermoset composite material. However thermoset composite material has the restriction on the storage conditions. Because of this reason, we conducted a study of applying the thermoplastic composite to a inflatable structure to eliminate the restriction

As the first step in this study, we examined the rigidization of the thermoplastic composite which is assumed to be used for the inflatable structure. This paper describes the feasibility of applying the thermoplastic composite to the inflatable structure from the result of the test data

Key Words: Inflatable structure, thermoplastic composite

Introduction

The need for light weight and small launch volume of the large space structure such as deployable satellite antenna is growing rapidly. Figure 1 shows an example of inflatable technology applied to the planar array antenna.

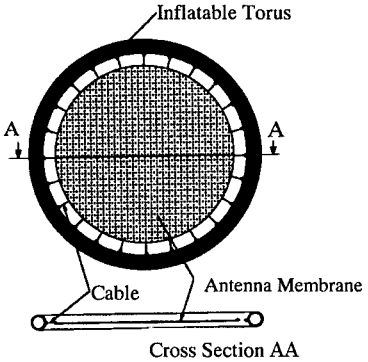

Fig. 1 Example of Planar Array Antenna

The inflatable structure provides a frame from which the antenna membrane can be suspended and tensioned to maintain the required surface tolerance of a planer array antenna[5]. The space inflatable structures are paid attention for such need. To apply inflatable structure in space, it is effective to make the structure rigid after it is fully deployed to eliminate the need for a constant supply of gas to maintain structure integrity of the system and reduce the damage of the debris and meteoroid. The inflatable rigidizable structure, once deployed to the final shape, is made rigid by a chemical reaction. The thermal rigidization of the thermoset composite structures have been studied[1,4]. The thermoset composite material have a problem of the short storage period. We have been investigating materials, and processing techniques and inflatable element design for the thermoplastic composite material. Some materials can be stored in many environment for a period of years without degradation.

A typical section view of inflatable structure is shown in Figure 2.

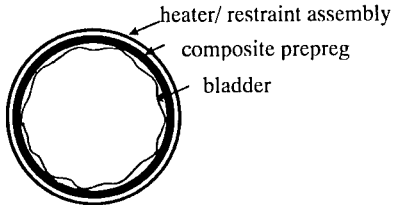

Fig. 2 Typical Section of Inflatable Structure

The composite laminate consists of three elements[3]: the bladder, the composite prepreg , and the heater and restraint assembly. The heater and restraint assembly provides resistive heat to plasticize the composite laminate that control the final shape. The bladder retains internal gas pressure and pushes the prepreg out against the heater/restraint. The composite prepreg is packaged before rigidization, then is regidized in order to become the main structural element after deployment is complete. Many studies have been made on the application of the thermoset composite to a composite prepreg. However thermoset composite has the restriction on the storage conditions. Because of this reason, we considered the application of the thermoplastic composite which dose not have the restriction. The problem which we have to consider next is the low flexibility of the thermoplastic composite. We considered the application of a cowoven fabric to solve this problem. The cowoven fabric offer the desired high flexibility without preheating[2].

Experimental Procedures and Results

Thermoplastic Cowoven Fabric

The cowoven fabric of the thermoplastic composite material consists of the glass fiber and the thermoplastic polymer in a continuous multifilament form. The coweave technique unites the glass and polyamide multifilament yarns during the weaving operation. Thermoplastic yarns are woven with glass yarns to form a fabric. Unidirectional fabric was investigated in this study. In unidirectional fabric, only glass filaments are woven in the warp direction and polyamide filaments are woven in the fill direction.

Processing Test

All specimens consisted of three elements[3]: the bladder, the composite prepreg and the restraint similar to the inflatable structure. Figure 3 shows the specimen configuration.

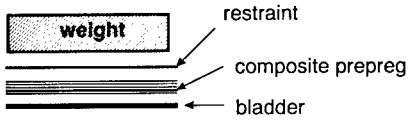

Fig. 3 Specimen Configuration

These specimens were placed into the furnace and were heated to the melt temperature at a pressure, and the weight was applied to the specimen as shown in Figure 3. The specimens were kept at the specified pressure and temperature for a time period of about 5 minutes before being removed to a quenching. The quenching was conducted by atmosphere. Forming temperature was monitored by reading the thermocouple placed on the specimen.

All specimens were quenched under the pressure which is below the glass transition temperature. A summary of the test conditions used for the material of this study is shown in Table 1.

Table 1 Summary of the Test Conditions

Test Case	1	2	3	4
Fiber	EGF(E Glass fiber), 135TEX			
Fabric Construction	Plain			
Temperature(℃)	234.6	254.2	233.7	230.7
Pressure(kPa)	0	12.7	19.6	39.2
Holding Time(min)	5	5	5	5

Microscope was used to examine the quality of the laminate rigidization. Figure 4 and 5 show the surface view of the specimen at the test case 1 and 3 respectively.

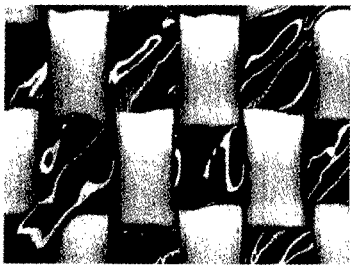

Fig. 4 Surface View of Case 1

Fig. 5 Surface View of Case 3

The photomicrograph in Figure 4 indicated that the thermoplastic fibers didn't wet out the glass fibers sufficiently, while the Figure 5 indicated the good regidization that the thermoplastic fibers wetted out the glass fiber.

All specimens indicated the same good regidization for more than 19.6 kPa pressure. The test result indicated that pressure was needed more than 19.6 kPa gauge internal pressure to make rigid the thermoplastic cowoven fabric.

FabricationTest

The cylinder which was 140 mm in diameter and 220 mm in length was manufactured and made rigid under 19.6 kPa (gauge) internal pressure in the furnace to evaluate the feasibility of the basic inflatable element fabrication.

The composite laminate of the cylinder consisted of three elements[3]: the bladder, the composite prepreg, and the restraint assembly. The bladder was a layer of 0.05 mm thick FEP film. The composite prepreg layer consists of the four plies of cowoven glass fabric that is shown in Table 1. The restraint consists of a layer of 0.1 mm thick glass fiber fabric impregnated with a Teflon resin. This composite laminate is a set of aluminum alloy end cap at the both of ends. The specimen configuration is shown in Figure 6

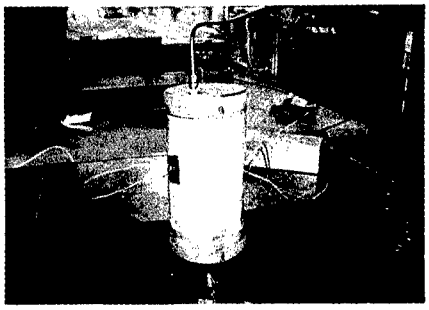

Fig. 6 Specimen Configuration

The cylinder was made rigid at 1 atmosphere ambient pressure. The cylinder was kept at the specified internal pressure and temperature in the furnace for a time period of about 5 minutes. Forming temperature was monitored by the three thermocouples placed on the circumference of the cylinder. Forming pressure was monitored by the pressure gauge.

A summary of the processing conditions used is shown in Table 2.

Table 2 Processing Condition

Molding Condition	
Temperature(°C)	254.7
Pressure(kPa)	19.6
Holding Time(min)	5

The cylinder indicated the good rigidization that thermoplastic fibers were melted and wetted out the glass fibers. The test result indicated that there was a feasibility of basic inflatable element fabrication using the method that internal gas pressure pushed the prepreg out against the restraint. However the cylinder was fabricated in the furnace without heating by the film heater in this test.

Conclusions

As the first step in this study, we conducted the tests regarding the rigidization of the thermoplastic composite under the condition that simulated applying for the inflatable structure. At first , the fundamental processing condition could be clarified from the result of the processing test. The most important processing condition is the pressure condition. 1.96 kPa pressure could be determined as the minimum value used for rigidization. Next , the applicability of the processing condition to the inflatable structure was confirmed from the result of the fabrication test. These results lead us to the conclusion that the thermoplastic composite could be applied to the inflatable structure.

References

1. M.S.Grahne, D.P.Cadogan, and C.R.Sandy: "Advanced Antenna Systems Utilizing Inflatable & Planer Array Technologies", IAF-00-M.2.06, 51st Internal Astronautical Congress, Oct 2000.
2. E.M.Silverman and Robert J. Jones: "Property and Processing Performance of Graphite/peek Prepreg Tapes and Fabrics, SAMPE Journal July/August 1988, pp.33-40.
3. M.S.Grahne, D.P.Cadogan, and C.R.Sandy: "Development of the Inflatable Shield In Space (ISIS) Structure for the NGST Program", IAF-00-I.1.04,51st Internal Astronautical Congress, Oct 2000.
4. D.P.Cadogan, Stephen E., and Scarborough: "Rigidizable Materials for use in Gossamer Space Inflatable Structures", AIAA 2001-1417, 42nd AIAA/ASME/ASCE/AHS/ASC Structure, Structural Dynamics, and Materials Conference & Exhibit AIAA Gossamer Spacecraft Forum, April 2001.
5. H.Tsunoda and Y.Senbokuya: "Shape Measurement of a Flat Stretched Lightweight Membrane for Planar Antenna Structure", 42nd AIAA/ASME/ASCE/AHS /ASC Structures, Structural Dynamics and materials Conf., AIAA-2001-1597, (2001).

Proceedings of 7th Japan International SAMPE
Symposium & Exhibition, Nov. 13-16, 2001

Research on Applicability of Shape Memory Polymers (SMPs) to Inflatable and Deployable Space Structure

Junichiro Ishizawa#1 Kichiro Imagawa#1 Junichi Yoshikawa#1
Shunichi Hayashi#2 Norio Miwa#2

#1:Technology Research Department, Office of Research and Development,
National Space Development Agency of Japan
#2:Nagoya Research and Development Center, Mitsubishi Heavy Industries
2-1-1 Sengen, Tsukuba, Ibaraki, 305-8505, JAPAN
E-Mail: ishizawa.junichiro@nasda.go.jp

Abstract

Demand for inflatable and deployable structures for space use produce many schemes for them. As one of the possibilities, we focus on Shape Memory Polymers (SMPs), which can be inflated or deployed simply by means of their shape memory effect. In this research, two types of SMPs have been investigated, foam type for inflatable structure, and fiber-reinforced type for deployable structure and actuator. Evaluated properties indicate that SMPs have enough applicability to space structures.

Key Words: Shape Memory Polymers (SMPs), Inflatable, Space Structure, Polyurethane

Introduction

Technology of inflatable and deployable structures enables launch vehicles, of which fairing sizes are limited, to transport huge structure to space. However, because of their complex mechanism to form desired shapes, a non-negligible number of malfunctions has been occurred. Some deployable and inflatable structures put into practice, but they were too complex and heavy. We focused on Shape Memory Polymers (SMPs), which are lighter, cheaper, lager in recovery volume ratio than shape memory metals. Characteristics of SMPs are shown in Table1.

Table 1 Characteristics of SMPs Compared with Shape Memory Metals

Superior	Inferior
Large recovery volume	Poor resistance
Low cost	to space environment
Light	Much out-gassing
Good workability	Low recovery power

Effect of SMPs

Shape memory effect of SMPs depends on their glass transition function. Figure 1 shows the concept of shape memory effect of SMPs, which are rubbery and flexible over Glass Transition Temperature (Tg), glassy and

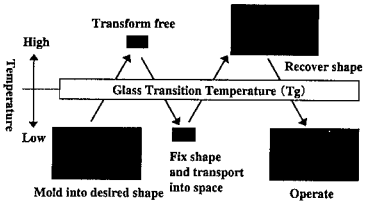

Fig.1 The concept of SMPs' Shape Memory Effect

rigid below it. SMPs can be inflatable and deployable simply and reliably.

Application of SMPs to space structures
Shown in Figure 2 is an example of application of SMPs to space structure. They can be applied to large space structure, such as solar paddles, antennas, etc..

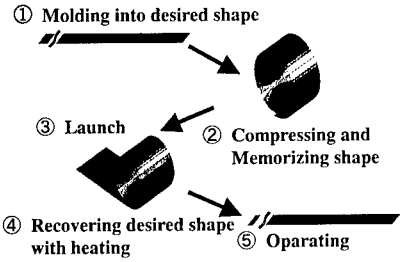

Fig.2 An Application of SMPs to Space Structure (ex. Solar Paddles)

Experimental

Polyurethane based SMP, "DiAPLEX"[(1),(2),(3)], manufactured by Mitsubishi Heavy Industries and being only SMP put into practical use, was chosen as samples. DiAPLEX has many features, being light, clear, colorable, high corrosion resistant and workable, and has flexibility of Tg selection. Two types of SMPs were prepared. One is carbon fiber reinforced SMP (FR-SMP) manufactured by hot pressing (in Figure 3) and deployable, 1-ply and 2-ply FR-SMPs were produced. The other is foam (SMP-Foam) for inflatable structure manufactured from isocyanate, polyol and water. Isocyanate and polyol react together to produce polyurethane, which is foamed by CO_2 generated by reaction of polyol and H_2O. FR-SMP was produced to apply to space structures for the first time, while SMP-Foam has been under researching [(4)]. In addition, UV irradiated samples were prepared in order to investigate resistance of SMP to UV. The total flux of each UV irradiated sample is 50 equivalent solar days (ESD).

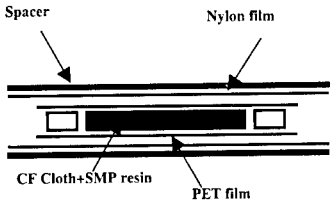

Fig.3 Manufacture of FR-SMP by Hot Press

Dynamic viscoelasticity of SMP samples were investigated at temperatures between 223K and 473K, with torsion mode for FR-SMP and with compression mode for SMP-Foam. Solar absorptance (alpha-S) and normal emittance (epsilon-N) of irradiated and unirradiated samples were measured. Durability of the materials against UV irradiation was judged by evaluating the alpha-S and epsilon-N changes. Outgassing of the samples was also evaluated with ASTM E 595. SMP-Foam has, however, too low density not to weigh enough for ASTM E595. Data of shape memory properties of SMP samples, fixation rate and recovery rate were obtained. They were acquired by comparing strain.

Results and Discussion

Dynamic viscoelasticity of SMPs
Figure 4 and Figure 5 show dynamic viscoelasticity of SMPs. At Tg, viscoelasticity changes significantly and so SMPs indicate typical shape memory effect.

Although 50ESD UV was irradiated, there are little change between their carves. It is considered that SMPs may keep their shape memory function beyond the range of 50 ESD UV irradiation. There may be enough time to inflate or deploy SMPs after putting into an orbit. Figure 5 also shows

an effect of carbon fiber, that 2-ply sample is stiffer than 1-ply one.

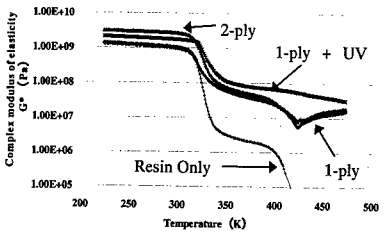

Fig.4 Viscoelasticity of FR-SMPs (Compared with Resin Only SMP)

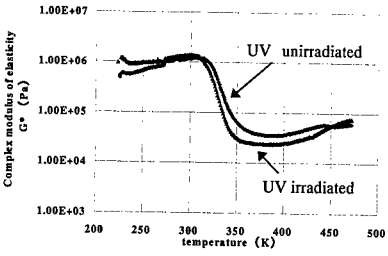

Fig.5 Viscoelasticity of SMP-Foam

Solar Absorptance and Normal Emittance Changes

Shown in Table 2 are data of solar absorptance and normal emittance changes of SMPs.

Table 2 Solar Absorptance and Normal Emittance Changes

Sample	Solar absorptance (alpha-S)		Normal emittance (epsilon-N)	
	Unirradiated	UV irradiated	Unirradiated	UV irradiated
FR-SMP	0.882	0.867	0.899	0.898
SMP-Foam	0.433	0.590	0.922	0.912

Solar absorptance of SMP-foam increased with UV irradiation. That of FR-SMP did not increase, and it may be due to black color of carbon fiber. It is found that SMPs are easily damaged by UV irradiation.

Outgassing of SMPs

Measured outgassing data of SMPs are shown in Table 3.

Table 3 Outgassing Data of SMPs

Samples	FR-SMP	SMP-Foam
Total Mass Loss (%)	0.678	3.582
Collected Volatile Condensable Materials (%)	0.001	0.057
Water Vapor Regained (%)	0.158	0.16
Judgement	Passed	Failed

PASSED: TML≦1% and CVCM≦0.1%

A total mass loss of SMP-Foam does not fulfill recommendation value. To use in space, SMP-Foam is desired to decrease its total mass loss.

Shape Memory Properties of SMPs

Shown in Table 4 are data of shape memory properties, fixation and recovery rate. As well as the result of viscoelasticity measurements, 50 ESD UV irradiation cannot deprive SMPs of shape memory function. Table 4 shows that FR-SMPs have a good shape recovery feature, and SMP-Foam a good shape fixation feature.

Table 4 Shape Memory Properties of SMPs

Sample	FR-SMP			SMP-Foam	
	Unirradiated		UV irradiated	Unirradiated	UV irradiated
	1ply	2ply	1ply		
Fixation rate	99.82	99.82	99.28	100	100
Recovery rate	100	100	100	98.32	97.54

Conclusion

In this research, many data have been taken and SMPs are considered by those data to have encouraging applicability to space structure. In particular SMP keeps its shape memory function despite of 50 ESD UV irradiation. However it is necessary to decrease the amount of outgassing and the damage by UV irradiation. In addition, the effects of other space environment, such as radiation, atomic oxygen irradiation, heat cycling, should be examined. Then application of SMPs to space structures will change space development drastically.

References

1. H.Tobushi and S.Hayashi:JSME Int. Journal, Ser. 1, 35(3), 296(1991).
2. S.Hayashi: Int. Progress in Urethanes, 6, 90(1993).
3. T.Takahashi and S.Hayashi: J. of Applied Polymer Science,60,1061(1996).
4. W.M.Sokolowski, A.B.Chmielewski, S. Hayashi and T. Yamada: Proceedings of the Electroactive Polymer Actuators and Devices, Smart Structures and Materials 1999, 3669, 179(1999).

Proceedings of 7th Japan International SAMPE
Symposium & Exhibition, Nov. 13-16, 2001

Light Sandwich Panels Utilizing Plastic Foam

Kichiro Imagawa, Junichi Yoshizawa, Junichiro Ishizawa(NASDA)

Hiroshi Mizuno, Koichi Saito, Mikio Tojo(MHI)

Nagoya Guidance & Propulsion Systems Works, Mitsubishi Heavy Industries,LTD.
1200 Higashi-tanaka, Komaki, Aichi 485-8561, JAPAN
E-mail: mikio_tojo@ngpsw.mhi.co.jp

Abstract

It is analytically found that light sandwich panels consisting of low-density plastic foam and CFRP plates can be lighter, cheaper and stiffer than conventional alumi-num honeycomb panel. Weghts of the panels that possess specified stiffness are calculated in consideration of mechanical property of materials and panel thickness. Result of the calcuration enable us to find out optimun combinations of CFRP and foam thickness. It is proved from mechanical test of the proto-type panels that hot press without adhesives is able to combine CFRP panels and foam, and gives as same stiffness as that of analysis results. Tensile and compressive strength and stiffness (modulus of elasticity) of the panels that had been exposed to electrons radiation are obtained in order to evaluate space applicability. Outgas, thermo-optical proper-ties, and shielding effects of the CFRP plates are also evaluated.

Key Words: Composite Material, Light Weight, Sandwich Panel

Introduction

Since the satellite structure have to be light weight and highly stiffness unlike general structure, a sandwich structure with honeycomb is in practical use. The main components of a sandwich structure are skin, core, adhesive and joints. We have resear-ched on the light sandwich panels which does not require adhesive for the combination of CFRP skin and low-density foam. This new panels were compared with the existing panels as the primary evaluations and their basic characteristics data were obtained by using the prototype materials.

Evaluation of The Sandwich Panel

Equivalent Stiffness of Sandwich Panel

The stiffness of a sandwich panel is analyzed with the skin stiffness, thickness and spacing, without any deformation of its core. And the stiffness of light sandwich panels equivalent to aluminum alloy board are analyzed for comparison with their weight. The analytical equation is as follows:

$$E_{AL}\, t_{AL}{}^3 b / 12 = E_{CF}\, b\, t_{CF} (d+t_{CF})^2 / 2 + E_{CF}\, b\, t_{CF}{}^3 / 6 \quad (1)$$

where E: Modulus, b: Width, t: Thicknss, d: Core thickness, suffix AL: Aluminum, suffix CF: CFRP(Carbon Fiber Reinforced Plastics)

The results of comparison show that light sandwich panels consisting of low-density plastic foam and CFRP plates without ad-hesive are lighter than conventional

alumi-num honeycomb panel.(Fig.1) Also it is enable us to find out optimum combinations of CFRP and foam thickness under an equivalent stiffness.

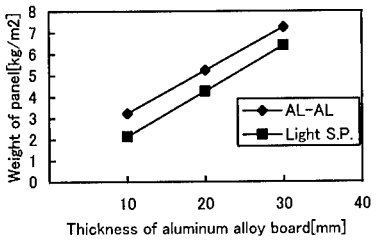

Fig.1 Weight of Sandwich Panel with Equivalently Stiffness for Aluminum alloy

Evaluation for Component of Structure

There are three kinds of specimens to eva-luate for component of a sandwich panel. Specimen A for CFRP skin consist of high-modulus fiber. Specimen B for panel rein-forcement and specimen C for combination part consist of middle-modulus fiber. And electron irradiation is conducted under the conditions shown in Table1 because of evaluation for space environmental resis-tance.

Table 1 Electron Irradiation Condition

Test No.	Electron Energy(MeV)	Fluence Rtio ($e/cm^2/s$)	Current (mA)	Fluence (e/cm^2)
(1)	0.5	$1.02x10^{13}$	8	$2x10^{16}$
(2)	0.5	$9.04x10^{12}$	8	$2x10^{16}$

(1): Atmosphere Helium for Specimen A and B
(2): Atmosphere Air for Specimen A, B and C
Radiation Temperature is Room Temperature.

In the test No.(1), the chamber is vacuumed down to less than 10 Torr, and then electron beams are irradiated horizontally into a vacuum chamber in which helium gas is flown at the flow rate of approximately 2 ml/min. In the test No.(2), electron beams are irradiated vertically in the air. The fluence ratio in each test is measured by using the charge collector installed at the test materials location. The fluence is set to $2x10^{16}$ (e/cm^2), equivalent to the 10-year period fluence in the space environment on the geosynchro-nous orbit. The test materials have to be vertically installed in the test No.(1) for horizontal irradiation of electron beams. Therefore, the materials are wrapped with 0.1 mm thick Kapton films, fixed during irradiation. Because it have to be considered that the Kapton films may shield electron beams, the result of using CTA (Cellulose Tri-Acetate; electron beam dose monitoring material) films indicated that the fluence decrease caused by Kapton films is 3%. The temperature of a test materials indicates below 85°C in any case of the electron beam irradiation conditions. The electron beam shield effect of the specimen A is evaluated by the following: The electron energy equivalent to 0.5 MeV is vertically irradiated to 4 types of thickness (1 to 4 mm) installed on CTA films and electron beam transmissions are calculated from the absor-bance changes of the CTA films after irra-diation.

Test Results

We obtained the data on the mechanical properties, outgas, and thermo-optical pro-perties (only for specimen A) before and after electron beam irradiation (in the helium gas atmosphere and in the air). The test results are shown in Table2-5.

Table 2 Mechanical Properties of Component(Ref.SACMA SRM 9-94)

Properties	Electron Irradiation	Specimen A	B	C
Tensile Strength	Before	523	758	460
(MPa)	After	473	724	464
Elastic Modulus	Before	96.9	47.6	40.3
(GPa)	After	98.1	44.7	40.4

Table 3 Bending Modulus of Sandwich Panel(Ref.ASTM C 393)

Properties	Electron Irradiation	Bending Modulus (kNm^2/m)
Test Results	Before	22.6
Analysis	Before	20

Panel Specification: Skin thickness 0.96mm and material is same as specimen A. Core thickness 20mm and material is low-density plastic foam.

Table 4 Outgas Properties after Electron Irradiation

Specimen	TML(%)	CVCM(%)	WVR(%)	REMARK
A	0.145	0.004	0.064	PASSED
B	0.193	0.008	0.046	PASSED
C	0.195	0.003	0.059	PASSED

PASSED: TML<1% and CVCM<0.1%

Table 5 Thermo-optical Properties for Specimen A

Electron Irradiation	Solar Absorptance (a_s)	Nomal Emittance (e_N)
Before	0.892	0.763
After	0.894	0.778

Conclusions

In this research, the result of the comparison in mechanical properties bet-ween a light sandwich panel and the existing honeycomb panel has clarified the range in which a light sandwich panel are advan-tageous. This is the effect due to no adhesive in forming a light sandwich panel. On the other hand, test results show that no deterioration caused by electron beams is recognized in the mechanical properties of skin material and that 2 mm or thicker skin material could prevent the core material from deteriorating attributable to electron beams. It is therefore considered that the reasonable compatibility of light-weight and high-stiffness design and electron beam resisting (core protection) design is vital as design elements of a light structure panel. The results of thermo-optical properties indicated that the effect of electron beam irradiation is hardly seen in solar absorptance, while nomal emittance increase after irradiation. Solar absorptance affect the thermal input to the inside, and nomal emittace affect the thermal emission to the outside. Both are used for the thermal design of spacecraft. The increase of nomal emittance is considered favorable for use as a spacecraft material. Therefore, it can be said from the above results that no deterioration caused by electron beam irradiation is observed in the thermo-optical properties of specimen A. At the solar absorptance of 0.89, however, solar beam causes a large quantity of thermal input, which will induce a temperature to rise in the inside of spacecraft. It is necessary to use with the thermal control material on the surface. It should be therefore concluded from the above results that the electron beam resistance of specimen A is satisfied in thermo-optical properties.

Reference

1.K.Imagawa and H.Mizuno: Proc. of 37th Aircraft Symposium , 1999 , pp537-540

Proceedings of 7th Japan International SAMPE
Symposium & Exhibition, Nov. 13-16, 2001

Development of super-lightweight waveguide for MUSES－C XHGA and horn antennas for MUSES-C XMGA

Osamu Amano #1,Toru Shibata #1, Akihito Watanabe #2 and Yukio Kamata #3

#1:NEC Engineering, Ltd.
4458,Ikebe-cho,Tsuzuki-ku,Yokohama,224-0053,JAPAN

#2:Sakase Adtech Corporation
14-10 Shimoyasuda, Maruoka-cho,Fukui,910-0363,JAPAN

#3:Institute of Space and Astronautical Science
3-1-1 Yoshinodai,Sagamihara,Kanagawa,229,JAPAN

Abstract

The 20th scientific satellite MUSE-C, shown in Fig.1, which aims at collecting the rock samples from the asteroid then returning them back to the earth, is scheduled for lunch in 2002 by ISAS. The satellite will have 5 antennas: one ϕ 1.6m X-band high gain antenna (XHGA),two X-band medium gain antennas (XMGA-A&B) and three X-band low gain antennas (XLGA-A,B & C).

Key Words: satellite, super light-weight, waveguide,horn antenna

1.Introduction

All 5 antennas are design with extremely low mass in order to meet the satellite's very tight weight budget. NEC has developed the Super-Lightweight (SLW) Waveguide for XHGA and horn antenna flares for XMGA-A&B in order to achieve the requirement of mass.

The SLW Waveguide and Horn antennas are used for both the transmitting frequency 8.41GHz and the receiving frequency 7.15 GHz.

Fig.1 MUSES-C IMAGE

The waveguide adopts the WR112 (inner size : 28.5m × 12.6mm , frequency range:7.05-10.0GHz) covering the above frequency.

2. SLW Waveguide

The SLW Waveguide for MUSES-C XHGA shown in Fig.2-1 is made from Triaxial Woven Fabrics Carbon Fiber (TWF −CF), Unidirectional Carbon Fiber (UD−CF) and 30 μm copper metal plate. TWF −CF, UD−CF and the copper metal plate are mainly used for strength, surface accuracy and surface conductivity respectively.

Fig.2-2 shows TWF−CF matrix.

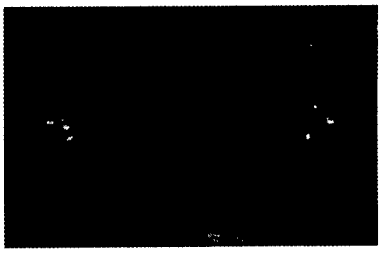

Fig.2-1 SLW Waveguide

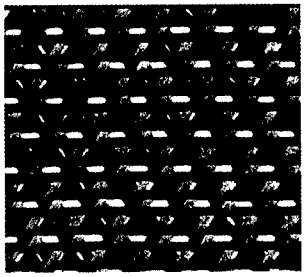

Fig.2-2 TWF−CF

The manufacturing of long waveguide as much as from one to two meter also become possible by using this structure.

Table.2-1 shows the major performance of the SLW waveguide compared with the conventional waveguide,etc .

The 480mm SLW waveguide made for MUSES-C XHGA shown in Fig.2-3 achieve the low transmission loss almost the same as the conventional waveguide at the frequency 7.15GHz / 8.41GHz.

Table2-1 Major performance the SLW Waveguide compared with the conventional Waveguide etc. (length:480mm)

item / Sample	Insertion Loss [dB/m] 7.15GHz	Insertion Loss [dB/m] 8.41GHz	Mass
SLW Waveguide	0.15 *1	0.15 *1	65g/m
	(0.15) *4	(0.15) *4	(107g)
Conventional Waveguide	0.13 *2	0.13 *2	385g/m
(t1.6mm,copper plated Al)	(0.14) *4	(0.14) *4	(258g)
ϕ4.3mm Coaxial Cable	0.83 *3	0.91 *3	52g/m
	(0.46) *4	(0.51) *4	(34g)

*1:measured value, *2:calculated value

*3:nominal value listed at a catalog

*4:The values in ( ) of this table show the values , including Waveguide-coaxial transformer or coaxial connector.

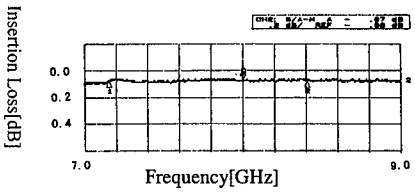

Fig.2-3 Insertion Loss of the SLW Waveguide (measured data)

Comparing with the conventional Waveguide, the mass of the SLW Waveguide is one sixth lighter the conventional waveguide.

And also, comparing with the coaxial cable, the mass of the SLW Waveguide is approximately as same as the coaxial cable and the transmission loss of the SLWW is one sixth lower than the coaxial cable.

We can achieve the excellent performance that the mass is almost the same as the coaxial cable and the transmission loss is almost the same as the conventional waveguide.

The value in ( ) of Table2-1 shows the insertion loss when it apply to the feeder of the MUSES-C XHGA. Even the short length,the SLW Waveguide still has the advantage in its low mass compared with the Metal Waveguide.

3.SLW Horn Antennas

The SLW Horn Antenna for MUSES-C XMGA shown in Fig.3-1 is made from Triaxial Woven Fabrics Carbon Fiber (TWF－CF) , Unidirectional Carbon Fiber

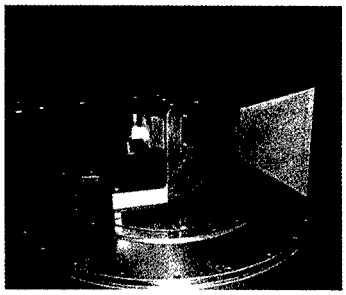

Fig3-1 SLW Horn Antenna

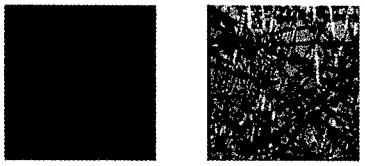

(a) (scale:1/1) (b) (scale:450:1)

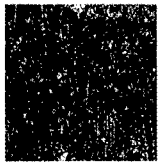

(c) (scale:450:1)

String's material: stainless

String's diameter:8 μ m (a)(b) for MUSES-C XMGA

2 μ m (c)

Fig. 3-2 Short Metal String Cloth

(UD－CF) and short metal string cloth instead of the copper metal plate in order to improve the thermal endurance. Fig.3-2 shows the short metal string cloth.

Table3-1 shows the major performance of the SLW Horn Antenna compared with the conventional Horn Antenna. The SLW Horn Antenna for MUSES-C XMGA achieves the Gain

characteristics almost the same as the conventional Horn Antenna at the frequency 7.15GHz / 8.41GHz and the mass is one sixth lighter than the conventional horn antenna. (See Fig.3-3 and Table3-1)

Table3-1 Major performance of the SLW Horn Antenna compared with the Conventional Horn Antenna

Item / Sample	Peak Gain [dBi] 7.15GHz	Peak Gain [dBi] 8.41GHz	Mass
SLW Horn Antenna (Stainless paper) *1	17.74 *2	18.80 *2	58g *2
Conventional Horn Antenna *1 (t1.6mm,Alminum)	17.71*2	18.88 *2	365g *3

*1:ApertureSize:90mm×130mm Length:160mm
*2:measured value *3: calculated value

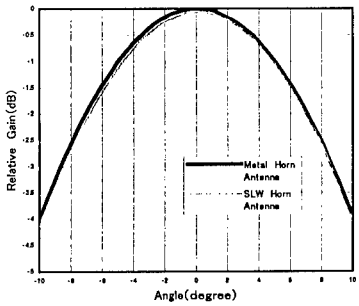

Fig.3-3 Antenna Radiation patterns at 8.41GHz (measured data)

4.Conclusion

The SLW Waveguide has already confirmed the characteristics under the specified environment for MUSES-C onboard equipment (thermal cycle, acoustic, vibration and shock) at PM phase.

The SLW Horn Antenna has already confirmed the characteristics under room temperature and the environment (vibration) at this time and is going to confirm the characteristics under the other Environment (thermal cycle and shock).

The inner layer of the SLW Waveguide is going to be changed from 30 μ m copper plate to a short metal string cloth to improve the thermal endurance and to use the thinner strings as shown in Fig3-2 (c) to improve the electrical performance.

5.References

1.Y.Kamata, M.Ichikawa,O.Amano and A.Watanabe :"A Development of light-weight Waveguide " The 2000 IEICE General Conference, B-1-124,2000,pp124

2.A.Watanabe,H.Tadokoro and Y.Arai : "Tensile Properties of Two-Reinforced CE/EP Single Ply Composites"43rd International SAMPE Symposium, 1998, pp1874-1882

3.S.Suesada and A.Watanabe: "Microwave Reflectivity of Carbon Fiber Triaxial Woven Fabrics for Antenna Aplication."44th International SAMPE Symposium, 1999, pp2301-2309

Proceedings of 7th Japan International SAMPE
Symposium & Exhibition, Nov. 13-16, 2001

Development of Passive Damping Device for Spacecraft Structures

Masahiro Takano*, Shiro Takada*, Shigenori Kabashima**, Takuo Ozawa**,
Ko Kojima**, Hiromi Seko** and Ideo Masuda***

*: Advanced Technology R & D Center, Mitsubishi Electric Corporation
8-1-1 Tsukaguchi-Honmachi, Amagasaki, Hyogo 661-8661, JAPAN
E-mail: takano@mec.crl.melco.co.jp
**: Mitsubishi Electric Corporation
***: National Space Development Agency of Japan

Abstract

This paper presents development and application of passive damping device to reduce vibration level of components induced in the environmental condition during launch. The restraining-type damping device consists of 2 different materials; one is a visco-elastic material with high damping ratio and the other is a restraint material with high stiffness. The damping device has been designed by modal strain energy method calculated by using finite element analysis, and optimized for specific eigen mode in order to achieve high damping efficiency. Furthermore, material properties such as out-gas of these materials were carefully tested in order to satisfy the specification for spacecraft use. The damping device was applied on a spacecraft panel of DRTS (Data Relay Test Satellite) and achieved about 1/4 of vibration level in acoustic vibration test.

Key Words: Spacecraft, Vibration Control, Damping Material, Visco-elastic Material,

Introduction

Spacecrafts are exposed in the environmental condition such as acoustic vibration during launch. On the other hand, vibration level of components on the spacecraft should be suppressed under the specific allowable level. For the purpose of the vibration level reduction, use of damping material is known as effective. Accordingly, in this paper, restraining-type damping device is developed and optimum size is examined to maximize the damping effect. Moreover, the application of the damping device to the spacecraft structures is described.

Optimum Size of Damping Device

In case of using a damping device, it is important to optimize the location, length and thickness of a damping device, in order to maximize the effect of attenuation without increasing the mass of the damping device. Accordingly, the effect of the damping device size to the loss factor was investigated by a theoretical analysis.

Analytical model

Figure 1 shows an analytical model for a small element, dx, in case that a restraining-type damping device is stuck to a spacecraft structure's panel. Figure 1(a) represents the undeformed shape and Fig.1(b) represents the deformed shape. Here, the axial displacement at the center of the i^{th} layer, that is, a CFRP layer, is u_i, and the shear strain of the $[i+1]^{th}$ layer, that is, a visco-elastic layer or a honeycomb layer, is γ_{i+1}. In addition, the axial force and the flexural stress of the visco-elastic layer or the honeycomb layer can be neglected, since the

elastic moduli of these layers are extremely small compared with that of the CFRP layer[1]. In Fig.1(b), the shear strain, γ_{i+1}, of the $[i+1]^{th}$ layer after the shear deformation results in the following equation according to a geometrical relationship.

$$\gamma_{i+1} = \frac{1}{t_{i+1}}\left\{u_i - u_{i+2} + \left(t_{i+1} + \frac{t_i + t_{i+2}}{2}\right)\frac{dw}{dx}\right\} \quad (1)$$

where, t_i is the thickness of the i^{th} layer. Next, Fig.1(c) shows the equilibrium of a laminated element. Here, F is the tensile force working on the CFRP layer, and τ is the shear stress operating on the visco-elastic layer or the honeycomb layer. A relationship leading to $dF_i = \tau_{i+1}bdx - \tau_{i-1}bdx$ is obtained from the equilibrium of force in the x direction. By substituting $F = Etb(du/dx)$ and $\tau = G\gamma$ into the above equation, the following equation are obtained.

$$E_c t_i \frac{d^2 u_i}{dx^2} = G_{i+1}\gamma_{i+1} - G_{i-1}\gamma_{i-1} \quad (2)$$

For i=1 and i=2n-1, Eq.(2) can be written,

$$E_c t_1 \frac{d^2 u_1}{dx^2} = G_2\gamma_2$$
$$E_c t_{2n-1} \frac{d^2 u_{2n-1}}{dx^2} = -G_{2n-2}\gamma_{2n-2} \quad (3)$$

where, n is the number of CFRP layers, E_c is the elastic modulus of the CFRP layer and G_i is the shear modulus of the visco-elastic layer or the honeycomb layer. The relationship between axial displacement, u, shear strain, γ, in each layer and deflection, w, can be calculated from Eqs. (1), (2) and (3).

Also, since the loss factor is expressed as the ratio of the dissipation energy to the total strain energy within one cycle in the eigen mode[2], the loss factor, η_0, of the area with the damping device is expressed by the following equation, provided that loss factors are assumed to be 0 for all layers except for the visco-elastic layer.

$$\eta_0 = \eta_v W_v / W_a \quad (4)$$

where, η_v is the loss factor of the visco-elastic layer, W_v is the shear strain energy of the visco-elastic layer, and W_a denotes the total strain energy of the area with the damping device.

In order to maximize the effect of attenuation, the optimum size of the damping device that gives the maximum η_0 should be calculated.

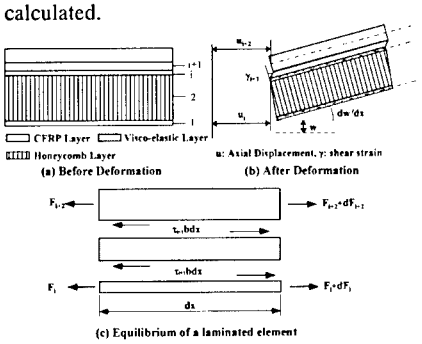

Fig.1 Analytical model

Results of Numerical calculation

The loss factor, η_0, was calculated by changing the length of the damping device, thickness and shear modulus of the visco-elastic layer. Calculation parameters used in the analyses are shown in Table 1. The relationship between the visco-elastic layer thickness and η_0 is shown in Fig.2. η_0 has a maximum value at the certain thickness of visco-elastic layer. Furthermore, the larger the shear modulus in the visco-elastic layer and the longer the length of damping device becomes, the thicker the optimum thickness of visco-elastic layer gets.

From the above, it is important to determine the optimum thickness of visco-elastic layer considering the length of the damping device and shear modulus of the

visco-elastic material, in order to use the damping device effectively.

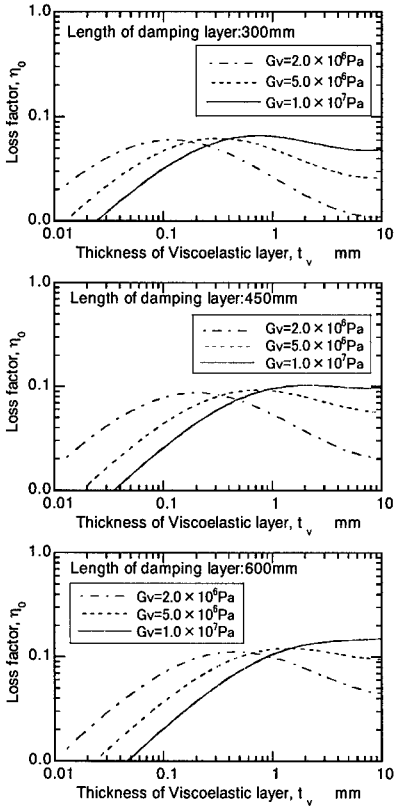

Fig.2 Relationship between loss factor, η_0, and thickness of visco-elastic layer

Table 1 Calculation Parameters

Damping device	
Length : l (mm)	300,450,600
Visco-elastic layer	
Thickness : t (mm)	0.01~10
Shear modulus : G (Pa)	$2,5,10\times10^6$
Loss Factor : η	1.0
Constraint layer (CFRP)	
Thickness : t (mm)	10
Elastic modulus : E (Pa)	1.15×10^{11}
Honeycomb sandwich panel	
Face sheet layer (CFRP)	
Thickness : t (mm)	0.36
Elastic modulus : E (Pa)	1.15×10^{11}
Honeycomb core layer (2^{nd} layer)	
Thickness : t (mm)	34.0
Shear modulus : E (Pa)	1.12×10^8

Application of Damping Device to Spacecraft Structure's Panel

The specific eigen mode of the DRTS structure's panel calculated by FEM is shown in Fig.3. In order to reduce the vibration response in this mode, three pieces of the damping device with 44 mm in width and 450 mm in length is stuck on the point A of the panel. The thickness of the visco-elastic layer was determined as 5 mm to maximize the effect of attenuation on the basis of the results in the former section.

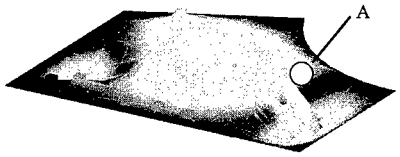

Fig. 3 Specific eigen mode of the panel

Estimation of reduction effect on vibration level

The loss factor of the whole structure after applying the above damping device to the spacecraft structure's panel is calculated by the modal strain energy (MSE) method.

In the following, the reduction effect of the vibration level is investigated by comparing the response with and without the damping device. The displacement X_j at a certain point becomes as follows.

$$X_j(\omega) = \sum_{i=1}^{n} \frac{\phi_{ji} \times \phi_{ki} F_k}{m_i(-\omega^2 + \eta_i \omega_i j\omega + \omega_i^2)} = \beta(\omega) \times \phi_{ki} F \qquad (5)$$

where, ϕ_{ji}, ϕ_{ki} are vector components of the response point j and the loaded point k for the following i^{th} mode, and ω_i and m_i are the natural frequency and modal mass of the following i^{th} mode, respectively. The generalized force $\phi_{ki}F_k$ is assumed to be the same with and without the damping device,

the reduction ratio of the response is obtained by comparing $\beta(\omega)$. In addition, the reduction ratio of the PSD of acceleration is obtained by comparing $\left\{\omega^2\beta(\omega)\right\}^2$ in the same method. Table 2 shows a comparison of maximum response around 300 Hz with and without the damping device. The values in the table were normalized by the response without the damping device. As shown in Table 2, the PSD of acceleration was expected to be reduced to 28% by the damping device.

Table 2 Analytical Results (Comparison of maximum response)

Analytical Case	Displacement	Acceleration PSD
w/o damping device	1.0	1.0
w/ damping device	0.58	0.24

Acoustic vibration test

The damping device was applied to DRTS structure's panel and an acoustic vibration test was carried out. The DRTS panel with the damping device is shown in Fig.4. In addition, as the experimental results, acceleration PSD with and without the damping device are shown in Fig.5. The acceleration PSD response with the damping device was reduced to 25% compared to without the damping device, which satisfied the allowable specifications of the loaded equipment. Furthermore, the experimental results show very good agreement with the analytical results, which shows that the analytical technique is effective enough to estimate the effect of the damping device.

Fig.4 DRTS panel with damping device

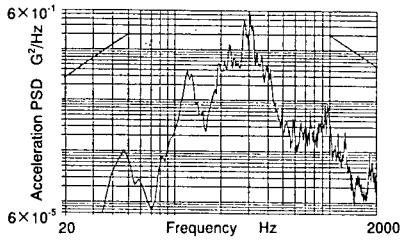

(a) without damping device

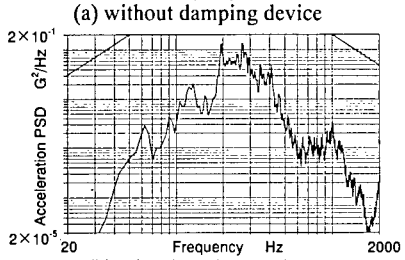

(b) with damping device

Fig.5 Experimental Results

Conclusions

A damping device was developed to reduce the vibration level of a spacecraft panel. Moreover, the damping device was applied to DRTS, Data Relay Test Satellite. Results are summarized as follows:

(1) Optimum thickness of visco-elastic layer was obtained in order to maximize the effect of damping device, considering the length of the damping device and shear modulus of the visco-elastic material.

(2) A simple technique was proposed in order to estimate the reduction of vibration level with the damping device.

(3) The acoustic vibration test results show very good agreement with the analytical estimation, and the vibration level with the damping device satisfied the allowable specifications of the loaded equipment.

References

(1) Ross, D., Structural Damping, Section Three, (1959), 49, Pargamon Press.

(2) Lall, A. K., J. Sound Vib., 123-2(1988), 247.

Proceedings of 7th Japan International SAMPE
Symposium & Exhibition, Nov. 13-16, 2001

Real Time Spectroscopic Observation of Degradation of Space Use Materials by Space Flyer Unit

Toshiaki YOKOTA, Susumu SASAKI#, Masahiro OTA*
and Hirohisa YOSHIDA*

Faculty of Science, Department of Physics, Ehime University, Matsuyama, Ehime 790-8577, JAPAN
E-Mail: yokota@phys.sci.ehime-u.ac.jp
#:The Institute of Space and Astronautical Science, Sagamihara, Kanagawa 229-8510, JAPAN
*:Faculty of Technology, Tokyo Metropolitan University,Minami Osawa, Hachioji, Tokyo 192-0397, JAPAN

ABSTRACT

The spectrometer (SPC) was set on the Space Flyer Unit (SFU) to observe the degradations of space use polymers against the space circumstances and to observe the luminous phenomena according to the interaction with space vehicle and space plasmas. The bare Upilex, aluminized Upilex and gold coated Upilex were selected for real time observations. Another samples were analyzed after the retrieve of the SFU.

SPC has been operated in a good condition for about ten months. The transmittances for aluminized and gold coated Upilex increase according as time. On the contrary, the transmittance for bare Upilex decreases according as time. These data are quite consistent with the results of laboratory simulation experiment prior to launch of SFU. SPC was able to observe the luminous spectra N, H, N_2, H_2, NH_3 and continuum associated with the exhaust of thruster.

Key Words: Degradation of materials, Spectroscopic observation, SFU.

INTRODUCTION

Many space vehicles have been put on the lower earth orbit. An atomic oxygen is most abundant in this region except for the UV light from the sun. It is pointed out that the surface of vehicle was degraded by interacting with the atomic oxygen and UV light and some luminous phenomena appear around a vehicle by interacting with space plasmas and surrounding gases come from thruster and out gas[1]. It is observed that the atomic oxygen has induced the degradation and the mass loss of material by striking the surface of vehicle. The details of these mechanisms are obscure in spite of many observations. The real time observation is inevitable to reveal these phenomena.

SPC has been constructed for real time investigation to reveal above phenomena. These observations have been planned on the basis of the laboratory simulation experiment prior to launch of SPC.[2,3] The bare Upilex (aromatic polymer), aluminized Upilex, and gold coated Upilex were selected as typical space use polymer. The degradation of these polymer was able to observe in real time by measurement of transmittance of laser diode

light. SPC was able to observe the luminous phenomena associated with the exhaust of thruster.

EXPERIMENTAL SET-UP

SPC was constructed for real time measurements of space circumstances and degradation of space use materials. SPC was modified from the commercial type monochrometer CT-10 (JASCO Co. Ltd.). It had the grating of 1200 grooves/mm, focal length was 10 cm, and aperture ratio was F3. The covering range of spectra was from 200 to 800 nm with resolution of 3 nm. The spectral intensity were sensed by a photomultiplier R-928 (Hamamatsu Co. Ltd.).

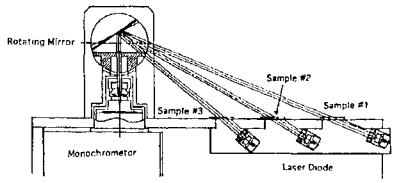

Fig.1 Setup for real time monitor.
#1: Alminized Upilex, #2: Gold coated Upilex, #3: Bare Upliex

Three space use materials have been set on the side panel of SPC. Each diode laser light beam (ML64110C; Mitsubishi Electric Co., Ltd.) pass through the sample was introduced to the entrance slit of SPC by an object mirror rotated by step motor (Fig.1). Three samples were a bare Upilex (Ube Industries Ltd.), aluminized Upilex, and gold coated Upilex. Both thickness of aluminum and gold were 14 nm and the coated side was set in order to expose to the space circumstances. SPC was able to observe the spectra around the SFU from ram to wake side by the rotation of object mirror.[4] Another samples attached on the panel of SFU were analyzed after retrieve of SFU.

OBSERVED RESULTS

The SFU and SPC have been operated in a good condition for about ten months after the launch. The large amount of data for optical transmittance and luminous spectra have been gathered. Time dependencies of transmitting intensity of laser diode light were obtained against two wave lengths (775.2 nm and 778.3 nm). Typical analyzed data are shown in Fig.2. The transmittance for bare Upilex decreases according as the elapse of time in the space circumstances. The transmittances for both aluminized Upilex and gold coated Upilex increase.

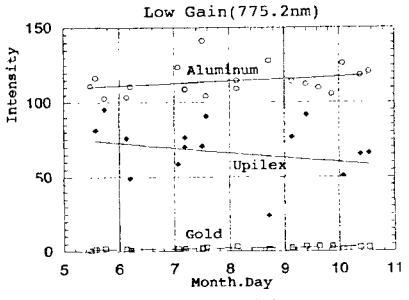

Fig.2 Time variations of real time transmittances obtained by SPC at λ=775.2 nm.

The surface of samples were analyzed by using various microscopic and spectroscopic method after the retrieve of SFU.[4] Surface reflection optical microscope was used to observe the surface morphology. Scanning probe microscopic observations were carried

out by SPI 3700 (Seiko Inst.) connected atomic force microscope and friction force microscope mode with resolution of 2.5×2.5 mm^2. Scanning electron microscopic observations were carried out by using JOEL 2000FX at the acceleration voltage of 200 V. Spectroscopic transmittances were observed by using Bio-Rad FTS 600 FT-IR spectrometer in wavelength range from 8000 cm^{-1} to 200 cm^{-1}. The electron spectroscopy for chemical analysis were performed at room temperature under a vacuum lower than 2×10^{-9} Torr with Hewlett-Packard Model 5650A.

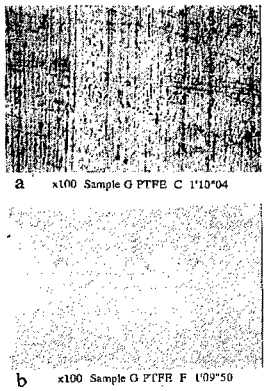

Fig.3 Optical microscopic observation of Upilex surface, (a) no flight, (b) retrieved after 10 months flight in the space. (magnification: ×100)

Substantial amount of damage was recognized on the surface of Upilex by the optical microscopic observation as shown in Fig.3. For instance, many scratch of micron order which were produced during the processing were observed on the surface, but all lines vanished after the flight. Some dust or space debris was found on the gold

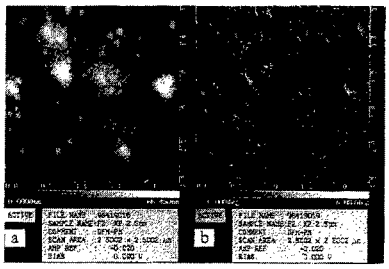

surface. It is determined that this dust contained SiOx by the result of electron

Fig.4 Surface etching images on gold surface by the scanning probe observation. The diameter of gold particle increases.

spectroscopy for chemical analysis. It is assumed that SiOx has come from the silicon adhesive used for the SFU frame and instruments. The surface etching was observed in picture of scanning probe observation (Fig.4). The average particle diameter was 7.2 nm and 27.5 nm in the 100 mm^2 area.[5]

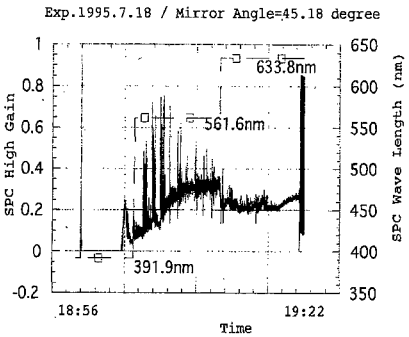

Fig.5 Observed spectra associated with exhaust of thruster.

SPC caught some luminous phenomena around the SFU. When the object mirror was set in the direction of thruster No.4 at the

mirror angle of 45.18 degrees, strong spectra were obtained for every exhaust of thruster gas. Typical spectra are shown in Fig.5. Mass analyzed data of surrounding atmospheres is shown in Fig.6 when thruster was exhausted.

DISCUSSION

SFU was in the lower earth orbit. In this orbit, the atomic oxygen density is 5×10^7 cm^{-3}, Helium density is 2×10^6 cm^{-3}, and atomic hydrogen density is 3×10^5 cm^{-3}. In the space, atoms, ions and high energy radiation, especially UV light from the sun, degrade the space use materials considerably. The source of another particles is the out gas from satellite itself and the thruster to control satellite. Atoms and ions collide with spacecraft at a relative speed of more than 8 km/s. This seems to be enough energy to interact with the surface of satellite.

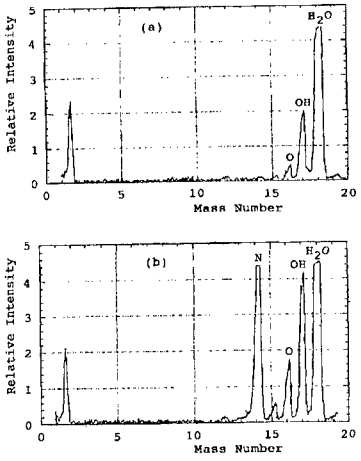

Fig.6 Mass analyzed data associated with exhaust of thruster. (a) after 30 sec, (b) just after.

In the laboratory experiment, the transmittance of polymer decreased by oxygen ion beam irradiation. Same tendency occurred in the case of UV light irradiation.[3] Surface color changed from the original yellow to brown for both irradiation, and transmittance of laser diode light decreases by irradiation. But, both transmittances of aluminized Upilex and of gold coated Upilex increased by the oxygen ion beam irradiation.[2] Optical transmittance increases up to 6.8 times if all of aluminum layer was sputtered out. Transmittance of aluminized Upilex increased up to 1.6 times after ten months flight. This value indicates that about 24 % of aluminum layer became thinner during the flight of 10 months. This value indicates that all of 14 nm aluminum layer may sputter out after more than 50 months flight. Up and down form of transmittance data in real flight indicates the fact that contamination adhere and sputtered out continuously. SiOx has came from the silicon adhesive used for the SFU frame and instruments. The same tendency occurs in the data of gold coated Upilex. Optical transmittance increases to 20 times when all of gold layer was sputtered. Increase of transmittance indicates that gold coated layer also became thinner a little, but not so much as aluminum. This data indicates that all of 14 nm gold layer may sputter out after more than 70 months flight. Transmittance of bare Upilex decreased according as the time during exposure to space. This is same as the laboratory irradiation experiments of oxygen ion beam and UV light.[2] These facts indicate that atomic oxygen sputtered out some of aluminum and gold layer (mass loss), and

that atomic oxygen and UV light cut the polymer chain. Moreover, it was found that the surface of retrieved Upilex was etched by the optical microscopic observation (Fig.3). The surface of retrieved gold was aggregated by the sun or cosmic radiation in the space (Fig.4).

The thruster gas dissociates to N_2, H_2, NH_3, etc. by the catalysis after exhaust as follows; Fig.6 shows mass analyzed data of surface gas environment of SFU after exhaust of thruster. The spectra of N, O, NH, OH, and H_2O were appear in the mass analyzed data. If spectral resolution of SPC is kept in mind, observed spectra 633.8 nm coincides with 1st positive band of N_2, and 391.9 nm coincides with 1st positive band of N_2 and N_2^+. 454.7 nm coincides with N_2^+, and 561.6 nm coincides with with spectra of N and N^+. The intensity of 633.8 nm is usually strong, and 561.6 nm is fairly strong, but 391.9 nm is weak. These spectra are coincident with the mass analyzed data. These spectra came from the shock heated plasmas at the surface of SFU, because its speed will be enough to dissociate and ionize the ejected gas.

CONCLUSION

SPC was able to detect the defects of space use materials by the real time observation of optical transmittance. It is concluded that the surface of Upilex was oxidized and polymer chain was broken by the space plasmas and the solar UV light, and that aluminum and gold were suffered mass loss by the space plasmas. The surface of satellite was not clean but contamination such as SiOx had come from the silicon adhesive used for the SFU frame and instruments. Strong spectra such as N_2 and N_2^+ were observed associated with the exhaust of thruster. Another luminous spectra were quite weak and were under the detectable limit of SPC.

ACKNOWLEDGEMENT

This work was supported under the ISAS and USEF for co-work. We thank Mr. H. Koyama and Mr. T. Takenouchi of JASCO Corporation and Mr. K. Kokubo, Mr. H. Kaneko, Mr. M. Abe, and Mr. H. Sawachi of Meisei Electric Company for construction and maintenance of SPC.

REFERENCES

1.(a) M. R.Torr and D. G. Torr, J. Geophys. Res. **90**, 1683 (1985);

(b) J. S. Pickett, G. B. Murphy, W. S. Kurth, and S. D.Showhan, J. Geophys. Res. **90**, 3487 (1985);

(c)M. R. Torr, Geophys. Res. Lett. **10**, 114 (1983);

2. T. Yokota, S. Sasaki, N. Kawashima, M. Ota, and M. Usui, Applied Spectroscopy, **48**, 121 (1994).

3. T. Yokota, S. Sasaki, M. Ota, H. Yoshida, and N. Kawashima, Applied Spectroscopy, **49**, 1463 (1995)

4. T. Yokota, S. Sasaki, and M. Ota, 21st ISTS, Omiya, Japan, p.1832, 1998

5. M. Takei, Y. Torii, K. Fusegi, M. Miyata, and M. Ichikawa, 47th International Astronautical Congress, Beijin, China, 1996

Proceedings of 7th Japan International SAMPE
Symposium & Exhibition, Nov. 13-16, 2001

Development of HOPE-X All-Composite Prototype Structure

Mayuki Niitsu #1 Tooru Kamita#2 Kiyoshi Uzawa#3

#1 : Mitsubishi Heavy Industries, Ltd.
10, Oye-cho, Minato-ku, Nagoya 455-8515, JAPAN
E-mail : mayuki_niitsu@mx.nasw.mhi.co.jp

#2 : National Space Development Agency of Japan (NASDA)
7-44-1, Jindaiji Higashi-machi, Chofu-shi, Tokyo 182-8522, JAPAN
E-mail : kamita.tooru@nasda.go.jp

#3 : GH Craft, Ltd.
11-6 Itazuma, Gotenba, 412-0048, JAPAN
E-mail : K-uzawa@Ghcraft.com

Abstract

HOPE-X (H-IIA Orbiting Plane Experimental) is a Japanese experimental reentry vehicle which has been developed by National Aerospace Laboratory (NAL) and National Aerospace Development Agency (NASDA).

Recently, the program has experienced thorough design change to achieve low-cost, lightweight and short schedule. The structure design concept was totally revised to meet these demands and the design solution is all-composite (CFRP) monocoque structure, instead of conventional aluminum semi-monocoque structure. To demonstrate feasibility of the design and manufacturing process, full-scale structural model was built as a prototype.

This paper presents outline of the prototype structure development, structure design feature, and related element tests.

Key Words : reentry vehicle, all-composite, honeycomb sandwich panel, non-autoclave curing technology

Introduction

HOPE-X is a Japanese experimental reentry vehicle which has been developed by NAL and NASDA. It's about 13m in length, 10m in width . Fig.1 shows the outlook of HOPE-X. Recently, the structural concept was total revised to achieve low-cost, lightweight and short-schedule. Design solution to these demands is all-composite monocoque structure using non-autoclave curing technology.

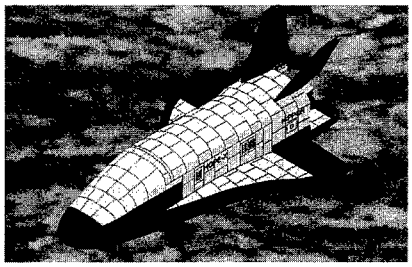

Fig.1 Outlook of HOPE-X

To demonstrate feasibility of the design and manufacturing process, it was decided to build full-scale structural testing model as a

prototype. There are following 3 objectives in this prototype development :

(1) To acquire capability of designing and manufacturing lightweight, all-composite structure with low cost.
(2) To establish innovative development frame work cooperating with a venture company.
(3) To conduct static load test and to validate analytical prediction as well as design and manufacturing themselves.

Preliminary design started in April, 2000 and vehicle assembly will be competed by the middle of August, 2001. It is only 17 months from start to finish, which is quite drastic schedule compression as a project of this scale.

In this prototype model development, new attempt to cooperate with a venture company is tried. A company with much experience in designing and manufacturing composite structure is involved along with NAL/NASDA/MHI. In order to effectively proceed with this project, design Built Team (DBT) consisting of selected engineers from each organization or company is organized.

Design Concept and Material

Composite Primary Structure

The primary structure is mostly made of honeycomb sandwich panel (OX aluminum core and CFRP face sheets). Structural concept is shown in Fig. 2. Whole structure is comprised of only 2 large parts, i.e. upper-fuselage and lower winged-body. The number of reinforcements such as ring frames and longerons is minimized to reduce manufacturing costs.

Most parts are jointed via adhesive bonding to reduce the number of fasteners and hence assembly cost. The exception is a wing upper skin where fastener joint is used to allow access to the internal equipments. All control surfaces, nose cap and leading edge are out-of-scope of this prototype development because they will be made of another material with higher heat resistant capability.

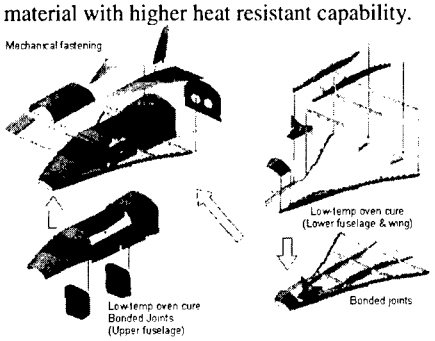

Fig.2 Structural Concept

Material Selection

To select composite material for HOPE-X primary structure, following requirements are considered :

(1) Pre-cured at 100deg-C or lower.
(2) Cured only with vacuum pressure
(3) Post-cured in free-standing state
(4) Tg higher than 190 deg-C
(5) Prepreg outlife longer than 30 days
(6) Wide process window

The first 3 requirements are indispensable for low-cost manufacturing of future launch vehicles. With these requirements satisfied, curing without autoclave is possible and large composite parts which won't fit in a autoclave can be manufactured. This leads to reduction in the number of parts and reduction in assembly cost. Low temperature pre-cure and freestanding post-cure are important as well to eliminate expensive tooling.

As there were no off the-shelf materials to meet these requirements, graphite/epoxy composite material was newly developed. The new material, TR30/#850 produced by Mitsubishi Rayon, can be pre-cured around 100 deg-C with vacuum pressure and maintain service temperature of 160 deg-C after post-cure around 180 deg-C. Preliminary results regarding unidirectional mechanical properties are shown in Fig.3.

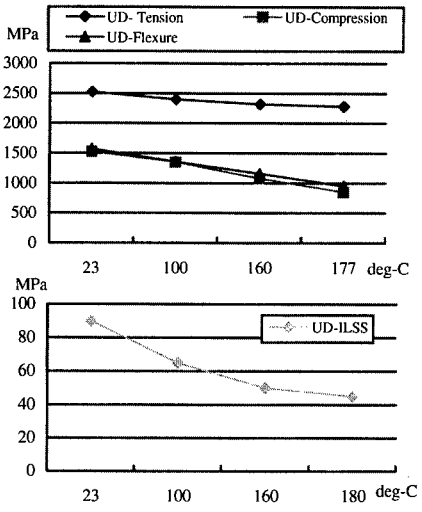

Fig.3 Basic Mechanical Properties

Process Window

Wide process window is quite important for low-cost manufacturing in that rigorous control of cure condition is unnecessary. In the early stage of material development, coupon tests were conducted to evaluate impact of cure condition on the quality of laminates.

Effect of cure pressure was of primary concern because it's usually difficult to apply ideal vacuum pressure during fabrication of large parts. Test specimens were prepared with different cure pressure, i.e. 100kPa and 90kPa and cross section of the laminates was inspected There was no quality reduction observed.

Effect of cure temperature was also evaluated. It was confirmed that variation of pre-cure temperature has little impact to the quality of laminates as long as post-cure is conducted in proper condition. Based on these evaluations, process specification is prepared which allows variation of cure condition as much as possible.

Initial Design Results

Structure design was conducted considering primary load conditions and stiffness requirements. All the primary load conditions are aerodynamic pressure during ascent phase when dynamic pressure is much severe than the other flight phases. Most of stiffness requirements are determined to prevent aeroelastic and aerodynamic problems.

As a result of initial design, it was found out that stiffness is a primary design driver. Sensitivity analysis was conducted to determine effective distribution of skin thickness and layout of structural parts. The design results are shown in Fig.4 and Fig.5. Although CFRP lay-up is mostly quasi-isotropic, structural weight is expected to be reduced by more than 20% compared to equivalent aluminum structure.

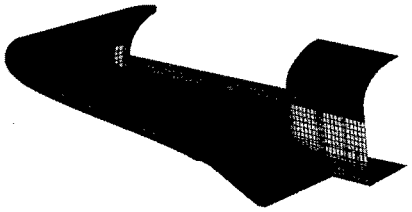

Face Sheet Thickness (One side of sandwich panel)

-Gray area	: 0.8mm
-Yellow area	: 2.4mm
-Dark green area	: 3.2mm
-Light blue area	: 4.0mm

Fig. 4 Skin Thickness

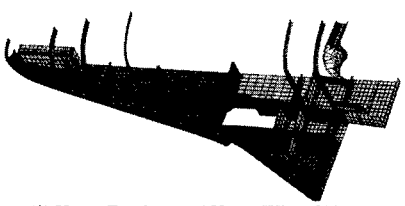

(*) Upper Fuselage and Upper Wing Skin are not shown.

Fig. 5 Layout of Structural Parts

Related Structural Tests

Element Tests

Various element tests have been conducted to acquire basic strength and stiffness data. Fig.6 shows peel test for bonded T-joints. As bonded joint of this type is extensively used for assembly, its strength capability, especially peel strength, is one of the key factors to determine feasibility of the design. Test results shows excellent peel strength higher than 100N/mm.

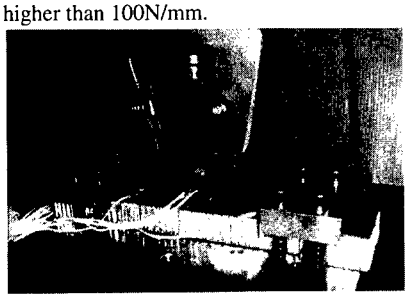

Fig. 6 T-Joint Peel Test

Component Tests

In addition to element tests, component tests are conducted to confirm structural integrity of critical area. Total 7 area were selected. 2 of them are structure with significant compression load and the rest of them are bonded joints. Fig.7 shows the compression test result of a longeron, which is located at mid fuselage and takes compression load due to fuselage bending. There was no unexpected failure mode(such as blooming) at unacceptably low load.

Fig.7 Longeron Compression Test

Recent Status

Manufacturing of upper fuselage and lower winged-body have been complete already as shown in Fig.8 and Fig.9. These two assemblies were just coupled. Post-cure will be conducted early August in this coupled configuration. Static load test is currently scheduled in October, 2001.

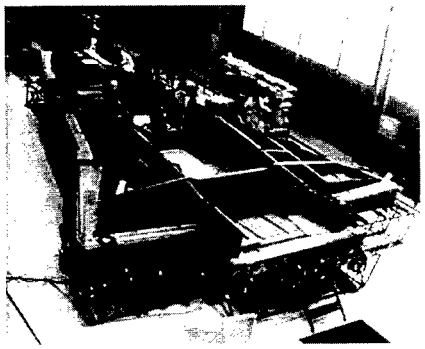

Fig. 8 Lower Winged-body Assembly

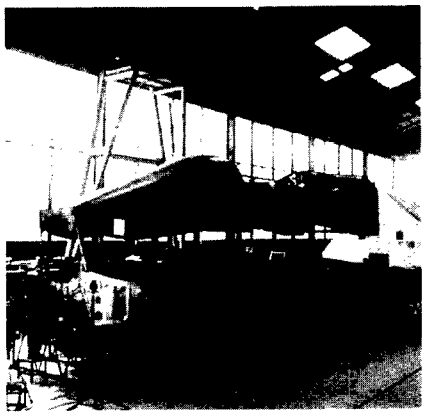

Fig. 9 Upper Fuselage prior to Coupling

Acknowledgement

Authors would like to thank design built team (DBT) for this program composed of the engineers from NASDA, NAL, MHI and GH craft.

Proceedings of 7th Japan International SAMPE
Symposium & Exhibition, Nov. 13-16, 2001

Structural Testing of a Full-Scale Composite Structure for an Aerospace Vehicle

Hideaki Murayama#, Toru Kamita# and Hirotake Igawa#

#: HOPE Joint Team Office (NAL/NASDA)
7-44-1 Jindaiji Higashi-machi, Chofu, Tokyo 182-8522, JAPAN
E-mail: murayama.hideaki@nasda.go.jp, kamita.toru@nasda.go.jp,
hirotake.igawa@nasda.go.jp

Abstract

National Aerospace Laboratory (NAL) and National Aerospace Development Agency of Japan (NASDA) have developed an experimental reentry vehicle, HOPE-X, for several years. Presently, the full-Scale structural model of HOPE-X is making of carbon fiber reinforced plastic (CFRP) as a prototype and the low temperature curing type of resin is used to fabricate with oven-curing technology.

This prototype model has been used to verify experimentally reliability of the structure that was made of CFRP with newly low cost manufacturing technology. Therefore, we implemented structural monitoring in the manufacturing process with health monitoring technique and will measure deformation of the structure in some structural tests that are scheduled for October 2001.

In this paper, structural monitoring with fiber-optic strain/temperature sensors conducted during post-cure of manufacturing process is described. We will also present results of the structural tests in our presentation of the conference.

Key Words: CFRP, cure, fiber-optic sensor, monitoring

Introduction

HOPE-X, which is shown in Fig.1, is an experimental reentry vehicle developed by NAL and NASDA for several years. It is about 13m long, 9m width and planned to be launched by H-IIA [1]. In the beginning of the project, we were planning to make it as a conventional aluminum semi-monocoque structure. But it generally requires the initial cost because of a huge number of structural parts and tooling. Therefore, the aluminum structure was changed into all-composite structure. It was expected that this drastic change would be useful to reduce not only the cost but also the weight of the vehicle.

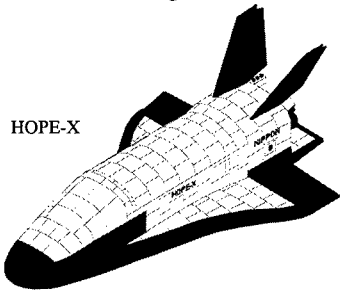

Fig.1 Outlook of HOPE-X

Presently, the full-Scale model of HOPE-X is making of CFRP and the low temperature curing type of resin is used to fabricate with

oven-curing technology instead of a large and expensive autoclave.

In the manufacturing process, high temperature post-cure in free-standing state was performed after low temperature pre-cure and assembling with bond in order to give the CFRP structure heat-resistance. However, if temperature distribution of the structure isn't uniform during post-cure, the process could lead to unexpected damage or deformation. Then the unwilling deformation might degrade the strength.

Therefore, we implemented post-cure monitoring by using fiber-optic strain and temperature sensors and health monitoring technique. In this paper, we present on the results of the post-cure monitoring with fiber-optic sensors after we describe about the design and the manufacturing of HOPE-X made of CFRP. These sensors will be also used for structural tests in October 2001. So the results of structural tests may be presented at the conference.

Design and Manufacturing of HOPE-X

Most components of HOPE-X are made of advanced composite materials (ACM) such as CFRP, either with single skinned or sandwich structures. The primary structure is comprised of two large parts, i.e. upper-fuselage and lower winged-body, and a number of reinforcement such as ring frames and longerons. They are mostly jointed by adhesive bonding. Fig.2 shows the structural concept schematically and this concept leads to a reduction of assembly cost.

Composite material for HOPE-X is TR30/#850 which is newly developed by Mitsubishi Rayon. This graphite/epoxy composite material can be cured at 100℃ with vacuum pressure. This means that we don't need an expensive autoclave and aren't restricted by the autoclave size.

A reentry vehicle such as HOPE-X is required to have heat-resistance close to AL-alloy. TR30/#850 is able to stand service temperature of 160 ℃ after post-cure at 180℃. So we planned to post-cure at 180℃ in free-standing state to give the structure heat resistance after pre-curing the structural components at 100℃ with vacuum pressure and assembling them by bonding joints.

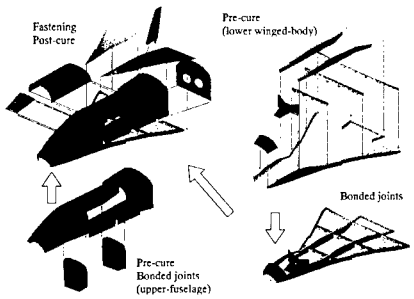

Fig.2 Structural Concept of HOPE-X

Post-Cure Monitoring

In the post-cure process, unexpected damage or deformation might occur due to uneven temperature distribution in the structure. So we attempted to monitor the strain and temperature distribution during post-curing. For post-cure monitoring, sensing system was significant and it was required to measure strain and temperature distribution accurately and easily in the factory. We selected two types of fiber-optic sensors for the monitoring, because they had advantage of distributed sensing in a field test. We describe these advantages on fiber-optic sensors below, and then we reported the sensing system and the results of the post-cure monitoring.

Fiber-Optic Sensors

Recently, fiber-optic sensors have been developed actively, and one can measure nearly all of the physical measurands of interest by them. Since they also have excellent characteristics such as high sensitivity, freedom from electromagnetic interference, good mechanical characteristics and distributed configuration, they have been applied to "smart structures" or "health

monitoring"

Capability of quasi or fully distributed sensing is especially significant advantage compared to conventional sensors. Quasi distributed sensing system makes measurements at a number of spatially selected points, usually with the purpose of detecting a parameter field of interest such as strain or temperature. On the other hand, fully distributed sensing system allows information about a parameter field to be obtained at any arbitrary point along the sensor length.

Brillouin optical time domain reflectometry (BOTDR) developed by NTT is a fully distributed sensor and can measure strain and temperature along the length of a fiber [2]. It was applied to the monitoring of the concrete setting temperature in a major dam at the Swiss Alps and the structural health monitoring of a Japanese racing yacht for America's Cup [3,4].

Fiber Optic Temperature Laser Rader (FTR) developed by HITACH is also a fully distributed sensor and can measure temperature. It has been used for fire alarm systems of coal-mine shafts, tunnel and etc.

In order to measure strain and temperature distribution, we used both BOTDR and FTR that were already commercialized.

Sensing System

The sensing system comprised BOTDR, FTR and sensing fibers. The specifications of BOTDR and FTR are shown in Table 1. The sensing fibers were also required to stand curing temperature, 180℃, as well as the CFRP structure. Therefore, coating material was more important than core and clad materials that had sufficient heat-resistance. A conventional optical fiber coated with ultraviolet curable resin as the sensing fiber of BOTDR (outside diameter = 0.25mm) was used. On the other hand, Teflon coating fiber (outside diameter = 0.90mm) was used for FTR. Although the ultraviolet curable resin coating changed in quality at 180℃, the sensing performance of BOTDR didn't change in the feasibility study.

These sensing fibers were installed in the outside of the CFRP structure after assembling the structural components that had been pre-cured. Fig.3 shows the sensing fiber on the upper-fuselage of HOPE-X. They were arranged in longitudinal direction and near the opening of the upper-fuselage because we were interested in global longitudinal deformation and considered adverse effect of the free boundary along the opening. Both sensing fiber for BOTDR and FTR were 54.8m in length.

In order to measure strain distribution of the structure with temperature variation by BOTDR, it is necessary to compensate for temperature effect. Since we were monitoring the temperature distribution by FTR, it was easy and adequate method to use FTR temperature data for temperature compensation of BOTDR strain data. Compensated strain distribution is given by

$$\varepsilon(z) = \Delta\varepsilon_{BOTDR}(z) - \Delta T_{FTR}(z) \times 20\ (\mu\varepsilon) \qquad (1)$$

where $\varepsilon(z)$ is compensated strain value at a point along the sensing fiber, $\Delta\varepsilon_{BOTDR}(z)$ is difference between initial strain measured by BOTDR before post-cure and strain measured during post-curing. $\Delta T_{FTR}(z)$ is difference between initial temperature measured by FTR and temperature measured during post-cure. Since the readout resolutions of BOTDR and FTR are 0.1m and 1m respectively, we could only compensate measured strain by 1m. But even if temperature in the structure was considered not to change for 1m, a measurement error didn't always increase because measured temperature was already average value regulated by the spatial resolution. The coefficient of $\Delta T_{FTR}(z)$, $20\mu\varepsilon$, is used to convert into strain.

Table 1 Example of Table

	BOTDR	FTR
Strain accuracy	±30με	NA
Temperature accuracy	±1℃	±1℃
Spatial resolution	1m	3m
Readout resolution	0.1m	1m

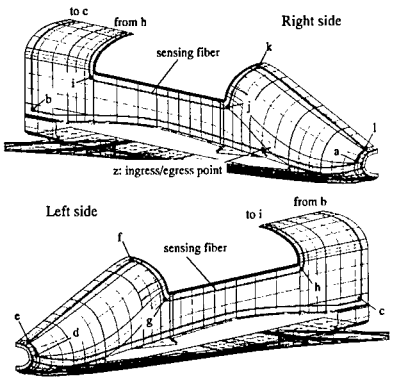

Fig.3 Sensing fibers on HOPE-X

Results

Before post-cure, we measured strain and temperature as initial value by BOTDR and FTR. Then measurements were implemented at appropriate intervals. Fig.4 shows temperature distributions measured by FTR. The letters in Fig.4, from a to l, and z, correspond the position marked with the letters along the sensing fiber in Fig.3. Temperature changed from 30℃ to 170℃ during post-cure. When strain distribution was measured by BOTDR after post-cure, temperature was about 40℃. Temperature distributions are almost uniform in the structure, so we can say that temperature in the oven was controlled adequately.

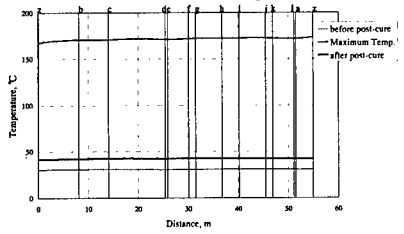

Fig.4 Result of FTR

Strain in the structure gradually increased by about 400με as shown in Fig.5. After post-cure, the CFRP structure contracted overall and strain was about –400με. Strain values near the ingress/egress point, z, were remarkable because it was boundary between the sensing fiber and the lead fiber. However, it seems that there wasn't extraordinary strain during and after post-cure. Therefore, it wasn't supposed that the post-cure process led to unexpected damage or deformation.

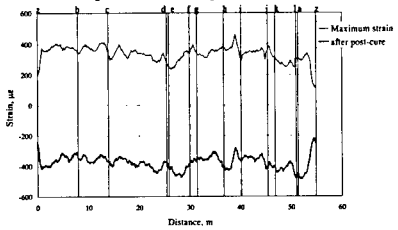

Fig.5 Result of BOTDR

Conclusions

By using fiber-optic sensors, we could successfully monitor strain and temperature distribution of HOPE-X made of CFRP during post-cure, and we assured the structural quality from the results. We can also access residual stress after curing process and will make use of the results in the structural tests scheduled in October 2001.

Acknowledgment

The authors thank Prof. K. Kageyama of Tokyo University, K. Nishiwaki of Mitsubishi Heavy Industries, Ltd. and K. Uzawa of GH craft, Ltd for their kind support.

References

1. T. Yamamoto, S. Asada, K. Nishiwaki, M. Niitsu, T. Kamita and G. Kimura: AIAA paper, 2001-1780 (2001)
2. T. Horiguchi, T. Kurashima and M. Tateda: IEEE Photon Tech. Lett., 1(5), 107 (1989)
3. L. Thévenaz, M. Niklès, A. Fellay, M. Facchini and P. Robert: Proc. of SPIE, 3330, 301 (1998)
4. H. Murayama, K. Kageyama, I. Kimpara, H. Naruse and A. Shimada: Proc. of SPIE, 3986, 324 (2000)

Proceedings of 7th Japan International SAMPE
Symposium & Exhibition, Nov. 13-16, 2001

Low Pressure Plasma Sprayed Yttrium-Silicates for Oxidation Protection of C/C-SiC Composite Structures

Thomas Ullmann[1], Martin Schmücker[2],
Hermann Hald[1], Rudolf Henne[3] and Hartmut Schneider[2]

DLR - German Aerospace Center
1: Institute of Structures and Design, Pfaffenwaldring 38-40, D-70569 Stuttgart
2: Institute of Materials Research, Porz-Wahnheide, Linder Höhe, D-51147 Cologne
3: Institute of Technical Thermodynamics, Pfaffenwaldring 38-40, D-70569 Stuttgart
GERMANY, E-mail: thomas.ullmann@dlr.de

Abstract

Due to oxidation sensitivity of carbon fibres above 400°C the use of C/C, C/SiC or C/C-SiC[1] for thermal protection systems (TPS) of reusable aerospace vehicles is limited under atmospheric reentry conditions. Therefore oxidation protection coatings are inevitable in terms of reusability and reliability of structures based on C-fibres. An effective two-layer coating system on C/C-SiC has been developed in order to improve both oxidation protection and erosion resistance. While the base layer consists of CVD-SiC, the outer erosion protection layer is composed of low pressure plasma sprayed yttrium-silicate. The coating system was qualified on C/C-SiC specimens by several test campaigns in a plasma wind tunnel at temperatures up to 1650°C. The thermal shock resistance was confirmed by tests within a solar furnace with the result of a very good adhesion to the bonding layer. Now it will be applied to larger structural components of C/C-SiC.

Key Words: yttrium-silicates, oxidation protection, coating, plasma spraying

[1] C/C-SiC – A special type of C/SiC composite developed and manufactured by DLR.

Introduction

The first effort in using reinforced ceramic composites for advanced heat shield components was conducted in the 1970's on structures to be used on the shuttle orbiter vehicles [1]. Here the nose cap and the leading edge of the wings are designed with C/C which is protected by an outer layer of silicon carbide against oxidation. Present TPS concepts are mostly based on C/SiC or C/C-SiC [2,3]. Though C/C-SiC shows relatively high erosion resistance compared to C/C, it is necessary to protect the carbon fibres from oxidation in terms of durability of the structural components. So far numerous efforts to develop more effective coating systems were made using different coating techniques and multilayer systems [4,5]. In order to be successful, it is very important that the coating technique itself supports both applicability and maintenance on larger structural components as well as repairability of possibly damaged surface areas after the vehicle's flight.

Oxidation Protection

As depicted in Fig. 2, there are a few critical factors which have to be considered when selecting materials for external oxidation protection coating systems. Mechanical

compatibility is the most important issue concerning adhesion to the underlying substrate. The coefficient of linear thermal expansion (CTE) of the coating material has to be similar of that of the substrate to avoid higher stresses at the interface. Parallel to the carbon fabric the CTE of C/C-SiC does not exceed $1.5 \cdot 10^{-6}$ K^{-1} (RT-1700°C). Thus the thermal expansion of the coating materials has to be quite low. As shown in Fig. 1, the bonding layer which stays in direct contact to the carbon fibres/matrix has to prevent any carbon diffusion to the outer coating system in order to avoid carbothermic reduction of oxidation resistant layers that are based on oxide or silicate materials. On the other hand, for effective oxidation protection, the top layer must provide a barrier to inward diffusion of oxygen. Furthermore one must consider that under reentry conditions the material is exposed to hypersonic gas streams in a low pressure and high temperature environment which demands low volatility for the surface material of the multilayer coating to attain adequate erosion resistance.

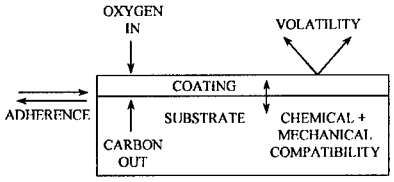

Fig.1 Criterias for oxidation protection layers on C/C-SiC

As already suggested, there is no single material which fulfils all issues mentioned above. Thus multilayer coating systems seems to be the best solution. In this study the low pressure plasma spraying (LPPS) of yttrium-silicates was performed on SiC-precoated C/C-SiC substrates. The SiC 'bonding layer' is an efficient carbon diffusion barrier and was applied by chemical vapour deposition (CVD) performed by an industrial supplier. There are two different compounds that are known in the system Y_2O_3-SiO_2 [6]. Both silicates show a rather high melting/decomposition temperature (Y_2SiO_5: 1980 °C; $Y_2Si_2O_7$: 1775 °C) and a very low CTE (e.g. Y_2SiO_5: $4.8 \cdot 10^{-6}$ K^{-1} / RT-1430 °C) and – compared to other ceramic materials – quite low oxygen permeability as well as low volatility at temperatures near the melting point [7].

Low Pressure Plasma Spraying

The development of spray parameters was performed with a DC low pressure plasma spray installation operated by DLR in Stuttgart. Here a computer-controlled robot system for precise guidance of the plasma torch inside the pressure chamber allows coating deposition at less than 100 hPa on substrates of up to 1 m^2 in size. The plasma jet leaves the torch by passing a Mach 3 Laval-nozzle with spray particle velocities exceeding 800 m/s [8]. The coating thickness of the yttrium-silicate layers varies between 100 and 200 µm and the temperature during deposition was measured by thermocouples 1.5 mm underneath the substrate's surface to be between 950 °C and 1200 °C. In this study two yttrium-silicate powders of different chemical composition were sprayed, as listed in Table 1.

Table 1 Plasma spray powders

	Powder 1	Powder 2
Composition Y_2O_3:SiO_2	50:50 wt.-%	75:25 wt.-%
Particle size	8-25 µm	5-30 µm
Phase content	$Y_2Si_2O_7$ + SiO_2	Y_2SiO_5 + $Y_2Si_2O_7$

Fig. 2 shows a cross section of the two layer coating system – LPPS-yttrium-silicate (top) and CVD-SiC (bottom). This coating was obtained from powder 1 (Table 1). The silicate layer (thickness: 130 µm) is interspersed by angular – sometimes even spherical shaped – particles of amorphous silica. These SiO_2 particles are residuals from the spray powder particles that did not

melt inside the plasma jet within the short traverse time of approximately 10^{-3} s.

Fig.2 Cross section of plasma a sprayed yttrium-silicate coating (SEM)

Thus they are projected to the substrate by the plasma jet and embedded by solidified droplets of yttrium-silicate during the coating build-up. Due to the high kinetic energy of the spray particles, the dense silicate material does not show the typical porous 'pancake-structure' usually known from plasma sprayed coatings. As a result, coatings with less than 4 % porosity are deposited. Due to a certain mismatch of the CTE between coating and substrate, microcracks – induced by tensile stresses – have been observed in the plasma sprayed layer. The mean width of these cracks is about 2-3 µm. It is confirmed by thermogravimetric measurements, that these microcracks are closed at temperatures above 1000 °C because of the larger thermal expansion of the coating material.

Qualification Tests

The specimens were tested with respect to the thermal shock resistance as well as to the oxidation protection efficiency of the coating system under simulated reentry conditions. For thermal shock conditions a solar furnace was used which is operated by DLR in Cologne. Reentry simulation was performed within the plasma wind tunnel test facility (PWK) at the Institute of Space Systems (IRS, University Stuttgart).

Solar furnace tests

The samples were exposed to 5 cycles between room temperature and 1400 °C (test condition 1) and also between room temperature and 1600 °C (test condition 2). Fig. 4 shows the test condition 2 for cycling up to 1600 °C. The mean thermal gradient was about 20 K/s. Obviously the relative mass loss of coated material is rather low compared to that of uncoated C/C-SiC.

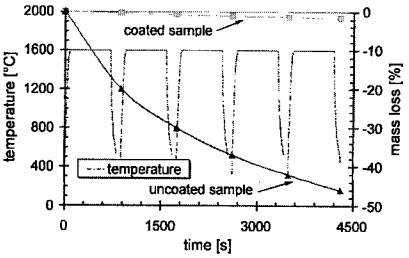

Fig.4 Relative mass loss of coated and uncoated C/C-SiC under thermal shock

After the tests at high temperatures there was no visible change on the surface of the specimen's coating, except the colour. Finally the samples were tested in the most critical temperature range between 700 °C and 1100 °C by rapid multiple thermal cycling. However, both types of coatings (Y_2SiO_5 /SiO_2 and $Y_2Si_2O_7$/Y_2SiO_5) show moderate relative mass loss rates of less than 1.7 %.

Arc jet testing

According to the well defined test parameters which were obtained by reentry simulations with SiC coated C/C-SiC [9], the total pressure was chosen to be 4.1 mbar. For the possibility of direct comparison of specimens with different coating systems, the first tests with the 2-layer LPPS/CVD coating system were performed at 1350 °C. Because no visible degradation was observed after 23 min at maximum temperature, it was decided to go on with tests at 1500 °C, 1600 °C and 1650 °C. The specific

mass loss rates of the specimens are depicted in Fig. 6. Some local hot-spots were observed on the plasma sprayed surface layer as the temperature exceeded 1650 °C. By the following SEM investigation, these spots have been identified as archings which obviously are the result of the generation of a gaseous phase (e.g. CO and/or SiO).

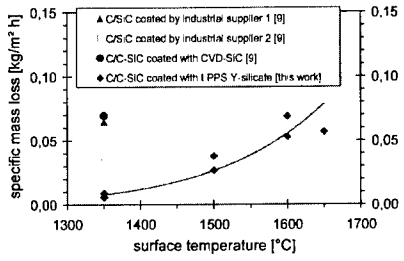

Fig.6 Specific mass loss rates of C/C-SiC with different coatings [9]

Examination by EDX and XRD has proven that the plasma sprayed silicates remain chemically stable even at temperatures up to 1650 °C.

Conclusions

The tests have proven that plasma sprayed yttrium-silicate layers show very low erosion effects under reentry conditions as well as high thermal shock resistance with good adherence to SiC coated C/C-SiC materials. The 2-layer system of a plasma sprayed top coating in combination with a thin CVD-SiC bonding layer performs adequate oxidation protection. Evaluation by SEM and creep tests up to 1250 °C indicate that plasma sprayed yttrium-silicate forms a dense glass-like top layer of high viscosity when approaching the melting point at approximately 1700 °C. After successful qualification of specimens protected by the new coating system, the current work now continues with upscaling the LPPS technique for applications on larger structural C/C-SiC components of a TPS system. Some initial practical experiences in terms of off-angle plasma spraying with a more complex shaped structure were achieved by coating a complete C/C-SiC panel of approximately 40 x 41 cm as it is shown by its rear side in Fig. 7.

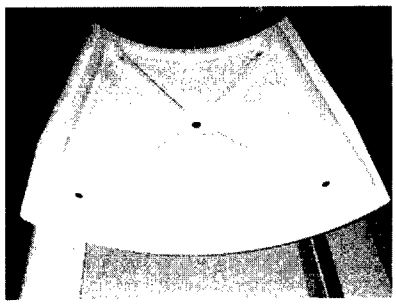

Fig.7 Rear side of a C/C-SiC panel with a plasma sprayed coating of yttrium-silicate

References

[1] D.M. Curry: Proc. of 1st ESA Workshop on Thermal Protection Systems, 122 (1993), ESA-WPP-053.

[2] H. Hald: J. High Temp. Chem. Processes, 3, 153 (1994).

[3] H. Hald: Proc. of 1st AAAF-Int. Symp. on Atmospheric Reentry Vehicles and Systems, on CD (1999).

[4] J.R. Strife and J.E. Sheehan: Am. Cer. Soc. Bull., 369 (1988).

[5] M.E. Westwood, J.D. Webster, R.J. Day, F.H. Hayes and R. Taylor: J. Mat. Sci., 31, 1389 (1996).

[6] S. Kumar and C.H. Drummond: J. Mat. Res., 7(4), 997 (1992).

[7] K. Ogura, M. Kondo and T. Morimoto: Proc. of 10th Int. Conf. Composite Mat., ICCM-10, IV, 767 (1995).

[8] R. Henne: J. Welding and Cutting, 2, E31 (1993).

[9] T. Ullmann et al.: Proc. of 3rd ESA Workshop on Thermal Protection Systems, 291 (1998), ESA-WPP-141.

Proceedings of 7th Japan International SAMPE
Symposium & Exhibition, Nov. 13-16, 2001

Erosion Phenomena of High Purity CVD-SiC under High Temperatures

T. Yoshinaka, and Y. Morino
National Space Development Agency of Japan 2-1-1 Sengen, Tsukuba, Ibaraki 305, Japan
E-Mail: Yoshinaka.Toshinari@nasda.go.jp

Abstract

To develop high performance thermal protection technologies for atmospheric re-entry vehicles, we conducted research on the erosion mechanism of Carbon/Carbon (C/C) materials with Chemical Vapor Deposited (CVD)-SiC thermal protection coatings. We evaluated the oxidation and erosion phenomena and believe that the quality of CVD-SiC thermal protection coatings is one of most the important factors.

We prepared high-purity CVD-SiC samples for this research and conducted static heating tests to compare the oxidation phenomena with those of C/C materials.[1],[2] The results show that the phenomena should be reviewed and the samples investigated once again. This paper describes the newest outcomes.

1. Introduction

High performance thermal protection systems (TPS) are essential for space transportation systems to withstand the severe conditions during the atmospheric re-entry phase. To establish the basic technologies for TPS, we conducted research on the erosion characteristics of C/C materials with CVD-SiC thermal protection coatings.[3],[4] The C/C materials are composed of the C/C substrate, the conversion SiC layer and the CVD-SiC layer. The C/C substrate provides lightweight, high temperature strength, and the CVD-SiC layer provides oxidation resistance. The conversion SiC layer, which is chemically converted from the C/C substrate, attaches the CVD-SiC layer to the C/C substrate. For some cases, a glass seal is applied to prevent oxygen from penetrating through cracks formed during production. The oxidation and erosion phenomena of the applied CVD-SiC must be then examined under the atmospheric re-entry environments to evaluate the thermal protection characteristics of the C/C materials.

SiC exhibits two types of oxidation behavior, passive and active oxidation, depending on the surrounding pressure and temperature combinations. Passive oxidation, as expressed by equation (1), is observed under high-pressures/low-temperature combinations. A protective SiO2 film prevents further oxidation and no mass loss is observed.

$$SiC + 3/2\ O2 \rightarrow SiO2\ (s) + CO\ (g) \uparrow \quad (1)$$

Active oxidation, as shown in equation (2), occurs under low-pressures/high-temperature conditions. No protective films are expected, and SiC erosion is observed because of significant SiO vapor formation.

$$SiC + O2 \rightarrow SiO\ (g) \uparrow + CO\ (g) \uparrow \quad (2)$$

The active-to-passive oxidation transitions are different for the types of crystals, impurities and production methods.[5] Therefore, it is important to investigate the transitions of the proposed CVD-SiC to evaluate the erosion characteristics the C/C materials.

Research on C/C materials had been conducted through the cooperation with the National Aerospace Laboratory (NAL)[3] and Institut fur Raumfahrtsysteme Universitat Stuttgart (IRS).[4]

Static heating and plasma wind tunnel tests were performed to evaluate the erosion characteristics of the four kinds of materials shown in Table 1. One of the important outcomes is that the quality of SiC is important for evaluating the erosion phenomena.

Table 1 Materials evaluated in the cooperative research

C/C materials	SiO2/B2O3 glass seal	Type A
	No glass seal	Type B
SiC substrate	Sintered SiC	Type C
	CVD-SiC	Type D

High-purity CVD-SiC (Type E) was selected to investigate the oxidation phenomena due to the quality of SiC. We performed static heating tests to determine the active-to-passive oxidation transitions.[1],[2] The transitions were different,[2] and further investigations are necessary. This paper describes the newly acquired results from the samples investigated.

2. Samples

The remarkable feature of the Type E sample is high purity.[1),(2)] The degree of the impurities is on the order of parts per billion (ppb), and the influence of the impurities on the oxidation behavior can be considered minimum.

3. Experiments

We performed static heating tests using the Ultra-high Temperature Oxidation Sublimation Machine,[1),(2)] shown schematically in Fig. 1, at Japan Ultra-high Temperature Research Center (JUTEM). The apparatus consists of a Xe lamp, ellipsoidal mirror, douser, low-pressure chamber, sample support, pyrometer, evacuation system, and gas feeder.

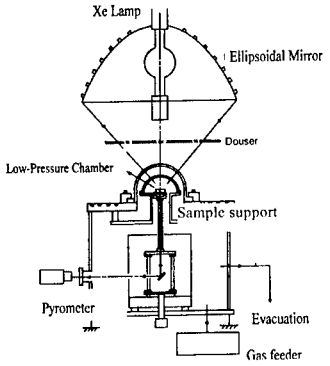

Figure 1 Schematic diagram of Ultra-high Temperature Oxidation and Sublimation Machine

The schematic diagram of the experimental system[2)] is shown in Fig. 2. The sample was placed on the attachment, installed in a low-pressure chamber, mounted on the sample support, and heated by a Xenon lamp and ellipsoidal mirror. Since ultraviolet light contained in the Xenon ray may accelerate the SiC erosion, we placed protective materials (CVD-SiC and Sintered SiC) on the upper surface of the sample.

The support pins were placed between the attachments and the dummy to prevent their contact. The sample temperatures were measured primarily by the thermo-couple and by the pyrometer for backup.

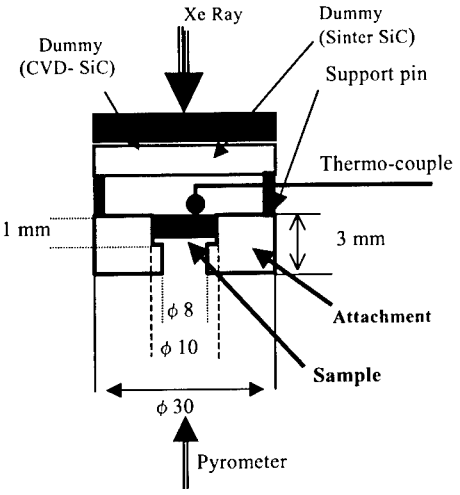

Figure 2 Schematic of the experimental system

4. Results

We investigated the samples based on outer appearance and the surface Scanning Electron Microscope (SEM) observations. We observed damage of CVD-SiC crystals and generation of glassy materials. Typical examples are shown in Fig. 3 with one unheated sample.

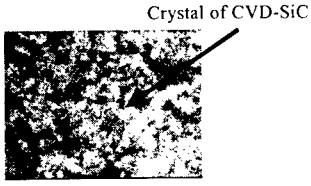

(a) Unheated
Damaged CVD-SiC crystal

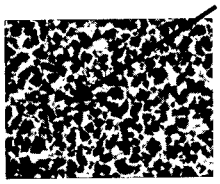

(b) 1560℃-100Pa

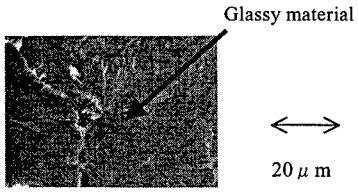

(c) 1560℃-2000Pa

Figure 3 SEM observations

In addition, we observed generation of glassy material and slight damage of CVD-SiC crystals for some samples. A typical example is shown in Fig. 4. SiC was identified by Electron Spectroscopy for Chemical Analysis (ESCA).

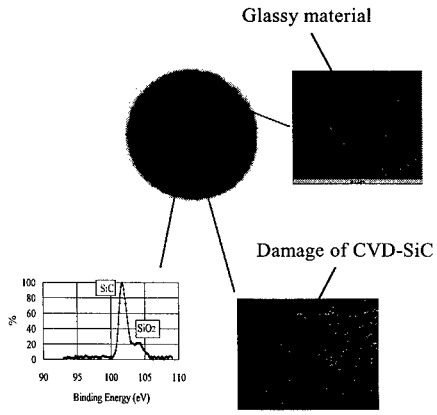

Figure 4 Investigation of the 1500℃-30Pa case

5. Discussion

5.1 Erosion rates

The erosion rate K (kg/m^2-H) of CVD-SiC under static heating N2/O2 environments is schematically shown in Fig.5.[6] In the active oxidation region, K increases with the oxygen partial pressure to a maximum value at the active-to-passive oxidation transition ($PO2^t$). When the oxygen partial pressure increases above $PO2^t$, K decreases discontinuously. Similar phenomena were observed in the previous research. [2],[4],[6],[7]

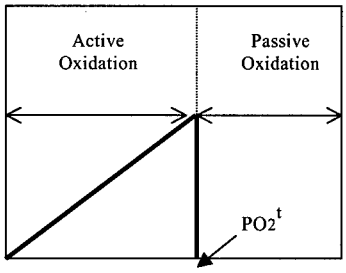

Figure 5 Typical erosion behavior of CVD-SiC

The acquired erosion rates [2] are shown in Fig. 6. Plus (minus) means a mass decrease (gain). The maximum erosion rates were observed at 50Pa/1560℃, and at 75Pa/1650℃. The erosion rate at 10Pa/1500 ℃ exceeds those of the same temperature.

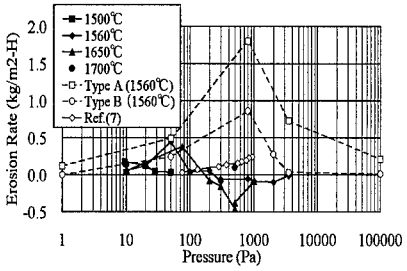

Figure 6 Acquired erosion rates

5.2 Oxidations

According to 5.1 above, the active-to-passive oxidation transition should be located at 1500℃/10Pa, 1560℃/50Pa, and 1650℃/75Pa.

However, we observed damage of CVD-SiC crystals at higher pressures as shown in Fig. 3(b).

In addition, we observed both glassy material generation and damage of CVD-SiC crystal as shown in Fig. 4.

Based on the previous evaluations,[1],[2] the generation of the glassy material means passive oxidation, and the damage of CVD-SiC crystal means active oxidation.

The results of the 1560℃/100Pa case mean the erosion rates decreased in spite of active oxidation

occurred. The results of the 1500℃/30Pa case mean both passive and active oxidation occurred. The further investigation on the mixing of passive and active oxidation is necessary.

5.3 Active to passive oxidation transition

Based on the above, we suggested a new active-to-passive transition of Type E as shown in Fig. 7 in comparison with those of previous research.[(1)~(7)] The transition of the Type E sample is located within previously reported results.[(2)]

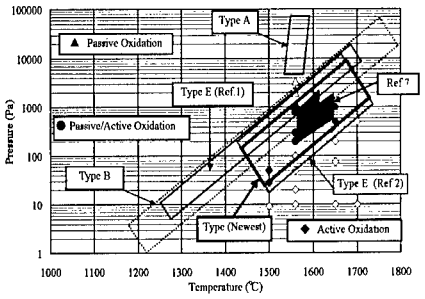

Figure 7 Comparison of the active to passive transitions

6. Concluding remarks

(1) We determine a new active-to-passive oxidation transition of high-purity CVD-SiC mainly by SEM observations.
(2) Further investigation on the mixing of passive and active oxidation is necessary.

7. Suggested future works

(1) The experimental methods should be improved to investigate the mixing of both oxidations.
(2) Plasma wind tunnel tests should be performed to investigate the oxidation phenomena of CVD-SiC under the plasma flow conditions.

8. Acknowldements

The authors would like to thank Prof. T .Goto (Tohoku University) and Prof. Monika Auweter-Kurtz (IRS) for their guidance and instructions in our research. In addition, the authors thank JUTEM personnel for the facility operation for our experiments and Advanced Engineering Services (AES) personel for SEM observation and ESCA analysis.

References

[1] T. Yoshinaka, M.Mizuno, and Y. Morino, "Oxidation Behavior of Pure Chemical Vapor Deposited SiC under Static Heating Conditions," 39 th AIAA Aerospace Sciences Meeting and Exhibit, Reno USA, AIAA 2001-0981, 8-11 January, 2001.

[2] T. Yoshinaka, Y. Morino, "Oxidation Phenomena of High Purity CVD-SiC under Atmospheric Re-entry Conditions," AIAA-NAL-NASDA-ISAS 10 th International Space Planes and Hypersonic Systems and Technology Conference, Kyoto Japan, AIAA 2001-1781, 24-27 April, 2001.

[3] Y. Morino, K. Yudate, and T. Yoshinaka, "Research on C/C Composite for the HOPE Re-entry Vehicle," 44 th International Astronautical Congress, Graz, Austria, IAF-93-I.3.223, Oct. 16-22, 1993

[4] T. Yoshinaka, Y.Morino, G. Hilfer, T. Wegmann, and M. Auweter-Kurtz, "The Oxidation behavior of C/C materials," 48 th International Astronautical Federation Congress, Melbourne, Australia, IAF-98-I.3.03, Sept28-Oct2, 1998.

[5] T. Narushima, T. Goto, Y. Iguchi, T. Hirai, and Y. Iguchi, "High Temperature Oxidation of Silicon Carbide and Silicon Nitride," Materials Transactions, JIM, Vol.38, No.10 (1997), pp.821-835.

[6] T. Goto, T. Narushima, Y. Iguchi, and T. Hirai, "Active to Passive Transition in the High-Temperature Oxidation of CVD SiC and SiN4," Corrosion of Advanced Ceramic 165-176

[7] T. Narushima, T. Goto, Y. Iguchi, and T. Hirai, "High-Temperature Active Oxidation of Chemically Vapor-deposited Carbide in an Ar-O2 Atmosphere," Journal of the American Ceramic Society Vol.74, No.10

Proceedings of 7th Japan International SAMPE
Symposium & Exhibition, Nov. 13-16, 2001

Development of C/C Ion Optics for Spacecraft Ion Engine

Ikkoh Funaki[##], Ken Goto[#], Hitoshi Kuninaka[#], Yukio Shimizu[#]
Kazutaka Nishiyama[#] and Kyoichiro Toki[#]

[##]University of Tsukuba, Tsukuba, Ibaraki, 305-8573, JAPAN.
e-mail: funaki@kz.tsukuba.ac.jp
[#]Institute of Space and Astronautical Science, Sagamihara, Kanagawa, 229-8510, JAPAN.

Abstract

An ion beam optics for a 20-cm-diam. 1kW-class microwave discharge ion thruster was fabricated and tested. The optics consists of three, 1-mm-thick, flat, carbon-carbon (C/C) composite panels with about 2800 holes, whose 3-mm-diam. holes were mechanically drilled and positioned in ±0.02 mm accuracy. When mounted on an aluminum ring, the intervals of three grids were kept at 0.5 mm by three sets of spacers, and in an operation with a microwave plasma source, the ion beam current of more than 200 mA was successfully extracted.

Introduction

Nowadays ion thrusters are recognized as one of the most efficient spacecraft propulsion system that are used for optimizing many near earth sattelites, or even for propelling interplanetary explorers.[1] As shown in Fig.1, our ion thruster has microwave powered plasma sources and an ion optics that extracts and accelerates ions[2]; then a thrust is produced as a repulsive force. The ion engine's edge over other thrusters relies heavily on its high exhaust velocity which is an order of magnitude larger than conventional chemical rocket engines. If the propellant is exhausted at a high velocity, propellant mass can be saved because only small amount of propellant is needed to produce the same thrust. This will benefit the satellite by increasing the payload mass, or much longer mission time is possible for the same amount of propellant because the lifetime of satellites is restricted by their fuel consumption.

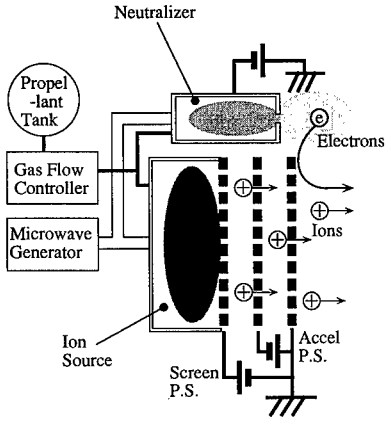

Fig. 1 Schematics of Microwave Discharge Ion Thruster System.

The above mentioned ideal acceleration will be conducted by an ion optics, whose function was described in Fig.2. The large electric field, which is realized between the

biased screen grid and the accelerator grid in an interval of about 0.5 mm, leads to the extraction of ions from the plasma source. This is because inside the acceleration region electrostatic force drives the ions up to 1.5 kV (corresponding to Xe ion velocity of 46 km/s), and efficient energy conversion from electrical energy to ion velocity is established. For the properly focused ion beam and acceleration, not only the grid-to-grid spacing but also the grid hole alignment have to be kept with an accuracy ± 0.02 mm. Also, such an accuracy should be obtained for the entire 1-mm thick grid plate. So far, molybdenum was usually used for the optics, but even molybdenum has a limit on durability when the ion bombardment and corresponding erosion occurs. The grid erosion mechanism is explained as follows. Even if the ions are properly focused when they are passing through a grid hole of an accelerator grid, charge exchange ions are produced as a result of the interaction between slow neutral atoms leaking from the screen grid and the fast ion beam. The created slow ions are attracted to the negatively biased accelerator grid, and steadily erode the surface of the accelerator grid. If the erosion advances to a severe level, beyond which electron backstreaming of electrons from the neutralizer occurs due to accelerator aperture enlargement form sputter erosion, the ion extraction and acceleration in the space charge condition collapses and the thruster reaches its end-of-life. The erosion of the accelerator grid is, threfore, considered the most important life-limiting factor of the ion engine. Among materials being considered for the ion thruster, a C/C composite is the most promising candidate since that has high resistivity than that of metal optics, leading to three times or more longer durability than, for example, that of molybdenum. Hence, many research institutes as well as commercial companies are now extensively developing C/C grid for the ion thruster.[3]

The difficulty of the C/C ion optics resides in contradicted requirements: a precisely machined thin plate should be placed in structurally strong way to survive a very severe vibrational condition during the spacecraft launch. Due to this difficulty, as far as we know, the 100 mm diam. optics was the first C/C optics that was qualified[3][4], and now we are developing a larger grid for a higher power ion thruster. In this paper, design, material selection and initial fabrication and testing of the 200-mm-diam. C/C ion optics were described and the need for improvement on mechanical strength was discussed.

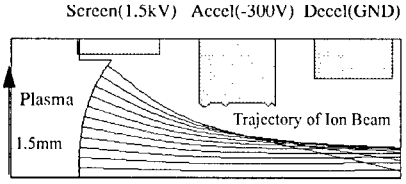

Fig. 2 Ion Optics for Ion Thruster.

Design and Fabrication of C/C Ion Optics

The first fabrication test of ion optics for 200 mm diam. ion thruster was conducted. Even for very thin structure of 1-mm thickness, the test fabrication resulted in a flatness of 0.5mm and a hole placement accuracy of 0.02 mm. Followings are the details of this optics design.

Geometry of Ion Optics

270 mm in diameter and 1 mm in thickness, flat, circular grids were fabricated from a 30-cm-square C/C panel (Fig.3). The effective diameter for ion beam extraction is 200 mm, in which about 2800 straight holes are drilled and located in a 3 mm pitch. The hole diameters are different for each grid: 3.0 mm for the screen grid, 1.8 mm the accelerator grid, and 2.4 mm for the decelerator grid.

Selection of C/C Material

The grids were fabricated by piling thin fiber sheets. Each sheet contains short pitch based carbon fibers to obtain a quasi-isotropic C/C reinforced in a direction parallel to the surface. This panel was also reinforced by the chemical vapor infiltration (CVI) process, and relatively large flexural modulus was obtained as is summarized in Table 1. Other than short fiber sheets, woven long fibers would be the best as far as mechanical strength is concerned. However, woven fiber is impractical for this case due to a very thin sheet below 1 mm, hence other kinds of design is required for using long fibers. For example, in Ref.[5], Mueller et al. fabricated a 0.46-mm-thick screen grid by piling six thin sheets consisting of pitch-based unidirectional long fibers. This panel was also reinforced by the CVI process, and larger flexural modulus compared to the short fiber carbon sheets was obtained. However, the flexural modulus showed strong anisotropy which inherently depends on the direction of the unidirectional fibers; furthermore, machining becomes difficult for these plates, requiring a laser drilling that usually cannot establish a straight hole; but a tapered hole is typically created. As a result of this fabrication difficulty of the long fibers, we decided to adopt the short fiber sheets.

Table .1 Mechanical Property of C/C Composite

Density	1.85 g/cc
Flexural Strength	180 MPa
Tensile Strength	110 MPa
Elastic Coefficient	68 GPA

Grid Mount Structure

Spacing between each grid is kept at 0.5 mm intervals by the rigid mount system shown in Fig.3. The C/C grid plates are mounted via ceramic spacers to an aluminum ring, and the grids are separated from each other by the spacers. Their gaps are precisely adjusted when they are torqued to the ring. With this fastened grid attachment, the grid increases its strength and the grid-to-grid gap can be controlled to ±0.04 mm accuracy.

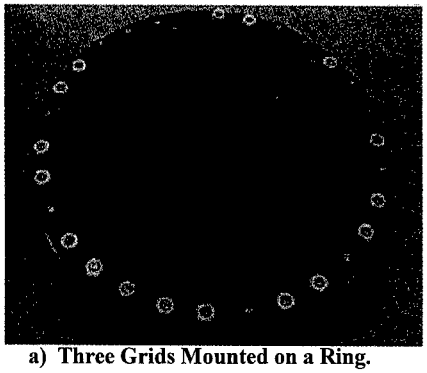

a) Three Grids Mounted on a Ring.

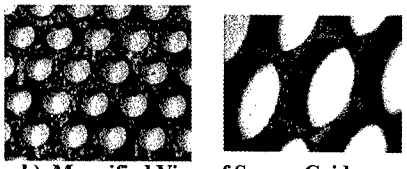

b) Magnified View of Screen Grid.

Fig. 3 The C/C Ion Optics.

Initial Tests of Ion Optics

Sputter Yield Measurement

To evaluate the erosion rate against ion bombardment, the sputter yield, which is the ratio of eroded atoms against the influx of ions, was measured. The measurement was conducted using an approximately a 15-cm-diam. DC discharge plasma source operated inside a 2-m-diam. space chamber, into which a test piece of 10 mm x 10 mm x 1 mm was immersed. Then the test piece was biased to a specific negative value during a specific amount of time, and the sputter yield is calculated as the ratio between the eroded weight against inflow ion current during the test. Usually, the most severely eroded grid (accelerator grid) is biased to around -300 V,

and for that typical biasing voltage, the sputter yield of 0.1 was obtained. This is one third that of molybdenum, which is so far used for many ion thrusters, and hence the result assures three times of longer lifetime for the same thruster operational condition.

Operation of Ion Thruster System

The first test of the ion optics with a microwave plasma source was conducted in a limited low power condition to confirm the applicability of 200 mm diam. C/C ion optics (Fig.4). For a microwave input power of 50 W, ion acceleration was successfully demonstrated up to a screen voltage of 1.3 kV and an accelerator grid voltage of - 300 V. So the short fiber structure is applicable to the ion thruster if several hours of aging was conducted: in the aging, some kinds of micro edges which might exist on the surface of the C/C optics would be removed by arcing between the grids. The ion beam extraction is 250 mA for a propellant gas xenon's mass flow rate of 6 sccm, which corresponds to a thrust of 15 mA for the above biasing condition.

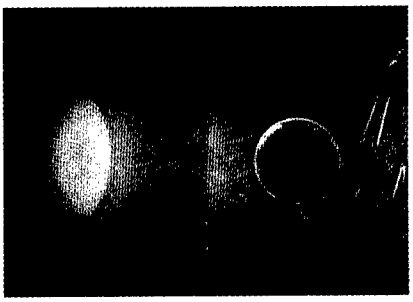

Fig. 4 Operation of Ion Thruster with the C/C Ion Optics.

Summary

Typical ion thrusters can generate a thrust of 30 mN for an input electrical power of 1kW, hence, for example, only a thrust as much as 90 mN is used for a 3 kW-class medium-size spacecraft. This is three orders of magnitude lower than conventional chemical thrusters. Accordingly, to take advantage of high-specific impulse achieved by efficient electrostatic acceleration of ions, these low-thrust ion thrusters are required to operate several tens of thousands hours. For a long-life ion thruster, the C/C composite is expected as the best material since it has both good sputtering characteristics as well as structural strength required to survive the spacecraft launch. Hence our new 200 mm in effective diameter ion thruster employed a 1-mm-thick carbon-carbon composite plate for an ion optics. The optics was attached to a microwave plasma source, and ion beam was successfully extracted in a space chamber experiment.

Although the above mentioned initial fabrication and test was successful, in order to optimize the extraction of the ion beam, thinner screen grid is necessary. What we need for our 200 mm diam. optics is 0.5 mm thick grid with an open area ratio of 70%, with which the total ion beam, and correspondingly the thrust, will be improved by about 10%. However, reducing the thickness will directly weaken the structure. Hence, it is important to study the structural response toward the vibrational condition during launch, and to estimate the ultimate limit of the thickness. In addition to these evaluations, some trials to improve structural strength are going on by changing the property of the C/C composite.

Acknowledgment

The authors would like to acknowledge the valuable fabrication and support by Nippon Carbon Co., Ltd.

References

1. E. Choueiri: Aerospace America, 37(12), 68(1999).
2. H. Kuninaka and S. Satori: J. Propulsion and Power, 14(6),1022 (1998).
3. I. Funaki, et al.: J. Propulsion and Power, 17(5), 2001, in press.
4. H. Kuninaka, et al.: AIAA paper 2000-3276, (2000).

Proceedings of 7th Japan International SAMPE
Symposium & Exhibition, Nov. 13-16, 2001

Development of Titanium Matrix Composite Rings

Takeshi YAMADA#, Akira FUKUSHIMA#, Chikara FUJIWARA#,

Masashi HIROTA#, Yukio KAWACHI# and Shinichi YAMAMOTO#

#: Research Institute of Advanced Material Gas-Generator (AMG),

1-13-4 Kitaohtsuka, Toshima-ku, Tokyo, 170-0004, Japan

E-mail: takeshi_yamada@mx.nasw.mhi.co.jp

Abstract

Titanium matrix composite (TMC) rings were fabricated by foil-fiber-foil process route using sprayed coil-preforms and titanium alloy (Ti-4.5Al-3V-2Fe-2Mo mass%; SP-700) foils. A continuous SiC fiber (SCS-6), together with a molybdenum wire as a spacer, was wound into a coil form. SP-700 powder was then sprayed on the coil to fix the fiber. After spraying, the molybdenum wire was easily removed, and the fiber spacing of sprayed coil-preforms was kept very uniform. The SCS-6/SP-700 composites were consolidated by a hot isostatic pressing at 1048K for 2 hours under an argon gas pressure of 120 MPa. It was machined to the final ring configuration. The burst strength of the TMC ring with four notches at the inside was evaluated by a spin test in a vacuum. The TMC ring was burst at 51183 rpm, which is 15% lower than the speed calculated based on the material data.

Key Words: titanium matrix composite, gas turbine, spray, spin test

Introduction

SiC fiber reinforced titanium alloy matrix composites (TMCs) are attractive for high strength application in the aerospace industries. When titanium alloy bladed rings (blings) are reinforced in the hoop direction by TMCs, about 30 to 50% weight saving can be expected for this component compared with the conventional disk and blades [1]. While a number of fabrication methods have been used for TMCs, matrix-coated-fiber (MCF) process may be the strongest candidate for TMC rings and disks manufacturing [2]. The MCF process is a new fabrication route for TMCs, which uses electron beam physical vapor deposition (EB-PVD) to pre-coat continuous SiC fiber with a thick layer of matrix alloy. They were laid-up and hot-pressed to the finished TMC. However, the coated fiber is still developing material and it is difficult to get the enough amount of the coated fiber.

In this study, sprayed coil-fiber-preforms were newly developed to fabricate a TMC ring by foil-fiber-foil process, and the burst spin test of the ring was also carried out.

Experimental Procedures

Composite Material

A continuous SiC fiber (SCS-6) and a molybdenum wire of 0.1mm diameter, as a

spacer, were wound into a coil form. Matrix alloy (Ti-4.5Al-3V-2Fe-2Mo mass%; SP-700) powder was then sprayed on the coil to fix the fiber using a low-pressure-plasma spraying. The molybdenum wire was removed after sprying. The SCS-6/SP-700 composite with 24 SiC fiber layers was fabricated by foil-fiber-foil process using the sprayed coil-preforms and SP-700 foils of 0.2mm thickness. They were consolidated by a hot isostatic pressing at 1048K for 2 hours under an Ar-gas pressure of 120MPa. It was machined to the final ring configuration, as shown in **Fig.1**. Tow TMC rings were fabricated in this study, and one was used for the spin test and the other for the cut inspection. X-ray radiographic inspection of the TMC ring was also carried out to check the reinforcement location

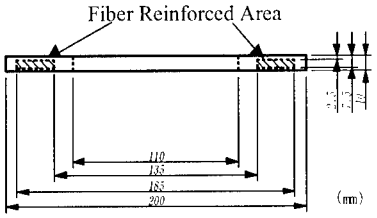

Fig.1 Dimensions of the TMC ring

Spin Test

The burst strength of the TMC ring with four notches at the inside was evaluated by a spin test in a vacuum. Notches were 4mm in depth, and they were located at the angles of 0, 90, 180 and 270 degree. The test ring was attached to an arbor disk with a drive shaft. The rotation speed and vibration of the shaft were recorded up to the burst speed.

Results and Discussions

TMC Ring Fabrication

Appearance of the sprayed coil-preform is shown in **Fig.2**. The molybdenum wire was easily removed from the preforms. The fiber spacing of sprayed coil-preforms was kept very uniform, and the average pitch of fiber was 0.2mm. **Figure 3** shows the appearance of the TMC ring fabricated in this study. The

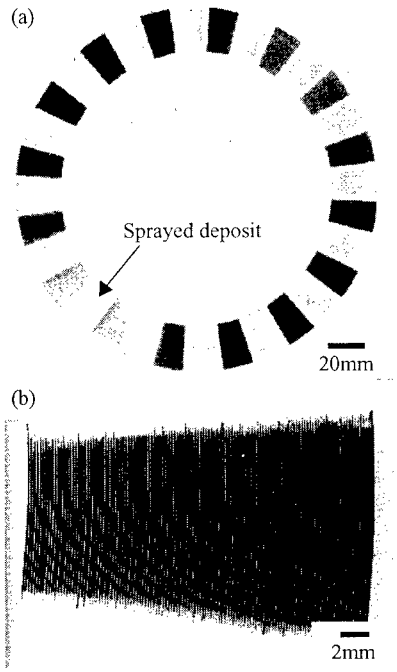

Fig.2 Sprayed coil-preform; (a) low and (b) high magnification.

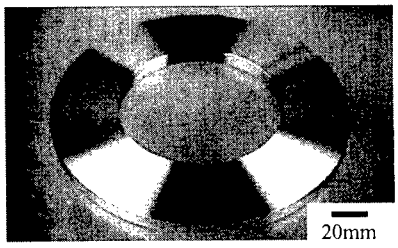

Fig.3 TMC ring model

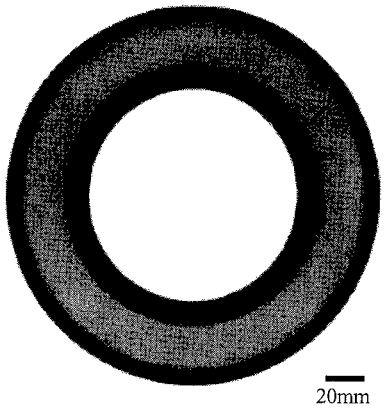

Fig.4 X-ray radiographic photograph of the TMC ring.

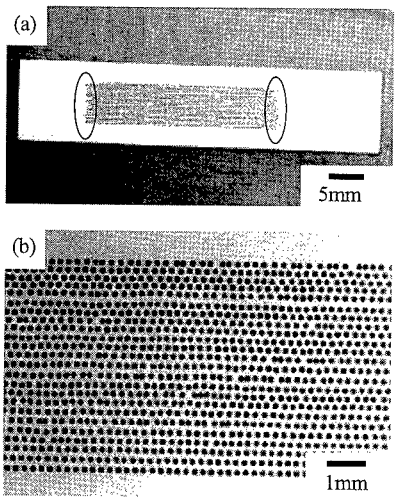

Fig.5 Cross-section of the TMC ring

TMC rings were successfully machined to the final configuration without any distortions caused by thermal residual stress. **Figure 4** shows the X-ray radiographic photograph of the TMC ring. The light-colored area in the **Fig.4** is the fiber-reinforced area. The SiC fiber position in the ring almost meats the design requirement (Fig.1), which was located in the range of the diameter from 135.9mm to 182.1mm.

While the fiber spacing in this composite ring was controlled to be almost uniform, small amount of closely spaced fibers was found, as shown in **Fig.5**. This may be due to the fibers free from the constraint of the sprayed deposit, and they may be moved by the matrix flow during the consolidation. At the inner and outer ends of the fiber-reinforced area, low fiber-volume-fraction (V_f) parts were observed in the TMC ring, as indicated by open circles in **Fig.5(a)**. It seems this can not be helped due to the process limitation of the foil-fiber-foil method. It is very difficult to place preforms with each end of the fibers strictly on the straight line along the staking direction.

Spin Test

The TMC ring burst at 51183 rpm, and it broke into 4 pieces, as shown in **Fig.6**. The primary failure occurred at the inner end of the fiber-reinforced area in the TMC ring, and many pull-out-fibers were observed at the primary fracture surface of the ring, as shown in **Fig.7**. This indicates the ring was burst due to the tensile overload in the hoop direction. Maximum stress of the ring in the

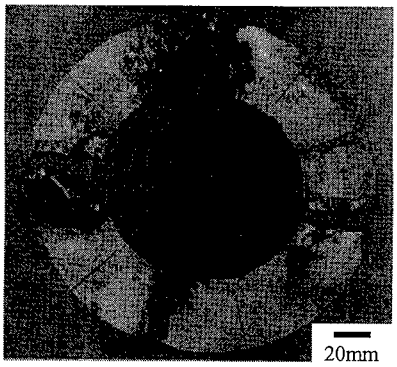

Fig.6 Burst TMC ring

rotation speed at 51183 rpm was estimated to be 1383MPa by a finite element analysis, which is 85% tensile strength of the coupon specimen with the same V_f of 33%. This degradation may be caused by the low V_f area at the inner end of fiber-reinforced area and by the multi-axis loading.

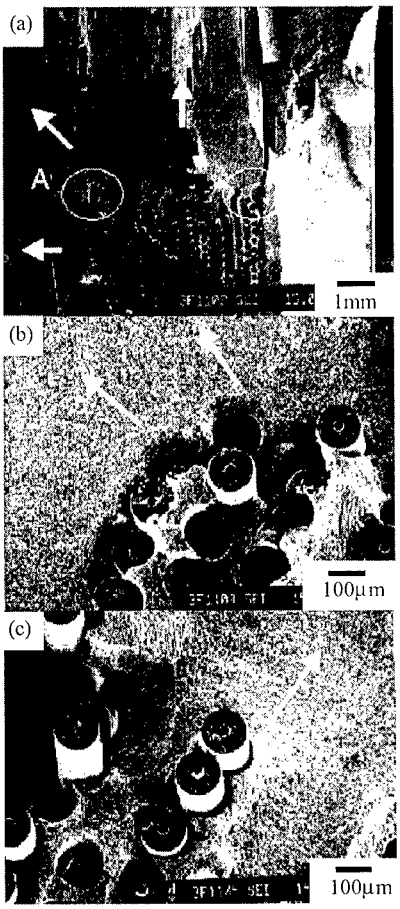

Fig.7 Fracture surface of the TMC ring: (a) primary fracture part, and close-up (b) A and (c) B area.

Conclusions

In this study sprayed coil-preforms were newly developed in order to fabricate the titanium matrix composite rings by foil-fiber-foil process, and the burst strength of the ring with four inside notches was evaluated by a spin test in a vacuum. Considering the results obtained, our conclusions are as follows.

1) The fiber spacing of the coil-preforms was kept very uniform, and the average pitch of the fiber was 0.2mm.
2) While the fiber distribution in the TMC ring was almost uniform, it was difficult to control the preform ends to be straight along the stacking direction.
3) The ring burst at 51183 rpm, which is 85% tensile strength of the coupon specimen with the same fiber volume fraction of 33%.
4) The primary fracture of the ring occurred at inner end of the fiber-reinforced area, and it was due to the tensile overload in the hoop direction.

Acknowledgment

The authors are grateful to Mr. M.Senda and Mr. A.Kono, Mitsubishi Heavy Industries, Ltd., Mr. M.Terasawa and Mr. Y.Azuma, Churyo Engineering Co. Ltd., and Mr. T.Nakao and Mr. K.Kondo, Tamagawa Engineering Co. Ltd. for helpful discussions and technical support.

References

1. S.Mall and T.Nicholas (eds.): *"Titanium Matrix Composites"*, TECHNOMIC, Lancaster, PA, 1998, pp.1-23.
2. C.M.Ward-Close et al.: Mater. Sci. Eng., A263, 314 (1999).

Proceedings of 7th Japan International SAMPE
Symposium & Exhibition, Nov. 13-16, 2001

Multiaxial Weibull Analysis of Graphite – from the Launch Failure of M-V-4 Rocket –

Eiichi Sato# and Junjiro Onoda#

#: The Institute of Space and Astronautical Science
3-1-1 Yoshinodai, Sagamhara, Kanagawa 229-8510, JAPAN
E-mail: sato@materials.isas.ac.jp

Abstract

In February 2000, the Institute of Space and Astronautical Science launched M-V-4 rocket with an unexpected failure. Intensive post-flight study has been pursued, and it has been finally concluded that the failure originated in a fracture of a nozzle throat insert made of graphite before 4 s after the launch. In the study, precise analyses of heat input, thermal conduction and stress in that part have been performed, and the multi-axial Weibull analysis has been, firstly as the authors know, applied to a real engineering part. A design procedure of a brittle, thermally-stressed part has been, thus, established.

Key Words: graphite, fracture, Weibull analysis, solid rocket motor

Introduction

The Institute of Space and Astronautical Science (ISAS) launched M-V-4 rocket on February 10, 2000 with an unexpected failure. M-V rocket is the largest solid propellant satellite launch system in the world, launched first in 1997. M-V-4 rocket intended to launch a new and advanced X-ray astronomical observatory, ASTRO-E, with a weight of 1700 kg. After the failure, intensive study to trace the origins has been pursued, and it has been finally concluded that the failure originated in a fracture of a nozzle throat insert made of graphite before 4 s after the launch, and that the fracture of the graphite must have originated at an inner or external crack preexisting with a diameter of 3 mm or more.

In the study, precise analyses of heat input, thermal conduction and stress in the throat insert have been performed, and the fracture probability of the throat insert has been calculated through Weibull analysis. The theory predicts that fracture becomes easier when any tensile principal stress is accompanied with other principal stresses of compression. When a part is loaded mainly by thermal stress generated by its temperature gradient, any tensile principal stress is accompanied with other principal stresses of compression. The above theory reveals that the multi-axial effect appears most strongly in this stress state.

In the present analysis, the multiaxial Weibull analysis has been, firstly as the authors know, applied to a real engineering part, and a distinct multiaxial effect has been revealed. A design procedure of a brittle, thermally-stressed part has been, thus, established.

Fracture statistics

A brittle material, such as ceramics and graphite, fractures through crack growth which has been preexisting in the material. Therefore the strength of the material is determined by the maximum preexisting crack size in it, which is expressed by Weibull statistics [1]. When a part is loaded mainly by thermal stress generated by its temperature gradient, any tensile principal stress is accompanied with other principal stresses of compression. Although an empirical multiaxial fracture rule has been once proposed [2,3], the multiaxial fracture statistics is indispensable for theoretically rigorous analysis.

The uniaxial fracture statistics is given as follows. First, we define the cumulative fracture probability of infinite element dv_i,

$$F_i = \left(\frac{\sigma}{\sigma_0}\right)^m dv_i, \tag{1}$$

and then the cumulative fracture probability

$$G = 1 - \exp\left[-\int_V \left(\frac{\sigma}{\sigma_0}\right)^m dv\right] = 1 - \exp\left[-\left(\frac{\sigma_R}{\sigma_0}\right)^m V_E\right],$$

$$V_E = \int_V \left(\frac{\sigma}{\sigma_R}\right)^m dv. \tag{2}$$

The distribution of G is called the Weibull distribution, m the Weibull parameter, and V_E the effective volume.

In the multiaxial case, formulation has been established considering the mixed mode fracture by Matsuo [4] and Lamon and Evans [6]. Modification based on the empirical fracture criteria, $(K_I/K_{Ic})^2+(K_{II}/K_{IIc})^2=1$, has been done by Oda et al. [6]. Here K_I and K_{II} are mode I and II stress intensity factors, respectively, and c denotes their critical values. As shown in Fig. 1, an infinitesimal element having a circular crack of diameter $2c$ stressed by $(\sigma_1, \sigma_2, \sigma_3)$. The growth criteria of the crack is then given by

$$1 = \left[\frac{K_I^2}{K_{Ic}^2}+\frac{K_{II}^2}{K_{IIc}^2}+\frac{1}{(1-\nu)^2(1+\nu)}\frac{K_{III}^2}{K_{Ic}^2}\right]_{max} = \frac{4c}{\pi}\frac{z}{K_I^2}, \tag{3}$$

where σ_R and τ are the normal and shear stresses on the crack, respectively, and z is the equivalent normal stress given by

$$z = \left\{\sigma_R^2 + \frac{4}{(2-\nu)^2}\frac{K_{Ic}^2}{K_{IIc}^2}\tau^2\right\}^{1}, \quad \sigma_R > 0. \tag{4}$$

Using the equivalent normal stress, we obtain the multiaxial probability function as follows:

$$G = 1 - \exp\left[-\int_V \frac{1}{\pi d^3}\left[\int_{\substack{semi-\\sphere}} \left(\frac{z}{\sigma_0}\right)^m \sin\varphi \, d\varphi \, d\theta\right] dv\right]$$

$$I = \int_0^{\pi}\left(\cos^4\varphi + \frac{4}{(2-\nu)^2}\frac{K_{Ic}^2}{K_{IIc}^2}\cos^2\varphi\sin^2\varphi\right)^{m/2} \sin\varphi \, d. \tag{5}$$

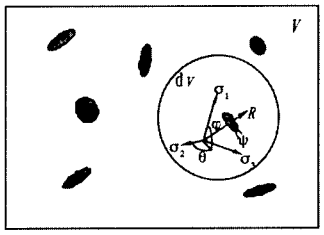

Fig.1 Schematic diagram for multiaxial fracture statistics

Fracture Behavior of Graphite

A material which follows Weibull statistics (eq.2) shows a linear relationship between $\ln(1/(1-G))$ and $\sigma V^{1/m}$ in a double logarithmic plot, which is called the Weibull plot. The results of large number of tensile tests (performed in this study and during the development of another rocket) revealed that the graphite shows good Weibull statistics with the Weibull parameter m=20, as shown in Fig. 2.

Multiaxial fracture behavior was studied through compression-torsion tests. Figure 3 shows the results in the form of fracture surface in the maximum and minimum principal stresses (σ_1 and σ_3) plane. The lines are theoretically estimated fracture surfaces (eq.5). The weakening by applying

compressive minimum principal stress σ_3 can be clearly observed, and the data implies that K_{IIc}/K_{Ic} =1.2; it is the first experimental verification of multiaxial Weibull analysis. The estimation of 1.2 is consistent with previous ambiguous measurements of 1.2–1.4 in graphite [7].

Analysis of Throat Insert

Fracture probabilities of the throat insert have been, then, calculated through substituting the stress and temperature distribution into the multiaxial Weibull analysis. Here, in addition to temperature dependence of the strength, the other fracture modes, compressive and shearing, have been also considered. Table 1 shows the results at the time of 1 and 4 s after the launch, until which the fracture has been identified to initiate. The probabilities in compressive and shearing mode have been also estimated to be negligibly small. The tensile (and thus total) probabilities are below 0.00006–0.000009% at 1 s after the launch and below 0.3–0.06% at 4 s.

This analysis has been performed with assumptions giving larger probability on the case of uncertainty, for example, the heat input to the throat insert. In addition, a uniform and infinite stress field has been assumed for each finite element, though the stress field has shown narrow peaks. Therefore the probabilities listed in Table 1 indicate the maximum limits. Since the maximum limit of the probability at 4 s after the launch has been calculated below 0.3%, the throat insert could not fractured because of the insufficient margin of safety.

Many other possibilities of the origin of the fracture of the graphite throat insert at the very beginning of the flight have been examined using FTA. Eliminating each possible origin listed in FTA, finally we have concluded that the fracture of the throat insert must have originated in a preexisting inner crack of diameter more than 3 mm or

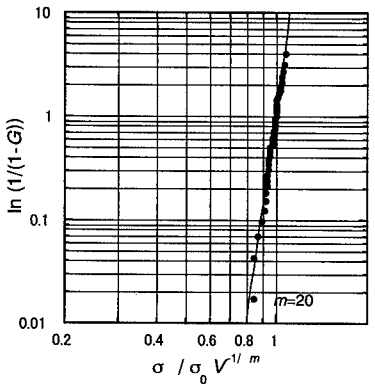

Fig.2 Weibull plot of the graphite

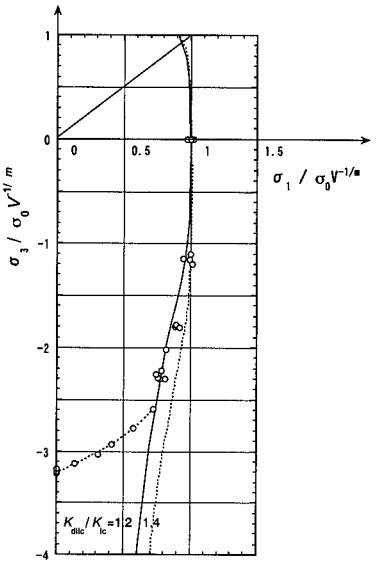

Fig.3 Fracture surface of the graphite

an external crack of depth more than 3 mm.

Using a brittle material to an important part, non-destructive inspection (NDI) is indispensable, though that for graphite has not been attempted except ultrasonic testing

Table 1 Calculated Fracture Probability

Time	K_{IIc} /K_{Ic}	Tensile Statistic Fracture	Compressive Minimum Principal Stress	Compressive Maximum Shear Stress	Total Fracture Probability
X+ 1 s	1.2	5.5E-7	9.8E-18	2.1E-19	5.5E-7
	1.3	1.8E-7			1.8E-7
	1.4	8.8E-8			8.8E-8
X+ 4 s	1.2	2.6E-3	1.2E-20	3.3E-22	2.6E-3
	1.3	9.9E-4			9.9E-4
	1.4	5.7E-4			5.7E-4

(UT) for the components in the first high temperature gas-cooled reactor in Japan named HTTR [9]. Although fracture statistics cannot determine the direction of the dangerous cracks, NDI for HTTR was targeted only the horizontal cracks, and its reliability is somehow doubtful. We have tried the UT procedure, however we have concluded that the graphite ingot of 1070 mm diameter and 350 mm height is too large to obtain sufficient S/N from the permitted crack of diameter 3 mm orienting to any direction.

Concluding Remarks

The precise analyses of heat input, thermal conduction and stress in the throat insert have been performed, and the fracture probability of the throat insert has been calculated through multiaxial Weibull analysis. The maximum limit of the probability at 4 s after the launch has been calculated below 0.3%, which implies that the throat insert could not fractured because of the insufficient margin of safety.

As a consequence of the discouraged conclusion of difficulty in reliable NDI and significant engineering development of 3D-C/C composite in recent years, we have decided to redesign the main motors of M-V rocket with throat inserts made of 3D-C/C. At present we are in the course of redesign and verification procedure. On the other hand, the study of NDI is continuing with a target of smaller throat inserts of sounding rockets and auxiliary motors of M-V rocket, which are now under way of redesign through multiaxial fracture statistics.

Acknowledgment

We received fruitful advises and reviews by the members of the investigative committee of M-V-4. Especially, Prof. Y. Matsuo and Prof. Y. Tanabe of Tokyo Inst. Tech. and Prof. M. Tokuda of Mie Univ. are acknowledged. Cooperation by Nissan Motors (at present, IHI Aerospace), Genes and Japan Power Engineering and Inspection are also acknowledged.

References

1. W. Weibull, Ingenioersvetenskapsakad., Handl., 151 (1939), 45.
2. K. Sato, Trans. Japan Soc. Mech Eng., 39-220, (1973), 1096, (in Japanese).
3. S. Sato, R. Kurumada, K. Kawamata,K. Kosaka, K. Arai, Depart. mech. Eng., Ibaraki Univ., 35 (1987), 105, (in Japanese).
4. Y. Matsuo, Trans. Japan Soc. Mech Eng., 46-406, A, (1980), 605, (in Japanese).
5. J.Lamon and A.G.Evans, J.Am.Ceram. Soc., 66 (1983), 177.
6. I. Oda, M. Matsui, T. Soma, M. Masuda, N. Yamada, J. Ceramic Soc. Japan, 90 (1988), 539, (in Japanese).
7. S. Sato, T. Okeda, T. Kimura, Iwaki Branch, Japan Soc. Mech Eng., (1997), 33, (in Japanese).
8. for example, H. Tada, The Stress Analysis of Cracks Handbook, Del Research co., Hellertown, (1973).
9. M. Ishihara, S. Hanawa, T. Iyoku and S. Shiozawa, Tanso, 196, (2001), 39, (in Japanese).

Proceedings of 7th Japan International SAMPE
Symposium & Exhibition, Nov. 13-16, 2001

Thermal Characteristics of a High-Thermal-Conductivity Graphite Sheet for Spacecraft Thermal Control

H. Nagano†, A. Ohnishi†† and Y. Nagasaka†††

†School of Integrated Design Engineering, Keio University
3-14-1, Hiyoshi, Yokohama 223-8522, JAPAN.
hosei@pub.isas.ac.jp

††Institute of Space and Astronautical Science
3-1-1, Yoshinodai, Sagamihara 229-8510, JAPAN.

†††Department of System Design Engineering, Keio University
3-14-1, Hiyoshi, Yokohama 223-8522, JAPAN.

Abstract

In order to apply a new material – a graphite sheet, which has characteristics of high thermal conductivity, lightweight and flexibility, as a material for spacecraft thermal control applications, the thermophysical properties, such as thermal diffusivity, total hemispherical emittance and solar absorptance, have been measured. Additionally, the thermal conductivity was evaluated.

Key Words: Graphite Sheet, High Thermal Conductivity, Thermal Control, Spacecraft.

Introduction

In the field of space development, designing lightweight thermal control systems of the spacecrafts are required. We have proposed a new material, "graphite sheet (GS)", developed by Matsushita Electric Industrial Co., Ltd., for spacecraft thermal control applications such as radiators, thermal doublers, thermal paths and heaters. The GS has characteristics of high thermal conductivity, lightweight and flexibility like a piece of paper. In order to use the GS as a thermal control material, it is essential to know the reliable thermophysical properties such as thermal conductivity, total hemispherical emittance and solar absorptance. In this paper, the temperature dependence of thermal diffusivity and total hemispherical emittance, and incident angle dependence of solar absorptance for the GS are described. Additionally, the thermal conductivity is calculated using the measured thermal diffusivity, and evaluated by comparing with the other high-thermal-conductivity materials.

Graphite Sheet

The GS has been prepared from aromatic polyimide films by heat treatment at 2900 - 3300 K in an inert atmosphere. The process for making highly oriented graphite sheets from polyimide films is as follows: (1) At temperatures between 700 and 900 K, the thermal decomposition reaction proceeds preferentially on the imide group, and a planar and heterocycle carbon precursor with the nitrogen contained are made. (2) Carbonization occurs by denitrification and dehydrogenation, and aromatic rings are developed above 1300 K. (3) At temperatures above 2900 K, lamination layers have been grown and highly oriented graphite films are produced. Figure 1 shows the scanning

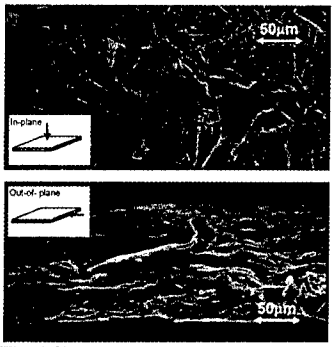

Fig. 1 SEM Images of a) surface and b) cross-section features of the graphite sheet.

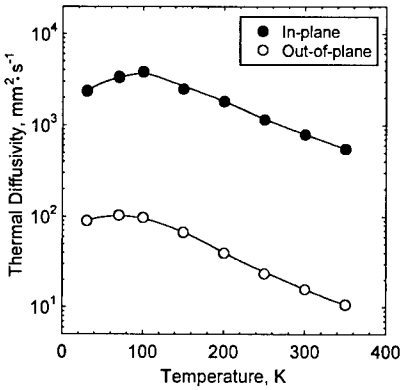

Fig. 2 Temperature dependence of in-plane and out-of-plane thermal diffusivities of graphite sheet.

electron microscope (SEM) photos of (a) the surface and (b) the cross-sectional view of the GS structures. It is remarkable that the GS is organized in different structures between the in-plane and the out-of-plane directions.

Measurement Method

The in-plane thermal diffusivity and the out-of-plane thermal diffusivity of the GS have been measured over the temperature range from 30 to 350 K by using a laser-heating ac calorimetric method [2, 3]. The uncertainty of the present measurement is estimated to be within ±3.5 % (in-plane) and ±11-52 % (out-of-plane) [4].

The total hemispherical emittance of the GS has been measured over the temperature range from 173 to 373 K by using a calorimetric method [5]. The uncertainty of this apparatus is estimated within ±3 % [6].

The solar absorptance of the GS has been calculated from the spectral reflectance, which was measured by using a spectroscopic method over the wavelength range from 0.26 to 2.5 μm [7]. This wavelength region is verified solar absorptance of thermal control materials. The uncertainty of the present measurement is estimated within ±2%.

Results and Discussions

Thermal Diffusivity

The results of the in-plane and out-of-plane thermal diffusivities measurement in the temperature range from 30 to 350 K are shown in Fig. 2. It is clear that both the in-plane and out-of-plane thermal diffusivities of the GS have large temperature dependences. They have the maximum values around 100 and 70 K, respectively. It is confirmed that the GS has extreme anisotropy between in-plane and out-of-plane directions. The value of the anisotropy ratio increases from 25 to 50 as the temperature increases.

Thermal Conductivity

The thermal conductivity of the GS is calculated by the following equation.

$$\lambda = \rho \cdot c \cdot a \qquad (1)$$

where λ : Thermal Conductivity, ρ : Density, c : Specific Heat, a : Thermal Diffusivity. The specific heat of the pyrolytic graphite was used for calculating thermal conductivity, since the value of the specific heat is independent of the degree of graphitization [8, 9]. The calculated thermal conductivity of the GS, compared to the

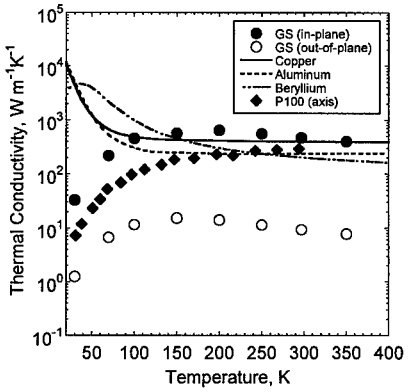

Fig. 3 Temperature dependence of thermal conductivities for graphite sheet, pure metals and P100 carbon fiber.

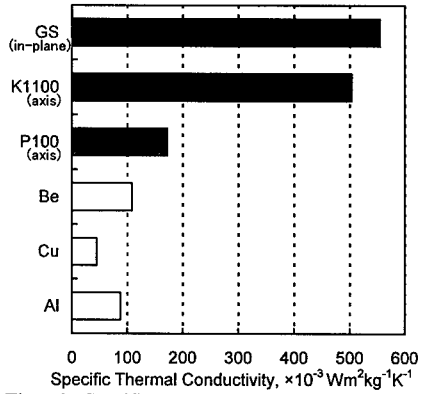

Fig. 4 Specific thermal conductivities for graphite sheet, carbon fibers, pure metals.

conductivities of pure aluminum, pure copper, pure beryllium [10] and P100 carbon fiber [11], are shown in Fig. 3. Above 150 K, The in-plane thermal conductivity is significantly greater than those of pure aluminum and pure beryllium, and is somewhat larger than the conductivity of pure copper over the present temperature range, while the out-of-plane thermal conductivity of the GS is smaller than those of metallic materials. Additionally, the in-plane thermal conductivity for the GS is greater than the conductivity in the axial direction of the P100 fiber presently used for spacecraft thermal designs.

The specific thermal conductivity, κ is calculated by the following equation.

$$\kappa = \lambda / \rho \qquad (2)$$

Figure. 4 shows the specific conductivities of GS, metallic materials and carbon fibers at room temperature. It is clear that the graphite materials (P100 fiber, K1100 fiber [12] and GS) have far greater specific thermal conductivities than those of metallic materials. Among the graphite materials, the GS is the highest in value of the specific thermal conductivities. Taking into account that the GS can diffuse heat two-dimensionally in the in-plane directions, while carbon fibers can diffuse only one-dimensionally, the GS should be a more useful material for spacecraft thermal management components.

Total Hemispherical Emittance

The result of total hemispherical emittance measurement in the temperature range from 173 to 373 K is shown in Fig. 5. The total hemispherical emittance increase as the temperature increases. The value of the total hemispherical emittance changes from 0.22 to 0.32 as the temperature increases.

Solar Absorptance

The measured spectral hemispherical reflectance in the incident angle range from 5 to 60□ in the wavelength range from 0.26 ~ 2.5 μm for the GS is shown in Fig. 6. In this wavelength region, the reflectance falls in the 20 to 45 % range. Although the remarkable incident angle dependence of the spectral reflectance between 5□ and 30□ is not confirmed, it is clear that the reflectance at 60□ is larger than those at 5□ and 30□. The values of the solar absorptance for incident angles of 5□, 30□ and 60□are 0.72, 0.72 and 0.67, respectively.

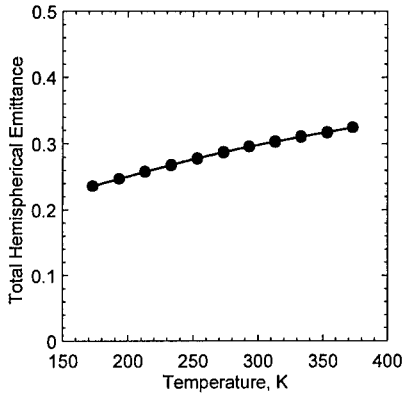

Fig. 5 Temperature dependence of total hemispherical emittance of graphite sheet.

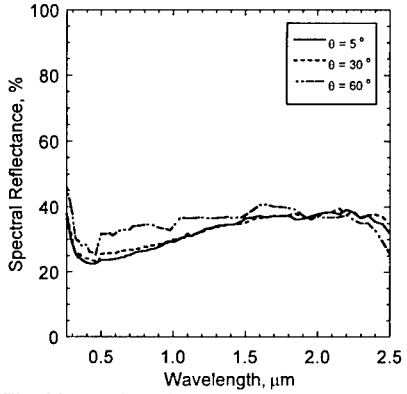

Fig. 6 Spectral hemispherical reflectance of graphite sheet for the incident angles at 5, 30 and 60 deg.

Conclusions

In order to apply a high-thermal-conductivity graphite sheet as a material for spacecraft thermal control applications, temperature dependence of thermal diffusivities and total hemispherical emittance, and incident angle dependence of solar absorptance have been measured. Additionally, thermal conductivities were calculated, and it was confirmed that the GS has high potential as a material for spacecraft thermal control applications on the ground of its high thermal conductivity and lightweight.

Acknowledgments

We would like to thank Dr. H. Kato of National Research Laboratory of Metrology for many helps during this research. We would also like to thank Mr. N. Nishiki of Matsushita Electric Industrial Co., Ltd. for supplying graphite sheets.

References

1. M. Murakami, K. Watanabe and S. Yoshimura, *Appl. Phys. Lett.*, 48 (23) 1594 (1986).
2. H. Kato, *Proc. 20th Jpn. Symp. Thermophys. Prop.*, 400 (1999).
3. H. Nagano, H. Kato, A. Ohnishi and Y. Nagasaka, *High Temp. - High Press.*, 33 (3) 253 (2001).
4. H. Nagano, H. Kato, A. Ohnishi and Y. Nagasaka, *Int. J. Thermophys.*, 22 (1) 301 (2001).
5. A. Ohnishi, T. Hayashi and H. Nagano, *Proc. 4th Jpn. Symp. Thermophys. Prop.*, 1 (1983).
6. H. Nagano, H. Kato, A. Ohnishi and Y. Nagasaka, *AIAA 34th Thermophys. Conf.*, No. 2000-2510.
7. A. Ohnishi, and T. Hayashi, *Proc. Int. Symp. 'Environmental and Thermal Systems for Space Vehicles'*, 467 (1983).
8. A. T. Butland, R. J. Maddison, *J. Nucl. Mater.*, 49 (1) 45 (1974).
9. A. Magnus, *Annalen der Physik*, 70, 303 (1923).
10. Y. S. Touloukian, R. W. Powell, C. y. Ho and P. G. Kelemens, *Thermophysical Properties of Matter*, Vol. 1, Thermal Conductivity of Metallic Solids, IFI/Plenum, New York/Washington, 1970.
11. J. Heremans, I. Rahim and M. S. Dresselhaus, *Phys. Rev. B*, 32 (10) 6742 (1985).
P. M. Adams, H. A. Katzman, G. S. Rellick and G. W. Stupian, *Carbon*, Vol. 36, No. 3, 1998, pp. 233-245.

Proceedings of 7th Japan International SAMPE
Symposium & Exhibition, Nov. 13-16, 2001

Design and Test Results of a Variable Emittance Radiator Device

Sumitaka Tachikawa†, Akira Ohnishi†
Akira Okamoto‡, Yasuyuki Nakamura‡, Yuichi Shimakawa‡, Toru Mori‡ and Atsushi Ochi‡

†: Institute of Space and Astronautical Science
3-1-1 Yoshinodai, Sagamihara, Kanagawa 229-8510, JAPAN
E-mail: sumitaka@pub.isas.ac.jp

‡: NEC corporation
4035 Ikebe-chyo, Tsuzuki-ku, Yokohama, Kanagawa 224-8555, JAPAN

Abstract

The Smart Radiation Device (SRD) is a thin and light tile which is made from a ceramic material. The material undergoes a metal-insulator transition at around room temperature and this allows the infrared emissivity of the device to change from low to high as the temperature is increased from 173K to 375K. This is beneficial for thermal control applications on spacecraft. For example, bonded only to the external surface of the spacecraft, the SRD controls the heat radiated to deep space without electrical instruments or mechanical parts which are used for changing emissivity. It reduces the energy consumption of the electrical heater for thermal control, and decreases the weight and the cost of the thermal control system.

In this paper, design and preliminary test results of the SRD will be presented.

Key Words: radiator, spacecraft, variable emittance, thermal control

Introduction

Spacecraft usually expel excess heat into deep space by radiators to keep the temperature of all the elements of a spacecraft system within the allowable limits for all mission phases. The amount of heat radiated into deep space is not constant because the temperatures of these components are affected by heat inputs which are highly variable with time over the life of the mission. So some devices are required for thermal control. The thermal louver is one of the thermal control devices and it has been used to regulate the rate of heat flow into deep. But, it is heavy and expensive, especially for high power consumption spacecraft. At the moment, the density of the instruments on the spacecraft tends to be high and the mission tends to be complex, so developing a lighter and more economical thermal control device with high performance is necessary.

We are now developing a variable emittance radiator named SRD. It is a light ceramic tile that changes its emissivity according to its temperature without using control instruments. The SRD has significant advantages, such as weight, so we can use the new device without any constraints and can control the temperature of the spacecraft easily in comparison to the thermal louver.

Smart Radiation Device

The SRD is a black ceramic tile which is 200μm thick and weighs only 1.2kg/m^2. Figure 1 shows a photograph of a test piece of the SRD. The size is 30mm×30mm. The SRD are made of $La_{1-X}Sr_XMnO_3$ or $La_{1-X}Ca_XMnO_3$ which are manganese oxides with a perovskite-type structure and made by replacing La^{3+} with Sr^{2+} or Ca^{2+} in parent material $LaMnO_3$. By this substitution, Mn^{3+} changes to Mn^{4+} in order to keep their electrical charge. The metallic state in these compounds is stabilized by the double-exchange interaction[1]. As a result, they have the special property of metal-insulator transition at around room temperature and the electrical conductivity of the compounds changes drastically depending on the temperature.

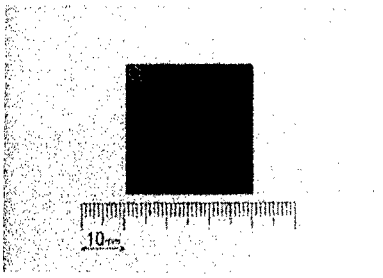

Fig.1 Test Piece of SRD.

In the beginning, we made some trial SRD which were made of $La_{1-X}Sr_XMnO_3$ or $La_{1-X}Ca_XMnO_3$. The molar ratio(X) dependence of the total hemispherical emittance became clear and the optimum molar ratio for these materials was confirmed[2]. As a result, we selected $La_{0.825}Sr_{0.175}MnO_3$ and $La_{0.7}Ca_{0.3}MnO_3$ for the materials of the SRD.

Optical Properties

The total hemispherical emittance of the SRD was measured by using the calorimetric method. Figure 2 shows the temperature dependence of the total hemispherical emittance for the SRD. The total hemispherical emittance changes in the temperature range of 173K~373K and especially the emissivity of $La_{0.825}Sr_{0.175}MnO_3$ changes drastically under 280K and that of $La_{0.7}Ca_{0.3}MnO_3$ changes drastically under 260K. $La_{0.825}Sr_{0.175}MnO_3$ has a high emissivity of 0.65 at high temperatures and a low emissivity of 0.28 at low temperatures, so the variability of the total hemispherical emittance Δε is 0.37. And $La_{0.7}Ca_{0.3}MnO_3$ has a high emissivity of 0.61 at high temperatures and a low emissivity of 0.19 at low temperatures, so the variability of the total hemispherical emittance Δε is 0.42.

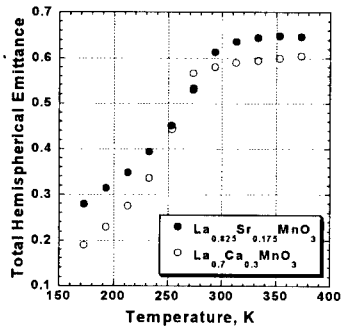

Fig.2 Temperature Dependence of Total Hemispherical Emittance of SRD.

The solar absorptance was measured spectroscopically with an integrating sphere in the wavelength region of 0.26~2.5μm. Figure 3 shows the spectral reflectance of the materials. The spectral reflectance of both materials is low. The solar absorptance of $La_{0.825}Sr_{0.175}MnO_3$ is 0.84 and that of

$La_{0.7}Ca_{0.3}MnO_3$ is 0.87. These are so high that we are trying to reduce them by multi layer coating which reflects the visible sunlight and acts as an antireflection coating for the thermal IR.

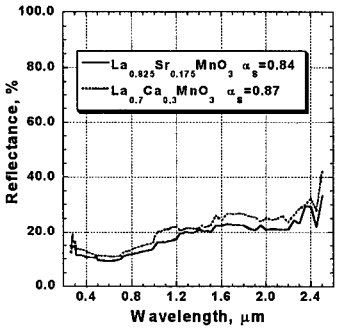

Fig.3 Spectral Reflectance of SRD.

Space Qualification Tests

Radiation durability is required for operation in space because it affects the life of the spacecraft. To evaluate the space degradation of optical properties, space environmental simulation tests were performed on the ground with independent radiation by protons, electrons and UV. Table 1 shows the radiation conditions.

Table 1 Radiation Conditions

SOURCE	ENERGY	FLUENCE
Protons	0.5MeV	5.0×10^{14}p/cm^2
	1.0MeV	1.0×10^{13}p/cm^2
	2.0MeV	2.0×10^{12}p/cm^2
Electrons	0.5MeV	1.0×10^{15}e/cm^2
	1.0MeV	5.0×10^{14}e/cm^2
	2.0MeV	2.0×10^{14}e/cm^2
UV	11.5SC	11532.8ESH

Figure 4 shows the temperature dependence of the total hemispherical emittance for $La_{0.825}Sr_{0.175}MnO_3$. The emissivity of irradiated samples was similar to that of the non-irradiated material within the measuring tolerance.

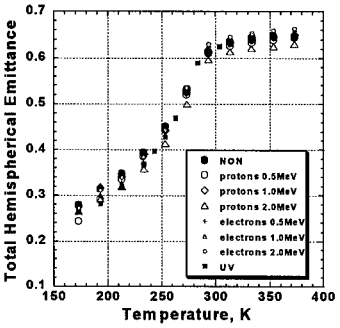

Fig.4 Temperature Dependence of Total Hemispherical Emittance of SRD.

Table 2 shows the solar absorptance of $La_{0.825}Sr_{0.175}MnO_3$ before and after irradiation. Each variation of these samples is less than 0.01.

Table 2 Solar Absorptance of SRD.

SOURCE		BEFORE	AFTER
protons	0.5MeV	0.88	0.88
	1.0MeV	0.90	0.90
	2.0MeV	0.88	0.88
Electrons	0.5MeV	0.90	0.89
	1.0MeV	0.89	0.89
	2.0MeV	0.88	0.88
UV		0.88	0.88

We confirmed that there was no degradation of $La_{0.825}Sr_{0.175}MnO_3$ for protons, electrons and UV irradiation. The radiation tests for $La_{0.7}Ca_{0.3}MnO_3$ have not been completed yet.

Improvement of SRD

In order to improve the SRD, we have been trying a new design as follows.

1. Design for the improvement of the optical properties.
2. Design for the reduction of the weight.

We have been trying to make a new composition, $La_{1-X-Y}Sr_XCa_YMnO_3$, which is combined $(La,Sr)MnO_3$ with $(La,Ca)MnO_3$ in order to improve the optical properties[3]. From the measurement results, we predict that this will be a new material, which has better optical property. But, the solar absorptance has not been improved yet.

It is very important for space applications to use light elements. In order to reduce the weight of the SRD, we designed a new one which is composed of a thin variable emittance layer and the ZrO_2 substructure. By introducing a thick film process, we could make a thinner SRD which is under 70μm thick and weighs under 430g/m^2[4].

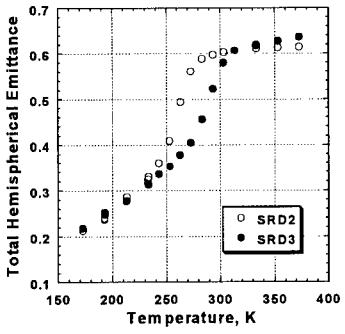

Fig.5 Temperature Dependence of Total Hemispherical Emittance of New SRD.

Figure 5 shows the temperature dependence of the total hemispherical emittance of the new SRD. In this figure, SRD2 was made of $La_{0.775}Sr_{0.115}Ca_{0.11}MnO_3$ by the old production process. On the other hand, SRD3 was made with the same compounds, but used the new production process. A striking phenomenon is the small increase in the transition temperature T_C of SRD3 compared with SRD2. We interpret this effect as an increase in charge-carriers due to a loss of La.

Summary and Conclusions

In summary, we confirmed that the manganese oxide with a perovskite-type structure could be used for the material of the SRD, by measuring the optical properties and through irradiation tests. Moreover, we have successfully developed a new SRD, by introducing a new design and a new manufacturing process. The new SRD is lighter and stronger than the old one. In addition, the new design and new manufacturing process make the element faster and easier to handle, and reduce its cost.

The SRD will be used in ISAS's scientific satellite MUSES-C which is going to perform a sample return mission to a near earth asteroid. After that, the film SRD will be tested by the flight of INDEX which is a small engineering satellite and will be exposed to all kinds of degrading environmental loads.

Acknowledgment

The authors would like to thank K.Shimazaki for his cooperation.

References

1. Y.Okimoto et al.: Physical Review B, 55(7), 4206(1997).
2. K.Shimazaki et al.: Proc. Of 8th International Symposium on Materials in Space Environment, (2000).
3. S.Tachikawa et al.: SAE Paper No.2000-01-2277, 30th ICES.
4. S.Tachikawa et al.: SAE Paper No.2001-01-2342, 31st ICES.

Proceedings of 7th Japan International SAMPE
Symposium & Exhibition, Nov. 13-16, 2001

JSCE Recommendations for Upgrading of Concrete Structures with use of Continuous Fiber Sheets

K. Maruyama [1] and T. Ueda [2]

1: Department of Civil and Environmental Engineering, Nagaoka University of Technology, Nagaoka, 940-2188, JAPAN
2: Department of Civil Engineering, Hokkaido University, Hokkaido, 060-0813, JAPAN

Introduction

Continuous fiber reinforced polymers (FRP's) have become attractive for design engineers as retrofit or strengthening materials for the existing RC structures after the disaster caused by the Great Hanshin Earthquake in 1995. High strength, lightweight and easy handling of FRP sheets become strongly beneficial for retrofit or strengthening of RC structures. Authorities in Japan, such as Railway Technical Research Institute, Japan Highway Public Corporation as well as the Ministries of Construction and Transportation, have been studying the effectiveness of FRP sheets for retrofit or strengthening of existing RC structures. With a lot of experimental works they have made their own design guidelines for their specific applications with specified type of fiber [1-4]. Considering the situation of FRP sheets applications in Japan, the Japan Society of Civil Engineers (JSCE) decided to establish the unified and more widely applicable design recommendations of FRP sheets for retrofit or strengthening of the existing concrete structures as well as repair and enhancement of durability of concrete structures. Since 1998 the authors have been working as a chairman and co-chairman in the JSCE research committee to establish the design recommendations of FRP sheet for upgrading of RC structures. The recommendations are now published both in Japanese and in English.

Different from the other recommendations, the recommendations are formatted and described based on the performance of RC structures with FRP sheets [5-7]. It means that the descriptions in the design part are made as how to evaluate the contribution of FRP sheets in terms of flexure, shear and ductility of RC members as well as enhancement of durability.

The recommendations involve other features, such as the construction part, the proposed test methods for FRP sheets and field applications. This paper describes the

Different from the contribution to shear capacity, the contribution of sheet to ductility depends upon the existing structural performance. As mentioned before, FRP sheet wrapping increases both the shear capacity and the confinement effect of cracked concrete. These effects should provide the member a large deformation capacity.

Contribution to Durability

The JSCE has adopted the way how to verify the durability of concrete structures in the standard specifications in 1999 [8]. In particular, the intrusion of chloride ion into concrete is expressed in the diffusion equation. Then, a role of FRP sheet can be evaluated as shielding against the intrusion of chloride ion for a certain period. The shielding effect of FRP sheet is taken as a formula below.

$$C_d = \gamma_{cl}\left[(C_0 - C_i)\left\{1 - erf\left(\frac{0.1 \cdot c}{2\sqrt{D_d (t - t_f)}}\right)\right\} + C_i\right] \quad (7)$$

$$(\text{however}, t > t_f)$$

$erf(x)$: the error function, expressed as

$$erf(x) = \frac{2}{\sqrt{\pi}} \int_0^x e^{-\xi^2} d\xi .$$

where: γ_{cl}: safety factor that covers the uncertainty of calculations of chloride ion concentration at the locations of steel reinforcement (may generally be set to 1.3), C_0: chloride ion concentration on the surface of the structure (kg/m^2), C_i: chloride ion concentration (kg/m^3) at the locations of steel reinforcement at the time of upgrading, c: cover thickness (mm), D_d: diffusion coefficient of chloride ions for cover concrete (cm^2/year), t: remaining design life (years), t_f: the period the continuous fiber sheets expected to block chloride ions (years).

Referring to the existing data for surface coating materials, the period (t_f) is determined as 10 years for one layer of FRP sheet under ordinary environment, and 5 years under sever condition. When two layers of FRP sheet are adopted, the values of period could be multiplied by 1.5. It is necessary to get further in-situ data.

Construction Practice

The proposed evaluation equations in the recommendations are based on the proper construction practice. In particular, the bond between FRP sheet and concrete is most of importance. A lot of attention has to be paid on how to treat adhesive materials, on how to treat the surface of concrete, on how to attach sheets and to cure them. The chapter of construction practice represents a summary of extended experiences from the actual execution of upgrading works on site. Inspection at each stage of construction is necessary for completing the good works. Finally, there are still many things left to the workmanship for conducting the upgrading works by use of FRP sheet. It may be necessary to establish a system to examine the workmanship for ensuring the proper construction practice of FRP sheets.

Test Methods

The committee proposed 9 test methods to determine the mechanical and durable properties of FRP sheet. Those are to determine (1) tensile strength of sheet, (2)

essence of the recommendations.

Contribution of FRP Sheet to the Flexural Capacity

The contribution of FRP sheet to the flexural capacity of concrete members can be evaluated by the traditional flexural theory such that plane sections remain planes, only when the peeling of sheet is not expected. The detailed observation may show that the tensile strain in FRP sheet measured is a little smaller than expected. However, for the design purposes the difference can be neglected for both the serviceability limit state and the ultimate limit state. The current research shows that the happening of peeling can be estimated by examination of tensile stress of the sheet at the location of flexural cracking. In other words, when the tensile stress of sheet can satisfies the Eq.(1), then peeling can be neglected.

In the equation, the interfacial fracture energy Gf is introduced. The value can be obtained by the proposed test method for the bond properties of FRP sheet. When there is no test date, then 0.5 N/mm is recommended.

$$f_f \le \sqrt{2G_f E_f / n_f \cdot t_f} \qquad (1)$$

where, f_f: tensile stress of sheet calculated at flexural cracking, G_f : fracture energy of peeling of sheet, E_f : elastic modulus of sheet, n_f : number of layers of attached sheet, t_f : thickness of sheet

Contribution to Shear Capacity

The contribution of FRP sheet to the shear capacity of RC member can be evaluated by the traditional truss model as shown in Eq. (1). However, the ultimate stress of sheet in the truss model should be estimated properly because the FRP sheet is quite elastic up to failure and has no stress redistribution (Fig. 1).

$$Vu = Vc + Vs + Vf \qquad (2)$$

$$Vf = K \cdot Af \cdot f_f \cdot z \cdot (\sin\alpha + \cos\alpha)/s_f \qquad (3)$$

Where, Vu: ultimate shear capacity of RC members with FRP sheet, Vc: concrete contribution, Vs: contribution of shear reinforcing bars, Vf: contribution of FRP sheet, K: coefficient of effectiveness of CFRP sheet, Af: cross sectional area of FRP sheet, f_f : tensile strength of FRP sheet, z: lever arm length, α: angle of fiber to longitudinal direction, s_f: =1 or spacing of FRP strip.

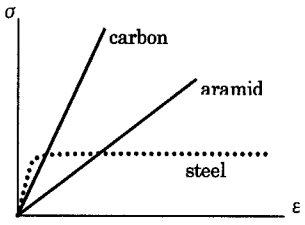

Stress-strain Diagram of FRP

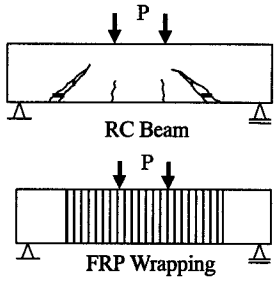

Fig. 1 Stress-Strain Diagram of FRP and RC Beams

Comparing with steel reinforcement, FRP's (both carbon fiber and aramid fiber) are quite elastic up to failure with less ultimate strain as shown in Fig.1. This property prevents strain redistribution which is typical phenomenon with steel reinforcement because steel has yielding property. In other words all steel stirrups within the length equivalent to the effective depth in a shear span, can carry the yield stress at the ultimate. On the other hand, FRP sheet can not transfer stresses uniformly within a shear span and has the stress concentration. Therefore, the equation derived from the truss model should account for the non strain redistribution of FRP using K factor. Otherwise, the contribution of FRP sheet to the shear capacity can not be evaluated properly.

The committee surveyed current research works on FRP sheet contribution to shear as well as field applications. Based on the examination and discussion the committee has proposed two ways to evaluate the FRP sheet contribution to shear. One is to introduce a correction factor to take account of non-strain redistribution, and the other is to calculate the contribution numerically using the bond characteristics of FRP sheet to concrete. In the former case, previous test results were surveyed widely and reevaluated the contribution of FRP sheet in terms of the tensile strength, the modulus of elasticity, the cross sectional area of FRP sheet as well as the concrete strength. With a lot of parametric studies, the correction factor (K) is proposed in the following form.

$$0.4 \le K = 1.68 - 0.67R \le 0.8 \qquad (4)$$

$$R = (\rho_f \cdot E_f)^{1/4} \left(\frac{f_{fud}}{E_f}\right)^{2/3} \left(\frac{1}{f'_{cd}}\right)^{1/3} \qquad (5)$$

$$0.5 \leqq R \leqq 2.0$$

Where, $\rho_f = A_f/(b_w \cdot s_f)$, E_f: modulus of elasticity of FRP sheet, f_{fud}: design strength of FRP sheet, f'_{cd}: concrete strength.

The effectiveness of the equation is shown in Fig.2. Since the collected data are limited in the shape and dimension of test specimens. Then the equation has a limit for application. The collected data range as d=200-540 mm, a/d=1.1-3.6, f'c=21-45MPa, f_f=2480-4300MPa, E_f=87-252GPa. When applying the equation to RC members outside these ranges, additional examination must be required.

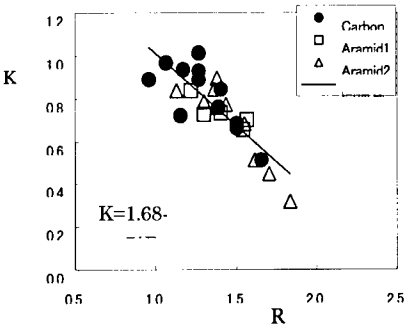

Fig. 2 Correlation of K with R by test results

The alternative method to evaluate the FRP sheet contribution to shear can be briefly explained as follows. As shown in Fig. 3, it is assumed that a portion with a major diagonal crack in the shear span undertakes a rigid body movement. FRP sheet which wraps the portion confines the movement. The contribution of FRP sheet should be

evaluated introducing the bond property of the sheet to concrete in terms of bond stress and local slippage. It requires a lot of numerical calculation by computer, but this way is applicable for wide range of structures.

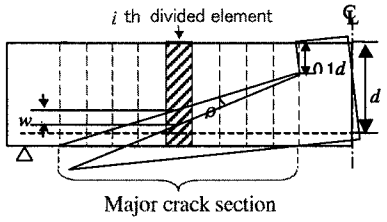

Fig. 3 Model of beam

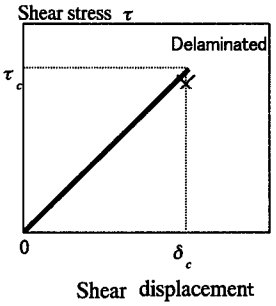

Fig. 4 Constitutive law for bond

Contribution to Ductility

Mechanism on how FRP sheet contributes to the ductility of RC members is much more complicate than that on how the sheet contributes to the shear capacity. Even for ordinary RC members, the ductility is still difficult to determine analytically. It is, however, observed in the experimental works that RC members with relatively higher shear capacity to flexural capacity exhibit large ductility. This fact is taken in the JSCE seismic design code for concrete structures expressing that the ductility ratio is a linear function of the ratio of shear capacity to flexural capacity.

The contribution of FRP sheet to ductility can not be attributed only to the increase of shear capacity by sheet, but also to the confinement of cracked concrete by sheet wrapping (Fig.5). Conducting the parametric study of existing experimental data, the following equation is proposed.

$$\mu = 1.16 \cdot \frac{(0.5V_c + V_s)}{V_{mu}} \cdot \left(1 + \alpha_o \cdot \frac{\varepsilon_f \cdot p_f}{V_{mu}/(B \cdot z)} \right) + 3.58 \qquad (6)$$

where, μ : ductility ratio (ratio of yield deformation to ultimate deformation), Vmu: shear force at the ultimate flexural capacity, B: width, αo: coefficient (same value of Young's modulus of steel can be taken).

The equation is verified as shown in Fig.3. The equation has also a limit for application since the collected data are within the ranges of d = 300 – 800 mm, a/d = 4.0 – 5.7, f'c = 18 – 24 MPa, ff = 2050 – 3430 MPa, Ef = 78 – 252 Gpa, axial stress = 3.2 - 5.9 MPa.

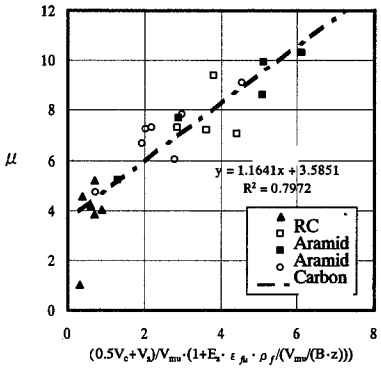

Fig. 5 Correlation of μ

anchorage strength between sheets, (3) bond strength between sheet and concrete, (4) bond strength between sheet and steel plate, (5) adhesive strength between sheet and concrete, (6) tensile fatigue strength of sheet, (7) accelerated exposure test, (8) freezing and thawing test, and (9) resistance against water, acid and alkali. Most of test methods are concerned with the property of sheet itself, but the bond test represents the interface strength among sheet, adhesive material and the surface condition of concrete. Since the tensile strength of sheet and the bond strength between sheet and concrete are important to the contribution of sheet to the flexural and shear capacity of RC members, some aspect of the test method is discussed.

Tensile Strength Test Specimens

The shape and size of specimen are shown in Figure 6 and table 1. The previous studies show that the specimen gives good results for both carbon fiber sheet and aramid fiber sheet.

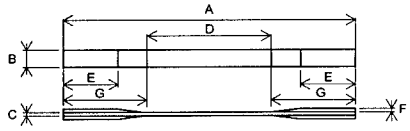

Fig. 6 Tensile test specimen

Bond Strength Test

Test specimen is shown in Figure 7. Two concrete blocks (100 x 100 x 300 mm) are aligned to match the center of cross section. Each has a steel bar mounted at the center of cross section. After alignment of two blocks, two FRP sheets (more than 50 mm width x 400mm length) are attached on the opposite sides. In order to obtain consistent data, sheets in one side should be anchored sufficiently. The left parts of sheets are measured. The load is applied by pulling a steel bar at the both ends. Strain gages should be attached on the both surfaces of sheet. Based on the strain distribution of sheet as shown in Fig. 8, the bond strength is determined.

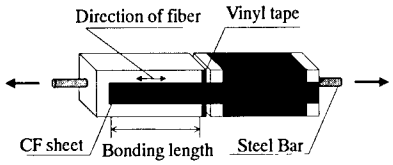

Fig. 7 Test Specimen for Bond

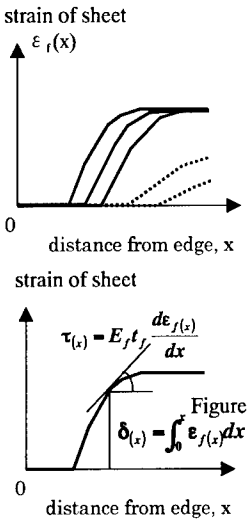

Fig.8 Strain Distribution of Sheet

Concluding Remarks

FRP sheets have advantageous material properties, such as high strength, lightweight, high resistance to corrosion. Making the application of FRP sheets to upgrading structures more effective, the contribution of the sheet should be evaluated sufficiently in the performance of structures as a whole. JSCE has surveyed the current technical state of the art and published the recommendations for the retrofit and strengthening of RC structures by FRP sheets. The recommendations are, of course, not perfect. With further understandings on the mechanism and with computational invention, the evaluation could be improved by numerical analyses.

Appendix: Contents of Recommendations

Part 1 Recommendations for Upgrading of Concrete Structures with Use of Continuous Fiber Sheets

Ch.1 General
Ch.2 Basics of Upgrading
Ch.3 Materials
Ch.4 Loads and Environmental Actions
Ch.5 Detailed Inspection of Existing Concrete Structures
Ch.6 Performance Verification for Upgraded Concrete Structures
- 6.1 General
- 6.2 Design strength of materials in existing structures
- 6.3 Safety factors
- 6.4 Verification of safety
- 6.5 Verification of serviceability
- 6.6 Restorability
- 6.7 Change of performance of upgraded structures with the elapse of time
- 6.8 Verification of structural details

Ch.7 Upgrading Work
Ch.8 Work Records
Ch.9 Maintenance of Upgraded Concrete Structures

Part 2 Test Methods for Continuous Fiber Sheets

1. Test Method for Tensile Properties of Continuous Fiber Sheets
2. Test Method for Overlap Splice Strength of Continuous Fiber Sheets
3. Test Method for Bond Properties of Continuous Fiber Sheets to Concrete
4. Test Method for Bond Strength of Continuous Fiber Sheets to Steel Plate
5. Test Method for Direct Pull-out Strength of Continuous Fiber Sheets with Concrete
6. Test Method for Tensile Fatigue Strength of Continuous Fiber Sheets
7. Test Method for Accelerated Artificial Exposure of Continuous Fiber Sheets
8. Test Method for Freeze-Thaw Resistance of Continuous Fiber Sheets
9. Test Method for Water, Acid and Alkali Resistance of Continuous Fiber Sheets

References

1. Railway Technical Research Institute (RTRI). (1996), *Design/Construction Guidelines on the Seismic Retrofitting of Railway Viaduct Columns using Carbon Fiber Sheet*. (in Japanese).
2. Railway Technical Research Institute (RTRI). (1996), *Design/Construction Guidelines on the Seismic Retrofitting of Railway Viaduct Columns using Aramid Fiber Sheet*. (in Japanese).
3. Railway Technical Research Institute (RTRI) . (1997), *Design/Construction Guidelines on the Seismic Retrofitting of Subway RC Columns using Carbon Fiber Sheet*. (in Japanese).
4. The Hanshin Highway Public

Corporation. (1997), *Design/Construction Guidelines on the Seismic Retrofitting of RC Bridge Piers using Carbon Fiber Sheet*. (in Japanese).
5. The Building Research Institute of Japan. (1998), *US-Japan Research Collaboration on the Hybrid Structures – The Retrofitting Design Guidelines on the Application of Continuous Fiber Sheets*.
6. ACI Committee 440.(1999), *Guidelines for the Selection, Design, and Installation of Fiber Reinforced Polymer (FRP) Systems for Externally Strengthening Concrete Structures*, ACI.
7. JSCE Concrete Committee. (2001), *Recommendations for Upgrading of Concrete Structures with Use of CFRP Sheet*, JSCE
8. JSCE (1999), *Standard Specifications for Design and Construction of Concrete Structures – Verification of Durability* -, JSCE. (in Japanese)
9. JCI Committee TC952 (1998), *Technical Report on Continuous Fiber Reinforced Concrete*, JCI

Table 1 Dimension of specimen (unit: mm)

A	B	C	D	E	F	G
≧200	12.5±0.5	≦2.5	≧100	≧35	1 - 2	≧50

Proceedings of 7th Japan International SAMPE
Symposium & Exhibition, Nov. 13-16, 2001

Development and Application of Carbon Fiber Composites for Large-span Structures

Kenichi Sugizaki#

#: General Manager, Institute of Technology, Shimizu Corporation, Tokyo, Japan
3-4-17 Nakajima, Koto-ku, Tokyo 135-8530, JAPAN
E-mail: sugizaki@tech.shimz.co.jp

The authors are engaged in the development and application of large-span structural systems for twenty-first century using a new material, CFRP. In this report, the pilot project: TRY2004 is introduced, and the Double-layer Space Frame and the Monocoque Roof using CFRP as a structural material are outlined. Structures with CFRP perform well from the point of view of specific strength, specific stiffness, heat insulation, corrosion resistance, etc. The authors believe that the composites will be one of the best structural materials of the 21st century.

The authors confirmed the structural performance of CFRP as a material, component, and the double-layer space frame in structural experiments. This structure has been used for the roof of a factory cafeteria (Photo 1 and Photo 2).

Photo 1 Internal View of "TRUSS HOLL" in Ehime Pref.

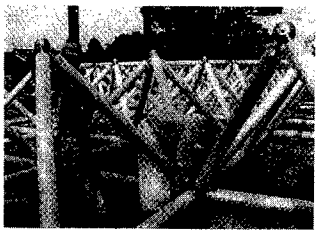

Photo 2 Under Construction

Continued in space frame, the authors started to develop the monolithic formed (Monocoque) roof structure made of CFRP. In this structure, the finish and the structure are unified, and it is big characteristic that we could realize the free curved surface such as RC shell by the light sandwiched structure. We made the sandwiched structure that the surface of CFRP layer (we will call it skin layer from now on) is the main structural material the basis. Figure 1, 2 show the design form example and the basic section detail.

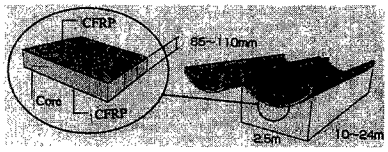

Fig. 1 Design Form Example

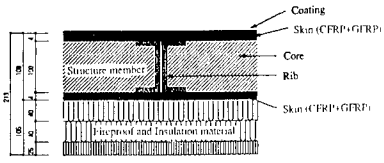

Fig. 2 Section Detail

The objects of it are the gymnasium of elementary school and junior high school, and the existing PCa roof materials are removed without strengthening the existing columns and beams in the short period of summer vacation, and also replace it to the large Monocoque roof made of CFRP.
Picture 3, 4 shows the case of Kusatsu-city elementary school gymnasium in Shiga pref. (completion Sep. 1999) and Toin-cho elementary school gymnasium in Wakayama pref. (completion Sep. 2000) among the application of CFRP roof for seismic rehabilitation of the existing roof. All the constructions were completed during the summer vacation, and it is said that the brightened gymnasium is reputed very well among the children.

Photo 3 School Gymnasium after Replacement in Kusatsu-city

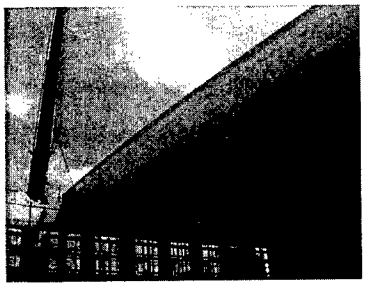

Photo 4 School Gymnasium under Construction in Toin-cho

The characteristics of the facilities using CFRP structural material are shown as following:

1) It is able to realize lightweight space structure of free curve that used to be difficult.
2) It is able to realize the long-life space of free maintenance.
3) The seismic strengthening in replacing the existing roof would be easy.
4) It is able to complete the construction in short term because of the lightweight roof and able to begin to use it earlier.

It is able to create a space that could not realize in the past by making use of the characteristic written above effectively, and the authors think that this specialization is the first step to be admitted as the structural material of 21st century. The author will end this paper wishing many people who approve to this thought increase, and we strongly wish to promote projects cooperating with many researchers, engineers and architects all over the world.

Proceedings of 7th Japan International SAMPE
Symposium & Exhibition, Nov. 13-16, 2001

Strength Evaluation on Bolt Joints of Pultruded GFRP Members

Iton Chou[1], Keiji Kamada[2] and Tadashi Kimura[2]

1: Technology Planning Group, Technical Development,
Ishikawajima-Harima Heavy Industries Co., Ltd.
3-2-16, Toyosu, Koto-ku, Tokyo 135-8733 JAPAN

2: Fundamental Research & Engineering Group,
Ishikawajima Inspection & Instrumentation Co., Ltd.
3-1-15, Toyosu, Koto-ku, Tokyo 135-8732 JAPAN

E-mail: iton_chou@ihi.co.jp

Abstract

The experimental investigation on the tensile strength of bolt joints in pultruded GFRP(Glass Fiber Reinforced Plastics) members used for pedestrian bridges are described in this paper. Adding biased cloth layer into the members was effective in improving the tensile strength of bolt joints. Also, taking longer edge distance for bolt holes was effective and gave higher tensile strength. The fracture modes of joints using large diameter bolts were shear failure for all types of specimen.

Key Words: FRP, Pultrusion, Bolt joints, Strength evaluation

Introduction

A lot of steel bridges and pre-stressed concrete bridges on seaside in Japan are attacked by the salt injury and have corrosive damages. Therefore, for the instance, GFRP was applied for the crossing bridge of the road park in Ikei-Tairagawa route in Okinawa prefecture, due to the strong resistance to the salt injury and corrosion damage[1-3]. In the development of the bridge, structural experiments on the strength evaluation of bolt joints were performed in order to affirm the soundness of the structure[4]. The strength evaluation on bolt joints is important especially for joints using large diameter bolts in civil engineering and bridge structure fields. However, most of design manuals describe the strength evaluation on joints using small diameter rivets[5-8].

In this paper, the experimental results on the tensile strength of bolt joints in pultruded GFRP members are reported. Effects of stacking sequences in the members and the edge distance on the tensile strength of bolt joints were examined. Also, the fracture modes and processes in the GFRP members were observed for the future designing of bolt joints and new development on bridges.

Experiments

Figure 1 shows the configuration

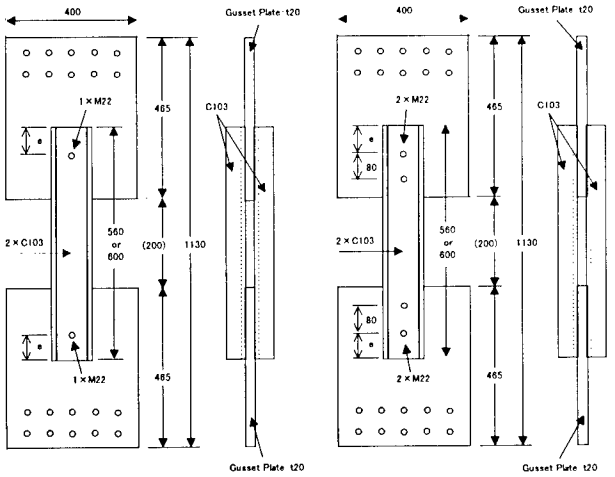

(a) Single bolt fastened specimen (b) Double bolt fastened specimen

Fig. 1 Configuration and dimension of test specimens (unit in mm)

Table 1 Stacking sequence of Type A specimen

Fiber angles	Kinds of layer	layer/bundle	Inner/Outer surface
Random	Chopped Strand Mat	1 layer	Inner
0/90°	Roving Cloth	1 layer	
±45°	Biased Cloth	2 layers	
0°	Roving	672 bundles	
0/90°	Roving Cloth	1 layer	
Random	Chopped Strand Mat	1 layer	Outer

Table 2 Stacking sequence of Type B specimen

Fiber angles	Kinds of layer	layer/bundle	Inner/Outer surface
Random	Chopped Strand Mat	1 layer	Inner
0/90°	Roving Cloth	1 layer	
±45°	Biased Cloth	3 layers	
0°	Roving	632 bundles	
±45°	Biased Cloth	1 layers	
0/90°	Roving Cloth	1 layer	
Random	Chopped Strand Mat	1 layer	Outer

(a) Single bolt fastened specimen

(b) Double bolt fastened specimen

Fig. 2 Tensile testing conditions

and dimension of test specimens. Single and double M22 bolt fastened specimens were employed in the tensile test. Edge distance, "e" in Fig. 1, was set to be 50 and 70 mm. The pitch between M22 bolts in the case of double bolt fastened specimen was 80 mm. C103 member (103×50×9.3) is channel cross section Glass fiber/Vinyl-ester resin composites manufactured by the pultrusion process. Two types of stacking sequences for the C103 member as described in Tables 1 and 2 were employed. Type A stacking sequence is the same to that used for the members of the truss structure under deck for the GFRP pedestrian bridge constructed in Okinawa prefecture. In addition, the case of edge distance e=50mm is the same to that applied for the bridge in Okinawa.

Four specimens for each case of specimen were used for evaluating the tensile strength of bolt joints. Totally eight cases of specimen type were considered in this study. Test specimens were fabricated by Asahi Glass Matex Co., Ltd.

Tensile tests were carried out in a constant cross head rate (approximately 2mm/min) using a 6MN capacity structural testing machine. Testing conditions are shown in Fig. 2.

Table 3 Summary of tensile strength in M22 bolt joints

Number of bolt hole	Edge distance e (mm)	Type of stacking sequence	Maximum load (kN)		
			Mean	Maximum	Minimum
1	50	Type A	92	100	82
	50	Type B	110	113	107
	70	Type A	123	130	113
	70	Type B	145	166	131
2	50	Type A	175	191	166
	50	Type B	191	243	162
	70	Type A	227	236	214
	70	Type B	268	303	226

Results and discussions

Tensile strength data obtained by the experiments are summarized in Table 3. Here, maximum loads are used for the strength evaluation. The followings can be drawn from the result.

(1) The tensile strength of double bolt fastened specimens is almost twice higher than that of single bolt fastened specimens in the case of Type A stacking sequence.

(2) The tensile strength of double bolt fastened specimens is about 1.8 times higher than that of single bolt fastened specimens in the case of Type B stacking sequence.

(3) The tensile strength of Type B stacking sequence specimens is 10 to 20 % higher than that of Type A stacking sequence specimens. Adding biased cloth layers is effective in improving the tensile strength of bolt joints.

(4) Test specimens in case of the edge distance e=70mm gives 30 to 40 % higher tensile strength than those in the case of the edge distance e=50mm. Taking longer edge distance is more effective than adding biased cloth layers into GFRP pultruded members for improving the tensile strength of bolt joints.

(5) Maximum load data in Type B stacking sequence specimens deviates more than that in Type A specimens. The trend is obvious especially for double bolt fastened specimens.

Fracture modes of the specimens are shown in Fig. 3. The dominant fracture mode is shear

failure for M22 bolt joints, clearly observed from Fig. 3. The characteristic fracture mode is the delamination at the interface between the biased cloth layer and the roving layer. Some layers of roving bundles can be seen at both ends of C103 members. This phenomenon indicates that the tensile strength would be improved if the delamination can be arrested, for instance, by modifying the stacking sequence of the member.

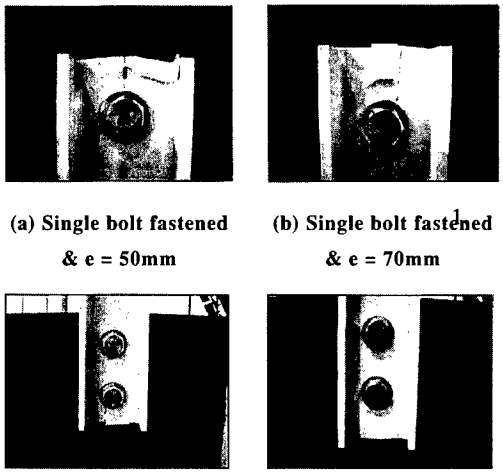

(a) Single bolt fastened & e = 50mm **(b) Single bolt fastened & e = 70mm**

(c) Double bolt fastened & e = 50mm **(d) Double bolt fastened & e = 70mm**

Fig. 3 Fracture modes of test specimens

Conclusions

The experimental study on the strength evaluation of M22 bolt joints gives the following remarks.

(1) Adding biased cloth layers into pultruded GFRP members is one of the methods in improving the tensile strength of bolt joints.
(2) Taking longer edge distance is also one of the methods in improving the tensile strength of bolt joints. This method is more effective than adding biased cloth layers.
(3) The dominant fracture mode in M22 bolt joints is shear failure.
(4) The characteristic fracture mode is the delamination at the interface between the biased cloth layer and the roving layer. This phenomenon indicates that the tensile strength would be improved if the delamination can be arrested, for instance, by modifying the stacking sequence of pultruded GFRP members.

References

1. N. Kitayama, S. Saeki, and K. Yamashiro: Proc. of 55th Annual Conf., The Japan Society of Civil Engineers, I -A, No.230 (2000) (in Japanese)
2. K. Nonaka: Nikkei Construction April 28th, 28 (2000) (in Japanese)
3. The Engineering Plastic Journal: No.712, (2000) (in Japanese)
4. I. Chou, K. Kamada, T. Kimura, S. Saeki, and K. Yamashiro: Proc. of 2000 Annual Meeting, Japan Society of Mechanical Engineers, Materials and Mechanics Division, 341 (2000) (in Japanese)
5. Morrison Molded Fiber Glass Company: Design Manual
6. The European Structural Polymeric Composites Group: EUROCOMP Design Code and Handbook
7. F. L. Matthews (eds.): "Joining Fibre-Reinforced Plastics", Elsevier, 1987
8. The Japan Reinforced Plastic Society: FRP Structural Design Manual, 1994 (in Japanese)

Proceedings of 7th Japan International SAMPE
Symposium & Exhibition, Nov. 13-16, 2001

Investigation on the Buckling Strength of the Steel Square Pipe Filled with the Urethane Resin Foam

Naoki Yamamoto[1], Nayomon Uno[2], Kotaro Inose[3], Keiji Kamada[4], Tadashi Kimura[4]

1: Ishikawajima-Harima Heavy Industries Co., Ltd, Technical Research Laboratory, Structure & Strength Dept. ,3-1-15, Toyosu, Koto-ku, TOKYO 135-8732 JAPAN

2: Ishikawajima-Harima Heavy Industries Co., Ltd, Bridge & Road Construction Div., 1-9-10, Mouri, Koto-ku, TOKYO 135-8322 JAPAN

3: Ishikawajima-Harima Heavy Industries Co., Ltd, Advanced Production Engineering Center, Production Engineering Dept., Shin-Nakahara-chou-1, Isogo-ku, Yokohama City, KANAGAWA 235-8501 JAPAN

4: Ishikawajima Inspection & Instrumentation Co., Ltd., Fundamental Research & Engineering Group, 3-1-15, Toyosu, Koto-ku, TOKYO 135-8732 JAPAN

E-mail: naoki_yamamoto@ihi.co.jp

Abstract

This paper describes the experimental and analytical results on the buckling behavior of the resin-filled and the hollow steel pipes. The experimental results indicated that the resin-filled pipe was superior to the hollow one for the buckling strength and the ductility. The resin-filled pipe collapsed due to the delamination between the resin foam core and the steel pipe, or due to the cracking in the resin foam core. In addition analytical models which could explain the load-displacement relationships obtained in the experiments were built for both of the resin-filled pipe and the hollow one.

Key Words: Urethane Resin Foam, Buckling , Steel Square Pipe , FEM Analysis

Introduction

Conventional methods for reinforcing steel pipes are to fill concrete in and to weld stiffeners to the pipes. In this study, the hollow steel square pipes filled with and without the urethane resin foam core were employed for the examination on the buckling behavior(1). The resin-filled steel pipes were light, and the buckling strength was improved due to avoiding the local buckling by filling the urethane resin foam into the hollow pipes.

In addition to the buckling tests, the non-linear analysis using FEM (Finite Element Method) was performed for both of the resin-filled pipe and the hollow one. The analytical load-displacement relationship agreed well with experimental results.

Experimental Study

Test Specimens

In order to decide the size of the test specimens, the followings were considered:

① Because the purpose of tests is to confirm that the resin-filled pipe is superior for the buckling strength to the hollow one, it is necessary that hollow pipes buckle in the elastic region not in the plastic region.

② The capacity of the 6MN structural testing equipment is enough for the plastic buckling strength of the hollow steel pipe.

③ The column buckling mode does not appear before the plate buckling mode appears.

The drawing of the test specimen is shown in Fig.1.

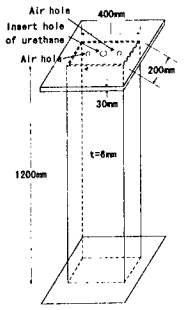

Fig.1 Test specimen

To both ends of the test specimens, 30mm thick steel flanges were welded for transforming the compression load to the specimens.

Two test specimens were steel pipes filled with the urethane resin foam, and other two test specimens were hollow steel pipes.

The density of the urethane resin foam was 0.15g/cm^3. When the pipe was filled with the urethane foam, the equipment for reinforcing was used because the urethane resin foam expanded and high-level stress occurred as inserting urethane foam (see Fig.2).

Fig.2 Conditions of filling urethane resin foam into the hollow pipe

Experimental Methods

The buckling tests were carried out using the 6MN structural testing equipment. The outline of the test is show in Fig.3.

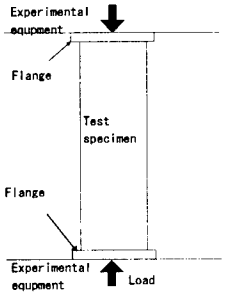

Fig.3 The outline of the test

The displacement in the loading direction was measured by the dial gauges which placed on the flanges.

Experimental Results

The load-displacement relationships are shown in Fig.4.

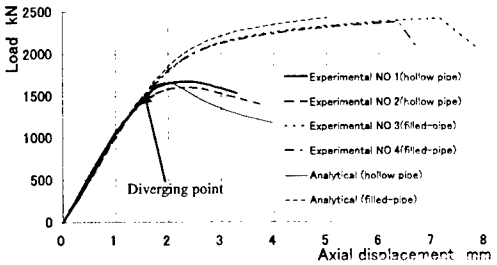

Fig.4 Load-displacement relationship for hollow pipes and filled pipes

It was clarified that the buckling strength and ductility were superior to those of hollow pipes.

The buckling mode of the hollow pipe is shown in Fig.5

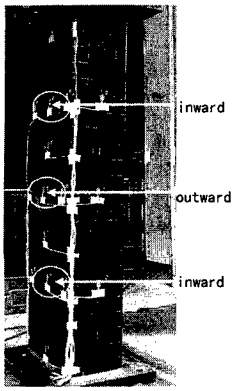

Fig.5 The buckling mode of the hollow pipe

There were 3 buckling waves for the hollow pipes. On the other hand, the collapse mode of the resin-filled pipes occurred at near flange as shown in Fig.6.

Fig.6 Collapse mode of the pipe filled with urethane resin foam

By cutting the cross section at which the collapse mode occurred, it was observed that the resin-filled pipe collapsed due to the delamination between the resin foam core and the steel pipe, or due to the cracking in the resin foam core as shown in Fig.7.

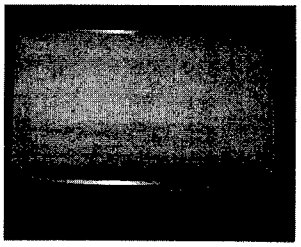

Fig.7 (a) Cross section view of the collapse mode(delamination)

Fig.7 (b) Cross section view of the collapse mode(cracking)

Analytical Study

Analytical model

FEM analysis with the assumption of a large displacement behavior and an elasto-plastic relationship was performed.

The analysis model of the filled-resin pipe is shown in Fig.8.

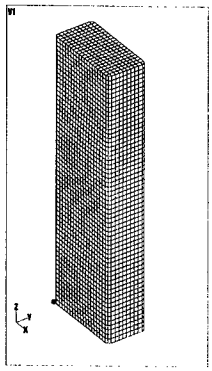

Fig.8 FEM analysis model (filled-resin pipe)

The shell elements were used for the steel pipes, and the solid elements were used for the urethane resin foam.

The result of tensile tests of steel was used as the stress-strain relationship of the shell elements. The yield stress of steel was 330N/mm^2.

Until the diverging point (at which the experimental tangent modulus of the hollow pipes began to differ from the filled-pipes), it was assumed that the Young's modulus of the urethane resin foam was zero. And after the diverging point, the Young's modulus of the urethane resin foam was assumed to be equal to the experimental tangent modulus.

Analytical Methods

Instead of the load, enforced displacements were given at the end face of the pipe. At the other end face, all freedoms of nodes were fixed.

The initial imperfections were given as half waves with L/1000 amplitude (L: length of the pipe) and buckling mode with B/150 amplitude (B: width of the pipe).

ABAQUS was used, as FEM analysis code.

Analytical Results

For the hollow pipe, the buckling mode in the experiment was same to that obtained by the FEM analysis as shown in Fig.9.

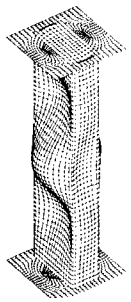

Fig.9 Buckling mode of the hollow pipe

The load-displacement relationship are shown in Fig.4, together with the experimental results .

For the hollow pipes, analytical results agreed well with the experimental results up to the maxim-load. And for the resin-filled pipes, analytical results also corresponded to the experimental results, too.

Conclusions

Experimental and analytical studies were carried out on the resin-filled and the hollow pipes. The followings were obtained.

① Superiority of the resin-filled pipe was confirmed for the buckling strength and the ductility.

② The resin-filled pipe collapsed due to the delamination between the resin foam core and the steel pipe, or due to the cracking in the resin foam core.

③ The analysis models which express the experimental load-displacement relationships were built for both of the resin-filled pipe and the hollow one.

Acknowledgement

We would like to express our appreciation to Dai-Nippon Ink and Chemicals, In. for the work to fill the urethane resin foam into the hollow pipe and for the useful advice.

References

(1) N.Yamamoto, K.Inose, N.Uno, K.Kamada, T.Kimura, "Evaluation on the buckling strength of the pipes filled with the urethane resin foam" Proceedings of the 56th Annual Conference of the Japan Society of Civil Engineers, I-B225(2001) (in Japanese)

Proceedings of 7th Japan International SAMPE
Symposium & Exhibition, Nov. 13-16, 2001

Bending Response of Thick-Walled Laminated Composite Pipes

Ming Xia[#1], Hiroshi, Takayanagi[#1], Hiroshi, Tsuda[#1], Kei Urabe[#1] and Kiyoshi Kemmochi[#2]

#1: Smart Structure Research Center (SSRC)
National Institute of Advanced Industrial Science and Technology (AIST)
AIST Tsukuba Central-2, Tsukuba, 305-8568, Japan
Email: ming.xia@aist.go.jp

#2: Faculty of Textile Science and Technology, Shinshu University
3-15-1, Tokida, Ueda, 386-8567, Japan

Abstract

Based on the classical laminated-plate theory, an elastic solution is presented for multi-layered fiber-reinforced composite pipes under pure bending. Moreover, detailed stress/strain responses for a filament-wound fiber-reinforced sandwich pipe are investigated by numerical analysis. The analytical model was sandwich pipe consisting of resin material for the core layer and filament-wound composite for the skin layers. It was observed that the axial stress at the inner surface could be larger than that at the outer surface when the pipe had the filament-wound layers with highly anisotropy

Key Words: Anisotropic analysis, Elastic solution, Laminated composite cylindrical pipe, Bending

Introduction

Filament-wound composite pipes are used in many applications because of their high specific strength. Applications include, but are not limited to, storage containers, pipelines and pressure vessels. In these applications, it is essential to maintain structural integrity for preventing catastrophic failure. Filament-wound fiber-reinforced composite pipes have been the subjects of numerous experimental [1-5] and theoretical investigations [6-8]. However, most studies on cylindrical fiber-reinforced composite pipes have focused on pipes subjected to internal pressure and biaxial loading. For analysis of cylindrical pipes subjected to bending, Lekhnitskii [9] provided formulations for only one layer with anisotropy. In the present study, an elastic solution for multi-layered filament-wound composite pipes was presented using the theory of cylindrical orthotropic elasticity. Stress/strain responses for a filament-wound fiber-reinforced sandwich pipe were investigated. The materials for each layer were homogeneous or cylindrically orthotropic.

Stress Analysis

Figure 1 shows the cylindrical

coordinate for multi-layered fiber-reinforced composite pipe subjected to bending load. Alternate-ply layers are those in which the principal material directions of the adjacent layer have an opposite fiber orientation $(\pm\phi)$ with respect to the axial direction. The orthotropic unit of the lay-up angle $(\pm\phi)$ is referred to as an orthotropic layer of angle ϕ.

The stress σ_z along the direction of the z-axis is written as [9]

$$\sigma_z = Ar\sin\theta - \frac{1}{S_{33}}\left(S_{13}\sigma_r + S_{23}\sigma_\theta\right) \tag{1}$$

The constitutive equations are given by

$$\begin{aligned}\varepsilon_r &= R_{11}\sigma_r + R_{12}\sigma_\theta + S_{13}Ar\sin\theta \\ \varepsilon_\theta &= R_{12}\sigma_r + R_{22}\sigma_\theta + S_{23}Ar\sin\theta\end{aligned} \tag{2}$$

and

$$R_{ij} = S_{ij} - \frac{S_{i3}S_{j3}}{S_{33}} \qquad (i, j = 1, 2, 4) \tag{3}$$

where S_{ij} are the compliance constants with respect to the material symmetry.

A stress function $F(r,\theta)$ can be introduced to give the stress fields, which are expressed as follows

$$\begin{aligned}\sigma_r &= \frac{1}{r}\frac{\partial F}{\partial r} + \frac{1}{r^2}\frac{\partial^2 F}{\partial\theta^2} \\ \sigma_\theta &= \frac{\partial^2 F}{\partial r^2} \\ \tau_{r\theta} &= -\frac{\partial^2}{\partial r\partial\theta}\left(\frac{F}{r}\right)\end{aligned} \tag{4}$$

The stress function satisfies the equation of compatibility:

$$\frac{\partial^2\varepsilon_r}{\partial\theta^2} + r\frac{\partial^2(r\varepsilon_\theta)}{\partial r^2} - \frac{\partial^2(r\gamma_{r\theta})}{\partial r\partial\theta} - r\frac{\partial\varepsilon_r}{\partial r} = 0 \tag{5}$$

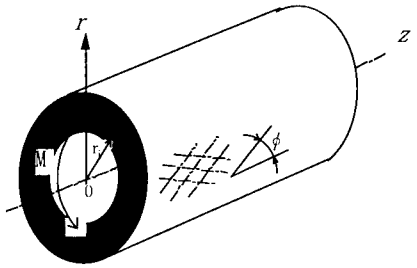

Fig. 1 Multi-layered fiber-reinforced composite pipe subjected to bending loading

Substituting Eqs. (1)-(4) into Eq. (5), we obtain the following differential equation

$$\begin{aligned}&R_{22}\frac{\partial^4 F}{\partial r^4} + (2R_{12} + R_{44})\frac{1}{r^2}\frac{\partial^4 F}{\partial r^2\partial\theta^2} + R_{11}\frac{1}{r^4}\frac{\partial^4 F}{\partial\theta^4} \\ &+2R_{22}\frac{1}{r}\frac{\partial^3 F}{\partial r^3} - (2R_{12} + R_{44})\frac{1}{r^3}\frac{\partial^3 F}{\partial r\partial\theta^2} - R_{11}\frac{1}{r^2}\frac{\partial^2 F}{\partial r^2} \\ &+(2R_{11} + 2R_{12} + R_{44})\frac{1}{r^4}\frac{\partial^2 F}{\partial\theta^2} + R_{11}\frac{1}{r^3}\frac{\partial F}{\partial r} \\ &= 2(S_{13} - S_{23})A\frac{\sin\theta}{r}\end{aligned} \tag{6}$$

Load function takes Lekhnitskii's stress function [9], as follows

$$F^{(k)}(r,\theta) = f(r)\sin\theta \tag{7}$$

Substituting the above stress function into Eq. (6), we obtain

$$\begin{aligned}&R_{22}r^4 f^{(4)} + 2R_{22}r^3 f^{(3)} - (R_{11} + 2R_{12} + R_{44})r^2 f'' \\ &+(R_{11} + 2R_{12} + R_{44})rf' - (R_{11} + 2R_{12} + R_{44})f \\ &= 2(S_{13} - S_{23})A\frac{\sin\theta}{r}\end{aligned} \tag{8}$$

Substituting the solution of Eq. (8) into Eqs. (4) and (2), we can analyze the stress and strain.

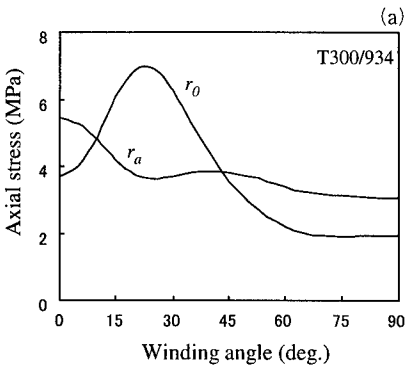

Fig. 2 Effect of the winding angle on the axial stresses of pipe with (a) T300/934 and (b) E-Glass/Epoxy

(r_0: Inner surface; r_a: Outer surface)

Numerical Results and Discussion

The formulation was applied to an example of a composite pipe with three layers. The pipe has an isotropic-core layer and two orthotropic-skin layers, which are made of the same material in the inner and outer layers. The elastic solutions are obtained for the sandwich pipe subjected to a bending moment of 1 kN. The pipe has an inner radius of 50 mm, a core-layer thickness of 20 mm, and skin-layer thickness of 2 mm. The material properties are given in Table 1.

Table 1 Material properties of skin layers and resin

Properties	T300/934	E-Glass/Epoxy	Resin
E_x (GPa)	141.6	43.4	1.2
E_y (GPa)	10.7	15.2	1.2
G_{zz} (GPa)	3.88	6.14	0.46
ν_{yx}	0.268	0.29	0.30
ν_{zy}	0.495	0.38	0.30

Figure 2 shows the axial stress curves varying with the winding angle under the bending load. The effect of the winding angle on stress variation is much larger for the carbon fibers (T300/934) than for the glass fibers (E-Glass/Epoxy) because carbon fibers have larger anisotropic properties. As shown in Fig. 2, both inner and outer surfaces of the sandwich pipe are subjected to almost constant axial stresses when the

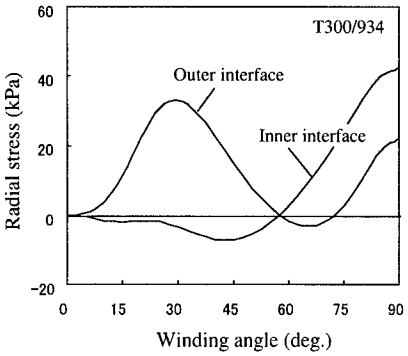

Fig. 3 Effect of the winding angle on the radial stresses of a pipe

winding angle is larger than 60^0, and the axial stress at the outer surface is higher than that at the inner surface. For a pipe within a certain range of winding angles, however, it is observed that the axial stress at the inner surface is higher than that at the outer. It is well known that this situation should be prevented in the case of pipes with isotropic or lower anisotropic materials.

Figure 3 shows the variation of the radial stress for the two interfaces between the core and skins. The radial stresses at the interfaces may be tensile or compressive for pipes with different winding angles. The outer interface is subjected to larger radial stress than the inner interface when the winding angle varies from zero to about 58^0, while the inner interface has higher stress when the winding angle is larger than 58^0. For a pipe with longitudinal fiber orientation (ϕ =0), it is observed from Fig. 3 that the axial stress equals to zero. This is because stress states degenerate into those of isotropic materials in the case of the transverse isotropy of composites with respect to the longitudinal direction.

Conclusions

A method was presented to analyze the stress/strain and deformation of multi-layered fiber-reinforced composite pipe under pure bending. Using the formulations derived in the present study, the stresses and deformation of the filament-wound sandwich pipe subjected to bending load were investigated and discussed. It has been shown that the stresses and strains depend strongly on the winding angle when the pipe has the filament-wound layers with highly anisotropy, such as T300/934. It was observed that the axial stresses and strains at the inner surface could be higher than those at the outer surface for a pipe within certain range of winding angles.

Acknowledgement

Dr. M. Xia wishes to express his appreciation to New Energy and Industrial Technology Development Organization (NEDO) for its financial support in the course of this study.

References

1. K. L. Alderson, K. E. Evans, Composites, 23, 167 (1992).
2. D. Hull, M. J. Legg, B. Spencer, Composites, 9, 17 (1978).
3. P. D. Soden, R. Kitching, P. C. Tse, Composites, 20, 125 (1989).
4. M. W. K. Rosenow, Composites, 15, 144 (1984).
5. B. Spencer, D. Hull, Composites, 9, 263 (1978).
6. T. Nishiwaki, A. Yokoyama, Z. Mackawa H. Hamada, S. Mori, Composite Structures, 32, 293 (1995).
7. H. Cho, G. A. Kardomateas, C. S. Valle, ASME J Appl. Mech. 65, 184 (1998).
8. M. Xia, H. Takayanagi, K. Kemmochi, Composite Structures, 51, 273 (2001).
9. S. G. Lekhnitskii, "*Theory of Elasticity of an Anisotropic Elastic Body*", San Francisco, Holder-Day, 1963.

Proceedings of 7th Japan International SAMPE
Symposium & Exhibition, Nov. 13-16, 2001

Dynamic Properties of Laminated Fiber Reinforced Rubber as a Shock Absorber for Bridge Restrainer System

Yasushi Nishimoto#, Yukihide Kajita##, Nobutaka Ishikawa##, Shinjiro Nishikawa# and Nobuyasu Ikoma#

#: SHIBATA INDUSTRIAL CO., LTD
1058, Nakao, Uozumi-cho, Akashi, Hyogo 674-0082, JAPAN
E-mail: Yasushi_Nishimoto@sbt.co.jp
##: Department of Civil and Environmental Engineering, National Defense Academy, JAPAN
1-10-20, Hashirimizu, Yokosuka, Kanagawa 239-8686, JAPAN

Abstract

Many bridges were severely damaged by the 1995 Hyogo-ken Nanbu Earthquake. Because of this lesson, the fundamental design concept was changed so that the girder may be prevented from falling down even if the same earthquake occurs. To this end, many researchers have studied so far the shock absorber for a bridge restrainer system from the viewpoints of both the high-energy absorption and the reduction of impact load. The static and high-speed compression tests were performed previously in order to examine the static and dynamic properties of the laminated fiber reinforced rubber. In this paper, the weight dropping impact test was carried out to investigate the buffer effect of the laminated fiber reinforced rubber. It is recognized that the laminated fiber reinforced rubber is much better material than the usual rubber with respect to the reduction of the impact load at high input energy.

Key Words: Shock absorber, Laminated fiber reinforced rubber, Weight dropping impact test

Introduction

The 1995 Hyogo-ken Nanbu Earthquake caused the destructive damage to highway bridges. Falling-down and nearly falling-down of girders occurred at 9 sites [1]. Because of this lesson, the Design Specifications of Highway Bridges [2] is revised so that the recurrence of falling-down of girders may be prevented even if an equivalent earthquake occurs. Therefore, the description about bridge restrainer systems is added to this new Design Specifications of Highway Bridges. Besides this specification, it is proposed that the falling-down prevention devices are equipped with shock absorbers such as a rubber. In case of severe earthquakes, a shock absorber is required to reduce the impact load that acts on the falling-down prevention devices and to absorb the kinetic energy of girders simultaneously. However, it is difficult to satisfy these two performance requirements at the same time. A material which has the high stiffness can absorb a large amount of the energy. On the other hand, that material cannot reduce the impact load. Therefore, it is necessary to develop a new kinds of shock absorber, which may be satisfied the two performance requirements simultaneously. In this study, we focus on a laminated fiber

Photo1. Structure of laminated fiber reinforced rubber

Photo2. Overview of the weight dropping machine

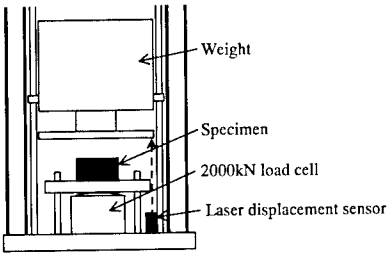

Figure1. Test setup and location of the measurement devices

Table1. Material properties of laminated fiber reinforced rubber

	Fiber			Rubber
	High tension (HMF)	Middle tension (MMF)	Low tension (LMF)	Hardness degree of 65 (R60)
Material	6-nylon	6,6-nylon	Vinilon	Natural rubber
Tensile strength	5292 (N/3cm)	2646 (N/3cm)	1764 (N/3cm)	20 (MPa)
Elongation percentage at break	40 (%)	25 (%)	20 (%)	600 (%)

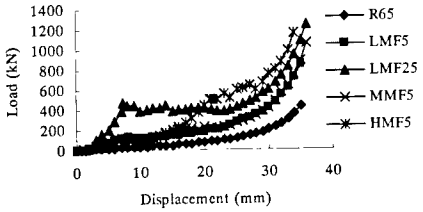

Figure2. Load ~ displacement curves

reinforced rubber newly developed as a shock absorber as shown in Photo 1. It is expected that the laminated fiber reinforced rubber is more useful shock absorber than the usual rubber, because it was found from the static compression test [3] that the load displacement curve of the laminated fiber reinforced rubber shows the elasto-plastic behavior because the fibers break at a certain load level. In this paper, the weight dropping impact test was carried out in order to examine the buffer effect of the laminated fiber reinforced rubber as a shock absorber, that is, to investigate the energy absorption and the load reduction effect.

Weight dropping test

Test setup and specimens

The weight dropping impact test was performed by using the weight dropping machine as shown in Photo 2 and Figure 1. The shape of the specimen is a rectangular cross section that has 150mm long, 150mm wide and 50mm high. In this test, three kinds of fiber are prepared. These kinds of the fiber have different tensile strength as shown in Table 1. The laminated fiber reinforced rubber is produced that the fibers are laminated into the rubber with hardness degree of 65. In this test, five kinds of specimen are used, that is, the natural rubber with hardness degree of 65 (R65) and laminated fiber reinforced rubber which has 5 layers of the low tension fiber (LMF5), 25 layers of the low tension fiber (LMF25), 5 layers of the middle tension fiber (MMF 5) and 5 layers of the high tension fiber (HMF5).

Test condition and Measuring system

The static compression test on the laminated fiber reinforced rubber is carried out ahead of the weight dropping test because the energy which is applied to the specimen is determined. Figure 2 shows the load-displacement curves on the static compression test. The required energy for breaking the fibers can be obtained from the results of the compression test. This required energies of LMF5, LMF25, MMF5 and

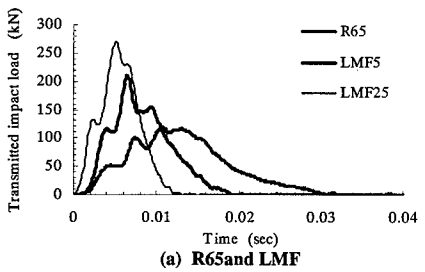

(a) R65and LMF

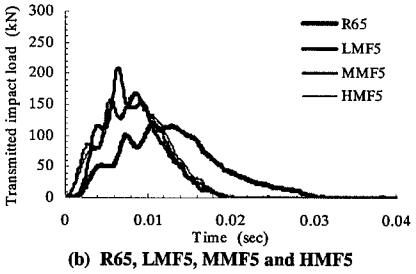

(b) R65, LMF5, MMF5 and HMF5

Figure 3. Time history of the transmitted impact load (input energy E_i = 1.0kN·m)

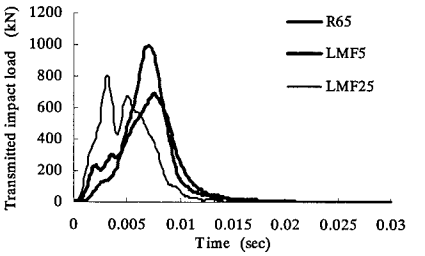

(a) R65and LMF

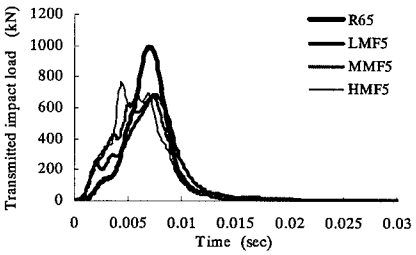

(b) R65, LMF5, MMF5 and HMF5

Figure 4. Time history of the transmitted impact load (input energy E_i = 10.0kN·m)

Table 2. Maximum transmitted impact load

Specimen	Maximum transmitted impact load :unit (kN)	
	E_i=1.0kN·m	E_i=10.0kN·m
R65	114.8	991.5
LMF5	203.8	687.1
LMF25	268.9	803.9
MMF5	167.5	670.9
HMF5	168.4	765.6

HMF5 are 0.51, 1.13, 1.33 and 2.96 kN·m, respectively.

The falling weight was set at W = 4.0 kN and the falling height was set at H = 0.25 and 2.5m (impact velocity V_i = 2.21 and 7.00m/s, respectively), that is, the input energy (the applied impact energy) was set at E_i =1.0 and 10.0kN·m. The input energy E_i = 1.0kN·m is the energy that the laminated fibers in all kinds of specimen may never break. On the other hand, the input energy E_i = 10.0kN·m is the energy that the laminated fibers in all kinds of specimen break perfectly. As for the measurement items, the transmitted impact load is measured by using the 2000kN load cell and the traveling distance of the weight is measured by using the laser displacement sensor as shown in Figure 1.

Results and consideration

Figures 3 and 4 show the transmitted impact load-time relations. It can be seen from Figure 3 that the maximum transmitted impact load of the laminated fiber reinforced rubber is larger than that of the natural rubber and the impact duration of the laminated fiber reinforced rubber is shorter than that of the natural rubber. This is because he stiffness of the laminated fiber reinforced rubber in elastic region is larger than that of the natural rubber. In other words, the laminated fibers don't break because of the small input energy. However, it is found from Figure 4 that when the input energy is larger, the maximum transmitted impact load of the laminated fiber reinforced rubber becomes smaller than that of the natural rubber. The reason why the maximum

Table 3. Energy absorption ratio

Specimen	Energy absorption ratio (%)	
	E_i=1.0kN·m	E_i=10.0kN·m
R65	72.1	85.0
LMF5	86.6	88.7
LMF25	88.9	90.4
MMF5	89.3	87.8
HMF5	86.5	85.5

transmitted impact load is reduced is that the laminated fiber reinforced rubber absorbs the kinetic energy by breaking the laminated fibers. Table 2 shows the maximum transmitted impact load. In Table 2, the hatching figures represent that the laminated fibers break. For example, when the natural rubber with hardness degree of 65 is compared with the LMF5 specimen (low tension fiber, 5ply), the maximum transmitted impact load of the laminated fiber reinforced rubber become about 0.7 times smaller than that of the natural rubber. Therefore, the laminated fiber reinforced rubber is effective as a shock absorber rather than the natural rubber from the viewpoint of the reducible effect of the transmitted impact load at high input energy.

Table 3 shows the energy absorption ratio (ΔE). The energy absorption ratio is defined as follows

$$\Delta E = \frac{E - E'}{E} \times 100 \qquad (1)$$

in which E and E' are the kinetic energy before and after the collision, respectively. The velocity of the weight is obtained by differentiating the traveling distance with respect to time. It can be seen from Table 3 that the energy absorption ratio of the laminated fiber reinforced rubber is larger than that of the natural rubber in every test case. Therefore, the laminated fiber reinforced rubber can absorb the kinetic energy of the weight, that is, the velocity of the weight after the collision can be smaller.

Conclusions

The following conclusions are drawn from this study.

1) In the case of the small input energy, the transmitted impact load of the laminated fiber reinforced rubber is larger than that of the natural rubber. Because the stiffness of the laminated fiber reinforced rubber is larger when the laminated fibers don't break.

2) On the other hand, in the case of the large input energy, the transmitted impact load of the laminated fiber reinforced rubber is about 0.7 times as that of the natural rubber because of breaking the fibers

3) The laminated fiber reinforced rubber can absorb the kinetic energy better than the natural rubber. As a result, the velocity of the weight after the collision is smaller.

As the results of the weight dropping impact test on the laminated fiber reinforced rubber and the natural rubber, it is concluded that the laminated fiber reinforced rubber is useful material as a shock absorber for bridge restrainer system.

References

1. Kawashima, K. and Unjoh, S., (1997), "Impact of Hanshin/Awaji Earthquake on seismic design and seismic strengthening of highway bridges", Journal of Structural Mechanics and Earthquake Engineering, No.556/I-38, 1-30.

2. Japan Road Association, (1996), Design Specifications of Highway Bridges, Part V Seismic Design. (in Japanese)

3. Nishimoto, Y., Kajita, Y., Ishikawa, N. and Nishikawa, S., (2000), "An experimental study on dynamic properties of laminated fiber reinforced rubber as shock absorber of bridge restrainer system", Journal of Structural Engineering, JSCE, Vol.46A, 1865-1874.

Proceedings of 7th Japan International SAMPE
Symposium & Exhibition, Nov. 13-16, 2001

Experimental Study on Effects of Resins on Bond Force Transfer of Carbon Fiber Sheet-Concrete Interface

Dai Jianguo[1], Sato Yasuhiko[1] & Ueda Tamon[1]
1:Division of Structural and Geotechnical Engineering, Hokkaido University
060-8628 Kita 13, Nishi 8, Kitaku, Sapporo, JAPAN
E-mail: daijg@eng.hokudai.ac.jp

Abstract

This paper presented results of a series of single-lap shear bond tests to clarify the bond force transfer capacity of carbon fiber sheet (CFS)-concrete interface, in which resin was treated as a main experimental parameter. Influences of different epoxy resins' Young's Modulus (0.35~3GPa), and different adhesive layer thickness (0.5mm, 1.0mm, 2.0mm) were observed. CFS stiffness (1 to 3 layer CFS) was also changed to compare effects of resins in the cases of different FRP sheet/adhesive stiffness ratio. Based on the experimental results, influences of resins on tensile strength of CFS, force transfer capacity of CFS-concrete interface and failure types were discussed. It could be seen from the experiments that changing thickness of resins in adhesive layer from 1.0mm to 2.0mm will increase the interface force transfer capacity significantly especially in the case of CFS-concrete interface with 3 layers CFS. Applying moderately soft resins can improve the load transfer capacity of CFS-concrete interface as well. However, it must be noted that harmful decrease of CFS tensile strength will be brought out by using low-Young's modulus resin as CFS immersing matrix. As a result, during the sheet bonding construction period soft resin can be regarded as a choice of not immersing matrix but interface bond adhesive. Based on the analysis of experimental data, a sandwich bonding system was proposed to improve the bond effects of CFS-concrete interface.

Keywords: Carbon fiber sheet-concrete interface, Soft epoxy resin, Sandwich bonding system, Bond force transfer

Introduction

To get good bonding effects of CFS--concrete interface, many experimental parameters such as bond length, concrete strength and surface processing, stiffness of CFS, and bond width, primer's effects and anchorage have been studied in the past[1-6]. It is widely known the CFS strengthening effects strongly rely on the performance of adhesives. However, work related to effects of resins has been seldom reported though different types of resins with a wide range of tensile Young's modulus from 1Gpa to 12GPa have been used in previous studies. Saadatmanesh, etc.[7] and Ritchie, etc.[8] verified a two-part, rubber-toughened epoxy to be a most suitable choice. Chajes etc. applied four types of adhesives in their experiments and found the resin (with Young's modulus of 0.25GPa and elongation of 60%) itself failed ahead of concrete failure [2]. In general, not soft resins but resins with high Young's modulus are preferred to achieve higher maximum bond stress. Trough appropriate bonding system, however, it is possible for applying moderately soft resin to adjust the stress distribution in concrete surface and alleviate the problem of peeling off. And also, to get accurate constitutive model for bond interface, it is necessary to quantify the influences of resin mechanical properties such as Young's modulus and fracturing strain. Moreover, the influences of resin's thickness in adhesive layer need to be clarified. To reach the goals, the paper presented a basic experimental approach to discuss the effects of resins on bond force transfer at CFS-concrete interface.

Outline of Experiment

Test setup

A single-lap shear bond test method was applied in the research (Fig.1).

The test setup included a steel basement connected to the strong floor, concrete block (40x20x60cm), CFS with the width of 10cm externally bonded to the concrete block, and connectors between the end of CFS sheet and actuator, which contained two hinges, ensuring that the end of CFS can be rotated in all direction freely. To achieve uniform pull-out force, two steel plates were adhered to both sides of CFS. Additional bolts were used to enhance the bond between sheet and steel plates. In order to avoid the local damage of concrete block, unbonded area was set by using vinylon to separate concrete surface from sheet. Strain gages were arranged with interval of 1.0cm along the pull-out direction on the surface of CFS. To check whether the load was eccentric or not, some strain gages were attached on the un-bonded area of sheet symmetrically (Fig.1).

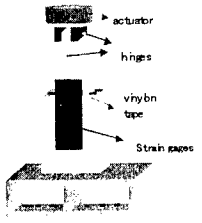

Fig.1 Single-lap shear bond test setup

Experimental materials

CFS and adhesives used in the study have mechanical properties shown in Table.1 and Table.2 respectively. Concrete with the same mixing ratio applied in the experiments had the average compressive strength of 33.1MPa.

Table 1 Mechanical properties of CFS

Density (g/m^2)	Thickness (mm)	Tensile strength (MPa)	Young's modulus E_{cB}(GPa)	Fracture strain ε_u(%)
1.8~2.0	0.11	3480	230	1.5

Table 2 Properties of adhesives

Type	CN-100	SX325	FR-E3P
Compressive modulus(GPa)	0.35	1.0	2.5
Mixture ratio (resin/hardener)	1:1	2:1	2:1

Bonding system

Concrete surface was smoothly dealt with concrete sanders (Makita PC9001) till coarse aggregates were heavily exposed. After the primer (FP-NS) was cured for 24 hours, adhesive resins, CFS and resin matrix were set. Through calculating the weight, thickness of resins was controlled. There are two bonding systems named as plate bonding and sheet bonding. In this paper the later was applied and the resins used for CFS matrix and for adhering layer were same. It has been known that using primer improves the bond effects of CFS-concrete interface[2]. To study the necessity of primer when lower Young's modulus resins SX-325 and CN-100 with moderate and lower viscosity were used, two more specimens without using primer (series 5 in table 3) were prepared.

Experimental results and discussion

Description of failure types

In this study, the following four types of failure were observed: (1) Peeling-off of CFS was totally developed without CFS fracture, and concrete surface (a thin layer beneath the concrete surface) failure occurred (Fig 2.1); (2) Partial peeling-off of CFS was developed and CFS fractured (Fig2.2), concrete surface failure occurred; (3) Peeling-off of CFS was initiated but not fully developed, CFS fractured, and concrete-adhesive interface failure (Almost no concrete damage occurred) occurred (Fig.2.3); (4) CFS fractured without peeling-off (Fig2.4).

Fig2.1 Failure type 1

Fig2.2 Failure type 2

Fig2.3 Failure type 3

Fig2.4 Failure type 4

Table 3 Test results of specimens

Test Series	No. of specimens[1]	Failure type	Failure load P_u(KN)	σ_{cfs}^f (MPa)[3]
1	R1-L1-T1	1	35.3	3209
	R1-L2-T1	1	51.3	2332
	R1-L3-T1	1	52.04	1577
2	R2-L1-T1	2	53.01	4819
	R2-L2-T1	4	38.81[2]	1764
	R2-L3-T1	2	43.34[2]	1313
3	R3-L1-T1	4	22.5	2045
	R3-L2-T1	4	43.2	1964
	R3-L3-T1	2	72.9	2209
4	R1-L1-T2	4	46.8	4255
	R1-L1-T3	1	46.8	4255
	R1-L3-T2	1	75.6	2291
	R1-L3-T3	1	45.9	1391
5	R2-L1-T1(NP)	2	45.9	4173
	R3-L1-T1(NP)	3	22.5	2045

Note 1: R-N1-L-N2-T-N3, N1 is resins' type: (1,2 and 3 mean FR-E3P, SX325 and CN-100 respectively); N2 is the number of CFS layer; N3 is the thickness of adhesive resins: (1,2 and 3 mean 0mm, 2.0mm and 0.5mm respectively, NP means that primer was not used).
Note 2: Eccentric tensile failure was observed
Note 3:σ_{cfs}^f is the nominal tensile stress of CFS at failure, $\sigma_{cfs}^f = P_u / nbt$, b is width of CFS, t is thickness of 1 layer CFS, n is number of CFS layer.

Effects of primer

By comparing Fig.2.2 with Fig.2.3, it can be seen that for R3 (resin CN-100), the primer has obvious effects on bond failure. The concrete-adhesive interface of specimen without primer failed ahead of concrete surface failure. Moreover it can be known from Table 3, specimen R3L1T1 and R3L1T1 (NP) failed under the same ultimate load due to CFS fracturing. For R3L1T1 peeling-off was not initiated, which means that the force transferring ability is higher than that of R3L1T1 (NP). For R2 (resin SX325), in both cases of with and without primer, concrete surface failure happened but the ultimate load was increased by 15.4% due to the using of primer.

Effects of Resins' Young's Modulus

For all the specimens using R1 (high stiffness resin FP-E3P) except specimen R1L1T2 with a thick adhesive layer, total peeling-off with concrete surface failure happened. CFS fracturing was not observed. While for all specimens using R2 (moderately soft resin SX325) and R3 (soft resin CN-100), the failure happened due to the CFS fracturing. For R2 series with two and three layers, though peeling-off happened, the failure load was lower because of the eccentric loading effects. This means that eccentric load could cause the earlier peeling-off and decrease the load transfer capacity. For Series R3, it can be seen the using of soft resin for CFS matrix will decrease the CFS tensile strength significantly. It is difficult to predict the ultimate bond force of CFS-concrete interface exactly because CFS failed ahead of total peeling-off. However, it can be said at least that the actual load transfer capacity of the interface would be higher than the observed values. Figure 3 shows the influence of Resins' Young's modulus on the ultimate load transfer value of CFS-concrete interface with 1 and 3 layer CFS.

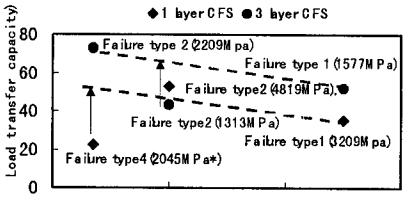

Fig.3 Resin's effects on load transfer capacity

*: the values shown in the brackets in figure.3 is nominal tensile strength of CFS at failure σ_{cfs}^f

The arrows in Fig.3 show the actual load transfer capacity could become high. The low observed values were due to the CFS failure under eccentric load. It must be noted when resins with Young's modulus of 0.35GPa was applied as CFS immersing matrix, the CFS nominal tensile strength at failure became around 2000MPa, which is far below the actual ultimate tensile strength of CFS.

Effects of adhesive's thickness

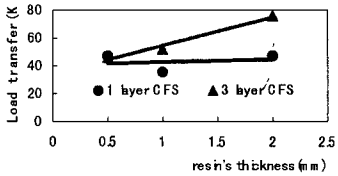

Fig.4 Relationship between resin's thickness and load transfer capacity

It can be seen from Fig.4 that the increasing of adhesive thickness can improve the interface load transfer only slightly in the case of CFS-concrete with one layer, because the load transfer capacity was controlled by CFS breakage. While in the case of three layer CFS where peeling-off controlled the load transfer capacity, the influence is significant. The increasing percentage is above 60% when the resin thickness changes from 0.5mm to 2.0mm.

A Solution to improve the load transfer ability of CFS-concrete interface

Base on the experimental results and above analysis of this study, a sandwich bonding system, consisting of primer resin, soft resin as adhesive layer and harder resin as immersing resin for carbon fiber sheet, is proposed as shown in Fig.5.

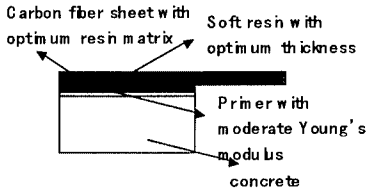

Fig.5 Sandwich bonding system

Primer will play a role of preventing adhesive-concrete interface failure, soft resin will improve the load transfer capacity of CFS-concrete interface, and resin matrix with optimum stiffness and fracturing strain will ensure the tensile strength of carbon fiber sheets.

Conclusions

Based on the results of this study, the following conclusions here can be drawn up for the range of experimental variables in this study:

1. Soft resin can be applied in adhesive layer to improve the load transfer capacity of CFS-concrete interface. Between soft resin and concrete, primer is necessary to prevent adhesive-concrete interface failure (or ensure concrete failure to happen).
2. Soft resin is not suitable for the matrix of carbon fiber sheet (CFS) because it will decrease the nominal tensile strength of CFS significantly.
3. Increasing the thickness of adhesive layer will improve the load transfer capacity especially in the case of high CFS stiffness.
4. The sandwich bonding system proposed here is a selectable way to improve CFS-concrete bond properties. To quantify and optimize the improving effects, further experimental and theoretical verifications are needed.

Acknowledgement

The authors would like to express their appreciation to Toho Earth-tech Co. Ltd. for the material supply, Mr. Saito in Nittestsu Compsite Co. Ltd. for his kind suggestion and material supply, and to the students in the author's laboratory for their kind assistances during experiments.

Reference

1.Talisten、Bjorn, Defining anchor lengths of steel and CFRP plates bonded to concrete, International journal of adhesion and adhesives. V17, n4, Nev., 1997 319-327

2.Michael J. Chajes et.al(1996), Bond and Force Transfer of Composites Material Plates Bonded to Concrete, ACI Structural, V,93, No.2, pp.208-217

3.Brian Miller et.al(1999),Bonded between CFRP Sheets and Concrete, Proc. ASCE 5th Materials Congress, Cincinnati, OH, L.C. Bank, Editor, May 10-12, , pp240-247

4.Mitsui, Masakazu et.al, Relations between Surface Roughness Indexes and Bond Strength Between CFRP Sheets and Concrete. Journal of the Society of Materials Science,Japan v49 n6 June 2000 685-691

5.Sato, Y., et.al, Fundamental Study on Bond Mechanism of Carbon Fiber Sheet, J.Materials, Conc. Struct., Pavements, JSCE, No.648/V-47, 71-87, 2000.5

6.K. Brosens et.al, Anchorage Design for Externally Bonded Carbon Fiber Reinforced Polymer Laminates, ACI SP 188-56, pp635-645

7.Saadatmanesh, H., et.al, Fiber Composites Plates Can strengthen Beams, Concrete International, V.12, No.13, Mar.1990,pp.65-71

8.Ritchie, P.A., et.al, External Reinforcement of Concrete Beams Using Fiber Reinforced Plastics, ACI Structural Journal, V.88., No.4., July-Aug.,1991, pp.490-500

Proceedings of 7th Japan International SAMPE
Symposium & Exhibition, Nov. 13-16, 2001

Retrofitting RC Beams with Innovative Hybrid Fiber Sheets

Zhishen Wu#, Koji Sakamoto#, Hedong Niu# and Tetsuji Kurokawa#

#: Department of Urban & Civil Engineering, Ibaraki University
Nakanarusawa 4-12-1, Hitachi 316-8511, JAPAN
E-mail: zswu@ipc.ibaraki.ac.jp

Abstract

In this paper, bending tests on RC beams strengthened with hybrid fiber sheets, consisting of different types of fibers, were conducted to investigate the effect on failure mechanism and strengthening effects. In contrast to the normal bonding method with single type of continuous fiber sheets, significant improvements can be achieved in ductility, stiffness and crack-resistance through externally bonding hybrid fiber sheets.

Key Words: Fiber Reinforced Polymers, Hybrid, Ductility, Stiffness, Bonding

Introduction

The application of fiber reinforced polymer (FRP) sheets (or plates) (such as glass, aramid, and carbon fiber sheets or plates molded with either epoxy or polyester resin), as an externally bonded reinforcement, have been widely accepted as an effective technique of strengthening and upgrading structurally inadequate or damaged concrete structures. Unlike the cold worked steel, they stay elastic until failure and fail in a noticeably brittle way. Therefore, the following two disadvantages may consist in an FRP-strengthened system:

1) The FRP-strengthened concrete structures can fail momentarily without any foreboding due to the FRP rupture or debonding of FRP sheets;
2) The strengthening effects with either aramid or glass fiber sheets on stiffness increase before the yielding of steel reinforcement and load increase at the yielding of steel reinforcement are not significant. Even for the case of carbon fiber sheets with a regular Young modulus equivalent to steel reinforcement, the effects are still not enough due to the reason that the reinforcing ratio of FRP sheets is relatively low.

One idea to incorporate the ductility and the stiffness is to use a hybrid composite which consists of different types of fiber sheets such as glass, aramid, vinylon, and carbon fiber composites with different strengths and stiffnesses, which fail at different strains during load history, thereby allowing a gradual failure of the composites [1,2].

In this paper, the strengthening effect and fracture behavior of RC beams strengthened with hybrid composites are investigated through bending tests on different hybrid composites including high strength carbon fiber sheet (hereinafter denoted by SS for short), high modulus carbon fiber sheet (hereinafter MS for short) and a newly developed PBO (Polypara-phenylene-benzo-bisthiazol) fiber sheet (hereinafter PS for short) which demonstrate better tolerance to impact than carbon and aramid FRP systems as shown in Fig. 1.

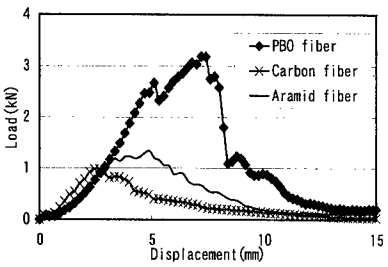

Fig. 1 Result of Impact Test

Description of Test Program

Test Specimens

Three types of beam specimens are designed in this study. The dimensions and cross-sectional details of the test beam as shown in Fig. 2, where Type A and B are FRP-strengthened notched RC beams with different reinforcing steel bars, Type C was unnotched one. Table 1 summarizes the material properties of specimens. Three types of fiber sheets were provided to investigate the strengthening effect of hybrid fiber sheets and the detailed reinforcing sheets are listed in Table 2.

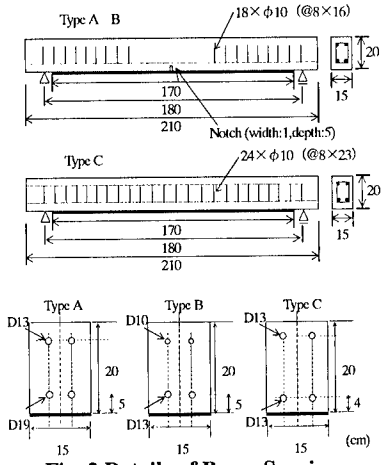

Fig. 2 Details of Beam Specimens

Table 1 Summary of Material Properties

Concrete	TypeA	Compressive strength (MPa)	33.8
		Modulus of elasticity (GPa)	34.4
	TypeB	Compressive strength (MPa)	49.3
		Modulus of elasticity (GPa)	35.1
	TypeC	Compressive strength (MPa)	49.3
		Modulus of elasticity (GPa)	35.1
Steel SD295A	D19	①Tensile strength (MPa) ②Yielding strength (MPa)	①:385 ②:515
	D13		①:358 ②:504
	D10		①:403 ②:577
High-strength Carbon Fiber Sheet (SS)		Modulus of elasticity (GPa)	230.0
		Tensile strength (GPa)	3.7
		Thickness (mm)	0.111
		Unit weight (g/m^2)	200
High-modulus Carbon Fiber Sheet (MS)		Modulus of elasticity (GPa)	540.0
		Tensile strength (GPa)	1.9
		Thickness (mm)	0.143
		Unit weight (g/m^2)	300
PBO Fiber Sheet (PS)		Modulus of elasticity (GPa)	240.0
		Tensile strength (GPa)	4.0
		Thickness (mm)	0.128
		Unit weight (g/m^2)	200

Table 2 Test Specimens

Specimens	Reinforc-ing bars	Fiber sheet type	Total Layers
NR-D19-A	D19	-	-
2SS-D19-A		SS(2 layers)	2
2PS-D19-A		PS(2 layers)	2
2SS1MS-D19-A		SS(2 layers) + MS(1 layer)	3
2PS1MS-D19-A		PS(2 layers) + MS(1 layer)	3
1SS-D13-C	D13	SS(1 layer)	1
2SS-D13-C		SS(2 layers)	2
2PS-D13-B		PS(2 layers)	2
2SS1MS-D13-C		SS(2 layers) + MS(1 layer)	3
2PS1MS-D13-B		PS(2 layers) + MS(1 layer)	3

Test Setup and Procedure

Type A, B and C beams were subjected to four-point and three-point bending test, respectively, as shown in Fig. 3. The loading rate is controlled as 1kN/min, but prior to occurrence of crack, loading is kept at each step of 1KN to examine whether or not crack is initiated.

The instrumentation of each beam specimen is composed of: 1) two LVDTs at mid-span for deflection measurement, 2) electrical strain gauges bonded on the tension steel bar to measure its deformation, 3) clip gauge bonded to the lateral faces of the test beam for crack-width measurement and 4)electrical strain gauges bonded on the surface of fiber sheets, some of them are illustrated in Fig. 3 and 4.

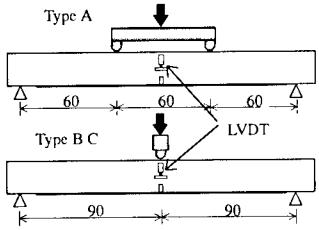

Fig. 3 Loading Scheme

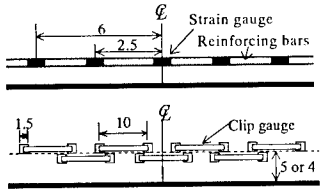

Fig. 4 Measurement Arrangement

Test Results and Discussions

Table 3 Experimental Results

Specimens	Initial cracking load (kN)	Steel yielding load (kN)	Failure load (kN)	Falure mode	Concrete crushing	FRP Peeling by shearing	Partial rupture of sheet
NR-D19-A	15.5	70.0	96.9	Flexural failure	O	-	-
2SS-D19-A	12.1	83.0	122.0	Deb. failure	-	O	-
2PS-D19-A	8.1	86.7	119.9	Deb. failure	-	O	-
2SS1MS-D19-A	16.5	104.5	118.5	Shear failure	-	-	-
2PS1MS-D19-A	16.0	—	116.5	Shear failure	-	-	-
1SS-D13-C	9.1	42.0	63.4	Flexural failure	O	-	O
2SS-D13-C	12.5	46.5	71.2	Deb. failure	O	O	-
2SS1MS-D13-C	13.0	61.5	86.5	Deb. failure	O	O	O
2PS1MS-D13-B	21.6	69.5	92.8	Concrete crushing	O	O	O

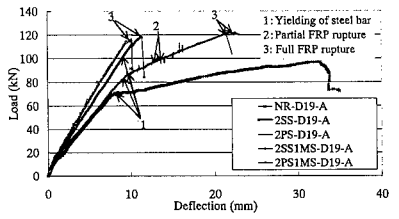

(a) Type A specimens

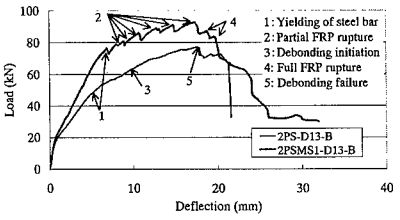

(b) Type B specimens

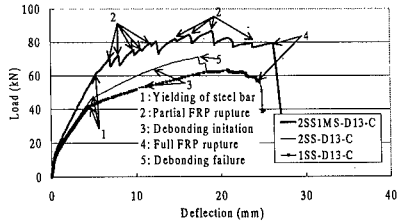

(c) Type C specimens

Fig. 5 Load-Deflection Relations

Experimental Results

The loads for crack initiation, yielding of steel bars and final failure and failure modes of all specimens are summarized in Table 3. The strengthening effect of different fiber sheets on the retrofitted system can be clearly illustrated in Fig. 5. The detailed discussions will be made in what follows.

Discussions

Four-Point Bending Test on Type A

As shown in Fig. 5(a), yielding and failure loads can be enhanced through bonding two layers of same fiber sheets to the bottom of RC beams as compared to those of the RC control beam. Adopting hybrid fiber sheets with higher modulus type of carbon fiber sheet yields great enhancements in yielding load and stiffness of the strengthened beams, comparing with both control beam and strengthened beams with single type of SS or PS fiber sheet (2 layers). Unfortunately, due to over-reinforcement in 2SS1MS-D19-A and 2PS1MS-D10-A, they failed in brittle shear failure and did not show superior to the ones strengthened with single fiber sheets in ductility. Therefore the structural strengthening design should avoid brittle shear failure due to over-reinforcement to effectively and efficiently utilize the strengthening effect of FRP composites.

Three-Point Bending Test on Type B and C

In order to avoid such shear failure as happened in Type A beam strengthened with hybrid sheets and fully utilize the hybrid effect, tension steel bars were changed from D19 to D13 and three-point loading was applied. This greatly improved the failure modes, as shown in Table 5 and Fig. 5(b), (c).

Both Fig. 5(b) and (c) shows that the stiffness, yielding and failure loads of strengthened beams with hybrid fiber sheets can be enhanced as compared to those of the single type of sheets. Due to the concrete crushing at the failure load, 2PS1MS-D13-B specimen did not see an increase in ductility comparing with 2PS-D13-B specimen. With regard to 2SS1MS-D13-C specimen, a superior performance can be observed. In addition, a pseudo-yielding plateau can be observed in Fig. 5(b) and (c) after yielding

of steel bars, which can be attributed to the fact that gradual rupture of higher modulus fiber sheet led to stress redistribution in hybrid sheets.

In order to compare the strengthening effect between PBO fiber sheets and high strength type of carbon fiber sheets, the pseudo-yielding plateau is magnified in Fig. 6 and the load drop versus the times is depicted in Fig. 7. A larger load drop can be observed for the high strength type of carbon fiber sheets during the load history due to the partial rupture of fiber sheets, which may fails the retrofitted system. At this point, PBO fiber sheets possess higher energy absorption performance and keep stable load drop when subjected to impact action from the partial rupture of fiber sheets.

Seen from Fig. 8, it is found that crack resistance of the structure can be improved by hybrid fiber sheets. However, no significant increase can be found in initial cracking load.

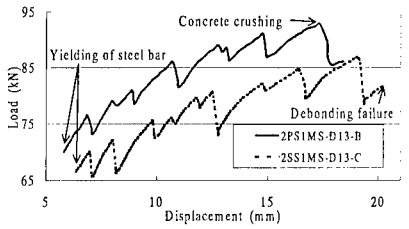

Fig. 6 Pseudo-Yielding Plateau

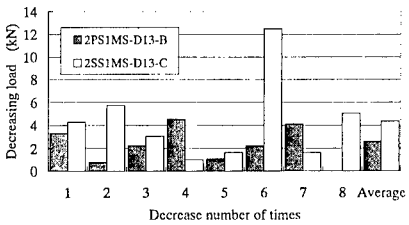

Fig. 7 Load Drop Due to the Partial Rupture of FRP Composites

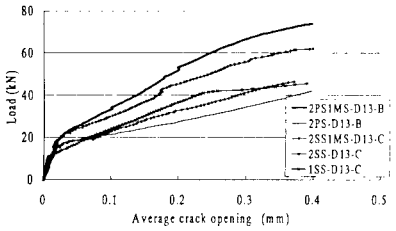

Fig. 8 Load versus Crack Opening

Conclusions

Through performing flexural tests on RC beams strengthened with hybrid fiber sheets, the following conclusions can be drawn:

(1) The structural stiffness and yielding load can be significantly improved through hybrid fiber sheets with high modulus type of carbon fiber sheet, which is higher than steel reinforcement in modulus.

(2) The hybrid strengthening effects with hybrid finer sheets on overall structural performance can be realized through rational structural strengthening design.

(3) PBO fiber sheets with high energy absorption performance may stabilize the strengthened structure with hybrid fiber sheets with a lower load drop during the partial rupture procedure of fiber sheets.

References

1. A.G. Razaqpur and M.M. Ali: Proc. of 1st ICCI'96, 401(1996)

2. H.G. Harris, W. Somboonsong, F.K. Ko and R. Huesgen: Proc. of 2nd ICCI'98, 66(1998)

Proceedings of 7th Japan International SAMPE
Symposium & Exhibition, Nov. 13-16, 2001

A Sensitivity Analysis for Shear Capacity of RC member Retrofitted with Continuous Fiber Sheet

Akihisa Kamiharako[1], Takumi Shimomura[2], Kyuichi Maruyama[2], and Takayuki Shinbo[2]

1: Department of Earth and Environmental Science, Hirosaki University
3 Bunkyo-cho, Hirosaki Aomori, 0368561 JAPAN
E-mail: kami@cc.hirosaki-u.ac.jp
2: Department of Civil and Environmental Engineering, Nagaoka University of Technology
1603-1 Kamitomioka-machi, Nagaoka Niigata, 9402188 JAPAN

Introduction

To repair and/or to strengthen existing Reinforced Concrete (RC) structures, Continuous Fiber (CF) sheet made of carbon or aramid has been increasingly applied in Japan [1]. Since CF sheet has no yielding point as steel reinforcement, it is necessary to know sheet strain in order to evaluate stress carried by CF sheet. In the RC member retrofitted with CF sheet, the sheet over concrete crack delaminates from concrete surface in accordance with crack opening. Therefore, the sheet strain depends on crack width and delaminating sheet length. From that point of view, the authors have developed an evaluation method for shear capacity of RC members retrofitted with CF sheet, in which bonding and delaminating behavior between sheet and concrete is considered [2]. This study will conduct a sensitivity analysis for shear capacity of retrofitted members by using the proposed evaluation method. The influences of various factors on failure mode and shear capacity will be clarified through the parametric analysis. The efficient retrofitting design of CF sheet will be discussed on the basis of the analytical results.

Summary of The Evaluation Method for Shear Capacity

Calculation method

The detail of the formulation is shown in Reference 2. Shear capacity of RC member retrofitted with CF sheet (V_u) is calculated as:

$$V_u = V_c + V_s + V_f \tag{1}$$

where V_c and V_s are shear force carried by concrete and stirrups respectively and V_f is shear force carried by CF sheet. The calculation methods for V_c and V_s conform to the JSCE design specification [3]. Shear force carried by CF sheet (V_f) is calculated by the proposed evaluation method, which is based on the coupled mechanical models: the rigid

body model shown in Fig.1 and the bond constitutive model in Fig.2.

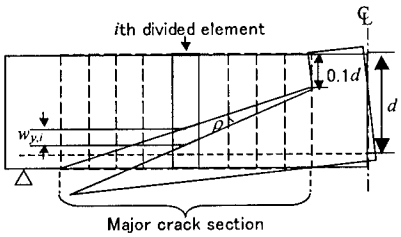

Fig. 1 Rigid body model

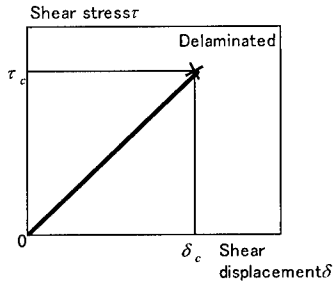

Fig. 2 Constitutive model

The calculation procedure is summarized in Fig. 3. Crack opening is calculated by the rigid body model and the assumed rotary angle. Stress analysis is executed at each divided element, in which bonding, delaminating and rupture of CF sheet are taken into account. The total shear force carried by CF sheet in the member is evaluated as the sum of the shear forces in the divided elements:

$$V_f = \sum_{i=1}^{n} V_{f,i} \qquad (2)$$

The ultimate shear force carried by CF sheet is defined as the maximum value obtained by Eq. (2) while the rotary angle is increased step by step. The proposed computational method can automatically distinguish the typical failure modes of the member retrofit-

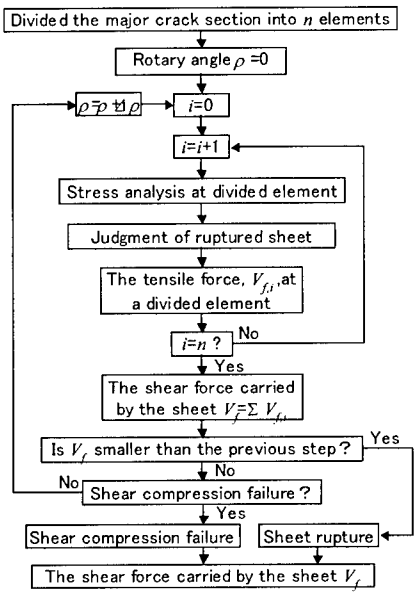

Fig. 3 Calculation flow

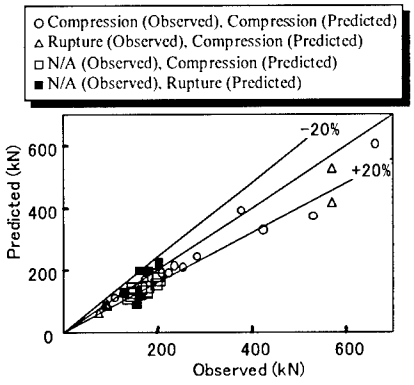

Fig. 4 Verification of the evaluation method

ted with CF sheet: the sheet rupture mode and the shear compression failure one.

Applicability

The authors have verified the applicability of the proposed method in Reference 2. The result is shown in Fig. 4. Even though the failure mode is not completely predicted, the shear capacity is predicted with sufficient accuracy by the proposed method.

Table 1 Calculating condition

Overall depth of member, h	350mm
Effective depth of member, d	300mm
Thickness of sheet, t_f	0.05 to 0.6mm
Elastic modulus of sheet, E_f	80 to 440 kN/mm^2
Tensile strength of sheet, f_{fu}	1000 to 4000 N/mm^2
Critical shear stress τ_c	7.5N/mm^2
Critical shear displacement δ_c	0.2mm

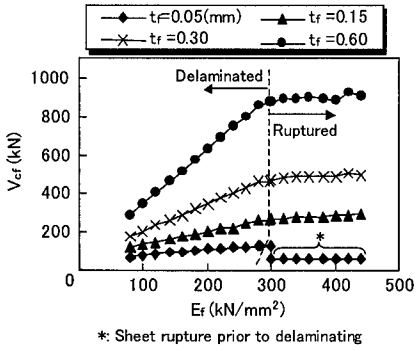

Fig. 5 Relationship between elastic modulus of sheet and the shear force

Discussion about Material Property of The Sheet

Elastic modulus

The influence of the elastic modulus of CF sheet on the shear capacity (V_f) is analytically investigated by the proposed method. Calculating conditions are summarized in Table 1. The tensile strength of the sheet is assumed as constant value: 3000 N/mm^2.

Figure 5 shows the relationships between the elastic modulus of CF sheet and the shear capacity of the member with different number of sheet layers. In cases that the elastic modulus of the sheet is smaller than 300 kN/mm^2, the sheet delaminates without rupturing. In such cases, the failure mode of the member will be the shear compression failure mode. The shear capacity increases linearly with increasing of the elastic modulus. On the other hand, in cases that the elastic modulus is greater than 300 kN/mm^2, the failure mode of the member will be the sheet rupture mode. The shear capacity depends on the tensile strength of the sheet in this failure mode. What we have to care is that, if the thickness of the sheet is too thin, the sheet may rupture before delaminating. In this case, the shear capacity of the member will be reduced. It implies that the minimum amount of affixed sheets should be noted in the practical design.

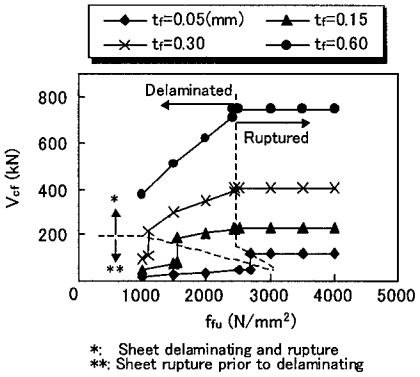

Fig. 6 Relationship between tensile strength of sheet and the shear force

Tensile strength

The relationship between the tensile strength of CF sheet and the shear capacity of the member is shown in Fig.6. Calculation condition is same as the previous section. Elastic modulus of the sheet is assumed as 240 kN/mm^2.

Figure 6 shows that the sheet ruptures prior to delaminating if the tensile strength is low and the thickness is thin. To avoid this undesirable failure mode, the tensile strength of the sheet must be higher than the delamination initiation stress. In the range where the failure mode is the sheet rupture mode, the shear capacity of the member increases with increasing of the tensile strength of the sheet. However, the shear capacity will no more increases after the failure mode changes to the shear compression mode.

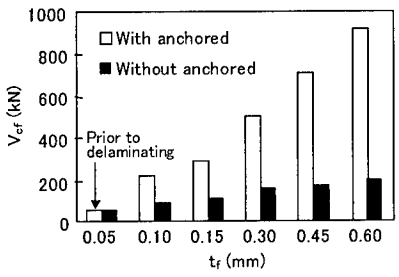

Fig. 7 Effectiveness of anchoring

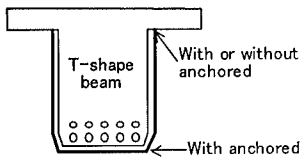

Fig. 8 Anchoring method

Anchoring method

In actual existing RC structures, CF sheet cannot always fully enclose the cross section. For example, in T-shape beam as Fig.8, mechanical anchorage of the sheet should be adopted. Figure 7 shows the analytical results on the effectiveness of the anchorage on the shear capacity of the member. Anchoring method assumed in this analysis is shown in Fig. 8.

If the sheet is not anchored at the end, sufficient performance cannot be expected because the sheet will suddenly debond when the sheet stress meets the delamination initiation stress.

Conclusion

The following conclusions can be drawn in this study:

(1) If the thickness or number of layers of the sheet is not enough, the sheet may rupture before delaminating. In such case, sufficient shear capacity cannot be ensured.

(2) To increase tensile strength of the sheet is effective to increase shear capacity of retrofitted member in case that the failure mode is the sheet rupture mode.

(3) Sufficient shear capacity is not ensured if the sheet is not anchored at the end.

References

1. JCI-TC952: Technical Report on Continuous Fiber Reinforced Concrete, 1998

2. A. Kamiharako, T. Shimomura, and K. Maruyama: Concrete Library International, (37), 147 (2001)

3. Japan Society of Civil Engineers: "*Standard Specification for Concrete Structural Design*", 1996

Proceedings of 7th Japan International SAMPE
Symposium & Exhibition, Nov. 13-16, 2001

Ductility Evaluation of RC Member Retrofitted with Continuous Fiber Sheet

Futoshi Katsuki#1, Kyuichi Maruyama#2 and Hiroshi Mutsuyoshi#3

#1: Shibaura Institute of Technology, Dept. of Civil Engineering
3-9-14 Shibaura, Minato-ku, Tokyo 108-8548, JAPAN
E-mail: katuki@sic.shibaura-it.ac.jp
#2: Nagaoka University of Technology, Dep. of Civil and Environmental Engineering
1603-1 kamitomiokamachi, Nagaoka-shi, Nigata 940-2188, JAPAN
#3: Saitama University, Dep. of Civil and Environmental Engineering
255 Shimo-Ohkubo, Saitama-shi, Saitama 338-8570, JAPAN

Abstract

The design ductility ratio of the members retrofitted with the continuous fiber sheets has been determined every structure and reinforcement from the results by the full-scale specimens under reversed cyclic load test. It is because the upgrading ductility of members retrofitted with the continuous fiber sheet differs by various factors such as types of the reinforcement, section size of the member, axial force, and ratio of tensile reinforcement etc.. Therefore, it is not possible to use the design equation of ductility ratio proposed in previous report for other members and new reinforcements. Then, authors tried the proposal of new design ductility ratio style that could be designed regardless of the type of the continuous fiber sheets by adding dynamic characteristics and the quantity of the sheets to the improvement effect of the ductility ratio as a parameter. Still, the design equation of new ductility ratio proposed in this paper was examined using the result of the columns retrofitted AFRP and CFRP sheets under cyclic load in past research.

Key words: Ductility, Carbon, Aramid

Introduction

The JSCE (Japan Society for Civil Engineers) Concrete Committee on FRP has already established "Recommendation for Design and Construction of Concrete Structures Using Fiber Reinforced Materials" in 1997. Then, the new committee on FRP sheet, which was setup in 1998, has been commissioned to establish a new design and construction method for retrofit of RC/PC structures using FRP sheet. This paper describes outlines of the seismic retrofitting design method mainly on ductility of retrofitted concrete structures by FRP sheet.

Results of previous report

Dimension and material properties of the specimens in the research of previous report [1-3] are shown at Table 1. All specimens are columns of rectangular cross section reinforced by lateral ties. Continuous fiber sheet used for seismic retrofitting of the members are Kevlar sheet (A-1), Technora sheet (A-2) and carbon fiber sheet (C). Still, the experimental result of ductility ratio μ_f in each specimen is also shown in the table. The ductility ratio μ_f of upgraded members

Table1 Dimension and material properties of the specimens

Specimen		T-0	T-1	T-2	T-3	T-4	T-5	K-0	K-1	K-2	K-3	K-4	C-1	C-2	C-3
Sheet type		Non	A-2	A-2	A-2	A-2	A-1	Non	A-1	A-1	A-1	A-2	C	C	C
B	cm	70	60	60	80	80	70	45	45	45	45	45	70	70	70
H	cm	70	60	60	80	80	70	30	30	30	30	30	70	70	70
d	cm	64	54	54	74	74	64	26.5	26.5	26.5	26.5	26.5	64	64	64
a	cm	320	290	290	300	300	300	150	150	150	150	150	320	320	320
N	kN	1921	1176	1176	2352	2352	1959	79.38	79.38	79.38	79.38	79.38	1921	1921	1921
f_{sy}	MPa	349	345	349	345	345	316	368	368	368	368	368	349	349	349
p_w	%	0.89	0.98	0.98	0.80	0.80	0.89	1.17	1.17	1.17	1.17	1.17	0.89	0.89	0.89
f_{wy}	MPa	345	325	317	319	319	325	394	394	394	394	394	345	345	345
A_w	mm^2	63.6	63.6	63.6	63.6	63.6	63.6	31.7	31.7	31.7	31.7	31.7	63.6	63.6	63.6
S	cm	15	10	10	15	15	15	25	25	25	25	25	15	15	15
f'_c	MPa	36.65	21.95	27.34	22.54	24.01	20.09	29.40	31.16	32.05	30.38	30.87	38.22	37.14	38.91
f_{fu}	MPa	0	2950	2950	2842	2896	2666	0	2401	2401	2401	2663	4312	4312	4322
t_f	mm/n_f	0	0.14	0.14	0.22	0.36	0.29	0	0.19	0.19	0.19	0.17	0.111	0.111	0.111
n_f	-	0	1	3	2	2	3	0	1	2	2	1	3	5	8
E_f	MPa	0	82.32	82.32	79.38	80.85	117.6	0	127.4	127.4	127.4	87.22	251.9	251.9	246.0
μ_f	-	4.20	7.20	9.45	7.30	7.05	10.30	5.20	7.70	9.90	8.60	9.40	7.26	7.85	9.07

is determined using the envelope in the hysteresis curve for load-peak displacement ($P-\delta$ curve) obtained through reversed cyclic load test. The limit displacement δ_{limit} at which the load-carrying capacity at the yield point δ_y can be maintained is divided by the yield displacement. However, the ductility ratio μ_f in the table is set to the average for positive direction load and negative direction load.

Results of study

The experimental data on the contribution of A-1, A-2 and C types sheets are organized in terms of the relationship between the ductility ratio μ_f and the ratio of shear capacity to flexural one $R_{c,s,f}$ (ex. Fig1). $R_{c,s,f}$ is as follows:

$$R_{c,s,f} = (V_c + V_s + (E_f / E_s) \cdot V_f) / V_{mu} \quad (1)$$

where V_c, V_s and V_f are the shear contribution due to concrete, shear reinforcing bars and continuous fiber sheets, respectively. V_{mu} is the maximum shear force when a member reaches the existing flexural load-carrying capacity M_u. E_s and E_f are the modulus of elasticity for reinforcing bar and continuous fiber sheet respectively. V_f is as follows:

$$V_f = A_f \cdot f_{fu} \cdot z / S_f \quad (2)$$

where f_{fu} is the tensile strength of the sheet. A_f is total cross-sectional area of the sheets in space S_f. S_f is spacing of the sheet. z is lever arm length (generally set to d/1.15, d is effective depth). The values for V_c, V_s, V_f and V_{mu} are calculated using the mean values of the material strengths for concrete, steel and continuous fiber sheets, and with all material factors and member factors set to 1.0. From the regression line of each data in this Figure, the ductility ratio of members retrofitted by A-2 sheets is greatly different from the others, though that retrofitted by A-1 and C type sheets agrees almost.

Here, the relationship between ductility ratio and $R_f = V_f / V_{mu}$ was summarized in Figure 2. In the legend of Figures 2, the values of $R_{c,s} = (V_c + V_s) / V_{mu}$ are also shown.

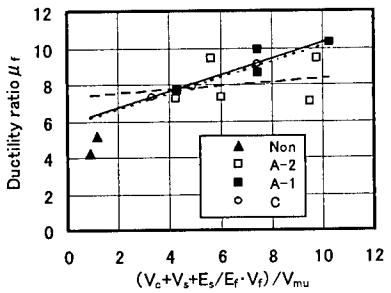

Fig.1 Relationship between μ_f and $R_{c,s,f}$

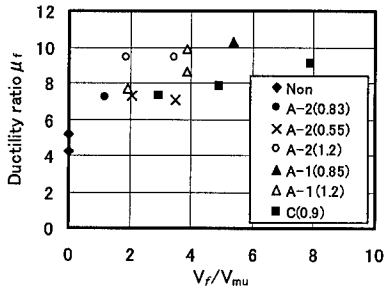

Fig.2 Relationship between μ_f and R_f

On the specimens in which the value in the legend is near for 1.0, the ductility ratio is comparatively improved, as the quantity of continuous fiber sheet increases. However, it is proven that the ductility ratio of the specimens in which this value is 0.55 is not almost improved, even if the quantity of continuous fiber sheet increases. Therefore, Using $R_{c,s,f}$ in the simplicity, ductility ratio of the members retrofitted with the type of three sheets cannot be integrated by the effect of the experimental data of specimens of which $R_{c,s}$ is small. Then, experimental data are organized again in terms of the relationship between the ductility ratio and $(V_c+V_s)/V_{mu}\cdot(1+E_s/E_f(V_f/V_{mu}))$ (ex. Fig3).

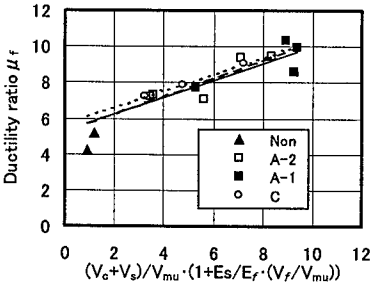

Fig.3 Ductility ratio of members upgraded with continuous fiber sheets

From the regression line of each data in this Figure, it can be seen that, by organizing the ductility of the member retrofitted A-1, A-2 and C type sheets in terms of the relationship with $(V_c+V_s)/V_{mu}\cdot(1+E_s/E_f(V_f/V_{mu}))$, it is possible to integrate both and evaluate them as a linear relationship.

The proposal of the design ductility ratio

In the JSCE standard, considering the lowering of V_c by the action repeatedly after the bending yield of reinforcement, ductility ratio of the RC members has been evaluated in the term of $(0.5\cdot V_c+V_s)/V_{mu}$. Then, by multiplying *0.5* in V_c, the ductility ratio of the member retrofitted by the continuous fiber sheets should be evaluated. The basic formula that determines the ductility ratio is shown in **Equation (3)**.

$$\mu_f = a\cdot\frac{(0.5\cdot V_c+V_s)}{V_{mu}}\cdot\left(1+\frac{E_s}{E_f}\cdot\frac{V_f}{V_{mu}}\right)+b \quad (3)$$

And, shear contribution V_f due to the continuous fiber sheet retrofitted in the bridge axis cross is substituted in **Equation (3)**. In addition, reinforcement quantity and ultimate strain of the continuous fiber sheet are clarified.

$$\mu_f = a\cdot\frac{(0.5\cdot V_c+V_s)}{V_{mu}}\cdot\left(1+\frac{E_s}{V_{mu}}\cdot\frac{A_f\cdot f_{fu}\cdot z}{E_f\cdot S_f}\right)+b$$

$$= a\cdot\frac{(0.5\cdot V_c+V_s)}{V_{mu}}\cdot\left(1+\alpha_o\cdot\frac{\varepsilon_{fu}\cdot\rho_f}{V_{mu}/(B\cdot z)}\right)+b \quad (4)$$

where a,b: Constant got from the regression line. B: Member width. ε_{fu}: Ultimate strain of the sheets ($\varepsilon_{fu}=f_{fu}/E_f$). α_o: Coefficient used to calculate member ductility ratio (for columns shear-reinforced with lateral ties, α_o may be used as the modulus of elasticity for the lateral ties). ρ_f: Shear reinforcement ratio of the sheets. ρ_f is as follows:

$$\rho_f = A_f/(S_f\cdot B)=2\cdot n_f\cdot t_f\cdot S'_f/(S_f\cdot B) \quad (5)$$

where t_f: Thickness of one play of the sheets. n_f: Number of plies of the sheets. S'_f: Width of the sheet.

Referring to the results [1-7] of members reinforced by lateral ties under reversed cyclic load tests, the experimental data on the contribution of continuous fiber sheets are organized in terms of the relationship between the ductility ratio and $(0.5\cdot V_c+V_s)/V_{mu}\cdot\{1+\alpha_o\cdot\varepsilon_{fu}\cdot\rho_f/V_{mu}/(B\cdot z)\}$.

The results are shown in Figure 4. It can be seen that, by organizing the ductility of the members retrofitted with A-1, A-2 and C type sheets in terms of the relationship with $(0.5 \cdot V_c + V_s)/V_{mu} \cdot \{1 + \alpha_e \cdot \varepsilon_{fu} \cdot \rho_f / V_{mu}/(B \cdot z)\}$, it is possible to integrate both and evaluate them as a linear relationship.

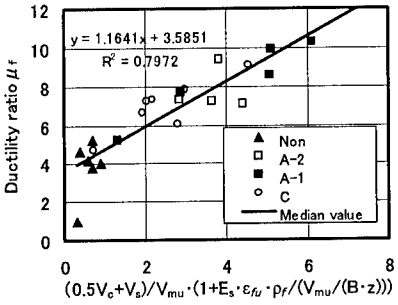

Fig.4 Ductility ratio of members upgraded with continuous fiber sheets $(0.5 \cdot V_c + V_s)/V_{mu}$

However, as can be seen from the horizontal axis in the figure, the proposed function for evaluating ductility ratio is a relatively accurate one developed through various trials. In these recommendations, a member factor is introduced based on the regression equation for the test results in order to proposed a calculation **Equation (4)**. Therefore, on the **Equation (4)**, both material factor and member factor used for calculation of V_c, V_s and V_{mu} are set to 1.0.

$$\mu_{fd} = \left[1.16 \cdot \frac{(0.5 \cdot V_c + V_s)}{V_{mu}} \cdot \left(1 + \alpha_e \cdot \frac{\varepsilon_{fud} \cdot \rho_f}{V_{mu}/(B \cdot z)}\right) + 3.58\right] / \gamma_{bf} \quad (6)$$

where γ_{bf} : Member factor used for calculation of μ_{fd} (generally set to 1.3)
ε_{fud} : Design ultimate strain of continuous fiber sheets. ε_{fud} is as follows:

$$\varepsilon_{fud} = f_{fud} / E_f = (f_{fuk} / \gamma_{mf}) / E_f \quad (7)$$

where f_{fuk} : Characteristic value of tensile strength of the sheets. γ_{mf} : Material factor of the sheets (generally set to 1.2).

Conclusion

On this paper, by organizing the ductility of the members retrofitted with Aramid fiber sheets and Carbon fiber sheets in terms of the relationship with $(0.5 \cdot V_c + V_s)/V_{mu} \cdot \{1 + \alpha_e \cdot \varepsilon_{fu} \cdot \rho_f / V_{mu}/(B \cdot z)\}$, it is possible to integrate both and evaluate them as a linear relationship. In addition, the values for the modulus of elasticity E_f and shear reinforcement ρ_f for the continuous fiber sheets used in previous tests are in the range of 80 – 235 kN/mm^2 and 0 – 2.54$\times$ 10^{-3}, respectively. Therefore, it is important to note that **Equation (6)** is only applicable within these ranges. And, **Equation (6)** confirms that ductility ratio can be ensured for reinforcement of reinforced concrete columns with the typical rectangular section using carbon fiber sheets and Aramid fiber sheets. Accordingly, when the conditions are markedly different from those of rectangular reinforced concrete columns, a separate safety study is required.

References

1. Railway Technical Research Institute: Design Construction Guidelines on the Seismic Retrofitting of Railway Viaduct Columns using Carbon Fiber Sheet, 1996.
2. Railway Technical Research Institute: Design Construction Guidelines on the Seismic Retrofitting of Railway Viaduct Columns using Aramid Fiber sheet, 1996.
3. Research Institute on Strengthening of Concrete Structures by Aramid Fibers: Design Construction Guidelines on the Retrofit of RC Piers using Aramid Fiber Sheet, 1997.
4. Masukawa, J. and et al.: Seismic Retrofit of RC Piers Using Carbon Fiber and Aramid Fiber Sheets, Proceedings of the Symposium on Utilization of Non-Metallic Materials for Concrete Structures, pp.193-198, 1996
5. Osada, k. and et al. : Seismic Retrofit of RC Piers Using Carbon Fiber, Concrete Research and Technology, JCI, pp.189-203, 1997
6. Osada, K. and et al.: Seismic Retrofit of RC Piers Using Carbon Fiber, Concrete Research and Technology, JCI, pp.189-203, 1997.
7. Hakamada,F: Experimental and Analytical Study on Seismic Retrofit of RC Wall Type Piers and Seismic Retrofit of RC Structures Using Carbon Fiber Reinforcing Polymers, Proceedings of the Symposium on Seismic Resistant Technology of Concrete Structures, 1997.

Proceedings of 7th Japan International SAMPE
Symposium & Exhibition, Nov. 13-16, 2001

Strengthening Behavior of Carbon Fiber Sheet Using Flexible Layer

Hideyuki Komaki#, Yoshio Sohda#, Toshiya Maeda##, and Kentarou Tsubouchi###

#: Central Technical Research Laboratory, Nippon Mitsubishi Oil Corporation
8, Chidori-cho, Naka-ku, Yokohama, 231-0815, Japan
E-mail:hideyuki.komaki@nmoc.co.jp

##: Technology Department Civil Engineering Division, Shimizu Corporation
SEAVANS SOUTH, 2-3, Shibaura 1-chome, Minato-ku, Tokyo, 105-8007, Japan

###: Research and Development Department, Nippon Mitsubishi Oil Corporation
3-12, Nishishimbasi 1-chome, Minato-ku, Tokyo, 105-8412, Japan

Abstract

Carbon Fiber Sheet (CFS) is used for strengthening of concrete structures due to its excellent durability and easy application. However, when CFS is bonded to the lower side of reinforced concrete (RC) bridge slabs or RC beams in order to increase the bending load capacity, CFS does not exhibit enough tensile capacity by the delamination failure of CFS. In this study, to reduce this delamination phenomenon, bending experiments were conducted using RC beams strengthened by CFS with a highly flexible material, called flexible layer, inserted between the concrete and CFS. As a result, it was found that the insertion of flexible layer relieves the stress concentration on CFS and improves the bonding behavior of CFS, thereby improving the strengthening effect of CFS.

Key Words: Carbon Fiber Sheet, Flexible Layer, Bending Strengthening, Bond Behavior, Stress Dispersion

Introduction

Carbon Fiber Sheet (CFS) is widely used to strengthen concrete structures because of its light weight, high tensile strength, and non-corrosiveness. The bonding characteristics of CFS with the reinforced concrete (RC) greatly influence the strengthening effect, because the stress is transmitted from the concrete to CFS by an adhesive such as epoxy resin. However, in many experiments the delamination failure of RC members strengthened by CFS has been observed[1,2].

To reduce this delamination phenomenon, the authors propose a strengthening method in which a highly flexible material, called flexible layer, is inserted between the concrete and CFS. This paper reports the results of bending experiments using RC beams and the reduction of the delamination phenomenon due to the insertion of flexible layer.

Outline of Experiment

Figure 1 shows the details of the test specimen. The length of the test beam is 2,200mm, the width is 200mm, and the thickness is 200mm. CFS was bonded to the lower side of the test beam with a general epoxy resin after base work with a

sander and primer. The weight of CFS is 300g/m^2, the strengthening length of CFS between the two fulcrums is 1,740mm, and the fiber direction of CFS is parallel to the longitudinal reinforcement. Flexible layer was spread on the strengthened surface of the test beam after the application of the primer. The thickness of flexible layer is 0.5mm. Table 1 shows the details of the experimental specimens, and Table 2 shows the mechanical properties of the materials.

A loading test was then carried out after more than 7 days of CFS bonding at room temperature. The distance between the loading points is 300mm, and the distance between the fulcrums is 1800mm. The loading test measured the load, displacement, strain of tensile reinforcement, and strain of CFS. Figure 2 shows the arrangement of the strain gages for the tensile reinforcement and CFS.

Experimental Results

The results of the experimental specimens are shown in Table 3. Figures 3 and 4 show the relationship between the

Table 1 Details of Experimental Specimens

Specimen	Number of CFS (ply)	Thickness of Flexible Layer (mm)
SP-0	–	–
SP-C	1	–
SP-C-E500	1	0.5
SP-C2	2	–
SP-C2-E500	2	0.5
SP-C2-E1000	2	1.0

Table 2 Mechanical Properties of the Materials

CFS	Fiber Weight (g/m^2)	Tensile Strength (MPa)	Elastic Modulus (GPa)	Rupture Strain (x 10^{-6})
	300	4,120	236	15,500
Flexible Layer	Tensile Strength (MPa)	Elastic Modulus (GPa)	Extension (%)	
	1.7	1.0	123	
Steel Bar	Yield Strength (MPa)	Tensile Strength (MPa)	Extension (%)	
	370	526	25.5	
Concrete	Compressive Strength (MPa)			
	33.3			

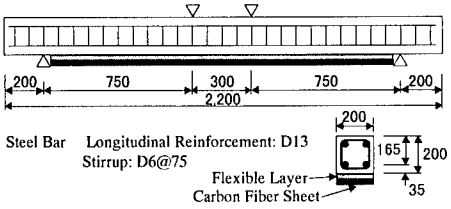

Fig.1 Detail of Test Specimen

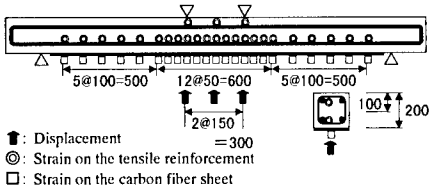

Fig.2 Arrangement of Strain Gages

Table 3 Experimental Results of Specimens

Specimen	Yield Load*1 (kN)	Ultimate Load (kN)	Strength Improvement	Ultimate Displacement (mm)	Ultimate Strain of CFS (x10^{-6})	Failure Mode
SP-0	40.2	44.1	1.00	22.7	–	Flexure
SP-C	44.4	78.3	1.78	21.7	7,790	CFS Delamination
SP-C-E500	45.4	101.0	2.28	33.4	15,750	CFS Breakage
SP-C2	61.6	109.0	2.47	16.4	71,70	CFS Delamination
SP-C2-E500	61.2	148.0	3.36	40.7	13,080	Delamination*2
SP-C2-E1000	50.7	132.0	2.99	45.5	14,500	Delamination*2

*1: Load at the Yield Strain of Tensile Reinforcement (1,800x10^{-6})

*2: Delamination of Cover Concrete of Tensile Reinforcement

specimen displacement and the load. The ultimate load of specimen SP-C strengthened by CFS increased by 78% compared to the control specimen SP-0. The ultimate strain of CFS of SP-C was $7{,}790 \times 10^{-6}$. The failure mode was delamination of CFS, the same as in previous studies. A photograph of this failure mode is shown in Photo 1. In contrast, the ultimate load of SP-C-E500 with an inserted flexible layer increased by 128% compared to SP-0. The ultimate strain of CFS was $15{,}750 \times 10^{-6}$, and the failure mode was CFS breakage. A photograph of this failure mode is shown in Photo 2. This result indicates that CFS achieves over 90% of its tensile strength by using flexible layer. It is thus confirmed that flexible layer suppresses the delamination of CFS and that the strengthening effect of CFS is improved greatly.

In the case of SP-C2 series, the effect of flexible layer was the same as for SP-C series. The failure mode was delamination of cover concrete of tensile reinforcement. A photograph of this failure mode is shown in Photo 3. Specimen SP-C2-E500 with a thickness of 0.5mm flexible layer had a higher strengthening effect than specimen SP-C2-E1000 with a thickness of 1.0mm. Therefore in this study it is considered that the best thickness of flexible layer is 0.5 mm.

The strain distributions of CFS and tensile reinforcement of specimens SP-C2 and SP-C2-E500 are shown in Figures 5 to 8.

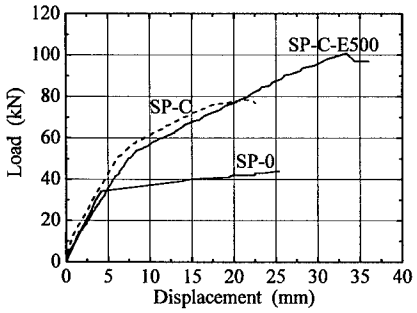

Fig.3 Load – Displacement Relationship

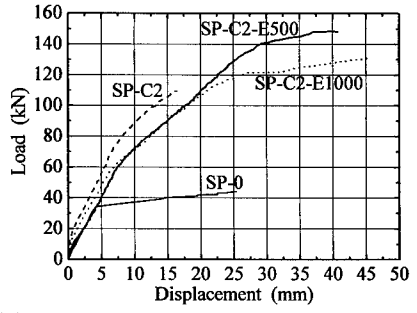

Fig.4 Load – Displacement Relationship

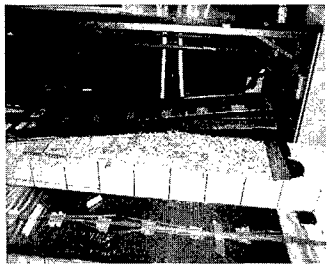

Photo 1 Failure Mode of Specimen SP-C2

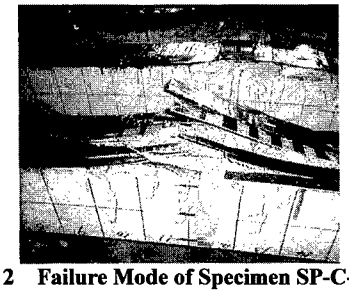

Photo 2 Failure Mode of Specimen SP-C-E500

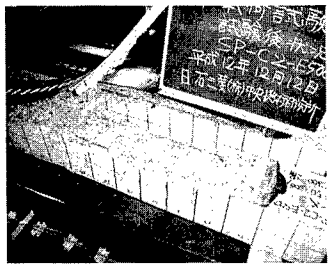

Photo 3 Failure Mode of Specimen SP-C2-E500

As for specimen SP-C2 without flexible layer, the strain of CFS was not distributed equally at the early stage of loading. At the ultimate condition, the strain of CFS at the moment area showed about $7{,}000 \times 10^{-6}$ equally. In contrast, as for specimen SP-C2-E500 with an inserted flexible layer, the strain of CFS was distributed equally at the early stage of loading. This result indicates that the tensile stress of CFS is distributed equally. At the ultimate condition, the strain of CFS showed high values and was distributed over a wide area. At the side area of RC beam, CFS strain of SP-C2-E500 with an inserted flexible layer was higher than that of SP-C2 at the same load. This phenomenon confirmed that flexible layer eases stress concentration of CFS and that CFS resists high load over a wide range. Regarding the strain distribution of the tensile reinforcement, tensile reinforcement resists load over a wide range by the effect of flexible layer, as in the case of CFS.

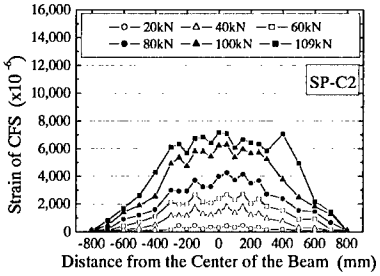

Fig.5 Strain Distribution of CFS in Specimen SP-C2

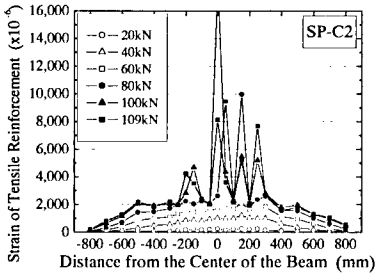

Fig.6 Strain Distribution of Tensile Reinforcement in Specimen SP-C2

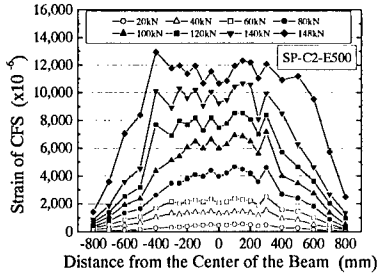

Fig.7 Strain Distribution of CFS SP-C2-E500 in Specimen

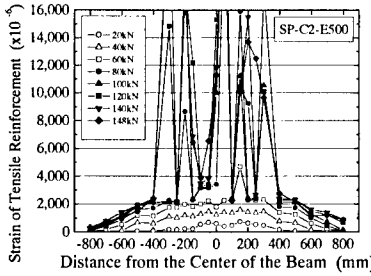

Fig.8 Strain Distribution of Tensile Reinforcement in Specimen SP-C2-E500

Conclusions

Flexible layer controls the delamination of CFS, and the strengthening effect of CFS is improved greatly.

Due to flexible layer, CFS demonstrates over 90% of its tensile strength.

Flexible layer eases the stress concentration of CFS and tensile reinforcement. Therefore, CFS and tensile reinforcement resist load over a wide range.

References

1. Y. Takahashi, Y. Sato, T. Ueda, T. Maeda and A. Kobayashi: Proc, of 3rd International Symposium of Non-Metallic(FRP) Reinforcement for Concrete Structures, Vol1, 327 (1997).

2. K. Ono and H.G. Park: Proc, of 8th KKNN Seminar in Civil Engineering, 171 (1998).

Proceedings of 7th Japan International SAMPE
Symposium & Exhibition, Nov. 13-16, 2001

Crushing Properties of FRP Pipe Bolted Joint to Steel Component - Integrated Crush Experiments -

Hiroshi Saito#, Ryuji Inai#, Tamotsu Nakatani##, Atsushi Yokoyama# and Hiroyuki Hamada#

#: Division of Advanced Fibro Science, Kyoto Institute of Technology
Matsugasaki, Sakyo-ku, Kyoto 606-8585, JAPAN
E-mail: hhamada@ipc.kit.ac.jp
##: Crash Safety, Japan Automobile Research Institute
2530 Karima, Tsukuba, Ibaraki 305-0822, JAPAN
E-mail: ntamotsu@jari.or.jp

Abstract

In this study the crushing performance of FRP tube, which was jointed to the steel component by bolts, was evaluated (Integrated Crush Experiments). The number of bolts and the diameter of bolts were varied. Two defferent fracture aspects were observed; one was bearing failure around the holes and bolt failure, and the other was progressive crushing without bolt failure, which was obtained in crushing test by using FRP pipe only (Element Crush Tests). In bolt jointed FRP and steel component, it is very important to optimise the number of bolts and holes in designing of FRP components. We proposed one of the designing guides from real data. The stress calculation method applied on the rivets jointing was used. Calculated results and actual fracture morphologies were compared in order to evaluate validity of designing guide.

Key Words: Bolt Joint, Crushing Energy Absorption, Progressive Crushing, Buckling Fracture

Introduction

Crushing is the most important keyword in car, aircraft, ship, helicopter and so on due to create safety society. The construction with high crushing performance can protect the passengers from the accident. In order to save energy a lightweight construction should be needed and fibre reinforced composites are suitable material system for this demand. Also it is well known that the crushing performance of fibre reinforced composites is very high. Therefore safety and lightweight construction can be achieved by using FRP.

Crushing tests under compressive load by FRP tubes have been preformed and typical fracture aspects called progressive crushing was confirmed. These tests were carried out by using only FRP tube, that is without connection to any other components, so that these are called "element crush test". In actual applications, FRP tube would be inserted into the body, for example behind bumper and in front of crush tube made by steel in the case of passenger car body. The simple question is arisen, that is how to connect the FRP tube to the car body. In order to find the answer of these questions there are two procedures; one is numerical simulation of car body in the case of crushing accident and the other is performing complex experiments. In the simulation the material property should be

expressed properly. From experimental approaches although experimental set up would be complex and expensive, we could confirm the crushing performance of FRP tube in the car body. Here, this experiment is called "Integrated Crushing Experiments" (ICE). Both efforts from simulation and ICE enable to urge usage of FRP tube in the car body indeed.

In this paper one of examples of ICE was presented, in which FRP tube was connected with steel circular column by steel bolts. The compressive load was applied to the FRP tube and the possibility of progressive crushing was examined.

Detail in the Body Text

Materials and Experimental Set Up

Material was glass cloth epoxy composite tube. Surface treatment on the glass fibre was amino-silane coupling agents. Geometry of tube was 50mm of inner diameter and 2.5mm of wall thickness. Weft fibres were aligned to the longitudinal direction of the tube.

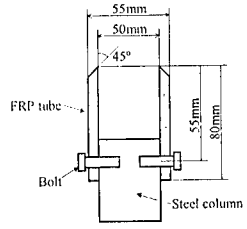

Fig.1 Test Instruments of Integrated Crushing Experiments

"Integrated Crush Experiment" (ICE) set-up is shown in Fig.1. FRP tube with 45° chamfer at the one end is connected to steel circular column with 50mm diameter, because the column is inserted into the FRP tube. The length of FRP tube was 80mm and the several holes were made at the distance from the top of the chamfer of 55mm length. The number of holes was 4 or 8, and 6mm or 8mm diameter bolts were inserted to these holes. Compressive load was applied through flat steel plate from the above of the chamfer at 2mm/min speed. Load-displacement curve was recorded and fracture aspects were observed at both chamfer region and bolt connected region.

Results

Fig.2 shows the load-displacement curves in the cases of M8 bolts with 4 holes (case 1), M8 bolts with 8 holes (case 2) and M6 bolts with 8 holes (case 3). In case 2 and case 3, X mark was indicated in the figures. This means that bolts were failed during compression test, so that the experiments were stopped. In case 2 the load kept at constant value, 43kN approximately. This feature is very similar to load- displacement curve in the case of progressive crushing by element crush test, in which FRP tube with 45° chamfer at the one end was set on the steel plate. Table 1 summarises the results of ICE in this paper, here the maximum crush load, and mean crush load, specific energy absorption value (Es) indicated. Es value in case 2 was 63kJ/kg, which is almost same or slightly higher value as results of element crush test by using same material and same geometry. Fig.3 shows photographs of over view of fractured tube and closed-up of bolted joint area. In the cases of 1 and 3, in which steel bolts were broken down, and the chamfer part was crashed. Bearing failure could be observed in the longitudinal direction. In case 2 although small bearing fracture was detected, the material at the chamfer part was crushed to both inside and outside of the tube, which would be starting of progressive crushing.

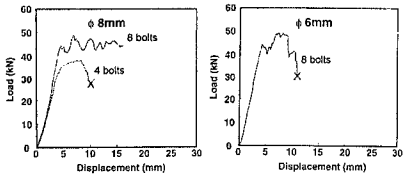

Fig.2 Load-Displacement Curves of Bolt Jointed FRP Tubes

Table 1 The Results of Integrated Crushing Experiments

Specimen	Max Crush Load (kN)	Mean Crush Load (kN)	Es (kJ/kg)
M8 x 4	36.8	---	---
M8 x 8	48.0	43.4	63.4
M6 x 8	47.5	---	---

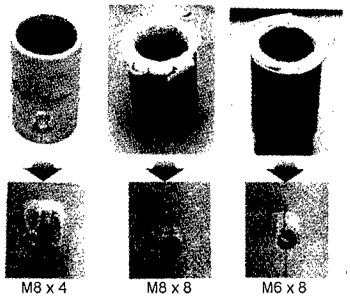

Fig.3 Photographs of Each FRP Tubes after Compression

Discussion

From these results progressive crushing was shown only in case 2, in which FRP tube had 8 holes. Only few delaminations were observed around the holes, fracture was mainly occurred at the tip of tapered region. This means that compressive stress of FRP tube had reached at the bearing strength of FRP tube before shear stress of a bolt reached the tolerant shear stress. Therefore bolts were safe and FRP showed progressive crushing.

In case 1, however the tip of tapered region of FRP tube was not buckled so much, delaminations and large buckling were shown around the holes. Because the contrary phenomenon of case 2 was happened, that is, shear stress of a bolt had reached at the tolerant shear stress before compressive stress of FRP tube reached the bearing strength. Therefore FRP tube did not show progressive crushing and bolts were failed. From load-displacement curve of Fig.2 and a picture of Fig.3, the region around the holes was delaminated and buckled by bolts at the displacement between 5mm and 8mm, in which load varied gradually. Therefore it is estimated that delaminations and buckling around the holes progressed in this duration.

In case 3, however fracture was slightly observed at the tip of FRP tube, bolts were failed. Here we proposed a hypothesis, that is there were 2 statuses during compressive test. This hypothesis is based on the estimation that shear stress generated in bolts was quite near the tolerant shear stress of bolts. In first status FRP tube started buckling, and conversely shear stress of bolts did not exceed the tolerant shear stress. In second status, fracture of FRP tube stopped and shear stress of bolts was equal or not exceeded the tolerant shear stress. Therefore in this hypothesis, buckling of FRP tube progressed intermittently and failure of bolts progressed gradually by repeating each status alternatively. Table 2 shows the summary of the statuses of compressive stress of FRP tube and shear stress of bolts in each case.

In order to generate progressive crushing in FRP tube and not to fail the bolts, stress status should be like case 2. Thus when FRP tube is jointed to the other components by bolt joint for example, stress distribution must be a critical parameter in order to occur progressive crushing in FRP tube. Thus it is very important to optimise the number of bolts and holes in designing

of FRP components.

Table 2 the status of compressive stress of FRP tube and shear stress of bolts

Case No.		Compressive stress applied on FRP tube	Shear stress applied on bolts
1		$\sigma_{FRP} > \sigma_{FRP,B}$	$\tau_{bolt} < \tau_{bolt,B}$
2		$\sigma_{FRP} < \sigma_{FRP,B}$	$\tau_{bolt} > \tau_{bolt,B}$
3	a	$\sigma_{FRP} > \sigma_{FRP,B}$	$\tau_{bolt} < \tau_{bolt,B}$
	b	$\sigma_{FRP} < \sigma_{FRP,B}$	$\tau_{bolt} \leq \tau_{bolt,B}$

where σ_{FRP}: compressive stress of FRP tube, $\sigma_{FRP,B}$: bearing stress of FRP tube, τ_{bolt} : shear stress of bolts, $\tau_{bolt,B}$: tolerant shear stress of bolts.

In this paper, we proposed one of the designing guides from real data. Here, the stress calculation method applied on the rivets jointing was used as the reference. Buckling would not be occurred and FRP pipe would show progressive crushing, when the compressive stress at projection area of hole, σ_{FRP} which is bearing stress, is smaller than the bearing strength of FRP, σ_C. This relationship can be expressed by following simple equation.

$$\sigma_{FRP} = \frac{P}{ndt} < \sigma_C \qquad (1)$$

Here P is applied load to the component, n is the number of bolts, d is a diameter of bolt and t is the thickness of FRP tube. Real σ_{FRP} values are shown in next Table 3.

In order to discuss these results, each σ_{FRP} was compared with real fracture morphologies. As shown in Fig. 3 buckling did not recognised in case 2, in which σ_{FRP} was 300MPa. Oppositely slight buckling was occurred around the holes in case 3, in which σ_{FRP} was 396MPa. In case 1, σ_{FRP} was so higher than 300MPa of case 2, and large buckling and delaminations were shown around the holes. Thus σ_{FRP} and real fracture morphologies around the holes have certain relationship, and it is possible to determine the optimum number of bolts from the equation 1. Therefore tolerant bearing strength of FRP, and the thickness of tube should be known beforehand, and applied mean load during progressive crushing should be estimated from previous experiments. If the diameter of bolts was determined finally, the optimum number of bolts was calculated from the equation. At the moment compressive or bearing strength has not been measured, so that it is difficult to discuss in more detail. However in case 2 which showed progressive crushing without any failure of bolts, σ_{FRP} was the lowest. Further we will discuss the relationship between strength and generated stress by using simple equation and the optimum number of the connected bolts would be determined.

Table 3 Compressive Stress of FRP at Projection Area of Hole

Case	P (kN)	The number of bolt	d*t (mm^2)	σ_{FRP} (MPa)	Comment
1	36.8	4	8*2.5	600	Buckled.
2	48.0	8	8*2.5	300	Not buckled.
3	47.5	8	6*2.5	396	Slightly buckled.
Ref. data	5.0	1	6*3	278	Buckled. Matrix is vinyl ester.

Conclusion

In this study, it was evaluated that the effects of bolt jointing between FRP tube and the other components on the energy absorption performance. The optimisation of the number of bolts and holes is necessary in designing stage of this kind of jointed FRP components. Therefore we proposed one of the designing guides from real data.

Proceedings of 7th Japan International SAMPE
Symposium & Exhibition, Nov. 13-16, 2001

Numerical Simulation for Crashing Behavior of FRP Tube under Impact Loading

Motoharu Tateishi
Nippon MARC
2-7-1, Nishi-Shinjuku, Shinjuku-ku, Tokyo、Japan

Atsushi Yokoyama, Hiroyuki Hamada
Division of Advanced Fibro-Science, Graduate School
Kyoto Institute of Technology
Matugasaki, Sakyo-ku, Kyoto, 606-8585, Japan
TEL +81-75-724-7754 FAX +81-75-724-7337
E-mail yokoyama@ipc.kit.ac.jp

Key Words: FRP tube, Progressive Crushing, FEM, Composite materials

Abstract

Tapered FRP tubes have high energy absorption performance under axial compressive load. FRP will be useful for structural material of a shock absorber in the various industries. And in order to evaluate the behavior of this material, several experimental tests and numerical simulations using FEM are carried out recently. However, it is difficult to simulate properly the behavior of tapered FRP tubes, so called "Progressive Crushing" with FEM, because the fracture mechanism contains various kinds of fractures such as delimitation, fiber fracture and so on. In this study, we proposed a special FEM model based on experimental data that is useful for the crush-worthiness analysis of FRP tube.

1. Introduction

As science-technology progresses, various new materials are developed and applied to structural parts. In the automobile industry, where energy saving and weight reduction is an important issue, Fiber Reinforced Plastic (FRP) is currently the focus of attention as an alternative material to metal, which has been mainly used up till now. Therefore, it has become an important task to evaluate the strength and simulate crushing behavior of FRP tubes. One method is to put the numerous test results into a database and estimate how FRP absorbs energy. On the other hand, several studies on simulation of the crushing behavior of FRP using FEM analysis have also been reportedly done. However, the crushing behavior of FRP itself is a very complicating

phenomenon, and it is difficult to obtain accurate results with currently available algorithms. Also, these simulations usually require huge amount of CPU time that is not acceptable for practical use. The objective of this study is to develop a numerical model that represents the FRP crushing behavior with accuracy, in order to enable FEM analysis to be performed with practical simulation run time.

2. Progressive Crushing / Numerical model

FRP tubes are known to have high-energy absorption performance under axial compressive load. The crushing behavior seen under such load conditions is called Progressive Crushing. FEM is often used to simulate progressive crushing, and some criteria for this kind of simulation have been reported. However, there are several problems that make it difficult to simulate Progressive Crushing accurately. Then, we will first define the characteristics of Progressive Crushing, and find out the necessary numerical models in here. The breaking pattern of the FRP tube shown in Fig 2.1 under axial compressive load is shown in Fig 2.2. Glass cloth and epoxy are used as the material. The breaking starts at the top end of the tube and progresses successfully, and the material deforms both inwards and outwards of the tube. During progression of crushing, the peak load value does not change so much, while displacement increases. This behavior is called Progressive Crushing, and its characteristics can be used effectively for shock absorbing purposes because of its high-energy absorption rate. Fig 2.3 shows the cross section of the broken tube. Various crushing behaviors such as delamination and fiber fracture can be seen. In order to simulate a phenomenon as complicated as this, a special numerical model is needed. The numerical models that represent the formation mechanism of the petal-like breaking pattern, and the progress of the formed breaking pattern are especially important. In this study, we propose the latter numerical model this time.

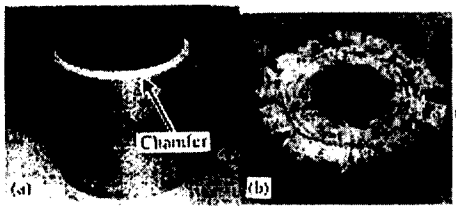

Fig2.1 FRP tube

Fig2.2 Crush pattern

Fig2.3 Cross section

3. Numerical Model of the Crushing Progress

3.1 Finite elements

A four-node thick-shell element with global displacements and rotations as degrees of freedom was used in this study to model the crushing of an FTP tube. And we used MSC.MARC Version 2001 with user subroutine functionality for implementation of our proposed constitutive law for FRP crushing behavior.

3.2 Elastic constitutive law

The ordinal orthotropic constitutive law for composite material was used in order to describe the elastic behavior

3.3 Definition of trigger

We assume that an element that is under crushing always has trigger. Therefore we only perform the crushing check for the element that has trigger. After completion of element crushing, this trigger moves to the neighbor element automatically. In this study, we took a simplified algorithm of setting these triggers on the elements that has taper as an initial condition, then these triggers migrate according to the element connectivity since it is not easy task to control trigger migration automatically for general occasion. However, this algorithm may not always work for arbitrary loading conditions apparently. We will continue to investigate algorithms that work for more general occasions in order to overcome this limitation.

3.4 Crushing criteria

The crushing is determined with the following criteria.

$$\sigma_{yp} \geq \sigma_{11} \quad \text{Remain Elastic} \quad (2)$$

$$\sigma_{yp} < \sigma_{11} \quad \text{Crushing occur} \quad (3)$$

If crushing behavior is detected by Eq.3, the relation between stress and strain is changed as follows.

$$\begin{Bmatrix} \delta\sigma_{11} \\ \delta\sigma_{22} \\ \delta\tau_{12} \\ \delta\tau_{23} \\ \delta\tau_{31} \end{Bmatrix} = \begin{bmatrix} E_{11}R_f & 0 & 0 & 0 & 0 \\ 0 & E_{22} & 0 & 0 & 0 \\ 0 & 0 & G_{12} & 0 & 0 \\ 0 & 0 & 0 & G_{23} & 0 \\ 0 & 0 & 0 & 0 & G_{31} \end{bmatrix} \begin{Bmatrix} \delta\varepsilon_{11} \\ \delta\varepsilon_{22} \\ \delta\gamma_{12} \\ \delta\gamma_{23} \\ \delta\gamma_{31} \end{Bmatrix} \quad (4)$$

Where

$\sigma_{y\,p}$ Primary crushing stress

R_f Stiffness reduction factor due to crushing

δe_{ii} Incremental direct strain components in local coordinates system

$\delta\gamma_{ij}$ Incremental shear strain components in local coordinates system

$\delta\sigma_{ii}$ Incremental direct stress components in local coordinates system

$\delta\tau_{ij}$ Incremental shear stress components in local coordinates

system

R_f governs the work hardening characteristic. If this factor is big enough, then the stress will increase after initial crushing initiated up to the secondary crushing stress, σ_{ys}. The secondary crushing stress σ_{ys} is the critical stress that governs the progression of the petal-like crushing pattern in circumferential direction. Therefore the entire crushing behavior of FRP tube is described with these principal factors, R_f and σ_{ys}. Especially the factor R_f has dependencies of axial stiffness and circumferential stiffness.

4. Analysis Examples with proposed Numerical Model

The finite element model using thick shell elements with rigid surface on the top edge is illustrated in Fig.4.1. This rigid surface represents the weight used in experiment and which moves downward by prescribed displacement in this analysis. Table 4.1 shows the material constants. For this analysis example, we performed three analyses, one is standard model (Case 1), and second one is that circumferential fairure strength is set at 0(Case 2) and the last case(Case 3) is calculated under the reduced circumferential failure. Fig 4.2 shows the load-displacement curve of the three cases. The figure shows that the tube crushes when the load reaches critical point, and displacement progresses alone after the crush occurs but no load increase at all in Case2. Especially in Case 1, we confirmed that the maximum load vibrates after the crush occurs. The amplitude and cycle of this vibration is determined by primary crushing stress, secondary crushing stress and stiffness reduction factor after crushing.

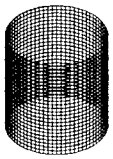

Fig.4.1 FEM Model

Table 4.1 Inelastic constants

	σ_{yp}	σ_{ys}
Case1 (Standard)	-9.7E+01	9.7E+01
Case2		0.0(not included)
Case3		7.0E+01

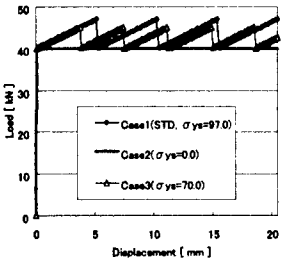

Fig.4.2 Comparison of Load-Displacement Curve

Proceedings of 7th Japan International SAMPE
Symposium & Exhibition, Nov. 13-16, 2001

Development of Lightweight and High Stiffness "New KP-Sheet" for Automotive Headliners by Controlling of Glass Fiber Arrangement

Yutaka Araki#, Shigeru Takano#, Seiji Hanatani##, Masahiko Ito##, and Hideho Kubo##

#: Technical Research Laboratory, Kawasaki Steel Corporation
##: K-Plasheet Corporation
1, Kawasaki-cho, Chuo-ku, Chiba 260-0835, JAPAN
E-mail: y-araki@kawasaki-steel.co.jp

Abstract

For the development of lightweight and high stiffness KP-Sheet, the effects of glass fiber content and glass fiber arrangement to the thickness direction were studied. The value of the elastic slope increased with increasing of the expansion-molded thickness. Although the moldable thickness limit increased with increasing of glass fiber content, the value of the maximum elastic slope was not enhanced at over 50wt% of the glass fiber content. By controlling the glass fiber arrangement to the thickness direction, the spring back force of glass fibers was enhanced. The thickness of the free expanded KP-Sheet increased more than 30% at the same unit weight. As the result, the elastic slope of a new KP-Sheet became 1.5 times as high as that of an ordinary one.

Key Words: Stampable sheet, Automotive headliner, Expansion molding

Introduction

KP-Sheet is a stampable sheet containing polypropylene and glass fiber, and produced by the licensed technology of Arjo-Wiggins, which is similar to that of a paper making method. It has a distinct characteristic of expanding in thickness due to the spring back force of glass fiber when the sheet is heated up to the melting temperature of polypropylene.[1,2]

Utilizing lightweight and high stiffness properties of the expansion-molded articles, KP-Sheet is being used as a base material of automotive headliners.[3] Mechanical properties of the expansion-molded articles depend on the glass fiber content, the glass fiber arrangement, the expansion ratio, and so on.

In this study, the effect of glass fiber content and the glass fiber arrangement on the stiffness property of the expansion-molded articles was investigated.

Experimental Details

Production of KP-Sheet

KP-Sheet webs were produced by a paper making method using chopped glass fiber filament and polypropylene powder as raw materials. The unit weight of the webs was set at 635g/m^2, and the glass fiber content in them was changed from 45 to 60 wt %.
A hot melt film was overlaid in one side of the webs and a polyester scrim was overlaid

in another side of them and they were heated together up to 205 °C and pressed at 0.3MPa for 15 seconds. After cooling, they were changed to consolidated sheets.

Molding of KP-Sheet

The consolidated sheets were heated up to 200°C in a far-infrared oven, and expansion-molded by a cold mold in a desired thickness.

Observation of Glass Fiber Arrangement

The glass fiber arrangement to the thickness direction was observed by soft X-ray photographs using specimens of KP-Sheets expanded freely at 200 °C.

Bending Test

The specimens used in this study for three point bending test were 150mm in length and 50mm in width cut out from the expansion molded articles. Bending tests were conducted at 50mm/min of a crosshead speed and 100mm of a span length. The load was applied from the surface of the hot melt film laminated. Elastic slope was defined as the slope of load-deflection curves at the early stage.

Results

Effect of Glass Fiber Content on Elastic Slope

The relation between expansion molded thickness and elastic slope in each glass fiber content was shown in Figure 1. The value of the elastic slope increased with increasing of the expansion-molded thickness. The moldable thickness limit in a case of 45wt% of the glass fiber content was 2.8mm due to the weak spring back force of glass fibers and the value of elastic slope was just 4N/mm, however, they increased with increasing of the glass fiber content. When the glass fiber content was 50wt%, the elastic slope increased to 5.5 N/mm because the moldable thickness increased to 3.4mm. In cases of over 55wt%, although the moldable thickness limit increased, the value of the maximum elastic slope was not enhanced and was nearly the same as that of 50wt%.

Effect of Glass Fiber Arrangement on Elastic Slope

According to Figure 1, it was found that the elastic slope increased with increasing of the expansion-molded thickness and the most suitable glass fiber content was 50 wt%. Then, for the improvement of the expansion ratio, the production conditions for arranging glass fibers to the thickness direction were studied at this glass fiber content.

As shown in Figure 2, the webs are formed when foam and water are drained out and a mixture of glass fiber and polypropylene are accumulated on the forming belt during paper-making process. It was predicted that the accumulating angle " θ " should affect to the glass fiber arrangement to the thickness direction, therefore, some webs were

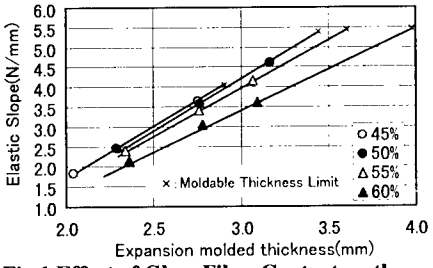

Fig.1 Effect of Glass Fiber Content on the Elastic Slope

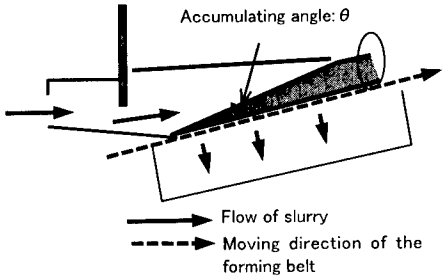

Fig.2 Schematic Diagram of Paper-making Machine

produced under a condition of high accumulating angle. According to the soft X-ray photographs shown in Figure 3, it was found that the glass fibers were strongly arranged to the thickness direction at that condition.

The relation between free expansion thickness and elastic slope of expansion molded articles of KP-Sheets produced by the ordinary condition as well as a high accumulating angle are compared in Figure 4 and 5. The compression ratio was set at 0.9 in the both molded articles.

The free expansion ratio of a new KP-Sheet is 30% higher than that of an ordinary one. It is due to the glass fiber arrangement to the thickness direction as shown in Figure 3 resulting in the strong spring back force of glass fiber. The elastic slope increased with increasing of the thickness. The elastic slope of a new KP-Sheet is 1.5 times as high as that of an ordinary one at the same unit weight. It means that it is possible to decrease 20% of the unit weight at the same elastic slope resulting in cost reduction of molding articles.

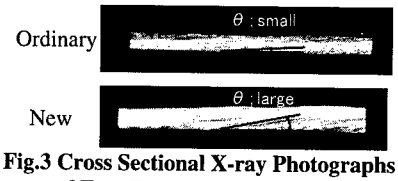

Fig.3 Cross Sectional X-ray Photographs of Free Expanded KP-Sheets

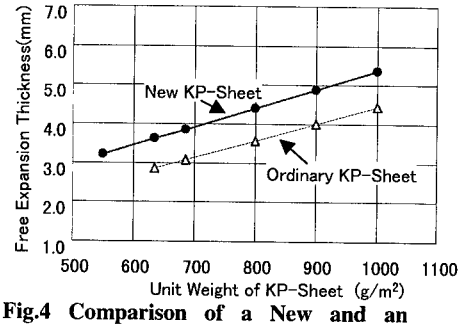

Fig.4 Comparison of a New and an Ordinary KP-Sheets in the Free Expansion Thickness

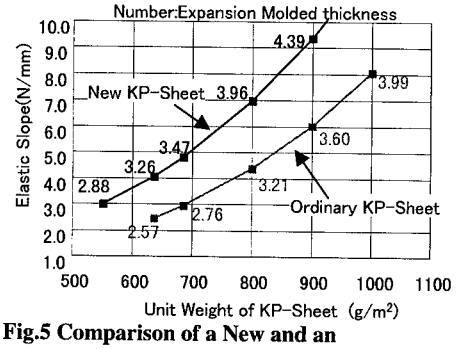

Fig.5 Comparison of a New and an Ordinary KP-Sheets in the Elastic Slope

Discussion

The elastic slope of expansion-molded articles is affected by the glass fiber content and the thickness of the molded articles as shown in Figure 1.

Supposing that glass fibers are uniformly distributed in the molded article and the number of glass fibers existing in cross sectional unit area is the same, the second moment of area I is shown as follows;

$$I=w\cdot Af\cdot n\cdot h^3/12 \qquad (1)$$

where w: width, h: thickness, Af: cross sectional area of a glass fiber, n: number of glass fibers existing in a cross sectional area $Af\cdot n$ means the existing probability of glass fibers, therefore, it is shown as follows;

$$Af\cdot n=(G/h)/\rho f \qquad (2)$$

where G: unit weight of glass fiber, ρf: density of glass fiber.

Supposing that the strength at the points of glass fibers' intersections formed by the matrix polypropylene's bonding does not change by changing of the expansion ratio or the existing amount of polypropylene at the intersections, the elastic slope is in proportion to the unit weight and the square

measure of the thickness. It is experimentally confirmed that this proportional relation exists as shown in Figure 6.

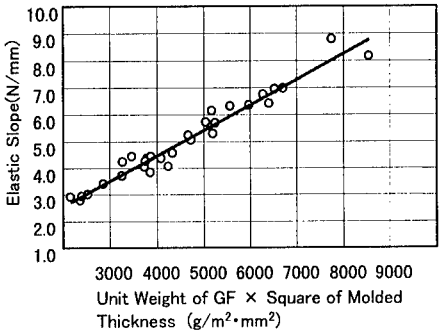

Fig.6 Relationship between Elastic Slope and the product of Unit Weight of GF and square of Molded Thickness

Then, for investigating the effect of the glass fiber content, the result of Figure 1 was transferred to the relation between the glass fiber content and the square measure of the thickness as shown in Figure 7. Although the elastic slope is in proportion to the unit weight of the glass fiber, which is the same result of Figure 6, the plots are not on the same line. Each line depends on the glass fiber content, and the slope decreases with increasing of glass fiber content. Over

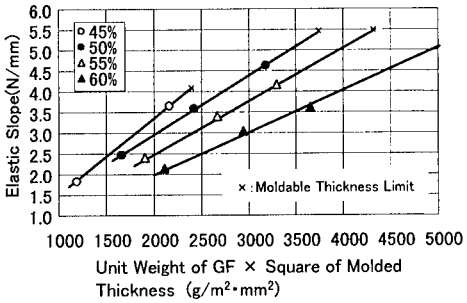

Fig.7 Relationship between Elastic Slope and the product of Unit Weight of GF and square of Molded Thickness in each Glass Fiber Content

50wt% of the glass fiber content, although the moldable thickness limit increases, the value of the maximum elastic slope is not enhanced as shown before. It should be because that the number of glass fibers' intersection increased with increasing of glass fiber filaments and it brings about the shortage of polypropylene for bonding the intersections. As the result, over 50wt% of the glass fiber content, the increased amount of the elastic slope by increasing of the moldable thickness may balance with the decreased amount by the weakened bonding strength at the intersections, and no change was seen in the value of the maximum elastic slope.

Conclusions

(1) By controlling the glass fiber arrangement to the thickness direction, the free expansion ratio is enhanced about 30wt%, which resulted in 1.5 times increase in the elastic slope.

(2) Newly developed KP-sheet realized about 20 wt% decrease in the unit weight at the same elastic slope, which results not only in the cost reduction of molded articles but also in applying this lightweight and high stiffness material to functional modular headliners.

References

1. H. Yoshitake, O. Nishimura, K. Se, Y. Araki, T. Sunada and H. Kubo, Plastic Age, 94,124(1996)

2. H. Kubo, Y. Satoh, Y. Araki, Kawasaki Steel Technical Report, 39,84(1998)

3. S. Hanatani, H. Kubo, O. Nishimura, Kawasaki Steel Technical Report, 32(1),87(2000)

Proceedings of 7th Japan International SAMPE
Symposium & Exhibition, Nov. 13-16, 2001

Investigation of Durability and Reasonable Design Method for Elastic Chain

Katsumasa Tokubuchi#, Yoshio Nishino# and Nobuyasu Ikoma#
#: SHIBATA Industrial Co., Ltd., Engineering and Development Division
1057 Nakao, Uozumicho, Akshi, Hyougo 674-0082, JAPAN
E-mail: Katsumasa_Tokubuchi@sbt.co.jp

Abstract

In general, steel chains are using for mooring of small scale floating structure which ship mooring or navigation buoy. When large scale sea waves act to these structures, mooring chain will be tensioned by oscillation of buoy body. In addition, steel chain links are touched by these self-load, and link's diameter will decrease because of abrasion at touch point of chain links. Then, mooring chain will be broken by impulsive tension. We suggest that using 'Elastic Chain' as buoy mooring chain. 'Elastic Chain' has composite structure, steel chain and rubber material. It is better than normal steel chain on abrasion and reduction of impulsive tension. However, 'Elastic Chain' is expensive compare with steel chain. And, We investigate the method of reasonable design method of 'Elastic Chain' using lumped mass mooring chain simulation, and we aim cost down of 'Elastic Chain' by shortening of the installing length. In the result, it can be 1/3 length of all mooring cable that 'Elastic Chain' length. And, in the length of 'Elastic Chain' is 1/3 to mooring line, occurrence impulsive tension is 50% compare with all steel chain using. Additionally, We carry out the investigation of Elastic Chain's durability for used at real sea environment. The using term is 7.5years. In the result, the rubber material of Elastic Chain was keep the strength compare with original rubber strength.

Key Words: mooring, tensile load, lumped mass.

Introduction

In generally, steel chain is using for mooring of small scale floating structure(i.e. Navigation signals for maritime transportation, Ship mooring buoy, etc.). However, the tensile strength is decrease by abrasion. And, mooring chain breaking will occurs when high wave by typhoon or low pressure act to floating structure moored by steel chain.

Steel chains diameter will be decrease at contact point between chain links. This is occurred by floating structure's moving. Then, impulsive tension will act to those mooring line, and chain breaking occur [1].

Therefore, it is need that reduction of chain abrasion and impulsive tension at mooring line for prevention of the disaster. And, We suggest to use "Elastic Chain" for mooring of floating structure. Elastic Chain has composite structure of rubber material and steel chain links as indicated by Fig.1. Steel chain is opened space between links and buried within rubber. Addly, rubber material is filled in those space. Elastic Chain has characteristics of elongation to tensile load. And, if Elastic Chain is installed at a part of mooring line, impulsive tension will be reduced to compare with using only steel chain[2].

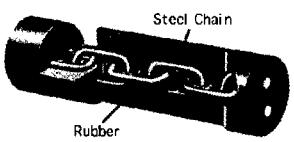

Fig.1 Structure of Elastic Chain

However, initial cost when install Elastic Chain at actual floating structure is expensive to compare

with using only steel chains because of many process and materials for making of Elastic Chain. Consequently, two ideas is need for cost down of using Elastic Chain: (1)Reduction the running cost of mooring line by improvement of durability using Elastic Chain and (2)Investigation of minimum length of Elastic Chain for reduction of impulsive tension and prevention of mooring line abrasion.

In this paper, we would like to investigate above two ideas from each point of view, durability of Elastic Chain and reasonable design using numerical simulation.

Investigation for Durability of Elastic Chain

Investigation for Abrasion

In this section, the example of installation of Elastic Chain is introduced at real sea environment while 7.5years. The installation site were 57m depth. And, Elastic Chain's specification were 25m length, 200mm diameter, and 38mm diameter steel chain were buried within the Elastic Chain. And, two Elastic Chains were connected when using for buoy mooring.

Fig.2 is diameter variation of the Elastic Chain. The diameter decreased at 15m point along length. This point correspond to the start of catenary curve from seabed. And, it occurred many times that contact of the Elastic Chain's surface and sand or stones at seabed. However, remarkable abrasion of buried steel chain within Elastic Chain did not occurred at this point. It is conceivable that surface covering by rubber is contribute to extension of life span of mooring line at sea environment.

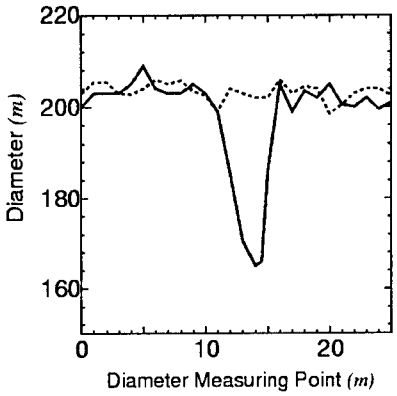

Fig.2 Diameter Variation of the Elastic Chain

Rubber Material Durability

In this section, rubber material durability is investigated. The investigation were carried out by measurement of hardness and tensile strength of rubber material that sampled from Elastic Chain introduced above section. The test piece for tensile strength test were dambel shape provided Japan Industrial Standard(JIS).

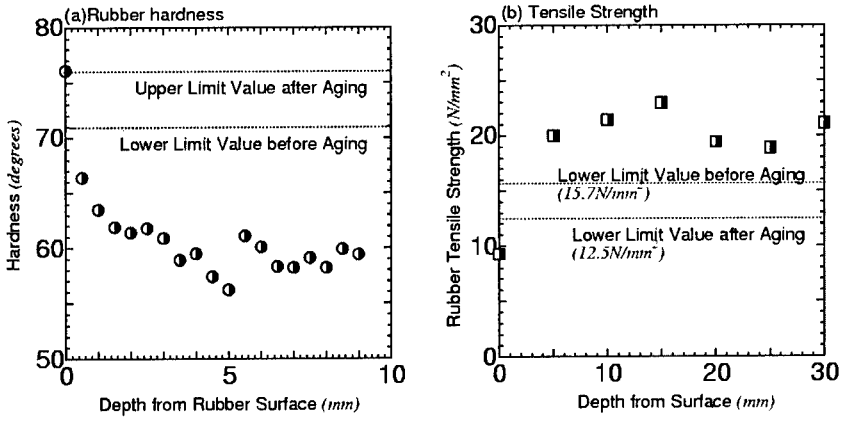

Fig.3 Hardness and Tensile Strength of Rubber Material of Elastic

Fig.3(a) is indicated of variation of rubber hardness along the depth direction of cross section of Elastic Chain. The hardness were lower than lower limit value of rubber hardness before aging except for sample at surface of Elastic Chain. Fig.4(b) is tensile strength variation of the rubber material along the same direction of hardness measurement..

From this result, the strength of rubber material were higher value lower limit tensile strength before aging except for
sample at surface of Elastic Chain.
From these result, rubber material's hardness and tensile strength were maintained even if Elastic Chain used long term at real sea environment.

Reasonable Design Method of Elastic Chain

Calculation Model

Next, design method of Elastic Chain is investigated using numerical simulation. The using calculation model is lumped mass model for single point buoy mooring(Fig.4). The acting forces are fluid forces and tensile loads between any mass points (buoy and mooring line). And, fluid forces were acted by water particle acceleration and velocity for water wave motion. These wave motion (water particle acceleration, velocity, and water surface) is calculated by Stokes 4th order assumption[3]. Kinematic equation of any mass points is indicated by Eq(1), (2) and mass points acceleration, velocity, and position are calculated by this equation.

$$F_{Hi}=\rho C_M V_i(du_i/dt-d^2x_i/dt^2)$$
$$+1/2\rho C_D A x_i|u_i-dx/dt|(u_i-dx/dt)$$
$$F_{Vi}=\rho C_M V_i(dw_i/dt-d^2z_i/dt^2)$$
$$+1/2\rho C_D A z_i|u_i-dz/dt|(w_i-dz/dt) \quad (1)$$
$$m_i d^2x_i/dt^2=F_{Hi}+T_i\cos\phi_i-T_{i+1}\cos\phi_{i+1}$$
$$m_i d^2z_i/dt^2=F_{Vi}+T_i\sin\phi_i-T_{i+1}\sin\phi_{i+1}$$
$$+f_i+m_i g \quad (2)$$

Where, F_H, F_V: fluid force act to mass points, du_i/dt, dw_i/dt u, w: acceleration and velocity of water particle, d^2x_i/dt^2 , d^2z_i/dt^2, dx/dt, dz/dt : velocity of mass points, V, m: volume and mass of mass point, C_M, C_D: inertia coefficient and drag coefficient, ρ:

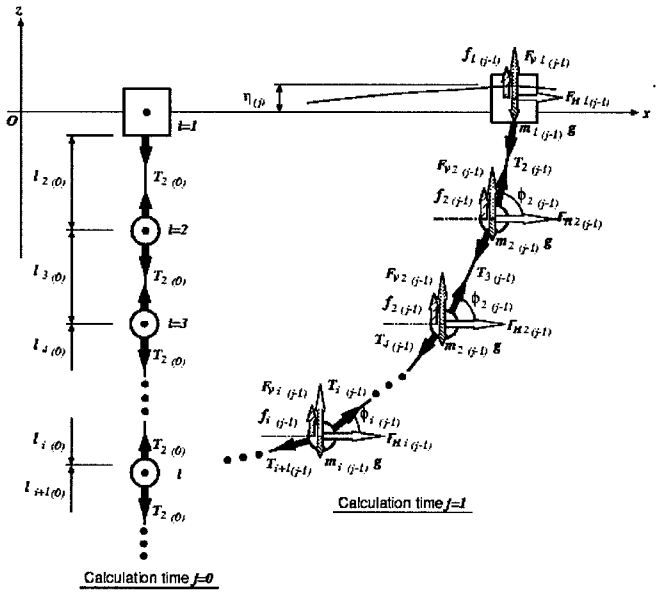

Fig. 4 Lumped Model for Single Point Mooring buoy

density of sea water, Ax, Az : projection area, f : buoyancy of any mass point, g : gravity acceleration, T : tensile load between mass points.

In addition, tensile loads between mass points are calculated by Hooke's low. The spring module of Elastic Chain is got by linearize of elongation character of Elastic Chain because of the character's non-linearity is larger than steel chain .

Investigation of Installing Point and Length of Elastic Chain

Tensile load of Mooring line would be calculation using the method indicated above section. The investigation would be carried out on the assumption that single point mooring buoy. The mooring system's specifications indicated in Table1. And, wave height is 9m, wave period is 10s.

Table1 Mooring System

Water Depth	30m
Moor line length	35m
Buoy shape	ϕ3.6m x 2mH (draft 1.3m)
Steel Chain	ϕ50mm Stud link chain
Elastic Chain length	9m - 35m

Calculation situations are 10 cases. In these cases, length ratios of Elastic Chain to entire mooring line length are 0.3, 0.5, and 0.7. And, installation points of Elastic Chain are anchor side, buoy side, and middle point of moor line.

Fig.5 is comparison of average peak tensile load to case of only steel chain using. From this calculation result, tensile load of installing Elastic Chain to entire mooring line is reduced 10% compared with the tensile load of using only steel chain. And, it is obvious that tensile load is reduced by Elastic Chain using. On the other hand, the tensile load become 40-50% of using only steel chain when the ratio of Elastic Chain length is 0.3 of entire mooring chain. And, character of tensile load reduction become steady on the calculation case that Elastic Chain is installed at anchor side.

Conclusions

Conclusions from these investigation:

(1)Elastic Chain has durability against long term using at real sea environment. Burying steel chain's diameter is kept by surface covering rubber material. And, strength of rubber material has initial value when Elastic Chain is manufactured.

(2)Tensile load of mooring line is possible using lumped mass model. And, tensile load is reduced 50% of using only steel chain for moor line when Elastic Chain's length is 30% of entire mooring line. From this result, initial cost of Elastic Chain using become reasonable in comparison with that Elastic Chain is installed on entire mooring line.

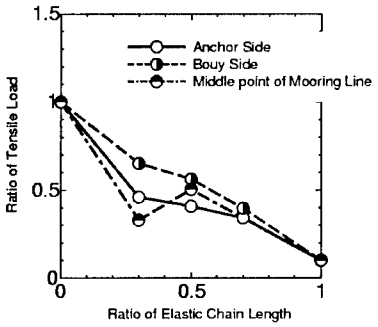

Fig. 5 Comparison of Calculated Average Peak Tensile Load

References

1. K.Tokubuchi and Y.Nishino: The Investigation of Elastic Chain's Durability and Reduction of Impulsive Tension, 15th Ocean Engineering Symposium, p.p.103-110(2000)

2. N.Ikoma and K.Tokubuchi: Experimental Investigation for Effect of Impact Load Reduction in RUBBER JOINER, PROCEEDINGS OF JISSE-5, p.p.1355-1360(1997)

3. Y.Tsuchiya, M.Yamaguchi: SOME CONSIDERATIONS ON WATER PARTICLE VELOCITIES OF FINITE AMPLITUDE WAVE THEORIES, Coastal Engineering in Japan, Vol.15, p.p.43-57(1972)

Proceedings of 7th Japan International SAMPE
Symposium & Exhibition, Nov. 13-16, 2001

Synthesis and Properties of Polyethylene-Clay Hybrids

Makoto Kato# and Arimitsu Usuki#

#: TOYOTA CENTRAL RESEARCH AND DEVELOPMENT LABORATORIES, INC.
Nagakute-Cho, Aichi-gun, Aichi-ken 480-1192 JAPAN
E-mail: makoto@mosk.tytlabs.co.jp

Abstract

Polyethylene-clay hybrids have been prepared successfully by melt compounding with maleic anhydride grafted polyethylene(MA-g-PE), organophilic clay and polyethylene. In these polyethylene-clay hybrid, the silicate layers of the clay were exfoliated and dispersed to the monolayers. The hybrids exhibit higher tensile yield strengths, tensile moduli compared to those of polyethylene. When the 5wt% clay were loaded, the tensile yield strength and the tensile modulus of the hybrid exhibited 1.4 and 1.8 times higher respectively compared to those of polyethylene/MA-g-PE mixture. The gas permeability of that clay hybrid decreased 30 % as compared with polyethylene/MA-g-PE mixture.
Key Words: Clay, Hybrid, Polyethylene

Introduction

A clay mineral is a potential nanoscale additive because it comprises silicate layers in which the fundamental unit is a 1 nm thick planar structure. If the nanometer dispersion of the silicate layers in a polymer matrix could be achieved, the mechanical properties might be further improved and/or new unexpected hybrid properties synergistically might be derived from the two components. In our previous works, we have synthesized nylon 6-clay hybrid (NCH) in which 1 nm thick silicate layers of clay minerals are exfoliated and homogeneously dispersed in the nylon 6 matrix [1]. The NCH exhibits various superior properties such as high strength, high modulus and high heat resistance compared to conventional nylon 6 [2].

Polyethylene is one of the most widely used polymers. But polyethylene clay hybrid could not be prepared easily because polyethylene is hydrophobic and has poor miscibility with clay silicates. We have already developed successfully a direct-intercalation process in which PP is modified using maleic anhydride, followed by melt compounding method [3]

So, we tried to prepare polyethylene clay-hybrids using melt compounding. There are two objects of this study. The first one is to prepare the polyethylene-clay hybrids using above compounding method in which the nanometer dispersion of the silicate layers are achieved in the matrix. The second objetct is to clarify the mechanical properties and gas permeation properties of the polyethylene-clay hybrids.

Experimental

Materials

The materials used for the preparation of the samples are Octadecylamine modified montmorillonite (ODA-CWC, inorganic content c.a.70wt%) from Nanocor Inc., polyethylene (KF380, melt flow index 4.0g/10min) from Japan Polychem co.,

maleic anhydride grafted polyethylene(Fusabond 226D, base resin type LLDPE, grafted maleic anhydride 0.90wt%, melt flow index 1.5g/10min, MA-g-PE) from E. I. du Pont de Nemours and Company.

Preparation of polyethylene-clay hybrids

Three types of hybrids with different compositions of the organophilic clay, MA-g-PE and PE were prepared as shown in Table 1. The dry mixed pellets of polyethylene and MA-g-PE (weight ratio PE/MA-g-PE = 7:3) were supplied into twin screw by using the feeder and the powdery ODA-CWC was added from another feeder. The mixture was melted-blend between 200-220 ℃ by using above twin screw extruder, pale-yellow or pale-brown strands of the hybrids were obtained. The obtained strands were cooled in a water bath , pelletized with a cutter, and dried under vacuum at 60 ℃ . The contents of the inorganic clay were measured by burning the samples. The results are listed in Table1. In orders to study the effect of the clay on the mechanical properties and gas barrier properties of the hybrids, three composites based polyethylene and MA-g-PE without clay were also prepared as listed in Table1.
The dried pellets of the hybrids were injection-molded into test pieces for the measurement of the mechanical. Also, for the measurement of the gas barrier permeability properties, the thin films(thickness 100 μ m) of the hybrids were obtained were molded with T-die film unit.

Evaluation of the Dispersibility of the Clay in Polyethylene Matrix

The dispersibility of the silicate layers in the hybrids was evaluated by using the X-ray diffractometer. The X-ray diffraction (XRD) patterns of the thin films of the hybrids were obtained by using a Rigaku X-ray diffractometer, RAD-B, with Cu-Ka radiation at 30kV and 30mA.

Measurement of mechanical properties and permeability

The tensile test was measured at 23 ℃ according to ASTM. The speed of the closshead was 10mm/min. The gas permeability of nitrogen gas was measured at 60 ℃ by using a Yanaco gas permeation measurement apparatus, GTR-30. The permeation area of the gas is 16.2 cm^2.

Results and Discussion

Evaluation of the Dispersibility of the Clay Layers in the Hybrids

Direct evidence of the nanometer dispersion of the silicates layers of the clay is provided by the XRD patterns of the obtained hybrids (Figure1). In Figure1, the peak of ODA-CWC around $2\Theta = 4^\circ$ is disappeared in the XRD patterns of the all hybrid samples. The diffraction strength of the hybrid samples are gradually increased toward low angle, although the XRD patterns of the PE1 exhibit slightly shoulder, and are stronger than that of polyethylene and MA-g-PE

Table 1. Compositions of the Prepared Hybrids Based on PE, MA-g-PE, and ODA-CWC and of the Related Samples

sample	matrix	inorganic clay contents, wt%
PE1	KF380	0
PE2	Ma-g-PE	0
PE3	PE1/PE2=7/3	0
PECH1	PE1/PE2=7/3	5.4
PECH2	PE1/PE2=7/3	3.5
PECH3	PE2	5.2

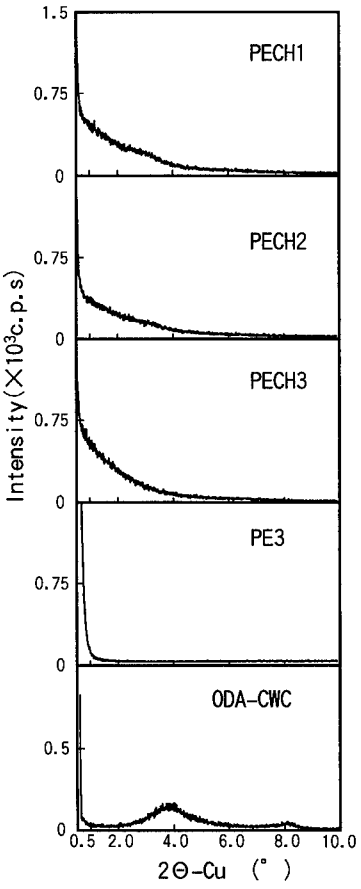

Figure 1. XRD patterns of the Obtained Polyetylene-Clay hybrids , Related Sample, and ODA-CWC

mixture (PE3). Since the peak of ODA-CWC shows the interlayer distance which is obtained by the XRD of (001) diffraction face, these results indicate that the interlayer distance of silicate layers in the hybrid samples are expanded beyond 100 Å as a average. Also, NCH, completely dispersed silicate layers in the nylon 6 matrix, exhibits no peak but exhibits a gradual increase in the XRD strength. Therefore, the nanometer dispersion of the silicates layers in the polyethylene matrix could be achieved. In previous our work [3], it was pointed out that the miscibility between maleated oligomer(or polymer) and matrix polymer was important for dispersion of the silicate layers. The shoulder of the XRD patterns of the PECH1 may be attributed to a few of the unexfoliated layers according to the miscibility between polyethylene and MA-g-PE.

Mechanical properties Study of the Polyethylene-clay hybrids

The mechanical properties of the polyethylene-clay hybrids and neat polyethylenes without clay are summarized in Table2. The tensile strengthes of the hybrids are higher than those of each matrix. In order to clarify the effect of the hybridization with the clay, the relative strengthes and moduli of the clay hybrids to those of each matrix were calculated and are shown in Table 2. In the cases of PECH1 and PECH2 where those matrix were mixture of polyethylene (PE1) and MA-g-PE(PE2), the strength and modulus is increased according to contents of inorganic clay. The tensile modulus of the PECH1 which 5wt% inorganic clay were loaded exhibits 1.8 times higher than that of the matrix (PE3), although the ultimate elongation of PECH1 is as same as that of the matrix. Also, in the case of PECH3 which the matrix was MA-g-PE(PE2), the modulus and the strength of the hybrid is higher the matrix respectively, although the ultimate elongation of the hybrid is slightly lower than that of matrix. These results indicate that in the polyethylene-clay hybrids the strength and the modulus is increased drastically and that the ultimate elongation is not almost decreased.

Table2. Tensile Properties of the Hybrids and Related samples

sample	tensile properties			
	tensile modulus (MPa)	tensile yield strength (MPa)	tensile yield point (%)	ultimate elongation (%)
PE1	102	7.3	7.1	>500
PE2	118	9.3	8.0	180
PE3	99	7.5	7.7	>500
PECH1	180(1.8)	10.3(1.4)	5.6	>500
PECH2	140(1.4)	9.4(1.3)	6.8	>500
PECH3	157(1.3)	12.6(1.4)	7.0	155

The values in parentheses are the relative values of the hybrids to those of each matrix

Gas Permeability Study of the Polyethylene-clay hybrids

Table 3 presents the gas permeability constants of nitrogen gas for the clay hybrids and related samples. Polyethylene-clay hybrids show superior gas barrier properties. In the cases of PECH1 and PECH2 the permeability constants of the hybrids are decreased as an increase of the inorganic clay content. The permeability of the PECH1 decreased 30% as compared with the matrix(PE3). However the inorganic clay content of the PECH1 are almost same as that of the PECH3, the permeability of the PECH3 decreased 35% as compared with the matrix(PE2). The gas barrier property of the PECH3 is slightly better than that of PECH1. The difference of the dispersebility of the clay silicates layers in the matrix influences to the difference of the gas barrier property between PECH1 and PECH3.

Table3. Gas Permeability of the Hybrids and related samples.

sample	gas permeability constant ($cm^3(STP)\cdot cm\cdot cm^{-2}\cdot s^{-1}\cdot cmHg^{-1}$)
PE1	7.01×10^{-10}
PE2	7.28×10^{-10}
PE3	7.09×10^{-10}
PECH1	5.04×10^{-10}
PECH2	5.21×10^{-10}
PECH3	4.64×10^{-10}

Conclusion

We have successfully prepared the polyethylene-clay hybrids by using maleic anhydride modified polyethylene. In these the silicate layers were exfoliated and dispersed on a nanometer level in polyethylene matrix. The polyethylene clay hybrid exhibits superior gas barrier properties. The gas permeability of the hybrid is decreased 30% as compared with that of polyethylene matrix.

References

1. Usuki, A.; Kawasumi, M.; Kojima, Y.; Fukushima, Y.; Okada, A.; Kurauchi, T.; Kamigaito, O. J. Mater. Res., 8, 1179 (1993)
2.Kojima, Y.; Usuki, A.; Kawasumi, M.; Fukushima, Y.; Okada, A.; Kurauchi, T.; Kamigaito, O. J. Mater. Res. ,8, 1185(1993).
3. (a) Usuki, A.; Kato, M.; Okada, A.; Kurauchi, T. J. Appl. Polym. Sci. ,63, 137(1997). (b) Kawasumi, M.; Hasegawa, N.; Kato, M.; Usuki, A.; Okada, A. Macromolecules ,30, 6333(1997),. (c) Hasegawa, N.; Kawasumi, M.; Kato, M.; Usuki, A.; Okada, A. J. Appl. Polym. Sci, 67, 87(1998).

Proceedings of 7th Japan International SAMPE
Symposium & Exhibition, Nov. 13-16, 2001

Development of New Type High Performance Potassium Titanate for Friction Material Use

Hidefumi Konnai# and Yoshio Aso##

#: Research Laboratory, Kawatetsu Mining Co., LTD.
1, Niihama-cho, Chuo-ku, Chiba 260-0826, JAPAN
E-mail: h-konnai@kawako.kawatetsu.ne.jp

##: Chiba Works, Kawatetsu Mining Co., LTD.
1, Kawasaki-cho, Chuo-ku, Chiba 260-0835, JAPAN
E-mail: y-aso@kawako.kawatetsu.ne.jp

Abstract

Potassium titanate has a needle-like fiber (ca. 0.5 μm in diameter, ca. 10 μm in length) as its general form, and is widely used as reinforcement material of plastic and the friction material of brake pad. It is suspected, however, that there is a wrong effect to the human respiratory organs due to respirable fibers (under 3 μm in diameter, over 5 μm in length, and over 3 in length / diameter).

To get rid of this suspicion, two kinds of new type potassium titanates, TIBREX-RPN and TIBREX-AF, have been developed by controlling their chemical compositions and crystal growing processes. TIBREX-RPN is potassium hexatitanate (K2O・6TiO2) having very few respirable fibers. TIBREX-AF is potassium octatitanate (K2O・8TiO2) fine particles of 0.5 μm in mean diameter and has no respirable fibers. These new type materials are becoming popular to make disk brake pad and other FRP products.

Key Words: Potassium Titanate, Respirable Fiber, Friction, Brake Pad.

Introduction

Potassium titanate is a multiple oxide as shown in the following general formula: $K_2O \cdot nTiO_2$ ($K_2Ti_nO_{2n+1}$). Both potassium hexatitanate of n=6 and potassium octatitanate of n=8 are chemically and thermally stable and have been widely used in industries. The shape of conventional potassium titanate is shown in Fig.1. It is microscopic fibers of about 0.5 μm in diameter and about 10 μm in length, and is classified as "whiskers".

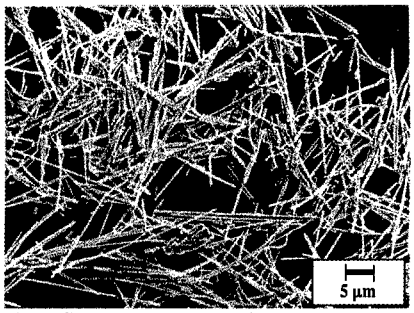

Fig.1 SEM photograph of Fiber-type

One of the major applications is as a reinforcing filler for engineering plastics to

give them such properties as high-strength, high-modulus, and high heat-resistance. Materials for dynamic uses such as in gears, cams, and bearings are required to show excellent frictional properties so that there is no occurrence of abrasion, noise, torque variation, heat generation, deformation etc. among the various interactions between materials

Improvement in brake performance by the use of potassium titanate fiber was reported by National Aeronautics and Space Administration (NASA) [1]. For this reason, potassium titanate fiber has also been widely used as a blending material for brake pads owing to its superior friction and wear properties.

In accordance with the recent general trend to give importance to the preservation of the global environment and human safety, the concern about the possible induction of human health problems by microscopic fibrous materials has been growing. Representative researches on this property include hypothesis by Stanton and that by Pott [2,3,4]. ILO (International Labor Organization) define the respirable fibers whose use should be controlled in the workplace as those having fiber-size of less than 3 μm in diameter, greater than 5 μm in length, and greater than 3 in aspect ratio (ratio of length to diameter) [5]. DFG (Deutsche Forschung Gessellschaft) classify such fibers as fibrous dust and also recommend that their use be controlled [6].

Demand for the non-fibrous potassium titanate has been growing, mainly in Japan and in Europe and United States, in applications that require good frictional properties, and that do not require fibrous form.

New type potassium titanate: TIBREX

Owing to the anisotropy of during crystal growth, it is apt to take the fibrous shape in the reaction stage of the synthesis. Conventionally, synthesis technologies have been developed, in which the anisotropy during the crystal growth is promoted to acquire high aspect-ratio (ratio of fiber length/fiber diameter) fibers and so obtain high reinforcing property. On the contrary, development of a new shape-controlling technology that suppresses anisotropy is required for non-fibrous type potassium titanate.

TIBREX-RPN

By the use of a newly developed synthesis method incorporated with a unique shape-controlling technology, TIBREX-RPN was introduced in the market in 1995, as a product that practically does not contain any respirable fiber. Since then, it has been widely used as a blending material in the disk brake pads for general passenger cars both in Japan and overseas, building a proven record of performance. The shape of TIBREX-RPN is shown in Fig.2. Its low aspect ratio is clear.

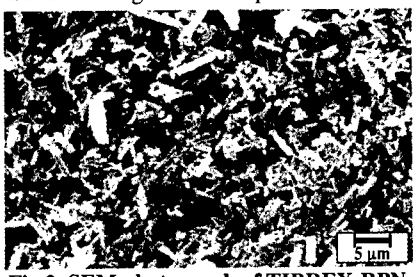

Fig.2 SEM photograph of TIBREX-RPN

In a disk brake a disk rotor made of cast iron and rotating along with the wheels is sandwiched between the two parts of the caliber, pressing the pad as a friction material against the rotor, thereby stopping rotation. The brake pad blended with TIBREX-RPN shows various features such as stable coefficient of friction, low water-absorption, low rotor-abrasion (damage to opposite faces) and small amount of squeal noise.

TIBREX-AF

TIBREX-AF is a non-fibrous potassium titanate recently introduced into the market.

As shown in Fig.3, it is made of fine particles with a sharp particle-size distribution at 0.5 μm. Used in brake pads, application in other compact frictional parts where fine-particle composition is advantageous is anticipated.

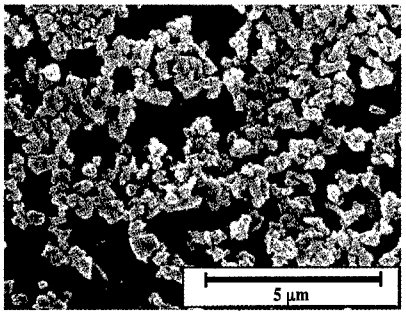

Fig.3 SEM photograph of TIBREX-AF

Fig.4 shows the size distributions of length and diameter of the TIBREX-AF, TIBREX-RPN, and the conventional fiber-type, measured with an image-analyzing device into which the SEM images of these were fed. The results show that TIBREX-AF does not contain any respirable fibers, that is, fibers of 3 μm less in diameter, 5 μm more in length, and with aspect ratio of 3 more. The typical properties of TIBREX-RPN and TIBREX–AF are shown in Table 1.

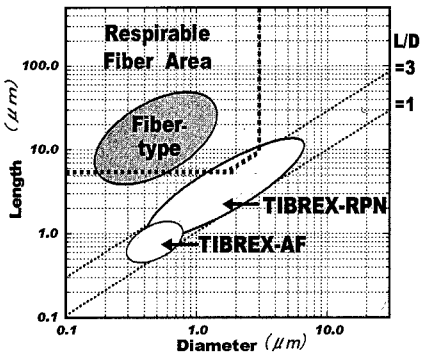

Fig.4 Size distribution of potassium titanate

Table 1 Typical properties of TIBREX

Grade	TIBREX-RPN	TIBREX-AF
Shape	Low-Aspect Ratio	Non-Fibrous Fine Particle
Substance name	Potassium Hexatitanate	Potassium Octatitanate
Chemical formula	K_2O6TiO_2	K_2O8TiO_2
CAS-RN	12056-51-8	59766-31-3
EINECS-RN	-	261-919-2
Color	White	White
Density(g/cm^3)	3.58	3.45
Bulk density	0.4	0.3
Median size(μm)	1.5	0.5
BET(m^2/g)	3	15
Mohs hardness	4	4
Water content	Less than 0.8%	Less than 1.0%
pH(dispersed in water	9.0	10.5
Import registration	Registered on EPA	TSCA:Inventory

Characteristics of the pad blended with TIBREX-AF

The brake performance of the brake pad blended with TIBREX-AF, a non-fibrous form of potassium octatitanate, was investigated. As a control of the experiment, a brake pad blended with the fiber-type potassium octatitanate of popular use was adopted.

Formulations and testing method

Both TIBREX-AF blended pad and fiber-type blended pad were trial-manufactured. These pads were NAO (Non-Asbestos Organic) blended, as shown in Table 2.

Table 2 Brake pad formulations

Ingredient		Content wt%	
Binder	Phenolic Resin	8	
Organic Component	Aramido Fiber	8	
	Rubber Particle		
	Cashew Particle		
Inorganic Fillers	Mineral Fiber	45	
	Barium Sulfate		
	Calcium Carbonate		
	and Others		
Lubricants	Graphite	17	
	Antimony Sulfide		
Metallic Component	Copper Fiber	7	
Potassium Titanate	Fiber-type	15	0
	TIBREX-AF	0	15
Total		100	100

Hardness and shear strength of the pads were measured in conformity with JIS-D4421 and JIS-D4422, respectively. The

brake performance was tested in the P1 category, where the nominal maximum speeds exceeding 140Km/h, in the Dynamometer Test for passenger cars in conformity with JASO C406. The material employed in the disk rotor was Gray Iron Casting of FC 250.

Test-results

The hardness and the shear strength of the TIBREX-AF pad were found higher by as much as 20%.

As for the brake performance, with regard to such properties as effectiveness, fade, recovery, and water recovery, obtained in Dynamometer Test, no substantial differences were found between pads blended with TIBREX–AF and with fiber-type. Fig.6 shows the relation between temperature of the disk rotor and its friction coefficient in the Second Fade Test. It shows that there is no fade, i.e., lowered friction coefficient at high temperatures.

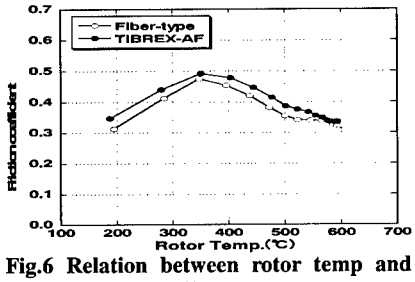

Fig.6 Relation between rotor temp and friction coefficient

Total number of motion controlling actions by the brake was 627 times in the Dynamometer Test. After the Test, the wear loss in thickness of the pads and the rotor were measured. The TIBREX-AF pad showed about 20% less wear loss of the pad and about 40% less loss of the rotor, compared with those for the fiber-type pad.

Fig.7 is the summary of the wear of the pads and the rotor. TIBREX-AF showed that it gives excellent wear-resistance to the pad and lowers abrasion of the rotor.

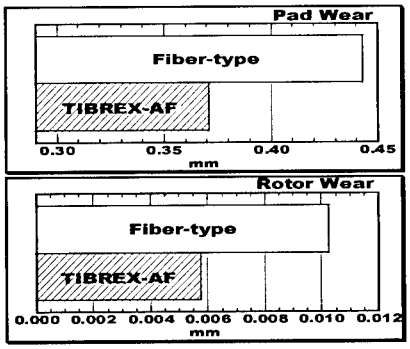

Fig.7 Wear performance

Conclusion

TIBREX, a new type potassium titanate, has the non-fibrous form designed in consideration of safety of the environment where it is used.

TIBREX-RPN has been already employed in the brake pads for general passenger cars, with proven performance. TIBREX-AF, developed for securing higher safety than TIBREX-RPN, contains practically no respirable fibers. It shows friction characteristics identical with the conventional fiber-type in the brake comparison test, and superior performance compared with the fiber-type in terms of pad and rotor abrasions.

Application of these two kinds of potassium titanate of new shape different from conventional types other than for frictional parts is expected in the future.

References

1. NASA: TN D-8363, 1976.
2. IARC: Scientific Publications (8) 289, 1973.
3. M.F.Stanton et al.: J. Nat. Can. Inst, 67, 965 (1981).
4. IARC: Scientific Publications 1(30), 1980.
5. ILO: Occupational Safety and Health Series No.64, 1989.
6. DFG: List of MAK and Value, 1996.

Proceedings of 7th Japan International SAMPE
Symposium & Exhibition, Nov. 13-16, 2001

Advanced seat fabrics with deodorization function for vehicles

Tomiko M. Suzuki[a], Kazuhiro Fukumoto[a], Norio Sato[a],
Yoshio Yamada[b], Masao Owaki[c], Masahiro Maekawa[d], Shigeyoshi Miura[e],
Osamu Araki[f], Akihiro Matsuyama[f], Masako Furuta[f]

a: Living Environment Lab., Materials Div.II, Toyota Central R&D Labs.,Inc.
41-1, Yokomichi, Nagakute-cho, Aichi 480-1192, JAPAN
E-mail: tomiko@mosk.tytlabs.co.jp
b: Body System Engineering Div., Toyota Motor Corporation
1, Toyota-cho, Toyota, Aichi 471-8572, JAPAN
c: Material Engineering Dept., Quality Div., Toyota Motor Corporation
1, Toyota-cho, Toyota, Aichi 471-8572, JAPAN
d: Organic Material Dept., Material Engineering Div.II, Toyota Motor Corporation
1, Toyota-cho, Toyota, Aichi 471-8572, JAPAN
e: Resins Technical Dept.II, Kansai R&D Center, Dainippon Ink & Chemicals, INC.
1-3, Takasago, Takaishi, Osaka 592-0001, JAPAN
f: Engineering Center, Fabric Engineering Dept., Toyoda Boshoku Corporation
3-201, Kamioguchi, Oguchi-cho, Aichi 480-0141, JAPAN

Abstract

"Air quality of the living environment" is one of the important issues today. In the vehicle compartment, there has been a need to purify the air by removing odors such as tobacco smoke. Tobacco smoke contains 4,000 or more kinds of the volatile organic compounds (VOC) such as nitrogen compounds, aldehydes, acetic acids, hydrocarbons. In order to improve air quality, we developed seat fabrics with deodorization function. The deodorization function was made by applying adsorbents to the back of the fabrics. The composite adsorbents we invented, contain silica-copper(II) sulfate complex and activated carbon. Especially, silica-copper(II) sulfate complex are chemical adsorbents for nitrogen compounds that are mainly odors from tobacco smoke. It was found that the seat fabrics reduced each component of odors (VOC) to less than 1/10. Also, the lifetime was estimated more than five years. Consequently, a more comfortable space for passengers is created and maintained.

Key Words: seat fabrics, deodorization, adsorbent

Introduction

In recent years, vehicles have been required not only for the means of transportation, but also for the riding comfort. According to the research for car user[1], 95% of passengers felt discomfort at the odors in the vehicle compartment. Moreover, a main cause of odors was tobacco smoke. Tobacco smoke contains 4,000 or more kinds of the volatile organic compounds (VOC) such as nitrogen compounds, aldehydes, acetic acids, hydrocarbons. Especially, it became apparent that the removal of nitrogen compounds was

effective for reducing unpleasantness[2, 3]. However the conventional physical adsorbents such as activated carbon were not effective for removing nitrogen compounds. This study was performed to develop chemical adsorbents for nitrogen compounds and apply the deodorization function to the seat fabrics that occupy a large area in the vehicle compartment.

Experimental Procedure

Materials

Activated carbon, silica, sepiolite were used as adsorbents. The physical properties of these porous materials are shown in Table 1. $CuSO_4 \cdot 5H_2O$ was selected as adsorbents for nitrogen compounds. It was used as impregnation ingredients on the silica. Copolymerization acrylic resin emulsion (Tg: -40℃) were used as back-coating agents. Textile fabrics (moquette) made from polyester yarn was used as car seat fabrics.

Table 1 Physical properties of porous materials

porous material	pore diameter (nm)	specific surface area (m^2/g)
activated carbon	1.7	850
silica-1	2.5	700
silica-2	17	300
sepiolite	1.0×0.5	300

Preparation of silica-copper (II) sulfate complex

4.7g of $CuSO_4 \cdot 5H_2O$ was dissolved in 45ml of water with stirring. Then, 30g of silica was added to the clear aqueous solution, and further stirred for 10 minutes. The mixture was dried at 100℃ for 12hr.

Preparation of seat fabrics

The back-coating agent with deodorization function was prepared as follows. 45g of activated carbon, 29g of silica -copper(II) complex and 150g of water were mixed to 110g of acrylic resin emulsion. The nonvolatile content was 34%. This back-coating agent was applied to the back of the fabrics so that dryness weight might become about $100g/m^2$. By drying at 135℃ for 15 minutes, the seat fabrics with deodorization function were prepared. For comparison, the seat fabrics without adsorbents were also prepared (untreated).

Removal odors: evaluation using model gas

Adsorption capability of the adsorbent was examined for trimethylamine which was representative adsorbate for nitrogen compounds. Adsorption capability of the seat fabrics was measured using mixed model gas, which consisted of trimethylamine, ammonia, acetaldehyde and toluene. The adsorbents or seat fabrics were put into non-permeable bags (5L). The gases generated by vaporization were introduced into the bag. The bags were kept at 25℃ for 24hr after sealing. The final concentration of the gas remaining in the bag was measured using a gas chromatograph. From each concentration, the amount of gas removed was calculated and adsorption isotherms were obtained. Comparison of adsorption capability was performed in the amount of gas removed at 10ppm of the equilibrium concentration.

Removal odors: real vehicle model evaluation using tobacco smoke

This evaluation was carried out using a acrylic resin box measuring 45 × 45 × 45cm. The volume was 1/33 scale of a real vehicle. The seat fabrics measuring 40 × 40cm were placed in the acrylic resin box with six lit cigarettes and the box was shut down. The seat fabrics were taken out and left indoors for three days. The seat fabrics were put into the new acrylic resin box and left for one day. Seven panelists smelled the air in the acrylic resin box, and evaluated about "odor intensity" and "pleasantness/ unpleasantness" shown in Table 2, which were provided by ministry of the

environment Japan. Gas samples were collected with adsorption tubes containing tenax GC. Following thermal desorption, the contaminants were quantitated by gas chromatograph with FID. Moreover, estimating of functional lifetime was evaluated[1].

Table 2 Standard of sensory test

Odor intensity	Pleasantness/Unplesantness
5: Very strong odor	3: Very pleasant
4: Strong odor	2: Pleasant
3: Odor easily sensed	1: Rather pleasant
2: Weak odor with the kind of recognizable odor	0: Neither pleasant nor unpleasant
1: Barely recognizable odor	-1: Rather unpleasant
0: No odor	-2: Unpleasant
	-3: Very unpleasant

Removal odors: real vehicle evaluation using tobacco smoke

This evaluation was carried out using a real vehicle. The deodorization function was applied to the front side of the seat. The total area was $4m^2$. One lit cigarette was placed in a vehicle and left with windows shut at 80℃ for 16hr. Seven panelists were carried out the odor sensory test at 40℃.

Results and Discussion

Development of adsorbents for trimehtylamine

We examined efficiency of adsorbents using trimethylamine that was polarity and bulky nitrogen compounds. The results of the adsorption capability are shown in Fig.1. Silica-1 was the most highly efficient in evaluated porous material. It was presumed that silica-1 had many adsorption sites of silanol groups which formed hydrogen bonds with trimethylamine[4]. Silica-1 impregnated copper(II) sulfate which forms a stable complex with nitrogen compounds[3] was more effective. Silica -copper(II) sulfate complex was about 9 times more effective than conventional adsorbents such as activated carbon and sepiolite[1]. Also, the odors adsorbed by physical adsorbent such as activated carbon might be released into the air if the temperature rises. We examined that the chemical adsorbents such as silica-copper(II) sulfate complex did not release the odors under high temperature (80℃) by the odor sensory test.

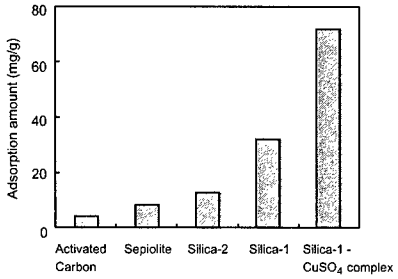

Fig.1 Amount of trimethylamine adsorbed by porous materials

Structure of prepared seat fabrics

The cross-sectional photographs of seat fabrics using the mixed adsorbents, silica-copper(II) sulfate complex and activated carbon were shown in Fig.2. It was confirmed that the adsorption resin layer containing two kinds of adsorbents was formed to the back of the fabrics. The acrylic resin of the adsorption resin layer had the function of both back-coating and fixing the adsorbents. It had numerous pores that increased contact surface with adsorbents and the odors.

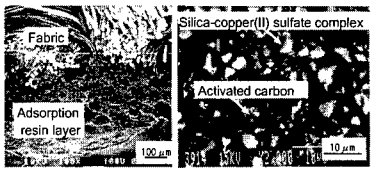

a) Secondary electron image

b) Backscatterd electron image (expansion of adsoption resin layer)

Fig.2 Cross-sectional photographs of the seat fabrics with deodorization function

Adsorption capability for model gas

The adsorption amount of the seat fabrics in mixed model gas is shown in Table 3. The developed seat fabrics adsorbed each odor, and especially adsorption of amine was excellent. On the other hand, untreated seat fabrics did not adsorbed any odors. This result suggests that the developed fabrics are effective for removing odors.

Table 3 Efficiency of advanced seat fabrics

Adsobate	Adsorption amount (mg/m^2)	
	Development	Untreatment
Trimethylamine	1100	0
Ammonia	300	0
Toluene	840	0
Acetoaldehyde	100	0

Adsorption capability for tobacco smoke

The result of odor sensory test using the real vehicle model for tobacco smoke is shown in Table 4. Developed seat fabrics improved 1.5 points of odor intensity and 0.6 points of unpleasantness. It became clear that the developed seat fabric was very effective in reducing the strength of odors and displeasure. Moreover as a result of analyzing gas chromatography, the seat fabrics reduced each component of odors to less than 1/10. The nitrogen compounds such as pyridine, nicotine were especially reduced.

Table 4 Result of odor sensory test

	Odor intensity	unpleasantness
Development	1.9	-1.1
Untreatment	3.4	-1.7

Estimation of functional lifetime

The functional lifetime was evaluated for tobacco smoke. As a result, it was estimated that if people smoke two cigarettes a day in the vehicle compartment, the functional lifetime was more than 5 years.

Real vehicle evaluation

The adsorption capability of the real vehicle equipped the seat with deodorization function was evaluated. The structure of the seat fabrics is shown in Fig.3. As a result of the odor sensory test for tobacco smoke, the capability of removing odors in the vehicle compartment was similar to that of the model evaluation using the acrylic box.

The seat fabrics with deodorization function are used for vehicles.

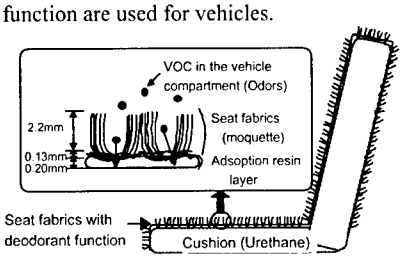

Fig.3 Structure of the seat fabrics with deodorization function for vehicles

Conclusions

1. Silica-copper(II) sulfate complex were efficient chemical adsorbents for nitrogen compounds.
2. The seat fabrics with deodorization function was obtained by applying silica -copper(II) sulfate complex and activated carbon to the back of the fabrics.
3. The seat fabrics showed removing odors such as tobacco smoke in the vehicle compartment.

References

1. Y. Yamada, O. Araki, M. Sugiura, M. Horii, T. Sekihara and A. Matsuyama: JSAE Rev., 13, 82(1992).
2. M. Matsuo : JASE Proc. of Spring Convention, 49(1997).
3. Y. Yamada, M. Owaki, T. M. Suzuki, K. Fukumoto, S. Miura, M. Furuta, A. Matsuyama : JSAE Rev., 21, 543(2000).
4. T. M. Suzuki, K. Fukumoto, S. Onoda : J. Odor Research and Eng., 32(1), 15(2001).

Proceedings of 7th Japan International SAMPE
Symposium & Exhibition, Nov. 13-16, 2001

Development of the Thermoplastic Elastomer Based on a Waste Rubber

Hirotaka Okamoto#, Kenzo Fukumori#, Mitsumasa Matsushita#, Norio Sato#,
Yasuaki Tanaka*, Tomoaki Okita*, Shigeki Otsuka+, and Yasuyuki Suzuki+

#TOYOTA Central R&D Labs., Inc, Nagakute, Aichi, 480-1192, JAPAN,
*TOYODA Gosei Co. Ltd., Kitajima, Inazawa, Aichi, 492-8540, JAPAN,
+TOYOTA Motor Corporation, Toyota, Aichi, 471-8572, JAPAN
E-mail: h-okamoto@mosk.tytlabs.co.jp

Abstract

A new rubber recycling technology to produce a polyolefin thermoplastic elastomer (TPO) based on EPDM waste was developed. In this technology, the devulcanization of EPDM waste and the compatibilization of the EPDM and PP would occur continuously and finally attain to the production of the TPO. In the TPO obtained under optimized conditions, EPDM phase was dispersed with a size of 1-micrometer order in continuous PP phase. The TPO shows rubbery elasticity and recovers its original length after elongation in a similar manner to commercial one. These properties may be due to a suitably formed phase structure (i.e., loosely crosslinked EPDM domains dispersed in PP matrix). The appropriate control of the devulcanization reaction for EPDM waste may contribute to the production of the TPO showing good properties

Key Words: Polyolefin, Thermoplastic Elastomer, Recycle, EPDM waste, Shear Flow Reactor, Rubbery Elasticity

Introduction

Recently, a continuous rubber recycling technology has been developed for vulcanized ethylene-propylene-diene rubber (EPDM) waste[1]. In this process, the breakages of carbon-sulfur crosslinking points occur selectively under the control of shear stress, reaction temperature and internal pressure. The devulcanized rubber exhibits excellent mechanical properties nearly equal to neat rubber. This recycling technology has been utilized manufactually and the devulcanized rubber has been used as materials for automotive parts. In this study, for the aim at the production of highly valuable materials such as thermoplastic elastomer, a more sophisticated technology has been developed.

Polyolefine thermoplastic elastomer (TPO) is generally made by melt-blending of EPDM with polypropylene (PP) or polyethylene (PE). Because TPO contains a large amount of EPDM, about 2/3 or more by weight, it exhibits the rubbery elasticity. The continuous thermoplastics phase is responsible for the reprocessability of TPO by heating. In order to disperse the EPDM, dynamic vulcanization procedure is often introduced in the melt-blending process. EPDM molecules form themselves into individual domains by the vulcanization and converted from continuous phase into disperse phase. Partially vulcanized EPDM is simply blended with PP in some TPOs instead of performing dynamic vulcanization.

The devulcanized rubber obtained by this developed method contains gel component which corresponds to loosely crosslinked network chain and its density is variable by controlling the devulcanization reaction. In this study, we have developed an enhanced technology to produce a TPO based on waste EPDM rubber.

Experimantal

Material

The waste EPDM was obtained from the weather strips (automotive waterproofing parts), which were generated in the process for manufacturing. It was sulfur-vulcanized rubber compounded with carbon black, process oil, etc. It was roughly crashed into small pieces in the size of about 5 mm for the following process.

A neat commercial PP was used as a polyolefin thermoplastics. According to the manufacturer data, the PP is generally used for extrusion products and its melt flow rate is 3.0g/10min.

Equipment

The TPO samples were produced with the "Shear Flow Reactor" based on a twin screw extruder. A schematic diagram is shown in Fig. 1. In the initial zone, the crashed EPDM would be pulverized by shearing. In the following zones, the devulcanization (selective breakages of crosslinking points in the EPDM) and compatibilization of the EPDM and PP would occur continuously and finally attain to the production of the TPO. In order to obtain some desirable TPO, screw geometry and configuration for the reactor and reactive conditions were suitably adjusted.

Characterization

The measurement of Mooney viscosity and the gel fraction of the devulcanized EPDM which was obtained without blending PP were performed to characterize the degree of devulcanization. The morphorogies of the obtained TPOs were observed with a transmission electron microscope (TEM). Mechanical properties such as tensile strength (T_b), elongation at break (E_b), tensile modulus, and others of the TPO were measured according to ASTM. Elastic recovery behaviors of the TPOs were investigated by elongation-recovery tests (maximum strain: 50%).

Results and Discussion

In the TPO obtained under optimized conditions, EPDM phase was dispersed with a size of 1-micrometer order in continuous PP phase (Fig. 2). The TPO showed good

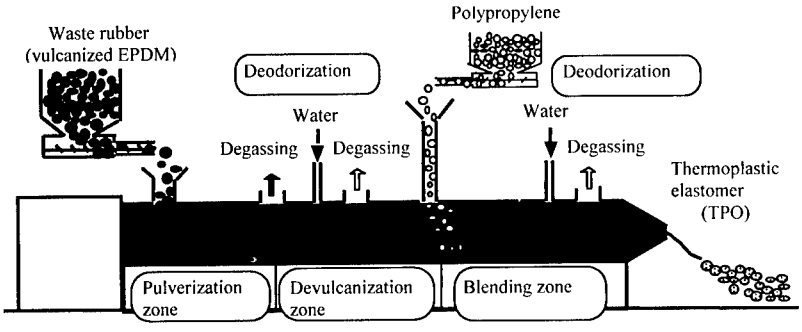

Fig.1 A schematic diagram of the processing system for polyolefin thermoplastic elastomer (TPO) based on waste rubber.

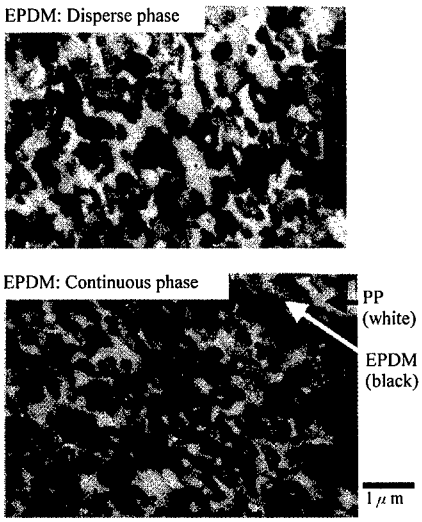

Fig. 2 TEM images of developed TPO. (EPDM/PP =80/20(wt%))

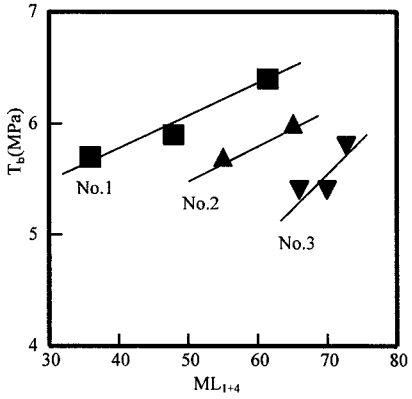

Fig.3 Relationship between tensile strength of TPO and Mooney viscosity of devulcanized EPDM. Numbers correspond to different screw configurations. No.1: the highest shear stress and pressure configuration, No.3: the lowest one

processability for injection molding. On the contrary, EPDM formed continuous phase in other TPOs in which Mooney viscosity of the EPDM was too high, i.e., there were large amounts of crosslinking in the EPDM. The morphorogical changes did not occurred for these samples even if the EPDM was melt-blended with PP intensively. The EPDM with extremely low Mooney viscosity also formed continuous phase in TPO. It is shown that the appropriate control of the devulcanization reaction for EPDM waste is important to the suitable morphorogy formation of the TPO. It is thought that both of the existence of the loosely crosslinked network chains and carbon black particles in the devulcanized EPDM contribute to the formation of EPDM disperse phase in TPO. Both may act as appropriate domain formation of EPDM molecules. The domain formation may be disturbed by insufficient or excess devulcanization of EPDM waste. Consequently, EPDM forms continuous phase.

Mechanical properties of the TPO also depended on degrees of devulcanization of the EPDM. Fig. 3 shows the relationship between tensile strength of the TPO samples and Mooney viscosity of the devulcanized EPDM samples. Numbers in Fig. 3 correspond to the difference in shear stress and pressure in the pulverization zone and the devulcanization zone decreased in number order. In other words, the shear stress and pressure applied on EPDM waste was the highest in configuration-1 and was the lowest in configuration-3. When the reactive conditions were changed in the same screw configuration, T_b of the TPO increased with Mooney viscosity. It is thought that the restraint of excess heat generation is important because the viscosity increases with decreasing the temperature in the pulverization zone and the devulcanization zone of the reactor. In comparison with the screw configurations, T_b decreased with the screw configuration number increasing. It is evident that T_b becomes higher under higher shear stress and internal pressure without the degradation by heat.

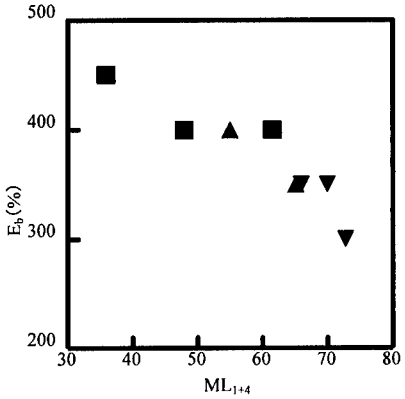

Fig. 4 Relationship between elongation at break of TPO and Mooney viscosity of devulcanized EPDM. Marks correspond to those in Fig. 3.

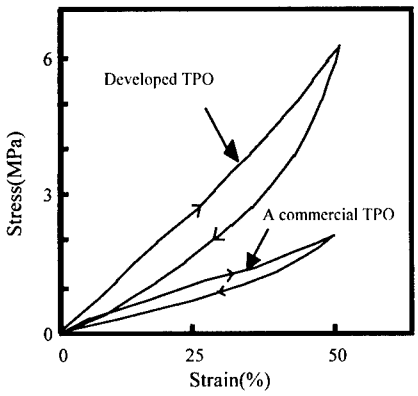

Fig. 5 Stress-strain curves in elongation-recovery measurement.

Elongation at break of the TPO decreased with the increase in Mooney viscosity and did not depend on the screw configuration as shown in Fig. 4. The increase in the viscosity causes the decrease in E_b. However, the TPO using the EPDM with the viscosity of lower than 60 shows both of plasticity (i.e., lost of rubbery properties) and high extensibility. It may be concluded that the TPO shows good tensile properties with Mooney viscosity of the devulcanized EPDM in the range of 60 to 65.

The TPO with good tensile properties recovered its original length after elongation in the elongation-recovery tests as shown in Fig. 5. This behavior was similar to a commercial one. It is shown that the developed TPO has rubbery elasticity. The TPO showed higher slope of the stress-strain curve, which was equivalent to higher modulus, than commercial one. These properties may be due to the presence of carbon black particles in the EPDM phase and bound EPDM rubber chains with the carbon black. In the case of the EPDM with Mooney viscosity of lower than 60, TPO showed poor rubbery elasticity and did not recover to its original length after elongation procedure.

Conclusions

A new rubber recycling technology by the continuous process in which the devulcanization of EPDM waste and the compatibilization of the EPDM and PP proceed to produce TPO was developed. In the TPO obtained under optimized conditions, the EPDM component forms the disperse phase with a size of 1-micrometer order in continuous PP phase. The TPO showed rubbery elasticity and good recoverable property after high elongation. These properties may be due to the presence of loose crosslinking structure and carbon black particles in the EPDM. It is concluded that devulcanization reaction for EPDM waste is the most important to the production of the TPO showing good properties

Reference

1. K Fukumori, M. Mouri, N. Sato, H. Okamoto, M. Matsushita, H. Honda, K. Nakashima, Y. Suzuki, and M. Owaki: Gummi Fasern Kunststoffe, 54, 48 (2001).

Proceedings of 7th Japan International SAMPE
Symposium & Exhibition, Nov. 13-16, 2001

Designing of CFRP baseball bats

Tsuyoshi NISHIWAKI

Research and development dept. ASICS Corp.
2-1, 6-chome, Takatsukadai, Nishi-ku, KOBE, 651-2271, JAPAN
Email: waki@tiger4.sp.asics.co.jp

Abstract

This paper describes the designing process of FRP regulation baseball bat. FRP baseball bat has some superior properties such as high durability and easy control of restitution rather than conventional metal and wooden bats. For the important parameters of the baseball bat, coefficient of restitution, the measurement method and dependency on geometrical parameter are discussed. Moreover designing method based on the numerical simulation is also proposed.

Key Words: FRP, Baseball Bat, Coefficient of Restitution, Numerical Simulation

Introduction

For sporting gears, the first application examples of fiber reinforced plastics (FRP) are tennis racket and/or golf shaft. On the other hand, the baseball bats have been made of aluminum or specific wood. Impact energy of the baseball bats at the ball hitting is much larger than that of tennis racket and golf shaft. For instance, in the regulation baseball bat, the ball with a diameter of 70mm, the weight is 145g. Impact velocity is usually 140 km/h. and the ball velocity hit is larger than the impact. Therefore the application of FRP has been delayed. However new issues in the conventional materials have been focused. At first, the specific wood is decreasing against various environmental problems such as forest destruction and acid rain. Secondary the metal bat causes hard listening of players. Thirdly both the conventional materials have been had the low durability. Based on the above background, I started the development of FRP regulation baseball bat. In this report, the designing process and some experimental and simulation results are described.

Mechanical Properties of Baseball Bat

Restitution Property

One of the most important properties in the bat is the restitution property.[1] Figure 1 is a schematic illustration of experimental method for the measurement of restitution. The system is constructed by the air gun, CCD camera, image processor and personal computer. The coefficient of restitution, e can be calculated by Eqn.1 under some assumptions,

$$e = \frac{v_1 + (\frac{m}{M} + \frac{ml^2}{I})(v_1 - v_0)}{v_0} \qquad \text{Eqn.1}$$

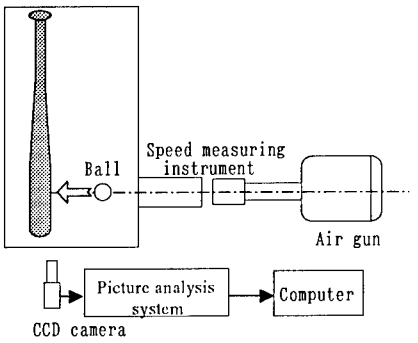

Fig.1 Illustration of coefficient of restitution measurement system

where, m and M denote the weight of ball and bat. I and l represent the moment inertia of the whole bat and the distance between hit point and the gravity position, respectively. The postscripts of v, 0 and 1 means the ball velocities at pre and post impacts. The bat is suspended by a fine string, this is equivalent with the free condition. By using this system, v_0 and v_1 are measured and e is calculated. Table 1 lists the basic geometrical properties of baseball bats used. Figure 2 shows the coefficients of restitution obtained from metal and wood plotted against the impact position. It was clarified that e was highest at l=150mm in both the bats. It was also found that the metal bat had the higher e rather than the wood bat. However the wood bat has the wider sweet area, which produce the high restitution.

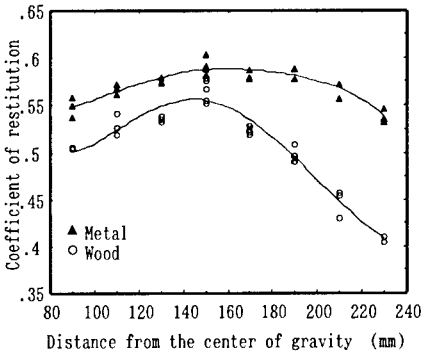

Fig.2 Coefficient of restitution plotted against the distance from the center of gravity in case of v_0 = 130 km/hr

Mechanical Properties

Two mechanical properties are focused in this study. One is the bending stiffness and

Table 1 Physical properties of baseball bats used in this study

Bat type	Weight [g]	Length [mm]	Max. diameter [mm]	Center of gravity [mm]	Moment of inertia [kg.cm2]
Metal	829.9	840	70	473	540
Wood	898.6	860	64	483	580

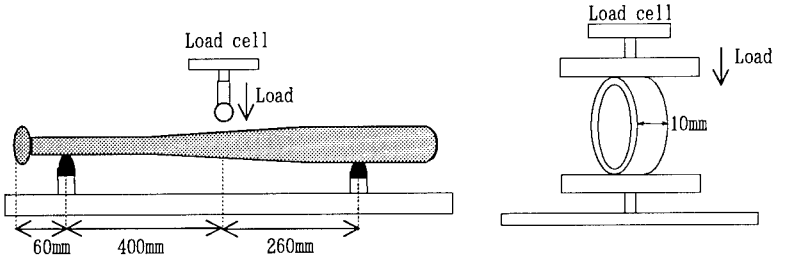

(a) Flexural experiment (b) Compressive experiment

Fig.3 Experimental measurement method of baseball bat properties

the other is lateral compressive stiffness at the batting portion measured by Fig.3 (a) and (b) methods, respectively. Table 2 shows the lists of the static properties obtained. The metal bat has the higher flexural stiffness and the lower compressive stiffness, as compared with the wood bat.

Table 2 Mechanical properties measured

	Stiffness [kgf/mm]	
Bat type	Flexural	Lat. Compressive
Metal	34.857	29.141
Wood	10.286	130.98

Numerical Simulation

In order to clarify the relationship between restitution and static mechanical properties, the explicit finite element analyses were performed. Figure 4 shows the numerical model used. The ball was represented by 3-d. solid model which has the equivalent stiffness. The bat was modeled by thin shell elements with the constant thickness of 2.5 mm. The ball impact velocity is set to be 130 km/h. The impact point is 130mm apart from the bat top. In this simulation, the bat was subdivided into two portions, which has the independent elastic modulus. The elastic modulus of the batting portion, E_1 correspond to the lateral compressive stiffness, the modulus of tapered portion, E_2 correspond to the bending stiffness. In these simulations, two kinds of analyses were performed. E_2 dependency upon the restitution are checked under the constant of E_1, 70GPa. Next, E_1 dependency upon the restitution are checked under the constant of E_2, 70GPa. The dependencies of these moduli on the restitution property are independently shown in Fig.5. Judging from this figure and Fig.2, it was found that the stiffness of the batting portion mainly made a great influence on the restitution property.

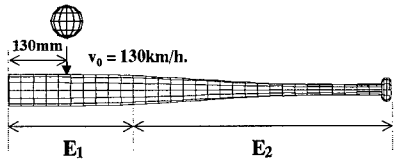

E_1 : Young's modulus of the batting part
E_2 : Young's modulus of the tapered part

Fig.4 Numerical model used in ball impact simulation

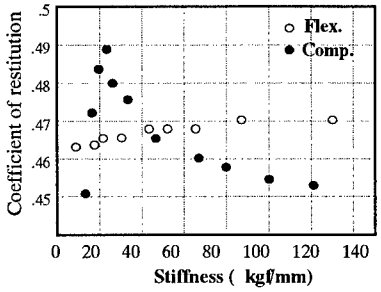

Fig.5 Relationship between coefficient of restitution anbat stiffness obtained from numerical simulation

This result can be understood by the phenomenon that only the ovalization of the batting portion is caused in the contact phase. In other words, the whole flexural deformation cannot be caused during the contact time.

Designing of baseball bat by using the numerical simulation

As already mentioned, the designing of the batting portion is very important for the control of coefficient of restitution. The portion is a cylindrical structure, high strain energy is caused at the impact. Namely the strength analysis is required in this designing. In this research, the lateral compressive analysis of CFRP cylindrical tube is effective for predicting the strength and stiffness of the batting portion in FRP baseball bat. In this section, numerical model of cylindrical FRP laminates is proposed and the validity is checked by a comparison with experimental results. Figure 6 shows the numerical model which can consider the heterogeneity of FRP.

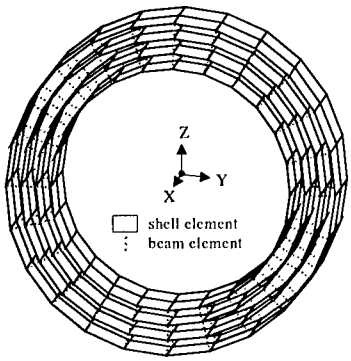

Fig.6 Quasi-three-dimensional model [2]

In the prediction of the strength, the onset and propagation of local failures such as transverse crack, interlaminar delamination and fiber breakage must be predicted. The proposed model has two type elements. The direct application of the conventional homogeneous model is not proper, because the homogeneous model cannot separately consider the above local failures. The stacking sequence used is $[\theta / -\theta]$sym. (θ = 15, 30, 45 and 60), where θ= 90 indicates the hoop direction. The outer and inner diameters are 70 and 61mm, respectively. The nominal thickness is 4.5mm. The length is 30mm. Figure 7 shows the comparison between analytical and experimental curves. Judging from this figure, the numerical

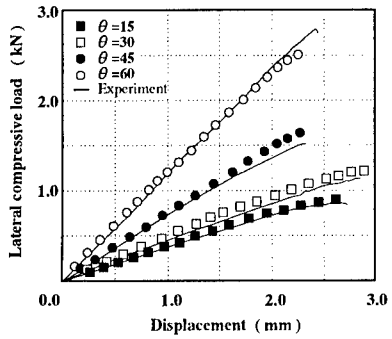

Fig.7 Comparison of load-deflection curves between analytical and experimental results

model shown in Fig.6 is effective for the prediction of mechanical behaviors of FRP cylindrical tubes with any fiber orientation angles.

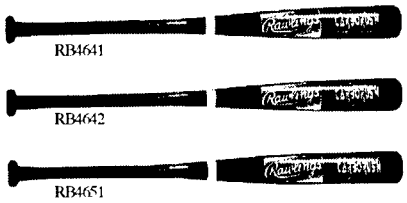

Fig.8 Finished FRP baseball bat

Figure 8 shows the designed FRP regulation baseball bats. From the current research, it was found that impact feeling depended on the bending stiffness. In case of the application of FRP to the baseball bat designing, various properties can be produced. For example, high restitution with soft impact feeling, wide sweet spot for hard impact and so on can be easily designed.

Conclusions

As the designing example of FRP related products, the designing process of the regulation baseball bat was described. In this designing, it was found that the lateral compressive and flexural stiffness made influences on the restitution property and the feeling at the impact, respectively. This is a representative application example of advantages in FRP, orthotropicity and tailoring.

References

1. Nishikawa, N. and Nishiwaki, T., Sports sangyou-gaku kennkyuu, 5, 2, (1995), pp.641-647.
2. Nishiwaki, T., Compos.Struct., 32, (1995), pp.635-640.

Proceedings of 7th Japan International SAMPE
Symposium & Exhibition, Nov. 13-16, 2001

Dynamic Response of FRP Structure after Impact

Norihiko TANIGUCHI#1 and Tsuyoshi NISHIWAKI#1

#1: Research and Development Department, ASICS Corporation,
6-2-1 Takatsukadai, Kobe 651-2271, JAPAN
E-mail: nori@tiger4.sp.asics.co.jp

Abstract

The stress wave propagation behaviors in unidirectional GFRP laminates are experimentally investigated. A simple technique has been developed in order to obtain the time history of stress wave. The calculated stress wave velocity is compared with the theoretical value. Results show that the experimental value is in a good agreement with the theoretical value. The effects of initial stress on wave propagation behaviors are also discussed. It is demonstrated that wave velocity increases with increasing of initial tensile stress. However, the increasing rate is affected by the induced wavelength.

Key Words: Wave propagation, GFRP, Initial stress, Dispersion.

Introduction

Generally speaking, dynamic response is the most dominant property in the practical designing. Stress wave, which is induced by impact load, makes a great influence on dynamic response of FRP structure. Therefore, evaluating the wave propagation behavior has been one of the great interests for a long time.

A number of experimental and analytical approaches have been performed in order to clarify the above problems [1]-[3]. However, these research activities have met with limited success for practical designing, since the analytical models are assumed to be infinite, and boundary conditions and/or initial conditions are ignored. In order to design the FRP structure more practically, considering these conditions are obviously important.

The purpose of this present paper is to evaluate the wave propagation behavior under various initial loading and boundary conditions. First, the wave velocity measured is compared with the theoretical vale in order to check the validity of the proposed experimental technique. Then, the effect of initial tensile stress upon the wave velocity is investigated experimentally. Finally, the dependencies of specimen thickness and length upon wave velocity are discussed.

Experiment

Specimen

Unidirectional GFRP laminates (volume fraction of fibers V_f = 62%, fiber orientation θ=0deg.) were used. The specimens were cut, ^{l}260mm×^{b}20mm×^{t}1.5mm, as shown Fig.1. For evaluating the wave propagation behavior, strain gages (KSN-2-120-E5-11) are located at specimen surface, where the word "Gage 1F" and "Gage 2F" denote the front surface gages, and "Gage 1B" and Gage 2B" indicate the back ones. Mechanical properties of specimen are listed in Table 1.

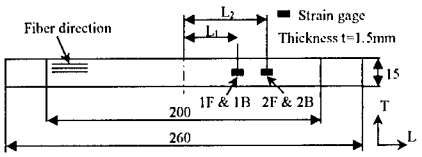

Fig.1 Geometry of specimen used in this study

Table 1 Mechanical properties of specimen

Young's Modulus E_L, E_T	46.3 GPa, 15.8GPa
Shearing Modulus G_{LT}	17.5 GPa
Poisson's ratio ν_{LT}	0.33
Fiber volume fraction V_f	62.3 %

Experimental Procedure

The overall set up of experimental system is shown in Fig.2. In this system, impact load was transversely applied at the centerline of specimen by swinging the cylindrical bar, steel bar (diameter d=10mm). Namely, the specimen was subjected to the line impact. It is noted that both the ends of specimen clumped. The swing angle, q, between steel bar and specimen is θ=30 deg in this study, the impact velocity is 1.11 m/sec.

The data obtained from this experiment is constructed by the time history of strain after impact. The strain value is derived from the strain gage on specimen surface. The sampling time for strain gages is 1μsec.

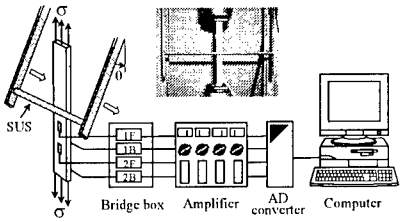

Fig.2 A schematic illustration of measurement

Results

Typical examples of strain gage outputs with various gage layouts are given in the following remarks.

Gage layout (a)

In gage layout (a), four single strain gages are located at the front and back surfaces of the plate. The gage positions, L_1 and L_2, are 40mm and 60mm, respectively. Typical examples of strain gage outputs along fiber direction are shown in Fig. 3. The waveforms obtained from the front and back surface gages are seen to be almost symmetric at the same station (Gages 1F and 1B, or 2F and 2B). This symmetric behavior implies that the transverse flexural wave appears as the predominant wave system.

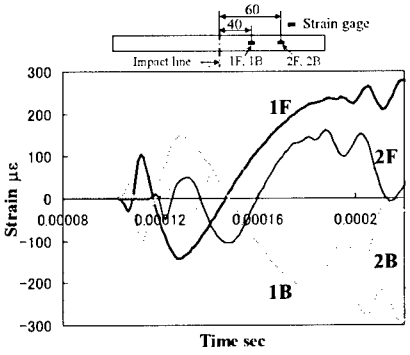

Fig.3 Time series of strain – gage layout (a)

Gage layout (b)

In gage layout (b), two single strain gages are located at the front surface only, which L_{1F}=40mm and L_{2F}=41mm. Figure 4 shows the typical time histories of obtained strain.

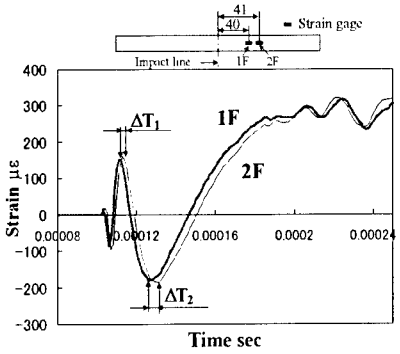

Fig.4 Time series of strain – gage layout (b)

In this study, wave velocity can be calculated from the following equation,

$$V = \frac{L_2 - L_1}{\Delta T} \qquad (1)$$

where ΔT denotes the time interval of wave peaks propagating from Gage 1F to 2F. The average wave velocities, V_{1b} and V_{2b}, measured from ΔT_1 and ΔT_2 in Fig.4 are respectively,

$$V_{1b} = 727.89 \text{ m/sec}$$
$$V_{2b} = 409.71 \text{ m/sec}$$

The theoretical wave velocity can be calculated by [4],

$$V^2_{Theory} = \frac{c_0^2}{2\varepsilon}\left\{1+\varepsilon+\frac{1}{K^2k^2} \pm \sqrt{\left(1+\varepsilon+\frac{1}{K^2k^2}\right)^2 - 4\varepsilon}\right\} \qquad (2)$$

where c_0, K and ε are material constants and k is wavelength.
The corresponding theoretical value obtained using the above equation (2) are,

$$V_{1btheory} = 746.19 \text{ m/sec}$$
$$V_{2bthoery} = 405.92 \text{ m/sec.}$$

The measured values are a good agreement with that from calculated ones.

Gage layout (c)

In gage layout (c), two single strain gages are located at the front surface as well as gage layout (b), where L_{1F}=60mm and L_{2F}=61mm. Typical time history of longitudinal strain are shown as Fig.5. The important point to note is that the waveform is completely different from that of gage layout (b). Namely, the waveform disperses as propagating.
The comparison of measured and calculated wave velocity V_{1c} is:

$$V_{1c} = 443.27 \text{ m/sec}$$
$$V_{1cthoery} = 474.70 \text{ m/sec.}$$

These values appear to agree well.

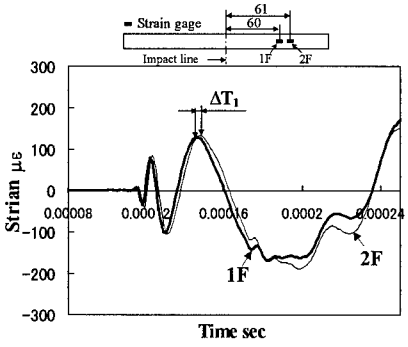

Fig.5 Time series of strain – gage layout (c)

Discussion

Initial stress dependency on wave velocity

In order to investigate the effect of initial stress, the wave velocity was measured under the various tensile loading conditions. In this section, two types of gage layout, gage layout (b) and gage layout (c), are adopted for measuring the wave velocity. The measured wave velocities plotted against the applied tensile stress are shown in Fig.5.
As clearly shown in this Figure, wave velocity V_{1b} is seen to be almost constant with increasing of tensile stress. On the other hand, wave velocity V_{1c} increases with increasing of the applied stress.

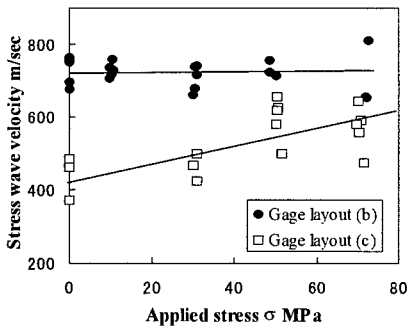

Fig.5 The intial tensile stress dependency upon wave velocity V_1

The most important point to note is that the increasing rate of wave velocity is obviously different. This result implies that the waveform, which is determined by wavelength, amplitude and frequency, makes a great influence of initial stress dependency upon wave velocity.

The effect of specimen thickness on wave velocity

Figure 6 shows the comparison of strain gage outputs of L_{1F}=40mm with various specimen thickness. It is clear that waveform change with changing of specimen thickness. Stress wave velocity V_{2h} was measured from t=1.0mm, 1.5mm, 3.0mm and 5.0mm.

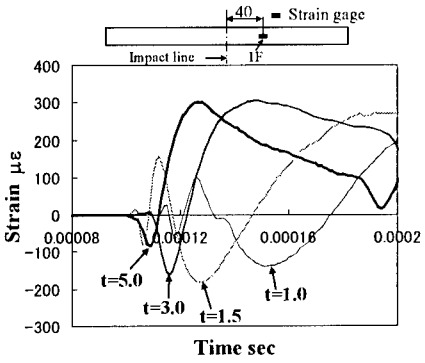

Fig.6 Time series of strain with various specimen thickness t mm

Table 2 shows the comparisons of wave velocity V_2 with various specimen thickness. The result demonstrates that the wave velocity increases with increasing the specimen thickness. Judging from this result, specimen thickness makes a great influence of wave velocity.

Table 2 The comparison of V_2 with various thickness

t mm	t=1.0	t=1.5	t=3.0	t=5.0
V_2 m/sec	329.4	409.7	884.9	1387.9

The effect of specimen length on wave velocity

Time histories of strain gage output with various specimen length are shown as Fig.7. The traces of the surface gage are seen to be almost same in shape. It is concluded that the wave velocity is independent of specimen length. However, it is noted that the reflection waves arrives faster in case that specimen length is getting shorter.

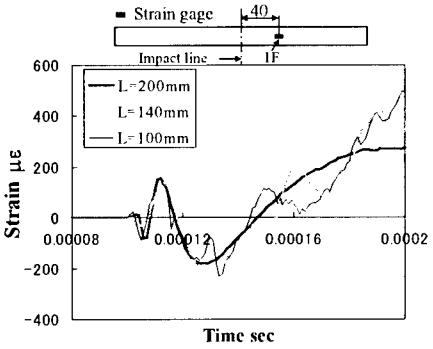

Fig.7 Time series of strain with various specimen thickness

Conclusions

(1) Stress wave velocity was measured by using the simple technique.

(2) Wave velocity increase with increasing of initial tensile stress. However, the increasing rate is dependent on wavelength.

(3) Specimen thickness makes a great influence of wave velocity. On the other hand, wave velocity is almost independent on specimen length.

References

1. R.M.Christensen, "Mechanics of Composite Materials", John Wiley and Sons, Inc., ISBN 0-89464-501-3, Cap. VII, 1979.
2. I.M.Daniel and T.Liber, Experimental Mechanics, pp.9-16, January, 1979
3. N. TAKEDA, et al., J. Composite Mater., Vol. 15, pp.157-174, 1981
4. T. HAYASHI, et al. ISBN 4-526-02427-9

Proceedings of 7th Japan International SAMPE
Symposium & Exhibition, Nov. 13-16, 2001

Prototype of A Finite Element Foot Model

Takeshi Asai#, Tsuyoshi Nishiwaki## and Hiroyuki Nunome###

#: Fac. of Educ., Yamagata Univ., Yamagata-city, Yamagata, 990-8560, JAPAN
##: ASICS Co., Takatsukadai, Kobe-city, Hyougo, 651-2271, JAPAN
###: Research Center of Health, Physical Fitness & Sports, Nagoya University, Furo-cho, Chikusa, Nagoya-city, Aichi, 464-8601, JAPAN
E-mail: asai@kescriv.kj.yamagata-u.ac.jp

Abstract

The purpose of this study was the development a foot joint skeletal model using the finite element method for the analysis of physical exercise, sports injury and footwear design. The basic shape of the finite element foot joint model was described using a commercial foot skeletal model for computer graphics and anatomical data, and the solid model was defined after simplifying that model.In the vertical drop test simulation, the contact time of the foot model and the floor model was about 22 ms, and the vertical peak force was about 8400 N for the model weight of 60 kg. It seems that a good approximation is acquired when comparing the actual ones with that values in the experiment [5]. It was observed that the highly stressed regions were the metatarsals, the navicular and the calcaneus in both the linear static analysis and dynamic transient analysis.

Key Words: Finite Element, Foot, Sport.

Introduction

The understanding of the impact mechanics during human motion is important for research within the fields of motion analysis and footwear design. Many fundamental and applied human motions are influenced by complex deformations, internal stresses and the shock wave of the foot skeletal system. It is difficult to directly measure the internal stresses and shock wave in vivo. However, these stresses and shock wave can be predicted using a mathematical or numerical model of the foot skeleton. The purpose of this study was the development a foot joint skeletal model using the finite element method for the analysis of physical exercise, sports injury and footwear design.
Several researchers reported some studies about a foot joint skeletal model used for stress analysis using 2D or 3D finite element method [1]. The stress distribution in the foot depends on the geometry and structure of the foot model. Hence, it is necessary to model the foot in all the three dimensions in order to provide a more realistic representation. The majority of finite element problems uses implicit methods to carry out a linear static analysis and a transient analysis. Static problems can be usually analyzed quasi-statically, but the technique is only cost effective if the problem incorporates significant nonlinearities. The time step of the implicit analysis must subdivide the shortest natural period of interest in the structure, but that of explicit analysis must subdivide the shortest natural period of the mesh. Therefore, in this study, the linear static analysis was used for the implicit time

integration code, and the dynamic transient analysis was used for the explicit time integration code.

Methods

The basic shape of the finite element foot joint model was described using a commercial foot skeletal model for computer graphics and anatomical data, and the solid model was defined after simplifying that model (Fig. 1). The axis system of the model is chosen such that, with respect to the foot, the X-axis is horizontal and in the external-internal direction, the Y-axis is vertical along the tibia pointing in the upward direction and the Z-axis completes the right-handed rectangular coordinate system (Fig. 2).

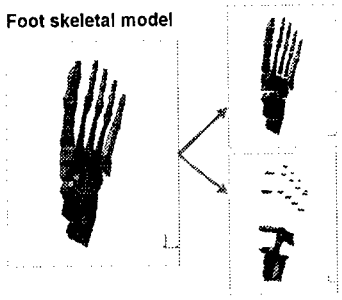

Fig.1 Structure of a foot-joint model

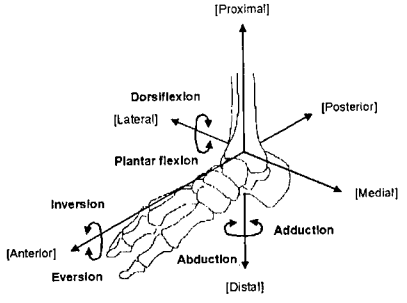

Fig.2 Configuration of foot-joint model

The hard tissue parts of this foot model consisted of 23 bone models such as the calcaneus, matatarsal, etc., and the soft tissue parts that were modeled consisted of 15 joint models such as the talocalcanean (subtalar) joint, calcaneocuboid joint, etc. The ligaments and retinacula were not geometrically represented, consequently, the stiffness of the soft tissue parts were estimated including the function of the ligaments and retinacula. The finite element meshes were made from the solid model using a commercial pre-post processor (MSC.Patran), and the linear static analysis was solved using an implicit FEM code (MSC.Nastran). More over, the dynamic transient analysis was performed using an explicit FEM code (MSC.Dytran). As material properties, the Young modulus of the hard tissue of the finite element foot joint model was 7.3 KPa, and Poisson ratio was 0.3 [2]. The Young modulus of the soft tissue was defined for 5 cases from 1 Pa to 5 Pa at intervals of 1 Pa in the linear static analysis. As the boundary condition, a vertical load of 300 N was defined on the trochlear surface of the talus. The bottom of the calcaneus and the head of the matatarsal were constrained (Fig. 3).

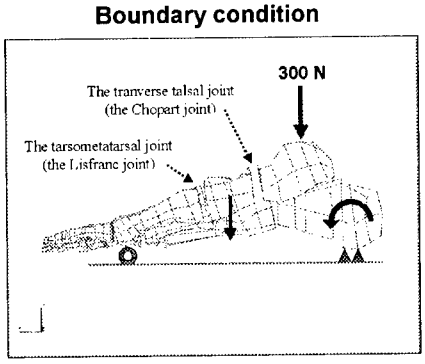

Fig. 3 Boundary condition of liner static analysis

For the dynamic transient analysis,

the Young modulus of the soft tissue was defined by higher values, and added mass including the muscles, retinacula, skin, etc (Table 1). The initial vertical velocity at impact was –1.0 m/s (Fig. 4). The initial rotational velocity were 0 rad/s and 8.7 rad/s.

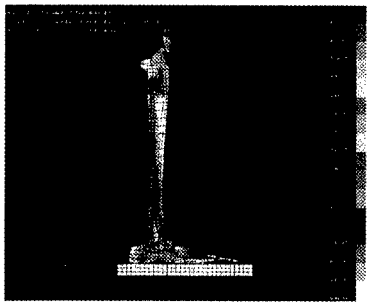

Fig.4 Vertical drop test in transient analysis

Table 1 Material properties on the transient dynamic analysis

Parts	Young's	Poison ratio
Hard Tissue	7300 MPa	0.3
Soft Tissue	1000 MPa	0.4
Ankle Joint	10000	0.4
Fibula	73000	0.3
Plantar	1500 MPa	0.4
Ground	61 MPa	0.3

Results and Discussions

In the experiment using a cadaver foot, the displacement of the inside arch height by a vertical load (300N) was 2.90 mm, while the same result for Case 4 of this study was 2.70 mm. The plantar flexion angle of the calcaneus of the cadaver was 1.8 deg. while that for Case 4 was 3.0 deg. It seems that, in this simulation model, the stiffness of the soft tissue is slightly lower than that of a real human foot (cadaver). It is considered that the motion pattern of the foot model during vertical loading is qualitatively similar to that of the experiment (Fig. 5).

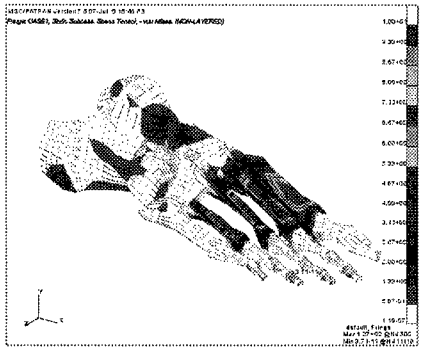

Fig.5 Stress contours on deformed shape in Case 5

In the vertical drop test simulation, the contact time of the foot model and the floor model was approximately 22 ms, and the vertical peak force approximately 8400 N (for the model weight of 60 kg) suggesting that the experiment represents a good approximation of real life [5]. However, the vertical peak force for this boundary condition was much higher than that reported for real human running [3, 4].

The vertical peak force of translation with an inclined initial position (0.26 rad) was lower than that for an upright initial position (0 rad). Also, the vertical peak force associated with translation and rotation with an inclined initial position (–1.0 m/s and 8.7 rad/s) was lower than that of translation alone (–1.0 m/s and 0 rad/s). It seems that, in this simulation, rotational motion of the foot and leg reduces the vertical peak force at impact (Table 2). It was observed that in both the linear static analysis and dynamic transient analysis, the highly stressed regions were the metatarsals, the navicular and the calcaneus (Fig. 6-8).

Conclusions

The finite element foot model of this study had simple structure and material

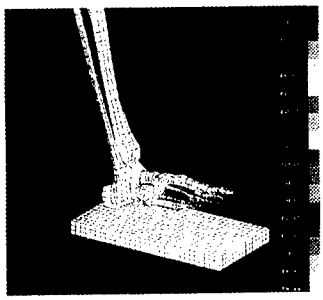

Fig.6 An example of the stress contour on the deformed shape at 0 ms in the transient analysis

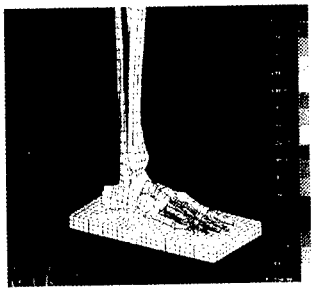

Fig.7 An example of the stress contour on the deformed shape at 30 ms in the transient analysis

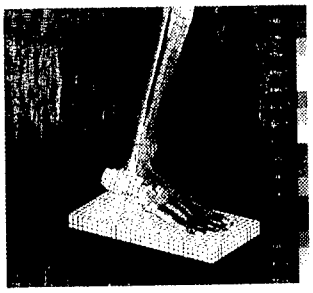

Fig.8 An example of the stress contour on the deformed shape at 60 ms in the transient analysis

properties. In the comparison the vertical contact force and contact time of experiment with that of simulation, it seemed that good agreement was obtained. It is considered that the highly stressed regions were the metatarsals, the navicular and the calcaneus.

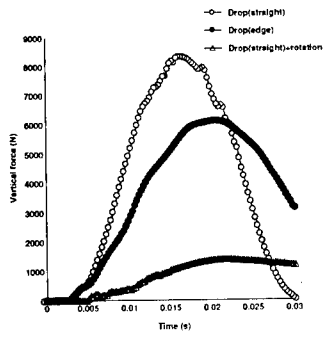

Fig.9 Vertical force in transient analysis

Table 2 Initial condition and vertical peak force in transient analysis

	Initial position (rad.)	Trans. velocity (m/s)	Rotat. velocity (rad/s)	Peak force (N)
Transient 1	0.0	-1.0	0.0	8322
Transient 2	0.26	-1.0	0.0	6108
Transient 3	0.26	-1.0	8.7	1385

References

1. Beaugonin M. and Haug E.: SAE, 962428, 239(1996).
2. Jacob S., et al.: Mechanics Research Communications, 23(4), 387(1996).
3. Lafortune M. A. and Lake M. J.: J. Biomechanics, 28(9), 1111(1995).
4. Nigg, B. M. (eds.): "*Experimental techniques used in running shoes research. In Biomechanics of Running Shoes*", Human Kinetics, Champaign, 1986, pp29.
5. Nishiwaki T. and Nasako M.: Proc. of sympo. on sports engineering. JSME, 9(1998).

Proceedings of 7th Japan International SAMPE
Symposium & Exhibition, Nov. 13-16, 2001

A Kinetic Comparison Between Dominant and Non-dominant Legs during Soccer Full Kick

Hiroyuki NUNOME#, Takeshi ASAI##, Yasuo IKEGAMI# and Shinji SAKURAI#
#Research Center of Health, Physical Fitness & Sports, Nagoya University,
Furo-cho, Chikusa, Nagoya-city, Aichi, 464-8601, JAPAN.
##Faculty of Education, Yamagata University,
Yamagata-city, Yamagata, 990-8560, JAPAN.
E-mail: nunome@htc.nagoya-u.ac.jp

Abstract

The ability to kick the ball with both legs is regarded as a desirable skill in soccer players. However, most data related to maximal soccer kick demonstrated the kinetic aspects only for the dominant side. This study investigated the asymmetrical aspects through a comparison of kinetic parameters between the dominant and non-dominant legs. Five male Brazilian U-17 players were volunteered. Three high-speed video cameras recorded the kicking motion of both legs at 200 Hz. A three-link kinetic chain was used to compute torques due to musculature and motion-depended interaction. A remarkable difference was found between the two legs for the interaction torque occurred at the knee joint. The interaction torque of the dominant leg particularly contributed to the knee extension motion whereas that of the non-dominant leg was small enough to be negligible. These results suggest the interaction torque is a substantial source to increase the knee extension angular velocity of the dominant leg during maximal soccer kick.

Key Words: soccer kick, kinetics, dominant leg, non-dominant leg

Introduction

The most successful players shot for goal with both left and right feet during high-level competition including World Cup (Starosta, 1988). Thus, the ability to kick the ball with both legs is regarded as a desirable skill in soccer. Although several studies have found no difference for the muscle strength between both legs, Mclean & Tumilty (1993) and Barfield (1995) showed a faster ball speed could be generated by dominant leg than non-dominant leg. This may attribute to some asymmetry of the leg motion during kicking. To understand how the asymmetry is produced, its kinetic aspects were investigated using a three-dimensional video analysis technique.

Methods

Informed consent was obtained from five male Brazilian U-17 club players (height = 176.2 ± 6.1 cm; mass = 70.6 ± 7.2 kg; career = 9.6 ± 0.5 yrs) who volunteered to participate in this study. Their dominant leg was right. After a short period of warm-up, they were instructed to perform maximal instep kicks with both legs to the center of goal, which was located at a distance of 11 m in front of them. Three

electrically synchronized high-speed video cameras (NAC Inc., Tokyo, Japan) were used to sample the kicking motion at 200 fps (shutter speed was 1/2000 s).

Of three trials, the one trial in which the ball contacted closest to the center of goal was analyzed. A digitizing system (DKH Inc., Tokyo, Japan) was used to manually digitize anatomical body landmarks including: right and left shoulders, hips, knees, ankles, heels and toes. The center of the ball was also digitized in its initial stationary position and in all the available frames after it left the foot. The direct linear transformation (DLT) method was used to obtain the 3-D coordinates of each landmark. The performance area ($1.5 \times 1.5 \times 1.8$m) was calibrated with a net root mean square error of 5 mm.

According to a procedure described by Feltner and Dapena (1989), the kicking leg was modeled as a three-link kinetic chain composed of the thigh, shank and foot to compute torques due to musculature and motion-depended interaction. Segment mass, center of the mass location and moment inertial values were derived from the data of young living athletes (Ae, 1996), which would be more appropriate for the subjects in the present study.

Both torques and angular velocities were separated into orthogonal components using unit vectors included in anatomically-relevant references frames (Fig. 1). Hip torque and angular velocity vectors were separated into three components: adduction ($+X_{AH}$)/abduction ($-X_{AH}$), flexion ($+Y_{AH}$)/extension ($-Y_{AH}$) and external rotation ($+Z_{AH}$)/internal rotation ($-Z_{AH}$). Knee torque and angular velocity vectors were separated into two components: extension ($+X_{KA}$)/flexion ($-X_{KA}$) and external rotation ($+Z_{KA}$)/internal rotation ($-Z_{KA}$). Ankle torque and angular velocity vectors were separated into two components: dorsi-($+Y_{AA}$)/plantar-flexion ($-Y_{AA}$) and inversion ($+Z_{AA}$)/eversion ($-Z_{AA}$).

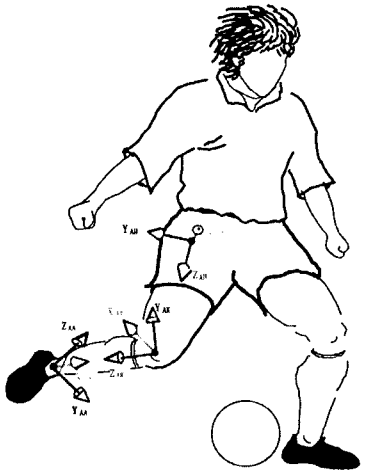

Fig. 1 Right-hand orthogonal reference frames fixed on each joint center.

The impact of the foot with the ball produces a sudden deceleration of the kicking leg, which causes a serious distortion of the kinetic data near impact. To avoid such systematic errors, the time-dependent coordinate data were digitally smoothed in a forward order (toward the impact) by a second-order Butterworth low-pass filter at 12.5 Hz.

Although this smoothing procedure may have minimized the risk of systematic errors stemming from impact, the reverse order filtering to eliminate phase distortion was canceled, thereby making the data prone to phase distortion.

Results

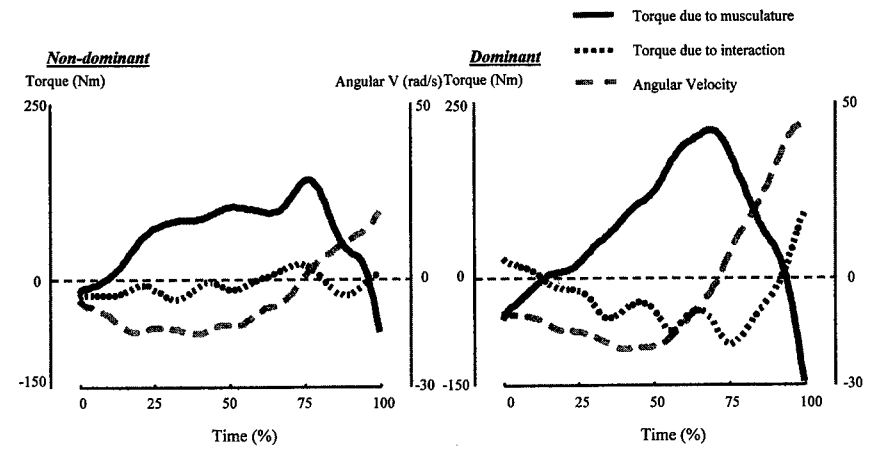

Fig. 2 Changes of torques due to musculature and motion-depended interaction and angular velocity of a typical subject for knee extension (+)/flexion (-).

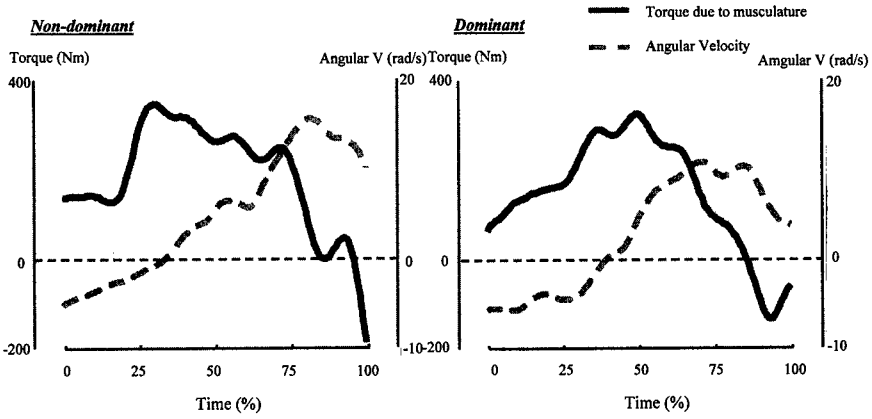

Fig. 3 Changes of torques due to musculature and angular velocity of a typical subject for hip flexion (+)/extension (-).

The average ball velocities of the dominant and non-dominant legs were 31.8 ± 2.6 m/s and 26.5 ± 1.6 m/s, respectively. The initial ball velocity of the dominant leg was significantly ($p < .01$) faster than that of the non-dominant leg.

Fig. 2 and 3 show the changes of torques and angular velocities of a typical subject for the knee extension (+)/ flexion (-) and hip flexion (+)/extension (-). In all graphs, analyzed portion was started from toe-off of the kicking leg which corresponding 0 % of the time and ended ball impact which corresponding 100 %.

As shown in Fig. 2, although the knee extension torque due to the musculature was dominant in both legs, its peak and integrated values (angular impulse)

were quite larger in the dominant leg than in the non-dominant leg. The peak value of the knee extension angular velocity was also quite larger in the dominant leg than in the non-dominant leg. A remarkable difference was observed between the two legs for the changes of torque due to motion-depended interaction. The interaction torque in the dominant leg tended to angularly accelerate the knee to the positive direction (extension) close to ball impact. In contrast, the magnitude of the interaction torque in the non-dominant leg was small enough to be negligible.

As shown in Fig. 3, although the hip flexion torque due to the musculature was dominant in both legs throughout the kicking, its angular impulse was slightly larger in the non-dominant leg than in the dominant leg that resulted in somewhat larger flexion angular velocity of the hip in the non-dominant leg.

Discussion

A proximal to distal sequence of segment motions has been recognized in kicking motions. In the present study, the sequential pattern of motion was confirmed in both legs. However, the knee extension angular velocity was quite lager in the dominant leg, which accounts for the lager ball velocity generated by the dominant leg.

Putnam (1991) showed a substantial influence of the interaction torque during a punt kick by showing the interaction torque always tended to angularly accelerate the distal segment in the positive direction as long as the proximal segment is rotating and the knee is not hyper-extended. In the dominant leg, besides the larger magnitude of the musculature torque and its angular impulse, the interaction torque angularly accelerated the knee to the positive direction (extension) close to ball impact; thereby partially support the results of Putman (1991).

In contrast, the interaction torque did not act to assist the angular acceleration of the knee in the non-dominant leg. As the motion of the proximal segment indirectly affect the interaction torque, the larger hip flexion angular velocity observed in the non-dominant leg may disturb the effective function of the interaction torque on the knee extension motion.

Conclusions

The present study clarified several aspects of asymmetry in soccer maximal kick. The torque due to motion-depended interaction is a substantial source to increase the knee extension angular velocity in the dominant leg during kicking.

References

1. Barfield, W. R. Effects of selected kinematic and kinetic variables on instep kicking with dominant and nondominant limbs. Journal of Human Movement Studies, 29, 251 (1995).
2. Levanon, J. and J. Dapena. Comparison of the kinematics of the full-instep kick and pass kicks in soccer. Med. Sci. Sports Exerc. 30(6), 917 (1998).
3. Putnam, C. A. A segment interaction analysis of proximal-to-distal sequent segment motion patterns. Med. Sci. Sports Exerc. 23(1), 130 (1999).
4. Starosta, W. Symmetry and asymmetry in shooting demonstrated by elite soccer players. "*Science & Football*", E. and FN. Spon, London, 1988, pp. 346-55.

Proceedings of 7th Japan International SAMPE
Symposium & Exhibition, Nov. 13-16, 2001

The relationship between the vertical movement of rotational axis and swing speed on the swing movement

Shin-ichi Inoue[1], Kenji Saitou[2] and Ross Sanders[3]

1:Faculty of Culture and Education, Saga University
2:Faculty of Science and Engineering, Saga University
3:Department of Physical Education, Sport & Leisure Studies, University of Edinburg

Abstract

In most movements of ball games, it is important to increase the swing speed at the ball impact. The purpose of this study is to investigate the relationship between the vertical movement of rotational axis of the swing and swing speed on the swing movements. To examine the relationship, an experiment and computer simulation in terms of Instep Kick in soccer was carried out. The results were as follows.

1. Experts were founded to lift the rotational axis of the swing leg to a greater degree than novices.
2. Computer simulations of the swing leg developed by combining data of torque patterns data of the thigh and the leg from the novices with kinematic data of the trochanter major from the expert group resulted in a slight increase in swing speed. When just the kinematic data from the most accomplished expert alone was used, a remarkable increase in swing speed was seen.

These results suggest the movement pattern such as lifting the rotational axis of the swing leg was useful in increasing the swing speed.

Introduction

In soccer, it is important to strike the ball accurately and quickly. To achieve this soccer player often use the Instep Kick. Generally, in order to kick the ball harder, the greater foot velocity needed. Ohta 3) reported experts swung their swing leg faster with upward velocity of center of gravity faster in an experiment comparing the Instep Kick of novices and experts. Accordingly, we hypothesized that experts would lift the rotational axis of their swing leg (trochanter major) faster than would novices, and the movement of lifting the rotational axis would contribute to increase the swing speed. The first purpose of this study is to examine this hypothesis by comparing the Instep Kick skill of a novice group to an expert group. The second purpose of the study is to examine the relationship between the movement of rotational axis and swing velocity of the foot in the Instep Kick. Then, computer simulation of the swing leg performed by using torque data of the thigh and the leg from each novice and kinematic data of the rotational axis from experts was used to examine whether the swing velocity of each novice was improved by these simulations.

Experiment

The subjects were 18 male expert soccer players who had played for at least 7 years, and 8 male novice players. The Instep Kick of each subject was recorded by high- speed video camera (250Hz) from a sagittal plane. Each body landmark was translated to coordinates on a computer, from which the kinematic data of the hip and the knee joints of the swing leg were obtained by using the "Mathematica Ver.3.0" program. The dynamical parameter was that of Chandler et al 1). The period of time from the landing of pivot foot to the ball impact of the swing leg

was used as swing phase.

Results of experiment

Figure 1 illustrates the means for the horizontal and vertical displacements of the trochanter major for the novice group and the expert group. Time bases were normalized to 100% of the swing phase.

The horizontal displacement of experts' data was slightly greater than that of

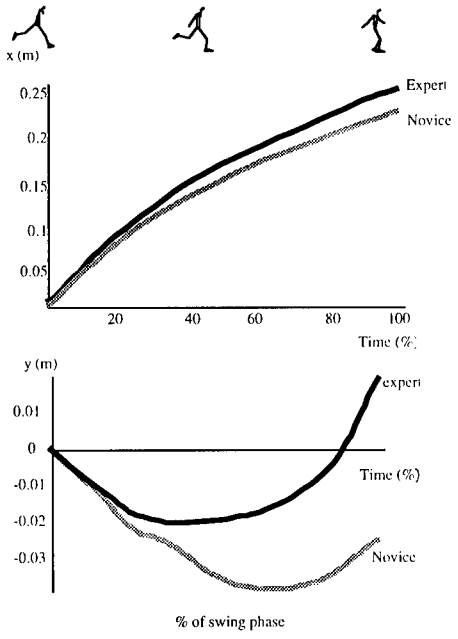

Fig. 1 Displacement of rotational axis on expert and novice group
Above: Holizontal component
Below: Vertical component

novices'. But the shape of the graph was similar. In contrast, a remarkable difference was seen between the novices' and experts' vertical displacement. The characteristic of the novices' pattern is a continuous descent of trochanter major to a point of 80 percent of the whole movement time, followed by a slight ascent. On the other hand, experts' descent of the trochanter major stopped at the 30 percent of whole movement time point, where it remained for a while, followed by an ascent from the 50 percent of whole movement time point.

Figure 2 illustrates the mean horizontal and vertical velocity of trochanter major of novices and experts. The horizontal velocity of experts was slightly faster than novices'.

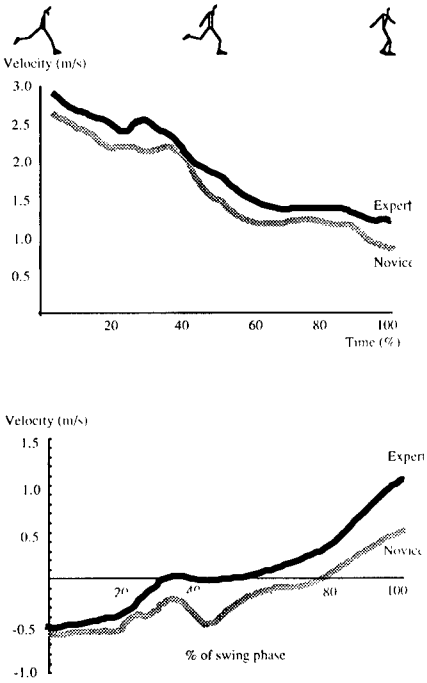

Fig. 2 Velocity of rotational axis on expert and novice group
Above: Holizontal component
Below: Vertical component

The vertical velocity of both subjects showed deceleration from the landing point for a while. But experts showed an increase in velocity from the early part of the swing phase to the latter phase.

These results indicate that the experts compared with novices lifted their rotational axis from the middle phase of the forward

swing in the Instep Kick.

Simulation

Figure 3 shows a model of the Instep Kick and the equation of motion built by the model. This model consists of segment representing thigh and combined shank with foot, and representing each torque is assumed to be generated on the hip joint and knee joint.

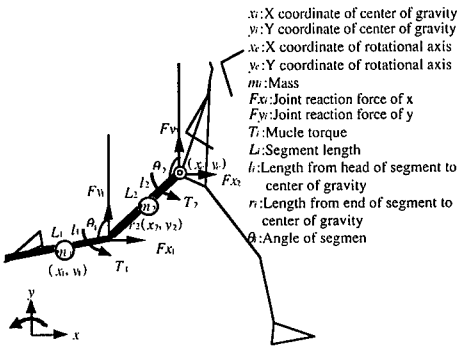

$$m_i \cdot \ddot{x}_i = Fx_i - Fx_{i-1} \quad (Fx_0 = 0)$$
$$m_i \cdot \ddot{y}_i = Fy_i - Fy_{i-1} - mg \quad (Fy_0 = 0)$$
$$I_i \cdot \ddot{\theta}_i = Fx_{i-1} \cdot r_{i-1} \cdot \cos\theta_i + Fy_{i-1} \cdot r_{i-1} \cdot \sin\theta_i + Fx_i \cdot l_i \cdot \cos\theta_i + Fy_i \cdot l_i \cdot \sin\theta_i + T_i - T_{i-1} \quad (r_0 = 0)$$

$$x_i = -L_{i-1} \cdot \sin\theta_{i-1} - l_i \cdot \sin\theta_i + x_c$$
$$y_i = L_{i-1} \cdot \cos\theta_{i-1} + l_i \cdot \cos\theta_i + y_c \quad (L_3 = 0)$$

Fig.3 Swing model for simulation and equation of motion

There are two input values for this simulation. One is for muscle torque of novice subjects exerted on the hip and knee joints, and the other is kinematic data on the rotational axis (trochanter major) of the expert subjects. Two rotational axis data are used for this simulation, one is the average data of the expert group (simulation1), and the other is the data of a subject who accomplished the fastest swing speed among all subjects (simulation2). Figure 4(Above) shows the displacement and velocity of horizontal and vertical axis on the rotational axis, which is used for two simulations. The initial angle value and angular velocity for each segment of each novice subjects was used, and the motion of equation were solved numerically by these initial conditions. The method of solution for this motion of equation as the differential equation is the Runge-Kutta method.

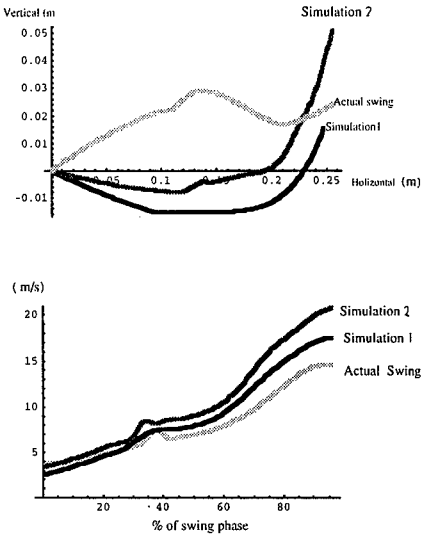

Fig.4 Above: Displacement of rotational axis for actual swing of Subject B.K.and used in Simulation 1 and 2
Below: Linear velocity of foot on actual swing (Subject B.K) and Calculated by each simulation

Results of Simulation

Figure 4(Below) shows the result of a simulation done on a novice subject (B.K.).The top graph is the displacement of the rotational axis, and bottom graph is the liner velocity of foot on actual swing and

calculated by each simulation.

At impact, the slowest swing was the actual swing, the second slowest was simulation 1 which used the average data of the expert subjects group, and simulation 2 which used the data of elite subject showing the fastest swing speed.

Table 1 shows the actual swing velocity at impact for each novice subjects and the results of two simulations. According to each average velocity data, actual swing velocity was 17.41m/s, simulation 1 was 17.95m/s, this was slightly faster than actual swing. Simulation 2 was 20.53m/s, which was much faster than the actual swing.

These results indicate that even though generated muscle torque in hip and knee joint are the same, the movement of rotational axis significantly influences the foot swing velocity. And since the velocity lifting the rotational axis in simulation 1 is faster than in simulation 2, we expect that lifting the rotational axis fast before impact is necessary to improve the swing velocity.

Table 1. Liner velocity of foot at impact on actual swing for each novices and calculated by each simulations.

(m/s)

Subject	Actual swing	Simulation 1	Simulation 2
S.I.	17.75	18.70	21.22
U.R.	19.39	18.62	21.08
B.K.	14.45	17.27	20.23
S.K.	17.73	17.92	20.64
A.M.	17.66	17.35	19.61
T.K.	16.52	15.00	17.50
N.G.	17.76	18.08	20.38
M.S.	17.98	20.62	23.54
Mean	17.41 (±1.42)	17.95 (±1.59)	20.53 (±1.69)

Discussion

On the movement of the Instep Kick in soccer, according to the hypothesis in this study, experts compared with novices lifted the trochanter major of swing leg quickly before impact. Actually, expert players seen on T.V. etc. jump upward after kicking the ball.

Then we carried out two computer simulations to examine the effect of the rotational axis. Also the result of simulations suggests that lifting the rotational axis of the swing leg was useful in increasing the swing speed.

We have an another result that we simulated the angular velocity of free pendulum with various vertical movements of the rotational axis of the pendulum2). In the result of the simulation, we recognized the effect that the lifting the rotational axis contributed the increase of the angular velocity.

In generally, the instruction method of sports activity including the Instep Kick doesn't mention the importance of lifting the rotational axis, but it is necessary to instruct this movement skill to increase the swing speed.

Reference

1.Chandler, RF, Clauser CE, Mcconville JT, Reynolds HM, Young JW: Investigation of Inertial Properties of the Human Body.U.S. Government Printing Office, 68(1975).

2. Shin-ichi Inoue, Tomoki Itoh. The influence of the movement of pivot lift on the in-step kick. Proceeding of 8 th Japan Society of Sports Industry, 73(1999).

2. Ohta,N:Biomechanical approach on the Instep Kick. Master's thesis of Faculty of Culture and Education, Saga University, (1998).

Proceedings of 7th Japan International SAMPE
Symposium & Exhibition, Nov. 13-16, 2001

Angular velocity of upper limb and torso in baseball pitches before and after ball-release

Kenji Saitou [1], Shin-ichi Inoue [2], Yuji Ohgi [3], Chikara Miyaji [4] and Shozo Takai [5]

1: Faculty of Science and Engineering, Saga University
1 Honjo, Saga 840-8502, JAPAN
E-mail: saiken@cc.saga-u.ac.jp
2: Faculty of Culture and Education, Saga University
3: Faculty of Environmental Information, Keio University
4: Japan Institute of Sports Sciences
5: Institute of Health and Sport Sciences, University of Tsukuba

Abstract

Angular velocities of joint motion in the upper limb and torso during baseball pitches were examined with a device consisting of six accelerometers. The magnitude and the time of maximal angular velocity before and after ball-release were compared between fast ball pitch and curve ball pitch. The angular velocities of forearm pronation and internal rotation of the shoulder at ball-release were higher in fast ball pitch. Maximal angular velocities of these motions were not significantly different between fast ball and curve ball pitches. From these results, forearm pronation inevitably occurs before and after ball-release during baseball pitch. In contrast, the maximal angular velocity of elbow extension was significantly different between fast ball pitch and curve ball pitch. In a curve ball pitch, the less flexed elbow joint makes forearm supination easier and reduces the torsion generated at the elbow as the forearm supinates and the shoulder rotates internally. In a curve ball pitch, to reduce elbow extension and to delay forearm pronation and internal rotation of the shoulder, the pitcher reduces the angular velocity of both forward flexion and torso rotation.

Key words: Angular velocity - baseball pitch - accelerometer - ball-release - pitch type.

Introduction

The understanding of body motion during baseball pitches has advanced with electromyography [6] and the use of three-dimensional video analysis, which is a direct linear transformation (DLT) method [1]. DLT methods provide much information simultaneously about the motion of body segments. Furthermore, the measurement devices used do not restrain the subject's movement during the experiment. However, DLT is less accurate for determining the coordinates of joints between various body segments. In contrast, the accelerometer has some advantages for the measurement of joint motion, particularly for rotations of small radii about a longitudinal axis, such as forearm pronation during baseball pitch [3, 5]. Furthermore, useful information concerning the type of motion and ball speed is acquired easily using a few small accelerometers [4, 7]. In this study, we measured joint motion of forearm, elbow, shoulder, and upper torso with a device consisting of six accelerometers. We examined differences

between fast ball and curve ball pitches.

Methods

Nine college baseball pitchers (all right-handed) participated in this study. The device for measuring the angular velocity consisted of pairs of accelerometers arranged in each axis of a three-dimensional coordinate system (Fig. 1).

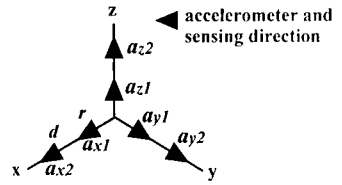

Figure 1. Device consisting of six accelerometers. Arrows represent accelerometers and the sensing directions.

Acceleration signals A_{x1}, A_{x2}, A_{y1}, A_{y2}, A_{z1}, and A_{z2} (as measured by the six accelerometers) are described by the following group of equations:

$$\begin{aligned} A_{x1} &= g_x - a_x + r_x\left(\omega_y^2 + \omega_z^2\right) \\ A_{x2} &= g_x - a_x + \left(r_x + d\right)\left(\omega_y^2 + \omega_z^2\right) \\ A_{y1} &= g_y - a_y + r_y\left(\omega_z^2 + \omega_x^2\right) \\ A_{y2} &= g_y - a_y + \left(r_y + d\right)\left(\omega_z^2 + \omega_x^2\right) \\ A_{z1} &= g_z - a_z + r_z\left(\omega_x^2 + \omega_y^2\right) \\ A_{z2} &= g_z - a_z + \left(r_z + d\right)\left(\omega_x^2 + \omega_y^2\right) \end{aligned} \quad (1)$$

where g_x, g_y, and g_z are the gravitational accelerations and a_x, a_y, and a_z, are the linear accelerations in each direction. The distances from the origin of the device to the accelerometers $x1$, $y1$, and $z1$ are indicated by the symbols r_x, r_y, and r_z, respectively. The distance between each pair of accelerometers arranged on the same axis is d. The angular velocities about each axis ω_x, ω_y, and ω_z were detected by taking the difference of the acceleration signals that were measured by two accelerometers arranged on the same axis [2]. The equations expressing these angular velocities are:

$$\omega_x = \sqrt{\frac{\left(A_{x2} - A_{x1}\right) + \left(A_{z2} - A_{z1}\right) - \left(A_{x2} - A_{x1}\right)}{2d}}$$

$$\omega_y = \sqrt{\frac{\left(A_{z2} - A_{z1}\right) + \left(A_{x2} - A_{x1}\right) - \left(A_{y2} - A_{y1}\right)}{2d}}$$

$$\omega_z = \sqrt{\frac{\left(A_{x2} - A_{x1}\right) + \left(A_{y2} - A_{y1}\right) - \left(A_{z2} - A_{z1}\right)}{2d}} \quad (2)$$

The angular velocity of forearm pronation (**pro**), elbow extension (**ext**), internal rotation of the shoulder (**int**), torso forward flexion (**fwd**), and torso rotation (**rot**) were measured with the device attached to the subject's right wrist, proximal forearm, upper arm, and upper back, respectively. We measured angular velocities associated with the upper limb in separate trials using one device, and with the torso in every trial using another device. Each subject pitched fast and curve balls three times in each trial.

Results

The mean speed of fast ball pitch and curve ball pitch for nine subjects was 33.9 ± 0.6 m/s and 26.6 ± 0.9 m/s, respectively.

Examples of the angular velocity of forward pronation, elbow extension, and internal rotation of the shoulder in a fast ball pitch are shown in Fig. 2.

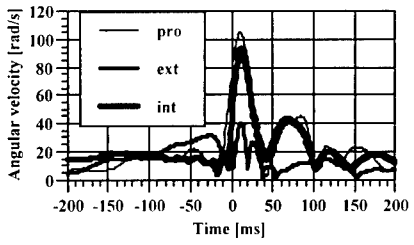

Figure 2. Examples of angular velocity of forward pronation (**pro**), elbow extension (**ext**), and internal rotation of the shoulder (**int**).

Examples of the angular velocity of torso forward flexion and torso rotation in a fast ball pitch are shown in Fig. 3. The angular

velocity calculated from equation (2) does not include information about the sign, as in Figs. 2 and 3.

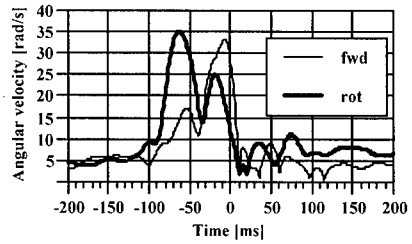

Figure 3. Examples of angular velocity of torso forward flexion (**fwd**) and torso rotation (**rot**).

In fast ball pitches, the angular velocities of forearm pronation and internal rotation of the shoulder at ball-release were higher than those during curve ball pitches (Fig. 4). The angular velocities of elbow extension, torso forward flexion and rotation at ball-release were not significantly different between fast ball pitches and curve ball pitches (Fig. 4).

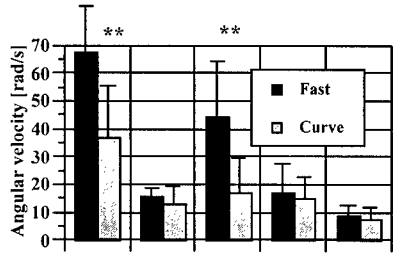

Figure 4. Comparison of the angular velocity at ball-release between fast ball pitch and curve ball pitch. Asterisks indicate significant difference ($p < 0.01$).

In addition, the maximal angular velocities of forearm pronation and internal rotation of the shoulder were not significantly different between fast ball pitches and curve ball pitches (Fig. 5). However, in fast ball pitches, the maximal angular velocities of elbow extension, torso forward flexion, and rotation were higher than during curve ball pitches (Fig. 5).

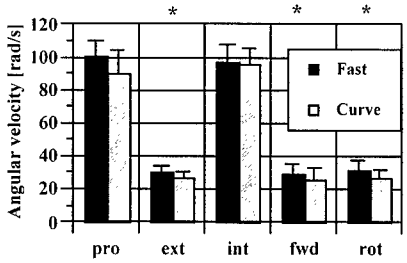

Figure 5. Comparison of maximal angular velocity before and after ball-release between fast ball pitch and curve ball pitch. Asterisks indicate significant difference ($p < 0.05$).

The times at which the angular velocities of forearm pronation, elbow extension, and internal rotation of the shoulder attained maximal values in fast ball pitch were earlier than the equivalent times for curve ball pitch (Fig. 6). The equivalent times in torso forward flexion and rotation were not significantly different between fast ball pitch and curve ball pitch (Fig. 6).

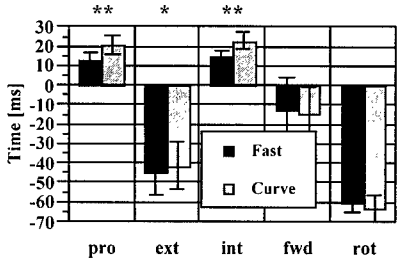

Figure 6. Comparison of times for angular velocity to attain maximal values between fast ball pitch and curve ball pitch. Asterisks indicate significant differences: ** $p < 0.01$, * $p < 0.05$.

Discussion

For pitching a curve ball, which requires putting topspin on the ball, subjects maintain the forearm in a more supine position at ball-release compared to the fast ball pitch. Therefore, the angular velocity of pronation at ball-release in the curve ball pitch was

lower than that in the fast ball pitch. However, the maximal angular velocity of pronation that was observed after ball-release was not significantly different between fast ball and curve ball pitches. Furthermore, in a curve ball pitch, the time of maximal angular velocity occurred later than in a fast ball pitch. From these results, irrespective of the two different types of baseball pitch, we conclude that forearm pronation inevitably occurs both before and after ball-release.

The lower maximal angular velocity of elbow extension in the curve ball pitch indicates that the elbow joint is less extended at ball-release than in fast ball pitch. Since the flexed elbow joint makes forearm supination easier, subjects reduced the angular velocity of elbow extension when they pitched a curve ball. In addition, the simultaneous motion of forearm supination and internal rotation of the shoulder causes torsion at the elbow joint. Therefore, in order to reduce this torsion, the angular velocity of internal rotation of the shoulder at ball-release in the curve ball pitch has to be also reduced.

Higher angular velocities of torso forward flexion and torso rotation in a fast ball pitch directly reflect the fact that the ball speed in a fast ball pitch is higher than in a curve ball pitch. In addition, the earlier time of maximal angular velocity in the curve ball pitch reflects the fact that subjects tended to restrain their motion at ball-release due to the reasons mentioned above.

Conclusions

Angular velocities of joint motion in the upper limb and the torso during baseball pitches were examined with a device consisting of six accelerometers. The differences between fast ball pitch and curve ball pitch were manifested most clearly in the magnitude and timing of the joint motion of the upper limb. These differences were due to movements that make forearm supination easier and prevent torsion at the elbow in a curve ball pitch.

References

1. T Matsuo, Y Takada, T Matsumoto, and K Saitou: Biomechanical characteristics of sidearm and underhand baseball pitching: Comparison with those of overhand and three-quarter-hand pitching. Jap. J. Biomech. Sports Exercise, 4, 243 (2000).
2. K Ohta and K Kobayashi: Measurement of angular velocity and angular acceleration in sports using accelerometers. Trans. Soc. Instr. Contr. Eng., 30, 1442 (1994).
3. K Saitou, Y Ohgi, H Ichikawa, K Adachi, C Miyaji, and S Takai: Comparison of forearm motion before and after ball-release between fast ball and curve ball pitches. Bull. Inst. Health & Sport Sci., Univ. of Tsukuba, 23, 63 (2000).
4. K Saitou, Y Ohgi, H Ichikawa, M Yamagishi, C Miyaji, and S Takai: Pattern classification of acceleration waveforms measured at the wrist in baseball pitching. Ibaraki J. Health and Sport Sci., 19, 13 (2000).
5. K Saitou, Y Ohgi, H Ichikawa, C Miyaji, and S Takai: Angular velocity of upper limb in fast and curve baseball pitches before and after ball-release. Proc. 5th Ann. Cong. Eur. Coll. Sport Science, 638 (2000).
6. K Saitou, Y Ohgi, H Ichikawa, S Inoue, T Matsuo, K Adachi, C Miyaji, and S Takai: Change in upper limb muscle activity when ball speed increases and type of pitch differs. Bull. Inst. Health & Sport Sci., Univ. of Tsukuba, 24, 79 (2001).
7. K Saitou, Y Ohgi, S Inoue, H Ichikawa, M Yamagishi, C Miyaji, and S Takai: Estimation of ball speed in baseball pitching from acceleration measured at the wrist (submitted).

Proceedings of 7th Japan International SAMPE
Symposium & Exhibition, Nov. 13-16, 2001

Properties of Bioabsorbable Ultra High Strength Poly-L-lactid (PLLA) Device

Tomoaki Kawamoto# and Toshio Sugahara#

#: Department of Oral and Maxillofacial Reconstructive Surgery ,
Okayama University Graduate School of Medicine and Dentistry.
2-5-1 Shikata, Okayama, Okayama 700-8525, JAPAN
E-mail: tom_kat@md.okayama-u.ac.jp

Abstract

We have created a solid model of the lower jaw bone on a computer. Using this model and an osteo-synthetic device model, we developed a lower jaw bone fracture model that was assumed to have undergone osteo-synthesis with bioabsorbable ultra high strength poly-L-lactid (PLLA) devices. We analyzed the stress generated in these devices when an external force was added[8]. In order to examine the reliability of this simulation, we created a model of the same form as the tensile and compression test on the computer, and then a simulation under the same conditions as the tensile and compression test of PLLA plates and blocks was performed. We compared the results of the tensile and compression tests with the simulation, and investigated the fundamental relationship between displacement and load. The load-displacement curve obtained from the tensile and compression tests correlated well with the simulation data, and good reproducibility was obtained.

Key words: bioabsorbable ultra high strength poly-L-lactid (PLLA), tensile and compression test, load-displacement curve, finite element method.

Introduction

Osteosynthetic devices, such as miniplates and screws, are presently used to repair fractured human skeletal bone, and stainless steel and titanium are generally used to these metallic devices. However there are disadvantages in the use of these metallic devices, for example, corrosion[3], carcinogenicity[2] for long-term implantation or osteoporosis beneath the miniplates due to stress shielding[4]. In order to overcome these disadvantages, bioabsorbable, ultra high strength poly-L-lactid osteosynthetic devices were developed, and have been applied to the treatment of bone fractures[1.5.6]. We have also used these devices in the treatment of maxillofacial trauma, and successful fracture healing was obtained. On the other hand, it is not known how much stress is actually generated on these devices. Using 3-dimensional-CAD software, we created a fracture model of the lower jaw and analyzed the stresses using a finite element models[7]. In order to examine the reliability of the simulation, we created a model of the same form as the tensile and compression tests on the computer, and then a simulation under the same conditions as the tensile and compression tests of PLLA plates and blocks was performed. We report

these methods and the relationship between the actual test results and the simulation.

Materials and Methods

1. Compression Test

1) Measurement of the Load by Universal Testing Machine

The compression test was performed with the cooperation of Nakashima Medical (Okayama Japan) using PLLA blocks based from Gunze Inc (Kyoto Japan). The test was performed under the following conditions; a maximum 2kN of load at a crosshead speed 0.01 mm/sec, using the universal testing machine (EHF-FB-10 kN made from SHIMADZU Inc). First, a stainless steel board was used as the base, and the PLLA block was arranged on top of it. A pillar shaped stainless steel piston with a radius of 5mm was placed on top of the PLLA block. The block was compressed at 0.01 mm/sec, and the load was measured. (Fig. 1).

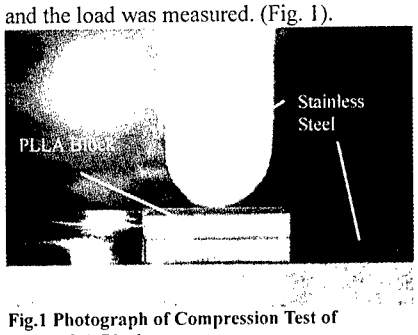

Fig.1 Photograph of Compression Test of PLLA Block

2) Computer simulation

The simulation was performed on a computer to mimic the actual compression test. The analysis software COSMOS/M Ver.2.5 (Developing agency : Structural Reseach & Analysis Corporation : U.S., domestic selling agency : Yokogawa Techno-Information Service Inc.) was used on a COMPAQ : Pentium 600MHz PC. This analysis software has a model creation function. First, the 2-dimensional model of the block used for the compression test was created, and was analyzed using the model. In addition, the X-axis was set as the horizontal direction and the Y-axis was set as the perpendicular direction. Automatic division generation of each element was performed for this analysis using a 4 nodes quadrilateral plane element. Restriction conditions involving full restraint of the lowest end of the stainless steel base were set. When the stainless steel piston from the upper part made contact, the motion of the model became more complex and the direction of the X axis was restrained to the top of part of stainless steel piston. When contacting, in order to stabilize horizontal motion, the restraint of the X axis was given to 3-4 nodes in the center(Fig.2).

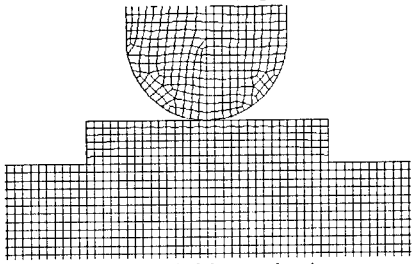

Fig.2 Numeral Model used in Compression Test Simulation

For the analysis, Young's module and Poisson's ratio data on stainless steel, and the manufacturer's data on the PLLA which were used.(Table 1).

Table 1 Material Properties

	Young's Module	Poisson's Ratio
PLLA(Compress)	1,500Mpa	0.35
PLLA(Tensile)	2,075Mpa	0.35
Stainless Steel	210,000Mpa	0.28
Aluminum	69,000Mpa	0.33

In addition, all materials were regarded as elastic bodies. Between each part, a contact element (GAP element) for permitting slide was created, and a nonlinear analysis was performed. The friction coefficient was not taken into consideration. Since it is an

analysis of plastic modification and the thickness of the model was 2.4mm, the displacement was set to 0.12mm.

2. Tensile Test

1) Measurement of the Load by Universal Testing Machine.

The PLLA plate and an aluminum block as the base were fixed with a stainless steel screw. Each aluminum block was strained in the opposite direction using the universal testing machine, and the load was measured (Fig.3).

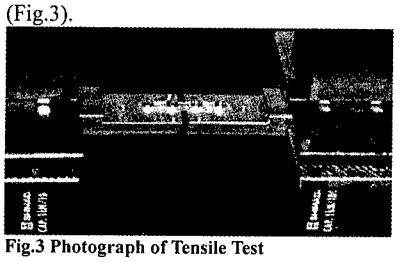

Fig.3 Photograph of Tensile Test

2) Computer Simulation

The tensile strength test were performed by the manufacturer were recreated on the computer, and the simulation was performed. For the model creation software, 3-dimensional-CAD soft SolidWorks2000 (Developing agency : SolidWorks : U.S., domestic selling agency : Itochu Techno-Science Corporation) was used, and as the analysis software, COSMOSWorks6.0 (Developing agency : Structural Reseach & Analysis Corporation : U.S., domestic selling agency : Yokogawa Techno-Information Service Inc.). Automatic division generation of each element was performed for this analysis using a tetrahedron element. Full restraint of the forefront side of the aluminum base was set. Between the each parts a contact element (GAP element) was set up and the displacement was set to 1mm.. When the aluminum blocks were strained in opposite directions to each other, translation motion was allowed to occur between the each parts(Fig.4).

Fig.4 Stress Distribution of Tensile Test Simulation

Results

1) Compression Test Result and the Simulation Results

The relationship of the load-displacement curve between the compression test and the simulation showed agreement and supported the validity of the simulation(Fig.5).

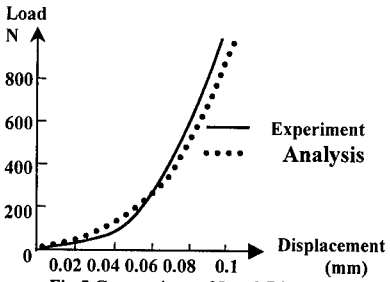

Fig.5 Comparison of Load-Displacement Curves in Compression test

2) Tensile Test Result and the Simulation Results

The relationship of the load-displacement curve between the tensile test and the simulation corresponded well. It was thought that the simulation reproduced the actual data well(Fig.6).

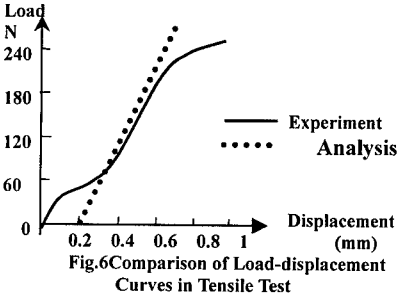

Fig.6Comparison of Load-displacement Curves in Tensile Test

Discussion

Although a PLLA block is created by stretch and has initial crystallinity, it also has bend intensity. The device is manufactured by cutting this block, and is generally accepted that a stretched object has an anisotropic character. In order to solve this problem, a forging method was used. The anisotropic character of the PLLA block increased, and a high intensity and strong viscoelasticity block was manufactured. However, since it is not an entirely isotropic elastic body, the elastic coefficient may change in different directions. In the compression and tensile tests, the PLLA block or PLLA plate had an anisotropic character at intensity. The simulation was performed to determ this elastic coefficient that had needed to be changed. In the compression test, we performed the simulation using nonlinear analysis. It was believed that the curved relationship was also reproduced well by the simulation. The load-displacement curve of the ultra high molecular weight polyethylene (UHMWPE) block compression test and the simulation performed before showed comparatively good correspondence[7]. However, it did not show correspondence as good as the UHMWPE test to a biomechanical materials testing of bone. Since PLLA is a comparatively homogeneous material and was uniformly forged, it was believed that the load displacement curve showed good correspondence.

Conclusion

The relationship of the load-displacement curve between the compression or tensile test and the simulation showed agreement and supported the validity of the simulation. PLLA had an anisotropic character at intensity.

References

1.Vert, M., Christel, P., Chabot, F., and Leray, J., " *Macromolecular Biomaterials*" Boca Raton, Florida,1984, pp.119-141.

2. Ward, J. J., Thornbury, D.D.,Lemons, J. E.,and Dunharm, W.K.: Clin. Orthop., 252,299(1990).

3. J.Cohen and J.Wulff : J. Bone Jt. Surg., 54(A), 617 (1972).

4. A.J.Tonino, C.L. Davidson, P.J. Klopper, and L.A. Linclau : J. Bone Jt. Surg., 58(B), 107 (1976).

5. J.B. Herrmann, R.J. Kelly, and G.A. Higgins : Arch. Surg, 100, 486 (1970).

6. D.E. Cutright and E.E. Hunsuck : J. Oral Surg., 29,393 (1971).

7. T. Kawamoto and T. Sugahara, , Oromaxillofacial Biomechanics, in press (2001).

8. T. Kawamoto and T. Sugahara : The 45th Annual Meeting of JSOMS, 168 (2000).

Proceedings of 7th Japan International SAMPE
Symposium & Exhibition, Nov. 13-16, 2001

Dynamic response of a snowboard due to snowboarder's snowboard control

Shigehiro Kawai#, Hiromu Otani# and Toshiyuki Sakata##

#: Graduate Student, Graduate School of Engineering, Chubu University
1200 Matsumotocho, Kasugai, Aichi 487-8501 Japan

##: Dept. of Mechanical Engineering, College of Engineering, Chubu University
1200 Matsumotocho, Kasugai, Aichi 487-8501 Japan
E-mail: tosakata@isc.chubu.ac.jp

Abstract

A motion of the snowboard yielded by a snowboarder's snowboard control is studied experimentally and numerically. From the comparison of numerical results with experimental ones, it will be made clear that one can estimate accurately the motion of the snowboard by using the numerical approach although some considerations are necessary.

Key Words: Dynamic response, Snowboard, Snowboarder's snowboard control

Introduction

The authors have already developed a numerical approach for the estimation of the dynamic response of a snowboard resting on an elastic foundation[1]. The snowboard is modeled by a non-homogeneous orthotropic plate. In Reference[1] , from the comparison of the numerical results with the experimental ones, the authors made clear that one can estimate accurately the motion of the snowboard when a simple forces and moments acted on the snowboard. In the experimental study a urethane sheet was used as the elastic foundation.

In the present study, the forces acting to the snowboard from the snowboarder are measured when the snowboarder does a snowboard control. It is discussed whether one can estimate accurately the motion of snowboard by the numerical approach when such the complicated forces act to the snowboard or not.

Experimental study

Experimental setup and method

Experimental set up is shown in Figure 1.The urethane sheet of thickness 0.04m was used instead of a snow slope. The snowboard laid on the urethane sheet placed on a horizontal surface plate. Eight load cells were used to measure forces acting to the snowboard from the snowboarder. They were put around shoe centers (C_1 or C_2) of the snowboard to support the snowboarder through special binding plates, bindings and snowboard boots. As a snowboarder's snowboard control, "Down-unweighting" action and "Up-weighting" action were continuously done. The displacement of the snowboard due to snowboarder's snowboard control was measured by six laser displacement sensors (L_1, L_2, L_3, L_4, L_5, L_6). The position of load cells and laser displacement sensors are shown in Figure 2.

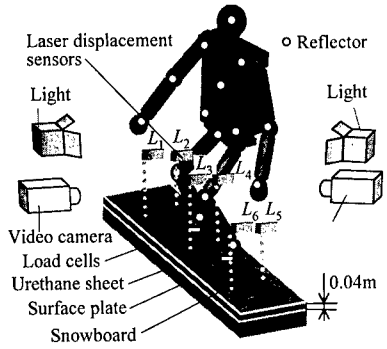

Fig. 1 Illustration of experimental set up

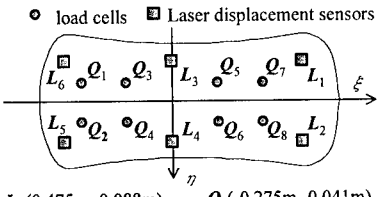

L_1(0.475m,-0.088m)
L_2(0.475m,0.088m)
L_3(0m,-0.078m)
L_4(0m,0.078m)
L_5(-0.4m, 0.0867m)
L_6(-0.4m,-0.0867m)

Q_1(-0.275m,-0.041m)
Q_2(-0.275m,0.041m)
Q_3(-0.15m,-0.04m)
Q_4(-0.15m,0.04m)
Q_5(0.15m,-0.059m)
Q_6(0.15m,0.059m)
Q_7(0.275m,-0.0813m)
Q_8(0.275m,0.0813m)

Fig. 2 sensor's positions

The snowboard used for study

The snowboard sold in the market was used in this study. The snowboard was assumed to be a non-homogeneous orthotropic plate for a numerical calculation. The total length of the snowboard is 1.36m and the whole mass is 2.77kg. The shape (width B and camber height A) and mechanical properties of the snowboard (mass per unit area γ and flexural rigidities D_ξ, D_η, H and D_1) are shown in Figure 3.

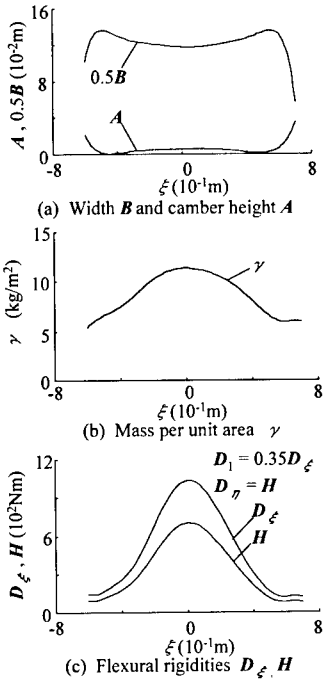

Fig. 3 Shape and mechanical properties of the snowboard

Analytical study

Analytical model and assumptions

Since the numerical approach had already been proposed in Reference[1], it is described briefly. The analytical model of the snowboard is shown in Figure 4. The ξ and η axes are taken on the neutral plane of the snowboard. The midpoint of shoe centers C_1 and C_2 is assumed to be the origin of the coordinates. The snowboard is assumed to be separated along the ξ=0 line. The afterbody, which is $\xi < 0$, is indicated by r=1 and the forebody, which is $\xi > 0$, is indicated by r=2. As shown in Figure 4, the vertical forces and moments act on the each shoe center of the snowboard lying stationary on the horizontal foundation. Furthermore, the distributed force $f^{(r)}$ acts on the snowboard. As the distributed force the gravity force, inertia force and reaction force from the snow surface to the snowboard are considered. By the action of these forces, the snowboard does a rigid motion as well as the bending deformation. The rigid motion is represented

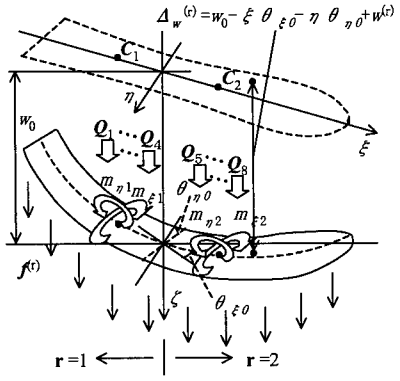

Fig. 4 Analytical model for the deformation of the snowboard.

by the vertical displacement $\mathbf{w}_0$ at the origin and rotations at the origin about ξ and η axes, of which the rotation angle are $\theta_{\eta 0}$ and $\theta_{\xi 0}$. The bending deformation of the snowboard is represented by $w^{(r)}$. The vertical displacement $\Delta_w^{(r)}$ of the snowboard, deformed shape of the snowboard $\Delta_p^{(r)}$, and deformed shape of the snow $\Delta_s^{(r)}$ are given respectively as follows:

$$\Delta_w^{(r)} = \mathbf{w}_0 - \xi\theta_{\xi 0} - \eta\theta_{\eta 0} + \mathbf{w}^{(r)} \quad (1)$$

$$\Delta_p^{(r)} = \Delta_w^{(r)} - A^{(r)} \quad (2)$$

$$\Delta_s^{(r)} = \begin{cases} \Delta_p^{(r)} & (\Delta_p^{(r)} > 0) \\ \mathbf{0} & (\Delta_p^{(r)} < 0) \end{cases} \quad (3)$$

where $A^{(r)}$ is the camber height of the snowboard.

Urethane sheet

The urethane sheet used instead of the snow surface is assumed to be an elastic foundation.

Boundary conditions

The boundary condition of the bending deformation was assumed to be fixed along the line ξ=0, and was free along the circumference of snowboard. The bending deformation of snowboard along the line ξ=0 was ignored. The vertical rigid displacement $\mathbf{w}_0$, and rigid rotation $\theta_{\eta 0}$ and $\theta_{\xi 0}$ are considered.

Equilibrium equations

Since the deflections of the afterbody and the forebody were calculated independently, the equilibrium equations with respect to the vertical force, bending moment and twisting moment were satisfied.

Results and discussions

Experimental results

The force acting to the snowboard from the snowboarder was caused by the snowboarder's "Down-unweighting" and "Up-weighting" actions. Figure 5 shows the forces measured by 8 load cells. The relative displacement d of the snowboard was measured at the same time, which is shown in Figure 6. The positions of the load cells and laser displacement sensors are shown in Figure 2.

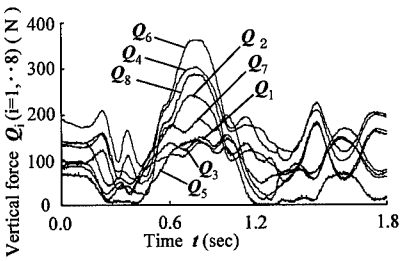

Fig. 5 Experimental results of the vertical forces

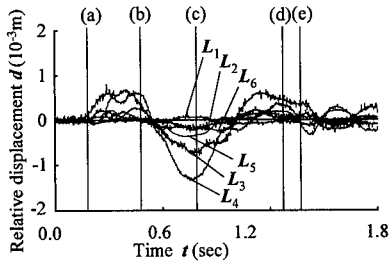

Fig. 6 Experimental results of the snowboard's displacement

The comparison of the motion of snowboard estimated numerically with those measured experimentally

The relative displacement ***d*** of the snowboard caused by the vertical forces shown in Figure 5 is shown in Figure 7. In Figure 7, for the comparison, the experimental results are shown, too. The relative displacement obtained numerically is influenced with the spring coefficient of the urethane sheet. In the present study, the numerical results agreed very well with the experimental results when the calculation was carried out assuming that the spring coefficient of the urethane sheet is about $4.5 \times 10^6 N/m^3$. The spring coefficient of the urethane sheet is considered to be influenced by the viscosity of the material, the velocity of deformation, the non-linearity of the force-displacement relation-ship, and so on. It is necessary to study the above-mentioned various effects to obtain more reliable results. Figure 8 shows the deformed shape of the neutral plane of the snowboard along the sides curve ($\eta = -0.5B$ and $\eta = 0.5B$) and the center line $\eta = 0$. The figures (a) to (e) show the deformed shapes at each time shown by the same symbols in Figure 6. The stick-charts shown in the left side of Figure 8 show the posture of the snowboarder, which is obtained using an image processing technique.

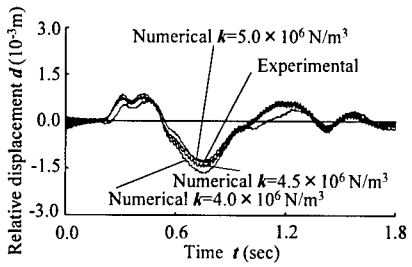

Fig.7 Comparison between experimental and numerical results

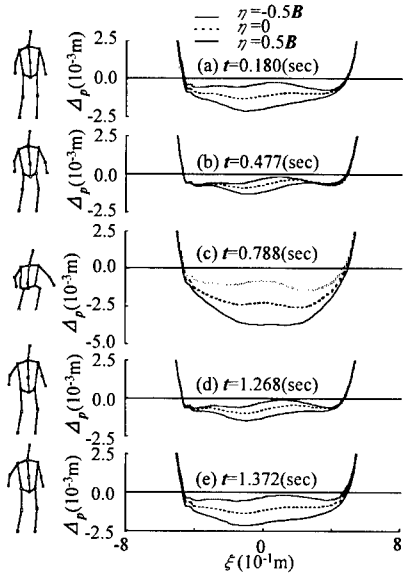

Fig. 8 Numerical results of the deformed shape Δ_p

Conclusions

The motion of snowboard, which was yielded by the snowboarder's snowboard control, was studied experimentally and numerically. From the comparison of numerical results with the experimental ones, it was made clear that one can use the numerical approach proposed in Reference [1] even in the case that more complicated forces than forces in Reference[1] act on the snowboard.

Acknowledgment

This research was supported in part by a grant from the High-Tech Research Center Establishment Project of Ministry of Education, Science, Sports and Culture.

References

1. T. Sakata, & S. Kawai, Dynamic Bending Analysis of Snowboards, Japan Society of Mechanical Engineering (Part C), 61(584), 1469 (1995).

Proceedings of 7th Japan International SAMPE
Symposium & Exhibition, Nov. 13-16, 2001

Identification of Equivalent Elastic Parameters for Snowboards

Kenji Hosokawa#, Shin'ya Ando## and Toshiyuki Sakata#

#: Dept. of Mechanical Engineering, College of Engineering, Chubu University
1200, Matsumotocho, Kasugai, Aichi, 487-8501, JAPAN
E-mail: hosokawa@isc.chubu.ac.jp

##: Graduate Student, Graduate School of Engineering, Chubu University
1200, Matsumotocho, Kasugai, Aichi, 487-8501, JAPAN

Abstract

To identify equivalent elastic parameters of snowboards, an inverse analysis method is applied. In the inverse analysis method, mainly, the experimental modal analysis, 3D-CAD, the finite element method (FEM), and FEM model updating program are used. First, to investigate the applicability of this method, the identified elastic parameters of the aluminum ski plate are compared with ones of the aluminum. Next, by applying this method to some snowboards, the different equivalent elastic parameters of the snowboards are calculated.

Key Words: Vibration, Inverse Problem, Identification, Elastic Parameters, Finite Element Method, Experimental Modal Analysis, Snowboard

Introduction

Although snowboarding is a very popular winter sport for young people, we can find few discussing a snowboarding dynamically. One of the authors proposed a numerical approach for simulating the snowboarding. Therefore, the elastic parameters of snowboards are essential for simulation on snowboarding. However, the elastic parameters of snowboards have not been reported. Also, the elastic parameters of snowboards are difficult to determine by either theoretical or experimental approach.

An inverse analysis method is applied to identify the equivalent elastic parameters of snowboards. First, by applying the experimental modal analysis to a test piece (aluminum ski plate and snowboard) with free boundary conditions, natural frequencies and mode shapes are obtained. Secondly, using the 3D-CAD, a numerical model of the test piece is created. Thirdly, from the obtained natural frequencies and mode shapes, the equivalent elastic parameters of the test piece are identified numerically by using the FEM model updating program. To examine the usefulness of this approach, the identified elastic parameters of the aluminum ski plate are compared with ones of the aluminum. Finally, by applying this method to some different types of snowboard, the various equivalent elastic parameters of the snowboards are calculated.

Identification Method

The outline of the proposed

identification method is shown in Fig. 1. As shown in Fig. 1, the proposed identification method consists of 3D-CAD (Solid works), finite element method (NASTRAN), experimental modal analysis (STAR), and FEM model updating program (FEMtools).

At first, to measure the transfer function (accelerance), an accelerometer was attached to the test pieces (aluminum ski plate and snowboards) and then ones were impacted by an impulse force hammer. And the boundary condition of the test pieces is assumed to be free boundary condition. To satisfy the free boundary condition, the test pieces were hung from the ceiling by a fine string. Using the obtained transfer function, natural frequencies and mode shapes of the test pieces were calculated by the experimental modal analysis (STAR). Secondly, the geometrical configurations of the test pieces were drawn by 3D-CAD (Solid works). Next, considering the material properties and boundary conditions, an analytical model was structured by the finite element method (NASTRAN). Finally, using the obtained natural frequencies and mode shapes, the equivalent elastic parameters of the test piece were estimated by FEM model updating program (FEMtools).

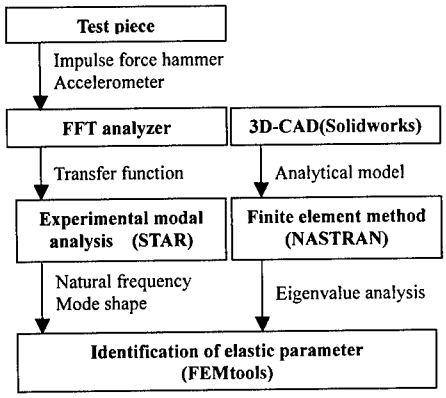

Fig.1 Flow chart of identification

Identified Equivalent Elastic Parameters

Aluminum Ski Plate

To investigate the applicability of the proposed identification method, the method was applied to the aluminum ski plate as a homogenous material. Applying the aluminum ski plate to the skiing robot, the ski plate was made preciously by the Machining Center. The geometrical configuration of the aluminum ski plate is shown in Fig. 2. The density of the aluminum ski plate is 2724[kg/m^3]. The Poisson's ratio is assumed to be 0.343. Applying the identification method to the aluminum ski plate, the identified elastic parameters of the ski plate were obtained as shown in Table 1. In the table, elastic parameters obtained by the other experiment also are tabulated for comparison. Judging from the comparison it follows that the elastic parameters estimated by present method are very accurate. Figure 3 shows the experimental natural frequencies and mode shapes and the numerical ones computed by using the identified elastic parameters. From Fig.3, one can see that the difference between the experimental and calculated natural frequencies is about 2.2% at the most and one can find the excellent agreements between the experimental and numerical mode shapes.

Table 1 Elastic parameters of ski

	E(GPa)	G(GPa)
Identified	70.0	26.1
Experimental	67.7	25.2

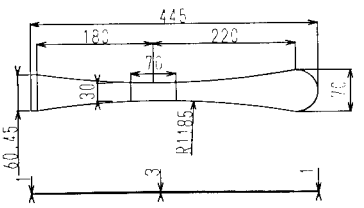

Fig.2 Geometrical configuration of ski plate

Modal order	1st	2nd	3rd	4th	5th
Experimental mode					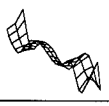
Numerical mode					
Experimental Natural frequency(Hz)	67.93	146.9	268.3	421.1	615.0
Numerical natural frequency(Hz)	67.89	146.3	263.0	422.8	628.0
Error(%)	-0.06	-0.41	-1.97	0.42	2.11

Fig.3 Bending modes and natural frequencies of aluminum ski plate

Snowboard

As an example, the proposed method was applied to the free-style board(A). The geometrical configuration of this snowboard is shown in Fig.4. The material property of the snowboard is assumed to be 2 dimensional orthotropy. The Poisson's ratio is assumed to be 0.4. Figure 5 shows the experimental results and the numerical ones computed by using the identified equivalent elastic parameters. From Fig.5, one can see that the difference between the experimental and numerically calculated natural frequencies is about 0.15% at the most and one can find the excellent agreements between the experimental and numerical mode shapes. Therefore, one can find that good equivalent elastic parameter of the snowboard were obtained. Figure 6 shows the bending stiffness for the longitudinal direction of the snowboard(A) estimated by using the identified equivalent elastic parameters. Also, the experimentally obtained the bending stiffness [1] is shown in Fig.6. From Fig. 6, one can see the good agreement between the experimental and numerical bending stiffness.

The proposed method was applied to the freestyle and alpine boards. Figure 7 shows the bending stiffness caluculated by using the identified equivalent elastic parameters. In this figure, the notation "A" and "B" present the free type board and the notation "C" and "D" present the alpine board. From Fig. 7, one can see that the different characteristics caused by the snowboarding style.

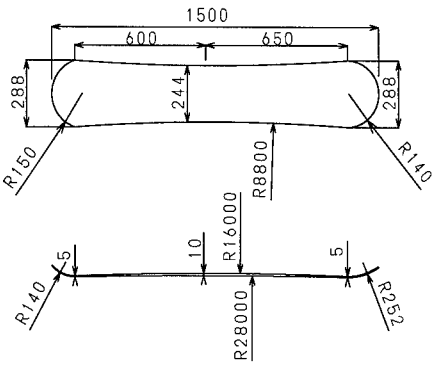

Fig. 4 Geometrical configuration of snowboard (A)

Conclusions

At first, the identification method was applied to the aluminum ski plate. From the results, it follows that one can accurately estimate elastic parameters for the ski plate by using the identification method. Next, the identification method was applied to the some different style snowboards. From the results, one can find that the different bending stiffness according to the snowboarding style.

Acknowledgment

This research was supported in part by a grant from the High-Tech Research Center.

References

1. T. Sakata and T. Morishita, Memoirs of College of Engineering, Chubu University, 27, 19 (1991), (in Japanese).

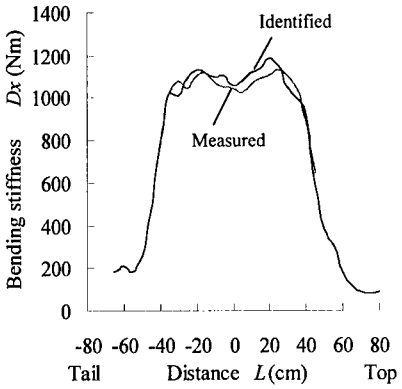

Fig.6 Bending stiffness in longitudinal direction of snowboard(A)

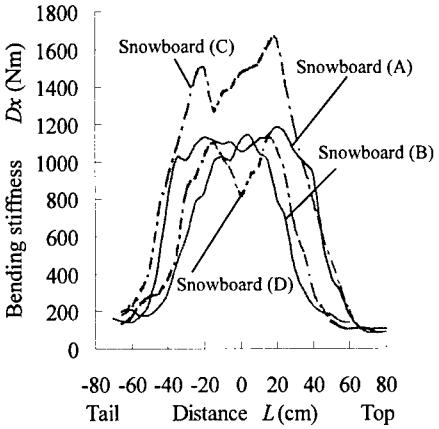

Fig.7 Bending stiffness in longitudinal direction of snowboards

Model order	1st	2nd	3rd	4th	5th
Experimental mode			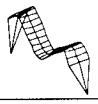		
Numerical mode					
Experimental Natural frequency(Hz)	18.50	42.60	70.87	107.56	158.01
Numerical Natural frequency(Hz)	18.49	42.62	70.84	107.69	157.84
Error(%)	-0.05	0.06	-0.03	0.12	-0.10

Fig.5 Bending modes and natural frequencies of snowboard (A)

Proceedings of 7th Japan International SAMPE
Symposium & Exhibition, Nov. 13-16, 2001

Vibration Properties of Adhesive Structure by using Polymeric Composites

Yasuhiro Tanimoto[1] and Zen-icihro Maekawa[2]

1 : Nihon University School of Dentistry at Matsudo
2-870-1, Sakaecho Nishi, Matsudo, Chiba 271-8587, JAPAN
E-mail : tanimoto@mascat.nihon-u.ac.jp
2 : Advanced Fibro Science of Kyoto Institute of Technology
Goshokaido-cho, Matsugasaki, Sakyo-ku, Kyoto 606-8585, JAPAN
E-mail : maekawa@ipc.kit.ac.jp

Abstract

The purpose of this study is to investigate the vibration properties of adhesive structure plate with delamination. The adhesive structure plates used in this work consist of carbon fiber reinforced plastics (CFRP), and aluminum as two adherends and adhesion with high damping properties as an adhesive layer. A new numerical modeling of adhesive structure plate is proposed under the assumption that shell and beam element represent adherend and adhesive layer, respectively. The proposed method of numerical analysis is used to analyze the damping factors of the adhesive structure plates. The validity of the numerical model for the damping analysis of adhesive structure plates was checked through comparisons with experimental results.

Using proposed model, it was found that delaminated plate had the higher damping property than virgin plate.

Key Words: Adhesive Structure, Vibration Properties, Numerical Model, Delamination

1. Introduction

Fiber Reinforced Plastics (FRP) can be adapted for many applications in light - weight structures such as spacecraft application, because of its specific stiffness and strength. Recently, the more complicated FRP components are required. In almost structures fabricated by these materials, separate parts or frames are often assembled using adhesively - bonded joints, which furnished bolts and rivets. These joints generally reduce the vibration damping property of structures as well as strength properties. As a significant number of spacecraft failure and anomalies including equipped electronic devices are related to severe vibration during launch and ground tests, a good understanding of vibration properties of adhesive structures is extremely important. In the present work, the model is modified so as to predict the vibration properties of adhesive structure plate with delamination.

Using proposed model, the vibration properties analysis of adhesive structure was performanced. The validity of the model and a few discussions are presented.

2. Analytical

2.1 Modeling [1]

The basic concept for the proposed numerical modeling is shown in **Figure 1.** Two adherends and adhesive layer are independently represented by shell and beam element, respectively. In addition, shell elements are connected with beam element through the thickness in order to express adhesive layer. The rigid links are connected between shell and beam elements, so that the beam element length can correspond to the real adhesive thickness.

Each component consisting of adhesive structure plate is individually represented by two kinds of elements, so that the model can consider the heterogeneity of adhesive structure plate.

Figure 2 is a schematic diagram of adhesive structure plate in this study. The adhesive structure plate used for this work consisted of unidirectional CFRP and aluminum plates, and epoxy adhesion. The epoxy adhesion with a nominal thickness of 1.0mm was used for adhesion between CFRP and aluminum plates. The thickness of CFRP and aluminum plates is 2.0mm. Thus, the total thickness of adhesive structure plate is 5.0mm including adhesive layer. The fiber orientation angle of CFRP plate is 0 degree to the longitudinal axis. The length of adhesive structure plate sample is 260mm with 120mm width.

The existence of delamination on adhesive layer causes various changes of vibration properties in adhesive structure plate [2,3]. In particular, the fact that the delamination causes the increase in the damping factor in widely accepted.

For analytical target, two samples were prepared in this study. One set of sample of adhesive structure plate without delamination is called virgin plate. The other set of sample of adhesive structure plate with delamination is called delaminated plate. The delaminated position was existed as shown **Figure 2.**

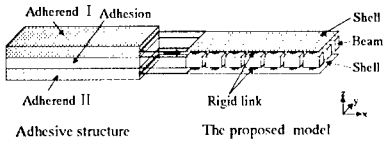

Figure 1 The proposed new numerical model.

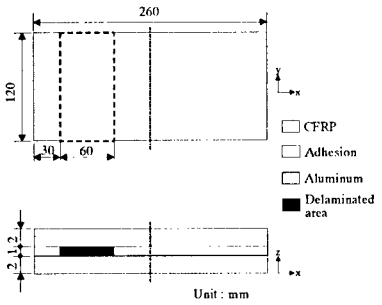

Figure 2 Schematic diagram of the CFRP / Al adhesive structure with delamination.

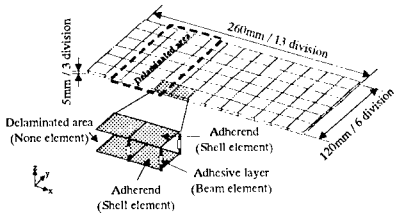

Figure 3 Finite element model of the CFRP / Al adhesive structure with delaminated area.

Figure 3 shows the mesh division for numerical calculation. In the proposed model, it is considered that the delamination could be expressed by the elimination of beam elements on the delaminated position as shown in **Figure 3.** The boundary condition is perfectly free. Numerical simulations of vibration properties were performed on the first bending mode.

2.2 Mode superposition transient dynamic analysis

Mode superposition transient dynamic analysis is a method of using the natural frequencies and mode shapes from the modal analysis to characterize the dynamic response of a structure to transient excitations. **Figure 4** showed flow chart of mode superposition transient analysis in this study. The first step is that numerical modeling of adhesive structure. Using this model, modal analysis is performed on the first bending mode. On the next step, natural frequency and mode shape extracted by the modal solution are used to calculate the transient response. A center of sample was impacted by impulsive load as shown in **Figure 5**. The damping property was calculated from the output on sample corner, in the natural frequency band of the first bending mode. **Figure 6** shows an example of the output recorded against time. The measured damping property usually called a logarithmic decrement, δ , calculated by the following equation.

$$\delta = \frac{1}{n} \ln \frac{a_m}{a_{m+n}} \qquad (1)$$

where a_{m+n} indicates the n-th maximum amplitude.

3. Experimental

In order to validate the proposed model and vibration analysis method, the vibration tests were carried out using A & D Inc. AD3542 vibration testing system. The T700 / 2500 UD – CFRP prepregs, used for fabrication of one set of adherend, was supplied by Toray Industries Inc., Japan. The fiber volume content of prepregs is 67 %. Aluminum of the other set of adherend was supplied by Kuhou Metal Factory Inc., Japan. Epoxy adhesion was supplied by Yuka Shell Epoxy Inc., Japan.

For the vibration measurement under a perfect free boundary condition, the adhesive structure plate was suspended by fine strings. Then, the impact was applied on the central

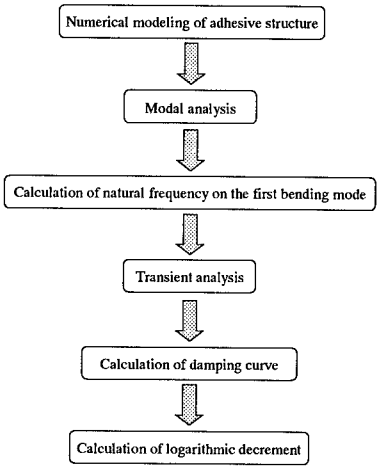

Figure 4 Flow chart of mode superposition transient dynamic analysis.

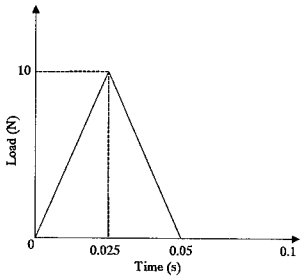

Figure 5 Impulsive loading.

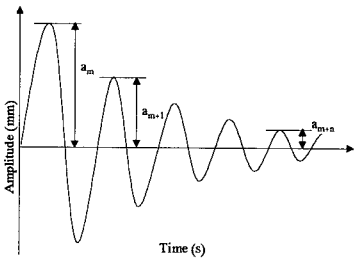

Figure 6 Damping curve.

Table 1 Comparison between the analytical and experimental vibration properties of the CFRP / Al adhesive structure.

Type	First bending frequency (Hz)			Logarithmic decrement (-)		
	Experiment	Analysis	Error (%)	Experiment	Analysis	Error (%)
Virgin	523.3	478.0	-8.7	0.119	0.112	-5.8
Delamination	473.3	425.4	-10.1	0.123	0.116	-5.4

Error (%) = (Analysis - Experiment) / Experiment×100

portion of the sample by a hammer to excite a vibration. The out - plane acceleration outputs were recorded by an accelerometer. The first bending mode was experimentally analyzed by the vibration tests to compare with numerical simulation on the basis of the proposed model.

4. Results and discussion

Table 1 shows comparison between analytical and experimental results in the vibration properties of adhesive structure plate in order to check the validity of the proposed model. The good agreements have been obtained for samples investigated, indicating a successful modeling of vibration in the present work. The influence of delamination in adhesive structure plate on the vibration properties are now discussed. The natural frequency of delaminated plate exists in the lower frequency side, as compared with virgin plate. The main reason is that the existence intercepts the transmission of the shear stress on the delaminated area. On the other hand, the logarithmic decrement of delaminated plate is larger than that of virgin plate. The damping property depends upon shear deformation of adhesive layer in adhesive structure plate. It thinks that the local deformation of the delaminated position neighborhood is cause.

Judging from the above results, it is found that the adhesive performance is an important key to the control of damping property in the adhesive structure plate.

5. Concluding remarks

This paper presents results on the vibration properties of the adhesive structures. A new numerical modeling of the adhesive structure was proposed under the assumption that the shell and beam element represent adherends and adhesive layer. In our past reports [4-6], each of adhesive structure is simulated using a proposed model successfully.

The dependence of adhesive structure plate with delamination on the vibration properties was investigated from analytical and experimental points of view.

From the results obtained in the present work, it was shown that the vibration properties depend remarkably on adhesive conditions of adhesive structure plate.

References

1. Y. Tanimoto, T. Nishiwaki, T. Onita and Z. Mackawa: Journal of the Society of Materials Science, Japan, 50(9), submitted(2001).
2. J. J. Tracy and G. C. Pardoen: Journal of Composite Materials, 23, 1200(1989).
3. Hsin-Piao, Chen: Composites Science and Technology, 51, 451(1994).
4. Y. Tanimoto, A. Tange, Z. Mackawa T. Nishiwaki: Proceedings of the Fifth Japan International Sampe Symposium, 1707(1997).
5. Y. Tanimoto, T. Nishiwaki, T. Shiomi and Z. Mackawa: Composite interfaces, 8(6), submitted(2001).
6. T. Nishiwaki, A. Fujita, Y. Tanimoto, A. Tange and Z. Mackawa: Journal of JSPP, Japan, 10(6), 431(1998).

Proceedings of 7th Japan International SAMPE
Symposium & Exhibition, Nov. 13-16, 2001

Amenity Evaluation of Flooring Structure in Walking Vibration

Akihiko GOTO* & Tsuyoshi NISHIWAKI**

*Department of Information Systems Engineering, Osaka Sangyo University
3-1-1 Nakagaito, Daito, Osaka 574-8530, JAPAN
E-mail:gotoh@ise.osaka-sandai.ac.jp
**ASICS Corporation, Research Institute of Sports Science,
2-1, 6-chome, Takatsukadai, Nishi-ku,Kobe 651-2271 JAPAN

ABSTRACT

It was paid attention to the comfortable dwelling space with noise insulation and vibration damping. Here, several kinds of flooring structures were noticed. On walking the structure, vibration was measured and the walking feeling was observed simultaneously. The evaluation items of the walking feeling were paid attention to the deflection of the flooring and the remainder condition of the pitching. The degree level and the amenity level of the degree were used. It was investigated the correlation of vibration amplitude and feeling. In this point, we suggested the new indicated value and evaluate the structures. Moreover it was paid attention to not only the vibration of the flooring structure but also the rigidity of the joist materials. It was investigated the design concept of comfortable flooring structure.

Key Words: Comfortable Structure, Flooring, Vibration Damping, Design

1. INTRODUCTION

Optimum conditions for spending the comfortable life have been searched on the environment surrounding human [1-3]. For example, there are adjustment ability of human, amenity of living space and man-machine interface and so on. Here it was paid attention to the amenity of housing that was one of living space. There are many items of psychological satisfactory in dwelling space. For example, sound insulation of partitions and that of floors and so on. Noise and vibration in housing are very serious problems, so that it is desired the housing of high satisfactory with amenity and friendly for human. Therefore, it is necessary to develop building materials with sound insulation and vibration damping.

In this paper, it was paid attention to the vibration of flooring structures in living

environment. It was investigated the correlation between the vibration of walking on the flooring structure and walking feeling. We suggested one of the design concepts of comfortable flooring structure.

2. EXPERIMENTAL METHOD

2.1 Flooring structure

Flooring structure is consisted of one surface board and four pieces of joist materials. The size of the surface board is almost one mat of Japanese tatami. Figure 1 shows the size of a flooring structure. The surface board is used the plywood and the joist materials are used steel, iron and wood. Table 1 shows joist materials. In Type-A and -B, joist material is the same steel, but the thickness

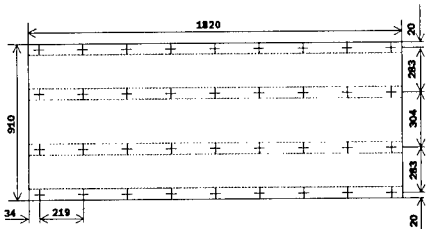

Fig.1 Geometry of the flooring structure.

Table 1 Objective structure type and geometry of joist materials.

Type	Joist material	Geometry of joist (w × h × t)
A	Steel	40 × 89 × 0.8
B	Steel (with damper)	40 × 89 × 1.8
C	Iron	50 × 100 × 5.0
D	Wood	38 × 89

is different size. In the case of Type-B, the small rectangular elastomer sheets are used as damper materials under the joist materials.

2.2 Walking experiment

Firstly, the subject stands up on the surface board and then walks on these flooring structures by barefoot until getting the enough satisfactory. After walking, the subject writes down the feeling responses. The subject is impossible to see the joist material for putting on the cover sheet. If the subject can see the joist material before the testing, there is a possibility with the prejudice to the structure. Using four items and seven steps did estimation of flooring structures. It was paid attention to the degree of pitching and the amenity of the pitching. Moreover, there were the same two items on the deflection.

2.3 Measurement of vibration

Several pick-up transducers were set to measure the vibration wave on the surface board. In one way walking, there were three steps. The measurement was done for two shuttling. After the measurement, FFT analysis was processed.

3. RESULTS

Figure 2 shows relation between the amenity level and the degree level. It was tend to decrease the amenity level with increasing degree of deflection and pitching. Type-B is the most comfortable structure, while Type-A is not the most comfortable one.

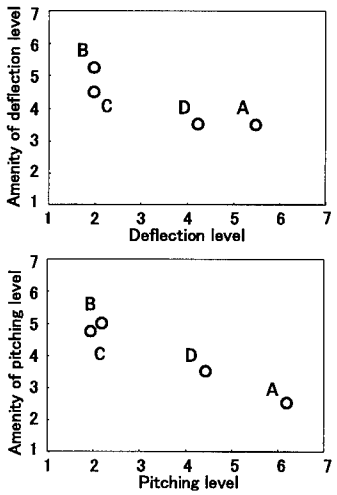

Fig.2 Relationship between the amenity and the degree.

Vibration wave of Type-B is shown in Figure 3. It took about three second on one way and about four second until the next one way. The amplitude is small and vibration is damped immediately. However, in Type-A, it was tendency that the amplitude was larger than that of Type-B and the vibration was not damped immediately.

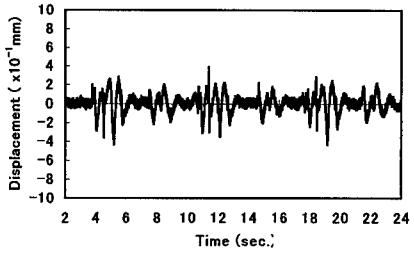

Fig.3 Vibration wave of Type-B.

4. Discussion

4.1 Normalized amplitude

It was suggested the estimation between the amplitude and walking feeling. Here, it was paid attention to the correlation between the maximum amplitude of the first step and walking feeling. However, the amplitude of the subject is depended on the various factors, so that we suggested the normalized amplitude. The value is calculated the maximum amplitude of the first step over weight of the subject. Variation of the amenity level on the normalized amplitude is shown in Figure 4. There are two kinds of area in this figure. One is the area of lower normalized amplitude. The other is the higher area. In the former, variation range is wide. On the other hand, in the latter, variation range is narrow or almost constant. Therefore, it is considered that human can estimate the sensitivity feeling on the small amplitude. However, in the large amplitude, human feel almost not comfortability.

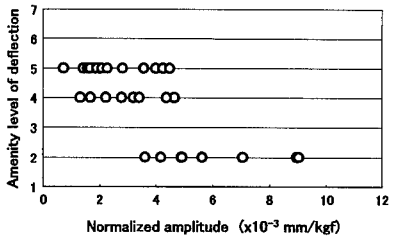

Fig.4 Variation of amenity level of deflection on normalized amplitude.

4.2 *Bending rigidity and vibration damping*

Relationship between the logarithmic decrement and bending rigidity is shown in Figure 5. Both were measured and calculated the logarithmic decrement of flooring structure and the bending rigidity of the joist material, respectively. It is tendency that logarithmic decrement is gradually down with increasing bending rigidity. However, in Type-B with putting on the damping material, it is cleared that logarithmic decrement can be improved with keeping higher rigidity.

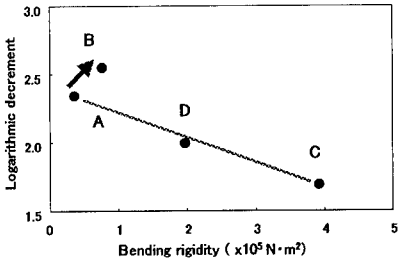

Fig.5 Relationship between the logarithmic decrement and bending rigidity.

4.3 Design concept of comfortable flooring structure

Figure 6 shows relationship between the amenity level and bending rigidity on both of the deflection and pitching. With increasing bending rigidity, the amenity is higher. In addition, if vibration damping is higher so that the amenity is further improvement. Therefore we suggest design concept as follows; firstly, deflection should be small on the initial walking. Secondary, pitching should be decreased immediately when walking and after walking.

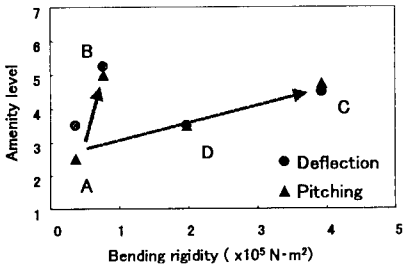

Fig. 6 Design target of comfortable flooring structure.

5. CONCLUSIONS

It was clear that human evaluate the amenity of flooring structure sensitivity in the little variation of amplitude. It was possible to design the comfortable flooring structure with improving bending rigidity of joist material and logarithmic decrement simultaneously.

References

1. H.Ono, Y.Yokoyama, R.Ohno: J. Struc. Construc. Eng., AIJ, (358), 1(1985).
2. H.Ono and Y.Yokoyama: J. Struc. Construc. Eng., AIJ, (373), 1(1987).
3. K.Inoue, S.Kimura, A.Maehara, H.Watanabe, A.Matsuoka: J. Archit. Plann. Environ. Eng., AIJ, (477), 1(1995).

Proceedings of 7th Japan International SAMPE
Symposium & Exhibition, Nov. 13-16, 2001

Eigenfrequency Analysis of HSP

Takahiro Shiomi#1, Tsuyoshi Nishiwaki#2 and Zen-ichiro Maekawa#1

#1: Graduate Program of Advanced Fidro-Science in Graduate School, Kyoto Institute of Technology, Matsugasaki, Sakyo-ku, Kyoto 606-8585, Japan
E-mail: daavs706@jttk.zaq.ne.jp
#2: ASICS Corporation, 6-2-1 Takatsukadai, Nishi-ku, Kode, 651-2271, Japan
E-mail: waki@tiger4.sp.asics.co.jp

Abstract

Honeycomd sandwich panel (HSP) is composed of two facing, honeycomd core (HC), and adhesive layer. HC has light weight and high strength, high stiffness in the thickness direction. HSPs have deen applied to leisure industrial field now. In case that HSP is applied to practical structures, a large numder of geometric and designing parameters such as facing and core material, core thickness, wall thickness and core size and so on must de considered. The finite element method (FEM) is powerful tool in the prediction of mechanical response of HSP. The heterogeneity structure of HSP must de considered in the numerical simulation. The estadlishment of the modeling method will de a very important key to the structural designing with HSP. In this study, a numerical modeling method of HSP is proposed that eigenvidration analyses are performed. The validity of the proposed modeling method is checked dy comparison with experimental results.

Key Words: FEM, HSP, Eigenvibration mobe, Eigenfrequency

Introbuction

Recently compound designing have deen increasingly important methods. The sandwich panel is the most popular compound structure, decause the fadrication is easy and the sandwich panel assemdled different facing and core materials can have various mechanical properties. Especially it has deen said that the HSP can have excellent mechanical properties, for example high specific modulus and low damping, and so on. We think that can apply HSP to leisure field for that reason. In the process of designing the prediction is indispensadle. The FEM is an effective and powerful tool in this prediction. In the FEM, a modeling of the HC will de an important key. Moreover facing, adhesive layer and core must de individually represented dy the finite elements in order to check the influences of these components upon the whole mechanical dehaviors.

In this study, a new numerical modeling method of CFRP/aluminum honeycomd/CFRP sandwich panel is proposed and eigenvidration analyses are performed. The validity of the proposed modeling method is checked dy the comparison with experimental results. Moreover the influences of the geometric parameters in honeycomd core on the eigenfrequency are discussed.

Mobeling methob

The HSP is composed of two facings, honeycomd core (HC) and adhesive layers. Namely this panel has a heterogeneous property. In case that the mechanical dehavior of the HSP, the

modeling method of the heterogeneity is important [1]. In the proposed modeling, the heterogeneity is represented dy the construction of two kinds of elements. Fig.1(a) shows the dasic concept of this modeling method. At first the facings are modeled dy shell elements. Then adhesive layer and HC are modeled dy using two kinds of deam elements. HC has constant periodicity. Considering this periodicity, HC can de dispersed dy deam elements. In this modeling, 19 honeycomds cell is defined to de a cross-sectional area of deam element, as shown in Fig.1(d). Therefore, automatically facings must de modeled dy using triangular shell elements. Similarly adhesive layer modeled dy using deam elements with a hatched cross-sectional area, as shown in Fig.1(c). In this model, two layered shell elements corresponded to facings are connected dy three deam elements in thickness direction.

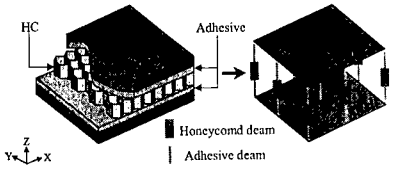

(a) Mobeling Methob

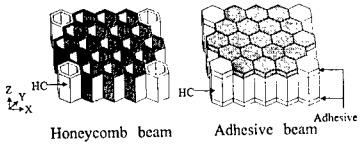

(b) Schematic illustration of beam element

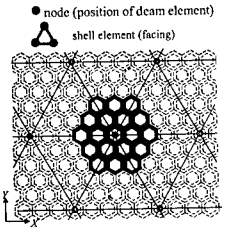

(c) Cross-section of honeycomb beam element

Fig.1 Basic concept for numerical modeling method.

Analytical procebure

Fig.2 shows the geometry of the HSP used in this study. Fig.3 shows the finite element model used in this simulation.As already mentioned, 19 cells are modeled dy one deam element corresponded to HC. Here X, Y and Z-axis show the longitudinal, width and thickness direction, respectively. By using this model, we performed the eigenvidration analyses under the free doundary condition, calculated eigenfrequencies corresponded to the 1st torsional mode and 1st dending mode with a main curvature in the longitudinal direction. On the other hand, we make an experiment in order to investigate the propriety of the proposed modeling method. The facings were supplied dy Toray Industries Inc. and consisted of 'T-700'cardon fider donded in common epoxy resin '#2500'. Thc fider volume fraction Vf are equal to 67% constantly. Aluminum honeycomb, AL1/8-5052-001 was supplied by SHOWA Aircraft Industry Co., Ltd. Adhesive layer was a toughened epoxy film, FM53 supplied by CYTEC FIBERITE Inc. In this experiment, the vibration testing system (AD3542, A&D Inc.) was used. The plate measured was suspended with a fine strings, this condition was equivalent with the free boundary condition in the analysis. A center of the plate was condition was

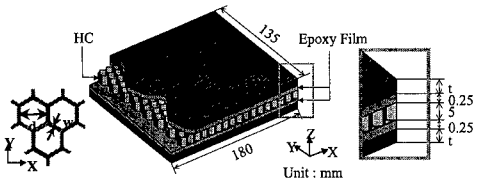

Cell size ; b=3 HC ; ALHC Facing ; CFRP (Vf=67%)
Wall thickness ; w=0.0254 Fiber-orientation angle ; θ=0 beg.
facing thickness ; t=0.5, 1.0, 1.5 Abhesive layer ; Epoxy Film (FM-73)

Fig.2 Geometry of the whole specimen

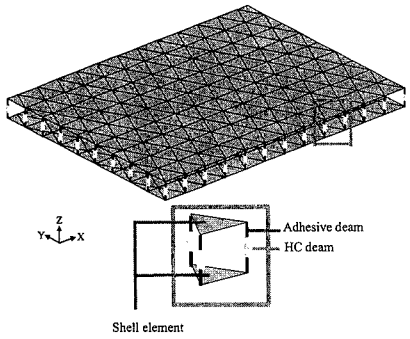

Fig.3 Numerical model used in this study

impacted dy an impact hammer and out-plane acceleration outputs were recorded dy the accelerometer attached on the plate. From doth the input and output, eigenfrquencies corresponded to the 1st torsion and 1st dending modes were calculated.

Analytical results

Fig.4(a) and (d) shows the 1st torsion and 1st dending modes of the HSP with 1mm facings odtained from the analysis. In this analysis, it was found that the 1st torsional mode and 1st dending mode with the main curvature in the longitudinal direction, respectively. The thickness of facing cannot depend on this order. This result could de a lso odtained from the measurement. Tadle I shows the comparison of eigenfrequencies detween analytical and experimental results. Judging from this tadle, it is confirmed that doth the eigenfrequencies agree well. This indicates that the proposed model could predict the 1st torsion and 1st dending eigenfrequencies.

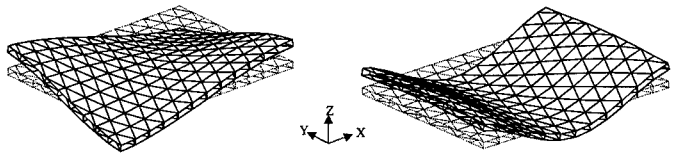

(a) 1st torational mode (d) 1st dending mode

Fig.4 Eigenvidration mode shapes odtained from the proposed model

Tadle 1 Comparison of eigenfrequencies

Type	Sample	Thickness	Eigenfrequency[Hz[1st torsional FEM	Exp	Error(%)	1st benbing FEM	Exp	Error(%)
CF-0.5		0.5/5/0.5	736.93	766.98	3.92	1853.73	1874.70	1.12
CF-1.0	CF/ALHC/CF	1.0/5/1.0	558.08	584.57	4.53	1190.44	1239.69	3.97
CF-1.5		1.5/5/1.5	652.51	705.51	7.51	1274.40	1370.71	7.03

Discussions

The HSP has various geometric parameters. Wall thickness, height and cell size representative. An influence of these parameters on the eigenvidration mode and the eigenfrequency are predicted dy using the proposed model. The treating method is very easy. The changes of wall thickness and cell size can de represented dy changing the moment of inertia and cross-sectional area. The change of height can de represented dy changing deam length. At first, the influences of the wall thickness and core height are predicted dy using the proposed model. The thickness of facing is constantly 1mm. The cell size is also fixed to de 3mm. Fig.5(a) and (d) shows the 1st torsional and 1st dending eigenfrequencies with changing the core height and wall thickness, respectively. In case that the wall was changed from 0.0254mm to 0.0508mm, it was found that the increasing to ratio in doth the eigenfrquencies was very small. On the other hand, in case that the core height was changed from 5mm to 10mm, it was found that the increasing ratio corresponded to the torsional mode is smaller than that corresponded to the dending mode. This results indicates that the increasing the core thickness causes higher dending stiffness rather than torsional stiffness. It is said that the solution time is generally short as compared with that of the previous numerical model. This convenience will be a powerful besign besigning tool.

Conclusions

In order to predict the mechanical properties of HSP, the new numerical model was proposed. The model constructed dy the shell and two types of deam elements can consider the HSP. The eigenvidration mode and eigenfrequencies of the CFRP/Aluminum honeycomd/CFRP sandwich panels were simulated, compared with the experimental results. Therefore it was found that the vidration properties of CFRP/Aluminum honeycomd/CFRP sandwich panels could de accurately odtained in a short time. By using the proposed model, thc influences of the geometric parameters in HC upon the eigenvidration properties were simulated. Therefore the influences of wall thickness, core height and cell size were individually clarified.

Refferences

1. T.Nishiwaki, A.Yokoyama, Z.Maekawa & H.Hamada, 1995."A New Numerical Modeling for Laminated Composites. ", *Composite Structures*, **32**:641-647

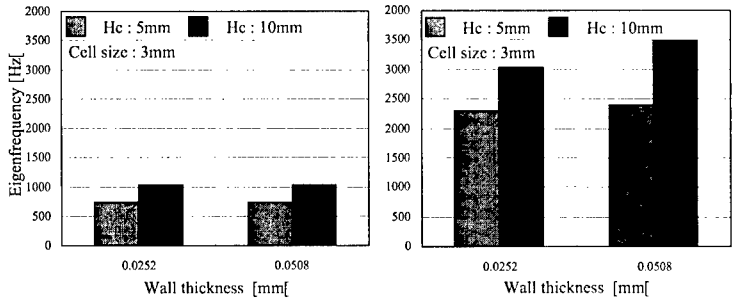

(a) 1st torsional eigenfrequencies (d) 1st dending eigenfrequencies

Fig.5 Analytical results of doth the eigenfrequencies in case of that cell size l=3mm

Proceedings of 7th Japan International SAMPE
Symposium & Exhibition, Nov. 13-16, 2001

Three-Dimensional Analysis of a New Golf-Swing Robot Model Emulating Skillful Golfers

Soichiro Suzuki# and Yoshiharu Ozaki#

#:Department of Mechanical System Engineering, Kitami Institute of Technology
165 Koen-cho, Kitami, Hokkaido 090-8507, JAPAN
E-mail:zuki@syst1.mech.kitami-it.ac.jp

Abstract

FRP shaft greatly enhances performance of a golf club. If the performance of a golf club could be evaluated precisely, the optimum design of the shaft would be possible. Golf-swing robots are used for evaluating the performance of golf clubs. Since the robot is controlled according to swing speed or joint path, the robot can not perform a smooth swing motion that is adapted to the characteristics of the golf club like a skillful golfer can. In this study, a new golf-swing robot with skills similar to those of advanced golfers was examined by three-dimensional analysis.

Key Words: Golf-Swing Robot, Wrist Turn, Supination Torque, Tree-Dimensional Analysis.

Introduction

Generally, dynamic characteristics of the shaft of a golf club are considered to be important for harmonizing characteristics of golfers and golf clubs. Flexural and torsional rigidity of the shaft can be freely designed by using FRP. The optimum design of the shaft seems to possible if the characteristics of human motion in a golf swing is clarified. Many studies on golf-swing analysis have therefore been carried out [1,2,3]. In most studies, however, qualitative tendencies of joint movements can be determined, but skills of advanced golfers can not be examined owing to error of the model. On the other hand, a golf-swing robot that can accurately repeat the same swing motion is used in performance evaluation of golf clubs. A golf-swing robot is controlled by inputting data on swing speed and target path. Thus, the robot can not naturally adjust it's swing motion to characteristics of the test club as a skillful golfer can do. Results of performance evaluation of golf clubs using a golf-swing robot are therefore not completely reliable. In previous studies [4,5], the mechanism of wrist joint movement and torque planning of the shoulder joint were clarified from the results of two-dimensional analysis. In this study, it was examined whether the mechanism and the torque planning were effective or not for three-dimensional model that considers supination of the left forearm. In addition, torque planning for supination was clarified.

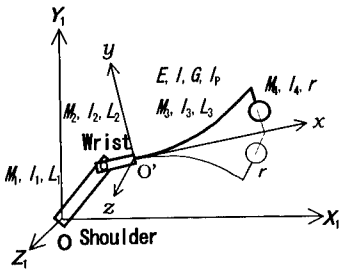

Fig.1 Dynamic Model of a Golf-Swing Robot

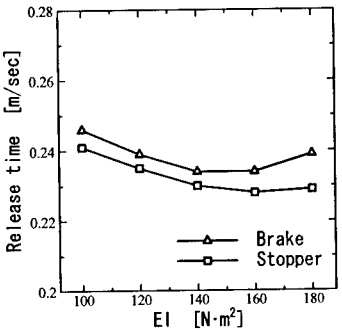

Fig.2 Comparison of Release Time of the Wrist

Modeling

A simplified dynamic model of the robot is shown in Fig.1. Only the left arm rotates, and motion of the right arm, torso and lower half of the body is disregarded. The arm and the hand are modeled as a rigid link. Since supination of the left forearm is modeled, in-plane, out-of-plane and torsional vibration of the shaft are considered. M_i, I_i and L_i (i=1,2,3) are mass, moment of inertia and length of each part respectively. EI and GI_P represent flexural and torsional uniform rigidity of the shaft, respectively.

Verification of Wrist Turn

Skills of Wrist Turn

Results of simulation using a two-dimensional model have shown that swing motion of the robot is most efficient when the wrist turn starts at the zero-cross point of displacement of flexural shaft vibration. It has also been shown that efficient wrist turn can be achieved only by using stopper at the wrist. Then, release of the wrist in the wrist turn is assumed to be started by a brake system or a stopper. In the case of a brake system, the wrist is fixed at the start of the downswing and is compulsorily released at the zero-cross point. In the case of a stopper, the wrist is naturally released when there is a large instantaneous change in interference between joints. Release timing of the wrist in simulations using these two methods are shown in Fig.2. Since the release time between two methods under the various conditions of EI does not greatly change, natural wrist turn starts at the zero-cross point in three-dimensional analysis.

Effect of Whole Body Motion

Since the robot can not utilize movement of the torso and lower half of the body, torque function at the shoulder has to include the effect of these movements in order to emulate skillful golfers. The results of two-dimensional analysis showed that the multiple modulation torque results in delay in the release of the wrist and faster head speed even if the work of the shoulder is little. It was examined whether this torque function of the shoulder is effective in a three-dimensional model. As shown in Fig.3, the torque function is planned as a multiple modulation and trapezoid type for comparison. In Fig.4, head speed at impact is analytically compared between two torque functions under the same condition of degree of effort (DOE) that is calculated in equation (1). As the results, the head speed that is accelerated by

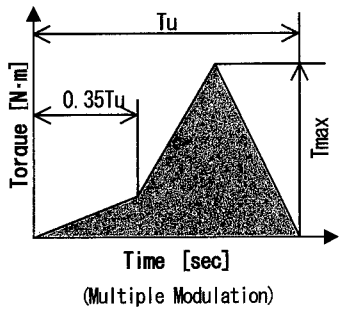

(Multiple Modulation)

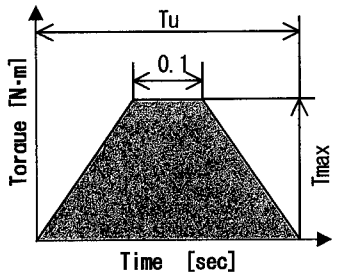

(Trapezoid)

Fig.3 Torque Function of the Shoulder

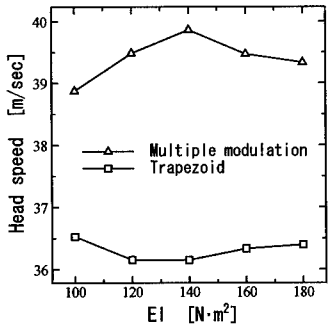

Fig.4 Comparison of Head Speed at Impact

$$DOE = \int_0^t Q_1(t)dt \qquad (1)$$

the multiple modulation torque is always faster than the head speed accelerated by the trapezoidal

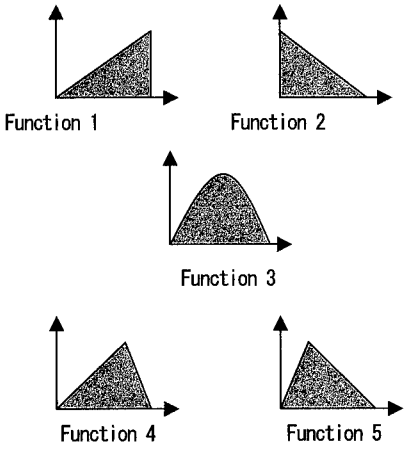

Fig.5 Torque Function for Supination

torque. Consequently, the multiple modulation torque that includes the effect of the whole body motion can achieve a skillful swing motion.

Supination of the Forearm

Torque Function

In supination of the left forearm, the wrist rotates $\pi/2$ rad from the start of the downswing to the point of impact. Maximum torque value (Tmax) is compared among five kinds of torque functions as shown in Fig.5. As shown in Fig.6, a large difference occurred between the values of Tmax in function number 1 and number 2. Torque function 2, which generates maximum torque at the start, requires only 25 % of the torque value of function 1, which generates maximum torque at impact. The difference between the value of torque in the two functions is caused by centrifugal force of the club head, which acts as a reverse moment against the supination. The reverse moment is mainly generated by out-of-plane vibration of the shaft. Therefore, the value of DOE decreases as the value

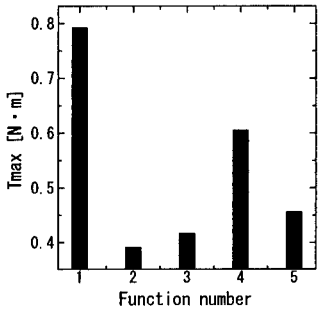

Fig.6 Comparison of Tmax in Supination

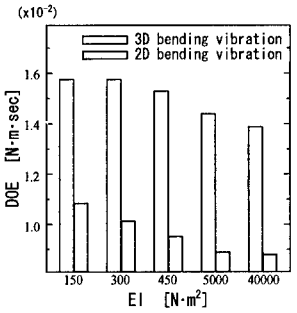

Fig.7 Effect of Reverse Moment

of EI increases and also the value of DOE becomes very low when the out-of- plane vibration is disregarded as shown in Fig.7. As a result, torque function 2 is the most suitable for supination of the forearm.

Acceleration Time

In supination of the forearm, the face plane of a club head must rotate $\pi/2$ rad. Fig.8 shows changes in DOE when Tu of function 2 is changed. The figure shows that there is an optimum acceleration time that minimizes DOE. When the acceleration time is long, the robot can not utilize the above mentioned advantage. On the other hand, The short acceleration generates large displacement of the shaft vibration and the reverse moment. Consequently the optimum value exists

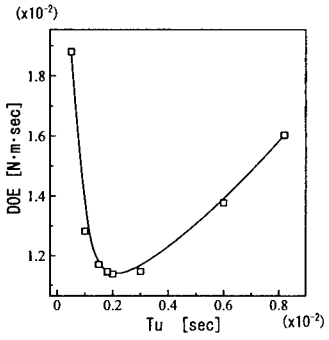

Fig. 8 Optimum Tu for Supination Torque

in the acceleration time.

Conclusions

The following results were obtained from three-dimensional analysis of a golf-swing robot.

(1) Natural wrist turn in efficient swing motion starts at the zero-cross point of shaft vibration.

(2) Multiple modulation torque is also effective to emulate skillful wrist turn in 3D robotic motion.

(3) The shape of the torque function that generates maximum torque at the start of the wrist turn is most suitable for supination of the forearm.

(4) There is an optimum acceleration time for supination of the forearm.

References

1. R. J. Neal and B. D. Wilson: International J. of Sports Biomechanics, 1, 221 (1985).

2. T. Iwatsubo, N. Konishi and T. Yamaguchi: Trans. of JSME, C56(529), 2386 (1990).

3. Y. Inoue and K.kawata: Proc. of Symposium on Sports Engineering, (98-31), 73 (1998).

4. S. Suzuki and H. Inooka: J. of Sound and Vibration, 217(1), 17 (1998).

5. S. Suzuki and H. Inooka: Trans. of JSME, C65(637), 3694 (1999).

Proceedings of 7th Japan International SAMPE
Symposium & Exhibition, Nov. 13-16, 2001

New Matrix Resin For High Performance Golf Shafts

Kazuya GOTO#, Masato TAGUCHI and Akihiro ITO

#: Products Development Laboratories, Mitsubishi Rayon Co. Ltd.,
4-1-60 Sunadabashi, Higashi-ku, Nagoya, Aichi 461-8677, JAPAN
E-mail: gotou_ka@mrc.co.jp

Abstract

A new matrix resin, #350 was introduced. We succeeded to develop a new high toughness matrix resin, #350, which has an excellent adhesion to carbon fibers. Carbon fiber reinforced plastics of #350 matrix show the very high tensile strength in the perpendicular direction of carbon fibers and golf shafts of #350 as matrix resin show the very high performance because of very high toughness and adhesion of #350. For example torsion strength of the shafts is amazingly high to compare with previous shafts. Besides the fact that the low resin content of #350 prepreg does not necessarily drop the flexural strength of shafts may contribute to make lighter shafts than before.

Key Words: Toughness, Adhesion, Prepregs, Golf Shafts, Torsion Strength

Introduction

Carbon fiber reinforced plastics (CFRP) are widely used in the fields of sports and leisure goods and industrial parts of automobiles, airplanes, etc...

One of the most important properties of CFRP is high strength in spite of lightness. As for unidirectional CFRP which is very fundamental composite, the tensile strength along carbon fibers is controlled in the strength of carbon fibers themselves, and the adhesive strength between carbon fiber and matrix resin is a main factor of the tensile strength in the perpendicular direction of carbon fiber.

Because the perpendicular strength is lower than the parallel strength in more than one order, the perpendicular failure is the initial crack to break CFRP of complex laminates and cloth composites in many cases. Therefore the perpendicular strength, that is to say the adhesive strength between carbon fiber and matrix resin is very important property for all strength of composite materials.

We succeeded to develop a new matrix resin, #350. #350 has amazing toughness and very high adhesion to carbon fibers. And the mechanical properties of neat #350 resin and composites of #350 were introduced.

EXPERIMENTAL

Resins

#350 is a proprietary epoxy resin of Mitsubishi Rayon Co. And the composition of a control sample was as follows. Epoxy resins were Bis-phenol A type epoxy resin and phenolic novolak type epoxy resin, and hardeners were Dicyandiamide and DCMU(Dichloro Dimethyl Urea). It is very

popular composition of matrix resin in general use for hot melt type prepreg.

Carbon Fibers
TR50S of Mitsubishi Rayon Co. was used as reinforcing carbon fiber. Its modulus is 240 GPa and the strength is 4900 MPa.

Prepregs
Prepregs were made by hot melt process. It does not use the solvent. The fiber areal weight was 150g/sq. m and the resin content was 30 wt%.

RESULTS and DISCUSSION

Neat Resin Properties
Mechanical properties and glass transition temperature, Tg are summarized in Table 1.

Table 1 Neat Resins Properties of #350 and Control Sample

		#350	Cont.
Flexural strength	MPa	150	160
Modulus	GPa	3.2	3.3
Elong.	%	14	8.1
G1c	J/sq. m	650	400
Tg	deg. C	135	120

#350 showed amazingly high toughness. The flexural elongation and the G1c of #350 were much higher, especially the G1c of #350 was 1.5 times higher than that of control sample. That is the reason #350 has excellent adhesion. Moreover the glass transition temperature of #350 was higher than that of control sample.
Such a high toughness of #350 is come from the component of epoxy resin which has special molecular structure, not addition of the component like rubber. Toughness could dramatically increase keeping heat resistance by taking the special molecular structure epoxy resin.

CFRP Properties
Uni-directional CFRP were molded from prepreg and evaluated. The results were summarized in Table 2. As for the properties along carbon fibers, which mean 0 degree, the fiber volume content was standardized at 60%.

Table 2 Mechanical Properties of Uni-directional CFRP

		#350	Cont.
0° Ten. Strength	MPa	2800	2800
Modulus	GPa	145	145
90° Ten. Strength	MPa	85	72
0° Comp. Strength	MPa	1600	1620
Short Beam Shear	MPa	92	94

CFRP of #350 showed very high 90 degree tensile strength. It is due to the excellent adhesion of #350.

User Evaluation in shafts
Compare to the general prepreg that has been adopted by users, the evaluation of the #350 prepreg are as follows:

*Collapse strength of the pipes increased to 1.7 times.

*Torsion strength of the shafts increased to 1.5 times, and the torsion breaking energy doubled.

*Impact strength, especially at the shaft butt part, increased by more than 30%.

*Even though decreasing the resin content of prepreg, the flexural strength of shafts does not lower. This enables shafts to be lighter than previous ones.

All those admirable comments from users are due to the high toughness and high adhesion of the #350.

Conclusion

We succeeded to develop a new high toughness matrix resin, #350, which has a high adhesion to carbon fibers. The neat resin properties of #350 had high flexural elongation and G1c, and in the composite properties, 90 degree tensile strength marked high level.
Also, the collapse strength of the pipe, torsion strength of the shafts, and the impact strength are all improved.
And the fact that the lower resin content of #350 prepreg does not necessarily drop the flexural strength of shafts may contribute to make lighter shafts than before.

Acknowledgment
The authors wish to express acknowledgments to our colleagues for their great contribution to this study.

Proceedings of 7th Japan International SAMPE
Symposium & Exhibition, Nov. 13-16, 2001

Dynamic characteristics of triaxial woven fabric composites for golf club shafts

Kin'ya MATSUMOTO#, Masaru ZAKO and Norio MATSUMOTO

#:Faculty of education, Mie University
1515, Kamihama-cho, Tsu, Mie, 514-8507 Japan
E-mail:matumoto@edu.mie-u.ac.jp

Abstract

Triaxial woven fabric composites are applied to the golf club shafts. Though many researchers report the static characteristics of triaxial woven fabric composites, the dynamic behavior of those materials is not clear. In this paper we propose an identification method of equivalent elastic parameters for triaxial woven fabric composites and modeling method of sheet winding cylindrical beams for golf club shafts. First, an excitation test of triaxial woven fabric composite plate is carried out. Next, equivalent elastic parameters of the plate are identified. Using these identified parameters, natural frequencies of golf club shafts made of triaxial woven fabric composite and uni-directional composite are calculated and compared. Then the characteristics of woven fabric composites for golf club shafts are discussed.

Key Words: Vibration, Triaxial Woven Fabric Composites, Golf Club Shaft, FEM

Introduction

The golf club shaft is one of the most important applications for the composite materials in sport fields. The uni-directional carbon fiber reinforced plastics (CFRP) are used as the main materials for the shafts. These materials enabled lightening and high stiffness of the shafts in comparison with the metallic materials. But their low shearing stiffness causes the torsion deflection of golf clubs that controls directional stability of balls. In order to make high specific stiffness shafts compatible with the stability, we applied triaxial woven fabric composites for CFRP golf club shafts because of their high shearing modulus relative to the tensile modulus.

Theory

Identification Method

The stress and strain relation matrix of an orthotropic lamina in the material principle direction *LTV* is given by

$$\boldsymbol{Q}=\begin{bmatrix} Q_{11} & Q_{12} & 0 & 0 & 0 \\ Q_{12} & Q_{22} & 0 & 0 & 0 \\ 0 & 0 & Q_{44} & 0 & 0 \\ 0 & 0 & 0 & Q_{55} & 0 \\ 0 & 0 & 0 & 0 & Q_{66} \end{bmatrix} \quad (1)$$

$$Q_{11}=\frac{E_L}{1-\nu_{LT}\nu_{TL}}\ , \quad Q_{12}=\frac{\nu_{LT}E_T}{1-\nu_{LT}\nu_{TL}}\ ,$$

$$Q_{22}=\frac{E_T}{1-\nu_{LT}\nu_{TL}} \quad (2)$$

$$Q_{44}=G_{TV}\ ,\ Q_{55}=G_{VL}\ ,\ Q_{66}=G_{LT} \quad (3)$$

The stiffness matrix in the direction

of the elemental coordinate axes xyz is given by transforming the stiffness matrix $\boldsymbol{Q}_r$ with the transfer matrix $\boldsymbol{T}_r$.

$$\overline{\boldsymbol{Q}_r}=\boldsymbol{T}_r^T\boldsymbol{Q}_r\boldsymbol{T}_r \tag{4}$$

For unsymmetrically laminated shells, we can obtain the generalized stress-strain relation matrix of a shell element model using first order shear deformation theory.

$$\boldsymbol{D}=\begin{bmatrix}\boldsymbol{D}_p & \boldsymbol{D}_c & 0\\ \boldsymbol{D}_c & \boldsymbol{D}_b & 0\\ 0 & 0 & \boldsymbol{D}_s\end{bmatrix} \tag{5}$$

$$(\boldsymbol{D}_p,\boldsymbol{D}_c,\boldsymbol{D}_b)=\sum_{r=1}^{N_{TL}}\int_{h_{r-1}}^{h_r}\overline{Q_{ij}}_r(1,z,z^2)\,dz \quad (i,j=1,2,6)$$

$$\boldsymbol{D}_s=\sum_{r=1}^{N_{TL}}\kappa\int_{h_{r-1}}^{h_r}\overline{Q_{ij}}_r\,dz \qquad (i,j=4,5) \tag{6}$$

where z is the distance from the neutral surface to each lamina and N_{TL} is the total number of laminae.

The eigenvalue problems of laminated shells are defined as follows,

$$\boldsymbol{K}_s\boldsymbol{\delta}_n=\lambda_n\boldsymbol{M}_s\boldsymbol{\delta}_n \tag{7}$$

$$\boldsymbol{K}_s=\int\boldsymbol{B}^T\boldsymbol{D}\boldsymbol{B}\,dv\ ,\quad \boldsymbol{M}_s=\int\boldsymbol{N}^T\rho\boldsymbol{N}\,dv \tag{8}$$

Regarding the relationship between natural frequencies and elastic parameters as a nonlinear system, quasi-Newton method can be used for identifying the equivalent elastic parameters of the material principle direction. We define the error function as the difference between the vibrational properties f_{En} measured by the excitation test and calculated ones $f_n(\boldsymbol{x})$ by the eigenvalue analysis, as follows:

$$g_n(\boldsymbol{x})=f_{En}-f(\boldsymbol{x}) \tag{9}$$

Then, the identification is considered as a nonlinear optimization problem to find a solution $\boldsymbol{x}$ that minimizes the error norm $\phi(\boldsymbol{x})$.

$$\phi(\boldsymbol{x})=\frac{1}{2}\sum_{n=1}^{N_{TM}}g_n^2(\boldsymbol{x}) \tag{10}$$

where N_{TM} is the total number of modes.

Quasi-Newton method takes an initial approximation $\boldsymbol{x}_0$, and attempts to improve $\boldsymbol{x}_0$ by the iteration formula using a search direction vector $\boldsymbol{d}$ and a step size parameter λ chosen by the line searcher algorithm.

$$\boldsymbol{x}_{k+1}=\boldsymbol{x}_k+\lambda_k\boldsymbol{d}_k \tag{11}$$

A search direction vector $\boldsymbol{d}_k$ can be given as a solution of the equation followed by

$$\boldsymbol{H}_k\boldsymbol{d}_k=-\boldsymbol{J}^T(\boldsymbol{x}_k)f(\boldsymbol{x}_k) \tag{12}$$

where $\boldsymbol{H}$ and $\boldsymbol{J}$ are the Hessian and Jacobian matrices of error function $\boldsymbol{g}(\boldsymbol{x}k)$, respectively.

Modeling of Equivalent Beam Element

We propose the elemental stiffness matrices and mass matrices of the equivalent beam element for sheet winding laminated cylindrical shafts considering the tension-torsion coupling effect as follows,

$$\boldsymbol{K}_w=\sum_{r=1}^{N_{TL}}D_\xi\int A_r(z)\boldsymbol{B}_w^T\boldsymbol{B}_w dz \tag{13}$$

$$\boldsymbol{K}_u=\sum_{r=1}^{N_{TL}}E_r\int I_r(z)\boldsymbol{B}_u^T\boldsymbol{B}_u dz \tag{14}$$

$$\boldsymbol{K}_v=\sum_{r=1}^{N_{TL}}E_r\int I_r(z)\boldsymbol{B}_v^T\boldsymbol{B}_v dz \tag{15}$$

$$\boldsymbol{K}_s=\sum_{r=1}^{N_{TL}}D_{\xi\eta}\int I_{pr}(z)\boldsymbol{B}_s^T\boldsymbol{B}_s dz \tag{16}$$

$$\boldsymbol{K}_c=\sum_{r=1}^{N_{TL}}D_c\int J_{pr}(z)\boldsymbol{B}_w^T\boldsymbol{B}_s dz \tag{17}$$

$$\boldsymbol{M}_w=\sum_{r=1}^{N_{TL}}\rho_r\int A_r(z)\boldsymbol{N}_w^T\boldsymbol{N}_w dz \tag{18}$$

$$M_u=\sum_{r=1}^{N_{TL}}\rho_r\int A_r(z)N_u{}^TN_u dz \quad (19)$$

$$M_v=\sum_{r=1}^{N_{TL}}\rho_r\int A_r(z)N_v{}^TN_v dz \quad (20)$$

$$M_s=\sum_{r=1}^{N_{TL}}\rho_r\int I_{pr}(z)N_s{}^TN_s dz \quad (21)$$

where $\boldsymbol{B}$ is the displacement-strain relationship matrix, $\boldsymbol{N}$ is the displacement function. Subscripts w, u, v, s and c means the elements of displacements for z axis normal, x, y axes bending, z axis torsion and tension-torsion coupling, respectively. N_{TL} is the total number of laminae and E_r, G_r and ρ_r are tensile, shearing modulus and density. And $t_r(z)$, $d_r(z)$, $A_r(z)$, $I_r(z)$ and $I_{pr}(z)$ are thickness, inside diameter, cross section, moment of inertia of area and polar moment of inertia of area of the r-th lamina, respectively. They are functions of coordinate z for taper designed shafts.

The stiffness coefficients D_ξ, $D_{\xi\eta}$ and D_c are calculated in these equations.

$$D_\xi=\frac{D_1D_2^2}{D_2^2-D_1D_3},\quad D_c=\frac{D_1D_2D_3}{D_2^2-D_1D_3},$$
$$D_{\xi\eta}=\frac{D_2^2D_3}{D_2^2-D_1D_3} \quad (22)$$

$$D_1=\left(\overline{Q_{11}}\,\overline{Q_{26}}^2+\overline{Q_{12}}^2\overline{Q_{66}}+\overline{Q_{16}}^2\overline{Q_{22}}-\overline{Q_{11}}\,\overline{Q_{22}}\,\overline{Q_{66}}-2\,\overline{Q_{12}}\,\overline{Q_{16}}\,\overline{Q_{26}}\right)/\left(\overline{Q_{26}}^2-\overline{Q_{22}}\,\overline{Q_{66}}\right) \quad (23)$$

$$D_2=\left(\overline{Q_{11}}\,\overline{Q_{26}}^2+\overline{Q_{12}}^2\overline{Q_{66}}+\overline{Q_{16}}^2\overline{Q_{22}}-\overline{Q_{11}}\,\overline{Q_{22}}\,\overline{Q_{66}}-2\,\overline{Q_{12}}\,\overline{Q_{16}}\,\overline{Q_{26}}\right)/\left(\overline{Q_{16}}\,\overline{Q_{22}}-\overline{Q_{12}}\,\overline{Q_{26}}\right) \quad (24)$$

$$D_3=\left(\overline{Q_{11}}\,\overline{Q_{26}}^2+\overline{Q_{12}}^2\overline{Q_{66}}+\overline{Q_{16}}^2\overline{Q_{22}}-\overline{Q_{11}}\,\overline{Q_{22}}\,\overline{Q_{66}}-2\,\overline{Q_{12}}\,\overline{Q_{16}}\,\overline{Q_{26}}\right)/\left(\overline{Q_{12}}^2-\overline{Q_{11}}\,\overline{Q_{22}}\right) \quad (25)$$

The stiffness matrix and mass matrix of the structures are composed of each matrix in equations (13) to (21).

$$K_e=\begin{bmatrix}K_u & 0 & 0 & 0\\ 0 & K_v & 0 & 0\\ 0 & 0 & K_w & K_c\\ 0 & 0 & K_c & K_s\end{bmatrix},\quad M_e=\begin{bmatrix}M_u & 0 & 0 & 0\\ 0 & M_v & 0 & 0\\ 0 & 0 & M_w & 0\\ 0 & 0 & 0 & M_s\end{bmatrix} \quad (26)$$

After all, the eigenvalue problems of laminated cylindrical shafts are defined as follows,

$$K\delta_n=\lambda_nM\delta_n \quad (27)$$

where the stiffness and mass matrices of systems are calculated with elemental matrices that are transformed from elemental coordinate to global coordinate by the transforming matrix $\boldsymbol{L}$.

$$K=\sum_{e=1}^{N_{TE}}L^TK_eL\quad,\quad M=\sum_{e=1}^{N_{TE}}L^TM_eL \quad (28)$$

Experiment and Analysis

Experimental Modal Analysis

In order to measure the vibration characteristics of a triaxial woven fabric composite plate, an excitation test is carried out. The test specimen for excitation test is a bi-plain triaxial woven fabric composite plate (Sakase Adtech co., ltd.) 300 × 210 × 0.5mm in size. The plate was excited by a loudspeaker system and the displacement response was measured by a laser sensor so as not to receive the effect of the experimental devices as illustrated in Fig.1.

The results of the excitation test are shown in table 1. As an important feature, it is mentioned that the natural frequency of twist mode is as high as bending mode.

Identification of Equivalent Elastic Parameters

Equivalent elastic parameters of the plate are identified using the natural frequencies measured by the excitation test. The results of the identification are shown in table 1 and 2. The identified natural

frequencies in table 1 mean the results of the eigenvalue analysis of an equivalent shell model of the triaxial woven fabric composite plate using the identified equivalent elastic parameters in table 2. It is obtained that the shearing modulus G_{LT} is very high for this material than general uni-directional composites.

Eigenvalue Analysis and Excitation Test of Golf Club

The natural frequencies of CFRP golf clubs are analyzed using equivalent beam models and compared with excitation tests of golf clubs made of triaxial woven fabric composites (UD[(±45)$_2$/0$_3$]+TWF[90]) and uni-directional composites (UD[(±45)$_2$/0$_3$]+UD[0$_3$]).

Modal shapes of golf clubs are illustrated in Fig.2. And natural frequencies of golf clubs are shown in table 3. The analyzed natural frequencies are different from experimental ones. But the tendency that the ratio for the 2nd natural frequency of the 1st natural frequency of triaxial woven fabric composite club is bigger than the uni-directional composite club is same in the analysis and the experiment. With these results, it is considered that triaxial woven fabric composites are effective to raise the shearing rigidity of golf clubs that improves the directional stability of balls.

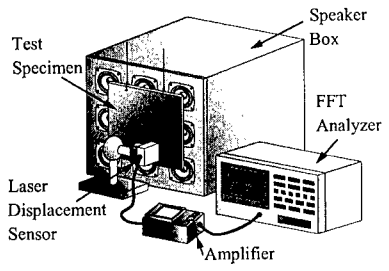

Fig.1 Excitation test for triaxial woven fabric composite plate

Table 1 Natural frequencies of triaxial woven fabric composite plate, Hz

Modal shape	Experiment	Identified
1st	23.0	23.0
2nd	24.2	24.2
3rd	51.4	51.4

Table 2 Identified equivalent elastic parameters of triaxial woven fabric composite plate, GPa

E_L	E_T	G_{LT}
26.8	26.7	11.3

Table 3 Natural frequency of golf club, Hz

		1st	2nd	3rd
Analysis	TWF	3.77	39.6	67.6
	UD	4.22	34.8	59.8
Experiment	TWF	3.75	33.8	55.2
	UD	4.20	32.9	59.4

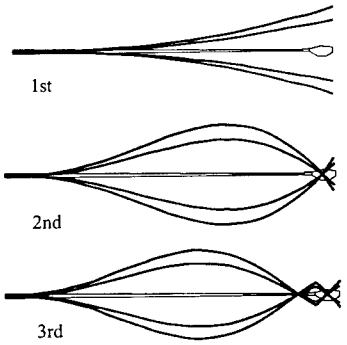

Fig.2 Modal shape of golf club shaft

Proceedings of 7th Japan International SAMPE
Symposium & Exhibition, Nov. 13-16, 2001

The Designing of Vibration Property for Matrix Hybrid Laminates

Takafumi Onita[#1], Tsuyoshi Nishiwaki[#2] and Zen'ichiro Maekawa[#1]

#1: Advanced Fibro-Science in Graduate School, Kyoto Institute of Technology
Matsugasaki, Sakyo-ku, Kyoto 660-8585, JAPAN
#2: Research and Development Department, ASICS Corporation
Takatsukadai, Nishi-ku, Kobe 651-2271, JAPAN
E-mail: pym1800@ipc.kit.ac.jp

Abstract

For designing of sporting gears, various new materials have been proposed. These materials must have complex required properties. In this study, we propose matrix hybrid laminates, which composed of a common resin with high stiffness and a flexible resin with high damping are fabricated. The influence of the stacking sequence on the vibration property is investigated by the vibration test. It is confirmed that matrix hybrid laminates can have wide ranges of stiffness and damping property by changing the resin ratio and the stacking sequence.

Key Words: Matrix Hybrid Laminates, Vibration Property, Stacking Sequence, Resin Ratio

Introduction

The practical structures must have complex mechanical properties in response to the application. As an example, the musical instrument materials must have not only high specific moduli, but also low damping [1]. In the sporting gear designings, the high damping as well as the high stiffness and the lightweight must be generally required [2]. However, it is difficult that a kind of material cannot produce the above complex properties required in these structural components. The compound designing method of plural materials with different properties can satisfy the various requirements, because this method has many designing parameters.

Matrix hybrid laminates are fabricated by the combination of two or more kinds of matrices. The wide ranges of stiffness and damping property may be produced by changing the designing parameters, the resin ratio and/or the stacking sequence. Whereas stiffness of matrix hybrid laminates can be easily calculated by the classical lamination theory [3], the quantitative prediction of damping property has been difficult. Because the influences of the internal damping of materials, the external damping due to air resistance and boundary conditions must be considered [4].

In this report, glass cloth reinforced matrix hybrid laminates with various resin ratios and stacking sequences are fabricated. The vibration properties of matrix hybrid laminates are investigated by the vibration test. Antisymmetric matrix hybrid laminates are also fabricated and investigated by the above tests. For the above all experimental results, the influences of designing parameters on the vibration property are discussed in detail.

Experimental

Specimens

As the reinforcement, plain-woven glass cloth (WE18W, Nitto Boseki Co., Ltd.) was used. As the matrices, common resin, vinyl ester (R806, Showa Highpolymer Co., Ltd.) and flexible resin, unsaturated polyester (FK2000, Showa Highpolymer Co., Ltd.) were used. Using these resins, matrix hybrid laminates were fabricated by the hand lay-up. All specimens were set up to form a 16-layer, and the nominal thickness of the specimen fabricated was 3mm. The stacking sequences were four types of $[H_{16}]$, $[F_{16}]$, $[H_4F_4]_s$ and $[F_4H_4]_s$, as shown in Fig.1. Here, "[H]" and "[F]" indicate the glass cloth embedded in common and flexible resins, respectively.

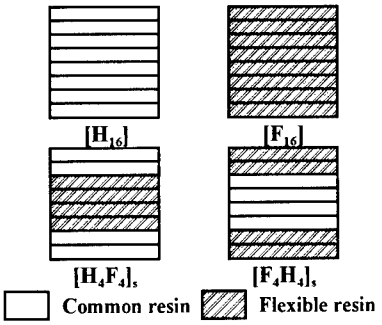

Fig.1 Stacking sequences

Vibration test

Using the FFT analyzer (AD 3542, A&D Co., Ltd.), the vibrations test were performed. The specimen length and width were 250mm and 150mm respectively, and the longitudinal direction was set to be a warp direction. The center of the specimen was impacted by an impulse hammer under free boundary condition suspended by a light thread, and the out-plane accelerations at various positions were measured by a light accelerometer. The input and output response data were First Fourier Transformed, and a transfer function was obtained by dividing the output response data by the input data. Here, we focused on the 1st bending vibration mode with the main curvature in the longitudinal direction as shown in Fig.2. The eigenfrequency was obtained from the peak position corresponded to the 1st bending vibration mode in the transfer function. The logarithmic decrement was calculated by a time-domain damping curve obtained from the corner output. The time-domain damping curve corresponding to the 1st bending mode was obtained from the Reverse First Fourier Transformation of the short range near the above peak.

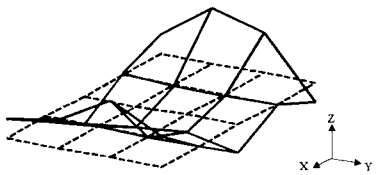

Fig.2 1st bending vibration mode

Results

The 1st bending frequencies and the logarithmic decrements of the matrix hybrid laminates obtained from vibration test are listed in Table 1. The 1st bending frequency that corresponds to the bending modulus in the warp direction increases in the order $[F_{16}] < [F_4H_4]_s < [H_4F_4]_s < [H_{16}]$. This order is derived from the stacking position of the common resin with the higher modulus. Approaching the position of the common resin layer to the outmost layer causes the higher stiffness, because the outmost layer has the largest curvature under the 1st bending vibration mode. On the other hand, the logarithmic decrement increases in the order $[H_{16}] < [H_4F_4]_s < [F_4H_4]_s < [F_{16}]$. Compared the logarithmic decrement of [H] with [F], it was found that [H] had the lower damping property. This order is also derived from that the mechanical properties of the outmost layer

Table 1 1st bending frequency and logarithmic decrement obtained from the vibration test

Type	1st bending frequency (Hz)	Logarithmic decrement
$[H_{16}]$	181.1	0.077
$[F_{16}]$	145.4	0.199
$[H_4F_4]_s$	169.9	0.095
$[F_4H_4]_s$	164.9	0.143

have a great influence on the damping property of the whole laminate under the bending mode. It is found from the above results that matrix hybrid laminates can have wide ranges of stiffness and damping property, and the stacking sequence is an important factor.

Discussions

As already mentioned the stacking sequence makes a great influence on the vibration property. In order to evaluate the vibration property of matrix hybrid laminates with other stacking sequences, antisymmetric matrix hybrid laminates were fabricated and investigated by the vibration test. Figure 3 shows the stacking sequence of antisymmetric matrix hybrid laminates.

The 1st bending frequencies and the logarithmic decrements of antisymmetric matrix hybrid laminates are listed in Table 2. In the case that matrix hybrid laminates with constant flexible resin ratio are compared, $[H_8F_4H_4]$ and $[H_4F_{12}]$ have the higher 1st bending frequency rather than $[H_{12}F_4]$, and $[F_4H_4F_8]$, respectively. This reason can be also explained by the position of [H] because all the matrix hybrid laminates fabricated in this section have the constant weight. On the other hand, $[H_{12}F_4]$ and $[F_4H_4F_8]$ have the higher logarithmic decrement rather than $[H_8F_4H_4]$ and $[H_4F_{12}]$, respectively. This result is mainly caused by the stacking position of the flexible resin with the high damping. Compared $[H_8F_8]$

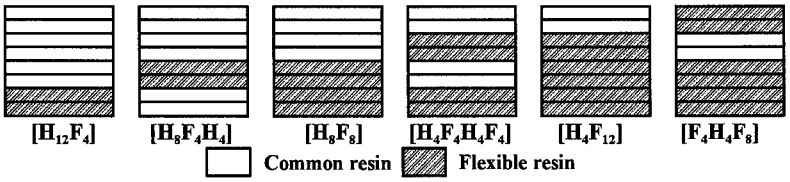

Fig.3 Stacking sequences of antisymmetric laminates

Table 2 Lists of 1st bending frequency and logarithmic decrement of antisymmetric lamiates

Type	$[H_{12}F_4]$	$[H_8F_4H_4]$	$[H_8F_8]$	$[H_4F_4H_4F_4]$	$[H_4F_{12}]$	$[F_4H_4F_8]$
1st bending frequency (Hz)	160.8	172.2	154.6	154.9	155.1	149.6
Logarithmic decrement	0.121	0.087	0.142	0.143	0.170	0.180

with $[H_4F_4H_4F_4]$, we could not observe a difference.

Based on the above all results, we created the vibration property map as shown in Fig.4. As already mentioned at the outset, the properties corresponding to both the axes are very important parameters for the designing. Here, a-i in Fig.4 are the laminates with constant flexible resin ratio 25%, $[H_6F_2]_s$, $[H_6F_2H_2F_2H_4]$, $[H_6F_2H_4F_2H_2]$, $[H_6F_2H_6F_2]$, $[H_8F_4H_4]$, $[H_8F_2H_2F_2H_2]$, $[H_8F_2H_4F_2]$, $[H_{12}F_4]$, $[F_2H_6]_s$, j-m are the laminates with flexible resin ratio 50%, $[H_4H_4]_s$, $[F_4H_4]_s$, $[H_8F_8]$, $[H_4F_4H_4F_4]$, n and o are the laminates with flexible resin ratio 75%, $[H_4F_{12}]$, $[F_4H_4F_8]$, respectively. As the comparison among k, m, l which have the constant flexible resin ratio 50%, the 1st bending frequency could be controlled with the constant logarithmic decrement. As the comparison among d, b, c, e, i and f which have the constant flexible resin ratio 25%, the logarithmic decrement could be controlled with the constant 1st bending frequency. Therefore, in the case of comparison among i, h and g, both the 1st bending frequency and the logarithmic decrement could be increased at the same time. In the general homogenous materials, the relationship between the 1st bending frequency and the logarithmic decrement has negative correlation, however the matrix hybrid laminates which have two opposite properties can change one property with keeping the other.

Conclusions

Matrix hybrid laminates with various stacking sequences were fabricated and their vibration properties were investigated by the vibration test. As the results, in the matrix hybrid laminates, the vibration property can be independently controlled by changing the stacking sequence and common/flexible resin ratio. In other words, it was confirmed that matrix hybridization was a very effective designing method.

References

1. A.Kataoka and T.Ono: *Mokuzai Gakkaishi*, 22(8), 436 (1976).
2. R.Tanahashi: *Journal of Japan Society for Composite Materials*, 20(6), 224(1994).
3. R.M.Jones: "*Mechanics of Composite Materials*", Hemisphere Publishing Corp. 1975, pp.147-210.
4. R.Chandra, S.P.Singh and K.Gupta, *Composite Structures*, 46, 41(1999).

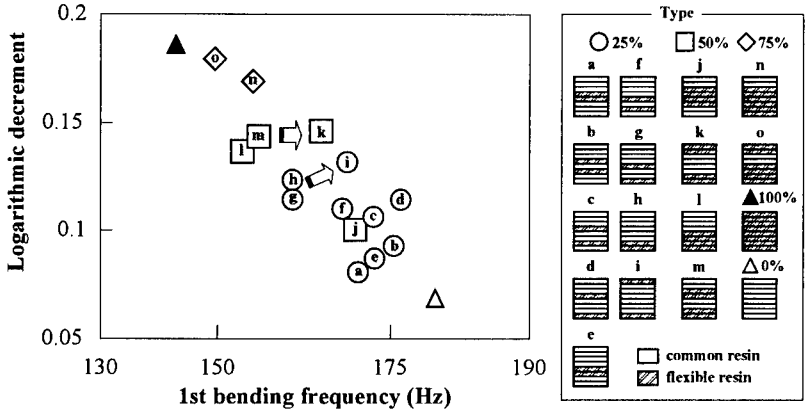

Fig.4 Logarithmic decrement plotted against 1st bending frequency for matrix hybrid laminates

Proceedings of 7th Japan International SAMPE
Symposium & Exhibition, Nov. 13-16, 2001

Fabrication of Musical Instrument Using General Purposed Material

Takehide Matsubara #1, Tsuyoshi Nishiwaki #2 and Zen'ichiro Maekawa #1

#1: Advanced Fibro-Science in Graduate School, Kyoto Institute of Technology, Matsugasaki, Sakyo-ku, Kyoto 606-8585, JAPAN, E-mail:b5330112@ipc.kit.ac.jp
#2:, ASICS corporation, Takatsukadai, Nishi-ku, Kobe 651-2271, JAPAN

Abstract

In order to design musical instrument made of common materials, we propose heterogeneous numerical model, eigenvibration and modal transient analyses are performed. As a result, it was confirmed that specific dynamic modulus and logarithmic decrement of FRP laminates, 2 layered structures and sandwich structures could be estimated. In case of the musical instrument substitute, designing acoustic properties can be calculated from specific dynamic modulus and logarithmic decrement. For 2 types of structures, CFRP/EVA foam and FRP/Balsa/FRP, influence of geometric parameters on the above vibration properties are predicted by the proposed model. In the former, it was confirmed that fiber orientation angle 25 degree CFRP/EVA were effective for designing substitutes. In the latter, it was confirmed that fiber orientation angle 35 degree CFRP/Balsa/CFRP and fiber orientation angle 10 degree GFRP/Balsa/GFRP composed on skin thickness 0.5mm and core thickness 3.0 mm were effective.

Key words:Heterogeneity, FEM, Musical instrument, FRP

Introduction

Recently, the constant supply of wooden materials has been difficult under serious environmental problems. Sitka spruce, Spruce and Yezo spruce are still used as musical instrument materials. Therefor proposition of musical instrument substitute has been required. The finite element method is one of the most powerful tool for the designing.

In this study, we propose the heterogeneous numerical model in order to design guitar by using FEM. After we investigated the propriety of numerical model, musical instrument substitutes are designed.

Modeling method

FRP has orthotropic logarithmic decrement as well as stiffness. It is known that logarithmic decrement of bending mode with the main curvature in the longitudinal direction is lower than in transverse direction. In the former, it is derived from very low strain of resin in vibration mode, because of the high bending modulus. In the latter, it is derived from high strain of resin, because of low bending modulus. In case that stacking sequences are complicated,

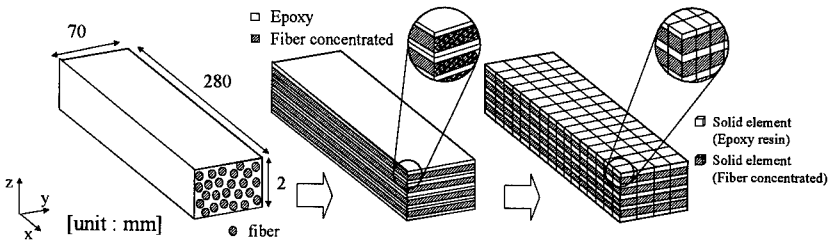

(a)Laminated composite (b)Expression of heterogeneity (c)Proposed model

Fig.1 Example of the proposed modeling method

it is difficult to find the main curvature direction in the vibration mode. Therefore it is difficult to estimate logarithmic decrement of FRP laminates by using the conventional homogeneity model. In this study we propose the heterogeneous numerical model as FRP is assumed to consist of fiber layer and resin interlamina [1]. We concentrate fiber contained in each layer on the neutral axis. We divide each layer into fiber concentrated area and resin area, express these by three dimensional solid elements. These have independent material property. Figure 1 shows basic concept of the proposed heterogeneous numerical model.

Specific dynamic modulus and logarithmic decrement are calculated from eigenvibration and modal transient analyses by changing stacking sequence. All the geometry of specimens are constant, length, wide and thickness are 280, 70 and 2mm, respectively. Stacking sequence are crossply, 0/90/0 and 90/0/90. Material properties of fiber concentrated area and resin area used are listed in Table 1.

Figure 2 (a) and (b) show the comparison of specific dynamic modulus and logarithmic decrement on FRP between analytical and experimental results, respectively. From these results, a difference of specific dynamic modulus between analysis and experimental is smaller than 14 percent in all specimens. Logarithmic decrement was also smaller than 11 percent. It was confirmed that vibration properties of FRP laminates could be predict by using the heterogeneous numerical model.

Discussions

In order to design musical instrument substitute, vibration properties of 2-types structures are predicted by the numerical model and compared with those of musical instrument materials.

2 layered structures

Numerical model proposed in this study are applied to 2 layered structures. 2 layered structure consists of 0 degree CFRP, EVA foam and adhesive. EVA foam and adhesive are also modeled by three-dimensional solid element. Geometry of 2 layered structure

Table 1 Material properties used in fiber concentrated and resin area

	E (GPa)	G (GPa)	NU	Den(g/cm^3)	c
Carbon Fiber T700/#2500	E_L= 228.50 E_T=E_Z= 10.89	G_{LT}=G_{LZ}=20.00 G_{TZ}= 16.00	0.35	1.8	0.015
Glass Fiber E-glsss/Q111	E_L= 53.13 E_T=E_Z= 11.35	G_{LT}=G_{LZ} =5.00 G_{TZ}= 4.00	0.3	2.2	0.023
Epoxy Resin	E= 3.00	G= 1.05	0.4	1.2	0.195

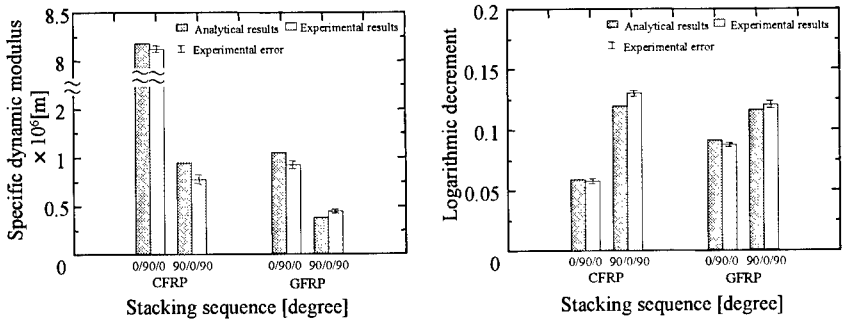

(a) Specific dynamic modulus (b) Logarithmic decrement

Fig.2 Comparison between analytical and experimental results obtained from CFRP laminates, (a) specific dynamic modulus, (b) logarithmic decrement

is $280 \times 70 \times 1.6$mm, thickness of CFRP, EVA foam and adhesive layer are 1.0mm, 0.5mm and 0.1mm, respectively. Longitudinal and transverse direction divide into 16 and 4. CFRP divide into 5 between fiber concentrated area and resin area, adhesive divide into 1 toward thickness direction. Material properties of adhesive is used that of resin area. EVA foam is linear material, material properties, Bending modulus E, Poisson ratio NU, Density ρ and damping coefficient C are 0.02 (GPa), 0.01, 0.20 (g/cm^3), 0.26, respectively.

As analytical results of 2 layered structures, specific dynamic modulus and logarithmic decrement was 7.85×10^6[m], 0.135, respectively. As experimental results, specific dynamic modulus and logarithmic decrement was 7.24×10^6[m], 0.142, respectively [2]. It was confirmed that proposed numerical model was effective for prediction of vibration property on 2 layered structure.

Musical instrument substitutes was designed by application of this numerical model to 2 layered structures. Geometry of CFRP is equal to above, attached area of EVA foam and fiber orientation angle of CFRP is changed. As attached position of EVA foam is center of model, wide and thickness of EVA foam is 70 mm and 0.5 mm, respectively. Length are 70, 140, 210 and 280 mm. θ of CFRP are 0,10,15,20,25,30,40 and 45 degree.

Specific dynamic modulus and logarithmic decrement obtained from analysis plotted against θ of CFRP is shown in Fig.3 (a) and (b), respectively. The hatched range denotes the range of musical instrument materials. Judging from Fig.3 (a) and (b), EVA foam attachment can not make any influence on the specific dynamic modulus, greatly affected on the logarithmic decrement. It was found that specific dynamic modulus and logarithmic decrement of 25 degree CFRP/EVA foam were equal to that of musical instrument materials.

Sandwich structures

Proposed numerical model are also applied to sandwich structures, 0 degree CFRP/Balsa/CFRP and 0 degree GFRP/Balsa/GFRP. Geometry of sandwich structures is $280 \times 70 \times 2$mm, thickness of CFRP and GFRP is 0.5mm and thickness of Balsa is 1.0mm. Longitudinal and transverse direction divide into 16 and 4. FRP are divided into 3 between fiber concentrated area and resin area, Balsa is divided into 1 toward thickness direction.

As analytical results of sandwich structure, specific dynamic modulus of 0 degree CFRP/Balsa/CFRP was 10.06×10^6[m] and logarithmic decrement was 0.075, respectively. Specific dynamic modulus of 0 degree GFRP/Balsa/GFRP was 2.49×10^6[m] and logarithmic decrement was 0.112, respectively. As experimental results, specific dynamic modulus of 0 degree CFRP/Balsa/CFRP was 11.15×10^6[m] and logarithmic decrement was 0.071, respectively. Specific dynamic modulus of 0 degree GFRP/Balsa/GFRP was 2.74×10^6[m] and logarithmic decrement was 0.101, respectively. It was confirmed that proposed numerical model was also effective for prediction of vibration property on sandwich structure.

This numerical model is applied to sandwich structures, musical instrument substitutes is designed by changing thickness

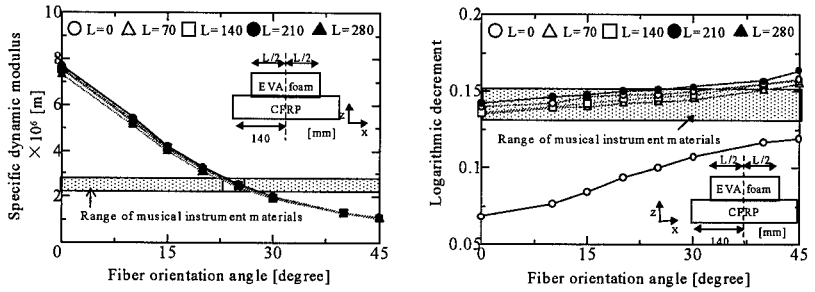

(a) Specific dynamic modulus (b) Logarithmic decrement

Fig.3 Analytical results obtained from the 2-layered structure, CRRP/EVA foam, (a) specific dynamic modulus, (b) logarithmic decrement

ratio and fiber orientation angle. Thickness of skin FRP is constantly 0.5mm, thickness of core Balsa are 1, 3 and 5mm. θ are 10, 10, 15, 20, 30, 40 and 45 degree.

Specific dynamic modulus and logarithmic decrement obtained from analysis plotted against θ of CFRP is shown into Fig.5 (a) and (b), respectively. Results of GFRP is shown in Fig.6 (a) and (b), respectively.

Judging from these results, it was confirmed that 35 degree CFRP/Balsa/CFRP and 10 degree GFRP/Balsa/GFRP with core thickness 3.0mm was valid for designing the musical instrument substitutes.

Conclusion

In this study, we proposed the heterogeneous numerical model as FRP was assumed to consist of fiber and resin. Proposed model was applied to 2 layered structures and sandwich structures. As a result, 25 degree CFRP/EVA foam, 35 degree CFRP/Balsa/CFRP and 10 degree GFRP/Balsa/GFRP with core thickness 3.0mm were effective for designing the musical instrument substitutes. It is thought that design and fabrication of guitar is possible by using this numerical model.

Reference

1. T.Nishiwaki, A.Yokoyama, Z.Maekwa and H.Hamada, Journal of Composite Structures, 32, 641 (1995)
2. T.Matsubara, T.Nishiwaki and Z.Maekwa, Journal of Textile Machinery Society of Japan, 53(11), 225 (2000)

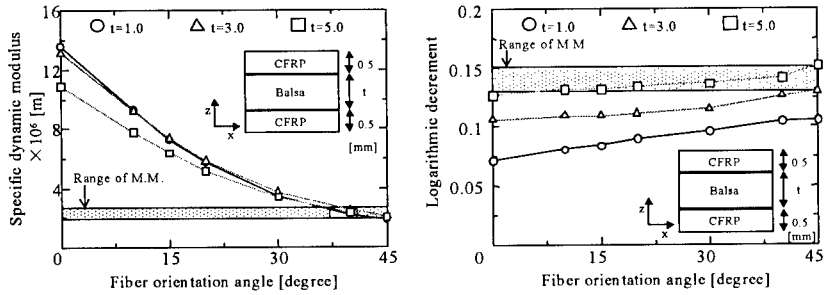

(a) Specific dynamic modulus (b) Logarithmic decrement

Fig.4 Analytical results obtained from the sandwich structure, CRRP/Balsa/CFRP, (a) specific dynamic modulus, (b) logarithmic decrement

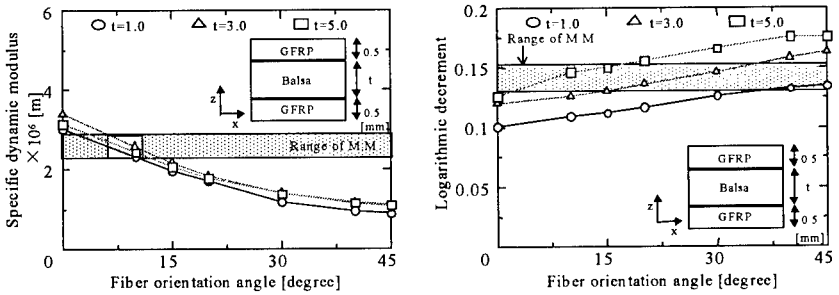

(a) Specific dynamic modulus (b) Logarithmic decrement

Fig.5 Analytical results obtained from the sandwich structure, GRRP/Balsa/GFRP, (a) specific dynamic modulus, (b) logarithmic decrement

Proceedings of 7th Japan International SAMPE
Symposium & Exhibition, Nov. 13-16, 2001

Prediction and Estimation of the Power of Thermoplastic Composite Tennis Racket

Yoshihiko Kawazoe #

#: Dept. of Mechanical Engineering, Saitama Institute of Technology,
1690 Fusaiji, Okabe, Saitama, 369-0293, JAPAN
E-mail: ykawa@sit.ac.jp

Abstract

It is heard that although a thermoplastic composite racket gives comfort feeling during tennis impact, it is inferior to the ordinary composite racket in power. This paper predicts and estimates the performance of thermoplastic composite and compares it with that of ordinary racket in terms of the restitution coefficient, the maneuverability, and the power. It is based on the experimental identification of the racket dynamics and the simple nonlinear impact analysis. The predicted results could explain the mechanism of difference in performance between the thermoplastic composite racket and the ordinary composite racket.

Key Words: Sports Engineering, Tennis Racket, Thermoplastic Composite

Introduction

At the current stage, very specific designs are targeted to match the physical and technical levels of each user. The optimum racket depends on the physical and technical levels of each user. Actually, however, the terms used in describing the performance of tennis rackets are based on the feeling of an experienced tester or a player. Accordingly, there are many unclear points regarding the relationship between the performance estimated by a player and the physical properties of a tennis racket. It is said that a thermoplastic composite racket gives comfort feeling during tennis impact, but it is inferior to the ordinary composite racket in power [1]. This paper predicts and estimates the performance of thermoplastic composite and compares it with that of ordinary racket in terms of the restitution coefficient, the maneuverability, and the power. It is based on the experimental identification of the racket dynamics and the simple nonlinear impact analysis [2-9].

Racket Physical Properties and Prediction of the Restitution of Coefficient between a Ball and a Racket

The main specifications and physical properties of the test rackets are shown in Table 1. The racket called FX-110TP is a thermoplastic(TP) composite racket (341 g including the weight of strings), while the racket called Ex-110 is a conventional composite racket (365 g including the weight of strings). The TP material is made of reinforced fiber and thin resin film. Standard modulus 12 K carbon fiber and a Nylon 6 based resin were selected for its suitable physical properties and cost balance [1].

In Table 1, the sign I_{GY} denotes the moment of inertia about the center of mass, the sign

Table 1 Specification and Physical Properties of Rackets.

Racket	FX−110TP	EX−110
Total length	685 mm	685 mm
Face area	705 cm^2	705 cm^2
Mass	341 g	366 g
Center of gravity from grip end	314 mm	325 mm
Moment of inertia I_{GY} about Y axis	36.3 gm^2	40.7 gm^2
Moment of inertia I_{GX} about X axis	1.40 gm^2	1.68 gm^2
1st frequency	127 Hz	132 Hz
Strings tension	55 lb	53 lb

I_{GX} the moment of inertia about the longitudinal axis of racket head.

Since the experimental modal analysis showed that the fundamental vibration mode of a hand-held racket is similar to the mode of a freely supported racket, it is assumed in terms of power that the racket is freely supported [2,7].

The impulse could be approximately derived using a model assuming that a ball with a concentrated mass and a nonlinear stiffness collides with the nonlinear spring of strings supported by a rigid frame, where the measured restitution coefficient e_{BG} inherent to the materials of ball/strings is employed as one of the sauce of energy loss. The contact time T_c could be derived, if it is determined by the natural period of a whole system composed of the mass m_B of a ball, equivalent compound stiffness K_{GB} of a ball and strings, and the reduced mass M_r of a racket.

On the basis of the approximation of the force-time curve of impact as a half-sine pulse and the application of its Fourier transform to the experimentally identified racket vibration model, the initial amplitude of racket vibration due to impact can be derived. The energy loss due to the racket frame vibration can be derived from the amplitude distribution of the velocity and the mass distribution along a racket frame.

The coefficient of restitution (COR) e_r between a ball and a racket can be estimated by considering the energy loss E_1 due to frame vibration as well as the energy loss E_2 due to large instantaneous deformation of the ball and strings. The coefficient of restitution e_r corresponds to the total energy loss E ($=E_1 + E_2$) could be obtained as

$$e_r = [1 - 2E(m_B + M_r) / (m_B M_r V_{BO}^2)]^{1/2} \quad (1)$$

Figure 1 shows a simple forehand ground stroke model used in this study. A player hits a coming ball V_{Bo} of the velocity with the racket head velocity V_{Ro} given by $L_X(\pi N_s / I_s)^{1/2}$, where the sign L_X denotes the distance between the player's shoulder joint and the impact location on the racket face, N_s the constant torque around the shoulder joint, and I_s the moment of inertia of arm/racket system around the shoulder joint.

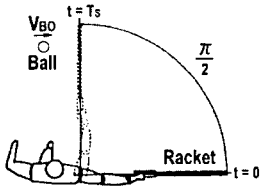

Fig.1 Simple forehand groundstroke swing model.

The predicted restitution coefficient e_r of a thermoplastic composite racket has been lower than that of a conventional composite racket, particularly at the off-center of the racket, where a player hits the ball (V_{Bo} = 10 m/s, N_s = 56.9 Nm).

Predicted Post-impact Ball Velocity and the Sweet Area in Terms of Power

Here we introduce the rebound power coefficient e defined by the ratio of rebound velocity V_B against the incident velocity V_{BO} of a ball when a ball strikes the freely supported racket at rest (V_{Ro} = 0) , written as Eq.(3) . The rebound power coefficient e can particularly estimate the rebound power of a racket for a volley.

$$e = -V_B / V_{BO} = (e_r - m_B/M_r)/(1+m_B/M_r) \quad (3)$$

When a player hits the ball with pre-impact racket head velocity of V_{Ro}, the coefficient e can be expressed as

$$e = -(V_B - V_{Ro}) / (V_{BO} - V_{Ro}) \quad (4)$$

Figure 2 shows the predicted rebound power coefficient e when a player hits the ball at the longitudinal axis and off the longitudinal axis (V_{Bo} = 10 m/s, N_s = 56.9 Nm). It also shows the sweet area with respect to the rebound power coefficient e.

The post-impact ball velocity V_B could estimate the power of the racket when a player hits the ball. The V_B can be expressed as Eq.(5).

$$V_B = -V_{Bo}\, e + V_{Ro}(1+e) \quad (5)$$

The predicted pre-impact racket head velocity V_{Ro} (N_s = 56.9 Nm) of a thermoplastic composite racket has been higher than that of a conventional composite racket.

Figure 3 shows the predicted post-impact ball velocity V_B when a player hits the ball at the longitudinal axis and off the longitudinal axis of the racket (V_{Bo} = 10 m/s, N_s = 56.9 Nm). It also shows the predicted sweet area with respect to the post-impact ball velocity V_B.

It is seen that the thermoplastic composite racket is lower than that of a conventional racket in terms of the post-impact ball velocity or power. However, there is no big difference.

Conclusions

It is said that a thermoplastic composite

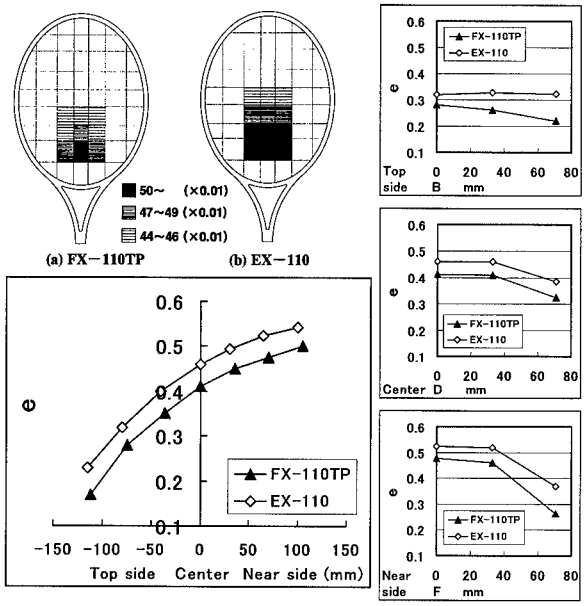

(a) on the longitudinal (b) off the longitudinal

Fig.2 Predicted rebound power coefficient e (N_S=56.9Nm, V_{BO}=10m/s)

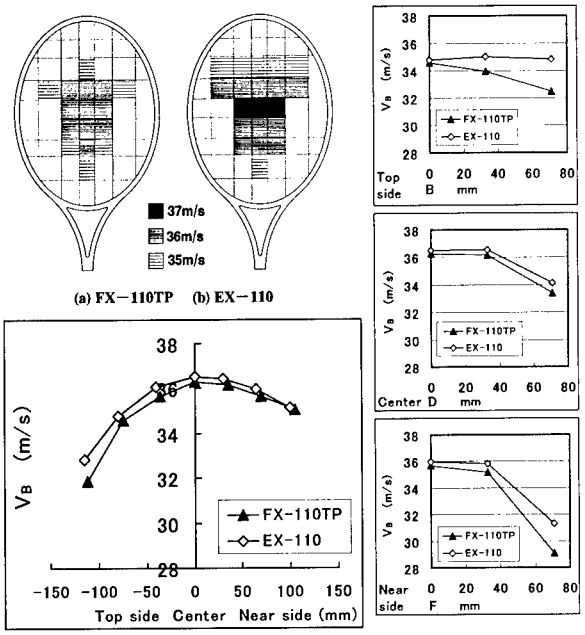

(a) on the longitudinal (b) off the longitudinal

Fig.3 Predicted post-impact ball velocity V_B

racket gives comfort feeling during tennis impact, but it is inferior to the ordinary composite racket in power. The predicted results could explain the mechanism of difference in power between the thermoplastic composite racket and the ordinary composite racket. Although the thermoplastic composite racket is lower than that of a conventional racket in terms of the post-impact ball velocity or power, there is no big difference between them.

Acknowledgment

This work was supported by a grant-in-Aid for Science Research B and a Science Research C of the Ministry of Education, Science, and Culture of Japan, and a part of this work was also supported by the High-Tech Research Center of Saitama Institute of Technology.

References

1. K. Muroi & Y. Shimizu, Proc. of 5th Japan International SAMPE Symp., 1317 (1997).
2. Y. Kawazoe, Dynamics and computer aided design of tennis racket. Proc. Int. Symp. on Advanced Computers for Dynamics and Design '89, 243(1989).
3. Y. Kawazoe, Theoretical and Applied Mechanics, Vol.41, 3(1992).
4. Y. Kawazoe, Theoretical and Applied Mechanics, Vol.42, 197(1993).
5. Y. Kawazoe, Theoretical and Applied Mechanics, Vol.43, 1994, pp.223-232.
6. Y. Kawazoe, *Science and Racket Sports*, E & FN SPON, 1994, pp.134-139.
7. Y. Kawazoe, Theoretical and Applied Mechanics, Vol.46, 1997, pp.165-176.
8. Y. Kawazoe, 5th Japan Int. SAMPE Symp., 1320 (1997).
9. Y. Kawazoe, Proc. of 6th Japan International SAMPE Symp, 783(1999).

Proceedings of 7th Japan International SAMPE
Symposium & Exhibition, Nov. 13-16, 2001

Estimation of the Improvement of the Shock vibrations at the wrist joint using the Thermoplastic Composite Tennis Racket

Yoshihiko Kawazoe #

#: Dept. of Mechanical Engineering, Saitama Institute of Technology,
1690 Fusaiji, Okabe, Saitama, 369-0293, JAPAN
E-mail: ykawa@sit.ac.jp

Abstract

It is reported that a tennis racket using thermoplastic composite with a thin flexible unidirectional tape prepeg (UD flex tape) has good damping characteristics and therefore gives soft impact feel to the player during tennis impact. This paper predicts and estimates the performance of thermoplastic composite and compares it with that of ordinary racket in terms of the shock vibrations at the wrist joint when a player hits the ball, which is closely related to the feel or comfort. It is based on the experimental identification of the racket/arm system and the simple nonlinear impact analysis. The predicted results could explain the mechanism of difference in the feel between the thermoplastic composite racket and the ordinary composite racket.

Key Words: Tennis Racket, Thermoplastic Composite, Feel

Introduction

It is reported that a tennis racket using thermoplastic composite with a thin flexible unidirectional tape prepreg (UD flex tape) has good damping characteristics and therefore gives soft impact feel to the player during tennis impact [1]. This paper predicts the performance of thermoplastic composite racket and compares it with that of ordinary racket in terms of the shock vibrations at the wrist joint when a player hits the ball, which is closely related to the feel or comfort. It is based on the experimental identification of the racket/arm system and the simple nonlinear impact analysis [2-12]. The details of specifications and physical properties of the test rackets are shown in literature [2]. The racket called FX-110TP is a thermoplastic (TP) composite racket (341 g including the weight of strings), while the racket called Ex-110 is a conventional composite racket (365 g including the weight of strings). The TP material is made of reinforced fiber and thin resin film. Standard modulus 12 K carbon fiber and a Nylon 6 based resin were selected for its suitable physical properties and cost balance [1].

Prediction of the Waveforms of Shock Vibrations at the Grip and at the Wrist Joint

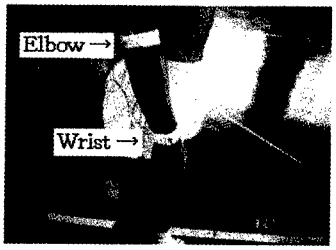

Fig.2 Location of Wrist joint

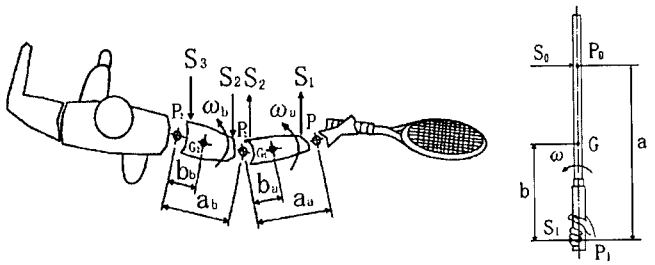

Fig.1 Impact model for the prediction of the shock force transmitted to the arm joints from a racket.

Figure 1 shows an impact model for the prediction of shock forces transmitted to the arm joints from a racket, where a male tournament player hits flat forehand drive. Figure 2 shows the locations of attached accelerometers at the wrist joint and the elbow joint in the experiment.

The impact force S_0 at P_0 causes a shock force S_1 on the player's hand P_1, a shock force S_2 on the elbow P_2, and finally a shock force S_3 on the player's shoulder P_3 during the impact at which the player hits the ball with his racket. The gravity force and muscular action are not taken into account. Accordingly, we consider the racket to be freely hinged to the forearm of the player, the forearm being freely hinged to the arm and the arm freely hinged to the player's body. We can deduce that the inertia effect of the arm and the forearm can be attributed to a mass M_H concentrated in the hand; therefore the analysis of impact between ball and racket can be carried out by assuming that the racket is free in space, as long as the mass M_H is applied at point P_1 of the hand grip. If the impact force S_0 between a ball and the racket is given when the ball hits the racket, the shock force S_1 can be obtained [10-12].

The vibration characteristics of a racket can be identified using the experimental modal analysis and the racket vibrations can be simulated by applying the approximate impact force-time curve to the hitting portion on the string face of the identified vibration model of the racket. When the impact force component of k-th mode frequency f_k in the frequency region applies to the point j on the racket face, the amplitude $X_{ij\,k}$ of k-th mode component at point i can be derived using the residue $r_{ij\,k}$ of k-th mode between arbitrary point i and j. The energy loss due to the racket vibration induced by impact can be derived from the amplitude distribution of the vibration velocity and the mass distribution along a racket frame when an impact location on the string face and the impact velocity are given. The coefficient of restitution e_r (COR) can be derived considering the energy loss E during impact. Furthermore, the force-time curve of impact between a ball and a racket considering the vibrations of a racket frame can be approximated.

$$S_0(t) = S_{0\,max} \sin(\pi t / T_c) \quad (0 \leqq t \leqq T_c) \quad (1)$$

where

$$S_{0\,max} = (\pi/(2T_c))(V_{BO} - V_{Ro})(1 + e_r)\, m_B/(1 + m_B/M_r). \quad (2)$$

The contact time T_c during impact can be determined against the pre-impact velocity ($V_{BO} - V_{Ro}$) between a ball and a racket assuming the contact time to be half the natural period of a whole system composed of the mass m_B of a ball, the equivalent stiffness K_{GB} of ball/strings, and the reduced mass M_r of the racket.

The shock acceleration $A_{nv}(t)$ at the hand grip considering the equivalent mass M_H of the arm system can be represented as

$$A_{nv}(t) = S_0(t)\,[1/(M_R + M_H) - (a/I_G)X] \quad (3)$$

where X denotes the distance between the center of mass of racket-arm system and the

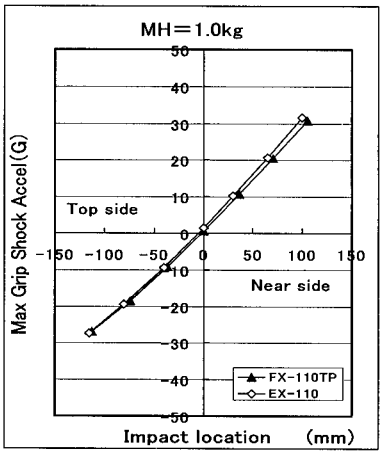

location of hand grip, a the distance between the center of mass of racket-arm system and the impact location of the racket, I_G the moment of inertia around the center of mass of racket-arm system, respectively. The maximum shock force S_{1max} transmitted to a wrist joint corresponds to the maximum impact force S_{0max}. Figure 3 shows the predicted maximum shock acceleration at the grip of hand-held racket. There is no big difference between two rackets. The vibration acceleration component of k-th mode at the location i of handgrip is represented as

$$A_{ij,k}(t) = -(2\pi f_k)^2 r_{ijk} S_{0j}(2\pi f_k) exp(-2\pi f_k \zeta_k t) sin(2\pi f_k t) \quad (4)$$

Fig.3 Predicted Maximum shock acceleration at the grip.

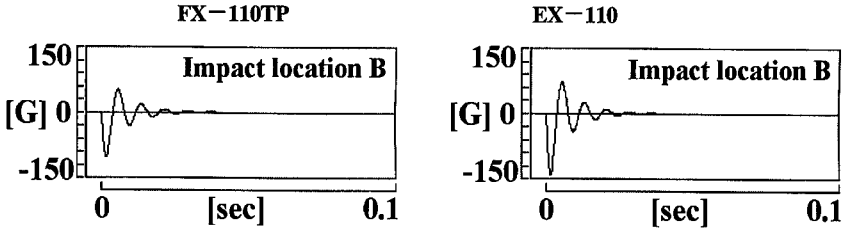

(a) Predicted shock vibrations at the wrist joint (Impact location : Top side B)

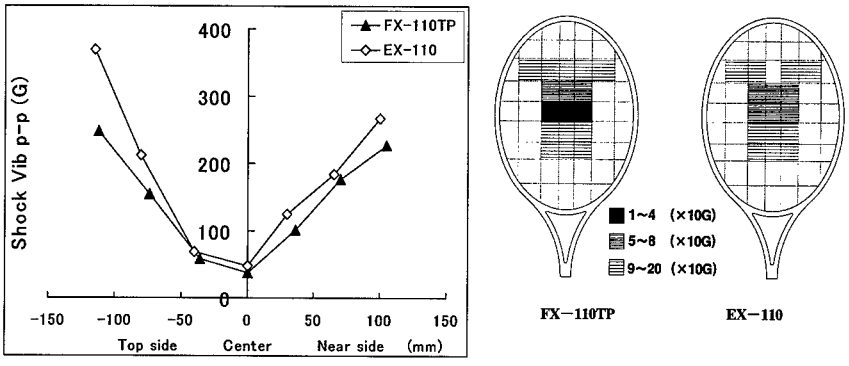

(b) Shock vibrations peak value at the wrist vs. impact locations (Impact velocity : 30m/s)

Fig.4 predicted shock vibrations at the wrist joint.

where j denotes the impact location between ball and racket on the string face, ζ_k the damping ratio of k-th mode, $S_{0j}(2\pi f_k)$ the fourier spectrum of Eq.(1).
The summation of Eq.(3) and Eq.(4) represents the shock vibrations at the handgrip.
Figure 4 shows the predicted shock vibrations of a wrist joint. Figure 4(a) is a comparison of two rackets when a ball strikes a racket face on the topside. The impact velocity between a ball and a racket face is 30 m/s. The damping ratio of a hand-held racket in the actual impact is estimated as about 2.5 times that of the one identified by the experimental modal analysis with small vibration amplitude. Furthermore, the damping of the waveform at the wrist joint was 3 times that at the grip portion of the racket handle. Figure 4(b) shows the shock vibrations peak value (Fig 5) at the wrist against the longitudinal impact locations on the racket face (Impact velocity : 30m/s). It also shows the predicted sweet area with respect to the shock vibrations at the wrist joint.
The shock vibrations of thermoplastic composite racket is smaller than those of conventional racket. It is predicted to be comfort when the ball is hit with.

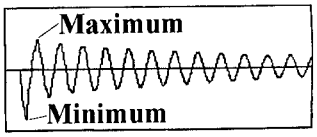

Fig.5 Peak- peak value of the wave form.

Conclusions

This paper has investigated the tennis racket performance in terms of the feel or comfort. It predicted the effect of the thermoplastic composite rackets on the impact shock vibrations of racket handle and the player's wrist joint when a player hits flat forehand drive. The prediction is based on the identification of the racket characteristics, the damping of the racket-arm system, equivalent mass of the player's arm system and the approximate nonlinear impact analysis in tennis. The predicted results could explain the mechanism of difference in the feel between the thermoplastic composite racket and the conventional composite racket. The result of the comparison shows that the shock vibration of the thermoplastic composite racket is smaller than that of the conventional racket. It is predicted to be comfort when the ball is hit with.

Acknowledgment
This work was supported by a grant-in-Aid for Science Research B and a Science Research C of the Ministry of Education, Science, and Culture of Japan, and a part of this work was also supported by the High-Tech Research Center of Saitama Institute of Technology.

References
1. K. Muroi & Y. Shimizu, Proc. of 5th Japan International SAMPE Symp., 1317 (1997).
2. Y. Kawazoe, Proc. of 7th Japan International SAMPE Symp, (2001). to be appeared.
3. Y. Kawazoe, Dynamics and computer aided design of tennis racket. Proc. Int. Symp. on Advanced Computers for Dynamics and Design '89, 243(1989).
3. Y. Kawazoe, Theoretical and Applied Mechanics, Vol.41, 3(1992).
4. Y. Kawazoe, Theoretical and Applied Mechanics, Vol.42, 197(1993).
5. Y. Kawazoe, Theoretical and Applied Mechanics, Vol.43, 1994, pp.223-232.
6. Y. Kawazoe, *Science and Racket Sports*, E & FN SPON, 1994, pp.134-139.
7. Y. Kawazoe, Theoretical and Applied Mechanics, Vol.46, 1997, pp.165-176.
8. Y. Kawazoe, 5th Japan Int. SAMPE Symp., 1320 (1997).
9. Y. Kawazoe, Proc. of 6th Japan International SAMPE Symp, 787(1999).
10. Casolo,F. & Ruggieri, G., *Meccanica*, Vol.24, 1991, pp.501-504.
11. Y. Kawazoe & K. Yoshinari, *Tennis Science & Technology*, Blackwell Sciences, 2000, pp.91-99.
12. Y. Kawazoe, Theoretical and Applied Mechanics, Vol.49, 2000, pp.11-19.

Proceedings of 7th Japan International SAMPE
Symposium & Exhibition, Nov. 13-16, 2001

Processing and Properties of Carbon Fiber Reinforced Composites with New Amorphous, Asymmetric, Addition Type Polyimides (Triple A-PI)

Toshio Ogasawara [#1], Rikio Yokota [#2], Yu Shigenari [#3], Kiyoshi Miyagawa [#3], Hideki Ozawa [#4], Mitsushi Taguchi [#4], and Takashi Ishikawa [#1]

#1: National Aerospace Laboratory of Japan (NAL)
6-13-1, Osawa, Mitaka-shi, Tokyo, 181-0015, JAPAN
#2: Institute of Space and Astronautical Science (ISAS)
3-1-1 Yoshinodai, Sagamihara-shi, Kanagawa, 229-8510, JAPAN
#3: IHI Aerospace Co., Ltd.
900, Fujiki, Tomioka-shi, Gunma, 370-2398, JAPAN
#4: Ube Industries, Ltd.
8-1, Goi-minamikaigan, Ichihara-shi, Chiba, 290-0045, JAPAN
E-mail: ogasat@nal.go.jp

Abstract

This paper presents experimental results for the processing and mechanical properties of carbon fiber reinforced composites with newly developed amorphous, asymmetric, and addition type polyimides (Triple A-PI). The imide oligomers were synthesized from the reaction of 2,3,3',4'-biphenyltetracarboxylic dianhydride (a-BPDA), 4,4'-oxydiaminine (ODA), and phenylethynyl phthalic anhydride (PEPA). Even though the molecular weight of the imide oligomer is relatively low, the cured polymer exhibits excellent mechanical properties because of its irregular and asymmetric structure. Unidirectional carbon fiber reinforced composites were fabricated by prepreg consolidation. The composites exhibit high glass transition temperature, and excellent shot beam shear strengths at elevated temperature compared to PETI-5.

Key Words: Asymmetric imides, Composite

Introduction

The phenylethynyl terminated polyimide, PETI-5 developed by NASA Langley Research Center (LaRC) possesses good processability and excellent mechanical properties in an adhesive and composite matrix resin [1-3]. Undoubtedly, PETI-5 is one of the most excellent matrix materials for high temperature polymer composites up to 200 °C.

Recently, new addition type polyimides were developed from the reaction of 2,3,3',4'-biphenyl-tetracarboxylic dianhydride (a-BPDA), diaminine, and phenylethynyl phthalic anhydride (PEPA) [4,5]. The new polyimides are referred to as "Triple A-PI (TA-PI)" from the characteristics of the polymer (amorphous, asymmetric, and addition type). Both the imide oligomers and cured polymers have significantly irregular and asymmetric structure derived from asymmetric (a-) BPDA. Therefore, even though the

molecular weigh of the imide oligomer is relatively low, the cured polymer exhibits excellent mechanical properties, with high glass transition temperature (Tg>300°C) [4,5].

This paper presents experimental results for processing and mechanical properties of carbon fiber reinforced composites with "Triple A-PI". It is known that the lower molecular weight oligomer had the lower melt viscosity, when cured, the higher Tg, and lower fracture toughness. Therefore, the effect of oligomer molecular weight on the composite properties was also investigated.

Experimental Procedure

Synthesis of Triple A-PI

The synthetic scheme for the imide oligomer is shown in Fig. 1. a-BPDA (2,3,3',4'-BPDA, mp 172°C), 4,4'-ODA (mp 187°C), and PEPA (mp 151°C) were used as-received. The imide oligomers with different molecular weight (calc. 1578 (n=2.5), 2494 (n=4.5), and 5245 g/mol (n=10.5)) were synthesized. Detailed descriptions regarding the synthesis of the imide oligomer were reported elsewhere [4,5].

The dynamic rheological behaviors of the imide oligomers were determined by a Rheometrics RDS-II dynamic rheometer at a heating rate of 3°C/min. The compacted resin disk was loaded in parallel plates with 7.9 mm diameter. The top plate was oscillated at a fixed strain of 10 %, and a fixed frequency of 10 Hz.

Processing of composites

The amide acid / NMP (N-methyl-2-pyrrolidinone) solutions were impregnated into Toray T-800 carbon fiber (12K/bundle). The properties of the unidirectional prepreg tapes and imide oligomers are summarized in Table 1. Unidirectional (UD) composites were fabricated in an autoclave. In order to obtain a well-consolidated T800/TA-PI composite, the solvent (NMP) and reaction by-products (H_2O) should be removed before applying pressure. For the purpose, the prepreg was held at 250°C for 0.5 hr. Subsequently, pressure (0.3 MPa) was applied and the temperature was increased to 370°C and held for 1 hr.

Evaluation of Mechanical Properties

Dynamic mechanical analyses (DMS) for the unidirectional (UD) composites were performed on Rheometrics RSA II. A beam specimen, 2 mm in width, 1.1 mm in thickness, 56 mm in length, was prepared, and three point bending load with 48 mm span width was applied at a fixed strain of

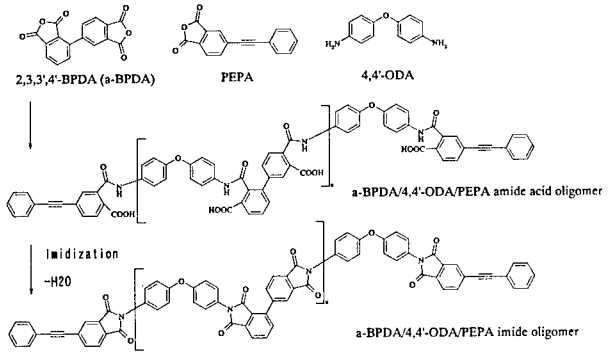

Fig.1 Synthetic scheme of the imide oligomers from the reaction of a-BPDA, 4,4'-ODA, and PEPA

0.02% and a fixed frequency of 1 Hz under a constant heating rate of 3.75 °C/min. The storage (E'), loss (E") moduli, and tan δ were measured as a function of temperature. Short beam shear strength (ASTM D2344) was determined on 12 ply specimens (12mm length, 6.35mm width, 2.2mm thickness) at RT, 177, and 300 °C. Five composite specimens were tested under each condition. Three point flexural strength (ASTM D790, span width 25 mm) was determined on 6 ply specimens (70 mm length, 12.7 mm width, 1.1 mm thickness) at RT. Three composite specimens were tested.

Table 1 Oligomer, Prepreg and Composite Properties

	n=2.5	n=4.5	n=10.5
Molecular weight (calc.), Mn	1578	2494	5245
Imide oligomer Tg, (°C) *	189	230	237
Imide oligomer minimum melt viscosity (Pa sec)	3.4 (336°C)	124 (347°C)	1750 (369°C)
Cured polymer Tg, (°C) *, **	351	341	308
Prepreg solids (wt %)	36.4	30.4	
Prepreg volatiles (wt %)	15.6	15.3	
Carbon fiber areal weight (g/m^2)	240	240	
Prepreg areal weight (g/m^2)	365	350	
Composite fiber fraction (vol. %)	64.2	69.6	
Composite porosity (vol. %)	0.8	4.0	

* Estimated by DSC technique
** Cured at 370°C for 1 hr.

Results and Discussion

Rheological Properties of Imide Oligomers

The dynamic rheological behaviors of the imide oligomers are shown in Fig.2. The minimum viscosities were 3.4, 124, and 1750 Pa sec for oligo-2.5 (Mw~1578), -4.5 (Mw~2494), and -10.5 (Mw~5245), respectively, which corresponded to the viscosities reported for PETI-5 (5.0, 90, and 1000 Pa sec for Mw~1250, ~2500, and ~5000) [3]. It should be noticed that the melt viscosities above 310°C are not stable because of the phenylethynyl group reaction, and the melt viscosity below 310°C is more important for actual composite processing than the minimum viscosity. Therefore, lower molecular weight is suitable to improve processbility.

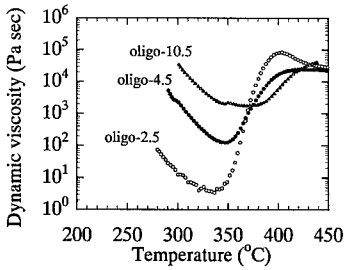

Fig. 2 Dynamic viscosity of the imide oligomers (n=2.5, 4.5, 10.5)

Mechanical Properties of UD-Composites

The lower molecular weight oligomer is expected that it had a higher Tg and lower mechanical properties, because of the higher crosslink density. In this study, the UD-composites with oligo-2.5 and -4.5 were fabricated, and mechanical properties were investigated. Fig.3 shows a DMA trace of the T800/TA-PI composites. The estimated Tg determined from E' by setting up tangents to the linear portion of the curve before and after the modulus drop off was approximately 320°C and 290°C for the TA-PI(2.5) and TA-PI(4.5) composites, respectively. Short beam shear strengths for the T800/TA-PI (2.5, 4.5) and IM7/PETI-5 composites are shown in Fig.4 [2]. The T800/TA-PI(2.5) composite exhibites higher SBS strength at elevated temperature, which attributes to higher Tg as well as proper fiber volume fraction compared to the TA-PI (4.5) composite. Although thermoplastic deformation was slightly observed before

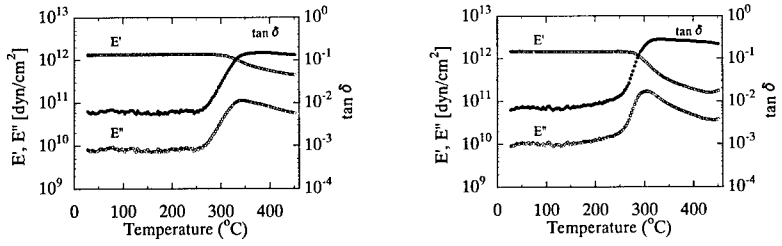

(a) T800/ TA-PI(2.5)

(b) T800/TA-PI(4.5)

Fig. 3 Dynamic Mechanical Analysis (DMS) trace of the Unidirectional T800/TA-PI Composites.

interlaminar fracture at 300°C, the apparent SBS strengths for the T800/TA-PI composites were quite excellent. Flexural strengths of the TA-PI(2.5) and TA-PI(4.5) composites were 2151 MPa, and 2194 MPa, respectively. In spite of high crosslink density due to low molecular weight, the T800/TA-PI composites exhibit excellent mechanical properties. It is supposed that the irregular and asymmetric structure of Triple A-PI produces excellent mechanical properties such as fracture toughness, and elongation to failure.

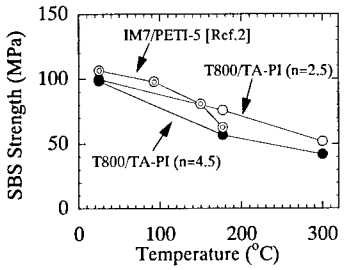

Fig. 4 Short Beam Shear (SBS) Strength of the T800/TA-PI (2.5, 4.5) and IM7/PETI-5 Composites.

Conclusion

Processing and mechanical properties of the T800/TA-PI composites were investigated. In spite of low molecular weight (<2500), the T800/TA-PI composites exhibit excellent shot beam shear strengths at elevated temperature with high glass transition temperature. This is due to the irregular and asymmetric structure of the TA-PI polymer derived from a-BPDA.

Acknowledgement

The authors wish to sincerely thank Mr. Asano, Mr. Koike, and Mr. Machii of Arisawa Manufacturing Co., Ltd. for the development of prepreg processing.

References

1. P. M. Hergenrother, and J. G. Smith, Jr, Polymer, 35(22), 4857 (1994)

2. T. H. Hou, B. J. Jensen and P. M. Hergenrother, *J. Comp. Mater.*, 30[1], 109-122 (1996)

3. J. G. Smith, Jr., J. W. Connell, and P. M. Hergenrother, *J. Comp. Mater.*, 34[7], 614-628 (2000)

4. R. Yokota, S. Yamamoto S. Yano, T. Sawaguchi, M. Hasegawa, H. Yamaguchi, H. Ozawa, and R. Sato, *Proc. of 7th Int. Conf. on Polyimides in Electronic Packing, The Society of Plastics Engineers, Oct. 16-18,* (2000)

5. R. Yokota, S. Yamamoto S. Yano, T. Sawaguchi, M. Hasegawa, H. Yamaguchi, H. Ozawa, and R. Sato, *High Perform. Polym.*, 13, S61-S72 (2001)

Proceedings of 7th Japan International SAMPE
Symposium & Exhibition, Nov. 13-16, 2001

Cyanate Ester Resin Formulations for Aerospace Applications

Akio Oshima#, Hiroyasu Ihara# and Tetsuji Watanabe#

Masaaki Shinagawa## and Hiroshi Onoda##

#: Central Technical Research Laboratory, Nippon Mitsubishi Oil Corporation
8, Chidori-cho, Naka-ku, Yokohama, Kanagawa, 231-0815 Japan
E-mail : tetsuji.watanabe@nmoc.co.jp

##: Carbon Fiber Business Division, R&D Department
Nippon Mitsubishi Oil Corporation
3-12, Nishi Shimbashi 1-Chome,Minato-ku, Tokyo, 105-8412 Japan

Abstract

Cyanate ester is used as the matrix resin for CFRP, especially for aerospace applications that need low moisture pick-up. Nippon Mitsubishi Oil Corp. (NMOC) has developed new cyanate ester resin formulations suitable for prepregs and for resin transfer molding (RTM). The new formulations have good handleability and processability, without compromising the inherent properties of the cyanate resin. The neat resin properties before and after curing will be discussed in comparison with the epoxy resin system, and the mechanical properties of the composites will be described using high modulus PAN and pitch-based carbon fibers.

Key Words: Cyanate ester, Prepreg, RTM, Matrix

Introduction

The use of carbon fiber reinforced plastics (CFRP) for satellite parts is increasing because of their light weight, near-zero coefficient of thermal expansion (CTE) and other advantages compared to metals. The carbon fiber mainly provides the mechanical properties, such as strength, modulus, and CTE, while the matrix resin contributes to the heat resistance, moisture absorption, and so on. Before 1990, epoxy resin systems were usually chosen and used because of their availability, low cost and proven track record. But because of its relatively high moisture pick-up, epoxy resin sometimes showed poor dimensional stability and also caused problems with optical and electrical instruments. In the 1990's, cyanate resin matrixes began to be used for specific parts of satellites because of the lower moisture absorption. Although the cost of cyanate resin was much higher than that of epoxy and it is still expensive now, cyanate resin is widely used in aerospace applications. But prepregs made with cyanate resins are not comparable with epoxy prepregs in terms of their handleability, processability or shelf life. To resolve these issues, NMOC has developed

two cyanate resin systems for prepregs and another system for RTM.

Results and Discussions

The designations of the newly developed cyanate ester resin formulations are shown in Table 1. NM20 is the 180°C cured formulation for RTM. NM25 and NM31 are both used for prepregs and are the 130°C and 180°C cured types, respectively. The 180°C cured systems (NM20 and NM31) can be used in parts that need high service temperatures around 180°C. The 130°C cured type (NM25) is for parts that do not require high Tg. Curing at 130°C leads to lower processing costs and smaller residual stress in the CFRP.

Table 1 Cyanate Resin Formulations

	Application	Cure condition
NM20	RTM	180°C x 2h
NM25	Prepreg	130°C x 3h
NM31	Prepreg	180°C x 2h

Temperature-Viscosity Properties

Viscosity is an important property for resin systems both for prepregs and for RTM. The temperature-viscosity curve was measured with a rheometer (Rheometrics, RDS-II) in the parallel plate mode. The rate was 10 Hz, and the ramp rate was 2°C/min. Fig. 1 shows the comparison of the temperature-viscosity curves of the several formulations (#1, #2 and #3) and NM31. #1 and #2 resins were less tacky in a prepreg at the room temperature, and #3 was too tacky. The excess resin flow was observed by #1 and #3 formulations during the usual auto clave curing. Improving on these properties, NM31 has a lower viscosity at room temperature than #1 and #2, and higher minimum viscosity compared to #1 and #3 formulations. The differences in the viscosity values were not very large, adequate tack and drapability were obtained, and the resin flow was controlled well.

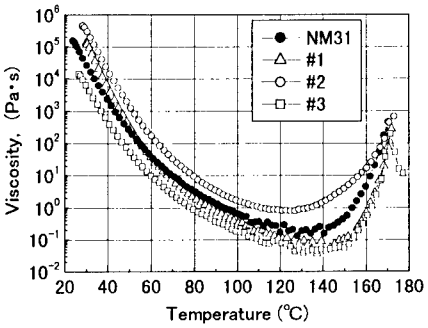

Fig. 1 Temperature-Viscosity Curve of NM31

Figure 2 shows the temperature-viscosity curves of NM25 for prepreg and NM20 for RTM. NM25 had almost the same viscosity as NM31 at room temperature, so the tack and drapability of the prepreg were adequate. There was no problem with excess resin flow with NM25 because the cure reaction started at a lower temperature and the minimum viscosity was much higher than for NM31. For RTM, a low viscosity is required during the resin transfer. The viscosity of NM20 is about six orders lower than that of the resins for the prepreg. It enables the production of RTM at low temperatures; this results in a longer pot life of the resin, and the resin can therefore be adopted for large structural moldings.

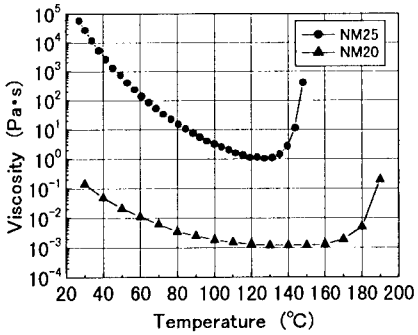

Fig 2 Temperature-Viscosity Curve of NM25 and NM20

Glass Transition Temperature (Tg)

The Tg value was measured using a DSC (Seiko Instruments, DSC-200) with a ramp rate of 20°C/min. The Tg was determined to be the midpoint of the transition range. Table 2 shows the Tg values of the 180°C cured resins. As shown in Table 1, the cure condition both for NM20 and NM31 was 180°C x 2h. The post curing was conducted at 232°C (450°F) x 2 h to get higher thermal resistance. The Tg of both resins was raised to 240°C by post curing; this is a very high level for thermoset resins.

Table 2 Tg of Cured Resins (180°C cure)

	NM20	NM31
180°C x 2h	170	188
232°C x 2h Post Cure	240	246

Table 3 shows the Tg of the 130°C cured type, that is, NM25 cured at 130°C x 3h. The level of the Tg is in the acceptable range for parts that do not need heat resistance.

Table 3 Tg of Cured Resin (130°C cure)

	NM25
130°C x 3h	145
180°C x 1h Post Cure	165

Flexural Test of the Cured Resin

Sometimes it is difficult to prepare a large specimen only from a neat resin without defects such as small voids, so the test results for large specimens tend to vary widely. In this developmental work, a small specimen (60 x 3 x 3 mm) was used to minimize the deviation in the flexural test. The span was 30 mm, L/D=10, and the crosshead speed was 1 mm/min. Table 4 and Fig. 3 show the results of the flexural test of the cured neat resins. NM20 and NM25 have good strain values of about 6%. The strength and strain values of NM31 are lower than those of the other two resins, but as described below there is no problem with the composite properties.

Table 4 Flexural Properties

		NM20	NM25	NM31
Strength	MPa	150	144	133
Modulus	GPa	3.0	3.1	3.2
Strain	%	6.0	6.3	4.7

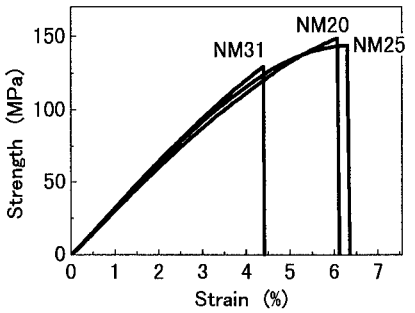

Fig. 3 Flexural Test of Cured Resin

Flexural Properties of Post Cured Resins

Fig. 4 shows the effect of the post curing on the flexural properties. Better strain and strength values were observed as a result of the post curing. In the case of conventional epoxy resin, the strength and strain are usually reduced by post curing. This point is thus an advantage of the cyanate resin with high thermal resistance by post curing.

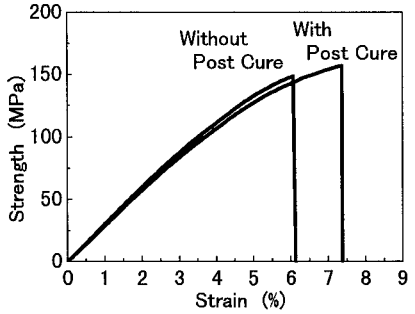

Fig. 4 Flexural Test of NM20

Moisture Absorption

The moisture absorption properties of the cured cyanate resins were compared with the conventional epoxy resin at room

temperature and 50% relative humidity. Fig. 5 shows the results for NM31 and the epoxy resin. The moisture absorption of cyanate reaches equilibrium much faster than that of the epoxy; the value was between 0.2 – 0.3% for the three developed resin systems.

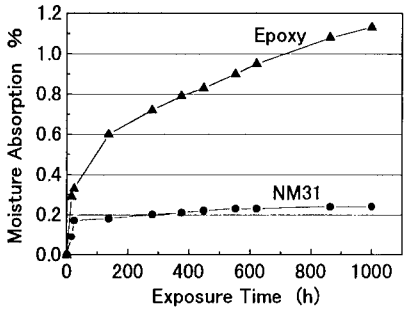

Fig. 5 Moisture Absorption of Cured Resins (25℃, 50% RH)

Mechanical Properties of the Composites

The pitch-based carbon fiber YSH-50A-60S from Nippon Graphite Fiber Corp. and the PAN-based carbon fiber M60J from Toray were chosen to confirm the mechanical properties of the CFRP.

Table 5 Mechanical Properties of YSH-50A/NM25

Fiber		YSH-50A-60S	
Resin		NM25	25P*
0 ° Tensile Strength	MPa	2080	2080
Modulus	GPa	321	317
Elongation	%	0.58	0.57
0 ° Compressive Strength	MPa	525	529
Modulus	GPa	262	265
Elongation1	%	0.34	0.31
0 ° Flexural Strength	MPa	925	936
Modulus	GPa	239	255
Elongation1	%	0.44	0.41
ILSS	MPa	82	84

*25P is the epoxy resin matrix from NMOC

Table 6 Mechanical Properties of M60J/NM25

Fiber		M60J	
Resin		NM25	#2500*
0 ° Tensile Strength	MPa	2220	2010
Modulus	GPa	360	365
Elongation	%	0.59	0.60
0 ° Compressive Strength	MPa	838	785
Modulus	GPa	334	-
Elongation1	%	0.28	-
0 ° Flexural Strength	MPa	1186	1080
Modulus	GPa	296	305
Elongation1	%	0.40	-
ILSS	MPa	79	69

*The values in the right column are the catalogue values from Toray, using #2500 epoxy resin matrix.

There was no apparent difference between the values with NM25 and epoxy matrix, thus confirming the good properties of the cyanate resin. Mechanical tests of YSH-50A/NM31 were also conducted and almost the same properties were confirmed.

Conclusions

New cyanate resin formulations for carbon fiber prepreg and RTM were developed. The resins for the prepreg have good handleability and processability, with the inherent good properties of low moisture absorption. Tests of the mechanical properties of CFRP using the other fibers, especially high modulus fibers, will be conducted in the near future. The RTM process with cyanate resin is still not popular, but the CFRP properties must be tested in comparison with epoxy resin.

Proceedings of 7th Japan International SAMPE
Symposium & Exhibition, Nov. 13-16, 2001

A Low Temperature Cure Material For Large Scale Prototype Model Construction

Kazutami MITANI#, Shigetsugu HAYASHI and Koki WAKABAYASHI

#: Products Development Laboratories, Mitsubishi Rayon Co. Ltd.,
4-1-60 Sunadabashi, Higashi-ku, Nagoya, Aichi 461-8677, JAPAN
E-mail: mitani_ka@mrc.co.jp

Abstract

A new low temperature cure material, #850, was introduced. #850 can be initial cured at 80°C and be free-standing postcured at 180°C. It can be used for high temperature applications, because glass transition temperature of postcured #850 laminate is as high as 195°C. #850 is suitable for molding a large scale and complex shaped composite part, for its prepreg life is longer than 30 days despite its low temperature curability. Using #850 prepreg system is quite cost effective especially for small volume manufacturing such as prototype model construction, because it gives void free composite by a conventional vacuum bag only molding process in which a low cost wooden mold can be used because of the low initial cure temperature.

Details of processing including heat generation and cure shrinkage are discussed. Mechanical and thermal performance UD prepreg laminates are also presented.

Key Words: Prepregs, Vacuum Bagging, Low Temperature Cure

Introduction

Carbon fiber composite are widely used in the fields of sporting goods and high-speed industrial machines as well as aerospace industries, where both low weight and high strength are desired. Historically, the cost of manufacturing composite parts has become relatively high, because recent market pressure and carbon fiber manufacturer's efforts are leading to the cost reduction of carbon fiber. To better exploit the vast applications of this high performance material, manufacturing processes (resins and methods) require cost effective processing without sacrificing the high performance of the fibers and the matrix. This combination of best material and lowest cost processing is being vigorously pursued on a global basis.

Low temperature curable prepreg is the latest solution for this purpose [1, 2]. Tooling cost should be estimated as the cost divided by the number of parts produced with one tooling effort. If more than one hundred parts are produced, the cost of tooling would not be a significant problem. But, if only one or two parts are manufactured with one tooling (as is the case of prototype programs), the reduction of tooling cost has a significant impact. Low temperature curable prepreg reduces the tooling cost by employing wooden or plaster tools instead of metal ones. However, the application of the low temperature curable prepreg (which can be molded with low cost wooden tools) has been

rather limited due to its high temperature performance and prepreg life, each of which is generally limited as compared with conventional autoclave cure prepregs.

In the early 1990s, the first long out time low temperature curing system, #820, was introduced, with a 4 weeks long out time at room temperature. #820 was welcomed by the market not only for its low temperature cure property, 80°C×5 hours or 90°C×2 hours, but also for its high mechanical properties which were equal to conventional 120°C cure systems such as MRC #340 resin system. Low temperature cure property was further improved by #830, which can be cured at 70°C within 3 hours maintaining 4 weeks long out time. #830 was used for the construction of the America's Cup class yacht by vacuum bag molding.

In 2000, a new low temperature curable system with high temperature performance, #850, was introduced. Typical cure cycle of #850 is 5 hours at 90°C in a vacuum bag followed by a freestanding post-cure at 180°C (about 350°F) for 4 hours. With this post-cure, #850 obtains excellent high temperature properties, and the extended prepreg out time (> 4 weeks) of #850 enables this material to be used for large-scale composite structures often found in aerospace applications.

EXPERIMENTAL

Materials

#850 is a proprietary epoxy resin of Mitsubishi Rayon Co. TR30M is an aerospace grade standard modulus PAN based carbon fiber from Mitsubishi Rayon Co. Unidirectional prepreg was made by hot-melt (non-solvent) process.
The UD prepreg has an areal fiber weight of 190 g/m2 and resin content of 34% by weight.

Laminate Molding Procedure

Conventional lay-up procedure and bag style can be applied to #850.
The following cure cycle was employed. The mold was heated from room temperature to 60°C in 1 hour, and held at 60°C for 1 hour, followed by heating up to 100°C in 1 hour, and a 5 hours hold at 100°C. The dwell at 60°C is recommended to ensure the temperature uniformity for large-scale molding.
For freestanding post-cure, the laminate was heated as it took 1 hour to reach 100°C, and 16 hours to reach 180°C, then it was held at that temperature for 4 hours.
Detail in the laminate molding procedure was reported in the previous paper[3].

Testing

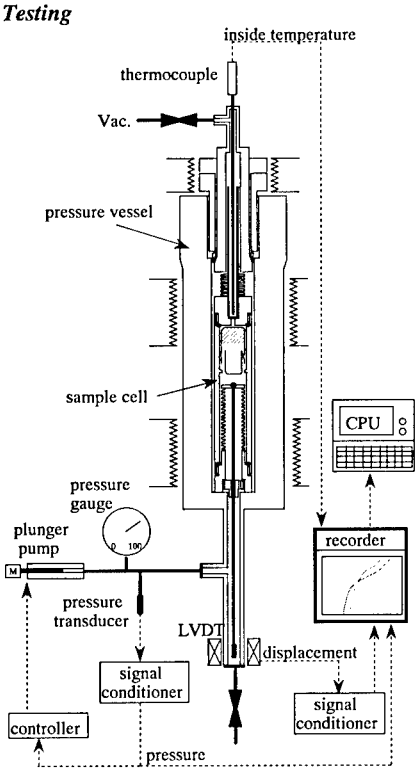

Fig.1 Schematic Diagram of the P-V-T Apparatus

Cure shrinkage of the #850 resin was measured with a P-V-T apparatus, which was designed by one of the authors [4].

The sample resin is confined in the sample cell of the P-V-T apparatus with mercury as show in Fig. 1, and cure shrinkage is detected as stretching of the bellows of the sample cell.

Cure cycle of 5 hours at 90°C or 15 hours at 80°C followed by post-curing at 180°C for 4 hours was applied under 10MPa. Heating rate was fixed at 1K/min for cure the shrinkage measurement.

Other testing procedures were as detailed in [3].

RESULTS and DISCUSSION

Heat Generation by DSC

DSC curve at the rate of 10K/min has a sharp peak at 170°C with an onset point at 150°C, giving total exotherm of 530 J/g. With the slower scanning rate of 5K/min, peak temperature and onset point were observed to shift down to 126°C and 104°C respectively. However, the total exotherm was observed to be constant.

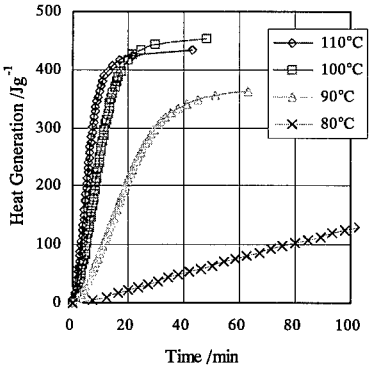

Fig.2 Heat generation during isothermal cure

Isothermal cure exotherm curves in Fig.2 indicate that the degree of cure after initial cure of 100°C is more than 85%, while it is 75 to 80% after 90°C initial cure. In the region of low degree of cure (less than 50%), the reaction rate is approximately tripled by every 10K over 90°C, while the reaction rate at 80°C is 10 times slower than that at 90°C. In spite of the slow reaction rate at 80°C, the isothermal reaction curve of 80°C indicates that it is possible to obtain a rigid green composite with enough strength at 80°C, if the proper length of cure cycle is used.

Cure Shrinkage by P-V-T Apparatus

Figure 3 shows how specific volume of #850 changes during cure cycle. Specific volume of uncured (raw) #850 is 0.832cm^{3}g^{-1} at 90°C, and the specific volume converges to 0.80cm^{3}g^{-1} during 5 hour holding.

Indeed the correspondence between the heat generation obtained by DSC and the cure shrinkage obtained P-V-T apparatus was not good, it is confirmed that 5 hour holding is long enough for 90°C initial cure.

Likewise, specific volume of 0.799 cm^{3}g^{-1} at 80°C was obtained after 15 hour of 80°C holding. Because 0.799 cm^{3}g^{-1} at 80°C corresponds to 0.801 cm^{3}g^{-1} at 90°C, it was confirmed that it is possible to obtain a sufficient degree of cure by 80°C initial cure, if the proper length of cure cycle is used.

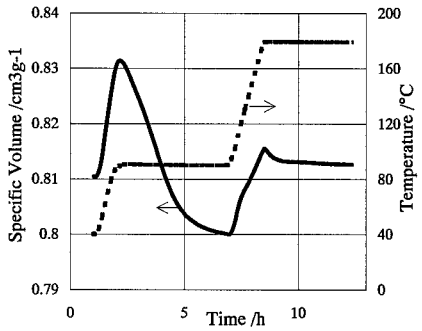

Fig.3 Shrinkage of #850 resin during 2 step cure (90°C for 5 h followed by 180°C for 4h, heating rate = 1K/min)

In Fig. 4, specific volume during cooling process is also shown. At 90°C, specific volume of after post-curing is larger than that before post-curing. The increase of specific volume indicates that cross-linkings generated by post-curing prevent the packing of molecules and cause increase of free volume of the resin.

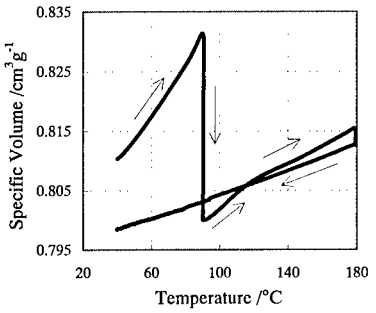

Fig.4 Specific volume of #850 resin during the cure cycle including cooling

Mechanical Properties

Mechanical properties of TR30M/#850 are summarized in Table 1. The performance of TR30M/#850 is very similar to first generation 177°C (350°F) cure epoxy systems.

Table 1 Mechanical Properties of TR30M/#850

		23°C	180°C
0° Ten. Strength	MPa	2030	2190
Modulus	GPa	138	145
Elong.	%	1.36	1.35
0° Comp. Strength	MPa	1420	1000
90° Ten. Strength	MPa	57.2	
Modulus	GPa	8.21	
Elong.	%	0.74	
Short Beam Shear	MPa	100	45
0° Flex. Strength	MPa	1480	853
Modulus	GPa	108	102
Elong.	%	1.4	0.85

Conclusions

#850 prepreg is a low temperature curable and freestanding post-curable system which gives low void composite by a conventional vacuum bag only molding process. It can be initial cured at 80°C using low cost wooden or plaster molds. The heat resistance of the post-cured composite is high enough that it can be used under severe condition such as 140°C environment. The long out time of #850 (more than 30 days) enable the material to be used for producing large scale and complex shaped composites.

Acknowledgment

The authors wish to express acknowledgments to our colleagues (K. Goto, T. Saito, Y. Suzumura, T. Kaneko, Y. Takagi, A. Ito, H. Koba) for their great contribution to this study.

References

1. K. Jackson: Proc. of 43rd SAMPE International Symposium, 1 (1998)
2. G. F. Xu, L. Repecka, and J. Boyd: Proc. of 43rd SAMPE International Symposium, 9 (1998)
3. K. Mitani, K. Wakabayashi and S. Hayashi: Proc. of 46th SAMPE International Symposium 2293 (2000)
4. K. Mitani, M. Furuyama and K. Fukuta: Proc. of 3rd Japan International SAMPE Symposium 834 (1993).

Proceedings of 7th Japan International SAMPE
Symposium & Exhibition, Nov. 13-16, 2001

Effect of Thermal Cycling and Aging on the Mechanical Properties of Carbon/BMI Composites for the Next-Generation SST Structures

Hisaya Katoh[1], Toshiyuki Shimokawa[1,2] and Christian Marais[3]

[1] Advanced Composite Evaluation Technology Center,
National Aerospace Laboratory of Japan,
6-13-1 Ohsawa, Mitaka, Tokyo, 181-0015, JAPAN
E-mail:katoh@nal.go.jp

[2] (Now) Department of Aerospace Engineering,
Tokyo Metropolitan Institute of Technology,
6-6 Asahigaoka, Hino, Tokyo, 191-0065, JAPAN
E-mail:Shimoka@timt.ac.jp

[3] Département Matériaux et Systèmes Composites,
Office National d'Etudes et de Recherches Aérospatiales,
29, avenue de la division Leclerc, Châtillon, 92322 Cedex FRANCE
E-mail:Christian.Marais@onera.fr

Abstract

The paper investigates the effects of long-term thermal cycling and isothermal aging on the residual compressive strength of carbon fiber / BMI matrix composite laminates. Two kinds of composites from the same family were tested by static compression load and examined by microscopy after subjecting to various aging conditions. The compression tests were carried out on non-holed and open-hole specimens. Damage was separately assessed by weight loss and observed by electron and light microscopes on aged open-hole coupons. Over the glassy range of the composites, it appears that the residual compressive strength is not only depending on both weight loss and cracking. In prospect, it appears necessary to develop a model for each parameter and include them in a more complex mechanical model. This reserch examines the effect of thermal cycling and isothermal aging conditions (temperatures and times) on the mechanical properties and attempts to explain the role of the overall aging process.

Key Words: Polymer matrix composites, Compressive strength, Degradation, Cracking, Thermal cycling and aging

Introduction

Carbon fiber / polymer matrix composite laminates have high potentialities as light structural materials for the next generation supersonic transport but they must undergo rigorous physical and mechanical testing to be qualified. Particularly, the long-term behavior is a major barrier to expand their use in such aircraft structures. The

problems associated with aging, durability and predicting life of polymer matrix composites have been highlighted by many aerospace industries. To predict the response of new generation of composite materials, it is therefore proposed to establish a relationship between mechanical characterization and damage achieved after aging through experimental proofs. Delamination or cracking can severely degrade the performance of composite materials. As a result, structural design using polymer matrix composites is based on very conservative design allowable. There is a strong need to develop composite materials that are more tolerant of damage.

Materials and Specimens

Two kinds of composite materials from the BMI resin family were used to investigate the effects of thermal cycling and isothermal aging on compressive strength. One sort of materials was prepared by NAL (National Aerospace Laboratory of Japan) and consisted of Cytec Fiberite prepregs made of G40-800 carbon fibers and 5260 BMI resin. The other sort was prepared by ONERA (National Aerospace Research Agency of France) and consisted of Hexcel prepregs made of T800H carbon fibers and F655-2 resin. The two kinds of materials were 32-ply laminates with a stacking sequence of $[+45/0/-45/90]_{4s}$ and cut into the geometry appropriate to the thermal cycling and isothermal aging in ovens. For each laminate, a series of panels were unnotched for non-holed compression tests and another panels with a center hole of 6.35 mm in diameter for open-holed compression tests. In addition, small square coupons from the same laminates were machined (40 mm × 40 mm), polished and used for examining of cracks during thermal cycling and isothermal aging.

Experimental Procedure

Panels and coupons were thermal-cycled up to 1,000 cycles in an oven and a holding of 5 minutes at the lowest and highest temperatures. A first series was conducted between –50 and +120°C, a second series between –50 and +150°C and another between –50 and +180°C. Then, these three series were isothermally aged at 120, 150 and 180°C respectively. Three isothermal aging times were 1,000, 3,000 and 6,000 hours for each temperature. After thermal cycling and isothermal aging, the coupons were removed and examined by a light microscope for counting cracks initiated on free edges. Likewise, the unnotched and open-hole panels were removed and machined into the specimens for compression tests. Then damaged free edges from panels were taken away. Hence, only damaged areas from surfaces and holes were preserved within the test specimens (Shimokawa et al [1]).

Test Results and Discussion

For all specimens from two kinds of composite laminates, damage and compression syrength were analyzed and numerous significant observations gained from the experimental works were discussed.

Degradation Assessment

First, weight losses have been collected during thermal cycling and isothermal aging on the small open-holed square coupons. Data show that there is not very much or not at all in the development of weight losses for 1,000 cycles because dwell times are very short as five minutes. Cumulated hours at the maximum temperature were only 83 hours. Moreover, for each thermal cycling, there were continuously remove and recovery about humidity and therefore weight losses are not significant on the degradation of composite laminates. During the isothermal aging, only 180°C is a temperature capable possibly to degrade the BMI structure. It is true that the BMI resin is recommended for

use temperatures at least equivalent otherwise higher than the test temperatures. Particularly, oxidation at 180°C is more effective than at lower temperatures and gives rise a removal of various volatile products (Salin and Seferis [2]). However, as indicated in Fig. 1, even at 180°C weight loss decreases very slightly.

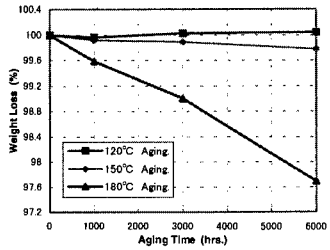

Fig. 1 Weight loss versus aging time at three temperatures of T800H/F655-2 composites

During isothermal aging, transverse and longitudinal cracks are increased. Fig. 2 shows a photomicrograph of the T800H/F655-2 composite aged at 180°C for 6,000 hours.

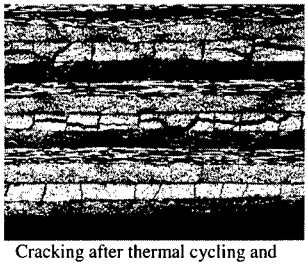

Fig. 2 Cracking after thermal cycling and isothermal aging at 180°C/6000h of the quasi-isotropic T800H/F655-2 composite.

In all cases, crack distribution is homogeneous in the eight 0° plies. If one consider only transverse cracking, Fig. 3 shows a straightforward representation of transverse crack densities as a function of aging time for all coupons and at the three temperatures. Crack density is the average number of transverse cracks crossing entirely a layer and determined per one millimeter long.

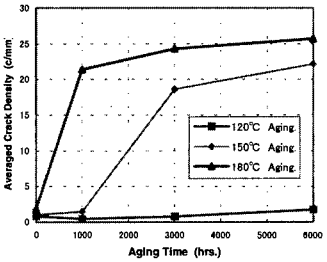

Fig. 3 Transverse crack densities of the quasi-isotropic T800H/F655-2 composite.

This figure illustrates clearly the existence of two diagnostic points in transverse cracking. The first point is the onset of cracking only insured by thermal cycling at 180°C for G40-800/5260 whereas a small number of cracks were already observed for T800H/F655-2 at 120°C and 150°C. For thermal cycling at 120°C and 150°C, the onset is superimposed on the time axis for G40-800/5260. This point is followed by a transition region in which cracks develop very rapidly at 150°C and 180°C. The second diagnostic point marks the end of the development at which a crack saturation is reached and maintained. This type of plot also shows the effect of temperature on the crack density versus time.

Compression Test

Compression tests were carried out at room temperature and conducted by means of a hydraulic testing machine. Static compression load was applied at the rate of 1.0 mm/min. Load versus deflection plots were recorded for all tests and obtained results were linked to damage from the respective examined and aged coupons. Isothermal aging and compression tests were carried out on the Japanese specimens by ONERA and inversely. The compression test method used by NAL is described in ref. [1] and that used by ONERA is the Airbus Industrie method (AITM [3]).

Each result is an average value obtained from two test specimens. For the two laminates and all the test configurations, either before or after aging, compressive strength decreases slightly with temperature. The sequence of events that leads to the final failure seems the same for all aging times and test temperatures. Examination of failed specimens shows that compressive failure of the quasi-isotropic laminate seems bring about the kinking of fibers in the 0° plies then damage propagates around. This is followed by delamination of the laminate.

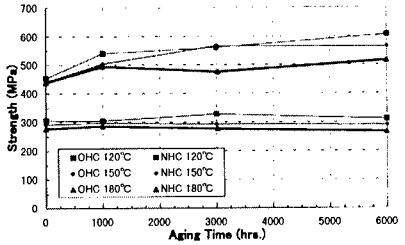

Fig. 4 Compressive strength versus aging time of non-holed (upper curves) and open-holed (lower curves) specimens from QI G40-800/5260 composite.

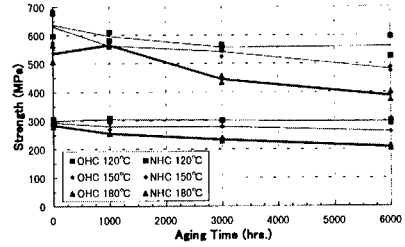

Fig. 5 Compressive strength versus aging time of non-holed (upper curves) and open-holed (lower curves) specimens from QI T800H/F655-2 composite.

A discussion about degradation tendencies can be made from compression data regarding damages as functions of aging time. We have an evolution of the compressive strength and the other hand, a development of damage consisting of weight loss and cracking. Fig. 4 and 5 show the failure strength at the three temperatures on non-holed and open-hole specimens from the two quasi-isotropic (QI) carbon/BMI composites.

It appears clearly significant results and fundamental differences between the two materials. Though compressive strength measurements of two composites are in the same order of magnitude, the evolution of curves is significantly different. For the T800H/F655-2 composite, all the failure strengths of non-holed specimens decrease monotonously due to the damage which develops for thermal aging. The decrease of the failure strength of open-hole specimens is slighter at 180°C even slighter still for the two other temperatures than those respectively from non-holed specimens. On the contrary, the shape of curves of the G40-800/5260 are reversed though very slightly for the open-hole specimens. This evolution was already noted on other composites (Plunkett et al [4]).

Acknowledgments

H. Katoh and T. Shimokawa would like to acknowledge Kawasaki Heavy Industries Ltd for supplying Japanese composite laminates. Also, C. Marais would like to thank the European Aerospace Defense and Space company for supplying French composite laminates, their facilities and technical support.

Reeferences

1. T. Shimokawa, Y. Hamaguchi, Y. Kakuta, H. Katoh, T. Sanda, H. Mizuno and Y. Toi, "Effect of Isothermal Aging on Ultimate Strength of High-Temperature Composite Materials for SST Structures", *Journal of Composite Materials, Vol.33, N° 12*, 1999.
2. Salin, I.R. and Seferis, J.C., "Mass transfer effects in degradation of bismaleimide matrix composite", *Journal of Applied Polymer Science, Vol. 62, 1023*, 1996.
3. AITM, "Fibre reinforced plastics, determination of notched, unnotched and filled hole compression strength", *AITM 1-0008*, 1997, published by Airbus Indutrie, France.
4. Plunkett, R.B., Tsang, P.H., Lesko, J.J., Wood, J.D. and Rufin, A.C., "Assessment of residual composite properties as influenced by thermal mechanical aging", *Proceedings of the ASME Aerospace Division, AD-Vol. 52*, 1996.

Proceedings of 7th Japan International SAMPE
Symposium & Exhibition, Nov. 13-16, 2001

Strengthening of Short Fiber Reinforced Polyimide Composites in Space Environment

Yoshihito Ozawa#

#: Department of Mechanical Engineering, Faculty of Education, Fukushima University
1, Kanayagawa, Fukushima 960-1296, JAPAN
E-mail: ozawa@educ.fukushima-u.ac.jp

Abstract

In this paper, the tensile strength and Young's modulus of short carbon fiber reinforced polyimide (SCFR-PI) composites in high vacuum and temperature conditions are investigated. In order to clarify the mechanical behavior of SCFR-PI composites, tension tests are performed by the use of thermal fatigue testing equipment. After tension tests, the damage propagation in the SCFR-PI specimens was observed by a scanning electron microscope and an optical microscope. Even though tested at the same temperature 298 K, the tensile strength for the SCFR-PI specimens kept in high vacuum condition is higher than that in the atmospheric condition. Furthermore, the SCFR-PI has higher equivalent Young's modulus than that in the atmospheric condition. In high vacuum condition, the degas and/or moisture desorption from the matrix and from the interface between the matrix and fibers occur. There is found to exist the effect of vacuum condition on the tensile strength and Young's modulus of SCFR-PI composites and the microfractures.

Key Words: Short Fiber Reinforced Composites, Mechanical Behavior, Space Environment, Temperature and Vacuum Condition.

Introduction

Short fiber reinforced organic composites have high specific strength and can be easily processed by the injection molding. Therefore, they are increasingly being used in large variety of engineering applications, especially the manufacture of aircraft structural components and space structural components [1]. The structural components in the orbit of a satellite around the earth experience high vacuum condition, and cyclic temperature change with wide range. Large thermal stresses and residual stresses develop in the structural components of the composites [2, 3]. The performance of the fibers, the polymer matrix and the interface between them may change in space environment. These components must be certified for service under a range of severe space environmental conditions.

In this paper, the tensile strength and Young's modulus of short carbon fiber reinforced thermoplastic polyimide (SCFR-PI) composites are examined in high vacuum and temperature condition. Tension tests with the aid of acoustic emission method are performed in the temperature and environmental system developed by the author. In order to consider the microfractures of SCFR-PI composites and their AE characteristics, the damage

propagation in the specimens is observed by a scanning electron microscope (SEM) and an optical microscope.

Test Specimens and Experimental Procedure

Test Specimens of SCFR-PI Composite

The material used in this study is a short carbon fiber reinforced thermoplastic polyimide composite which contains short carbon fibers of 20% or 30% by weight. The average fiber length and diameter are 130 μm and 8 μm, respectively. SCFR-PI specimens were made by an injection molding method as shown in Fig. 1.

Experimental Procedure

Tension tests for the SCFR-PI specimens in high vacuum and temperature environmental conditions were performed by using the thermal fatigue testing equipment for advanced composite materials. This testing equipment has an advanced temperature and environmental system in order to conduct thermal fatigue test at temperature range 93 K to 473 K (-180°C to 200°C) and vacuum levels down to 10^{-4} Pa (10^{-6} torr).

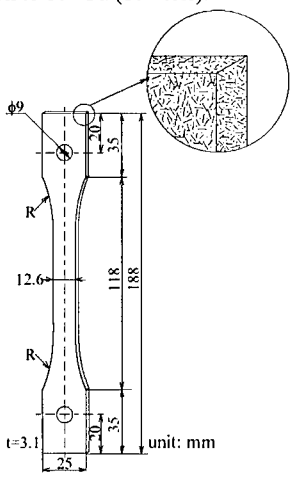

Fig.1 Geometry of SCFR-PI Composite Specimen

The specimens were subjected to tensile load in the longitudinal direction of the specimen. The testing speed was kept at 0.2 mm/min throughout the tests. Before the tension tests, the specimens were hold in the temperature and environmental system and kept in the high vacuum condition 10^{-4} Pa at 298 K (25°C) for 15 days.

The relationship between the load P and the loading point displacement δ was recorded in an X-Y recorder. All the AE signals detected by a wideband AE transducer were monitored and recorded during the tests. After the tests, the recorded signals were processed by a personal computer, and the damage propagation in the SCFR-PI specimens was observed by SEM and an optical microscope.

Experimental Results and Discussion

Fig. 2 shows the load P - loading point displacement δ curve for the SCFR-PI specimens of 20 wt% and 30 wt% tested at temperature 298 K (25°C) in high vacuum condition 10^{-4} Pa. The P-δ curves for the specimens tested at 298 K in the atmospheric condition 10^{5} Pa are also shown in Fig. 2. The solid line indicates the result of the specimen tested in high vacuum condition, and the broken one shows that in the atmospheric condition. The tensile strength σ_b and equivalent Young's modulus E* of SCFR-PI composites in each case are summarized and shown in Table 1.

The damage in the specimens after the tests was observed by using a SEM and an optical microscope. The fiber pull-out length for the specimen in high vacuum condition is shorter than that in the atmospheric condition. Considering our observation for the fracture surfaces, it can be said that the interfacial bonding strength between carbon fibers and the resin matrix becomes much better in high vacuum condition [4].

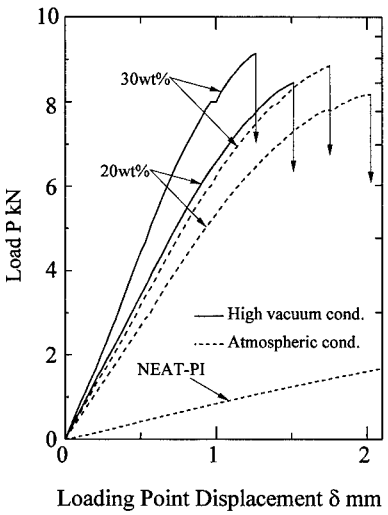

Fig.2 P - δ Curve for SCFR-PI Specimens Tested at Temperature 298 K

Table 1 Tensile Strength and Equivalent Young's Modulus of SCFR-PI Composites

Condition	σ_b MPa fiber fraction		E* GPa fiber fraction	
	20wt %	30wt %	20wt %	30wt %
High Vacuum	211	228	26.1	36.3
Atmospheric	205	223	23.3	25.5

at 298 K

Even though tested at the same temperature 298 K, the tensile strength for the SCFR-PI specimen tested in high vacuum condition is higher than that in the atmospheric condition as shown in Table 1. Furthermore, the SCFR-PI has higher equivalent Young's modulus than that in the atmospheric condition. The strengthening of SCFR-PI composites is attributed to the nonexistence of air around the specimens. The organic composite contains some kind of evaporated substance and moisture in the matrix resin[5]. In high vacuum condition, the degas and/or moisture desorption from the matrix and from the interface between the matrix and fibers must occur, and thus the matrix resin is shrank. The residual stresses yield in the composites owing to the mismatch between the coefficient of moisture expansion of matrix and that of fibers. It is noted that the degas and/or moisture desorption may change the performance of each material and the microfractures of SCFR-PI composites.

In our previous paper[6, 7], we have investigated the mechanical behavior of CFRP cross-ply laminates at various temperatures in high vacuum condition 10^{-4} Pa and the atmospheric condition 10^5 Pa. The values of tensile strength of CFRP cross-ply laminates σ_b are 599 MPa in high vacuum condition, and 528 MPa in the atmospheric condition. The values of E* for the specimens in high vacuum condition and in the atmosphere are 46.2 GPa and 46.4 GPa, respectively. From these experimental result of SCFR-PI composites and CFRP cross-ply laminates, the mechanical behavior of SCFR-PI composites is found to be quite different from that of CFRP cross-ply laminates.

Composite properties are strongly dependent on the arrangement and distribution of fibers: *the fiber architecture.* There is interest in understanding the distribution of stresses within the composite, and the consequences of this for stiffness and other mechanical properties. The basic results of the shear lag treatment can be used to predict the elastic deformation of the short fiber reinforced composite (*the Rule of Averages*) [8]. All the fibers in the composites are aligned in the loading direction and at random position along their length. By taking account of fiber end stress transfer, the stress-strain relationship for the composites is obtained from

$$\sigma_1 = \varepsilon_1 \left[fE_f \left(1 - \frac{(E_f - E'_m)\tanh(ns)}{E_f ns} \right) + (1-f)E_m \right] \quad (1)$$

in which f is the fiber volume fraction, and s is the aspect ratio of a fiber. E_f and E_m are Young's moduli of the fiber and the matrix, respectively. n and E'_m are given by

$$n = \left[\frac{2E_m}{E_f(1+\nu_m)\ln(1/f)} \right]^{1/2} \quad (2)$$

$$E'_m = E_f(1 - \operatorname{sech}(ns)) + E_m \quad (3)$$

The prediction of Eq. (1) is examined for the strength and Young's modulus of SCFR-PI composites. It is found that the rule of averages gives the good prediction of Young's modulus of the composites in the atmospheric condition, however the rule is not applicable to the prediction of the strength. For SCFR-PI in high vacuum condition, the rule can not be used to evaluate the strength and Young's modulus of SCFR-PI composites. Arrangements in short-fiber systems are more complex, and methods of characterizing them must be described for evaluation of SCFR-PI composites in high vacuum and temperature condition.

Conclusions

The tensile strength and Young's modulus of SCFR-PI composites at the temperature 298 K in high vacuum condition 10^{-4} Pa and in the atmospheric condition is investigated in this paper. The main results are summarized, as follows:

(1) Even though tested at the same temperature 298 K, the tensile strength for the SCFR-PI specimens kept in high vacuum condition is higher than that in the atmospheric condition. Furthermore, the SCFR-PI has higher equivalent Young's modulus than that in the atmospheric condition. The rule of advantage can not be used to evaluate the strength and Young's modulus of SCFR-PI composites in high vacuum condition.

(2) The strengthening of the SCFR-PI composites is attributed to the nonexistence of air around the specimens. In high vacuum condition, the matrix resin is shrank owing to the degas and/or moisture desorption from the matrix and from the interface between the matrix and fibers, and thus the residual stresses yield in the organic composites. The interfacial bonding strength between carbon fibers and the resin matrix becomes much better in high vacuum condition. The methods of characterizing them must be described for evaluation of SCFR-PI composites in space environment.

References

1. K. Kishimoto, M. Notomi and T. Koizumi: Eng. Fracture Mech., 49(6), 943(1994).
2. Y. Ozawa, K. Noguchi, and K. Sugiura: Proc. of ICM&M'97, JSME, 523(1997).
3. Y. Ozawa, K. Sugiura and K. Noguchi : Thermal Stresses '97, 461(1997).
4. Y. Ozawa, K. Sato and K. Kishimoto, Proc. International Workshop on Sensing and Evaluation of Materials System (ISRE2000), 92(2000).
5. Y. Sung and Y.Y. Chen: ASME EEP-Vol. 25, 287(1998).
6. Y. Ozawa and H. Suzuki: ASME EEP-Vol. 25, 209(1998).
7. Y. Ozawa, K. Sugiura and H. Suzuki: Thermal Stresses '99, 441(1999).
8. D. Hull and T.W. Clyne: *An Introduction to Composite Materials*, 2nd Ed., Cambridge University Press, Cambridge, 1996, pp. 105-132.

Proceedings of 7th Japan International SAMPE
Symposium & Exhibition, Nov. 13-16, 2001

Thermal Properties of New Continuous Amorphous Pitch-based Carbon Fiber for Space Applications

Noriyuki Kiuchi and Tsutomu Kihara
Central Technical Research Laboratory, Nippon Mitsubishi Oil Corporation.
8, Chidori-cho, Naka-ku, Yokohama, 231-0815, Japan
E-mail: noriyuki. kiuchi@nmoc.co.jp

Takayuki Matsumoto and Gen Ishikawa
Head office, Nippon Graphite Fiber Corporation
E-mail: ngf03@cd.mbn.or.jp

Hirohata Plant, Nippon Graphite Fiber Corporation
E-mail: risuken@bc.mbn.or.jp

Abstract

The Nippon Graphite Fiber Corporation (NGF) has developed a new continuous amorphous pitch-based carbon fiber (XN-05) with a low modulus of 50 GPa. The newly developed XN-05 has several unique characteristics with regard to its thermal properties and impact properties. The first is that XN-05 has low thermal conductivity (TC) and a positive coefficient of thermal expansion (CTE). Hybrid CFRP that has a zero-CTE and a high modulus of 175 GPa was developed with XN-05 and high modulus pitch fiber (YS-90A). The second is that the thermal properties of XN-05 barely change even after high temperature treatment, unlike mesophase pitch-based carbon fibers (CF). The graphitic structures of XN-05 do not grow in temperature as high as about 3000℃. Therefore, the low TC and the positive CTE can be maintained during processing of high temperature materials (C/C composites etc). It was concluded that the developed fiber XN-05 is quite suitable as reinforcement for controlling the thermal properties of CFRP and high temperature materials.

Key Words: Positive CTE, Low TC

1. Introduction

It is known that the amorphous CF (XN-05), which has a low modulus of 50 GPa and a high compressive fracture strain, contributes to the improvement of the impact properties of CFRP [1]. XN-05 also has unique thermal properties, including low thermal conductivity (TC) and a positive coefficient of thermal expansion (CTE). The thermal properties of XN-05 can be maintained even after treatments at high temperature. In this paper, research applying the thermal properties of XN-05 is reported for CFRP and high temperature materials including C/C composites.

2. Experimental Procedures

2.1 CTE of hybrid CFRP with XN-05 and High modulus CF (YS-90A)

2.1.1 Material

The characteristics of the amorphous CF (XN-05) and pitch-based high modulus CF (YS-90A) are shown in Table 1 (source: NGF catalog).

Table 1 Characteristics of XN-05 and YS-90A

		XN-05	YS-90A
Tensile strength	MPa	1100	3550
Tensile modulus	GPa	54	880
Elongation	%	2.0	0.3
Density	Mg/m^3	1.65	2.18
CTE	$10^{-6}/K$	4.6	-1.5
TC	W/mK	4.7	500

Note 1) CTE: Coefficient of thermal expansion
Note 2) TC: Thermal Conductivity

The characteristics of prepreg made with XN-05 and YS-90A are shown in Table 2. The lay up of the hybrid CFRP are shown in Table-3. SF-YS90A-75 is a thin fabric with YS-90A.

Table 2 Characteristics of prepreg

Prepreg (PP)	AFW g/m^2	RC wt%	MPT mm
SF-YS90A-75 (Fabric-PP)	71.6	42	0.076
XN-05 PP	101	37	0.12

Table 3 Lay up of hybrid CFRP

Prepreg	Lay up
(0,90): Fabric SF-YS90A-75	$[(0,90)_4/45/(0,90)_2/-45/(0,90)_2]_S$
	Ratio of XN-05: 23.6 vol %
±45 : XN-05 Unidirectional	$[(0,90)_4/45/(0,90)_4/-45/(0,90)_4]_S$
	Ratio of XN-05: 17.0 vol %
	(0,90) only, YS-90A: 100 vol %

2.1.2 Measurement and calculation of CTE

The CTE of the hybrid CFRP was measured with a laser interferometry type thermal expansion meter (Lix-1, Shinku-Riko, Inc.). The CTE of the hybrid CFRP was estimated by changing the ratio of XN-05 to YS-90A based on the Tsai-Wu law. The calculated CTE was compared with the measured CTE of the hybrid CFRP. The modulus of the hybrid CFRP was also calculated, and the calculated modulus was compared with that of a quasi-isotropic CFRP made with high modulus carbon fibers.

2.2 Thermal properties of XN-05 after high temperature treatment

2.2.1 Material

XN-05 as received (NGF product) and XN-05 after high temperature treatment (HTT) at 2965℃ were used to measure the CTE along the fiber axis and the TC at room temperature. Next, C/C preforms and C/C composites were prepared with XN-05 or mesophase pitch-based CF (Meso-CF). Table 4 shows the specifications of the C/C preforms and C/C composites.

Table 4 Specifications of C/C preforms and C/C composites.

Specimens	Heat history	Vf %	Density Mg/m^3
Preform with XN-05	1000℃ carbonization	60	1.47
Preform with Meso-CF	1000℃ carbonization	60	1.50
C/C with XN-05	2000℃×30min. (Holding time)	61	1.71
C/C with Meso-CF	2000℃×30min. (Holding time)	61	1.85

Note 1) Matrix: phenolic precursor
Note 2) Stacking sequence: unidirectional laminates
Note 3) Meso-CF: mesophase pitch-based CF

2.2.2 Measurement of dimensional change and thermal expansion of C/C materials at elevated temperatures

The dimensional change and thermal expansion behavior of C/C preforms and C/C composites along the fiber axis were evaluated in an inert atmosphere up to 2000℃ with a laser displacement sensor. The dimensional change of the C/C preform with XN-05 was compared with that of a C/C preform with Meso-CF. Next, the thermal expansion behavior of C/C was investigated.

3. Results and Discussion

3.1 CTE of hybrid CFRP with XN-05 and YS-90A

Fig. 1 shows the CTE of the hybrid CFRP made with XN-05 and YS-90A. The measured CTE of the hybrid CFRP increased from a

negative value to a positive value as the ratio of XN-05 increased. The SF-YS90A-75 fabric layer in the hybrid CFRP shows a negative-CTE, while the XN-05 layer showed a positive CTE. The CTE of the hybrid CFRP was determined by the combination of the CTE of both layers. From the measured data, it was found out that the hybrid CFRP showed a zero-CTE with an XN-05 ratio of about 20 % to YS-90A. The ratio of XN-05 with a zero-CTE corresponded to that estimated from the calculation. In the ratio of XN-05 with a zero-CTE, the estimated modulus of the hybrid CFRP from calculation was 175 GPa, which was much higher than that of the conventional quasi-isotropic laminates with zero-CTE (CFRP with XN-50 that has modulus of 520 GPa). The hybrid CFRP with XN-05 and YS-90A was concluded to have a zero-CTE as well as a high modulus.

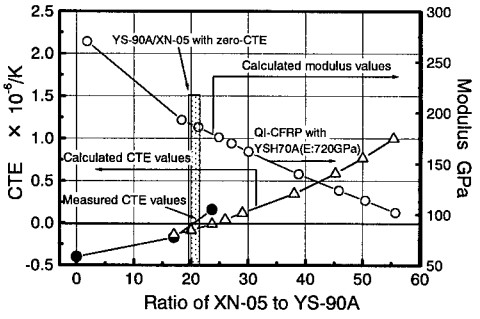

Fig. 1 CTE of hybrid CFRP with XN-05 and YS-90A

3.2 *Thermal properties of XN-05 after high temperature treatment (HTT)*

Fig.2 and Fig. 3 show the CTE and TC (Thermal conductivity) of XN-05 before and after HTT, including high modulus PAN-CF and mesophase pitch CF. The CTE of XN-05 showed a positive value. The TC of XN-05 had a small value compared with the conventional PAN-CF and mesophase pitch CF.

Moreover, the change in the CTE and TC of XN-05 after HTT was very small. In other words, these unique properties of XN-05 can be maintained after a heat history up to about 3000℃. The reason for this result is that XN-05 does not generate the preferred orientation of graphitic structure along the fiber axis with HTT.

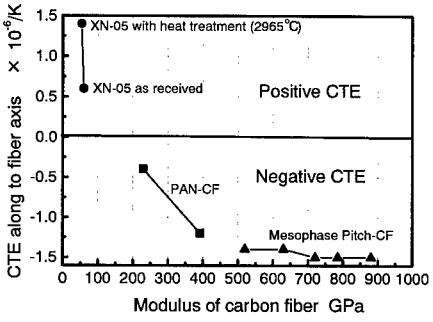

Fig. 2 CTE of XN-05 as received and XN-05 after HTT

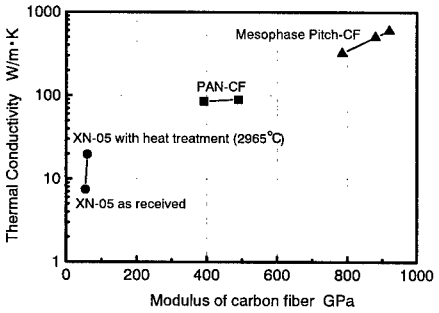

Fig. 3 TC of XN-05 as received and XN-05 after HTT

3.3 *Thermal properties of C/C materials at elevated temperatures*

The dimensional changes of C/C preforms made with XN-05 or mesosphere pitch CF from room temperature to 2000℃ are shown in Fig. 4. The heat history of the C/C preforms was up to 1000 ℃. Therefore, the microstructure of the C/C preforms can change during HTT. The dimensional changes include the thermal expansion and the growth of the crystal structures in the preforms.

The dimensional change of the C/C preform made with mesophase pitch CF was much larger than that of C/C made with XN-05. Moreover, the dimensional change of the C/C preform made with XN-05 showed a correspondence between the heating procedure and cooling procedure. In contrast, the dimensional change of the C/C preform with mesophase pitch CF had a large value in heating and a very small value in cooling. It is thought that the crystal growth of CF along the fiber axis dominates the dimensional change of the material. XN-05 does not show the crystal growth compared with the mesophase pitch fiber. The mesophase pitch fiber generally progresses in the degree of preferred orientation of the graphitic layers along the fiber axis with HTT. This difference in the crystal growth causes the difference in dimensional changes.

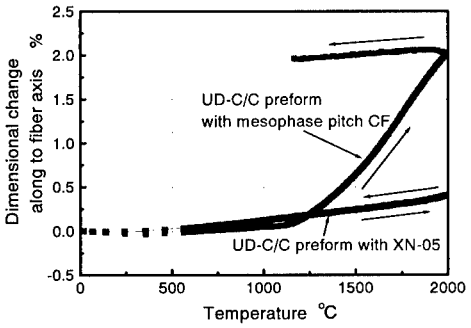

Fig. 4 Dimensional change of C/C preforms in HTT

The thermal expansion properties of C/C with XN-05 and C/C with mesophase pitch CF at elevated temperatures are shown in Fig. 5. The C/C was made with HTT of 2000℃. In this case, the dimensional change should be thermal expansion of the material only. The thermal expansion of C/C with XN-05 was much larger than that of the C/C with the mesophase pitch CF. It is thought that the CTE of XN-05 and the mesophase pitch CF as reinforcements influences the CTE of the C/C. It is known that the thermal expansion of the C/C is very small, which is an advantage for thermal shock. The small expansion behavior of the C/C is a disadvantage for connecting with materials that have large thermal expansion. In this case, the large CTE of the C/C made with XN-05 was thought to be a unique property. It is expected that the combination of XN-05 and the conventional pitch CF can relieve the mismatch in the CTE between the C/C and the other materials including metal.

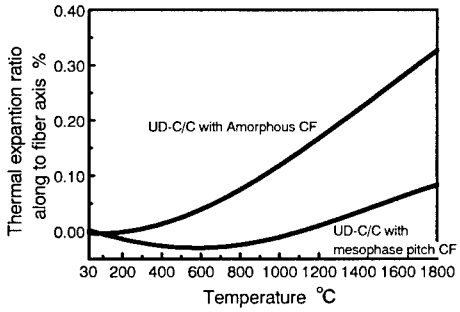

Fig. 5 Thermal expansion of XN-05 of C/C materials at elevated temperatures

4. Conclusions

The developed fiber XN-05 with a low modulus of 50 GPa has low thermal conductivity (TC) and a positive coefficient of thermal expansion (CTE). The low TC and the positive CTE can be maintained after HTT up to 3000℃. Hybrid CFRP that has a zero-CTE and a high modulus (175 GPa) was developed with XN-05 and high modulus pitch fiber (YS-90A). C/C materials with XN-05 showed little dimensional change at elevated temperatures. As a result, it was concluded that the XN-05 was quite suitable as reinforcement to control the thermal properties of CFRP and high temperature materials.

References

1. N.Kiuchi et al, 45th International SAMPE, 2000, p330-341

Proceedings of 7th Japan International SAMPE
Symposium & Exhibition, Nov. 13-16, 2001

Evaluation of the Burst Strength of FW-FRP Composite Pipes with Low-Modulus Carbon Fiber after Impact

Shuichi Wakayama#, Toshiaki Takekusa#, Satoshi Kobayashi#,

Noriyuki Kiuchi* and Takayuki Matsumoto**

#: Graduate School of Engineering, Tokyo Metropolitan University
1-1 Minami-Ohsawa, Hachioji, Tokyo 192-0397, JAPAN
E-mail: koba@ecomp.metro-u.ac.jp
*: Central Technical Research Laboratory, Nippon Mitsubishi Oil Corporation
**: Nippon Graphite Fiber Corporation

Abstract

Impact tests of filament-wound carbon fiber composites pipes were carried out using a drop-weight impact test device developed by the authors. Burst pressure of composite pipes was also measured in order to investigate the burst strength degradation due to impact damage. Depth of fiber breakage region caused by impact test was evaluated after burst strength test. The burst strength of FW-FRP composite pipes after impact was demonstrated to decrease as the increase in cross sectional ratio of damage area. Low-modulus carbon fibers were wound on the surface of the pipes in order to reduce the impact damage. Consequently, it reduced the impact damage and enhanced the residual burst strength.

Key Words: FW-FRP Composite Pipe, Impact Test, Burst Strength, Low-Modulus Carbon Fiber

Introduction

Filament winding technology are extensively used in commercial manufacture of FRP pressure vessels such as air cylinders for self-contained breathing apparatus, oxygen cylinders for medical uses, fuel gas cylinders and so on. In case of daily use of FW-FRP vessels, there are possibilities of impact loading such as dropping and/or knocking vessels. In this point of view, it is very important to clarify the strength degradation mechanism after impact and to improve the impact resistance.

There were some investigations for burst strength degradation after impact [1-4]. Most studies dealt with surface fiber break length, though fiber break depth is also influential on the burst strength.

In the present study, we conducted internal pressure test on FW-CFRP composite pipes after impact test. Impact damages, which consist of fiber break length and depth, were evaluated as functions of absorption energy. To improve the impact resistance, low modulus amorphous carbon fiber, which has high compressive strain, were applied to the surface of composites pipes. The effectiveness of the hybridization was confirmed.

Experiments

Specimen configuration is shown in Figure 1. Specimens consist of aluminum alloy (A6063-T6) liner and CFRP layer.

Carbon fiber used was T700S-24K supplied by Tray Inc. Matrix was Epoxy resin. Composite pipes were fabricated using filament winder. To improve the impact resistance, low modulus amorphous carbon fiber XN05-30S, supplied by Nihon Graphite fiber Inc., was wound on the surface of the composite pipes. XN05 has high compressive strain and it was reported that hybrid composite using XN05 has high impact resistance properties [5]. Five T700S-24K layers were wound on the liner and two additional XN05-30S layers were wound on some specimens. In the present study, specimens without/with low modulus fiber are defined as specimen A and B, respectively. Specimen B was expected to have higher impact resistance.

Impact tests apparatus were shown in figure 2. Mass of the impactor is 7kg and initial impactor height is 0.45m, which means potential energy of the impactor is 30 J. Impactor radius, R was selected as 3, 10 and 20 mm for specimen A, and 3 and 10 mm for specimen B. Absorption energy was calculated from the initial impactor height and rebound height measured by video camera. Some of the specimens after impact tests were sectioned and observed by optical microscopy.

Internal pressure tests were conducted using the apparatus shown in Figure 3. In the present study, strength of hoop direction is most concerned and axial strength is very weak, so deformation in the axial direction was constrained by the shaft centered in the pipes. Surface of the specimen was observed by video camera during the internal pressure test.

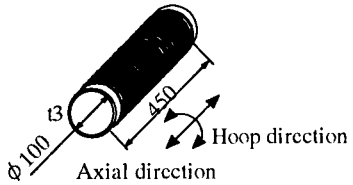

Figure 1 Schematic of the specimen.

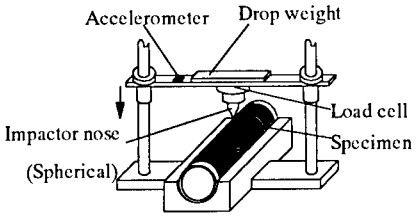

Figure 2 Schematic of the impact test apparatus.

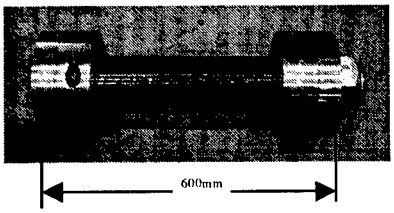

Figure 3 Internal pressure test apparatus.

Experimental Results and Discussions

Impact tests

Figure 4 shows the schematic of surface damage after impact tests. In all conditions, indentation and splitting were observed. Damage areas were larger in the case of impactor radius, R, =10 mm. Fiber breakage were observed only in the specimen A with R = 10. In the case of R = 20 for specimen A, no damages were observed.

Figure 5 shows the result of cross-sectional damage observation. Figure 5 indicates that fiber breakage is caused by micro-buckling. Delamination and plastic deformation of the linar were also observed. There were fiber breakages below the indentation regions of specimen A, however, no fiber breakages were observed in specimen B.

Figure 6 shows the absorbed energy at impact tests. Absorbed energy decreased as the impactor radius became larger. There are no differences in the absorbed energy between specimen A and B at the same

impactor radius, though different damage states were observed. It is considered that the most of impact energies were utilized for plastic deformation of liners.

Internal pressure tests

Figure 7 shows damage progress under internal pressure tests. Splitting progress were observed for specimen A, R = 3 and 10 mm, prior to burst. On the other hand, no microscopic damages were observed for specimen A, R = 20 and specimen B, R= 3 and 10 mm. These specimens burst in a catastrophic manner.

Figure 8 shows burst strength after impact tests comparing to the strength of virgin specimen. Residual strength became larger as the impactor radius, R, became larger. To evaluate the effect of low modulus amorphous carbon fiber on the impact resistant properties, residual strength ratio, which is defined as strength after impact normalized by strength of virgin specimen, are shown in figure 9. Residual strength ratios of specimen B were larger than specimen A. This indicates the high impact resistant by applying the XN-05 fibers.

To clear the effect of damage scale on the residual strength, fiber breakage area were calculated for specimen A. Fiber breakage area is defined as the length of fiber break length measured by surface observation multiplied by fiber breakage depth. Fiber breakage depth was measured after internal pressure tests. Impact damage region was very different from burst damage region, so fiber breakage depth can be measured easily. Figure 10 shows the relation between strength ratio and cross sectional area of fiber breakage. Strength ratio linearly decreased as cross sectional area of fiber breakage increased. That is, it is clarified that not only fiber break length but also fiber breakage depth should be considered to estimate the residual strength after impact.

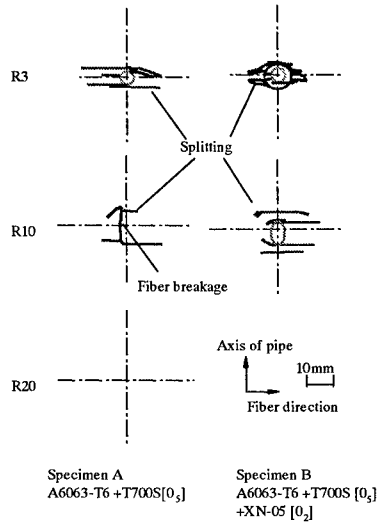

Figure 4 Schematic of impact damage.

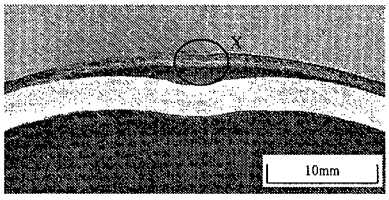

(a) Cross-sectional view.

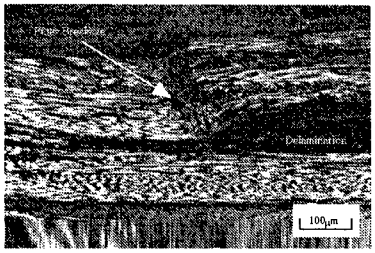

(b) Enlargement of X.

Figure 5 Impact damage (Specimen A, R = 3mm).

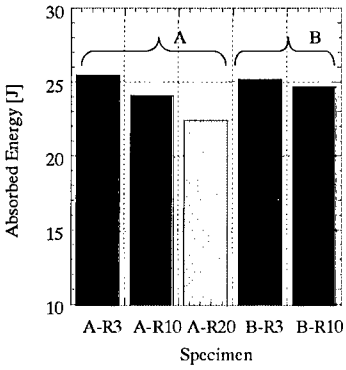

Figure 6 Impact absorbed Energy.

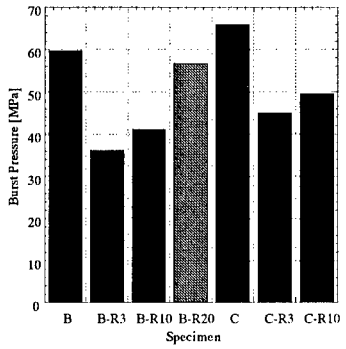

Figure 8 Burst pressure.

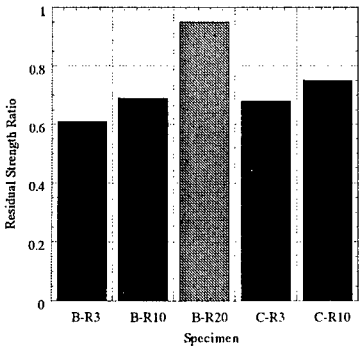

Figure 9 Residual strength ratio.

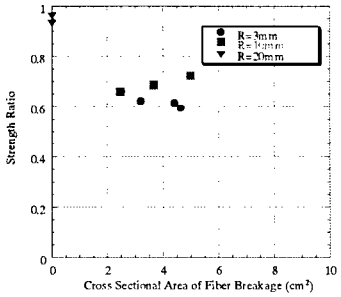

Figure 10 Strength ratio of specimen A as a function of cross sectional area of fiber breakage.

Conclusion

Internal pressure test of FW-CFRP composite pipes after impact test were carried out.

1. Impact absorbed energy become larger as the radius of the impactor become smaller.
2. There are no effects of low modulus amorphous carbon fiber on the absorbed energy.
3. Residual burst strength ratio become larger by applying low modulus amorphous carbon fiber on the surface of the pipes.

Acknowledgment

This research has been supported by Grant in Aid for Scientific Research under grant no. 12555181.

References

1. A. P.Christoforou and S. R.Swanson, Trans. of the ASME, 110, 180 (1988).
2. K. L. Alderson and K. E. Evans, Composite Structures, 20, 37 (1992).
3. S. A. Matemilola and W. J. Stronge, J. Pressure Vessel Technology, 119, 435 (1997).
4. J. Curtis, M. J. Hinton, S. Li, S. R. Reid and P. D. Soden, Composites Part B, 31, 419 (2000).
5. N. Kiuchi, Y. Sohda, T. Matsumoto, G. Ishikawa, Y. Arai, Proc. 25th Sym. Comp. Mater. (Japan- Korea Joint Session), 91 (2000)

Proceedings of 7th Japan International SAMPE
Symposium & Exhibition, Nov. 13-16, 2001

Interply Hybrid Laminates with Improved Flexural Impact Resistance

Shinichi Takemura [1], Hideyuki Ohno [2], Albert S. Kobayashi [3]

1: Nippon Mitsubishi Oil Corporation
8, Chidori-cho, Naka-ku, Yokohama 231-0815, JAPAN
E-mail: shinichi.takemura@nmoc.co.jp

2: Nippon Graphite Fiber Corporation, Web: http://plaza6.mbn.or.jp/~NGF
3-12, Nishi-shimbashi 1-chome, Minato-ku, Tokyo 105-8412, JAPAN

3: Department of Mechanical Engineering, University of Washington
Box 352600, Seattle, Washington 98195-2600, U.S.A.

Abstract

The compression side of a polyacrylonitrile (PAN)-based carbon fiber laminate, TORAYCA T700S, was reinforced with a thin layer of low modulus carbon fiber, GRANOC XN-05 in order to avoid the compression-dominated flexural failure of the T700S laminate. A three-point bend, impact test showed that the impact resistance of the hybrid laminate was considerably higher than that of the T700S monolithic laminate since a higher compressive failure strain of the XN-05 layer suppressed the compressive failure of T700S at the point of impact. A finite element (FE) analysis suggests that the compressive failure strength of the T700S layer in the hybrid laminate was elevated since the XN-05 layer suppressed the microbuckling failure on the compression side of T700S.

Keywords: Impact resistance, Hybrid laminate

Introduction

Flexural failure in PAN-based carbon fiber/epoxy unidirectional laminates tends to initiate on the compression side under three-point bend loading since the compressive failure strain is lower than that in tension [1]. A low modulus carbon fiber/epoxy laminate, XN-05/25P, has considerably higher compressive failure strain than that of the high strength PAN-based carbon fiber/epoxy, T700S/#2500. A thin layer of XN-05 was placed on the one-side of the T700S laminate to form an interply hybrid laminate. Impact load was applied on the XN-05 layer side in a three-point bending mode.

A damage mechanics based FE analysis was also performed with the ABAQUS finite element package in order to delineate the mechanisms for improving the impact resistance of the hybrid laminates [2]. The compressive strength obtained from a compressive testing of the Celanese method was initially used. Then the compressive strength of T700S in the hybrid laminate was elevated to reflect the restraining effect of the XN-05 layer. Finally, the increase in the compressive strength of T700S was demonstrated by correlating the experimental and FE results.

Drop weight impact testing

Materials

All impact specimens were produced from prepregs. The low modulus carbon fiber/epoxy prepreg used as a thin outer reinforcing layer was GRANOC XN-05/25P manufactured by Nippon Graphite Fiber Corporation. The PAN-based carbon fiber/epoxy prepreg used in this study was TORAYCA T700S/#2500 manufactured by Toray Industries, Inc. Table 1 shows the properties of carbon fibers, prepregs, and unidirectional laminates. The compressive properties of unidirectional laminates were measured in accordance with the ASTM D 3410-87 standard test method [3]. The compressive failure strain of 2.9 % of the XN-05 laminate is higher than the 1.4 % of the T700S laminate.

Two types of unidirectional interply hybrid laminates were fabricated by varying the XN-05 to T700S ratio as shown in Table 2. Two monolithic laminates were also fabricated and impact tested. For the hybrid laminate, the thin outer reinforcing layer of XN-05 was placed on the compressive side of T700S. All laminates were cured at a temperature of 130 °C with a nominal thickness of 2 mm. The longitudinal impact specimens with nominal dimensions of 10 mm wide and 80 mm long were cut out from the unidirectional laminates.

Impact tester

A low velocity impact testing was performed with an instrumented drop weight impact tester. The impact load was applied on the XN-05 layer side for the hybrid laminates at a support span of 60 mm. The impact hammer with a 3 mm-radius loading tip weighted 20.7 N. The supports had 6 mm-radius points. The impact hammer was dropped from a height of 300 mm to 600 mm with impact velocities of 2.3 m/sec to 3.2 m/sec, respectively.

Table 1 Carbon fiber, unidirectional laminate, and prepreg properties

			XN-05	T700S
Fiber Properties	Tensile strength	MPa	1180	4900
	Tensile modulus	GPa	55	230
	Elongation	%	2.0	2.1
	Density	g/cm^3	1.65	1.80
Prepreg Specifications	Fiber weight	g/m^2	100	125
	Resin content	wt %	37	33
	Thickness	mm	0.109	0.119
	Resin		25P	#2500
Unidirectional laminate properties	0° Tensile strength	MPa	650	2650
	Tensile modulus	GPa	34	127
	Elongation	%	1.8	1.8
	0° Compressive strength	MPa	880	1470
	Compressive modulus	GPa	32	120
	Failure strain	%	2.9	1.4

Table 2 Impact test specimen specifications

	Interply hybrid		Monolithic	
	Type 1	Type 2	All-XN05	All-T700S
Reinforcing layer on compression side	XN-05 1ply	XN-05 3 ply	-	-
Primary material	T700S 16 ply	T700S 14 ply	XN-05 19 ply	T700S 17 ply

Experimental results

Typical impact load-deflection relations and the absorbed impact energy are shown in Figs. 1 and 2, respectively. The absorbed impact energy was partitioned into initiating failure energy and propagating failure energy.

The impact properties of the hybrid laminates were higher than those of the monolithic laminates due to the reinforcing effect by the XN-05 layer. Type 2 laminate yielded the highest impact load and absorbed impact energy followed by those of Type 1 laminate. The 3-ply XN-05 layer in Type 2 laminate suppressed compressive failure at the top of the T700S layer better than the 1-ply XN-05 layer in Type 1 laminate. For monolithic laminates, the all-XN05 laminate had a lower impact load than the all-T700S laminate but the absorbed impact energy was higher than that of the all-T700S laminate due to higher failure deflection.

The ratio of tensile/compressive failure region on the failed surface was evaluated from micrographs. The all-T700S laminate showed that the compressive failure region accounted for 82 % of the total failed surface and the flexural failure was thus governed by compressive properties. Although the all-XN05 did not break completely, it did not fail in compression. The tensile failure region of Types 1 and 2 hybrid laminates increased to 31 % and 44 %, respectively, compared to 18 % of the all-T700S laminate.

Finite element analysis

Simulating longitudinal failure

A half segment of the impact specimen was modeled. The left side edge of the FE model, which corresponds to the mid-span of specimen, was fixed in x direction and a symmetry boundary condition was imposed on the cross section. The right side edge was fixed in y direction. The finite elements were assumed to fail longitudinally. The longitudinal (0°) tensile/compressive failure strengths, shown in Table 1, were prescribed for both T700S and XN-05 layers. When the longitudinal tensile/compressive stresses exceeded the prescribed failure strength at the Gaussian integration point of the finite element, the modulus of elasticity, E_{11}, the shear modulus, G_{12} and G_{13}, were reduced near to zero. A displacement based FE analysis was performed by applying a y-direction displacement at the mid-span and the reaction force at the support was calculated.

Analytical results

The FE model of the all-T700S and the all-XN05 laminates reproduced the impact load-deflection relations well and showed that the failure strengths obtained from the

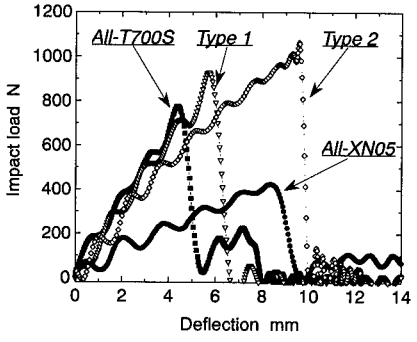

Fig. 1 Impact load-deflection responses

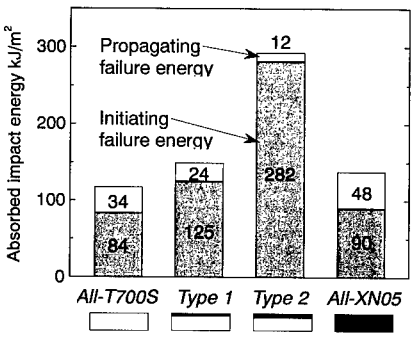

Fig. 2 Absorbed Impact energy

ASTM test method are appropriate for the FE analysis of the monolithic laminates.

For hybrid laminates, the compressive strength, 1470 MPa of T700S, which was obtained by compressive test of the Celanese method, was also prescribed initially. As shown in Fig. 3, the FE results for Type 2 laminate, identified as the FE model #1, were considerably lower than the test data since the FE model predicted the premature compressive failure at the top of the T700S layer. The longitudinal stress distribution though the thickness shows the increase in the compressive failure strength of the T700S layer. Fig. 4 shows the longitudinal stress distribution through the thickness of Type 2 laminate at a deflection of 10 mm, which corresponds to the failure deflection in the impact test. The FE analysis suggested that the longitudinal compressive stress at the top of the T700S layer was 2404 MPa, which was higher than the compressive strength, 1470 MPa, of T700S. When the compressive failure strength of T700S in the FE model of the hybrid laminates was elevated to 2355 MPa, the FE result, identified as the FE model #2, reasonably reproduced the impact load-deflection responses as shown in Fig. 3. Similarly, when the compressive strength, 1960 MPa of T700S, was prescribed for Type 1 laminate, the FE results was consistent with the experimental data.

Conclusions

The higher compressive failure strain of the XN-05 layer suppressed the microbuckling failure of the T700S layer in the hybrid laminate. This resulted in an increase in the compressive failure strength of T700S and an improved flexural impact resistance of the hybrid laminates.

References

1. P. K. Mallick, Fiber-Reinforced composites: Materials, Manufacturing, and Design, Second edition, Marcel Dekker, Inc., New York, 1993
2. ABAQUS Version 5.8, Hibbitt, Karlsson and Sorensen, Inc., 1998
3. D3410-87, "Standard Test Method for Compressive Properties of Unidirectional or Crossply Fiber-Resin Composites", ASTM Standards and Literature References for Composite Materials , American Society for Testing and Materials, Philadelphia, 1990

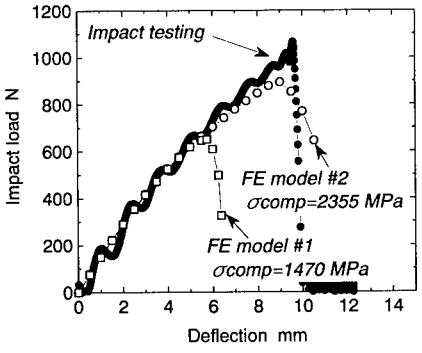

Fig. 3 FE results for Type 2 laminate

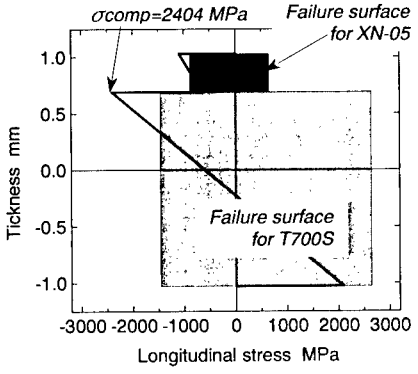

Fig. 4 Stress distribution for Type 2 laminate

Proceedings of 7th Japan International SAMPE
Symposium & Exhibition, Nov. 13-16, 2001

Curing Process in SMC Roll Forming

- Effects on Characteristics and Formability -

Tsutao Katayama[1], Masahiro Shinohara[2], Masahiro Hakotani[3], Go Kamada[4], and Keizo Nishii[4]

1: Department of Mechanical Engineering, Doshisha University
1-3 Tatara Miyakodani, Kyotanabe, Kyoto 610-0321, JAPAN
2: Department of Mechanical Engineering, Maizuru National College of Technology
234 Shiraya, Maizuru, Kyoto 625-8511, JAPAN
E-mail : sinohara@maizuru-ct.ac.jp
3: Mitsui Takeda Chemicals, Inc.
2-26-1 Muraoka Higashi, Fujisawa, Kanagawa 251-8555, JAPAN
4: Graduate Students, Doshisha University
1-3 Tatara Miyakodani, Kyotanabe, Kyoto 610-0321, JAPAN

Abstract

SMC roll forming has some advantages compared with other molding method, which are a lower forming energy, a short production time, a controllability in fiber orientation, a possibility for long-sized products and so on. SMC roll forming consists of two processes, the forming process and the curing process. Until now, we have spent much time for investigating the forming process. However, the curing process is an important factor that characterizes SMC roll forming.
In this paper, we investigated the effects of curing condition on the stiffness and the dimensional accuracy in the curing process. First, we tried to clarify the relationship between time and temperature in the specimen as characteristics in curing process. And we predicted curing times for various heating temperature. Next, we examined the dimensional accuracy and stiffness of the products cured in various conditions considering cure characteristics. Finally, we confirmed superiority of curing condition sets in order to improve the stiffness and the dimensional accuracy.

Key Words : SMC Roll Forming, Curing Process, Curing Time, Heating Temperature

Introduction

We have attempted to apply roll forming, which is known as a metal rolling [1-3], to SMC. SMC roll forming has some advantages compared with other molding

method, which are a lower forming energy, a short production time, a controllability in fiber orientation and a possibility for long-sized products and so on. SMC roll forming is consists of two processes, the forming process in which the material deforms to the target shape and the curing process in which the material cures. Until now, setting of the forming condition and deformation characteristics has been established in the forming process. However, the curing process is an important factor that characterizes SMC roll forming. Therefore, it is desired that various characteristics in the curing process are found at present.

In this study, we investigated the effects of curing condition on the stiffness and the dimensional accuracy in curing process. First, we tried to clarify the relationship between time and temperature in the specimen as characteristics in curing process. And we predicted curing times for various heating temperature. Next, we examined the dimensional accuracy and stiffness of the products cured in various conditions considering the cure characteristics. Finally, we confirmed superiority of curing condition sets in order to improve the stiffness and the dimensional accuracy.

SMC Roll Forming

Materials and Forming Machine

Contents of SMC in this study are shown in Table 1.

Table 1 Contents of SMC.

	[wt %]
Resin (UP, TP, etc.)	25.0
Glass fiber	30.0
$CaCO_3$	45.0

This SMC is cut out and 5 sheets of SMC are laminated. Afterwards, the preparatory molding is carried out in order to set the initial thickness of the specimen to 9 [mm].

Forming Process

Then, the specimen is inserted into the arrow direction as shown in Fig.1 and we form repeatedly until the web thickness becomes the target thickness. Like the above, the product with channel shaped cross section is formed by continuous roll forming. The product has the cross section of 75[mm] x 20[mm] x 5[mm] (= width x flange height x web thickness) as shown in Fig.2.

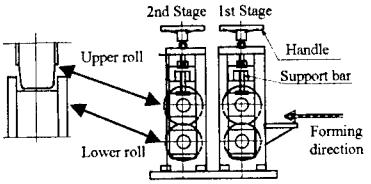

Fig.1 Roll forming machine.

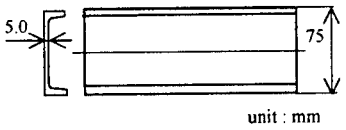

Fig.2 Size of specimens.

Curing Process

After the forming process, the specimen is cured by curing system as shown in Fig.3.

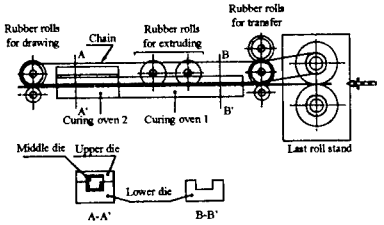

Fig.3 Curing system.

Curing Characteristics

It is possible to know, by observing the relationship between temperature and

time of the material, for characteristics of curing. Then, in this chapter, the relationship between heating time and temperature in specimen was investigated, and various phenomena were examined. And, curing completion in this study shall mean exothermic reaction end in the specimen. The curing condition in this study is shown in Table 2.

Table 2 Curing condition.

Displacement of middle die		free	
		Oven-1 [°C]	Oven-2 [°C]
Heating temperature condition	He-12	120	120
	He-13	130	130
	He-14	140	140
	He-15	150	150
	He-16	160	160
	He-17	170	170

Temperature History in the Specimen

In this section, in order to estimate the gelation time and completion time of the exothermic reaction in the specimen, we clarify the relationship between time and temperature in the specimen.

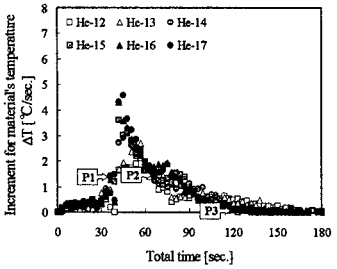

Fig.4 Increment for temperature in the specimen vs. total time.

Fig.4 shows the relationship between time and increment for temperature in the specimen. In this figure, ΔT_i shows the incremental value of temperature in the specimen derived by eq. (1).

$$\Delta T_i = \frac{T_i - T_{i-1}}{\Delta t} \qquad (1)$$

In this figure, paying attention to the discontinuity of this curve, we can guess the 3 points of total time as follows.

P1 : Completion time of first stage of curing at the curing oven 1. (Total time = 36 [sec.])

P2 : Start time of exothermic reaction and completion time of gelation in the specimen.

P3 : Completion time of exothermic and curing reaction in the specimen.

Fig.5 shows the relationship between heating temperature condition and each point of total time. From this figure, start and completion time of exothermic reaction at each heating temperature is found and it is able to guess the completion time of curing. And when the heating temperature increases, the gelation time (P2) comes to be shorter.

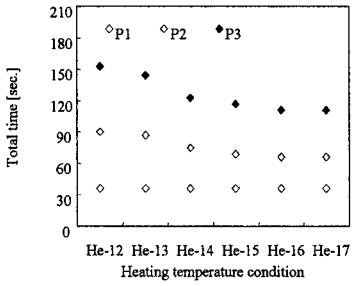

Fig.5 Total time vs. heating temperature condition.

Dimensional Accuracy of the Specimen

The relationship between each heating condition and total strain of the specimen is shown in Fig.6. In this figure, the total strain to the longitudinal direction is almost constant in every heating temperature condition. However, the total strain to the lateral direction increases as the heating

temperature comes to higher. In the case of higher heating temperature, the gelation time comes to be short, so the gelation occurs at the same time in the whole specimen. At this time, the specimen compressed by the middle die and deforms to the longitudinal and lateral direction equally. The size of the specimen in this study to the longitudinal direction is larger than to the lateral direction, so the total strain to the lateral direction is larger compared to the longitudinal direction.
In the case of lower heating temperature, the specimen keeps preformed dimension before and after curing process, so lower heating temperature condition is desirable.

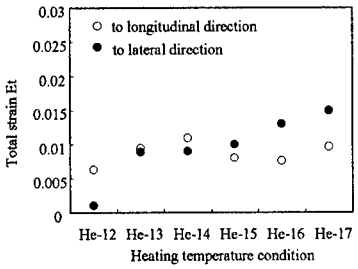

Fig.6 Total strain vs. heating temperature condition

Effect on Mechanical Properties

In this study, in order to estimate the effect of curing condition on mechanical properties, tensile test of the web part of the specimen is carried out and Young's modulus of the specimen is found.
Fig.7 shows the relationship between heating temperature condition and Young's modulus of the specimen derived by tensile test. In this figure, Young's modulus of the specimen is slightly increases at higher heating temperature condition.
In the case of higher heating condition, as above mentioned, the gelation occurs at the same time in the whole specimen, and the specimen compressed by the middle die. So the density at the web part of the specimen increases and Young's modulus of the specimen increases.
Therefore, in respect of Young's modulus, the higher heating temperature condition is desirable.

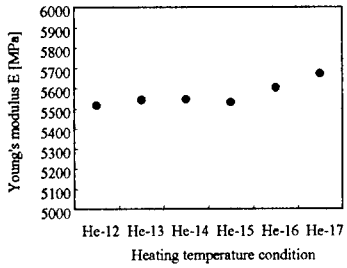

Fig.7 Young's modulus vs. heating temperature condition.

Conclusion

We investigated the relationship between time and temperature in the specimen as characteristics in curing process and investigated the effects of curing condition on the dimensional accuracy and the stiffness of the specimen.
Following results were obtained.

(1) By measuring the increment for temperature in the specimen, it is possible to estimate the curing time.
(2) The products cure at lower heating temperature keep preformed dimension before and after curing process.
(3) In respect of Young's modulus, the higher heating temperature condition is desirable.

References

1. Hirai, T, Eu-Jap. Exch. on Materials, Tech Met., 92 (1992)
2. Hirai, T. JSPP, 6-12, 922 (1994)
3. Katayama, T. et al, Journal of JSMS, 45-8, 871 (1996)

Proceedings of 7th Japan International SAMPE
Symposium & Exhibition, Nov. 13-16, 2001

Comparison of Strength and Damage for Notched FRP Plates made by Injection Molding with that of Machining

Toshihiro Yamamoto# and Hiizu Hyakutake#

#: Fukuoka University, Faculty of Engineering, Department of Mechanical Engineering
8-19-1 Nanakuma, Fukuoka 814-0180, JAPAN
E-mail: yamamott@fukuoka-u.ac.jp

Abstract

The strength and damage for notched FRP plates made by injection molding (IM specimen) and that of machining (M specimen) have been investigated. This is accomplished by obtaining experimental data of the static tension and fatigue tests on the notched plate of short glass fiber-reinforced polycarbonate. To evaluate the damage near the notch root, we measured the luminance distributions by means of the luminance-measuring system with a CCD camera. On the basis of the idea of the stress concentration and the similarity of stress distribution near the notch root, the experimental results of IM specimen were compared to that of M specimen.

Key Words: FRP, notch, fatigue, damage

Introduction

Because of their importance in design applications, the fracture and fatigue of notched FRP specimens have been the subject of much research. Such notch is gained by two methods; injection molding of the notched FRP plates and machining by cutting the FRP plates.

The aims of the present research are to investigate the effect of the machining of notch on the strength of the short fiber reinforced plastics. This is accomplished by obtaining experimental data of the static tension and fatigue tests on the notched plate made by injection molding (IM specimen) and that of machining (M specimen) of short glass fiber-reinforced polycarbonate.

To evaluate the strength and the damage near the notch root, we used a fracture criterion for notched FRP plates in static load [1] and a fatigue failure criterion for notched FRP plats [2]. The validity of the fracture criterion [1,3] and the fatigue failure criterion [2] were confirmed previously for notched FRP plates. The criterion is based on the idea of stress concentration and the similarity of stress distribution near the notch root.

Prior to fracture, the damaged zone initiates and grows near the notch root of notched FRP plates under static and cyclic loading. To evaluate the damage, we measured successively the luminance distributions by means of the luminance-measuring system with a CCD camera [2, 3].

Theory

Studying stress distribution near the notch root, Hyakutake et al. [1] have obtained a fracture criterion for FRP plates having intermediate notch-root radii in static

load. The severity near the notch root is determined by both the maximum elastic stress σ_{max} and the notch- root radius ρ [1]. It is suggested that the elastoplastic stress distributions near the notch root after small-scale yielding or damage are the same in all specimens, for which both the σ_{max} and ρ are equal in all cases.

Based on the evidence mentioned above, the fracture criterion for a notched plate under static load is expressed as [1]

$$\sigma_{max} = \sigma_{max,c}(\rho) \qquad (1)$$

where σ_{max} is the maximum elastic stress at fracture and is determined as the product of the nominal stress and the geometrical stress concentration factor. The parameter $\sigma_{max,c}$ is governed by the notch-root radius ρ, and it is independent of notch depth and notch angle and so on.

Under the condition of cyclic loading, it is considered that the initiation of fatigue damage near the notch root is determined by both the magnitude of severity and the repetition of loading. The fatigue failure criterion in cyclic loading is expressed as [2]

$$\sigma_{max} \cdot (N_d)^m = C(\rho) \qquad (2)$$

where N_d is the number of loading cycles to fatigue damage initiation. The parameter m and C are the material constant. The details of N_d will be described later.

Experimental Procedure

The material used was a short glass fiber-reinforced polycarbonate. The plate contains 30 % E-glass fiber by weight. The length of glass fiber is 1 mm or less. Two kinds of notched specimen were used: notched plates made by injection molding (IM specimen) and that of machining by cutting the same FRP plates (M specimen). The notch- root radius, notch depth and width of specimen are the same in both IM specimen and M specimen. The notch-root radius ρ ranged from 0.2 to 10 mm. The notch angle is 90° for IM specimen and 0° for M specimen.

Figure 1 shows transmitted light photographs near the notch root. It is evident that the orientation of the fiber near the notch root for IM specimen is different from that for M specimen.

Static tension tests were performed by using an Instron-type testing machine at a constant cross-head speed of 0.5 mm/min. Fatigue tests of pulsating tension were made on a servohydraulic material test system at frequency 2 Hz.

To evaluate the damage, we measured the luminance distributions near the notch root by means of the luminance- measuring system with a CCD camera [2,3].

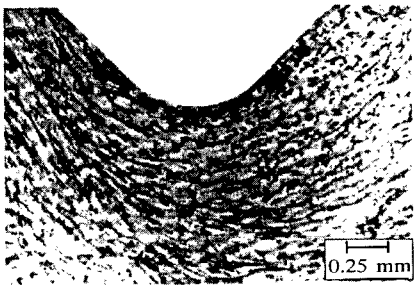

(a) IM specimen

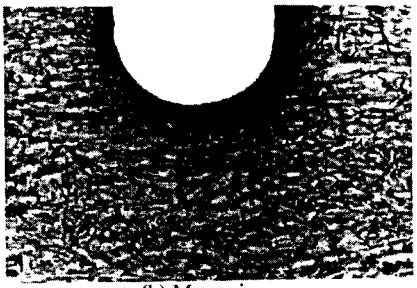

(b) M specimen

Fig. 1 Transmitted light photographs near the notch root (ρ = 0.5 mm).

Results and Discussion

Figure 2 shows the processes of damage initiation and growth near the notch root under static tension. The patterns with light and shade correspond to the value of luminance that was made at four steps, 75, 70, 65 and 60%. The value of relative luminance is the ratio of the luminance at a stress to the luminance before testing. The damage is accumulated severely at the region where the value of relative luminance is small. The processes of damage initiation and growth of IM specimen under static tension were similar to that of M specimen.

The relation between the area of damaged zone and the maximum elastic stress σ_{max} is represented in Fig. 3. It can be

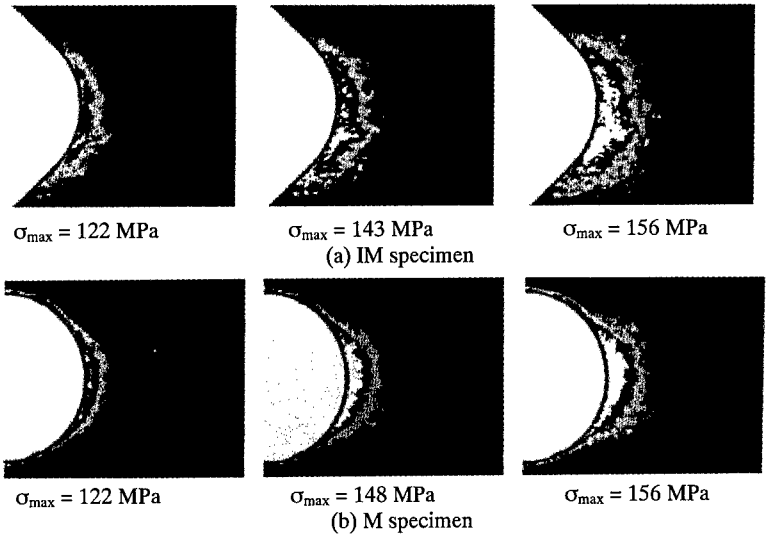

Fig. 2 Growth of damaged zone near the notch root (ρ = 2 mm)

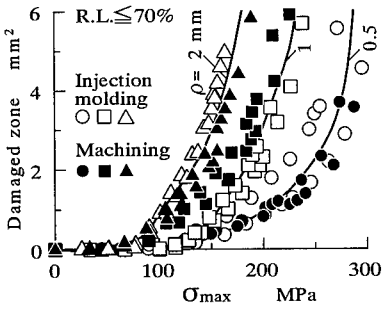

Fig. 3 Area of damaged zone versus the maximum elastic stress σ_{max} under static tension.

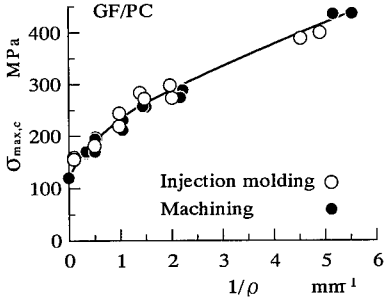

Fig. 4 Maximum elastic stress at fracture, $\sigma_{max,c}$ versus notch-root radius ρ under static tension.

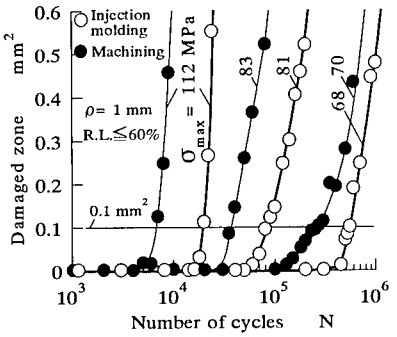

Fig. 5 Growth of the area of fatigue-damage zone.

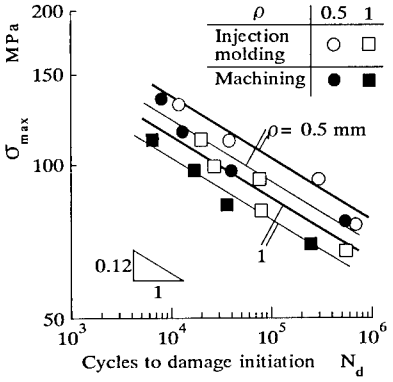

Fig. 6 The relation between the maximum elastic stress σ_{max} versus the cycles to fatigue damage initiation N_d.

seen that the area of damaged zone has a one-to-one correspondence with a notch-root radius. There is no difference between IM specimen and M specimen.

Figure 4 shows the maximum elastic stress at fracture in static tension versus notch-root radius. As can be seen from Fig. 4, each experimental point of IM specimen fell in close proximity to the characteristic curve for M specimen.

Fatigue damage is accumulated severely at the region where R.L. is small. The growth curves of the area of fatigue-damage zone where R.L. $\leqq$ 60 % are shown in Fig. 5. When the area of fatigue-damage zone increased to the value of 0.1 mm^2, the fatigue-damage zone increased rapidly. We determined that N_d is the number of loading cycles at the area of fatigue-damage zone = 0.1 mm^2 [2].

The growth curve of fatigue-damage zone for IM specimen is different from M specimen subjected to the same value of the maximum elastic stress.

Figure 6 shows the relationship between the maximum elastic stress and the fatigue-damage initiation N_d for a constant notch-root radius ρ. The processes of fatigue damage initiation of IM specimen were different from that of M specimen. As can be seen from Fig. 6, the number of loading cycles to fatigue damage initiation of IM specimen were longer than that of M specimen.

Conclusions

The strength and process of damage initiation for notched FRP plates made by injection molding (IM specimen) and that of machining (M specimen) have been investigated.

For static tension tests, the strength and process of damage initiation of IM specimen were similar to that of M specimen.

On the other hand, the process of fatigue damage initiation of IM specimen was different from that of M specimen. The number of loading cycles to fatigue damage initiation of IM specimen were longer than that of M specimen.

References

1. H. Hyakutake, H. Nisitani and T. Hagio, JSME Int. J., 32(2), 300(1989).
2. H. Hyakutake and T. Yamamoto: Proc. 5th Japan Int. SAMPE Symposium, 119 (1997).
3. H. Hyakutake and T. Yamamoto, Science and Engineering of Composite Materials, 6(2), 121(1997).

Proceedings of 7th Japan International SAMPE
Symposium & Exhibition, Nov. 13-16, 2001

Effect of Thermal Treatment on Mechanical Properties of a Carbon/Epoxy Composite

Keiji OGI#, Tetsuro SHIRAISHI# and Takayuki TOKUNAGA##

#: Department of Materials Science and Engineering, Ehime University
3 Bunkyocho, Matsuyama, Ehime 790-8577, JAPAN
##:Graduate school of Science and Engineering, Ehime University
3 Bunkyocho, Matsuyama, Ehime 790-8577, JAPAN
E-mail: kogi@en2.ehime-u.ac.jp

Abstract

This paper presents the effect of thermal treatment on mechanical properties of carbon fiber reinforced epoxy (CF/Epoxy) composites. At first, the shrinkage strain, the mechanical properties such as Vickers hardness of resin, transverse modulus and strength and Weibull parameters of transverse strength are measured for carbon/epoxy unidirectional laminates after four-hour thermal treatment. Then, the effect of thermal treatment temperature on transverse cracking behavior in a cross-ply laminate is experimentally investigated. The change in the residual stress due to thermal treatment is also estimated for the cross-ply laminate. Finally, the fracture surfaces of transverse cracks are observed using the scanning electron microcopy (SEM) to reveal the effect of thermal treatment on fracture behavior. It is found that the unidirectional laminate shrinks in only the transverse direction after thermal treatment. The hardness of the resin increases with increasing thermal treatment temperature below 150 ℃ while transverse modulus and strength are independent of temperature below 150 ℃. Transverse cracks in cross-ply specimens after thermal treatment initiate at lower stresses than the critical stresses in virgin specimens. It is deduced from SEM observation of fracture surfaces that the fiber/resin interface is weakened by thermal treatment that may lead to reduction in the transverse strength at 200 ℃.

Key words: Thermal Treatment, Transverse Modulus, Transverse Strength, Transverse Cracking, Residual Stress

Introduction

As composite materials have been widely used in various industrial fields, it is essential to quantitatively evaluate effect of thermal history on mechanical properties and geometrical change. Fiber reinforced thermoplastic composites shrink in the transverse direction during a curing process [1]. Shrinkage is also observed when a composite is subjected to high temperature during thermal treatment. While some researches have been conducted for other material systems [2,3], effect of thermal treatment on mechanical properties and fracture behavior of this composite has received little attention in the literature.

In the present study, we measured shrinkage strain and change in Vickers

hardness of resin, Young's modulus and strength of a unidirectional CF/Epoxy composite after thermal treatment. Then, transverse cracking behavior in a cross-ply laminate was studied taking transverse strength and residual stress into account. In addition, fracture surfaces were observed by scanning electron microscopy (SEM) to reveal the fracture behavior.

Experiment

Material and thermal treatment

The CF/Epoxy unidirectional and cross-ply ($[0°/90°_3]_S$) laminates were fabricated by means of an autoclave system at a curing temperature of 180 °C. In some unidirectional laminates, thermocouples and heat-resistant strain gages were embedded between prepregs and cocured. The specimens were cut out of unidirectional and cross-ply laminates and heated for four hours at temperatures 70, 110, 150 and 200 °C in air under the atmospheric pressure. The longitudinal and transverse strains in the unidirectional laminate were measured during thermal treatment.

Mechanical tests and fracture behavior

After polishing the cross-section of virgin and thermally-treated [90°] specimens, Vickers hardness of resin between fibers were measured for applied load 1 gf. Tensile tests were performed for [90°] specimens to measure transverse modulus E_2 and strength S_2. Weibull parameters of transverse strength S_2 were also measured assuming that S_2 obeys the following two-parameter Weibull distribution:

$$F = 1 - \exp\left\{-\frac{V_S}{V_0}\left(\frac{\sigma_2}{\sigma_0}\right)^n\right\} \qquad (1)$$

where F, V_S and V_0 denote probability of failure at transverse stress σ_2, standard volume and volume of the specimen, respectively, and n, σ_0 are shape and scale parameters, respectively. Fracture surfaces of [90°] specimens with and without thermal treatment were observed by means of SEM focusing on fiber/matrix interfaces. Tensile tests were also conducted for cross-ply specimens to measure transverse crack density as a function of applied stress at room and high (110 °C) temperatures. Gage length for transverse cracking was 60 mm which corresponds to gage length of the two strain gages on the specimen.

Results and Discussion

Shrinkage strain

Figure 1 shows change in the transverse strain in the unidirectional specimens during thermal treatment. The strain increases with increasing temperature and then decreases while temperature is kept constant. The strain decrease during cooling and compressive permanent strain is observed at room temperature. The permanent strains (-730, -650, -2500 με for 110, 150, 200 °C) are comparable to the shrinkage strains during thermal treatment. On the other hand, the longitudinal strain decreases with

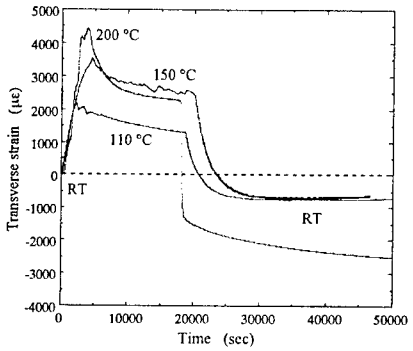

Fig. 1 Transverse Strain in Unidirectional Laminates during Thermal Treatment.

Table 1 Vickers Hardness, Transverse Modulus, Transverse Strength and its Weibull Parameters

T ℃	H_V (1gf)	E_2 MPa	S_2 MPa	n	σ_0 MPa
RT	22.2	8.28	74.1	5.15	256
70	23.1	N/A	N/A-	N/A	N/A
110	23.8	8.11	N/A	N/A	N/A
150	25.2	8.34	76.5	6.21	215
200	23.9	8.15	63.4	5.48	205

temperature rise and returns to zero at room temperature.

Hardness, Modulus and Strength

Table 1 summarizes the Vickers hardness of resin H_V, transverse modulus E_2 and strength S_2 and Weibull parameters of S_2 for various thermal treatments. The scale parameter σ_0 was computed with the use of $V_0 = 1\,\text{mm}^3$ and $V_S = 448\,\text{mm}^3$. Hardness increases with an increase in temperature below 150 °C while it decreases at 200°C. The increase in hardness is attributed to post-cure effect of resin while the decrease at 200°C may be ascribed to deterioration of resin due to high temperature over glass transition temperature (about 160 °C). Transverse modulus E_2 and strength S_2 are insensitive to thermal treatment except for reduction in strength S_2 at 200 °C. The shape parameter n dose not change largely with temperature whereas the scale parameter σ_0 decreases with increasing temperature.

Fracture behavior

Figure 2 shows SEM photographs of fracture surfaces of [90°] specimens with and without thermal treatment. In the thermally-treated specimen (200 °C), amount of resin attached to fiber/resin interfaces is small compared with the virgin specimen. This indicates weakness of interface strength after thermal treatment, which leads to reduction in transverse strength S_2 at 200 °C.

Transverse cracking

Figure 3 shows transverse crack density as a function of applied stress in cross-ply specimens with and without thermal treatment. Critical stress for transverse cracking decreases with increasing thermal treatment temperature T and the crack density is larger at higher temperature T.

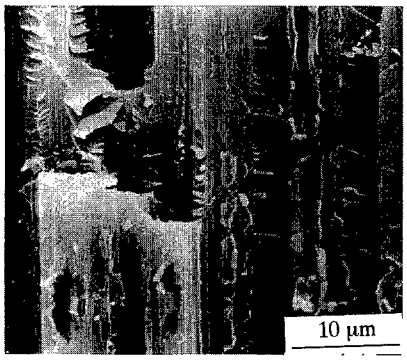

(a)

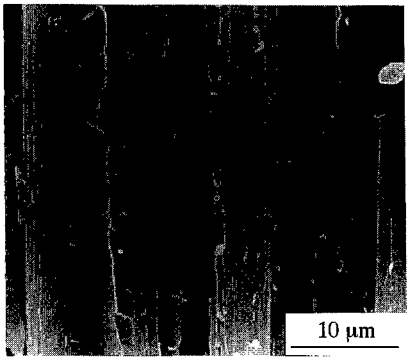

(b)

Fig. 2 SEM Photos Showing Fracture Surfaces; (a) Virgin and (c) 200℃.

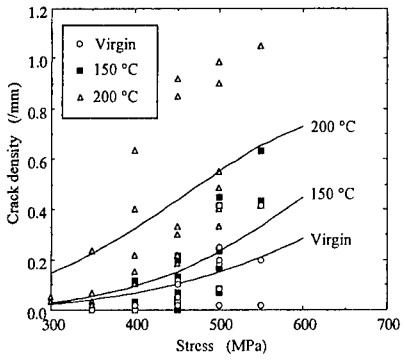

(a)

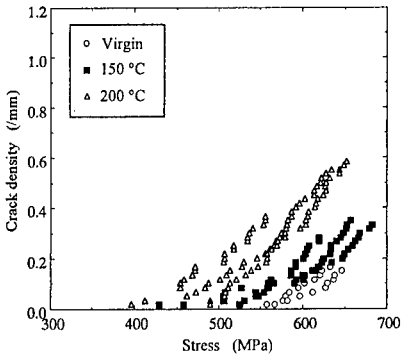

(b)

Fig. 3 Transverse Crack Density VS. Stress at (a) 25 ℃ and (b) 110 ℃.

Transverse cracking behavior can be explained by residual stress in conjunction with a probabilistic failure model. The shrinkage in the transverse direction increases the residual stress in the 90° ply (36 MPa at room temperature for a virgin specimen) by 5.2, 4.6, 17.8 MPa for thermal treatment of 110, 150 and 200 °C, respectively. Transverse crack density ρ is expressed by the following equation [4]:

$$\rho = \frac{1}{L_e}\left[1-\exp\left\{-\frac{V_e}{V_0}\left(\frac{\sigma_2+\sigma_{2,T}-\sigma_C}{\sigma_0}\right)^n\right\}\right] \quad (2)$$

where L_e is the element length [4] obtained using a shear lag analysis, V_e, σ_2 and $\sigma_{2,T}$ denote the element volume, transverse stress and residual stress in the 90° ply and σ_C denotes strength increment due to constraint effect [4]. With the use of $L_e = 1.234\,\text{mm}$, $V_e = 10.96\,\text{mm}^3$, $\sigma_C = 10.0\,\text{MPa}$ together with the material properties shown in Ref. [5] and in Table 1, the transverse crack density is predicted through Equation (2). Predicted crack density is shown in Figure 3 (a) as solid lines. Predictions agree qualitatively well with the experimental results.

Concluding Remark

Effect of thermal treatment on mechanical properties of CF/Epoxy composites is studied. Transverse modulus and strength are insensitive to thermal treatment below 150 °C except hardness of resin. Thermal treatment of 200 °C decreases the transverse strength and strength for transverse cracking. Reduction in the strength results from an increase in the residual stress in the 90° ply due to shrinkage in the transverse direction.

References

1. A. S. Crasto and R. Y. Kim, Proc. 8th Japan-US Conf. Compos. Mater., 813 (1998).
2. K. A. Lindsey and C. D. Rudd, J. Materials Science Letters, **12**, 894 (1993).
3. R. Tucker, P. Compston and P. -Y. B. Jar, Composites Part A, **32**, 129 (2001).
4. N. Takeda and S. Ogihara, Compos. Sci. Tech., **52**, 183 (1994).
5. K. Ogi, H. S. Kim, T. Maruyama and Y. Takao, Compos. Sci. Tech., **59**, 2375 (2000).

Proceedings of 7th Japan International SAMPE
Symposium & Exhibition, Nov. 13-16, 2001

Electro-Conductive Plastic Compounds filled with Stainless Steel Micro Fiber

Kenji Yoshino and Ryozo Sakamoto

KAWASAKI STEEL Techno-research Corporation, Process & Products Engineering Divsion
1, Kawasaki-cho, Chuo-ku, Chiba 260-0835 Japan
E-mail: yoshino@tsc.ktec.co.jp

Abstract

Plastic compounds filled with stainless steel micro fiber(SMF), named as "SUSTEC", exhibit very uniform good electric conductivity and low frictional electrification properties. SMF is a curved fine fiber(10μm in mean dia. and 300μm in mean length) made by grinding the stainless steel sheet. A low sloughing and particulate contamination free properties, an excellent wear resistance, a low warpage and good dimensional stability are also important characteristics of SUSTEC. These characteristics are attributable to the ductile and isotropic nature of SMF and its three dimensional fine network structure in the compounds. SUSTEC compounds are applied to electric/electronic parts which require the basic properties free from dust contamination and charging of static electricity, e.g. the tray for IC packages.

Key Words: Stainless Steel Micro Fiber, Electrically Conductive Plastics.

Introduction

Many electrical and electronic parts using plastics have Electro-Magnetic Interference(EMI) and Electro-Static Discharge(ESD) problems, because plastics are electrical insulation materials and transparent against electromagnetic radiation. There are a number of ways to solve EMI and ESD problems, for example, an electroless and electrolytic plating, a spray coating, a vacuum metallising and a conductive paint. One of the best way is the use of electrically conductive plastics such as stainless steel fiber loaded plastics.

This paper describes characteristics of "Stainless Steel Micro Fiber" developed and produced by KAWASAKI STEEL Techno-research Corporation.

Stainless Steel Micro Fiber(SMF)

SMF is a curved fine fiber(10μm in mean dia. & 300μm in mean length) made by grinding the stainless steel sheet(Fig.1).

Fig.1 Stainless Steel Micro Fiber(×30)
Average Size: 10μm in dia., 300μm in length
Specific Gravity:7.9, Specific Surface:0.30 m^2/g

Properties of SMF Loaded Plastic Compounds

Electroconductivity

Figure 2 shows the volume resistivity of stainless steel fiber loaded ABS. In the case of SMF loaded ABS, the electroconductivity appears in the range of 6-8 volume percent. That of stainless steel long fiber(SUS-L, $\phi 8\mu m \times 6mm$) loaded ABS appears only at 0.5 volume percent. It is considered that the difference between SMF and SUS-L is attributable to the aspect ratio of fiber. SUS-L has the advantage that the low loading levels in the range of 0.5-1.5 volume percent are sufficient to satisfy ESD or EMI requirements. However, as can be seen from the vertical curve of SUS-L in Fig.2, it is difficult to control the volume resistivity of 10^3 Ω·cm or above. On the other hand, the volume resistivity of SMF loaded ABS can be controlled accurately in the range of 10^1- 10^5 Ω·cm by changing the SMF content.

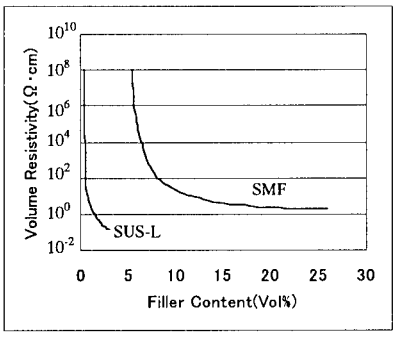

Fig.2 Volume Resistivity of Stainless Steel Fiber Loaded ABS
SUS-L:Stainless Steel Long Fiber($\phi 8\mu m \times 6mm$)
SMF:Stainless Steel Micro Fiber($\phi 10 \times 300\mu m$)

Homogeneous Electric Conductivity

The relationship between the distance from gate of moldings and the volume resistivity is shown in Table 1. The volume resistivity decreases with increasing distance from gate. At the same time, specific gravity also increases. One of the cause of variation of volume resistivity is the variation of filler content. The degree of variation of SUS-L loaded ABS is larger than that of SMF loaded ABS.

Table1 The Effect of Distance from Gate of Moldings on Volume Resistivity

No.	SMF43wt% Loaded ABS		
	S.G.	Filler Content (wt%)	VR (Ω·cm)
1	1.643	41.6	4.7×10^4
2	1.642	41.6	2.0×10^4
3	1.645	41.7	7.8×10^3
4	1.651	42.0	4.4×10^3
5	1.661	42.4	2.4×10^3
6	1.669	42.8	1.0×10^3
7	1.668	42.7	9.9×10^2
No.	SUS-L 9wt% Loaded ABS		
	S.G.	Filler Content (wt%)	VR (Ω·cm)
1	1.121	7.3	3.4×10^1
2	1.126	7.8	7.1×10^0
3	1.128	8.0	5.1×10^0
4	1.133	8.5	2.7×10^0
5	1.140	9.1	1.3×10^0
6	1.153	10.3	7.8×10^{-1}
7	1.164	11.3	3.5×10^{-1}

Filler Content:Caluculated Value from Specific Ggravity(ABS:1.05, filler:7.9)
SUS-L:Stainless Steel Long Fiber
S.G.:Specific Gravity

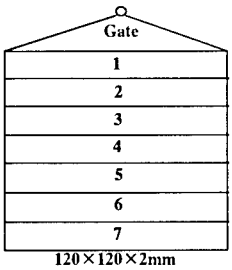

Table 2 shows the surface resistivity of SMF loaded polypropylene moldings(IC chip tray). At any points on the molding, SMF loaded composite reveals a very homogeneous surface resistivity.

Table 2 Surface Resistivity of IC Chip Tray

Position	SR(Ω/sq)	Position	SR(Ω/sq)
①	6.0×10^4	⑥	5.5×10^4
②	5.9×10^4	⑦	6.0×10^4
③	6.2×10^4	⑧	5.8×10^4
④	5.6×10^4	⑨	5.5×10^4
⑤	5.8×10^4	⑩	5.5×10^4

Material : SMF 38wt% Loaded PP,
SR:Surface Resistivity

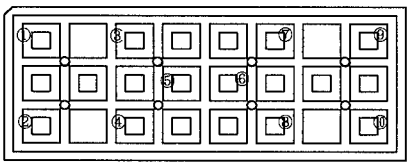

8 pin gates, Tray Size:135mm×320mm

Anisotropy

Stainless steel fiber loaded plastic moldings have a very small anisotropy(Table 3). Especially, anisotropy of mold shrinkage is almost equal to 1.0. For this reason, the moldings of stainless steel fiber loaded plastics exhibit a very low warpage and good dimensional stability.

Low Sloughing and Particulate contamination-Free Properties

Table 4 shows the volume wear obtained with the thrust washer test apparatus. The volume wear of SMF loaded polypropylene is very small compared with that of polypropylene. Furthermore, SMF loaded polypropylene exhibits 1/5 volume wear of carbon black loaded polypropylene which has same surface resistivity.

The low sloughing and particulate contamination-free properties are attributable to the ductile nature of stainless steel fiber.

Table 3 Anisotropy of Stainless Steel Fiber Loaded ABS Moldings

Test Items	Direction	SMF 43wt% ABS	SUS-L 9wt% ABS
Flexural Strength	// (MPa)	74	70
	⊥(MPa)	58	59
	// / ⊥	1.28	1.17
Flexural Modulus	// (MPa)	4670	2870
	⊥(MPa)	3630	2750
	// / ⊥	1.29	1.04
Mold Shrinkage	// (%)	0.24	0.38
	⊥(%)	0.26	0.38
	⊥ / //	1.08	1.00
Surface Resistivity	// (Ω/sq)	2.7×10^5	3.9×10^1
	⊥(Ω/sq)	2.7×10^5	4.8×10^1
Volume Resistivity	// (Ω·cm)	3.9×10^4	5.5×10^0
	⊥(Ω·cm)	4.4×10^3	2.7×10^0

//:Flow direction, ⊥:Transverse direction
Specimen:Cutting from 120x120x2mm plaque

Table 4 Thrust Washer Test of SMF Loaded Polypropylene

Test	Test Sample	Volume Wear (mm^3)
1	Polypropylene(PP)	20.7
	SMF60wt% PP	1.3
2	Carbon Black 22wt% PP	10.3
	SMF 38wt% PP	2.0

Test Method:JIS K7218
Test 1; Pressure:137N, Velocity:15m/min, Elapsed time:60min, Counterface:S45C
Test 2 ; Pressure:50N, Velocity:30m/min, Elapsed time:100min, Counterface:S45C

Conclusions

SMF loaded plastic compounds are available as a commercial name "SUSTEC". SUSTEC has excellent characteristics as a electrically conductive plastics, such as a controlable and homogeneous resistiveity, a low warpage and good dimensional stability, a low sloughing and particulate contamination-free properties.

Proceedings of 7th Japan International SAMPE
Symposium & Exhibition, Nov. 13-16, 2001

Silver Coated Carbon Black Epoxy Composites: PTC Effect and Electric Wave Shielding Effectiveness

Hisaichi Ohnabe[1] and Kenichi Kamada[2] and Farid El-Tantawy[1*]

1: Department of Biocybernetics, Faculty of Engineering, Niigata University
8050 Igarashi 2-nochou, Niigata City, Niigata 950-2181, JAPAN
2: Graduate School of Science and Technology, Niigata University
* On leave from: Faculty of Science, Suez Canal University, Ismailia, Egypt
Email: ohnabe@bc.niigata-u.ac.jp

Abstract

In the present paper we report on the successful preparation of a new functional conductive epoxy resin, silver coated carbon black composite with a positive temperature coefficient of resistance (PTC) and effective electric wave shielding properties. The correlation between electrical conductivity and the volume of silver coated carbon black has also been investigated. The temperature dependence of electrical properties was analyzed. We performed a study of the mechanisms related to the DC electrical conductivity of epoxy resin loaded with different concentrations of silver coated carbon black. The morphology of silver coated carbon black was displayed by using scanning electron microscopy (SEM). We have concluded that the silver coated carbon black is a promising composite for heating elements, temperature sensors and electric wave shielding applications.

Key Words: epoxy resin, silver coated carbon black, electrical heater, electric wave shielding

1. Introduction

Dispersion of a conductive filler into an insulating polymer matrix yields a composite material characterized by a sharp increase of its bulk electrical conductivity, when the volume fraction of filler is increased above a threshold value [1,2,3]. With increasing temperature, most such composites display a sharp increase of their resistance. This effect, known as the positive temperature coefficient of resistance (PTC) is pronounced in semi- crystalline and amorphous polymers. In fact, the mechanism involved in the change of the electrical properties of the composites is still under debate in the literature. Recently, shielding against electric waves has become a critical and functional requirement for plastic housings and others in order to protect the electronic components from environmental electric wave shielding. In the present paper, experimental and theoretical studies of the electrical properties and electric wave shielding effectiveness of silver coated carbon black epoxy composites are also presented.

2. Experimental

Silver coated carbon black is used as the conducting filler. The matrix is epoxy, mixed with bisphenol A type liquefied epoxy, with gravity of 1.10g/ml. Dispersion of silver coated carbon black into the liquid epoxy and hardener matrix is achieved by use of a centrifuge mixer for 1 minute. The composite material is then cast in a Teflon

mould and cured in a controlled chamber at 20 ^{0}C. The filler/epoxy ratios (weight ratio) are 6:4, 5:5, and 4:6. The three series are abbreviated as TP-A, TP-B and TP-C, respectively. The shape, size of the TPs and the positions of thermocouples are illustrated in Fig.1.

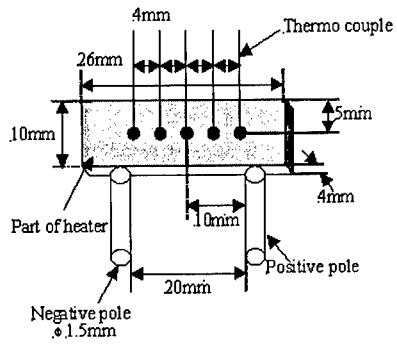

Fig.1 TP shape, size and positions of thermocouples

3. Results and Discussion

3.1 Resistance -Temperature studies

Preliminary studies indicate that epoxy composite filled with silver coated carbon black will increase the static resistance as shown in Fig.2. This is because at a low content of filler there is no physical contact between the conductive aggregates. However, with increasing content of filler the network conducting aggregates are formed and therefore the resistance sharply increases. In a comparison between the present work and an epoxy filled with carbon black without silver coating (Fig. 2(b)), it is observed that the resistance of epoxy filled with silver coated carbon black has a lower resistance compared with epoxy-carbon black at the same value of the volume fraction of the filler. This indicates that the silver coated carbon black has better adhesion interaction with epoxy interface, as was confirmed by using scanning electron microscopy (SEM).

Figure 2(a) shows the variation of the resistance with temperature for different volume fractions of silver coated carbon black. It is clear that at low temperature the resistance increases only slightly up to certain temperature, and then abruptly increases. This abrupt increase depends on volume of the silver coated carbon black content. The slight increase of resistance may be due to the bulk thermal expansion of the epoxy matrix and increases the separation distance between the conductive aggregates. On the other hand the abrupt increase in resistance can be ascribed to the increase in viscosity and the decrease in the surface energy among conductive aggregates [2,3]. This leads to an increase in the separation distance among conductive aggregates and forms a hard barrier, which hinders the charge carriers from hopping and/or tunneling from one site to another. As a consequence resistance increases sharply. Another possible mechanism of increasing resistance is the increase of the barrier high energy among conductive aggregates. This activation energy (E_a) can be calculated by the following equation:

$$R = R_0 \exp(-E_a / KT) \qquad (1)$$

where K is Boltzman constant, and T is absolute temperature.

The calculated values of E_a as a function of silver coated carbon black content are shown in Fig.3. In order to give more insight into the conduction mechanism of conductivity, we calculate the hopping energy (E_h) among conductive aggregates by the following equation:

$$R\sqrt{T} = R_0 \exp(-E_h / KT) \qquad (2)$$

The calculated values of E_h as a function of filler content are shown in Fig.4 from which it is reasonable to conclude that the values of E_a are not close to the values E_h. This shows that the conduction mechanism within epoxy composites obeys the tunneling conduction mechanism. Thus the decrease of E_a with increasing filler content indicates that the inclusion of filler within an epoxy matrix

improves the interface among conductive aggregates and changes the morphological structure of epoxy composites. This is confirmed by the results from the SEM.

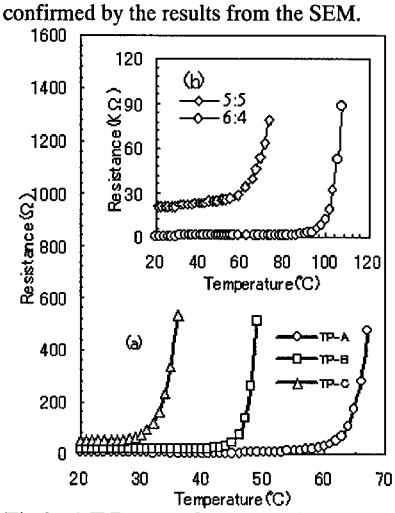

Fig.2: a) T-R curve for epoxy silver coated carbon black, b) T-R curve for epoxy filled carbon black.

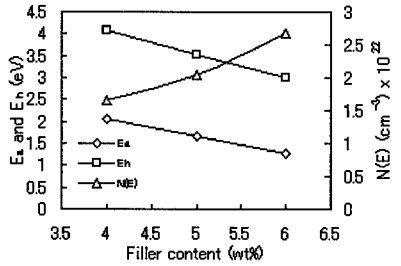

Fig.3 The Variation of E_a, E_h and N (E) vs. filler content for epoxy composites.

3.2 Current – Voltage - Temperature Dependence for composite material

Figure 4(a)(b)(c) shows the Current – Voltage - Temperature characteristics of TP-A, TP-B, and TP-C. In Fig.4 (a)(b)(c), it can be seen that the current increases with increasing applied voltage up to a certain voltage (namely the peak voltage), and then it decreases again. It is interesting to note that the peak voltage also decreases with increasing silver coated carbon black content. This means that the addition of silver coated carbon black enhances the cross-linking density into the epoxy matrix. We believe that the decrease of current, after the peak voltage is reached, is attributable to the increase of the TP temperature due to the Joule heating effect. The resistance therefore increases (i.e. current decreases). Also it is clear that temperature increases, with increasing applied voltage.

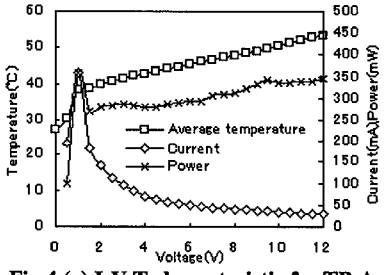

Fig.4 (a) I-V-T characteristic for TP-A

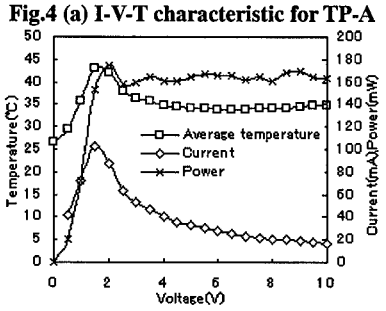

Fig.4 (b) I-V-T characteristic for TP-B

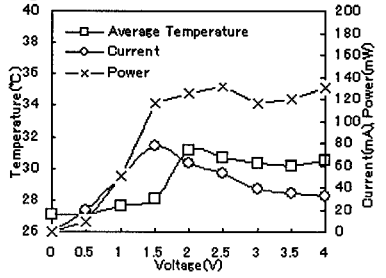

Fig.4 (c) I-V-T characteristic for TP-C

3.3 Morphological study

SEM results for TP-A and TP-B are

shown in Fig.5 (a) and (b) respectively. They reveal that the average diameter of silver coated carbon black particles is 12 μ m. The quantity of epoxy particles in TP-A is denser than in TP-B. The silver coated carbon black particles are also more homogeneous and better dispersed in TP-B than in TP-A. Finally, in TP-B the silver coated carbon black are connected and more tight compared to TP-A.

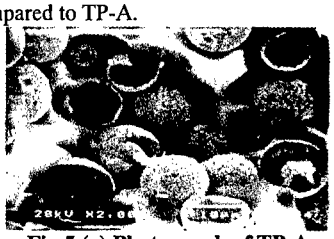

Fig.5 (a) Photograph of TP-A

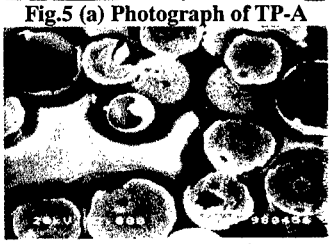

Fig.5 (b) Photograph of TP-B

3.4 Electric wave shield

The electric wave shield is calculated by the following equation [4].

$$\begin{cases} SE = R + A + B \\ R = 50.51 - 10\log(f\rho) \\ A = 1.726t\sqrt{f/\rho} \end{cases} \quad (3)$$

where R is reflection loss, A is absorption loss, f is the frequency, t is the TP thickness, ρ is the resistively.

The variation of shield effect with frequency at thickness 0.1cm is illustrated in Fig.6. It can be seen that the shield effect increases with increases in filler content. This implies that silver coated carbon black has enhanced the connectivity between conductive particles within an epoxy composite. It is worth mentioning that the shield effect slightly decreases with increasing frequency. This means that epoxy filled silver coated carbon black is a good composite for electric wave shielding applications.

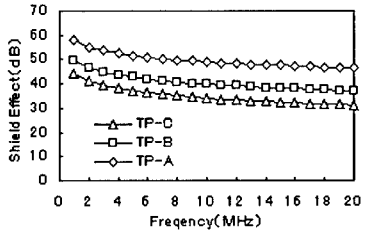

Fig.6 Shield effect vs. frequency

4. Conclusions

1. Static conductivity depends on the morphology and fractal aggregates of the conducting filler.
2. Conductivity changes with temperature during PTC effect depend on the volume fraction of silver coated carbon black.
3. The silver coated carbon black-epoxy composites can be used for temperature sensor and current limiter applications.
4. High electric wave shielding can be obtained using a high volume of silver coated carbon black

Acknowledgment

The authors are most grateful thank to Prof. Dr. H. Hisada, for his help and encouragement. We also thank Mitsubishi Materials Corporation and Yuka Shell Epoxy Corporation, Japan for providing the silver coated carbon black and epoxy.

References

1. H. Hosaka, H. Ohnabe: Conference Yonezawa JSME Touhoku Branch, 13 (1999) (Japanese).
2. F. El-Tantawy, K. Kamada, H. Ohnabe: 38th Conference JSME Hokuriku Shin-etsu Branch, 379(2001) (Japanese).
3. F. El-Tantawy, K. Kamada, M. El-Ashry, H. Ohnabe: Asia Polymer Symposium, 118 (2001).
4. R. Sakamoto: Journal of Japan Rubber association, 58(9), pp. 588~596, (1985).

Proceedings of 7th Japan International SAMPE
Symposium & Exhibition, Nov. 13-16, 2001

Long-Term Multi-Physics Performance of Functional Ceramic Composite Material Systems

K. Reifsnider, X. Huang, and N. Olson

Materials Response Group, Department of Engineering Science and Mechanics
Virginia Tech, Blacksburg, VA, USA

Abstract

Ceramic composite functional composite systems have become important elements of next-generation power systems, including fuel cells and advanced turbines. These CMC systems are functional in several domains of physics and mechanics, including electrochemistry, thermal management, and mechanical response. This functional behavior is highly coupled, requiring the solution of "multi-physics" models to describe their operational characteristics. That situation is further complicated by the fact that the properties of the CMC system constituents are functions of time and service history, and by the fact that they are not necessarily uniformly distributed throughout the engineering component. This paper outlines some of the salient elements of this problem and outlines some basic precepts that form an approach to predictive modeling for such systems.

Introduction

One of the most significant developments in the field of composites is the use of layered ceramic composites as functional materials, especially for engineering components used in the manufacturing, processing, and power industries. In many cases, this has become literally an enabling technology. This is especially true for fuel cells, where solid oxide fuel cell systems (SOFCs) hold a singular promise of efficient use of available energy, distributed power, and reliable energy for the industrial and civil sectors.

SOFCs are solid-state electrochemical devices made by bonding porous electrodes to an ionically conducting electrolyte. The anode of such an SOFC is typically nickel/Zirconia cermet; the cathode may be a doped lanthanum manganite; and the electrolyte is most often a stabilized zirconia. This tri-layer composite is, in turn, bonded to interconnects that provide an electrical connection between the anode of one cell to the cathode of the adjacent cell in a stack that produces useable levels of power. These interconnects must be compatible with the other cell materials at operating temperatures (generally of the order of 800 to 1000 °C), be chemically and physically stable in reducing and oxidizing environments, and have sufficient mechanical strength to act as the structural component of the stack.

Considerable investigative effort has been dedicated to the characterization of the mechanical properties of the constituent materials in an SOFC. Armstrong [1] and Rug, et. al [2] have discussed both the physical and mechanical properties of Lanthanum Chromite[1], and quotes the flexural strength of that material as a function of density and grain size for acceptor-substituted Lanthanum Chromites. Armstrong also discusses the effect of heat treatment at different oxygen partial pressures on Ca-substituted and Sr-substituted lanthanum

[1] A candidate material for ceramic interconnect.

chromites, in terms of the microstructure of those materials. His work, and the work of others, makes it clear that the properties of the constituents may change with time as a function of the operating history and environment. Moreover, the bonded interfaces in such systems are also subject to changes in material state with operating time. As a result, cell performance can also be expected to change with time. Indeed, changes in cell performance have been observed in all such known prototype systems. It should be emphasized that these changes may be small in some cases, and they do not threaten the promise of SOFC fuel cell performance, but they do define their life and must be understood, modeled, and predicted. That is the objective of the present work.

Long-Term Performance of Fuel Cells

Fuel cells degrade with time; eventually they become less efficient and operation is terminated. This degradation is often caused by corrosion of the components. Stationary cells that are used around the clock may be required to last up to ten years (90,000 hours) whereas an automotive cell designed to operate for only one or two hours a day for ten years will have a life of around 3000-5000 hours[4]. Limited data on the life of fuel cells now in use is reported to the public.[2-7] The following is a sample of current available data on the life expectancy of fuel cells for each of the major types. All numbers are in hours, and are total life expectancy, not time before refueling

TYPE OF FUEL CELL	APPROXIMATE LIFE (HOURS)
PEM	10,000[3]
PAFC	40,000[4]
PEFC	15,000[3]
MCFC	7,000-10,000[4]
AFC	15,000[4]
SOFC	30,000[4] - 69,000[3]

Multi-Scale Multi-physics Modeling

What controls the life of SOFCs? Local mechanical failures (microcracking and delamination) are certainly possible failure modes.[8] But more often life is controlled by performance, i.e., the power output and efficiency of the fuel cell. And typically, this performance is controlled by the electrochemical reactions at the electrode (anode and cathode) - electrolyte interfaces, or the regions near the interface where the electrochemical reactions occur. Huang, Reifsnider, and Case [9] have recently described the construction of performance metrics that can be used to represent engineering behavior in terms of the controlling electrochemical processes in those reaction regions. They note that these processes occur in a number of physical domains, the electrochemical reactions at the interfaces, the transport of reactant gases to reaction sites, the generation and diffusion of heat, and the equilibrium of internal stresses. They have established solution methods for the system of simultaneous integral-differential equations that are strongly coupled by shared state variables to determine the performance of the cell as a function of the micro-constituent material properties and property changes. These solutions connect the global performance micro-level cell structure.

However, the material constants in those equations are functions of time, point wise local conditions, and history of operation. For the present discussion, to answer the question of what controls the life of SOFCs, we must consider one more scale of behavior. Models (and simulations) of electrodes (and electrode/electrolyte interfaces) in SOFCs are being developed. (See reference 11 for a good review.) These models typically estimate conductivity, polarization resistance, and

impedance of electrodes in terms of the porosity, microstructure, local geometry and con-nectivity. Those details determine the local kinetics and electrochemical reactions of the electrons, electrolyte ions, and gas molecules, and thereby, largely determine the performance of the fuel cell at the global level. (Sunde [10] notes that unless the porosity of the electrodes is significantly less than 30 percent, mass transfer in porous electrodes is not controlling.) Hence, the evolution of the physical constants in those models with time and history of operation control the life of the SOFC.

Multi-physics models are critical in bridging the gap between the micro-level structure and material evolution, and the global performance metric. It is also an indispensable tool in the engineering design process of SOFCs. Material characterizations are usually performed at controlled homogeneous conditions; local working conditions inside a cell/stack are far from uniform; multi-physics models are needed to take advantage of any experimental data to predict the cell/stack performance. There has been evidence [11] that the electrochemical degradation rates are functions of some local intensive variables, such as local current density. Multi-physics models are needed to predict global performance taking into account the non-uniform local degradation rate. Mechanical failure driving forces are sensitive to the temperature gradient generated by any transient processes, such as start-up, shutdown, and load fluctuations; multi-physics models are required to assess the cell/stack responses under these transient conditions.

Multi-physics Models; Example Solutions

In the Materials Response Group, we have built a simple model for an SOFC single cell and developed an associated solution scheme. The electrochemical, thermal, and gas transport processes are modeled. A resistor in the external circuit is used to simulate the electric load. The coupled integral-differential equations are solved and the distribution of all intensive variables can be obtained, as shown in Figure 1. The performance curve is easily calculated by integration on these intensive variables. Following are examples of a solution.

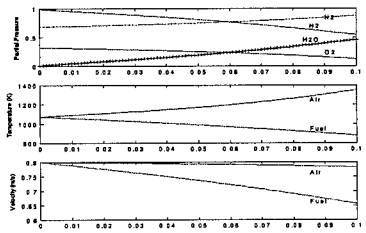

Figure 1. A steady-state solution of the multi-physics model. Shown above are the variation of some state variables along the stream line: hydrogen and oxygen are consumed, the generated heat are removed by the air stream.

During operation, the microstructure of the interfaces and material properties evolve. As a result, the overvoltage increases. The mechanisms at the micro-level are still not fully understood. But the kinetics of these processes can be measured in some controlled operation conditions [11]; the result can subsequently be incorporated into the multi-physics model to predict the performance evolutions. The performance drop after the conductivity of the electrolyte has decreased 20% is shown in Figure 2.

The operation of SOFCs involves processes in a wide range of temporal scales. The characteristic rate[2] of electrochemical process is faster than the gas transport process, which is in turn faster than the heat diffusion process.

[2] The rate to achieve a steady state from a disturbed state.

Indeed, we can take advantage of this natural temporal hierarchy.

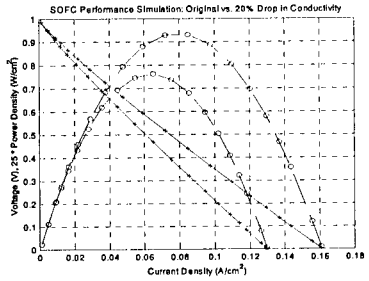

Figure 2. Performance decrease due to the decrease of conductivity.

In solving the time-dependent problems, we assume that temperature field is in a steady state when solving the time-marching equations of gas transport and we assume the gas partial pressure is steady when we solve the electrochemical equations. Thus the computation task for the time-dependent problem becomes manageable. A simulated transient response of a SOFC is shown below. The inlet gas pressures and temperatures are kept constant. A disturbance was introduced to the external load, which is represented by the Heaveside step function. The transient response of the current, voltage, and temperature are calculated and shown in Figure 3.

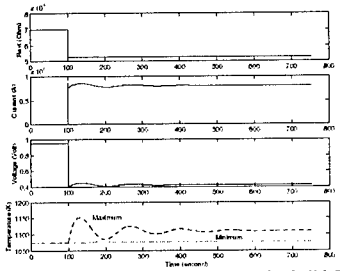

Figure 3. Simulated transient response of a Solid Oxide Fuel Cell. The voltage, current, and temperature are calculated following a sudden drop of external resistance *R-ext*. The inlet gas pressure, temperature, and composition are kept constant.

SUMMARY

The present paper has outlined the behavior and philosophy needed to define the long-term multi-physics performance of functional ceramic composite systems. An approach to modeling that response was suggested, based on solutions of coupled models of the associated balance equations which incorporate changes in material states and stress states as a function of service history. The need for experimental data to support such robust modeling was identified.

REFERENCES

1. Armstrong, T.R., Baskaran, S., and Paulik, S.W., 2000, (private communication)
2. Ruh, R. and Mazdiyasni, K.S., J. Am. Ceram. Soc., Vol. 80, No. 4, 1997, pp. 903-908
3. Eberl, Ulrich. "Fuel Cells For Everyone" http://w4.siemens.de/FuI/en/archiv/zeitschrift/heft2_98/artikel05/index.html.
4. Kordesch, Karl and Günter Simader Fuel Cells and their applications, 1996 VCH [1]mbH, Weinheim, and VCH publishers, inc., New York.
5. Beardsley, Tim http://www.sciam.com/explorations/122396explorations.html accessed June 18, 2001.
6. Tavast, Johan, and Peter Torstensson. "Fuel cells." http://exergy.se/goran/cng/alten/proj/97/fc/fc.html
7. "Strategic Planning for the Hydrogen Economy: the Hydrogen Commercialization Plan" http://www.ttcorp.com/nha/commpln.htm October 2000.

8. Lowriek, F.L. and Rowlings, R.D., J. European Ceramic Soc., Vol. 20, 2000, pp. 751-760
9. Huang, X., Reifsnider, K.L., and Case, S.W., in press
10. Sunde, S., J. of Electroceramics, Vol. 5, No. 2, 2000, pp. 153-182
11. Jorgensen M., Holtappels P., and Appel C. (2000), *J. Appl. Electrochem.* **30** 411-418

Proceedings of 7th Japan International SAMPE
Symposium & Exhibition, Nov. 13-16, 2001

Fibre/matrix interface shear strength measured *in situ* for SiC/SiC composites with different matrices and interfaces

I. J. Davies[#], T. Ogasawara[$], and T. Ishikawa[$]

[#] Kyoto Institute of Technology, Matsugasaki, Sakyo-Ku, Kyoto 606-8585, Japan
E-mail: davies@ipc.kit.ac.jp

[$] Structures Division, National Aerospace Laboratory, 6-13-1 Ohsawa, Mitaka-Shi, Tokyo 181-0015, Japan

Abstract

The mechanical properties of ceramic matrix composites are known to depend mainly on the fibre/matrix interface shear strength and fibre strength Weibull parameters measured *in situ* the composite. In the present work the authors review two methods to obtain the fibre/matrix interface shear strength and their application to a 3-D woven SiC/SiC composite.

Key Words: interface shear strength, Weibull parameters, in situ fibre strength, SiC/SiC.

Introduction

The application of ceramic matrix composites (CMCs) as high temperature structural materials has led to calls to better understand the relationship between microscopic parameters (e.g., fibre strength) and macroscopic behaviour (e.g., tensile strength). Recent work [1] has shown the macroscopic behaviour of CMCs to be mainly controlled by three microscopic parameters, namely the fibre/matrix interface shear strength, τ, together with the fibre strength Weibull parameters, S_o and m, measured *in situ* the composite. It should be noted that τ, S_o, and m are linked through the following equation [1]:

$$\tau = \frac{r\lambda(m)S_0}{4<h>} \quad (1)$$

where r is the fibre radius, $<h>$ is the mean fibre pullout length, and $\lambda(m)$ is a function only of m.

The authors will briefly review two methods that may be used to obtain τ and apply these to a 3-D woven SiC/SiC composite.

Review of methods to obtain τ

In situ fibre strength (ISFS) method

The first method under investigation [1] may be summarised as follows. The strength, S, of individual fibres at the fracture surface of a CMC specimen that failed under tensile loading may be determined *in situ* a scanning electron microscope (SEM) by measuring the fracture mirror radius, r_m, and using the following equation:

$$S = \frac{A_m}{\sqrt{r_m}} \quad (2)$$

where A_m is an empirical constant and typically 2.5 MPa·m$^{1/2}$ for amorphous SiC

fibres [2]. If a large number of data points is collected than S may be plotted against cumulative failure, F, such that S_o and m may be extracted through fitting the well-known Weibull equation:

$$F = 1 - e^{-\left(\frac{S}{S_o}\right)^m} \quad (3)$$

Following appropriate correction factors being applied to S_o and m [1], the value of τ may be obtained using eqn. (3) together with a value for $<h>$ obtained using optical microscopy (OM) [3] or SEM [4,5]. The ISFS method is believed to yield accurate data for τ due to its assumption of multiple matrix cracking (which is known to exist in most CMC systems). However, a major disadvantage of this method is the large amount of S data required to obtain an accurate value for S_o and m, thus resulting in a laborious and time consuming procedure.

Fibre pullout length (FPL) method

Whereas the ISFS method required accurate value of S_o, m, and $<h>$ be obtained in order to evaluate τ, the FPL method [6] is able to evaluate τ using only the distribution of fibre pullout lengths, h. The distribution of h values may be obtained from analysing the fracture surface of the CMC using either OM [3] or SEM [4,5] and then compared to the following equation [6]:

$$\Phi\{\xi\} = 1 - \int_{\xi^{m+1}}^{\infty} \left[1 - \xi\beta^{-1/(m+1)}\right]^m e^{-\beta} \partial\beta \quad (4)$$

with

$$\lambda = R/(2\tau), \quad \beta = \left(T/\Sigma\right)^{m+1}, \quad \xi = h/(\lambda\Sigma)$$

and $$\Sigma = \left[\frac{A_o S_o^m \tau(m+1)}{2\pi r^2}\right]^{1/(m+1)}$$

where $\Phi\{\xi\}$ is the cumulative failure in nondimensional form for fibre pullout lengths $\leq h$, T is the maximum stress in the fibre between crack surfaces, and A_o is the fibre surface area. The value of τ may be obtained through iteration of τ in eqn. (4) to the experimental distribution of h.

Although easier to apply to CMCs due to the need to measure only the distribution of h, the FPL method was derived making the assumption of a CMC containing only a single matrix crack whereas CMCs are known to generally exhibit multiple matrix cracking. However, it will be shown later that qualitative estimates of τ may still be obtained from the FPL method through use of an appropriate correction factor.

The next part of this work illustrates how these two methods were applied to a 3-D woven SiC/SiC composite.

Experimental Procedure

The initial CMC investigated in this work comprised of surface-modified Tyranno® Si-Ti-C-O fibres woven into a 3-D orthogonal configuration. Matrix densification for the composite was achieved through the repeated polymer impregnation and pyrolysis of a precursor similar to polytitanocarbosilane (PTCS). Following machining to a suitable test geometry, selected specimens were repeatedly impregnated and sealed with a glass-based material in order to act as an oxidation barrier; specimens with no oxidation barrier were denoted "unsealed" whilst those subject to the oxidation protection treatment were denoted "sealed". Mechanical testing of the composite has been detailed elsewhere [7] but essentially comprised of uniaxial tensile loading at temperatures between room temperature and 1380 °C in either vacuum or air. Following mechanical testing, the fracture surfaces of specimens were investigated using OM (to measure fibre pullout length) and SEM (to measure *in situ* fibre strength).

Results and Discussion

Fig.1 illustrates *in situ* fibre strength curves for the SiC/SiC composite tested under different conditions whilst Table 1 summarises results obtained using eqns. (1) – (3). Regarding Table 1, values of τ for the unsealed composite tested in vacuum were in the approximate range 5~9 MPa and, when combined with the superior tensile strength of these specimens (280~400 MPa [8]), indicated the necessity of low τ in this composite system. In contrast to this, τ for the unsealed composite tested in air was in the approximate range 55~60 MPa and, when combined with the poor mechanical properties of these specimens (<100 MPa [8]), suggested the fibre/matrix interface to have been oxidised. Finally, τ for the sealed composite tested in air was similar that of the unsealed composite tested in vacuum, indicating the glass-based sealant to provide excellent oxidation protection for the test conditions employed.

Fibre pullout length distributions for the composite have been presented in Fig. 2. Although not shown here [9], values of τ obtained from eqn. (4) were always underestimated by a factor of 3.43 ± 0.35 [9] compared to those obtained using the ISFS method, presumedly due to the ISFS method assuming the presence of multiple matrix microcracking whereas the FPL method (erroneously) assumed the presence of only a single matrix microcrack.

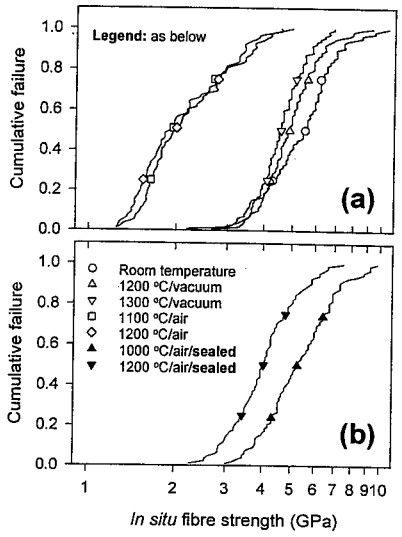

Fig. 1 *In situ* fibre strength curves for a SiC/SiC composite: (a) unsealed [4], and (b) sealed [5].

Taking into account the "correction factor" of 3.43 ± 0.35 [9], values of τ qualitatively estimated for SiC/SiC composites, based on the previous system, but with different fibre/matrix interfaces and matrices [10] have been presented in Table 2. It may be seen that values of τ for 4 out of the 5 specimens (all tested at room temperature) were <10 MPa and thus similar

Table 1 Values of S_o, m, and τ obtained using the "*in situ* fibre strength" method for a SiC/SiC composite [4,5].

	Test condition	S_o GPa	m	τ MPa
Unsealed	Room temperature	3.86 (+/- 0.13)	4.19 (+/- 0.05)	4.94 (+/- 0.16)
	1200 °C/vacuum	3.45 (+/- 0.20)	5.72 (+/- 0.10)	6.27 (+/- 0.35)
	1300 °C/vacuum	3.18 (+/- 0.34)	6.56 (+/- 0.11)	9.13 (+/- 0.96)
	1100 °C/air	1.37 (+/- 0.15)	2.91 (+/- 0.13)	54.75 (+/- 5.40)
	1200 °C/air	1.26 (+/- 0.18)	2.68 (+/- 0.11)	60.50 (+/- 8.43)
Sealed	1000 °C/air	4.22 (+/- 0.29)	4.00 (+/- 0.07)	3.92 (+/- 0.26)
	1200 °C/air	3.12 (+/- 0.31)	4.64 (+/- 0.10)	6.06 (+/- 0.61)

to those shown in Table 1 for the original composite. It would thus appear that both the ISFS and FPL methods may prove useful for the estimation of τ in CMCs.

Acknowledgements
The authors wish to sincerely thank Dr. M. Shibuya of Ube Industries Ltd., Dr. J. Gotoh of Kawasaki Heavy Industries Ltd., and T. Hirokawa and T. Tanamura of Shikibo Ltd. for the manufacture and supply of all materials used in this study.

References
1. W. A. Curtin, J. Amer. Ceram. Soc., 74(11), 2837 (1991).
2. I. J. Davies and T. Ishikawa, Int. J. Maters. Prod. Tech., 16(1-3) 189 (2001).
3. I. J. Davies, T. Ishikawa, M. Shibuya, and T. Hirokawa, Comp. Sci. and Technol., 59(3) 429 (1999).
4. I. J. Davies, T. Ishikawa, M. Shibuya, and T. Hirokawa, Comp. Sci. Technol., 59(6) 801 (1999).
5. I. J. Davies, T. Ishikawa, M. Shibuya, T. Hirokawa, and J. Gotoh, Composites Part A, 30(4) 587 (1999).
6. M. D. Thouless, O. Sbaizero, L. S. Sigl, and A. G. Evans, J. Amer. Ceram. Soc., 72(4), 525 (1989).
7. T. Ishikawa, K. Bansaku, N. Watanabe, Y. Nomura, M. Shibuya, and T. Hirokawa, Comp. Sci. Technol., 58 (1998) 51.

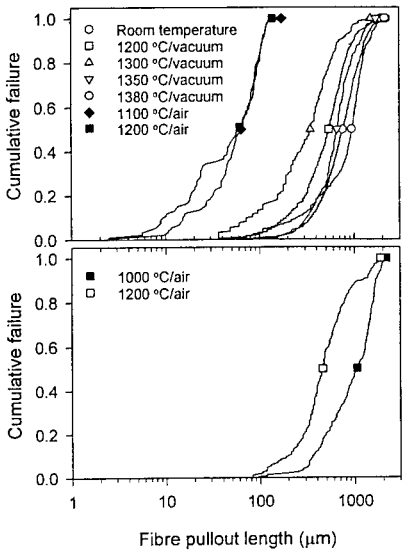

Fig. 2 Fibre pullout length distributions for a SiC/SiC composite [9]: (a) unsealed, and (b) sealed.

8. I. J. Davies, T. Ogasawara, and T. Ishikawa, J. Ceram. Soc. Jpn., 109(7) 643 (2001).
9. I. J. Davies and T. Ishikawa, Composite Interfaces, 7(5-6) 479 (2001).
10. I. J. Davies, T. Ogasawara, and T. Ishikawa, J. Maters. Sci. Letts., submitted

Table 2 Estimated values of τ obtained using the "fibre pullout length" method for SiC/SiC composites with different interfaces and matrices [10].

		Fibre/matrix interface shear strength, τ	
Specimen name	Mean fibre pullout length, <h> (μm)	Fibre pullout method (MPa)	Corrected value (MPa)
ZM-10	733 ± 34	1.05	3.60 ± 0.37
ZM-20	991 ± 49	0.77	2.64 ± 0.27
ZM-21	1484 ± 79	0.44	1.51 ± 0.15
ZM-22	≤100	-	≥50
ZN-23	427 ± 33	2.80	9.60 ± 0.98

Proceedings of 7th Japan International SAMPE
Symposium & Exhibition, Nov. 13-16, 2001

High Temperature Behavior of Sintered SiC Fiber-bonded Ceramics

Shinji Kajii, Mitsuhiko Sato, Kenji Matsunaga, Toshihiko Hogami and Toshihiro Ishikawa

Ube Research Laboratory, Ube Industries, LTD.
1978-5 Kogushi, Ube, Yamaguchi, 755-8633, JAPAN
E-mail: 27500u@ube-ind.co.jp

Abstract

A sintered SiC fiber-bonded ceramic was synthesized by hot-pressing 8 harness satin woven fabrics of an amorphous Si-Al-C-O fiber at 1850 ℃ and 50MPa. The sintered SiC fiber-bonded ceramic composed of perfectly close-packed structure of the hexagonal columnar fibers with a very thin interfacial carbon layer around the fibers. This material showed excellent heat-resistance up to 1800℃. The sintered SiC fiber-bonded ceramics were joined with mixture of β -SiC powder, Al_2O_3, B and C by hot-pressing. The initial joining strength (200MPa) at room temperature was almost maintained even at 1700℃.

Key Words: Sintered SiC fiber-bonded ceramic, Heat resistance, Joining, Bending strength

Introduction

A sintered SiC fiber-bonded ceramic was synthesized by hot-pressing an amorphous Si-Al-C-O fiber [1-2]. This material showed a perfectly close-packed structure of the hexagonal columnar fibers with a very thin interfacial carbon layer around the fibers. The sintered SiC fiber-bonded ceramic showed high fracture energy and good bending strength up to 1700℃ . This material showed excellent thermal conductivity up to very high temperatures and high thermal shock behavior.

This material is of considerable interest for potential use in advanced gas turbine. By the way, a flexibility of the shapes of this material is limited such as a board and cylinder, because of using hot-press in the product process. The engineer often requires fabrication of complex shaped components. One attractive way of achieving this is to build up complex shapes by joining geometrically simple shapes. The majority of the techniques used are based on the joining of monolithic ceramics with metals either by diffusion bonding, metal brazing or diffusion welding [3-6]. Generally, the service temperatures for these joints are below 700℃. Thus other joining techniques are needed to obtain the high temperature joints. Recently, the technique for joining SiC based ceramics by reaction-sintering, powder sintering, and polymer pyrolysis methods have been investigated [7-10]. The joints using polymer pyrolysis method have lower strength due to porosity.

On the other hand, the strength of the reaction-sintering joints decreased at high temperature.

In this paper, the SiC powder sintering method for the joining of sintered SiC fiber-bonded ceramic will be reported. Heat-resistance of sintered SiC fiber-bonded ceramic is also reported. The mechanical properties of the SiC powder sintering joints of sintered SiC fiber-bonded ceramics was investigated.

Experiments

Specimen preparation

Eight harness satin woven fabrics with thickness of about 200 μ m were prepared with the amorphous Si-Al-C-O fiber. Laminated materials, prepared with the fabrics, were hot-pressed at 1850 ℃ and 50MPa to obtain the sintered SiC fiber-bonded ceramic. During the hot-pressing, the amorphous Si-Al-C-O fiber was converted into a sintered SiC fiber by way of a decomposition, which released CO gas. And sintering process accompanied by a morphological change from a round columnar shape to a hexagonal columnar shape. The production process of the sintered SiC fiber-bonded ceramic was shown in Figure 1.

Commercially available β -SiC powder (Betarundum, Ibiden LTD.) was used as the starting powder of the joining layer. The contents of the additives were 1 mass% Al_2O_3, 1 mass% B, and 1 mass% C. The powders were ball-milled with Si_3N_4 balls in ethanol for 24 hours. The slurry was dried, then the mixed powder were used to the following joining operation. The sintered SiC fiber-bonded ceramics were cut into pieces of size about 8 mm(t) × 24 mm(W) × 20 mm(L). The direction of the joining plane normal was perpendicular to the piled direction of the sintered SiC fiber-bonded ceramics. The mixed powders about 0.26g

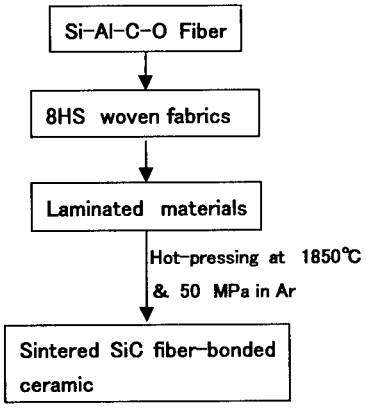

Fig.1 Production process of the sintered SiC fiber-bonded ceramic.

were set between the specimens. The joining specimen was prepared by hot-pressing at 1800℃, 40MPa and for 3hrs. The Joining specimen was shown in figure 2.

measurement

Scanning electron micrograph (SEM) was obtained with a Hitachi S-5000 operating at 5kV. Four-point bending strength was measured using an Instron Model 8562 Testing Machine at room temperature to 1700℃. Testing was done at

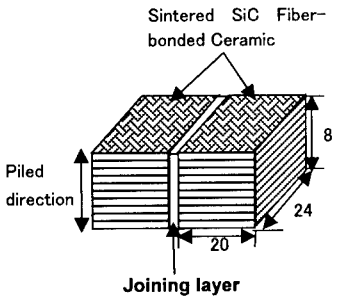

Fig.2 Appearance and dimension in mm of the joining specimen.

a cross-head speed of 0.5mm/min with 10 mm inner and 30 mm outer span. Specimen size was 3 mm(t) × 4 mm(W) × 40 mm(L). Bending bars were machined from the joining specimen, with joints in the middle of the bending bars.

Result and Discussion

The cross-section of the sintered SiC fiber-bonded ceramic was shown in figure 3 (a). The sintered SiC fiber-bonded ceramic exhibited perfectly close-packed structure of the hexagonal-columnar fibers with a very thin interfacial carbon layer. Figure 3 (b) showed an SEM photograph of the fracture surface of the sintered SiC fiber-bonded ceramic. Fibrous fracture behavior and large amount of pullout can be confirmed. It has been found that the aforementioned interfacial carbon layer plays an important role in producing the fibrous fracture behavior with large fracture energy.

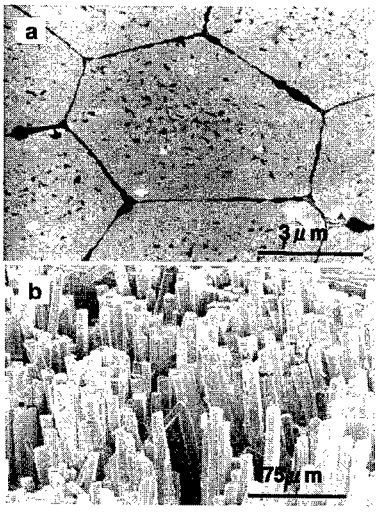

Fig.3 (a) Cross-section of the sintered SiC fiber-bonded ceramic, (b) fracture surface of the sintered SiC fiber-bonded ceramic.

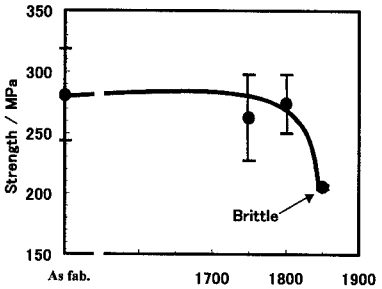

Fig.4 Heat-resistance of the Sintered SiC fiber-bonded ceramic.

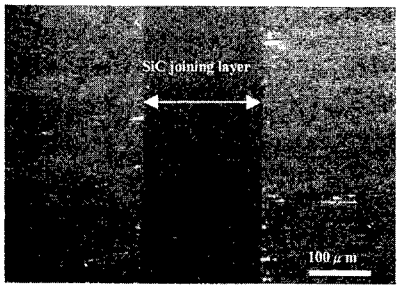

Fig.5 Microstructure of the sintered SiC fiber-bonded ceramics and 180 μ m sintered SiC joint.

Figure 4 showed the heat-resistance of the sintered SiC fiber-bonded ceramic. The initial strength was preserved after heat-treatment at 1800℃ for 3hours in Ar. In this case, the fibrous fracture behavior was preserved under the above heat-treatment condition. However, the strength of this material was reduced to 200MPa by heating in Ar for 3hours at 1850℃. And fracture behavior showed brittle fracture pattern. With increasing heat-treatment temperature, the grain size of SiC increased. In the case of the heat-treatment at 1850 ℃ , the interfacial carbon layer partially can not be detected, which caused by the SiC grain growth between the adjacent fibers. Because

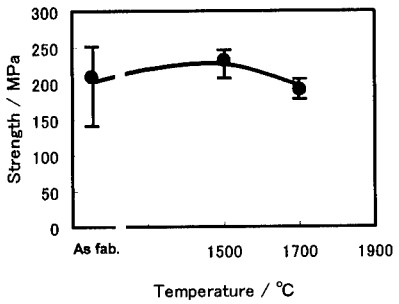

Fig.6 Temperature dependence of 4-point bending strength for the sintered SiC fiber-bonded ceramic containing joints.

of these properties, the temperature under 1800 ℃ was employed for the joining. Figure 5 showed the microstructure of the sintered SiC fiber-bonded ceramic and SiC sintered joints. The thickness of the joint was 180 μ m. The joining layer consists of the dense SiC-crystalline without any voids and clacks.

The room and high temperature bending strength of the sintered SiC fiber-bonded ceramic was determined and compared to the strength of the jointed material by four-point bending tests. The room-temperature strength (280MPa) of the sintered SiC fiber-bonded ceramic was perfectly maintained up to 1700℃. Figure 6 shows the temperature dependence of the bending strength for the sintered SiC fiber-bonded ceramic containing joints. The bending strength values of joined material at room temperature and 1700℃ were 209.2 $\pm$ 45 and 190.8 $\pm$ 15 MPa, respectively. These bending strength values were comparable to those of bulk materials. In the bending specimens containing joints, fracture always occurred in around the bulk material/joint interface and propagated to the joint.

Conclusion

The sintered SiC fiber-bonded ceramic composed of perfectly close-packed structure of the hexagonal columnar fibers with a very thin interfacial carbon layer around the fibers. This material was shown excellent heat-resistance up to 1800℃. The SiC sintering method for the jointing of the sintered SiC fiber-bonded ceramic has been developed. The initial joining strength (200MPa) at room temperature was almost maintained even at 1700℃.

References

1. T. Ishikawa, S. Kajii, K. Matsunaga, T. Hogami, Y. Kohtoku and T. Nagasawa: Science, 282, 1295(1998).
2. T. Ishikawa, S. Kajii and T.Hisayuki: Proc. of 24th Annual Conf. on Composites, Advanced Ceram., Mater., and Struct.:B, Ceram. Eng. & Sci. Proc., 21(4), 323(2000).
3. C.H. Bates, M.R. Foley, G.A. Rossi, G.J. Sandberg and F.J. Wu: Ceramic Bulletein, 69(3), 350(1990).
4. O.M. Akselsen: J. Mater. Sci., 27, 1989(1992).
5. T.J. Moore: J. Am. Ceram. Soc., 68(6), C151(1985).
6. M. Nakamura, M. Mabuchi, N. Saito, Y. Yamada, M. Nakanishi, K. Shimojima and I. Shigematsu: J. Ceram. Soc., Japan, 106(9), 927(1998).
7. T. Iseki, K. Arakawa, H. Matsuzaki and H. Suzuki: Yogyo-Kyokai-shi, 91(8), 11(1983).
8. S. Yajima, K. Okamura, T. Shishido, Y. Hasegawa and T. Matsuzawa: Am. Cerm. Soc. Bull., 60(2), 253(1981).
9. T.Iseki, M. Imai and H. Suzuki: Yogyo-Kyokai-shi, 91(6), 9(1983).
10. M. singh: Scripta Materialia, 8, 1151(1997).

Proceedings of 7th Japan International SAMPE
Symposium & Exhibition, Nov. 13-16, 2001

High Temperature Creep Deformation and Thermal Stability of 3-D Woven Tyranno ZMI fiber / Si-Ti-C-O Matrix Composite

Yutaka Ohsawa#1, Shijie Zhu#2, Toshio Ogasawara#3, Takashi Ishikawa#3 and Yasuo Ochi#4

#1: Graduate Student, University of Electro-Communications
1-5-1 Choufugaoka, Choufu city, Tokyo 182-8585, JAPAN
#2: Institute of Industrial Science, The University of Tokyo
4-6-1 Komaba, Meguro-ku, Tokyo 153-8904, JAPAN
#3: Advanced Composite Evaluation Technology Center, National Aerospace Laboratory of Japan
6-13-1 Ohsawa, Mitaka, Tokyo 181-0015, JAPAN
#4: University of Electro-Communications
1-5-1 Choufugaoka, Choufu city, Tokyo 182-8585, JAPAN

E-mail: ogasat@nal.go.jp

Abstract

The tensile creep behaviors of an orthogonal 3-D woven Si-Zr-C-O (Tyranno ™ ZMI) fiber / Si-Ti-C-O matrix composite (CMC) were investigated in air at 1573-1723K. For stresses between 60 and 140MPa, the creep rate decreased continuously with time, with no apparent steady-state regime observed at 1573-1723K. Under the test conditions, the microstructure of Tyranno™ ZMI fiber and Si-Ti-C-O matrix was unstable, resulting in weight loss and SiC grain growth. As a result, the viscosity of the fiber and matrix increased because the increase in viscosity caused a continuously decreasing creep rate, which made steady-state creep impossible under these conditions.

Key Words: Ceramic Matrix Composite, Creep deformation, Thermal stability

Introduction

Tyranno™ fiber (UBE Industries Ltd., Japan) is a kind of silicon carbide fibers derived from organic silicate polymer which includes Ti or Zr as a second metallic element and has good oxidation resistance compared to carbon fibers.

In the present work, tensile creep behavior of an orthogonal 3-D woven Tyranno™ ZMI fiber (Si 56%, Zr 1%, C 34%, O 9%) / BN interface / Si-Ti-C-O matrix composites was investigated at 1573-1723K in air. The influence of the thermal stability of the composite on creep behavior was also studied.

Material and Method

Tyranno™ ZMI fiber bundles containing 1600 fibers with BN coating were woven into an orthogonal 3-D configuration with fiber volume fraction of 0.17, 0.17, and 0.02 in the x, y, and z directions, respectively. The thickness of BN interphase was approximately 0.5μm. Polytitanocarbosilane was used as the matrix precursor with repeated impregnation and pyrolysis cycles until satisfactory densification was achieved. Specimens had 30mm in gauge length, 4mm

in thickness, 4.6mm in width, and 110mm in the overall length.

Creep testing was conducted on a servo-hydraulic testing system (Model 8501, Instron, USA) at 1573K, 1673K, and 1723K in air. A high temperature furnace and a contact-type extensometer (gauge length 12.5 mm, Model 2632, Instron, USA) were used for this experiment. The initial loading rate for creep testing was 1.0 MPa/s. The creep tests were performed under constant load.

The rate of pyrolysis was measured with a thermogravimetric analyzer (TGA) (STA-449C, NETZSCH-Gerätebau, Germany) at 1673K, 1723K and 1773K under argon gas flow condition. X-ray diffraction (XRD) analysis was conducted using a Cu-Kα radiation under conditions of 40kV and 200mA with an X-ray diffractometer (Model RINT2500, Rigaku, Japan) in order to evaluate crystallization behavior of the composite.

Experimental Result and Discussion

Creep deformation behavior

Tensile creep curves (creep strain versus time) at 1673K are shown in Fig.1. For creep stresses between 60 and 120MPa, the creep rate decreases continuously with time, with no apparent steady-state regime observed.

In many cases, steady state creep rate, $\dot{\varepsilon}_{cr_s}$, under applied creep stress, σ_c, is represented by the power-law creep equation as follows:

$$\dot{\varepsilon}_{cr_s} = A\sigma_c^n \exp\{-Q/RT\} \qquad (1)$$

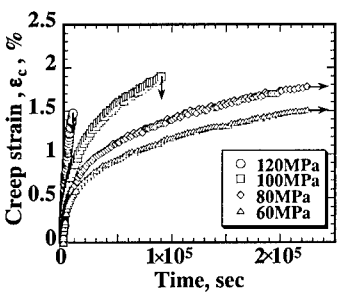

Fig.1 Tensile creep strain versus time in air at 1673K.

where A is the dimensionless constant, n is the stress exponent, Q is the apparent activation energy, R is the universal gas constant (8.315J/mol), and T is absolute temperature. In this paper, similar relationship was applied for creep strain rate at creep time, t:

$$\dot{\varepsilon}_{cr} = At^p\sigma_c^n \exp\{-Q/RT\} \qquad (2)$$

where p is a constant. The stress dependence of tensile creep rate at creep time of 1x 10^3, 5x 10^3, 1x 10^4, 2x 10^4, and 5x 10^4 sec. is shown in Fig.2 at temperature of 1673K. The stress exponents, n, which was determined from a linear-regression analysis of the $\log\dot{\varepsilon}_c$-versus-$\log\sigma_c$ plot, are approximately 1.2 for each creep time stage, and correspond to a Newtonian-type viscous flow (n=1). Although it should be noticed that the creep rate in Fig.2 was not steady state, these stress exponents are similar to that found for the creep of Nicalon™ (Si-C-O) fibers, indicating that the creep rate of the composite was controlled by fiber creep[1].

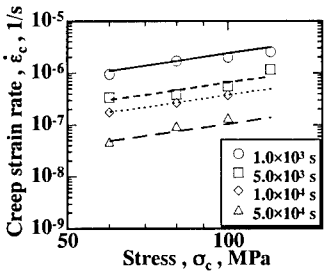

Fig.2 Creep strain rate versus stress in air at 1673K.

The apparent activation energy, determined from a plot of the $\log\dot{\varepsilon}_{cr}$-versus-$1/T$ plot in Fig.3 for applied stress of 80MPa, is approximately 190kJ/mol. This value is similar to the activation energy of steady state creep found in Nicalon™ / C-interphase / CVI-SiC composites [2]. The time exponents, p, determined from the $\log\dot{\varepsilon}_c$-versus- $\log t$ plot shown in Fig.4 for temperature of 1673K, is almost constant to be –0.8 up to 10^5 sec. The calculated curves using Eq.(2) with n=1.2, p=0.8, Q=190 (kJ/mol), A=1.18 are superimposed on Fig.2, Fig.3 and Fig.4. The

parameter A is applied for stress in megapascals, time in seconds, and temperature in Kelvin. Comparison of the predicted and measured values indicates good agreement by this simple relation.

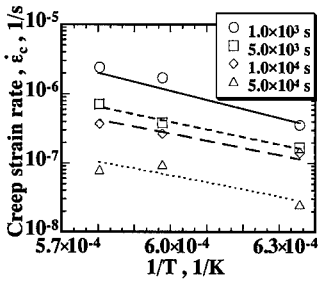

Fig.3 Creep strain rate versus reciprocal of absolute temperature in air at 80MPa.

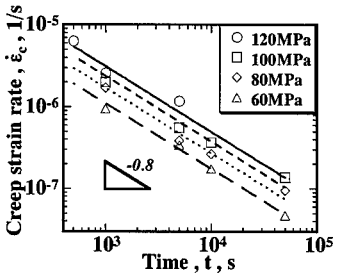

Fig.4 Creep strain rate versus time in air at 1673K.

The pyrolysis and crystallization behavior of the composite

The TGA results are shown in Fig.5, where ΔW and W_0 are the weight-loss and the initial weight of the composite, respectively. It was obviously observed that the weight decreased with exposure time. The weight loss almost saturates at 1773K for 20 hour.

It was reported that the pyrolytic rate of the Tyranno^{TM} fibers can be analyzed by means of Avrami- Erofeev equation as follows[3]:

$$-\ln(1-X) = k \cdot t^m \qquad (3)$$

where k and m are the rate constant and the rate exponent, and X is the pyrolysis ratio as follows:

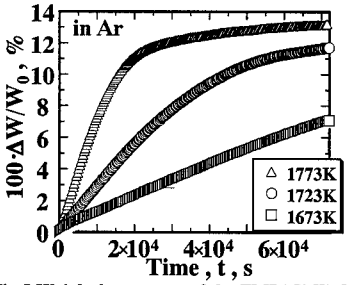

Fig.5 Weight loss curves of the ZMI / Si-Ti-C-O composite at various temperatures.

$$X = \Delta W_t / \Delta W_f \qquad (4)$$

where ΔW_t and ΔW_f are the weight-change at time t, and the saturated weight loss, respectively. Following equation is obtained when the logarithm of both sides of the Eq.(3) is taken:

$$\ln\{-\ln(1-X)\} = \ln k + m \cdot \ln t \qquad (5)$$

Fig.6 shows the application of Ep.(5) to data tested for 5hour. The exponent, m, determined from the mean value of the slope of the ln{-ln(1-X)} -versus- ln$t$ plot shown in Fig.6, is approximately 1. The apparent activation energy for the pyrolysis, found from the Arrhenius plots for the rate constants k determined from the y-intercept of the ln{-ln(1-X)}- versus-ln$t$ plot shown in Fig.6, is 173kJ/mol.

Fig.7 shows the decomposition curves of the composite during the creep time calculated by Eq.(3).

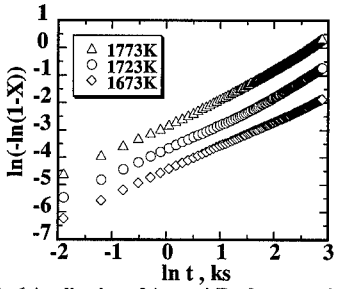

Fig.6 Application of Avrami-Erofeev equation to experimental results.

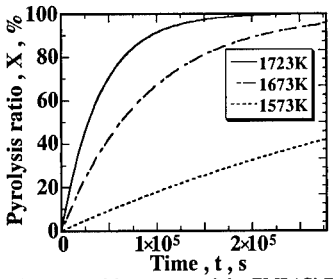

Fig.7 Decomposition curves of the ZMI / Si-Ti-C-O composite calculated by equation (3).

At 1673K and 1573K, the pyrolysis ratio does not saturate, which suggests the composite is not chemically stable during thecreep test condition.

Fig.8 shows the X-ray diffraction patterns from the composite surface heated at 1723K. The diffraction peak intensities derived from silicon carbide increased with time. A full width of half maximum intensity (FWHM) of diffraction peaks was evaluated for peak angle from the 111 reflection of β-SiC. Using the determined FWHM, the apparent crystallite size was estimated using the Scherrer's relationship:

$$D = \kappa\lambda / w\cos\theta \qquad (6)$$

where λ, θ, w and κ indicate the wavelength of Cu-Kα radiation, the Bragg angle of the 111 reflection, the half-width (FWHM) corrected a mechanical broadening width ($2\theta = 0.160^\circ$), and the Scherrer's constant(=0.9), respectively. Fig.9 shows SiC crystallite sizes as a function of time at 1723, 1673K.

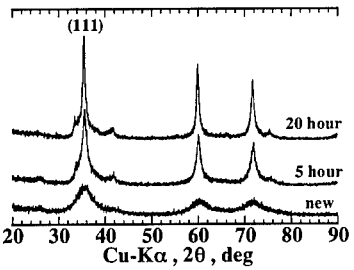

Fig.8 X-ray diffraction patterns from ZMI / Si-Ti-C-O composite surfaces heated at 1723K.

Crystallite size increased with time, which indicates that SiC grain growth occurred during creep testing.

As a result, the viscosity of the fiber and matrix increased. This caused a continuously decreasing creep rate and made steady-state creep impossible.

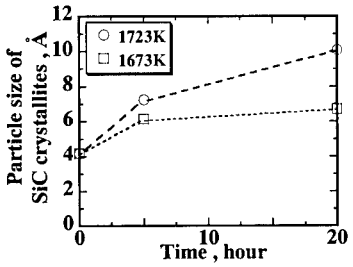

Fig.9 SiC crystallite size as a function of exposure time at 1723, 1673K.

Conclusions

The tensile creep behavior of a 3-D woven Tyranno™ ZMI fiber / BN interface / Si-Ti-C-O matrix composite at 1573-1723K in air and the influence of the thermal stability of the composite on creep behavior were investigated. The following conclusions were made:

(1) No apparent steady-state creep regime observed in this creep test condition. Transient creep behavior of the composite is represented by the simple power-law.

(2) Under the test conditions, the microstructure of the composite is unstable, resulting in weight loss and SiC grain growth, which made steady- state creep impossible under the condition.

References

1. R. Bodet and J. Lamon: J. American Ceramic Society, 79(10), 2673 (1996)
2. S. Zhu, M. Mizuno, Y. Kagawa and Y. Mutoh: Composite Science and Technology, 51, 833 (1999).
3. T. Shimoo, M. Sugimoto, Y. Kakehi, and K. Okamura: J. Japan Inst. Metals, 55(3), 294 (1991)

Proceedings of 7th Japan International SAMPE
Symposium & Exhibition, Nov. 13-16, 2001

Distribution of fibre/matrix interface shear strength within a single fibre bundle for a 3-D woven SiC/SiC composite tested at 1100 °C in air

I. J. Davies[#], T. Ogasawara[$], and T. Ishikawa[$]

[#] Kyoto Institute of Technology, Matsugasaki, Sakyo-Ku, Kyoto 606-8585, Japan
E-mail: davies@ipc.kit.ac.jp

[$] Structures Division, National Aerospace Laboratory, 6-13-1 Ohsawa, Mitaka-Shi, Tokyo 181-0015, Japan

Abstract

The distribution of fibre/matrix interface shear strength, τ, within a single fibre bundle was investigated for a 3-D woven SiC/SiC composite tested at 1100 °C in air. The mean fibre pullout length, $<h>$, varied between zero at the bundle perimeter to 59 μm at the centre. The lowest value of τ was 60.2 MPa at the centre but this increased significantly towards the fibre bundle perimeter and reached values in excess of 2 GPa. Such a wide variation in τ within a single fibre bundle had not been observed by previous researchers, most likely due to the lack of τ data for composites with short fibre pullout lengths.

Key Words: interface shear strength, SiC/SiC, fibre bundle, fibre pullout.

Introduction

The mechanical properties of ceramic matrix composites (CMCs) are known to mainly depend on the fibre/matrix interface shear strength, τ, together with the Weibull parameters, S_o and m, of the fibre strength measured *in situ* the composite [1]. Highest tensile strength, σ, for SiC/SiC CMCs have generally been achieved using low values of τ (typically <10 MPa) with subsequent large fibre pullout lengths [2-4]. These low values of τ require the use of fibre/matrix interfaces based on layered materials such as pyrolytic carbon (py-C) and boron nitride (BN). However, one major problem with both py-C and BN is their extreme oxygen sensitivity above 500 °C. Oxidation of the fibre/matrix interface may increase τ to such an extent that crack deflection mechanisms at the fibre/matrix interface are suppressed, leading to brittle failure of the composite and poor mechanical properties. Although the oxidation damage within CMCs has been examined by several authors [5,6], the data obtained has generally been qualitative in nature. In the present work the authors aim to examine the distribution of τ within a single fibre bundle for a SiC/SiC composite.

Experimental Procedure

The CMC under investigation was comprised of surface-modified Tyranno® LoxM Si-Ti-C-O fibres (800 fibres per bundle) woven into a 3-D orthogonal configuration. Matrix densification of the composite was achieved through the repeated polymer impregnation and pyrolysis of a

precursor similar to polytitanocarbosilane. This composite system has been the subject of recent work by the authors [2-4, 7, 8].

Following machining to a suitable test geometry, the composite was heated in air to 1100 °C at 0.75 °C·s^{-1} and then loaded under tension to failure; the total time spent at 1100 °C being on the order of several minutes. The composite fracture surface was then investigated using a scanning electron microscope (SEM) and the following parameters measured for each fibre within a single randomly chosen fibre bundle towards the centre of the specimen; (i) x position, (ii) y position, (iii) fibre pullout length, h, and (iv) whether the fibre exhibited a fracture mirror. A total of 698 fibres (out of the 800 expected within a single fibre bundle) could be measured due to the shielding of fibres by their neighbours and the presence of holes where fibres had pulled out; these phenomena being especially prevalent for fibres with large pullout lengths.

In the present work, τ was estimated within different zones of the fibre bundle using the following equation [1]:

$$\tau = \frac{r\lambda(m)S_0}{4<h>} \qquad (1)$$

where r is the fibre radius, $<h>$ is the mean fibre pullout length, and $\lambda(m)$ is a function only of m. Values of 2.47 GPa and 2.91 were used for S_o and m, respectively, based on previous work by the authors [3]. Strictly speaking, S_o and m would also be expected to vary according to the extent of oxidation damage but, as shown later, any change in S_o and m would most likely be insignificant compared to the change in τ. The value of $<h>$ in Eqn. 1 was calculated using individual h data whilst r and $\lambda(m)$ were 4.03 μm [4] and 1.43, respectively.

Results and Discussion

Fig. 1(a) illustrates the positional dependence of fibre pullout length within the single fibre bundle. It can be clearly seen that the majority of fibres within the bundle exhibited either zero or negligible fibre pullout which are generally indicative of brittle failure, i.e., suppression of crack deflection mechanisms at the fibre/matrix interface due to τ being excessively high. This conclusion was confirmed in Fig. 1(b) that illustrates the vast majority of fibres with low h values to have also exhibited a flat fracture surface; as opposed to a fracture mirror that typically occurs when crack deflection mechanisms are present. Nearly all the fibres with higher h values and fracture mirrors were concentrated towards the centre of the fibre bundle, thus suggesting the oxidation damage to have been concentrated at the perimeter. Such a result would indicate the oxygen to have entered the fibre bundle from the perimeter.

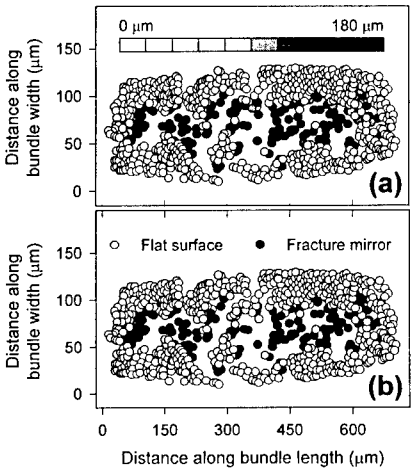

Fig. 1 Positional dependence of properties within a single fibre bundle: (a) fibre pullout length, and (b) existence of flat surface or fracture mirror. Note that fibre pullout lengths in (a) have been shown using a logarithmic scale.

Even though the fibres towards the centre of the bundle exhibited the largest h values, these h values were still considerable smaller

compared to those measured for specimens tested at room temperature or in vacuum, i.e., in the absence of oxidation damage. Figure 2 compares fibre pullout length distributions for the composite tested under a variety of conditions [3] with $<h>$ being 810 μm for the specimen tested at room temperature compared to 70 μm for the specimen under investigation (1100 °C/air). This data would suggest that even the fibres with largest h values in the present specimen possessed substantially oxidised fibre/matrix interfaces.

As mentioned earlier, for the calculation of τ to be shown later, it was assumed that S_o and m were constant within the fibre bundle. However, it can be seen from Fig. 3(b) that S_o and m were in fact considerable different at the centre and perimeter of the fibre bundle with S_o and m at the bundle perimeter being lower and higher, respectively, compared to fibres near the bundle centre. This result compares greatly with the specimen tested at room temperature (Fig. 3(a)) which shows no difference between S_o and m (and hence, most probably $<h>$ and τ) for the two regions.

The next step was to investigate the variation of properties along the (symmetrical) minor axis of the fibre bundle from the perimeter to the centre. Essentially, the data in Fig. 1 was divided into horizontal strips and the data averaged for each strip.

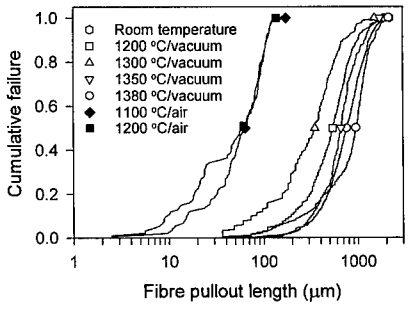

Fig. 2 Fibre pullout length distributions for a SiC/SiC composite tested under various conditions [3].

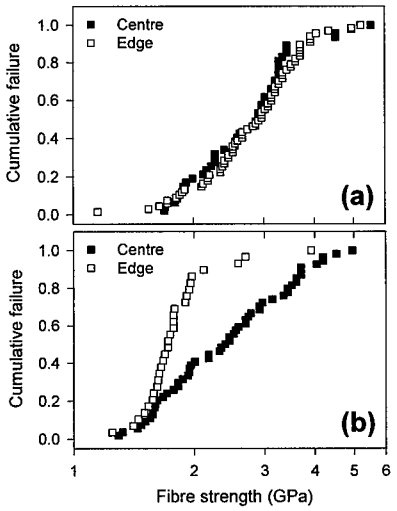

Fig. 3 Fibre strength distributions measured *in situ* a SiC/SiC composite: (a) room temperature, and (b) 1100 °C in air. "Centre" and "Edge" refer to the general position within the fibre bundle where the measurements were taken.

The result of this procedure has been presented in Fig. 4 with the fraction of fibres exhibiting fracture mirrors (Fig. 4(b)) being again seen to closely correlate with $<h>$ (Fig. 4(a)). The values of $<h>$ varied between zero at the perimeter to 59 μm at the centre whilst the lowest non-zero value of $<h>$ was 1.7 μm at approximately 15 μm from the bundle perimeter. It can be seen from Eqn. 1 that τ is inversely proportional to $<h>$ which suggests the ratio of τ between the centre and perimeter of the fibre bundle to be approximately 35 at the lowest non-zero $<h>$ region (i.e., 59/1.7); the value at the perimeter of the bundle where $<h>$ was zero being necessarily greater than 35.

Values of τ obtained from Eqn. 1 have been presented in Fig. 5 as a function of the distance from the fibre bundle perimeter. The lowest value of τ obtained was 60.2 MPa at the centre of the fibre bundle and this value

agreed closely with the value of 54.75 MPa obtained previously [3] for the centre of a fibre bundle tested under similar conditions.

The value of τ increased gradually away from the bundle centre to reach 128 MPa at a distance of 39 μm from the bundle perimeter but then increased significantly to reach ≥2 GPa for the smallest non-zero $<h>$ region. Such high values of τ have not previously been noted in SiC/SiC composites and are probably due to the fact that τ has not been measured within composites exhibiting very small h values.

In conclusion, the present work appears to show a very wide range of τ values to exist within a single fibre bundle that was partially oxidised at 1100 °C in air. In future work the authors will aim to refine this technique in order to obtain more accurate values for τ.

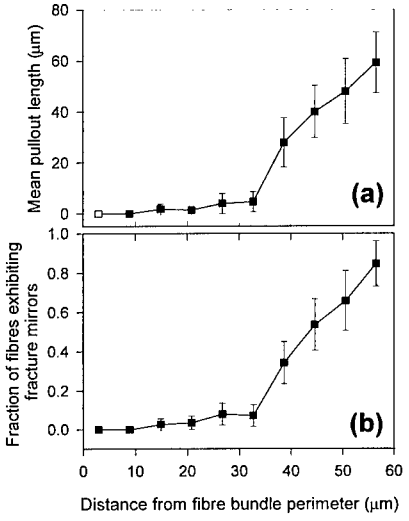

Fig. 4 Distribution of fibre properties along the minor axis within a single fibre bundle: (a) mean fibre pullout length, and (b) fraction of fibres exhibiting fracture mirrors.

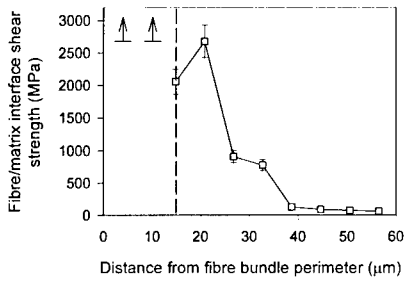

Fig. 5 Distribution of fibre/matrix interface shear strength along the minor axis within a single fibre bundle.

Acknowledgements

The authors wish to sincerely thank Dr. M. Shibuya of Ube Industries Ltd., Dr. J. Gotoh of Kawasaki Heavy Industries Ltd., and T. Hirokawa and T. Tanamura of Shikibo Ltd. for the manufacture and supply of all materials used in this study.

References

1. W. A. Curtin, J. Amer. Ceram. Soc., 74(11), 2837 (1991).
2. I. J. Davies, T. Ishikawa, M. Shibuya, and T. Hirokawa, Comp. Sci. and Technol., 59(3) 429 (1999).
3. I. J. Davies, T. Ishikawa, M. Shibuya, and T. Hirokawa, Comp. Sci. Technol., 59(6) 801 (1999).
4. I. J. Davies, T. Ishikawa, M. Shibuya, T. Hirokawa, and J. Gotoh, Composites Part A, 30(4) 587 (1999).
5. F. E. Heredia, J. C. McNulty, F. W. Zok, and A. G. Evans, J. Am. Ceram. Soc., 78(8), 2097 (1995).
6. J. A. Celemin and J. Llorca, Compos. Sci. Technol., 60, 1067 (2000).
7. T. Ishikawa, K. Bansaku, N. Watanabe, Y. Nomura, M. Shibuya, and T. Hirokawa, Comp. Sci. Technol., 58 (1998) 51.
8. T. Ogasawara, T. Ishikawa, N. Suzuki, I. J. Davies, M. Suzuki, J. Gotoh, and T. Hirokawa, J. Maters. Sci., 35, 785 (2000).

Proceedings of 7th Japan International SAMPE
Symposium & Exhibition, Nov. 13-16, 2001

Shear Modulus of 3-D Woven Ceramic Matrix Composite

Takuya Shiraishi[1], Toshio Ogasawara[2], Takashi Ishikawa[2] and Naoyuki Watanabe[3]

1: Graduate Student, Department of Aerospace Engineering,
Tokyo Metropolitan Institute of Technology
6-6 Asahigaoka, Hino, Tokyo 191-0065, JAPAN
E-mail: takuya@aswat1.tmit.ac.jp
2: Advanced Composite Evaluation Technology Center,
National Aerospace Laboratory of Japan
3: Department of Aerospace Engineering, Tokyo Metropolitan Institute of Technology

Abstract

In this work, torsional rigidities of beam specimens with rectangular cross section were measured in torsional tests to estimate shear moduli of an orthogonal 3-D woven ceramic matrix composite (CMC). The in-plane shear modulus estimated from torsional tests almost corresponded with the values obtained by tensile tests of ±45° specimens. The shear moduli were calculated by the finite element analysis based on the homogenization method. By assuming the suitable macroscopic elastic modulus of the matrix, the analytical results were in good agreement to the experimental results.

Introduction

Many studies about nonlinear stress-strain behavior of ceramic matrix composites (CMCs) have been made [1, 2]. There were a few studies focusing on reduction of shear modulus under tensile loading [3], however, no study for 3-D woven CMCs. In this work, torsional tests for beam specimens with rectangular cross section were conducted to estimate shear modulus of an orthogonal 3-D woven CMC. The experimental results were compared with the results measured in tensile tests of $\pm 45°$ specimens and numerical results by the finite element analysis based on the homogenization method.

Experimental Procedure

Material Description

The material under investigation was an orthogonal 3-D woven ceramic matrix composite [4]. Tyranno™ Lox-M (Si-Ti-C-O) fiber was used for reinforcement, and Si-Ti-C-O matrix was impregnated into the fiber preform by using a polymer impregnation and pyrolysis (PIP) processing. Fiber volume fractions in the x, y, and z directions were 19%, 19%, and 2%, respectively.

Tensile Tests

In order to measure the initial elastic moduli of this composite, tensile tests were performed for 0/90 and $\pm 45°$ orientations under the constant displacement rate of 0.1 mm/min. For $\pm$ 45° orientations, three specimens were evaluated to investigate the scattering of the results. Specimen configuration and dimensions are shown in Fig. 1(a). Strain gages were used to measure the longitudinal and transverse strains.

Torsional Tests

Figure 2 shows the schematic configuration of the torsional test. By using an optical lever, two twist angles θ_a and θ_b at

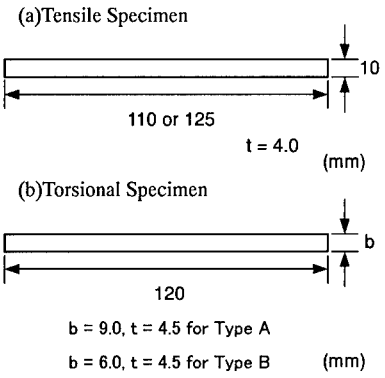

Fig. 1 Dimensions of Specimens used for Tensile and Torsinal Tests

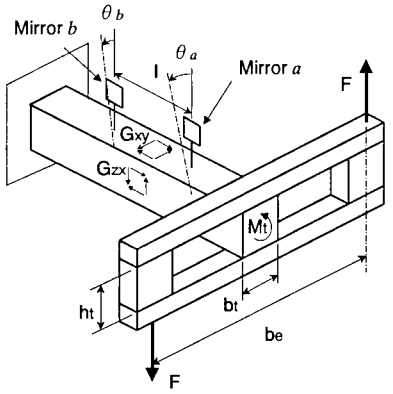

Fig. 2 Schematic Illustration of the Torsional Test

points a and b are measured as a function of torque ($M_t = F \times b_e$). The separation between two points was 50mm. Load was applied with dead weight. When torsion angle per unit length, ω, is given from $\omega = (\theta_a - \theta_b)/l$, torsional rigidity of the specimen is obtained with M_t/ω. The torsional tests were conducted for the specimens with two different cross sections as shown in Fig. 1(b) Type A and Type B.

Results and Discussion

Tensile Tests

The experimental results on initial elastic moduli are listed in Table 1. Figure 3 and 4 show stress-strain curves for No.1 and No.3. In-plane shear modulus G_{xy} was obtained from the following equation

$$G_{xy} = E_{45}/\{2(1+\nu_{45})\} \qquad (1)$$

where E_{45} and ν_{45} are Young's modulus and Poisson's ratio in 45° direction, respectively. The obtained shear moduli (G_{xy}) are 46, 49 and 50GPa. The average is 48.3GPa and its standard deviation is 2.1GPa. The matrix elastic moduli of the CMC seem to be similar to those of fiber [2]. Therefore the composite behaves almost isotropically in linear elastic region. However, once matrix begins to crack, stress-strain behavior in the ±45° specimen is far different from that in the 0/90 specimen is observed. In the 0/90 specimen, after the matrix crack saturation at 0.7% of strain, the applied load is carried almost only by the fibers. Consequently the stress-strain curve shows a nearly linear behavior until its failure. On the other hand, in the ±45° specimen, as the matrix cracks grow, the matrix cannot effectively carry the load because the crossed fibers deform like a pantograph. Finally, when the longitudinal strain reaches 2.3%, the transverse strain is approximately 1.0%.

Table 1 Results of the Tensile Tests

No.	Orientations	E (GPa)	G_{xy} (GPa)
1	0/90	125	-
2	±45°	112	46
3	±45°	120	50
4	±45°	118	49

Torsional Test

Torsional rigidity of a beam with rectangular cross section is obtained from the following equations [5]

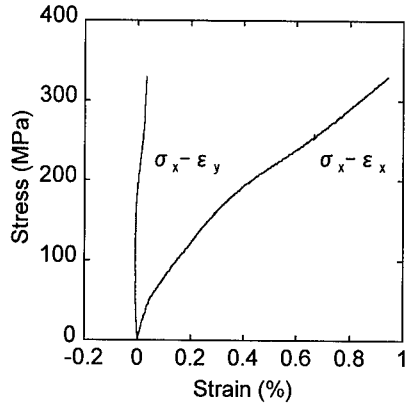

Fig. 3 Stress-Strain Curve in Uniaxial Tension parallel to the Fiber (0/90, No.1)

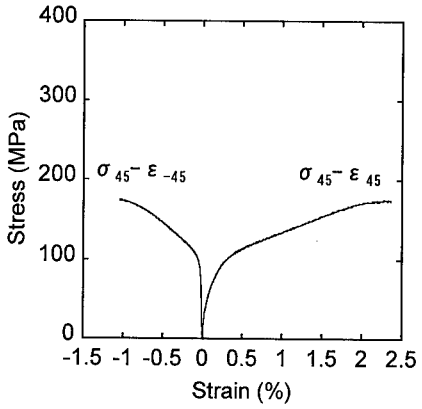

Fig. 4 Stress-Strain Curve in Uniaxial Tension at Angle 45° to the Fibers (No.3)

$$M_t/\omega = G_{xy}\beta(c)b_t h_t^3 \tag{2a}$$

$$\beta(c) = \frac{32c^2}{\pi} \times \sum_{k=1,3,5,\ldots}^{\infty} \frac{1}{k^4}\left(1 - \frac{2c}{k\pi}\tanh\frac{k\pi}{2c}\right) \tag{2b}$$

$$c = \frac{b_t}{h_t}\sqrt{\frac{G_{zx}}{G_{xy}}} \tag{2c}$$

where, b_t and h_t are the width and height of the specimen, respectively. By substituting experimental values of M_t/ω, b_t and h_t into Eqs.(2), a curve on G_{zx}-G_{xy} plane can be described. The intersection point of two curves obtained from two different cross section specimens gives the solution of G_{zx} and G_{xy}. In Fig. 5, the solid line shows the result of Type A; M_t/ω =8.48Nm^2, b_t =9.0mm and h_t=4.5mm, and the dotted line shows the result of Type B; M_t/ω =4.33Nm^2, b_t=6.0mm and h_t=4.5mm. Then the intersection point of these curves determines shear moduli of this material as G_{xy}=45GPa and G_{zx}=36GPa. Taking the scattering of the experimental results in the tensile tests into consideration, the estimated shear modulus (G_{xy}=45GPa) seems to be reasonable.

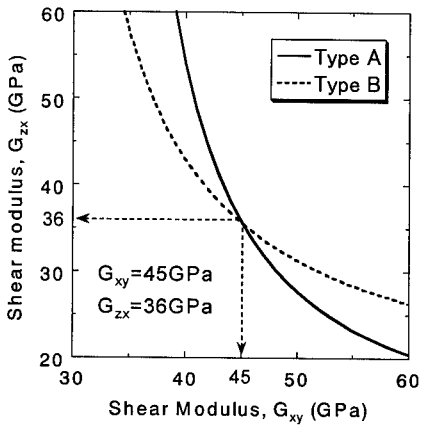

Fig. 5 Estimation of Shear Moduli

Calculation of Shear Modulus by FEM

An orthogonal 3-D woven composite can be regarded as three-dimensional periodic structure of base cell which is the smallest unit structure. Macroscopic elastic modului of periodic nonhomogeneous material such as these composites can be calculated by FEM based on homogenization method [6]. The base cell model of this CMC is shown in Fig. 6. Dimensions of fiber bundles were measured by microscopic observation. Young's modulus of fiber is 187GPa and, Poisson's ratios of fiber and matrix are assumed to be 0.2. It is impossible to determine Young's modulus of matrix directly, which contains micro voids.

Therefore, the elastic modulus of matrix was estimated by parametric study using FEM Analysis.

The numerical results are indicated in Fig. 7. Using the value E_x=125GPa from the tensile test, Young's modulus of the matrix is estimated as 150GPa. Then shear moduli G_{xy} and G_{zx} are 48.5GPa and 34.3GPa, respectively. Comparing with the results of tensile and torsional tests, the analytical results obtained by FEM are in good agreement with the experimental results.

Conclusion

Shear moduli G_{xy} and G_{zx} were estimated by means of torsional tests of specimens with two different rectangular cross sections. Comparing estimated shear modulus G_{xy} from tensile test of $\pm 45°$ specimen, it was proved that the torsional test was an effective method to estimate shear modulus. Shear moduli were calculated by FEM based on homogenization method. A good correspondence between the analytical results and the experimental data was obtained, and the validity of the analytical model was demonstrated.

In this work, only the initial shear moduli were obtained from the torsional rigidities. In the future work, by using the torsional tests for specimens with matrix cracks due to tensile tests in advance, the reduction of shear modulus under tensile loading will be evaluated.

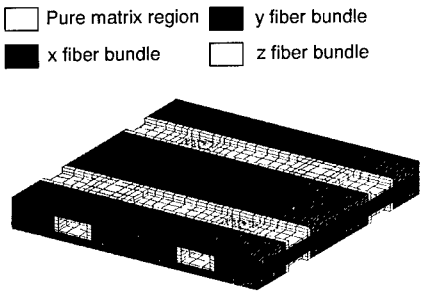

Fig. 6 FEM Model of Base Cell

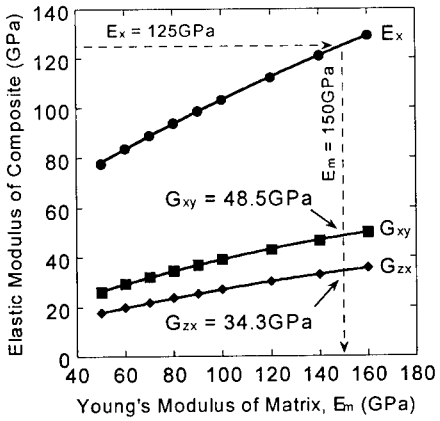

Fig. 7 Equivalent Elastic Moduli of the Composite estimated by the Homogenization Method as a Function of Matrix Young's Modulus

References

1. A. G. Evans and F. W. Zok: Journal of Materials Science, 29, 3857 (1994).
2. H. Ito, T. Ogasawara, N. Watanabe and T. Ishikawa: Journal of the Japan Society for Composite Materials, 27(2), 112 (2001).
3. C. Cady, F. E. Heredia and A. G. Evans: J. Am. Ceram. Soc. 78(8), 2065 (1995).
4. T. Ishikawa, K. Bansaku, N. Watanabe, Y. Nomura, M. Shibuya and T. Hirokawa: Composites Science and Technology, 58, 51 (1998).
5. T. Ishikawa, K. Koyama and S. Kobayashi: Journal of the Japan Society for Aeronautical and Space Sciences, 23(263), 678 (1975).
6. N. Watanabe and K. Teranishi: Proc. AIAA 36th SDM Conference, Vol. 1, New Orleans, LA, USA (1995), pp. 1955-1963.

Proceedings of 7th Japan International SAMPE
Symposium & Exhibition, Nov. 13-16, 2001

Characterization of Thermal Shock Fracture Behavior in Ceramic Materials by Disk-on-Rod Tests

Shuichi WAKAYAMA#, Kousuke NISHINO# and Shinya ARAI#

#: Department of Mechanical Engineering, Tokyo Metropolitan University
1-1 Minami-Ohsawa, Hachioji-shi, Tokyo 192-0397, JAPAN
E-mail:wakayama@ecomp.metro-u.ac.jp

Abstract

The thermal shock fracture behavior in ceramic materials was characterized by Disk-on-Rod tests. The central region of heated specimen was quenched by means of contacting with a cool metal rod. AE signals during thermal shock fracture were detected by an AE transducer attached on the opposite end of metal rod. The transient thermal stress field was calculated by FEM from temperature distribution on the specimen measured by a high speed IR camera (30 frames/s). The formation and arrest of maincrack was observed at the center of the specimen. It is important that the critical stress for maincrack formation during thermal shock fracture was evaluated by AE analysis and found equivalent to the critical stress evaluated by plane bending tests.

Key Words: Ceramics, Thermal Shock Fracture, Disc-on-Rod Test, Maincrack Formation

Introduction

The thermal shock fracture behavior of ceramics has been investigated using many traditional thermal-shock-testing methods such as the water quench [1,2]. Recently, new experimental methods are proposed and applied to the investigation of macroscopic crack propagation process during thermal shock fracture, based on fracture mechanics [3-5]. However the characterization of microfracture process under thermal shock as well as transient thermal stress field is indispensable, since thermal shock fracture is caused by the accumulation of microscopic damages such as microcrackings due to thermal stress.

In this study, new experimental technique for the investigation of thermal shock fracture behavior, Disk-on-Rod test, is proposed. The temperature fields in the specimen were measured and used to calculate the 2 dimensional thermal stress field. Furthermore, fracture process was evaluated by AE measurement. The formation of maincrack due to propagation and/or coalescence of microcracks was focused in the present paper. Especially, the critical stress for maincrack formation is evaluated from obtained experimental data and compared with the results of mechanical biaxial bending tests. Consequently, thermal shock fracture process in ceramics was well understood.

Experimental Procedure

Materials

The material used were alumina ceramics (ADS-11) offered from Toshiba Ceramics Co., Ltd. The relative density and mean

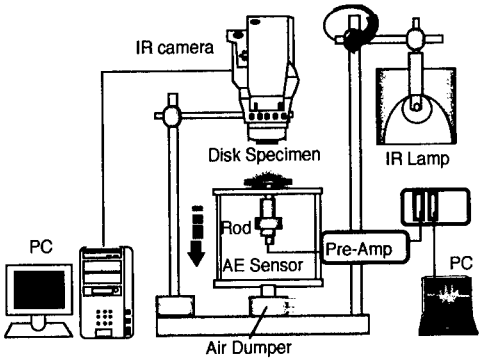

Fig.1 Disk-on-Rod Test Apparatus

grain size were 97.7% and 6 μm, respectively. Disk specimens were cut from the rod materials and both surfaces were polished.

Disk-on-Rod Tests

In this study, for characterizing the thermal shock fracture process, new experimental technique, Disk-on-Rod test was developed. A thin disk specimen was heated uniformly to the required temperature by an infrared lamp and only the central part of disk was quenched by means of contacting with a Cu rod. The disk specimens have diameter of 20 mm and thickness of 0.6mm, and a contacting area has 4 mm diameter, therefore 2-D thermal stress field was obtained. The apparatus of Disk-on-Rod test and AE measuring system are shown in Fig. 1 schematically. Contacting speed was controlled by an air damper to restrain the AE noise due to contacting. And temperature distributions on disk surface were measured by a high-speed infrared camera (30 frames/s). Then thermal stress was calculated from temperature distribution using FEM analysis.

In order to evaluate the fracture process, AE signals during thermal shock fracture were detected by AE sensor attached on the bottom end of metal rod, which was used for both coolant and wave guide. AE sensor, in which amplifier is instrumented, with resonant frequency of 180 kHz was used, then the initiations of microcracks could be detected with excellent sensitivity. The total gain of the AE system was 75 dB (main amplifier; 20 dB and pre-amplifier with sensors; 55 dB) and the threshold level was 40 dB, i.e.18 μV at the input terminal of the pre-amplifier.

Results and Discussion

Determination of Thermal Stress

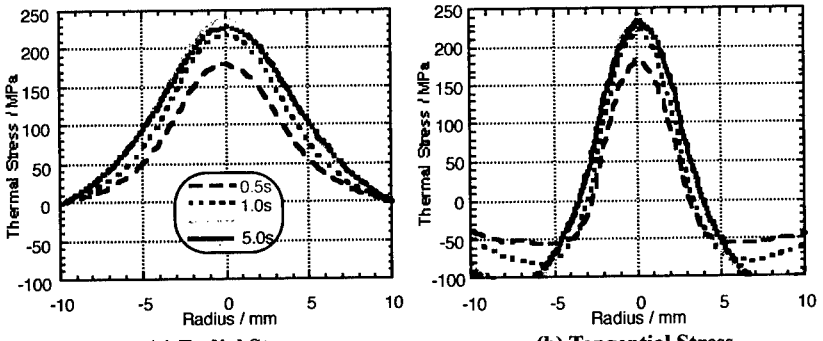

(a) Radial Stress **(b) Tangential Stress**

Fig.2 Thermal Stress during Disk-on-Rod Test

The temperature on specimen surface was measured by 1/30 s using a high-speed infrared camera system during Disk-on-Rod test and concentric temperature field was obtained. The thermal stress field was computed from the obtained 2-dimensional temperature distribution using FEM code (ANSYS), as shown in Fig. 2 (a), radial stress, and (b), tangential stress. The obtained stress field was axi-symmetric according to the concentric temperature distribution. It is understood from the figure that the center of the disk is subjected to equi-biaxial maximum stress and the stresses decrease to the outer region along the radial direction. It is important that radial stress is tension in the whole of disk specimen, while tangential stress has the transition point from tension to compression at 4mm from the center of the disk. Both stresses show the maximum at 3s.

Fracture Behavior during Disk-on-Rod Tests

Figure 3 shows a fractured specimen (a) and equi-biaxial thermal stress and AE behavior during Disk-on-Rod test (b). It is observed in Fig. 3 (a) that the maincrack was formed at the center of specimen subjected to the maximum biaxial stress and propagated to the outer region with small crack deflection. The specimen was separated into 4 peaces, which demonstrates that the fracture was in brittle manner. The author have reported that the crack arrest and re-propagation was observed during the Disk-on-Rod tests of alumina with lower strength [6]. It is considered that these deference in fracture behavior was resulted from the deference in strain energy at the maincrack formation.

It is recognized in Fig. 3 (b) that both cumulative AE events and energy increase remarkably at 1.5 s. Since the formation of maincrack was observed at the AE increasing point in the previous study, it is understood that the critical stress for maincrack formation during thermal shock fracture, σ_{th}, can be determined by Disk-on-Rod test. Those values ranged from 250 to 300 MPa independently from the initial temperature of the specimen.

Maincrack Formation under Thermal Shock

In order to investigate the critical stress for maincrack formation, the plane bending tests were carried out using same geometry specimens and a loading rod with 4mm diameter. Figure 4 shows the result of plane bending test and a fractured specimen. Similarly to the thermal shock fracture, it is observed in Fig. 4 (a) that the maincrack was initiated at the center region of the

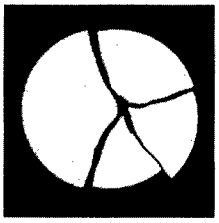

(a) Fractured Specimen

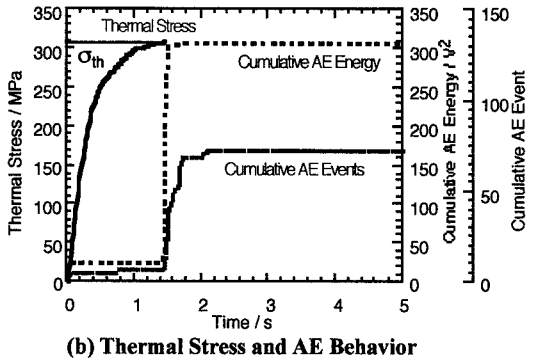

(b) Thermal Stress and AE Behavior

Fig.3 Thermal Stress and AE Behavior during Disk-on-Rod Test and Fractured Specimen

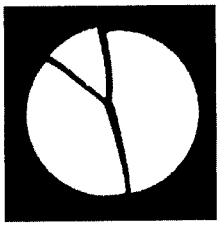

(a) Fractured Specimen

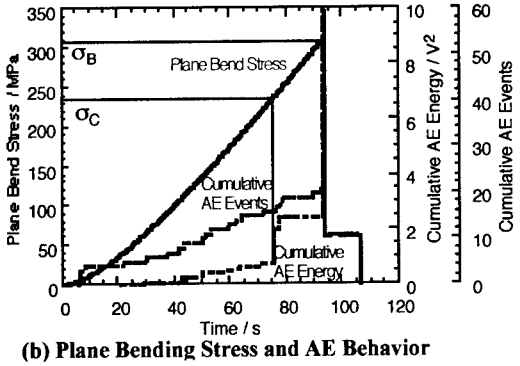

(b) Plane Bending Stress and AE Behavior

Fig.4 Result of Plane Bending Test and Fractured Specimen

specimen subjected to equi-biaxial stress. In Fig. 4 (b), the AE increasing point can be observed before maximum bending stress, therefore it is understood that the critical stress for maincrack formation under mechanical loading, σ_C, can be determined. Those critical stresses for Material B were evaluated as 180 – 240 MPa; those are lower than the critical stress for maincrack formation under thermal shock as mentioned above. Considering the influence of stress corrosion cracking due to water during bending test at room temperature, it can be concluded that the critical stresses for maincrack formation under thermal shock and mechanical loading are equivalent to each other.

Conclusions

In the present study, new experimental technique, Disk-on-Rod test, was developed and applied to the characterization of thermal shock fracture process in ceramics. The thermal stress fields were computed from temperature distributions measured by high-speed IR camera and fracture process was evaluated by AE measurement, both of which are significant for understanding the thermal shock fracture behavior. From these results, the following conclusions were obtained.

(1) The maincrack was formed at the center of disk specimen subjected to maximum equi-biaxial stress.
(2) The critical stress for maincrack formation was evaluated and it was almost equivalent to the critical stress for maincrack formation in plane bending test.
(3) Thermal shock fracture process consisting of crack initiation, propagation and arrest was well understood.

Acknowledgment
The authors would like to thank Toshiba Ceramics Co., Ltd. for their offer of ceramic samples.

References

1. W. D. Kingley: J.Am.Ceram.Soc. 38(1), 3(1955).
2. D. P. H. Hasselman: J.Am.Ceram.Soc., 52(11), 600(1969).
3. G. A. Schneider and G. Petzow: J.Am.Ceram.Soc. 74(1), 98(1991).
4. W. P. Rogers and A. F. Emery: J. Mater. Sci. 27(1), 146(1992).
5. Y. Mizutani, N. Nishikawa and M. Takatsu: J. Ceram. Soc. Japan 103(5), 494(1995)
6. S. Wakayama: Progress in Acoustic Emission 9, III73(1998).

Proceedings of 7th Japan International SAMPE
Symposium & Exhibition, Nov. 13-16, 2001

Development Study of Carbon-Carbon Turbine Disk for ATREX Engine

Ken Goto, Hiroshi Hatta, Tetsuya Sato, Nobuhiro Tanatsugu
The institute of space and astronautical science
3-1-1 Yoshinodai, Sagamihara, Kanagawa, 229-8510 Japan
Email: kgoto@pub.isas.ac.jp

Abstract

Cold spin test of 3DC/C disk were carried out to elucidate the feasibility for the turbine disk of ATREX engine. The fly-out behavior occurred before the total fracture of the disk and the shaft vibration simultaneously increased. The fly-out behavior was characterized by the delamination of the fiber bundles from the surface of the 3DC/C disk. Partial siliconization was shown to be effective to improve the onset speed of fly-out behavior. The machinability of 3DC/Cs for turbine blade are also examined and the tip radius can be machined with 0.5 mm.

Key Words: Carbon-Carbon, Turbine disk

Introduction

Carbon-carbon composites (C/Cs) can maintain high strength and toughness up to extreme high temperature more than 2273 K. From this strong point, C/Cs has been expected to use for the turbine disk material of the air-turbo-ram-jet engine (ATREX), which ISAS has been developing for the future propulsion system of the space launcher. The requirements for the turbine disk from the system study of the ATREX engine are; (1) disk diameter = 300 mm, (2) peripheral speed at the disk tip must be more than 390 m/s, (3) surrounding atmosphere is high temperature hydrogen gas (1500 K). From our pervious study [1, 2], the rotation speed could be reached 513 m/s at the total fracture by using r-θ-z three dimensional fiber reinforced C/C (3DC/C) disk. However, the fly-out behavior coming from the micro fracture of the C/C disk occurred before the final failure and the vibration amplitude simultaneously increased. In this study, the mechanism responsible for the fly-out behavior are examined through the understandings of the experimental evidences. Using these understandings, the preventive measure was proposed and tested for 3DC/C disk. In addition, the machinability of the 3DC/Cs for the turbine blade tip sharpness was also examined for the design of the turbine system.

Experimental Procedure

(1) Material

C/C disk used in this study was the r-θ-z three dimensional fiber-reinforced C/C using high strength carbon fiber (Torayca T-800). Fiber volume fractions in each direction, r, θ and z are set to , 5 %, 40 % and 15%, respectively. The carbon matrices were infiltrated by the repetition of the densification cycles; infiltration of phenolic resin and carbonization. The final bulk density was reached to 1.42 x 10^3 kg/m^3. The C/C disk were machined to the final shape (inner diameter = 300 mm, outer diameter = 400 mm and thickness = 15 mm) by conventional milling technique. The siliconization around the outer surface of 3DC/C disk by the melt Si impregnation and the gaseous route were examined as the preventive methods for fly-out behavior. The turbine blade tip were modeled as shown in Figure 1 with changing the tip radius, R, by conventional machining.

(2) Mechanical test

Cold spin tests were carried out in a vacuum chamber by using a spin tester driven by air turbine. The 3DC/C disk assembled with the rotation fixture was adjusted rotation balance by changing the weight of the fixture. To avoid the fiber damage, the rotation balance of the C/C ring itself was not adjusted. The objects flying-out from C/Cs were detected by the AE sensor adhered to the aluminum target located around the specimen as shown in Figure 2. The spin test were also carried out for the model turbine disk using the fixture as shown in Figure 3. To characterize the fly-out behavior, the toughness of the 3DC/C were measured by CT (Compact tension) specimen machined from 3DC/C disk as shown in Figure 4.

Result and Discussion

(1) Fly-out behavior

Figure 5 shows the surface of 3DC/C disk after rotation test at the maximum speed of 270 m/s. From this figure the θ- and z-directional fiber-bundles were shown to be flew-out from the disk and only the r-directional fiber bundles remained. From the observation of the fly-out objects and surface of the 3DC/C disk after rotation, the fly-out behavior are modeled as shown in Figure 6; θ-directional fiber bundles at the surface were delaminated from the edge made by machining and this delamination increased and finally delaminated layer fractured. Using this fracture model, the fly-out behavior can be characterized by the stress concentration at the tip of the delamination. The delaminated layer is loaded by the hoop stress generated in the disk and also centrifugal force as shown in Figure 7.

Considering these two loading modes, energy release rate, G, can be estimated as a function of delamination length as shown in Figure 8. G has its minimum with delamination length and the onset of fly-out can be described with comparing this minimum G and critical energy release late of the inter-layer, Gc. From Fig. 8, G is also the function of rotation speed and layer thickness, h. To increase the critical rotation speed where the fly-out occurs, the following two methods are considered to be effective; (1) decrease layer thickness, i.e., use fine texture and (2) increase Gc itself. The minimum G of the 3DC/C disk used in this study is estimated ≈ 10 J/m^2 and this value agrees with Gc of graphite (5 to 20 J/m^2).

(2) Preventive method for fly-out behavior

One of the effective preventive methods for fly-out behavior is the increase of inter-layer bonding strength by siliconization. Figure 9 (a) and (b) show the 3DC/C disks with partial siliconization at outer surface area; (a) for melt Si impregnation and (b) for the gaseous route. Large area of the 3DC/C disk is shown to be siliconized for melt Si impregnation and only slight surface area for the gaseous route. The effectiveness of partial siliconization was firstly examined by the toughness measurement using CT specimen.

Figure 10 shows the load versus crack opening displacement relations of 3DC/C and 3DC/C with melt Si impregnation (3DC/C-Si). Usually, 3DC/Cs possess large fracture resistance and Gc increase with crack extension mainly due to the fibers running perpendicular to the crack plane. However, the fly-out behavior was occurred at only surface of the disk and the resistance described above could not operate. Thus, the initial value of Gc measured by CT specimen is meaningful for understanding the fly-out behavior. The initial Gc for 3DC/C was estimated as ≈ 5 J/m^2 and ≈ 40 J/m^2 for 3DC/C -Si. Using this Gc for 3DC/C-Si, the critical speed for fly-out behavior could be increased from 200 to 340 m/s. However, this speed of 340 m/s is still lower than the requirement speed of

ATREX engine (390 m/s). The cold spin test for the improved Si improved disk will be carried out and the result will be discussed farther in near future.

(3) Machinability of 3DC/C

The sharpness of the turbine blade tip edge is the key factor for turbine system. To achieve high rotation speed and avoid thermal stress, the turbine disk should be directly machined from 3DC/C disk. Figure 11 shows the edge of the model turbine blades with various R. As shown in the figure, the edge could be machined until R = 0.5 mm and the edge was broken at R = 0.1 mm. The cold spin test were performed with this model blade with R = 0.5 mm and the blade maintain its shape up to 470 m/s and this speed is enough for the ATREX engine.

Conclusions

(1) The fly-out behavior can be modeled by the delamination of the layers from the 3DC/C disk surface.
(2) Siliconization of the surface area of 3DC/C disk was shown to be effective for preventing fly-out behavior.
(3) 3DC/C can be machined with its tip radius = 0.5 mm and the blade maintain its shape with rotation speed up to 470 m/s.

References

[1] K. Goto, H. Hatta and N. Tanatsugu, Proceedings of The 6 th Japan International SAMPE Symposium, 1111-1114, 1999
[2] K. Goto, H. Hatta and N. Tanatsugu, Proceedings of the 10th Iketani Conference on Materials Reserach Toward the 21st Century, eds. T. Okubo, T. Kishi and T. Saito , June 26-30, 2000, Karuizawa, Japan

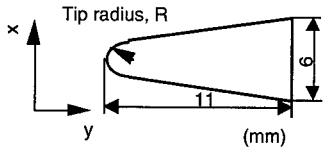

Figure 1 Model turbine blade.

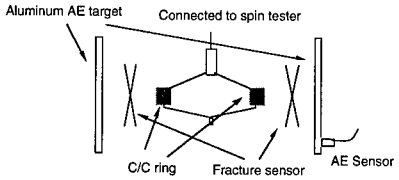

Figure 2 Set up for cold spin test.

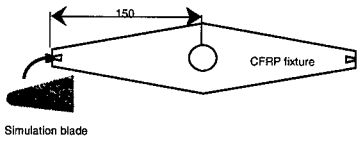

Figure 3 The fixture for model turbine blades.

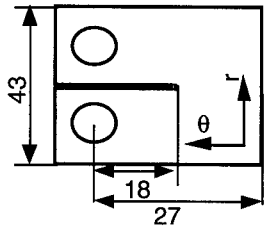

Figure 4 Shape and dimension of CT specimen.

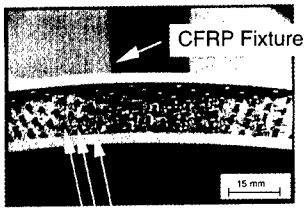

Figure 5 Surface of 3DC/C disk after rotation test.

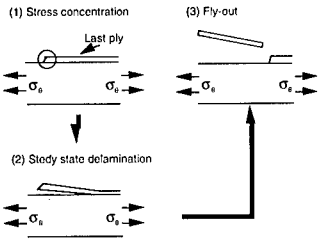

Figure 6 Fly-out process.

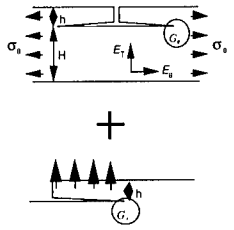

Figure 7 Loading mode for fly-out behavior.

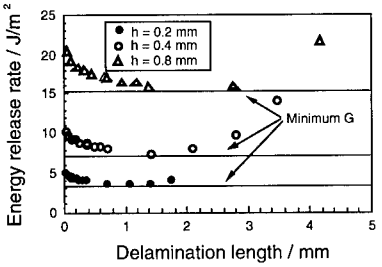

Figure 8 Energy release rate, G, as a function of delamination length.

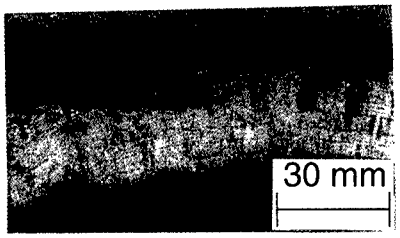

Figure 9 (a) 3DC/C disk with melt Si impregnation.

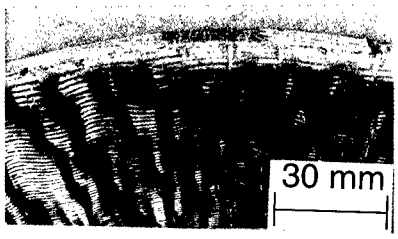

Figure 9 (b) 3DC/C disk with siliconization with gaseous route.

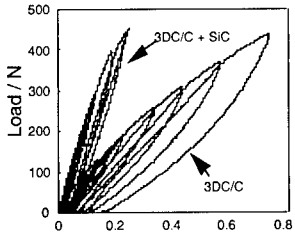

Figure 10 Load versus crack opening displacement curve of 3DC/C and 3DC/C-Si.

Figure 11 Edge of the model turbine blade.

Proceedings of 7th Japan International SAMPE
Symposium & Exhibition, Nov. 13-16, 2001

Ceramic coatings for oxidation protection of C/C composites

T. Aoki*, H. Hatta**, H. Fukuda***

* National Aerospace Laboratory of Japan, 6-13-1 Osawa, Mitaka, Tokyo 181-0015, Japan, takuya@nal.go.jp
** The Institute of Space and Astronautical Science, 3-1-1 Yoshinodai, Sagamihara, Kanagawa 229-8510, Japan
*** Science University of Tokyo, 2641 Yamazaki, Noda, Chiba 278-8510, Japan

Abstract

Two concepts are proposed to suppress cracking in the oxidation-resistant coating for carbon fiber reinforced carbon matrix (C/C) composites. The first idea is a SiC/C multi-layered coating. The aim of this coating is to prevent through-the-thickness cracking by reducing the thickness of each SiC layer. Even if the coating fractures occurs, for example, by external load, this coating is thought to be still effective by the mechanism of crack deflection. The other is a sinusoidal SiC coating. This coating suppresses through-the-thickness cracking by reducing thermal stress in the coating using the CTE anisotropy of C/C composites. In the present paper, both the concepts were demonstrated to be promising.

Key Words: C/C composites, Oxidation-resistant coatings, Coating cracks

Introduction

During the cooling process after the coating treatment, a huge mismatch in coefficient of thermal expansion, CTE, between ceramic coatings and C/C composites gives rise to a large number of through-the-thickness coating cracks. These through-the-thickness cracks allow the oxygen diffusion to the C/C substrate, and lead to severe oxidation-degradation in the substrate [1]. To improve the oxidation-resistance of C/C composites, therefore, the suppression of the through-the-thickness coating cracks is required. In this paper, SiC/C multi-layered and sinusoidal SiC coatings were examined for the suppression of through-the-thickness cracks in oxidation-resistant coatings on C/C composites. Plausibility of these coatings was discussed from experimental and theoretical points of views.

Coating concepts

SiC/C multi-layered coating

The multi-layered coatings are composed of extremely thin SiC and pyrolytic carbon layers alternately laminated as shown in **Fig.1**. The main role of the SiC layer is oxidation protection and that of the pyrolytic carbon layers is to eliminate mechanical interactions among the SiC layers and to isolate each SiC layer.

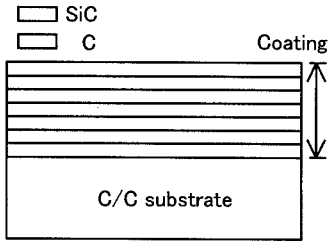

Fig.1 Schematic description of the SiC/C multi-layered coating.

When the thickness of a coating becomes less than a critical value, the coating cracks disappear. This phenomenon occurs due to the reduction in the energy release rate during the formation of a through-the-thickness crack [2]. As discussed afterward, the critical thickness for the present SiC coating is 0.2μm. We also experimentally confirmed that a relatively thick pyrolytic carbon layer (about 15μm) on a C/C composite did not induce cracks. Thus if SiC layers with the thickness less than 0.2μm and pyrolytic carbon layers are alternately laminated, we can possibly obtain a thick crack-less coating.

Sinusoidal SiC coating

Shioya *et al.* reported that by making the coating surface sinusoidal, tensile thermal stresses in the coating can be reduced [3]. In addition to this effect, in the present study, we have used the CTE anisotropy of C/C composites. While the in-plane CTE of C/Cs is smaller than that of SiC coatings, that in the out of plane direction is much larger than that of SiC. Thus, when SiC coatings are applied on the substrates with the carbon fibers inclined certain angles with the coating surface, we can diminish the CTE mismatch between the both materials. This implies that by making the surface sinusoidal, a drastic reduction in thermal stress will be achieved and suppression of coating cracks would be made especially for 1D- and 2D-C/Cs.

Experimental procedure

Two kinds of unidirectionaly reinforced C/C composites were used. The first C/C was produced by the Preformed-Yarn method and supplied by Across Co., Japan (PY-C/C). The other was fabricated by Sentan Zairyou Co., Japan (SZ-C/C). The reinforcing fiber of the PY-C/Cs was TORAYCA-M40 (Toray Co., Japan) and the volume fraction of the fibers, V_f, and the heat treatment temperature, HTT, were 50% and 2000°C, respectively. The SZ-C/Cs were reinforced by XN-35 (Nippon Graphite Fiber Co., Japan) and HTT was 2500°C. SiC/C multi-layered and sinusoidal SiC coatings were formed by the chemical vapor deposition, CVD, using $SiCl_4$, C_3H_8 and H_2 gases. Both the SiC and pyrolytic carbon layers were deposited at 1200°C under a total gas pressure of 10 Torr.

Results and discussion

Critical thickness for SiC single-layered coating

The critical thickness of the SiC single-layered coating was examined using the unidirectional PY-C/C with the dimensions of 15×15×3mm. **Fig.2** shows the variation of the observed crack spacing, 2λ, the distance between adjacent cracks, as a function of the coating thickness. The 2λ decreases up to 0.2μm with the decrease of coating thickness. The coating cracks, however, almost disappeared at a thickness of 0.2μm although localized small cracks were still slightly observed only above matrix rich regions of the substrate C/C. The coating thickness, when coating crack almost disappeared, was defined as the critical thickness, h_c.

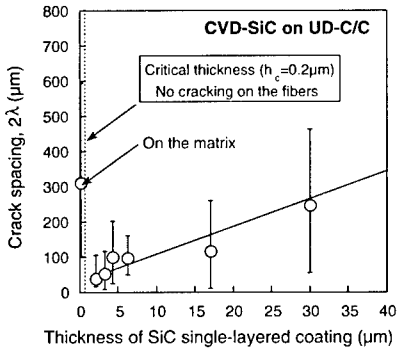

Fig.2 Relationship between the observed crack spacing and the thickness of SiC single-layered coating.

Effectiveness of SiC/C multi-layered coating

To confirm the validity of the present concept, SiC/C multi-layered coatings were deposited on the off-axis substrates cut from unidirectional SZ-C/Cs. In the experiment, the cutting angle between the coating plane and the carbon fiber axis, θ, shown in **Fig.3** was varied. The substrate dimensions were 20×10×3mm. The off-axis

substrates were used so as to increase the in-plane CTE of the substrates. By this procedure, we can freely set the critical thickness, h_c, and then we can chose h_c at values which we can easily form the multi-layered coatings.

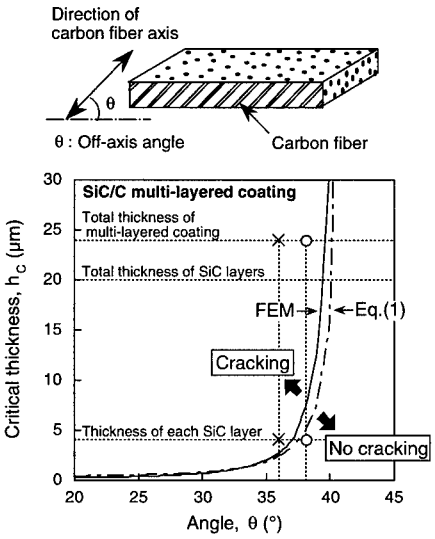

Fig.3 Critical thickness, h_c, of SiC single-layered coating as a function of the cutting angle, θ.

Beuth [2] has given h_c by setting the energy release rate, G_{ch}, during the formation of a through-the-thickness channeling crack equal to G_{IC}, as;

$$h_c = \frac{2\overline{E_{SiC}}G_{IC}}{\sigma_{SiC}^2 \pi g(\alpha,\beta)} \quad (1)$$

where E_{SiC} is the Young's modulus, G_{IC} the mode-I critical energy release rate of the coating, σ_{SiC} the tensile stress in the coating. The $g(\alpha,\beta)$ is a function of Dunders parameters, α and β [2], being modulus ratios between the coating and substrate. The critical energy release rate, G_{IC}, of the SiC coating was assumed to be 30 J/m^2. In Fig.3, the critical thickness, h_c, calculated from Eq.(1) and finite element analysis, FEA, is shown for SiC single-layered coating as a function of θ.

Fig.4 shows the cross-sectional views of a SiC/C multi-layered coating applied on off-axis substrates. The total thickness of the coatings was about 24μm, and thickness of each SiC and pyrolitic carbon layers were about 4μm and 0.8μm, respectively. In the coating with the 36° substrate, many through-the-thickness cracks were seen in the layer. On the other hand, in the 38° coating, no through-the-thickness crack was observed. The difference in the observed morphology can be clearly explained in **Fig.3**. In the 38° coating, the thickness of each SiC layer, equal to about 4μm, is lower than the critical thickness (5~7μm). Thus isolation of the each SiC layer by inserting the pyrolitic carbon layers lead to crack-less coating. In the 36° coating, however, each SiC layer was thicker than h_c, causing coating cracks.

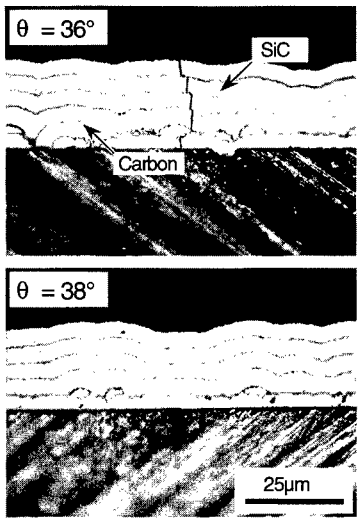

Fig.4 Cross-sectional views of SiC/C multi-layered coatings applied on off-axis SZ-C/C substrates.

We also formed a single-layered SiC coating with a thickness of 20μm on the same off-axis substrates, θ = 36°~38°. In these coatings, we clearly observed through-the-thickness cracks.

This example, therefore, successfully demonstrated that the SiC/C multi-layered coating is effective to suppress the through-the-thickness cracks in the coating.

Effectiveness of sinusoidal SiC coating

The thermal stress in a sinusoidal SiC coating was calculated by use of FEA. **Fig.5** shows the calculated result for a configuration with coating thickness 125μm, wave height 3.6mm, and wave length 4mm, which was assumed to be applied on a unidirectional PY-C/C. The X and Y axes represent the horizontal position in the coating, and the maximal principle stress in the sinusoidal coating normalized by the stress in the flat coating, respectively. As shown in this figure, a large stress was obtained only at the coating surface and near the interface at the bottom and top of the wavy coating. Hence we can expect the cracks induced at these points would be arrested within the coating.

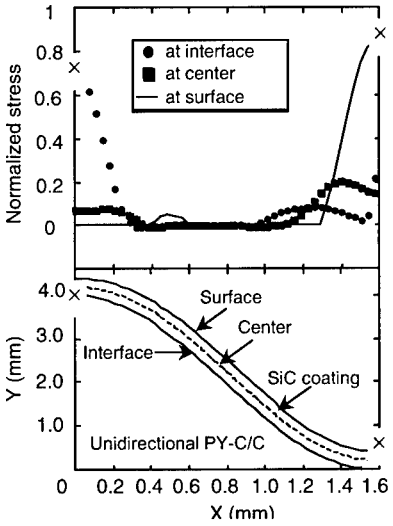

Fig.5 Normalized maximal principle stress in a sinusoidal SiC coating.

Note that if we do not assume the anisotropic substrate, i.e., isotropic substrate, then we got higher stress in the coating. This anisotropic effect is a difference from Shioya's analysis. **Fig.6** shows the cross-sectional view of a sinusoidal SiC coating applied on a QI-C/C substrate. Coating cracks were successfully suppressed by use of the sinusoidal configuration. Thus the remaining problem is the optimization of sinusoidal configuration to make the wave flatter and how to utilize this concept to the 3D-configuration.

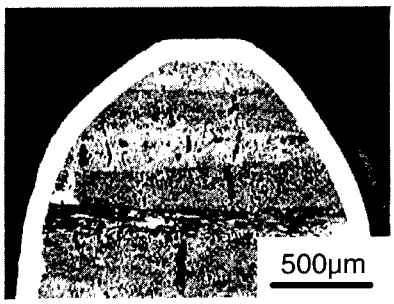

Fig.6 Cross-sectional view of a sinusoidal SiC coating.

References

1. H. Hatta, T. Aoki, Y. Kogo, and T. Yarii: Composites, Part A, 30, 515 (1999).
2. L. Beuth: Int. J. Solids Structures, 29(13), 1657 (1992).
3. T. Shioya, K. Uenishi: *Proc. of theYokohama Int. Gas Turbine Congress*, Yokohama, III, 93(1995).

Proceedings of 7th Japan International SAMPE
Symposium & Exhibition, Nov. 13-16, 2001

Effect of Interfacial Morphology Formed by Conversion Pretreatment of CVD-SiC Coating on C/C Composites

Daisuke Maruyama #1, Hiroshi Hatta #2 and Yasuo Kogo #3

#1 : Graduate Student, Science University of Tokyo
#2 : Research Division of Space Propulsion, The Institute of Space and Astronautical Science, 3-1-1 Yoshinodai, Sagamihara 229-8510, JAPAN
#3 : Department of Material Science and Technology, Science University of Tokyo, 2641 Yamazaki, Noda 278-8510, JAPAN
Mail: maru@pub.isas.ac.jp

ABSTRACT

Silicon-carbide-coating on carbon/carbon matrix composites (C/Cs) were generally formed by a CVD method with the conversion treatment along the coating interface to improve bonding strength between coating and C/C composite. To clearify the mechanisms for the bonding improvement, the interfacial shear strength of SiC-coated C/C composites with various conversion time was measured by a plunger method and the surfaces and cross-sections were observed by SEM and EPMA. These results gave clear micro-image during formation of the conversion layer and the strengthening mechanism of the bonding by the conversion treatment.

KEY WORDS:
C/C Composite, SiC Coating, Conversion Treatment, Bonding Strength

INTRODUDTION

C/C composites are unique materials which posses exceptional high heat resistance along with light weight, high stiffness and high strength [1,2]. However, C/C composites are known to possess a serious shortcoming, i.e., easily oxidized to evaporate above temperatures of about 773K [3,4]. To overcome the oxidation problem, ceramic coatings have been applied on the surfaces of C/C composites and SiC is regarded as most promising material for the oxidation protection coating. However, thermal mismatch strain between C/C and SiC coating often leads to coating debonding. For producing strong bonding, the interphase layer by direct chemical reaction of the gaseous silicon with carbon in the substrate is often formed before forming CVD-SiC coating. It has been reported that the bonding strength between coating and substrate increases by the conversion treatment, although the strengthening mechanism has not clarified. In this study, the bonding strength of

SiC-coating is measured by a plunger method for the coating changing conversion treatment time. In addition, micro-structure of the conversion layers is observed with SEM and EPMA so as to identify strengthening mechanisms.

EXPERIMENTAL PROCEDURE

1. C/C composite

The C/C composite used for the substrates was fabricated by the preformed yarn process and supplied by Across co. Ltd. This C/C was unidirectionally reinforced with Torayca M40 and had a total fiber volume fraction of 50%.

2. Conv.-treatment and SiC coating

The SiC coating was produced with a hot-wall type CVD reactor. The SiC coating was composed of two layers; a thin SiC conversion layer (sub μm) and a thick CVD coating layer. The conversion layer was formed by direct chemical reaction of the gaseous $SiCl_4$ with carbon in the substrate by the reaction,

$$Si + C \rightarrow SiC.$$

The CVD-layer was formed from a $SiCl_4$ /C_3H_8 /H_2 system. Both of the Conversion and CVD layers were formed under the conditions of deposition temperature, 1473K, and total pressure, 1.3 kPa.

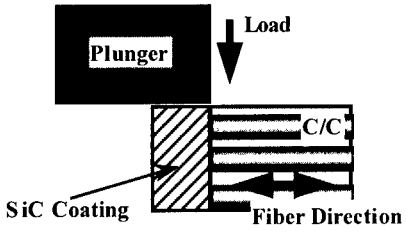

Fig.1 Schematic drawing of plunger method for the measurement of interfacial bonding strength.

3. Shear tests by plunger method

The interfacial fracture between a SiC coating and the C/C composite was induced by a test fixture shown in **Fig.1**. The bonding strength was evaluated by the average shear stress, an interfacial fracture load divided by interfacial fracture area.

RESULTS AND DISCUSSION

1. Bonding strength

The interfacial shear fracture stresses of the SiC coating by plunger method are plotted as a function of conversion treatment time in **Fig.2**. As shown in this figure, the bonding strength of the SiC coating increased linearly with the conversion treatment time.

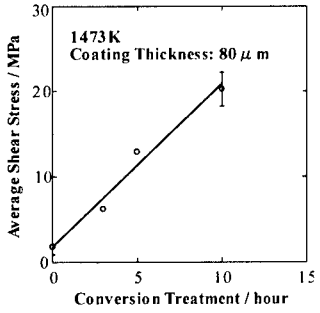

Fig.2 Relation between bonding strength and conversion time.

2. Observations of conversion layer

Figures 3 and **4** show surfaces of a bare C/C (non coated) and a C/C substrate with conversion treatment for 13 h. It can be seen in **Fig.4** that SiC formed by conversion treatment is at first formed in the matrix region. This behavior might be due to low graphitization and thus high reactivity of the matrix region. **Figure 4** also shows that thin SiC film by the present conversion treatment was formed only near the

surface of the substrate and defects, and little amount of SiC was produced at the inside of the substrate. From this observation, it is concluded that the SiC formation is ruled by diffusion of inner carbon. The SiC formation in pore surfaces in the C/C substrate gradually proceeded into deep places, as shown in **Fig.5** and **6**. At the converted places, the growth rate of CVD-SiC had higher growth rate than non-converted inner surfaces. Therefore, the whole pore are easily filled with CVD-SiC after long conversion treatment, and these filled portion of SiC might act as anchors against delamination of SiC coating.

3. Observations of C/C substrate after plunger tests

Figures 7 and **8** show fractured surfaces by plunger tests for C/C substrates with conversion treatment for 3h and 10h, respectively. As shown in **Fig.7**, SiC coating with 3h of conversion time debonded at interface between coating and substrate. On the other hand, 10h-treated SiC coating partly fractured in the C/C substrate as shown in **Fig.8**. **Figure 9** shows the cross section of C/C substrate with 10h conversion treatment after plunger test. In this figure, it was observed that SiC coating didn't debond perfectly but coating is partly bonded on the substrate even after the plunger test. As mentioned above, by giving long conversion treatment, CVD-SiC is filled in C/C substrate. These penetrated parts operate as the anchors against cracks propagating along interface between coating and substrate when shear load applied on the interface. Thus, this anchor effect is concluded to be the principal factor of increasing bonding strength by the conversion treatment.

CONCLUSIONS

(1) The formation of conversion SiC layer starts from near surface matrix region.
(2) The conversion SiC layer is formed by diffusion of carbon from inner substrate.
(3) When conversion treatment time is short, CVD-SiC isn't filled in substrate pores. As this result, cracks propagates along interface between coating and substrate. When conversion treatment time becomes long, CVD-SiC is easily filled in substrate defects, this penetrated SiC operates as anchors and the strengthen the interfacial bonding.

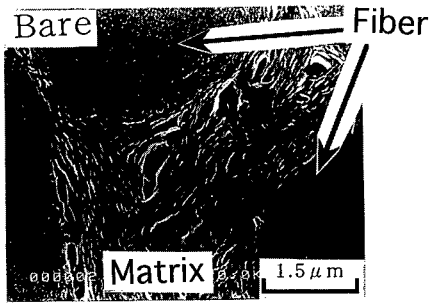

Fig.3 A typical surface of bare C/C.

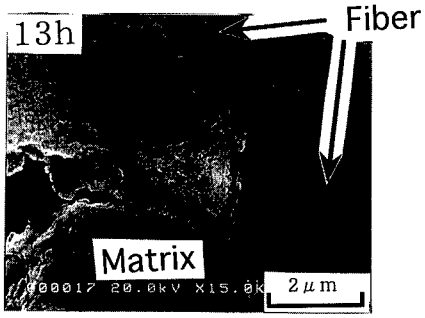

Fig.4 A surface of C/C after 13h conversion treatment.

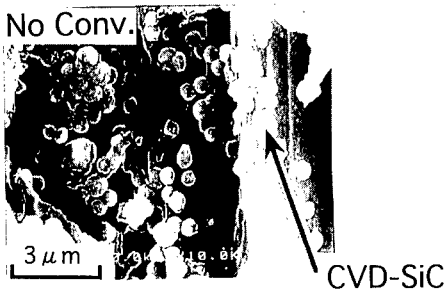

Fig.5 A near surface cross section of C/C without conversion treatment after plunger test.

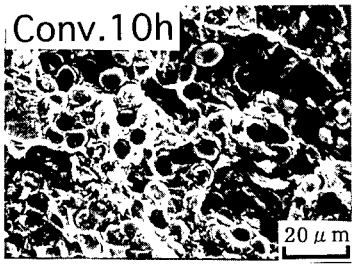

Fig.8 A fracture surface of C/C with 10h conversion treatment after plunger test.

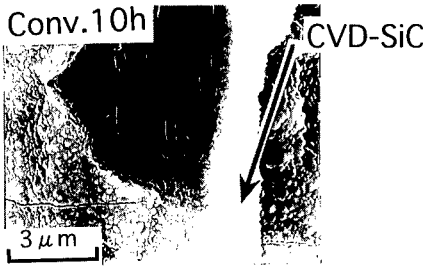

Fig.6 A near surface cross section of C/C with 10h conversion treatment after plunger test.

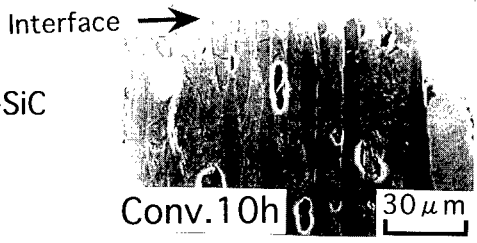

Fig.9 A near surface cross section of C/C with 10h conversion treatment after plunger test.

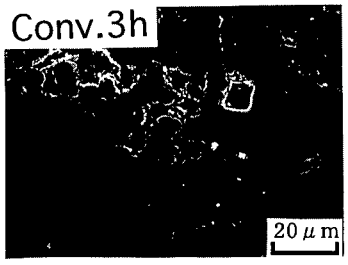

Fig.7 A fracture surface of C/C with 3h conversion treatment after plunger test.

REFERENCES

[1] G. Savage, "Carbon-Carbon Composites" Chapman and Hall, 1993.

[2] C.R. Thomas, "Essentials of Carbon-Carbon Composites," Roy.Soc.Chem.,1993.

[3] J.E. Sheehan, "Carbon-Carbon Materials and Composites", "NASA RefPub.", 1992.

[4] J.R. Strife and J.E. Sheehan, "Ceramic Coating for Carbon-Carbon Composites", "Am. Ceram. Soc. Bul., 67[2], 369-374 (1988).

Proceedings of 7th Japan International SAMPE
Symposium & Exhibition, Nov. 13-16, 2001

Fatigue Behavior of C/C Composite Impregnated with Si

H.N.Ko[1], S.Hanzawa[2] and K.Nakano[2]

1: Nakanihon Automotive College
Sakahogi-cho, Kamo-gun, Gifu-ken 505-0077, JAPAN
E-mail: ko@nakanihon.ac.jp
2: NGK INSULATORS, LTD.
Suda-cho, Mizuho-ku, Nagoya-city, 467-8530, JAPAN
E-mail: hanzawa@ngk.co.jp, nakano@ngk.co.jp

Abstract

Rotary bending and static fatigue tests were performed on the new composite smooth specimens at room temperature. The material used was a carbon fiber reinforced carbon composite impregnated with Si, developed by NGK INSULATORS, LTD. Two kinds of materials with different carbon fibers were studied to examine the impregnation effect on the fatigue strength. The assumed fatigue limit under rotary bending was much lower than the static bending strength. The static fatigue strength was also lower than the static bending strength. Regardless of carbon fibers, the strength was decreased by Si impregnation. It was considered that the damage or fracture mechanism was changed by the generated SiC.

Key Words: Cyclic fatigue, Static fatigue, C/C composite, C/C composite impregnated with Si

Introduction

The new composite, which was a carbon fiber reinforced carbon (C/C) composite impregnated with Si, was developed by NGK. This material has the characteristics such as oxidation and wear resistance, compared with C/C composites [1]. The applications of this material, as well as C/C composites, require at least a degree of strength and stiffness [2]. The fatigue strength must be studied on the present materials to make their reliability higher as structural materials, since the fatigue strength is generally lower than the static strength. However, the basic data on the fatigue behavior of the present material (Si-C/C), as well as C/C composites, are still not sufficient to clarify the fracture mechanism. As for the aspect, the fatigue behavior of Si-C/C smooth specimen was examined at room temperature under rotary bending and static fatigue, as the same manner in the study [3] on ceramics. Two kinds of materials with different carbon fibers were studied to examine the impregnation effect on the fatigue strength. The strength characteristics were also compared with those of C/C composites having no Si impregnation. Based on the results obtained, the difference of the fatigue strength characteristics in Si-C/C and C/C composites were discussed.

Experimental Procedure

The material used was a C/C composite impregnated with Si, obtained from NGK (Japan). Si impregnation was performed on a C/C composite at 1873 K under decompression; the C/C composite was made using pre-formed yarn method, developed by across co. LTD. Two kinds of laminate plates with different carbon fibers (T300 and T700 by Toray Industries, Inc.) were made; the tensile strength was higher for T700 than for T300. In the

present study, the materials are called as Si-T300C/C and Si-T700C/C; the materials without Si impregnation are called as T300C/C and T700C/C. The microstructure is composed of carbon fiber, carbon, silicon and silicon carbide.

The specimen had a cylindrical shape, as shown in Fig.1. The diameter of the middle part was 10 mm and each end of the specimen had a larger diameter of 12 mm for chucking. The specimen was ground perpendicularly to its axis to make the finished surface smooth. The machine used was an Ono's rotary bending fatigue testing machine (147Nm) operating at 3420 cycles per minute. The loading type of the machine was four-point bending, and the stress state of the specimen was reversed bending. The static and static fatigue tests were performed using the non-rotating fatigue machine; in these tests the orientation of the fibers at the specimen surface was taken parallel to the loading axis, since the specimen is an anisotropic body. Fracture features and acoustic emission (AE) characteristics were also examined.

Results and Discussion

Cyclic and Static Fatigue Behavior

Rotary bending test was carried out mainly within the range 10^4 to 10^8 stress-cycles. Some specimens were tested at cyclic number more than 10^8 to examine the existence of a knee; 10^8 stress-cycles is equivalent to about 20 days under the present test condition. Test points of two present materials, represented by open or solid symbols, are shown in Fig.2; the arrowed points indicate those stopped testing. The fatigue life increases as the stress amplitude decreases, and the fatigue limit seems to be about 20 MPa for Si-T300C/C. A similar S-N relationship was obtained on Si-T700C/C, and the fatigue limit seemed to be about 50 MPa. As some specimens are fractured at more than 10^7 stress-cycles, the existence of a knee must be studied in future.

The static bending strength, obtained by the non-rotating fatigue machine, is shown at N=1 for each material. The

Fig.1 Specimen.

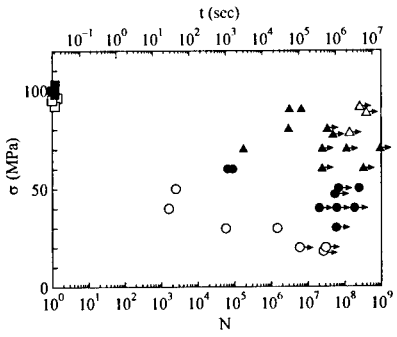

Fig.2 Test results for two kinds of present materials under (○, ●) rotary bending, (△, ▲) static fatigue and (□, ■) static test; open and close symbols indicate the data for Si-T300C/C and Si-T700C/C, respectively.

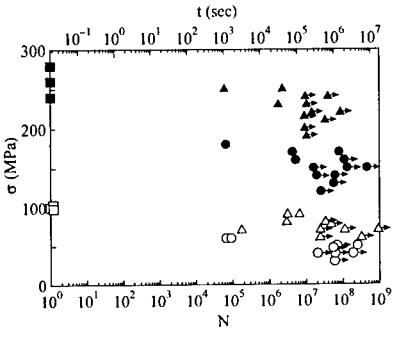

Fig.3 Test results for Si-T700C/C and T700C/C under (○, ●) rotary bending, (△, ▲) static fatigue and (□, ■) static test.

values were about 90 and 100 MPa, respectively. The strength was clearly different in C/C composites with different carbon fibers. In Si-C/C composites, however, the strength difference became smaller. Test points under static fatigue were also plotted on the graph. As can be

seen in the figure, the static fatigue behavior exists in Si-T700C/C. The static fatigue limit seems to be about 70 MPa, and this value is higher than the fatigue limit. In Si-T300C/C, the scatter was relatively large, but the static fatigue behavior was confirmed, increasing and holding the constant applied stress.

The results for Si-impregnated material were compared with those for C/C composite. As shown in Fig.3, the strength becomes smaller by Si impregnation. C/C composite has the similar fatigue behavior, although the static fatigue strength means that a specimen does not maintain its deformation condition. In static and static fatigue tests, the fracture means the separation of a specimen for Si-C/C, but not for C/C, since the fracture features are different in two materials, as described later.

AE under Four-Point Bending

AE event count was examined using rectangular specimens with 3 mm thick and 4 mm wide under four-point bending test whose crosshead speed was 0.5 mm/min to know the degree of damage under the fracture process. As shown in Fig.4, AE event count, indicating the initiation of damage or its progress, increases with increasing stress. Although the location of the damaged zone could not be detected, AE event occurred at very low stress for Si-C/C compared with C/C; Si impregnation may induce a defect or a crack.

AE event count was examined under the constant stress lower than the ultimate flexural strength to know the damage process under static fatigue. The result, obtained under the constant stress whose magnitude is 90 % of the ultimate flexural strength, is shown in Fig.5. The rapid increase in the number of AE event occurs when applying the stress, and AE event occurs although its number decreases as the time proceeds. The cracks between yarns are observed, and thus the progressive damage is believed due to the crack growth. On the other hand, in C/C composites, the damage such as delamination between plies progresses, leading to the reduction of Young modulus, and thus the deformation

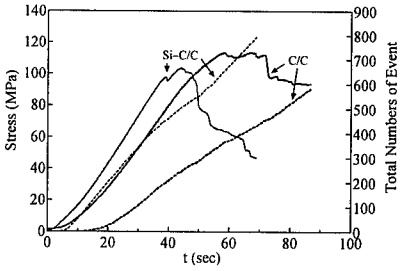

Fig.4 AE event count for Si-T700C/C and T700C/C rectangular specimens under four-point bending.

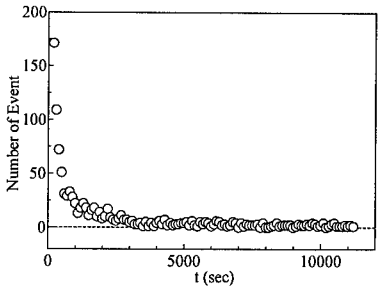

Fig.5 AE event count for Si-T300C/C rectangular specimen under static fatigue (σ =65 MPa).

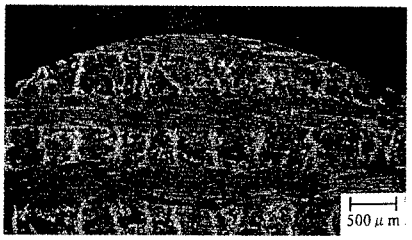

Fig.6 Fracture surface after rotary bending test (σ = 30 MPa, N=1.47X10^6).

condition may not be maintained.

Fracture Features

A typical macrophotograph of a fracture surface under rotary bending is shown in Fig.6. The fracture origin could not be detected even by minute observations. The fracture occurred perpendicularly to the specimen axis, like ceramics, as shown in

Fig.7(a). The shape of a fracture C/C specimen, however, showed the stepwise failure, as shown in Fig.7(b). This is believed due to the difference in the interfacial strength of plies/plies. In the case of the laminated composites used in the present study, it seems that plies/plies or yarns/yarns interfacial strength characteristics are important [4]. The interlaminer test results, performed on a double notched specimen, showed that the strength was higher for Si-C/C than for C/C; the measured values were 12 MPa for Si-T300C/C and 4 MPa for T300C/C, respectively.

The relationship between stress and strain was examined at specimen surfaces subjected to the maximum tensile and compressive stresses. The results, obtained by the non-rotating fatigue machine on Si-C/C and C/C, are shown in Fig.8. In C/C specimens, the buckling of fibers or the delamination between plies was observed at compressive side; the delamination was seen near the stress of 170 MPa in the figure. The fatigue limit of a C/C specimen is believed to be related to the damage generated at compressive side. In Si-C/C, however, the fracture seemed to initiate from the tensile side. The fatigue fracture mechanism is believed to be different in Si-C/C and C/C specimens due to the role of generated SiC; the fiber/matrix interface characteristics, as well as the above interfacial ones, must be studied for further explanation on fracture mechanism.

Conclusions

Rotary bending and static fatigue tests were carried out on C/C composite impregnated with Si at room temperature. Two kinds of materials with different carbon fibers were studied to examine the impregnation effect on the fatigue strength. The assumed fatigue limit under rotary bending was much lower than the static strength. The damage occurred under static fatigue, and the assumed static fatigue limit was also lower than the static strength. The strength was decreased by Si impregnation, and the strength difference

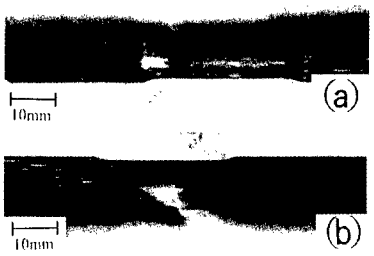

Fig.7 Fracture specimens after rotary bending test for (a) Si-C/C and (b) C/C.

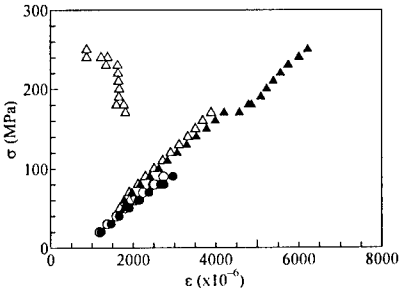

Fig.8 Relationship between stress and strain at specimen surface for (○, ●) Si-T700C/C and (△, ▲) T700C/C; open and close symbols indicate the values of compression and tension, respectively.

due to the carbon fibers became smaller in Si-impregnated materials. The results, such as fracture features, AE characteristics and the relationship of stress against strain, indicated that the damage or fracture mechanism was changed by Si impregnation. This was believed due to the role of generated SiC.

References

1. S. Hanzawa and K. Nakano: Ceramics Japan, 34, 474 (1999).
2. G. Savage: Carbon-carbon composites, Chapman & Hall, 1993, p.246.
3. H. N. KO: Fracture Mechanics of Ceramics, Vol.12, Plenum Press, New York, 1996, pp.15-29.
4. C. Tallaron, D. Rouby, P. Reynaud and G. Fantozzi: Key Engineering Materials, 164-165, 329 (1999).

Proceedings of 7th Japan International SAMPE
Symposium & Exhibition, Nov. 13-16, 2001

The Role of Three Dimensional Reinforcement on Fracture Behavior of Carbon-Carbon Composites

Mohamed S. ALY-HASSAN*, Hiroshi HATTA**, Shuichi WAKAYAMA*, Emi MIYAZAKI***,
Ken GOTO** and Kiyoshi MIYAGAWA****

* Tokyo Metropolitan University, Department of Mechanical Engineering,
1-1 Minami-Ohsawa, Hachioji-shi, Tokyo, 192-0397 Japan
**The Institute of Space and Astronautical Science, 3-1-1 Yoshinadai, Sagamihara, Kanagawa 229-8510, Japan
*** Kogakuin University, Tokyo, Japan & ****IHI Aerospace Co. Ltd., Japan
E-mail: aly-has@pub.isas.ac.jp

Abstract

Fracture behavior of 2D and 3D carbon/carbon composites, 2D-C/Cs and 3D-C/Cs, was experimentally compared by the compact tension method. The 3D-C/Cs were shown to possess far higher fracture resistance than the 2D-C/Cs. This high fracture resistance of the 3D-C/Cs was explained in terms of extremely low shear resistance and high shear deformation. The former low shear resistance is shown that to be derived from many interfacial cracks between fiber bundles and pure matrix. These cracks appear due to 3D mechanical constraints by the 3D reinforcement. The latter behavior is induced by the entangled three-dimensional reinforcement structure.

Key Words: 2D and 3D C/Cs, Fracture Resistance, Compact Tension Test.

Introduction

Carbon fiber reinforced carbon matrix composites, C/Cs, maintain their high strength over 2000o C. C/Cs are highly expected in high temperature applications especially in aerospace and nuclear energy industries [1-3]. However, when C/Cs are actually used, we must solve various problems due to serious shortcomings that C/Cs are holding. Well-known shortcomings are the weakness against oxidation and low inter-laminar strength. To overcome the latter lack, 3D-C/Cs have been introduced.

However, many properties of the 3D-C/Cs have not been sufficiently examined, probably due to the extremely high cost. However, few papers mentioned about 3D-C/Cs and most of studies directed to 2D-C/Cs [3-9]. Hence, there is no clear image about the effect of three-dimensional reinforcement on various mechanical properties. In this paper comparison was made for the fracture behavior of 3D-C/C and 2D-C/C. Using compact tension test, fracture behaviors of both materials are clarified. Then, the obtained difference in fracture pattern between 3D-C/C and 2D-C/C is explained in terms of microstructures and basic mechanical responses in tension, compression and shear.

Materials

The 2D-C/Cs, produced via preform yarn method by Across Co., had 0/90 lamination and fiber volume fraction of 50%. The reinforcing fiber of this C/C was Torayca M40 supplied by Toray Co. Two kinds of 3D-C/Cs with different void contents were used, produced by IHI Aerospace Co. These C/Cs were reinforced with pitch-based fibers and had a fiber volume fraction of 36 % (12% each direction). The source materials of these were unidirectionally reinforced CFRP rods, which were arranged into a preform reinforced in orthogonal directions. Then the preform was HIP-treated over 500 atm., where impregnation material was coal tar pitch, followed by heat treatment over 2000 ^{0}C. These HIP cycles were repeated several times to yield C/C with 1.9 and 2.0 g/cm^3. In this paper, the abbreviation LD and HD are used to indicate low density and high density of 3D-C/C respectively.

Experimental Procedures

Micro-Structure

Voids distribution and cracks were observed using an optical microscope prior to mechanical tests. Later SEM was used to scan the damage of fracture surfaces that produced by mechanical tests.

Characterization of Mechanical Properties

To characterize the materials, stress-strain relations under tensile, compressive and shear loading were obtained. The Iosipescu method was adopted to determine the shear responses. At least one test for each material was repeated loading and unloading to measure residual shear strain as a function of applied load. The compressive tests were performed according to JIS for carbon materials. Screw-driven mechanical testing machine, Autograph AG-5000A, was used for all the mechanical tests under cross head speed 0.05 mm/min.

Compact Tension Tests

Compact tension, CT, tests were performed to compare fracture behavior of the materials. The pre-crack was introduced by diamond wheel with a thickness of 0.4 mm, then by a sharp blade until 0.1 mm. During the CT test, the crack growth length was measured using a travelling microscope with a magnification of 25 times. To easily determine the crack propagation, surfaces of the specimens were diamond polished with 15 □m disk and thinly painted white. Crack opening displacement, COD, was monitored at the crack edge by a clip gauge. Loading-unloading cycle tests were performed by mentioned above testing machine under cross head speed of 0.1mm/min. Energy release rates were determined from measured load-COD relation and following equation;

$$G = \frac{P^2}{2B}\frac{dc}{da} \qquad (1)$$

where P, B, c, and a are load, thickness of the specimen, compliance measured at the loading point, and crack extension length, respectively.

Results

Mechanical Properties

1- Micro-Structures

Although many transverse cracks and micro-voids can be seen in 2D-C/C, the interlaminar crack is hardly observed. On the other hand in the 3D- LD, large scale debonding is observed along the interfaces between fiber bundles and pure matrices and large scale near-closed-voids are been in matrix pockets formed between fiber bundles running three dimensionally. In 3D-HD, the matrix pockets almost filled with matrix carbon. See Fig. 1.

2- Tensile and Compressive Properties

The comparison of tensile and compressive responses of 2D- and 3D-C/Cs are shown in Figs. 2 and 3 respectively. It can be seen in these figures that the tensile S-S curves of all the test materials exhibited linear relation. On the other hand compressive curves showed strong non-linearity. The tensile strength of 3D-LD was slightly higher than 3D-HD but the compressive strength showed opposite tendency. The tendency of the tensile strength is due to higher interfacial strength of 3D-LD than that of 3D-HD and compressive strength feature was probably derived from internal deficits.

3- Shear properties

Shear S-S curves for all the test materials are compared in Fig.4. It follows from this figure that 2D-C/C has relatively high strength with low ultimate strain. On the other hand, 3D-C/Cs have low maximum stress and very large fracture strain about 7 %. It should be noted that the S-S curves for both 3D C/Cs almost coincided.

The repetition of shear loading and unloading yielded residual strain. The residual shear strains of 2D- and 3D-C/Cs are compared in Fig.5 as a function of the maximum stress during each lording and unloading cycle. The residual strain was small in 2D-C/C, but was large from the first cycle and increased rapidly in 3D-C/C. This result clearly shows that the shear deformation in 3D-C/C proceeded inducing defects and might due to the large-scale interfacial cracks induced in the processing stage.

CT Tests

Typical load and crack opening displacement, P-COD, relations of 2D-C/C and 3D-C/C obtained by compact tension tests. During the measurement of 3D-LD, COD became huge amount and a clip gage out-ranged. Thus after that only COD was determined at the maximum and minimum load of each cycle. The difference of fracture behavior is observed not only between 2D-C/C and 3D-C/Cs but also between 3D-C/Cs. In the CT specimens three modes of deformation, tension, compression and shear, appear. As mentioned above, the shear S-S curve for both 3D-C/Cs is almost the same and both the tensile S-S curves are linear. Hence the discrepancy between the 3D-C/Cs should be derived from that of compressive S-S curve. Actually, non-linear stress analysis during CT tests revealed that regions with compressive failure spread to large area in 3D-LD but not large in 3D-HD. This results is based on the fact that compressive strength of 3D-LD is much lower than 3D-HD.

Compliance was determined from the linear region of reloading curve then using Eq. (1) energy release rate during stable crack growth, G, was calculated as a function of crack extension length, da. Regarding to 3D-LD, determination of G was given up due to the compressive failure. It can be seen from the comparison of Gs that G for 3D-C/C is 3 orders of magnitude higher than that for 2D-C/C.

From Eq. (1) parameters directly affects G are P and dc/da. Fig.5 shows the relation between maximum load in a cycle, P, and Δa. Although 2D-C/C attained peak P at 1000N, 3D-HD maintained monotonic increase in P. Thus the characteristics of the curves are different but this difference can not explain the 3 order discrepancy of G. On the other hand, dc/da-Δa relation yielded sufficient difference. Thus, the main reason for the large difference in G is large deformation of 3D-C/C.

Discussions

High Toughness Mechanisms of 3D-C/C

Main factor for high toughness behavior of 3D-C/Cs compared with 2D-C/C is easy deformation of 3D-C/Cs. This large deformation is induced mainly by shear deformation. Residual CODs during CT tests and residual shear strain for 2D-C/C and 3D-HD were observed as a function of P. In these relations both residual deformations show similar trend and this tendency supports the statement that the large deformation during CT test was induced mainly by shear. As we discussed earlier, easy shear deformation of 3D-C/C is due to many large-scale interfacial cracks. On the other hand, it was already shown that thermal residual stresses in 3-dimensional composites are much higher than that in 2-dimensional composites. It is due to 3 dimensional constraint [10]. This high value of thermal residual stress induces the interfacial cracks, which induce easy shear deformation. In addition 3- dimensionally entangled reinforcement prevent early ultimate fracture to yield high deformation capability. Therefore we can conclude that 3D-C/Cs have easy shear deformation capability and exhibit high toughness behavior.

Fracture Mechanics Approach

In the above discussion, we simply applied fracture mechanics procedure for the materials include large nonlinear deformation. It may be questionable to use fracture mechanics procedure, in particular, for 3D-C/Cs with large residual COD. It is clear by nonlinear FEM analysis that shear residual strain appears in 3D-C/C even at the free boundary of the CT specimen. This suggests that if we enlarge specimen size, obtained toughness value should be larger than present ones. Thus the presented G especially for 3D-C/C might be specimen geometry dependent. Thus, we must consider appropriate measure for this kind of materials.

Furthermore, FEM calculation revealed that observed crack extension length did not coincide with calculated one. We might observe matrix or interfacial cracking. Thus, crack length with fiber fracture might be much smaller. The data in this paper include such kind of contradictions. Nevertheless, we followed the fracture mechanics approach. Because it is meaningful to show difference of fracture behavior between 2D- and 3D-C/Cs and there is no precise approach to the authors` knowledge to show the difference.

Conclusion

The following conclusions were obtained through comparison of fracture behavior of 2D and 3D-C/Cs based on the previous results.

1) Fracture resistance of 3D-C/Cs was about 3 orders higher than that of 2D-C/C.

2) Tri-axially reinforced 3D-C/Cs have extremely low shear resistance and high shear deformation capability.

3) High fracture toughness of 3D-C/Cs is attributed to the deformation characteristic.

References

1- C.R. Thomas "*Essentials of Carbon-Carbon Composites*" The Royal Soc. of Chem. (1993).
2- E. Fitzer, "*Carbon Reinforcements and Carbon/Carbon Composites*" Springer (1998).
3- A.G. Evans: J. Mater. Sci., 29, 3857 (1994).
4- T.J. Mackin, T.E. Purcell, M.Y. He, and A.G. Evans: J. Am. Ceram. Soc., 78(7), 1719 (1995).
5- H. Hatta, Y. Kogo, H. Asano, and H. Kawada: JSME Int. J., Series A, 42(2), 265(1999).
6-Y. Kogo, H. Hatta, H. Kawada, and T. Machida: J. Comp. Mater., 32(13), 1273 (1998).
7- P. Brondsted, F.E. Heredia, and A.G. Evans: J. Am. Ceram. Soc., 77(10), 2569 (1994).
8- M.S. Aly-Hassan, H. Hatta, S. Wakayama, T. Watanabe, and K. Goto: Proc. of 43rd of JSASS/JSME Structures Conference, 161(2001).
9- M.S. Aly-Hassan, H. Hatta, S. Wakayama, and K. Goto: Proc. of 16th Symposium of Space Materials and Structures,ISAS, 76(2000).
10- IHI: Reference Publication, (2001).

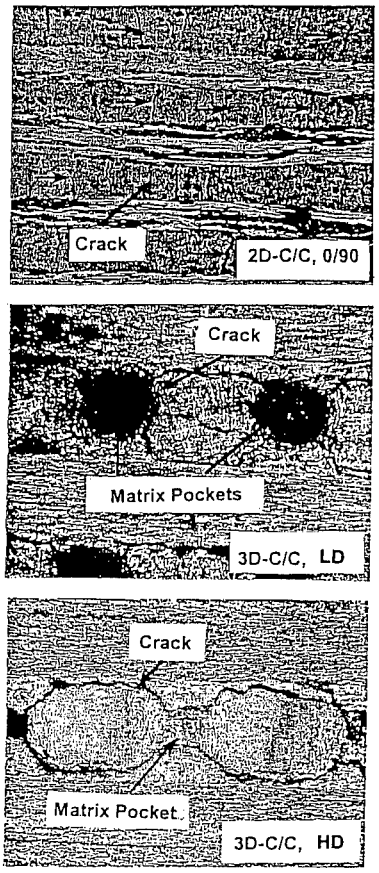

Fig. 1 Micro-Structures

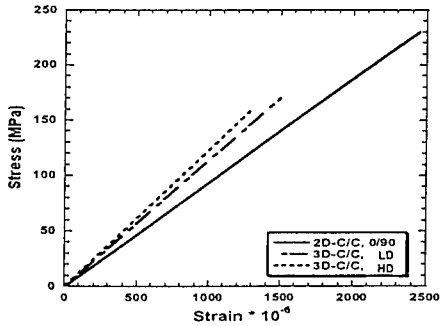

Fig. 2 Tensile Stress-Strain Curves

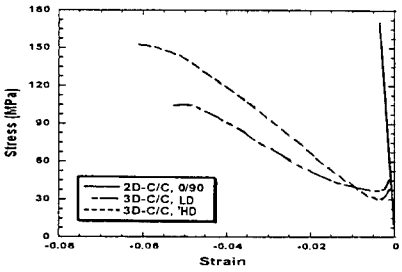

Fig. 3 Compression Stress-Strain Curves

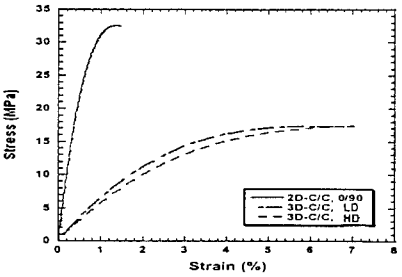

Fig. 3 Shear Stress-Strain Curves

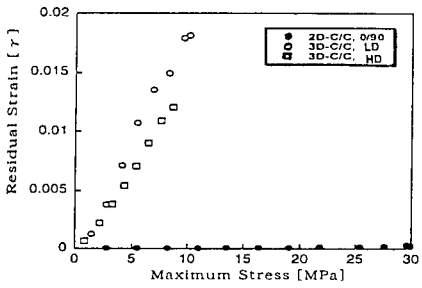

Fig. 4 Residual Strain vs. Maximum Stress

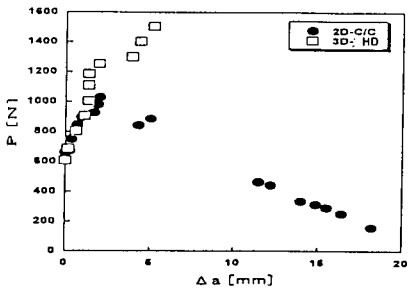

Fig. 5 Maximum Load vs. Δa

Proceedings of 7th Japan International SAMPE
Symposium & Exhibition, Nov. 13-16, 2001

Thermal Shock Damage in Carbon-Carbon Composites

Yasuo Kogo[1], Kastutoshi Nakazaki[2], Takumi Katagiri[2], and Hiroshi Hatta[3]

1: Department of Materials Science and Technology, Science University of Tokyo
2641 Yamazaki, Noda, Chiba 278-8510, JAPAN
E-mail: kogo@rs.noda.sut.ac.jp

2: Graduate Student, Science University of Tokyo

3: Research Division of Space Propulsion
The Institute of Space and Astronautical Science
3-1-1 Yamazaki, Sagamihara, Kanagawa 229-8510, JAPAN

Abstract

Thermal shock behavior of unidirectional and cross-ply carbon-carbon (C/C) composites was experimentally examined. Water quench tests were carried out with various temperature differences (ΔT) up to 1000K. Results showed that catastrophic failure, usually observed in monolithic ceramics did not occur in C/C composites even at ΔT of 1000K, but microscopic damage, which was delamination between fiber/matrix interfaces and/or matrix fracture, was observed near the specimen surface. Numerical analysis revealed that the maximum stress induced in the composite was much higher than the transverse tensile strength of the UD C/C composites. This implies that stress relaxation mechanism occurred in the C/C composites.

Key Words: Carbon-carbon composites, Thermal shock, Water Quench Test

Introduction

Carbon-carbon (C/C) composites are attractive for use in thermostructural applications because of their high temperature mechanical properties and lightweight. For example, the interest of aerospace industries in the composites as turbine systems, rocket propulsion components, and heat shields of reentry vehicles has rapidly increased [1].

In actual operation conditions, the materials will be subjected to severe thermal transients, which will induce considerable thermal stresses. Because of this, knowledge of thermal shock resistance is indispensable for structural design of hot structures. However, thermal shock behavior of composites is generally complicated compared with monolithic ceramics [2-4], and is not fully understood yet. In this study, water quench tests were carried out on the unidirectional and cross-ply laminated C/C composites to investigate damages induced by the thermal shock.

Experimental Procedure

Materials investigated in this study were unidirectional (UD) and Cross-ply laminated (CP) C/C composites. They were reinforced with high modulus type of carbon fibers (Toray M40) with a total volume

fraction of 50% (nominal). They were fabricated by the preformed yarn method [5], in which the hot pressing temperature of 873K and the heat treatment temperature of 2273K (Across co. ltd., Japan).

The C/C composite plates were machined into rectangular bars, and one end of the specimens was sharpened as shown in Fig.1. The sharp tip is necessary to avoid formation of thick air layers on the specimen surface when the specimen enters into water. As already reported [6,7], heat transfer at specimen surface is increased by making a sharp end due to a change in a boiling condition on the surface. This results in a more severe thermal shock condition compared with that without the sharp end.

In the thermal shock tests, the specimen was heated in an inert atmosphere and kept for 15 min. at a given temperature difference (a maximum of 1000K). Then, the specimen was made to fall freely and stopped in the water bath. Both falling height and falling depth from the water surface were set to 600 mm following the Japanese standard for the thermal shock test of ceramics (JIS-R1615). In order to investigate macro- and microscopic damage induced in the composites, cross sections of the specimens were observed by SEM.

To understand effect of the thermal shock on mechanical properties, Young's modulus was measured before and after the quench by four-point flexure tests with a sufficiently low stress level (about 1/20 of fracture stress). Inner and outer spans were set to 27 and 81mm. After the quench, fracture stress was also obtained. For the fracture test of the UD C/C composites, transversely reinforced specimens were tested in tension, because effect of the damage was expected to be easy to detect compared with a longitudinal specimen.

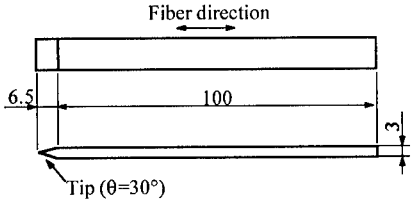

Fig.1 Geometry of specimen

Results and Discussion

Damage observation

In all the thermal shock tests, no macroscopic damage was observed for both UD and CP C/C composite specimens. This means C/C composites possess superior thermal shock resistance compared with monolithic ceramics. Figure 2 shows cross-sectional views of UD C/C composites before and after the quench at ΔT of 1000K. Compared with the specimen before the quench, fracture of matrix and/or delamination at fiber/matrix interface was observed near the surface of the quenched specimen. They were clearly observed in the magnified view (Fig.3). The same type of micro-damage was observed in all the UD and the CP specimen at all ΔT. Although the area of the micro-damage could not be

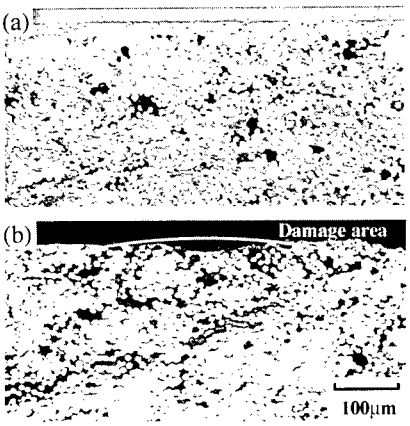

Fig.2 Cross-sectional view of UD C/C composites (a) before, and (b) after thermal shock

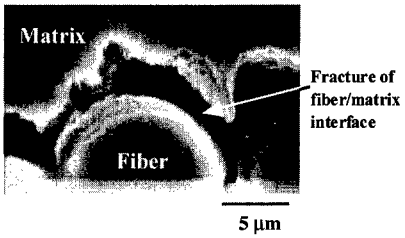

Fig.3 Magnified view of micro-damage in UD C/C composites

obtained quantitatively due to the diffculity in determination of boundaries, the area tended to increase with increasing ΔT.

Mechanical Properties

Figure 4 (a) shows change in the longitudinal Young's modulus (E) and the transverse tensile strength (σ_f) of the UD C/C composites. Young's modulus kept its original value even after the thermal shock test up to ΔT of 1000K. Furthermore, as shown in Fig.4 (b), Young's modulus was not degraded even after the cyclic thermal shock test at ΔT of 1000K. It is reasonable to think that the fibers in the composite were intact even after the thermal shock, though the micro-damage was introduced in the matrix and/or the interface. Similarly, the transverse tensile strength (σ_f) was unaffected by the thermal shock as shown in Fig.4 (a), although σ_f must be controlled by the strength of the matrix and/or the interface. One possible reason is that the critical flaw controlling σ_f was larger than the damage introduced by the thermal shock. It was reported that the as-received UD C/C composites contains cracks with maximum size of about 0.4 mm [8]. Since the damage introduced by the thermal shock was much smaller than 0.4 mm, σ_f was expected to be unaffected by the thermal shock.

As in the case of UD C/C composites, the CP C/C composites showed no

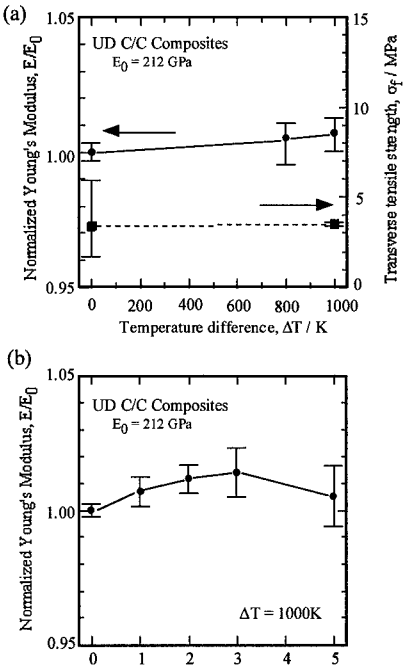

Fig.4 Effect of thermal shock on mechanical properties of UD C/C composite. (a) Effect of ΔT, (b) Effect of thermal shock cycle

degradation in Young's modulus and bending strength even after the cyclic thermal shock at ΔT of 1000K. These results showed that the C/C composites posses superior thermal shock resistance.

Transient Thermal Stress Analysis

For estimating the thermal stress induced in the specimen, finite element analyses were carried out. Linear elastic two-dimensional model was used assuming the plane strain condition. The cross-section was modeled using 8-nodes isoparametric elements. Temperature dependence of transient heat flow on the specimen surface was obtained independently from the experiments using silver specimens with a thermocouple [9]. Temperature dependence

of Young's modulus, coefficient of thermal expansion, and thermal conductivity was also considered referring to the experimental results previously reported for the same materials [10].

The calculated maximum thermal stresses induced in the UD C/C composites are shown in Fig.5. Even at ΔT around 200K, the maximum thermal stress exceeds the transverse tensile strength of the UD C/C composites. This means the maximum stress cannot predict the macroscopic thermal shock fracture. This must be because transient thermal stress was relaxed by the formation of the microscopic damage area. This is a unique stress relaxation mechanism to the composites.

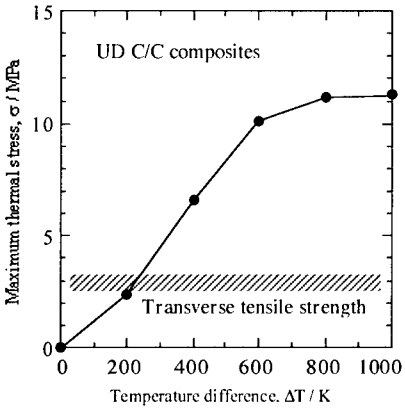

Fig.5 Maximum thermal stress induced in UD C/C composites during thermal shock test

Conclusions

Thermal shock resistance of UD and cross-ply C/C composites was investigated by the water quench tests. Even at ΔT of 1000K, no macroscopic damage was introduced in the C/C composites, although microscopic damage was observed near the surface.

The results of thermal stress analyses suggested that the formation of the microscopic damage introduced near the surface was a unique stress relaxation mechanism to the composites.

References

1. G. Savage: "*Carbon-Carbon Composites*", Chapman & Hall, London, 1993, pp. 346-353.
2. Y. Kagawa, N. Kurosawa, and T. Kishi, J. Mat. Sci., **28**, 735 (1993).
3. H. Wang and R.N. Singh: Int. Mater. Rev., **39**, 228 (1994).
4. H. Wang, R. N. Singh, and R. A. Lowden: J. Am. Ceram. Soc., **79**, 1783 (1996).
5. A. Okura, and T. Cho: "*Advanced Composites in Emerging Technologies*", 1992, pp.348-53.
6. T. Sakuma, U. Iwata and H. Takaku: Trans. Japan Soc. Mech. Eng. A, **57**, 2741 (1991). (*in Japanese*)
7. T. Sakuma, U. Iwata and H. Takaku: *ibid.*, **58**, 1424 (1992.). (*in Japanese*)
8. H. Hatta, Y. Nakayama, K. Goto, T. Aoki, Y. Kogo, and H. Fukuda: Trans. Japan Soc. Mech. Eng., A., **65**(638), 2073 (1999). (*in Japanese*)
9. Y. Kogo, M. Kamiya, H. Hatta, and T. Ishikawa: Proc. 9th U.S.-Japan Conf. Comp. Mater., 831(2000).
10. H. Hatta, Y. Kogo, N. Tanatsugu, H. Ohnabe, T. Mizutani, H. Kawada, and T. Shigemura: The Institute of Space and Astronautical Science Report, 85, 4 (1996). (*in Japanese*)

Proceedings of 7th Japan International SAMPE
Symposium & Exhibition, Nov. 13-16, 2001

Compressive stress enhancement by EB treatment of C/C composite spring

Atsushi KIMURA, Takashi TORIYAMA, Akihiro MIZUTANI
Kazuya OGURI*, Akira TONEGAWA* and Yoshitake NISHI

Department of Materials Science, Tokai University,
1117 Kitakaname, Hiratsuka, Kanagawa, 259-1292 JAPAN
E-mail: am026429@keyaki.cc.u-tokai.ac.jp
*Department of Physics, Tokai University
1117 Kitakaname, Hiratsuka, Kanagawa, 259-1292 JAPAN
E-mail: am026429@keyaki.cc.u-tokai.ac.jp

Abstract

A recovery treatment of fracture origins has been developed for C/C composites applied for aerospace and rapid transit engineering by using sheet electron beam irradiation. The EB irradiation of 150 Mrad largely enhanced spring constant and resistance to compressive stress.

Key Words: C/C composite, spring constant, Electron beam irradiation

Introduction

C/C composites have been applied as high-strengthened light structural materials in the fields of aerospace and rapid transit engineering [1,2]. Furthermore, in the first step in producing, it is often difficult to handle the fractured fibers in the bundling machine, because carbon fiber often fractured. Since carbon atoms diffuse at high temperatures, heat treatment is typically used to enhance the fracture stress of carbon fiber [3]. Such carbon atom migration probably reconnected the separated crack planes near the crack tips and might occupy free volume [4] in glassy structure. Thus, the crack tips became dull, and then the inter-atomic bonding density became high in carbon fiber, simultaneously. However a traditional recovery process usually takes long time for heat treatment. In order to modify the fracture strain for short time at lower temperature, carbon fiber has been often treated with electron beam (EB) irradiation [5]. Electron beam (EB) irradiation of high electrical potential (170 kV) is used to migrate carbon atoms in a carbon fiber. Namely, the EB irradiation not only enhanced the fracture strain, but also may enlarge the tensile strength on fracture. If the EB treatment can be also effective for C/C composite spring, it can be applied for aerospace and rapid transit engineering. Thus, the purpose of the present work is to study effects of EB treatment on spring constant and resistance to compressive stress of C/C composite spring.

Experimental Procedure

The C/C composite spring (Dr. Takao Nakagawa, President, Across Ltd, 16-27, Nishiki–cho 2, Warabi, Saitama, JAPAN, E-mail:across@sannet. ne.jp) is shown in Figure 1. The sizes were 50 mm in diameter and 25 mm in length. HIP treatment was performed for 7 hour from 673 to 873K under 11.8MPa. After that, heat treatment was performed at elevated temerature up to 2273 K under Ar atmosphere, where the heating rate was 20 deg/hour.

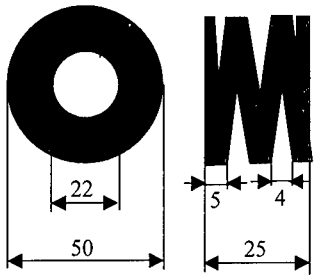

Figure 1 Schematic drawing of C/C composite spring

The sheet electron beam irradiation was homogeneously performed using an electron - curtain processor (Type CB175/15/180L, Energy Science Inc., Woburn, MA)[5-8].

The acceleration potential and the irradiating current density were 170 kV and 0.89 x 10^{-2}mA/cm^2, respectively. The EB treatment was applied intermittently (i.e., not continuously). The conveyer speed was 10 m/min. Irradiation time was kept constant at 0.23 s in order to control the temperature in each of the four samples. The temperature of the sample was below 323 K just after the EB irradiation. The irradiation dose was controlled by the integrated irradiation time in each of the samples. Here, the total amount of absorbed dose value was converted by the absorbed dose of the distillation water. Although the EB generation was in vacuum, the irradiated specimen was kept under protective nitrogen at atmospheric pressure in the apparatus. Namely, specimen was irradiated by electron beam through the titanium thin film window attached to vacuum chamber (240 mm in diameter). The distance between sample and window is 35 mm. The oxygen concentration was less than 400 PPM in this atmosphere.

Table 1. Condition of EB irradiation

Acceleration potential	170 kV
Irradiating current	2.0 mA
Irradiation dose	0 Mrad 51.84 Mrad 151.20 Mrad 250.56 Mrad
Atmosphere	Nitrogen with atmospheric pressure Oxygen concentration is less than 400 ppm

To evaluate compressive strength on elasticity, a compression test was performed. Figure 2 shows schematic drawing of compression test of C/C composite spring. The C/C composite spring on fixed stand was homogeneously compressed. The stress rate was 3.3×10^{-2} N/s.

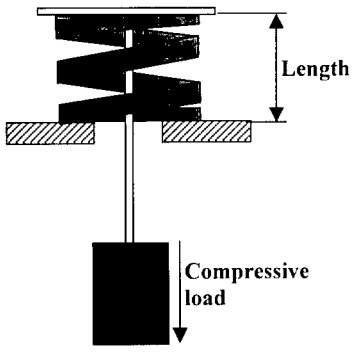

Figure 2 Schematic drawing of compressive test of C/C composite spring.

Results and Discussion

The compressive test was performed below 15 kPa. Figure 3 shows compressive stress-strain curve of C/C composite springs before and after EB irradiation. The compressive strain enhanced the resistance to compressive stress. Although the steep slope above 0.12 of strain was observed in the untreated C/C spring, the dull slope of initial curve below 0.12 of strain was found. The EB treatment enhanced the resistance to compressive stress below 5 kPa, as shown in Figure 3. On the other hand, the steep slopes of curves above 5 kPa were observed in all C/C springs at different EB doses. Namely, the EB treatment enhanced the spring elasticity. The spring compressive elasticity for the treated sample (151.20 Mrad) is about 170% larger than that for untreated sample.

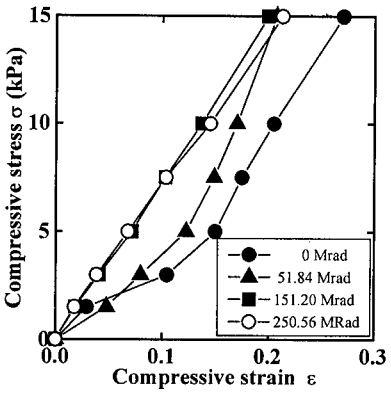

Figure 3 Compressive stress – strain curve of carbon-carbon composite spring samples.

Figure 4 shows change in resistance to compressive stress against irradiation dose at different compressive strains. Although the EB irradiation slightly enhanced the resistance to compressive stress at 0.05 of compressive strain, the EB irradiation below 150 Mrad strongly enhanced the resistance to compressive stress above 0.15 of compressive strain. Increase in resistance to compressive stress was 5 kPa below 150 Mrad.

Figure 5 shows change in the spring constant of C/C composite spring against EB irradiation dose. The EB treatment of 150 Mrad enhanced spring constant from 1.0 to 2.0 N/mm of C/C composite spring.

The excess EB irradiation of 250.56 Mrad slightly decreased resistance to compressive stress (see Fig. 4) and spring constant (see Fig. 5).

If the EB treatment forcibly diffuses carbon atoms into free volume and incoherent interface because of high electrical potential (170 kV), such carbon atom migration probably decreased the dangling bonds, dulled the edge of sharp crack tips and probably reconnected the separated crystal planes near the crack tips. In order to evaluate the inter-atomic bonding density, density of dangling bonds (DDB: mol^{-1}) is obtained by dangling bond signals of graphite, which can be detected by means of electron spin resonance (ESR) spectrometer [5]. Here the microwave frequency range used in the ESR analysis was the X-band. The field modulation was 100 kHz. Spin density was calculated using a Mn^{2+} standard sample. The EB irradiation decreased the density of dangling bond (spin) [5]. Namely, the EB treatment forcibly diffused carbon atoms to free volume, incoherent interface and increased the inter-atomic bonding density in carbon fiber. Therefore, the EB irradiation of 150 Mrad largely enhanced spring constant and resistance to compressive stress of C/C composite spring.

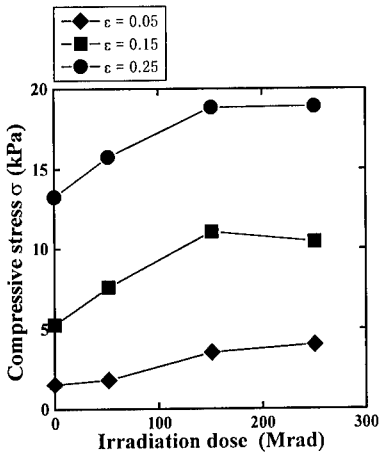

Figure 4 change in compressive stress against irradiation dose at different compressive strains.

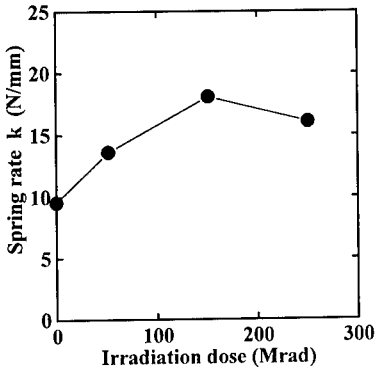

Figure 5 Change in spring constant of C/C composite spring against EB irradiation dose.

Conclusions

A recovery treatment of fracture origins has been developed of C/C composite spring by using sheet electron beam irradiation. When the EB treatment is performed, the compressive strength of C/C composite spring was improved. The EB irradiation of 150 Mrad largely enhanced resistance to compressive stress and spring constant. On the other hand, excess EB irradiation (250 Mrad) slightly decreased compressive stress and spring constant.

Acknowledgement

Authors would like to thank Dr. Takao Nakagawa, (President of Across Ltd.) and Dr. Hirotaka Nagao for their usuful and fantastic technology to prepare C/C composite spring.

References

1. J. D. Brooks and G. H. Taylor, Carbon, 3, 185(1965).
2. T. Chang and A. Okura, Transactions ISIJ,27, 229(1987)
3. C. R. Rowe, D. L. Lowe, Bienn. Conf. Carbon, 13,170(1977).
4. M.H.Cohen and D. Turnbull, J. Chem. Physics., 43139 (1965).
5. Y. Nishi, T. Toriyama, K. Oguri, A. Tonegawa & K. Takayama, J. Maerials Research 2001, in press.
6. Y. Nishi, S. Takagi, K. Yasuda & K. Itoh, J. Applied physics, 70,367(1991).
7. Y. Nishi, H. Izumi, J. Kawano, K. Oguri, Y. Kawaguchi, M. Ogata, A. Tonegawa, K. Takayama, T. Kawai, M. Ochi, J. Materials Science, 32, 3637.(1997).
8. K. Oguri, K. Fujita, M. Takahashi, Y. Omori, A. Tonegawa, N. Honda, M. Ochi, K. Takayama and Y. Nishi., J. Materials Research, 13, 3368(1998)

Proceedings of 7th Japan International SAMPE
Symposium & Exhibition, Nov. 13-16, 2001

Tensile Failure Mechanisms of C/C Composites

Tatsuzi Aoi #1 , Hiroshi Hatta #2 and Yasuo Kogo #3

#1 : Graduate Student , Science University of Tokyo
#2 : Research Division of Space Propulsion,The Institute of Space and Astronautional Science, 3-1-1 Yoshinodai, Sagamihara 229-8510, JAPAN
#3 : Department of Material Science and Technology, Science University of Tokyo, 2641 Yamazaki, Noda 278-8510,JAPAN
E-mail : aoi@pub.isas.ac.jp

Abstract

In order to improve tensile strength of carbon/carbon composites (C/Cs), it is important to clarify their tensile failure mechanisms. In the present paper, the tensile strength of C/Cs was intentionally changed by varying density and heat treatment temperature. Then, the tensile failure mechanisms of these C/C composites were discussed based on the experimental evidence. It was concluded through the discussion that in high density C/Cs tensile strength was mainly ruled by the interfacial bonding between the fiber and matrix. On the other hand in low density C/Cs, tensile fracture was controlled by load transfer capability within the matrix.

Key Words: C/C composite, Tensile strength, Bulk density, Heat treatment temperature.

INTRODUCTION

Carbon fiber reinforced carbon matrix composites (C/Cs) usually possess a much lower strength than that expected from the rule of mixture. For example, the ultimate elongation of typical C/Cs is only 30-50% of that of reinforcing fibers. Hence, it is extremely important for the improvement of C/C strength to understand mechanisms yielding such strength degradations. In the present study, special attention was placed on the effect of the bulk density and heat-treatment-temperature of the C/Cs on the tensile fracture strain. In addition, the effect of the interfacial strength on the tensile strength of the C/Cs was attempted to be evaluated.

EXPERIMENTAL

1. MATERIALS

Two types of carbon fibers, high strength (IM600-6K by Toho-rayon co. Ltd.) and high modulus types (UM46-6K by Toho-rayon co. Ltd.), were examined for the reinforcements of C/Cs. All the C/Cs had cross-ply lamination

and a total fiber volume fraction of 60%. The precursor of all the C/Cs were phenol-matrix CFRP carbonized at 1273K. Then half of the carbonized C/Cs were re-impregnated with phenol resin, re-carbonized at 1273K, and heat-treated at 2273K. This cycle was repeated 1 to 6 times. After the carbon impregnation, the C/Cs were heat treated at 2573K, 2873K, and 3273K to compare the tensile properties. The remaining halves were applied HIP (Hot Isostatic Pressing) processing from 1 to 5 times and heat-treated at 2573K. For the HIP process, pitch was used for matrix-precursor.

2. TENSILE TEST

Tensile strength and fracture strain of the C/Cs were measured using an INSTRON type tensile testing machine. The specimens of the tensile tests were a strip-of-paper type with 200mm length, 10mm width, and 1.5mm thickness. Aluminum tabs with a length of 60mm and a thickness of 1mm were glued on the gripping portions of the IM600-C/Cs. In contrast, for UM46-C/C, aluminum tabs was required 80mm in length to prevent tab debonding.

RESULTS AND DISCUSSION

A relation between bulk density and tensile strength of IM600-C/C was shown in Fig.1. As shown in this figure, the tensile strength of HIPed IM600-C/Cs has decreased with increase in bulk density (1.7~2.0g/㎤). This is caused by strengthening of fiber/matrix interface bonding with repetition of the HIP process [1]. This feature of tensile fracture is similar to that in long fiber reinforced ceramic matrix composites. On the other hand, in the low density region of 1.3~1.7g/㎤, the tensile strength of IM600-C/Cs increased with increasing bulk density.

The relation between the bulk density of IM600-C/C and fracture strain was shown in Fig. 2. In the low density region of 1.3~1.7g/㎤, fracture strain remained almost constant value. This indicates that the strength rise by the density rise of low density C/C is principally due to the increase in Young's modulus. In Fig. 3, the effect of filling matrix carbon to defects in the C/Cs is calculated. As this figure shows, the filling effect cannot explain the increase in Young's modulus. When bulk density is extremely low, the matrix in C/C only partially restrains the fiber as shown in Fig.4. Therefore, if a tensile load is applied, the load is supported only by straight fibers but not by curved fibers. As the bulk density rises, the load transfer capability by the matrix gradually comes out. Then load-bearing capability gradually appears in the curved fibers. Thus this effect has capability to explain the increase in Young's modulus.

Concerning to the effect of heat treatment temperature, HTT, the tensile strength of IM600 C/Cs monotonically decreased with HTT as shown in Fig.1 and 2. During the HTT, the diameter of carbon fiber was found to decrease and fiber cross-sections were distorted as shown in Figs. 5, 6, and 7. By these changes, the fibers might be damaged and deterioration the fiber strength was supposed to occur. It is noted here that the HTT of IM600 during the fiber production stage might be 1500-1800 K, which is much lower than HTT in the present

study. Hence the deterioration of fiber with high temperature HTT is easily understandable.

The relation between the bulk density and tensile strength of UM46-C/Cs is shown in Fig. 8. As shown in this figure, the tensile strength of UM46-C/Cs increased with density up to 1.7g/㎤. This is the same behavior as that of IM600-C/Cs. However, strength degradation is not clearly seen in terms of HTT. It is due to high heat treatment temperature of UM46 when it was fabricated. Although change of a fiber / matrix interface was expected during HTT, the interfacial bonding strength might not be changed. The matrix precursor of the present C/Cs was phenolic resin and the resin tends to yield glassy carbon matrix. Thus prompt graphitization should be extremely difficult [2]. On the other hand, a pitch or CVI is reported to be easy to form graphite upon heat treatment. Therefore, if the same examination as this research is performed by pitch, interfacial bonding strength control might become possible.

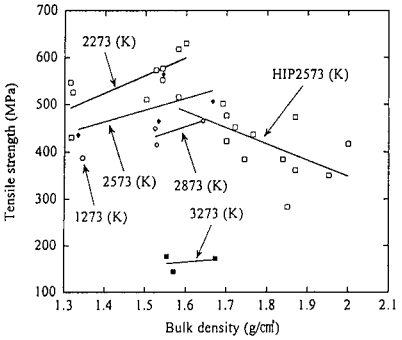

Fig.1 Tensile strength as a function of bulk density of IM600-C/C composites

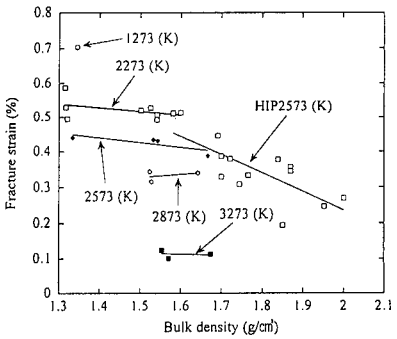

Fig.2 Fracture strain as a function of bulk density of IM600-C/C composites

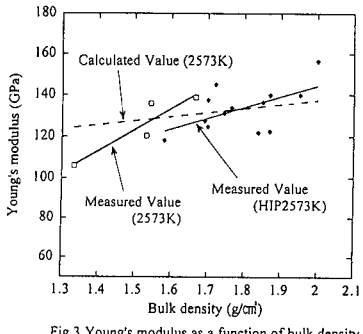

Fig.3 Young's modulus as a function of bulk density of IM600-C/C composites

REFERENCES

[1] H. Hatta, K. Suzuki, T. Shigei, S. So,iya, Y. Sawada, "Strength Improvement by Densification of C/C Composites", Carbon 39, 83-90 (2001).

[2] Shiushichi Kimura, Yashhiro Tanaka, Nobuyuki Takase, Pressure Graphitization of Matrix in Carbon Fiber/Glass-Like Carbon Composite, Bulletin of the Chemical Society of Japan, 1981, (9), p.1474~1480.

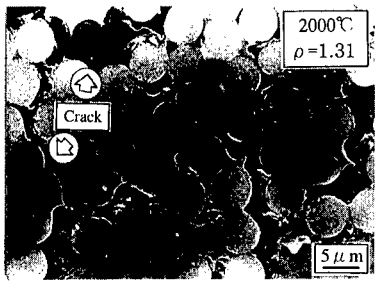

Fig.4 SEM microstructure of IM600-C/C (ρ =1.31)

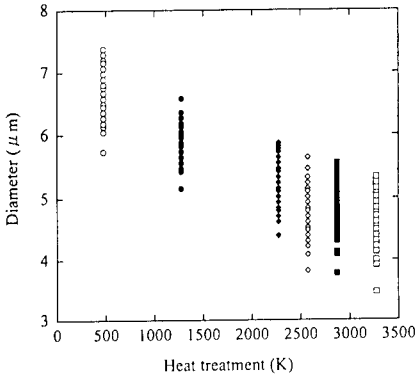

Fig.6 Diameter IM600-fibers after heat treatment

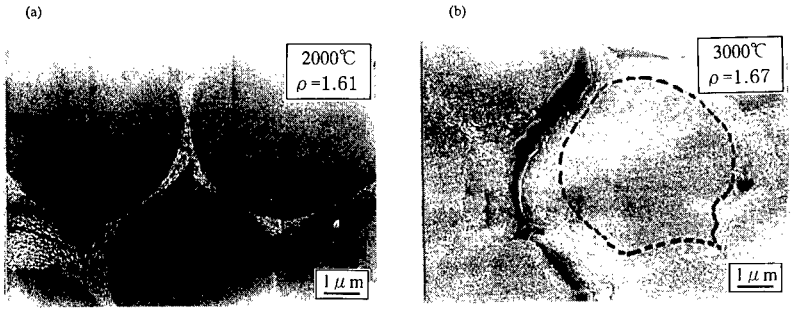

Fig.5 SEM microstructure of IM600-C/Cs after heat treatment at 2273K (a), and 3273K (b)

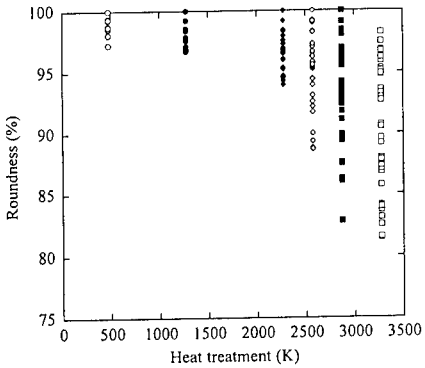

Fig.7 Roundness of fiber as after heat treatment of IM600-C/C composites.Round equals to Diameter of a fiber(small) / Diameter of a fiber (large)×100.

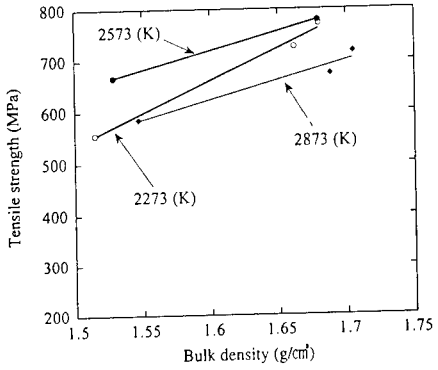

Fig.8 Tensile strength as a function of bulk density of UM46-C/C composites

Proceedings of 7th Japan International SAMPE
Symposium & Exhibition, Nov. 13-16, 2001

Corrosion Mechanisms of Metal-Matrix Composites

L.H. Hihara

Department of Mechanical Engineering
University of Hawaii at Manoa
2540 Dole St., Honolulu, HI 96822
E-mail: hihara@wiliki.eng.hawaii.edu

Abstract

Metal matrix composites (MMCs) are metals that are reinforced with fibers or particles to improve or tailor properties such as stiffness, strength, thermal conductivity, thermal expansion, friction, and wear resistance. Corrosion resistance is normally given secondary consideration, and therefore, it is not uncommon for MMCs to possess low corrosion resistance resulting in their restricted usage. The corrosion resistance of MMCs is usually inferior to that of their monolithic matrix alloys. Overviews and examples on the corrosion mechanisms affecting MMCs will be presented.

Key Words: Corrosion, Metal-Matrix Composites

Introduction

Research devoted to corrosion behavior of MMCs has been sparse in comparison to research on fabrication and mechanical properties. MMCs typically have been designed for superior properties over monolithic materials, but not for resistance to environmental degradation. Consequently, MMC corrosion is not well understood, and some MMCs have very low resistance to corrosion and undergo severe degradation.

The presence of the reinforcement fibers and particles and the processing associated with MMC fabrication can cause accelerated corrosion of the metal matrix in comparison to the monolithic matrix alloy.

Sources of Corrosion in MMCs

Accelerated corrosion in MMCs may originate from electrochemical, chemical, and physical interaction between MMC constituents; and from processing related problems. The primary sources of MMC corrosion that will be discusses are 1) galvanic interaction between MMC constituents; 2) chemical dissolution of interphases; 3) physical presence of the reinforcements; and 4) processing related problems.

Galvanic Corrosion

Galvanic corrosion between the matrix and reinforcements or interphases is one of the primary concern regarding the corrosion behavior of MMCs. The rate of galvanic corrosion is governed by the type of reinforcement and matrix material, the environment, and the amount of reinforcement particles or fibers.

Galvanic corrosion is particularly a concern for active metals (in environments not conducive to passivation) that are reinforced with conductive, noble fibers or particles. For example, 6061-T6 Al would have galvanic corrosion rates approximately three orders of magnitude higher than that of Ti-15V-3Cr-3Sn-3Al (Ti 15-3) if reinforced with an equal area fraction of graphite (Gr) fibers and exposed to aerated 3.15 wt% NaCl (Figure 1). The intersection of the anodic

polarization curve of the matrix metal and the cathodic polarization curve of the reinforcement indicates the magnitude of the galvanic corrosion current density (i_{GALV}).

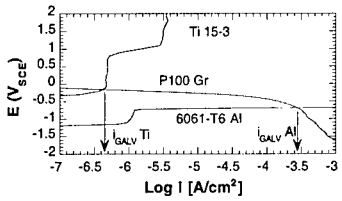

Figure 1: Anodic polarization diagrams of Ti 15-3 [1] and 6061-T6 Al [2] in deaerated 3.15 wt% NaCl at 30°C. Cathodic polarization diagram of P100 Gr fibers [2] in aerated 3.15 wt% NaCl at 30°C. Scan rate = 0.1 mV/sec.

Galvanic corrosion rates may also be sensitive to dissolved oxygen depending on the matrix material and reinforcement. The polarization diagrams (Figure 2) indicate that the galvanic corrosion rate for 6061-T6 Al coupled to carbon-cored SiC monofilaments with filament ends exposed (SiC_{MF}) in 3.15 wt% NaCl would increase by approximately two orders of magnitude when the solution is oxygenated.

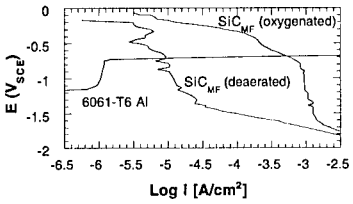

Figure 2: Anodic polarization diagram of 6061-T6 Al in deaerated 3.15 wt% NaCl at 30°C [2]. Cathodic polarization diagrams of SiC_{MF} in deaerated and oxygenated 3.15 wt% NaCl at 30°C.[3] Scan rate = 0.1 mV/sec.

The electrolyte may also have significant effects on galvanic corrosion rates. Figure 3 demonstrates that the galvanic corrosion rate for 6061-T6 Al coupled to Gr fibers in aerated 3.15 wt% NaCl is significantly greater than that in 0.5 M Na_2SO_4.

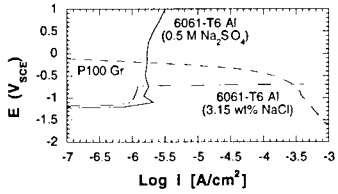

Figure 3: Anodic polarization diagram of 6061-T6 Al in deaerated 3.15 wt% NaCl and 0.5 M Na_2SO_4 at 30°C.[2] Cathodic polarization diagram of P100 Gr fibers in aerated 3.15 wt% NaCl at 30°C. [2] Scan rate = 0.1 mV/sec.

The type of reinforcement also has a significant affect on the anticipated rate of galvanic corrosion between the matrix and reinforcement materials. It is indicated in Figure 4 that the galvanic corrosion rate between 6061-T6 Al and the various reinforcements would ranked from highest to lowest in aerated 3.15 wt% NaCl as follows: P100 Gr > carbon-cored SiC_{MF} with ends exposed > tungsten-cored boron MF (B_{MF}) with ends exposed > hot-pressed (HP) SiC > Si. The galvanic corrosion rate can also significantly increase as the area fraction of the reinforcements increase.

Chemical Dissolution of Interphases

Degradation of MMCs may also occur by chemical rather than electrochemical reactions. Certain types of reinforcement phases and interphases may undergo chemical degradation, which cannot be predicted using electrochemical analysis. For example, in MMCs containing Al and carbon, the formation of the Al_4C_3 interphase can be problematic, since it readily hydrolyses in water to form methane gas (Figure 5).

Physical Presence of Reinforcements

The physical presence of the reinforcements may also have secondary effects on MMC corrosion. The reinforcements, which are

usually inert in comparison to the matrix, are often left in relief as the matrix corrodes leaving behind a network of crevices that trap corrosion products and exacerbate corrosion. In Si/Al MMCs, for example, localized anodic regimes spread over the MMC surface in 0.5 M Na_2SO_4 in which aluminum should passivate. It was likely that corrosion products trapped in the crevices formed by the network of particles in relief acidified the solution and prevented passivation (Figure 6).

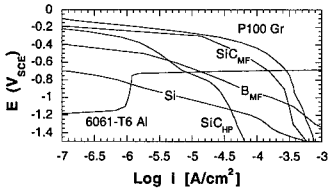

Figure 4: Anodic polarization diagram of 6061-T6 Al [2] in deaerated 3.15 wt% NaCl at 30°C. Cathodic polarization diagrams of P100 Gr fibers [2], SiC monofilament (MF) [1], boron MF, hot-pressed (HP) SiC [2], and Si [4] in aerated 3.15 wt% NaCl at 30°C. Scan rate = 0.1 mV/sec.

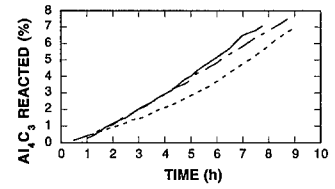

Figure 5: Hydrolysis of hot-pressed Al_4C_3 immersed in pure water. [2]

Processing Related Problems

These problems do not directly arise from the reinforcement, the matrix alloy, or the interaction between the reinforcement and matrix alloy. Problems in this category may include corrosion induced by contaminates or residuals of processing, or by corrosion exacerbated by less than ideal processing conditions.

An example are some types of Gr/Al MMCs that were found to have been contaminated with microstructural chlorides during processing. [2] Figure 7 and 8 show two Gr/Al MMC samples processed by the same method that have been stored in identical laboratory air for over 10 years. The sample in Figure 7 shows extensive degradation; whereas that in Figure 8 is relatively free from degradation, indicating the sensitivity of corrosion performance of these MMCs to processing parameters.

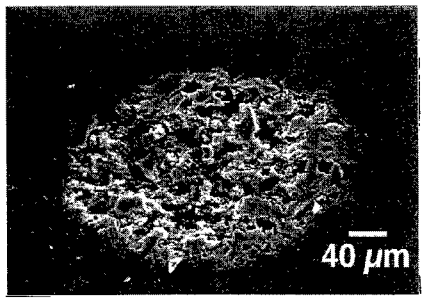

Figure 6: Region of localized corrosion on Si/Al MMC exposed for 120h in aerated 0.5 M Na_2SO_4 at 30°C in the open-circuit condition. [4]

The presence of microstructural chlorides in the Gr/Al MMCs were confirmed during microscopy analyses and evident in anodic polarization diagrams. [5] Figure 9 shows an anodic mixed-electrode polarization diagram that was constructed using the mixed-potential theory (MPT) and the polarization diagrams of 6061-T6 Al and P100 Gr exposed to 0.5 M Na_2SO_4. The MPT-generated diagram (Figure 9) shows that a 6061-T6 Al matrix should passivate during the anodic scan. The anodic polarization diagram of the actual Gr/6061-T6 Al MMC, however, showed that pitting is induced at approximately -0.6 V_{SCE}. Buonanno [6] verified that Gr/Al MMCs free of microstructural chlorides (processed using pressure infiltration) have polarization diagrams resembling that of the mixed-

electrode model. Other types of MMCs have also shown behavior as predicted by the MPT: Particulate Si/Al MMCs (Figure 10) and SiC_{MF}/Ti 15-3 (Figure 11).

Figure 7: Gr/Al MMC disintegrating in laboratory air. Greater than 10 years exposure.

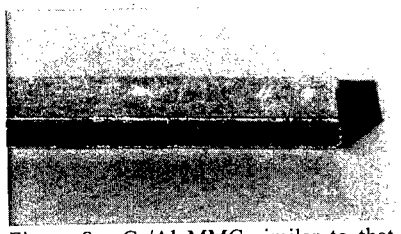

Figure 8: Gr/Al MMC similar to that in Figure 7 with over 10 years exposure in laboratory air, but with no visual signs of degradation.

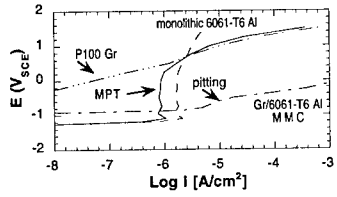

Figure 9: Anodic polarization diagrams of P100 Gr, monolithic 6061-T6 Al, and an actual Gr(P100)/6061-T6 Al MMC exposed to deaerated 0.5 M Na_2SO_4 at 30°C. The discrepancy between the polarization diagram generated by the MPT and that of the actual MMC is due to microstructural chlorides. Scan rate = 0.1 mV/sec. [5]

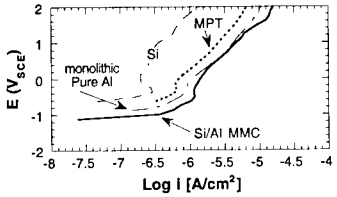

Figure 10: Anodic polarization diagrams of Si, pure Al, an Si/Al MMC, and that generated with the MPT exposed to deaerated 0.5 M Na_2SO_4 at 30°C. Scan rate = 0.1mV/s. [4]

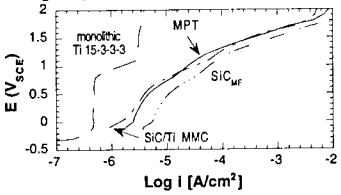

Figure 11: Anodic polarization diagrams of SiC_{MF}, Ti 15-3, an actual SiC_{MF}/Ti 15-3 MMC, and that generated with the MPT exposed to deaerated 3.15 wt% NaCl at 30°C. Scan rate = 0.1 mV/sec. [1]

Summary

The corrosion of MMCs are usually more severe than their monolithic matrix alloys, and therefore, these materials must be thoroughly studied and understood before they can be safely put into service.

Acknowledgements

The author is grateful to the Shell Foundation, Office of Naval Research, National Science Foundation, and TRW, Inc. for funding projects discussed in this work.

References

1) C. Tamirisa, M.S. Thesis, University of Hawaii at Manoa, 1993.
2) L.H. Hihara, Ph.D. Thesis, MIT, 1989.
3) P.K. Kondepudi, M.S. Thesis, University of Hawaii at Manoa, 1992
4) Zi Jian Lin, M.S. Thesis, University of Hawaii at Manoa, 1995.
5) L.H. Hihara and R.M. Latanision, Corrosion 47,1991, p335.
6) M.A. Buonanno, Ph.D.Thesis, MIT, 1992.

Proceedings of 7th Japan International SAMPE
Symposium & Exhibition, Nov. 13-16, 2001

The Properties of the Titanium Matrix Composites Manufactured by Spray-Winding Techniques

Akira Kono#1, Takeshi Yamada#1, Chikara Fujiwara#1 and Masashi Hirota#2

#1: Nagoya Aerospace Systems, Mitsubishi Heavy Industries, Ltd.
10, Oye-cho, Minato-ku, Nagoya 455-8515, JAPAN
#2: Nagoya Guidance & Propulsion Systems, Mitsubishi Heavy Industries, Ltd.
1200, O-aza, Higashi Tanaka, Komaki, 485-8561, JAPAN
E-mail: akira_kono@mx.nasw.mhi.co.jp

Abstract

Silicon carbide fiber (SCS-6) reinforced Ti-4.5Al-3V-2Fe-2Mo (SP-700) composites were manufactured by spray-winding process, which is a potential low cost manufacturing process, and their mechanical properties were evaluated in comparison with conventional foil-fiber-foil process. The ultimate tensile strengths to fracture of the spray composites were much lower than those of foil composites. The low tensile strengths of spray composites may result from contamination of matrix brought by powder material and spraying process.

However, the tensile strengths of spray composites did not improve even after the contamination was suppressed by controlling spray atmosphere. The fracture surfaces of tensile test specimens of the spray composites showed separation of interface between fiber and matrix, which is not, observed in foil composites. Not only matrix contamination but also other factors such as interfacial strength would affect the lower tensile strengths of spray composites.

Key Words: Continuous Fiber, Titanium Matrix Composite, Spray, Manufacturing

Introduction

Continuous fiber reinforced titanium matrix composites are attractive as potential aerospace structural material due to their high specific mechanical properties and improved high temperature capability[1]. Particularly, when the fan rotor ring is reinforced by TMCs in the hoop direction, weight saving of more than 30% has been expected. In the Japanese government support program, manufacturing process of TMC ring is being researched and developed.

Spray-winding process is one of the most cost effective manufacturing process. Actually the manufacturing cost of TMC ring has been demonstrated to be reduced by 60% by applying spray winding process, compared with conventional foil-fiber-foil process. The problem of the spray winding process is degradation of mechanical properties caused by matrix contamination. However, the tensile strengths of the spray composites (Ti-6242/SCS-6, vol % fiber, from 35 to 40 %) were shown to be in the range from 1540 to 1930 MPa, by maintaining contamination levels to be less than 1500 ppm[2]. In this paper, SiC fiber reinforced titanium matrix composites were manufactured by spray-winding process with a control of atmosphere to suppress the contamination and their mechanical

properties were evaluated.

Experimental Procedure

Materials

The reinforcements used in this study were the SCS-6, which is continuous silicon fiber with an average diameter of 140 μm. These fibers were produced by chemical vapor deposition process. The outer coating of the fiber is carbon-rich, which prevents detrimental interaction between the fiber and titanium during composite processing.

The matrix was titanium alloy (SP-700) with composition of Ti-4.5Al-3V-2Fe-2Mo. The matrix powder was produced by Ar-gas atomizing. The particle size distribution used in this study is from 32 to 65 μm.

Experiments

Tension test

The spray composites with five layers were manufactured by means of the following process. A fiber was spirally wound onto the stainless steel foil, 0.3mm thick, which was wound onto the cylindrical substrate. And then matrix material was low-pressure-plasma-sprayed onto the fiber. To make matrix contamination lower, the spray process was developed. Before low-pressure plasma spraying, the purge of argon gas was conducted. The monotape preform was removed from stainless steel foil. They were consolidated by hot isostatic pressing (Hiping) at 1048K for 7.2ks under a Ar-gas pressure of 120MPa. The tensile specimens with gage dimensions of 15mm long by 5.0mm wide were machined from composite plates. The volume fraction of these composites was about 33 vol %. Two kinds of composites were made from the monotapes (one is produced by conventional spray process, the other is by developed process). These tensile specimens were tested at room temperature in air at a constant crosshead speed.

Interstitial impurity analysis

To examine the impurity level of matrix material, chemical analysis was conducted. Vacuum fusion method was adopted as a chemical analysis method. The impurity levels of foils, powders and sprayed deposits were measured.

Results and discussion

Mechanical properties

Tensile test results of the spray composites are shown in Fig.1. with properties of the foil composites and monolithic SP-700 [3), 4)]. The volume fraction of foil composites was about 28 vol %. Although the tensile strength of the foil composites in the longitudinal direction was much higher than those of monolithic sheets, the tensile strength of the spray composites was slightly lower than those of monolithic sheet. It means the fibers of the spray composites do not reinforce material effectively.

As for the strengths of the composites in the transverse direction, the strengths of both foil and spray composites were lower than those of monolithic sheet. The strengths of the spray composites were lower than those of foil composites.

With regard to the influence of sprayed processes, the strengths of the spray composites did not vary with sprayed processes.

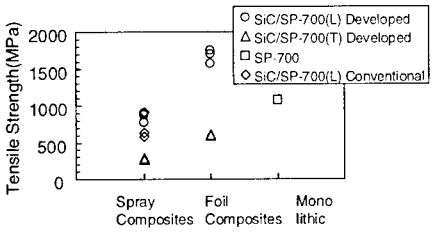

Fig.1 Tensile strength of the SCS-6/SP-700 Composites and SP-700 monolitic

Fig.2 shows scanning electron microscope (SEM) micrographs of fracture surfaces of tensile test specimen from SCS-6/SP-700 fabricated by spray-winding process ((a),(b) and (e)) and by foil-fiber-foil process ((c),(d) and (f)).
In the fracture surface of the foil composites, typical dimple pattern is observed in the matrix between the fibers as shown in Fig.2 (d). In case of the spray composites, cleavage fracture is observed, as shown in Fig.2 (b). From the fracture surface of the spray composites in the longitudinal direction, the crack seems to propagate along the debonded

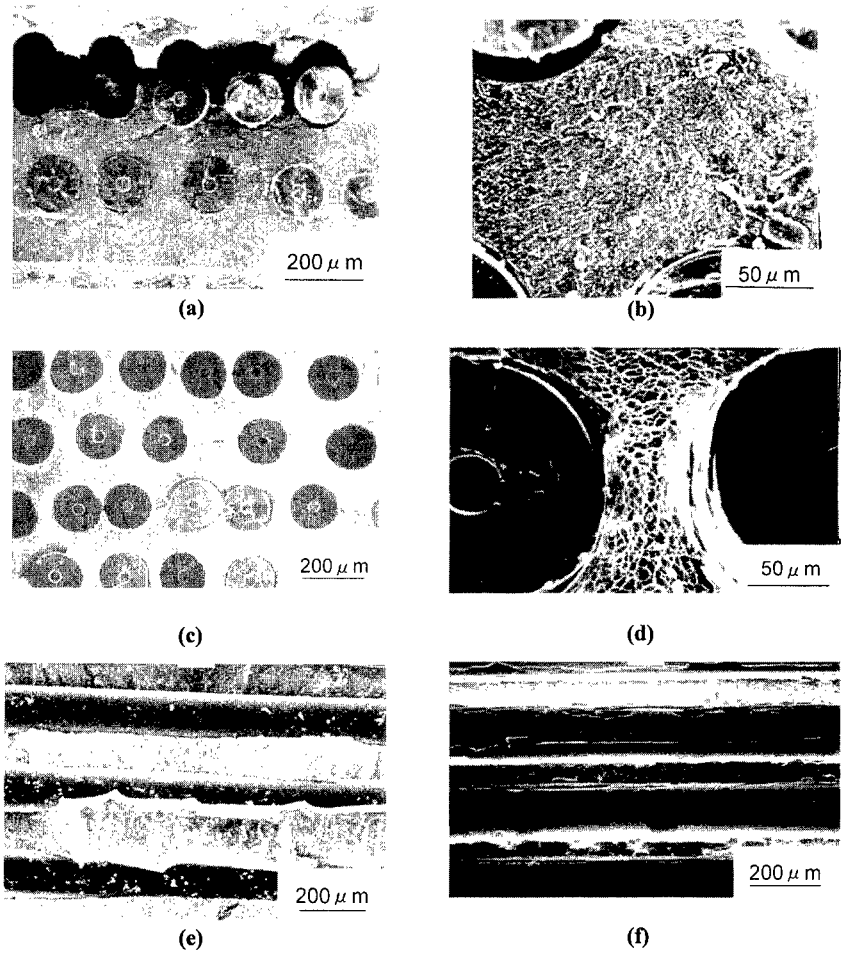

Fig.2 Microstructure of tensile fracture surface of the TMC specimen [(a) and (b); sprayed composite, longitudinal. (c) and (d); foil composite, longitudinal. (e); spray composite, transverse. (f); foil composite, transverse.

interface between fiber and matrix. In case of transverse direction, in the fracture surface of the foil composites, some amounts of a layer of matrix were observed to remain on to the fiber. In the case of spray composites, the matrix and fibers were completely separated. The interfacial strength between fibers and matrix also varied with manufacturing process routes.

Table 1 Interstitial impurity analysis of matrix

material	O(%)	N(%)
foil	0.07	0.01
powder		
as received	0.14	0.01
as sprayed	0.36	0.04
(conventional)		
reference data	0.50	-
(Magnetron sputtering)		

Table 1 shows the impurity level of matrix material in foils and powders, and sprayed deposits. The oxygen levels in the magnetron sputtering matrix (Ti-6-4) are also summarized in Table1. Oxygen and nitrogen levels in the sprayed matrix were higher than those in the foil matrix. This may be the cause of the embrittlement of matrix. As for the influence of oxygen content of matrix on tensile strength, it is reported the tensile strengths of the composites (SCS-6/Ti-6-4, vol % fiber, from 35 to 40 %) with a high oxygen content are in the range from 1500 to 1800 MPa, which are lower than those predicted by the rule of mixtures[5]. But this value was higher than those of the monolithic material (1000MPa). Not only the embrittlement of the matrix with a high oxygen content but also another factors, such as interfacial properties, would affect the tensile strengths of the spray composites.

Conclusion

In this paper, the SCS-6/SP-700 composites were manufactured by spray-winding process, and their mechanical properties were evaluated. The following conclusions were obtained.

(1) Spray composites is inferior to foil composites in the strength in both longitudinal and transverse directions, irrespective of contamination levels of matrix.
(2) From the composites processed with the fiber-winding process, cleavage fracture is observed. The composite fractures of interface between fiber and matrix vary with the manufacturing processes.

The research and development mentioned above includes research conducted under the entrustment contract with New Energy and Industrial Technology Development Organization (NEDO), as a part of the National Research and Development Program of Agency of Industrial Science and Technology (AIST), Ministry of International Trade and Industry (MITI).

References

1. S.Mall.T.Fecke and M.A.Foringer: "Titanium Matrix Composites", Shankar Mall and Theodore Nicholas (eds.), Thecnomic Publishing Co.Inc, 1998, pp.1-11
2. Stewart.J.Veeck, George.Wolter and Jay.Jacson: Adv.Powder Metall Part Mater, NO.5, 1994, pp365-375
3."Material Properties Handbook, Titanium Alloys", pp685-692
4. C.Fujiwara, M.Yoshida, M.Matsuhama, S.Ohama: Proc.10th Int. Conf. On Composite Materials (ICCM), (1997).
5. F.Leucht and H.J.Dudek : Materials Science and Engineering, A188,1994, pp.201-210

Proceedings of 7th Japan International SAMPE
Symposium & Exhibition, Nov. 13-16, 2001

Development of Titanium Matrix Composite Rings

Takeshi YAMADA#, Akira FUKUSHIMA#, Chikara FUJIWARA#,

Masashi HIROTA#, Yukio KAWACHI# and Shinichi YAMAMOTO#

#: Research Institute of Advanced Material Gas-Generator (AMG),

1-13-4 Kitaohtsuka, Toshima-ku, Tokyo, 170-0004, Japan

E-mail: takeshi_yamada@mx.nasw.mhi.co.jp

Abstract

Titanium matrix composite (TMC) rings were fabricated by foil-fiber-foil process route using sprayed coil-preforms and titanium alloy (Ti-4.5Al-3V-2Fe-2Mo mass%; SP-700) foils. A continuous SiC fiber (SCS-6), together with a molybdenum wire as a spacer, was wound into a coil form. SP-700 powder was then sprayed on the coil to fix the fiber. After spraying, the molybdenum wire was easily removed, and the fiber spacing of sprayed coil-preforms was kept very uniform. The SCS-6/SP-700 composites were consolidated by a hot isostatic pressing at 1048K for 2 hours under an argon gas pressure of 120 MPa. It was machined to the final ring configuration. The burst strength of the TMC ring with four notches at the inside was evaluated by a spin test in a vacuum. The TMC ring was burst at 51183 rpm, which is 15% lower than the speed calculated based on the material data.

Key Words: titanium matrix composite, gas turbine, spray, spin test

Introduction

SiC fiber reinforced titanium alloy matrix composites (TMCs) are attractive for high strength application in the aerospace industries. When titanium alloy bladed rings (blings) are reinforced in the hoop direction by TMCs, about 30 to 50% weight saving can be expected for this component compared with the conventional disk and blades [1]. While a number of fabrication methods have been used for TMCs, matrix-coated-fiber (MCF) process may be the strongest candidate for TMC rings and disks manufacturing [2]. The MCF process is a new fabrication route for TMCs, which uses electron beam physical vapor deposition (EB-PVD) to pre-coat continuous SiC fiber with a thick layer of matrix alloy. They were laid-up and hot-pressed to the finished TMC. However, the coated fiber is still developing material and it is difficult to get the enough amount of the coated fiber.

In this study, sprayed coil-fiber-preforms were newly developed to fabricate a TMC ring by foil-fiber-foil process, and the burst spin test of the ring was also carried out.

Experimental Procedures

Composite Material

A continuous SiC fiber (SCS-6) and a molybdenum wire of 0.1mm diameter, as a

spacer, were wound into a coil form. Matrix alloy (Ti-4.5Al-3V-2Fe-2Mo mass%; SP-700) powder was then sprayed on the coil to fix the fiber using a low-pressure-plasma spraying. The molybdenum wire was removed after sprying. The SCS-6/SP-700 composite with 24 SiC fiber layers was fabricated by foil-fiber-foil process using the sprayed coil-preforms and SP-700 foils of 0.2mm thickness. They were consolidated by a hot isostatic pressing at 1048K for 2 hours under an Ar-gas pressure of 120MPa. It was machined to the final ring configuration, as shown in **Fig.1**. Tow TMC rings were fabricated in this study, and one was used for the spin test and the other for the cut inspection. X-ray radiographic inspection of the TMC ring was also carried out to check the reinforcement location

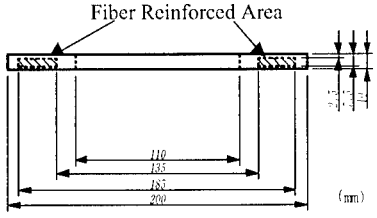

Fig.1 Dimensions of the TMC ring

Spin Test

The burst strength of the TMC ring with four notches at the inside was evaluated by a spin test in a vacuum. Notches were 4mm in depth, and they were located at the angles of 0, 90, 180 and 270 degree. The test ring was attached to an arbor disk with a drive shaft. The rotation speed and vibration of the shaft were recorded up to the burst speed.

Results and Discussions

TMC Ring Fabrication

Appearance of the sprayed coil-preform is shown in **Fig.2**. The molybdenum wire was easily removed from the preforms. The fiber spacing of sprayed coil-preforms was kept very uniform, and the average pitch of fiber was 0.2mm. **Figure 3** shows the appearance of the TMC ring fabricated in this study. The

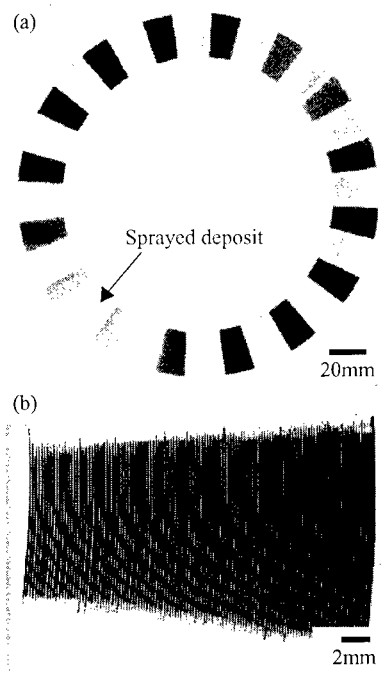

Fig.2 Sprayed coil-preform; (a) low and (b) high magnification.

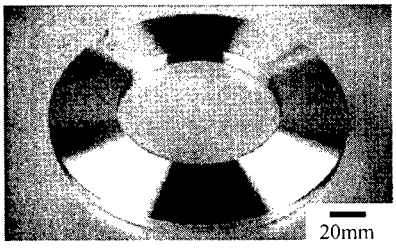

Fig.3 TMC ring model

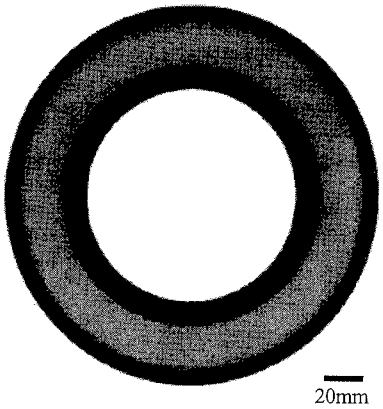

Fig.4 X-ray radiographic photograph of the TMC ring.

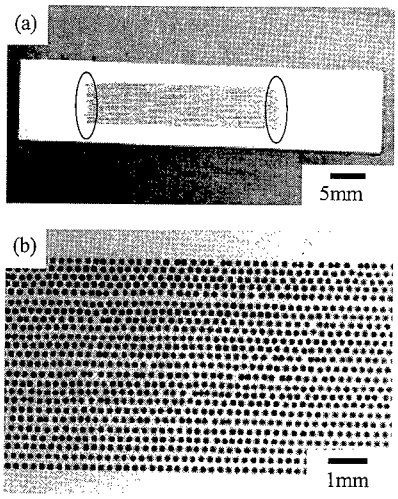

Fig.5 Cross-section of the TMC ring

TMC rings were successfully machined to the final configuration without any distortions caused by thermal residual stress. **Figure 4** shows the X-ray radiographic photograph of the TMC ring. The light-colored area in the **Fig.4** is the fiber-reinforced area. The SiC fiber position in the ring almost meats the design requirement (Fig.1), which was located in the range of the diameter from 135.9mm to 182.1mm.

While the fiber spacing in this composite ring was controlled to be almost uniform, small amount of closely spaced fibers was found, as shown in **Fig.5**. This may be due to the fibers free from the constraint of the sprayed deposit, and they may be moved by the matrix flow during the consolidation. At the inner and outer ends of the fiber-reinforced area, low fiber-volume-fraction (V_f) parts were observed in the TMC ring, as indicated by open circles in **Fig.5(a)**. It seems this can not be helped due to the process limitation of the foil-fiber-foil method. It is very difficult to place preforms with each end of the fibers strictly on the straight line along the staking direction.

Spin Test

The TMC ring burst at 51183 rpm, and it broke into 4 pieces, as shown in **Fig.6**. The primary failure occurred at the inner end of the fiber-reinforced area in the TMC ring, and many pull-out-fibers were observed at the primary fracture surface of the ring, as shown in **Fig.7**. This indicates the ring was burst due to the tensile overload in the hoop direction. Maximum stress of the ring in the

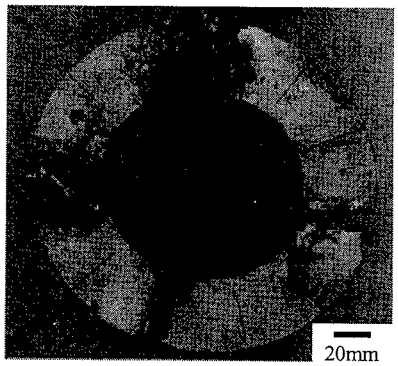

Fig.6 Burst TMC ring

rotation speed at 51183 rpm was estimated to be 1383MPa by a finite element analysis, which is 85% tensile strength of the coupon specimen with the same V_f of 33%. This degradation may be caused by the low V_f area at the inner end of fiber-reinforced area and by the multi-axis loading.

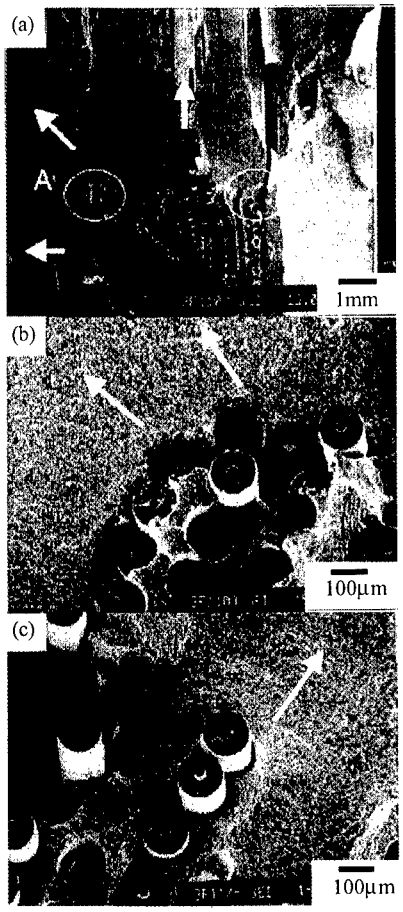

Fig.7 Fracture surface of the TMC ring: (a) primary fracture part, and close-up (b) A and (c) B area.

Conclusions

In this study sprayed coil-preforms were newly developed in order to fabricate the titanium matrix composite rings by foil-fiber-foil process, and the burst strength of the ring with four inside notches was evaluated by a spin test in a vacuum. Considering the results obtained, our conclusions are as follows.

1) The fiber spacing of the coil-preforms was kept very uniform, and the average pitch of the fiber was 0.2mm.
2) While the fiber distribution in the TMC ring was almost uniform, it was difficult to control the preform ends to be straight along the stacking direction.
3) The ring burst at 51183 rpm, which is 85% tensile strength of the coupon specimen with the same fiber volume fraction of 33%.
4) The primary fracture of the ring occurred at inner end of the fiber-reinforced area, and it was due to the tensile overload in the hoop direction.

Acknowledgment

The authors are grateful to Mr. M.Senda and Mr. A.Kono, Mitsubishi Heavy Industries, Ltd., Mr. M.Terasawa and Mr. Y.Azuma, Churyo Engineering Co. Ltd., and Mr. T.Nakao and Mr. K.Kondo, Tamagawa Engineering Co. Ltd. for helpful discussions and technical support.

References

1. S.Mall and T.Nicholas (eds.): *"Titanium Matrix Composites"*, TECHNOMIC, Lancaster, PA, 1998, pp.1-23.
2. C.M.Ward-Close et al.: Mater. Sci. Eng., A263, 314 (1999).

Proceedings of 7th Japan International SAMPE
Symposium & Exhibition, Nov. 13-16, 2001

Development of Aluminum MMCs Brake Rotor by Pressure-less Metal Infiltration Process

Heishiro Takahashi#, Hisao Kamii#, Satoshi Chonabayashi#, Takehisa Inoue#

#Joint Development Center by Taiheiyo Cement Co., Ltd. & Akebono Brake Ind. Co., Ltd.
c/o CTC of Taiheiyo Cement Co., Ltd., 〒360-8566 5310 Mikajiri Kumagaya-City, Saitama Pref.
E-mail: heishirou_takahashi@taiheiyo-cement.co.jp

Abstract

Aluminum Metal Matrix Composites (hereinafter referred to as MMCs) are developed by various production methods such as Molten metal infiltration process, Powder metallurgy process, Casting process, Hot pressure welding process and so forth, depending on its usage. If a pressure-less metal infiltration process (PRIMEX™ Process) is used, MMCs with a high volume fraction of a reinforcement material can be produced, which have less segregation of a reinforcement material and give a high cost performance. MMCs (which is the reinforcement material with volume fraction of 37Vf(%) produced by pressure-less metal infiltration process belonging to the category of Molten metal infiltration process) is superior in the mechanical properties such as thermal resistance, wear resistance, etc. As a result of performance evaluation testing on MMCs rotor, rotor wear has been found small with good brake effectiveness stability.

In conclusion, there has come out a possibility of putting MMCs into practical use.

Key-word : Pressure-less Metal Infiltration Process

Introduction:

This technology is what AKN Ltd. introduced from Lanxide in U.S.A., and Taiheiyo Cement, AKN's parent Co. and Akebono Brake Ind. are now jointly making an application development to brake parts. This time, we produced MMCs by the pressure-less metal infiltration process evaluated material characteristics and performance of rotor.

Testing Methods:

The powder of Al_2O_3 was used as ceramics for reinforcement in consideration of thermal resistance. By press-forming the powder of Al_2O_3, a preform was produced. After heating a preform in a nitric atmosphere and infiltrating aluminum, we cooled and processed to various test pieces, and evaluated material characteristics.

In the meantime, we produced a brake rotor in the same way and conducted performance evaluation.

(1) Evaluation of MMCs material characteristics

Various test pieces being made, organizational

observation and evaluation of mechanical characteristics were performed.

As comparison materials, FC－200 (hereinafter referred to as FC), SiC 20vf(%)MMCs (hereinafter as SiC—MMCs), and AC4C (hereinafter as AC4C) were selected and the same evaluation was conducted.

(2) Performance evaluation of rotor

Fig.1 shows the disc rotor we produced. By our dynamo testing machine, rotor performance, thermal resistance (on occurrence of scoring) and stabilization of effectiveness were checked and confirmed. Also, we conducted car testing for a final evaluation purpose.

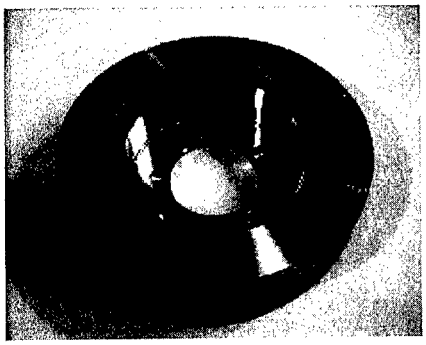

Fig.1 MMC s Disk-Rotor

Test Results:

(1) Material characteristics of MMCs

Material characteristics are shown in Table-1. The density of MMCs is a little bit at higher side as compared with SiC—MMCs and AC4C, but is less than half of FC. The thermal conductivity of the same is higher than FC.

Fig.2 shows the result of elastic modulus. When a reinforcement material exceeds 20vf(%), it was found that MMCs' elastic modulus becomes higher than FC. For Al_2O_3 37vf(%)MMCs, its elastic modulus was 130Gpa.

A disc rotor has a repetitive action of heating and cooling. Fig. 3 shows tensile strength and elongation of MMCs at room temperature after experiencing high temperature. SiC－MMCs lowered strength after heating at 400℃ for 5 hours, but the material in question did not show any change of strength.

From the above results, tensile strength and elastic modulus were found over FC, and we selected MMCs with Al_2O_3 fraction volume 37vf(%) and with stabilized strength after high temperature history.

(On the material in question hereunder)

Fig. 4 shows a microscopic photo of fine structure. The material shows an aluminum infiltrated condition into fine parts.

Table.2 MMCs Mechanical Property

Items	The Material	FC200	SiC -MMCs	AC4C-T6
Density (g/cm³)	3.14	7.10	2.80	2.68
Elastic Modulus (GPa)	130	95～120	81	74
Tensile Strength (MPa)※1	269	230	254	280
CTE (10^{-6}/℃)※2	17.4	11.7	17.5	21.5
Thermal Conductivity (W/mk)※2	86.2	52.3	160.0	159
Specific Heat (J/gK)	0.83	0.51	0.83	0.88
Fatigue strength (MPa)	115	—	105	130

※1.Thermal Condition:25℃

※2.Thermal Condition.:25～300℃

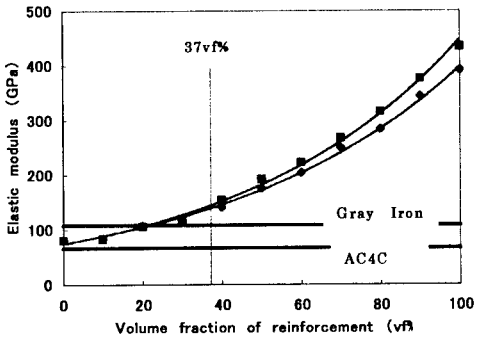

Fig.2 Coefficient of Expansion

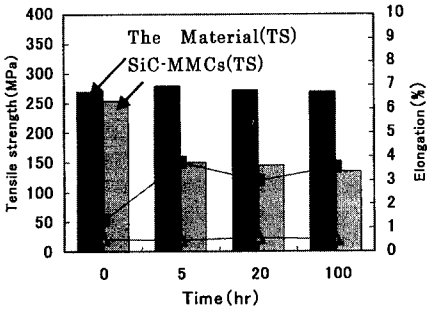

Fig.3Tensile Strength of HighThermal Hysteresis

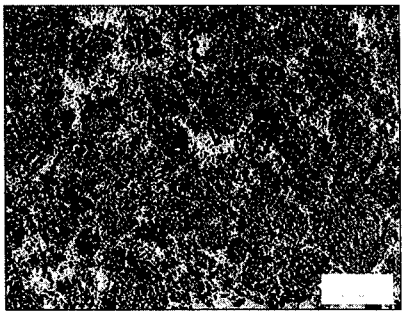

Fig4 Fine Structure 100 μ m

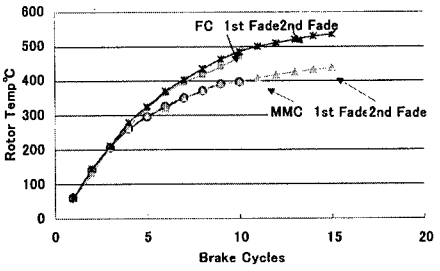

Fig.5 Rotor Temperature Change

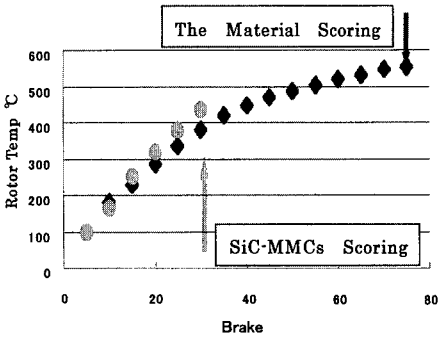

Fig.6 Scoring Test

(2) Performance evaluation of rotor

Fig. 5 shows a rotor temperature change by JASO fade test. The material was found to be nearly 100℃ lower than FC at the final temperature of No.2 fade. This is due to the thermal conductivity of the material being at high level. This result is nearly consistent to FEM analysis value, dynamo test value and car testing. Fig.6 shows thermal resistant limit by scoring test. While scoring for SiC—MMC occurred at about 450℃, the material did not cause scoring until the temperature of 100℃ higher.

Fig.7 shows the change of frictional coefficient on a friction material and rotor. The frictional coefficient of FC changed along a temperature increase, but that of the material was found to remain nearly at a same level. Fig.8 shows a wheel condition after a travel motion. FC showed some stain after running 300km, but any stain was not observed for the material even after a 4300km run.

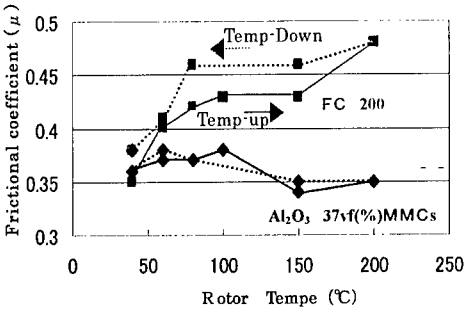

Fig.7 Change of Frictional Coefficient

Fig.8 Wheel Stain

A disc rotor was produced from the material, and as a result of performance evaluation, each evaluation item showed a good result.

Conclusion:

It is proper that Al_2O_3 fraction volume for MMCs brake rotor produced by pressure-less metal infiltration process is 37vf(%). The rotor in question is a light-weight and has a stable brake effectiveness. Its thermal resistance is restricted because of matrix being aluminum, but other characteristics are superior to conventional FC rotors, and it has been confirmed that an application to a practical car use is possible.

Proceedings of 7th Japan International SAMPE
Symposium & Exhibition, Nov. 13-16, 2001

Mechanical Properties and Microstructure of Squeeze Casting $Al_{18}B_4O_{33}w$ / Magnesium Alloy Composites

Gen Sasaki#, Makoto Yoshida# and Hideharu Fukunaga##

#: Department of Mechanical Engineering, Hiroshima University
1-4-1 Kagamiyama, Higashi-Hiroshima 739-8527, JAPAN
E-mail: gen@hiroshima-u.ac.jp
##. Kure National College of Technology
2-2-11 Aga, Kure 737-8506, JAPAN

Abstract

$Al_{18}B_4O_{33}$ whisker reinforced AZ91D (Mg-9%Al-1%Zn) and ZK60 (Mg-6%Zn-0.4%Zr) magnesium alloy composites were fabricated by squeeze casting. Some composites were fabricated under the semi-solid conditions. The low reactivity between whisker and matrices during fabrication and heat-treatment processes are caused by the formation of a stable and uniform reaction layer 20-30 nm in thickness on the whisker. These composites exhibit good strength and age hardening ability. In AZ91D matrix composites, the reaction layer is single-like crystalline $MgAl_2O_4$, which grew epitaxially on the whisker. On the other hand, in ZK60 matrix composite, the reaction layer is polycrystalline complex oxide containing Zr, Zn and Mg elements.

Key Words: Composite, Magnesium alloy, Aluminum borate, Interfacial layer, Aging behavior, Bending strength

Introduction

Recently, magnesium alloys are great watched as the next generation lightweight materials. However, the mechanical properties of magnesium alloys at room and high temperature is lower than that of practical aluminum and titanium alloys. In order to improve the properties of magnesium alloys, the combination with the ceramics reinforcement is effective. Especially, SiC, Al_2O_3 and carbon have been attempted for the reinforcement of magnesium alloy [1-3]. Recently, it is found that $Al_{18}B_4O_{33}$ whisker has good mechanical properties and is effective for the reinforcement of many aluminum alloys. But this whisker reacts with aluminum-magnesium alloys at the interface during the fabrication and the heat-treatment [4]. The mechanical properties of the composites are affected by the interfacial structure, strongly. But the interfacial reaction between $Al_{18}B_4O_{33}$ whisker and practical magnesium alloys and the effect to the mechanical properties has still unknown. In this study, the effect of the mechanical properties and the interfacial structure for the fabrication condition in AZ91D and ZK60 magnesium matrix composites were investigated.

Experimental Procedure

The reinforcement is $Al_{18}B_4O_{33}$ whisker (Shikoku Chemicals Co. Type M-20) with 0.5-1μm in diameter and 10-20μm in length. Matrices are AZ91D and ZK60 magnesium

alloys. The composition of AZ91D and ZK60 are Mg-9%Al-1%Zn and Mg-6%Zn- 0.4%Zr, respectively. Whisker preform was fabricated by the sintering of the whisker under the condition of 850°C for 1h. The composites were fabricated by the squeeze casting under the conditions of preform preheating temperature: 200 °C, die temperature: 700°C, molten alloy temperature: 570-840 °C and squeeze pressure: 50-160 MPa. Some AZ91D matrix composites were fabricated under the semi-solid condition (solid fraction (fs): 50%). The bending strength and the aging behavior were estimated. Microstructure and interfacial structure in the composites were observed by SEM (Topcon/ SM-520) and TEM (JEOL/JEM-4000EX and 3010).

Result and Discussions

Mechanical Properties

Table 1 shows the bending strength of the composites. Composites have higher strength than the monolithic alloys. These composites have good strength for practical use. The bending strength of AZ91D monolithic alloy could not be estimated because of high plastic deformation. In AZ91D matrix composite, the strength of the composites fabricated by the molten alloy (fs=0%) is higher than that of the semi-solid condition (fs=50%). The degradation of the strength is caused by the fracture of the whisker in preform during the squeeze casting. In actual, the mean whisker length in preform before casting, in composites after 0%fs casting and 50%fs casting is 12.08, 8.28 and 5.24 μm, respectively. The whisker shortened by the high pressure of squeeze casting. The strength and the whisker length in 50%fs as-cast composites were low and short.

Fig. 1 shows the aging behavior of AZ91D monolithic alloy and composite fabricated under the condition of 0 and

Table1 Bending strength of $Al_{18}B_4O_{33}$ whisker / AZ91D and ZK60 alloy composites.

Matrix	AZ91D			ZK60	
	Monolithic	Composite		Monolithic	Composite
Solid fraction (fs%)	0	0	50	0	0
Bending Strength (MPa)	(165)*	564	518	605	675

(* Tensile strength of as-cast alloy)

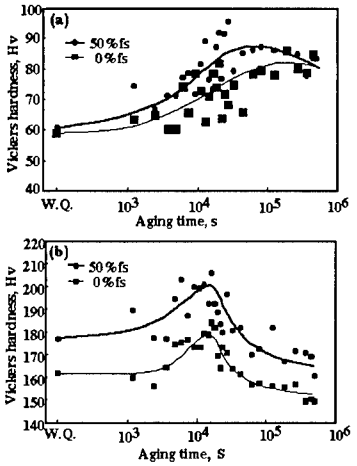

Fig.1 Age hardening curves of (a) monolithic AZ91D alloy and (b) $Al_{18}B_4O_{33}$ whisker/AZ91D alloy composites.

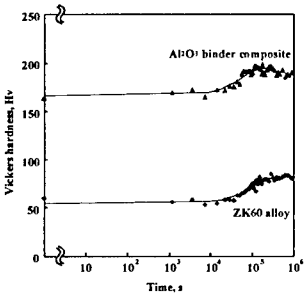

Fig.2 Age hardening curves of monolithic ZK60 alloy and $Al_{18}B_4O_{33}$ whisker/ZK60 alloy composite.

50%fs. Both of the monolithic alloy and composite shows the obvious good aging behavior. Hardness of 50%fs composite is higher than that of 0%fs composite. As liquid phase penetrate preferentially into the preform during squeeze casting process, the composites has many post liquid phase (β phase, $Mg_{17}Al_{12}$) in the matrix. Consequently, 50%fs composite shows high hardness because of high hardness of β phase. The reach time to highest hardness of the composites is faster than that the monolithic alloy. This is caused by the stress around the interface between the reinforcement and the matrix. This is the conventional phenomenon for many composites.

Fig. 2 shows the aging behavior of ZK60 monolithic alloy and composites. The composite shows good aging behavior. But the reach time to highest hardness of the composites is same as that of the monolithic alloy.

Microstructure

(a) AZ91D matrix composite

Fig. 3 shows the high-resolution TEM image of the interface between $Al_{18}B_4O_{33}$ whisker and AZ91D matrix in as-cast composites. There is a uniform reaction layer between $Al_{18}B_4O_{33}$ whisker and magnesium with a thickness of 20-30nm. The reaction layer is $MgAl_2O_4$ with spinel structure and covered with the whisker completely. $MgAl_2O_4$ layer grew on the whisker epitaxially.

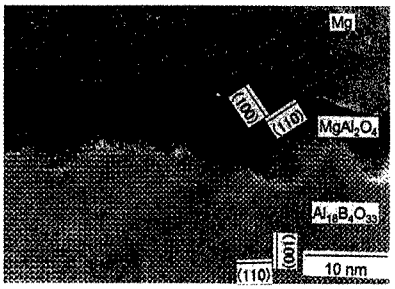

Fig. 3 Microstructure of the interface between $Al_{18}B_4O_{33}$ whisker and matrix.

Fig 4 is the extracted whisker from the composites. Fig.4 (a) shows the whisker from as-cast composite. The whisker surface is very clear and smooth, which is same as the as-received whisker. The interfacial reaction during squeeze casting is very little. Fig. 4 (b) shows the whisker from the heat-treated composites at 700 °C for 1h, which is the molten condition of matrix alloy. The whisker surface becomes to roughen with small irregularities. But this roughness is very flat compared with the magnesium contained aluminum alloy matrix composites [5]. It seems that the uniform reaction layer prevents a further reaction of the whisker with the matrix. In actual, the degradation of the strength of the heat-treated composites was not observed and the heat-stability of this composite is very good [6].

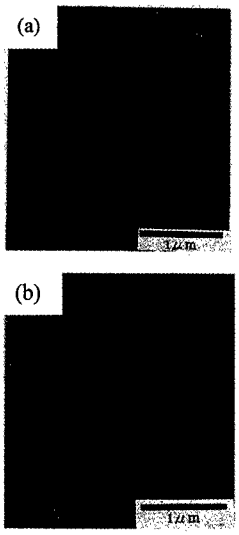

Fig.4 Extracted whisker from $Al_{18}B_4O_{33}$ whisker/ AZ91D matrix composites prepared by squeeze casting. (a) As-cast and (b) heat- treated at 700°C for 1h.

(b) ZK60 matrix composite

Fig. 5 is the extracted whisker from as-cast $Al_{18}B_4O_{33}$ whisker/ ZK60 matrix composites. The whisker surface is very clear and smooth but has little irregularities. Fig. 6 is the microstructure and EDS analysis around the interface between whisker and matrix in composite. There is an interfacial reaction layer, which covered with the whisker completely. This layer forms polycrystalline of complex oxide containing Zr, Zn and Mg elements. But the phase of this layer could not be identified. This layer prevents the direct reaction between the whisker and the matrix during fabrication and heat-treatment process. If the many interfacial reaction layer are produced by long fabrication and heat-treatment process times, it seems that the strength and age hardening behavior of the composites decreases because of consumption of Zn element in the matrix by the interfacial reaction. This composite is not stable compared with AZ91D matrix composites.

Fig. 5 Extracted whisker from as-cast $Al_{18}B_4O_{33}$ whisker/ ZK60 alloy matrix composite.

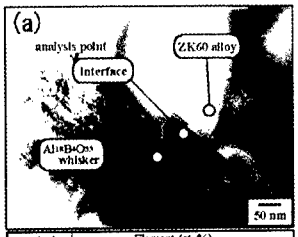

Analysis point	Element (at. %) Al	Mg	O	Zn	Zr
$Al_{18}B_4O_{33}$ whisker	45.54	5.46	49.00	0.00	0.00
interface	13.93	41.80	15.99	7.05	21.24
ZK60 alloy	0.55	90.11	7.20	0.01	2.12

Fig. 6 TEM image and EDS analysis of the interface in $Al_{18}B_4O_{33}$ whisker/ ZK60 alloy composite.

Conclusions

$Al_{18}B_4O_{33}$ whisker/ AZ91D and ZK60 alloy composites were fabricated by squeeze casting. The relationship between mechanical properties and interfacial reaction was investigated.

(1) Both composites have good strength and age hardening behavior. Only AZ91D matrix composite shows the shortening of peak hardening time.

(2) Both composites show the interfacial reaction at fabrication process. The whisker was covered with 20-30 nm interfacial layers in thickness, completely. As this layer prevents the direct reaction between whisker and matrix, the mechanical properties of composites has stable at high temperature.

References

1. D. M. Lee, B. K. Suh, B. G. Kim and C. H. Lee: Mat. Sci. Tech., 13, 590 (1997).
2. K. Kaneda, T. Choh: J. Jpn. Inst. Light Metals, 46, 321 (1996).
3. J. Kiehn, E. Bohn and K. U. Kainer: Key Eng. Mat., 127-131, 861 (1997)
4. K. Suganuma, T. Fujita, G. Sasaki and N. Suzuki: J. Jpn. Inst. Light Metals, 41, 270 (1991).
5. G. Sasaki, L. J. Yao, M. Yoshida, J. Pan, H. Fukunaga: J. Jpn. Inst. Metals 63,5, 577(1999)
6. G. Sasaki, M. Yoshida, J. Pan, N. Fuyama, T. Fujii and H. Fukunaga: Mat. Sci. Forum 350-351, 215 (2000)

Proceedings of 7th Japan International SAMPE
Symposium & Exhibition, Nov. 13-16, 2001

High Strain Rate Superplasticity of TiN Particulate Reinforced Aluminum Composites

Tsunemichi Imai#, Liang Zhen## and Makoto Takagi###

#: National Institute of Advanced Industrial Science & Technology, Nagoya, 462-8510, Japan
E-mail:ts-imai@aist.go.jp
#:Harbin Institute of Technology, Harbin, China 150001
###:Aichi Institute of Technology

Abstract

High strain rate superplasticity (HSRS) is an efficiently near-net shape forming to apply metal matrix composites (MMC) to automobile components, semi-conductor packing, structures in aerospace industry and even for housings in IT industry . The objectives of this study is to investigate the effect of matrix alloy elements on the HSRS in TiN particulate reinforced aluminum composites and to discuss the superplastic deformation mechanism of the HSRS composite. TiN/1N90 produced a m value of about0.4 and total elongation of 200% at strain rate of about $10^{-2}s^{-1}$ and at 928K which is below liquid temperature of 1N90 pure aluminum. And TiN/2014 and TiN/2017 Al composite with Vf = 0.15 exhibited a m value of about 0.4 at strain rates higher than $10^{-1}s^{-1}$ and maximum tensile elongation of about 200~350% at a strain rate of about $3x10^{-1}s^{-1}$ at 818k which was above the solid temperature of matrix. However, the total elongation of the TiN/2014 is larger than that of the TiN/2017 and amount of Mg included to 2014Al is larger than that of 2017Al so that Mg is thought to have an effect on total elongation of TiN/Al composites. However, TiN/Al-1Mg indicates the total elongation less than 100% which means that 1wt%Mg has not positive effect on improving total elongation of TiN/Al composites.

Key Words: TiN, Aluminum composites, Superplasticicty.

INTRODUCTION

High strain rate superplasticity (HSRS) of metal matrix composites (MMC) has a great potential to establish an efficiently near-net shape forming for automobile components and semi-conductor packing structures in aerospace, since the HSRS is usually associated with lower flow stress and total elongation of 250~600% at high strain rates of 10^{-2}~$10s^{-1}$[1-13]. Deformation mechanism of the HSRS should be different from the mechanism of conventional superplastic materials since the strain rate at which the HSRS occurs is 10~1000 times higher than the conventional one and the optimum temperature at which the maximum elongation is obtained is near or just above the solid temperature of aluminum matrix. Although it has been pointed out that the primary deformation mechanisms of the HSRS materials are grain boundary sliding and interfacial sliding involving a liquid phase, phenomenon of the HSRS is affected by factors such as the grain size, the interface structure and so on. But how interface structure could affect to the HSRS has not yet been understood entirely. The objectives of this study is to investigate the effect of aluminum alloy elements on the HSRS in TiN/aluminum alloys composites and to discuss the superplastic deformation mechanism of the HSRS composite.

TiN particles(average size=1μm) were used as the reinforced material. Volume fraction of TiN is V_f=0.15. 2014Al、2017Al, 1N90 pure and Al-1Mg were used as matrix. Table 1 shows chemical compositions of these aluminum powders used.

The TIN/Al composites were sintered under

Materials	Cu	Fe	Si	Mn	Mg	Zn	Al
2014*	4.38	0.24	0.05	0.6	1.5	0.01	93.61
2017*	3.84	0.03	0.56	0.64	0.58		94.35
1N90**	6	43	41	5	3	17	99.98
Al-1Mg*	0.12	0.49	0.36	0	1.04	0.02	97.97

**:ppm, *:wt%

a pressure of 200 MPa at 773K for 20min and then extruded with an extrusion ratio of 100 at 773K. Hot rolling after extrusion was also used to build fine grain size and to make reinforcement dispersed uniformly. Tensile specimens with a 4 mm width and about 15mm gage length were made. Specimens were pulled at 773~ 928K and at strain rates ranging from $1x10^{-3}$ to $2s^{-1}$. Microstructures and fracture surfaces were examined by SEM.

EXPERIMENTAL RESULTS AND DISCUSSION

HSRS of TiN/1N90

Sherby et al proposed a deformation model of the HSRS in which fine grains with high angle boundaries and subgrains near the grain boundaries contribute to grain boundary silding. 1N90 pure aluminum made by powder metallurgical method. which produced a m value of 0.3~0.45 and total elongation of 300~450% at strain rate of about $10^{-2}s^{-1}$ consisted of fine grain of 10~20μm and subgrain of 1~2μm . It is, therefore, thought that the superplastic characteristics of 1N90 could support the deformation model in which the constitutive equation is expressed as follow

$$\dot{\varepsilon} = k(D_l/L\lambda^2)((\sigma-\sigma_0)^n \qquad (1)$$

where $\dot{\varepsilon}$ is the strain rate, k is a materials constant, D_l is the lattice diffusion coefficient, L is the grain size with high angle grain boundaries, λ is the subgrain size, σ is the flow stress, σ_0 is threshold stress and n is the stress factor (n = 1/m).

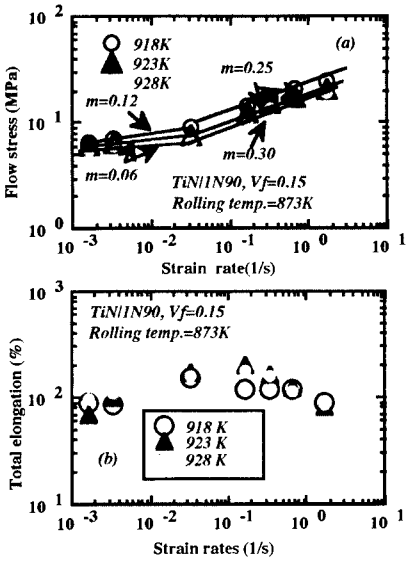

Figs. 1 Superplastic characteristics of TiN/1N90 Al composites

Fig.1 shows relationship between total elongation and strain rate of TiN/1N90 pure Al composites hot-rolled after extrusion. TiN/1N90 deformed at 918, 923 and 928K indicated m value of about 0.3 at the strain rate higher than $3x10^{-2}s^{-1}$. And maximum total elongation of about 200% is obtained at the strain rate of $2x10^{-1}s^{-1}$ at 923K and 928K which is just below the melting temperature of pure 1N90 aluminum. Apparent activation energy of TiN/1N90 is estimated to be 730~760 KJ/mol in temperature range from 918K to 928K which is higher than activation energy, 142KJ/mol, of pure aluminum. The TiN/1N90 could produce HSRS(High Strain Rate Superplasticity).

HSRS of TIN/2014 Al composites

The superplastic characteristics of the TiN/2014 Al composite with Vf = 0.15 are shown in Figs.2 as a function of testing

The superplastic characteristics of the TiN/2014 Al composite with Vf = 0.15 are shown in Figs.2 as a function of testing temperature. The composite deformed at 798 and 818K exhibits m value of about 0.37 at strain rates higher than $4x10^{-2}s^{-1}$, although the m value of about 0.24 at 773K and lower m value of about 0.15 in the strain rate less than $2x10^{-2}s^{-1}$ are obtained. Maximum tensile elongation of about 370% of the composite was obtained at a strain rate of about $3x10^{-1}s^{-1}$ at 818k which was

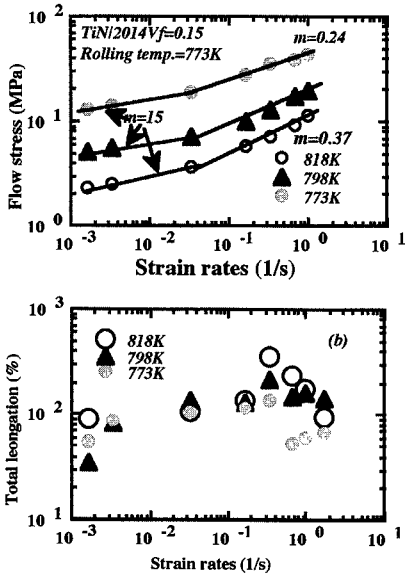

Figs. 2 Superplastic characteristics of the TIN/2014 composite

above the solid temperature of 2014 Al matrix. The results indicate that TiN/2014 produced high strain rate superplasticity (HSRS).

Fig.2 indicates superplastic characteristics of the TIN/2017 composite. m value of about 0.20 in the TIN/2017 composite is obtained in the strain rate range less than $10^{-1}s^{-1}$ and the temperature of 773~838K and the composites indicates m value of 0.3~0.34 in the strain rate range more than $10^{-1}s^{-1}$.

However, maximum total elongation of about 200% is shown at the strain rate of about $4x10^{-2}s^{-1}$ and at 818K which is lower as compared with one of 370% in the TiN/2014 Al composite. The apparent activation energy of TiN/2014 is 424~618KJ/mol in the temperature range of

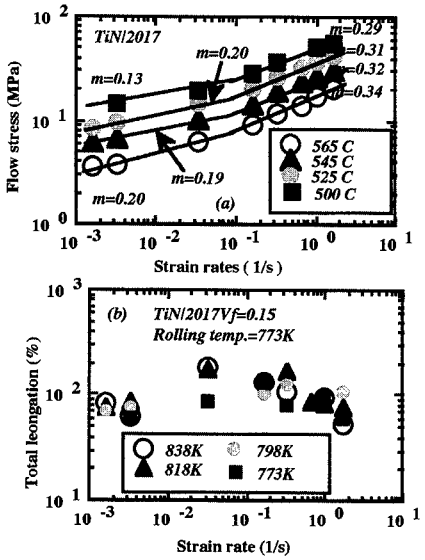

Fig.3 Superplastic characteristics of TiN/2017 composite

773~818K. On the other hand, activation energy of the TiN/2017 is 216~409KJ/mol. Amount of Mg included in 2014 aluminum is larger than those of 2017 Al so that Mg might have a positive effect on HSRS. Therefore, superplastic characteristics of TiN/Al-1Mg composite is investigated.

HSRS of TiN/Al-1Mg Al composites

The strain rate sensitivity value, m, of the TiN/Al-1Mg composite pulled at 853 and 873K became 0.24~0.27 in the strain rate more than $10^{-1}s^{-1}$, but the m value in the composite deformed at 893K indicates about 0.36. Total elongation of the

activation energy of TiN/Al-1Mg composite is estimated to be 207~346KJ/mol which is lower activation energy as compared with those of TiN/1N90, TiN/2014 and TiN/2017 Al composites.

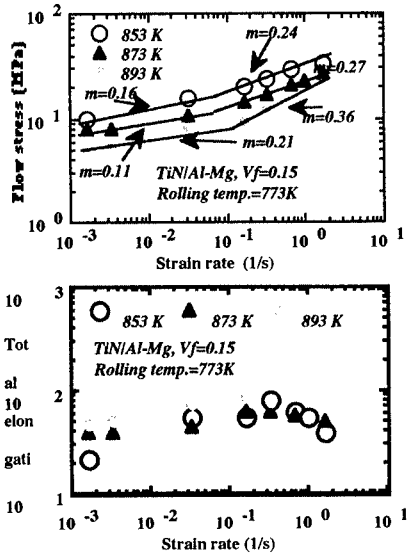

Fig.4 Superplastic characteristics of TiN/2Al-1Mg composite

CONCLUSIONS

Superplastic characteristics of TiN/1N90 pure aluminum, TiN/2014, TiN/2017 and TiN/Al-1Mg aluminum composite hot-rolled after extrusion, were investigated. The following results were obtained:

(1)TiN/1N90 shows m value of about 0.3 in the strain rate more than $3x10^{-2}s^{-1}$ and total elongation of 200% at strain rate of about $10^{-1}s^{-1}$ and at 923K ~ 928K.

(2)TiN/2014 Al composite indicates the m value of about 0.37 in the strain rate range more than $10^{-1}s^{-1}$ and in temperature of 798~818K. And also maximum tensile elongation of about 370% is obtained at the strain rate of about $10^{-1}s^{-1}$ and at 818K

(3) TiN/2017 Al composites indicate the same m value as that of TiN/2014 al composites but total elongation obtained is about 200%.

(4)TiN/Al-1Mg composite indicates a total elongation of about 100% at the strain rate of $10^{-1}s^{-1}$ and at 853~893K.

REFERENCES

1.T.G.Nieh, C.A.Henshall and J.Wadsworth, Scripta Metall. et Mat., 18(1984) 1405

2.T.Imai, M.Mabuchi, Y.Tozawa and M. Yamada, J.Mat.Sci.letters 9(1990) 255

3.M.Mabuchi,T.Imai,K.Kubo,H.Higashi,Y. Obada and T.Tanimura, Materials Letters, 11(1991)339

4.T.Imai, G.L'Esperance & B.D.Hong, Scripta Metall. et Mat., 31-3(1994)321

5.M.Mabuchi, K.Higashi, Y.Okada, S. Tanimura , T.Imai and K.Kubo, Scripta Metall. et Mat. 25 (1991)2517

6.T. Imai, G.L'Esperance, B.D.Hong & J.Kusui, in Proceedings of ECCM-6 , Edited by A.R.Bunsell, A.K.Kelly & A.Massianh,(Woodhead Publishing Limited 1993) P.533

7.T.G.Nieh, T.Imai, J.Wadsworth and S.Kojima, Scripta Metall. et Mat., 31-12 (1994)1685

8.T.Imai,G.L'Esperance,B.D.Hongand S.Kojima, Scripta Metall. et Mat., 31-3 (1995)1333

9. I.Tochigi, T.Imai andK.Ai, Scripta Metall. et Mat., 32-11(1995)1801

10.M.Kon, J.Kaneko and M.Sugamata, J.Japan STP, 35(1994)823

11.H.Xiaoxu, L.Qing, Ciki Yao and Y.Mei, J.Mat. Scie. Letters, 10(1991)964

12. J.Pilling, Scripta Metall.,13(1989)1375

13.T.Hikosaka,T.Imai,T.G.Nieh and J. Wadsworth, Scripta Metall. et Mat., 31-9 (1994) 1181

Proceedings of 7th Japan International SAMPE
Symposium & Exhibition, Nov. 13-16, 2001

Application of Intermetallic Compounds Parts by Spark Plasma Sintering Process of Cu-Al Elemental Metal Powders

Tamotsu Nakamura#, Shigekazu Tanaka#, Kunio Hayakawa#,
Haruki Imaizumi# and Hideki Kawaguchi#

#: Shizuoka University, Faculty of Engineering, Department of Mechanical Engineering
3-5-1 Johoku, Hamamatsu, 432-8561, JAPAN
E-mail: tmtnaka@ipc.shizuoka.ac.jp

Abstract

The powder mixtures of Cu-33at%Al were milled by a mechanical alloying (MA) process, and the mechanical-alloyed powder mixtures were sintered using the spark plasma sintering (SPS) process at a heating temperature 800°C during 9 minutes under punch pressure 50MPa. It has been confirmed that the sintered parts have excellent mechanical properties, for example, the relative density is 100 %, the hardness *HV* is more than 700, and the compressive fracture strength is more than 1GPa. Some parts with different geometries have been sintered by the SPS process of Cu-33at%Al and the tribological characteristics have been investigated for considering some application to dies of forming processes.

Key Words: Intermetallic Compounds, Spark Plasma Sintering, Cu-Al Powders, Forming Dies

Introduction

Intermetallic compounds are attractive materials with excellent potential for use at elevated temperatures. However, the major problems limiting its use for structural components are low elongation in tension and impact toughness at a low temperature and so poor workability and formability. The intermetallic compounds are considered to be more useful in practical applications, if various parts including intermetallic compounds could be manufactured by a near net shape processing such as a powder metallurgical process.

The authors have developed a new near net shape manufacturing process of parts including intermetallic compounds by a spark plasma sintering (SPS) process. It has been confirmed in the previous reports [1-5] that Cu-Al or Ti-Al elemental powders can be sintered with chemical reaction and some parts including intermetallic compounds can be manufactured and the sintered parts have excellent mechanical properties, for example, the relative density is 100 %, the hardness *HV* is more than 700, and the compressive fracture strength is more than 1GPa.

In the present paper, some parts with different geometries are tried to manufacture by the SPS process of Cu-33at%Al and the tribological characteristics are investigated for some applications to dies of forming processes.

Experimental Procedures

Table 1 shows the chemical composition of the copper and the aluminum pow-

ders used. The copper powder used is an electrolytic precipitation powder of a commercially pure copper, and occurs irregularly shaped agglomerates with size of -100 mesh (less than 150 μm). The aluminum powder used was produced by an atomization process of a commercially pure aluminum and is nodular shape with size of -100 mesh (less than 150μm).

The powder mixture of Cu-33at%Al mixed simply were milled by a mechanical alloying (MA) process during 24 hours under the conditions with the frequency 10.5Hz and the ball to powder weight ratio 20 using a cylindrical ball-mill. The average particle diameter of the mechanical alloyed powder was about 20~50 μm.

Figure 1 shows a principle scheme of the spark plasma sintering (SPS) process. The powder mixtures are sintered directly by a resistant heating and a phenomenon of microscopic electric discharge between the particles under a punch pressure in a graphite die. The sintering is carried out at a temperature T = 800°C during 9 minutes under the punch pressure p = 50MPa and the degree of vacuum about 10^{-2}Torr. It has been confirmed in the previous paper [1-5] that the billets sintered under the conditions include intermetallic compounds Cu_9Al_4 and CuAl.

Table1 Chemical composition of elemental metal powders used

(a) Copper

Elements	Cu	Pb	Ag	Si	S
wt%	99.5	0.057	0.002	0.01	0.001

(b) Aluminum

Elements	Al	Si	Fe	Cu	Cu+V	Oth
wt%	99.79	0.06	0.15	tr	tr	tr

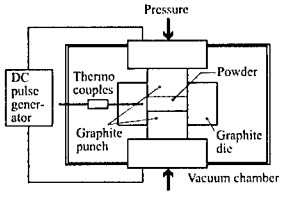

Fig.1 Principle scheme of spark plasma sintering (SPS) process

Figure 2 shows four kinds of billets with various geometries which are sintered using the different punches made of graphite as shown in **Figure 3**.

Effect of Height on Hardness of Billets

Figure 4 shows the effect of the billet (A) height h and lubrication at the die on the Vickers hardness HV. In the case without lubricant at the die, the hardness HV keeps constant high values about 760 until h = 10mm, but reduces to 650 at h = 15mm. However, HV keeps about 760 until h = 15mm when the inner surface of the die was lubricated by a Boron-Nitride (BN).

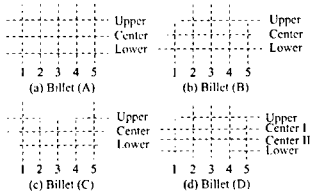

Fig.2 Four type of billets with different geometries

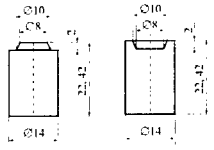

Fig.3 Punch geometries

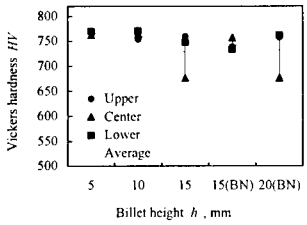

Fig.4 Effects of billet heights and lubrication at die on Vickers hardness

Effect of Lubrication at Punches on HV

Figure 5 shows the effects of lubrication by BN at the punches on *HV* distributions of the sintered billet (B). The HV values at the central portion are lower than those at the peripheral portion of the billets in the case without any lubricant at the punches as shown in Fig.5(a), while the *HV* keeps uniform high value about 750 when the punch ends are lubricated by BN as shown in Fig.5(b). The same results were obtained in the case of the billets (C) and (D). Therefore, the powder particles can be easy to move along the punch surfaces in spite of the different reductions at the central portion and the peripheral portion when the effective lubricant are used. As a result, the uniform hardness can be obtained for different geometries of various billets.

Figure 6 shows the cross sections of the billets (B), (C) and (D) sintered with the different heights. All the billets were sintered successfully and had uniform hardness *HV* = 750 and the relative density of 100%.

Simultaneous Sintering of Twin Billets

Figure 7 shows the simultaneous sintering method of twin billets (A). **Figure 8** shows the effects of the compaction pressure p and the billet height h on *HV*. Both of the twin billets keep uniform high values of *HV* = 750 under the conditions ranging with p = 0~400MPa and h = 5~15mm.

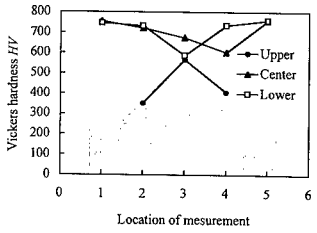

(a) No lubrication

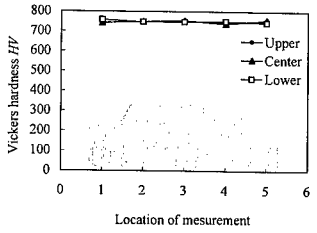

(b) Lubrication by BN

Fig.5 Effect of lubrication by BN at punch on *HV* distribution

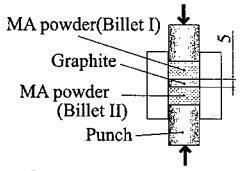

Fig.7 Simultaneous sintering method of twin billets (A)

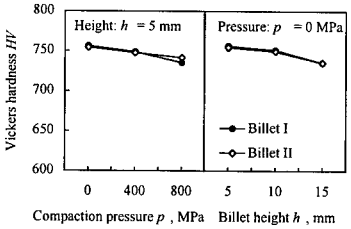

Fig.8 Effect of compaction pressure and height of billets on *HV* in simultaneous sintering of twin billets

(a) Billet (B) **(b) Billet (C)** **(c) Billet (D)**

Fig.6 Cross sections of billet sintered into various geometries with different height

Frictional Characteristics by Ring Compression Type Friction Test

Some ring compression type friction tests were carried out to investigate the frictional characteristics of the dies by the SPS process. The dies were manufactured by sintering Cu-33at%Al elemental metal powders and were built up by reinforcement as shown in **Figure 9(a)**. The test results were compared with those in the case of dies made of tool steel alloy (SKD11 in JIS). A commercially pure aluminum (A1050) and copper (C1100) were used as ring blanks as shown in **Figure 9(b)**. Three mineral oils with different viscosity VG2, VG26 and VG1000 were used as a lubricant.

Figure 10 shows the relationship between the friction coefficients and the viscosity using the different dies. All the friction coefficients are highest without lubricant and decreases with the increasing of viscosity. The friction coefficients with the Cu-Al die are a little bit lower than those with the SKD11 die in case of the aluminum blank, while the friction coefficient with the Cu-Al die is higher than those with the SKD11 in case of the copper blank.

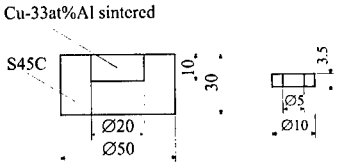

(a) Die **(b) Ring blank**

Fig.9 Die and ring blank for ring compression type friction test

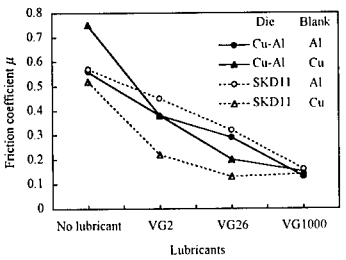

Fig.10 Variation of friction coefficient with viscosity using different dies

Conclusions

Cu-33at%Al elemental metal powders have been mechanical alloyed and sintered by the SPS process to manufacture some parts with different geometries for application to some application for dies of forming processes. As a result, the following conclusions were obtained.

1. Some billets of various geometries with different heights were sintered successfully with uniform high hardness when the dies and the punches are lubricated by Boron-Nitride (BN).
2. Twin billets were successfully manufactured with uniform high hardness by the simultaneous sintering method.
3. The friction coefficients with the Cu-Al die are a little bit lower than those with the SKD11 die in the case of aluminum blank, while the friction coefficient with the Cu-Al die is higher than those with the SKD11 in the case of copper blank.

References

1. T. Nakamura, S. Tanaka, M. Hiraiwa, H. Imaizumi, & S. Suzuki, Proceedings of 5th ICTP, (1997), pp. 323-326.
2. T. Nakamura, Proceedings of 30th ISATA , (1997), pp. 603-610.
3. T. Nakamura, S. Tanaka, K. Hayakawa, H. Imaizumi, & Y. Morita, Proceedings of 5th SAMPE, (1997), pp. 465-470.
4. T. Nakamura, Proceedings of 31st ISATA (1998), pp. 481-488.
5. T. Nakamura, S. Tanaka, K. Hayakawa, H. Imaizumi, & M. Nishimura, Proceedings of 6th SAMPE, (1999), pp. 432-437.

Proceedings of 7th Japan International SAMPE
Symposium & Exhibition, Nov. 13-16, 2001

FABRICATION OF NICKEL BASED ACTIVE COMPOSITES

H. ASANUMA and G. HAKODA
Dept. of Electronics & Mechanical Engineering, Chiba University
1-33, Yayoicho, Inage-ku, Chiba-shi, Chiba, 263-8522, Japan

ABSTRACT

This paper describes fabrication of an active composite working at high temperatures. In this study, the concept of SiC/Al active composite was applied to nickel matrix composite. In this case, SiC/Ni layer was laminated on unreinforced nickel plate with aluminum insert. Fabrication condition of this material was examined and an appropriate condition, that is, hot pressing temperature 993 K, pressure 27 MPa, time 4.8 ks in a low vacuum of 1×10^2 Pa using 0.1mm thick insert was obtained. There remained a thick interaction layer of NiAl intermetallic phase around the bonded line of this material. The curvature of this composite increases with increasing temperature up to higher than 1200 K, which shows the possibility of it as an active material working at high temperatures.

1. INTRODUCTION

In the previous papers [1, 2], CFRP prepreg as a low CTE material and aluminum plate as a high CTE material was laminated to obtain an active and light material by thermal deformation due to large CTE mismatch in the fiber direction and joule heating of the carbon fiber in the CFRP layer. In order to increase the working temperatures, a FRM based active composite, that is, a laminate of FRM plate and unreinforced matrix plate as shown in Fig. 1 was proposed [3-5].
In this paper, a nickel based active composite aiming at high temperature use was tried to be fabricated and its working temperature was investigated.

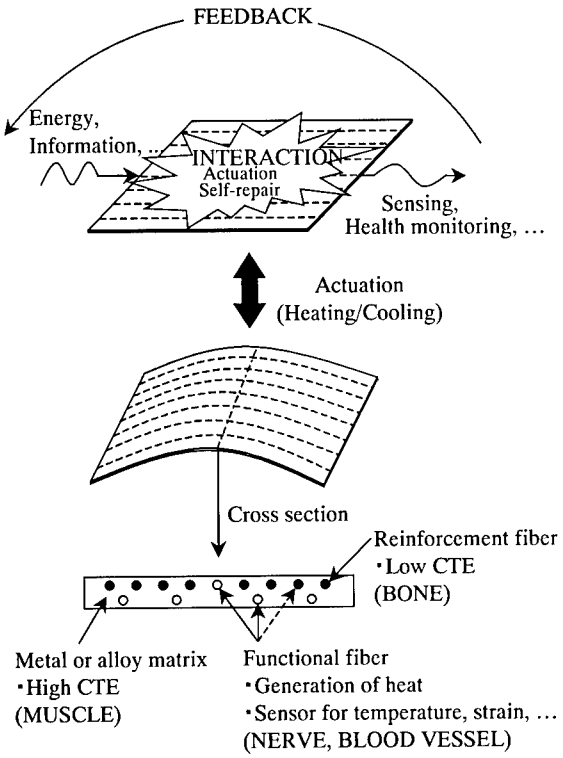

Fig. 1 A new FRM based active material.

2. EXPERIMENTAL

Nickel plates of 0.1 and 0.3mm thickness, 30mm width, 60mm length and 99.7% purity were used as matrix, and SiC fiber of 0.14mm diameter was used as reinforcement. Pure aluminum foil or plate of 0.01, 0.018 or 0.1mm thickness was used as insert. These materials were piled up as shown in Fig. 2 and it was hot pressed under various conditions.
One of successfully obtained samples was heated up from room temperature to 1273K in an electric furnace, of which shape was recorded with a digital camera for calculation of its curvature.

3. RESULTS AND DISCUSSION

The materials were bonded only when 0.1mm thick aluminum plate was used. The hot pressing condition was selected as 993K, 27MPa, 4.8ks and 1×10^2Pa, where the

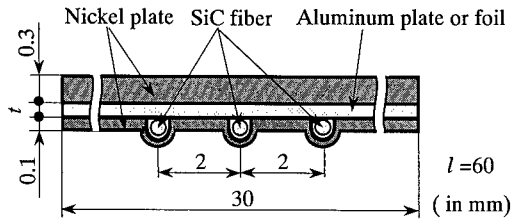

Fig. 2 Cross sections of the materials piled up for hot pressing.

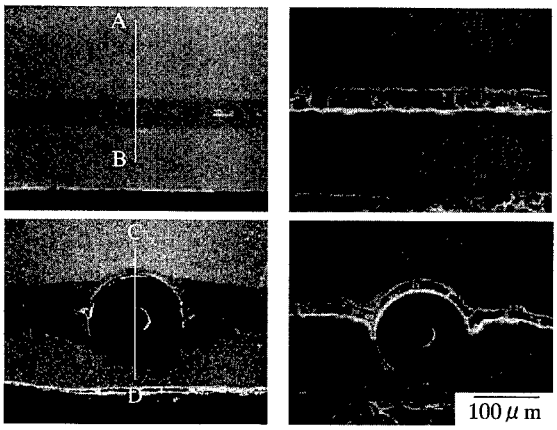

Fig. 3 SEM images of cross sections of the specimens hot pressed under (a) 993K, 27MPa, 4.8ks and (b) 973K, 16MPa, 1.2ks. The analyses lines by EPMA are indicated in figures (a).

microstructure as shown in Fig. 3(a) was obtained. In the Fig. 3(b), the microstructure obtained when hot pressed under 973K, 16MPa, 1.2ks and 1×10^{2}Pa is shown for comparison. Most of the reaction zone observed in the successful microstructure proved to consist of NiAl intermetallic phase due to the results of the EPMA line analysis as shown in Fig. 4 and XRD analysis.

A sample fabricated under the some hot pressing condition as that of the one shown in Fig. 3(a) was heated and its curvature change depending on the temperature increase was obtained as shown in Fig. 5. According to this figure, its curvature continues to increase up to the temperatures higher than 1200K and the shape drastically changes as shown in the same figure, which means that this material system has possibility to work as a high temperature active composite. Though the sample tends to have a slight curvature in the width direction, this problem is thought to be solved by development of the continuous/discontinuous fiber type active composite [6].

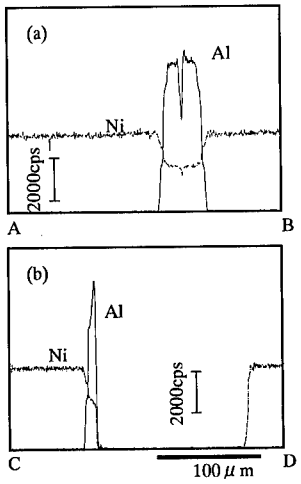

Fig. 4 Results of nickel and aluminum analyses by EPMA crossing the bondeded area (a) without and (b) with fiber as shown in Fig. 3 (a).

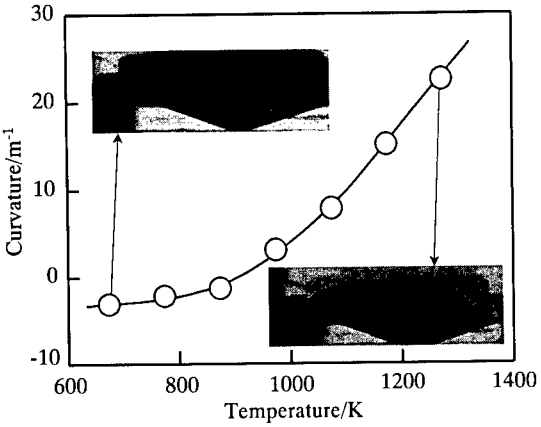

Fig. 5 Effect of temperature on curvature of the SiC/Ni active composite.

4. CONCLUSIONS

(1) The SiC/Ni active composite was successfully obtained under the hot pressing condition of 993K, 27MPa, 4.8ks and 1×10^2Pa by using an insert of 0.1mm thick aluminum plate.
(2) Its curvature continues to increase from room temperature up to the temperatures higher than 1200K and the shape drastically changes, which means that this material system has possibility to work as a high temperature active composite.

REFERECES

1. H. Asanuma et al., Proc. Japan Society for Composite Materials, 19, (1996)
2. H. Asanuma et al., 6th Materials and Processing Conference of JSME (M&P '98), 163, (1998)
3. H. Asanuma et al., Proc. 44th Intl. SAMPE Sympo., 1969, (1999)
4. H. Asanuma et al., Proc. Intl. Conf. on Smart Materials, Structures and Systems, 79, (1999)
5. H. Asanuma et al., Proc. 1999 JSME Annual Meeting, Vol. I, 375, (1999)
6. H. Asanuma et al., Proc. Mechanical Engineering Congress 2001, Vol. V, 321, (2001)

Proceedings of 7th Japan International SAMPE
Symposium & Exhibition, Nov. 13-16, 2001

Fabrication of TiB_2/Cu composites by reaction between Cu, Ti and B

Makoto Kobashi, Shinichi Yamamoto and Naoyuki Kanetake

Department of Materials Processing Engineering, School of Engineering,
Nagoya University, Nagoya 464-8603, JAPAN
E-mail: kobashi@numse.nagoya-u.ac.jp

Abstract

Copper matrix composites are gaining great interests as heat sink materials such as electronic packaging. In this study, TiB_2/Cu composites were synthesized by a reactive infiltration process. The reactive infiltration in this work makes use of;

(i) reaction between titanium and boron powders, which forms porous TiB_2

(ii) infiltration of molten Cu with synthesized porous TiB_2.

Adiabatic temperature of TiB_2 formation was controlled by adding Cu or TiB_2 powders, which absorbs the heat of reactions. When the adiabatic temperature was sufficiently controlled, TiB_2/Cu composites were successfully made, whereas the composite could not be made without controlling the adiabatic temperatures.

Key Words: Heat Sink, Combustion Reaction, Copper, Titanium Boride (TiB_2)

Introduction

Ceramic/Cu composites are regarded as a potential candidate for heat sink materials due to high thermal conductivity and controlled thermal expansion. One of the common processing routes for producing the Ceramic/Cu composite is high-pressure infiltration, in which molten Cu is forced to penetrate into the ceramic powder preform. However, this process requires special equipments to produce high pressure, and reaction at the interface is also a problem. For example, in SiC/Cu system, decomposition of SiC significantly deteriorates thermal conductivity of Cu matrix. *In situ* processing, in which the second phase is chemically formed during a fabrication process, can potentially solve the problem. In this work, *in situ* processing of TiB_2/Cu composites was investigated. Figure 1

shows the basic concept of this experiment. The blended elemental powders consisting mainly of Ti and B are compacted. The powder preform was put in a crucible and a Cu ingot was located on the preform. Then the whole specimen was heated to melt the Cu ingot and to induce reaction between Ti and B. The heat of TiB_2 formation is large enough to increase the temperature of the whole system, which results in making wettability between TiB_2 and molten Cu better. Thus, the molten Cu penetrates into the porous TiB_2 spontaneously.

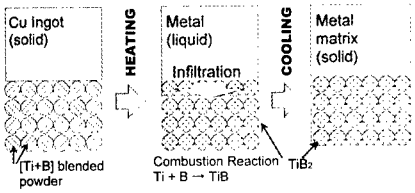

Fig 1 Basic idea of the present work

Experimental Procedure

B powder (<44μm), Ti powder (<44μm), Cu powder (<44μm) and TiB_2 (<44μm) powder were used as starting materials. The molar blending ratio of Ti and B was fixed to 1:2 (this blended powder is denoted as [Ti+2B] powder in following sections). Cu powder or TiB_2 powder was then mixed with the [Ti+2B] powder. The blending ratio of Cu or TiB_2 to the [Ti+2B] powder was varied from 30vol% to 60vol%. These powders were compacted in a cylindrical shape (15mm in diameter, 10mm in height) and located in an induction furnace with a Cu ingot (Fig.2). The specimen was heated up to 1473K in Ar gas atmosphere to make the composites. Vertical cross-sections were observed by scanning electron microscopy to identify whether the *in situ* reaction occurred.

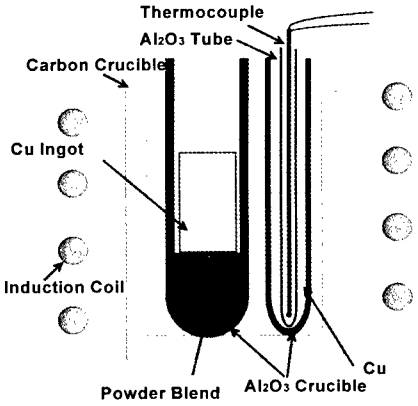

Fig.2 Experimental set-up for the infiltration experiment

Results

Combustion reaction between Ti and B

First of all, combustion synthesis of TiB_2 from [Ti+2B (with Cu addition)] powder was carried out to see if the appropriate reaction took place or not for producing TiB_2/Cu composites. Results showed that the heat of reaction between Ti and B was so high that the original shape of the blended powder compact could not be maintained when blending ratio of Cu was not sufficient. Figure 3 shows the macroscopic view of the

combustion-synthesized specimen made from (a) [Ti+2B (with 40vol%Cu)] and (b) [Ti+2B (with 50vol%Cu)]. Fig.3(a) shows that the specimen was broken into small pieces during the combustion reaction (self-breakage). However, the self-breakage was prevented by adding more than 50vol%Cu in the [Ti+2B] blended powder. The same tendency was also observed when TiB_2 powder was added in the [Ti+2B] powder.

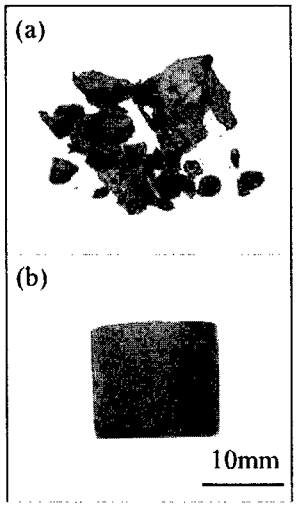

Fig.3 Macroscopic view of the combustion synthesized specimens
(a) [Ti+2B (with 40vol%Cu)]
(b) [Ti+2B (with 50vol%Cu)]

Infiltration Experiment

Three kinds of powder compacts;
(a) [Ti+2B] with 50vol%Cu (reactive)
(b) [Ti+2B] with 50vol%TiB_2 (reactive)
(c) TiB_2 (non reactive)
were applied to the infiltration experiment to identify the possibility of the spontaneous infiltration. Macroscopic views of the three specimens are shown in Fig.4. The spontaneous infiltration of molten Cu in the reactive powder phase was identified, whereas the infiltration into non-reactive TiB_2 powder phase did not take place

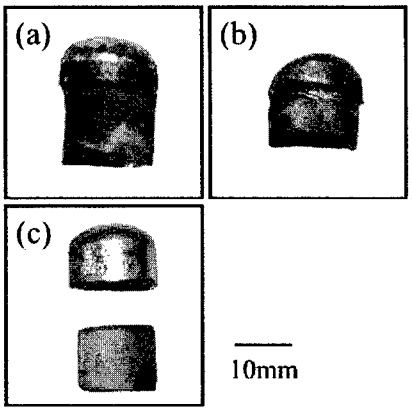

Fig.4 Macroscopic view of specimens after attempting spontaneous infiltration
(a) [Ti+2B] with 50vol%Cu (reactive)
(b) [Ti+2B] with 50vol%TiB_2 (reactive)
(c) TiB_2 (non reactive)

Microscopic Observation

Microscopic observation was carried out on cross-sections of the Cu infiltrated;
(a) [Ti+2B] with 50vol%Cu, and
(b) [Ti+2B] with 50vol%TiB_2
specimens (Fig.5 (a) and (b), respectively). X-ray diffraction analysis was carried out to identify what is synthesized by the reaction,

and X-ray peaks were observed only at appropriate angular positions of Cu and TiB_2. Dark particles in Fig.5 (a) and (b) are TiB_2 particles. Large TiB_2 (>10μm) in Fig.5 (b) is the blended powder and small (1-2μm) particles are reaction synthesized TiB_2. Thus, formation of TiB_2 was clearly identified in both specimens (no residual Ti or B was identified). Micro pore is not visible, which indicates the complete infiltration of molten Cu.

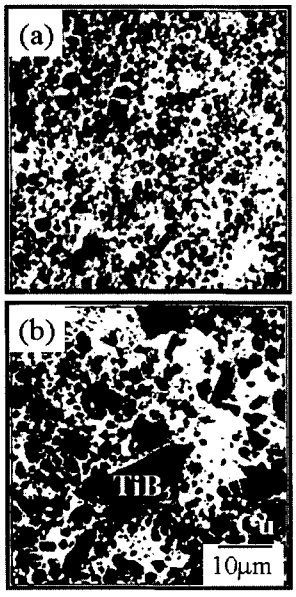

Fig.5 Cross-sections of the Cu infiltrated specimens.
(a) [Ti+2B] with 50vol%Cu
(b) [Ti+2B] with 50vol%TiB_2

Conclusions

Copper matrix composites reinforced by TiB_2 particle were synthesized using the reaction between titanium and boron. Cu or TiB_2 powder was blended with [Ti+2B] powder to make the reaction moderate.

Molten Cu infiltrated in [Ti+2B] powder compacts (with addition of appropriate amount of Cu or TiB_2 powders), whereas infiltration into non-reactive TiB_2 powder compact did not take place.

Complete conversion of Ti and B into TiB_2 was confirmed in both Cu added and TiB_2 added specimens.

Proceedings of 7th Japan International SAMPE
Symposium & Exhibition, Nov. 13-16, 2001

Surface Modification Technology for TiAl Alloys Using Reactive Plasma Process

Masahiro Inoue, Masanobu Nunogaki and Katsuaki Suganuma

The Institute of Scientific and Industrial Research, Osaka University
8-1 Mihogaoka, Ibaraki, Osaka 567-0047, JAPAN
E-mail: inoue@sanken.osaka-u.ac.jp

Abstract

The reactive plasma process with pre-irradiation of a relativistic electron beam was developed for direct surface modification of TiAl intermetallics in order to extend lifetime in several environments. The surface modified layers was successfully formed by nitridation and oxidation using this plasma process. The pre-irradiation of 20 MeV electron beam can influence the subsequent reaction behavior of TiAl with nitrogen and oxygen plasma. This plasma process is expected to apply to surface modification of the composites as well as the alloys with third elements.

Key Words: intermetallics, plasma, surface reaction, lifetime extension

Introduction

TiAl intermetallics are promising as one of the candidates for novel structural materials in aerospace and automobile industries [1]. In order to improve the mechanical properties of TiAl alloys, the microstructural control by heat treatment and the alloy design with third elements. Furthermore, the composite materials with ceramic or metallic particles and fibers have also successfully developed using skillful processes.

Although the success in improving mechanical properties of TiAl alloys, these material designs are not always sufficient for suppressing external chemical and physical damages. Therefore, the material designs for extending material's lifetime are important in order to establish practical applications of the alloys. In this situation, the surface modification techniques, which are compatibly performed with the materials designs for improving mechanical properties, are promising as an effective technology [2]. The surface modification processes are briefly divided into two categories; coating [2] and direct modification [3-5].

Recently, the present authors have developed the reactive plasma process for direct modification of metals [3,4,6] and intermetallics [5], in order to achieve lifetime extension. By using this process, the modified surface layers composed of ceramics with a compositional gradient have been successfully fabricated on these materials. This paper describes the processing details for modifying TiAl surface.

Experimental Procedure

The Ti-48at%Al alloy was fabricated by hot-pressing a commercial alloying powder (Kyouritsu Ceramic Materials Co., Ltd.) in vacuum. Plates of 5 x 8 x 1 mm^3 in

dimension were obtained from the hot-pressed disks. After polishing the plates, vacuum annealing was conducted at 623 K for 10.8 ks. The 20 MeV electron beam irradiation of 9 x 10^{15} – 3.6 x 10^{16} m^{-2} in fluence was performed for some plates at ambient temperatures prior to the plasma process.

The constitution of apparatus of the reactive plasma process was described in previous papers [3,4,6]. In this work, the nitridation and oxidation were performed at 1373 and 1073 K, respectively. The source plasma was generated using a Penning Ion Gauge (PIG discharge) under a gas pressure below 0.1 Pa.

The microstructure and constitutional phases of modified layers were characterized by scanning electron microscopy (SEM) and X-ray diffraction (XRD). Furthermore, the specimens were exposed in air at 1073 and 1273 K for 260 ks, as a preliminary investigation of oxidation resistance.

Results and Discussion

As the result of chemical reaction with a nitrogen plasma, the modified layer, composed of a double-layer structure, was obtained as shown in Fig. 1. The top surface layer mainly consist of a ternary nitride, Ti_2AlN [5]. In the sub-surface layer, which corresponds to a diffusion layer without nitride formation, the lamella structure of Ti aluminides is not observed. Because the reaction product has high melting point and hardness [5], heat and wear resistance are expected to improve by the nitridation.

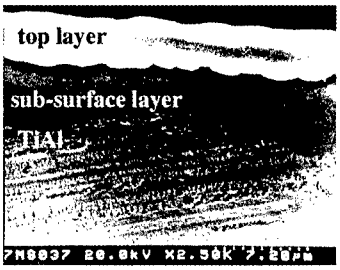

Fig. 1 Cross-sectional SEM micrograph of nitrided layer formed on Ti-48at%Al alloy at 1373 K. The specimen was chemically etched with the Kroll's reagent.

However, the ternary nitride is easily oxidized at initial stage of high temperature oxidation [7], and is insufficient to form the protective oxide scale. Hence, the oxidation resistance of TiAl alloys is hardly improved by the nitridation. Figure 2 (a) and (b) show the cross-sectional SEM micrographs of the nitrided specimen after exposing in air at 1073 and 1273 K for 260 ks. The specimens irreparably damaged by high temperature oxidation at 1273 K as shown in Fig. 2 (b). The oxidation resistance of the nitrided specimens is limited to ~1100 K.

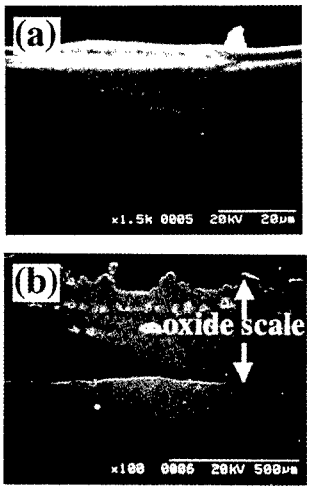

Fig. 2 Cross-sectional SEM micrograph of nitrided layer formed on Ti-48at%Al alloy, after exposing in air at (a)1073 and (b)1273 K for 260 ks.

On the other hand, the surface modification with an oxygen plasma is worthy to be investigated from the viewpoint

of protective scale formation against high temperature oxidation. As the result of the present examination, the modified layers were not definitely formed with an oxygen plasma below 973 K. Then, the processing temperature set to be 1073 K.

Figure 3 shows the cross-sectional micrograph of the oxidized specimen using reactive plasma process at 1073 K for 16.2 ks. The modified layer of ~10 μm in thickness was successfully fabricated by the reaction with an oxygen plasma. According to XRD pattern measured with X-rays incident perpendicular to the sample surface, a cubic ternary oxide, $Ti_5Al_3O_2$ [8], was detected as shown in Fig. 4 (a).

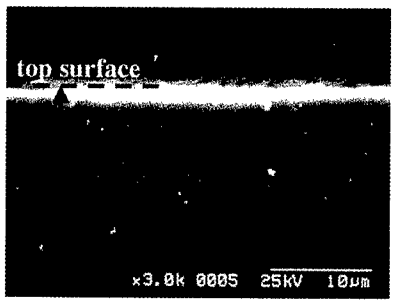

Fig. 3 Cross-sectional SEM micrograph of oxidized layer formed on Ti-48at%Al alloy at 1073 K.

In our project, the effect of pre-treatment using relativistic electron beam and low energy ion beam irradiation on the reactive plasma process is investigating as the technique for controlling thickness and constitutional phase of the modified layers. The effect of 20 MeV electron beam pre-irradiation on the chemical reaction of TiAl with an oxygen plasma is described below.

Figures 4 (b) and (c) show the XRD patterns of oxidized specimens prepared with the 20 MeV electron beam pre-irradiation. The reaction products apparently different depending on the fluence of electron beam pre-irradiation. In the case of the electron beam pre-irradiation of 9.0 x 10^{13} m^{-2} in fluence, different phases from $Ti_5Al_3O_2$ were formed by the reaction with oxygen plasma as shown in Fig. 4 (b). These diffraction peaks are not distinctly identified within the limits of this experiment. The precise analyses are further needed to identify the reaction products. The electron beam pre-irradiation above 1.8 x 10^{14} m^{-2} results in the formation of TiO_2 (rutile), as well as the unknown phases. Many lattice defects are formed in the alloy by the electron beam irradiation. Although the concentration of these defects sinks by annealing, the retained defects can influence to the ordering manner during reactive plasma process.

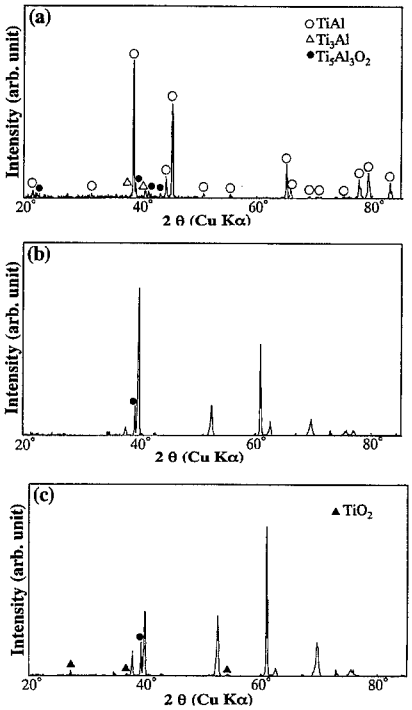

Fig. 4 XRD patterns of oxidized Ti-48at% Al alloy using reactive plasma process (a) without pre-treatments, and with 20 MeV electron beam pre-irradiation of (b) 9.0 x 10^{13} and (c) 1.8 x 10^{14} m^{-2} in fluence.

It still remains unclear whether these modified layers sufficiently exhibit oxidation resistance in air at elevated temperatures. Moreover, the protective scale formation is significantly influenced by alloying third elements. Therefore, the alloying or ion implantation with the elements which are useful for enhancing oxidation resistance, such as Nb, should be examined as the pretreatment, in order to establish the surface modification technology for TiAl alloys. This process is also expected to be applied to TiAl matrix composites as well as their based alloys.

Conclusions

The direct surface modification of Ti-48at%Al alloy was conducted by reactive plasma process using nitrogen and oxygen plasma. The modified layers were successfully formed by this process. The pretreatment by irradiating a relativistic electron beam clearly influences reaction behavior with the plasma.

References

1. S.C. Huang, J.C. Chesnutt, *"Intermetallic Compounds, vol.2"* (eds., J.H. Westbrook, R.L. Fleischer), John Wiley & Sons, Chichester, 1995, pp.73-90
2. M.J. Bennett and S.J. Bull: *"Oxidation of Intermetallics"* (eds., H.J. Grabke and M. Schütze), WILEY-VCH, Weiheim, 1997, pp.313-327
3. M. Nunogaki, Y. Susuki, K. Kitahama, Y. Nakata, F. Hori, R. Oshima, S. Emura, Proc. Mater. Res. Soc. Symp., 551, 303 (1999)
4. M. Nunogaki, M. Inoue, K. Kitahama: Mater. Trans., 42(3), 457 (2001)
5. M. Inoue, M. Nunogaki, K. Suganuma: J. Solid State Chem., 157, 339 (2001)
6. M. Inoue, M. Yamashita, K. Suganuma, M. Nunogaki: *in preparation*
7. N. Zheng, W. Fischer, H. Grübmeier, V. Shemet, W.J. Quadakkers, Scripta Metall. Mater., 33(1), 47 (1995)
8. W.J. Quadakkers, P. Schaaf, N. Zheng, A. Gil, E. Wallura, ref.2, pp.275-287

Proceedings of 7th Japan International SAMPE
Symposium & Exhibition, Nov. 13-16, 2001

Strain Measurements with FBGs Embedded into Cast Metal Alloys

Michele A. Caponero[#], Ferdinando Felli[§], Antonio Paolozzi[□]

[#]ENEA Frascati Research Center, Via Enrico Fermi 46, 00044 Frascati (Rome), Italy
Tel. +39 06 94005442, Fax. +39 06 94005400
e-mail: caponero@frascati.enea.it
[§]University of Rome *"La Sapienza"*, Dipartimento ICMMPM, Via Eudossiana 18
00184 Roma, Italy Tel. +39 06 44585601, Fax. +39 06 44585641
e-mail: ffelli@metal1.ing.uniroma1.it
[□]University of Rome *"La Sapienza"*, Dipartimento Aerospaziale, Via Eudossiana 18
00184 Roma, Italy, Tel. +39 06 44585301, Fax. +39 06 44585670
e-mail: paolozzi@nero.ing.uniroma1.it

Abstract

In this paper the experience gained in embedding sensorless optical fibers into cast metal alloys is extended to Fibre Bragg Gratings (FBGs). A zinc-aluminium alloys has been used to cast a smart slender bar to be used for static and dynamic tests. Strain measurements have been obtained directly by the embedded FBG.

Key Words: Embedding, Zinc alloy, FBG.

Introduction

The interest for embedding optical fibres into structural components is twofold. On one side the optical fibre should be, in analogy with all living beings, part of a nervous system capable of detecting all types of flaws or defects inside the structure. On the other side the structure provides a protection for the fibre itself. Embedding optical fibre into metal alloys presents problems concerning the high temperatures and the chemical reactivity of the metal melts. For this reason in the literature, differently from the case of composite materials, very few works are available on the embedding into metal alloys. Besides the works made by our research group we would like to mention some papers produced by Japanese colleagues [1,2]. Another important condition for manufacturing a metal smart structure is the good wettability of the fibre with respect to the hosting metal matrix. Low cost commercially available fibres are provided with either acrylate or polyimide coatings. Previous works [3-6] have shown that the embedding of organic coated optical fibres creates a not satisfactory interface fibre/metal matrix. It is possible to use custom made metallic coated optical fibres [3-5] but the cost and time of procurement may be very high. Furthermore if Fibre Bragg Gratings (FBG) are to be used, complications may be even higher. Therefore the easiest way is to remove the coating. The elimination of the polyimide is possible by burning it with a lighter but the fibre becomes brittle making difficult the

removal of burned residuals [5]. Consequently we have chosen to remove the acrylate coating with dichloromethane (CH_2Cl_2). Even if embedding into aluminium alloys is possible [3-5] in this preliminary work we preferred to use a less severe casting process using a lower melting point alloy. This choice was also forced by the use of (FBGs) that have a more limited temperature range with respect to the optical fibre. However the success of the tests performed in this work call for the realization in the near future of a smart bar made of an aluminium alloy. The objective of the paper is to prove the possibility of measuring strains by using an embedded FBG. In previous works we have already proved the feasibility of measuring strains by using a Michelson or Mach Zehnder interferometer [4-7] but those provides a global measurement, i.e., the strain integrated over the embedded fibre. With the FBG we are instead capable of making point measurements which could be used for performing an experimental modal analysis, useful for identification purposes.

Experimental

A Zn-Al bar with an embedded optical fibre containing an FBG has been manufactured. The FBG is an in fibre optical sensor that can measure strain induced by mechanical or thermal excitation. It is realized by a sort of photographic process by using an ultraviolet laser light. The exposition induce a periodic variation, of spatial wavelength Λ, into the fibre core. The grating length is about 1cm. When a broadband (50 nm) light is launched into the fibre the grating reflects only the component given by $\lambda_B = n_{eff}\,\Lambda$, where λ_B is the Bragg wavelength and n_{eff} the effective index of refraction. This property allow to multiplex many FBGs with different Bragg wavelengths within the same fibre. When the grating is subjected to strain λ_B will be shifted slightly. By measuring with an interrogation system this shift it is possible to retrieve the strain down to 1 $\mu\varepsilon$. As mentioned in the introduction the acrylate coating has been removed in correspondence of the sensor and for about the length of the bar. The bar dimensions were 0.2 x 0.005 x 0.0045 m. The alloy is commercially known as Galfan® (nominal composition 94.9% Zn, 5% Al, 0.1% misch metal). This alloy has optimal wettability with respect to the silica [6]. A vertical mould, made of graphite, has been used. The fibre has been placed vertically i.e., in the direction of casting and maintained in place by two cylindrical steel tubes blocked by properly wrapped aluminium foils. The fibre has been positioned off the neutral axis of the bar. The vertical position has been chosen to eliminate the effects induced by the floating of the fibre during the filling of the mould. In Fig. 1 is reported a photograph of the open mould soon after solidification of the specimen. It is visible the specimen with the feeder head before its removal. Also the optical fibre and the steel tube, used to prevent fibre from breaking in the ingress/egress from the specimen are shown.

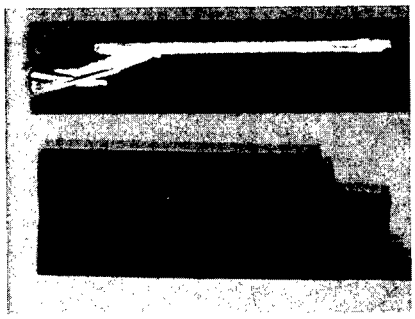

Fig. 1 Open mould with cast specimen.

A further bar has been manufactured in order to perform metallographic analysis to evaluate the quality of the fibre/matrix interface and to look for possible broken section of the fibre. The bar has been cut in

several pieces both in the longitudinal and transversal directions. The observation surfaces have been polished using silicon carbide papers and alumina in suspended particles. The metallographic specimen has been observed using the Scanning Electron Microscope (SEM). The bar has been tested statically using the set up reported in Fig. 2.

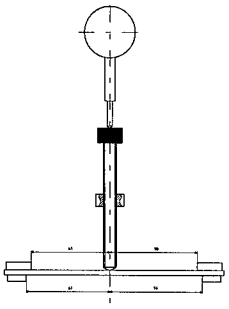

Fig. 2 Set up for static test.

A micrometric screw pushes the bar while the Micron Optics interrogation system provides the strains in terms of Bragg wavelengths. The limitation of the Micron Optics system is the rate of interrogation (100 Hz) that does not allow for a broad band test. From this the need of using a vibration exciter with relevant power amplifier (both from B & K) to force at low frequency the bar mounted horizontally. In Fig. 3 it is possible to recognize the cantilever bar (lower part of the picture), the optical fibre emerging from the bar and the vibration exciter in the centre connected through the big cable to the power amplifier.

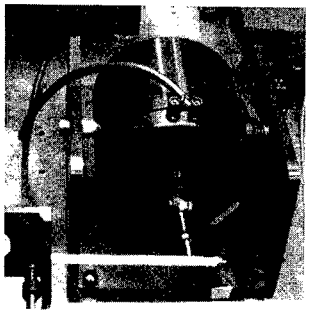

Fig. 3 Detail of set up for dynamic test.

Results and Discussion

The observation of the metallographic longitudinal and transversal sections have shown (Fig. 4) that the interface fibre/metal is very good and that the fibre is exempt from damages. The alloy starts solidification on the fibre surface and dendrides grow in the radial direction with respect to the fibre. Neither shrinkage cavities nor bobbles are present in the cast. In Fig.5 are reported in ordinate the readings

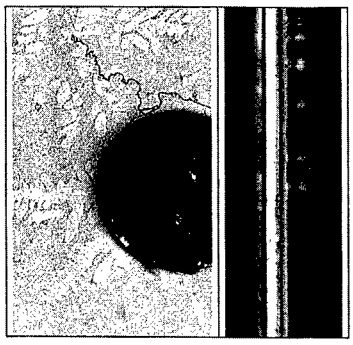

Fig. 4 SEM micrograph of optical fibre embedded into a Zn-Al alloy.

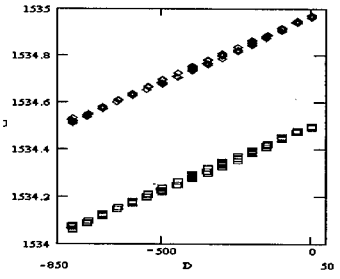

Fig. 5 Results from static tests.

from the interrogation system (Bragg wavelength in nanometer) and in abscissa the readings from the micrometer in μm. The experimental points from successive cycles of loading and unloading show a substantial repeatability of the measurement. The presence of the two curves shows a situation similar to what expected if one would have been using two FBGs "written" on the same fibre but characterized by Bragg wavelengths differing of about 0.5 nm. Instead the two wavelengths arose because of the manufacturing process of the specimen. We are aware of similar situation being encountered with FBGs embedded into thermoset based composite materials. The reason of this behaviour could be found in the birefringence induced on the fibre by the abovementioned manufacturing processes. As far as the dynamic tests are concerned, different forcing frequencies have been used. However due to the limitations on the sampling rate of the interrogation system (100 Hz) and on the data acquisition rate of the associated computer board (15 Hz) it was not possible to retrieve reliable sinusoidal responses above 4 Hz. For the sake of brevity only one response diagram is reported for the dynamic test (Fig. 4). Differently from Fig. 3 in ordinate is reported the value of the shifts of λ_B assuming $\lambda_B = 0$. when the bar is at rest. In abscissa is reported the time in seconds.

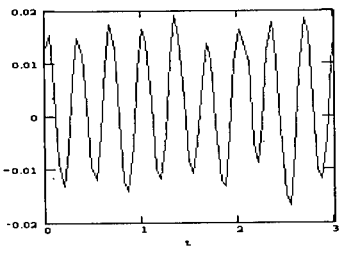

Fig. 6 Results from dynamic test at 4 Hz.

The not perfectly sinusoidal behaviour of the response could be imputed to the imperfect contact of the exciter rod with the bar (Fig. 3) as well as to the exciter itself whose response curves are given for frequencies above 10 Hz.

Conclusions

The embedding of an FBG in a Zn-Al alloy has been successful. However the signal reflected by the FBG has shown a splitting probably due to a birefringence induced by the casting process. The static tests have proved a very good repeatability. The dynamic tests were also quite satisfactory. However the interrogation system available could not allow neither higher frequency analysis nor a broad band tests. As a future development we plan to extend the experimentation to aluminium alloys and to broad band tests.

Acknowledgments

The research is sponsored by the Italian Space Agency (ASI) and the Ministry of the University and Scientific and Technological Research.

References

1. H. Asanuma, K. Ichikawa, T. K. Kishi: J. of Intelligent Material System and Structures, 7, 301 (1996).
2. O. Haga, H. Asanuma, H. Koyama: Advanced Composite Materials, 7(3), 239 (1998).
3. A. Paolozzi, F. Felli, A. Brotzu: Proc. of PACAM VI/DINAME 99, 639 (1999).
4. A. Paolozzi, F. Felli, M.A. Caponero: Proc. of 2nd Int. Workshop on Structural Health Monitoring, 257 (1999).
5. F. Felli, A. Paolozzi, M.A. Caponero: Aluminum Transaction, 2(2), 189 (2000).
6. M.A. Caponero, F. Felli, A. Paolozzi, I. Peroni: SPIE Symposium on Smart Materials, 4234, 152 (2000).
7. A. Paolozzi, F. Felli, Proc. 16th AIDAA Italian Congress, (2001).

Proceedings of 7th Japan International SAMPE
Symposium & Exhibition, Nov. 13-16, 2001

Superconducting Shape Memory Effect (SSME)

Naotada Hagiwara, Hiromasa Yabe, Tsunenori Suzuki and Yoshitake Nishi

Department of Materials Science, Tokai University
1117, Kitakaname, Hiratsuka, Kanagawa, 259-1292 JAPAN
E-mail: am026429@keyaki.cc.u-tokai.ac.jp

Abstract

In order to develop new shape memory materials operated by temperature, magnetic field, electrical current, pressure, and light frequency, the superconducting shape memory effect (SSME) induced by softening was studied using thermal expansion. In this study, we introduced two operating factors (temperature & magnetic field) induced volume change in the high T_c $YBa_2Cu_3O_{7-y}$ superconductors near 90K.

Key Words: Superconductor, Shape memory effect, YBCO, Softening, Magnetic field.

Introduction

The molar volume change on softening of metallic superconductor has been observed near superconducting transition temperature [1, 2]. Although most of the shape memory effects are operated by temperature change, the superconducting shape memory effects (SSME) induced by softening [3, 4] can be operated by changes in temperature (T), magnetic field (H), electrical current (I), pressure (P), and light frequency (ν) (see figure 1). Furthermore, since the atomic bonding force is strong at low temperature, the strong power can be expected for softening induced reversible shape memory effects of superconductor. SSME potential can potentially be used for an actuator. Therefore, the softening induced volume change has been studied for high Tc $YB_2Cu_3O_{7-y}$ superconductors.

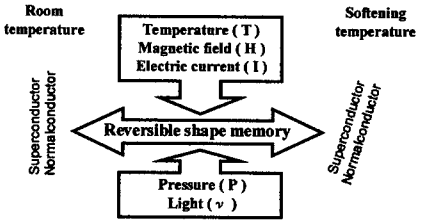

Fig. 1 Concept of shape memory effect induced by softening of superconductor bimetal.

Experimental Procedure

A directional oriented crystal was prepared by the QMG process [5] (4mm × 4mm × 2.2mm). The volume change was detected by a measurement system of low temperature uniaxial expansion with strain gage (see figure 2). The temperature was measured by a Au / 0.07 at% Fe - chromel thermocouple attached to the sample in a cryostat at equilibrium temperatures. Sample's cooling rate is 40K / min from temperature to liquid nitrogen, and hold 60 minute. The heating rate is 3K / min to room temperature. The strain was measured at elevated temperature (model no, KFL-05-120-C1-11, Kyowa Dengyo,

Tokyo). It was measured on the following two conditions to examine the magnetic field. The first condition was that the magnet was not put on sample, that is, non field cooling sample, NFC. The second condition was that the magnet was put on sample, that is, field cooling sample, FC. Magnetic force is 0.31T at liquid nitrogen temperature. Electrical resistivity was measured by using a standard four-probe technique. Offset temperature of superconductivity transition is 84.4K.

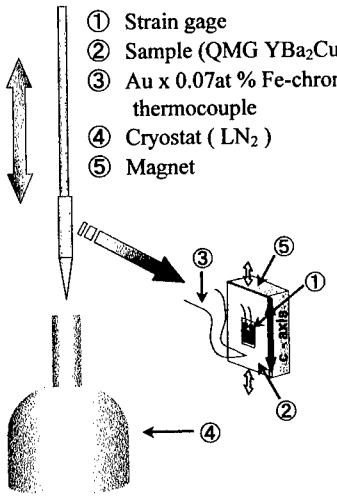

Fig. 2 Measurement system by low temperature uniaxial expansion system with strain gage.

Results and Discussion

1. Shape memory effect of non field cooling superconductor (YBCO)

Figure 3 shows the change in strain (ε) at elevated temperatures for non field cooled (NFC) sample. An excess strain on softening has been found from 84K to 110K. If the high T_c $YBa_2Cu_3O_{7-y}$ superconductor can be welded to supporting materials (see figure 1), softening induced excess strain can be found from near 90K. A positive temperature dependence of the excess strains (ε) was observed above 110K. In the temperature region, the material behaves like a metal. On the other hand, a negative temperature dependence of the excess strains (ε) was found from 84K to 110K.

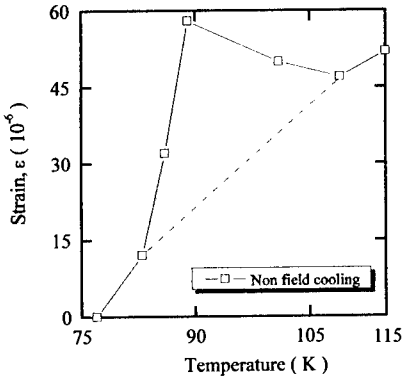

Fig. 3 Change in strain (ε) at elevated temperatures from 75 K to 115 K.

2. Shape memory effect of field cooling superconductor (YBCO)

Figure 4 shows the change in strain (ε) at elevated temperatures. The circle plots are for field cooled (FC) sample. The broken line is for non field cooled (NFC) sample.

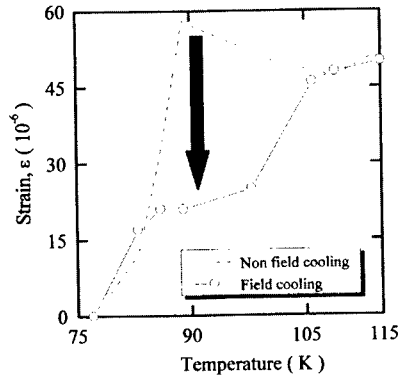

Fig. 4 Change in strain (ε) at elevated temperatures from 75 K to 115 K.

Magnetic field decreases the excess strain near 90K. If the sample is welded to supporting materials as shown in Fig. 1, the shape memory effect can be induced by the magnetic field. This means that reversible shape memory effects of superconductor can be developed.

3. Electron-electron scattering

Some models suggesting electron - electron pairs and groups as an exiton mechanism have been proposed [7-9], because the Bardeen-Cooper-Schriefer (BCS) electron-electron coupling [10] might be partially inapplicable for high Tc $YBa_2Cu_3O_{7-y}$ superconductors. Landau and Pomeranchuk [11] predicted the law from electron-electron scattering. Before the scattering, both electrons should be at the energy width (Boltzmann tail) within k_BT of the Fermi surface. If the electron-electron pair model were applied for the high T_c Y-Ba-Cu-O system, then the T^2-law would be found just above the onset temperature of the superconductivity transition. This was indeed observed in the present study for the high T_c Y-Ba-Cu-O system [12]. We defined a critical forming temperature (T_{ee}) of the electron-electron pairs and groups. The onset temperature (90K) of the excess strain ($\Delta\varepsilon$) corresponds to the T_{ee} temperature. In superconductors, hole, electron, their pairs and group act as Bose particles, whereas in normal state, they act Fermi particles. Near superconducting transition electrical transporters such as, electron or hole, convert from Fermi particles to Bose particles. Figure5 (b) shows a schematic drawing of the electron – electron scattering between T_{es} and T_{ee}. At the time of the collision of the electrons, both should be at the same energy level below the Felmi level, although the pairing life is short because of the scattering. If the transition chaos, that is, bonding electron orbital disordering, decreases the cohesive force, the excess volume increasing can be expected. To predict the molar volume change, change in lattice constants was reported by Dr. You [13]. Since the elevation of resistivity is too small near 110K, the large excess volume increases were apparently found below 110K. Therefore, a large volume change occurs in the temperature range from 84K to 110K, causing the shape change.

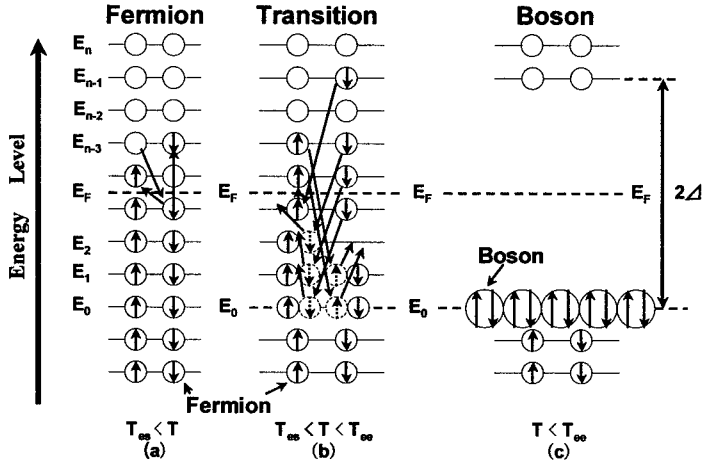

Fig. 5 Schematic drawing of fermion (a) electron-electron scattering (b) from T_{es} to T_{ee} and boson (c).

Conclusions

To develop new actuator, the thermal expansion of the high T_c $YBa_2Cu_3O_{7-y}$ superconductors was studied for application as an actuator using volume change on softening. A softening induced volume change was found below 110K. If the superconducting metal is welded to supporting materials, the bimetals will show the shape memory effects induced by magnetic field. Although most of the shape memory effects are operated by temperature change, the superconducting shape memory effect (SSME) may be also activated by changes in temperature, magnetic field, electrical current, pressure, and light frequency. We introduced two operating factors (temperature & magnetic field) induced by volume change in the high T_c $YBa_2Cu_3O_{7-y}$ superconductors.

References

1. M. Nohara, T. Suzuki, Y. Maeno and T. Fujita, A. Phys, Soc. 70, 3447 (1992).
2. G. Cao, Y. Li and R. Ma, Physica C, 178, 657 (1969).
3. N. Hagiwara, H. Yabe, K. Oguri, T. Asaka, T. Suzuki and Y. Nishi, J. Appl. Ele. and Mech, in press.
4. N. Hagiwara, H. Yabe, K. Oguri, T. Asaka, T. Suzuki and Y. Nishi, J. Adv. Sci., 12(3), 369 (2000).
5. M. Murakami, M. Morita, K. Doi, K. Miyamoto, Jpn. J. Appl. Phys, 28,1189 (1989).
6. T. Ojima, H. Yabe, R. Kondo, H. Izumi and Y. Nishi, J. Adv. Sci., 11(1), 33 (1999).
7. P. W. Anderson, Science, 235, 1196 (1987).
8. C. M. Varma, S. S. Rink and E. Abrahams, Solid State Commu, 62, 681-685 (1987).
9. W. Y. Ching, Y. Xu, G. L. Zhao, K.W. Wong and F. Zandiehnadem, Phys. Rev. Lett, 59, 1333-1336 (1987).
10. J. Bardean, L. N. Cooper and J. R. Schrieffer, Phys. Rev, 108, 1175-1204 (1957).
11. L. Landau and I. Pomeranchuk, Phys. Z. Sowjet, 10, 649 (1936).
12. Y. Nishi, A. Igarashi, S. Moriya, U. Kita and S. Tokunaga: J. Materials Sci. Lett, 8, 700-702 (1989).
13. H. You, U. Welp, Y. Fang, Phys. Rev, Vol. B 43 (4), 3660 (1991).

Proceedings of 7th Japan International SAMPE
Symposium & Exhibition, Nov. 13-16, 2001

Effects of Electron beam and UV light irradiation on clear time from misting for TiO_2 thin film

Rie FUJII, Kazuya OGURI, Masaki TETSUKA, Akira TONEGAWA,
Haru-Hisa UCHIDA, and Yoshitake NISHI

Department of Materials Science, Tokai University
1117 Kitakaname, Hiratsuka, Kanagawa, 259-1292 JAPAN
E-mail:am026429@keyaki.cc.u-tokai.ac.jp

Abstract

Effects of sterilization and blur free are induced by photo-catalytic reaction on the TiO_2 film surface irradiated by UV light. However it is possible to take long time for UV irradiation to improve the surface condition. To shorten the treatment time, the misting-free have been developed by sheet electron beam irradiation (SEBI). The minimum detectable time to clear vision has been about 10.0 ks for UV treatment, whereas the minimum detectable time to clear vision has been 3.45 s for SEBI treatment. The short time SEBI treatment induces clear vision on the TiO_2 film surface. Based on the results and Young-Dupré equation, the dipole factor is one of dominant factors for SEBI treatment.

Key Words: TiO_2, electron beam, blur.

Introduction

The blur free mirror for car attachment and the toiletry application for sterilization are famous application in the current Japanese market. Photo-catalytic reaction is well known on the TiO_2 film surface irradiated by an ultraviolet (UV) light [1]. It generates effects of sterilization and blur free. However, it takes long time to generate the effective reaction after UV light. Compared with the UV results, a sheet electron beam irradiation (SEBI) was performed for short time, when misting free condition occurs. Namely, the short time SEBI treatment induces clear vision on the materials surface [2-4]. Therefore, the time to clear vision was measured by TiO_2 film surface irradiated by UV and SEBI treatment in the present work. The effect is due to an enhancement of the interfacial energy between the TiO_2 and water. Using Young-Dupré equation [5,6], the dominant factor of surface free energy has been evaluated.

EXPERIMENTAL PROCEDURE

TiO_2 film was prepared by using magnetron-sputtering deposition under 4 x 10^{-3} Torr oxygen gas atmosphere for 4 h in 200 W RF condition. Sheet electron beam irradiation was homogeneously applied with an electron curtain processor (Type: CBI175/15/180L, Energy Science Inc., Woburn, MA; Iwasaki Electric Group Company, Tokyo) [7,8]. A tungsten filament in a vacuum generated the sheet beam. The acceleration potential and the irradiating current were 170 kV and 2.0 mA, respectively. The most important feature of sheet electron beam was homogeneous treatment, which was performed under protective nitrogen gas with the pressure inside the apparatus kept at atmospheric pressure. The concentration of impure oxygen gas was below 400 ppm. SEBI treatment was not continuously applied. In order to control the temperature of the surface of the sample, the irradiation time

was kept constant at 0.23 s. The sample was transported on a conveyer, and the speed of the conveyer was 10.0 m/min. The temperature of the surface of the sample was below 323 K just after the irradiation. Repeated application increased the total dosage of irradiation, as expressed by a following equation.

$$D = 21.6 \times I / S \times n$$

Here, the irradiation dosage was proportional to yield value of determination, irradiated current (I;mA), conveyer speed (S;m/min), irradiation times (N). The yield value of determination was calibrated by FWT nylon dosimeters. On the other hand, the length of Ti window is 38.0 mm. The irradiation time (ti) is 0.23 s per times at 10.0 m/min of conveyer speed.

A TiO_2 film surface, which had or had not been treated with SEBI, was subject to blowing for 3 s under saturated vapor pressure (misting experiment). The blowing rate was approximately 6 x 10^{-4} m^3/s under atmospheric pressure. Ultraviolet light is irradiated by black light. The time to clear vision was measured by a videotape recorder. The minimum detectable time to clear vision was 0.2 s. The start point of misting was considered to be just after the completion of blowing for 3 s under saturated vapor pressure. There are two different definitions of blur free for ultraviolet and sheet electron beam irradiated samples. In the case of ultraviolet light, the effect of super hydrophilic generates water fine drop. The UV light keeps the condition of clear vision. Its time was defined as the time to wet clear vision. On the other hand, the wet clear vision is induced by surface water wetability. for SEBI-treated samples, Thus, it shows a higher interfacial energy and induces the rapid deposition of fine water drops at heterogeneous active sites. Its time was defined time to dry clear vision.

Using Young-Dupré equation, the surface free energy was evaluated. Fowkes' equation [9-11] for interfacial tension was tried to extend the interface which included intermolecular interactions of polar and hydrogen bonding characters, besides of no polar one. In the calculation of the surface tension, the contact angle for three series of liquids, such as no polar, polar, and hydrogen-bonding liquids whose components were known, is used.

Results and discussion

Fig. 1 shows the relationship between the time to clear vision and the irradiation time of ultraviolet radiation treatment on a TiO_2 film surface under saturated humidity atmosphere. The UV light decreased the time to clear vision. When the ultraviolet irradiation treatment was performed for 3 hour on a TiO_2 film surface, the time to clear vision could not be detected; i.e., clear vision was achieved in spontaneously. However it takes long time to achieve the blur free condition. On the other hand, fig. 2 shows the relationship between the time to clear visionand the irradiation time of SEBI treatment on a TiO_2 film surface under saturated humidity atmosphere. The SEBI treatment on a TiO_2 film surface shortened the time to clear vision. The time to clear vision of a TiO_2 film surface that had been

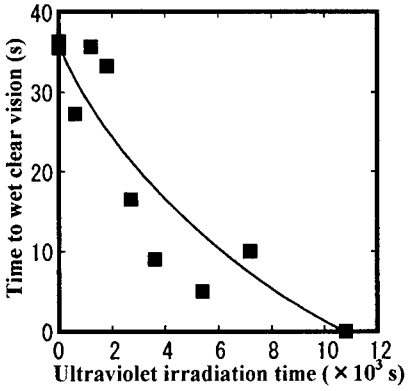

Fig. 1 Changes in the time to clear vision against radiation time of ultraviolet.

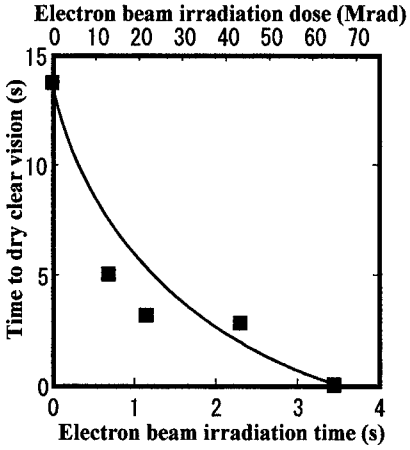

Fig. 2 Changes in the time to clear vision against total dosage of SEBI time.

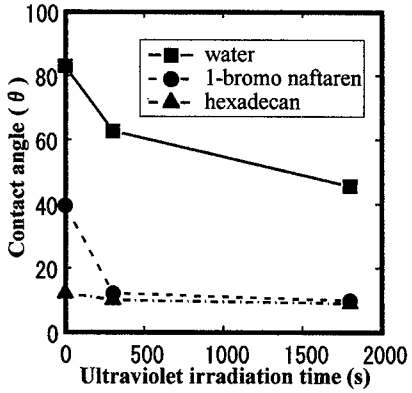

Fig. 3 Changes in three series liquids contact angle against total radiation time of ultraviolet.

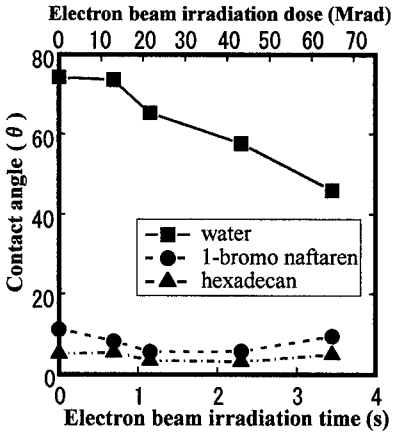

Fig. 4 Changes in three series liquids contact angle against total dosage of SEBI.

treated for 2.1 s (= 40 Mrad) of SEBI, was below 1 s. The time to clear vision of a TiO_2 film surface that had been subject for 3.45 s (= 64.8 Mrad) of SEBI treatment, could not be detected; i.e., clear vision was achieved in spontaneously. The blur was induced by the fine water deposition. The deposition process could be explained. SEBI treatment mainly activated the surface of a TiO_2 film by the addition of electrons to the surface. The nucleation frequency and extending rate were related to the interfacial energy [12,13]. This showed that the SEBI treatment time was shorter than that of the ultraviolet radiation treatment.

If these treatments increased the amount of energy, the short time to clear vision could be explained. Thus, it was important to know the interfacial energy of a water drop on the TiO_2 film surface. The surface energy of a solid could be expressed by an equation derived from Young's and Dupré's general theory. Fowkes' equation for interfacial tension was applied by using contact angles for three series of liquids. Fig. 3 & 4 show change in three series of liquids' contact angle against total ultraviolet radiation time and total dosage of SEBI to TiO_2 film surface. The UV irradiation decreased the contact angle of waterdrop. This effect was induced by photo-catalytic reaction on the TiO_2 surface irradiation by UV light. The SEBI irradiation decreased the contact angles of water and 1-bromo naftaren.

Namely, the reaction was the photo-induced super- hydrophilic and

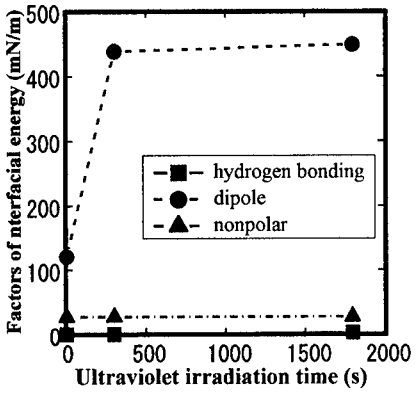

Fig. 5 Changes factors of interfacial energy against total radiation time of ultraviolet.

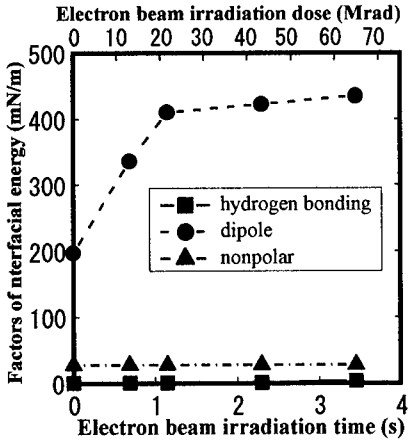

Fig. 6 Changes factors of interfacial energy against total dosage of SEBI.

simultaneously super-oleophilic conversation on the TiO_2 surface. Fig. 5 and 6 show change in interfacial energy against ultraviolet and electron beam irradiation times, respectively. Based on the results, the dipole factor was the dominant factors. The surfacetreated by SEBI and UV show higher interfacial energies than those of the non-treated surface. The increased energy induces the rapid deposition of fine water drops at heterogeneous active sites. It also induces an increase in nucleation frequency and an increase in extending rate of the fine water drops. Namely, we conclude that clear vision is achieved by the SEBI- and UV-induced active sites.

Conclusions

In summary, ultraviolet irradiation treatment (UV) and sheet electron beam irradiation [SEBI] decreased the time to clear vision of the TiO_2 surface. Based on the results of Young-Dupré equation, we concluded that these effects were dominated by the dipole factor. The UV irradiation for 3 hour and EB irradiation for 3.45 s became undetectable time to clear vision.

References

1. T. Watanabe : kogyo zairyo, 47, 56, (1999)
2. M. Takahashi, K. Fujita, Y. Ohmori, N. Honda, Y. Nishi and A. Tonegawa : Patent, JAPAN (Ref. No. HAE8-321688) (1996).
3. M. Takahashi, K. Fujita, Y. Ohmori, H. Jingu, N. Honda, Y. Nishi, and A. Tonegawa : J. Adv. Sci., 99(1996).
4. Y. Nishi, K. Oguri, K. Fujita, M. Takahashi, Y. Omori, A. Tonegawa, N. Honda, M. Ochi and K. Takayama : J. Mater. Res., 13, 3368(1998).
5. T. Young : Trans. Roy. Soc., London, 95, 65(1805).
6. A. Dupré : Thorie Mchanique debla Chaleur, (Paris, 1869).
7. Y. Nishi, S. Takagi and K. Yasuda : Phys. Lett. A, 141, 294 (1989).
8. Y. Nishi, S. Takagi, K. Yasuda and K. Itoh : J. Appl. Phys., 70, 367 (1991).
9. M. Kitazaki : The Adhesion Society of Japan, 8(3), 123 (1972).
10. M. Kitazaki : The Adhesion Society of Japan, 8(3), 131 (1972).
11. F. M. Fowkes : I.E.C., 56, 40 (1964).
12. D. Turnbll and J. C. Fisher : J. Chem. Phys., 17, 71 (1949).
13. M. Zinke-Allmang : Thin Solid Films, 346, 1 (1999).

Proceedings of 7th Japan International SAMPE
Symposium & Exhibition, Nov. 13-16, 2001

Microstructural Changes in an Al-Al_3Ti Composite by Equal Channel Angular Extrusion

Shigemitsu Hosoda and Yoshimi Watanabe

Department of Functional Machinery and Mechanics,
Shinshu University, 3-15-1, Tokida, Ueda 386-8567, JAPAN
E-mail: yoshimi@giptc.shinshu-u.ac.jp

Abstract

Equal channel angular extrusion (ECAE) is receiving increasing attention as a method to impose large plastic strains and develop ultrafine microstructures in metals. In this study, microstructural changes in an Al-Al_3Ti composite (Al- 5mass %Ti alloy) by ECAE are observed. It is found that ECAE leads to a significant hardness increase in the Al-Al_3Ti composite. It is also found that the size of Al_3Ti particle is decreased by the ECAE. In contrast, small effect is observed in the total volume fraction of Al_3Ti particle. It is concluded that a complete supersaturated solid solution without the Al_3Ti particles will not be introduced by the ECAE even if such a strong strain is applied.

Key Words: ECAE, MMC, Microstructure, Intermetallic compound

Introduction

Ultrafine-grained materials with the grain size of submicrometer order exhibit superior mechanical properties compared with conventional fine-grained materials. Several methods have been developed to obtain ultrafine-grained materials thorough severe plastic deformation [1-6]. Among them, the equal channel angular extrusion (ECAE) technique has been proved to be an effective method for the fabrication of various bulk ultrafine- grained materials. By using ECAE, very high shear strain can be obtained by multiple passes through a die without any change in the billet dimensions.

On the other hand, in our recent studies, it was found that a wear-induced supersaturated solid solution layer (supersaturated layer) was formed near the worn surface region by wear test of Al-Ti alloy (Al-Al_3Ti composite) [7, 8]. In this layer, there were no Al_3Ti particles, namely, a complete supersaturated solid solution was introduced by the wear test. Below the supersaturated layer, there was damaged layer where Al_3Ti particles were broken and re-oriented along the sliding direction. Although we have concluded that the formation of the supersaturated layer was a result of the large subsurface strains and plastic deformation during the wear test rather than from rapid quenching, there is no direct evidence for the above mechanism

In the present study, an Al-Al_3Ti composite which contains Al_3Ti platelets in an Al matrix, was extruded using the ECAE technique at room temperature. The microstructural changes of the composite by ECAE were studied by optical microscopy (OM), scanning electron microscopy (SEM) and X-ray diffraction (XRD) analysis. For the characterization of mechanical property,

the hardness change was measured by the Brinell hardness and Vickers micro-hardness testers.

Experimental Procedure

Rod shaped samples of an Al- 5 mass % Ti alloy, 10 mm in diameter and 55 mm in length, were prepared by casting. The schematic illustration of the ECAE die used in the present study is shown in Fig. 1. When a specimen is pressed through the die of the form illustrated in Fig. 1, the total strain, ε, accumulated by passage through the die can be calculated by

$$\varepsilon = (N/\sqrt{3})[2\cot(\Phi/2+\psi/2) + \psi\,\mathrm{cosec}(\Phi/2+\psi/2)] \quad (1)$$

where N is the number of separate passages through the die. For the present experiments where $\Phi = 90^\circ$ and $\psi = 0^\circ$, it follows from equation (1) that $\varepsilon = 1.15N$. The billet was rotated trough 90° clockwise between each cycle (In the literature, this route is often referred to as route Bc [3].)

The microstructures of the samples before and after the ECAE were observed using an OM and a SEM. To analyze the structural changes by the ECAE, XRD was carried out on a monochrometer-attached diffractometer with radiation from a Cu-Kα source. The hardness tests were performed by Brinell hardness tester and Vickers micro-hardness tester for the mechanical property characterization.

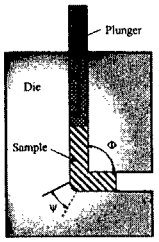

Fig. 1 A schematic illustration of the ECAE die used in the present study.

Results and Discussion

Hardness

Figures 2 shows hardness as a function of the number of passes of ECAE. It is apparent that ECAE leads to a significant hardness increase in the Al-Al_3Ti composite. It must be noted here that more than 100% of the total hardness increase is achieved after only one pass of ECAE. A similar result has also been reported in Al-Cu single-phase alloy [5].

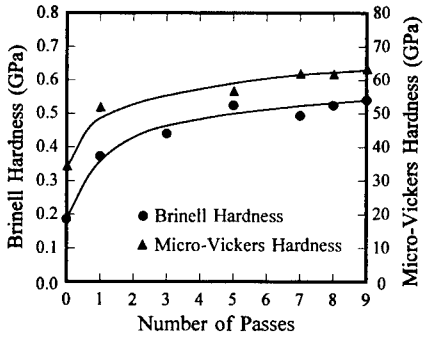

Fig. 2 Brinell hardness and Vickers microhardness as a function of the number of ECAE.

Microstructures

Figures 3 (a)-(d) shows typical SEM micrographs of samples before and after one, five and thirteen passes of ECAE, respectively. The SEM samples were cut perpendicular to the longitudinal axis of each pressed rod. Although the data from an energy disperse X-ray (EDX) analysis are not presented here, all of the particles in Fig. 3 were identified to be stoichiometric Al_3Ti intermetallic compound. It is seen from these figures that the size of Al_3Ti particles after the ECAE is smaller than that before the ECAE.

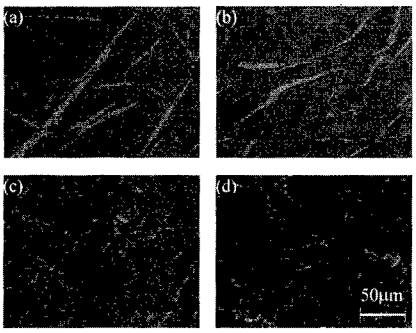

Fig. 3 Typical SEM micrographs of samples before (a) and after one pass (b), five passes (c) and thirteen passes (d) of ECAE.

In order to describe the above phenomena quantitatively, the distribution of the area-equivalent diameter of Al_3Ti particles for each sample was measured, and the results are shown in Fig. 4. It is seen that the area-equivalent diameter of Al_3Ti particles is decreased by ECAE. This result is in agreement with several previous investigations of ECAE [3, 6].

The volume fraction of Al_3Ti particles of each specimen was measured and the result is also shown in Fig. 5. It can be seen from this figure that the volume fraction has a tendency to become smaller by ECAE. However, despite the fact that there is a notable difference in the particle size, only small effect is observed in the volume fraction of particles.

XRD analysis

Figure 4 shows XRD patterns of the Al-Al_3Ti composite both before and after ECAE. It is seen from this figure that the Al and the Al_3Ti peaks exist both before and after ECAE. Therefore, we can conclude that a complete supersaturated solid solution without the Al_3Ti particles will not be introduced by ECAE even if such a strong strain is applied.

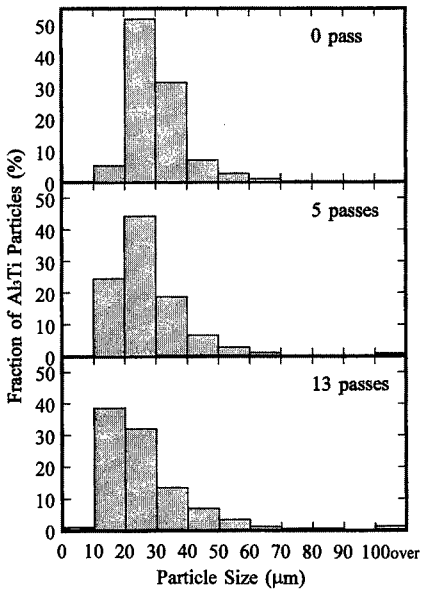

Fig. 4 The size distributions of Al_3Ti particles in the specimens before and after ECAE.

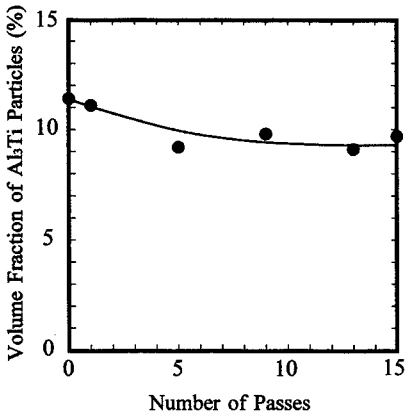

Fig. 5 Total volume fraction of Al_3Ti particles as a function of the number of ECAE passes.

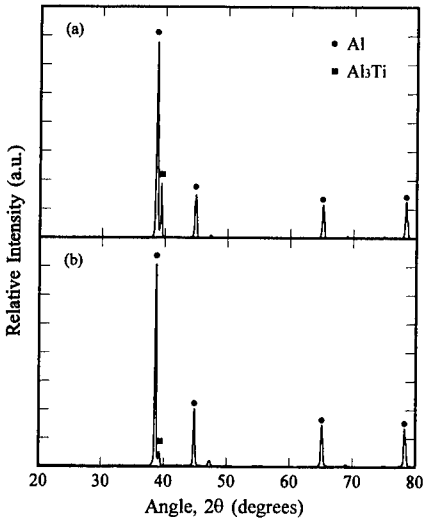

Fig. 6 XRD profiles of the Al-Al_3Ti composite both before (a) and after nine passes (b) of ECAE.

Future works

In the case of Al-Al_3Ti FGMs fabricated by the centrifugal solid-particle method, it is known that a large number of Al_3Ti particles are arranged with their platelet planes nearly perpendicular to centrifugal force direction [7, 9]. Moreover, it was shown that the orientation of Al_3Ti platelets is distributed with a gradient in the Al-Al_3Ti FGMs [10]. In this study, the billet was rotated trough 90° clockwise between each cycle (route Bc). Therefore, there was no observable orientation effect in Al_3Ti particles by ECAE. However, it is expected that the orientation of Al_3Ti platelets will appear by ECAE with no rotation of the billet (route A). We are currently investigating the orientation effect in Al_3Ti particles by ECAE with no rotation of the billet (route A).

Conclusions

In this study, microstructural changes are observed in an Al-Al_3Ti composite which contains Al_3Ti platelets in an Al matrix, by ECAE. The results are summarized as follows.

(1) The hardness of the Al-Al_3Ti composite was increased with increasing the passes of ECAE.

(2) Despite the fact that there is a notable difference in the particle size, only small effect is observed in the total volume fraction of particles.

(3) Al_3Ti XRD peaks exist in the specimen after ECAE.

(4) It can be concluded that a complete supersaturated solid solution without Al_3Ti particles will not be introduced by ECAE even if such a strong strain is applied.

Acknowledgment

This work was supported by Grant-in-Aid for COE Research (10CE2003) by the Ministry of Education, Science, Sports and Culture of Japan.

References

1. V. M. Segal, V.I. Reznikov, A.E. Drobyshevskiy and V.I. Kopylov: Russian Metallurgy, (Engl. Transl.), 1, 115 (1981).
2. V. M. Segal: Mater. Sci. Eng., A197, 157 (1995).
3. K. Nakashima, Z. Horita, M. Nemoto and T. G. Langdon: Acta Mater., 46, 1589 (1998).
4. Y. Saito, H. Utsunomiya, N. Tsuji and T. Sakai: Acta Mater., 47, 579 (1999).
5. M. Murayama, Z. Horita and K. Hono: Acta Mater., 49, 21 (2001).
6. D. H. Shin, I. Kim, J. Kim and K.-T. Park: Acta Mater., 49, 1285 (2001).
7. Y. Watanabe, N. Yamanaka and Y. Fukui: Metall. Mater. Trans. A, 30A, 3253 (1999).
8. K. Yokoyama and Y. Watanabe; Trans. MRS-J, 26, 303 (2001).
9. Y. Watanabe, N. Yamanaka, Y. Fukui; Z Metallkd; 88, 717 (1997).
10. Y. Watanabe, H. Eryu and K. Matsuura; Acta Mater., 49, 775 (2001).

Proceedings of 7th Japan International SAMPE
Symposium & Exhibition, Nov. 13-16, 2001

Stress Relaxation Test for Spring Sheet of Tin Coated Cu-Ni-Sn Alloy Applied for Advanced Automobile Connecting Materials

Kazuharu HAYASHI, Kuniyasu GEMMA, Mikio NISHIHATA #

Tatsuo KUNIMINE# and Yoshitake NISHI

Department of Materials Science, Tokai University, 1117, Kitakaname,

Hiratsuka, Kanagawa, 259-1207, Japan

E-mail: am026429@keyaki.cc.u-tokai.ac.jp

#: Nippon Bell-parts Co., LTD. 601-36, Ohwada-shinden, Yachiyo, Chiba, 276-0046, Japan

E-mail: nbp@fb3.so-net.ne.jp

Abstract

Using load cell attached in a new apparatus for high temperature relaxation test, the relaxation ratio of electric spring materials was continuously detected at different temperatures. Compared with conventional methods, the new apparatus showed a reliable data. An excellent stress relaxation ratio was obtained for a Cu-Ni-Sn alloy sheet, by using the testing at upper critical temperature of current automobile. Based on the results of the relaxation test below 423 K, we confirmed that the Cu-Ni-Sn and tin-coated Cu-Ni-Sn alloy sheets can be applied for connecting materials in automobile engine room.

Key Words: Stress relaxation, Elevated temperature, Thin plate spring, NB109

1. Introduction

It is important to know stress relaxation of spring materials. Stress relaxation ratio is usually evaluated by bending displacement. By definition, stress relaxation should be evaluated by a change in the stress under the constant distortion.

Nishihata, Kunimine & Arase have developed a new apparatus for high temperature relaxation test. Using load cell attached in the apparatus, the relaxation ratio was continuously detected at different temperatures. Here, the new testing apparatus was developed to evaluate stress relaxation ratio of spring materials. On the other hand, a Cu-Ni-Sn alloy sheet (NB109 [U.S. Patent: 4337089] invented by Nishihata), which shows low contact electrical resistance. However a stress relaxation character has not precisely studied at upper critical temperature of current automobile. Therefore, the purpose of the present work is to investigate the stress relaxation ratio of Cu-Ni-Sn and a tin-coated Cu-Ni-Sn alloy sheets at higher temperature in engine room of automobile.

2. Experimental

2.1 New Stress relaxation test apparatus

Stress relaxation measurement is enacted as specification E 328-86 in ASTM [1]. In this article, we developed a new stress relaxation measurement machine by reading a load directly. Figure 1 shows an illustrated mechanism of the new stress relaxation testing apparatus. The apparatus consisted of three parts of instruments; main body loading the stress to specimens, movable electric furnace heating the specimens and stress change detector, as shown in fig.1. After fixing the specimen at jig by pressure bolt, the 60% stress of spring limit (0.2% proof stress on bending test) of the specimen was loaded by load cell. To heat the loaded sample, the electric furnace was moved. After heating at high equilibrium temperature from 373 to 423 K, the stress relaxation ratio was measured.

The change in stress of the specimen is measured continuously at a high temperature for a long duration. A relationship between stress(σ) and load (W) can be expressed by a following equation for a rectangular test piece.

$$\sigma = 6Wl/bt^2 \qquad (1)$$

Here, l, b and t were span, width and thickness of a rectangular specimen. On the other hand, the stress relaxation ratio (R:%) was expressed by a following equation.

$$R = (W_r - W_f)/Wi \qquad (2)$$

Here, W_i and W_f mean an initial loading value and a measured load after a duration, respectively. Thus, accurate experimental data can be expected by the new apparatus to get stress relaxation ratio.

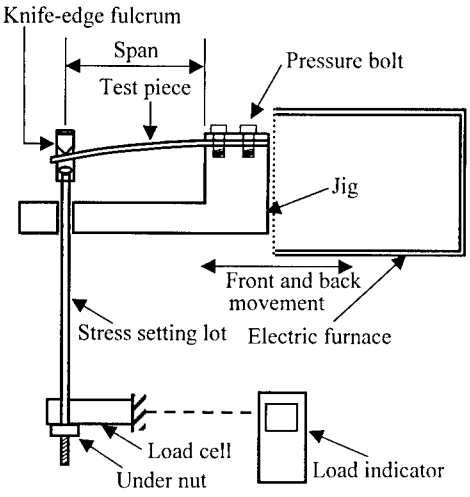

Fig.1 Schematic diagram of the new testing apparatus for stress relaxation

2.2 Specimens

A sheet of Cu-Ni-Sn spring alloy (NB109) was supplied for the new stress relaxation measurement. A chemical composition of the Cu-Ni-Sn (NB109) alloy was summarized in table1, together with brass and phosphor bronze.

An initial loaded stress in elastic deformation of static stress- strain curve was 60% of spring limit. Thus, the initial loaded stress of Cu-Ni-Sn (NB109) spring alloy and Sn coated NB109 alloy sheets were obtained and summarized in table 2, together with brass and phosphor bronze.

Table1 Chemical compositions of Cu-Ni-Sn (NB109) spring alloy, together with brass and phosphor bronze.

(wt%)

	Cu	Sn	P	Pb	Fe	Zn	Ni
NB109	Re.	1.00	0.059	—	—	—	1.00
Brass	60.68	—	—	0.0061	0.0039	Re.	—
Phosphor bronze	93.2	6.57	0.21	—	—	—	—

Table2 Initial loaded stress of Cu-Ni-Sn spring alloy and Sn coated NB109 alloy sheets, together with brass and phosphor bronze.

	σ_R (MPa)
Brass	132
Phosphor bronze	207
NB109	292
NB109 +Sn coated	253

3. Results

In order to correct the experimental value of the new testing method, a two-phase brass sheet was firstly used as a standard material. Figure2 shows the relationship between the stress relaxation ratio and loading time at different temperatures from 373 to 423 K. At the initial stage, the stress relaxation ratio of the brass increases remarkably. The large relaxation ratio was found at higher temperature testing. The stress was slowly relaxed after 50 hour loading. When the relaxation ratio after 100 hr loading were measured from fig.2, they were 21%, 35% and 54% at 373K, 398K and 423K, respectively. To investigate influences of temperature and time on stress relaxation ratio, Larson-Miller correlation was applied [2] and was shown in Figure 3, which was converted by the results in fig.2. The plots of data were distributed on the Larson-Miller correlation. Thus, a reliability of the new method was here warranted.

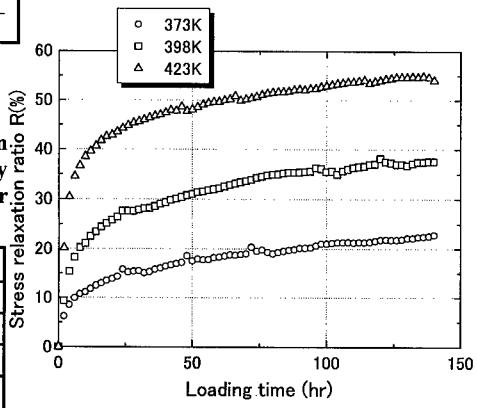

Fig.2 Stress relaxation curve of brass

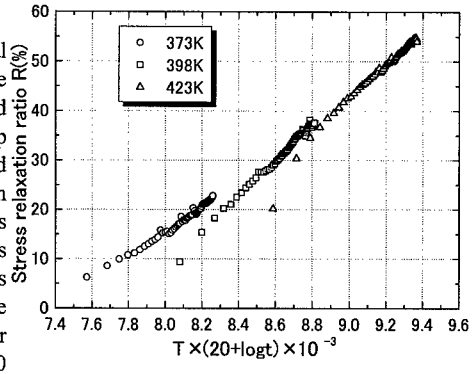

Fig.3 Stress relaxation ratio of brass by Larson-Miller correlation

Figure 4 shows the relationship between the stress relaxation ratio at 423K and loading durations in a new stress relaxation resistance alloy (NB109) specimens, together with a conventional automobile connecting material of phosphor bronze Sn-coated NB109 alloy. The resistance to stress relaxation of NB109 alloy and a Sn-coated NB109 alloy sheets show twice higher than that of the phosphor bronze. The superior resistance to relaxation was kept for the Sn-coated NB109 alloy sheet, which shows low electrical contact resistance.

As, shown in Fig. 5, Larson-Miller correlations of these results obtained by means of the new method were confirmed. The high resistance to relaxation was obtained for the Sn-coated NB109 alloy sheet.

From these results, we concluded that the NB109 alloy has an excellent property as unrelaxed spring of electrical contact material.

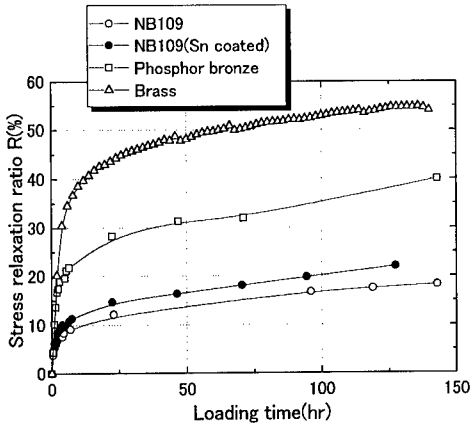

Fig.4 Stress relaxation curve of typical automobile connecting materials

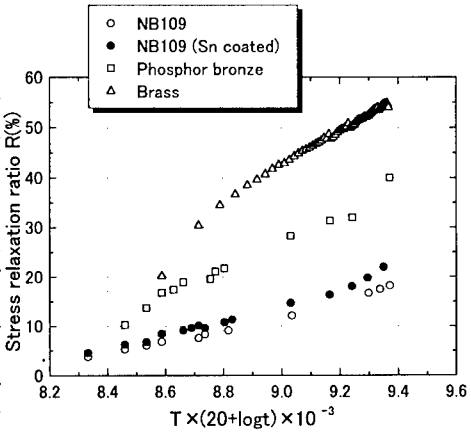

Fig.5 Stress relaxation ratio of typical automobile connecting materials at 423K by Larson-Miller correlation

4.Conclusion

The new apparatus, which have been developed by Nishihata et al., can be applied practically to continuous measurement of the stress relaxation for sheet materials. Experimental data obtained by means of the method are fitted enough on Larson-Miller correlation. In addition, it is recognized that a new Cu-Ni-Sn alloy (NB109 alloy) has twice stress relaxation resistance than a mass-produced phosphor bronze of typical connecting material. It is therefore expected that the NB109 alloy is wide used for current automobile. The new stress relaxation testing method will be adopted as an industrial global standard in the world.

References

1.Annual book of ASTM standards,Section3, E-328-86, 353-364 (1995)

2.I.Finner and W.H.Heller, '*Creep of Engineering Materials*' Mcgraw-Hill Book CO., INC. NewYork, 313-320, (1959).

Proceedings of 7th Japan International SAMPE
Symposium & Exhibition, Nov. 13-16, 2001

Particle Size Distributions in Al-Al_3Ni Functionally Graded Materials Fabricated by a Semisolid Forming

Koichi Matsuda[*1], Yoshimi Watanabe[*1], Kazuhisa Yamagiwa[*2]and Yasuyoshi Fukui[2]

1. Department of Functional Machinery and Mechanics, Shinshu University
3-15-1 Tokida, Ueda 386-8567, Japan
E-mail: zai5002@giptc.shinshu-u.ac.jp

2. Department of Mechanical Engineering, Kagoshima University
1-21-40 Korimoto, Kagoshima 890-0065, Japan
E-mail: fukui@mech.kagoshima-u.ac.jp

Abstract

In a resent study, it was shown that near-net-shape products having fine Al_3Ni intermetallic compound particles could be successfully fabricated by backward extruding at a molten aluminum and solid Al_3Ni intermetallic compound particles coexisting temperature. However, origin of fine Al_3Ni intermetallic compound particles is still open to question. We propose to measure the particle size distributions in the near-net-shape products. The FGM billets fabricated by a vacuum centrifugal method were heated to 650℃ to 680℃, at which temperature the FGM becomes a mixture of molten aluminum eutectic and solid Al_3Ni intermetallic compound particles. The billets were extruded to FGM cups by a semisolid forming. Microstructures of the near-net-shape products have been observed by optical microscopy. It is found that the size of Al_3Ni particles within the products is distributed in a gradually graded manner as well as the volume fraction of Al_3Ni particles. Based on the experimental results, the origin of the above microstructure has been discussed.

Key Words: Functionally Graded Material, Semisolid Forming, Particle Size, Intermetallics Compound.

Introduction

Intermetallics dispersed functionally graded materials (FGMs) are planed to compensate the own brittleness of intermetallics by ductile matrix and then to utilize the expected superior characteristics of intermetallics [1]. The authors have fabricated Al-Al_3Ni FGM tube by a centrifugal method and examined a probability as a structural and component material [2-4]. Here, the centrifugal method is an FGM fabrication method proposed by one of the authors [5]. Unfortunately, Al-Al_3Ni FGMs tested heretofore did not have sufficiently high strength due to the presence of relatively large Al_3Ni particles. These results indicate that a plastic forming operation for such a material would be very difficult, *i.e.*, low ability as a structural and component material. One possible way to overcome this difficulty may be in an application of hot working and heat treatment. However, this has not been successful because of the low resistance of Al_3Ni intermetallics to brittle fracture, even

in the case of hot working up to the melting point of the eutectics. On the other hand, another possible way to overcame a natural difficulty of forming of the present aluminum-base FGMs. That is, if the FGMs were worked under a coexisting condition of a liquid hypereutectic aluminum alloy and solid intermetallics, it must be possible to obtain a near-net-shape FGM product and it may widen the ability of the metal intermetallic FGMs.

In our previous study [6], it was found that the Al-Al_3Ni FGM cup with smaller Al_3Ni particles could be successfully fabricated by a semisolid forming over eutectic melting temperature of Al-Al_3Ni FGM. Although it is well known that mechanical properties of particle-dispersed composites and FGMs are influenced by not only by the volume fraction of dispersed particles but also by the particle size, the detailed study on the particle size distributions in the Al-Al_3Ni FGMs fabricated by the semisolid forming are not yet investigated. The aim of this study is, therefore, obtaining the information of the particle size distributions in Al-Al_3Ni FGMs fabricated by the semisolid forming.

Experimental Procedure

A configuration of the vacuum centrifugal system for FGM tube manufacturing is illustrated in Fig. 1. Using this system, Al-Al_3Ni FGM tube was fabricated from Al-20mass%Ni commercial ingot. Thick-walled FGM tube is initially cut into four pieces of bar having a circular arc cross-section, as illustrated in Fig. 2. The bar is then subject to hot working and a flat plate is obtained, for a preparation of FGM billets to examine the so–called semisolid or semimelt forming. As illustrated in Fig. 3, billets are held in a container such that the aluminum-rich plane of the FGM billet touches the punch head for testing the backward extruding to an FGM cup. Tested temperatures are 650℃, 660℃, 670 ℃ and 680 ℃ , at which molten hypereutectic aluminum and solid Al_3Ni intermetallics are coexisting. The container, which has both billet and punch, is heated and held at test temperature for 30 minutes in a crucible furnace. Then, it is place on press machine and the billet is extruded to an FGM cup.

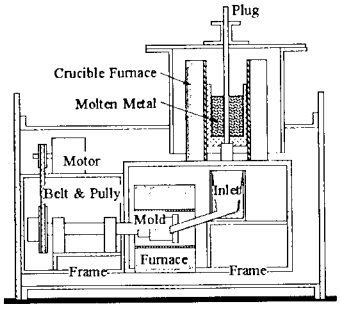

Fig.1 Schematic representation of vacuum centrifugal system.

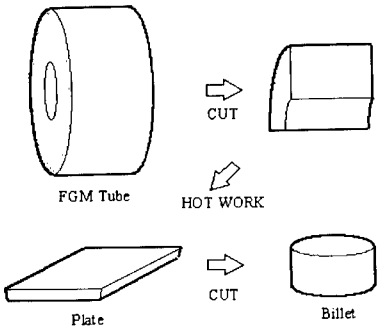

Fig.2 Process of the FGM billet preparation from FGM tube.

Results and Discussion

Microstructures in a present Al-Al_3Ni FGM cup are examined by an optical microscopic (OM) observation. Typical micrographs of Al_3Ni particles obtained in this study are shown in Fig. 4, where the gray part is aluminum matrix and black particles are Al_3Ni intermetallics. Figure 5 reveals that

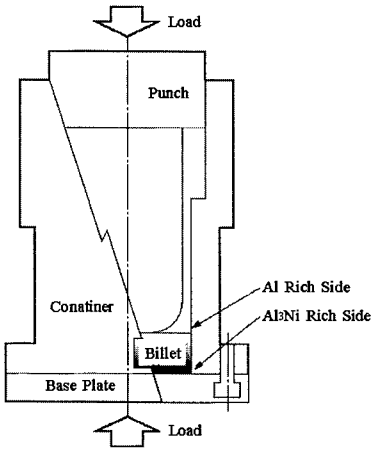

Fig.3 Schematic of the die and billets setting for the FGM backward extruding, where punch contacted with aluminum-rich surface.

the volume fraction of the Al_3Ni particles increases towards the cup's higher region because of at the early stage, Al_3Ni particles carried away by flow of eutectic aluminum alloy melt. Another important feature found in Fig. 4 is that the size of Al_3Ni particles varies depending on height. To discuss this phenomenon quantitatively, the particle size distribution of Al_3Ni particles is measured at each region as same as Fig.5. Here, for the convenience of analysis, the distribution of the cross-section diameter is calculated as area-equivalent diameter assuming the granular particles as spherical. In case of spherical shaped particles, since it is known that multiplication of $4/\pi$ by the average two-dimension diameter [7], the average three-dimensional diameter can be calculated from the cross-section diameter.

Figure 6 shows the average three-dimensional diameter of Al_3Ni particle. As can be seen, the average three-dimensional diameter is distributed in these specimens in a graded manner. Moreover, higher tested temperature gives a smaller particles size. One possibility is that the eutectic melt flow

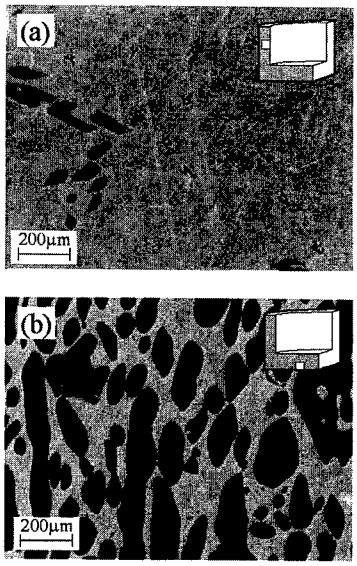

Fig.4 Micrographs showing the microstructure of cross section of extruded FGM cup at 670℃. (a) and (b) are wall and bottom region of the cup.

0	#
0	#
10	0
20	30
30	20
40	30
40	40

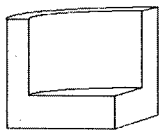

Schematics of specimen

40	40	40	50	60	60	70	70	70	60
40	50	50	50	60	70	70	70	60	60
30	50	50	60	60	70	70	60	70	60

Unit : vol%

Fig.5 The distribution of Al_3Ni particles in the extruded FGM cup at 670℃. The letter "#" indicates no particle in region.

(a)

70	50								
90	70								
130	60								
60	70								
100	80								
60	70								
50	50								
90	60	80	#	#	#	#	#	#	#
70	80	80	#	#	#	#	#	#	#
80	80	#	#	#	#	#	#	#	#

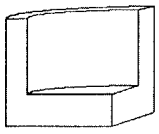

Schematics of specimen

Unit : μm

(b)

20	30								
30	30								
20	40								
60	50								
190	140								
130	130								
90	110								
160	100	90	110	120	110	110	130	100	110
160	130	110	120	120	130	120	120	120	140
170	170	160	210	140	150	150	140	150	210

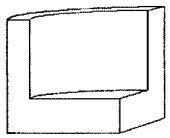

Unit : μm

(c)

20	30								
20	20								
60	30								
60	50								
90	90								
110	70								
100	100								
130	130	110	130	130	100	110	100	110	100
160	140	90	90	100	100	110	120	100	100
110	120	130	140	140	130	140	130	150	140

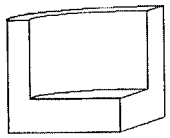

Unit : μm

Fig.6 Particle size distributions in the FGM cups fabricated at 660℃(a), 670℃(b) and 680℃(c). The letter "#" indicates no particle in region.

with higher viscosity breaks up the large intermetallics particles to fine granular. Another possibility is cooling rate difference

It is known that the crystallized particle size is influenced by the solidification process. In our previous study [3], it was found that the average Al_3Ni particle size in Al-Al_3Ni FGMs fabricated by the centrifugal *in-situ* method was gradually distributed in the specimens. It had been concluded that the difference in the particle size distributions was caused by the cooling rate. In this study, the higher tested temperature gives a faster cooling rate. Consequently higher tested temperature gives a smaller particles size

Summary

Near-net-shape products having a graded distribution of intermetallics are fabricated by semisolid forming. It is found that the average particle size was gradually distributed in FGM cup as well as the volume fraction of particles. It was also found that higher tested temperature gives a smaller particles size. From the experimental results, it can be concluded that the origin of particle size distributions within the FGMs is depended on shear stress of eutectic melt flow and cooling rate.

References

1. Y. Watanabe and Y. Fukui: Rec. Devel. Metal. & Mater. Sci., 4, 51, (2000)
2. Y. Fukui, Takashima and C.B. Ponton : J. Mater. Sci., 29, 2281, (1994)
3. K. Matsuda, Y. Watanabe and Y. Fukui: submitted to Ceramic Trans.
4. Y. Fukui, N. Yamanaka and Y. Enokida: Composite Part B, 28B, 37, (1997)
5. Y. Fukui and Y. Watanabe: Metall. Mater. Trans. A, 27A, 4145, (1996).
6. Y. Fukui, H. Okada and N. Kumazawa: Metall. Mater. Trans. A, 31A, 2627, (2000).
7. R.T. DeHoff and F.N. Rhines ed, "*Quantitative Microscopy*", McGraw-Hill Book Company, New York, 1968, pp.128-48

Proceedings of 7th Japan International SAMPE
Symposium & Exhibition, Nov. 13-16, 2001

High temperature mechanical characterization of low activation materials for fusion reactor

Satoshi Uchida, Tsuyoshi Sunamoto, Hiromasa Yabe, Noriyuki Inoue, and Yoshitake Nishi

Tokai University, 1117 Kitakaname, Hiratsuka, Kanagawa, 259-1292 Japan
e-mail : am026429@keyaki.cc.u-tokai.ac.jp

Abstract

Using in-situ hardness test at high temperature, the hardness values were measured for Fe-9Cr-2W-V-Ta steel (JLF-1) during isothermal heating from 373K to 1473K. The hardness changes against loading time can not be remarkably observed below 773K. Thus, we confirmed that JLF-1 steal with low activation can be applied for fusion reactor materials below 773K. Furthermore, to predict high temperature morphology changes induced by welding for reactor construction, hardness was measured below 1473K. Tremendous decreasing in hardness was found from 773K to 1073K. Based on X-ray diffraction analysis results, bcc phase can not found at 1473K, whereas fcc phase can not detect below 1093K. Thus, large stress relaxation, that is creep, from 873K to 1073K was observed and can be explained by wolfram carbide coarsening with chromium carbide annihilation.

Key Words:
High Temperature hardness, JLF-1,
Ferrite steel

1. Introduction

From the point of view of eco-materials development, it is important to study structural materials for fusion reactor. Fusion reactor is under developed, which is generating electric power without CO_2. If fusion can be realized on earth, using the fuel of deuterium found naturally in one barrel of seawater, the amount of electrical energy equivalent to that of 250 barrels of oil can be produced.

The structural material for fusion reactor has been operating from extremely low temperature below boiling point of helium to extremely high temperature above plasma formation temperature. Several types of low activation materials have been developed as candidate for fusion reactor structural components. Japanese Fe-9Cr-2W-V-Ta steel (JLF-1) of low activation materials was practical candidate for fusion reactor structural components under a surveillance test program in Japanese universities, which is low cost and shows high resistance to stress at high temperature [1-4]. In order to prevent activate, chromium was added. The structural material for fusion reactor has been operating at high temperatures. Thus, wolfram addition formed fine separated carbides to reinforce the matrix at high temperature. In addition, homogeneous mechanical properties, which can be applied for thick reactor wall and show good weld-ability [5,6], can be expected. Since it is important to investigate mechanical and phase characteristics at high temperature, the in-situ micro-hardness values have been measured for. Fe-9Cr-2W-

V-Ta steel at high temperature.

2. Experimental

2-1 Specimen

Samples were Fe-9Cr-2W-V-Ta ferrite steel (JLF-1) with low-activation. Chemical composition was summarized in Table 1. The specimens (5mm×5mm×5mm) were normalized at 1323K for 1hr and air-cooled. In addition, it tempered at 1050K for 1hr, and then air-cooled.

2-2 High-temperature hardness tester

In-situ Vickers hardness measurements at different high temperature from room temperature to 1473K were carried out by a high-temperature micro hardness tester (QM-2, Nikon Co. Tokyo). The furnace was controlled by proportional integral derivative actions (PID). The measuring sample was heated in vacuum (1.02×10-3Pa). The testing load was 100gf.

2-3 X-ray diffraction

The structures of the samples were examined by means of high-temperature X-ray diffraction apparatus (RINT2200, Rigaku Co. Tokyo). The heater was controlled by PID from room temperature to 1473K under nitrogen gas atmosphere.

3. Results and Discussion

3-1 Influence of loading time on Hv

Figure 1 shows changes in Vickers' hardness against loading time during isothermal heating from 1 to 100 s at different temperatures. The hardness changes against loading time can not be remarkably observed below 773K. Thus, we confirmed that Fe-9Cr-2W-V-Ta ferrite steel (JLF-1) with low activation can be applied for fusion reactor materials below 773K.

Furthermore, in order to predict high temperature morphology changes induced by welding for reactor construction, hardness was measured below 1473K. The longer the loading time, the lower the hardness becomes at high temperature over 873K. Large Hv decreasing from 70 at one second to 45 at 100 s was observed by isothermal heating for 100 s at 973K. On the other hand, Hv decreasing induced by long loading time is not so large above 1073K isothermal heating.

Fig.2 shows changing rate of Hv against temperature of Fe-9Cr-2W-V-Ta ferrite steel (JLF-1). The changing rate is about zero below 773K. The rate decreased above 773K below the minimum value. The minimum changing rate was found at 973K. The changing rate above 1073K slightly enhanced at elevated temperatures. The Hv decreasing against loading time can not be found at 1473K, as shown in Figure 1.

3-2 Influence of Temperature on Hv

Figure 3 shows change in Vickers hardness against temperature of Fe-9Cr-2W-V-Ta ferrite steel (JLF-1). Temperatures decreased the Hv. The slope of Hv decreasing was changed at different temperature ranges. Three ranges were divided at 773 and 1073K. Tremendous decreasing in hardness was found from 773K to 1073K. Thus, we observed that large stress relaxation, that is creep, from 873K to 1073K.

3-3 X-ray diffraction

Fig.4 shows X-ray diffraction patterns of Fe-9Cr-2W-V-Ta ferrite steel (JLF-1) at different temperature ranges. Isothermal

Table 1. Chemical composition of Fe-9Cr-2W-V-Ta ferrite steel (JLF-1)-HEAT2

(mass%)

C	Si	Mn	P	S	Cr	W	V	Ta	Fe
0.10	0.05	0.45	0.003	0.002	8.85	1.99	0.20	0.080	balance

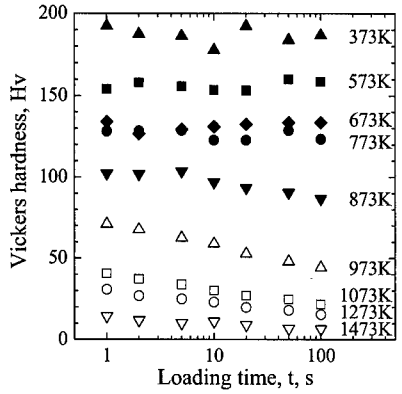

Fig.1 Change in Vickers hardness against loading time at different temperature

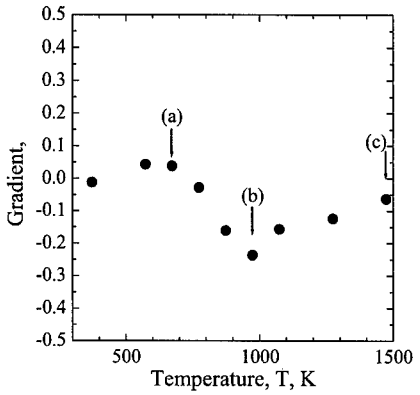

Fig.2 Change in gradient against temperature at Fig.1.

673K-heated sample, which can be applied for fusion reactor materials, shows body centered cubic phase, as shown in Figure 4 (a). The crystal structure of the 973K-heated sample, in which tremendous Hv decreasing was found in range (b) in Figure 3, is body centered cubic phase with chromium carbide, as shown in Figure 4 (b). Figure 4 (c) of the 1473K-heated sample in range (c) in Figure 3 shows face centered cubic phase with wolfram carbide. Based on X-ray diffraction analysis results, body centered cubic phase can not be found at 1473K, whereas face centered cubic phase can not be detected below 1093K.

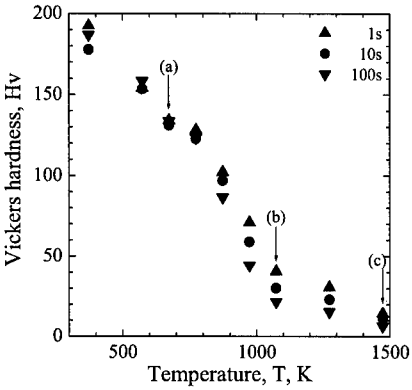

Fig.3 Change in Vickers hardness against temperature at different loading times of JLF-1.

Body centered cubic phase peaks as shown in (a) and (b) were found. High Hv and tremendous Hv decreasing against temperature were typical feature of body centered cubic phase with separated precipitated fine carbides. Based on the small X-ray diffraction peaks, the tremendous Hv decreasing (see Figure 3) from 773K to 1073K the large stress relaxation, that is creep, (see Figures 1 and 2) from 873K to 1073K were explained by wolfram carbide coarsening with chromium carbide annihilation.

On the other hand, face centered cubic phase peaks as shown in (c) were found. Low Hv and slight Hv decreasing against temperature were typical feature of face centered cubic phase.

4. Conclusion

Using in-situ hardness test at high temperature, the hardness values were measured for Fe-9Cr-2W-V-Ta

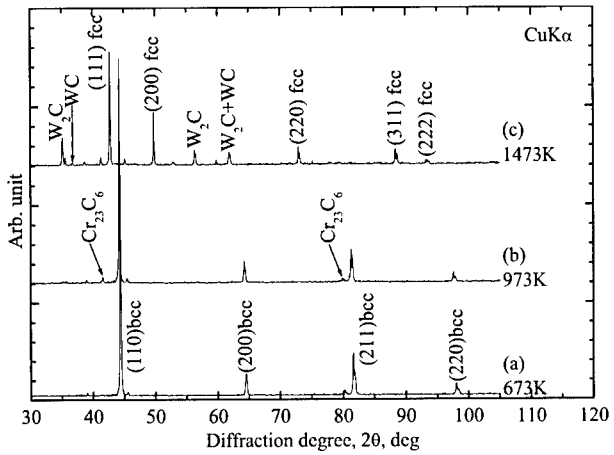

Fig.4 High-temperature X-ray diffruction spectra of JLF-1.
(a):673K, (b):973K, (c)1473K

steel (JLF-1) during isothermal heating from 373K to 1473K. The hardness changes against loading time can not be remarkably observed below 773K. Thus, we concluded that JLF-1 steal with low activation can be applied for fusion reactor materials below 773K. Furthermore, to predict high temperature morphology changes induced by welding for reactor construction, hardness was measured below 1473K. Tremendous decreasing in hardness was found from 773K to 1073K. Based on X-ray diffraction analysis results, bcc phase can not found at 1473K, whereas fcc phase con not detect below 1093K. Thus, large stress relaxation, that is creep, from 873K to 1073K was observed and can be explained by wolfram carbide coarsening with chromium carbide annihilation. By using this method, it is possible to obtain mechanical characteristics in short time with small sample without special forming of test piece.

References

1.A. Kohyama, Y. Kohno, K. Asakura, H. Kayano, : J. Nuclear Mater., 212-215, 684 (1994)

2. A. Kohyama, A. Hishinuma, D.S. Gelles, R.L. Klueh, W. Diets,K. Ehrlich, J. Nuclear Mater., 233-237, 138 (1996)

3. T. Hasegawa, Y. Tomita, A. Kohyama, J. Nuclear Mater., 258-263, 1153 (1998)

4. A. Kohyama, Y. Kohno, M. Kuroda, A. Kimura, F. Wan, J. Nuclear Mater., 258-263, 1319 (1998)

5. N. Inoue, T. Muroga, A. Nishimura, O. Motojima : J. Nuclear Mater., 258-263, 1248 (1998)

6. N. Inoue, T. Muroga, A. Nishimura, T. Nagasaka, O. Motojima S. Uchida, H. Yabe, K. Oguri, Y. Nishi, Y. Katoh, A. Kohyama : J. Nuclear Mater., 283-287, 1187 (2000)

Proceedings of 7th Japan International SAMPE
Symposium & Exhibition, Nov. 13-16, 2001

Textile Composites Models: Integration Strategies

Ignaas Verpoest, Stepan Lomov, Eugene Belov, Richard Parnas and Andreas Prodromou

Department MTM, Katholieke Universiteit Leuven, Kasteelpark Arenberg, 44, Heverlee (Leuven), Belgium
E-mail: Ignaas.Verpoest@mtm.kuleuven.ac.be

Abstract

Textile composites are characterised by a hierarchy of structure, which can be represented by a model of geometry and mechanical behaviour implemented as an integrated modelling and design tool for textile composites. The model of the textile geometry serves as a base for meso-mechanical and permeability models for composites, which provide simulation tools for analysis of composites processing and properties

Key Words: Textile composites, geometry, mechanical properties, permeability

Introduction

Reliable prediction of properties (and mechanical behaviour in the more broad sense) of composite materials is of primary importance for the success of usage of textile composites. The complexity of structure and presence of hierarchy of structural and scale levels lead to the complexity of predictive models, high level of approximation in them, and to the high level of uncertainty of the predictions, when errors are accumulated when the model progresses from one hierarchical level to another. The same hierarchy provides a very generic and reasonable route for construction of the predictive models.

Hierarchy of the textile composite structure

Table 1 shows the "staircase" of structural elements of a textile composite and modelling problems associated with each scale/structure level. Each level on the staircase is occupied by models, which use the input data of topology and spacing parameters of structural elements (i.e. weave pattern and warp/weft count) and properties

Table 1. Hierarchy of structure and models of a textile composite

Structure	*Elements*	*Models*
Yarn (tow)	Fibres	Fibre distribution in the yarn and its change under load/strain. Mechanical properties of the yarn
Fabric (woven, knitted...)	Yarns	Geometry of yarns in the fabric and its change under load/strain. Mechanical behaviour of the fabric repeat under complex loading.
Composite unit cell	Fabric Matrix	Mechanical properties (stiffness matrix/non-linear; strength). Permeability tensor.
Composite part	(Deformed) unit cells	Behaviour under loading. Flow of the resin Behaviour in the forming process.

of the elements themselves (i.e. yarns in a fabric) to predict properties of the structure (i.e. geometry of the fabric).

Level I. Fibre → Yarn: Fibrous structure of a yarn

Normally considered circular, elliptical or lenticular, textile yarns and tows have a complex fibrous structure [1]. Fine details of this structure can affect such properties of a composite as permeability and stress concentrations within yarns. The information of fibre distribution can be used for prediction of mechanical properties of yarns (see e.g. [2]). The fibrous structure can change under load. Consider compression of the yarn, as the most common type of deformation in the composites processing. Initially even distribution of fibres can became more sparse on yarn boundaries and more dense in the central region which can be simulated using conform mapping of deformed yarn cross-sections [1].

Level II. Yarn → Fabric

Internal geometry of a fabric

We shall consider here a woven fabric [3,4]. Consider a single repeat of the fabric. Assume further as given: (1) all the necessary yarn properties; (2) the topology of the yarn interlacing pattern within the fabric repeat; (3) the yarn spacing within the repeat. The problem is to compute the spatial placement of all yarns in the repeat. In more practical terms, this means: determine all the yarn heart-lines within the repeat and define the yarn cross-sectional shape and its dimensions normal to the yarn heart-line for each point along the yarn heart-lines.

The list of the necessary yarn properties includes the yarn geometry in free state and its behaviour in compression, bending and friction. Topology of the yarn interlacing inside a multi-layered woven structure is described with the matrix

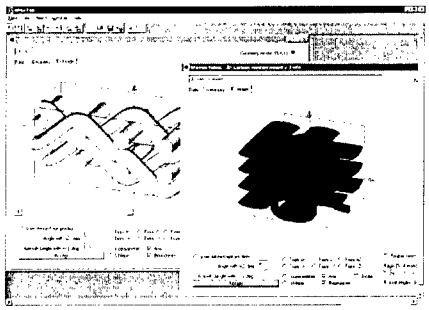

Fig. 1. *WiseTex* software

coding, proposed in [5]. It allows decomposition of yarns in the unit cell into elementary crimp intervals, which leads to a system of algebraic equations representing the minimum energy configuration of the yarns. Solution of the equations gives heights of out-of-plane and in-plane crimp of warp and weft yarns, and the complete yarn geometry is then reconstructed with the help of a spline approximate solution for the minimum energy problem on each crimp interval. This algorithm is implemented in the *WiseTex* software (Fig.1).

Geometrical modelling is supported by investigation of the structure of textile reinforcements and composite materials with X-ray computer tomography (Fig.2).

Once the geometrical model of a fabric is built, the model of fibre distribution inside yarns can be used to produce a complete description of the unit cell fibrous structure. In the simplest case such a model assumes even distribution of fibres, taking into account yarn compression inside the fabric, or more complex models of fibre distribution can be employed. The output data constitute input for meso-mechanical models of composites, which are described below.

Deformation of a dry fabric

Modeling of deformation of a dry fabric is a necessary part of any predictive model of preform formability. The compression model of a textile reinforcement is described

in [6]. The same approach can be applied for

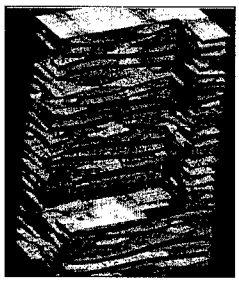

Fig.2. X-ray tomography image of a glass laminate

tension (bi- and uni-axial) of a woven fabric. Applied strain increases spacing of yarns in the fabric. Crimp heights in the deformed state are computed via the energy balance between the work of transversal forces during the change of crimp heights of warp and weft on one hand, and the change of bending energy of yarns on the other hand. The strain of the yarns in the crimp intervals is then computed and forces evaluated using a non-linear tension diagram of the yarn. A similar approach can be applied to shear and bending of the fabric [7,8].

Permeability of the reinforcement

The Lattice Boltzmann (LB) method, which is a meso-scopic approach based on the evolution of "fluid" particles in discrete co-ordinate and velocity space, is effectively used to model complex multi-phase flow

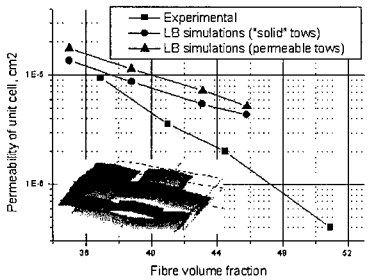

Fig.3. Results of Lattice Boltzmann computations of permeability

through porous media with an arbitrary internal geometry (Phelan et al. [9]). The reliability of the LB permeability prediction is affected to a great extent by the accuracy of the internal geometry description. This includes the description both of the tow path configuration and the fibre distribution in the tows. These data are readily provided by the textile geometry preprocessor.

The way the textile internal structure is usually described is limited to the description of a unit cell, which then is translated in two in-plane space directions to form a regular structure of the textile layer. It is well known that these regular structures are not the case in composite reality as illustrated in Fig.2 for plain-woven glass reinforcement. This highly irregular pattern is a result of non-uniform deformation of the reinforcement layers and of different nesting of the layers. This irregularity as well as non-uniform fibre distribution in tows can have a crucial effect on the permeability simulation, and explains discrepancies of the experimental and predicted data (Fig.3).

Level III. Fabric → unit cell of the composite

Meso-mechanical models for textile composites require one of two distinct, idealized geometrical input formats from a textile geometry preprocessor (TGP).

A first series of models uses the actual yarn co-ordinates to derive the reinforcement volume fraction, orientation distribution, yarn shape and curvature. This is the *Yarn Path Mode* of output of TGP. It is used by the meso-mechanical model based on Eshelby's transformation concepts. The model uses a short fibre analogy to describe the mechanical behaviour of curved yarn segments, combined with a Mori-Tanaka or self-consistent scheme to account for interaction effects [10]. The Yarn Path Mode is also used to transfer geometrical description of a textile to FE packages [11].

Models which use a mapping of an actual textile fibrous structure on a regular 3D mesh rely on another type of idealisation: a volume discretisation in which the original textile architecture is mapped into a 3D grid of simpler, homogenised elements (voxel partitioning). The TGP implements the *Fibre Distribution mode* (FD) as an interface to this model class, creating a 3D array of data which stores fibre content and average fibre orientation for sub-cells of desired size [12].

Level IV: unit cell → composite part

When properties of a unit cell of composite material are known, predictions on the uppermost hierarchical level become possible using general purpose or specialized FE packages. As shown on Fig.4, predictive models described above merge into an Integrated Design Tool, providing the long-waited solution for a designer of composite structures.

Conclusions

The modeling strategy proposed in the present work creates a link between models of the architecture of the textile reinforcement and meso-mechanical and permeability models of composites. It provides an opportunity to use manufacturer's fabric and yarns data, obtained on the standard equipment for textile testing, as a starting point for modeling of composite materials. This gives solid foundation for a *priori* predictions of mechanical properties of composites, allowing accounting for geometry peculiarities (complex crimp and porosity pattern) and yarn mechanical behavior. 2D and 3D textiles are easily constructed, providing great flexibility of input data. A user-friendly software application *WiseTex* allows easy manipulating of fabric and yarn data and visualization tools. The hierarchical concept applies to many different types of textile reinforcement structures, resulting in integrated design software for textile composite modeling.

References

1 Grishanov, S.A., Lomov, S.V., Harwood, R. and Cassidy, T.: J Text Inst, 88-1: 118; 352 (1997)

2 Rudin, A.E., Truevtsev, N.N. and Lomov, S.V. Fibres&Textiles East Europe, 4: 25 (1996); 5: 23 (1997)

3 Lomov, S.V., Gusakov, A.V., Huysmans, G., Prodromou, A. and Verpoest, I.: Comp Sci Techn, 60:2083 (2000)

4 Lomov, S.V., Huysmans, G. and Verpoest, I.: Text Res Jl, 71(6):534 (2001)

5 Lomov, S.V. and Gusakov, A.V. Technische Textilen, 38: 20 (1995)

6 Lomov, S.V. and Verpoest, I. J Reinforced Plastics Composites, 19(16):1329 (2000)

7 Lomov, S.V., Primachenko B.M. and Truevtzev, N.N. Int J Clothing Sci Techn, 3: 49 (1995)

8 Lomov, S.V., Truevtsev, A.V. and Cassidy, C. Text Res J, 70(12): 1088 (2000)

9 Spaid M. and Phelan F. Composites A, 29 A: 749 1998

10 Huysmans, G., Verpoest, I. and Van Houtte, P. Acta Materials 46: 3003-3013 (1998)

11 Lomov, S.V., Verpoest, I., Kondratiev, S.V. and Borovkov, A.I.. Proc.22nd International SAMPE Europe Conference, Paris, France, 379 (2001)

12 Prodromou, A. G., Ivens, J., Huysmans, G., Lomov S., and Verpoest, I. Proc. 12th International Conference on Composite Materials, Paris [s.p.] (1999)

Proceedings of 7th Japan International SAMPE
Symposium & Exhibition, Nov. 13-16, 2001

Cost-Effective Manufacturing Technology for Knitted Fabric Composites

Kazuaki Nishiyabu

Department of Mechanical Engineering, Osaka Prefectural College of Technology
26-12 Saiwai, Neyagawa, 572-8572 Osaka, JAPAN
E-mail: kazu@ipc.osaka-pct.ac.jp

Abstract

The aim of this paper is to introduce some manufacturing technologies for knitted fabric composites taking into account of cost effective to their performance. One of their examples is thermal or vacuum forming method using weft-knitted fabric reinforced thermoplastic composites for a high cycle production, and another example is a low internal pressure molding using cylindrical weft-knitted fabric reinforced thermosetting plastic composites for repairing a gas or sewage branch-pipes. It is concluded that weft-knitted fabric reinforced composites can be located in one of high cost-effective advanced composites materials by modifying the manufacturing process.

Key Words: Cost-effective manufacture, Weft-knitted fabric composites, Thermal forming, Vacuum forming, Low internal pressure molding

Introduction

In general, textile based composites have several unique properties, e.g. high fracture toughness, high impact absorption, high structural anisotropy and deformability, etc. However they are extremely complex for an estimation of their global mechanical properties with changing microscopic textile structures. Therefore it is very difficult for the practical design and manufacture of textile composites to accomplish a high cost-effectiveness to their performances. In order to overcome these designing difficulties, some simulation strategies have been proposed recently [1,2].

Under those situations, most of textile composites have been used so far for particular applications, such as sub-structural parts of space and aircraft. They tend to be used recently for civilian goods and huge structures, e.g. automobiles, sports and civil construction. I make a point that it is necessary for a wider spread of textile composites to realize their low cost manufacturing process. It will be able to be achieved by changing in business activities, because the fabrication cost of traditional textile fabrics, such as weaving, braiding and knitting, is extremely low nowadays for mass-production from a historical point of view, with a few exceptions of particular textile fabrics, such as real 3-axial structured solid fabric. Among all textile structures, weft-knitted structure, which is flexible and deformable apart from weaving and braiding, posses both high degree of designing freedom and high production efficiency with low cost machines and small factory space, because it is produced from only one yarn.

High Cost-Effectiveness of Weft-Knitted Structure

Knitted fabrics are classified into two types of knitted structures, i.e. Warp- and Weft-knitted fabrics by manufacturing method. Warp-knitted fabric is produced

from arrangement of many warp-yarns like weaving, and then the techniques can be applied for production of high-functional fabrics such as 3-dimensional thick fabric [3] and can be utilized for flexible composite [4], in spite of its low tailored flexibility. Weft-knitted fabric, on the other hand, can be produced from only one or more bobbins of yarn basically with intertwining and simple yarn-needle movement such as knit, tuck, miss and transfer [5]. Recently some of weft-knitted machine makers have developed full computer-controlled knitting machines, which can fabricate complex 3-D shaped and non-stitched sweater in each order [6,7]. Therefore this technique will contribute to the fabrication of reinforcements for "Real Tailored Textile Composites" with help of Information Technology in the near future.

Thermal Forming

Preparations of weft-knitted fabric and its composites sheet

As shown in Fig.1(a), the reinforcing fabrics are produced with weft-knitting machines such as V-flat bed or cylindrical type of machine, and impregnated with thermoplastic sheets by film stacking method. It should be noted that high melting viscosity of thermoplastic matrix results in poor impregnation and causes large deformation of flexible fabric. As solution to overcome these problems, commingled yarn or co-knitted yarn, which is arranged thermoplastic yarn and reinforcing yarn into the bundle or between yarns each other, can be utilized for each purpose. In the case of pre-sheet fabrication of knitted fabric thermoplastic composites, it is suitable to use combining co-knitted yarn with film stacking method, because of low fiber volume fraction in knitted structure and lower costs of yarn.

Hot-press forming and deep-drawing [8]

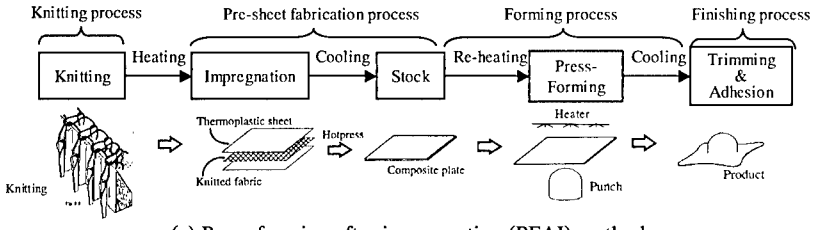

(a) Press-forming after impregnation (PFAI) method

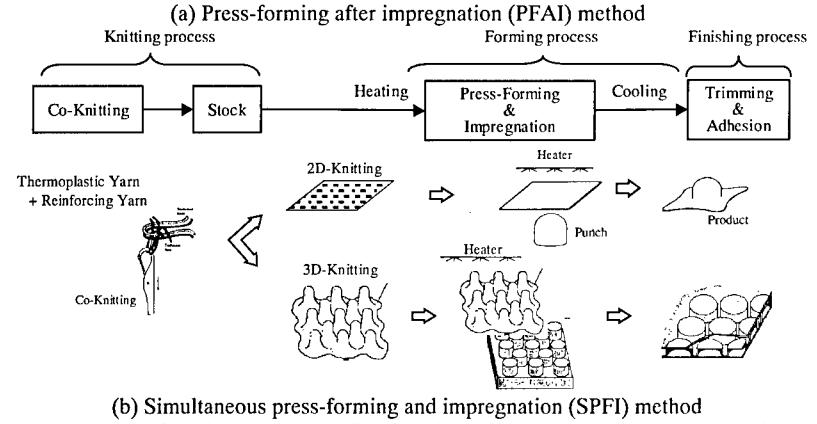

(b) Simultaneous press-forming and impregnation (SPFI) method

Fig.1 Thermal forming processes of weft-knitted fabric thermoplastic composites.

In the case of "Press-Forming After Impregnation (PFAI) method" as shown in Fig.1(a), the pre-sheet is press-formed with closed-dies after re-heating, and is cooled below the glass transition temperature of thermoplastic matrix. In this process, it is key point how to hold the pre-sheet of flexible knitted fabric. Moreover the deformation behavior of knitted loop should be paid an attention because it affects on mechanical properties of deformed products [9].

Fig.2 shows an example of convex product press-formed using weft-knitted carbon fiber (Torayca®, T300) reinforced polypropylene. This structure is originally derived from Ref. [10] patent.

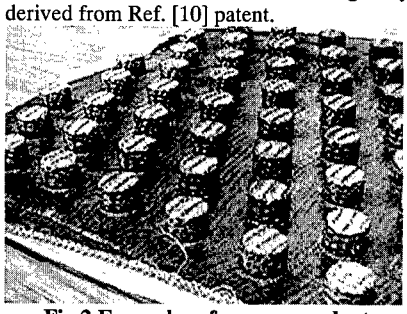

Fig.2 Examples of convex product press-formed using carbon weft-knitted fabric reinforced polypropylene.

In the case of "Simultaneous Press-Forming and Impregnation (SPFI) method" as shown in Fig.1(b), co-knitted fabric are press-formed with an impregnation simultaneously by heating. Therefore such a one step heating method has an advantage in lower cost and energy, but production cycle is lower because it needs to hold enough time for impregnation. Another advantage of this method is possible to utilize quasi-3 dimensional structure co-knitted fabric. Such a near-net shape of knitted pre-forming can be deformed with very low pressure and in keeping the predicted knitted structure. This is a real-tailored technology possible in weft-knitted technology.

Fig.3 shows an example of quasi-3D co-knitted Aramid (Technola®) fabric and its press-formed product.

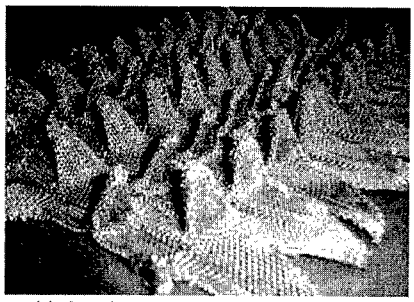

(a) Quasi-3D co-knitted Aramid fabric

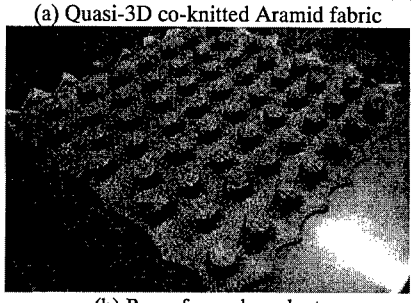

(b) Press-formed product

Fig.3 Example of quasi-3D co-knitted fabric and its press-formed product.

Vacuum Forming [11]

Vacuum forming is used for lots of productions of thermoplastic package covers and the protector for the enclosed product. This manufacturing method is very low cost. As shown in Fig.4, the thermoplastic sheet clamped mechanically is deformed with a mold after reheating and a vacuum is applied to assist in deforming the sheet. The thermoplastic sheet might be allowed to use fiber reinforced composites if the fiber arrangement and heating conditions can be taken into account sufficiently. Only knitted fabric is suitable reinforcement for vacuum forming, because of its high-deformability.

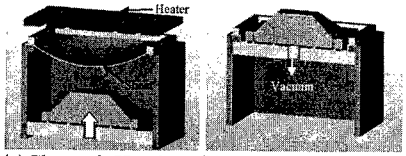

(a)Clamp & Heating (b)Forming & Vacuum

Fig.4 Generic vacuum forming process.

Fig.5 shows examples of convex products vacuum-formed using glass/polypropylene or carbon/polypropylene.

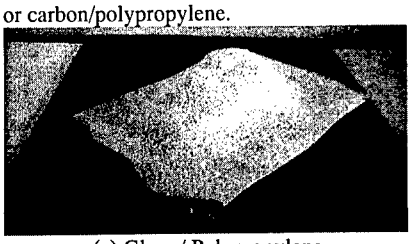

(a) Glass / Polypropylene

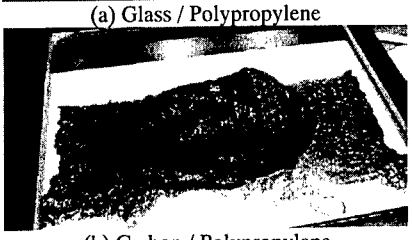

(b) Carbon / Polypropylene

Fig.5 Examples of vacuum formed products.

Low-Pressure Molding [12]

It is useful for repairing the sewage branch pipe as shown in Fig.6 and 7 to utilize a cylindrical weft-knitted fabric reinforced unsaturated polyester resin. The key technologies in such a particulate molding process are resin impregnation in low pressure and non-wrinkling in curved points. Therefore a knitted structure is suitable for such a low cost application.

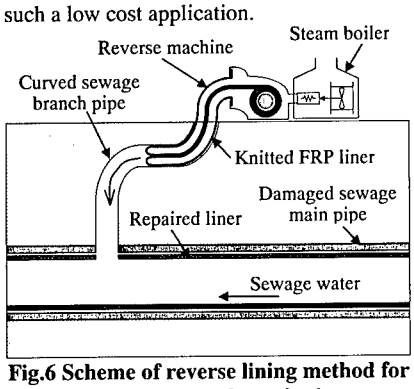

Fig.6 Scheme of reverse lining method for repairing sewage branch pipes.

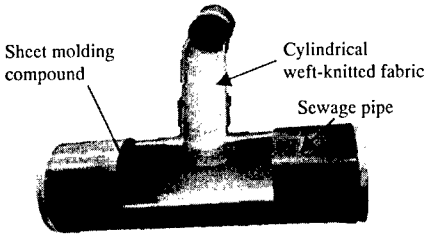

Fig.7 Cylindrical weft-knitted fabric used for lining of sewage branch pipe curved.

Conclusions

Some cost-effective manufacturing technologies using weft-knitted fabric composites were introduced in this paper. Though this technique never referred to be brand-new, the traditional textile technology of weft-knitted fabric can conduct a complemented role in cost-effective manufacture of near-net shape 3-dimensional and flexible advanced composite products.

References

1. I.Verpoest, et al., "Textile composites models: integrating strategies", Proc. of Japan-International SAMPE (JISSE-7) 2001.
2. N.Takano, et al., "The formation of homogenization method applied to large deformation problem for composite materials", Int. Jour. of Solids and Structures, **37,** 2000
3. Asahi Kasei, Co, "Fusion-I®", Japanese Patent, PAT: No.2125634, No.2720985
4. D.Phillips, "Characterization and development of 3D-knitted composites", Doctorial thesis of Katholieke Universiteit Leuven, Sep. 1999
5. D.J.Spencer, "Kniting technology 2nd ed.", Pergamon press, 1989
6. Stoll GmbH & Co., http://www.stoll.de/
7. Shima Seiki Co., http://www.shimaseiki.co.jp/
8. K.Nishiyabu, "Deep-drawing of knitted fabric thermoplastic composites", Proc. of Japan-International SAMPE (JISSE-4), 1992
9. K.Nishiyabu, et al, "Strain Distribution in Deep-drawing of Knitted Fabric Thermoplastic Composites", Proc. of Japan-International SAMPE (JISSE-7), 2001
10. D.Disselbeck, Hoechst Co., Fed.Rep. of Germany Patent No.3412846, Apr.5, 1984, US Patent No.4631221, Dec.23, 1986
11. K.Nishiyabu, et at., Japanese Patent, PAT-No.2001-121439 (In applied), 2001
12. Ashimori Co. Japan, Partem®

Proceedings of 7th Japan International SAMPE
Symposium & Exhibition, Nov. 13-16, 2001

BRAIDING TECHNOLOGIES FOR AIRPLANE APPLICATIONS USING RTM PROCESS

Tadashi Uozumi, Yutaka Iwahori**, Shigeo Iwasawa** and Takumi Yamamoto*

* MURATA MACHINERY, LTD., Braider Section
136, Takeda-Mukaishiro-cho, Fushimi-ku, Kyoto 612-8686, Japan
tuozumi@muratec.co.jp

** Japan Aircraft Mfg. Co.. Ltd. , Aerospace Division
3175, Showa-machi, Kanazawa-ku, Yokohama, 236-8540, Japan

ABSTRACT

Braiding is one of the useful textile techniques for fabricating near-net-shaped fiber preform. Automated braided preform fabrication process has been improved. Triaxial braiding was evaluated as a means of reducing the cost of producing airplane frames. Braided preforms were produced with carbon fiber, and deformed into near-net-shape. The preforms were molded using resin transfer molding (RTM) process with epoxy resin into I-beam frames and panels for investigating mechanical testing and the production cost. Mechanical testing and cost analysis indicated that the mechanical properties of the braided composites are superior to those of aluminum materials and that the combination of the braiding and the RTM process is less costly than the hand-lay-up and autoclave process.

Key Words: Braiding, RTM, CFRP frames

1. INTRODUCTION

In 1990's, textile machine producers, manufactures of textile fabrics and preforms, aerospace companies combined forces to further exploit the benefits of textile processes for fabrication of advanced composite materials, and the airplane manufactures began to show increased interest in textile processes. Textile processes offered the potential for major cost reductions and performance gains.

Braiding is one of the useful textile techniques for fabricating near-net-shaped fiber preform. Fabrication of braided preforms is highly automated and a good balance in off-axis properties can be achieved with braided configurations. The braided preforms are well suited for complex shapes and they have good drapability[1].

Braiding technologies have been improved by developments of combining robotic mechanism to make complex shaped preformes[2]. The automation of complete production systems including a braiding machine has also been improved[3]. The production cost includes the cost of labor, tooling, depreciation, materials and etc. The cost of labor is the biggest individual cost. Automation technology is the most efficient way to reduce the production costs.

Resin transfer molding (RTM) process is well suited for molding the textile reinforced composites. Recently low viscosity thermosetting resin systems have

been developed, so that they are capable of penetrating near-net-shaped large part cavities. In addition, the RTM process is best known its abilities to provide an excellent surface finish, and the cycle times are typically short.

In this paper, the main focus is on work performed in the development of frames or stringers for airplane shown in fig. 1. The frames were made using braiding / RTM process. Tensile and Compressive properties were evaluated the production cost of the braiding / RTM process was compared to that of autoclave processes.

This paper originated from research first presented in "Study on Low-cost CFRP Using Braided Preform / RTM Process," (society of Japanese Aerospace Company, 1999-2000)[4].

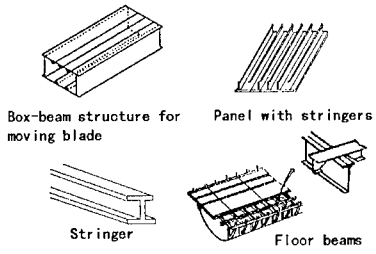

Fig. 1 Airplane applications for braid frames or stringers.

2. BRAIDING TECHNIQUE FOR FRAMES

Fig. 2 shows a schematic of a triaxial braided structure. Multiple yarns are intertwined on a mandrel to form tubular shape. Triaxial braid consists of three types of fiber orientation, $0°$,$+\theta°$ and $-\theta°$.

Braiding yarns make braiding angles ($\pm\theta°$) with axis of the braided fabric. Longitudinal yarns can be inserted into braided fabric in the longitudinal direction. The braiding angle can be varied within a layer to meet the design requirements. If a preform design must be formed to a thickness requiring more than one layer, several layers can be braided over each other to achieve the required thickness.

When the final product configurations can't be obtained directly from braiding process, the preform deforming process is used. In preform deforming process, braided fabric is deformed and flattened to make frame configurations such as 'I', 'J', 'T' and 'Z' shapes shown in Fig. 3. The braid construction after deforming is still same to the initial braid construction in a tubular braided fabric. At the ends in the transverse direction of them, braided fabrics are not cut out but folded up, so that braiding yarns are oriented continuously.

Fig. 4 shows variations of braid frame construction to make thick flange parts of 'I' frame, using other smaller braided fabrics, core materials or mandrels.

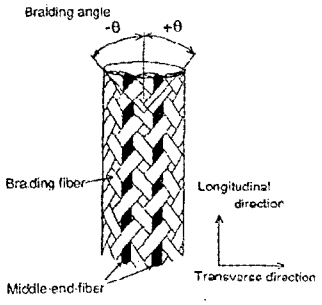

Fig. 2 Triaxial Braid.

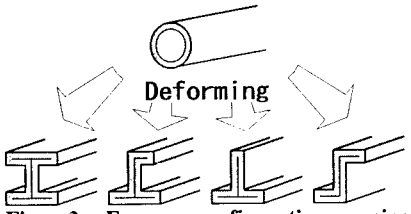

Fig. 3 Frame configurations using deforming process

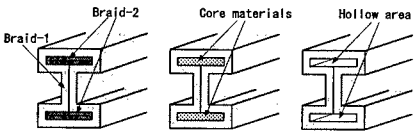

Fig. 4 Variations of braid frame construction.

3. RTM PROCESS

The RTM system is shown in Fig. 5 and consists of four units, pumping unit, heating unit, mold unit and vacuum unit. The preform after deforming process is put into the mold, and the mold with the preform is placed into the heater unit. The pump push and the vacuum pull within the mold are the driving force for bringing the resin into the preform. The required temperature can be controlled during the RTM process.

The RTM process is simple and consists of only few steps; Prepare the mod tooling, place the preform into the mold, close the mold, force or draw the resin into the mold, saturate the preform, cure everything, and demold the parts.

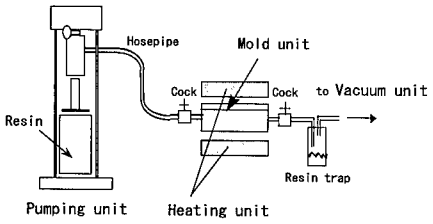

Fig. 5 Schematic of RTM system.

4. BRAIDED COMPOSITE 'I' FRAME

Fabrication

In this chapter, 'I' frame is described as an example of frames. Table 1 shows braided preform fiber architecture for two types of 'I' frames, 'I-60' and 'I-45'. 'I-60' has a 0° /±60° braid construction with 12K carbon fiber bundles and 6K carbon fiber bundles in the longitudinal and bias direction, respectively. 'I-45' has a 0° / ±45° braid construction with 12K carbon fiber bundles and 6K carbon fiber bundles in the longitudinal and bias direction, respectively.

The RTM process conditions are shown in table 2. The temperature was controlled during the RTM process with the PR-500 epoxy resin system. The temperature of the mold for filling the mold with the resin was 160℃. The temperature of mold for curing was 180℃

Table 1 Braided preform fiber architecture.

Type	I-60	I-45
0°yarn	Torayca T300-12K	Torayca T300-12K
Braid yarn	Torayca T300-6K	Torayca T300-6K
Braid angle(θ)	60°	45°
%0° , %±θ	33.3% , 66.6%	41.4% , 58.6%

Table 2 RTM process conditions.

Type	Vacum-Assited RTM
Resin system	Epoxy PR-500
Mold temp.	160℃ (for penetrating)
	180℃ (for curing)

Fig. 6 shows a photograph of 'I' frame composite and 'I' frame preforms of 'I-45'. As for two small 'I' frames, left one is a composite, and another is a braided preform. The dimensions of them are 50mm width, 50mm height and 2mm thickness. A large 'I' frame preform has same fiber architecture as small ones, and the dimensions are 100mm width, 100mm height and 2mm thickness.

Good quality 'I' frames were produced. Photomicrographic investigation of the areas in a flange part, in a web part and in a junction did not show any signs of the large voids.

Fig. 6 Photograph of 'I'frame composite and preforms.

Tensile and Compressive properties

Tensile and compression tests were carried out using flat plate specimens, 'P-60' and 'P-45', which have same fiber architectures as the 'I' frames, 'I-60' and 'I-45', respectively. Fig. 7 and 8 show the results of tensile and compression tests with aluminum materials, Al-7075 and Al-2024, as comparison. 'P-60' and 'P-45' indicated higher specific moduli and strengths than the aluminum materials. The test results make it clear that braided composite frames are qualified to use for frames or stringers of airplane.

5. CONCLUTIONS

Braided preforms were produced with carbon fiber, by the use of deforming process for airplane frames. The preforms were molded using resin transfer molding (RTM) process with epoxy resin into I-beam frames. Braided composite frames indicated superior tensile and compressive properties to aluminum materials.

Furthermore, cost analyses were also investigated. The results of cost studies indicated that Braiding / RTM process has approximately a 30% cost advantage over hand-lay-up / autoclave process. The braiding / RTM process is capable of applying to various frame configurations, and the process is be expected to extend the range of applications of composites for airplane.

References

1) H. B. Dexter, 28th International SAMPE Technical Conference, pp.404, (1996).
2) Z. Maekawa, H. Hamada, A. Yokoyama, H. Uchida, T. Uozumi and M. Hayashi, Japan International SAMPE Technical Seminar, pp.169, (1994).
3) T. Uozumi and M. Hirukawa, 6th Japan International SAMPE symposium, pp.497, (1999).
4) K. Takasaki, H. Uchida and etc, Society of Japanese Aerospace Company Contractor Report ISSN1345-2045 No.1406, 2000.

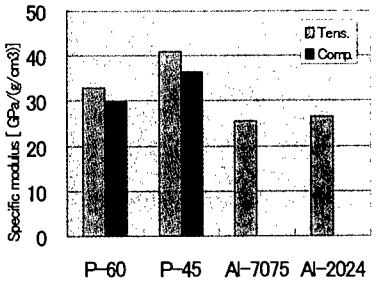

Fig. 7 Specific tensile and compressive moduli.

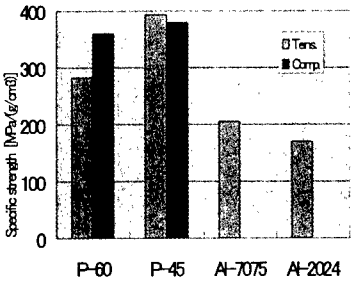

Fig. 8 Specific tensile and compressive strengths.

Proceedings of 7th Japan International SAMPE
Symposium & Exhibition, Nov. 13-16, 2001

Mechanical behaviors of braids under tensile loading

Miwako HANADA* ,Tsuyoshi NISHIWAKI**
Hiroyuki HAMADA***, Asami NAKAI*** and Teruko ISHII*

*:Aoba Gakuen Junior College 3-12-9 Setagaya, Setagaya-ku, Tokyo, 154-0017, E-mail: hanada@aoba.ac.jp **: ASICS Corp. Research Institute of Sports Science 6-2-1 Takatsukadai, Nishi-ku, Kobe, 651-2271, E-mail: waki@tiger4.sp.asics.co.jp *** :Kyoto Institute of Technology Matsugasaki, sakyo-ku, Kyoto, 606-8585, JAPAN

Abstract

Braids have been applied to various scenes in our life. Recently a sash clip and shoelace are representative examples of braids. The mechanical behavior is very complex, because the braids have a large deformability. The purpose of this study is to propose the evaluation method of the mechanical properties of braids under the tensile loading. From the load-displacement curve obtained, some mechanical properties which were used as the characteristic values could be defined. We directly measured Poisson's ratio by observation of the cross-sections of the braids under various tensile loading. Therefore the dependency of the tensile load on Poisson's ratio was quantified. Other three types of shoelaces made of polyester were also used as test specimens. The structures used are Naiki, Kamakura and Marukara braidings and their cross-sections are circle, oval and flat rectangle, respectively. Based on the above results, relationship between braiding structures and mechanical properties could not be clarified.

Key Words: Shoelace, Braid, Tensile Load, Mechanical behavior

Introduction

The braid is constructed by crossing three or more strands or threads under the constant pattern. The braiding pattern affects the cross-sectional shape and appearance. These braids have been used in our life more than 1,000-year past. However even a basic mechanical properties such as the stiffness and strength have not been reported. This is derived from the large deformability and interruption of bending stress and larger Poisson's ratio as compared with common materials.

In this study, the evaluation method of the mechanical properties of the braid under the tensile load was proposed in order to precisely clarify the mechanical behavior. The influences of braiding structure on the proposed mechanical property were discussed.

Experimental Method

The shoelace used has circular cross-section as shown in Fig.1, the braiding structure is called as Marukara-kumi. The diameter is 5.6mm. The tensile tests were performed by using Instron Testing Machine (type 4204). The span lengths, L_0=80, 100 and 150mm were used. In order to calculate Poisson's ratio another tensile test with

Sample	A
Geometry of cross-section	W, T
W[mm]	5.6
T[mm]	5.6
Area [mm²]	24.63

Fig.1 Cross-sectional properties of Sample-A

L_0=80mm was also performed. Poisson's ratio in the linear region of common materials is a constant value. However the braid has a large deformability, the load-deflection curve is not linear at the initial stage. In other words, Poisson's ratio must not be constant, the dependency of load value is very large. Accordingly the relationship between the cross-sectional area and the tensile load are measured. The braid wrapped by the nylon tube is stretched till four kinds of load values, 5, 10, 20 and 50N. These loading values were selected in the initial loading which caused the drastic change of cross-sectional area. Under the stretching of the values, epoxy resin is poured into the tube. After epoxy hardening, the test specimen is removed from the testing machine, and the cross-section at the specimen cut is observed by the microscope.

Result and Discussions

A typical load-displacement curve and cross-sectional photographs obtained from the braid with span length L_0=80 in shown in Fig.2. For the evaluation of the mechanical properties, the following characteristic values were calculated. ***a*** denotes a displacement at the point S that the load reaches 1.0 N. ***b*** denotes the displacement between point S and T. T denotes the intersection of the line *l* and horizontal axis. In ***b***, cross-sections of the above braids drastically changed. c denotes the displacement from point T to displacement at the maximum tensile load,

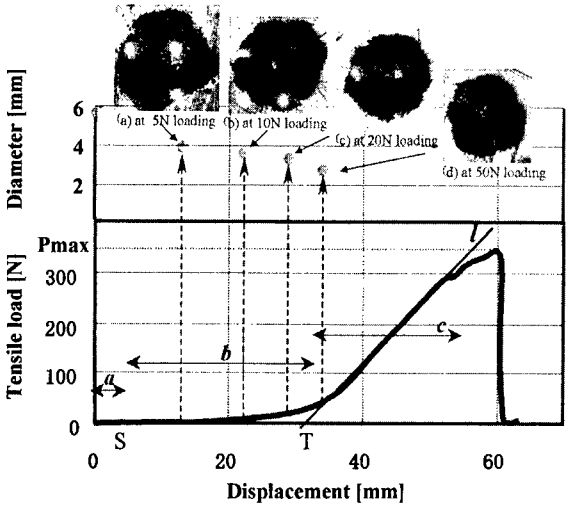

Fig.2 Load-displacement curve obtained from Sample-A with L_0=80mm. Upper graph shows the diameter plotted against displacement with 4 cross-sectional photographs.

P_{max}. By using the above parameters ε_1, ε_2, E_1 and E_2 were calculated by following equations as the mechanical properties of the braids subjected to tensile load.

$$\varepsilon_1 = b/(L_0+a)$$

$$\varepsilon_2 = c/(L_0+a)$$

$$E_1 = P_{max}/\varepsilon_2$$

$$E_2 = tan.l\ (L_0+a)$$

Here, ε_1 indicates the strain under the initial loading. ε_2 indicates the rupture strain of the braid which has the almost constant modulus. E_1 and E_2 are the slopes of the line connected with point T and P_{max} and the tangent to load-displacement curves, respectively. Both E_1 and E_2 correspond to the specific stiffness of the braid.

The results obtained are listed in Table 1. In these comparisons, it was found that all the mechanical properties obtained were almost constant. The proposed properties can not be affected by the overall length of the specimen. In other words, the properties are characteristic values of the braids.

Figure 2 also shows the diameter plotted against the displacement. This figure indicates that the above loading values, 5, 10 and 20 N are in the range of ***b*** and 50N is in the range of ***c***. The reduction in the diameter is notable in the initial loading. It was also confirmed that the cross-section at any tensile load maintained the circle. It was also found that Poisson's ratio could not be constant. Poisson's ratio ν can be calculated from the following equation

$$2\nu_{p\text{-}q} = \frac{\dfrac{D_p - D_q}{D_p}}{\dfrac{L_p - L_q}{L_p}}$$

Here, p and q denote the loading value. D_p and D_q denotes the diameters under the loading values of p and q, respectively. L_p and L_q denotes the displacements under the loading values of p and q, respectively. Table 2 shows the load dependency on Poisson's ratio. Poisson's ratio obtained between tensile loads of 0 and 5N is 1.90. Poisson's ratio of a normal isotropic homogeneous material must not be greater than 0.5. Because the 0.5 means the zero cross-sectional area. This too large Poisson's ratio, 1.90 indicates that the change of diameter is too large as compared with the longitudinal displacement. This is a specific characteristic of the braid. With increasing tensile load, Poisson's ratio decreases. This is derived from reduction in cross-sectional area of the braid.

Table 2 Tensile properties obtained from load-displacement curves

Range of load [N]	Poisson's ratio
ν 0-5	1.90
ν 5-10	0.17
ν 10-20	0.12

Finally, in order to check the influence of braiding structure upon the above 4 mechanical parameters, tensile tests

Table 1 Tensile properties obtained from load-displacement curves

Lo [mm]	Pmax [N]	ε_1	ε_2	E_1	E_2
80	352.4	0.32	0.33	1160	1080
100	337.5	0.25	0.24	1450	1420
150	310.3	0.28	0.24	1480	1280

of other braiding structures shown in Fig.3 were performed. The span length is constantly 100mm. In this figure these three kinds of shoelace called as Sample-B, -C and -D are also on the market. Sample-B, -C and -D have circle, oval and rectangular cross-sections whose structures are called as Marukara-kumi, Kamakura-kumi, Naiki-kumi, respectively.

The characteristic value which was calculated by above-mentioned technique based on the load-displacement curve is listed in Table 3. It was found that all properties obtained were affected by geometric parameters. It was found that Sample- C and -D had the higher stiffness and strength rather than other samples with circular cross-section. On the other hand, Sample- C and -D has smaller ε_1 and ε_2

Sample	B	C	D
Geometry of cross-section			
W[mm]	3.4	6.6	7.5
T[mm]	3.4	3.8	1.8
Area [mm²]	9.08	19.70	13.50

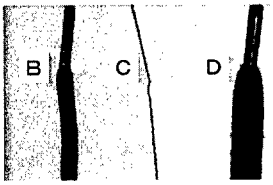

Fig.3 Cross-sectional properties of other Samples, Sample-B, -C and –D.

was almost constant in all samples. Judging from the results, the lower modulus and ther larger ε_1 of Sample-A and –B may be derived from the deformability of the circular cross-section. These results may be derived from that the circular cross-section in the braids can easily deformed, as compared with other cross-sections, oval and rectangular.

Conclusions

The evaluation method of the basic mechanical properties for braids under the tensile loading was proposed. Therefore some parameters, ε_1, ε_2, E_1 and E_1 could be defined. Another important parameter, Poisson's ratio was directly measured by the proposed technique and the relationship between Poisson's ratio and tensile loading value was quantified. The singular Poisson's ratio can make a great influence on the knotting and unknotting behaviors of the braids. Also the the braiding structure affected the mechanical properties, however the relationship could not be quantified.

References

1. Shouzaburou Fujita:Kumihimo wo sekkeisuru, Bijyutsu-shuppan, 1981, pp.2-12
2. Toshio Mori, Chikako Ito, Miyoko Iwasa: Mechanical characteristics and Sensory Evaluation of Flat Braids: Journal of Home Economics of Japan, 44(8), 655(1993)
3. Makiko Tada: "Comprehensive Treatis of Braids 1: Maru-dai braids": Texte,Inc.,Japan,1996, pp. 719-762

Table 3 Tensile properties obtained from load-displacement curves

Smple	L_0[mm]	P_{max} [N]	ε_1	ε_2	E_1	E_2
A	100	337.5	0.25	0.24	1450	1420
B	100	297.3	0.15	0.27	1110	1180
C	100	583.0	0.10	0.27	2160	3080
D	100	438.7	0.10	0.25	1770	1820

Proceedings of 7th Japan International SAMPE
Symposium & Exhibition, Nov. 13-16, 2001

Deformation Mechanism of Textile under Uni and Bi-axial Tensile Load

Kazuhiro SAKAKIBARA, Atsushi YOKOYAMA, Horoyuki HAMADA

Kyoto Institute of Technology
Matsugasaki, Sakyo-ku, Kyoto, 606-8585, Japan

Key Words: Textile, Biaxial tension test, Weave structure

Abstract

This textile preform is user for the reinforcement of textile composites. The deformation mechanism of textile greatly affect the mechanical behavior of it's composite under various external loadings. This study is to investigate the deformation mechanism of the textiles under uni and bi-axial tensile loading. Deformation state of the cross-section of the textile was observed using microscope. As the result of these experiments, The deformation state of the textile can be divide into two state. In first stage, the structure of textile such as crimp ratio and so on is mainly changed by tensile load. And in next stage the fiber bundle of textile is deformed and fractured by the external load. Using these result, we developed the numerical model of fabric which can simulate the deformation state under various external loadings.

1. Introduction

The geometric structure of the textile affects the mechanical property of the textile. Consequentially, the textile shows the nonlinear behavior in the anisotropy. It is difficult to predict the deformation behavior of the textile that shows the peculiar behavior. It is necessary to grasp the behavior of the whole fabric structure in which it is only in mechanical property that the fabric shows in order to predict the deformation behavior of the fabric. As the technique that solves these problems, the analysis using the computer is proposed. However, the construction of the numerical model that expresses the relationship between mechanical property that the textile shows and structure is required in order to use the analysis using the computer. Investigations by the experiment on mechanical property and deformation behavior of the textile

Table 1 Textile for target specimen

	Warp	Weft
Fiber orientation number per 100 mm^2	74	70
Initial crimp angle (degree)	18.8	30.5
Aspect ratio of initial cross-section	0.72	0.38

are necessary for the construction of this numerical model. In this study, the construction of this numerical model was made to be a purpose. Mechanical property and deformation behavior of the textile were investigated actually. And, Numerical model of the textile was constructed according to collected experimental data. The analysis simulation was practice using made numerical model. Analytical result was compared and was examined with the experimental data. And the effectiveness of the analysis was examined.

2. Experiment approach

The cloth made of the acrylic with the biaxial plain weave structure was used as specimen. The outline of the specimen is shown at Table 1. In this study, biaxial tensile testing machine was used as testing machine.

The dimension of the specimen was made to be 120mm length of the length and 120mm length of the width. The tensile velocity was made to be 1.00 (mm/sec.). The measurement of the strain made the point on specimen surface, and it calculated the strain by the relative displacement magnitude of the distance. The cross-sectional observation fixed specimen in the condition that put on the load, and it observed the cross section by the microscope.

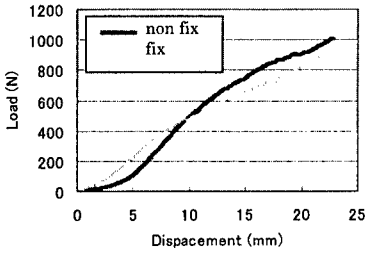

Fig 1 Load-displacement curve of textile

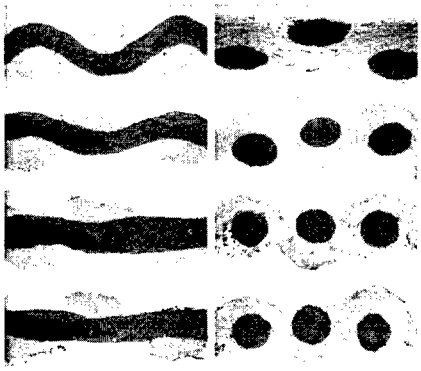

(a) Weft (b) Warp

Fig.2 Cross-section of deformed testile

3. Experimental result and discussion

In the uni-axial tensile test, the following are shown in Fig.1: Load-displacement curve in putting on the load to the weft yarn direction and load-displacement curve in fixing the

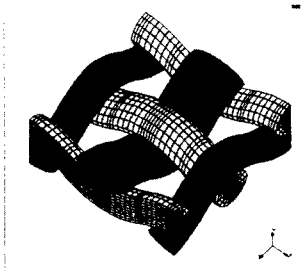

Fig. 3 Numerical model of textile

cross-direction displacement. As a result of comparing these 2 curves, it was confirmed that initial gradient differed. And, the tendency of the curve has changed 30%～50% range at the maximum load for the boundary in these 2 curves.

This phenomenon seems to be not material peculiar property but thing by the change of the fabric structure. Then, the deformation of the cross-sectional shape at each load was investigated. The parallel cross-section photograph in the weft under each load is shown in Fig.2-a. Parallel cross-section photograph in the warp also is shown in Fig.2-b. The tendency in the whole figure is observed. Fiber bundle of the load direction (weft) is extended, and the crimp angle decreases. Crimp angle which cross-direction fiber bundle (warp) makes grows with act on the deformation of fiber bundle of the load direction (weft). The deformation of crimp angle which fiber bundle of the load direction (weft) makes in point of time which reached 30% load at maximum load seems to be achieving limitative this phenomenon. The property which fiber bundle it of the load direction shows after the 30% load at the maximum load seems to have appeared in the gradient of the graph.

And, the cross-sectional shape of fiber bundle is observed. Cross-sectional shape changes on fiber bundle of the load (weft) direction from the ellipse to round shape in order to put on the load. Cross-direction fiber bundle (warp), since there is no the cross-direction load, the effect in which crimp angle of fiber bundle of the load direction decreases is received, and it changes from round shape to the ellipse.

Warp and weft influence, and there is, the fabric has formed the deformation behavior of the whole textile. It is necessary to consider the deformation behavior of not only fiber bundle but also cross-direction fiber bundle which it influences of the load direction, when the fabric is evaluated.

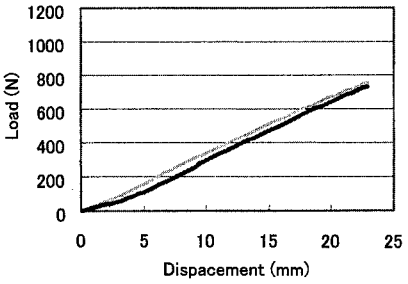

Fig.4 Load-displacement curve by calculation

4. Numerical proceedure

Proposed numerical model was constructed to be the smallest unit that consisted of 2 warp bundles and 2 weft ones. Element type that constituted the model used the three-dimensional and solid type. Plain weave structure that consisted of warp and weft was expressed. The numerical model is shown in Fig.3. The dimension of the model used the dimension measured by the cross-sectional observation. It was made to be length 2.7mm, width

2.8mm, and 1mm thickness. The X-axis direction is made to be orientation direction of the warp, and the Y-axis direction was made to be orientation direction of the weft.

The material property used information got from tensile test of fiber bundle of one. E1 and E2 were calculated according to two collinear approximation of the result graph. By setting E1 and E2, the no linearity of the material property was expressed. The yield stress was made to be 27.6MPa as E1=599MPa,E2=267MPa. The boundary condition was set at the condition equal to the experiment. The load was given in the weft direction, and the displacement velocity was made to be 1mm/time. 2-types were analyzed. Type 1:Without fix the cross-direction displacement. Type 2:Fix the cross-direction displacement.

5. Numerical result and discussion

Load-displacement curve according to the analytical result is shown in Fig.4. Initial gradient of the curve is different by fixation of cross-direction displacement. The gradient of the curve has changed the similar range for the boundary. Next, the deformation of crimp angle that the fiber bundle of the load direction made was noticed. The graph of the deformation of the crimp angle that the fiber bundle by the analysis makes in Fig.5 is shown, by the experiment makes in Fig.6 is shown. It was confirmed that the almost similar tendency in these two graphs. By these results, it seems to have appeared in not only setting of the material property constant but also analysis the effect of the fabric structure.

6. Conclusion

Fiber bundle affects the deformation behavior of the whole textile from the structure. It was possible that the analysis using the numerical model constructed by this consideration expressed the effect on mechanical properties that the fabric composition gives.

Therefore, the analysis using the three-dimensional model that expressed the fabric structure is effective as a means for predicting the deformation behavior of the textile.

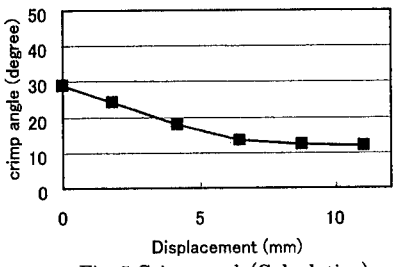

Fig. 5 Crimp angle(Calculation)

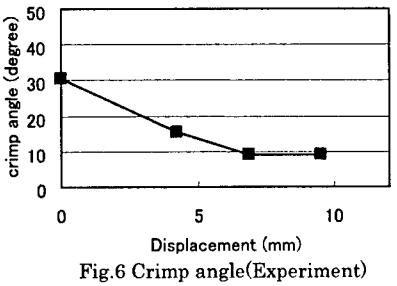

Fig.6 Crimp angle(Experiment)

Proceedings of 7th Japan International SAMPE
Symposium & Exhibition, Nov. 13-16, 2001

Strain Distribution in Deep-drawing of Knitted Fabric Thermoplastic Composites

Kazuaki Nishiyabu [1] Naoki Takano [2], Masaru Zako [2] and Reiko Fujitsu [2]

[1] Department of Mechanical Engineering, Osaka Prefectural College of Technology
26-12 Saiwai, Neyagawa, 572-8572 Osaka, JAPAN,
E-mail: kazu@ipc.osaka-pct.ac.jp
[2] Department of Manufacturing Science, Graduate School of Engineering, Osaka University
2-1 Yamada-oka, Suita, 565-0871 Osaka, JAPAN,
E-mail: takano@mapse.eng.osaka-u.ac.jp

Abstract

As manufacturing method of fiber reinforced thermoplastics (FRTP), the deep-drawing method is studied. Two types of knitted fabrics, i.e., plain and rib knitted fabric, are used as reinforcement because of their high drapability. The constituents are the aramid fiber and the polypropylene. The strain distribution during the deep-drawing process was measured very precisely based on the knitted structures, motivated by the fact that the function of the product is strongly dependent on the largely deformed knitted structures. This paper discusses the comparison for deformation behaviors of plain knitted fabric with rib knitted one. Clear differences in the strain distribution or forming mechanism were revealed between the plain and rib knitted fabric reinforced composite materials. From the experimental results, it is obvious that the deformation behaviors and the draping mechanism are quit different according to the knitted structures. These evidences are very useful for the microscopic structural designing of knitted fabric, which is used as reinforcements in deep-drawn products of fiber reinforced thermoplastic composites.

Key Words: Thermoplastic composites, Weft-knitted fabric, Deep-drawing, Strain distribution

Introduction

Fiber reinforced composite materials, which have high specific modulus and strength, are required for both achievement of lower cost manufacturing system and recycling available material selections. Thus it is a key technology in present to develop the cost-efficient fabrication methods for fiber reinforced thermoplastic composites, which have very complicated shapes. Deep-drawing method is one of the typical forming processes for continuous fiber reinforced composites [1], and it has some advantages in low cost and high cyclic production as compared with autoclave or tape lay-up method for manufacturing of thermosetting plastic composites. The production procedure is very simple as the below sequence: 1) impregnation, 2) heating, 3) forming and 4) cooling, because thermoplastic matrix is used. The sequential structural deformation of fiber reinforcements in each process significantly affects on the mechanical properties of forming products. In present, however, there is no definition for the evaluation method of deformable performance in microscopic scale. Therefore it is important to obtain the experimental information for strain distribution in fiber configurations during forming processes.

Experimental Details

Weft-knitted fabrics examined

The microscopic strain field of knitted fabric thermoplastic composites has been measured as experimental work for two types of typical weft-knitted fabrics, i.e. plain knitted and rib knitted fabrics as shown in Fig.1. Such knitted fabrics are prepared with Aramid fiber (Teijin Co., Technora®, T-360 Spunnized yarn, #10 (572de.)).

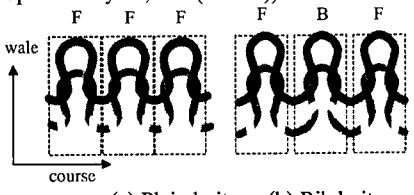

(a) Plain knit (b) Rib knit

Fig.1 Geometries of knitted structures.

Deep-drawing process

The knitted fabric reinforced polypropylene composite sheet was prepared with film stacking method and deep-drawn by semi-spherical punch with a low clamping force after reheating as shown in Fig.2.

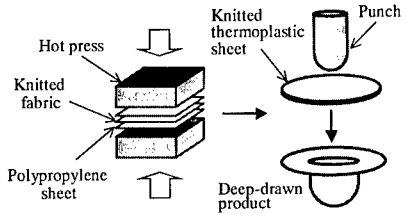

Fig.2 Scheme of deep-drawing process.

Definitions of Strain

With comparing the deformation behaviors of plain knitted fabric with rib knitted one, it is evidence from uni-axial tensile test of rib knitted structure that the rotation of sinker loop is more predominant than that of needle loop. Thus strain is defined as in-plane deformation of a unit of knitted loop for the plain knitted fabric composites (Eq.1a and 1b). With rib knitted ones, on the other hand, it is defined as in-plane deformation at a unit of grid because of the complicated deformation behaviors (Eq.2a and 2b).

For the case of plain knitted fabric:

$$\varepsilon_x = \frac{1}{2}\left(\frac{B'C'-BC}{BC} + \frac{D'A'-DA}{DA}\right)\times 100(\%) \quad (1a)$$

$$\varepsilon_y = \frac{1}{2}\left(\frac{A'B'-AB}{AB} + \frac{C'D'-CD}{CD}\right)\times 100(\%) \quad (1b)$$

For the case of rib knitted fabric:

$$\varepsilon_x = \frac{A'B'-AB}{AB}\times 100(\%) \quad (2a)$$

$$\varepsilon_y = \frac{B'C'-BC}{BC}\times 100(\%) \quad (2b)$$

Where ε_x: x-axial strain, ε_y: y-axial strain.

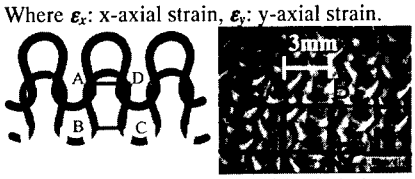

(a) Plain knit (b) Rib knit

Fig.3 Definition of strain.

Experimental Results

Fig.4 shows the strain distributions along wale direction of plain knitted fabric deep-drawn sheets with changing of punch stroke. In the case of low stroke (z=10mm), only 20% or less strain occurs almost wholly in both axial and lateral directions. When the stroke reaches to z=30mm, strain distribution affects significantly at the edges of C and C' points, where axial Y-strain concentrates up to 50% and lateral X-strain tends to be negative. As the stroke closes to the ultimate elongation of knitted fabric composites (z=50), axial Y-strain is extremely high, while lateral X-strain increases negatively to around 40%, in the region of E and F points.

From these strain distributions, a knitted loop make elongate to wale direction the largest at the edges, afterward the elongation of loop relaxes because the surrounding fabric is drawn to the cylindrical parts as the stroke increases in the case of plain knitted fabric composites. Therefore it is important for deep-drawing performance of knitted fabric composites to relax strain concentrations at flat, i.e., un-drawn parts.

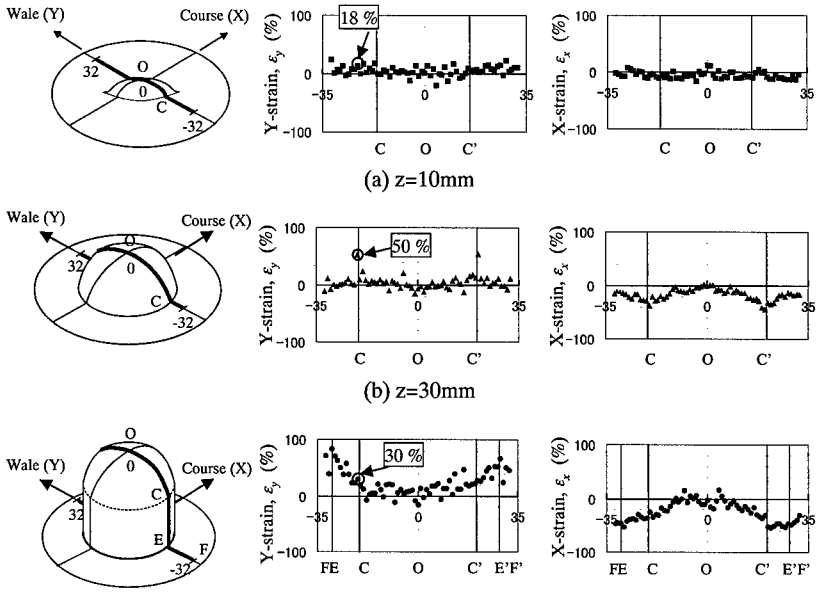

Fig.4 Strain distributions along wale direction (Plain knit).

Fig.4 shows the strain distributions along wale direction of rib knitted fabric deep-drawn sheets with changing of punch stroke. In the stroke of z=10mm, the axial Y-strain reaches to around 20% in the spherical region contacting to punch. Its tendency enhances as the stroke increase to z=30mm. When the stroke reaches to z=52mm, the axial Y-strain increases up to around 50% in spherical parts and over 90% in the bottom of the cylindrical ones.

Discussions

On speaking from macroscopic point of view of strain distribution in deep-drawn sheet, in the case of plain knitted fabric composites, the strain concentrates at the edge region and changes significantly between the spherical parts and cylindrical ones, but the strain distribution is uniform for rib knitted ones. The strain relaxation at the edge part is large for the plain knitted fabric composites, but it is lower for rib knitted ones. Therefore, on speaking the mechanism of draping, the drawing process is dominated for the plain knitted fabric composites, but the loop stretching is dominated for the rib knitted ones. The rib knitted fabric composites behave larger in the degree of anisotropy than plain knitted one.

From the deformation in outer shape of deep-drawn products for plain and rib knitted fabric composites shown in Fig.6, it is obvious that plain knitted fabric is larger in the measure of drawing than rib knitted one. In addition, the degree of anisotropy for rib knitted fabric is larger than that for plain knitted one.

From these experimental results, it is concluded that the deformation behaviors and the draping mechanism are quit different according to the knitted structures.

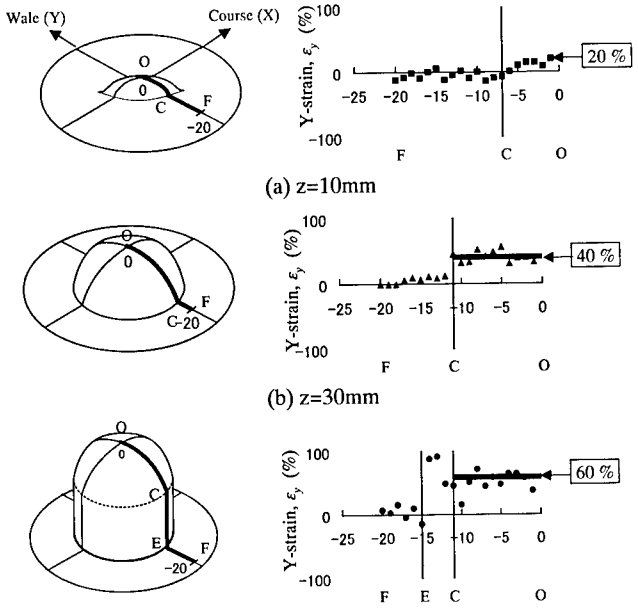

Fig.5 Strain distributions along wale direction (Rib knit).

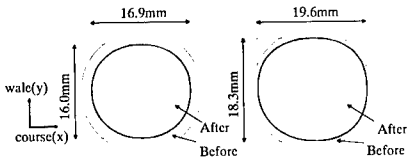

(a) Plain knit (b) Rib knit

Fig.6 Deformation in outer shape of deep-drawn products.

Conclusions

In this study, strain distribution during deep-drawing process of weft-knitted fabric thermoplastic composites was measured more preciously based on knitted structures. Clear differences in the strain distribution or forming mechanism were revealed between the plain and rib knitted fabric. These experimental results are useful for the microscopic structural design of weft-knitted fabrics, which are used for the reinforcements of deep-drawing products.

To conclude it can be stated that the consideration of strain distribution in combination with finite element analysis based on homogeneous method [2] is very useful for understanding the complicated deformation behavior of textile based composites, and for both material and process designing of complicated shape composite structures with repeated textile microstructures.

References

1. K.Nishiyabu, Deep-drawing of knitted fabric thermoplastic composites, Proceeding of International-Japan SAMPE (JISSE-4), 1992
2. N.Takano, et al., "The formation of homogenization method applied to large deformation problem for composite materials", Int. Jour. of Solids and Structures, 37, 2000

Proceedings of 7th Japan International SAMPE
Symposium & Exhibition, Nov. 13-16, 2001

Mechanical Properties of Square Braided Fabric

Takahisa Ueda1, Akio Otani1, Asami Nakai1 and Yoshimichi Fujii2

1 Division of Advanced Fibro-Science, Graduate School, Kyoto Institute of Technology, Matugasaki, Sakyo-ku, Kyoto, 606-8585, Japan
E-mail: nakai@ipc.kit.ac.jp

2 Seikow Chemical Eng. & Machinery, LTD Sioe 3-1-16 Amagasaki, 661-0976 JAPAN

Abstract

Cyclic compression test was performed on square braided fabric and the hysteresis loop in load and displacement was investigated. The observation of the cross section with optical microscopy was performed and the mechanism of deformation under compressive loading was clarified. Structure inside of braided fabric and compressive properties were extremely changed at first compression and then tended to converge to stable structure.

Key words: Square braided fabric, Cyclic compression test, Fiber orientation state.

1. Introduction

Braided fabric has a structure which exhibits the ability of long fiber bundle and the composite has excellent mechanical properties. The representative braided fabrics are classified into three kinds of braided fabrics, flat braided fabrics, tubular braided fabrics and square braided fabrics, according to the shape and the manufacturing technique. Especially, in the square braided fabric, the fiber bundles are continuously braided each other through the thickness and longitudinal direction. Therefore, when the square braided fabric was used as reinforcements of the composite, it is realized to prevent the delamination which has been the disadvantage of other laminated composites.

This study has currently focused on the relation between structure of braided fabrics and mechanical behavior of the fabrics on thick square braided fabric. Cyclic compression test was performed on square braided fabric and the hysteresis loop in load and displacement was investigated. Slices of cross-section of the braided fabrics were observed by optical microscopy for each compression loading and the observation results were related to the load-displacement behavior. From these results, mechanism of deformation on square braided fabric was clarified.

2. Experiment

2.1 Specimens

The cross section of fabricated square braided fabric is shown in Fig.1(a). Arrows in this figure indicate the direction of the movement of the spindles. 4 tracks (track a, b) constructs two different fiber bundle pass as shown in Fig.1(b); fiber bundle 'a' and 'b'. In Fig.1(b), narrow and wide line shows the outline of square braided and the fiber bundle pass respectively. The fiber bundle 'a' is composed by 2 straight lines connecting the corners diagonally and shows reciprocating motion. On the other hand, fiber bundle 'b' is composed by 4 straight lines connecting the 4 flat surfaces and shows round motion.

Aramid fiber bundle (HM-1055-7250d 12 μ m × 5000 filament; AKZO) was used and two fiber bundle was combined with 1 fiber bundle.

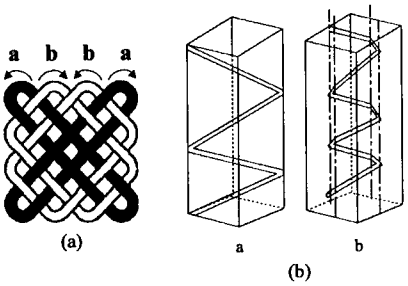

Fig.1 Square braided fabric.

The braiding angle θ, the angle between longitudinal direction and fiber bundle on route b appeared to the surface, were changed. Three types of specimen with different braiding angle of 22, 27, 35 and cross sectional area of 100mm^2 were fabricated.

2.2 Compression test

Cyclic compression test for the square braided fabric was performed by Instron universal testing machine (Type4206) with flat platters. Braided fabric for the test was 150mm in length. The diameter of upper and bottom platter was 100 and 150mm respectively. The square braided fabric was compressed and unloaded between 2000N and 0N for five cycles. Cross head speed is 1mm/min. The hysteresis loop in load and displacement was measured.

2.3 Observation of cross section

In order to investigate the change in fiber orientation states inside of the square braided fabric under the compression load, observation of the cross section was performed. During the compression tests, the specimen was impregnated with resin under certain compression loading. Then the polished cross-section of the braided fabrics was observed by optical microscopy at intervals of every 1mm.

From these pictures, the data of the shape and location of the cross section of fiber bundles could be taken, consequently, centroid of the fiber bundles could be calculated. From these data, 3 dimensional plots for the centroid of the fiber bundle before and after testing were constructed to examine the fiber orientation state and the deformation state of the square braided fabric.

3. Results

3.1 Compression properties

Typical hysteresis loop in load and displacement was shown in Fig.2. In the 1st compression cycle, compression curve was composed of two regions; the load increased slowly at first region and then load increased rapidly at second region. Reconstruction curve had only second region of compression curve and the residual deformation was about 40% of initial specimen size at un-loading point of 0N. After 2nd cycle, the hysteresis loop in load and displacement tends to converge at same curve.

Fig.3 shows the relation between compression ratio and the compression cycle. Here, compression ratio is the ratio of the compressive displacement at the maximum load to the initial thickness of the specimen before test as shown in Fig.3. Also, Fig.4 shows the relation between reconstruction ratio and the compression cycle. Here, reconstruction ratio is the ratio of the reconstructive displacement to compressive displacement as shown in Fig.4. The compression ratio is corresponded with the compressive strain at 2000N and the reconstruction ratio means a kind of residual strain. The compression and reconstruction ratio was changed largely from 1st cycle to 2nd cycle and then kept almost same value. These compression properties were the same in the 3 kinds of specimens with different braiding angle, therefore it was concluded that the angle did not affect to the compression properties. From there results, it is considered that the specimen was deformed largely in the first compression and the structure of the specimen was changed into more stable state, so that the deformation properties became the same after first cycle.

3.2 Deformation state

Figure 5 is the typical picture of cross section for the specimen before and after compression. In this figure, compression direction is ups and downs and the fiber bundles on the same track are filled with same pattern. When square braided fabric was compressed, the size was down in compression direction and up in transverse direction. However, the deformation to the transverse direction was not uniform, the center of the side face on the square braided fabric deformed to the transverse direction more than the corner edge deformation and the difference was defined as Δt. It was confirmed the shape of the fiber bundles were changed, however, the cross section of the each fiber bundles did not vary before and after compression.

From these pictures of the cross section, the centroid of the fiber bundles was calculated. Using data of the centroid of the fiber bundles, the fiber orientation state before and after compression was investigated.

First the crimp ratio, which describes the degree of undulation of fiber bundle, was defined as shown in Fig.6. The crimp ratio was calculated by dividing the sum of the length $l_1 \sim l_n$ by the length L between G_0 and G_n, that is, the crimp ratio is the ratio of length of fiber bundle to the linear distance at the both end. In the case of fiber bundle b, there was no difference in the crimp ratio between before and after compression (from 1.11 to 1.14). Whereas, crimp ratio increased in fiber bundle a after compression (from 1.14 to 1.23).

Next, braiding angle was investigated. Fig.7 is the schematic drawing of fiber orientation to consider the projected braiding angle on the X-Z and Y-Z plane. In this figure, longitudinal direction of braided fabric is Z direction, and the compression direction is Y direction. θ_{xz} and θ_{yz} were defined as the angle between Z direction and fiber bundle projected on X-Z and Y-Z plane respectively. These angles before and after compression were shown also in Fig.7. θ_{xz} and θ_{yz} of fiber bundle 'a' before compression were

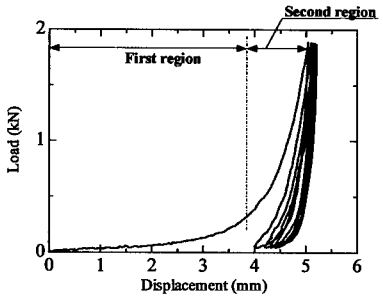

Fig.2 Load-displacement curve.

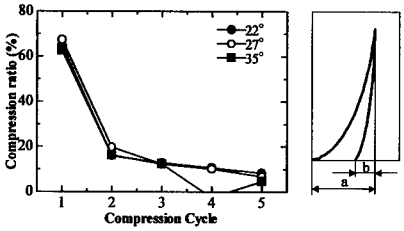

$$\text{Compression ratio} = \frac{a}{\text{Initial thickness}}$$

Fig.3 Relationship between compression ratio and compression cycle.

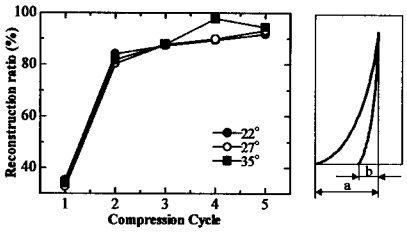

$$\text{Reconstruction ratio} = \frac{b}{a}$$

Fig.4 Relationship between reconstruction ratio and compression cycle.

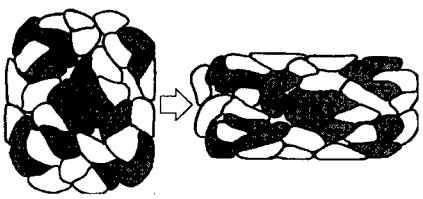

Fig.5 Deformation of cross section for square braided composite.

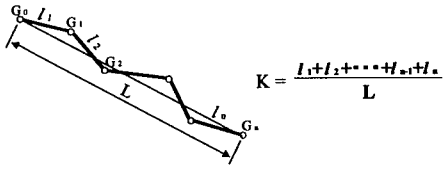

Fig.6 Definition of crimp ratio.

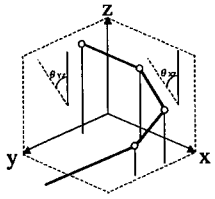

		Before	After
θ_{xz}	a	32.2	48.8
	b	39.3	51.6
θ_{yz}	a	34.8	27.5
	b	46.0	28.3

Fig.7 Projected braiding angle.

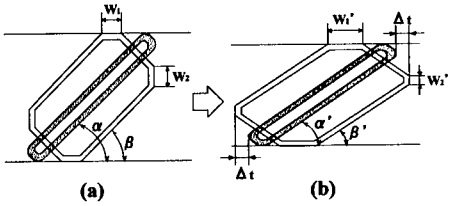

Fig.8 Deformation mechanism.

bigger than that of fiber bundle 'b', and these angle of 'a' and 'b' became almost same after compression. From the result, since the different braiding angle on different track was changed into the same braiding angle, it is considered that the fiber orientation state after 1st compression was stable condition for square braided fabric, therefore, the properties after 1st cycle compression were changed and then conversed.

4. Discussion

Figure 8 shows the possible deformation mechanism projected on X-Y plane considered with all results. Basically, the fiber bundles in the square braided fabric have some apparent bending parts on X-Y plane. The apparent bending parts must appear at the surface of square braided fabric. In the case of fiber bundle a, the fiber bundle is composed by 2 straight lines connecting the corners diagonally and there are little exposed at the corners. On the other hand, in the case of fiber bundle 'b', they have some apparent bending parts on X-Y plane as shown in this figure with w_1 and w_2.

After compression, the angle α and β of fiber bundle and thickness of the specimen decreased. In the case of fiber bundle a, the change in angle α was dominant. Whereas in the case of fiber bundle b, the width of apparent bending part was also changed in addition to change in angle β. The apparent bending part w_1 was increased because this part was contacted with compressive plates, on the other hand, the part w_1 on the side of the specimen was decreased because this part was pushed out on the free side of specimen by compression.

This mechanism can explain the change in the crimp ratio. Normally, the crimp ratio would be larger after compression, however, in the case of fiber bundle b, the fiber bundle could deform without restriction on the free surface. From this mechanism and the fact that the angle α is equal to β and the angle α ' is equal to β ', it was thought that there was a distance Δt between 'a' and 'b' fiber bundle as described in Fig.5.

Consequently, the square braided fabric could deform to stable fiber orientation after first compression, and kept same fiber orientation under more cyclic compressive loading. The difference in braiding angle before compression was normalized into same braiding angle after compression. With stable fiber orientation, the dimension and compressive properties was not also changed.

To protect the flowing away of the fluid from the cover plate and pillow block of the bulb, pump and so on, grand packing has been well used. Here, the deformation behavior of the grand packing subjected to cyclic compression loading is important factor which dominate the capability. These results in this study indicated that the square braided fabric appropriate for the usage as the grand packing, which is subjected to cyclic compressive loading.

Proceedings of 7th Japan International SAMPE
Symposium & Exhibition, Nov. 13-16, 2001

MECHANICAL PROPERTIES OF WEFT KNITTED FABRIC COMPOSITES

Surya D. Pandita, Gert Huysmans, Ignaas Verpoest

Department of Metallurgy and Materials Engineering, Katholieke Universiteit Leuven
Kasteelpark Arenberg 44, B-3001 Leuven, Belgium
E-mail: darma.suryapandita@mtm.kuleuven.ac.be

Abstract

New types of weft knitted fabrics were produced by modifying the knitting process. The tensile properties of these knitted fabric composites were investigated with different types of fibres and matrices. The degree of anisotropy in the tensile properties is influenced by the fibre orientation, which is related to the knitted structure. The impact properties of these knitted fabric composites are also investigated under low velocity impact loads. The impact damage is mainly flexural failure and no delamination was observed.

Key Words: Textile fabric composites, Mechanical Properties, Impact Failure.

Introduction

In the last decade, the mechanical properties of weft and warp knitted fabric composites have widely been investigated.[1-6] The in-plane mechanical properties of knitted fabric composites were reported to be lower than braided and woven fabric composites. These are due to a lower fibre volume fraction, the almost random fibre orientations, and for aramid fibres the weak interface.

In conjunction with the progress of computer applications in the knitting technology, many "exotic" knitted fabrics have been introduced recently. The new knitted fabrics are expected to have more dimensional stability without decreasing a lot of their conformability and to have higher mechanical properties. The aims of this paper are to investigate the tensile properties of new weft knitted fabric composites and their impact properties. Glass, aramid and carbon fibres were used. Thermoset (Epoxy) and thermoplastic (polypropylene) matrices were used to impregnate knitted fabrics. The tensile properties of knitted fabric composites with thermoset as matrix are compared to the tensile properties of woven fabric composites. Moreover, the tensile properties of knitted fabric composites with thermoplastic as matrix are compared to the tensile properties of randomly glass fibre mat/polypropylene composites.

Experimental

All weft knitted fabrics were supplied by the Flemish company VERDONCK-WINDHEY. Plain weave fabrics coded as R/420 were supplied by another Flemish company SYNCOGLAS. The knitted fabrics and woven fabrics were laid up with epoxy films F533, supplied by HEXCEL. Afterwards, the textile pre-pregs were cured in an autoclave with a pressure of 3 Bar and a curing temperature of 125 °C for 2 hours.

For the thermoplastic composites, knitted fabrics are made out of commingled

yarns. The knitted fabrics are then heated in a hot press with a pressure of 20 bar and a temperature of 200 °C (polypropylene matrix) or 220 °C (polyamide matrix) for 5 minutes. Then, they are cooled to 100 °C with a cooling rate of - 6 °C/min.

Tensile tests were carried out on an Instron 4505 installed with hydraulic grips. The tensile specimen dimensions were 210 mm by 2.5 mm. The gage length was 150 mm. An extensometer with a gauge length of 50 mm was attached to the specimens.

The impact properties of knitted fabric composites are evaluated under low velocity impact loads. The impact specimens were sandwiched in between two plate support fixtures using a tie-down bolt near each corner of the opening. In this impact investigation, the incident kinetic energy (IKE) was 3, 5, and 7 Joule/mm thickness. The composite thickness is about 3 mm. Impact damage assessment was performed by using ultrasonic C-scan and Tomography.

Results and Discussion

1. Tensile properties

1.1. Glass – epoxy composites

With similar process conditions, the fibre volume fraction of knitted fabric composites (about 30 %) is much lower than the fibre volume fraction of plain weave fabric composites (between 50 and 55%). Higher fibre volume fractions of knitted fabric composites may be achieved by applying higher pressure. The fibre volume fraction was determined by burning the matrix.

In the weft knitted structure, fibres are more oriented in the wale direction than in the course direction. Therefore, the highest tensile properties appear at the wale direction and the lowest properties at the course direction. Regardless the values of the fibre volume fraction, the mechanical properties of knitted fabric composites were compared to the mechanical properties of woven fabric composites. It is seen that the mechanical properties of knitted fabric composites were not always lower than the mechanical properties of woven fabric composites. The mechanical properties of double rib knitted fabric composites in the wale direction such as tensile stiffness and tensile strength properties are higher than the tensile stiffness and the tensile strength of woven fabric composites in the bias (45°) direction. Figure 1 shows the polar tensile curves of the investigated composites. Double-rib knitted fabric composites show the highest tensile properties and the highest degree of anisotropy. However, milano knitted fabric composites have the lowest tensile properties and the lowest degree of anisotropy.

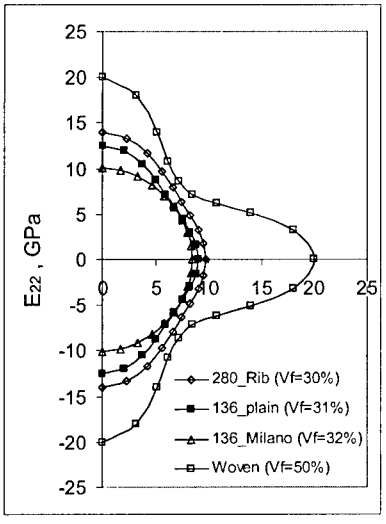

Fig.1 Polar Strength diagram of knitted fabric composites compared to woven fabric composites

1.2.Aramid-and carbon–epoxy composites

For aramid and carbon knitted fabric composites, the mechanical properties were much lower than what is expected as shown in figure 2. The mechanical properties of both carbon and aramid knitted fabric

composites were expected to be anisotropic like the mechanical properties of E-glass knitted fabric composites, whose highest properties are in the wale direction and the lowest properties in the course direction. However, the mechanical properties of carbon and aramid knitted fabric composites are almost similar in both wale and course directions. Moreover, they are lower compared to the mechanical properties of E-glass knitted fabric composites.

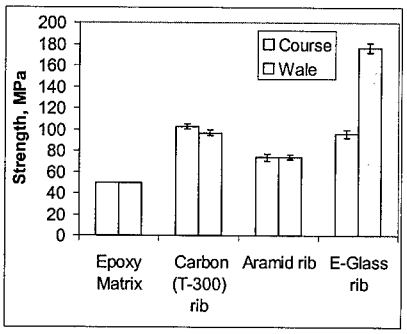

Fig.2 Strength properties of aramid and carbon composites

The low properties can be due to surface damage on fibres and bad interface properties. During the knitting process, fibres were subjected to external loads like tension, compression, shear, and friction loads. Those loads may generate surface damage on the fibres.

The low tensile properties are also influenced by the low transversal properties of carbon and aramid fibres. As in knitted fabric composites a wide fibre orientation distribution is found, the tensile properties are very much influenced by the low values of the transverse and shear stiffness and strength of the impregnated yarns.

At the final failure, a smooth fibre surface and smooth fibre print on the matrix indicated that the interface properties of aramid composites are very poor.

1.3. Glass – thermoplastic composites

Figure 3 shows a comparison of the mechanical properties of thermoplastic knitted fabric composites with the mechanical properties of GMT E-glass-polypropylene that are reported by Lee.[7] The fibre volume fraction of knitted fabric composites is about 40 %, whereas the fibre volume fraction of the GMT E-glass-polypropylene is selected at 30%. The mechanical properties of knitted fabric composites are higher in the wale direction, but lower in the course direction. For composites with polyamide as matrix, their mechanical properties are higher in both directions compared to composites with polypropylene as matrix.

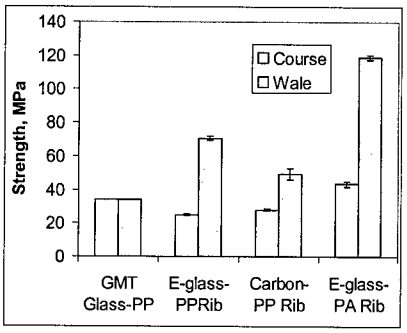

Fig.3 Strength properties of thermoplastic knitted fabric composites

2. Impact properties:

Knitted fabric composites will fail in the flexural mode (either tensile fracture or compressive buckling), because the complex fibre structure makes knitted fabric composites have a very high interlaminar fracture toughness, both in mode I or mode II. The nature of tensile failure in the impacted specimens is strongly related to the static tensile properties. In general, cracks caused during impact load are perpendicular to the direction of the weakest tensile

properties. For weft knitted fabric composites with a higher degree of anisotropy like double rib, these cracks are more located in the wale direction as shown in figure 4.

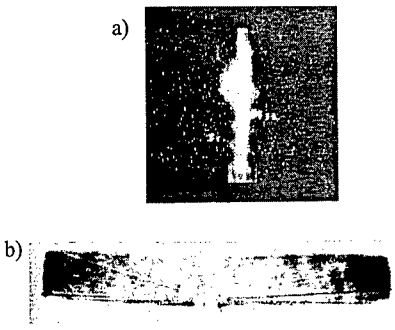

Fig.4 Rib knitted composites :a) Ultrasonic C-scan and b) Tomography

For milano weft knitted fabric composites with a lower degree of anisotropy, cracks are more distributed as shown in figure 5.

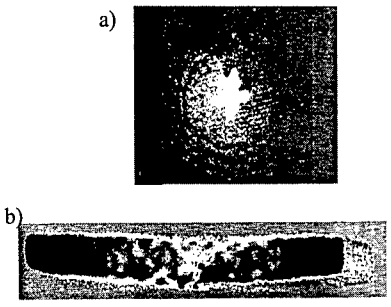

Fig.5 Milano knitted composites :a) Ultrasonic C-scan and b) Tomography

Conclusions

The mechanical properties of weft knitted fabric composites were investigated. For carbon and aramid knitted fabric composites, the tensile properties are lower than what is expected. This is due to surface defects on the fibres and poor interfacial properties. The nature of impact damage is correlated to the degree of anisotropy in the tensile properties.

Acknowledgement
S.D. Pandita is financed through grants of the Governmental Agency for Co-operation with Developing Countries (ABOS-VLIR) and the Concerted Research Action (GOA). SDP thanks to the Flemish government for supporting the IWT project on knitted fabric composites, collaboration with the Flemish company VERDONCK WINDHEY. SDP also thanks to the Flemish company SINCOGLAS for supplying woven fabrics R/420.

References

1.Verpoest, I., Gommers, B., Huysmans, G., Ivens, J., Luo, Y. Pandita, S., Philips, D., Proc. of 11th ICCM, 108 (1997)
2. A. Kelly and C. Zweben (eds.): "*Comprehensive Composite Materials, Vol.2*", Elsevier, London, 1999, pp. 523-669
3. Gommers, B., Verpoest, I., and Van Houtte, P., Proc. of 10th ICCM, 309(1995).
4. Ramakrisna, Composite Science and Technology, 57(1), 1(1997)
5. Huang, Z.M., Ramakrisna, S., Composites part A, 31 (5), 479(2000)
6. Wu, W.L, Kotaki, M., Fujita, A., Hamada, H., Inoda, M., Maekawa, Z.I, Journal of reinforced plastic and composites, 12(10) 1097(1993).
7. Lee, N.J., Jang, J., Composites part A, 30(6), 815(1999).

Proceedings of 7th Japan International SAMPE
Symposium & Exhibition, Nov. 13-16, 2001

Mechanical Properties of Knitted Fabric Composite with Hybrid Matrix Layer

Asami Nakai*, Akio Otani*, Takeshi Ishida** and Sotomi Gotoh***

*Kyoto Institute of Technology, Matsugasaki, Sakyo-ku, Kyoto 606-8585, JAPAN
E-mail: nakai@ipc.kit.ac.jp
**FRP Services and Company
***Material Processing and Engineering Inc.

Abstract

Structure of knitted fabric is that unidirectional fiber bundles are aligned in multi direction and linked with knitted yarn. Therefore, knitted fabric has good mechanical properties with no crimps and need low cost with omission of the stacking process. In this study, hybrid knitted fabric composites with flexible matrix were proposed. The effects of flexible matrix layer and flexible interphase on the bending properties of the knitted fabric composite were clarified.

Key words: Knitted fabric, flexible matrix layer, flexible matrix interphase.

Introduction

Of particular interest as reinforcements of composites is the use of warp knitting technology for the production of multi-axial warp knits (we describe as knitted fabric). Knitted fabrics allow the placement of warp, weft, and off-axis materials directly into the fabric structure. Moreover, in addition to the unidirectional fiber bundles, chopped strand mat can be also combined. One of the most attractive features of this type of fabric is the ability to combine multiple layers of oriented yarn in a single structure. Structure of knitted fabric is that unidirectional fiber bundles are aligned in multi direction and linked with knitted yarn. Therefore, knitted fabric has good mechanical properties with no crimps and need low cost with omission of the stacking process.

In previous study, we have fabricated knitted fabric composites with commercial unsaturated polyester resin and investigated the basic mechanical properties such as tensile, bending and lap joint property(1). In this study, in order to apply the knitted fabric composites to wide-range of usage, hybrid knitted fabric composites were proposed. This hybrid was defined as a usage of more than 2 kinds of materials for not only fiber and matrix and but also interface. Here, the terminology of hybrid fiber and hybrid matrix has already been used, whereas we proposed the terminology of hybrid interphase. In this study, the hybrid matrix and hybrid interphase were examined.

Knitted fabric composites with hybrid matrix layers of different properties were fabricated by using flexible resin. The chemical structure of used matrix was same; modified resins were used. We

have also developed the fiber reinforced composite materials with more flexible interphase than matrix resin(2-3). In the case of unidirectional fiber reinforced composite, woven fabric composite and braided fabric composites, we have succeeded in increasing the static and dynamic properties by the flexible interphase. The concept of flexible interphase was applied to knitted fabric composites. For these hybrid knitted fabric composites, the bending properties were investigated.

Materials and Specimen

Knitted fabric used in this study as reinforcements is shown in Fig.1. Structure of the knitted fabric is that unidirectional fiber bundles are aligned in 0 and 90 direction and linked with knitted yarn. Vinylester (R806, Showa high polymer Co., Ltd.) and unsaturated polyester (FK2000, Showa high polymer Co., Ltd.) were used as matrix resin. Compared with R806, FK2000 can be defined as flexible resin because they have lower modulus and higher ultimate strain. For the fabrication of flexible interphase, alkyd of unsaturated polyester resin was also used.

In this study, 7 kinds of specimen as shown in Table 1 were fabricated with the above-mentioned materials. For the bending test, the knitted fabric was laminated with 4 layers and the first character of the stacking sequence means compression side. Each stacking sequence was described with H, F, Fi1, Fi2; H is layer with R806 as matrix, F is flexible matrix layer with FK2000 and Fi1 is flexible interphase layer with alkyd of FK200 as interphase and R806 as matrix. Fi2 is flexible interphase layer with FK200 as interphase and R806 as matrix. In the case of Fi2 without alkyd, inside of fiber bundle would be filled with flexible resin.

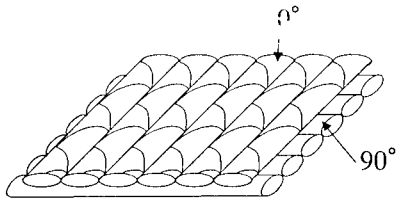

Fig.1 Knitted fabric.

Experimental results

Fracture aspects

Schematic drawing of the fracture aspects for bending test can be described with Fig.2. In specimen H, first the matrix crack occurred at the external layer (①), then the crack progressed to the second layer with increase in load

Table 1 Types of specimen.

	H	F	F-t	F-c	Fi1	Fi1-t	Fi2-t
Stacking sequency	HHHH	FFFF	FHHH	HHHF	$F_{i1}F_{i1}F_{i1}F_{i1}$	F_{i1}HHH	F_{i2}HHH
Young's Modulus (GPa)	20.8	9.8	16.8	17.5	20.3	21.3	18.4
Initial fracture stress (MPa)	260	-	190	186	260	258	301
Maximum stress(MPa)	603	100	595	409	543	571	507

(②). The final fracture occurred because of the buckling on longitudinal fiber bundle at the compression side (③), and of the fracture of the longitudinal fiber bundle at the tensile side (④). In specimen F with flexible layer for all layers, only the buckling of fiber bundle (H-③) occurred in external layer at compression side, that is ultimate fracture of specimen.

The specimens with flexible matrix layer at the compression side (F-c) exhibited the fracture progress as same as specimen H (H-①→②→③→④). In the case of the specimen with flexible matrix layer at the tensile layer (F-t), the occurrence of the matrix crack at the external layer was prevented and matrix crack occurred in the second layer at tensile side (⑤).

The specimens with flexible interphase layer at the tensile side (Fi1-t) also exhibited the fracture progress as same as specimen H. At the in-situ observation with CCD camera, it could be observed that the brittle crack propagation at the tensile side (①) was restrained. In the specimens with fiber bundle filled with flexible resin at the tensile side (Fi2-t), the occurrence of the matrix crack at the external layer was prevented and matrix crack occurred in the resin rich region of second layer at tensile side (⑥).

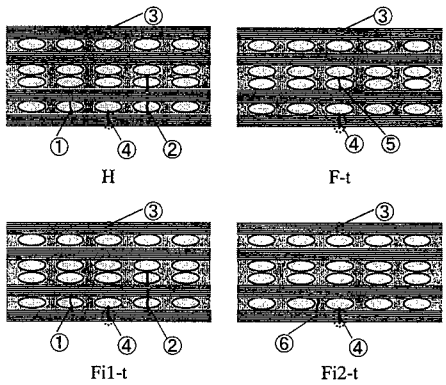

Fig.2 Fracture aspect of bending specimen.

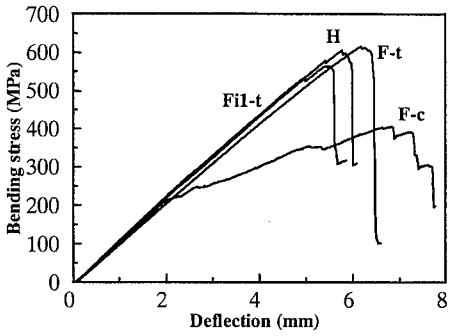

Fig.3 Stress-deflection curves of bending specimens.

Bending properties

Figure 3 shows the typical stress - deflection curves. The specimens with flexible matrix or interphase layer at the tensile side exhibited relatively elastic linear behavior as specimen H. Whereas, The specimens with flexible matrix layer at the compression side (F-c), decrement in slope of the stress-deflection curve occurred at the small strain. The bending modulus and strength were shown in Table 1.

Figure 4 shows the bending modulus divided by the modulus of specimen H. The specimen with flexible matrix layer showed lower modulus than specimen H, whereas the specimen with flexible interphase layer showed almost same modulus as specimen H

Figure 5 shows initial fracture stress divided by those of specimen H. Here. Initial fracture stress means the stress at which initial fracture occurred. The specimen with flexible interphase layer showed higher value than specimen H.

Figure 6 shows bending strength divided by those of specimen H. The specimen with flexible matrix layer at the tensile layer (F-t) and the specimen with flexible interphase layer (Fi1-t) exhibited almost same value as specimen H.

Figure 7 shows the relation between bending strength and the modulus. Comparing with specimen H and F-t, although the modulus was decreased, the strength kept same value. In the case of Fi1-t, the modulus was increased in addition that strength kept same value. Therefore, with flexible interphase layer or flexible matrix layer, material design would be achieved to satisfy the required mechanical properties.

Conclusion

In this study, hybrid knitted fabric composites with flexible matrix layer and flexible interphase layer were fabricated and bending properties were examined. As a results, it was confirmed that the knitted fabric composites with various mechanical properties could be designed with flexible matrix. As a future work, the dynamic properties such as impact testing will be investigated for the application of hybrid knitted fabric composites

Reference

(1) Asami Nakai, Akio Ohtani, Masahiro Yamanouchi, Hiroyuki Hamada, the Int. Conf. of 6th Deformation and Fracture of Composites(2000), 103

(2) A.Tange, T.Nishiwaki, H.Hamada, Proc.6th Japan International SAMPE Symposium, vol.2 (1999), 808

(3) K.Kitagawa, K.Sugimoto, H.Hamada, Proc.6th Japan International SAMPE Symposium, vol.2 (1999), 907

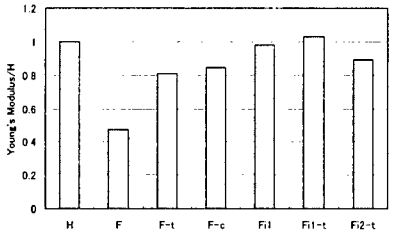

Fig.4 Ratio of Young's modulus.

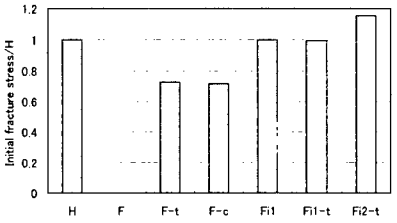

Fig.5 Ratio of initial fracture stress.

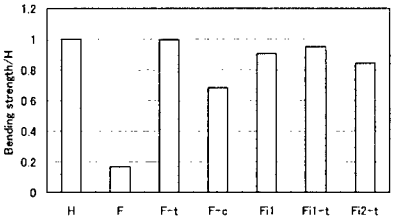

Fig.6 Ratio of bending strength.

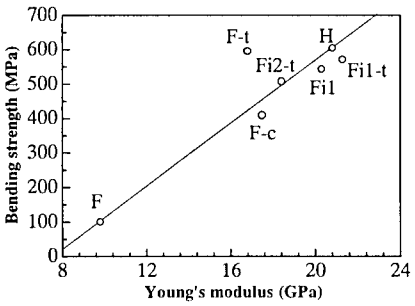

Fig.7 Relation between bending strength and Young's modulus.

Proceedings of 7th Japan International SAMPE
Symposium & Exhibition, Nov. 13-16, 2001

Local and Microscopic Analysis of Woven Fabric Composite Material under Bending by Finite Element Mesh Superposition Method

Naoki Takano [1], Masaru Zako [1] and Toru Okazaki [1]

[1] Department of Manufacturing Science, Graduate School of Engineering, Osaka University
2-1 Yamada-oka, Suita, 565-0871 Osaka, JAPAN,
E-mail: takano@mapse.eng.osaka-u.ac.jp

Abstract

A finite element mesh superposition method is applied to the damage propagation analysis of woven fabric composite materials under three-point bending. The microscopic heterogeneity consisting of fiber bundles and matrix resin is considered. The disorder of the lamination is also considered, which results in the loss of periodicity. Under bending condition, the damageoccurs locally, which also restricts the usage of the homogenized material model. To this end, the finite element mesh superposition method is adopted to analyze the local and microscopic damage propagation considering the micro-macro coupling effect.

Key Words: Finite element method, Heterogeneity, Woven fabric composite material, Damage

Introduction

Since after the series of micromechanical studies of composite materials considering the microscopic heterogeneity, a new multi-scale analysis using the homogenization method has been a matter of concern in the last decade. However, such micro-macro coupled analysis using the homogenization procedure is not strictly applicable to the evaluation of damage or fracture because the periodicity condition is not satisfied. Moreover, the homogenized material model can't be applied to a region under high strain gradient. To this end, the conventional micro-macro coupled method is not useful to the evaluation of damage.

To solve this problem, a finite element mesh superposition method is applied to the local damage propagation of woven fabric composite material under three-point bending. The microscopic heterogeneity consisting of fiber bundles and matrix resin is considered. The disorder of the lamination is also considered, which results in the loss of periodicity. Under bending condition, the damage occurs locally, which also restricts the usage of the homogenized material model. On the contrary, the local heterogeneity due to the disorder of lamination and the damage is modeled directly in the local mesh. To bridge the gap between the local and microscopic heterogeneity and the global structure, the homogenized model is still used in the global mesh. The local mesh can be superimposed onto the global mesh. Consequently, the local and microscopic heterogeneity can be studied in the framework of the multi-scale analysis.

Finite Element Mesh Superposition Method

The original idea of the finite element mesh superposition method was presented by

Fish [1] in the series of research works on the adaptive finite element method. That is, the refinement of mesh was available in more practical way than the conventional zooming technique or h-method. The authors have applied it to the modelling of local and microscopic heterogeneity of various composite materials.

Two kinds of finite element meshes are used; the one is the global mesh and the other is the local mesh. The global mesh is used to model the global structure and to analyze the global behavior. The homogenized material model is applied to the global mesh based on the microscopic and periodic heterogeneity. On the other hand, the local mesh is used to model the local heterogeneity such as the crack, void, inclusion, interface etc. Because such local heterogeneity can be replaced by the homogenized model, it is not considered in the global mesh. Then, by superimposing the local mesh onto the global mesh as shown in Fig.1, both the micro-macro coupling behavior and the local heterogeneity is considered. The concept of the global and local heterogeneity and the modified formulation was proposed in Ref. [2]. The accuracy was verified in case of mesh refinement [3,4]. The verification for the local heterogeneity was shown in [5] for a dissimilar inclusion, and in [6] for a crack problem. The applicability to an interface problem was reported in [7,8]. The fundamental study on the microscopic stress analysis under bending was reported in [8].

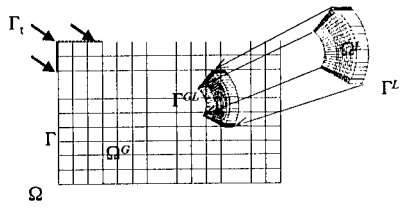

Fig.1 Superposition of local mesh onto global mesh.

Bending Analysis of Woven Fabric Composite Materials

We can find many literatures which study the micromechanical inplane behaviors of woven fabric composite materials considering the woven architecture. However, no numerical study can be found on the bending analysis. In addition, the effect of the disorder of lamination on the damage propagation under bending has never been analyzed within the framework of the homogenized modelling. The local and microscopic heterogeneity considered in this study is illustrated in Fig. 2.

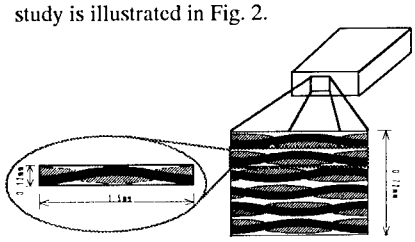

Fig. 2 Local and microscopic heterogeneity in woven fabric composite.

The above-mentioned heterogeneity is considered only in the local mesh, while the global mesh is used to analyze the global behavior based on the homogenized modelling. Fig. 3 shows the global and local meshes. Note that the local mesh occupies the region from the bottom surface to almost the neutral axis, which results in the non-uniform field in the local region. In addition, the disorder of the lamination is considered in the local mesh. Because it affects less to the global behavior, the homogenized model takes only the basic woven architecture into account as shown in Fig. 4. The dimensions are shown in Fig. 5.

The effect of the local damage on both the global and local behaviors is important. The formulation of the finite element mesh superposition method [2,5] tells that it can well consider that effect. The maximum stress criterion is used to judge the occurrence of damage after Ref. [9]. Once the

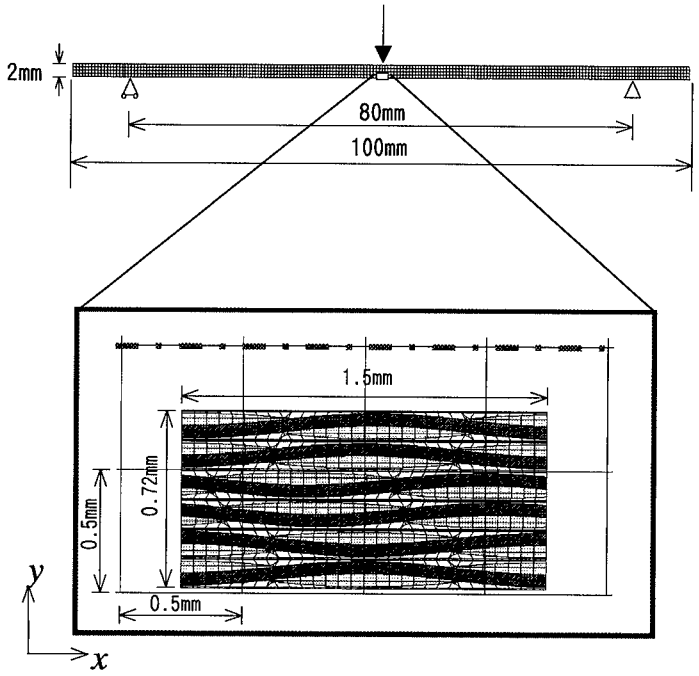

Fig. 3 Global and local meshes.

damage occurs, the degradation of the stiffness is considered by the reduction factors according to the damage mode [9].

The prescribed displacement was applied to simulate the three-point bending test. Fig. 6 shows the relation between the load and displacement. A sequential linear analyses were carried out to simulate the nonlinear behaviors. At the loading levels A and B, the stress distribution in the local mesh is shown in Fig. 7 (a) and (b), respetively. The stress distribution is not symmetric due to the disorder of the lamination.

Fig. 4 Unit woven structure to represent the global heterogeneity for homogenization.

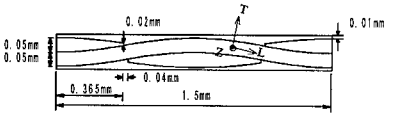

Fig. 5 Dimensions of the microscopic heterogeneity.

Discussion and Concluding Remarks

The advantages of the finite element mesh superposition method were recognized on the following point;

(1) The disorder of the lamination is the local heterogeneity, which can't be replaced by the homogenized model. The finite element mesh superposition method could consider its effect on the damage propagation.

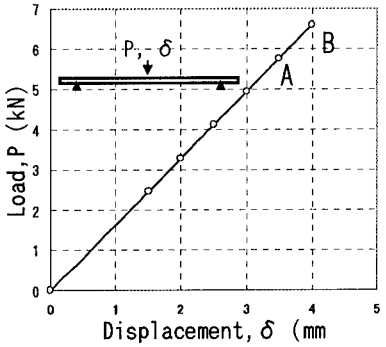

Fig. 6 Load and displacement curve.

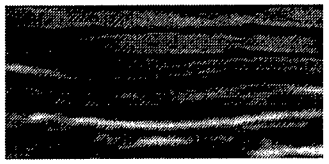

(a) At load level A

(b) At load level B

Fig. 7 Stress distribution in local region

(2) Under bending condition, the (macroscopic) strain field is non-uniform in the local region, which violates the assumption of the periodicity for the use of the homogenized model. The finite element mesh superposition method could be applied to this kind of problem.

(3) Once the damage occurs, the assumption of the periodicity is lost, which means the homogenized model can't be used. The finite element mesh superposition method could directly model the locally damaged situation.

On the contrary, some future works were recognized. In this analysis, the local region to be analyzed was too small to study the damage propagation. The application of the finite element mesh superposition method to the nonlinear problem should be studied further by exploring the incremental formulation of this method. Also, there may be some other problems in the three-dimensional analysis by this method, such as the large-scale analysis capability. They should be also the future works.

In conclusion, the advantages of the finite element method can supplement the limitations of the homogenized modelling.

References

1. J. Fish: Computers and Structures, **43**, 539 (1992).
2. N. Takano, M. Zako and M. Ishizono: Journal of Computer-Aided Materials Design, **7**, 111 (2000).
3. N. Takano, Y. Kashiwagi, Y. Ohnishi and M. Zako: Transactions of JSME, **65**A, 498 (1999) (in Japanese).
4. N. Takano, Y. Uetsuji, Y. Kashiwagi and M. Zako: Modelling and Simulation in Materials Science and Engineering, **7**, 207 (1999).
5. N. Takano, M. Zako and M. Ishizono: Transactions of JSME, **66**A, 220 (2000) (in Japanese).
6. N. Takano, M. Zako and T. Okazaki: JSME International Journal, Ser. A, in press (accepted).
7. N. Takano and M. Zako: Transactions of JSME, **67**A, 603 (2001) (in Japanese).
8. N. Takano, M. Zako, T. Okazaki and F. Kubo: Materials Science Research International, Special Technical Publication-2, 219 (2001).
9. M.G. Kollegal and S. Sridharen: Journal of Composite Materials, **34**, 240 (2000).

Proceedings of 7th Japan International SAMPE
Symposium & Exhibition, Nov. 13-16, 2001

Non-Constitutive Numerical Modeling for Plain-Weave Fabrics

Osamu Kuwazuru# and Nobuhiro Yoshikawa#

Institute of Industrial Science, The University of Tokyo
4-6-1 Komaba Meguro-ku, Tokyo 153-8505, JAPAN
E-mail: kuwa@telu.iis.u-tokyo.ac.jp

Abstract

A new methodology of material modeling is developed to analyze the complex mechanical behavior of plain-weave fabrics. The deformation of the fabrics is categorized into three kinds of thread deformation, that is, skewing, straightening and extension under the assumption of null friction and null flexural rigidity concerning with threads. We introduce a new strain-displacement relationship instead of the conventional method for material modeling by the constitutive law. By this strain-displacement relationship, the deformation of the fabric is translated as the axial extension and transverse compression of the threads. The finite element is derived by the total Lagrangian formulation, and solved by the Newton-Raphson method.

Key Words: Finite Element Method, Total Lagrangian, Discontinuity, Fabrics

Introduction

Woven fabrics has been utilized for membrane or composite structural members from the standpoint of high specific strength. However, its complicated mechanical behavior prevents adequate analysis and design of woven fabrics. The difficulty is mainly caused by the microscopic geometrical non-linearity arising from the discontinuity among threads. In other words, the woven fabric is not the continuum, and the conventional constitutive modeling is no longer available. The deformation analysis of unit weave structure[1-3] in the context of the representative volume element approach[4] is practical to obtain the mechanical property of plain-weave fabric, but its applicability is limited to the primitive type of deformation such as extension along the warp or weft.

In this study, we newly introduce the crimp parameter indicating the crimp condition of warp and weft to describe the three-dimensional thread rotation in in-plane problem, and define a new strain-displacement relationship suitable for the deformation mechanism of the plain-weave fabrics. Owing to this strain-displacement relationship, we constitute a new model by the continuum-like manner, and name it pseudo-continuum model. Use is made of the total Lagrangian formulation[5] to derive the finite element for the pseudo-continuum model. The numerical examples concerning the uniaxial tensile tests of plain-weave fabric demonstrate the validity of the proposed model.

Pseudo-Continuum Model

Problem Description

Under in-plane extension without wrinkling,

the plain-weave fabric undergoes three types of thread deformation, that is, skewing, straightening and extension[1] as shown in Fig.1. The skewing illustrated in Fig.1(a) means in-plane rotation of the thread, and the straightening in Fig.1(b) means anti-plane one. The extension illustrated in Fig.1(c) is the elastic elongation of the thread itself, whereas the elastic bending and shearing are neglected under the assumption of null flexural rigidity and null friction.

The warp and weft are made of an orthotropic and linear elastic material, and woven uniformly with orthogonal configuration. The weave is sufficiently dense and fine. We set ξ_1-ξ_2 coordinates so as to make ξ_1-axis indicate the weft direction, and denote the global Cartesian coordinates by x_1-x_2. The inclination angle of weft from x_1-direction is denoted by θ. Hereafter, the variables concerning the weft and warp are denoted by the suffix 1 and 2, respectively.

We set unit weave as the square of four cross-over points between warp and weft. Figure 2 shows the detailed configuration of the unit weave structure in which the cross-over point is indicated by the solid circle. The central thickness of thread is denoted by d_i, and the wave-length and wave height of the crimp $2p_i$ and h_i, respectively. The wave between the cross-over points corresponding to the half wave-length is approximately modified by a straight line, and its length is denoted by s_i. The values in initial undeformed state are represented by the upper tilde (~), hereafter.

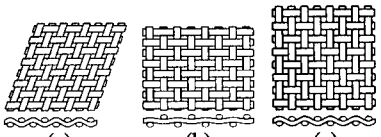

Fig.1 Specific deformation types

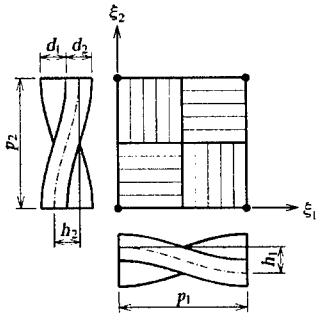

Fig.2 Unit weave structure

Crimp Parameter

The crimp height h_i and the central thickness d_i always hold the relationship:

$$h_1 + h_2 = d_1 + d_2 . \qquad (1)$$

h_i varies in the order of finite displacement, whereas d_i decreases in the order of infinitesimal strain. We assume d_i constant, and introduce a nondimensional parameter μ $(0 \le \mu \le 1)$ named crimp parameter for the parametric expression of the crimp heights of both threads by

$$\begin{cases} h_1 = \mu\,(d_1 + d_2) \\ h_2 = (1-\mu)(d_1 + d_2) \end{cases} . \qquad (2)$$

The weft is completely straightened at $\mu = 0$, and the warp straightened at $\mu = 1$. The crimp parameter is dealt with as a component of the displacement vector, hereafter.

Strain-Displacement Relationship

Figure 3 shows schematic deformation of the unit weave structure. The in-plane relative rotation angle between warp and weft caused by the skewing is estimated by $\zeta = \zeta_1 + \zeta_2$ as shown in Fig.3. In this study, ζ is approxi-

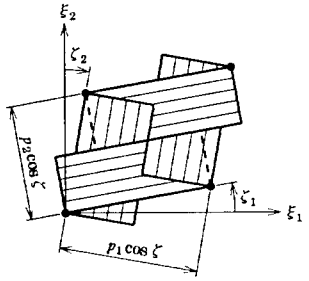

Fig.3 Deformation of unit weave structure

mated by $v_{1,2}+v_{2,1}$, where $v_{i,j}$ represents the displacement gradient $\partial v_i/\partial \xi_j$.

The skewing and straightening yield the variation of the spacing of threads from $\tilde{p}_i$ to $p_i \cos\zeta$ as shown in Fig.3. This variation is identical with the in-plane transverse compression of threads, since we employ null gap assumption between threads. The transverse compressive strain ε_{Ci} is, thus, defined as

$$\varepsilon_{C1} \equiv (\tilde{p}_2 - p_2\cos\zeta)/\tilde{p}_2$$
$$\approx 1-\sqrt{(1+v_{2,2})^2+v_{1,2}^2}\left\{1-\frac{1}{2}(v_{1,2}+v_{2,1})^2\right\} \quad (3)$$
$$\varepsilon_{C2} \equiv (\tilde{p}_1 - p_1\cos\zeta)/\tilde{p}_1$$
$$\approx 1-\sqrt{(1+v_{1,1})^2+v_{2,1}^2}\left\{1-\frac{1}{2}(v_{1,2}+v_{2,1})^2\right\}. \quad (4)$$

Considering the three-dimensional rotation of thread, we estimate the thread extension in terms of the axial tensile strain ε_{Ti} defined as

$$\varepsilon_{T1} \equiv (s_1-\tilde{s}_1)/\tilde{s}_1$$
$$=\sqrt{\phi_1^2(1+v_{1,1})^2+\phi_1^2 v_{2,1}^2+\psi_1^2\mu^2}-1 \quad (5)$$
$$\varepsilon_{T2} \equiv (s_2-\tilde{s}_2)/\tilde{s}_2$$
$$=\sqrt{\phi_2^2(1+v_{2,2})^2+\phi_2^2 v_{1,2}^2+\psi_2^2(1-\mu)^2}-1 \quad (6)$$

where ϕ_i and ψ_i are the constants obtained by

$$\phi_i = \tilde{p}_i/\tilde{s}_i, \quad \psi_i = (d_1+d_2)/\tilde{s}_i. \quad (7)$$

Although the above-mentioned strains are defined in the sense of infinitesimal strain, they are equivalent to the Green-Lagrange strain in the context of finite rigid-body rotation[5].

Constitutive Law

Young's modulus and Poisson's ratio of the threads are denoted by E_T, ν_T in the axial direction, and E_C, ν_C in the transverse direction, respectively. The plane stress state is plausible for the thread, so that the axial tensile stress σ_{Ti} and the transverse compressive stress σ_{Ci} are expressed by

$$\begin{Bmatrix}\sigma_{Ti}\\ \sigma_{Ci}\end{Bmatrix}=\frac{1}{1-\nu_T\nu_C}\begin{bmatrix}E_T & -\nu_C E_T\\ -\nu_T E_C & E_C\end{bmatrix}\begin{Bmatrix}\varepsilon_{Ti}\\ \varepsilon_{Ci}\end{Bmatrix}. \quad (8)$$

These stresses are equivalent to the second Piola-Kirchhoff stress. σ_{Ci} have to be non-negative, since it is caused by the contact pressure between warp and weft. If σ_{Ci} obtained by Eq.(8) becomes negative, the constitutive law is converted to that of uniaxial stress state represented by

$$\sigma_{Ti} = E_T\varepsilon_{Ti}, \quad \sigma_{Ci}=0, \quad \varepsilon_{Ci}=\nu_T\varepsilon_{Ti}. \quad (9)$$

Finite Element Formulation

For the sake of notational simplicity, the stress and strain vectors are defined as

$$\{\tau\} \equiv \{\sigma_{T1} \quad \sigma_{C1} \quad \sigma_{T2} \quad \sigma_{C2}\}^T \quad (10)$$
$$\{\gamma\} \equiv \{\gamma_{T1} \quad \gamma_{C1} \quad \gamma_{T2} \quad \gamma_{C2}\}^T \quad (11)$$

where the superfix T represents the matrix transpose, and their components are denoted by τ_i and γ_i, respectively. The variables used in the strain calculation are denoted by κ_i, and its vector form is defined as

$$\{\kappa\} \equiv \{v_{1,1} \quad v_{1,2} \quad v_{2,1} \quad v_{2,2} \quad \mu\}^T. \quad (12)$$

In order to deal with the geometrical nonlinearity, the incremental analysis from the time t to $t'=t+\Delta t$ is carried out. Then, the strain is approximated in the second-order in the vicinity of the time t, and expressed by using the summation convention as

$${}^{t'}\gamma_i = {}^{t}\gamma + {}^{t}R_{ij}\Delta\kappa_j + \frac{1}{2}{}^{t}S_{ijk}\Delta\kappa_j\Delta\kappa_k \quad (13)$$

where the left superfix t indicates the referred time, ${}^{t}R_{ij}$ and ${}^{t}S_{ijk}$ are the first and second-order derivatives of γ_i with respect to κ_j, respectively. In case of null body force, the principle of virtual work in the total Lagrangian form based on Eq.(13) yields the governing equation of the finite element analysis:

$$[{}^{t}K]\{\dot{U}\} = \{{}^{t'}F\} - \{{}^{t}Q\} \quad (14)$$

where $[{}^{t}K]$ is the tangent stiffness matrix, $\{\dot{U}\}$ the nodal velocity vector described in the global coordinates x_1-x_2, $\{{}^{t'}F\}$ the nodal external force vector and $\{{}^{t}Q\}$ the nodal internal force vector[5]. Use is made of the Newton-Raphson iterative procedure based on Eq.(14) to obtain the solution. The tangent

stiffness [K] may become singular from lack of the stiffness against skewing. A numerical regularization have to be employed to cope with such kind of numerical instability.

Numerical Example

The tensile test of a strip of plain-weave fabric shown in Fig.4 is investigated. The left end of the specimen is clamped, and the right end is pulled by a uniform displacement. The material property of threads is characterized as $E_T = 5.0$GPa, $E_C = 1.0$GPa, $\nu_T = 0.3$ and $\nu_C = 0.06$. The structural parameters of the plain-weave fabric are set by the central thickness of the thread $d_1 = d_2 =$ 0.14mm, the crimp wave-length $2\tilde{p}_1 = 2\tilde{p}_2 =$ 1.90mm and the crimp height $\tilde{h}_1 = 0.18$mm, $\tilde{h}_2 = 0.10$mm. Then, three cases are set for the different inclination angles of weave, that is, $\theta = 0°$, 45° and 90°. In these cases, the extensions in the direction of weft, bias and warp are analyzed. The nine-node element is employed for the finite element discretization shown in Fig.4, and the numerical integration is carried out by the Gauss quadrature.

Figure 5 shows the obtained load-displacement curves. The load and displacement are normalized by the width and length of the specimen, respectively. The stiffness in weft direction becomes slightly lower than that in warp direction by the difference of crimp height. Extremely low stiffness and highly nonlinear behavior are revealed in the result for bias loading. The distribution of the thread stresses along the left clamped edge can be evaluated by the proposed finite element as shown in Fig.6 for the case of $\theta = 45°$ at the load of 5N/mm. In case of the bias loading, there appears high stress concentration of σ_{Ti} near the corner of specimen as shown in this figure.

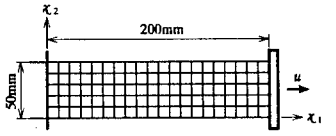

Fig.4 Specimen under uniaxial loading

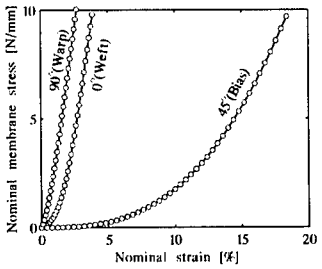

Fig.5 Load-displacement curves

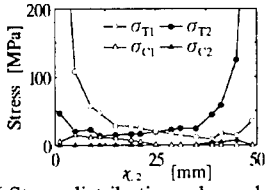

Fig.6 Stress distributions along clamped edge for $\theta = 45°$

Concluding Remarks

As a non-constitutive modeling, the pseudo-continuum model was proposed by using a new strain-displacement relationship suitable for the plain-weave fabrics. Through the numerical examples, the deformation behavior of the fabric was investigated, and versatility of the proposed model was elucidated.

References

1. R. Haas: NACA Report, No. 16, Part 1, 155 (1918).
2. S. Kawabata, M. Niwa and H. Kawai: J. Textile Institute, 64, 47 (1973).
3. S.Y. Luo and A. Mitra: Trans. ASME J. Appl. Mech., 66, 631 (1999).
4. Z. Hashin: Trans. ASME J. Appl. Mech., 50, 481 (1983).
5. T. Hisada and H. Noguchi: Nonlinear Finite Element Method and Its Application(in Japanease), Maruzen, Japan, (1995).

Proceedings of 7th Japan International SAMPE
Symposium & Exhibition, Nov. 13-16, 2001

Initial Fracture Behavior of Knitted Composites

Asami Nakai #, Toshiko Osada #, Tatsuro Fukui #, Miyako Inoda #

#: Kyoto Institute of Technology
Matsugasaki, Sakyo-ku, Kyoto 606-8585, JAPAN
E-mail: nakai@ipc.kit.ac.jp

Abstract

In this study, initial fracture behavior of knitted composite was considered. In order to clarify the initial fracture behavior, tensile testing of knitted fabric composites was performed and the knee point on the stress-strain curve was considered. Strain was obtained by both extensometer and strain gages. Strain values measured were different between extensometer and strain gages. Moreover, elastic moduli before and after the knee point were different with the location of the strain gages. The initial fracture at knee point and the difference in moduli before and after knee point were explained by the characteristic deformation of knitted fabric composite.

Key Words: Knitted Fabric Composite, Initial Fracture Behavior, Strain Gage, Knee Point.

Introduction

Micro fracture behaviors contribute to macroscopic mechanical behavior of composites. Therefore, the initiation of micro fracture, namely initial fracture is important to understand the mechanical properties of composites. It has been clarified that knee point on the stress-strain curve can be used for quantitative evaluation of initial fracture [1]. As a more active method for use of initial fracture, in case that the initial fracture occurs on an interface, the accurate identification of initial fracture can be used for the evaluation of interface property.

In this study, we challengingly tried to detect of initial fracture of knitted composites with knee point on the stress-strain curves. Here, the reason why the word of challenge was used is that the knitted fabric composite exhibited the extremely characteristic mechanical behaviors compared with other textile composite such as woven and braided composites; the mechanism of deformation and the heterogeneity of the textile structure described in the following section.

Knitting structure made by interlocking offers characteristic deformation behavior. The yarns of knits are consisted of a loop structure. The deformability is a direct consequence of the loop structure in the knit. The bent yarns have potential to be straightened before the yarn itself has to be extended. When knitted fabrics are used for composites, the mechanism of deformation would be complicated.

Moreover, knitted composite has heterogeneous structure. Here, heterogeneous structure is employed not for macroscopic mechanical properties of plate but for the unit cell base. The unit cell of woven and braided fabric is aggregation of the fiber crossing part, whereas the unit cell of knitted fabric is consists of the fiber crossing part and straight fiber which form loop structure. Therefore, there are resin

region without fiber at the center of loop, what is called the hole filled with resin. This heterogeneous structure causes the local variation in the strain depending on the measured position.

In this study, initial fracture behavior of knitted composite was investigated with tensile test. Initial fracture was detected on the local stress-strain curves of different position.

Experiment

Materials

Materials used in this study was glass fiber (D B450 1/2 445 Y23, Nippon Electrical Glass Co., Ltd.) as reinforcement and epoxy resin (Epikote 828, Japan Epoxy Resin Co., Ltd.) as matrix resin. Plain weft knitted fabric as shown in Fig.1 was used as reinforcements.

The plate with 1 ply of knitted fabric was prepared by hand lay-up method, and was cured for 48h at room temperature, followed by post cure for 2h at 100°C.

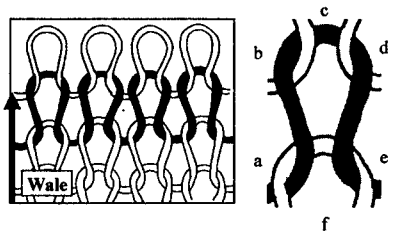

Fig.1 Plain weft knitted fabric.

Tensile testing

Tensile testing of knitted composites was performed by using an Instron 4206 universal testing machine. Dimensions of the specimen were 1 mm in thickness, 200 mm in length, and 20 mm in width. Test conditions were 100mm span length under a crosshead speed of 1 mm/min at room temperature.

As mentioned above, knitted fabric composites are considered to be not homogeneous but heterogeneous, that is, there are resin rich region and higher fiber volume fraction region from microscopic viepoint. It is important to decide which strain should be measured on the specimen. Strain obtained from the strain gage shows local strain, whereas, strain from the extensometer shows more global strain.

In this study, first, extensometer (gage length; 50mm) was used for the tensile testing of knitted composite. Then, tensile testing with strain gages (KFG-3-120-D16-11, Kyowa Electronic Instruments Co., Ltd., gage length; 3mm) was performed. Figure 2 shows the location of strain gages in the longitudinal direction. Strain gages in the longitudinal direction were attached at the two different location; one was along the fiber crossing part (position A(Fig.1 a-b)), and the other was without the loop fiber (position B(Fig.1 c-f)). Knee point on the local stress-strain curve was determined using least squares method [3].

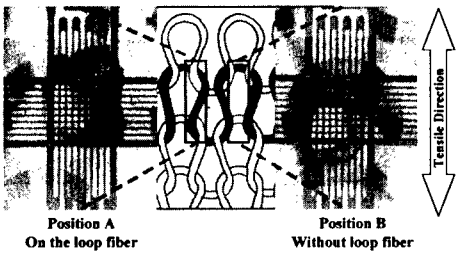

Fig.2 The location of strain gages in the longitudinal direction.

Results

Relationship between stress and strain

Figure 3 shows stress-strain curves of the knitted composites by using the strain gages. Knee point was found on the stress-strain curve shown in Fig.3. Strain at the knee point was shown in Table 1. However, the knee point could not be detected in the case of strain obtained by

extensometer. There are about 25 loops on the measured region, so that strain from the extensometer shows more global strain. Therefore, it is considered that small change in strain caused by an initial fracture disappeared in the global strain.

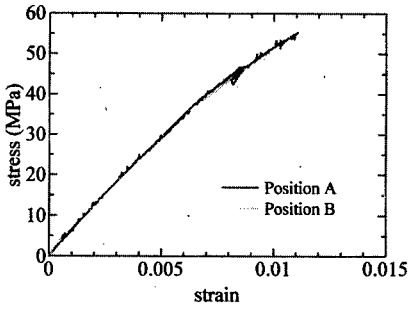

Fig.3 Stress-strain curves of the knitted composites by using the strain gages.

Table1 Mechanical Properties

	E_E (GPa)	E_1 (GPa)	Knee stress (MPa)	Knee strain (%)	E_2 (GPa)
Position A	5.62	6.03	27.40	0.456	5.73
Position B		6.29	22.03	0.354	5.60

Table 1 shows the elastic modulus (E_1) and the 2nd modulus (E_2) obtained by the strain gage and modulus (E_E) obtained by the extensometer as comparison. Here, the 2nd modulus was defined as the slope of stress-strain curve after knee point. Modulus by extensometer was lower than that of strain gages. Modulus of position A showed lower than that of position B, whereas, the 2nd modulus of position A showed higher than that of B.

Initial fracture behavior in knitted composites

During the tensile tests, the testing machine was periodically stopped and unloaded to 0, and observation using optical microscopy was performed to examine the initial fracture behavior.

Figure 4 shows fracture aspect by optical microscope around the knee point. Two types of fractures were observed; one was the delamination inside of fiber bundle at the loop head, the other was delamination at the fiber crossing part.

Discussion

From the viewpoint of deformation, the above results were considered. Figure 5 shows schematic drawing of deformation of knitted structure obtained by numerical analysis using Finite Element Method.
Deformation of fiber bundle at the line a-b and d-e is considered as follows; fiber at the line a-b and d-e was extended at the small strain, because of sliding at the fiber crossing

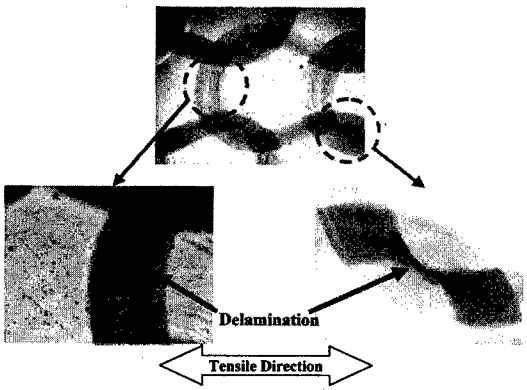

(a) Transverse crack (b) Fiber crossing part

Fig.4 Fracture aspect by optical microscope around the knee point.

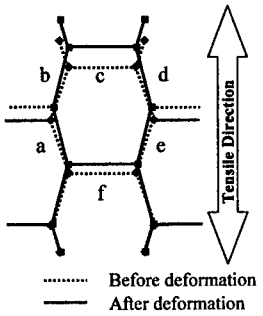

Fig.5 Schematic drawing of deformation of knitted structure obtained by numerical analysis using Finite Element Method.

part (a, b, d, and e) in addition to straightening of fiber itself (a-b, d-e). Then it was straightened fully, and finally straightening of fiber bundle was completed at the knee point. Therefore, fiber bundle acted as the materials aliened to fiber direction after the knee point. At the knee point, fiber bundles at the fiber crossing part (a, b, d, and e) are fastened each other, and then fracture at the fiber crossing part (shown in Fig.4 (b)) occur.

On the other hand, tensile load in loading direction was applied to the fiber bundle at the line b-c-d, and at the same time tensile load in fiber direction also applied when fiber bundle at the line a-b and d-e was straightened. Namely, two axial tensile load would be applied to line b-c-d, as a result, this fiber bundle at the line b-c-d was scarcely deformed in loading direction. There is also scarcely deformation of matrix at line c-f. At the knee point, transverse crack occurred at line b-c-d (shown in Fig. 4(a)). When transverse crack at line b-c-d occur, line c-f will be separated and easy to deform in loading direction.

As shown in Table 1, E_1 of position A showed lower than that of position B. As mentioned above, this is because the fiber bundle at the line a-b and d-e was straightened, whereas, the matrix and fiber bundle at the line b-c-d were scarcely deformed. In the case of E_2 after knee point, line a-b and d-e acted as the materials aliened to fiber direction, whereas, when transverse crack at line b-c-d occur, it would be easy to deform.

As shown above, even one loop exhibited very complex deformation state and this caused the local strain and initial fracture corresponding each location. Therefore, as a future work, other testing method needs to be considered, such as, using strain gage with shorter gage length, several gages on one specimen, or strain mapping technique. Also tension applied to knitted fabric in molding the composite would be examined.

Conclusion

In this study, initial fracture behavior of knitted composites was investigated. Tensile testing of knitted fabric composites was performed, here, strain was obtained by the strain gages or extensometer. Elastic moduli before and after the knee point were different with the location of the strain gages. Then, initial fracture behavior at the knee point was considered using optical microscopy. The initial fracture and the difference in moduli before and after knee point was explained by the characteristic deformation of knitted fabric composite. These results indicated that local stress-strain curve should be used for the detect of initial fracture using knee point on knitted fabric composites.

References

1. A. Nakai, T. Osada, H. Hamada and N. Takeda, Composites part A, 32, pp. 487-498, (2001)
2. A.Nakai, H.Hamda, N.Takeda, Proceedings of the 9th US-Japan Conference on Composite Materials, pp. 753-760, (2000)
3. Toshiko Osada, Machiko Mizoguchi, Masaya Kotaki, Asami Nakai, Hiroyuki Hamada, ICCM-13th, ID 1083, (2001)

Proceedings of 7th Japan International SAMPE
Symposium & Exhibition, Nov. 13-16, 2001

Effect of processing conditions on the mechanical properties of a 2-D braided SiC/SiC composite

A. Ohtani[#], I. J. Davies[#], T. Inoue[$], A. Nakai[#], and H. Hamada[#]

[#] Kyoto Institute of Technology, Matsugasaki, Sakyo-Ku, Kyoto 606-8585, Japan
E-mail: davies@ipc.kit.ac.jp

[$] National Institute of Advanced Industrial Science and Technology, 1-8-31 Midorigaoka, Ikeda, Osaka 563-8577, Japan

Abstract

The mechanical properties of a 2-D braided SiC/SiC composite were investigated as a function of processing temperature (1200 °C and 1400 °C). The specimen processed at 1200 °C possessed far superior mechanical properties with a mean flexural strength of 407 MPa, flexural modulus of 140 GPa, effective fracture energy of 3685 $J \cdot m^{-2}$, fracture toughness of 7.68 $MPa \cdot m^{1/2}$, and fibre pullout length of 348 μm. The difference in behaviour between the specimens was attributed mainly to the effect of the fibre/matrix interface shear strength.

Key Words: SiC/SiC, braided, CMC.

Introduction

Ceramic matrix composites (CMCs) have shown great potential as high temperature structural materials in aerospace and space applications. One of the main problems inhibiting the widespread acceptance of such materials is their high manufacturing cost; resulting from several factors such as the choice of raw materials and fibre placement method together with labour and energy intensive manufacturing procedures. Several advanced fibre placement methods exist, such as knitting, weaving, and braiding, together with simpler forms such as unidirectional and laminate machine or manual lay-ups. It has been suggested that braided fibre architectures may provide a good compromise between the complex multi-directional fibre placing of the more expensive kitted and woven procedures and the lower cost approach of unidirectional or laminate materials.

In the present work the authors have investigated the mechanical properties of a 2-D braided SiC/SiC composite manufactured at either 1200 °C or 1400 °C.

Experimental Procedure

The fibre utilised in the present work was Tyranno® LoxM (Type TM-S5, Ube Industries, Ltd., Ube City, Japan) with the following characteristics: 800 fibres per bundle, 11 μm nominal diameter, >3 GPa tensile strength, 180 GPa tensile modulus, and 2.37 $g \cdot cm^{-3}$ density. The fibre was braided into the form of a continuous tape (nominal width 50 mm) with an angle of ≈25° between the neighbouring fibre bundles along the major axis of the tape. The fibre preform for the composite was produced by cutting the tape into lengths of ≈40 mm and stacking the layers to result in a fibre preform comprising of 16 layers with an approximate size of 40 *x* 40 *x* 3 mm.

Matrix consolidation was accomplished using the polymer impregnation and pyrolysis (PIP) method in which a 25 mass% solution of polycarbosilane (PCS) in hexane was first vacuum impregnated into the fibre preform and left to dry. Pyrolysis of the PCS matrix and conversion to SiC was carried out at either 1200 °C or 1400 °C under a nitrogen atmosphere with a heating rate of 1 °C·min^{-1} up to the required temperature and followed by a holding time of 10 min and furnace cooling to room temperature. The final open porosity values (following 12 PIP cycles) were 6.1 and 13.9 vol% for the 1200 and 1400 °C specimens, respectively. The difference in final open porosity was attributed to the difference in processing temperature; the value for the 1200 °C specimen being typical of that for SiC/SiC composites infiltrated by repeated PIP [1].

Following manufacture, the resulting composite plates were cut and polished into specimens suitable for 3-point flexural and fracture toughness evaluation; 30 *x* 4 *x* 1 mm (span *x* width *x* depth) for flexural testing and 12 *x* 4 *x* 2 mm for the fracture toughness tests. Specimens for fracture toughness evaluation were tested in the single-edge double-notch beam (SEDNB) configuration using an initial notch to depth ratio of 0.5. The crosshead speed was 0.1 mm·min^{-1} for both tests. In addition to flexural strength, the flexural modulus and effective fracture energy were also calculated for the 3-point flexural test specimens.

The extent of fibre pullout is known to be an important indicator of fracture behaviour and the fibre/matrix interface shear strength, τ, in CMCs [2,3] with the fibre pullout length being measured for a large number of fibres close to the notch tip in each fracture toughness specimen.

Results and Discussion

Load/displacement curves for specimens tested under 3-point flexural loading have been presented in Fig. 1. The most important point to note is the relatively "graceful" failure exhibited by the 1200 °C specimen (Fig. 1(a)), i.e., a gradual decrease in load following the maximum load and suggestive of the presence of crack bridging mechanisms (presumably as a result of fibre debonding and pullout) and pseudo-ductile failure. Such a failure mode has been noted in previous SiC/SiC composites manufactured using the PIP method [1] and is generally desirable from the point of view of fracture toughness and effective fracture energy.

Mechanical properties measured using the 3-point flexural test have been presented in Fig. 2; namely flexural strength (Fig. 2(a)), flexural modulus (Fig. 2(b)), and effective fracture energy (Fig. 2(c)). The values of flexural strength (407 MPa) and effective fracture energy (3685 J·m^{-2}) for the 1200 °C specimen were significantly higher compared to those of the 1400 °C specimen; 355 MPa and 2196 J·m^{-2}, respectively. The

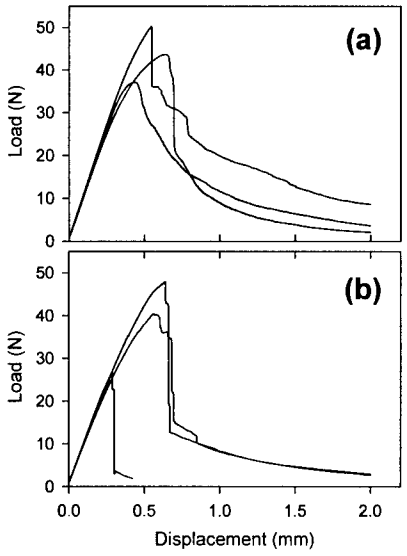

Fig. 1 Effect of processing temperature on flexural load/displacement curves: (a) 1200 °C, and (b) 1400 °C.

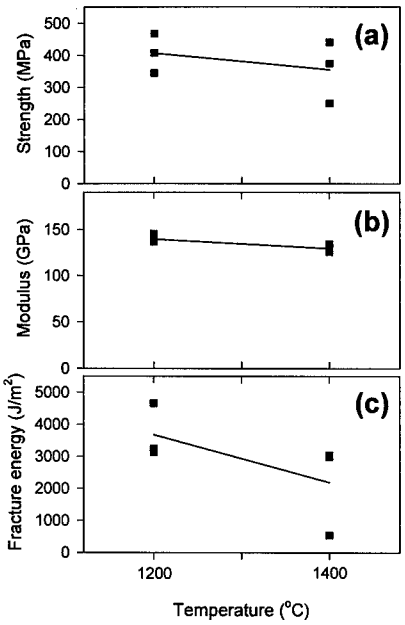

Fig. 2 Effect of processing temperature on flexural properties: (a) strength, (b) elastic modulus, and (c) fracture energy.

tensile strength of CMCs is known to depend on the fibre strength *in situ* the composite, S_o, and, to a greater degree, τ [2]. Although it may be the case that S_o was slightly lower in the 1400 °C specimen due to the increased processing temperature and resulting trend towards fibre decomposition [4], a more likely explanation would be that most of the difference between flexural strength and effective fracture energy was attributed to a difference in τ between the specimens. One reason to explain the difference in τ would be the difference in processing temperatures that resulted in different thermal stresses (higher for the 1400 °C case) once the specimens had cooled to room temperature. Further evidence for a significant difference in τ will be presented later. The flexural modulus was 140 GPa for the 1200 °C specimen and slightly lower at 129 GPa for the 1400 °C specimen (Fig. 2(b)). The elastic modulus of brittle materials is known to depend on both the amount and morphology of the porosity. The smaller amount of open porosity in the 1200 °C specimen would tend to lend itself towards a higher elastic modulus value as found in the present work.

The mean fracture toughness values were 7.68 and 2.49 MPa·m$^{1/2}$ for the 1200 °C and 1400 °C specimens, respectively. Fracture toughness specimens for the 1200 °C case exhibited tortuous fracture paths with multiple crack branching and evidence of fibre pullout, as might be expected for a composite with a relatively high fracture toughness. On the other hand, the 1400 °C specimen showed a crack path rather linear in nature. Although a fracture toughness of 7.8 MPa·m$^{1/2}$ is not unreasonable for many applications, it is still significantly less than that of either 3-D woven SiC/SiC composites (40 MPa·m$^{1/2}$) or even self-reinforced

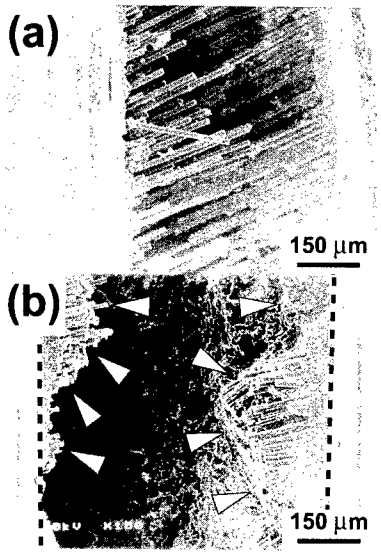

Fig. 3 Scanning electron micrographs illustrating fibre pullout at the notch tip of fracture toughness specimens: (a) 1200 °C, and (b) 1400 °C.

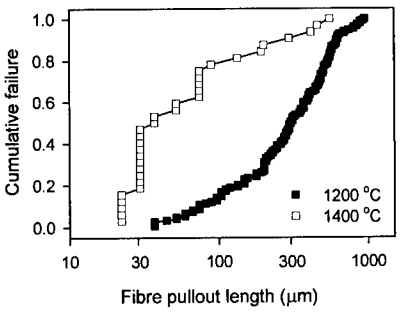

Fig. 4 Fibre pullout length distributions for braided SiC/SiC composites.

monolithic ceramics such as silicon nitride (10 MPa·m$^{1/2}$).

A comparison between the fibre pullout behaviour at the notch tip of the fracture toughness specimens (Fig. 3) showed the 1200 °C specimen to exhibit extensive fibre pullout on the order of several 100 μm whereas fibre pullout in the 1400 °C specimen was relatively minor with pullout lengths on the order of several fibre diameters. Distributions of fibre pullout lengths for both specimens have been presented in Fig. 4 with mean values of 348 μm (1200 °C) and 103 μm (1400 °C). The larger mean fibre pullout length for the 1200 °C specimen is indicative of a lower τ [3,5] that has been shown in previous work on SiC/SiC composites to result in superior mechanical properties [6]. Fibre strength is also known to have an effect on the fibre pullout length distribution [3]. However, the decrease in fibre strength for the 1400 °C specimen, required to cause such a large change in fibre pullout behaviour, would almost certainly have resulted in poor flexural strength and fracture toughness behaviour far below that noted in the present work. This result further confirms the assertion that the main reason for the difference in mechanical behaviour between the specimens was a difference in the fibre/matrix interface shear strength.

Conclusions

Mechanical properties were investigated for a 2-D braided SiC/SiC composite manufactured using the repeated polymer impregnation and pyrolysis of polycarbosilane at either 1200 °C or 1400 °C. The specimen processed at 1200 °C possessed far superior mechanical properties with a mean flexural strength of 407 MPa, flexural modulus of 140 GPa, effective fracture energy of 3685 J·m^{-2}, fracture toughness of 7.68 MPa·m$^{1/2}$, and fibre pullout length of 348 μm. Although the pore morphology and amount varied between the specimens, this did not appear to have a significant effect on the mechanical behaviour. Instead, most of the difference in mechanical behaviour was attributed to the effect of the fibre/matrix interface shear strength being different; presumably as a result of the processing temperature giving rise to different thermal stresses upon cooling to room temperature.

Acknowledgements

The authors wish to express their sincere thanks to Dr. M. Shibuya of Ube Industries, Ltd. for the supply of all fibres used in this study.

References

1. M. Takeda, Y. Kagawa, S. Mitsuno, Y. Imai, and H. Ichikawa, J. Amer. Ceram. Soc., 82(6), 1579 (1999).
2. W. A. Curtin, J. Amer. Ceram. Soc., 74(11), 2837 (1991).
3. M. D. Thouless, O. Sbaizero, L. S. Sigl, and A. G. Evans, J. Amer. Ceram. Soc., 72(4), 525 (1989).
4. G. Emig and R. Wirth, J. Maters. Sci., 30, 5813 (1995).
5. I. J. Davies and T. Ishikawa, Comp. Interfaces, 7, 479 (2001).
6. I. J. Davies, T. Ishikawa, M. Shibuya, and T. Hirokawa, Comp. Sci. Technol., 59, 801 (1999).

Proceedings of 7th Japan International SAMPE
Symposium & Exhibition, Nov. 13-16, 2001

Stitching of 3-Dimensional Preforms for the Production of High Performance Composite Parts

Dr. Juergen Wittig and Yuh-Schunn Sun

Altin Naehtechnik GmbH, Staakener Feldstrasse 39 – 41
13591 Berlin, Germany
E-Mail: juergen.wittig@altin-naehtechnik.de

Abstract

Widespread demand for reproducible dry preforms for the production of composite parts has promoted new developments in textile techniques. Altin Naehtechnik, a former producer of industrial sewing machines in Germany has developed a system which allows the combination of continuous moving industrial robots with discontinuously operating stitching systems. The developed stitching heads are carried via the manipulator along the seam line of the fixed work piece. The various types which are described allow the application of carbon fiber threads and can be used for shaping of the structures as well as for the reinforcement through the thickness. Patented new stitching techniques which allow the approach to the work piece from only one side or the reinforcement of the structure in the mould are explained. Almost any shape of preform can be produced by stitching, avoiding the use of time consuming braiding procedures. Examples for fixture designs and produced dry preforms are given.

Key Words: Stitching, Tufting, Preform, Reinforcement,

Introduction

The increasingly growing application of resin infusion techniques in the recent past has also increased the demand for reproducible textile preforms. Shaping of structures, the production of semi-solid preforms which can be handled without fiber misalignment, fixation of patches to a fabric structure and the reinforcement through the thickness are the major tasks to be fulfilled. Textile techniques therefore are in the focus of interest of the composite industry. Traditional stitching techniques known from the textile industry are limited to 2-dimendional structures. Weaving and braiding techniques are in general too slow and therefore too costly and have the disadvantage of high amounts of fiber undulations in the finished preform. Altin Naehtechnik, a former producer of industrial sewing machines in Germany has therefore developed and patented a complete new technique. By combining an industrial robot with special designed stitching heads it is nowadays possible to produce 3-dimensional preforms by the application of stitching technology.

The Robot System

Industrial six – axes robots which can guarantee the required accuracy are used to carry the stitching heads. The regular span of approx. 2500 mm can be extended by mounting the robot on a gantry system as it is known from modern tape laying machines. The control system allows the operation of up to 27 servo drives. Programming of the robot is done either by Teach-In mode, Off-line-Programming or by submitting of CAD data files to the control system. Besides collision control mechanisms the offline programming also allows the optimization and simulation in the design laboratory. A typical system is shown in Figure 1.

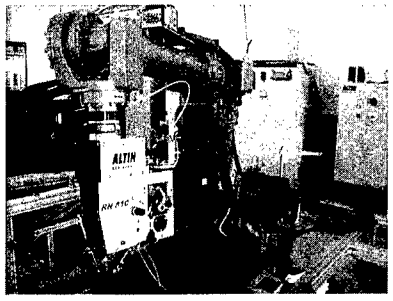

Fig.1 Robotic 3–D Stitching System

The Stitching Heads

Presently seven stitching heads for different applications and stitch types are available. All are equipped with special compensation gears which allows them to be continuously guided along the seam path whereby the needles show no sideward movement while in the fabric. The patented One Side Stitching head (OSS) as well as the tufting head allow the stitching of structures which have access from one side only, since no machine part is on the reverse side of the work piece.

One Side Stitching (OSS)

The new invented stitching system is a variation of a simple chain stitch. Two needles are penetrating the work piece from only one side and are manipulating the thread in such a way that the interlocking is generated on the surface of the fabric (Fig.2).

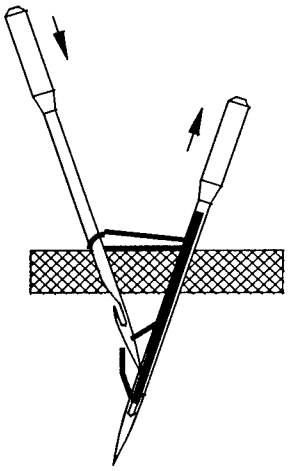

Fig.2 One Side Stitch

Since the thread is lying under 45° and 90° in the work piece it is possible to achieve a type of cross stitching by reversing the direction of the seam path. A structural cross- reinforcement in T-shaped parts can thus be applied in the areas of the high loads. Figure 3 shows the sketch of the seam pattern.

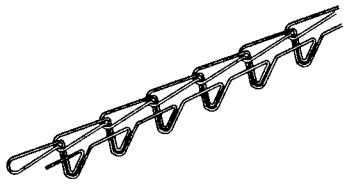

Fig.3 Seam Pattern of One Side Stitch

Tufting

Different from the above described two needle system, the Tufting head is using a single needle, inserting the thread in or through the fabric without producing any interlocking of the thread. The two resulting stitch patterns are shown in figure 4.

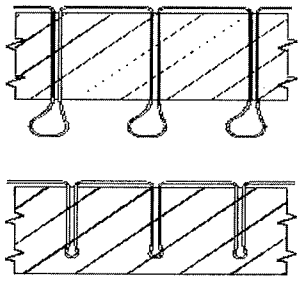

Fig. 4 Tufting Stitch Pattern

Unlike the OSS system the preform is therefore not as rigid, but due to the missing interlocking of the thread, lowest possible thread tensions can be achieved.

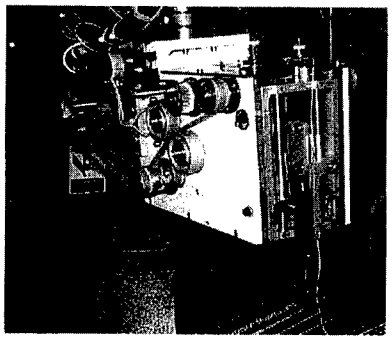

Fig. 5 Tufting Head

The major advantage of tufting however lies in its "in-mould-stitching" capability which allows the reinforcement of the structure already positioned in the resin infusion tool. The tufting head is shown in figure 5.

Double Lock Stitch

This commonly known stitch type is characterized by the use of one needle and two threads of which one is located in a small rotating bobbin underneath the fabric. It produces a similar looking seam line on booth sides of the structure. The stitching head shown in figure 6 was the first in a family of now seven stitching heads for robot application and is also capable of handling carbon fiber threads.

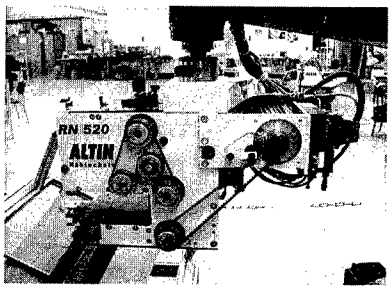

Fig. 6 Double Lock Stitch Head

Fixtures

The stitching procedures are reliable and proven in the industrial application. The fixation of the fabrics to be stitched, however is a challenge for every new composite structure. Figure 7 show a 3-dimensional impeller design as example. The target is to produce all seams with no or minimal replacement on a single fixation device.

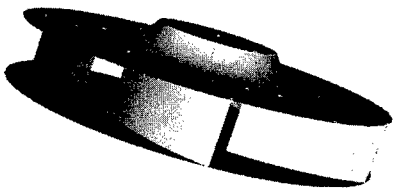

Fig. 7 Impeller Design

Although this cannot be achieved for every structure, the one side stitching techniques together with elaborated fixture design allows to come close to target. The fixture for the impeller is shown in figure 8.

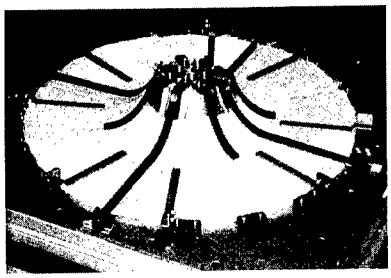

Fig. 8 Fixture for an Impeller

The stitching for a 3-dimensional aircraft part on a fixture is shown in figure 9. A double conical stringer for an aircraft application, produced solely by OSS technique, is shown in figure 10.

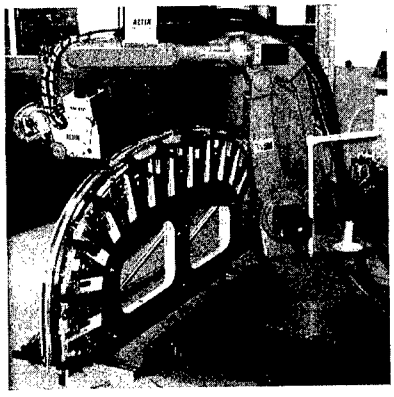

Fig. 9 Stitching of a curved Stringer

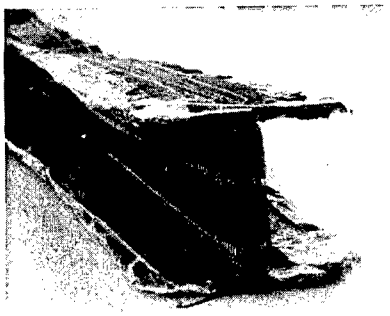

Fig. 10 Double conical Stringer

Conclusion

Stitching of dry fabric preforms has a high potential for the production of composite parts. Shaping as well as reinforcement through the thickness can be achieved. The possibility of distinct insertion of threads allows their use as a structural element in the design of the part for the achievement of improved performance. Delamination behavior on impact, known from conventional produced composite parts is substantially improved. The use of unidirectional or multiaxial fabrics for stitching allows to avoid time consuming braiding and weaving procedures with their high amount of undulated fibers in the product. With new developed patented stitching technologies almost every shape of preform can be produced. The industrial robots used to carry the stitching heads, guarantee the required accuracy and reproducibility as well as automation for high performance parts. Rail or gantry systems allow large stitching areas. Major International aircraft parts manufacturer have decided to use this technique for their production. Weight savings achievable by the use of composites almost impose this technique for automotive and marine applications.

Proceedings of 7th Japan International SAMPE
Symposium & Exhibition, Nov. 13-16, 2001

Modeling of Inter-fiber Sliding in Fabric Shaping Process

Yutaka Arimitsu, Shichiro Takahashi and Tsu-Wei Chou#

Department of Mechanical Engineering, Ehime University
3 Bunkyo-cho, Matsuyama 790-8577, JAPAN
E-mail: arimitsu@en1.ehime-u.ac.jp
#: Department of Mechanical Engineering, University of Delaware
Newark, Delaware 19716-3140, U.S.A.
E-mail: chou@ccm.udel.edu

Abstract

The pin-jointed network model has been widely used for the simulation of fabric forming process of Resin Transfer Molding. Inter-fiber sliding has been observed, when the molding surface has sharp corners. The radius of curvature of a corner influences the fabric deformation in some cases. We experimentally examine inter-fiber sliding in fabric shaping process, and propose the scheme of finite element analysis using the pin-jointed network model to simulate fabric shaping. Inter-fiber sliding at a node can be mechanically estimated from the axial force of the yarns.

Key Words: Fabric Shaping Simulation, Resin Transfer Molding, Finite Element Method, Inter-fiber Sliding

Introduction

It is of considerable practical significance to analyze fabric shaping process in Resin Transfer Molding (RTM). Main topics in this research are macroscopic deformation of fabrics (formability of fabric without wrinkles) and microscopic deformation of yarns (local yarn orientation, shape of texture and yarn spacing). The approaches analyzing fabric draping and shaping can be classified into two categories. One is the geometrical approach, meshing of the curved surface; for example, the fishnet algorithm [1,2], meshing with Computer Aided Design (CAD) system [3,4]. The other is the mechanical approach, minimizing elastic energy of fabrics; for example, Finite Element Method (FEM) using two-dimensional elements [5,6]. In the previous paper [7], we also reported the modeling of fabrics using truss (one-dimensional) elements and the commercial FEM system. In most studies of fabric draping/shaping, the pin-jointed network model (geometrical approach and modeling with one-dimensional elements) has been widely used. However no inter-fiber sliding was assumed in the FEM analysis with two-dimensional elements.

Recently, Lai et al. [8] proposed the modeling of fiber slippage using FEM. In the proposed model, the amount of fiber slippage is geometrically estimated from yarn curvature. They examined the effects of inter-fiber sliding experimentally, and reported that slippage became large near sharp corner. Yarn sliding has been observed in regions where the rate of shear angle

variation is higher (see Fig.1(a)), and where single yarn bending occurs (see Fig.1(b))[9]. Since inter-fiber sliding is related to friction between fibers, we take into account of the tensile force in yarns, in the present study.

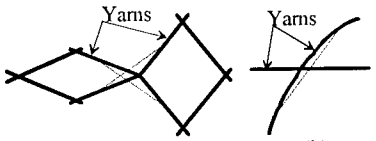

Fig.1 Patterns of inter-fiber sliding. (a) Large shear angle variation, (b) single yarn bending.

Experimental Results of Inter-fiber Sliding

Test Apparatus

We studied the effects of inter-fiber sliding by deep drawing with the cylindrical punch shown schematically in Fig.2. A distributed load of 50 N is applied to the fabric by the blank-holder.

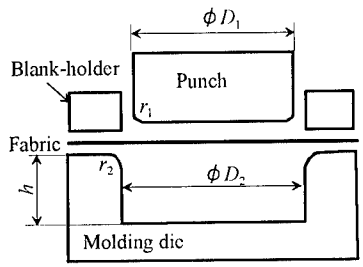

D_1 = 30, 34 mm, D_2= 32, 36 mm,
h = 10, 20, 26 mm, r_1 = 0.5 mm, r_2 = 2, 5 mm

Fig.2 Deep drawing with cylindrical punch.

Test Fabrics

Plain-weave rayon fabric of 100×100 mm^2 was used in this test. Structural parameters are listed in Table 1. We employ fibers of 0.15 mm diameter, to avoid the effect of waviness of woven fabrics.

Table 1 Properties of Fabrics

Material	Thickness (mm)	Spacing of warp (mm)	Spacing of weft (mm)
Rayon	0.25	1.5	1.9

Experimental Results

Deformation of plain-woven fabric is shown in Figs.3-6. Large shear deformation is observed on the side surface of the cylindrical punch and the blank-holder surface (see Fig.3).

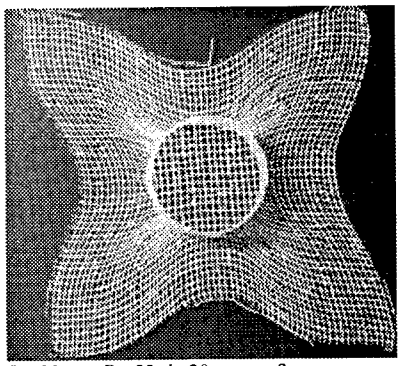

D_1=30mm, D_2=32, h=20mm, r_2=2mm.

Fig.3 Fabric deformation of deep drawing.

Inter-fiber sliding is negligibly small when the punch traveling h is small (see Fig.4).

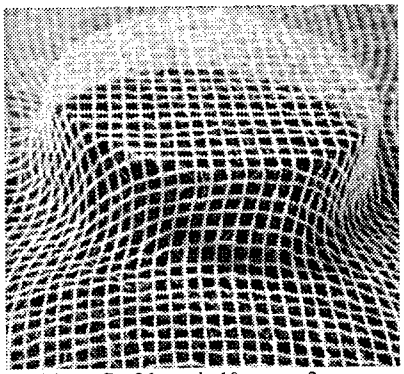

D_1=34mm, D_2=36mm, h=10mm, r_2=2mm

Fig.4 Fabric deformation without inter-fiber sliding.

Buckling of yarn by compression is observed on the side surface, when the punch traveling h is large and the radius r_2 of molding surface is small (see Fig.5).

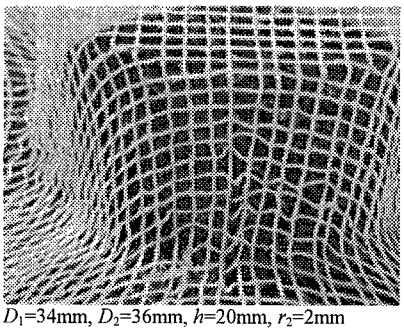

D_1=34mm, D_2=36mm, h=20mm, r_2=2mm

Fig.5 Buckling of yarns on side surface.

Inter-fiber sliding is also observed on the side surface, when h and r_2 are large (see Fig.6).

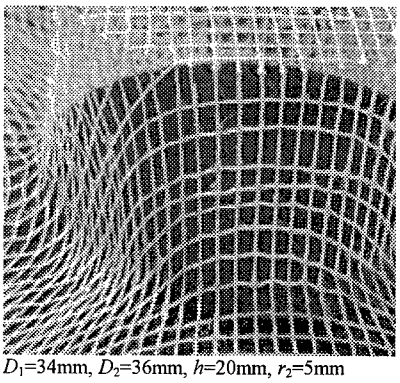

D_1=34mm, D_2=36mm, h=20mm, r_2=5mm

Fig.6 Inter-fiber sliding on side surface.

Network Model and Inter-fiber Sliding

We employ the pin-jointed network model, and each nodal point of the plain woven fabrics is connected to four line segments as shown in Fig.7(a). We evaluate the amount of sliding from the axial force of segments, and then we move the position of P(i, j) by sliding.

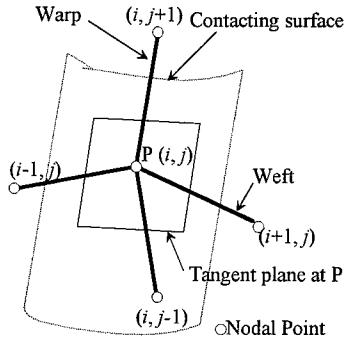

(a) Modeling of yarn deformation

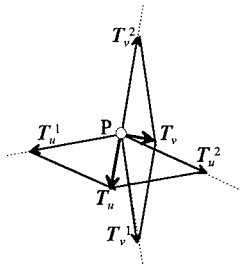

(b) Three-dimensional applied forces to node P

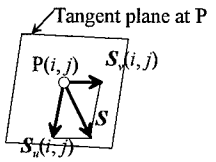

(c) Two-dimensional vectors on tangent plane

Fig.7 Modeling of inter-fiber sliding at node P.

Estimation of Inter-fiber Sliding

We evaluate the amount of sliding at every nodal point a fabric by the following local rule.

Forces $\boldsymbol{T}_u^1$ and $\boldsymbol{T}_u^2$ which can be evaluated from the axial forces of weft segments are applied to node P(i, j) of weft i and $\boldsymbol{T}_u$ is the resultant of them. Similarly, $\boldsymbol{T}_v^1$

and T_v^2 are applied forces from warp segments, and T_v is the resultant. These vectors are three-dimensional as shown in Fig.7(b).

If a node contacts on the punch or the molding surface, it moves along the contacting surface. To estimate the sliding movement of point P on the contacting surface, projection vectors $S_u(i, j)$ and $S_v(i, j)$ of the force vectors T_u and T_v onto the tangent plane are defined. These vectors $S_u(i, j)$, $S_v(i, j)$ and the resultant S are two-dimensional on the tangent plane shown in Fig.7(c). The direction of S denotes the sliding direction. We define the sliding factor β which depends on the number of sliding estimations and the status of friction between yarns. Then, we determine the value of β with reference to the experiments of fabric friction [10], empirically. We can estimate the amount of inter-fiber sliding at βS, and obtain the new draping point on the punch surface by re-projection onto it.

FEM Analysis

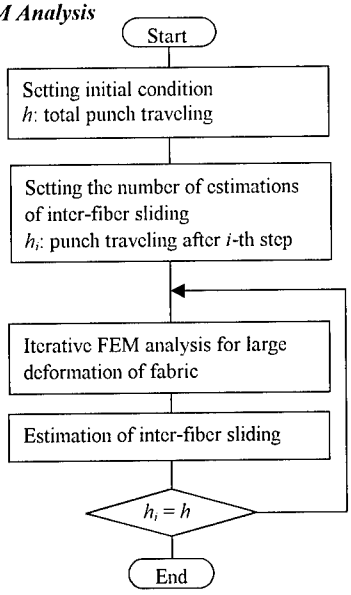

Fig.8 Flow chart of simulation.

We set the initial condition and the number of estimation of sliding. The iterative FEM analysis for large deformation is performed until the punch traveling distance approaches to h_i, which denotes the punch traveling distance without inter-fiber sliding. We estimate the inter-fiber sliding from temporary results of FEM, and employ LS-DYNA for the large deformation analysis. The flow chart is shown in Fig.8.

Conclusions

We have examined deep drawing of fabrics with a cylindrical punch. Large shear deformation of texture, buckling of yarn by compression and inter-fiber sliding are observed. We propose the strategy of FEM analysis for studying inter-fiber sliding.

References

1. C. Mack and H.M.Taylor: J. Textile Institute, 47, 477 (1956).
2. F. Van der Ween: International Journal for Numerical Method in Engineering, 31, 1415 (1991).
3. B. P. van West and S. C. Luby: Journal of Advanced Materials, 28(3), 29 (1997).
4. J. Wang, R. Paton and J. R. Page: Composite, Part A, 30(6), 757 (1999).
5. J. C. Gelin, A. Cherouat, P. Boisse and H. Sabhi: Composites Science and Technology, 56(7), 711 (1996).
6. L. Dong, C. Lekakou and M. G. Bader: Composites Part A, 31(7), 639 (2000).
7. Y. Arimitsu and Tsu-Wei Chou: Proc. of 23rd International SAMPE Tech. Conf., 551 (1999).
8. Chyi-Lang Lai and Wen-Bin Young: Polymer Composites, 20(4), 594 (1999).
9. J. Wang, J. R. Page and R. Paton: Composites Science and Technology, 58(2), 229 (1998).
10. L. Virto and A. Naik: Textile Research Journal 70(3), 256 (2000).

Proceedings of 7th Japan International SAMPE
Symposium & Exhibition, Nov. 13-16, 2001

Fabrication and Mechanical Behavior of Textile Reinforced SMC

Asami Nakai[1] and Takeshi Ohkawa[1]

1: Division of Advanced Fibro Science, Kyoto Institute of Technology
Goshokaido-cho, Matsugasaki, Sakyo-ku, Kyoto 606-8585, JAPAN
E-mail: nakai@ipc.kit.ac.jp

Abstract

In this study textile reinforced SMC was fabricated to improve the mechanical property of SMC, furthermore, to reinforce around the hole. Tensile test of textile reinforced SMC with a circular hole with a pin was conducted. SMC with textile showed higher tensile properties than SMC without textile. Particularly, the braided hole contributed to the improvement in the maximum load. These differences were due to continuous fiber around the circular hole. From the observation of the cross section the microfracture of textile reinforced SMC with a circular hole with pin was clarified.

Key words: SMC, Textile, Braided Hole, Machined Hole

Introduction

SMC (Sheet Molding Compound) is one of the typical composite materials, which consists of glass fiber mat and unsaturated polyester resin. SMC products have smooth surface without any particular technique, and this is a superior point of SMC. SMC molding process is simple, namely easy to fabricate complex shape products. From these reasons, SMC products have been used in structural parts of transportation vehicles, water tank, bathtub, and many other products.

Although SMC is widely used, the initial fracture occurs at relatively small strain. As one of the solutions, the use of textile as the reinforcements of SMC was proposed. The reason is that long fiber reinforcements of textile can improve the modulus and strength in SMC.

When the composite materials are used as structural members, connecting them with other members is the important problems. Mechanically fastened joints connecting each member by pins or bolts have been well known as one of the simplest joint methods. In producing the hole by machining, decrement in the mechanical properties of SMC is expected because of the stress concentration.

The braided fabric can make a hole without cutting fiber continuity around a hole. Therefore, the above-mentioned SMC reinforced with textile is also useful because braided fabric can reinforce around the hole in addition to improvement of the mechanical properties of SMC.

In this study, textile reinforced SMC was fabricated with braided fabric and cloth for the comparison. For the actual application, tensile test with pin in the circular hole was performed. Moreover, observations of the cross-section after

tensile test were carried out to clarify the microfracture in the specimens.

Experiment

Materials

In this study, to reinforce SMC, two types of textile were used. One was E-glass cloth (WE18W; Nitto Boseki Co., Ltd.) and the other was flat braided fabric. Materials used for flat braided fabric was glass fibers (ER575 F-165N, 17 μ m, 1000 filaments, Nippon Electrical Glass Co., Ltd.) as a reinforcement. A flat braided fabric with 2/2 intersection repeat was fabricated by using a flat braiding machine with 25 spindles. SMC (1740; Asahi fiber glass co., ltd.) was composed of random glass mats of short glass fiber and unsaturated polyester. SMC plates reinforced with textile were produced by compression molding machine with 300mm×300mm of the cavity mold.

In the case that laminate of SMC and textile fabric was compressed and molded, the unimpregnated region was observed. Therefore, in order to fill the resin into the fiber bundles and to help the impregnation of resin from SMC to textile, textile fabric was impregnated with paste resin used for SMC materials prior to molding. Processing conditions were as follows; 140 ℃ of molding temperature, 5.6MPa of molding pressure, 100% of charge ratio.

Tensile test

Geometry of the specimens for tensile test was 250mm in length, 25mm in width, and SMC was 4mm in thickness, and both SMC with cloth and SMC with flat braided fabric were 4.8mm in thickness. Static tensile test was performed with the gage length of 170 mm. The diameter of a hole was 6 mm. Tensile tests with pin were performed.

The types of specimen were as follows; SMC with machined hole (SHP), SMC with cloth with machined hole (CHP), and SMC with braided fabric with machined hole (MHP), SMC with braided fabric with braided hole (BHP).

Results and Discussions

It is known that in SMC specimens under tensile load, initial fracture, namely transverse crack, occurred at the interface in a fiber bundle. [1] For the textile reinforced SMC, the transverse cracks were also observed. In load-displacement (L-D) curves of these SMC products, load increased linearly at the beginning and showed a knee point. It was confirmed that the transverse cracks caused the decrement in slope of the stress-strain curves, that is, knee point.

Figure 1 shows L-D curves of SHP, CHP, MHP, and BHP. All specimens of SMC with textile showed higher properties than SMC without textile. The behavior of L-D curves, particularly after knee point, depended on the types of textile as the reinforcements. BHP with the fiber continuity around the hole had the highest property; the steepest slope and the highest maximum load of all the specimens.

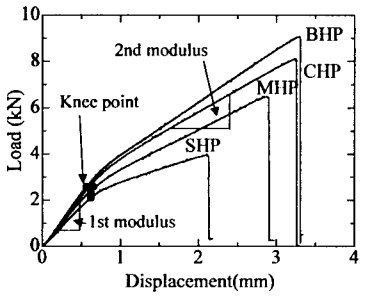

Fig.1 L-D curves of textile reinforced SMC

Tensile properties are summarized in Table 1. Here, 1st modulus and 2nd modulus represents the slope of L-D curves before and after knee point as shown in Fig.1. Knee point load and maximum load were obtained from L-D curves. Here, the normalized load is load divided by the thickness. Improvement ratio represents the knee point

and maximum load divided by the values of SMC without textile (SHP) respectively.

As shown in Table 1, the 2nd moduli of SMC with textile were higher than those of SMC without textile. The normalized knee point and maximum load of SMC with textile was higher than that of SMC. As for Improvement ratio, both that of knee point load and maximum load with textile showed value above 1.0 and the improvement ratio of maximum load was higher than that of knee point. Concerning SMC reinforced with braided fabric, BHP showed 1.30 in improvement ratio of knee point, and 2.01 in improvement ratio of maximum load. From these results, it is clear that SMC with textile, particularly braided fabric with circular hole, has higher property than SMC without textile because of the continuous fiber around the hole. Moreover, it is interesting result that maximum load of BHP was equal to that of F, that is, SMC reinforced with braided fabric without a hole.

Next, microfracture of textile reinforced SMC after tensile test was examined with optical microscopy; the photograph of cross-sectional area of specimen parallel to the longitudinal direction was focused. In the case of SHP, transverse cracks were observed as mentioned before. Figure 2 shows CHP around the hole, which shows that the cloth was delaminated. Further, in this photograph both transverse crack and the crack parallel to longitudinal direction occurred in one fiber bundle around the hole. The crack parallel to longitudinal direction was because of heterogeneity structure in thickness direction since textile was put only one side. As a result, it is considered that shear stress generated in the SMC before the delamination between textile and SMC.

Figure 3 is MHP around the hole and Fig. 4 is BHP. Delamination between textile and SMC was not observed in MHP and BHP even around the hole. In MHP, there are cracks parallel to longitudinal direction and transverse cracks as same as the CHP, because the fiber continuity was not kept around the hole. In BHP specimens, only the cracks parallel to the longitudinal direction were observed all over the specimen. It is expected that because the cracks only parallel to the longitudinal direction occurred, delamination could not occur until the final fracture in BHP.

Conclusion

In this study textile reinforced SMC was fabricated to improve the mechanical property of SMC, furthermore, to reinforce around the hole. Tensile test of textile reinforced SMC with a circular hole with pin was conducted. BHP showed the highest tensile property of all types of the specimen. Optical microscopic observation was conducted to understand microfracture of the specimen. From these results, usefulness of braided fabric for reinforcements of SMC by the continuous fiber around the hole was confirmed.

References

1. Etsuko Tanigaki, Hiroyuki Hamada "*Structural Designing of SMC Products*"pp.9-10 (1999)

Table 1 Tensile property of textile reinforced SMC with a pin

	Thickness (mm)	1st modulus (kN/mm^2)	2nd modulus (kN/mm^2)	Normalized load [knee (kN/mm)]	Normalized load [Max (kN/mm)]	Improvement ratio [knee (%)]	Improvement ratio [Max load (%)]
SHP	3.96	0.83	0.28	0.29	0.88	1.00	1.00
CHP	4.95	0.90	0.39	0.40	1.59	1.38	1.82
MHP	4.82	0.80	0.31	0.30	1.47	1.06	1.67
BHP	4.77	0.95	0.42	0.37	1.76	1.30	2.01

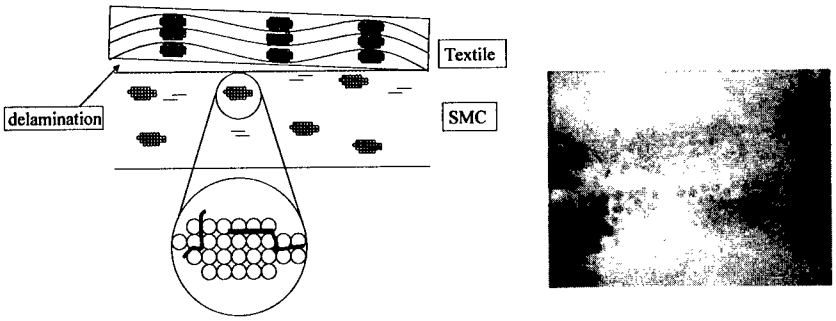

Fig. 2 Fracture aspect of CHP

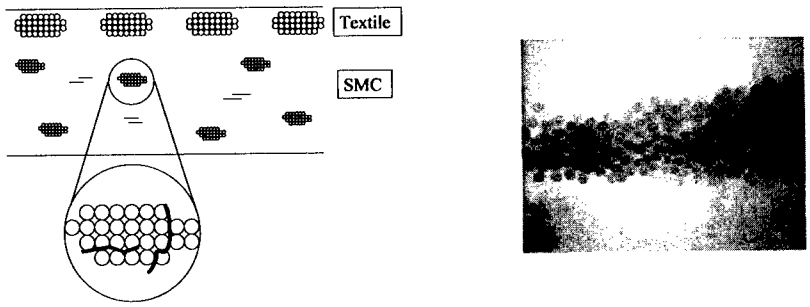

Fig. 3 Fracture aspect of MHP

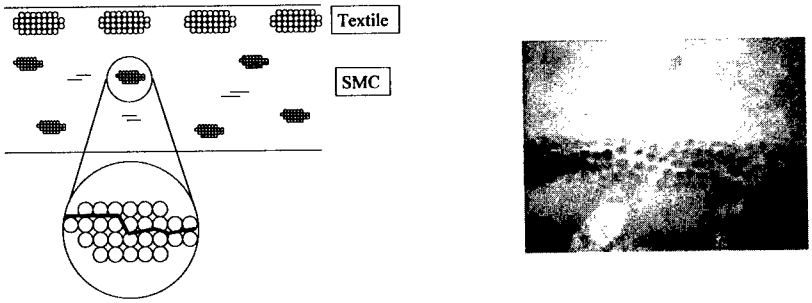

Fig. 4 Fracture aspect of BHP

Proceedings of 7th Japan International SAMPE
Symposium & Exhibition, Nov. 13-16, 2001

Ironing Assisted Deep-Drawing of Thermoplastics Reinforced with Continuous Carbon Fiber and Characteristics of The Products

Terufumi Machida# Toshihiko Okai# Kentaro Yoshimatsu ##and Masuhiro Okada###

#: Tamagawa University, Tamagawa-gakuen 6-1-1, Machida, Tokyo 194-8610, JAPAN
E-mail: machidat@eng. tamagawa.ac.jp

##:Molex Japan Co., Ltd. Fukami-higashi 1-5-4, Yamato, Kanagawa 242-8585, Japan

###:Yamaha Corp. Nakazawa-cho 10-1, Hamamatsu, Shizuoka 430-0904, Japan

Abstract

Continuous fiber reinforced thermoplastics were formed into cylindrical and square cups by using the newly developed ironing-assisted thermal drawing method. The forming limits increases with decreasing fiber contents and ironing ratio. By the addition of ironing, the accuracy in diameter and thickness, and the surface roughness were remarkably improved. For the redistribution of fiber, the radial strength uniformly increases with increase of wall position from bottom.

Key Words: Thermal Drawing with Ironing-Assisted , Continuous Fiber Reinforced Thermoplastics, Forming Limits, Accuracy of Product

Introduction

Since a plastic sheet reinforced with continuous fiber or long fiber has, in general, no plastic deformability, it is thought very hard for such materials to be formed in solid phase. For this reason some thermoforming processes for continuous fiber/thermoplastic composite sheets have been used only to produce a shallow dish[1]. In the previous papers[2～4], however, authors have already suggested that such long / fabric fiber reinforced materials are possible to be deep drawn into various shapes.

In the present paper, a newly developed deep-drawing of ACM or FRTP was successfully investigated to produce the high quality cylindrical cup. In this process, the local heating of flange and the ironing, that is clearance less than sheet thickness, are most important factors for the uniform draw-in. As predicted theoretically, limiting drawing ratio (L.D.R.) increases with decreasing of fiber volume fraction. The accuracy, surface roughness and tensile strength of product were confirmed to be excellent, too.

Experimental

Preparation of testing materials

Fabric carbon reinforced polycarbonate and polyetherimide are used. As illustrated in Fig.1, the plain-weave textiles of carbon fiber and PC or PEI films are alternately laminated to a given fiber content (v_f: 7 types, 0～45.2 vol%), then the materials are press-molded at elevated temperatures to be composite sheets having the thickness of 1.50 ± 0.05mm.

Deep drawing method

Deep drawing with ironing was conducted by using a hydraulic press of 100kN capacity, as illustrated in Fig.2. Electric sheath heaters, which are incorporated in the dies and blank holder, can heat locally the flange materials.

The ironing ratio or reduction of wall thickness was mainly set at 6.7%. From the clearance (cl) and blank thickness (t_0), the ironing ratio ϕ_0 is written as the following equation,

$$\phi_0 = 1 - cl / t_0 = 1 - (d_D - d_P) / (2t_0) \quad (1)$$

Results

Formability

Fig.3 shows the limiting drawing ratio and the possible cup depth (h/d_P). From the figure, it is seen that both Cf/PC and Cf/PEI are applicable for the process. The L.D.R. is uniformly lowered as the fiber content is increased, because the distance between fiber clusters is expanded and therefore the flange can shrink in the direction of circumference easily as the fiber content is decreased. The materials of v_f 7.5% were confirmed to show the highest value i.e. 7.14, when softened materials break on punch. In case of v_f 45.2%, the L.D.R. reaches the value of 2.78, while materials with no fiber have less formability because of easiness of necking on punch head.

Characteristics of drawn cup

With respect to the usually drawn cup of Cf/PC, which are obtained by the simple deep drawing (no ironing), the change of outer diameter is great in the range from the top to the wall and also the diameters of 0° direction become larger than those of 45°. In addition, the wall thickness increases rapidly with lowering the position from the cup shoulder. Such distributions are never expected for the product characteristics. In contrast with this, generally the accuracy of the product is remarkably improved.

The examples of products obtained in accordance with the individual methods are

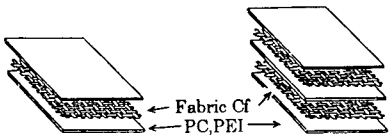

Fig.1 Constitution of materials

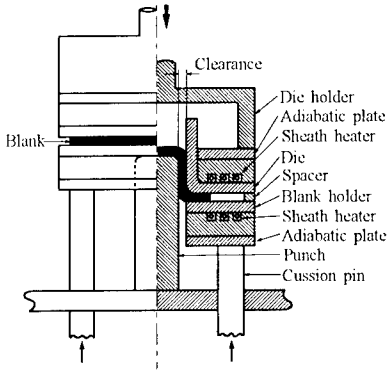

Fig.2 Apparatus for ironing-assisted deep-drawing

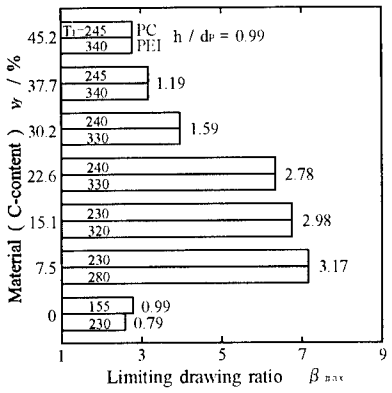

Fig.3 Increase of limiting drawing ratio and cylindrical cup depth with decrease of fiber content

photographically shown in Fig.4. Here, it is clearly noted that the appearance of cup is remarkably improved by the assistance of ironing and also no influence of material anisotropy on the flange draw-in is there.

The surface roughness measured at the central 5mm arc on the cup wall of Cf/PC are shown in Fig.5. With the cup produced by the process, R_{max} is slightly larger as the fiber content is smaller. For instance the value of 45.2 vol% Cf/PC remains in a range from 13.0 to 14.2㎛, which is comparable to the original value (R_{max}=3.8～4.2㎛). In contrast with this, the simply drawn cup has quite large values, for example 90～380㎛. Hence it is concluded that the assistance of ironing brings forth a distinct appearance of the smoothing effect.

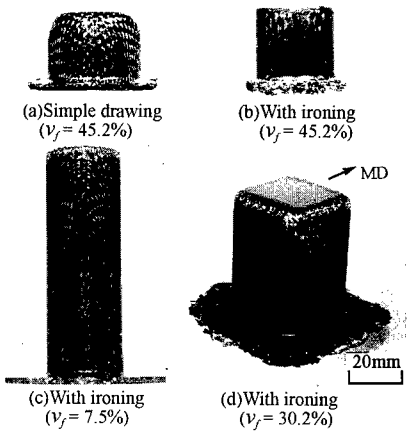

Fig.4 Appearances of fabric Cf/PC cups formed by using both the methods

Discussion

Evaluation of process

Because of its strain recovery, the one-operational process or deep-drawing with ironing was mostly promising to make a deepest cup of plastics composite materials.

Such the materials have strong planar anisotropy due to fiber direction. Hence in case of simple deep drawing, the fiber direction (0°) is apt to be drawn into the die hole and the 45° direction to make the circumferential shrinkage. This means that not only residual flange is liable to be formed, but also the fiber exposure or wall breakage by the local die gall is likewise liable to be produced as a result of the local increase of thickness[2].

Keeping such affairs in mind, the blank was compelled to flow homogeneously by applying of the ironing to the deep drawing. Such fruitful outcomes as predicted were obtained. This is because the continuous fiber is strong enough to exceed the flange shrinking resistance and ironing resistance and therefore the flange can be drawn into die hole.

Forming limit

The L.D.R. can be obtained theoretically on the principle of fiber amount constant, as follows[5,6];

$$\beta_{max} \fallingdotseq (2v_{fmax}/v_f)(1-\phi_o) \quad (2)$$

In the theory the limiting drawing ratio β_{max} is uniformly decreased with increasing ironing ratio ϕ_o for every capable fiber contents.

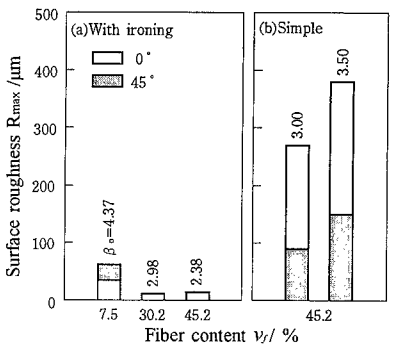

Fig.5 Comparision of surface roughness of formed cup wall between both the drawing methods (βo : drawing ratio)

Distribution of fiber and strength

The distribution of the fiber content in the formed cups, which are made of the Cf/PC with various fiber content is shown in Fig.6. It is seen that the value is raised by the aggregation of the fiber due to flange shrinking and by the extraction of plastics to brim, and the distribution in the 0° direction takes a little lower values on the wall region because of the extraction effect of the substrate plastics than that in the 45° direction.

Such the fiber displacement may distribute the strength of drawn cup wall. For examples, the radial tensile strength increases uniformly as the position comes near the cup brim, and its tendency becomes more clear in 45° than in 0° direction due to the fiber gathering effect, while the circumferential strength distributes a little.

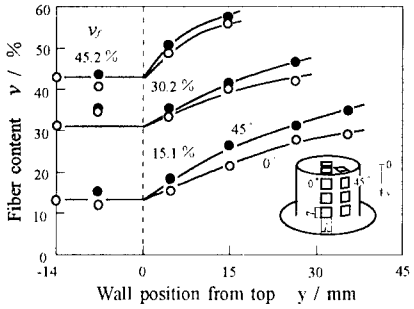

Fig.6 Changes in fiber volume content of various Fabric Cf / PC due to the ironing assisted deep-drawing

Conclusions

A novel process was successfully testified to produce a deep cup of fabric carbon reinforced plastics. Results are obtained as follows;

1) By deep-drawing assisted with local heating and with ironing, sheets of PC and PEI containing fabric carbon fibers are formed successfully.

2) As the fiber content is lowered, the limiting drawing ratio (L.D.R.) goes up uniformly.

3) By introducing the ironing the planar anisotropy of sheet has almost no effect on deep-drawability.

4) The product possesses higher quality such as accuracy in diameter and thickness, smooth surface, and higher tensile strength in radial direction than that of usual process.

Acknowledgment

The authors would like to thank Mr. Y. Kawashima, Sumitomo Heavy Industries Co. Ltd. for his useful suggestions and Kawasaki Steel 21st Century Foundation for its support.

References

1. K. Friedrich, M. How and J. Krebs: Composite Sheet Forming, ed. D. Bhattacharyya, Elsevier, 91(1997).

2. T. Machida, T. Okai, T. Masuyama and T.Ozawa: Jr. of The Japan Society for Technology of Plasticity, 29(326), 286(1988).

3. T. Machida, T. Okai, Y. Sanomura and T. Tanaka: Proceed. 1st Japan Int. SAMPE Symposium, 724(1989).

4. T. Machida, T. Okai, M. Okada and Y. Kawashima: Proceed. of the SPE 53rd Annual Technical Conference, 3094(1995).

5. T. Machida, T. Okai and K. Yoshimatsu: Advanced Technology of Plasticity 1996 (5th ICTP), 715(1996).

6. T. Machida, T. Okai, S. Kuramochi, G. Kimura and K. Yoshimatsu: 4th Int. Symposium Textile Comp., O-25-1(1998).

Proceedings of 7th Japan International SAMPE
Symposium & Exhibition, Nov. 13-16, 2001

Information on Pattern Figure in Textiles of Cultural Property

Akihiko GOTO*, Kumiko GOTO**, Asami NAKAI**,
Zen-ichiro MAEKAWA**, Masanori SATO***

*Department of Information Systems Engineering, Osaka Sangyo University
3-1-1 Nakagaito, Daito, Osaka 574-8530, JAPAN
E-mail:gotoh@ise.osaka-sandai.ac.jp
** Division of Advanced Fibro-Science, Kyoto Institute of Technology
Matsugasaki, Sakyo-ku, Kyoto 606-8585, JAPAN
***Nara National Cultural Properties Research Institute
2-9-1, Nijo-cho, Nara 630-8577, JAPAN

ABSTRACT

In our cultural history, textiles of the Nara period are very interested. Various pattern figures are drawn in the textiles. The geometric properties of the figure give much information to modern people. In this paper, we paid attention to geometric properties of pattern figures in textiles. Firstly, the algorithm of analyzing circle pattern figures was investigated and the measuring tool was developed. It was considered the ratio of the size of each circle pattern figure in a textile. Moreover, the ratio was compared with the different textiles. The regularity of the ratio of circle pattern figure was investigated.

Key Words: Textiles, Pattern Figure, Geometric Property, Culture Property

1. INTRODUCTION

It is very significant to investigate cultural properties on the 7th to 8th century. They have influences of two kinds of cultures. One is Japanese culture and the other is Chinese culture. By observing the cultural property, it is possible to search not only the skill of textiles and variations of geometric figures but also the idea and feeling of the ancient people. On these precious cultural properties, various researches have been done by using information technology.

In this paper, we paid attention to pattern figures of textiles in the Nara periods. In drawing pattern figures of the textile, there are beaded medallion, several kinds of circles and so on. Firstly, it aims to measure the geometric properties of these pattern

figures. The algorithm to extract geometric properties was investigated and the tool for the analysis was developed. Objective pattern figures were often included some damage and/or many parts of lost. However, if there are these cases, it is possible to predict total geometric properties by using this tool. Moreover, the geometric feature and ratio of various circle pattern figures was investigated.

2. OBJECTIVE PATTERN FIGURES

Examples of objective figures in textiles are shown in Figure 1. One is Nishiki silk with facing rhinoceroses in a beaded medallion design on a brown ground (Object 1). It is kept in Shosoin. This pattern figure is typical Nishiki silk with a beaded medallion design of Persian origin imported from China. It has lost most of the design. The circles around beaded medallion have not been sharp. Another is Nishiki silk with a hunting scene in a beaded medallion design on a green ground kept in Shosoin (Object 2). It has a sharp design. Moreover, Nishiki silk with a hunting scene in a beaded medallion design on a light blue ground kept in Shosoin and Nishiki silk with hunting lions in a beaded medallion design kept in Horyuji and so on were used as objects. Figure 2 shows illustration of the pattern figure. We paid attention to the beaded medallion and two kinds of circles. They were called the inner circle and the outer circle, respectively. Geometric properties of these figures were measured.

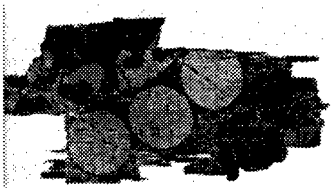

(a) Nishiki silk with facing rhinoceroses in a beaded medallion design on a brown ground (Object 1).

(b) Nishiki silk with a hunting scene in a beaded medallion design on a green ground (Object 2).

Fig.1 Examples of objective pattern figures.

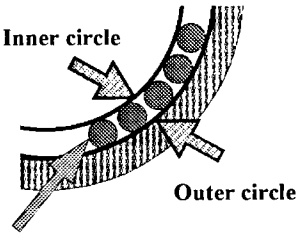

Beaded medallion

Fig.2 Illustration of objects.

3. MEASUREMENT OF GEOMETRIC PROPERTIES

3.1 Measurement procedure

First of all, pattern figures of analogue image in printed matter were used. They were digitalized by image scanner. And then objective circles of digital images were converted into numerical datum by the binary coded processing. Information of geometric properties was extracted by using the developed program.

3.2 Algorithm of measurement

Algorithm of measurement was able to find out an equal oval to the numerical datum. The flow chart of the algorithm is shown in Figure 3. Firstly, center position and radius of circle figure are predicted based on the numerical datum in consideration of the range of the error. By referring to this prediction, the range of an oval of breadth and the length radius is appropriately set. Next, the oval was drawn on the numerical datum. With setting value, breadth and length radius are varied gradually, respectively. Here, each oval was evaluated approximation degree to the numerical datum. In the beginning, the straight line which predicted center position of circle pattern figure is connected with the numerical datum curve was noticed. In addition, intersection of both this straight line and drawing oval is calculated. Therefore, distance between intersection of numerical datum curve (point a) and that of drawing oval (point b) is calculated. Figure 4 shows distance calculation between intersections. The distance is calculated by using all numerical data. All the distances are totaled. This processing is done for each drawing oval. The drawing oval with the minimum total of the distance is the optimum approximation curve of the numerical datum curve.

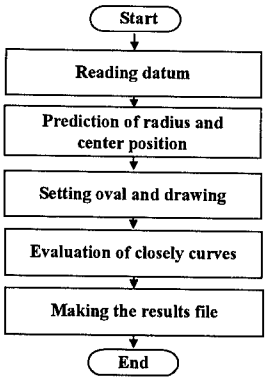

Fig.3 Flow chart of the algorithm.

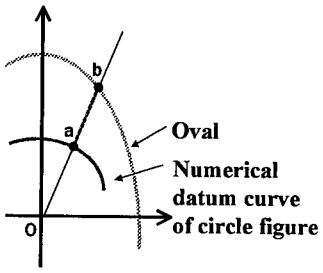

Fig.4 Distance between intersections.

4. RESULTS OF MEASUREMENT

Figure 5 shows an example of result by processing the developed algorithm. It is confirmed that the optimum approximation curve is very closely to the numerical datum

curve of circle figure. It is considered that the developed algorithm is useful for the analysis of geometric properties of pattern figures.

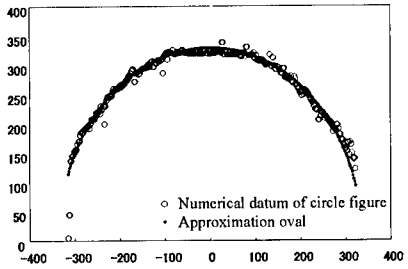

Fig.5 Example of comparison of numerical datum and approximation oval.

In the cases of object 1 and 2, the ratios of oval radius were calculated by transverse radius over longitudinal radius. Table 1 shows the radius ratio of each circle. In the case of object 1, the outer and the inner circle are a little sideways flat. However, the beaded medallion is almost the perfectly circle. In the case of object 2, all circles are almost the perfectly one. It is considered that the circle pattern figures were drawn as the perfectly circle.

Table 1 Radius ratio of each circle.

	Outer circle	Inner circle	Beaded medallion
Object 1	1.72	1.72	0.78
Object 2	1.24	1.05	1.22

5. DISCUSSIONS

The correlation of the outer circle, the inner circle and the beaded medallion in each object was investigated. Table 2 shows correlation of each circle. Here, the ratios of radius of each circle were calculated based on the radius of outer circle. When the radius of the outer circle express as 1, the inner circle and the beaded medallion express as about 0.8 and 0.1 respectively. It is considered that there is the regularity of the ratio of each circle in the pattern figure of culture properties. The figure that the ancient people created is accepted as beautiful shape at the present age. It is thought that finding such a relation gives one factor in the making design.

Table 2 Correlation of each circle.

	Outer circle :	Inner circle :	Beaded medallion
Object 1	1 :	0.79 :	0.084
Object 2	1 :	0.86 :	0.13

6. CONCLUSIONS

It is possible to measure the geometric properties of pattern figures in textile by the developed algorithm. It is cleared that each circle figure in different textiles was drawn by constant ratio.

In future work, the regularity of the geometric properties in textiles on various regions is investigated. Moreover, it is considered the sensibilities of both ancient and modern people on the regularity.

References

1. K. Matsumoto: "Shosoin textiles", Kyoto Shoin, 1993.

2. Nara National Museum: " Exhibition of Shoso-in Treasures", 2000.

Proceedings of 7th Japan International SAMPE
Symposium & Exhibition, Nov. 13-16, 2001

Interfacial properties of EB cured composite

Toshiko Osada, Machiko Mizoguchi, Asami Nakai, Hiroyuki Hamada

Advanced Fibro Science, Kyoto Institute of Technology, Matsugasaki, Sakyo, Kyoto, 606-8585, JAPAN
E-mail: hhamada@ipc.kit.ac.jp

Abstract

There are significant advantages to be gained in Electron Beam (EB) processing of composite materials over conventional thermal curing. Composite cured by EB can achieve the easy material handling and short curing time. In this study, EB cured plain woven reinforced epoxy composite was fabricated and Mode I fracture toughness test was performed to investigate the interfacial properties. As a result, stable crack propagation behavior and sub cracks, which are due to poor interfacial properties, were observed. It indicated that the interfacial properties of EB cured composite were extremely low.

Key Words: Electron beam cure, Mode I fracture toughness test, textile composite, interface

Introduction

There are significant advantages such as non-thermal and nonautclave curing, shorter curing time, and lower energy requirements, to be gained in Electron Beam(EB) processing of composite materials over conventional thermal curing. Particularly, for textile composite EB curing system would provide an important advantage. One of the most important problems in textile composite is impregnation. Using EB curing system, the impregnation and curing procedures can be separated, and enough time can be spent to impregnate completely. In addition, thermal stress can be reduced. When processing thick products using textile composite, thermal stress is large in the case of thermal curing. On the other hand, EB curing can overcome this problem. Hence, the EB curing process is suitable for textile composite.

In composite, it is well known that interfacial properties affect the properties of whole composite. In the textile composite, particularly in woven fabric reinforced composite, the initial damage occurs at interface. Therefore it should be very important to understand interfacial properties to achieve the high mechanical performance of composite.

In this study, EB cured woven fabric composites were fabricated and the interfacial properties were investigated. We have been considering the several interfaces, that is, interface around single filament, interface in fiber bundle, interface around fiber bundle, and interface between lamina. Interfacial properties between lamina were focused in this study. It was discussed using Mode I fracture toughness test with double cantilever beam specimen. The crack propagation behavior was precisely observed by microscope.

Experimental

Materials

Epoxy silane treated plain woven glass cloth (Nittobo, WE18W) was used as reinforcement. Matrix resin used is Bisphenol A type epoxy resin (Epicote 828, Yuka shell epoxy Co. Ltd.) and cationic photoinitiator (phenil-p-octyloxyphenil-iodoniumhexafluoroantimonate, OPPI, General Electric Co.). To give toughness to the resin, 1,4-bis[(3-ethyl-3-oxetanylmethosy)methyl] benzen, (XDO), was added.

XDO and OPPI were mixed with the epoxy resin, and then it is impregnated to the fabric in a vacuum chamber. 18 plies and 3mm thick double cantilever beam specimen with pre-crack were prepared for Mode I fracture toughness test. EB curing was performed with an electron beam which was produced by an accelerator with energy of 10MeV. Figure 1 shows schematics of EB curing facility. Specimens were put on a tray on a conveyer, and EB is rayed to the samples during passing below horn under accelerator. Rayed dose can be controlled by changing the speed of conveyer system. 150 kGy was totally rayed with a combination of 10kGy 3 pass and 30kGy 4 pass.

Mode I fracture toughness test

Mode I fracture toughness test was performed using INSTRON universal testing machine(Type 4206) according to JIS K7086. The testing speed was set at 1mm/min. After the test, the cross-section of the specimen along the crack was observed.

Results and discussion

Figure 2 shows the load-crack opening displacement curve. The load reached the maximum value and then decreased gradually. Figure 3 shows R curve obtained from figure 2 and crack length measured during test. The fracture toughness of crack initiation was 0.18 J/m^2, whereas that of thermal cured composite is 0.30 J/m^2. Figure 4 and 5 show the result of cross sectional observation and schematic illustration of crack propagation behavior respectively. The main crack propagated at the interface. The load-crack opening

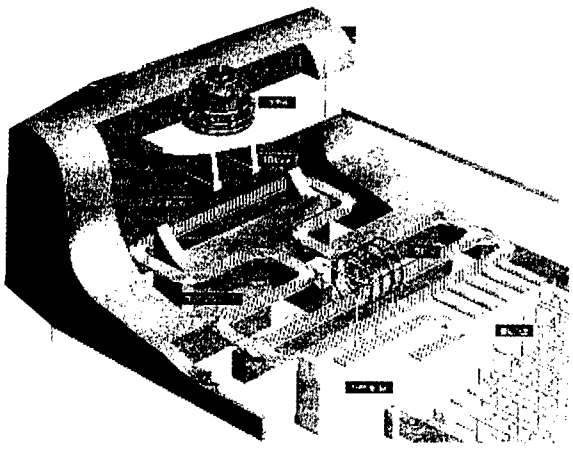

Figure 1 Facility for electron beam curing

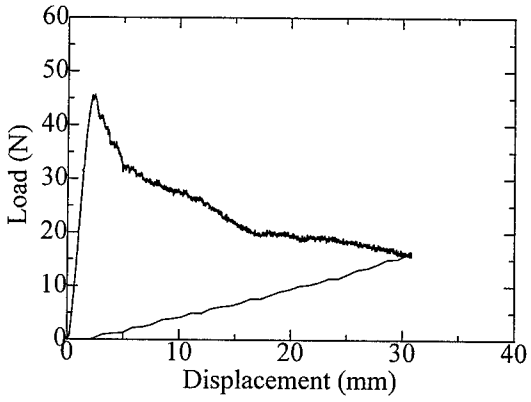

Figure 2 Load-crack opening displacement curve.

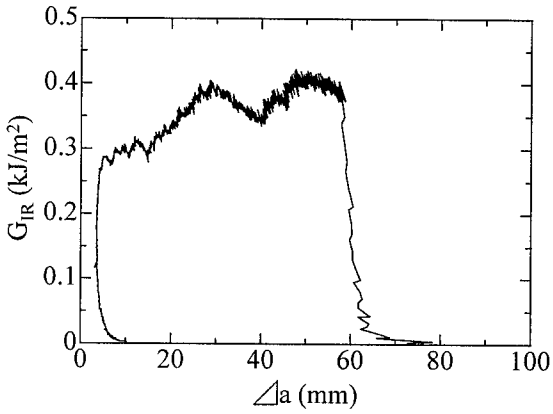

Figure 3 R curve.

displacement curve shown in figure 2 and the crack propagation behavior shown in figure 4 and 5 were due to stable crack propagation. The crack propagation behavior depends on the fracture toughness of interphase and resin[1-3]. When the fracture toughness of interphase is higher than that of resin, the crack propagated into resin area, and the crack propagation behavior is unstable. On the other hand, when the fracture toughness of resin is higher than that of interphase, namely the interfacial adhesion is poor, the crack propagated along glass cloth, in other words, at interphase. Therefore, the stable crack propagation behavior indicated that the interfacial adhesion in EB cured composite

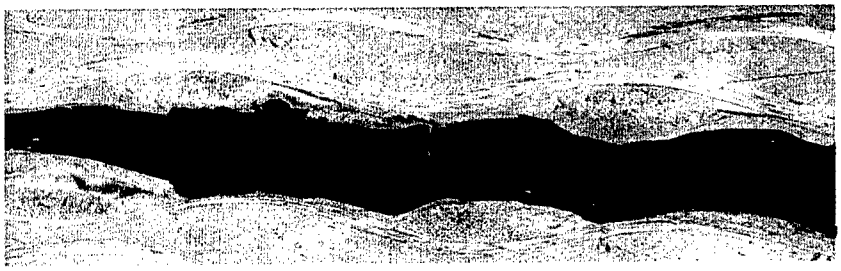

Figure 4 Cross sectional observation

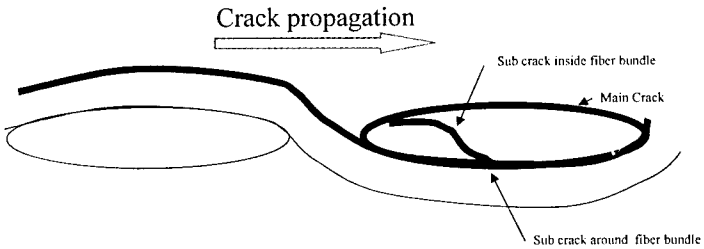

Figure 5 Schematic illustration of crack propagation behavior

was poor.

In addition, not only a main crack but also sub cracks were observed in figure 4 and 5. Cracks were observed in the fiber bundle and around the fiber bundle. The cause of the sub cracks would be also the poor interfacial adhesion both in and around fiber bundle.

It is reported that the EB cured epoxy resin has low fracture toughness, and the great effort have been made to obtain higher fracture toughness. When the fracture toughness of resin is low, it is expected that the crack tends to propagate into resin. From this point of view, the poor interfacial properties in EB cured composite were emphasized. It is well known that the interfacial properties affect the properties of whole composite. Therefore, to obtain higher mechanical properties of EB cured composite, the improvement of interfacial properties should be suggested in addition to the improvement of fracture toughness of resin.

Conclusions

EB cured woven fabric composites were fabricated and the interfacial properties were investigated using Mode I fracture toughness test using double cantilever beam specimen. The stable crack propagation behavior and sub crack were observed. It indicated that the interfacial adhesion in EB cured composite was poor.

References

[1] Y. Suzuki, Z. Mackawa, H. Hamada, Composite Part A, 28A, pp.257-266, 1997.
[2] Y. Suzuki, Z. Mackawa, H. Hamada, A. Yokoyama, T. Sugihara, M. Hojo, J. Mater. Sci, 28, 1725-1732, 1993.
[3] M. Mizoguchi, Y. Ma, K.Inomata, Y. Fujii, Proceedings of Ninth US-JAPAN Conference on Composite Materials, 2000.

Proceedings of 7th Japan International SAMPE
Symposium & Exhibition, Nov. 13-16, 2001

Investigation of interfacial properties using compact tension tests of glass cloth reinforced vinylester composite -Fractographic approach-

Hiroyuki Hamada #1, Yoshimichi Fujii #2, Machiko Mizoguchi #1 and Yoshihiko koyama #1

#1: Kyoto Institute of Technology
Matsugasaki, Sakyo-ku, Kyoto 606-8585, JAPAN
E-mail : kom00@ipc.kit.ac.jp
#2:Seikow Chemical Engineering & Machinery, Ltd. Shioe,Amagasaki, Japan

Abstract

Acid stress corrosion behavior of E or C glass cloth reinforced vinyl ester resin has been investigated using CT specimen. Basically E glass fibers easily degrade in acid solution, whereas C glass fibers are unti-corrosive fibers. It is expected that interfacial problems become an important issue in the case of C glass fiber reinforced composite particularly in long time service. On the fracture surface of CT specimen after immersion in acid solution the cracks initiating from inside of fiber bundles were often observed in our previous paper. In this paper modified CT specimen in which warp fiber bundle were removed near crack tip in order to make observation of cracks from inside of weft fiber bundle easier.

Keyword

CT test, interfacial degradation, C-glassfiber, fractography

Introduction

Fiber reinforced thermosetting matrix composite (FRP) has been in adversity against ecological movement in recent days, because easy recycling materials are very friendly to the earth. However in the civil engineering field long life construction requires FRP particularly in rehabilitations of concrete columus and sewage repair, moreover pipe, fan and tank in acid environments. Therefore, FRP has been still important material system in our social life. In acid environment acid stress corrosion was very sevior problem. Intesead of E glass fibers, C-glass fibers which is anti-corrosive fibers, should be used in such applications. Data base of C-glass fiber reinforced composites, however, is quite small [1,2]. In order to establish design guideline of C-glass fiber composites we started creep test in acid solution. Gradually fracture mechanism of C-glass fiber composites has been cleared [3]. Basically elastic modulus and tensile strength of C-glass fiber are lower than those of E- glass fiber. In acid environments C-glass never corrodes, however, interfacial degradation occurrs and this phenomena determined the life of the products of C-glass composite. In CT specimen under acid environments we observed the cracks initiating from inside of warp fiber bundle which was aligned to crack propagation direction. This generation of cracks intimate degradation of interfacial properties inside of fiber bundle and observation of these cracks in more detail is key to open the understanding of degradation behavior of C-glass composites. In normal CT specimen the fracture surface is very rough because of pulled-out warp fiber bundle, so that it is very difficult to identify interfacial cracks. In this paper we used modified

CT specimen in which warp fiber bundle were removed near crack tip. Accordingly the crack propagated inside or between weft fiber bundle and the fracture surface would be very smooth. It was expected that cracks initiating from inside of weft fiber bundle could be easily observed.

Materials and specimen

Material used in this paper was C-glass cloth supplied from Mie txtile Co as reinforcement and vinyl ester resin supplied from Showa Highpolymer Co., Ltd., Japan was used as matrix. E-glass fiber cloth was also used for comparison. Normal CT specimen was cut out from the panel fabricated by hand lay up method with 6 mm of thickness (24 ply). The specimen geometry is shown in Fig.1. In the proposed specimen warp fiber bundle were removed before fabrication of the panel. The area without warp fiber bundle was 10 mm from crack tip as shown. The tensile load was applied to the pins at 0.5mm/sec of cross head speed at room temperature under normal air condition.

SEM observation of fracture surface

Fig.2 shows SEM fractographic photographs of E and C glass composites by using normal CT specimen in which warp fiber bundle were not removed. The most characteristics feature is the pulled-out warp fiber bundle. The length of pulled-out fibers and its distribution from crack tip would be useful information to understand fracture mechanism. In the case of E-glass fiber composites after immersing under acid environments the length of pulled out fiber decreased and fracture surface became smooth . On the other hand in the case of C-glass fiber composites even after long immersion tests the length of pulled out warp fiber bundle were still long and the rough fracture surface was observed Apparently, degradation of C-glass fiber composites could not be understood by observation of state of warp fiber bundle. According to our precise observation of fracture surface, the cracks initiating from inside of weft were detected as shown in Fig.2. In the case of rough fracture surface, it was difficult to pay attention to those cracks, because these cracks often existed behind of warp fiber bundles. Fig.3 shows the fracture surface of modified CT specimen. Only weft fiber bundle were observed and it was easy to identify the cracks from inside of weft. In comparison between C-glass composite and E-glass composites number of these cracks is larger in C-glass composites. Therefore the interfacial properties as C-glass composite was comparatively lower than that of E-glass composites. Initially we detected these cracks in C-glass specimen after immersion of acid environments by using normal CT specimen. It was supposed that interfacial degradation occurred in C-glass composites by acid. However, in this paper many of cracks were observed even in air condition by using modified CT specimen. The difference of interfacial properties of C and E-glass composites might depend on composition of fiber or another possible reason might be that surface treatment on the C-glass fibers is not optimized. In long term usage in acid environments the interfacial degradation would be the most important issue in C-glass fiber composites. The modified CT specimen proposed in this paper would be useful to identify these cracks and it leads to well understanding of fracture behavior of C-glass fiber composites. Further modified CT specimen will be used.

Conclusions

In order to understand fracture mechanisms of C-glass fiber composites under acid environments we proposed modified CT specimen in which warp fiber bundles were removed near crack tips. This specimen enables easy observation of cracks initiating from inside of weft fiber bundle which means interfacial degradation. It was explained that the modified CT specimen would be useful to understand interfacial degradation.

REFERENCES

1.Hogg,P.J., Composites,14,3(1983)254

2. HKumosa,M.,Hull,Dand Price,J.N.,Journal of Meterials Science,22,(1987)331.

3.Maeda,M.Fujii,Y.,Hamada,H.,Proceedings of the fourth international conference on durability analysis of composite system-DURACOSYS 99,Recent Developments in Durability Analysis of Composite System(1999)202

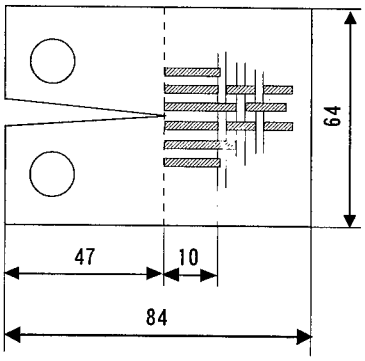

Fig.1 Geometry of modified CT specimen

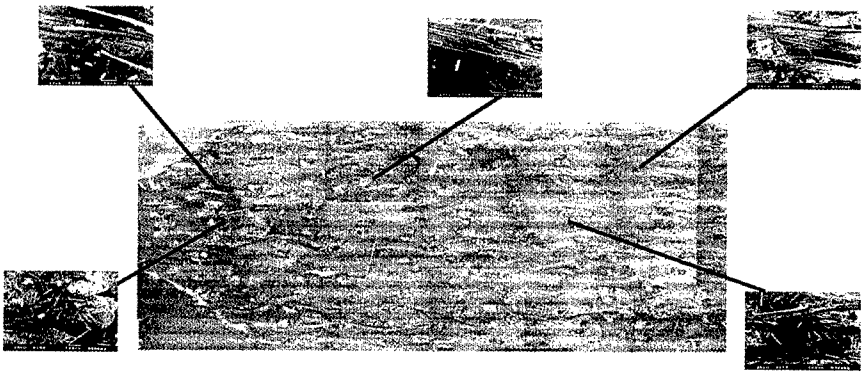

(a) E specimen

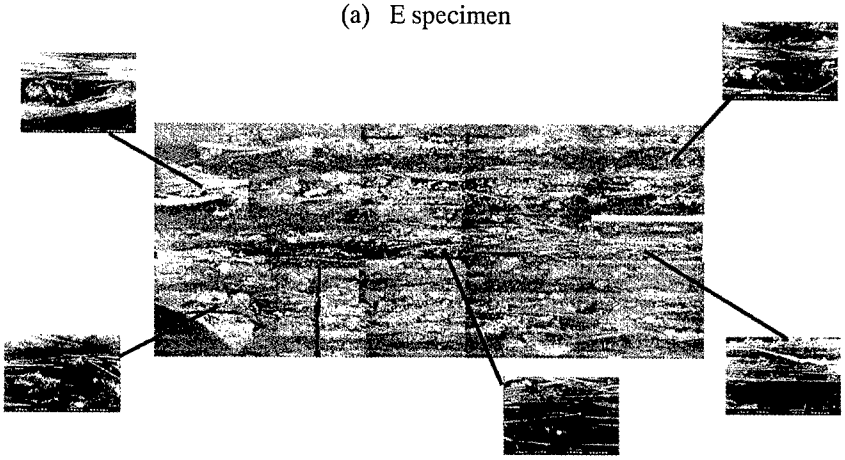

(b) C specimen

Fig.2 Fracture surface of normal CT specimen

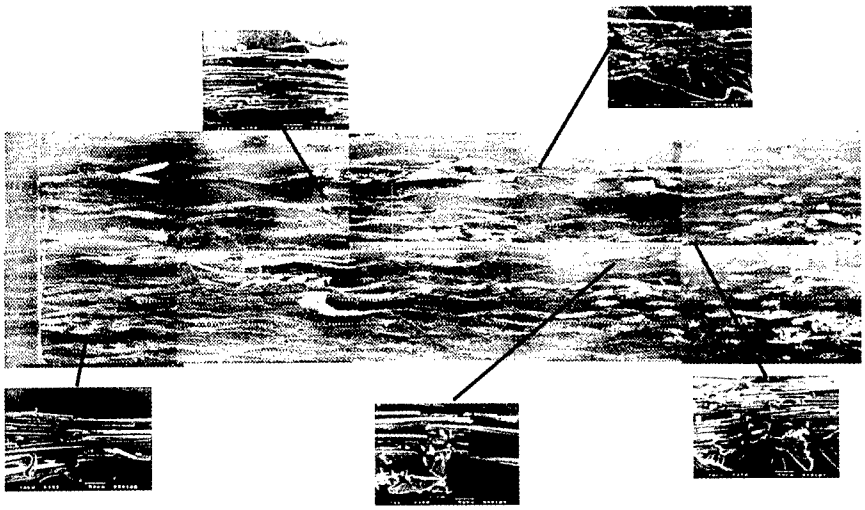

(a) E specimen

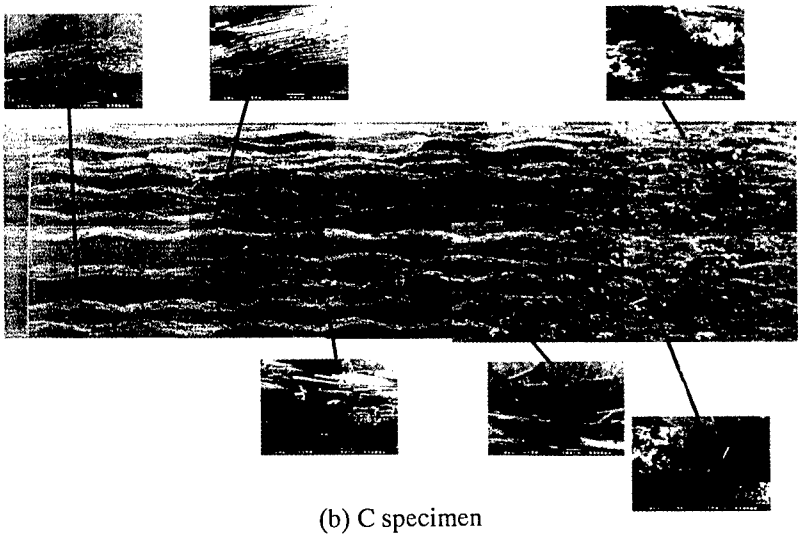

(b) C specimen

Fig.3 Fracture surface of modified CT specimen

Proceedings of 7th Japan International SAMPE
Symposium & Exhibition, Nov. 13-16, 2001

Mechanical Properties of Plain Woven Fabric Composites with Flexible Interphase

Satoshi Kobayashi#, Toshiko Osada* and Asami Nakai*

#: Graduate school of Engineering, Tokyo Metropolitan University,
6-13-1 Ohsawa, Mitaka, Tokyo 192-0392, JAPAN
E-mail: koba@ecomp.metro-u.ac.jp
*: Advanced Fibro Science, Kyoto Institute of Technology

Abstract

The interphase between fiber and matrix has a very important role, which includes the load transmission between fiber and matrix. In this study, the effect of interphase characteristics on the macroscopic behavior of plain woven laminates were most concerned. Basic mechanical properties of plain woven fabric composites with flexible interphase were evaluated experimentally. The effect of interphase thickness, which corresponded to the resin concentration in solution, on the cyclic properties were clarified.

Key Words: Flexible Interphase, Plain Woven, Static loading, Cyclic loading.

Introduction

Interface properties affect mechanical properties of fiber reinforced plastics (FRP) [1-3]. Various methods to improve the adhesion between fiber and matrix were developed. Recently, the concept of interphase has been recognized. That is, interface between fiber and matrix is not two dimensional plane but three dimensional region which has some volume. It is difficult to control the interphase properties, such as thickness, modulus and so on, and understand effects of interphase on the mechanical properties of laminates.

In the present study, we develop the method to fabricate woven fabric composites with flexible interphase. Static and cyclic tensile tests were conducted to clarify the effect of the interphase properties on the mechanical properties of laminates.

Experiments

Materials

E-glass plain woven fabric (WE18W, Nitto Boseki Co., Ltd) with 0.4wt% epoxy silane treated was used for a reinforcement. Epoxy resins were used for matrix and flexible interphase, Epikote 828 and Epikote 871 (both Yuka Shell Epoxy Co., Ltd). Epikote 871 has lower tensile modulus and higher ultimate strain than Epikote 828 and it was regarded to have more flexible properties than Epikote 828. Hardeners were 4,4-diaminodiphenylsulfon (DDS) and 1,2-diaminopropane for Epikote 828, 871 respectively.

Fabrication process of prepreg with flexible interphase was the conventional wetting method. First, the woven fabric was dipped into the mixture of Epikote 871 with 1,2-diaminopropane hardener and acetone. The acetone dilution had low viscosity for easy impregnation into the fiber bundles.

The woven fabric was dried at 65°C for 40 minutes and B-stage prepreg with flexible interphase was obtained. The resin concentration in acetone solution was varied among 0, 1, 3, and 5wt%.

Second, woven fabric was immersed into matrix resin bath. Here, the hardener for matrix resin was dissolved in acetone and methyl cellosolve. Before the immersion of woven fabric, matrix resin and hardener diluted with acetone were left in a vacuum chamber for 6 hours to remove the acetone well. The woven fabric impregnated into Epikote 828 was prepregnated at 130°C, 40 minutes. 5plies woven fabric composites were fabricated by air-bag fabrication method. Curing condition of composites was at 180°C for 120min.

Laminates fabricated by the above process were cut using diamond saw to make specimens. Specimen geometry is shown in Figure 1.

Static and Cyclic Tensile Tests

Static tensile tests were conducted using universal testing machine under displace control condition. Cross head speed was 0.5mm/min which corresponds to strain rate 0.007%/sec. Cyclic tensile tests were conducted using electro-hydraulic testing machine. Loading rate was 40kgf/sec which corresponds to strain rate 0.09%/sec. Maximum stress level was 240 MPa for each specimen, at which transverse cracks in weft fiber bundles go through the thickness. In both static and cyclic tensile tests, strain was measured by extensometer. Tests were continued until final failure.

Results and Discussion

Static Tensile Tests

Figure 2 shows typical stress-strain relationship for each specimen. There are nonlinear relationship in stress-strain behavior at early stage. This corresponds to initial damage initiation [4]. Table 1 shows average value of each property. Tensile strength of specimens with flexible interphase were larger than without interphase, which indicate the effectiveness of flexible interphase on the tensile properties. Each property becomes fine values at 3%wt, so 3%wt is most suitable for the present material system in case of applying to components under tensile loading.

Cyclic Loading

Figure 3 shows the relation between Young's modulus and number of cycles. Damages initiate at first cycle in all specimen, which results in large decrease in Young's modulus. Modulus reduction are considered to correspond to damage initiation and progress. 3wt% specimen has largest modulus under fatigue loading. That is, 3wt% concentration is most suitable to improve fatigue damage resistance.

Figure 4 shows SEM photographs of fracture surfaces of each specimen. Smooth fiber surface were observed in 0wt% and 1wt%. On the other hand, resin were attached to the fiber in 3wt% and 5wt%. We cannot recognized the fracture of 3wt% and 5wt% specimens initiated at whether interphase or matrix. Fracture mode changed from interfacial fractures in 0wt% and 1wt% to matrix fracture in 3%wt and 5%wt, which means the improvement in fatigue damage resistance is attributed to transition of the failure mode.

Conclusions

The method to fabricate woven fabric composites with flexible interphase was developed. The results of static and cyclic tensile tests indicate 3wt% concentration of the solution was most suitable to improve the properties of woven fabric laminates.

Acknowledgment

Professor Hiroyuki Hamada, Kyoto Institute of Technology, is gratefully acknowledged for his meaningful advices. Mr Nobuyoshi

Kajioka and Mr Masahiro Yamanouchi, Kyoto Institute of Technology, are also thanked for their help in fabricating specimens.

References

1. H. Ishida and J. L. Koenig: Composite Interfaces, Elsevier (1986).
2. D. Hull: An Introduction to Composite Materials, Cambridge Univ. Press (1982).
3. J. D. H. Hughes: Composite Science and Technology, 41, 13 (1991).
4. H. Hamada, et. al.: Proc. ICCM-13, ID 1557 (2001).

Table 1 Material properties

	Young's Modulus (GPa)	Strength (MPa)	Maximum Strain (%)
0wt%	23.7	317	1.59
1wt%	24.1	336	1.60
3wt%	24.8	338	1.67
5wt%	23.6	336	1.68

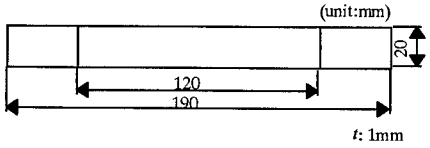

Figure 1 Specimen geometry.

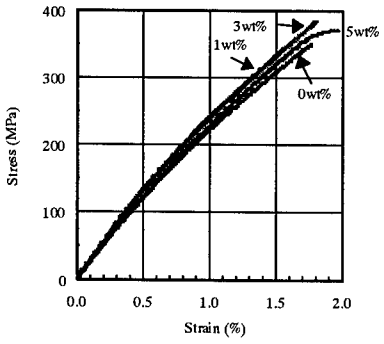

Figure 2 Typical stress-strain curve.

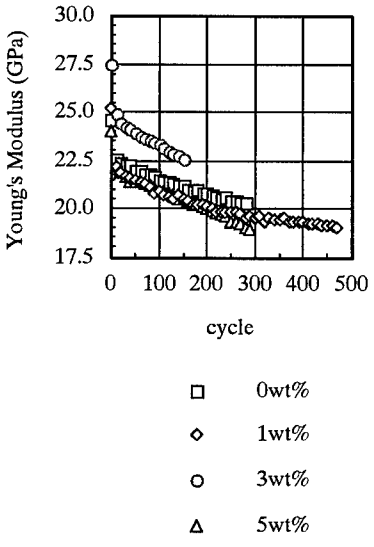

Figure 3 Young's modulus as a function of number of cycles.

(a) 0wt%

(b) 1wt%

(c) 3wt%

(d) 5wt%

Figure 4 Results of SEM observation.

Proceedings of 7th Japan International SAMPE
Symposium & Exhibition, Nov. 13-16, 2001

Initial Micro Fracture Behavior of Woven Fabric Composites

Toshiko Osada#, Tadayoshi Shimizu#, Asami Nakai#, and Hiroyuki Hamada#

#: Kyoto Institute of Technology
Matsugasaki, Sakyo-ku, Kyoto 606-8585, JAPAN
E-mail: b5330033@ipc.kit.ac.jp

Abstract

Knee point found on the stress-strain curve of tensile test was used to quantitative evaluation of interphase properties. Glass plain woven fabric treated with different concentration of acryl silane was used for reinforcement, and the matrix resin was vinylester. One ply composite was prepared, and static tensile test was performed.

Two kind of knee point was identified on the stress-strain curve by least squares method. Strain energies were calculated from the 1st and 2nd knee point stress and strain. It was confirmed that the 1st knee point shows the interfacial strength, and the energy between the 1st and 2nd knee point indicates the fracture toughness of interface inside of fiber bundle.

Key Words: Initial Fracture Behavior, Knee Point, Woven Fabric Composite, Interphase Property.

Introduction

It has been clarified that knee point on the stress-strain curve can be used for quantitative evaluation of initial fracture[1]. Initial fracture of woven fabric composites was confirmed to be transverse crack, that is, fracture at interface inside of fiber bundle. Consequently, knee point on stress-strain curve is also considered to be used for quantitative evaluation of interphase inside of fiber bundle.

In this study, in order to investigate the interfacial property, tensile tests of 1 ply composites with different concentration of silane coupling agent were performed. Knee point was determined on the stress-strain curve by least squares method. Next, initial fracture stress and strain energy were calculated and interfacial property was discussed using these results.

Micro fracture behavior

As previous study, tensile testing of 1 ply composites was performed and stress and strain at the knee points and the corresponding fracture process was discussed[1]. On the stress-strain curve, two kinds of knee point were found as shown in Fig,1. During the tensile tests, the testing machine was periodically stopped and observation of transverse cracks in weft fiber bundles using optical microscopy was performed.

Figure 2 shows the fracture aspect by optical microscopic observation. Transverse cracks appeared in weft fiber bundles, and the number of the cracks increased, and the crack was enlarged with increasing the strain.

The initiation of transverse crack appeared at the 1st knee point and when the initiated crack propagated throughout the weft fiber bundle the 2nd knee point occurs as shown in Fig.3.

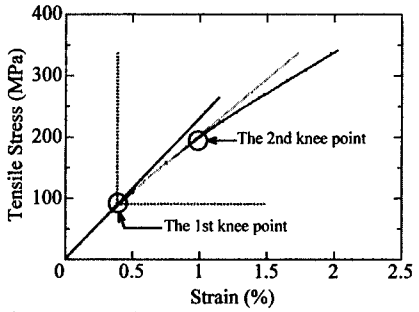

Fig. 1 Knee points on the stress-strain curve.

Materials

Materials used in this study were plain glass woven fabrics (WE18W: Nitto Boseki Co., Ltd., Japan) as reinforcement with 0.01, 0.4 and 1.0 wt% acryl silane coupling agent and vinyl ester resin (R-806; Showa Highpolymer Co., Ltd., Japan) as the matrix resin. The room temperature catalyst used was 0.7 phr methylethylketoneperoxide (MEKPO). 1 ply woven fabric composite was fabricated for tensile test to detect the onset and growth of transverse cracks clearly.

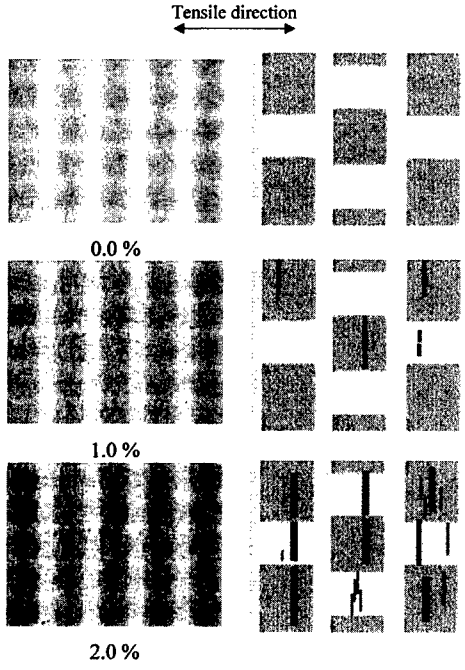

Fig. 2 Fracture aspect.

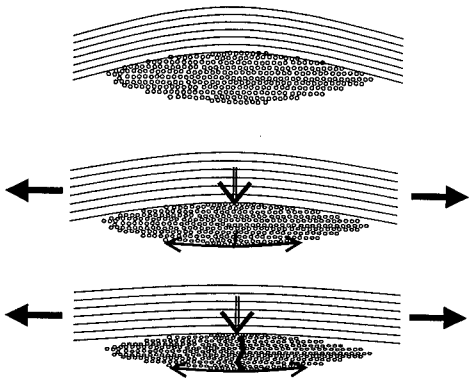

Fig. 3 Fracture process.

Knee point stress

Figure 4 shows the change in knee point stress with silane concentration. The 1st knee point stress of 0.4wt% specimen shows the highest value. As increasing the coupling agent concentration, the 1st knee point stress was decreased. It is supposed that there is an optimum concentration for the interfacial property. This phenomenon could be observed in case of single fiber embedded test [2]. On the other hand, the 2nd knee point stress decreased with increasing the concentration.

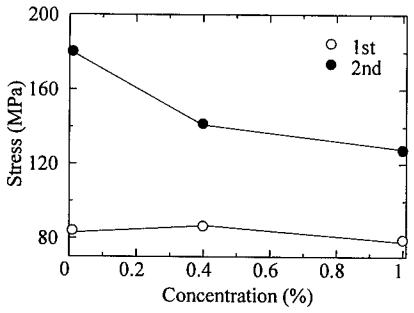

Fig. 4 Knee point stress.

Knee point energy

Strain energies were calculated from the 1st and 2nd knee point stress and strain. Here, the strain energy was defined as the area under stress-strain curve. As mentioned before, initiation of cracks appeared at the 1st knee point, and the cracks propagate throughout the weft fiber bundle at the 2nd knee point. Thus, strain energy until the 1st knee point represents the energy for the initiation of crack, the energy between the 1st and 2nd knee point is the energy for propagation of the crack, which is considered to indicate the fracture toughness of interface inside of fiber bundle.

Figure 5 shows the relationship between each strain energy and the silane concentration. In the case of 0.4wt%, energy until the 1st knee point shows the highest value as well as knee point stress. On the other hand, energy between the 1st and 2nd knee point decreased in the order of 0.01, 0.4, and 1.0wt%.

Discussion

We often use "optimum" surface treatment on the fibers discussing composite properties. However, the meaning of "optimum" has not always been cleared,

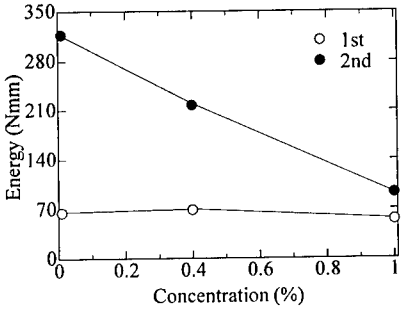

Fig. 5 Knee point strain energy.

because there are various kinds of composite properties, and strictly speaking, "optimum" surface treatment should be different corresponding to composite properties. In this paper we propose 1st and 2nd knee point to evaluate interphase properties inside of fiber bundle. Regarding the 1st knee point, it should be considered that interfacial strength could be evaluated. The dependence on concentration of silane coupling agent could be explained by the same discussion which was made on the results of single fiber embedded specimen [2].

For 2nd knee point, interfacial fracture toughness, which is not same as strength, might be evaluated from phenomenological viewpoints, because crack generated at the surface of weft fiber bundle propagated throughout the inside of fiber bundle between 1st and 2nd knee point. In this consideration strain energy between 1st and 2nd knee point would be important. As shown in Fig.6 the energy value of 0.01 wt% was the highest. We made the discussion in two different ways as follows.

Assuming that crack propagate along the interface between silane coupling agent and matrix, crack in 0.01 wt% with lower interfacial strength propagates easily, and might show lower energy value. On the other hand, assuming that crack propagate inside of interphase, since cross linking density around glass fiber become higher with increase in silane coupling agent, fracture toughness of interface become lower and crack propagate in brittle manner. This leads lower propagation energy. Thus, the results that the higher energy of 0.01 wt% and lower energy of 1.0wt% convey that crack propagate inside of interphase. From phenomenological viewpoints, the latter discussion explained properly the experimental results, interfacial fracture toughness of 1.0wt% is the lowest.

Conclusion

In this study, in order to investigate the interfacial property, tensile test of 1 ply composite was performed. Glass woven fabric treated with different concentration of acryl silane, were used for reinforcement. Two kinds of knee points were identified on the stress-strain curves by least squares method. Strain energies were calculated from the 1st and 2nd knee point stress and strain. It was confirmed that the 1st knee point shows the interfacial strength, and the energy between the 1st and 2nd knee point indicates the fracture toughness of interface inside of fiber bundle.

References

1. Toshiko Osada, Machiko Mizoguchi, Masaya Kotaki, Asami Nakai, Hiroyuki Hamada, ICCM-13th, ID 1083, (2001)
2. H. Ichihashi, H. Hamada, N.Ikuta, and Z. Maekawa, Transactions of the Society of Fiber Science and Technology, Vol.49, pp.169-175, (1993)

Proceedings of 7th Japan International SAMPE
Symposium & Exhibition, Nov. 13-16, 2001

Experimental Characterization of Off-axis Properties of Woven Fabric Composites

Hiroyuki Hamada#, Asami Nakai# and Shinji Ogihara*

#: Advanced Fibro Science, Kyoto Institute of Technology
*: Department of Mechanical Engineering, Science University of Tokyo, 2641 Yamasaki, Noda, Chiba 278-8510
E-mail: ogihara@rs.noda.sut.ac.jp

Abstract

Nonlinear stress-strain behavior in woven glass fiber reinforced epoxy composites under off-axis tension is investigated experimentally. An orthotropic plasticity model with three parameters is used. Composite systems with and without flexible interphase are studied. Effect of flexible interphase on the nonlinear off-axis behavior is discussed.

Key Words: Flexible Interphase, Glass Plain Woven Fabric Composite, Off-axis Loadng, Nonlinear Stress-Strain Behavior

Introduction

It is known that fiber composites exhibit nonlinear stress-strain response under off-axis loading. To model the nonlinear behavior of composites, many mechanical models have been proposed using two approaches. One is macroscopic and another is microscopic. In the macroscopic approach, composites are treated as a nonlinear elastic or plastic body. In the microscopic approach, attempts are made to describe the effective composite response using the properties of the fiber and matrix.

Hahn and Tsai [1] employed a complementary elastic energy density function which contained a biquadratic term for in-plane shear stress. The nonlinear stress-strain relation of unidirectional laminae under off-axis loading was predicted. Sun and Chen [2] developed the one-parameter plasticity model to describe the nonlinear behavior of unidirectional composites based on a more general approach [3]. The approach is based on a quadratic plastic potential and the assumption that there is no plastic deformation in the fiber direction. Ogi and Takeda [4] proposed a model based on a fourth-order complementary elastic energy function and the one-parameter plastic potential in which an anisotropy parameter changes with plastic deformation.

On the other hand, a method to fabricate woven fabric composites with flexible interphase is developed recently [5]. It is shown that composite strength can be enhanced by introducing flexible interphase.

In the present study, the nonlinear behavior of a woven glass/epoxy composite under off-axis tension is investigated experimentally. Composite systems with and without flexible interphase are used. Tensile tests are performed at off-axis angles, 22.5°, 45° and 67.5° as well as 0° and 90°. It is shown that a plastic potential function with

three parameters can be used for the woven composite. Effect of flexible interphase on the nonlinear stress-strain behavior under off-axis tension loading is discussed.

Experiments

E-glass plain woven fabric (WE18W, Nitto Boseki Co., Ltd) with 0.4wt% epoxy silane treated was used for a reinforcement. Both composite systems with and without flexible interphase are prepared. Epoxy resins were used for matrix and flexible interphase, Epikote 828 and Epikote 871 (both Yuka Shell Epoxy Co., Ltd). Epikote 871 has lower Young's modulus and higher failure strain than Epikote 828. Hardeners were 4,4-diaminodiphenylsulfon (DDS) and 1,2-diaminopropane for Epikote 828 and 871, respectively. Specimens are cut out of the panels in the direction of θ=0°, 22.5°, 45°, 67.5° and 90°. Tensile tests were performed on the specimens. Two strain gages (one is to obtain longitudinal strain and one transverse strain) are put at the center of the specimen. The crosshead speed was 0.5mm/min. The specimens were loaded up to failure.

Analytical Procedure

A yield function that is quadratic in stress is assumed for the general 3-D fiber composite as

$$\begin{aligned} 2f(\sigma_{ij}) = {} & a_{11}\sigma_{11}^2 + a_{22}\sigma_{22}^2 + a_{33}\sigma_{33}^2 \\ & + 2a_{12}\sigma_{11}\sigma_{22} + 2a_{13}\sigma_{11}\sigma_{33} + 2a_{23}\sigma_{22}\sigma_{33} \\ & + 2a_{44}\sigma_{23}^2 + 2a_{55}\sigma_{13}^2 + 2a_{66}\sigma_{12}^2 = k \end{aligned} \tag{1}$$

where k is a state variable and the stresses σ_{ij} refer to the principal material directions. By using the associated flow rule, the yield function is taken as the plastic potential function from which the incremental plastic strain can be derived as

$$d\varepsilon_{ij}^p = \frac{\partial f}{\partial \sigma_{ij}} d\lambda \tag{2}$$

where the superscript p denotes plasticity, and $d\lambda$ is a proportionality factor.

The increment of plastic work per unit volume is given by

$$dW^p = \sigma_{ij} d\varepsilon_{ij}^p = 2f d\lambda \tag{3}$$

Let the effective stress $\bar{\sigma}$ be defined as

$$\bar{\sigma} = \sqrt{3f} \tag{4}$$

The effective plastic strain increment $d\bar{\varepsilon}^p$ can be defined such that

$$dW^p = \sigma_{ij} d\varepsilon_{ij}^p = \bar{\sigma} d\bar{\varepsilon}^p \tag{5}$$

Consider a state of plane stress parallel to the $x_1 - x_2$ plane. The plastic potential function reduces to

$$2f = a_{11}\sigma_{11}^2 + a_{22}\sigma_{22}^2 + 2a_{12}\sigma_{11}\sigma_{22} + 2a_{66}\sigma_{12}^2 \tag{6}$$

The complete orthotropic plastic flow rule is defined if the parameters a_{11}, a_{22}, a_{12}, a_{66} and $d\lambda$ are determined. To determine $d\lambda$, the effective stress-effective plastic strain relation must be established. This can be accomplished from the results of tension tests on off-axis specimens.

Let the x-axis be the uniaxial loading direction which makes an angle θ with the fiber direction x_1-axis. The stresses referring to the material principal axes (x_1 and x_2) are related to the applied uniaxial σ_x as

$$\left.\begin{aligned} \sigma_{11} &= \sigma_x \cos^2\theta \\ \sigma_{22} &= \sigma_x \sin^2\theta \\ \sigma_{12} &= -\sigma_x \sin\theta\cos\theta \end{aligned}\right\} \tag{7}$$

Substitution of (7) into (6) and (4) yields

$$\bar{\sigma} = h(\theta)\sigma_x \tag{8}$$

where

$$h(\theta) = \sqrt{\frac{3}{2}\left\{a_{11}\cos^4\theta + a_{22}\sin^4\theta + 2(a_{12}+a_{66})\sin^2\theta\cos^2\theta\right\}} \tag{9}$$

For monotonic loading, we obtain,

$$\bar{\varepsilon}^p = \frac{\varepsilon_x^p}{h(\theta)} \tag{10}$$

The relation between $\bar{\sigma}$ and $\bar{\varepsilon}^p$ can now be obtained from the experimentally obtained relation between σ_x and ε_x^p.

Since the $\bar{\sigma}-\bar{\varepsilon}^p$ relation should be unique in monotonic loading for the given material, the parameters a_{11}, a_{22}, a_{12} and a_{66} must be chosen so that the resulting $\bar{\sigma}-\bar{\varepsilon}^p$ relations is independent of θ. It can also be shown that the plastic Poisson's ratio can be defined as

$$\nu_\theta^p = -\frac{d\varepsilon_y^p}{d\varepsilon_x^p} = -\frac{(a_{11}+a_{22}-2a_{66})\sin^2\theta\cos^2\theta+a_{12}\left(\sin^4\theta+\cos^4\theta\right)}{a_{11}\cos^4\theta+a_{22}\sin^4\theta+2(a_{12}+a_{66})\sin^2\theta\cos^2\theta} \quad (11)$$

In the discussions above, we can set $a_{11}=1$ without loss of generality.

Results and Discussion

Figure 1 shows the stress-strain curves of the woven composite. We have nonlinear stress-strain relations at all angles. The nonlinear strain becomes higher as the angle becomes larger until 45°. It can be seen that nonlinear strain is larger in composite with flexible interphase at the same loading angle.

To check the validity of the plasticity model and determine the parameters, we made the following procedure. We first assumed that the strains can be divided into two parts as

$$\varepsilon_i = \varepsilon_i^e + \varepsilon_i^p \quad (12)$$

where ε_i^e is the elastic strains and ε_i^p is plastic strains, and that the elastic strains are linear elastic ones and can be determined by

$$\varepsilon_x^e = \frac{\sigma_x}{E_x}, \quad \varepsilon_y^e = -\nu\frac{\sigma_x}{E_x} \quad (13)$$

where E_x is the initial longitudinal Young's modulus, ν is the initial longitudinal Poisson's ratio of the laminate and x and y denote longitudinal (loading) and transverse directions, respectively. We also assumed that the nonlinear part of strain comes from plasticity.

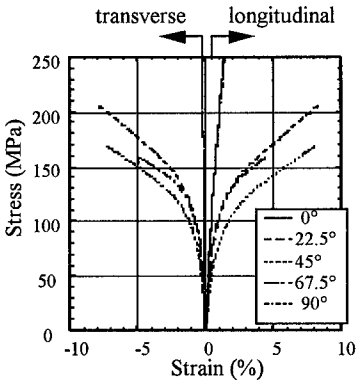

(a) Composite without flexible interphase

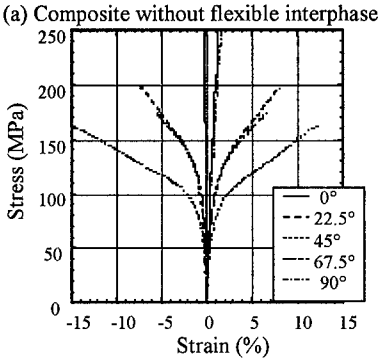

(b) Composite with flexible interphase

Fig.1 Stress-strain curves for woven glass fabric composites.

Our next task is to determine the parameters a_{22}, a_{12} and a_{66} and the effective stress-effective plastic strain curve. If we can obtain parameters which lead to a master effective stress-effective plastic strain curve from the data of all angles, we can confirm the validity of the plasticity model. We note that when θ=0, $h(0)$ is dependent on none of the parameters a_{22}, a_{12} and a_{66}. Thus, the effective stress-effective plastic strain curve for 0° can be used as the master

curve. Considering that $h(90)$ is dependent on only a_{22}, we can determine a_{22} so that the effective stress-effective plastic strain curve for 90° fits that for 0°. By using (9) and the experimental data of other angles, we can determine $a_{12}+a_{66}$. After that, we use (11) to determine a_{12} and a_{66}.

Figure 2 shows the effective stress-effective plastic strain curves from the experimental data of all angles. We can see that the curves gather on two curves. One is from on-axis data and one from off-axis. This implies that the nonlinear behavior of woven fabric composite cannot be described by using a single plastic potential. This may be due to the difference in the cause of nonlinear deformation under on-axis and off-axis loading. Possibly, nonlinear strain in on-axis data comes from damage such as matrix cracks and nonlinear strain in off-axis data from nonlinear shear behavior of matrix resin.

At this stage, we have $a_{22}=0.8$ and 1.5 and $a_{12}+a_{66}=2.5$ and 10 for composites without and with flexible interphase, respectively. The higher value of $a_{12}+a_{66}$ in composite with flexible interphase may be due to high value of a_{12} which indicates the effect of shear stress. Effect of flexible interphase on the nonlinear stress-strain behavior can be evaluated by this plasticity parameter.

Acknowledgment

Mr Nobuyoshi Kajioka and Mr Masahiro Yamanouchi, Kyoto Institute of Technology, are gratefully acknowledged for their help in fabricating specimens.

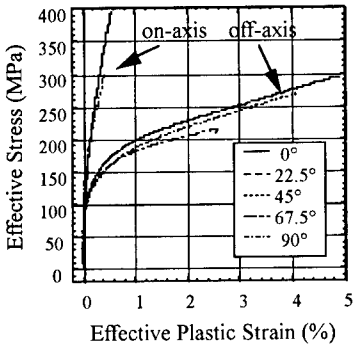

(a) Composites without flexible interphase

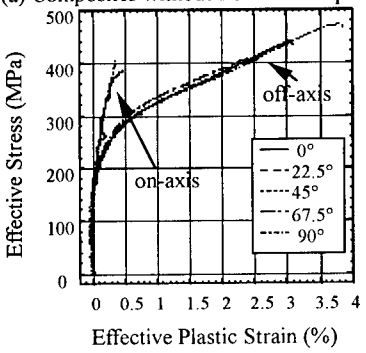

(b) Composites with interphase

Fig.2 Effective stress-effective plastic strain curves.

References

1. H.T.Hahn and S.W.Tsai: Journal of Composite Materials, 7,102-118 (1973)
2. C.T.Sun and J.L.Chen: Journal of Composite Materials, 23, 1009-1020 (1989)
3. D.Kenaga, J.F.Doyle and C.T.Sun: Journal of Composite Materials, 21, 516-531 (1987)
4. K.Ogi and N.Takeda: Journal of Composite Materials, 31, 530-551 (1997)
5. H.Hamada, et. al.: Proc. ICCM-13, ID 1557 (2001).

Proceedings of 7th Japan International SAMPE
Symposium & Exhibition, Nov. 13-16, 2001

Fundamental Study on Flexural Fatigue Properties in Flexible Printed Circuit
Properties of Phenoxy/Epoxy Resin with Mixing Ratio

Hiroyuki KAWADA#, Kuniyasu NAKAYA# and Akira KOBIKI#

#: Department of Mechanical Engineering, Waseda University
3-4-1 Okubo, Shinjuku, Tokyo 169-8555, Japan
E-mail:kawada@mn.waseda.ac.jp

Abstract

In the last decade, flexural fatigue properties of a flexible printed circuit(FPC) in mechanical moving parts of electronic devices have been studied to improve their reliability and flexibility. The phenoxy/ epoxy blend polymer is one of the candidates for the adhesive of the FPC, where a phenoxy resin is designated an epoxy one with a long molecular chain. And, it is important to examine the influence of the mixture ratio on the flexural fatigue properties. It is reported that the phenoxy/epoxy blend polymer showed the phase separation behavior in some cases. First of all, an affect of the mixture ratio on the mechanical and thermal properties of blends changed was investigated. It has been shown that the phase separation behavior appears in a part of the mixture ratio, and a part of the epoxy resin merges with the phenoxy resin. Next, from the result of the peeling test with the phenoxy/epoxy blend as the FPC adhesive, it is clarified that the peel strength in the copper foil and the adhesive interface have the same character at the mixture ratio due to the phase separation behavior.

Keywords : FPC, Phenoxy, phase separation and adhesive

Introduction

The flexible printed circuit (FPC) is used for the wiring technology in most electronic devices with miniaturizing and making of an electronic equipment high density. The FPC is a structure with thin layers, and it is thin enough to flex in smaller radii of curvature so that the FPC is used in mechanical parts of electrical devices. However it is necessary to increase the flexural fatigue life in order to attain high reliability of electronic devices. The FPC is made of a copper foil, an adhesive and an insulating film. It is reported that the number of cycles to failure of the FPC is determined by the fatigue failure of the copper foil [1], however, it also seems to be influenced by bonding properties of the FPC adhesive [2].

Recently, it is suggested that a phenoxy resin designated as an epoxy resin with a long molecular chain is an adhesive with a high bonding property for metallic materials. In general, the epoxy resin is one of the candidates for an adhesive for the FPC, however the phenoxy/epoxy blend is coming out for the next generation of adhesive for the FPC. It is investigated that the phase separation appears at some mixture ratios, and the epoxy resin merges

with the phenoxy resin [3-5]. This paper shows the relation between the mechanical and thermal properties of the phenoxy/ epoxy blend and the mixture ratio, and the mixture ratio dependence of peel strength of the FPC evaluated by a peeling test using the phenoxy/epoxy blend as an adhesive layer. It seems to be possible to increase reliability of the material by studying the dependence of the bonding properties on the mixture ratio.

Materials

The epoxy resin used in this study was AER260(Asahi Chemical Industrial Co., Ltd.) and the phenoxy resin was YP50-S(Touto Chemical Industrial Co., Ltd.). All the blends of the epoxy resin and the phenoxy resin had blend ratios of 100/0, 80/20, 60/40, 40/60, 20/80 for weight. The compounds were cured at 160℃ for 2 hours in a vacuum oven.

Examinations and results

Tensile test

The mechanical properties of the epoxy/ phenoxy blend were investigated by the tensile test measured using the tensile test machine at a room temperature with the dumbbell type test specimens, and at a crosshead speed of 0.5mm/min. Fig.1 shows typical stress-strain curves which were changed with various mixture ratios of the phenoxy resin. The maximum value of the breaking stress and strain was obtained at the phenoxy mixture ratio 20wt%. Fig.2 shows a microphotograph of the specimen surface using the scanning electron microscope (SEM) at the phenoxy mixture ratio 20wt%. At this ratio the phenoxy phase separated from the epoxy phase, and it seems to improve the breaking stress and strain by the phenoxy phase being the source of such as the micro crazes in the epoxy phase.

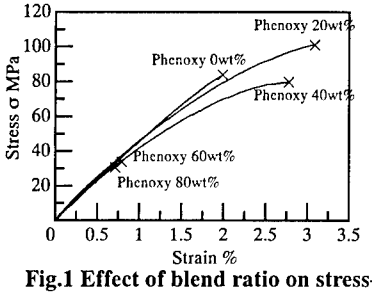

Fig.1 Effect of blend ratio on stress–strain curves

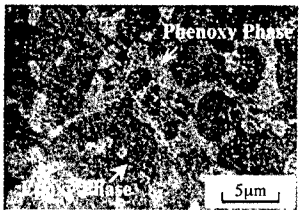

Fig.2 Phase separation of blend (Phenoxy 20wt%)

Thermal properties

The glass transition temperature T_g of the blends were measured by using the differential scanning calorimetry (DSC). The temperature was changed from 40 to 250℃, and the heating rate was 5℃/min. Fig.3 shows the changes of an endothermic amount with the temperature. The result at the phenoxy mixture ratio 0wt% shows the change of an endothermic amount in the temperature from 95 to 125℃, and it seems that this temperature range is the glass transition temperature of the epoxy resin. Next, it seems that the glass transition temperature range of the phenoxy resin is from 75 to 95℃ as the result of the phenoxy mixture ratio 80wt%. At the phenoxy mixture ratio 20 and 40wt%, the changes of an endothermic amount were observed in two temperature ranges. In these mixture ratios, the phenoxy phase

separated from the epoxy phase as shown in Fig.2. Fig.4 shows the changes of an endothermic amount from 75 to 95℃ and from 95 to 125℃. It shows that the change of an endothermic amount in the epoxy glass transition temperature range disappeared at the phenoxy mixture ratio 60wt% or more. The epoxy resin disappeared by merging with the phenoxy resin, and about 2/3 of the epoxy weight for the phenoxy weight merges with the phenoxy resin.

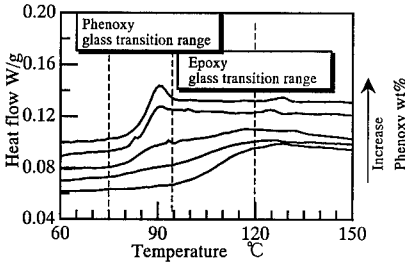

Fig.3 The glass transition behavior of the phenoxy/epoxy blends

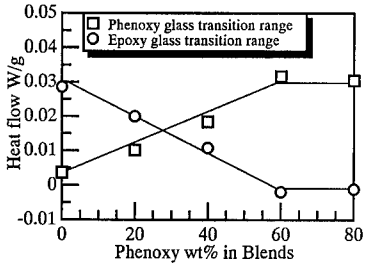

Fig.4 Endothermal amounts at T_g of epoxy and phenoxy range

Dynamic mechanical properties

The temperature dependence of the dynamic mechanical properties with various mixing ratios was investigated using the dynamic mechanical analyzer. The specimen's geometry was a rectangular bar for tensile test. The specimen was clamped securely at both ends and oscillated in tension at a frequency of 15Hz. The temperature dependence of the storage modulus was measured from 60 to 150℃ at a heating rate of 3℃/min. Fig.5 shows the temperature dependence of the storage moduli measured by the dynamic mechanical analyzer. At the mixture ratio 0, 20 and 40wt%, the decrease of the storage modulus was settled over 125℃ in the temperature, at the mixture ratio 60wt% and more, the storage moduli kept decreasing. Fig.5 shows that the epoxy phase was predominant at the mixture ratios 0, 20 and 40wt% because the storage moduli E' behaved as a thermosetting resin and that the phenoxy phase was predominant at the mixture ratio 60wt% or more because the storage moduli E' behaved as a thermoplastic resin.

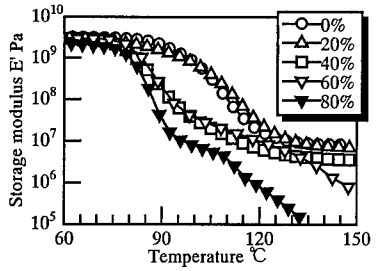

Fig.5 Effect of temperature on storage moduli in the phenoxy/epoxy blends

Peeling test

The peel strength with various mixing ratios was evaluated by the 90deg and 180deg peeling test. The specimen was a structure of three layers to be bonded, a copper foil of 18μm in thickness bonded to a polyimide film of 25μm in thickness with the phenoxy/epoxy blend. Moreover, a polyimide film side of the specimen was bonded to the aluminum backing plate and the copper foil was bent to peel using the tensile test machine at a room temperature

at a crosshead speed of 50mm/min. The fracture mode was not the cohesive failure but the adhesive failure. It was observed that the adhesive failure propagated in a constant load. Fig.6 shows the relation between the phenoxy mixture ratios and the peel strengths. As a result, it was found that the peeling angle was independent of the peel strength. The peel strength has been improved by an increase in the mixture ratio of the phenoxy resin overall. Furthermore, at the mixture ratio 20 and 40wt%, the peel strength did not change relative to the mixture ratio.

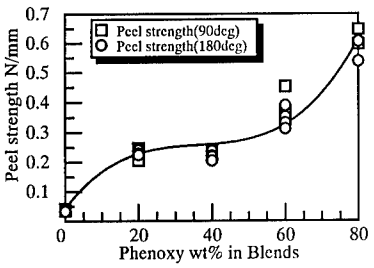

Fig.6 Peel strengths of the Copper foil and adhesive interface

Discussion

The phase separation greatly influences the fact that the peel strengths were constant at the mixture ratio 20 and 40wt%. Here, the wetting theory is introduced which is important to determine the peel strength. According to the wetting theory, the phase with high bonding stress adheres to the solid surface. Because the phenoxy bonding strength to the copper foil is higher than the epoxy one, the phenoxy phase in blend where the phase separated adheres to the solid surface. However, it seems that the composition at the mixture ratio 20wt% corresponds to one at 40wt% because the result of the DSC showed that the phenoxy phase was made from the phenoxy and epoxy resin, and the epoxy resin is merged with the phenoxy phase in a saturated state. In the peeling test, it was observed the peeling propagated in the copper foil/ adhesive interface so that it seems that the peel strength is influenced by interfacial chemical properties, therefore the peel strength at the phenoxy mixture ratio 20wt% corresponds to one at 40wt%. At the mixture ratio 60wt% or more, the composition where only the phenoxy phase exists without the phase separation. The peel strength was improved with an increase in the phenoxy weight in the peeling test, because the phenoxy phase at the mixture ratio 60 and 80wt% contains more phenoxy resin than the composition of the phenoxy phase at the mixture ratio 20 and 40wt%.

Conclusions

The following conclusions can be described on this study.

1. The maximum value of breaking stress and strain was observed at phenoxy mixture ratio 20wt% where phase separation was caused.
2. It seems that 2/3 of the epoxy weight for the phenoxy weight merges in the phenoxy resin.
3. As a result of phase separation, peel strengths were constant at the phenoxy mixture ratio 20wt% and 40wt%.

References

1) Hideto SUZUKI, Trans. JSME, 57 (534), A , 228 (1991)
2) Takeshi OSHIKUBO, et al., Trans. JSME, 65 (629), A, 48(1999)
3) Qipeng Guo, Polymer, 36, 4753(1995)
4)K.C.Teng, F.C.Chang, Polymer, 37, 2385 (1996)
5) H. K. Hseih, et al., Polymer, 39, 2175 (1998)

Proceedings of 7th Japan International SAMPE
Symposium & Exhibition, Nov. 13-16, 2001

Fatigue Properties of Quasi-Isotropic Alumina-Fiber Reinforced Plastic laminates

Hiroyuki KAWADA#, Nobuyuki KOBAYASHI# and Yusuke KOSHIKIYA#

#: Department of Mechanical Engineering, Waseda University
3-4-1 Okubo, Shinjuku, Tokyo 169-8555, JAPAN
E-mail: kawada@mn.waseda.ac.jp

Abstract

This paper presents an experimental investigation of internal damage propagation behaviors in the quasi-isotropic alumina FRP laminates (0/+45/-45/90)s under tension-tension fatigue loading. The onset and growth of the matrix cracks and the delaminations were observed by using an optical microscope during the fatigue tests. The matrix crack density and the normalized length of delamination were measured as a function of the normalized number of cycles. A different damage growth pattern was observed in each layer and the interface under the tension- tension fatigue.

Key Words: Quasi-Isotropic Alumina FRP, Tension-tension fatigue loading, Matrix crack and Delamination.

Introduction

Alumina fiber reinforced plastics (alumina FRP) have been regarded as heat insulating structures of the superconducting coil in the magnetic levitated train because of their superior specific strength and rigidity, and their adiabatic property, etc. On the other hand, it is known that the fiber orientation angle greatly influences the mechanical properties of the FRP, so that in many applications of alumina FRP, they are used in the form of multidirectional laminates. Generally, in the failure process of the alumina FRP laminates, particular internal damages such as matrix cracks and delaminations occur in each layer and between layers because of the discontinuity of the stiffness, etc. The matrix crack is a from of internal damage which occurs at an initial stage of the fatigue. Delamination seems to be the principal cause of the failure of laminates. Therefore, it is important to understand the internal damage propagation behavior from a microscopic viewpoint so as to obtain long term reliability in the quasi-isotropic alumina FRP as a structural material.

Up to now, the various properties of the cross-ply laminates have been investigated under the fatigue loading [1,2]. Some studies focused on the quasi-isotropic GFRP laminates [3] and quasi-isotropic CFRP laminates [4-6] under the fatigue loading. However, few studies on the quasi-isotropic alumina FRP laminates under fatigue loading have been conducted. In this study, the internal damage propagation behavior in the quasi-isotropic alumina FRP laminates (0/+45/-45/90)s under the tension-tension fatigue loading was investigated. In addition, the crack density in the each layer was measured and the relation between the crack density and the fatigue life was evaluated. These detailed results will become determinants of the damage-tolerant design.

Specimens and Test Procedure

The specimen geometry is shown in Fig.1. Quasi-isotropic alumina FRP laminates (0/+45/-45/90)s were adopted for the test specimen of this study. The fiber volume fraction of the laminate was about 60%. In order to avoid the stress concentration at the chacking part, the tabs made of GFRP were introduced at both ends of the laminate. The matrix crack and the delamination were observed directly with an optical microscope from the polished side of the laminates. The mechanical properties of the laminate through quasi-static tension tests are shown in Table1.

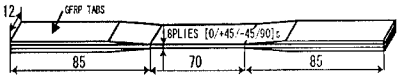

Fig.1 Geometry of specimen

Table1 Mechanical properties for Alumina FRP

Maximum stress σ_b MPa	Young's modulus E GPa	Failure strain ε_f %
352.8	49.4	0.83

Tension-tension fatigue tests were conducted by using a servo-hydraulic fatigue test machine at a room temperature with a sine waveform under the load-control conditions. The test conditions were stress ratio, R=0.1 and frequency, f=1 and 10Hz. The maximum value of the stress amplitude was set as 50-80% of the tensile strength of the quasi-isotropic alumina FRP laminate. In addition, direct observations of the damage were conducted by means of the interruption in the fatigue tests. The laminates were detached from the test machine whenever the number of cycles reached a previously decided value, and the internal damage was observed from the polished edge side with the optical microscope.

Results and Discussion

S-N Diagram

To clarify the fatigue properties, an S-N diagram is shown in Fig.2.

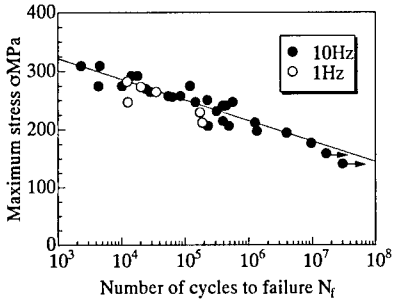

Fig.2 S-N curve

Fig.2 shows the S-N diagram approximated to a straight line, and the fatigue limit did not exist until the number of cycles to failure $N_f=10^7$. There were few differences between the frequency 1Hz and 10Hz, so it turned out that the fatigue life did not depend on the frequency in this study.

Definition of Matrix Crack Density and Normalized Length of Delamination

To evaluate the matrix crack quantitatively, the matrix crack density, D_{MC} mm^{-1} is defined as ;

$$D_{MC}=nl_o/A \quad (1)$$

where n is the number of matrix cracks, l_o is the ply thickness and A is the measured area. The normalized length of the delamination, D_d mm/mm is defined as ;

$$D_d=l_{total}/L \quad (2)$$

where l_{total} is the total length of the delamination and L is the measured length.

Internal Damage Progression Behavior

Fig.3 shows a representative internal damage photograph that was taken from the polished side of the laminates at the normalized

number of cycles, N/N_f=0.4. It can be seen that the delaminations occur at the 90/-45 and -45/+45 interfaces.

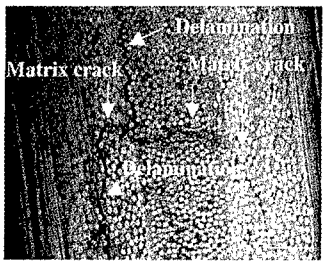

Fig.3 Typical internal damages under Fatigue Loading

The results of the matrix crack density and the normalized length of delamination in the fatigue tests are shown in Fig.4 and Fig.5, respectively. Fig.4 shows that the matrix cracks in the 90deg layer increased rapidly at the first stage of fatigue, and reached saturation at the normalized number of cycles, N/N_f=0.1. The matrix cracks in the -45deg layer occurred after the initiation of the matrix cracks in the 90deg layer increased gradually, and were saturated at N/N_f=0.4. The matrix cracks in the +45deg layer occurred at N/N_f=0.2, and increased rapidly. After that, the matrix cracks in the +45deg layer reached saturation at N/N_f=0.7. Fig.5 shows that both the 90/-45 and -45/+45 delaminations occurred at the first stage of fatigue, and increased gradually. The normalized length of delaminations increased rapidly at N/N_f=0.5, and was saturated at the vicinity of N/N_f=0.7.

The matrix cracks first occurred in the 90deg layer (Fig.6(a)), and the matrix cracks in the -45deg layer and 90/-45 delaminations were occurred from the tips of the matrix crack in the 90deg layer (Fig.6(b)). The -45/+45 delaminations occurred from the tips of the matrix cracks in the -45deg layer (Fig.6(c)), and then, the tips of the delaminations were propagated in the +45deg

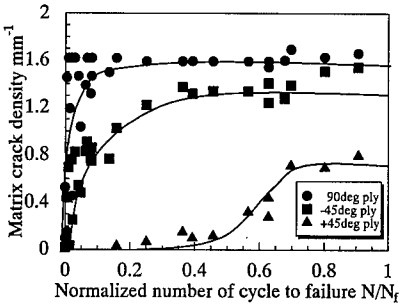

Fig.4 Matrix crack propagation behavior under the fatigue loading

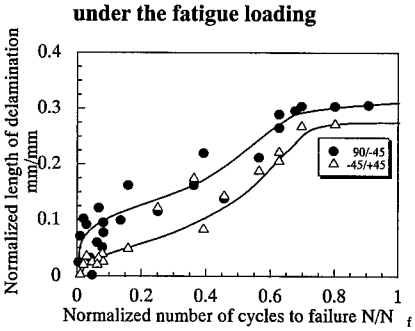

Fig.5 Delamination propagation behavior under the fatigue loading

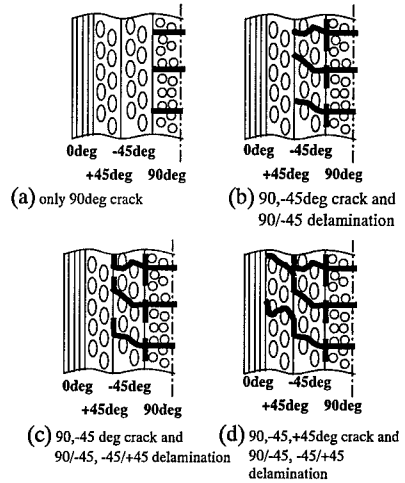

Fig.6 Schematic illustration of internal crack progress

layer and the matrix cracks in the +45deg layer were formed (Fig.6(d)).

Criterion for Damage-Tolerant Design

Internal damages grow as a number of cycles, and remarkably decrease the mechanical properties of the laminate. Therefore, it is thought that the design of a structure which is made of FRP laminates should not be based on the fatigue life but it is necessary to design it based on the damage onset number of cycles.

Next, the quasi-static compression tests were conducted by using the laminates applied by the fatigue loading until the number of cycles necessary to investigate the internal damage onset. Fig.7 shows the compression tests results at each normalized number of cycles. The relation between normalized compressive strength, σ_c/σ_{max} and the normalized number of cycles, N/N_f was investigated to clarify the main cause of the fatal damage to the laminates under fatigue loading. In the figure, the compressive strength is normalized by the virgin one.

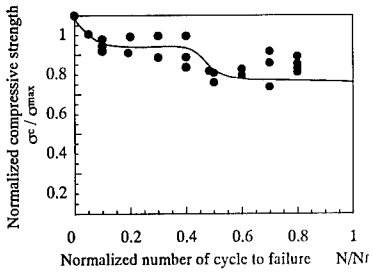

Fig.7 Normalized compressive strength at each normalized number of cycles

As a result, the virgin compressive strength of the laminates, σ_{max}, was 512MPa, and the normalized compressive strengths of the laminates applied by the fatigue loading to N/N_f=0.4 and 0.6, σ_c/σ_{max}, were 0.8 and 0.6 (σ_c=410 and 307MPa), respectively. These results show that the compressive strength declined between N/N_f=0.4 and 0.6 of the normalized number of cycles. On the other hand, Fig.5 shows that the 90/-45 and -45/+45 delaminations increased rapidly between N/N_f=0.4 and 0.6 of the normalized number of cycles. These results show that the internal damages which decreased the compressive strength were the delaminations and the normalized number of cycles at which internal damages occurred was the N/N_f=0.4. Therefore, considering the onset point of the internal damages shown by such a microscopic observation enables the damage-tolerant design of the FRP structures.

Conclusion

The S-N diagram approximated to a straight line and the fatigue limit did not exist until the number of cycles to failure, $N_f=10^7$. The internal damages under the fatigue loading were the matrix cracks in the 90, -45 and +45deg layer and the delaminations at 90/-45 and -45/+45 interface. It was shown that explaining the internal damage propagation behavior by the microscopic observation enabled the damage-tolerant design of the FRP structures.

References

1.Berthelot J-M, Le Corre J-F: Composite Science and Technology, 60, 1055(2000).
2.Nairn J.A.: Journal of Composite Materials, 23, 1106(1989).
3.Tong J., Guild F.J., Ogin S.L. & Smith P.A.: Composites Science and Technology, 57, 1527 (1997).
4.Masters J.E. & Reifsnider K.L.: ASTM STP, 775, 40(1982).
5.O'Brien T.K.: ASTM STP, 775, 140(1982)
6.Ogihara S, Takeda N, Kobayashi S & Kobayashi A: Composites Science and Technology, 59,1387(1999).

Proceedings of 7th Japan International SAMPE
Symposium & Exhibition, Nov. 13-16, 2001

Effect of Interphase on Hydrothermal Aging of Glass Fiber Reinforced Unsaturated Polyester Composite

Tohru Morii[1] and Sho Seino[2]

1. Department of Materials Science & Engineering, Shonan Institute of Technology
1-1-25 Tsujido-Nishikaigan, Fujisawa, Kanagawa 251-8511, JAPAN
E-mail: morii@mate.shonan-it.ac.jp
2. Graduate Student, Shonan Institute of Technology
1-1-25 Tsujido-Nishikaigan, Fujisawa, Kanagawa 251-8511, JAPAN
E-mail: sseino@mate.shonan-it.ac.jp

Abstract

This study dealt with the effect of binder on hydrothermal aging of glass fiber reinforced unsaturated polyester composite. The glass fiber rovings with different types (composition and amount) of binder were used as the reinforcement in order to examine the effect of binder on the interfacial degradation. By using these fiber rovings, unidirectional glass fiber roving reinforced unsaturated polyester composite rods were prepared and they were immersed in distilled water at 95°C. The weight changes due to water immersion were not sensitive to the amount of binder, however, they depended on the composition of binder. In the composite with the binder for chopped strand mat, the water penetrated to the dissolved interface, and as a result, the weight gain showed remarkable increase at longer immersion time. In the composite with the binder for continuous strand mat, the dissolution of the binder occurred at the vicinity of the specimen edges, and such dissolved region did not keep the water inside the material. As a result, the weight gain of this composite was lower than the others.

Key Words: Interphase, Aging, Binder, Weight change

Introduction

Glass fiber reinforced plastics have been widely used as water and corrosion resistant materials. Among them glass fiber mat reinforced thermosetting composites have often used as the structural materials under water environment such as water storage tank, bathtub, etc. When the material is exposed to the water environment for long-term period, however, the degradation of the material occurs due to water absorption. Water absorption often brings the degradation of the interface between fiber and resin, and it leads the reduction in mechanical properties. In glass fiber mat, glass fibers are treated by silane coupling agent and binder. Binder is applied in order to combine a certain number of filaments into fiber roving and to form the sheet from the fiber bundles. However, binder often dissolves by contact to the water, and it brings the significant scale of debonding at the interface region[1-3]. Such debonding led the significant reduction in mechanical properties[4-6]. Therefore water resistant of

binder is very important to establish superior water resistance of the glass fiber mat reinforced composites.

From these backgrounds, this study dealt with the effect of type and amount of the binder on the hydrothermal aging behavior of glass fiber reinforced unsaturated polyester composite. By using different types of fiber rovings, unidirectional glass fiber reinforced unsaturated polyester resin composites were fabricated, and they were immersed into hot water environment. After aging, weight change and change in mechanical properties were evaluated.

Experimental Procedure

Materials and Specimen Preparation

Matrix used was isophthalic based unsaturated polyester resin, and reinforcement was different types of glass fiber rovings. Details of the fiber rovings are summarized in Table 1. The binder applied to type-A and -B rovings was designated commercially for continuous strand mat, and the binder applied to type-C and type-D rovings was designated for chopped strand mat. The amount of binder in type-A roving was a standard for continuous strand mat, and the amount in type-C roving was the same with type-A roving. The amount of binder in type-B and -D rovings were almost half of type-A and -C rovings.

By using these materials, resin impregnated unidirectional glass fiber roving composite specimens were prepared. A certain number of rovings were aligned and combined to one bundle, and resin with hardener (methyl ethyl ketone peroxide) was impregnated under vacuum condition. Resin impregnated fiber bundle was pulled into the PTFE tubular mold and was cured at 80°C for 2 hours. After complete curing, the specimen was demolded. Fiber volume fraction of each composite was about 45%.

Weight Change Measurement

In order to evaluate the effect of binder on the weight change behavior, the specimens were immersed in distilled water at 100°C for fixed periods. Immersion times were 3, 10, 30, 100, 300 and 1000 hours. Before immersion, all the specimens were fully dried at 100°C under vacuum condition, and the initial weight of the specimen (W_o) was measured. After fixed period of immersion, the weight of the wet specimen (W_w) was measured, and then the specimen was re-dried at 100°C under vacuum condition. After reaching the fully dried condition, the weight of the re-dried specimen (W_d) was measured. From these weight measurements, the net weight gain (M_g) and the weight loss (M_l) were evaluated by;

$$M_g = \frac{W_w - W_d}{W_o}, \quad M_l = \frac{W_o - W_d}{W_o} \qquad (1)$$

In order to discuss the degradation of the interphase, cross-section of the specimens after weight measurement were observed by scanning electron microscope.

Experimental Results

Figs.1 and 2 show the changes of net weight gain (M_g) due to hydrothermal aging. In type-A and -B, where the binder for

Table 1 Summary of fiber rovings.

Type	A	B	C	D
Filament diameter	21μm			
Number of filaments	1,200 filaments			
Binder type for	Continuous strand mat		Chopped strand mat	
Weight reduction after burned-out	0.21%	0.11%	0.25%	0.13%

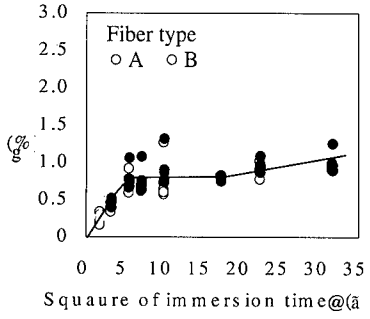

Fig.1 Changes of weight gain (M_g) due to water immersion for type-A and -B.

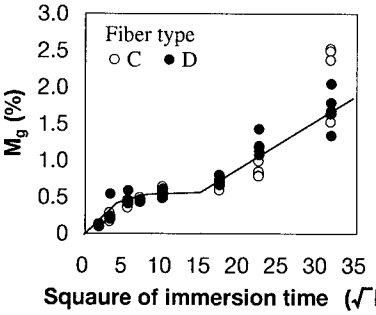

Fig.2 Changes of weight gain (M_g) due to water immersion for type-C and -D.

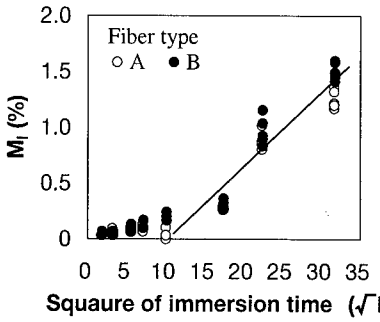

Fig.3 Changes of weight loss (M_l) due to water immersion for type-A and -B.

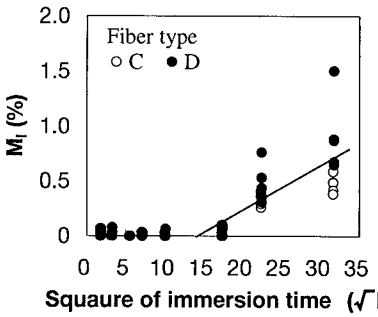

Fig.4 Changes of weight loss (M_l) due to water immersion for type-C and -D.

continuous strand mat were applied, M_g increased almost linearly to 30 hours independent of the amount of the binder, and after that, it reached equilibrium. However, it gradually increased again from 300 hours immersion. In type-C and -D, where the binder for chopped strand mat were applied, M_g increased in the same way with type-A and -B, however, M_g value in equilibrium was lower than type-A and -B. M_g in type-C and -D also began to re-increase linearly against the square root of immersion time at 300 hours immersion, and its gradient was much higher than type-A and -B.

Figs.3 and 4 show the changes of weight loss (M_l) due to hydrothermal aging. In type-A and -B, M_l was almost zero to 100 hours immersion, and after that, it increased linearly against the square root of immersion time independent of the amount of binder. In type-C and -D, the immersion time to begin increasing M_l was delayed to type-A and -B, and it increased linearly against the square root of immersion time from 300 hours immersion. In addition, the increasing rate of M_l was lower than type-A and -B.

The matrix resin and the glass fiber used for all the specimens were the same and the difference in these specimens was the binder only. Therefore it is considered that the difference in the weight change behavior is brought by the influence of binder. The

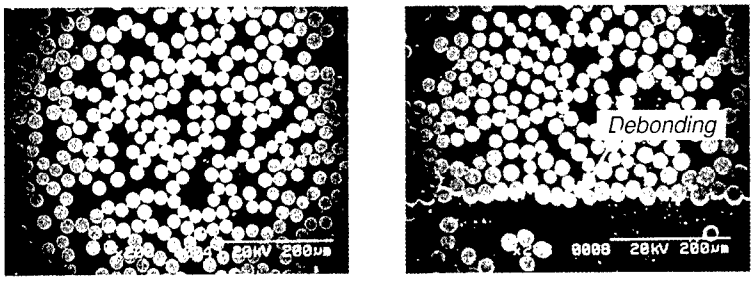

(a) (b)

Fig.5 Scanning electron micrographs of the cross-section for type-C specimens; (a) non-immersed specimen and (b) 1000 hours immersed specimen.

beginning of re-increasing M_g corresponded to the beginning of increasing M_l in all the specimens. This fact suggested that the water penetrated into the debonded interphase region resulted from the dissolution of the binder. As shown in Fig.5, the debonding at interphase region appeared as a result of water immersion, and such debonding increased with increasing the immersion time. However, the amount of M_g in re-increasing stage did not correspond to the amount of M_l. If the debonding occurs deeply inside the material, water can stay there even after taking out the specimen from the water bath. It is considered that such degradation phenomenon occurs in type-C and –D, and therefore they showed remarkable increase in M_g and M_l at longer immersion time. On the other hand, it is considered that the debonding only occurred at the vicinity of the specimen edges in type-A and –B, and therefore the water cannot stay inside the material. As a result, Mg did not increased remarkably at longer immersion time in these specimens.

Conclusions

This study dealt with the effect of binder on hydrothermal aging of glass fiber reinforced unsaturated polyester composite. The glass fiber rovings with different types of binder were used as the reinforcement in order to examine the effect of binder on the interfacial degradation. The weight changes due to water immersion were not sensitive to the amount of binder, however, they depended on the composition of binder. In the composite with the binder for chopped strand mat, the water penetrated to the dissolved interface, and as a result, the weight gain showed remarkable increase at longer immersion time. In the composite with the binder for continuous strand mat, the dissolution of the binder occurred at the vicinity of the specimen edges, and such dissolved region did not keep the water inside the material. As a result, the weight gain of this composite was lower than the others.

References

1. T. Morii, H. Hamada, Z. Maekawa, T. Tanimoto, T. Hirano and K. Kiyosumi: Composites Science & Technology, 49(3), 209(1993).
2. T. Morii, H. Hamada, Z. Maekawa, T. Tanimoto, T. Hirano, K. Kiyosumi and T. Tsujii: Composites Science & Technology, 50(3), 373(1994).
3. T. Morii, H. Hamada, Z. Maekawa, T. Tanimoto, T. Hirano and K. Kiyosumi: Polymer Composites, 15(3), 206(1994).
4. H. Hamada, Z. Maekawa, T. Morii, T. Tanimoto and A. Yokoyama: Composite Materials -Testing and Design-, ASTM STP 1274, 88(1996).

Proceedings of 7th Japan International SAMPE
Symposium & Exhibition, Nov. 13-16, 2001

Interfacial Properties of Braided Composites

Toshiko Osada#, Asami Nakai#, and Hiroyuki Hamada#

#: Kyoto Institute of Technology
Matsugasaki, Sakyo-ku, Kyoto 606-8585, JAPAN
E-mail: b5330033@ipc.kit.ac.jp

Abstract

Purpose of this study was to examine the effectiveness of interfacial property on braided composites from the viewpoint of fabric architecture. Tensile testing of braided composites was performed to determine the effect of binding agent on interfacial properties of braided composites.

In the case that fiber bundle continue, there are no effect of interface, whereas, in the case that fiber bundle does not continue, effect of interface appeared. Braiding angle greatly affected on the effectiveness of interfacial property and in the case of large braiding angle, the effects of interface were remarkable.

Key Words: Braided Composites, Initial Fracture, Interfacial Properties.

Introduction

It has been clarified that knee point on the stress-strain curve can be used for quantitative evaluation of initial fracture[1]. In the case of woven fabric composites, the initial fracture was confirmed to be transverse crack, that is, fracture at the interface inside of fiber bundle. By using these results, knee point on stress-strain curve was also used for quantitative evaluation of interface inside of fiber bundle. Thus, in case that the initial fracture occurs on an interface, the accurate identification of initial fracture can lead to the evaluation of interface property.

For the braided composites, the same approach would be used; we have already examined the stress-strain curve and the micro fracture behavior by in-situ observation. However, there are numerous design parameters for braided fabric, such as weaving structure and braiding angle, and so on. These factors have the effect on micro fracture behaviors, i.e., debonding between fiber and matrix at interface, debonding at fiber crossing part, transverse crack, and filament fracture. The difference in the location at which micro fractures occur is to be a factor for difference in effectiveness of interface property on the mechanical properties of composites.

In this study, the effectiveness of interfacial property on braided composites was investigated from the viewpoint of fabric architecture; continuity of fiber bundle and braiding angle. Tensile testing of braided composites was performed to determine the effect of binding agent on interfacial properties of braided composites. To investigate the effect of fiber continuity, two types of braided composite were used; a normal flat braided composite (Non-cut specimen) and a flat braided whose side edge fiber bundles were cut (Cut specimen). Moreover, two types of braiding angle were prepared in Cut specimen.

Experiment

Materials

Materials used in this study comprised of 2 types of glass fibers with different quantities of binding agent (ER575 CH653 and CH654, 17 μ m, 1000 filaments, Nippon Electrical Glass Co., Ltd.) as reinforcement. These glass fibers were referred to as Low, and High, according to the ratio of binding agent quantity (0.1: 2), whilst the quantity of coupling agent was constant for each fiber. Binding agent reduce the damage by friction of fiber, however, too much binding agent reduces the adhesive effect of the coupling agent [2].

Two types of braiding angle shown in Fig. 1 were prepared. Braiding angle of type A(20°) is smaller than that of type B(33°). In this study, braiding angle was changed only for Cut specimen.

Dimensions of the specimens are shown in Fig. 2. Tensile tests of braided composites were performed in order to consider the effect of binding agent on the mechanical properties with changing the continuity of fiber bundle and the braiding angle.

Micro-fracture behavior

In order to clarify the microscopic fracture process for these braided composites, in-situ observation were performed.

Figure 3 shows an example of fractured filaments observed in the Non-cut specimen obtained by optical microscopy. In Non-cut specimen, only the filament fracture occurred and the number of filament fracture increased with increasing strain.

Figure 4 illustrates the onset of delamination and growth between fiber bundles at the surface edge of Cut specimens obtained by replica observation. In the Cut specimens, initial microscopic damage was delamination of the fiber bundles at the center of the fiber crossing region. The delamination progressed along the fiber crossing part and then around the fiber bundles. As the tensile stress was increased further, the delamination reached the specimen surface and the fiber bundles were eventually pulled out of the matrix.

Effectiveness of interfacial property

Effects of continuity of fiber bundle

Table 1 shows initial fracture stress and strain obtained by knee point on stress-strain curve. Comparing the Low and High specimens, initial fracture stress and strain of High specimen shows higher than those of Low for the Non-cut specimen. On the other hand, in the case of Cut specimen, initial fracture strain of High specimen was smaller than that of Low specimen.

Initial fracture strain of Non-cut specimens agreed with the strain at which filament fracture occurred. For the Cut specimen, Table 2 shows the replica observation results. With excessive binding agent, the adhesion between fiber and matrix became lower so that delamination occurred at a lower strain. Strain at which

Fig. 1 Braiding angle.

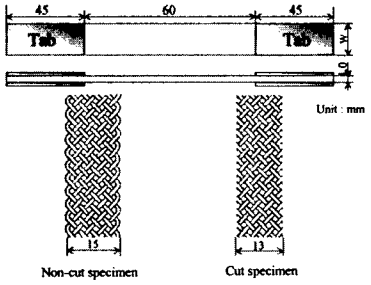

Fig. 2 Specimen geometry

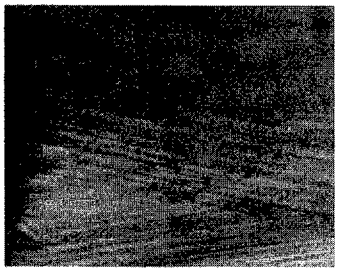

Fig. 3 Filament fractures.

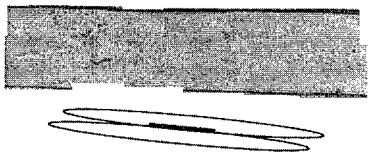

(a) initiation of delamination

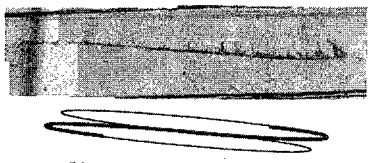

(b) Progress around fiber bundles

Fig. 4 Fracture at Cut specimens.

Table 1 Initial fracture stress and strain.

	Initial fracture stress (MPa)		Initial fracture strain (%)	
	Non-cut	Cut	Non-cut	Cut
Low	278	146	1.37	0.93
High	416	152	1.88	0.76

Table 2 Replica observation results of Cut specimen.

Strain (%)	Low	High
0		
0.5		initiation of delamination
0.6	initiation of delamination	
0.7		Progress between fiber bundles
0.9	Progress between fiber bundles	Progress around fiber bundles
1.1	Progress around fiber bundles	

delamination progressed between fiber bundles were agreed with initial fracture strain. From these results, it was clarified that knee point agreed with the initiation of initial fracture for the braided composites.

Initial fracture stress was increased with increasing binding agent quantity for the Non-cut specimen since filaments do not damage, whereas, initial fracture of Cut specimen was caused by the delamination around a fiber bundle, so that initial fracture stress was decreased with increasing binding agent quantity. Consequently, the effectiveness of binder agent was different depending on the continuity of fiber bundle; it was effective for filament strength on Non-cut specimen and interfacial strength around fiber bundle on Cut specimen.

Effects of braiding angle

Figure 5 shows relationship between initial fracture stress and binding agent quantity of two specimens. Initial fracture stress of type B is lower than that of type A. Decreasing ratio from the Low to High of type B is larger than that of type A. It is supposed that braiding angle greatly affect on the effectiveness of interfacial property, because the shear stress occurred at the interface became larger with increase in braiding angle. In the case of braided composites, the compressive stress and shear stress on the fiber crossing part occurred [3]. It was considered that the fiber crossing part did not fracture by the compressive stress. Therefore, the fracture of fiber crossing part was caused by the shear stress and in the case of large braiding angle the effects of interface property were remarkable.

Conclusion

In this study, the effectiveness of interfacial property on mechanical properties of braided composites was investigated from the viewpoint of fabric architecture. The effects of binder agent depended on the continuity of fiber bundle; it was effective for filament strength on Non-cut specimen and interfacial strength around fiber bundle on Cut specimen. Moreover, Cut specimen with large braiding angle showed lower initial fracture stress, it was cleared that braiding angle affect on the effectiveness of interfacial property.

References

1. Toshiko Osada, Machiko Mizoguchi, Masaya Kotaki, Asami Nakai, Hiroyuki Hamada, ICCM-13th, ID 1083, (2001)
2. A. Nakai, T. Osada, H. Hamada and N. Takeda, Composites part A, 32, pp. 487-498, (2001)
3. Asami Nakai, Akihiro Fujita, Atsushi Yokoyama and Hiroyuki Hamada, Design Methodology for a Braided Cylinder, Composite Structures, 32 (1995), pp. 501-509.

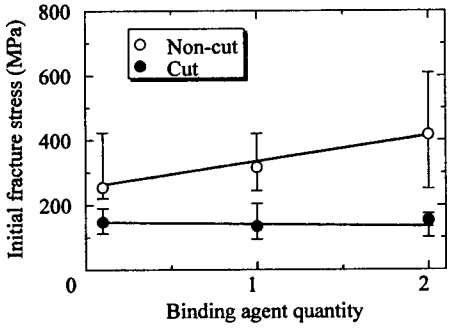

Fig. 5 Relationship between initial fracture stress and binding agent quantity.

Proceedings of 7th Japan International SAMPE
Symposium & Exhibition, Nov. 13-16, 2001

Novel functional polymer/YBCO superconductor ceramic composites for thermistor, electromagnetic shielding effectiveness and electrostatic charge dissipation

Farid El -Tantawy
Department of Physics, Faculty of Science, Suez Canal University, Ismailia, Egypt
E-mail: faridtantawy@yahoo.com

Abstract

The electromagnetic radiation is harmful to a man when its density is more than a certain value. It is very important to develop a new type of conductive polymer composites in order to prevent men from radiation. This paper presents the relationship between conductivity, shielding effectiveness (EMI) and electrostatic charge (ESD) of rubber filled with different contents of YBCO superconductor. The results showed that the good property of material, positive temperature coefficient of resistivity (PTC), temperature sensor and ESD applications. Furthermore, the shielding effect of the novel conductive composite to EMI and microwave radiation is well.

1. Introduction

Polymer composites materials have been studied for many years and really constitute a very active area for researches in material science. The physico-chemical properties of rubber filled with structured filler are influenced by factors such as: type of filler, particle size, volume fraction, surface area of filler, and processing condition [1]. These composites can behave as a very non-positive temperature coefficient (PTC) resistors; a property that has been exploited in a number of smart material applications including self-regulating heating cables, electrostatic charge dissipation (ESD) [1,2], electromagnetic interference (EMI) and others. In recent years, EMI problem or electromagnetic pollution has received wide attention because of the malfunctioning of the electronic equipments from the radiations generated from the source or emerging from other electronic equipments. With this consideration, we study the effect of YBCO on the electrical properties; ESD and EMI of rubber composites, aiming to get complete information, which might help the scientific and technical point of view.

2. Experimental Work

The matrix materials were butyl rubber (IIR), ethelene-propylene-diene rubber (EPDM), and the filler was $Y_1Ba_2Cu_3O_7$ high-T_c superconductor (YBCO). The YBCO system was prepared by solid-state reaction of a stoichiometric proportion of Y_2O_3, $BaCO_3$ and CuO. The reagents were sintered four times at a temperature 980 ^{0}C for 5 hrs. The final compound have zero resistance of about 100 K, surface area was about 16 g/cm^2 and average particle sizes were about 8 μm. Details of the formulation of the mixes are given in the **Table 1.** The rubber composites were prepared by two roll mill of 300 mm length, 170 mm diameter with speed of slow roll 18 rev/min and gear ratio 1.4, by careful control of temperature, time of mixing and nip gap. The vulcanization process was carried out under pressure of 500 KN/m^2 for 5 hours at 165 °C. The surface morphology was measured by a scanning electron microscope (SEM). The circuit used for I-V and dc electrical conductivity (σ) measurements were described elsewhere [1]. The total EMI of rubber films is equal to the sum of the reflection loss (R), absorption loss (A) and a correction factor (B). The correction factor can be neglected for plane waves. The reflection loss and

absorption loss could be expressed as follows [1]

$$R = 168 + 10\log(\sigma / \mu_r f) \quad (1)$$

$$A = 3.34t\sqrt{(\sigma\mu_r f)} \quad (2)$$

where μ_r: is the relative permeability, f: is the frequency, and t: is the sample thickness.

The static charge of the rubber composites was measured using static charge meter (SCM). The static energy is calculated using the relationship:

$$E = 0.5CV^2 \quad (3)$$

The amount of the bound rubber (B_r) was determined by the equation:

$$B_r = \left(1 - \frac{w_0 - w_1}{w_0 - w_f}\right) \quad (4)$$

where w_0, w_1: are the weights of the sample before and after extraction (1 g), respectively, w_f: is the weight of the filler in the sample.

The density of states at the Fermi-level $N(E)$ is given by:

$$D = \left(\frac{9}{8\pi\gamma E_a N(E)}\right)^{\frac{1}{4}} \quad (5)$$

where D: is the hopping distance, γ: is the inverse rate of all of the wave function and is about 18 A^0, and E_a: is the activation energy.

Table 1 Formulation of rubber mixture

Ingredients, phr	F10	F15	F20	F30	F40
IIR	90	90	90	90	90
EPDM	10	10	10	10	10
Pb-Stearate	1	1	1	1	1
YBCO	5	5	5	5	5
KPS	1	1	1	1	1
CN	1	1	1	1	1
Silane-69	1	1	1	1	1

KPS: Potassium peroxodisulfate
CN: Cobalt Naphthenate

3. Results and discussion

3.1 Morphology and electrical studies

The preliminary experiment shows that the microstructure of IIR changes with the insertion of the filler. **Fig. 1** shows the SEM of sample F40. It is seen that good adhesion and connectivity between filler and rubber interface. For more confirmation, B_r as a function of filler contents are 55, 56, 63, 74, and 85 % respectively. This is also an evidence for of the increased rubber to filler interaction.

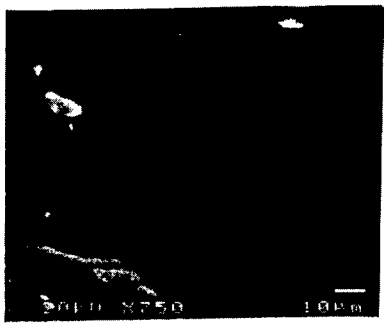

Fig.1: SEM of sample F40

Fig. 2 illustrates the temperature dependence of the electric resistivity $(\rho - T)$ of IIR filled with different content of YBCO. As we expected, the static resistivity at room temperature is markedly decreased with the increase of YBCO content. The decrease of free volume and intermolecular distance among conductive phases are one of the reasons for the increased interface adhesion and conductivity. This is confirmed by estimating the thermal expansion coefficient (α), with YBCO content, which are $8.3x\ 10^{-3}$, $6.3x\ 10^{-3}$, $5.1x\ 10^{-3}$, $4.3x10^{-3}$, and $2.3x\ 10^{-3}\ K^{-1}$ respectively.

In **Fig. 2** it is seen that, at relatively low temperature range, ρ is near slightly dependent on T. This may be attributed to the direct contact and block of conductive phases; which resist the breakage as the rubber is thermally expanded. While at moderate T, the ρ increases with the increased T; this is probably a result of the breakdown of conductive phases structures due to the thermal expansion of the rubber matrix and the increase of the barrier height energy among conductive phases. In other words, the rise of T will cause an appreciable increase in the intermolecular distance among conductive filaments, which leads directly to a drop of the tunneling probability and scattering of charge carriers at

the rubber layers between conductive phases. Finally, this belongs to relatively high T in which the separation distance between conductive phases becomes so large, simultaneously, the intrinsic conduction due to the carriers of the host materials begins to appear (i.e. thermal activation conduction mechanism), and the composite shows (NTCC) effect. The activation energy E_a as a function of YBCO content is calculated by using Arrhenious equation and is about 0.92, 0.81, 0.66, 0.44, and 0.21 eV, respectively. The hopping energy E_h are calculated by using the following equation:

$$\sigma\sqrt{T} = A\exp(E_h / KT) \quad (6)$$

The values of E_h as a function of YBCO content are 1.73, 1.21, 1.01, 0.87, and 0.69 eV respectively. In short the values of E_a and E_h are not close. This indicates that the conduction mechanism of ρ in IIR composites is controlling by tunneling effect [2]. Finally, the value of $N(E)$ as a function of YBCO content is 2.2×10^{20}, 4.3×10^{20}, 5.6×10^{20}, 7.2×10^{20} and 8.7×10^{20} cm^{-3}, respectively. This means that YBCO acts as a charge carrier reservoir into epoxy matrix.

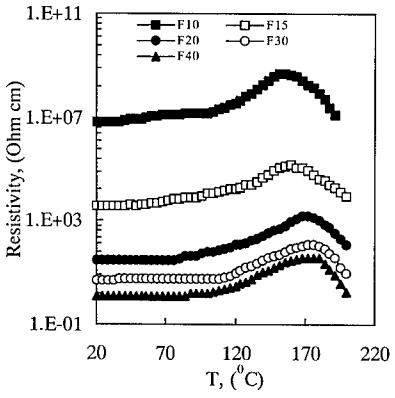

Fig. 2: $\sigma - T$ curves for all samples

3.2 $I - V - T$ studies

In **Fig. 3** the current–voltage $I - V$ characteristic of rubber composites were illustrated. It was observed that at low values of electric potential, the linear behavior is predominant without any remarkable change of the sample temperature. The increases of the electric potential above a certain limit leads to an increase in the Joule heating effect and consequently an increase in the whole sample temperature. As a result, a deviation of I – V characteristic from linear to non-linear at certain voltage, namely switch voltage that depends on filler content is observed. The current decreases beyond this switch potential leading to what is called a negative resistance behavior. It is interesting to mention that, the temperature increase linearly with the increase of the applied potential. This means that this composite can be used as switching effect application. **Fig. 4** shows the applied power density against heating temperature $P - T$ for rubber composites. It is clear that the temperature increase linearly with increasing applied potential. The increase of the temperature level at the same applied power with increasing filler content indicates that the fillers enhancing the stable structure of rubber matrix. The sensitivity of a thermistor is usually characterized by the constant β, which is defined by [2]:

$$\beta = \ln(R_1 / R_2)/(1/T_1 - 1/T_2) \quad (7)$$

The β values of IIR composites with different content of YBCO are 1450, 1766, 1900, 3015, and 4569 K respectively, which makes it possible to provide an effective heat generation with reasonable sensitivity for temperature sensor.

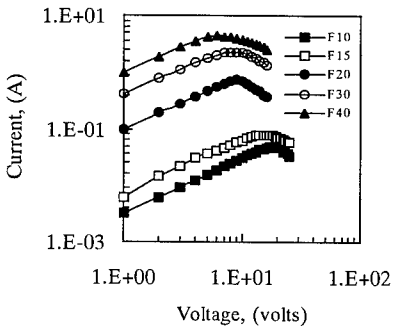

Fig. 3: $I - V$ curves for all samples

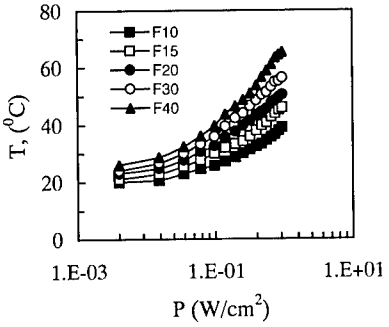

Fig. 4: $P-T$ **curves for all samples**

3.3 ESD and EMI studies

Static energy value as a function of YBCO content are 16×10^{-5}, $34\times10^{-6}, 11\times10^{-7}, 28\times10^{-8}$ and $61\times^{-9}$ J respectively. This means that there is a complete dissipation of ESD with decreasing conductive filler content. In more confirmation, the half-life time of leakage of electrostatic charge $(\tau_{1/2})$ was measured by corona discharge technique under applied voltage (V) about 15 KV, for t=20 s, and can be described by the following empirical formula and it was calculated at $t=\tau_{1/2}$ [1,2].

$$(V-V_0)=(V_m-V_0)\left(1-\exp\left(-\frac{t}{\tau_{1/2}}\right)\right) \quad (8)$$

The calculated values of $\tau_{1/2}$ versus YBCO content are 10, 21, 29, 42, and 63 s. it is seen that the discharge time $\tau_{1/2}$ increase with increasing YBCO content and more than 10 s, excepted sample F10, thus there is time dependence on surface potential could be registered. This indicates that the IIR composites with high YBCO content is not sufficient to remove any charge from the sample immediately and are considered as composites with good antistatic properties at low filler content but useful for EMI applications at high filler content. Fig. (5) shows the effect of YBCO content on EMI. It should be interesting to mention that the EMI increased with increasing filler contents. This ascribed to with increasing filler content the gaps between conductive phases becomes minimum and conductive phases becomes tighter and/or contacts enough. So the mobility carriers are easier to hop and/or transfer across gaps into epoxy matrix. This refers that at low loading level the composites cannot be effectively used for shielding effectiveness. While the higher loading levels of YBCO in the elastomer matrix give a higher shielding effectiveness of the order of 46 dB.

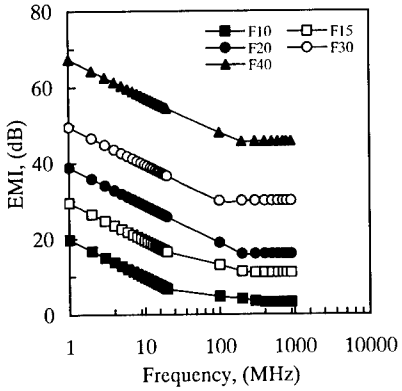

Fig. 5: EMI vs. IIR/YBCO composites.

Conclusions

1. The presence of YBCO modifies extensively the microstructure and cross linking density of rubber matrix.
2. Electrical conductivity is strongly affected by the YBCO content and the conduction mechanism governed by tunneling process.
3. IIR-YBCO composites are useful for temperature sensor and current limiter.
4. Low loading levels of YBCO in the composite can be used for the dissipation of electrostatic charge whereas high loading levels can be used for the EMI application.

References

1. F. El-Tantawy, and A. El-Gohary, Polymer International, 49(12), 6, (2000).
2. S. Koul and S. K. Dhawan, Polymer, 41, 9305, (2000).

Proceedings of 7th Japan International SAMPE
Symposium & Exhibition, Nov. 13-16, 2001

Excimer laser irradiation onto PET materials

K. Mizoguchi[1], A. Yamamoto[1], M. Ishikawa[1], A. Ohuchi[2], T. Ohie[3]

1) Shizuoka Univ. 2) NIMC. 3) Hamamatsu Photonics
1) 3-5-1 Johoku, Hamamatsu 431-8561

TEL&FAX +81(53)478−1192

E-mail : tckmizo@ ipc.shizuoka.ac.jp

Abstract

When excimer laser is irradiated on poly (ethylene terephthalate) (PET) fibers or films, fine roll-like structures appear on the surface. This phenomenon has a possibility to change the surface functionality, e.g. adhesion or wetting properties. Laser treatment reduces environmental pollution because it does not involve any solvent in contrast to conventional chemical processes.

The modified surface morphology was studied by using SEM and AFM. The roll-like structures on the surface were analyzed as functions of stretched degree, laser fluence and number of laser pulses.

In order to control the roll-like structures, we mainly concentrated on the mechanism of the structure formation. To clarify the structure formation mechanism, a simple model was proposed and computer calculation was attempted.

Key words

Excimer laser, Poly (ethylene terephthalate), Surface treatment, Roll-like structures

1. Introduction

Since excimer laser treatment onto polymeric materials was investigated in 1982 [1], this method has been used in various studies as a new, dry and uncontact surface treatment of polymeric materials. When excimer laser was irradiated onto PET materials, fine roll-like structure appears on the surface.

This phenomenon has a possibility to enhance surface functionality, for instance, adhesion, wettability and adsorption. In the case of fiber, the possibility as a tire code was studied [2]. If the adhesion between rubber and fiber become much stronger, we could expect to obtain a tire with higher performance.

We think that controlling of surface morphology is necessary to prepare new composite materials. In this study, we tried various experiments to clarify the mechanism of structure formation. On the basis of experimental results, a simple model for structure formation was proposed. And the computer calculation was attempted.

2. Experimental

2.1 Sample

PET fibers and stretched films were used as samples. The PET fiber (Teijin, T-03350) used in this experiment was a kind of plain woven fabric. The width of filament was around 20 μm. The PET films used are unstretched, uniaxialy stretched (x 2 or x 3), and biaxially stretched (3 x 3).

2.2 Excimer laser irradiation

Irradiation was conducted in air with KrF excimer laser (Lambda - Physik Model LPX-2000; wavelength = 248 nm). Fluence and the number of pulses were varied at each irradiation. Irradiation frequency was fixed at 1Hz to minimize thermal damage of the material.

2.3 Observation of surface morphology

The surface structure of the sample after laser irradiation was observed using the scanning electron microscopy (SEM; JEOL, JSM-5600). Roll width, distance and height were measured by the atomic force microscopy (AFM; Seiko Instruments Inc, SPA300).

3. Results and discussion

3.1 Effect of stretching

Fig.1 shows the SEM photographs of different stretched PET film surfaces after laser irradiation. The arrows on indicate the stretching directions. Though the roll-like structure was not observed, innumerable upheaves appeared on the surface of unstretched PET films (a). Fine roll-like structures were formed on the uniaxially stretched films (b). The rolls seemed to be perpendicular to the stretching direction. In the case of biaxial stretched films, bossy structures appeared (c).

These results indicate that the roll-like structure can be formed only after stretching and that the internal stress fields which is released by the excimer laser irradiation changes the surface morphology.

3.2 Effect of the number of pulses

3.2.1 Irradiation onto PET fiber

Fig.2 shows the surface morphology change of PET fiber with the number of laser pulses at fluence of 100mJ/cm^2. After 5 pulses, innumerable fine roll-like structures appeared on the surface (b). In the case of 1 pulse, it showed the even surface (a). At the fewer laser pulses than 20, the pattern of roll-like structures was complicated. With further increases in the laser pulses, however, the branches of roll-like structures disappeared gradually. These patterns of the rolls become perpendicular more clearly to the fiber axis. After 100 pulses, the surface showed the regular pattern. The cross section of rolls shows triangle waves.

At the moment of laser irradiation, we could see white smoke. Some gases or fragments may be generated from the surface.

3.2.2 Irradiation to PET film

Fig.3 shows the average roll size of stretched PET films (x 2) as a function of the number of laser pulse. As the number of laser pulse increased, the roll width and the roll distance were continuously developed although the roll height quickly reached an asymptotic value. The limited growth of the height may depend on the depth of the laser penetration. The size of the roll width was around 1~3 μm.

The surface morphology of the samples with different pulses was imaged by AFM (Fig.4). The left side of AFM image shows a bird's-eye view and the right one shows the cross section of the roll-like structure. Though various roll sizes of upheaves formed at 1 pulse, no roll-like structure was observed from a bird's-eye view. The small upheaves at 1 pulse were absorbed into the large rolls at 20 pulses. Clear roll-like structures appeared on the surface at 20 pulses. The increase in the roll size might be due to mergence of small rolls.

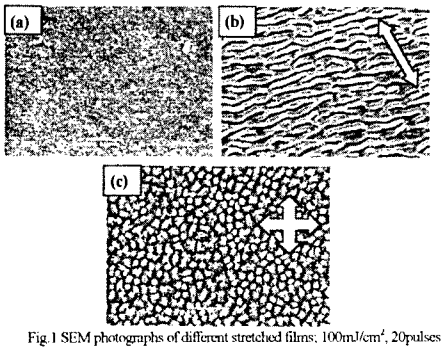

Fig.1 SEM photographs of different stretched films; 100mJ/cm^2, 20pulses
(a) unstretched (b) uniaxially stretched (×3) (c) biaxially stretched (3×3)

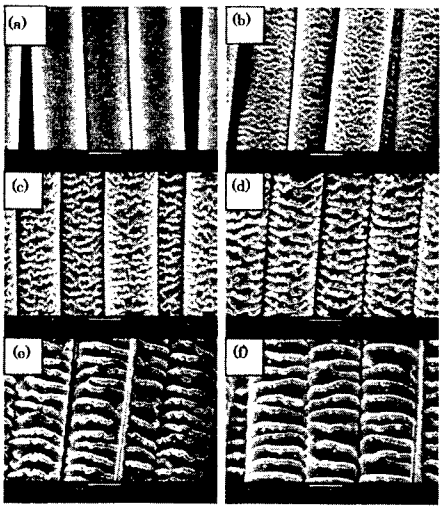

Fig.2 SEM photographs of PET fiber after different laser pulses (100mJ/cm^2)
a) 1 pulse b) 5 pulses c) 10 pulses d) 20 pulses e)50 pulses f)100pelses.

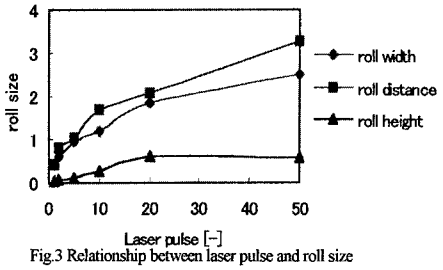

Fig.3 Relationship between laser pulse and roll size

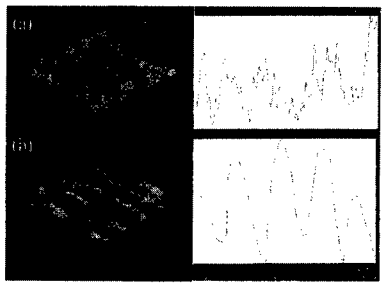
Fig.4 AFM view of PET film (2 fold stretching)
(a) 1pulse (b) 20 pulses

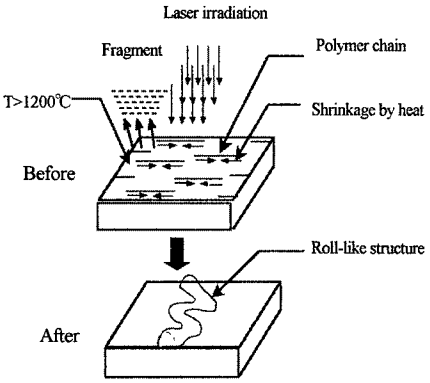

Fig.5 (a). Schematics of structure formation model

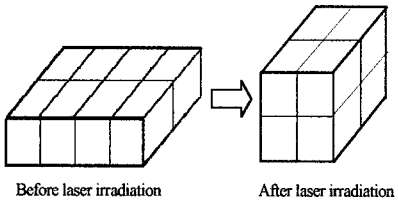

Fig.5 (b). Schematics of shrinkage of polymer chain

3.3 Model construction

3.3.1 Schematics of structure formation model

Considering the experimental results mentioned above, a very simple model for the structure formation was constructed. Fig.5(a) is an schematic representation of the structure formation. There are numerable stretched polymer chains on the PET surface. It was reported that the temperature on the laser-irradiated polymer surface exceeded 1200℃ [3]. Even though the temperature induced was much higher than the melting point of PET, 250℃, the change in surface morphology takes place within very thin surface layer around 1μm and a very strong temperature gradient should exist on the surface because of very short irradiation time, 20ns. Taking all results into consideration, the stretched polymer chains might shrink quickly to form the roll-like structure.

3.3.2 Computer calculation

3.3.2.1 Simple model for computer calculation

A very simple model using blocks was proposed for computer calculation as seen in Fig.5(a). As shown in Fig.5(b), the stretched orientation field melts as a result of laser irradiation, and then shrinks, resulting in the accumulation of the brocks in the central region. The computer calculation was performed with Mathematica™ based on the following assumptions.

- Polymer chains are expressed as several brocks of stretched orientation fields.
- Laser beam is irradiated at random on the surface.

3.3.2.2 Result of computer calculation

Fig.6 shows an example of the result of the computer calculation. At the high numbers of the shrinkage, the generated surface structure is in good agreement with the experimental results. Even though the computer calculation proposed here is very simple, the result seems to reasonably express structure change. The results suggest that the shrinkage of polymer chain play an important role for the generation of roll-like structures.

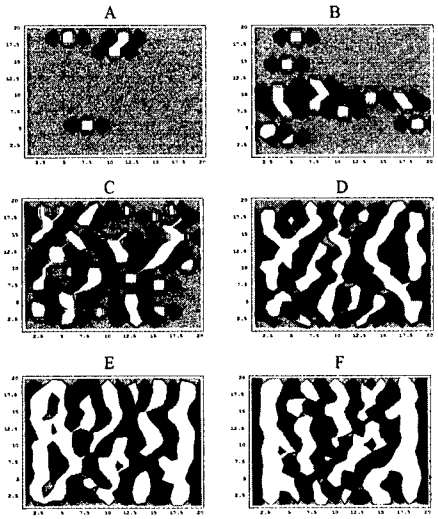

Fig.6 Various stages in the development of roll like structure

Number of shrinkage

A : 4 B : 16 C : 64 D : 256 E : 1024 F : 4096

4. Conclusions

After excimer laser irradiation to PET materials, clear roll-like structures appeared on the surface. In this study, various experiments were conducted to clarify the mechanism of structure formation. A simple model for the formation of the roll-like structure was proposed to perform computer calculation. The result of computer calculation reasonably expressed the formation of the roll-like structure.

4. Acknowledgement

The authors are grateful to Dr. T. Yamanaka of NIMC (Tsukuba) for his valuable suggestions on the model construction.

5. References

1. R. Srinivasan and W. Mayne-Banon, Appl. Phys.,Lett., 41, 576 (1982).
2. H. Watanabe and T. Tanaka, Settyakugakkaisi., 29, 12 (1993).
3. T. Bahners, W. Kesting, and E. Schollmeyer, Appl. Surf. Sci., 69, 12 (1993).

Proceedings of 7th Japan International SAMPE
Symposium & Exhibition, Nov. 13-16, 2001

Effect of fiber sizing treatment on mechanical properties of PE / Epoxy

Yuji Higuchi[1], Tadayoshi Shimizu[2], Machiko Mizoguchi[2] and Hiroyuki Hamada[2]

1: Osaka Gas Co., Ltd.
5-11-61 Torishima, Konohana-ku, Osaka 554-0051, JAPAN
E-mail: higuchi@osakagas.co.jp

2: Graduate School, Kyoto Institute of Technology
matsugasaki, Sakyo-ku, Kyoto 606-8585, JAPAN

Abstract

Tensile tests and pipe performance tests were carried out on PE/Epoxy in which the polyethylene fibers were treated with pre-treatment and/or sizing treatment. Tensile modulus of pre-treatment composites was higher than those of composites without pre-treatment even though tensile strength of both composites was almost the same. Knee point stress of the composites without pre-treatment decreased with sizing treatment. Pipe shape retention strength of pre-treatment composites was large compared to those of composites without pre-treatment and with sizing treatment. This difference in pipe performance was caused by the different interphase made from pre-treatment and/or sizing treatment, resulting in the different tensile performance.

Key Words: PE/Epoxy; sizing treatment; tensile properties; pipe performance

Introduction

Pipeline automatic lining system by inversing the hose is one of the rehabilitation methods for steel and cast-iron piping[1]. The performance of the rehabilitated pipe is closely related to the hose structure, selection of matrices as adhesive between pipe and hose, etc. Many researchers have studied the relation between these variables and the mechanical properties of pipe[2-4].

However, the effects of surface treatments to the fabric on performance of structural composites have not been investigated, in spite of the importance of interfacial properties in composite materials. One of the factors that determines the rehabilitated pipe performance is the permeability of the matrix to the fiber bundles. This paper describes an evaluation of the effect of pre-treatment and/or sizing treatment on the

tensile property and on pipe performance of PE/Epoxy composites. The materials adopted were polyethylene fabric/epoxy resin composites with pre-treatment and/or sizing treatment.

Experimental

Materials and preparation of the specimen

The polyethylene yarns (Dyneema SK60, 2400d, Toyobo Co., Ltd.) were knitted on a shuttle-knitting machine to produce plain fabric. Usually, as received fibers from the fiber manufacturing company are treated with binders such as oils and surfactants to protect the fiber surface and to improve handlability. In order to remove the binder, pre-treatment was performed. The plain fabric was immersed in cyclohexane under ultrasonic waves. This fabric was called 'refined' fabric. Sizing treatment was performed on the refined fabric. An epoxy dispersion-based sizing agent (EA-7) supplied by Nippon NSC Ltd was used. The concentrations of sizing agent were 5, 10 and 20 wt% in water. The refined fabric was immersed in the sizing solution and was dried at 110℃ for 45 min. The matrix used was a bisphenol-A type epoxy resin (SA-6382-2, Sanyu Rec Co., Ltd.). 8 types of specimen with the combination of 4 concentrations of sizing treatment and pre-treatment were prepared.

A flat plate with one ply of plain fabric was fabricated by a hand lay-up method. The fabric was dipped with a mixture of epoxy resin and hardener and dried under vacuum at 50℃ for 10 min. The composite was subjected to curing at 50℃ for 80 min. and post curing at 100℃ for 2h. The thickness of the flat plate was 1 mm in order to observe the fracture process under tensile load clearly. Tensile specimens were cut out in course and wale direction and had dimensions of 30 mm wide and 150 mm long, with 25 mm end aluminium tabs.

Measurements

The surfaces of polyethylene plane fabrics after sizing treatment were observed by scanning electron microscopy (SEM).

Tensile tests were conducted by an Instron universal testing machine (Type 4206) at room temperature. The test condition was 1 mm/min. crosshead speed. To observe the fracture process during tensile loading, the specimen was illuminated with high intensity light. Since the epoxy resin used was transparent, it was possible to see the fibre bundles in the composite.

Pipe shape retention tests were conducted in accordance with the manual published by Japan Gas Association. The rehabilitates pipes, which has a branch at the center of the pipe was made. Water pressure has conducted form the open end of the branch onto the pipe. The rehabilitation hose receives the pressure directly. The retention strength was determined by the time that the hose blockade with crush.

Results and Discussion

Figure 1 shows the specimen before tensile test. It seemed that transparency was low and the matrix did not permeated into the fiber bundles without pre-treatment. For the fiber with pre-treatment, the matrix permeated quickly in the fiber bundles, and transparency was high.

In the load–displacement curve, load increased, inclination fell at 0.3% strain,

inclination became large again from around 3.5% strain gradually, load reached maximum and the specimen broke. All specimens show the same tendency. The matrix crack had occurred innumerably. Many pieces of the matrix had come off and fallen along with the crack in the specimen without pre-treatment. However, the fallen pieces were not observed in the specimen with pre-treatment.

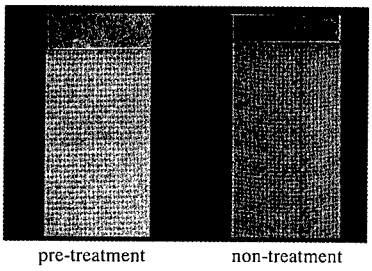

Fig.1 Specimen Observation

Figure 2 shows the relation between the tensile modulus and sizing treatment concentration in both pre-treatment and non-treatment specimen. Tensile modulus of pre-treatment composites is higher than those of non pre-treatment composites. Figure 3 shows the tensile strength. Pre-treatment and sizing treatment did not affect the tensile strength. It seems that the tensile strength in this case was dominated by the fiber strength. Figure 4 shows the knee point stress. Knee point stress decreases with an increase in the sizing treatment concentration. The binders and the sizing treatment agent, which coat the fiber, disturb the matrix to permeate into the fiber. On the other hand the matrix permeates easily into the fiber with pre-treatment and without sizing treatment.

Figure 5 shows the SEM photograph of specimen after tensile test. In the specimen

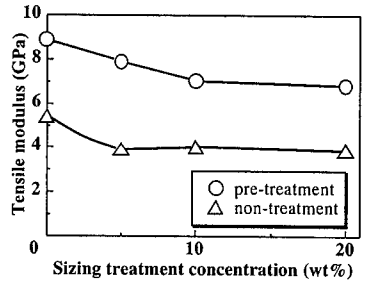

Fig.2 Tensile modulus of PE/Epoxy

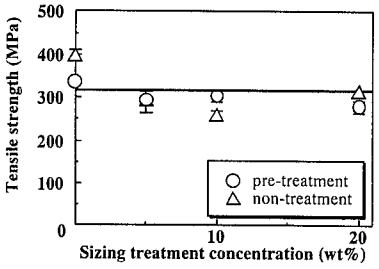

Fig.3 Tensile strength of PE/Epoxy

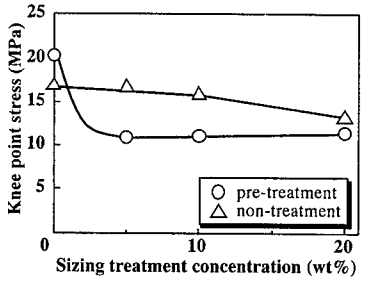

Fig.4 Knee point stress of PE/Epoxy

without pre-treatment (a), the matrix does not exist inside fiber bundle. However in the specimen with pre-treatment (b) and/or sizing treatment (c), the matrix existed inside fiber bundle. Hence the difference of permeability among these specimens became clear. In the specimen with pre-treatment and with sizing

treatment, a fiber is coated with the sizing treatment. The matrix cannot permeate into the fiber bundles.

Figure 6 shows the pipe shape retention tests. The specimen with pre-treatment has good shape retention strength compared to both the specimen without pre-treatment and the specimen with sizing treatment. The specimen with pre-treatment has large modulus and high permeability of the matrix into the fiber bundles. These tensile performances make the shape retention strength of the rehabilitation pipe high.

(a) Non-treatment

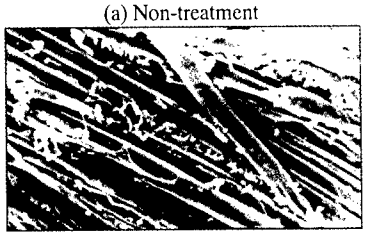

(b) Pre-treatment

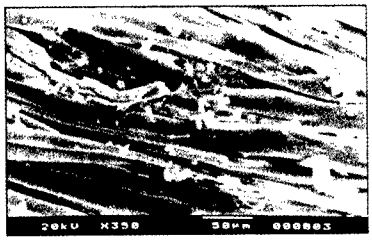

(c) Pre-treatment and sizing treatment

Fig.5 SEM observation after tensile

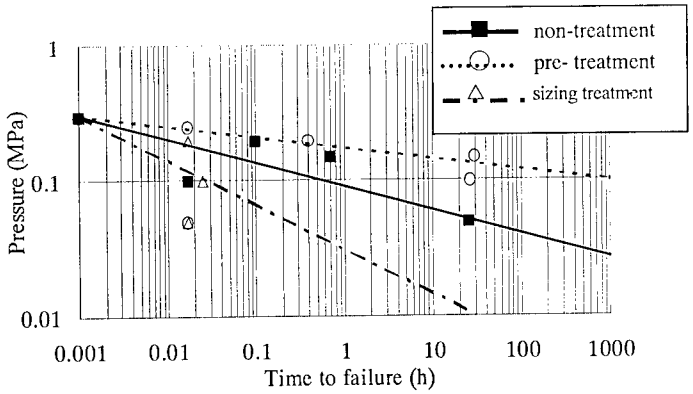

Fig.6 Pipe shape retention test

References

1. G. Brawley, et. al.: Proc. of 14th International Plastic Fuel Gas Pipe Symp., 75 (1995).
2. M.Mamoun,et.al.: Proc. of 14th International Plastic Fuel Gas Pipe Symp., 56 (1995).
3. K .Gunther.: Proc. of 14th International Plastic Fuel Gas Pipe Symp., 68 (1995).
4. Andraka.T.M."Cured-In-Place Lining Renews Gas Mains" Pipeline and Gas Journal,June1995,pp26-29

Proceedings of 7th Japan International SAMPE
Symposium & Exhibition, Nov. 13-16, 2001

Influence of Element Size on Damage Growth Simulation Based on FEM

Yoshinobu Shimamura[1], Yosuke Yamamura[1], Akira Todoroki[1] and Hideo Kobayashi[1]

1: Department of Mechanical Sciences and Engineering, Tokyo Institute of Technology
2-12-1 O-okayama, Meguro, Tokyo 152-8552, JAPAN
E-mail: yshimamu@ginza.mes.titech.ac.jp

Abstract

In damage growth simulation methods for composite laminates based on FEM, damage due to matrix cracking and fiber breaking is generally replaced into stiffness degradation of the elements. It is known that the element size affects the damage growth and load-displacement relationship. The decision of proper element size is, however, difficult because it depends on the modeling of the fracture modes sentenced above. In this study, damage growths of various element sizes are simulated, and damage growth and load-displacement relationship are compared to experimental results. As a result, a guideline to improve results is obtained.

Key Words: Damage Growth Simulation, Element size, FEM

Introduction

In damage growth simulation methods for composite laminates based on FEM, damage due to matrix cracking and fiber breaking is generally replaced into stiffness degradation of the elements. It is known that the element size affects the damage growth and load-displacement relationship [1,2]. The decision of proper element size is, however, difficult because it depends on the modeling of the fracture modes sentenced above. In this study, damage growths of various element sizes are simulated, and damage growth and load-displacement relationship are compared to experimental results. As a result, a guideline to improve results is obtained.

Simulation Procedure

The simulation procedure is described as follows [1,3].

(1) The D matrix is calculated based on the classical lamination theory.
(2) Strain components of each element are determined by FEM analysis with 2-dimensional plane stress elements
(3) Stress components of each lamina are calculated by using the classical lamination theory.
(4) A fractured lamina is estimated one by one according to Yamada's method [4].
(5) Reduction of moduli is applied to the fractured lamina.
(6) The above process is repeated until a given displacement is achieved.

In the simulation, triangle plane stress elements are adopted. Maximum stress criterion was used as the fracture criterion. Reduction of moduli of the lamina is as follows.

$$\text{Matrix cracking}: E_T^* = \frac{1}{100}E_T, G_{LT}^* = \frac{1}{n}G_{LT}$$
$$\text{Fiber breaking}: E_L^* = \frac{1}{100}E_L, E_T^* = \frac{1}{100}E_T, \quad (1)$$
$$G_{LT}^* = \frac{1}{100}G_{LT}, \nu_{LT}^* = \frac{1}{100}\nu_{LT},$$

where E_L, E_T, G_{LT}, ν_{LT} are longitudinal modulus, transverse modulus, shear modulus and major Poisson's ratio, respectively, and superscript * means degraded modulus. n depends on whether unidirectional or not, and is set to 1/2, 1/10 and 1/100.

Specimen and Analytical Model

Using GFRP laminates of stacking sequence $[90_8]_T$, $[0_8]_T$, $[0_2/90_2]_S$, $[0_2/45_2/90_2/-45_2]_S$ with an open hole, static tension tests were conducted under a displacement control. Specimen configuration is shown in Fig.1. An extensiometer was mounted on the specimens to measure a displacement over 50mm-gauge length. Damage propagation process is monitored by VTR because specimens are semitransparent.

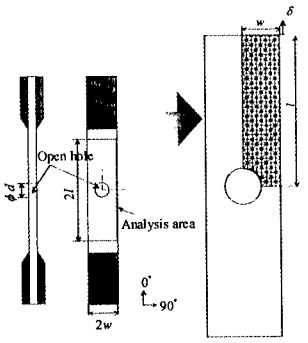

Fig.1 Specimen Configuration and Analytical Area

Damage growth of the laminates with an open hole was simulated by using the proposed method. In the analyses, a displacement was given at the upper edge of the mesh division. Material properties used in the analyses are listed in Table1. In Table1, subscripts L and T denote longitudinal and transverse, respectively.

Table 1 Material Properties

Longitudinal modulus, E_L	38.6 GPa
Transverse modulus, E_T	8.27 GPa
Shear modulus, G_{LT}	4.14 GPa
Major Poisson's ratio, ν_{LT}	0.26
Longitudinal tensile strength, F_{Lt}	1062 MPa
Transverse tensile strength, F_{Tt}	31 MPa
Shear strength, F_{LT}	72 MPa
Longitudinal compressive strength, F_{Lc}	610 MPa
Transverse compressive strength, F_{Tc}	118 MPa

Analytical Results

Unidirectional Laminates

In order to discuss the influence of element size for simple cases, damage growth of unidirectional laminates are simulated and compared to experimental results. For unidirectional laminates, reduction of shear stiffness due to matrix cracking is set to 1/100 because the element with matrix cracking cannot bear any shear force.

Fracture of $[90_8]_T$ laminates with an open hole is dominated by transverse stress at ligaments. This implies that accuracy of stress analysis affects predicted strength of laminates. Fig.2 shows the stress concentration factor of $[90_8]_T$ laminates with an open hole. As you know, sufficient fine mesh division is required to calculate the accurate stress concentrate factor.

For $[0_8]_T$ laminates with an open hole, splitting initiated from the shear stress concentrated points [5]. Excessive propagation of splitting is dominated by the stress intensity factor. This implies that finer mesh division might give rise to excessive crack propagation because the maximum stress criterion is used in this simulation.

Fig.3 shows the least square error of load-displacement relationship. Fig.3 shows that there is an optimum mesh size for splitting propagation simulation.

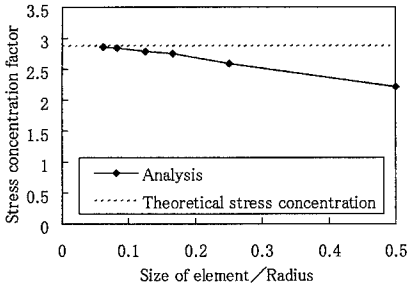

Fig.2 Stress Concentration Factor of $[90_8]_T$ Laminate

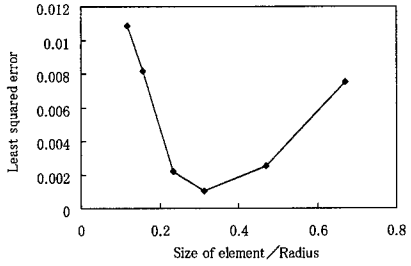

Fig.3 Least Square Error of Load-Displacement Relationship of $[0_8]_T$ laminate

Multidirectional Laminates

Damage growth of cross ply laminates and quasi-isotropic laminates with an open hole are simulated and compare to experimental results [5]. For multidirectional laminates, shear deformation of a lamina with matrix cracking is constrained by adjacent laminae. Since degree of the constraint is unknown, parameter survey is conducted in terms of reduction of shear stiffness. Reduction of shear stiffness are set to 1/2, 1/10 and 1/100 in the parameter survey.

Fig.4 shows propagation of splitting in 0° lamina in terms of reduction of shear stiffness. Fig.5 shows propagation of splitting in terms of element size.

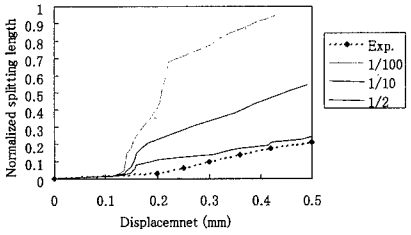

Fig.4 Influence of Stiffness Degradation Ratio

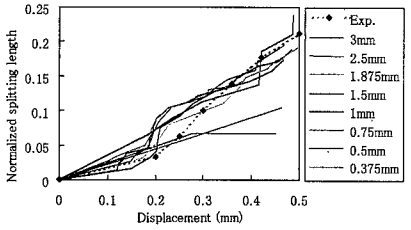

Fig.5 Influence of Element Size

Fig.4 shows that reduction of shear stiffness considerably affects propagation of splitting. The reduction ratio 1/2 is appropriate in view of Hashin's variational approach [6]. This implies that consideration of micro-mechanics is required to decide the reduction ratio.

Damage growth of crossply laminate is complicated because it consists of stress-dominant fracture, fracture machanics-domainant fracture, constraint by adjacent laminae and so on. Fig.5 shows that simulation results converge as element size decreases. Though sufficient fine mesh is required for $[90_8]_T$ laminate, moderate fine mesh is required for $[0_2/90_2]_S$ laminate to simulate damage growth.

Growth of matrix cracking in quasi-isotropic laminates in terms of element size is shown in Fig.6. The tendency is similar to that of crossply laminate. The

results converge as element size decreases, and unnecessary fine mesh division gives rise to increase of calculation time.

As a result, it is shown that the simulation results converge with decrease of element size for multidirectional laminates, and mesh division of 1/5-1/10 of diameter is enough to simulate damage growth from stress concentration region.

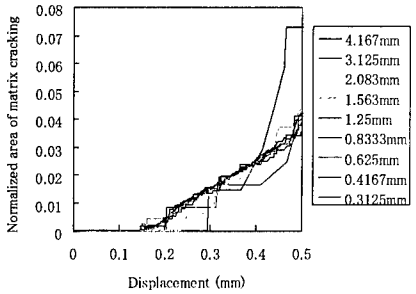

Fig.6 Influence of Element Size of Quasi-Isotropic Laminate

Conclusions

Influence of element size on damage growth simulation is investigated. As a result, it is shown that the simulation results converge with decrease of element size for multidirectional laminates, and mesh division of 1/5-1/10 of diameter is enough to simulate damage growth from stress concentration region.

References

1. Y.Shimamura, A.Todoroki, H.Kobayashi, H.Nakamura and T.Minowa: Trans.Japan Soc.Mech.Eng., 60A(579), 2498(1994) (in Japanese)
2. K.Y.Chang, S.Liu and F.K.Chang: J.Comp.Mater., 25, 274(1991)
3. M.Zako: "*Suuchi FukugouZairyo Rikigaku*", Yokendo, Tokyo, 1989, pp.8-39. (in Japanese)
4. T.Miyoshi, M.Shiratori, M.Zako and S.Sakata, "*YugenYosoHou*", Jikkyoshuppan, Tokyo, 1976, pp.39-41. (in Japanese)
5. Y.Shimamura, A.Todoroki, H.Kobayashi and H.Nakamura: Trans.Japan Soc.Mech.Eng., 62A(594), 1842(1996) (in Japanese)
6. Z.Hashin, Mech.Mater.4,121(1985)

Proceedings of 7th Japan International SAMPE
Symposium & Exhibition, Nov. 13-16, 2001

Experimental and Analytical Characterization of Microscopic Damage Progress in CFRP Angle-Ply Laminates

Akihisa TANAKA#, Satoshi KOBAYASHI#, Shuichi WAKAYAMA#,
Yu SHIGENARI*, Kiyoshi MIYAGAWA* and Shigeru SUZUKI*

#: Department of Mechanical Engineering, Tokyo Metropolitan Univ.
1-1 Minamiosawa, Hachioji-city, Tokyo 192-0397, JAPAN
E-mail:akihisa@ecomp.metro-u.ac.jp

*: IHI Aero Space Co.

Abstract

Microscopic damage behavior of carbon/epoxy angle-ply $[\pm\theta]_s$ (θ=15, 30, 45, 60 and 75°) laminates under tensile loading were investigated experimentally and analytically. Initiation and growth of microscopic damages were observed by optical microscopy and soft X-ray radiography. Matrix cracks and delamination initiated at the free edge in $[\pm15]_s$, $[\pm30]_s$ and $[\pm45]_s$ laminates. It was observed that delamination grew in the width direction in only $[\pm15]_s$ and $[\pm30]_s$ laminates. On the other hand, no damages were observed until final fracture in $[\pm60]_s$ and $[\pm75]_s$ laminates. Analytical approach based on damage mechanics analysis was also adapted to analyze these experimental results.

Key Words: Angle-Ply Laminate, Matrix Crack, Delamination, Damage Mechanics

Introduction

Carbon fiber reinforced plastic (CFRP) laminates are used in the aerospace field because of their high specific modulus and strength. However, it is well known that various microscopic damages such as matrix crack and delamination initiate and grow before final fracture in the failure process of CFRP laminates. These structures have been designed based on the safe-life concept which do not allow any initial damages. However, it is necessary that design criteria is shifted to risky side to reduce the weight of structures. To establish such damage tolerance design, it is necessary to clarify the mechanism of damages nucleation and the effects of damages on mechanical properties.

There are many studies about the damages in the transverse plies, example for the shear lag theory [1] and Hashin's model [2]. Actually it has also been confirmed that the matrix cracks initiate in off-axis plies, which are included in quasi-isotropic laminates, but there are little research about mechanism of behavior of these damages. In the present study, the damage behavior in off-axis plies of angle-ply laminates were characterized experimentally. These experimental results were analyzed using damage mechanics analysis.

Experimental Procedure

Material systems used in this study were two kinds of carbon-epoxy composites, T700S/2500 and IM700X/Q153. The mechanical properties of unidirectional composites for these materials are tabulated in Table 1. For each material system, $[\pm\theta]_s$ angle-ply laminates were fabricated. The range of θ was from 15° to 75° to evaluate the effect of the fiber orientation on microscopic damage progress. Specimen length was 150mm, width was 10mm and thickness was 0.55mm. To avoid the stress concentration at the grip, GFRP tabs, which

have 25mm length, were glued on both ends of specimens.

Quasi-static tensile tests were carried out at room temperature under constant cross-head speed of 0.5mm/min. In order to observe the microscopic damage progress, the specimen was removed from testing machine, and free edge observation by optical microscopy and internal observation by soft X-ray radiography were conducted. Observed area was 25mm length at the center. Matrix crack density was defined as the number of matrix crack per unit observed length.

Table 1 Mechanical properties of unidirectional composites.

	T700S/2500	IM700X/Q153
Longitudinal Young's Modulus, GPa	121	176
Transverse Young's Modulus, GPa	10.4	8.90
In-Plane Shear Modulus, GPa	4.80	6.22
In-Plane Poisson's Ratio	0.312	0.310

Table 2 Results of tensile tests of T700S/2500 angle-ply laminates.

Lamination Angle	15°	30°	45°	60°	75°
Young's Modulus, GPa	101	42.1	16.1	11.1	10.6
Ultimate Strength, MPa	814	392	161	67.8	61.0
Failure Strain, %	0.96	1.64	7.78	0.78	0.63

Table 3 Results of tensile tests of IM700X/Q153 angle-ply laminates.

Lamination Angle	15°	30°	45°	60°	75°
Young's Modulus, GPa	121	51.3	19.5	11.5	9.89
Ultimite Strength, MPa	622	329	143	73.1	62.5
Failure Strain, %	0.55	0.88	3.93	0.89	0.70

Experimental Results

Tensile test

The results of tensile test for T700S/2500 and IM700X/Q153 are summarized in Tables 2 and 3, respectively. It is recognized in the tables that stiffness and strength decrease with the increase in lamination angle for both materials. And for $[\pm 15]_s$, $[\pm 30]_s$ and $[\pm 45]_s$ laminates, the failure strains of IM700X/Q153 are about half of T700S/2500 and the strength is also lower. On the other hand, the failure strain and the strength of IM700X/Q153 are larger for $[\pm 60]_s$ and $[\pm 75]_s$ laminates.

Results of Free Edge Observation

Figure 1 shows the result of free edge observation for T700S/2500 $[\pm 30]_s$ laminates. For the $[\pm 15]_s$ and $[\pm 30]_s$ laminates, similar damage behaviors were observed. A matrix crack in outer ply and a delamination at a crack tip initiated at first on both materials. Then a matrix crack in inner ply initiated from a tip of the delamination. Although similar damage behavior was observed in IM700X/Q153, the number of matrix crack was smaller in IM700X/Q153 than T700S/2500.

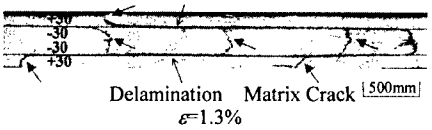

Fig.1 Damage in T700S/2500 $[\pm 30]_s$ laminate observed by optical microscopy (ε:laminate strain).

Figure 2 shows the results of free edge observation for $[\pm 45]_s$ laminates of both materials. First, a matrix crack in outer ply and a little delamination at a crack tip was observed on both materials. Then a crack from a tip of the delamination is initiated in the inner ply. As load increased, additional cracks are initiated along the

edges of specimen. The number of crack was almost the same between outer and inner ply for the T700S/2500, while the number in inner ply was smaller than in outer ply for the IM700X/Q153.

Figure 3 shows matrix crack density as a function of the laminate strain for $[\pm 45]_s$ laminate. As mentioned above, matrix crack densities in each ply increase almost equivalently for the T700S/2500, while the density in inner ply is lower than outer ply for the IM700X/Q153, which might be resulted from higher matrix toughness of IM700X/Q153 than T700S/2500.

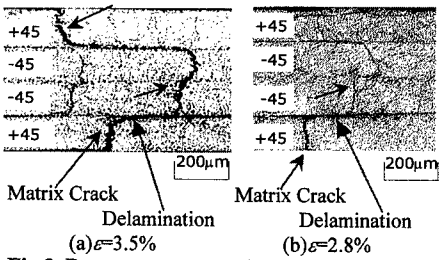

Fig.2 Damage progress in (a)T700S/2500 and (b)IM700X/Q153 $[\pm 45]_s$ laminate observed by optical microscopy (ε: laminate strain).

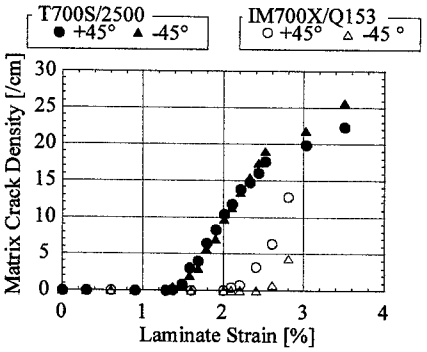

Fig.3 Matrix crack density as a function of laminate strain in T700S/2500 and IM700X/Q153 $[\pm 45]_s$ laminate.

Results of Internal Observation

The result of internal observation for T700S/2500 $[\pm 15]_s$ laminate is shown in Fig.4. For the $[\pm 15]_s$ and $[\pm 30]_s$ laminates, similar damage behavior is also observed in internal observation. It can be seen in the figure that triangular delaminations surrounded by the matrix cracks in outer and inner ply were initiated. As load increased, the delamination areas grew and new delaminations were initiated. Although similar delamination areas were observed for IM700X/Q153, the number of the delamination was less than T700S/2500.

On the other hand, the results of internal observation for $[\pm 45]_s$ laminates of both materials are shown in Fig.5. Similarly to the free edge observation, the cracks were observed along the free edge. The delamination hardly grew along the width direction. For the T700S/2500, the matrix cracks on each ply did not go through the width. On the other hand, for the IM700X/Q153, the matrix cracks in the outer ply went through the width, and little crack in the inner ply grew into the width direction.

For the $[\pm 60]_s$ and $[\pm 75]_s$ laminates, no microscopic damages were observed before the final failure. That is, fracture of these laminates was catastrophic.

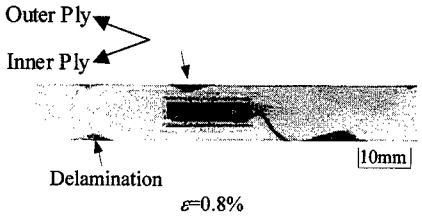

Fig.4 Damage progress in T700S/2500 $[\pm 15]_s$ laminate observed by soft X-ray radiography (ε: laminate strain).

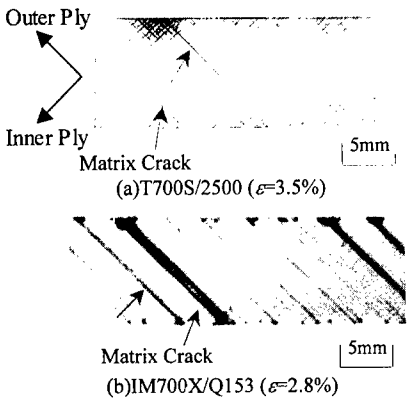

Fig.5 Damage progress in (a)T700S/2500 and (b)IM700X/Q153 $[\pm 45]_s$ laminate observed by soft X-ray radiography (ε: laminate strain).

Discussion

Damage Mechanics Analysis

Modulus reduction was calculated based on damage mechanics analysis proposed by Gudmundson and Zang [3]. The compliance matrix of laminate as functions of matrix crack densities in each plies is expressed as

$$\mathbf{S}(\rho^k) = \left((\mathbf{S}_0)^{-1} - \sum_{k=1}^{N} v^k \rho^k (\mathbf{A}^k)^T \sum_{i=1}^{N} \beta^{ki} \mathbf{A}^i \right)^{-1} \quad (1)$$

where v^k, ρ^k and β^{ki} denotes the volume fraction of ply k, the matrix crack density of ply k and the matrix related to the average crack opening displacements in ply k, respectively. $\mathbf{A}^k$ is the matrix represented with the compliance matrix of ply k and the unit normal vector on the crack surfaces in ply k. The laminate stiffness $\mathbf{E}(\rho^k)$ is calculated from $\mathbf{S}(\rho^k)$. Figure 6 shows the comparisons of the experimental result with the result calculated from the above equation. The experimental date just after damage initiation is lower than the calculation for each material. It is suggested that these results reflect the effect of the nonlinear shear behavior of unidirectional composites.

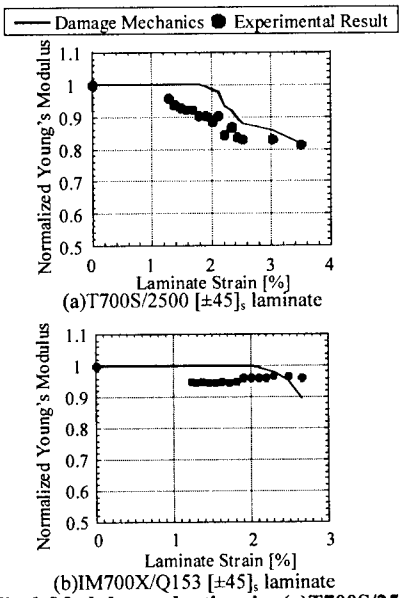

Fig.6 Modulus reduction in (a)T700S/2500 and (b)IM700X/Q153 $[\pm 45]_s$ laminate.

Conclusion

Microscopic damage behavior of angle-ply laminates under tensile load were studied. Following conclusions were obtained.

1. Matrix cracks and delamination were observed before final fracture in $[\pm 15]_s$ and $[\pm 30]_s$ laminates.
2. Although matrix cracks were observed, delamination hardly grew in the width direction in $[\pm 45]_s$ laminates.
3. No damages were observed until final fracture in $[\pm 60]_s$ and $[\pm 75]_s$ laminates.
4. It was confirmed that there was the effect of nonlinear shear behavior of unidirectional composites on modulus reduction.

Reference

1. J. -W. Lee, I. M. Daniel, J. Comp. Materials, *Vol.*24 (1990), 1225-1243
2. Z. Hashin, Engng Fract. Mech., 25 (1986), 771-778
3. P. Gudmundson, W. Zang, Int J. Solids Structures, *Vol.*30 (1993), 3211-3231.

Proceedings of 7th Japan International SAMPE
Symposium & Exhibition, Nov. 13-16, 2001

Analytical Prediction and Experiment of Transverse Lamina Cracking in Multidirectionally Reinforced Symmetric Laminates

Satoshi Abe, Kazuro Kageyama, Isamu Ohsawa, Makoto Kanai, and Tetsuji Kato#

#: The University of Tokyo
7-3-1 Hongo, Bunkyo Ward, the Metropolis of Tokyo, Japan, 〒113-8656
E-mail: abe@ygg.naoe.t.u-tokyo.ac.jp

Abstract

Composite materials have heterogeneous and anisotropic features, so damage behavior of composite laminate is complex. Damages of composite materials are classified to three modes, transverse lamina cracking, delamination, and fiber breakage. Transverse lamina cracking grows stably in early damage state. The prediction method of transverse lamina cracking is necessary for structural design based on damage tolerance. In this research, we tried to establish the transverse lamina cracking prediction method and did experiments to make sure of the prediction method.

Key Words: Transverse Lamina Cracking, Delamination, Damage Tolerance, and Failure Criteria

1. Introduction

When the composite laminate is subjected to mechanical load, transverse lamina cracks occur in the beginning. Transverse lamina cracks propagate and delamination occurs from cracks or free edge with load increase. Finally, whole material breaks with fiber breakage. Behavior of transverse lamina cracks should be studied for estimating initial state of damage processes of composite laminates.

When no damage is tolerated in structural design, the design strength is limited to onset of transverse lamina cracks. But when some extent damage is tolerated, the design strength is improved. The concept of the allowable damage growth makes design strength improved.

Transverse lamina cracks are supposed to occur when both failure criteria that are stress failure criterion and energy failure criterion. When ply group's thickness is thin, the failure criterion is not stress failure criterion but energy failure criterion, so material fails not at point A' but at point A in Fig.1.2. When ply group's thickness is thick, the failure criterion is not energy failure criterion but stress failure criterion, so material fails not at point C' but at point C. Combined failure criterion transits from energy failure criterion to stress failure criterion with ply group's thickness increase at point B.

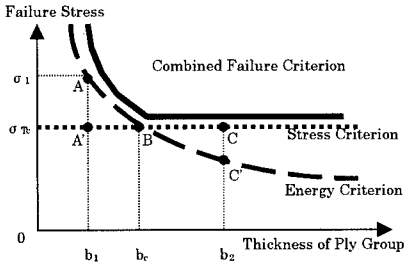

Fig. 1.1 Failure Criteria Transition

2. Damage Prediction Theory

2.1. Modeling of Laminates

The multidirectional symmetric n layer laminate $[\theta_n/\cdots/\theta_1]_s$ is divided into n-1 units, $U_{n-1},\cdots,U_1$, at the center of each layer. The laminate is expressed as a combination of the units. The symmetric laminate unit can be deal with as the $[\theta_m/90_n]_s$ laminate unit by coordinate transformation. We consider stiffness reduction of the laminate unit with cracks in 90° ply.

2.2. Calculating Method

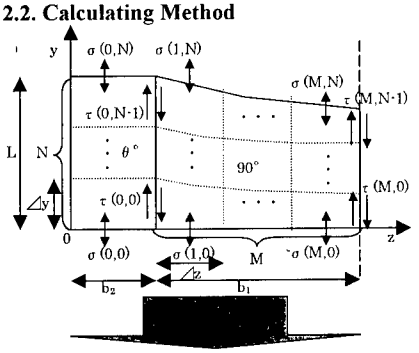

Fig. 2.1 Calculation of Stress Distribution

The 90° ply is divided into M × N elements in the z- and y- directions, respectively. The θ° ply is divided into N elements in the y direction, as shown in Fig.2.1. Tensile stresses σ (m,n) and shear stresses τ (m,n) are defined at boundaries of the divided elements. These stresses are calculated from equilibrium conditions of stresses, compatibility of strains, and boundary conditions. When the crack density is c(=1/2L:2L is the distance of cracks), and the average tensile stress σ_0 is applied, tensile stresses components σ (m,n) and shear stresses components τ (m,n) are obtained. The average tensile stress of the θ° ply $\sigma_{av}{}^{\theta}$ is obtained from the tensile stresses of θ° ply σ (0,n). The average strain of the unit ε_{av} is obtained from $\sigma_{av}{}^{\theta}$ because the tensile stiffness of the θ° ply does not change by cracks of the 90° ply. The stiffness of the unit is obtained by $\sigma_0/\varepsilon_{av}$. Although the above-mentioned method is the case of tensile stiffness, shear stiffness is calculated in the same method of tensile stiffness by replacing stresses and stiffness.

2.3. Energy Failure Criterion

First, damage is predicted based on energy balance. In the standpoint of energy balance, transverse lamina cracks are supposed to initiate or propagate when energy that is released by crack growth is equal to the change of potential energy of laminate.

Matrix cracking failure under mixed mode is predicted when following energy criterion [1)2)] is satisfied

$$\left(\frac{G_{\mathrm{I}}}{G_{\mathrm{I}c}}\right)^{\alpha}+\left(\frac{G_{\mathrm{II}}}{G_{\mathrm{II}c}}\right)^{\alpha}=1 \qquad (2.1)$$

where G_{I} and G_{II} are the energy release rate of mode I and II, respectively, and $G_{\mathrm{I}c}$ and $G_{\mathrm{II}c}$ are the fracture toughness of mode I and II, respectively. Cracks initiate and propagates when the total energy release rate $G(=G_{\mathrm{I}}+G_{\mathrm{II}})$ reaches mixed mode fracture toughness G_c as follows.

$$G=G_c \qquad (2.2)$$

When the mixed mode ratio, M_G, is defined as $G_{\mathrm{I}}/G_{\mathrm{II}}$, the mixed mode fracture toughness is obtained from Eqn.2.1 as follows;

$$G_c=(1+M_G)\left\{\left(\frac{1}{G_{\mathrm{I}c}}\right)^{\alpha}+\left(\frac{M_G}{G_{\mathrm{II}c}}\right)^{\alpha}\right\}^{-\frac{1}{\alpha}} \qquad (2.3)$$

When increment of crack density, $dc^{(1)}$ is given, the energy release rates are expressed as follows;

$$G=-\frac{b_1+b_2}{2b_1}\varepsilon_y'^2\frac{dS_{22}'}{dc^{(1)}}-\frac{b_1+b_2}{2b_1}\gamma_{xy}'^2\frac{dS_{66}'}{dc^{(1)}}$$

$$G_{\mathrm{I}}=-\frac{b_1+b_2}{2b_1}\varepsilon_y'^2\frac{dS_{22}'}{dc^{(1)}} \qquad (2.4)$$

$$G_{\mathrm{II}}=-\frac{b_1+b_2}{2b_1}\gamma_{xy}'^2\frac{dS_{66}'}{dc^{(1)}}$$

where dS_{ij} is stiffness reduction, and $dc^{(1)}$ is increase of crack density in 90° ply.

Critical strains are obtained at each ply. Crack is predicted to initiate or propagate in the ply that gives the smallest critical strain.

2.4. Stress Failure Criterion

Matrix cracking failure under combined loads is predicted when the following stress criterion[3] is satisfied

$$\left(\frac{f_\sigma \sigma_T}{\sigma_{Tc}}\right)^2 + \left(\frac{f_\tau \tau_{LT}}{\tau_{LTc}}\right)^2 = 1 \quad (2.4)$$

where σ_T and τ_{LT} are the average ply transverse and shear stresses, respectively, and σ_{Tc} and τ_{LTc} are the effective transverse tensile strength and shear strength of the ply under consideration, respectively. Factors, f_σ and f_τ, are the ratios of maximum stresses and average stresses in tensile and shear components. Crack is predicted to initiate or propagate in the ply that gives the smallest critical stress.

2.5. Thermal Residual Stress

Thermal residual stresses $\sigma_R^{(k)}$ occur in each layer because of the difference of thermal expansion coefficients in the longitudinal and transverse direction, respectively, as follow;

$$\boldsymbol{\sigma}_R^{(k)} = \mathbf{S}^{(k)}\left\{\boldsymbol{\varepsilon}^{(c)}(T) - \mathbf{R}_\varepsilon(\theta_k)\boldsymbol{\alpha}_0(T - T_0)\right\} = \mathbf{S}^{(k)}\boldsymbol{\varepsilon}_R^{(k)} \quad (2.5)$$

Where $\mathbf{S}^{(k)}$ is stiffness matrix of k ply. $\mathbf{R}_\varepsilon$ is a strain transformation matrix. α_0 is a thermal expansion coefficient vector. The origin of the stress-strain curve shifts because of thermal residual stress. The critical strain and stress are measured from the revised origin.

3. Experiment

3.1. Specimens

TR340H150; the carbon/epoxy pre-prig sheet of Mitsubishi Rayon Co., Ltd. is served to experiment. Material properties are shown in Table.3.1. The nominal ply thickness is 0.15mm. Temperature change by lamination is 100K. Cross-ply and quasi-isotropic were prepared with stacking sequences, as shown in Table.3.2.

Table. 3.1 Lamina Properties

E_L	115GPa	σ_T	82MPa
E_T	8GPa	τ_{LT}	110MPa
G_{LT}	3.5GPa	G_{Ic}	197J/m^2
G_{TZ}	2.5GPa	G_{IIc}	982J/m^2
ν_{LT}	0.34	α_L	-7.5*10^{-7}/K
σ_L	1924MPa	α_T	4.3*10^{-5}/K

Table. 3.2 Stacking Sequences

Cross-Ply	Quasi-Isotropic
$[0_1/90_1/0_1]_s$	$[45_1/-45_1/0_1/90_1]_s$
$[0_1/90_1]_s$	$[45_1/0_1/-45_1/90_1]_s$
$[0_2/90_2]_s$	
$[0_4/90_4]_s$	

3.2. Method of Experiment

Tension tests of the specimens were performed using the Shimadzu Autograph test machine in the stroke control mode at a loading rate of 0.5mm/min. When initial A.E. wave was detected, crosshead movement was stopped and reversed a little, and cracks were counted by the way of edge observation. This was repeated while strain was increased 1000 or 2000 $\mu\varepsilon$ until the specimen breaks.

4. Comparison of Results

Stress-strain and crack densities are shown in Fig.4.1~2, and relationships between 90° ply group's thickness and failure strain are shown in Fig.4.3, about cross-ply. Stress-strain and crack densities in quasi-isotropic are shown in Fig.4.4~5.

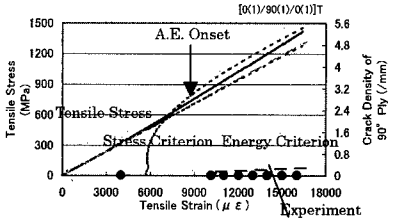

Fig. 4.1 Stress-Strain and 90° Ply's Crack Density of $[0_1/90_1/0_1]_T$

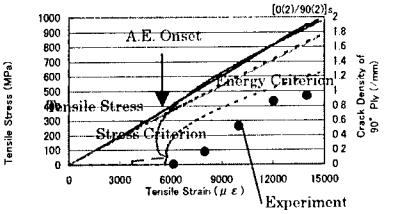

Fig. 4.2 Stress-Strain and 90° Ply Group's Crack Density of $[0_2/90_2]_s$

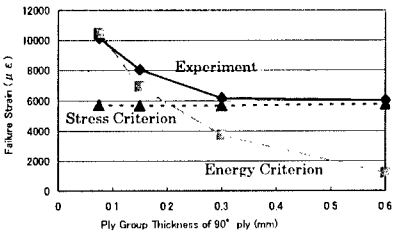

Fig. 4.3 Relationships between 90° Ply Group's Thickness and Failure Strain in Cross-Ply Laminates

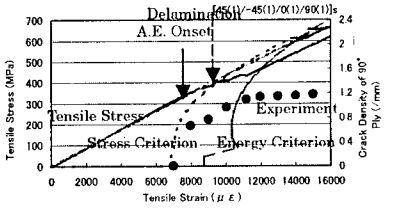

Fig. 4.4 Stress-Strain and 90° Ply Group's Crack Density of $[45_1/-45_1/0_1/90_1]_s$

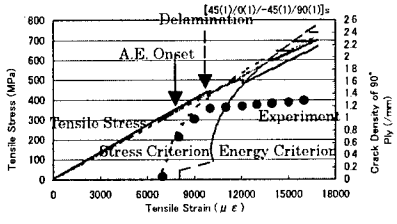

Fig. 4.5 Stress-Strain and 90° Ply Group's Crack Density of $[45_1/0_1/-45_1/90_1]_s$

In cross-ply laminates, transition of failure criterion with ply group's thickness was confirmed in transverse lamina cracks in 90° ply group. When the ply group is thin, the failure criterion is energy criterion. When the ply group is thick, the failure criterion is stress criterion.

In quasi-isotropic laminate, stacking sequence did not influence propagating tendency of transverse lamina cracks in 90° ply group. But in $[45_1/0_1/-45_1/90_1]_s$, transverse lamina cracks of 90° ply group gave -45° ply groups stress concentration, and it became easier for transverse lamina crack of -45° ply groups to initiate and propagate. In quasi-isotropic laminates, delamination prevented transverse lamina cracks from propagating by cutting off stress transmission between neighbor layers.

5. CONCLUSION

In the present paper, we calculated crack growth and stiffness reduction based on energy criterion and stress criterion. Crack propagating process was well predicted by our prediction method.

REFERENCES

1) Keiichiro Tohgo, Kenji Akizuki, and Yuji Sugiyama, "Ply Cracking Damage Theory and Damage Behavior in CFRP Cross-Ply Laminates", Journal of Japan Machinery Association, Vol64-621, No.97-0737, pp.30-37, May 1998

2) Keiichiro Tohgo, Yuji Sugiyama, and Kenji Akizuki, "Ply-Cracking Damage Theory and Its Application to Finite Element Method", Journal of Japan Machinery Association, March 1999

3) Iqbal Shahid, Fu-Kuo Chang, "Modeling of Accumulated Damage and Failure of Multidirectional Composite Plates Subjected to In-Plane Loads", Composite Materials: Fatigue and Fracture, Fifth Volume, ASTM STP 1230, R. H. Martin, Ed., American Society for Testing and Materials, Philadelphia, 1995, pp.186-214

Proceedings of 7th Japan International SAMPE
Symposium & Exhibition, Nov. 13-16, 2001

Statistical Strength Prediction of CFRP Cross-ply Laminates

Junji Noda#1, Tomonaga Okabe#2 ,Nobuo Takeda#3 and Masao Shimizu#1

#1: Department of Integrated Design Engineering, Keio University,
3-14-1 Hiyoshi, Kohoku-ku, Yokohama 223-8522, Japan
#2: National Institute of Advanced Industrial Science and Technology,
1-1 Umezono 1, Tsukuba 305-8568, Japan
#3: Graduate School of Frontier Sciences, c/o Komaba Open Laboratory (KOL),
The University of Tokyo, 4-6-1 Komaba, Meguro-ku, Tokyo, 153-8904, Japan
E-mail: noda@compmat.rcast.u-tokyo.ac.jp

Abstract

The failure process of CFRP cross-ply laminates (T800H/3631) is studied experimentally and analytically. The variation of Ultimate Tensile Strength (UTS) of laminates with various stacking sequences is measured and the damage process is observed. According to the simulated results of fiber bundle strength, it is found that there is little notch sensibility in spite of the existence of transverse cracks. To investigate the damage evolution process quantitatively, a new numerical model based on 3D-shear lag analysis is proposed in the present paper. The elastoplastic relation of epoxy matrix is considered effectively, which makes it possible to predict the UTS of laminates with good accuracy. Based on the analysis results of the proposed model, it is shown that the viscoplastic regions at the tip of transverse cracks reduce the concentration of stress and that the bundle strength is not affected by the existence of transverse crack.

Key Words: Transverse crack, Bundle strength, Computational simulation, Elastoplastic.

Introduction

For the case of cross-ply laminates subjected to uniaxial loading, the early stage of damage is dominated by transverse crack generated in the 90° plies. These transverse cracks propagate along the fiber direction and extend across the width of the laminate to the free edges of test specimens. The influence of these micro-damages on the UTS of cross-ply laminates was empirically considered, but the failure mechanism was not yet investigated quantitatively. Therefore, the purpose of the present work is the experimental and analytical investigation on the stress-strain relation and the UTS of the CFRP cross-ply laminates with various micro-damages.

At first the variation of UTS of laminates with various stacking sequences was measured and the damage process was observed. And these UTS and damage process were compared with those of unidirectional composites. Then, to investigate the damage evolution process quantitatively, we proposed an 3D-shear lag model based on experimental observation. Then, the failure behavior of the cross-ply

laminates was estimated quantitatively by the proposed numerical model.

Experimental Approach

Experimental Procedure

In the present study, a high strength CFRP composite (T800H/3631(Toray Industries, Inc.)) was used. Two types of stacking sequences of CFRP composites were prepared, one is the unidirectional composite $[0]_2$ and the other is the cross-ply laminates $[0_1/90_n/0_1]_{n=2,4,6}$ with dimensions of 5mm x 120mm x 0.3~1.2mm. The volume fraction was 60%. For various stacking sequences, to measure the stress-strain relation and ultimate tensile stress, the tensile test was carried out. For the accurate measurement of the transverse crack density, the replica of the specimen edge was taken.

Experimental Results

Figure 1 shows UTS versus laminate ratio. The laminate ratio r_L was defined by the following equation (1):

$$r_L = t_{90}/t_0, \qquad (1)$$

where t_0, t_{90} : the thickness of 0° ply and 90° ply, respectively. Therefore, r_L = 0 means UD.

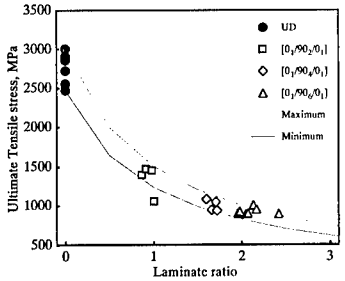

Fig.1 Ultimate Tensile Stress versus laminate ratio.

The tensile test results showed that the UTS of CFRP laminates decrerased with increasing laminates ratio, that is to say, the length of the transverse crack. This behavior can be considered to be stemmed from the reduction of the ratio of the effective cross-area which can sustain the actual load. Therefore the difference of the bundle strength, which defined as the value of stress to be shared by the fiber bundle in 0° plies, was checked for the each laminates ratio. The bundle strength σ_b was calculated by the following equation (2):

$$\sigma_b = \frac{\sigma_{UTS}}{V_f^{eff} \cdot V_0} \qquad (2)$$

where σ_{UTS} :UTS, V_f^{eff} :effective volume fraction in 0° ply and V_0 was expressed as:

$$V_0 = \frac{t_0}{t_0 + t_{90}} \qquad (3)$$

with:

$$\frac{1}{V_0} = 1 + r_L \qquad (4)$$

Figure 2 shows the relations between the bundle strength and the laminate ratio. The bundle strength is almost constant in spite of the difference in the laminate ratio. So, it is concluded that there is little notch sensibility in spite of the existence of transverse cracks.

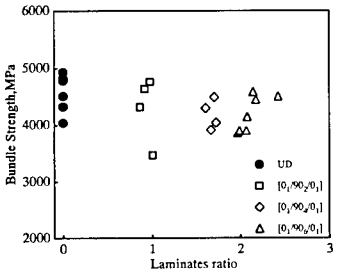

Fig.2 Bundle strength versus laminate ratio.

Inner Micro-damage Analysis

3D shear-lag model

In the present paper, a new numerical model based on the 3D-shear lag analysis was proposed to investigate the inner micro-damage process. For this purpose cross-ply laminates were modeled as shown in Fig. 3. The model was composed of N x M fibers

and transverse elements, which length was given by L. Each fiber and transverse element was partitioned into K elements. The present study assumed that the fibers were uniformly spaced by a distance d and were aligned in a square arrangement.

In the model the elastoplastic relation of the epoxy matrix is considered effectively. And the interface property between the lamina, 0° ply and 90° ply, was evaluated by the Berthelot method[1]. According to the parabolic shear-lag approach, the shear stress τ at the ply interface is given by

$$\tau = \frac{3G}{t_{90}}(u_0 - u_{90}) \qquad (5)$$

where u_0 , u_{90} : the average longitudinal displacement in 0° ply and 90° plies, respectively. Furthermore the shear modulus G is

$$G = \frac{G_{xz}^{90}}{1 + \frac{t_0 \cdot G_{xz}^{90}}{t_{90} \cdot G_{xz}^{0}}} \qquad (6)$$

where G_{xz}^{0}, G_{xz}^{90} : the transverse shear moduli of the 0° ply and 90° plies, respectively. We have already validated that the stress distribution obtained from the present analysis model has a good agreement with that of a finite element analysis.

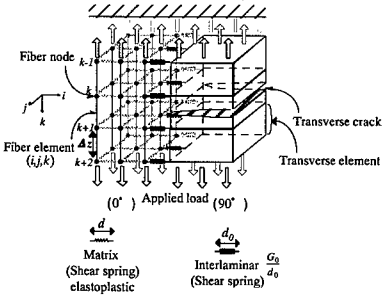

Fig.3 Schematics of 3D shear lag model.

According to the shear-lag concept wherein the tensile load carried by the matrix is neglected, the equilibrium equation for the stress $\sigma_{i,j,k}$ on a single fiber element is given by

$$A_1 \frac{d\sigma_{i,j,k}}{dz} = -\frac{\pi r}{2} \sum_{l=1}^{4} \tau_{i,j,k}^{l} \qquad (7)$$

where A_1 is the area of fiber cross section, r is the fiber radius and $\tau_{i,j,k}^{l}$ is the interfacial shear stress with l ranging from 1 to 4 as expressed as equation (5). Consequently, we use a finite difference method to solve equation (7) as

$$\frac{4E_f A_1}{\Delta z^2} \frac{\left[\gamma_{i,j,k}\left(u_{i,j,k+1} - u_{i,j,k}\right) - \gamma_{i,j,k-1}\left(u_{i,j,k-1} - u_{i,j,k}\right)\right]}{2 + \gamma_{i,j,k} + \gamma_{i,j,k-1}} + \sum_{l=1}^{4} h\left[\tau_{i,j,k}^{l}\left(1 - P_{i,j,k}^{l}\right) + \zeta_l P_{i,j,k}^{l} \tau_y\right] = 0 \qquad (8)$$

$$\frac{4E_f A_1}{\Delta z^2} \frac{\left[\gamma_{i,j,k}\left(u_{i,j,k+1} - u_{i,j,k}\right) - \gamma_{i,j,k-1}\left(u_{i,j,k-1} - u_{i,j,k}\right)\right]}{2 + \gamma_{i,j,k} + \gamma_{i,j,k-1}} + h\tau_{1,j,k} + \sum_{i=2}^{4} h\left[\tau_{i,j,k}^{l}\left(1 - P_{i,j,k}^{l}\right) + \zeta_l P_{i,j,k}^{l} \tau_y\right] = 0 \qquad (9)$$

$$\frac{4E_t A_2}{\Delta z^2} \frac{\left[\gamma_k\left(u_{k+1} - u_k\right) - \gamma_{k-1}\left(u_{k-1} - u_k\right)\right]}{2 + \gamma_k + \gamma_{k-1}} + \sum_{j=0}^{J-1} h\tau_{1,j,k} = 0 \qquad (10)$$

$P_{i,j,k}^{l} = 0$: *Elastic*, $P_{i,j,k}^{l} = 1$: *Plastic*

$\gamma_{i,j,k} = 1, 0$: *Fiber Element* (i,j,k) *is broken or not broken*

$\gamma_k = 1, 0$: *Fiber Element* (k) *is broken or not broken*

where A_2 is the area of transverse element cross section, E_f and E_t are Young's moduli of fiber and 90° ply, respectively. And the interfacial plastic parameter $P_{i,j,k}^{l}$ is 0 or 1 when the interface is elastic or plastic.

Monte Carlo Simulation

Considering the real situation, it is well known that the characteristic strength of a fiber are different from that of another fiber. These situation can be well described by using the Weibull of Weibull model proposed by Curtin[2]. The Weibull of Weibull theory gives the strength of each fiber element $\sigma_{i,j,k}^{S}$, and can be represented by equation (11).

$$\sigma_{i,j,k}^{S} = \left(\frac{L_0}{\Delta z}\right)^{\frac{1}{\rho}} \sigma_0^{i,j}\left[-\ln\left(1 - \eta_{i,j,k}\right)\right]^{\frac{1}{\rho}}, \qquad (11)$$

where $\sigma_0^{i,j}$ is the characteristic strength of the one fiber of length L_0 , ρ ' is the length

scaling Weibull modulus and $\eta_{i,j,k}$ is a random number.

Monte Carlo simulation is conducted by controlling the applied composite strain. In this simulation, the final failure is considered to be realized, once the applied composite stress decreases to 90% of the applied maximum composite stress.

Analysis Results

Figure 4 shows the comparison between the predicted and experimental results of UTS against laminates ratio, which shows this analysis model makes it possible to predict the UTS of cross-ply laminates with good accuracy. In order to study damage evolution process in the composite by simulation, the variation of the stress concentration at the tip of a transverse crack is examined, according to investigate the stress concentration factor (SCF) on the cross section with a transverse crack.

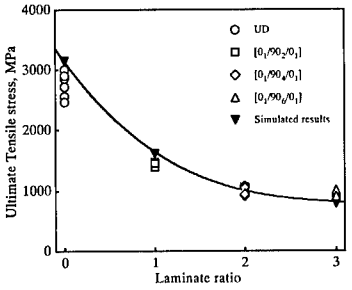

Fig.4 Comparison between experimental and simulated results.

Figure 5 shows the spatial distributions of SCF at the cross section with a transverse crack of 0° ply. At the low strain level, the stress concentration near the crack tip region induced fiber. However, at the high strain level, the stress concentration at the transverse crack tip diminishes and new fiber breakage occurs at the region far from the crack tip. The critical cluster which contributes to the final failure arises from this region where the stress concentration due to the transverse crack tip does not exists. These results can be explained using the plastic behavior of epoxy region. By virtue of this plasticity, the stress concentration at the crack tip is reduced. Therefore, the final failure of cross-ply composite is not affected by the existence of transverse cracks. This is the most important result of the present study.

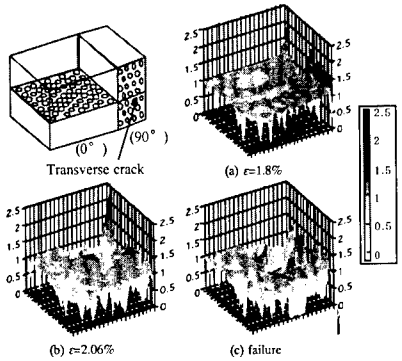

Fig.5 Spatial distributions of SCF.

Conclusions

A new numerical model based on the 3D-shear lag analysis was proposed. The elastoplastic relation of the epoxy matrix was considered effectively, which made it possible to predict the UTS of laminates with good accuracy. Based on the analysis results of the proposed model, it was shown that the viscoplastic regions at the tip of transverse crack reduce the concentration of stress and that the bundle strength is not affected by the existence of transverse cracks.

References

1. J.-M.Berthelot: Composites Part A, 27A, 989 (1996).

2.W.A.Curtin: Journal of Composite Materials Vol.34, No.15, 1301(2000)

Proceedings of 7th Japan International SAMPE
Symposium & Exhibition, Nov. 13-16, 2001

Design And Analysis Of Reduced Thickness Solar Panels

Steven Hahn and Tsuyoshi Ozaki

Advanced Technology R&D Center, Mitsubishi Electric Corporation
1-1-57 Miyashimo, Sagamihara, Kanagawa 229-1195, JAPAN
E-mail: hahn@zaiken.sow.melco.co.jp

Abstract

To satisfy opposing requirements for minimum stowed volume, high stiffness, and light weight, various honeycomb sandwich solar panel designs were considered with the object of reducing the thickness by approximately 20% while maintaining current levels of stiffness and weight. Two solutions were found. The first involves use of a higher modulus material for the panel faces. The second involves strategic placement of doublers to suppress the first vibration mode. Doublers constructed of high stiffness material were found to provide the most benefit. Since the use of high cost, high performance material is localized, the impact on panel acquisition cost is expected to be minimized.

Key Words: Solar Array, Sandwich Panel, Design

Introduction

The electrical power requirements of satellites have been steadily increasing in recent years, leading to requirements for increased solar array area. At the same time, the satellite structures are also growing, and the volume available within the rocket fairing for stowing the satellite during launch is limited, so simply increasing the number or size of the solar array panels is an unattractive solution. In the current study, designs for solar array panels for a 22 kW class satellite bus (Fig. 1) were sought which would provide increased surface area without requiring additional stowed volume.

Requirements

The solar array for a recent MELCO developed satellite provided a point of

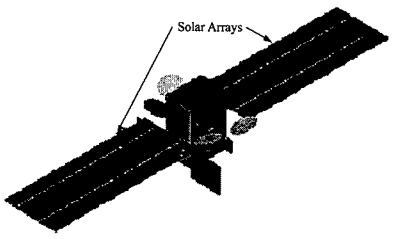

Fig. 1 22 kW Class Satellite Bus

departure for the study. That solar array comprised three 26 mm thick sandwich panels. The facesheets are constructed from three plies (0.102 mm facesheet thickness) each of M60J (Toray) carbon fiber prepreg arranged in a [0/±60] quasi-isotropic layup. It was determined that 8 panels of this size were required for a 22 kW class satellite. It was concluded from dimensional analysis that the stowed volume requirements could be met by reducing the thickness of each panel to 20 mm.

The natural frequency of the 26 mm thick panel array was 35 Hz in the stowed configuration. In order to prevent amplification of inertial loads due to vibrations experienced during launch, the natural frequency of the 22 kW array was also required to meet or exceed this value. Furthermore, as the available launch capability is best used for the satellite payload, it was required that the mass of each panel be less than that of the existing panels.

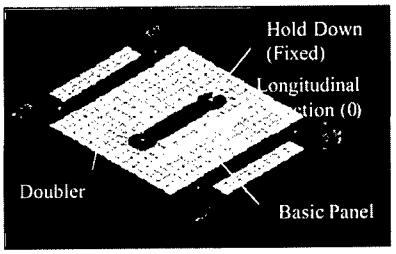

Fig. 1 Three Panel Solar Array FEM Model

Table 1 Baseline Results

	Run 0	Run 1
Description	26mm Baseline	20mm Baseline
Core thickness(mm)	25.4	19.05
Facesheet Thickness(plies[mm])	3[0.102]	3[0.102]
Facesheet Layup	[0/±60]	[0/±60]
Facesheet Material	M60J	M60J
Doubler Thickness(plies[mm])	None	None
Doubler Layup	–	–
Natural Frequency (Hz)	35.3	29.2
Panel Mass (kg)	5.85	5.00
Delta Mass	–	-14.6%

Approach

The finite element method (FEM) model of the stowed 3 panel array shown in Figure 2 was used for this study. The deployment direction indicated by the arrow was defined as the longitudinal direction, and the 0-degree direction of the facesheet laminate.

As shown in Table 1, the baseline model (Run 0) exhibited a natural frequency of 35.3 Hz, and a panel mass of 5.85 kg. The initial mode shape is illustrated in Figure 3. When the sandwich panel thickness was reduced to 20 mm and a new baseline taken (Run 1), the natural frequency dropped to 29.2 Hz. The mode shape was essentially the same as that of the 26 mm panel array shown in Figure 3.

From these baseline results, the material, thickness, and layup of the facesheets were varied, and the effect on the natural frequency and mass of the array was calculated. The effect of doublers was also evaluated, as

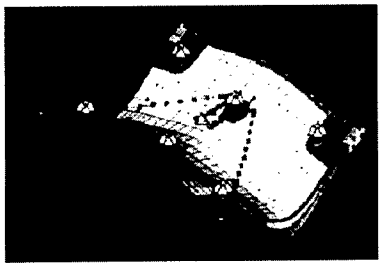

Fig. 2 Baseline Model Initial Mode Shape

well as the effect of changes to the material, thickness, and layup of these doublers.

Results

Table 2 shows the analysis results for various configurations with quasi-isotropic facesheet laminates. In Run 2, when the thickness of the baseline M60J facesheets was doubled, the natural frequency only increased to 32.2 Hz despite the mass surpassing the 5.85 kg requirement by 13%. At this point, the facesheet material was changed to a ultrahigh stiffness K13C (Mitsubishi Chemical) pitch-based carbon fiber prepreg. In Run 3, it was found that at the original facesheet thickness, this design essentially met the natural frequency requirement while achieving a mass reduction of 11%. By increasing the facesheet thickness by 33% (Run 4), both the mass and natural frequency requirements were completely satisfied. The initial mode shape of this configuration, shown in Figure 4, was similar to that exhibited by the baseline configuration.

These results established the feasibility of designing a reduced thickness solar array panel to meet the requirements of a 22 kW class satellite bus; however, as the ultrahigh modulus K13C fibers are more expensive than the lower performance baseline M60J fibers, it is desirable to limit their use. To this end, locally stiffened design configurations employing doublers on the baseline M60J facesheets were evaluated. As was shown in Figure 2, the doublers were applied in the longitudinal direction between the hold down mechanisms that attach the array to the satellite body so as to suppress the initial vibration mode shape.

The results of this evaluation are shown in Table 3. Evaluation of [0/±60] quasi-isotropic doubler designs in Runs 5 and 6, indicated that the panel mass would exceed the allowable value before the natural frequency

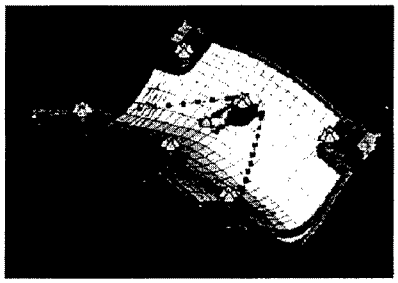

Fig. 3 Ultrahigh Modulus Model First Mode Shape

Table 2 Facesheet Material Change Results

	Run 0	Run 1	Run 2	Run 3	Run 4
Description	26mm Baseline	20mm Baseline	Double Thickness Facesheets	Increased Stiffness Facesheet	Increased Thickness Increased Stiffness Facesheet
Core thickness(mm)	25.4	19.05	19.05	19.05	19.05
Facesheet Thickness(plies[mm])	3[0.102]	3[0.102]	3[0.204]	3[0.102]	3[0.136]
Facesheet Layup	[0/±60]	[0/±60]	[0/±60]	[0/±60]	[0/±60]
Facesheet Material	M60J	M60J	M60J	K13C	K13C
Doubler Thickness(plies[mm])	None	None	None	None	None
Doubler Layup	-	-	-	-	-
Natural Frequency (Hz)	35.3	29.2	32.2	34.6	36.0
Panel Mass (kg)	5.85	5.00	6.62	5.19	5.77
Delta Mass	-	-14.6%	13.1%	-11.3%	-1.4%

Table 3 Doubler Results

	Run 0	Run 1	Run 5	Run 6	Run 7	Run 8	Run 9	Run 10
Description	26mm Baseline	20mm Baseline	Quasi-Isotropic Doubler	Increased Thickness Quasi-Isotropic Doubler	Unidirectional Doubler	Increased Thickness Unidirectional Doubler	Increased Thickness Unidirectional Doubler	Increased Stiffness Unidirectional Doubler
Core thickness(mm)	25.4	19.05	19.05	19.05	19.05	19.05	19.05	19.05
Facesheet Thickness(plies[mm])	3[0.102]	3[0.102]	3[0.102]	3[0.102]	3[0.102]	3[0.102]	3[0.102]	3[0.102]
Facesheet Layup	[0/±60]	[0/±60]	[0/±60]	[0/±60]	[0/±60]	[0/±60]	[0/±60]	[0/±60]
Facesheet Material	M60J	M60J	M60J	M60J	M60J	M60J	M60J	M60J
Doubler Thickness(plies[mm])	None	None	3[0.204]	3[0.306]	3[0.102]	9[0.306]	8[0.272]	6[0.204]
Doubler Layup	–	–	[0/±60]	[0/±60]	[0]3	[0]9	[0]8	[0]6
Natural Frequency (Hz)	35.3	29.2	31.1	32.2	31.7	35.2	34.8	35.8
Panel Mass (kg)	5.85	5.00	5.53	5.98	5.27	5.98	5.86	5.63
Delta Mass	–	−14.6%	−5.6%	2.2%	−10.0%	2.2%	0.2%	−3.9%

would increase to the required level. Results for unidirectional doubler designs considered in Runs 7 through 9 suggest that both the panel mass and natural frequency requirements can be essentially satisfied by providing 8 or 9 0-degree M60J plies in the doublers (Run 9 and 8, respectively). In Run 10, the doubler material was changed to K13C fiber reinforced composite in a [0]6 layup. This configuration was found to exhibit a natural frequency of 35.8 Hz, with a panel mass of 5.63 kg (4% less than the baseline), satisfying both requirements completely. The shape of the first vibration mode was very similar to that of the baseline design, as shown in Figure 5. Since the amount of high cost material used is limited, it is thought that this configuration represents a lower cost alternative to full K13C fiber reinforced facesheets.

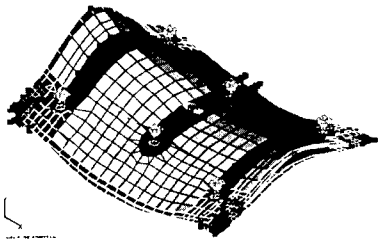

Fig. 4 Doubler Model First Mode Shape

Conclusions

By evaluating the performance of reduced thickness solar array panels, it was confirmed that both natural vibration frequency and mass property requirements could be satisfied through the use of ultrahigh modulus fiber reinforced composite materials in the panel facesheets. It was also determined that these competing requirements could be met at lower cost through selective application of ultrahigh modulus material in facesheet doublers. It is expected that reduced thickness solar array panels will contribute significantly to the development of future high power satellite systems at Mitsubishi Electric Corporation.

References

1. S. Hahn and T. Ozaki: Symposium of the Japan Soc. for Composite Materials, 89 (2001).

Proceedings of 7th Japan International SAMPE
Symposium & Exhibition, Nov. 13-16, 2001

Detailed Analysis of the Solar-B SOT Main Mirror Support Structure

Hidetaka Ishii and Tsuyoshi Ozaki
Mitsubishi Electric Co

1-1-57 Miyashimo, Sagamihara, Kanagawa 229-1195, JAPAN
E-mail: ishii@zaiken.sow.melco.co.jp

Introduction

Recently, requirements for high precision optical devices in order to resolve celestial objects such as the sun, the moon, and deep space more clearly are increasing. Especially in space applications, where the difference between minimum and maximum temperatures is so great, a high level of thermal stability is needed for the materials used for optical equipment structures. The optical space telescope structure (Fig. 1), under development by the National Astronomical Observatory (NAO) for the joint NAO and US National Aeronautics and Space Administration (NASA) SOLAR-B mission typifies these requirements.

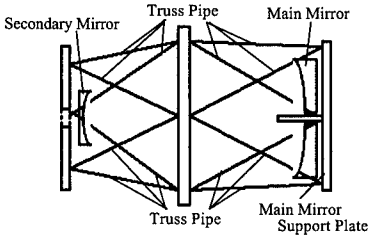

Fig1:Space Telescope

For many years, Invar alloys, which exhibit Coefficient of Thermal Expansion(CTE) values as low as 0.5ppm/K, have been used for optical equipment structures. But increasingly strict demands for low CTE and requirements for low density materials necessitated by increased size of the optical equipment have lead to a shift from Invar alloys to Carbon Fiber Reinforced Plastics (CFRP) which can have CTE values much lower than metals.

If the CFRP orientation is designed properly, it's possible to make the CTE of a CFRP laminate lower than 0.1ppm/K. Furthermore, as the density of CFRP is typically around 1.6g/cm^3, less than one fifth that of Invar alloys (8.5g/cm^3), CFRP strength-to-weight and stiffness-to-weight properties are much higher than metals. These properties make CFRP an ideal material for optical equipment used in space.

In this research, the strength of a CFRP optical structure for a space telescope comprising a truss constructed from CFRP pipes with CTE less than 0.1 ppm/K and a CFRP main mirror support plate was analyzed under random vibration loads experienced during launch to verify the feasibility of such low expansion CFRP structures for space telescope applications.

Design

Two types of carbon fibers were used for the CFRP pipes: a high modulus K13C fiber from Mitsubishi Chemical, and a high strength, intermediate modulus T800 fiber from Toray. An EX1515 cyanate ester resin from Bryte Technologies was used for the matrix of the CFRP pipes.The inner diameter of the CFRP pipes was 30mm; the length was 500mm, and the layup was [0/0/70/-70/0/90]s, where the outer two 0 degree plies were K13C, and the remaining plies were T800.

The main mirror support plate was constructed from a CFRP honeycomb sandwich panel. Plain weave fabric incorporating high strength, high modulus M60J fibers from Toray were used for the skin and the low density core. High strength Toray T300 fibers were used for the high strength core. The material properties of these honeycomb cores are shown in Table.1. EX1515 resin was used for the matrix material of the skin. A [0/60/-60]s quasi-isotropic layup was used in the skin to provide equivalent properties in all directions. The core thickness was 25 mm.

Table1: Properties of honeycomb core

	Low density core	High strength core
E_L(Mpa)	490.0	861.8
Ew(Mpa)	255.0	441.3
P_L(Mpa)	1.00	2.79
Pw(Mpa)	0.48	3.14
?(g/cm3)	0.049	0.158

FEM analysis of CFRP structure

Strength analysis of CFRP truss pipes

In order to verify that the strength of CFRP is higher than the loads experienced when the telescope is launched, a coarse finite element method (FEM) analysis model of the full space telescope structure was constructed using bar and shell elements and analyzed under random vibration loads. The axial loads on the truss pipes were extracted from this model. The maximum axial load was 1 t, much lower than the 1.9 t measured axial strength of the CFRP pipe(Fig.2,Fig.3). It was concluded that it is possible to use extremely low expansion CFRP truss pipes for the structure of space telescope.

Fig.2:CFRP Pipe

Fig.3:Pipe mesurements set up

Strength analysis of main mirror support plate

In order to evaluate the strength of main mirror support plate, a detailed FEM model of the lower part of the space telescope was constructed, and analyzed under linear static loads equivalent to random vibration loads experienced during launch. By restricting the FEM model to the lower part of the space telescope, it was possible to modelthe skin and honeycomb core of the main mirror support plate, as well as the joints between the truss and the plate, in accurate detail.

The number of elements in the detailed FEM

analysis model, shown in Figure 4, was nearly 37000.The CFRP truss pipes were modeled with bar elements, the main mirror support plate with laminated plate and solid elements (the skin was modeled with laminate elements, the honeycomb core with solid elements), the center ring plate with plate elements, and the joint parts between the truss pipes and the main mirror support plate with solid elements.

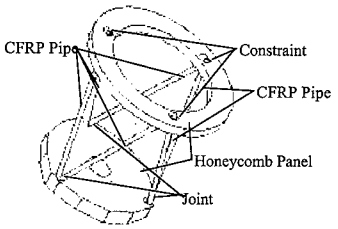

Fig.4:FEM analysis model

The 15.0 kg main mirror was modeled as a point mass at the center of main mirror support panel. It was expected that large stress concentrations would be observed near the connection points between the main mirror supports and main mirror support plate, and between the truss pipes and the main mirror support plate.

The points where the center ring plate is connected to the outer structure of the space telescope were fixed. Based on the results of the full telescope random vibration analysis presented above, the mass of each part in the analysis model was multiplied by the G level predicted for that part, and a uniform 1G load was applied to the entire analysis model.

Figure 5 shows the results of the initial FEM analysis. In this model only low density honeycomb core was used. As shown, high shear stress concentrations were observed around the joints between the truss pipes and the main mirror support plate.It was determined that the core would fail in shear during launch in the circled regions. To correct this deficiency, the low density core was replaced locally with high strength core, and the core segments were oriented to align the core direction of high strength (L-direction) with the direction in which the highest stresses were seen in the analysis results.(Fig.6,Fig.7).The results of analysis with this model are shown in Figure 8. With the increased core strength, the failure points due to shear stress seen in Figure 5 are gone, and the strength of the main mirror support plate for the space telescope was verified.

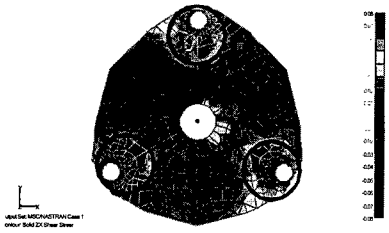

Fig.5:Analysis result of honeycomb core(shear stress)Without using high-strength cores

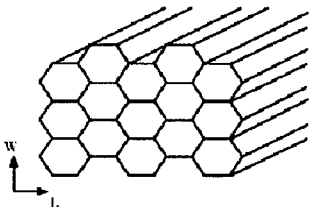

Fig.6:Cordinate system of honeycomb core

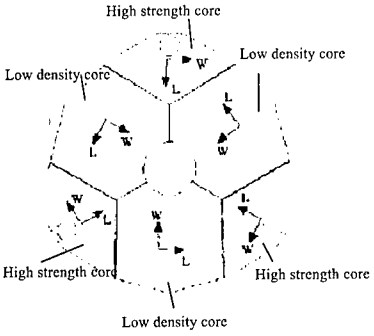

Fig.7:Direction of cores in panel

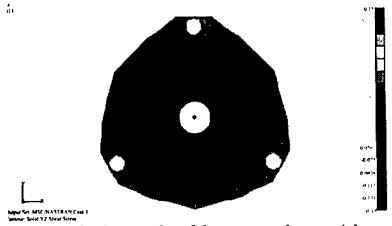

Fig.8:Analysis result of honeycomb core(shear stress)Using high strength cores

telescope was verified. Application to the upcoming SOLAR-B mission is expected to significantly reduce thermal deformation and telescope weight.

Summary

The structural integrity of low CTE CFRP truss pipes and a CFRP main mirror support plate was verified by comparing the results of analytic modeling with experimental strength data. Pipes designed for CTE less than 0.1 ppm/K were found to exceed strength requirements. By using high strength core locally for the points where high stress was seen, and aligning the core direction of high strength (L-direction) with the direction of high stress, a high strength, lightweight, and extremely low thermal deformation honeycomb sandwich panel design for the main mirror support plate that will survive launch loads was successfully achieved.

As a result, the feasibility of using of these elements for the optical equipment of a space

Reference

[1] Hidetaka Ishii and Tsuyoshi Ozaki,"FEM Analysis of CFRP Truss Pipes Structure for the Space Telescope" Proceedings of the 2001 Annual Meeting of JSME/MMD , pp79-80

Proceedings of 7th Japan International SAMPE
Symposium & Exhibition, Nov. 13-16, 2001

Buckling of Composite Structures with Higher-order Shear Deformation

Qing-Qing Ni, Jia Xie and Zenichiro Maekawa

Division of Advanced Fibro-Science, Kyoto Institute of Technology,
Matsugasaki, Sakyo-ku, Kyoto, 606-8585, Japan
Email: nqq@ipc.kit.ac.jp

Abstract

Recent researches verified that out-plane shear deformation was very important for the buckling analysis of composite structures. The key points for buckling analysis are to take account of shear deformation and to find a suitable displacement function to represent arbitrary edge conditions. In this paper, a higher-order shear deformation plate theory and the Ritz displacement function that takes the products of a two-dimensional polynomial function and a boundary function were used for buckling analysis.
Using higher-order shear deformation theory, the results were more accurate compared with thin theory or one-order shear deformation theory. Using the displacement function of the two-dimensional polynomial, arbitrary edge conditions of composite plates could be calculated, and a unified buckling analysis is established. Then the optimal lamination angle at which the non-dimensional buckling load is largest was obtained in any edge condition, and the buckling mode was represented, which is very useful for prediction of the buckling characteristics.

Keywords: Buckling, Shear deformation, Composite plates

Introduction

Fiber reinforced composite materials have been extensively used in modern engineering applications, due to their high specific strength and modulus. In such applications, buckling behavior may often be observed. In buckling analysis, classical thin plate theory is frequently used due to its analytical simplicity without considering the out-of-plane shear deformation. However, this simplification has resulted in a significant difference in some structural composite materials due to low out-of-plane shear modulus and/or significant thickness of the plate. In order to evaluate this difference, several shear-deformation theories have been proposed for buckling analysis by Reddy [3] and others. In this paper, the displacement function of a two-dimensional polynomial and a higher-order shear deformation plate theory were utilized. The laminated composite plates under combined shear and biaxial compression loading were investigated, and the critical buckling loads and buckling modes were obtained with various boundary conditions.

Analysis

The Rayleigh-Ritz method is usually used in buckling analysis. However the buckling load was obtained only under limited boundary conditions. The key point for buckling analysis is to find a suitable displacement function to represent specified

edge conditions. In previous work by one of the present authors [1-2], the pb-2 Ritz displacement function [4], which consists of the product of a basic and a two dimensional polynomial function, was used to analyze laminated composite plates with free, simply supported, and/or clamped edges. Here the higher-order shear deformation is taken into account.

Energy Expressions

The higher-order shear deformation theory developed [3] yields the following displacement field:

$$\begin{aligned} u_t(x,y,z) &= u_0(x,y) + z\theta_x(x,y) - \frac{4}{3t^2}z^3\left[\theta_x(x,y) + \frac{\partial w}{\partial x}\right] \\ v_t(x,y,z) &= v_0(x,y) + z\theta_y(x,y) - \frac{4}{3t^2}z^3\left[\theta_y(x,y) + \frac{\partial w}{\partial y}\right] \\ w_t(x,y,z) &= w_0(x,y) \end{aligned} \quad (1)$$

where $w_0(x, y)$ is the displacement along the z-axis in the middle plane. $\theta_x(x, y)$ and $\theta_y(x, y)$ are the bending slopes along the x-axis and y-axis, respectively.

The total potential energy for a composite plate is given by

$$\Pi = \frac{1}{2}\int_V \Delta\varepsilon_L^T [\bar{Q}] \Delta\varepsilon_L dV + \int_V \tau^T \Delta\varepsilon_N dV \quad (2)$$

where ε_L , ε_N are strains of the linear and non-linear items, respectively. τ^T is the stress tensor. For combined shear and compression, it results in the following form.

$$\tau^T = \{-N_x/t \quad -N_y/t \quad -N_{xy}/t \quad 0 \quad 0\} \quad (3)$$

N_x, N_y are the applied compression stresses in the x and y direction, respectively, and N_{xy} is the shear stress.

Polynomial Displacement Functions

The following polynomials are used in the present analysis [4].

$$\begin{aligned} w_0(\xi,\eta) &= \sum_{i=1}^{n} c_i \phi_i(\xi,\eta) \\ \theta_x(\xi,\eta) &= \sum_{i=1}^{n} d_i \psi_{xi}(\xi,\eta) \\ \theta_y(\xi,\eta) &= \sum_{i=1}^{n} e_i \psi_{yi}(\xi,\eta) \end{aligned} \quad (4)$$

where,

$$\begin{aligned} \phi_i(\xi,\eta) &= f_i(\xi,\eta)\phi_{xi}(\xi,\eta) \\ \psi_{xi}(\xi,\eta) &= g_{xi}(\xi,\eta)\psi_{xI}(\xi,\eta) \\ \psi_{yi}(\xi,\eta) &= g_{yi}(\xi,\eta)\psi_{yI}(\xi,\eta) \end{aligned} \quad (5)$$

Here, the normalized coordinates $\xi = x/a$, $\eta = y/b$ are used. c_i, d_i, e_i are coefficients; f_i, g_{xi}, g_{yi} are two-dimensional polynomials; and ϕ_I, ϕ_{xI}, ϕ_{yI} are boundary functions.

Substituting the above displacement function into equation (2), and minimizing the total energy by differentiation, the buckling load and mode can be obtained.

Numerical results

The mechanical properties of a laminate used in the analysis are as follows.

$b = 500$ mm, $a/b = 1$, $b/t = 10$

$E_2 = 10.0$ GPa, $G_{12} = 0.5E_2$, $\nu_{12} = 0.25$

$E_1/E_2 = 25$, $G_{13} = 0.5E_2$, $G_{23} = 0.3E_2$

where, a, b are plate size in x and y direction, respectively. t is the plate thickness. ν_{21} is determined by the reciprocal theorem, whilst the non-dimensional buckling load is defined as:

$$K = Nb^2 / \pi^2 D \quad (7)$$

where $D = E_2 t^3 / [12 (1 - \nu_{12}^2)]$.

To compare first-order shear deformation theory (FSDT) and higher-order shear deformation theory (HSDT), the results of buckling loads for laminated composite plates by using these two theories are shown in Table 1. It can be seen that the difference is noted. When the ratio of the width to thickness, b/t, is small, i.e., the plate is thick, the difference by these two theories becomes large. This indicates that the buckling load will be larger, that is the structures will be more dangerous by the FSDT than by the HSDT.

Symmetrically laminated square plates

Symmetrically laminated cross-ply or angle-ply square plates were used in this

analysis. The cases of biaxial compression loading, combined with positive shear ($N_{xy}/N_x=1$) were investigated. Figure 1 shows the effect of *b/t* on buckling load for symmetrically laminated cross-ply plates. It is shown that for the ratio *b/t*>40, the effect of *b/t* becomes small, and after this it seems to be constant. The buckling load for *b/t*>40 in the clamped 4 edges is almost three times larger than that in the simply supported 4 edges boundary condition. Figure 2 shows the effect of lamination angle on buckling load for symmetrically laminated angle-ply plates in three different boundary conditions. It is found that the buckling load is symmetrical and has a maximum value at the lamination angle of 45° for the clamped 4 edges and simply supported 4 edges conditions. However, it was unsymmetrical with the maximum value at angle of about 40^0 in the clamped 2 edges and simply supported 2 edges condition. The cases of biaxial compression loading, combined with negative shear load ($N_{xy}/N_x=-1$) were also investigated. For symmetrically laminated cross-ply plates, the effect of aspect ratio *a/b* on the non-dimensional buckling load for three types of supported conditions, combined with positive or negative shear load is shown in Fig.3. It can be seen that when *a/b* is less than 1, the non-dimensional buckling load decreased rapidly, and it becomes to be constant from *a/b*=2 and, the

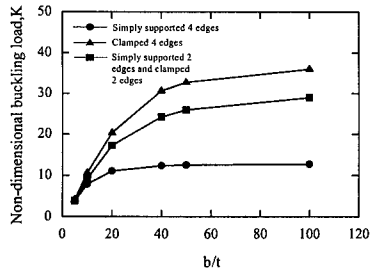

Fig.1 Effect of *b/t* on the Non-dimensional buckling load for (0/90 deg)s laminated composite plates.

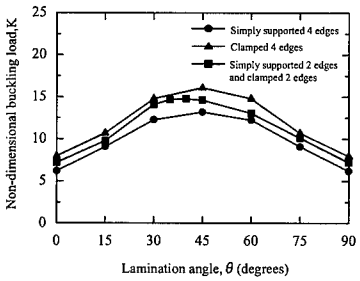

Fig.2 Effect of different supported conditions on the buckling load for (θ /- θ)s laminated composite plates.

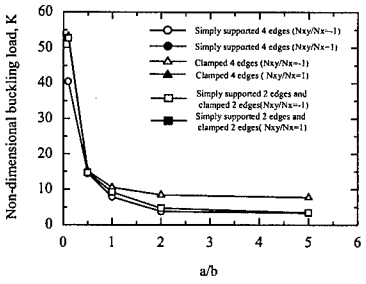

Fig.3 Effect of aspect ratio *a/b* on the buckling load combined with positive or negative shear load for symmetric cross-ply laminates.

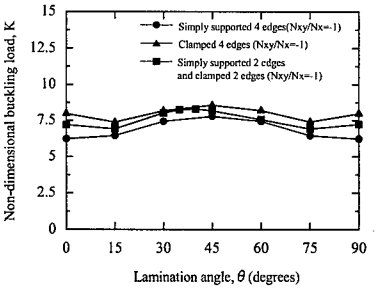

Fig.4 Effect of different supported conditions on the buckling load combined with negative shear load for symmetric angle-ply laminates.

two different cases almost get the same values, that is the direction of shear loading has no effect on the buckling load. But for symmetrically laminated angle-ply plates, in comparison with Fig.2, the non-dimensional buckling loads combined with a negative shear load presented in Fig.4 are much lower than those with a positive shear load. This means that for symmetrically angle-ply laminates, the direction of shear loading has significant effect on the non-dimensional buckling load.

buckling mode

The buckling modes for the laminated composite plates under simply supported condition have been obtained Figs 5 and 6 show the buckling modes of symmetrically cross-ply plates subject to biaxial compression loading combined with a positive or negative shear load. These figures illustrate how the buckling behavior is affected by shear loading direction. Using these figures, the buckling behavior may be predicted much clearer.

References

[1] Q-Q. Ni, S. Kataoka, Transactions of the JSME (A), Vol.64, 522-528 (1998).

[2] Q-Q. Ni, J. of Soc. Mat. Sci., Japan, Vol.46, 1362-1368 (1998).

[3] J. N. Reddy, J. Appl. Mech., Vol.51, 745 (1984)

[4] K. M. Liew, C. M. Wang, Eng. Struct., Vol. 15, 55-60 (1993).

[5] Timoshenko, S. P. & Gere, J. M., *Theory of Elastic Stability* (2nd edn).McGraw-Hill, New York, 1961.

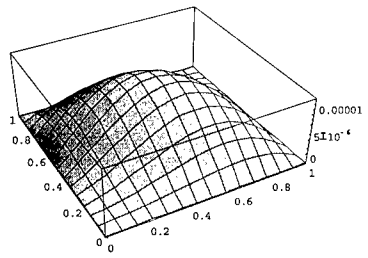

Fig.5 Representation of the buckling mode for a $(0^{\circ}/90^{\circ})$s laminated composite plates under biaxial compression loading combined with positive shear load.

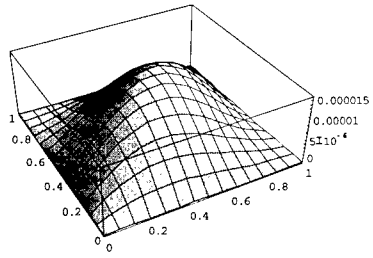

Fig.6 Representation of the buckling mode for a $(0^{\circ}/90^{\circ})$s laminated composite plates under biaxial compression loading combined with negative shear load.

Table 1 Effect of HSDT and FSDT on Non-dimensional buckling load, K.

	4S		4C		2S and 2C	
b/t	K (HSDT)	K (FSDT)	K (HSDT)	K (FSDT)	K (HSDT)	K (FSDT)
5	3.2183	4.0625	3.2525	4.1676	3.2183	4.1082
10	7.7934	8.7620	8.5633	10.4983	8.1798	9.7381
20	11.7989	12.2058	15.8418	17.8045	14.1898	15.5327
50	13.6895	13.7752	22.2289	22.9399	18.6988	19.1957
100	14.0279	14.0095	23.8625	24.0963	19.8160	19.9817

Proceedings of 7th Japan International SAMPE
Symposium & Exhibition, Nov. 13-16, 2001

Damage Accumulation in Composite Laminates under Quasi-Static Transverse Loading

Yuichiro Aoki [1] and Hiroshi Suemasu [2]

1: Graduate Student, Department of Mechanical Engineering, Sophia University
2: Department of Mechanical Engineering, Sophia University
7-1 Kioicho Chiyoda-ku Tokyo 102-8554 Japan
E-mail: aoki-y@sophia.ac.jp

Abstract

A numerical analysis is performed to study an impact damage in composite laminates. A special interface element is proposed to simulate the delamination propagation in laminates. The energy stored in the element per unit area is equal to the interlaminar fracture toughness. This element is incorporated in a commercially available finite element code and applied to the DCB problem. The convergence of the solution is quite smooth, good agreement with the theoretical results is obtained. The present method is applied to the damage accumulation problem of CFRP laminates.

Key Words: Composite laminate, Interface, Delaminations, Finite element analysis

Introduction

Composite laminates are used in many engineering applications such as aerospace structures because of the need for reducing weight. But structures made of composite laminates are susceptible to impact damage [1-4]. The impact damages, being difficult to detect from outside of structures, may cause severe reduction of compressive strength (Compression after impact: CAI)[4]. Design loads of the structures are often limited by the degraded compressive performance due to possibilities of the existence of these damages. Therefore, the mechanism of damage accumulation due to impact must be well understood in order to utilize composite laminated structures to their full advantage.

Many researchers have studied the failure process of composite laminates based on the damage mechanics [e.g.5,6]. To know the delamination propagation problem, however, the damage-mechanics-based analyses may not be sufficient and fracture mechanical theory must be incorporated. Suemasu et. al have explained a damage propagation problem in axi-symmetric plate subjected to quasi-static loading analytically[7,8] and numerically[9]. Aoki has numerically studied the stability of the damage by three-dimensional finite element analysis [10].

In the present paper, a mechanism of damage accumulation in composite laminates is numerically studied by using three-dimensional finite element method. A special interface element is proposed to simulate the delamination propagation hereafter.

Finite element analysis

Modeling of quasi-isotropic laminates

A square composite laminate (150 mm × 150 mm × 4 mm) of stacking sequence

$[-45/90/45/0]_4$ shown in Fig.1 is numerically solved. Elastic properties of each ply are summarized in Fig.1. Multiple circular delaminations (diameters d = 20 mm) are placed at its center is calculated. A commercially available finite element code of

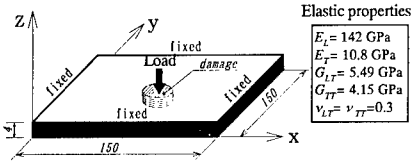

ABAQUS 5.8 is adopted.

Fig.1 Composite laminates subjected to a concentrated load

A finite element mesh is shown in Fig.2. A three-dimensional 20-node isoparametric brick elements and 15-node wedge elements (only at the center of the delaminated area) are used. The geometrical nonlinearity due to the finite deflection is considered. Contact problem at the delaminated surfaces is considered through using a nonlinear spring element between the double nodes at the delaminated surface, which has high stiffness in compressive direction and no resistance in tensile direction. Energy release rates are calculated along the circular delaminations by using virtual crack closure technique.

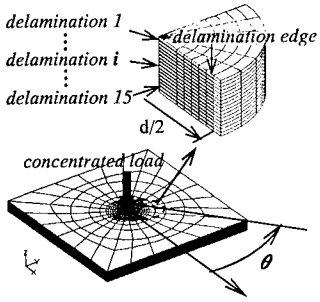

Fig.2 Finite element mesh of square laminate

Interface element

An interface element is proposed to simulate the damage propagation. A 16-node element is developed to incorporate between the 20-node brick element (Fig.3). The elements which need to have no thickness are placed where delaminations are expected to propagate. In this figure, x, y, z and ξ, η are global and local coordinate system, respectively.

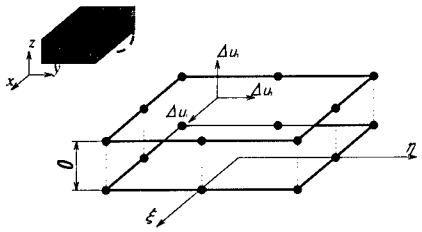

Fig.3 Interface element

The relative displacements Δu_k between the double nodes in in-plane (k=1,2) and out-of-plane (k=3) directions are defined as

$$\Delta u_k = \sum_{i=1}^{8} \phi_i(\xi,\eta)\Delta u_k^{(i)} \quad (k = 1,2,3) \quad (1)$$

where $\phi_i(\xi, \eta)$ are shape functions. The energy $\Phi(\xi, \eta)$ stored in a unit area is defined as

$$\Phi(\xi,\eta) = G_t\left[1-\exp\{-\varphi(\xi,\eta)\}\right] + \frac{1}{2}k_c\left(|\Delta u_3| - \Delta u_3\right)^2 \quad (2)$$

$$\varphi(\xi,\eta) = \alpha\Delta u_3^{\,2} + \beta(\Delta u_1^{\,2} + \Delta u_2^{\,2})$$

where G_t is critical total energy release rate, and α and β are coefficients associated with critical relative displacements. The second term in Eq.(2) is introduced to consider the contact problem. The stored energy and traction are plotted against a relative displacement Δw in Fig.4. The traction is defined to reduce when the relative displacement exceeds a certain value. This interface element is incorporated into the finite element code by using the USER SUBROUTINE command.

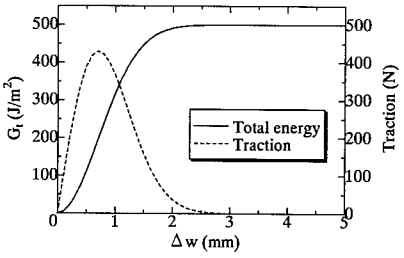

Fig.4 Relationship between potential energy and traction

Numerical results

Energy release rate distribution

The energy release rate distributions along the delaminations are computed for the damaged model. Fig.5 shows the distributions of the total energy release rates when the applied load is 300 N. The center displacement was about 0.4 mm for this case. The nonlinearity is not significant at this displacement level. The energy release rate tends to be large at the mid-surface, where transverse shear stress (τ_{xz} and τ_{yz}) is usually maximum. The energy release rate at the delaminations near the both surfaces tends to be large in the stiffer principal material direction of the delaminated portion outsides the corresponding delamination. The distributions are almost uniform at the delamination inside. It is because anisotropy of the portions outside the delamination are weak.

Fig.6 shows the distributions of the total energy release rates when P=2280N. Center displacement is about 1.5 mm, which is 6 times larger than the delaminated ligaments. The fiber directions of the layers just above and below each delamination are indicated by the shorter and longer lines with arrows in each figure. The maximum value exceeds 200 J/m^2 and the delaminations may propagate around this load level. The direction of maximum energy release rate changes from the material principal direction of the upper delaminated portion to that of the layer just below. The difference between the radial moduli of the layers above and below the delamination is plotted in Fig.7. The shape is similar to the energy release rate distribution.

We may conclude that the distribution of energy release rate is dominated by the value of the material elastic property when the deflection is small and bending is dominant and by the stiffness difference of the laminas just below and above the delamination when the deflection is large and the in-plane stress is dominant.

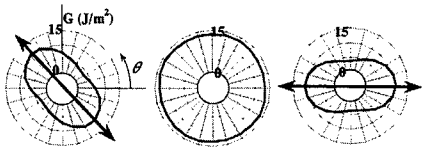

Fig.5 Energy release rate distribution along the delamination edges at P=300 N

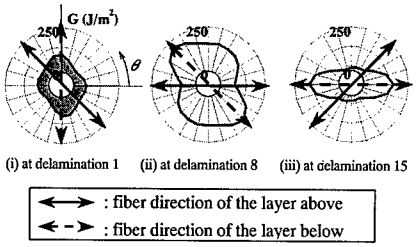

Fig.6 Energy release rate distribution along the delamination edges at P=2280 N

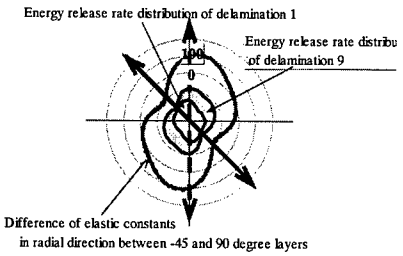

Fig.7 The stiffness difference between the layers whose orientations are -45° and 90°

Analysis of crack propagation

To demonstrate the validity of the present interface element, crack propagation in a double cantilever beam (25 mm×150 mm×4 mm) is solved as a three-dimensional problem. The length of an initial delamination is 30 mm. Elastic properties of the composite are same as that of the ply of the square laminate. The fiber direction is same as the beam axis.

The finite element mesh is shown in Fig.8. The values of critical total energy release rate used in this analysis are 200, 500, 600 J/m^2. Coefficients α and β are 100 mm^{-2}, which means that the maximum stress is attained at the relative displacement of 0.065 mm. The analysis is performed by a displacement control.

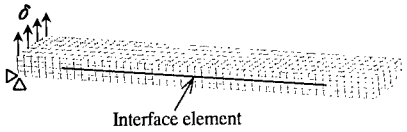

Fig.8 Double cantilever beam and finite element modeling

The applied load is plotted against crack opening displacement in Fig.9. Since the process zone is large, stiffness of the beam reduces at the very early stage of loading. The present results agree well with theoretical ones based on a beam theory plotted by broken lines in the propagation stages.

The distribution of the normal stress σ_{33} at the plane of delamination is shown in Fig.10.

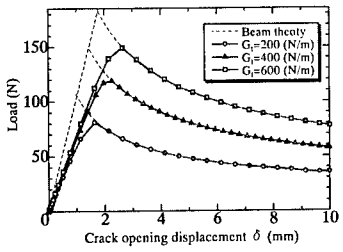

Fig.9 Relationship between load and crack opening displacement

Stress in the newly delaminated surface is nearly zero and reaches maximum at the crack tip area. The area of high stress shows an edge effect. The process zone, that is, stress increased area in this figure is fairly large.

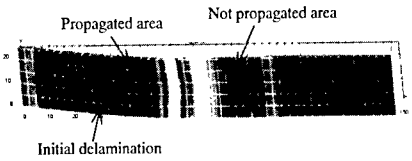

Fig.10 Stress distribution at the interface

Summary

The mechanism of damage accumulation during impact is well disclosed by the present finite element analysis through the energy release rate distributions. We could propose an efficient interface element for crack-like damage propagation for three-dimensional problem.

References

1. S. Liu and F. K Chang : J. Composite Materials, 28, 10, 1994, 940-977.
2. S. A. Hichen et. al : Composites, 26, 1995.
3. Shang-Lin Gao, et.al: Proceedings of ICCM-11, Gold Coast, Australia, 14th-18th July 1997.
4. T. Ishikawa, et. al : Composite Science & Technology, 55, 1995, 349-363.
5. O. Allix and P. Ladevèze : Composite Structures, 22, 1992, 257-267.
6. V. Albouys, et. al : Proceedings of ICCM-12, Paris, France, 5th-9th July 1999.
7. H. Suemasu and O. Majima : J. Composite Materials, 30, 4 ,1996, 441-453.
8. H. Suemasu and O. Majima : J. Composite Materials, 32, 2 ,1998, 123-140.
9.O.Majima and H.Suemasu : J. Japan Society for composite materials, 26,6,2000,219-226
10.Y.Aoki and H.Suemasu : Trans.Japan Society of Mechanical Engineers, A, in press

Proceedings of 7th Japan International SAMPE
Symposium & Exhibition, Nov. 13-16, 2001

A Phenomenological Constitutive Model for Off-Axis Viscoplastic Behavior of Unidirectional CFRP

M. Kawai [1] and Y. Masuko [2]

[1] Institute of Engineering Mechanics and Systems,
University of Tsukuba, Tsukuba, Ibaraki 305-8573, JAPAN
E-mail: mkawai@kz.tsukuba.ac.jp
[2] Graduate School of Systems and Information Engineering, University of Tsukuba

Abstract

A constitutive model to describe the rate-dependent behavior of unidirectional fiber-reinforced composites is developed from phenomenological points of view. Unidirectional composites are assumed to be transversely isotropic. Constitutive modeling is based on the irreversible thermodynamics with internal variables. Constitutive relations are systematically derived from the free energy and dissipation functions; these thermodynamic potentials are defined using a transversely isotropic tensor of the fourth rank. Validity of the proposed model is evaluated on the basis of the stress-strain responses of a thermoplastic resin system under different loading-rate conditions at elevated temperature.

Key Words: Unidirectional Composite, Off-axis Loading, Viscoplasticity, Constitutive Modeling

Introduction

Nonlinear deformation of polymer matrix composites depends on time, loading rate and temperature, which becomes more significant under off-axis loading conditions. This is due to the inherent characteristics of the polymer matrices employed. For accurate evaluation of the performance and life of the structural components made of polymer matrix composites, therefore, it is crucial to develop engineering procedures to predict the deformation and fracture by appropriately considering the time, rate and temperature dependence.

Macromechanical modeling of the viscoplastic behavior of unidirectional fiber systems was attempted by Sun and coworkers [1,2]. Gates and Sun [1] extended the time-independent Sun-Chen model [3] for plane stress conditions to develop a viscoplasticity model based on overstress. Yoon and Sun [2] proposed another plane-stress viscoplasticity model; they extended the Bodner-Partom model [4] for the viscoplastic behavior of isotropic materials using the effective stress and effective inelastic strain of the Sun-Chen model [3]. By comparison with experimental results, it is shown that the Gates-Sun model [1] and the Yoon-Sun model [2] can describe the monotonic tensile deformation behavior and its rate-dependence for unidirectional polymer matrix systems under plane-stress off-axis loading conditions at room and high temperatures.

In these viscoplasticity models, a single scalar internal variable is assumed to describe the rate-dependent nonlinear behavior. However, it has not been validated

experimentally that the internal state associated with the macroscopic inelastic deformation of unidirectional fiber composites is represented in terms of an isotropic scalar variable. Actually, the Bauschinger effect has been observed for the fiber-reinforced composites subjected to tensile pre-strain in the range of nonlinear response [5]. Such an anisotropic response cannot be described in terms of a single scalar variable. To represent accurately the internal state associated with the macroscopic inelastic behavior of fiber-reinforced composites from macroscopic and phenomenological points of view, therefore, both scalar and tensor (second rank or even higher) variables are required.

The present study aims to develop a three-dimensional constitutive model to describe the viscoplastic behavior of unidirectional fiber-reinforced composites from a macromechanics point of view. A particular emphasis is placed on a general formulation in which the internal state associated with inelasticity is described using both isotropic (scalar) and kinematic (tensor of the second rank) hardening variables. The formulation is based on the irreversible thermodynamics [6] for the inelastic behavior of transversely isotropic continua. Applicability of the proposed constitutive model is evaluated by comparing the predicted and experimental results on unidirectional AS4/PEEK under monotonic off-axis tensile loading at different strain-rates and stress-rates [7].

Viscoplasticity Model for Transversely Isotropic Materials

For two tensors $\mathbf{x}$ and $\mathbf{y}$ of the second rank, the trace operation $tr(\mathbf{xy})$ is denoted as $\mathbf{x}\cdot\mathbf{y}$ in the following.

State Relations of Internal Variables

At any instant of monotonic inelastic deformation, it is assumed that the internal state is described by a scalar ρ and a symmetric second-rank deviatoric tensor $\boldsymbol{\xi}$. To define the thermodynamic force variables associated with the assumed internal variables, the Helmholtz free energy ψ is introduced. If uncoupled physical processes take place at the same time, the total free energy function is expressed by the sum of the free energy functions for respective processes [6]. In the present study, the free energy is expressed as

$$\psi = \psi_e(\boldsymbol{\varepsilon}^e) + \psi_p(\boldsymbol{\xi}, \rho) \tag{1}$$

where $\boldsymbol{\varepsilon}^e$ is the elastic strain tensor; i.e. the difference between the total strain $\boldsymbol{\varepsilon}$ and the viscoplastic strain $\boldsymbol{\varepsilon}^p$:

$$\boldsymbol{\varepsilon}^e = \boldsymbol{\varepsilon} - \boldsymbol{\varepsilon}^p \tag{2}$$

The free energy components in the right-hand are specified as

$$\psi_e(\boldsymbol{\varepsilon}^e) = (1/2)\boldsymbol{\varepsilon}^e \cdot \mathbf{C}\boldsymbol{\varepsilon}^e \tag{3}$$

$$\psi_p(\boldsymbol{\xi}, \rho) = (1/3)H\,\boldsymbol{\xi}\cdot\boldsymbol{\xi} + h(\rho) \tag{4}$$

where $\mathbf{C}$ in Eq. (3) denotes the transversely isotropic elastic tensor of the fourth rank, H in Eq. (4) is a material constant and $h(\rho)$ represents a positive function of the scalar internal variable.

From the assumed free energy, the thermodynamic forces $\boldsymbol{\sigma}$, $\mathbf{p}$ and r associated with $\boldsymbol{\varepsilon}^e$, $\boldsymbol{\xi}$ and ρ are obtained as

$$\boldsymbol{\sigma} = \partial\psi / \partial\boldsymbol{\varepsilon}^e = \mathbf{C}(\boldsymbol{\varepsilon} - \boldsymbol{\varepsilon}^p) \tag{5}$$

$$\mathbf{p} = \partial\psi / \partial\boldsymbol{\xi} = (2/3)H\boldsymbol{\xi} \tag{6}$$

$$r = \partial\psi / \partial\rho = \partial h / \partial\rho \tag{7}$$

Evolution Equations of Internal Variables

To prescribe the evolution equations of the assumed internal variables, a dissipation function is defined. To derive the non-linear hardening format of Armstrong-Frederick type [6], we assume the following form:

$$\Omega_{vp} = [K_0/(m+1)]W_{vp}^{\,m+1} \tag{8}$$

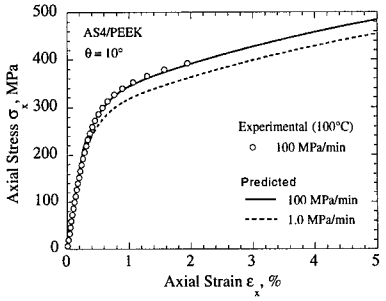

Fig.1 Predicted off-axis stress strain curves for $\theta = 10°$

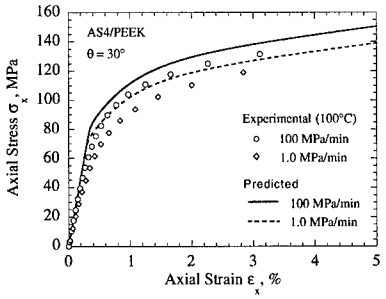

Fig.2 Predicted off-axis stress strain curves for $\theta = 30°$

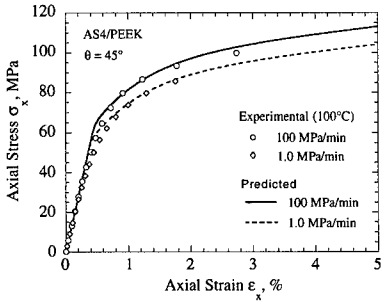

Fig.3 Predicted off-axis stress strain curves for $\theta = 45°$

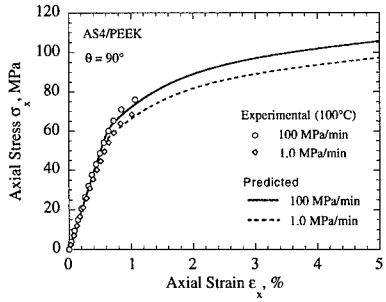

Fig.4 Predicted off-axis stress strain curves for $\theta = 90°$

The invariant function W_{vp} in the right-hand side is specified as

$$\mathbf{s}^* = \mathbf{s} - \mathbf{p} \tag{9}$$

$$W_{vp} = W + (L/2H)\sqrt{(3/2)\mathbf{p}\cdot\mathbf{A}\mathbf{p}}^2 - (HL/2)\sqrt{(2/3)\boldsymbol{\xi}\cdot\mathbf{A}\boldsymbol{\xi}}^2 \tag{10}$$

$$W = \left\langle U(\mathbf{A},\mathbf{s}^*) - r - \sigma_0 \right\rangle \tag{11}$$

$$U(\mathbf{A},\mathbf{s}^*) = \sqrt{(3/2)\mathbf{s}^*\cdot\mathbf{A}\mathbf{s}^*} \tag{12}$$

where $\mathbf{s}$ in Eq. (9) is the deviatoric part of the Cauchy stress $\boldsymbol{\sigma}$, σ_0 in Eq. (11) represents the size of the initial elastic region, i.e. $U(\mathbf{A},\mathbf{s}) = \sigma_0$, and K_0, L and m denote material constants. The angular brackets < > define the operation: <x> = x ($x \geq 0$); <x> = 0 ($x < 0$), i.e. the Macauley brackets. The stress invariant U (i.e. equivalent stress) is defined in terms of the fourth rank tensor $\mathbf{A}$ that describes the initial anisotropy (transverse isotropy). It is assumed that $\mathbf{A}$ transforms a deviatoric tensor (of the second rank) to another deviatoric tensor; this condition is imposed so that the derived viscoplastic strain would satisfy the incompressibility.

The time-rate of the viscoplastic strain is derived from Eq. (8) as

$$\dot{\boldsymbol{\varepsilon}}^p = \nu_0(\partial\Omega_{vp}/\partial\mathbf{s}) = (3\dot{P}/2U)\mathbf{u} \tag{13}$$

where

$$\dot{P} = v_0 K_0 W^m = K W^m \quad (14)$$

$$\mathbf{u} = \mathbf{A}\mathbf{s}^* \quad (15)$$

In the same way, we can obtain the time-rate of the assumed internal variables as

$$\dot{\boldsymbol{\xi}} = -v_0(\partial\Omega_{vp}/\partial\mathbf{p}) = \dot{\boldsymbol{\varepsilon}}^p - (3L/2H)\dot{P}\mathbf{v} \quad (16)$$

$$\dot{\rho} = -v_0(\partial\Omega_{vp}/\partial r) = \dot{P} \quad (17)$$

where

$$\mathbf{v} = \mathbf{A}\mathbf{p} \quad (18)$$

Taking into account Eqs. (6) and (7), the time rates of the kinematic-hardening and isotropic-hardening variables can be expressed as

$$\dot{\mathbf{p}} = (2/3)H\dot{\boldsymbol{\varepsilon}}^p - L\dot{P}\mathbf{v} \quad (19)$$

$$\dot{r} = (\partial^2 h/\partial\rho^2)\dot{P} \quad (20)$$

Simulation

To examine the applicability of the proposed viscoplasticity model, the off-axis tension behavior of unidirectional AS4/PEEK at different strain rates and stress rates [7] is simulated.

Predictions using the proposed combined hardening model and its isotropic and kinematic hardening versions agree with each other when monotonic tensile behavior is analyzed. Since the present study primarily aims to evaluate the predictive capability of the rate-dependent nonlinear behavior under off-axis loading, the simulation using the isotropic hardening model is presented.

The predictions for the off-axis tensile behavior at two different stress rates of 100 and 1.0 MPa/min are compared with the experimental results in Figs. 1(a)–(c). These figures show the verification of the proposed model for the viscoplastic behavior under monotonic loading conditions, since the material constants of the constitutive model have been identified using the constant strain-rate test results. From these figures, it is obvious that the macromechanics model favorably describes the rate dependence of the off-axis nonlinear behavior for the unidirectional AS4/PEEK at high temperature.

Conclusion

A three-dimensional macroscopic constitutive model to describe the viscoplastic behavior of unidirectional fiber composites has been developed on the basis of irreversible thermodynamics approach. A particular emphasis is placed on a general description of the internal state associated with viscoplasticity of material using scalar and second-rank tensor variables. A basic analysis of the rate-dependent nonlinear deformation of unidirectional AS4/PEEK under off-axis loading at high temperature was made using the proposed model. The proposed model succeeds in accurately describing the nonlinearity and the rate dependence of the off-axis tensile behavior of unidirectional AS4/PEEK at high temperature.

References

1. T.S. Gates and C.T. Sun: AIAA Journal, 29(3), 457 (1991).
2. K.J. Yoon and C.T. Sun: J. Composite materials, 25, 1277 (1991).
3. C.T. Sun and J.L. Chen: J of Composite Materials, 23, 1009 (1989).
4. S.R. Bodner and Y. Partom: ASME J. Applied Mechanics, 42, 385 (1975).
5. G.J. Dvorak and M.S.M. Rao: Int. J. Eng. Sci., 14, 361 (1976).
6. J. Lemaitre and J.L. Chaboche: *Mechanics of Solid Materials*, (1985), Cambridge University Press.
7. M. Kawai, Y. Masuko, Y. Kawase, and R. Negishi: International Journal of Mechanical Sciences, 43(9), 2069 (2001).

Proceedings of 7th Japan International SAMPE
Symposium & Exhibition, Nov. 13-16, 2001

Modeling of Bearing Failure in Bolted Composite Joints

Yi XIAO# and Takashi ISHIKAWA#

#: Advanced Composites Evaluation Technology Center, National Aerospace Laboratory
6-13-1, Osawa, Mitaka-shi, Tokyo, 181-0015, Japan
E-mail xiaoyi@nal.go.jp

Abstract

A modeling of bearing failure has been developed using general-purpose FEM code ABAQUS in the bolted composite joints. The fundamental approach consists of contact problem at the pin/hole interface, progressive damage, large deformation problem and material nonlinear problem. A complex approach based on a nonlinear shear elasticity theory of Hahn & Tsai fused with a continuum damage mechanics (CDM) approach can be also utilized to represent the material nonlinear behavior during loading. The damage accumulation criteria using the hybrid method based on Hashin and Yamada-Sun's failure criteria are adopted, and the stress redistribution analysis using a degradation model for the damaged ply is performed.

Key words: *CFRP Laminated Composites, Bearing Failure, Progressive Damage, Continuum Damage Mechanics (CDM).*

Introduction

Degradation and failure of aircraft structures are frequently initiated at the joints, so that safety, durability and reparability are strongly influenced by the adequacy of joint design. The next generation supersonic transport (SST) aircraft make extensive use of advanced composite materials in both primary and secondary structure, and the mechanically fastened joints have been used.

The main aim of the study describe here is to develop a model of bearing failure in the bolted composite joints, which is easy to implement and easy to use, moreover, has only a few parameters. The fundamental approach consists of contact problem at the pin/hole interface, progressive damage, large deformation problem and material nonlinear problem. A complex approach based on a nonlinear shear elasticity theory fused with a damage mechanics approach can be also utilized to represent the material nonlinear behavior during loading. The damage accumulation criteria using stress based on the hybrid method of Hashin and Yamada-Sun's failure criteria are adopted, and the stress redistribution analysis using a degradation model for the damaged ply is performed. The accurate prediction result includes progressive damage and strength response of the joints that agrees well with the existing experimental data.

Analytical Modeling

Experimental characterization

In order to evaluate the relationship between bearing strength and damage progress behavior in bolted composite joints, a detailed and significant experimental investigation have been performed in the authors previous works [1]. Based on the experimental observation, major mechanism of the bearing failure can be explained in following.

(1) The microscopic damage behavior such as the fiber kink-band of 0° plies and delamination appeared to be the dominant mode in the onset of damage. Out-of-plane shear cracks and large-scale delamination were the major reason for final failure.

(2) Lateral constraint condition by the washer suppressed out-of-plane deformation, and it was recognized as an important parameter to improve the joint strength.

Table 1. Damage variable FV_i and failure index

Failure mode	Failure index	Damage variable
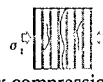 Matrix compression failure	$\sigma_2 \le 0,\ e_m^2 = \left(\frac{\sigma_2}{Y_c}\right)^2 + \left(\frac{\sigma_{12}}{S_c}\right)^2$ (Hashin failure criteria)	FV_1 (D_2, D_6)
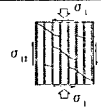 Fiber compression-shear failure	$\sigma_1 \le 0,\ e_{fs}^2 = \left(\frac{\sigma_1}{X_c}\right)^2 + \left(\frac{\sigma_{12}}{S_c}\right)^2$ (Yamada-Sun failure criteria)	FV_2 (D_1, D_2, D_6)

The matrix compression failure and fiber compression-shear failure (fiber buckling or kink-band of 0° plies) are dominant in-plane failure modes in laminated composites under compression. Therefore, the principal objective in this study is that an accumulative damage model will be developed to estimate the extent of in-plane compression damage for the bearing failure mode in composite joints.

Nonlinear Shear Constitutive Relationship

It is well know that unidirection composites show a nonlinear behavior for the shear deformation along the fiber direction without damage. Hahn & Tsai formulated the nonlinear shear stress/strain relationship using a high order elasticity theory [2], and it can be written in following simple form

$$\varepsilon_{12} = G_{12}^{-1}\sigma_{12} + \alpha\sigma_{12}^3 \qquad (1)$$

where G_{12}, σ_{12}, ε_{12} are the initial ply shear modulus, shear stress, shear strain, respectively. α is a nonlinear parameter constant of the material that has to determined experimentally.

Next, the function given by Eq. (1) has to be rewritten in an incremental form in the following equation to be implemented in a finite element program.

$$\sigma_{12}^{(i+1)} = \frac{1 + 2\alpha\left(\sigma_{12}^{(i)}\right)^3\left(\varepsilon_{12}^{(i)}\right)^{-1}}{1 + 3\alpha G_{12}\left(\sigma_{12}^{(i)}\right)^2} G_{12}\varepsilon_{12}^{(i+1)} \qquad (2)$$

Accumulated Damage Criteria and Property Degradation Rule

Damage progress analysis carried out in this study is almost similar to usually damage-mechanical expression technique [3,4]. The following procedure is adopted: first perform a stress analysis using the finite element method, then apply a set of failure criteria to check for failure at each element, and third, if the failure has occurred, degrade the material properties. This procedure must be repeated for increasing load levels until properties have been degraded at so many integration points that the joint fails.

Accordingly, it is necessary that adopting the internal state variable represent the mechanic effect of damaged materials and implement in FEM codes. For each failure mode, damage variable FV_i is shown in Table 1. The condition of the damage production at each element using stress based on the hybrid method of Hashin and

Table 2. Dependence of the material properties on the field variables

Failure state	*Failure index*		*Material properties*			
	FV1	*FV2*	E_1	E_2	ν_{12}	G_{12}
No Failure	0	0	E_1	E_2	ν_{12}	G_{12}
MTRX/Comp. Failure	1	0	E_1	D_2E_2	$D_2\nu_{12}$	D_6G_{12}
FIB/Comp-Shear Failure	0	1	$D_1^{1st}E_1$	D_2E_2	$D_2\nu_{12}$	D_6G_{12}
MTRX/Comp & FIB/Comp-Shear Failure	1	1	$D_1^{2nd}E_1$	D_2E_2	$D_2\nu_{12}$	D_6G_{12}

Yamada-Sun's failure criteria is adopted [5,6]. The failure index (e_m, e_{fs}) exceeds 1.0, the failure has occurred.

Material degradation within the damaged ply must be considered according to each failure mechanism in each ply. The degraded effective ply stiffness matrix can be presented as follows:

$$Q_{ij}^{D} = \begin{bmatrix} Q_{11}^{0} & Q_{12}^{0} & 0 \\ Q_{12}^{0} & Q_{22}^{0} & 0 \\ 0 & 0 & Q_{66}^{0} \end{bmatrix} \begin{bmatrix} D_1 & & \\ & D_2 & \\ & & D_6 \end{bmatrix} \quad (3)$$

where D_1, D_2 and D_6 are, respectively, the material degradation factor which depends on each damage variable, and the dependence is shown in Table 2. D_1^{1st}, D_1^{2nd} represents degradation values on D_1 of primary and secondary. In this analysis these degradation factors D_i can be examined from a numerical parameter study. In order to avoid the problem that the number of parameter to be examined becomes enormous, for D_2 and D_6 with the constant are approximately 0.3 [7], only D_1 will be varied. Following examination procedure is performed: (Ⅰ) For D_1^{1st} varies from 0.07 to 0.3, three finite element meshes in Fig. 1 were used for the analysis of the load-displacement curve, and the effect of the element mesh on the load response was examined. (Ⅱ) Using the results the optimum element mesh and D_1^{1st} value in proportion to the onset damage were determined by procedure (Ⅰ), D_1^{2nd} will be examined as an exponential function of D_1^{1st}.

Finite Element Analysis

FE Model

Consider the problem of the middle lap in a double lap configuration, the composite plate is loaded with an in-plan load P (Fig. 1) for the pinned-joint. A two-dimensional finite element model is created using the commercial code ABAQUS [8]. Due to symmetry of the analytical model, only half

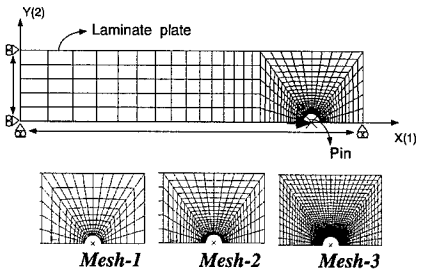

Fig.1 FEM mesh, boundary conditions and three mesh types

of the laminate is modeled and symmetry boundary conditions are applied in the planes defined in Fig. 1. For a $[45/0/-45/90]_{2S}$ laminated plate was modeled with 4-node plane stress elements (CPS4R). To simulate the contact between the pin and the laminate plate, the pin circumference is modeled as a rigid surface and the hole edge as a deformable surface. The material properties of the unidirectional CF/PIXA composite for the analysis are shown in Table 3.

To simulate the behavior of progressive damage in the joint, the failure criterion and constitutive equation formulated are implemented in ABAQUS through the user subroutine USDFLD, and the solution for the non-linear problem is obtained using repetition incremented method. The flowchart of progressive damage simulation, which built in the above algorithm, is shown in Fig. 2.

Verification and Comparisons

Table 3 Mechanical properties of CF/PIXA material

Elastic properties of CF/PIXA	
Longitudinal modulus, E_1 (GPa)	152.4
Transverse modulus, E_2 (GPa)	8.06
Shear modulus, G_{12} (GPa)	4.69
Poisson's ratio	0.34
Strengths of CF/PIXA	
Longitudinal tensile strength, X_t (MPa)	2293
Longitudinal compression strength, X_c (MPa)	948.2
Transverse tensile strength, Y_t (MPa)	66.2
Transverse compression strength, Y_c (MPa)	(210)*
In-plane shear strength, S_c (MPa)	155.3

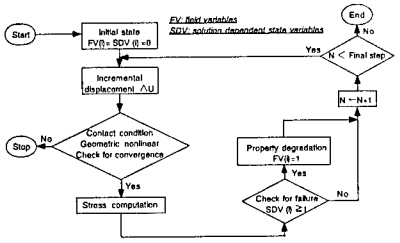

Fig. 2 Flow chart for damage simulation

A verification of the accuracy of the model is performed by comparison of strength response and damage pattern with experimental data. The comparison with experimental result of the load-displacement curve in joint response using CF/PIXA materials is shown in Fig. 3. Based on this, it is possible to predict nonlinear response behavior in the load-displacement curve until the last structural failure, if appropriate D_i is selected. Fig. 4 shows the comparison of damage simulation with the experimental result of X-radiograph for different load stages and failure modes. The inside damage aspect which appeared by the analysis agrees well with the experimental result.

Conclusions

A damage-mechanical approach was developed for predicting the bearing failure of pinned joints. Nonlinear algorithm containing the shear deformation without damage and bearing damage were considered in the model. The effect of the stiffness degradation factors D_1^{1st} and D_1^{2nd} on the strength and response of the joints appear to be very significant. Based on the model, reproducing the inside damage aspect was tried. The predictions of the analysis agreed with the experimental data quite well.

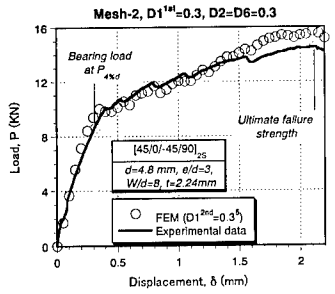

Fig. 3 Comparison with experimental data for the joint response

References

1) Y. Xiao and T. Ishikawa: Proceedings of 13th ICCM, ID1559 CD-ROM (2001).
2) H.T. Hahn, S.W. Tsai: *J. Compos. Mater.*, **7**, 102(1973).
3) ABAQUS/Standard version 5.8, Example Problem Manual, HKS Inc., USA, 1998; I: 3.2.25.
4) F.K. Chang & L.B. Lessard: *J. Compos. Mater.*, **25**, 2(1991).
5) Z. Hashin: *J. Appl. Mech.*, **47**, 329(1980).
6) S. E. Yamada & C. T. Sun: *J. Compos. Mater.*, **12**, 275(1978).
7) S. C. Tan and J. Perez: *J. Reinforced Plastics and Composites,* **12**, 1043(1993).
8) ABAQUS/Standard version 5.8, User's Manual, HKS Inc., USA, 1998.

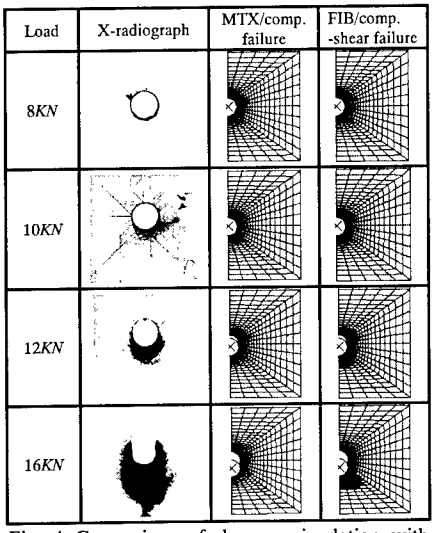

Fig. 4 Comparison of damage simulation with experimental results for different load stages and failure modes (only showing at 45° ply)

Proceedings of 7th Japan International SAMPE
Symposium & Exhibition, Nov. 13-16, 2001

Rate Dependence of Linear and Nonlinear Behaviors of Unidirectional CFRP Under Off-Axis Loading at High Temperature

Masamichi Kawai [1], Yoichi Masuko [2] and Manabu Kohashi [3]

[1] Institute of Engineering Mechanics and Systems,
University of Tsukuba, Tsukuba 305-8573, JAPAN
E-mail: mkawai@kz.tsukuba.ac.jp
[2] Graduate School of Systems and Information Engineering, University of Tsukuba
[3] Undergraduate Course of Engineering Mechanics, University of Tsukuba

Abstract

Deformation of a unidirectional carbon fiber-reinforced polymer-matrix composite T800H/Epoxy under off-axis loading at high temperature is examined with a particular emphasis on elucidation of loading-rate dependence. Monotonic tensile stress-strain curves at high temperature are accompanied with marked nonlinearity for all off-axis angles. Loading rate has significant influences on the off-axis flow stress in the regime of nonlinear stress-strain response. In view of a permanent strain remaining after unloading, this implies that the off-axis nonlinear deformation of this composite may involve an irrecoverable inelastic part with a viscoplastic nature. It is also observed that the elastic modulus evaluated on the basis of the initial gradient of the stress-strain curve of off-axis specimen depends on loading rate. The present study thus reveals that both viscoelastic and viscoplastic effects on the stress-strain relationship should be considered to characterize accurately the matrix-dominated behavior of polymer matrix composites at elevated temperature.

Key Words: Rate Dependence, Off-Axis Loading, Unidirectional CFRP, High Temperature

Introduction

Polymers used as constituents of composite materials, which range from amorphous to moderately crystalline, exhibit viscoelastic and viscoplastic responses to load, regardless of the magnitudes of stress and strain [1]. Viscoelastic and viscoplastic effects in polymers become marked as the temperature increases due to the aid of thermal activation. A strong tendency of polymers for the time- and rate-dependent behavior should have important influences on the mechanical responses of polymer matrix composites (PMCs), especially when they are subjected to off-axis loading. To the high-temperature durability of PMC laminates for advanced aerospace structures, therefore, their matrix-dominated responses to shear loading are crucial.

Effects of loading rate on the off-axis tensile behavior of a unidirectional AS4/PEEK were studied by Gates and Sun [2], Yoon and Sun [3], and Kawai et al. [4]. These studies primarily focused on the rate dependence of the nonlinear deformation for the unidirectional system of AS4/PEEK at a relatively large strain. On the rate dependence of the system in the range of an apparently linear response at a small strain, however, very few studies are reported. The rate effect at a small strain should also be carefully taken into account to characterize the rate dependence of the off-axis behavior of unidirectional PMCs, since the elastic modulus of polymer usually depends on loading rate [1] and accordingly such a viscoelasticity effect may also brings about the rate dependence of the initial gradient of the off-axis stress-strain curve. By closely observing the reported test results [3,4], we can actually find the rate dependence of the initial elastic moduli for unidirectional PMCs under off-axis loading. For accurately evaluating the performance and reliability of structural PMCs, therefore, it is important to elucidate the viscoelastic and viscoplastic effects on the deformation in both linear and nonlinear regimes.

The present study aims to examine the rate dependence of the off-axis deformation behavior at small and large strains for a unidirectional carbon fiber-reinforced composite T800H/Epoxy. Monotonic tension tests are performed using off-axis plain coupon specimens at three different stress rates at 100°C.

Material and Experimental Procedure

Material and Specimen

The material used in the present study is a unidirectional fiber composite fabricated using the autoclave method from the prepreg (P2053-17, TORAY) which consists of the carbon fiber (T800H) and the thermosetting epoxy resin (#2500). The volume fraction of the fibers is V_f = 63.8 %, and the lay-up of the virgin laminate is $[0]_{12}$. The T800H/Epoxy prepreg was cured at 130°C for two hours.

Six kinds of plain coupon specimen with a different off-axis angle (θ = 0, 10, 15, 30, 45, 90°) were cut from 400 mm by 400 mm unidirectional laminate panels. The shape and dimensions of the off-axis specimens are based on the testing standard JIS K 7073 [5]; the specimen length L = 200 mm and the thickness t = 1.7 mm. The specimen width is 10 mm for θ = 0°, and 20 mm for other off-axis angles. Rectangular-shaped aluminum-alloy tabs were attached on both ends of the specimens using epoxy adhesive (ARALDITE); the thickness of end-tabs is 1.0 mm.

Experimental Procedure

Static tension tests were carried out at 100°C at three different rates of 100, 10 and 1.0 MPa/min. The specimens were heated up to 100°C in air without applying the load, and they were preconditioned in the test environment for 60 minutes prior to test.

The longitudinal and lateral strains of each specimen were monitored with two-element L-type rosette strain gauges. These strain gauges were mounted back to back at the center of specimens.

The monotonic tension tests at 100°C were performed using a servo-hydraulic testing machine MTS-810. To raise the temperature of specimens, a heating chamber with a precise digital control capability was employed. The specimens were clamped in

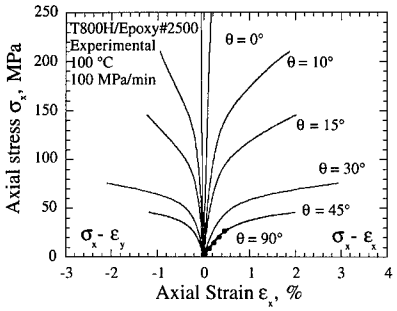

Fig.1 Axial stress-strain relationships for all off-axis angles (100 MPa/min)

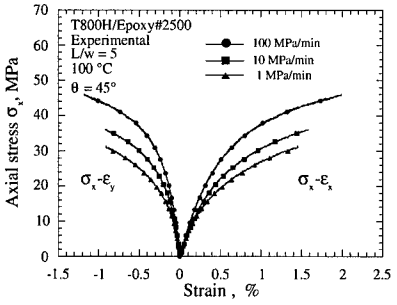

Fig.2 Rate dependence of the off-axis stress-strain relationships (θ= 45°)

the heating chamber by the high-temperature hydraulic wedge grips fitted on the testing machine.

Experimental Results and Discussion

Off-Axis Tensile Behavior

Tensile stress-strain curves of T800H/Epoxy at 100°C with a constant stress rate of 100 MPa/min are presented in Fig. 1 for various off-axis angles θ. The first quadrant of this figure exhibits the stress-

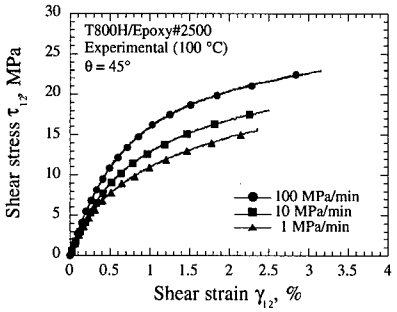

Fig.3 Rate dependence of the shear stress-strain relationships

strain response in the loading direction ($\sigma_x - \varepsilon_x$), and the second quadrant displays the relationship between the longitudinal stress σ_x and the lateral strain ε_y. A significant nonlinear behavior is clearly observed for the off-axis angle in the range $10° \leq \theta \leq 45°$. The off-axis fracture strains are larger than 2 % in this range of off-axis angle.

The off-axis angle dependence of the Young's modulus E_x and the Poisson ratio ν_{xy} are accurately predicted by the orthotropic linear elasticity theory [6]. The off-axis tensile strengths are appropriately described using the Tsai-Hill criterion [6]. Similar features of the off-axis stress-strain responses were observed at different stress-rates of 10 and 1.0 MPa/min.

Rate Dependence of Off-Axis Tensile Behavior

Comparisons between the off-axis stress-strain curves at 100°C under three different stress rates of 100, 10, and 1.0 MPa/min are presented in Fig. 2 for the case θ= 45°. It is obvious that the axial flow stress σ_x in the nonlinear regime becomes smaller at lower

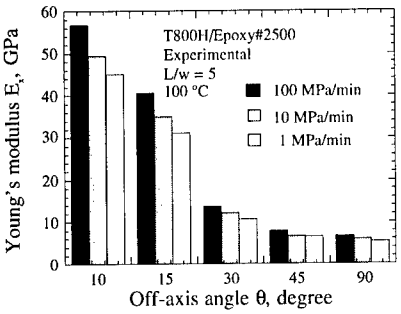

Fig.4 Rate dependence of the initial gradients of the off-axis stress-strain curves

stress rate; the same tendency was observed for all off-axis angles except 0°.

Fig. 3 shows the shear stress-strain curves based on the off-axis tension test results for θ = 45° at 100, 10 and 1.0 MPa/min; the stress and strain components are taken with respect to the material principal coordinate system. In the nonlinear regime, the shear flow stress τ_{12} is smaller at lower strain rate. The rate dependence of the shear flow stress is comparable with that of the axial flow stresses under off-axis loading. This indicates that the rate dependence of the off-axis flow stress of this system at 100°C is controlled by the viscous nature of the epoxy matrix.

Fig. 4 shows the rate dependence of the elastic modulus that is evaluated on the basis of the initial gradient of the off-axis stress-strain curve. From this figure, it is clearly observed for $\theta > 0°$ that the initial slope tends to become lower at a lower stress rate. It is believed that the rate dependence of the initial slope of the off-axis stress-strain curve reflects the viscoelastic property of the epoxy matrix.

Conclusions

The rate dependence of the linear and nonlinear deformation under off-axis tensile loading was examined for the unidirectional carbon fiber-reinforced composite T800H/Epoxy at high temperature. The monotonic tension tests were performed at three different stress rates: 100, 10 and 1.0 MPa/min, respectively.

Except for the fiber direction $\theta = 0°$, the flow stress in the nonlinear regime depends on loading rate, and it becomes smaller at a lower rate. The rate dependence of the off-axis flow stress almost agrees with that of the in-plane shear flow stress. These observations reveal that nonlinear response of T800H/Epoxy is apparently viscoplastic and this comes from the characteristic of the epoxy matrix. The rate effect was also observed at a small strain; the initial slope of the off-axis stress-strain relationship becomes less at a lower loading rate. This reflects the viscoelasticity of the epoxy.

References

1. L.E. Nielsen: *Mechanical Properties of Polymers and Composites*, Marcel Dekker, New York, 1975.
2. T.S. Gates and C.T. Sun: AIAA Journal, 29(3), 457 (1991).
3. K.J. Yoon, and C.T. Sun: Journal of Composite Materials, 25, 1277 (1991).
4. M. Kawai, Y. Masuko, Y. Kawase, and R. Negishi: International Journal of Mechanical Sciences, 43(9), 2069 (2001).
5. Japanese Industrial Association (JIS): Japanese Industrial Standard K 7073, (1988).
6. D. Hull, *Introduction to Composite Materials*, Cambridge University Press, UK, 1982.

Proceedings of 7th Japan International SAMPE
Symposium & Exhibition, Nov. 13-16, 2001

Evaluation of Crack Closure in Epoxy Resin Plates with Embedded SMA Wires by Finite-Element Analysis

Eisaku Umezaki# and Tadashi Ichikawa#

#: Nippon Institute of Technology
4-1 Gakuendai, Miyashiro, Saitama 345-8501, Japan
E-mail: umezaki@nit.ac.jp

Abstract

Crack closure in epoxy resin plates with embedded linear shape-memory alloy (SMA) wires as an actuator in smart structure members was investigated as a function of the duration of the supply of electric current to the SMA wire under a tensile load using finite-element analysis (FEA), and discussed comparing with that obtained from photoelastic experiments. The simulated isochromatics near the crack tip were drawn on the basis of stresses obtained from the FEA, and used to calculate the stress intensity factor. The analytical results were in good agreement with those obtained using photoelastic experiments. Therefore, the simulated isochromatics suggested the possibility of applications in the prediction of the intensity of the crack closure.

Key Words: Smart Structure, Shape Memory Alloy, Crack, Crack Closure, Epoxy Resin Plate, Finite-Element Analysis, Actuator

Introduction

Recently, one of the authors has investigated the fundamental characteristics of shape-memory alloy (SMA) wires, which are an effective actuator in smart structures, embedded in epoxy resin plates to develop a smart structure which prevents crack generation and closes generated cracks in machine parts and structure members[1-3]. The temperatures of the SMA wires embedded in the plates must exceed the austenite finishing temperature, A_f, at which the SMA wires recover completely in the memorized shape, to close cracks efficiently. In those studies, the amount of electric current supplied to SMA wires to recover the SMA shape was controlled so that the temperature of the SMA wire surface in the atmosphere approached A_f. Therefore, the recovery power of SMA wires may not be used efficiently in the plates because the temperatures of SMA wires in the plates may not exceed A_f.

Then, the authors have attempted to estimate the temperatures of SMA wires in epoxy resin plates heated by supplying electric current using an infrared thermography technique and the finite-element method. Consequently, the temperatures of SMA wires in epoxy resin plates have been found to be approximately half to 2/3 of the temperature of a SMA wire in the atmosphere[4].

In this study, in consideration of those results, we investigated crack closure

in an epoxy resin plate with an embedded linear SMA wire heated by supplying electric current using finite-element analysis, and evaluated whether the finite-element analysis was effective for estimating the crack closure, in comparison with photoelastic experiments.

Photoelastic Experiment

Experimental Method

Figure 1 shows the shape and dimensions of the specimen used. The SMA used was a TiNi wire with 0.5mm diameter, 290MPa maximum recovery stress, 6% shape recovery and 58°C austenite finishing temperature, A_f[5]. The SMA wires had a 14.1GPa Young's modulus and Poisson's ratio of 0.3 at 20°C after shape-memory heat treatment.

One linear SMA wire of 200mm length with approximately 6% prestrain was embedded in an epoxy resin plate; the epoxy resin plates were produced from Araldite-CY230: hardener-HY956 = 100: 20 in a weight ratio. The epoxy resin plate, in which the SMA wire was not embedded, had 2.8GPa Young's modulus, 0.35 Poisson's ratio, and 0.058mm/N photoelastic sensitivity at 20°C. The SMA wire was fixed during the formation of the plate to prevent recovery of the SMA shape during high heat generation in the initial stage of molding. A steel plate of 0.15mm thickness

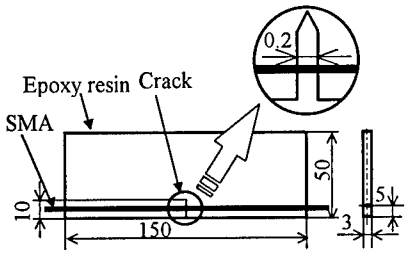

Fig.1 Shape and dimensions of specimen used for crack closure function tests

with silicon grease applied to the surface to a thickness of about 0.025mm was placed in the mold before adding the mixture of Araldite and hardener, in order to form a notch of about 0.2mm to simulate a crack.

An electric current of 1.5A was supplied for 60s to the SMA wire in the specimen under a tensile load of 515N in a photoelastic measuring apparatus, and thereafter the current was switched off. Photoelastic fringes, known as isochromatics, generated near the crack tip, were recorded using an 8mm video camera, and used to calculate the stress intensity factor, K_I, using the Irwin method[6].

In order to evaluate the function of crack closure in the specimen, we used the variation rate of K_I, R_{KI}, defined by

$$R_{KI} = \frac{\left(K_{I(0)} - K_{I(t)}\right)}{K_{I(0)}} \times 100\ (\%), \quad (1)$$

where $K_{I(0)}$ is K_I before current was supplied to the SMA wire, and $K_{I(t)}$ is that at time t after the current supply. The crack in the specimen is closed when R_{KI} is negative, and open when R_{KI} is positive.

Experimental Results

Figure 2 shows variations in isochromatics near the crack tip in the specimen for a 60s duration of current supply. In these figures, the SMA wires are indicated by the black horizontal lines, and the cracks by the black segmented lines at the lower center. The spread of the isochromatics generated at the crack tip became small with time. Therefore, it is understood that the crack closes.

Finite-Element Analysis

Analytical Method

Crack closure in an epoxy resin plate with an embedded linear SMA wire was evaluated as a function of the duration of the supply of electric current to the wire

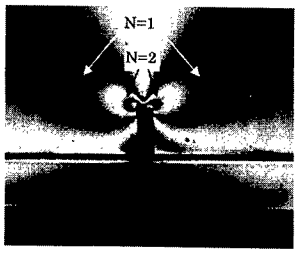

(a) t=0s

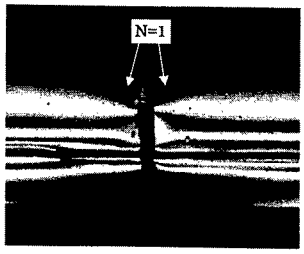

(b) t=60s

Fig.2 Variations in isochromatics (N: Fringe order)

under tensile loads using the finite-element method (FEM). Simulated isochromatics, which are obtained by $2\alpha t(\sigma_1-\sigma_2)$, where σ_1 and σ_2 are the principal stresses on the structure surface, were used to evaluate crack closure.

Figure 3 shows the finite-element model, which had the same shape as that in Fig.1. However, the right-hand half of the experimental specimen was used for the analytical model because the specimen was symmetrical. The shape at the crack tip for the model was the same as that for the experimental specimen.

The material properties of the SMA wire and the epoxy resin plate were the same as those for the experiment specimen except the Young's moduli, of which temperature dependability was taken into consideration.

In the analytical model, eight-node three-dimensional elements were used. The number of elements was 8,328 and the number of nodes was 10,043.

Recovery stress and strain of the SMA wire, which depended on the temperature of the wire, were given to the wire under a tensile load of 515N, which was the same as that for the experiment. The SMA wire heated supplying an electric current generate heat to rise with time. In this study, the heat was calculated as a function of the duration of electric current by Joule's heat analysis using the FEM, and given to the SMA wire as a source of heat. The same model as that used in this study was used in the heat analysis except that a load did not act on the model.

The simulated isochromatics near the crack tip were drawn on the basis of stresses obtained from the FEA, and used to calculate the stress intensity factor. The analysis was carried out for 60s. MARC was the analytical software used.

Analytical Results

Figure 4 shows variations in simulated isochromatics obtained by the FEA. In these figures, the isochromatics shown in the left-hand half were obtained by copying those shown in the right-hand half. The results showed that a spread of simulated isochromatics generated at the crack tip became small with time in the same way as the experimental results. Therefore, it is understood that the crack closes.

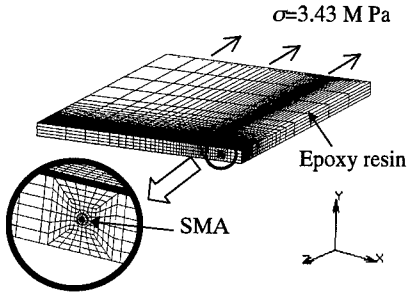

Fig.3 Analytical model

Comparison of Experimental and Analytical Results

Figure 5 shows a comparison between variations in R_{KI} obtained from isochromatics and those obtained from simulated isochromatics. From Figs.2, 4 and 5, analytical isochromatics near the crack tip and around the SMA were similar to experimental isochromatics, and the analytical R_{KI} was in good agreement with the experimental one. These results showed that the proposed method was effective in determining the stress intensity factor.

Therefore, crack closure in an epoxy resin plate with embedded SMA wires heated by supplying electric current, and the stresses inside the plate, which are difficult to determine using experiments, can be evaluated using the FEA.

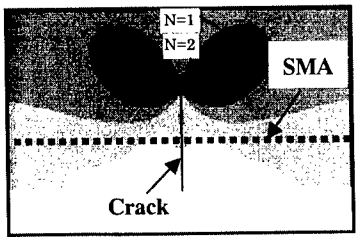

(a) t=0s

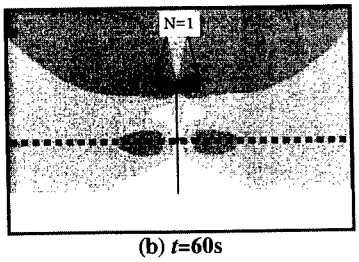

(b) t=60s

Fig.4 Variations in simulated isochromatics obtained using FEM (N: Fringe order)

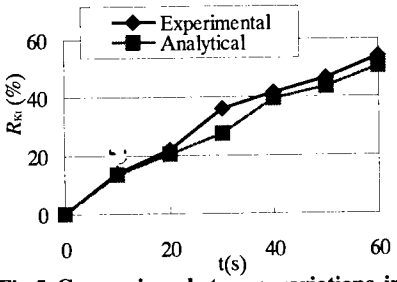

Fig.5 Comparison between variations in R_{KI} obtained from isochromatics and simulated isochromatics for a current supply of 60s

Conclusions

Crack closure in an epoxy resin plate with an embedded SMA wire heated by supplying electric current was evaluated using the FEA. The analytical results were in good agreement with those obtained from photoelastic experiments. Therefore, the simulated isochromatics obtained from FEA suggested the possibility of application in the prediction of the intensity of crack closure.

References

1. E. Umezaki: Prepr. of Jpn. Soc. Mech. Eng., (in Japanese), No.98-1,Vol. II, 129 (1998).
2. E. Umezaki, E. Kawahara and H. Watanabe: JSME Int. J., Series C, 41(3), 470 (1998).
3. E. Umezaki: Mater. Sci. Eng.: A 285, 363 (2000).
4. E. Umezaki and T. Ichikawa: Trans. Materials Research Society of Japan, 26(1), 179 (2001).
5. in Catalog of Furukawa NT Alloy, Furukawa Electric Co., Ltd.
6. E. Umezaki, Y. Nanka and H. Watanabe: Proc. of International Conference on Material Engineering, Lecce, Italy, 267 (1996).

Proceedings of 7th Japan International SAMPE
Symposium & Exhibition, Nov. 13-16, 2001

Numerical Prediction of Permeability Tensor for Sheared Woven Fabric by Asymptotic Homogenization Theory

Naoki Takano [1], Masaru Zako [1] and Toru Okazaki [1]

[1] Department of Manufacturing Science, Graduate School of Engineering, Osaka University
2-1 Yamada-oka, Suita, 565-0871 Osaka, JAPAN,
E-mail: takano@mapse.eng.osaka-u.ac.jp

Abstract

The permeability is a key parameter in the RTM process simulation. This paper presents a novel computational method to predict the three-dimensional permeability tensor using the asymptotic homogenization theory. The prediction is based on the microstructure of the composite materials. In this paper, the sheared woven fabric after draping or performing is studied. The non-diagonal term in the permeability tensor can be easily estimated by the proposed method. Furthermore, the microscopic flow field can be analyzed as well as the macroscopic permeability tensor. The microscopic flow field includes important information rather than the permeability tensor which is the averaged values.

Key Words: Permeability, RTM, Numerical analysis, Homogenization theory

Introduction

Resin transfer molding (RTM) has been a matter of concern in the last decade in the research works of cost-effective and affordable polymer matrix composite materials. We can find many studies on the numerical simulation of the RTM process, some of which includes also performing or draping process simulation. Most of the current RTM simulation is based on the Darcy's law. It describes the flow velocity of the viscous fluid in a porous media. The Darcy's law says the velocity is proportional to the pressure gradient, and is in inverse proportion to the viscosity ratio. A coefficient is also used, which is called the permeability tensor. This is a second order tensor.

For the RTM simulation, the permeability tensor must be determined by preliminary experiment. Some papers report that a difficulty lies in the measurement of permeability tensor accurately. The convenient prediction rules exist only for the uni-directional fiber reinforced composites. Especially, the permeability tensor for the sheared woven fabrics in the draping or performing process is very hard to be measured. This is mainly because the non-diagonal term appears in the permeability tensor due to the loss of orthogonality.

In order to predict numerically the permeability tensor for arbitrary reinforcing architecture, we propose a multi-scale analysis by the asymptotic homogenization theory. The original formulation of this theory for a solid-fluid mixture was presented by Terada et al. [1]. The authors [2-4] have applied it to the prediction of the permeability tensor for uni-directional fiber reinforced composites and textile composites. The accuracy was validated for uni-directional fiber reinforced composites by comparison with the conventional prediction rules [4].

In this paper, the multi-scale computational method by the homogenization theory is applied to the prediction and evaluation of the permeability of sheared woven fabric. The description of the formulation is omitted in this paper; see Refs.[1-3].

Microstructure-based RTM process simulation

The proposed multi-scale analysis is based on the microstructural information. Because the Darcy's law describes the macroscopic behavior, the permeability tensor is derived by the homogenization theory as the volumetric average of the microscopic and characteristic flow velocity in the unit microstructure. The outline of the microstructure-based RTM process simulation using the homogenization theory is illustrated in Fig. 1. See [3] for more detail.

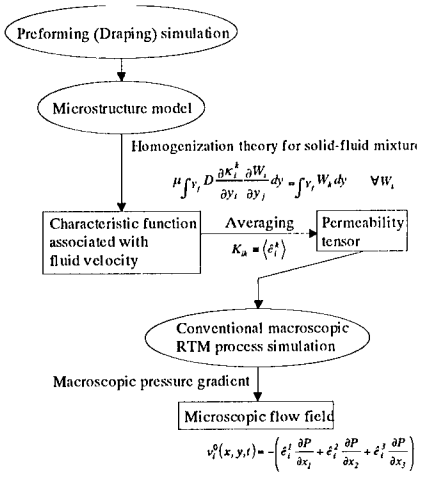

Fig.1 Outline of the microstructure-based RTM process simulation.

Prediction of Permeability Tensor for Sheared Woven Fabric

In this paper, plain woven fabric reinforced composite material isstudied. We assume that the warp yarn and the weft yarn are the same as shown in Fig. 2(a). It is a unit microstructure model descretized by finite elements. We assume that this woven fabric is sheared as shown in Fig. 2(b). The volume fraction and the cross-sectional area of the yarn are assumed to be same between undeformed and sheared fabrics.

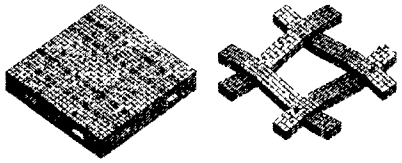

(a) Undeformed plain woven fabric

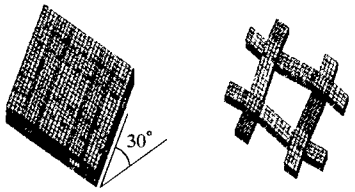

(b) Sheared fabric

Fig. 2 Unit microstructure models of undeformed and sheared fabrics.

The calculated permeability tensor is shown in Eqn. 1 for the undeformed fabric and in Eqn. 2 for the sheared fabric. The viscosity ratio of resin is assumed to be 10^{-1} Pa·s.

$$K_{undeformed} = \begin{bmatrix} 2.77\times10^{-3} & 0 & 0 \\ & 2.77\times10^{-3} & 0 \\ \text{sym.} & & 7.82\times10^{-3} \end{bmatrix} \ (\mathrm{m^2/Pa\cdot s}) \quad (1)$$

$$K_{sheared} = \begin{bmatrix} 2.41\times10^{-3} & 8.51\times10^{-4} & 0 \\ & 3.39\times10^{-3} & 0 \\ \text{sym.} & & 6.96\times10^{-3} \end{bmatrix} \ (\mathrm{m^2/Pa\cdot s}) \quad (2)$$

The in-plane isotropic permeability tensor was obtained for the undeformed plain woven fabric. For the sheared fabric, the non-diagonal term was predicted using the same numerical algorithm.

Once the permeability tensor is known, we can predict the flow

characteristics from macroscopic point of view. Moreover, the proposed multi-scale method provides us microscopic flow field under a given macroscopic pressure gradient condition as shown in Fig. 1.

Microscopic Evaluation of Permeability Characteristics

The evaluation of the microscopic flow field is available using the proposed multi-scale method. In this study, the following four cases of the typical macroscopic conditions with respect to the pressure gradient are supposed.

Case 1: $\frac{\partial P}{\partial x_1}=1,\ \frac{\partial P}{\partial x_2}=\frac{\partial P}{\partial x_3}=0$

Case 2: $\frac{\partial P}{\partial x_1}=\frac{\partial P}{\partial x_2}=\frac{1}{\sqrt{2}},\ \frac{\partial P}{\partial x_3}=0$

Case 3: $\frac{\partial P}{\partial x_1}=\frac{1}{2},\ \frac{\partial P}{\partial x_2}=\frac{\sqrt{3}}{2},\ \frac{\partial P}{\partial x_3}=0$

Case 4: $\frac{\partial P}{\partial x_1}=0,\ \frac{\partial P}{\partial x_2}=1,\ \frac{\partial P}{\partial x_3}=0$

Then, the microscopic flow velocity can be defined as shown in Fig. 1. We can understand well the microscopic flow field in the unit microstructure using the commercial graphics tool [3]. In our previous report [3], we proposed a histogram display of the microscopic flow field. We have shown the effects of the woven architecture on the macroscopic permeability and the microscopic flow field can be well evaluated by the histogram display.

In this paper, we show that the microscopic flow front can be predicted using the particle trace display. An example of the particle trace animation is shown in Fig. 3 for the undeformed fabric under the condition case 2. We finally obtained the microscopic flow front as shown in Figs. 4 and 5 for the undeformed and sheared fabrics, respectively.

Conclusion

The multi-scale computational method can predict both the macroscopic permeability tensor and the microscopic flow field. There is no way at this moment to measure such microscopic flow behaviors, whilst the proposed method can easily calculate all possible quantities from both macroscopic and microscopic standpoints for arbitrary reinforcing architecture.

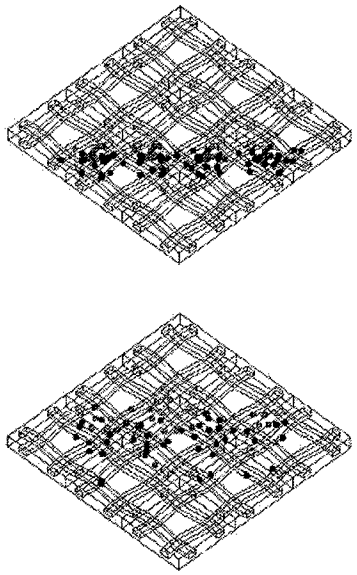

Fig. 3 Particle trace display of microscopic flow field.

References

1. K.Terada, T.Ito and N.Kikuchi: Computer Methods in Applied Mechanics and Engineering, **153**, 223 (1998).
2. N.Takano, K.Terada, M.Zako and T.Yoshioka: Journal of the Japan Society for Composite Materials, **26**(5), 171 (2000) (in Japanese).
3. N.Takano, K.Terada, M.Zako: Journal of the Society of Materials Science Japan, **50**(5), 488 (2001) (in Japanese).
4. N.Takano: Journal fo the Japan Society for Composite Materials, **27**(1), 4 (2001) (in Japanese).

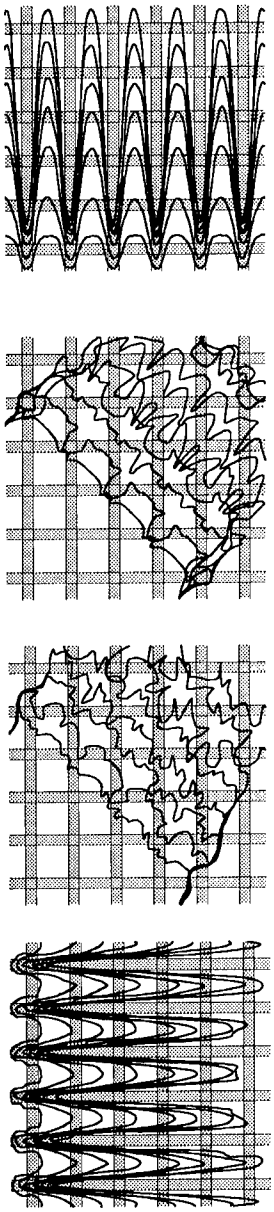

Fig. 4 Microscopic flow front for undeformed fabric for cases 1 to 4.

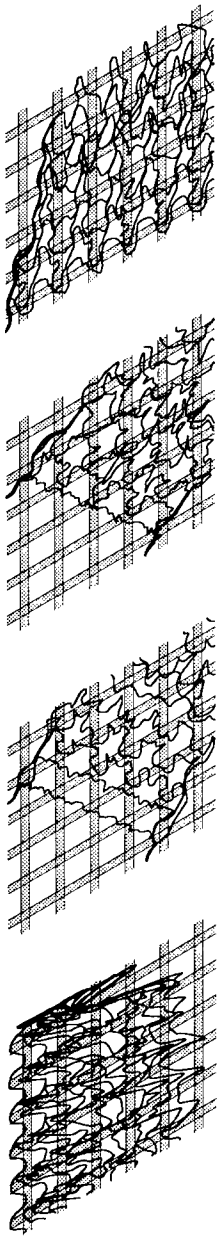

Fig. 5 Microscopic flow front for sheared fabric for cases 1 to 4.

Proceedings of 7th Japan International SAMPE
Symposium & Exhibition, Nov. 13-16, 2001

A Study of Bridging the Gap between Atomistic and Mesoscopic Simulation for Materials Design

Satoru Yamamoto and Shi-aki Hyodo

Frontier Research Group V, Toyota Central R&D Labs., Inc.
Nagakute, Aichi 480-1192, JAPAN
E-mail: e0857@mosk.tytlabs.co.jp

Abstract

A cooperation procedure to bridge the gap between atomistic and mesoscopic simulation is presented. The Flory-Huggins χ-parameters for coarse-grained model in a mesoscopic simulation are estimated by an atomistic simulation, calculating the energy of mixing for each pair of components. Mesoscopic structures of binary polymer blend are simulated with realistic χ-parameters by using the dissipative particle dynamics (DPD). This bridging method from atomistic to mesoscopic level is applied to prediction of the mesoscopic structure of hydrated Nafion membrane. The simulated structure is in good agreement with experimental reports. For a reverse bridging method for different scale simulations, a molecular structure at interface is extracted from the simulated mesoscopic structure by mapping to the concentration profile of each component. In the case of binary polymer blend, the complicated morphology is successfully generated by this procedure.

Key Words: Dissipative Particle Dynamics, Mesoscopic Simulation, Polymer Blend, Polymer Electrolyte Membrane.

Introduction

An atom-based simulation such as molecular dynamics method has come into wide use for materials design. However, we are often in face of difficulty on the cooperation over wide range of dominant time- and length-scale for the system. Although a possible molecular structure can be simulated by the atom-based simulation, it is less realistic to predict mesoscopic structure, for example morphology of polymer blend and composite, which often dominates an actual material property. It is therefore inevitable to adopt a mesoscopic simulation technique such as the dissipative particle dynamics (DPD) for an effective materials design [1]. In this study, we present an idea for bridging the gap between atomistic and mesoscopic simulation, namely χ-parameter between two components in DPD model is estimated through the atomistic simulation [2], and then an atom-based model is extracted from a density profile of DPD results by using Monte Carlo technique. We demonstrate a series of this procedure for immiscible polymer blend system.

Method

In a mesoscopic simulation, a coarse-grained molecular model is used for studying the morphology of inhomogeneous materials with the Flory-Huggins χ-parameter between models. It is a one way

to bridge from atomistic to mesoscopic simulation that χ-parameter is estimated by an atomistic simulation. And, extracting molecular model at an interface based on the concentration profile in mesoscopic simulation is a way of bridging in opposite direction. This cooperation procedure is shown in Fig.1 and is described in following sections.

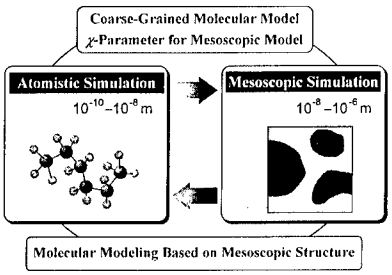

Fig.1 Conceptual Illustration of Cooperation between Atomistic and Mesoscopic Simulations

From Atomistic to Mesoscopic Simulation

The dissipative particle dynamics (DPD) is one of mesoscopic simulation methods and is based on the dynamics of coarse-grained particles interacting by conservative, dissipative, random forces, and spring force for polymer system [1].

$$\mathbf{f}_i = \sum_{j \neq i} \left(\mathbf{F}_{ij}^{C} + \mathbf{F}_{ij}^{D} + \mathbf{F}_{ij}^{R} + \mathbf{F}_{ij}^{S} \right) \qquad (1)$$

The repulsion parameters between particles in the conservative forces are related to the χ-parameters, which can be calculated from the energy of mixing ΔE_{mix} by an atomistic simulation [2],

$$\chi = V_{\mathrm{seg}} \left(\frac{\Delta E_{\mathrm{mix}}}{RT} \right) \qquad (2)$$

where V_{seg} is the volume of one polymer segment corresponding to the particles size in DPD. ΔE_{mix} is defined by the cohesive energy densities E_{coh}/V for pure components and their blends, calculated from the cohesive energy E_{coh} per a volume V by using molecular mechanics (MM) and molecular dynamics (MD) techniques.

$$\Delta E_{\mathrm{mix}} = \frac{1}{2}\left(\frac{E_{\mathrm{coh}}}{V} \right)_1 + \frac{1}{2}\left(\frac{E_{\mathrm{coh}}}{V} \right)_2 - \left(\frac{E_{\mathrm{coh}}}{V} \right)_{12} \qquad (3)$$

Mesoscopic structure is simulated by DPD with realistic χ-parameters in cooperating an atomistic simulation.

Molecular Modeling from Meso-Structure

According to the simulated mesoscopic structure by DPD, a molecular structure is generated by Monte Carlo technique (Fig.2). This procedure is as follows:

1. Consider the concentration profile ϕ for the specific composition.
2. Generate an atom of desired molecule at a random position.
3. Acceptance or rejection for adoption of the generated atom is decided based on the concentration profile of the composition.
4. By repeating 3 and 4 for connecting atoms to the latest accepted one, molecular structure is generated.
5. The above operation is continued until the concentration of the specific component reach the desired one.

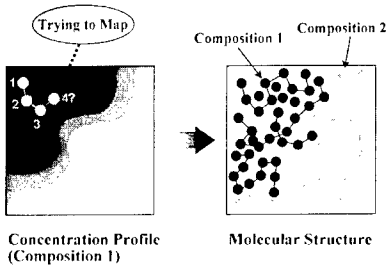

Fig.2 Mapping Molecular Structure Based on Concentration Profile of Mesoscopic Structure

Applications

Mesoscopic Simulation

We demonstrate DPD simulation coupling with realistic χ-parameters for binary polymer blend of (a)PE-PP, (b)PE-PS, and (c)PP-PS. The estimated χ-parameters for these mixtures by atomistic simulations are listed in Table 1. It is predictable that miscibility is in (a)>(c)>(b) order. Figure 3 shows concentration profiles of each polymer for these mixtures by DPD simulation. It is recognized that thickness of interface is well corresponding to this miscibility order.

Table 1 χ-Parameter of Binary Blend

Mixture	PE-PP	PE-PS	PP-PS
χ-Parameter	0.09	0.71	0.21

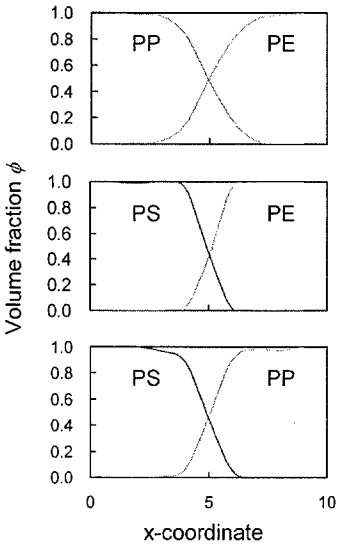

Fig.3 Concentration Profiles at Interface of Binary Polymer Blend

For more practical application of this procedure, the mesoscopic structure of hydrated Nafion membrane is simulated. Nafion is perfluorinated sulfonic acid membrane and is used in the polymer electrolyte fuel cell [3]. There are some models for structure of membrane, however, which are still under discussion. Coarse-grained Nafion model is constructed and χ-parameters of them are calculated. DPD simulation reveals the sponge-like structure as shown in Fig.4. Water particles and hydrophilic particles of Nafion side chain form aggregates or clusters and are embedded in the hydrophobic phase of Nafion backbone. Magnitudes of water clusters and their dependence on the water content are in good agreement with experimental reports. Although this sponge-like structure is essentially identical to the cluster-network model based on experimental studies, the shape of water clusters is not spherical but irregular, and the water regions are indistinguishable structures of water clusters and their channels.

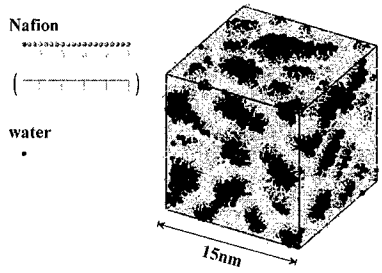

Fig.4 Sponge-like Structure of Hydrated Nafion Membrane

Molecular Modeling

Molecular structure is generated by Monte Carlo technique based on the concentration profile at the interface for binary polymer blends discussed in previous section (Fig.3). Figure 5 shows carbon atoms of each polymer backbone and their connected bonds. Molecular structures are successfully obtained by this procedure.

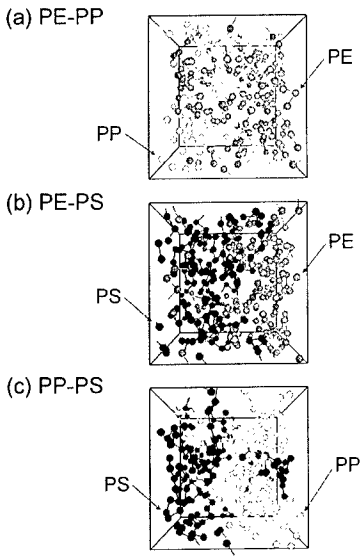

Fig.5 Molecular structure at Interface of Binary Polymer Blend Based on Mesoscopic Structure in Fig.3

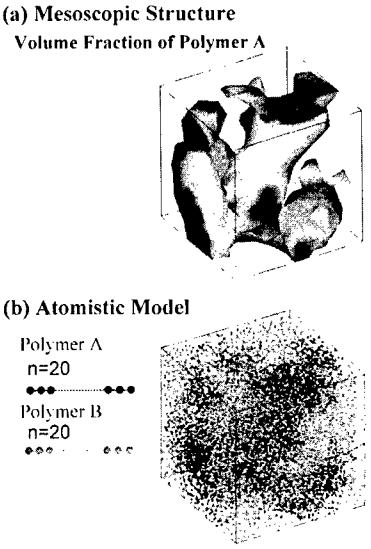

Fig.6 Atomistic Modeling of Complicated Morphology of Binary Polymer Mixture

Then, we applied this procedure to the complicated morphology of binary polymer blend as shown in Fig.6. In this system, a generated atomistic structure is well corresponding to the density profile of mesoscopic structure. By using this atomistic model, we can perform a molecular dynamics simulation to study more realistic material properties such as gas diffusion at the interface.

Conclusions

We propose a cooperation procedure to bridge the gap between atomistic and mesoscopic simulation, and demonstrate it for binary polymer blends in successful. For an application of the bridging method from atomistic to mesoscopic level, the mesoscopic structure of hydrated Nafion membrane is simulated by DPD with realistic χ-parameters. The predicted structure of membrane is in good agreement with the experimental reports. For a bridging method for different scales in an opposite direction, the mapping of molecular structure is applied to the complicated interface of binary polymer blend, and the molecular structure is successfully generated.

Acknowledgment

The authors thank Prof. H. Tanaka and members of *Polymer Workshop* sponsored by 'The Association for the Progress of New Chemistry' for helpful discussions and useful comments.

References

1. R. D. Groot and T. J. Madden: J. Chem. Phys., 108(20), 8713 (1998).
2. F. H. Case and J. D. Honeycutt: TRIP, 2, 259 (1994).
3. T. D. Gierke, G. E. Munn, and F. C. Wilson: J. Polym. Sci. Polym. Phys. Ed., 19, 1687 (1981).

Proceedings of 7th Japan International SAMPE
Symposium & Exhibition, Nov. 13-16, 2001

Image-based Modelling of Microstructures of Porous Ceramics to Study the Micro-Macro Coupling Effect

Naoki Takano [1] Futoshi Kubo [1], Masaru Zako [1] and Keiichi Kimura[2]

[1] Department of Manufacturing Science, Osaka University
2-1 Yamada-oka, Suita, Osaka 565-0871 JAPAN,
E-mail: takano@mapse.eng.osaka-u.ac.jp
[2] Synergy Ceramics Laboratory, Fine Ceramics Research Association
2-4-1 Mutsuno, Atsuta-ku, Nagoya 456-8587, JAPAN
E-mail: kimura@mtb.biglobe.ne.jp

Abstract

For the development of functional materials, the design and control of their microstructures will be an essential technique. Hence, the authors have developed a practical CAE (Computer-Aided Engineering) tool to study the relation between the microstructures and the macroscopic properties using the mathematical homogenization method. The CAE tool includes the three-dimensional image-based modelling capability to reduce the cost for the modelling of very complex microstructures.

This paper presents the outline of the developed CAE tool and an application to a real porous ceramics with needle-like random pores. The numerically predicted elastic constants were compared with the measured values, and very good coincidence was obtained.

Key Words: Microstructure, Numerical analysis, Homogenization Method, Porous ceramics

Introduction

In the field of computational mechanics in the last decade, we can find many studies on the multi-scale numerical analysis for various composite materials considering their microscopic heterogeneity. The mathematical homogenization method based on the asymptotic expansion method has been applied to the micro-macro coupled stress analysis, elasto-plastic analysis, large deformation analysis and buckling analysis of PMCs and MMCs [1-3].

In this paper, the homogenization method is applied to the microscopic stress analysis of porous ceramics with needlelike random pores. Three-dimensional image-based modelling technique is employed which provides the voxel element model semi-automatically. The homogenized macroscopic elastic constants were calculated and compared with the experimental result. The microscopic stress was predicted under four-point bending condition.

Development of Multi-scale CAE Tool

Image-based modelling

Because the microstructure of real materials are very complex, an automatic or semi-automatic mesh generator is essential for the development of a practical CAE tool. Hence, the three-dimensional image-based modelling technique is employed. It has been applied to, for instance, the modelling of porous architecture of human bone [4]. The outline of the image-based modelling used in this study is illustrated in Fig.1. Because very

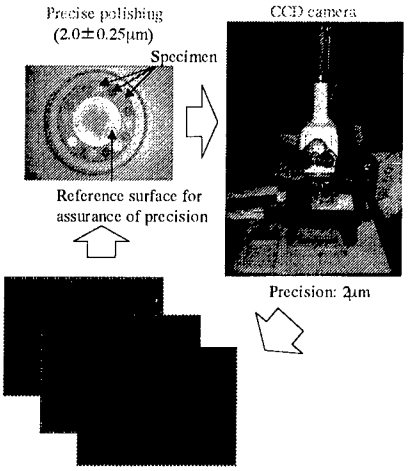

Fig.1 The outline of three-dimensional image-based modelling.

high resolution was required to express the complex microstructures, the specimen were polished precisely by every 2.0μm, but the CT scan was not used. The cross-sectional view was obtained by CCD camera, which was transformed automatically into the voxel finite element mesh.

Homogenization method

The homogenization method is one of the applied mathematical theory for the multi-scale analysis of various heterogeneous materials. It has both the homogenization capability and the localization capability. The former enables us to calculate the homogenized macroscopic properties based on the microstructure considering the constituents' properties and the microscopic geometrical information. Based on the assumption of the periodicity of the microstructures, a unit cell is used that represent the microscopic heterogeneity. The localization capability enables us to calculate the microscopic quantities such as stresses and strains as well as the macroscopic quantities.

Because a large-scale problem has to be solved to express the complex microstructure, the developed CAE tool can solve approximately two million finite elements model. Please refer [3] for more detail.

Image-based Modelling and Homogenization of Porous Alumina

A porous alumina with needle-like pores was studied. Two types of specimen were prepared. The one has approximately 3% porosity ratio, and another has approximately 23% porosity ratio. Fig.2 shows the image-based model of the whole polished region, i.e., 800x800x100μm. The size of each voxel cubic finite element is 2μm.

We first studied on the extraction of a unit cell model from the whole model in Fig.2, so that the extracted unit cell can well represent the heterogeneity in random porous alumina.

Fig. 3 shows two unit cell models with 280x280x100μm volume and 980000 elements. Two unit cell models were extracted from different location. The homogenized elastic constants were calculated. A slight orthotropy was found, which is due to the manufacturing process of this porous alumina. The calculated elastic constants by two unit cell models were in very good agreement. The Young's modulus in the 1st and 2nd directions was approxi-

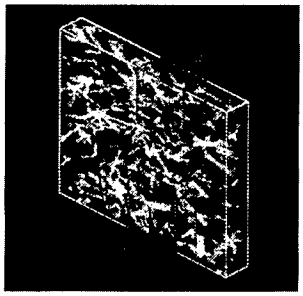

Fig.2 Porous alumina with 3% porosity ratio expressed by voxel element model (800x800x100μm).

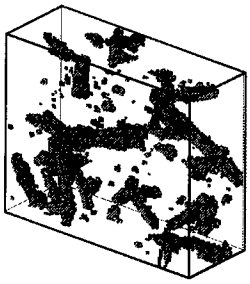

(a) Unit cell model A

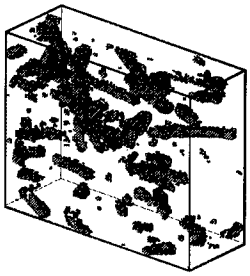

(b) Unit cell model B

Fig. 3 Unit cell models with one million elements extracted from different location (280x280x100μm).

mately 379 GPa, and that in the 3rd direction was approximately 365 GPa, while the alumina's Young's modulus is 405 GPa. The measurement of Young's modulus and Poisson's ratio was conducted only in the 3rd direction, because the orthotropy was not predicted before calculation. The measured Young's modulus in the 3rd direction was 366 GPa, which agrees quite well with the numerical prediction. The Poisson's ratio was 0.232 by both numerical prediction and measurement. This result tells us more than one million elements model with 2μm resolution is enough to represent the microscopic heterogeneity and to predict the homogenized macroscopic properties regardless of the location of the unit cell model for random microstructure architecture.

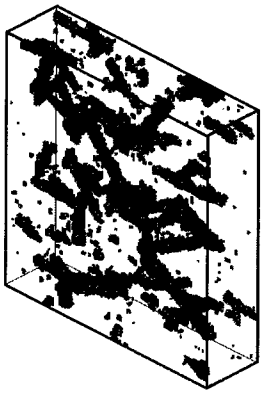

Fig.4 Unit cell model with two million elements (400x400x100μm).

To verify this, two million elements model with 400x400x100μm volume was studied next as shown in Fig.4. The calculated elastic constants agreed very well with the previous calculation.

Once the strategy to determine the unit cell model is found, we can apply our calculation to various materials. Fig. 5 shows the unit cell model of similar porous alumina with approximately 23% porosity ratio. In this case, the homogenized property was recognized in the matrix or tensor form.

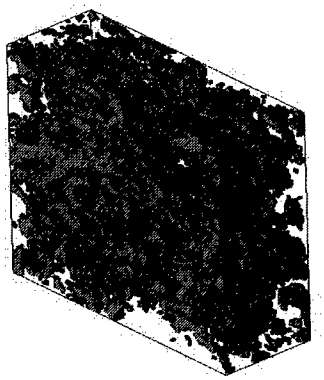

Fig. 5 Unit cell model of porous alumina with 23% porosity ratio (280x280x100μm, 980000 elements).

Micro- and Macroscopic Stresses under Four-point Bending

A four-point bending test was simulated using the above-mentioned homogenized properties. Fig. 6 shows the problem's setup. Fig. 7 shows the calculated macroscopic stress distribution. In Fig.8, tensile longitudinal stress is shown. Due to the symmetry, only a quarter part was analyzed. The calculated macroscopic stress was in good coincident with the classical beam theory. At the point where the maximum macroscopic stress is observed, the microscopic stress in the unit cell was calculated. Fig. 8 shows an example of the microscopic stress distribution for a unit cell model of porous alumina with 23% porosity ratio. We can find that the maximum microscopic stress is much higher than the macroscopic stress due to the stress concentration along the needle-like pores.

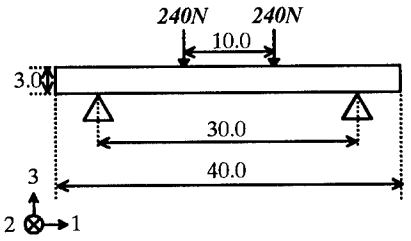

Fig. 6 Four-point bending problem

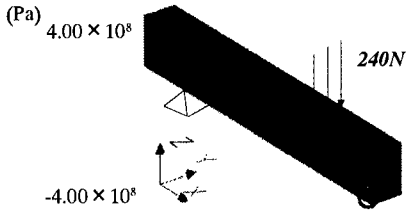

Fig. 7 Calculated macroscopic stress distribution for a quarter part of the four-point bending specimen.

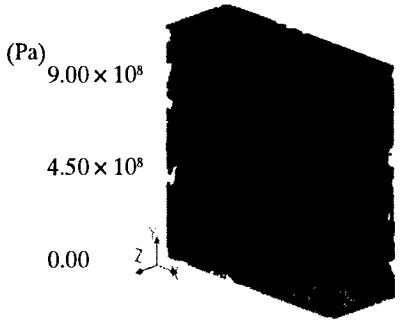

Fig. 8 Microscopic stress distribution in unit cell for porous alumina with 23% porosity ratio.

Conclusions

A practical multi-scale CAE tool was developed, and was applied to porous ceramics with very complex random microstructures. The numerically predicted elastic constants was in very good agreement with the measured values, which proves the validity and the reliability of the developed tool.

Acknowledgment

This research was supported by NEDO, under the Synergy Ceramics Project promoted by METI, Japan.

References

1. J.L.Lions: *"Some Methods in the Mathematical Analysis of Systems and Their Control"*, Science Press, Beijing (1981).
2. N.Takano, Y.Ohnishi, M.Zako and K.Nishiyabu: International Journal of Solids and Structures, **47**(44), 6517 (2000).
3. N.Takano, M.Zako, F.Kubo and K.Kimura: Materials Science Research International, Special Technical Publication-2, JSMS, 66 (2001).
4. S.J.Hollister and N.Kikuchi: Biotechnogy and Bioengineering, **43**, 586 (1994).

Proceedings of 7th Japan International SAMPE
Symposium & Exhibition, Nov. 13-16, 2001

Fracture Behavior of Micro Structure in Tibial Pleateau under External Loading -The Effect of Aging on the Stress Wave Propagation –

Tsuneo HIRAI
Prof. em. Of Doshisha University
Miyamagi-Nanasegawa, Kyotanabe, Kyoto, 610-0313, Japan

Atsushi YOKOYAMA
Kyoto Institute of Technology
Matsugasaki, Sakyo-ku, Kyoto, 606-8585, Japan

Yoshinobu WATANABE
Kyoto Prefectural University of Medicine
Kawaramachi-Hirokoji, Kamigyo-ku, Kyoto, 620-0856, Japan

Key Words: Biomechanics, Bone Fracture, FEM, Stress Wave

Abstract

The external load is transmitted to the cortical bone by way of cancellous bone and the stress propagation in the bone is greatly affected by the microstructure of the bone. So the mechanism of stress distribution process in the bone is request to organize the finite element division consisting with solid phase as bone tissue and surrounding liquid phase as marrow. The solid and liquid tissue are modeled by two independent planes being connected by imaginary elements at the points between these two planes. It is expressed minute debonding fracture at an imaginary element working between beam elements and touching of liquid phase under impact loading. According to the assumptions, the related shear stress distributions on each lateral truss element are obtained characteristic and suggested for healing operation method on fractured cancellous bone.

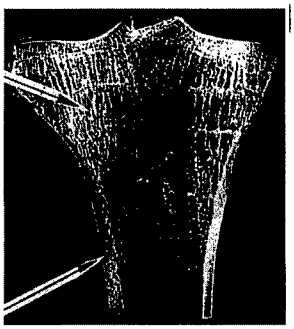

Fig.1 X-ray image of bone

1. Introduction

It is considered recently an activity to analyze numerically on fracture of cancellous bone in tibial plateau under eccentric dynamic loading being expressed by an interpretation under biomechanical analysis. The lateral above fracture are divided into three types: so type 1 is split fracture type, type II is split depressed fracture type,

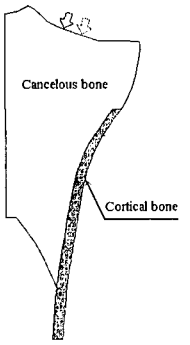

Fig.2 Schematic diagram of living bone

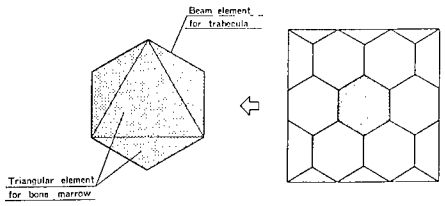

Fig.3 Numerical model of living bone

type III is isolated depression. Split fracture type is most common in young,

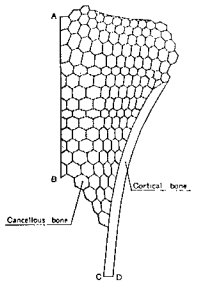

Fig.4 Finite element mesh of target bone

in contrast, the isolated depressed fracture may be observed in old peoples. The difference of these populations is believed to depend on the rigidity of proximal tibia and a little effect viscosity of mallow. This study is designed to evaluate stress wave dispersion under impact loading by numerical method to explain the mechanism of lateral tibial plateau fracture.

In this study, the numerical model of living bone is proposed to simulate the fracture behavior of tibia bone under dynamic compressive loading. This proposed model can express the transient process of stress living bone due to adopt independent model of solid tissue and liquid tissue.

2. Numerical model of living bone

The living bone can be divided into two different phases such as solid tissue and liquid tissue. The combination of these phases makes complicated microstructure of bone. The living bone

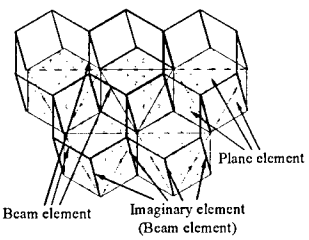

Fig.5 Numerical model of imaginary element in target bone

can be assumed to be the composite structure. In this study, the numerical model of the living bone is developed by assuming the internal structure of the bone as composite materials with complicated structure. Fig.1 shows X-ray photograph of tibia bone and Fig.2 is schematic diagram of the structure of the tibia bone. At center of tibia bone, the cancellous bone is allocated to absorb the external load. And the cortical bone is located at surface of the cancellous bone. This cortical bone transfer external load to under leg. The cancellous bone consists of solid tissue and liquid tissue. The structure of cancellous bone decides the transfer mechanism of the external load and the fracture mechanism of the tibia bone. So the model of cancellous bone is key technology to simulate the fracture mechanism of living bone.

Fig.3 shows numerical model of cancellous bone. The component of the cancellous bone is modeled independently. So the solid tissue is expressed by the beam element and the liquid tissue is modeled by the plane triangular element.

Honeycomb shaped finite element mesh expressing solid and liquid phases as shown in Fig.4

4. Results and Discussions

The proposed model has two independent sub models such as solid tissue and liquid tissue. To control the combination of the material constants of these two sub models, various state of bone can be expressed such as younger or older people's bones. Fig.6 shows stress distribution state at early stage in three type of combination of the material constant. In these result, type A express young bone and type B,C is correspond to older people bone by changing the combination of material constant of solid and liquid tissue. It is considered dividing two phases that stress wave propagated horizontally to subchondral region about 0.4ms after loading by the results assuming imaginary elements as shown in Fig.6-A. Following this, the stress wave propagates vertically to the lateral cortical shell with time. The behaviours are shown in Fig.6 for young and old people and the results

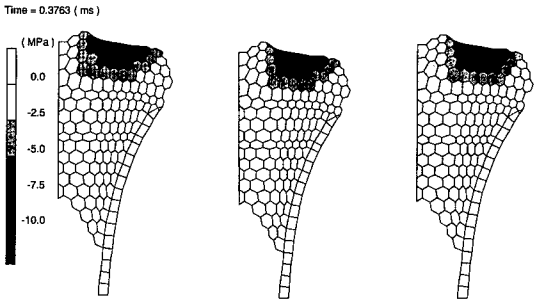

Fig.6 The result of stress wave dispersion in proximal tibia

obtained under imaginary element

analysis. The deference of stress distribution is not observed in all type of bone. The stress dispersion processes with bone fracture are also obtained by using imaginary element model as shown in Fig.7. In the case of 30% reduction of modulus in bone element shown as old people, perpendicular high stress band act and expand to split fracture at out side domain of tibial plateau, that is, depart from symmetrical line of cancellous bone as shown in Fig.9-B. The stress distribution in obedience to increase of viscosity in liquid phase is shown in Fig.9-C showing tendency of generally incremental reduction. Furthermore, the shear stress distributions of solid tissue can be obtained by using this numerical model as shown in Fig. 9. These distributions are calculated the serial beam element located on a line A1- A18. From this result, the old bone have high risk to occur the split fracture of cancellous bone. By using these results, this proposed model can be decided to be effective for investigation of fracture process in various type living bone.

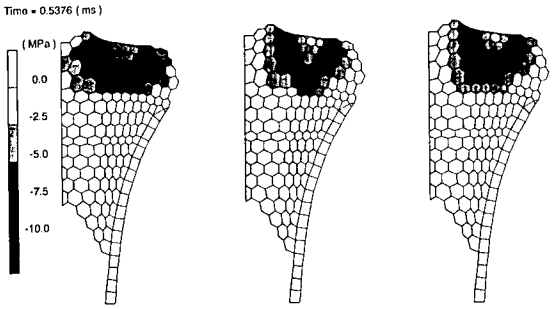

Fig.7 The result of stress wave dispersion in proximal with bone fracture

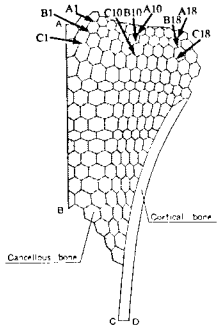

Fig.8 Location of calculated beam element of shear stress.

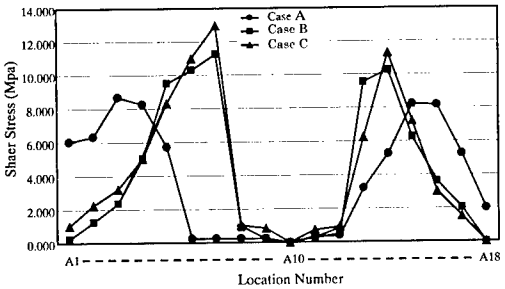

Fig. 9 Sher stress distribution of solid tissue on line A1- A18

Proceedings of 7th Japan International SAMPE
Symposium & Exhibition, Nov. 13-16, 2001

The New Progress and Developing Tendency of NDT for Advanced Composite Materials and Structures

Xu Kebei

NDT lab, Beijing Institute of Aeronautical Materials
P. O. Box 81-6, Beijing, 100095, China
E-mail: kebei.xu@biam.ac.cn

Abstract

In this paper, some latest developments of non-destructive testing (NDT) techniques , such as Laser-based Ultrasonic, Air-coupled Ultrasonic, Lamb waves, Thermography, Laser-Shearography, Industrial CT, Real-Time Imaging of X-Ray, Electromagnetism and Eddy Current, applied in the fields of composite materials and manufactures are introduced briefly. In succession, author indicates that the innovations and integrations of NDT technologies, the correct characterization and the accurate quantification to defects by non-destructive evaluation (NDE) means, and standardization of NDT methods for advanced composites will become some very interesting and magnetic subjects in the future. Besides, the reality and representative of man-made defects will also be a noticeable problem for improvement of NDT technology.

Key Words: Composite Materials, NDT, Development, Tendency

Introduction

NDT techniques are applied in every stage of developing and applicating a production, from design, research, manufacture to service and maintenance stage, so it plays an active and important role for optimizing the designation, improving the performance, decreasing the cost, ensuring the quality and prolonging the life-span of the production. In the latest decades, advanced composite materials and processings are developed rapidly. Composites are inhomogeneous and anisotropic materials, and composite components are usually manufactured by one-off process. This brought challenges to the NDT of composites which was derived from the NDT of metallic materials. On the other hand, those challenges stimulate the rapid development of the new NDT techniques & methods. Especially in the latest decade, along with the research and application of composite materials and components, some new progresses have been developed, including Laser-based Ultrasonic, Air-coupled Ultrasonic, Lamb waves, Thermography, Laser-Shearography, Industrial CT, Real-Time Imaging of X-Ray, Electromagnetism and Eddy Current.

The New progress in NDT for Composites

Laser-based Ultrasonic

Laser-based ultrasonic (LBU) is such a technique that one laser beam is transmitted to the surface of the tested object to generate ultrasonic, and another laser probe is used to receive and detect that ultrasonic signal. LBU has many outstanding advantages over the conventional ultrasonic system in some

aspects as follows:

First, effects caused by curvature or sloping surface could be ignored, since the minimum size of the interesing flaw of the large composite structures is about 6～12mm, which is typically 10^4 times larger than the optical wavelength. The distance over which the incident laser beam will remain approximately the same diameter is more than 50m. This enormous depth of focus means that changes in the distance between the laser and the surface of the part caused by curvature or sloping surfaces will not cause a change in the laser spot size and thus will not affect the characteristics of the ultrasonic beam that is generated. [1]

Secondly, it is not necessary to use the large and complicated scan equipment. When the ultrasonic pulse-echo C-scan is employed, the system have to be consisted of not only the long tracks (often up to 10m) in tow directions for leading transducer's movement, but also a 2-D complicated framework for adjusting transducer's pose, and a device for keeping the precise distance from the transducer to the object. When the C-scan of ultrasonic through-transmission is selected, the primary requirements for the synchronous movements of the two transducers and their relative precise positions make the system much more complicated. When LBU is used, the scan system is a small simple device that only consists of two optic mirrors to rotate in two vertical axes, but it has a capacity of rapid scanning over a large area.

Thirdly, LBU is suitable for complicated forms. There are a lot of complicated shapes of stiffeners in the "T" or "Π" shape in composite components and structures. For those cornered positions, conventional ultrasonic couldn't be performed automatically and efficiently, but LBU could do it easily because of its non-touch, non-couplant and small focus.

In late 90's, LBU techniques were transformed from laboratory to industry. Typical applications were developed in the large composite structures in the field of research, fabrication and service, such as fuselage planes, rudder skin and radome.[2]

Air-coupled Ultrasonic

The extremely high sound attenuation of the composite makes ultrasonic inspection with 2 to 10MHz become very difficult, especially for high thickness and low density structures, such as honeycombs and foam sandwiches. There are two resolutions, one way is to enhance the power of transmitted ultrasonic, another way is to decrease the inspecting frequency. When ultrasonic frequency is reduced to tens or hundreds of kilo-Hz, the attenuation of ultrasonic at such low frequencies in air becomes lower than the one with higher frequencies. This principle is used to make the ultrasonic instrument with higher power which works at low frequencies could travel through large and loose composite components. Therefore, air-coupled ultrasonic, without touch, couplant and being eroded by liquid, is becoming very attractive and interesting for the field inspection.

With the increasing of the thickness to travel through, the capacity to identify exiguous differences in composite becomes weak. How to improve the capacity of detecting small defects is the key techniques for air-coupled ultrasonic inspection. In latest years, a great deal of researches are focused on the structure design of transducers and the methods how to place the transmitting and receiving probe.

Pertinent researches indicate that, for thermoset carbon composite panel at 1/4 in. thickness, tested with 400kHz air-coupled and focused transducers, a Teflon insert of 1/16 in. in diameter could not be found. In the case that tested with the 50 kHz air-coupled and flat transducers, when the couple of transducers are arranged in straight through-transmission, a Teflon insert

of 1/2 in. in diameter could not be found, when the couple of transducers are arranged in displaced through-transmission, a Teflon insert of 3/8 in. in diameter could be found. Air-coupled ultrasonic at 50 kHz could penetrate through about 100mm-thick foam block and find the delamination in it.[3]

Lamb Waves

Lamb wave is one kind of ultrasonic. It is composed of longitudinal wave and transverse wave in special condition, and could be produced in composite lamination. The speciality and complexity of Lamb waves' excitation, vibration and transmission make it have potential advantages for finding out the porosity and delamination in composite lamination, the disbond and unbond between the scarfskin and the core.

The early researches in the field of composite materials and structures were aimed at adhesive structure of metallic panel to metallic panel[4]. Through analyzing the Lamb waves' signal, the thickness and setting state of adhesive could be known. Increasing the space between transmitting and receiving transducers by taking advantage of the character of the Lamb waves that could travel a long distance, the detecting efficiency could be obviously improved, and this approach is applied wildly at the stages of service and maintainence of the airplanes. Recently, the researches of leaky Lamb waves (LLW) aiming at composite laminates are an active subject. The experimentations indicate that the C-scan technique combined with LLW is more efficient than the conventional C-scan for finding out dense porosities and quantitatively evaluating the percentage of the porosities.[5]

Thermography

Thermography could be used to inspect the subsurface disbonds and delaminations, damaged cores and the inclusions of foreign materials through detecting local differences in either heat capacity or thermal conductivity of the composite materials or structures. This method has outstanding character of high speed and efficiency, and is mainly used to inspect the large scale composites of laminates or honeycomb structures. The use of square pulse heating could provide higher signals of the defects but reduce the ability to resolve the details in the thermal patterns. The flash techniques are faster and could supply more details of the impact damage structures. In the latest years, a plenty of researches is concentrated on increasing the acquirable depth and the measure accuracy of the defects, and some improvements have been acquired.

In the field of exploring how to increase the inspecting depth, one researching approach is that different types of excitations, such as electrical, sonic and light are employed, another researching approach is that the phase analysis of a long pulse with different evaluation frequencies, such as 0.31Hz, 0.12Hz and 0.05Hz are employed.[6] An algorithm for quantitatively analyzing the depth of defects is studied. Experimentation indicates that the depth determination could be performed with thermal wave imaging by analyzing the temperature variation as a function of time over the defects.[7]

Laser-Shearography

Laser-shearography is also named Electronic-shearography. This method records a coherent superposition of two laterally displaced images of the surface of the sample with a CCD camera, replacing the panel coated with special chemical materials in laser holography, so laser-shearography could overcome the fatal shortage that laser-holography is extremely sensitive to environmental influences (vibration). This creates condition for laser-shearography that could be applied out of the laboratory.

Compared with laser-holography images, primary laser-shearographic images are always very noisy, so the image processing is an important and valuable task. The applications of phase shifting and/or special filtering techniques can significantly improve the image quality as well as the defects visibility.

Laser-shearography could inspect an area up to $10m^2$ at one time when pulse laser is used and proper loading technique is exerted, so it is a very high efficient NDT method. [8]

Industrial CT & Real-Time Imaging of X-Ray

Ceramic matrix composites (CMC) are becoming top-priority materials for manufacturing heat resistant parts of advanced aircraft engine. In order to overcome the shortage of high friability, some ways for improving toughness through designing and manufacturing various structures of CMC are used, such as self-strengthening, bionic structure and so on.

Woven SiC matrix composite is one kind of self-strengthening composites. There are a lot of large porosities or voids distributing in woven fibres. In the light of material design, the size of single void less than 1mm is permitted if the content of porosities is below 10%. To the very loose composites, neither the ultrasonic with higher frequency nor the one with lower frequency, could be successfully applied. The reasons are extremely serious attenuation for high frequency sonic, and the low resolving ability for low frequency sonic. It is the same to the optical methods, such as thermography and laser-shareography. Industrial computed tomography (ICT) with mini-focus and low energy could successfully resolve the above problems. According to the relationship that the CT values of image elements are direct proportion to the image resources, the CT values of porosities are clear difference to the fibers', so ICT could measure the size and content of the voids and porosities in this kind of ceramic matrix composites by analyzing and calculating the various CT values of ICT images. Relative experimentations give the results of five samples with 6.6%, 7.2%, 12.4%, 15.7% and 8.0% porosities.

Laminated SiC matrix composite is one kind of bionic composites. Real time imaging by microfocus X-ray could effectively minimize the geometric unsharpness of images so it has a great capability of probing micro defects. When a lower voltage within 40 to 100 kV and a micro current within 70 to 100 μA are selected, this real time imaging techniques could find out a micro crack with a width in 14.7 μm along irradiating direction, a mini void or inclusion diameter in 118 μm and a flake of monolayer with thickness in 100 μm across irradiating direction in a sample with a thickness about 2mm.

Electromagnetism & Eddy Current

Based on the theory of electromagnetics that the magnitude of counterforce to detecting coil caused by ferromagnet are inverse proportion to the square number of distance between them, electromagnetic meter could measure the thickness of non-ferromagnetic coats, including a great number of composites layers on ferromagnetic materials, but the maximal range of current advanced electromagnetic meters is only up to 30mm and the ferromagnetic matrixes must exist under the coats. For the honeycomb sandwich structure with the thickness in 40 to 80 mm, conventional instruments could not meet the require. EM-99 electromagnetic meter made in BIAM could achieve above target through inspired with a large coil for making a great electromagnetic field and receiving with a small coil for reducing error caused by the shape of composite structure, and the precision of 0.3mm could be reached.

The conductivity of graphite provides the possibility for eddy current testing. An experimentation presents that utilizing a special structure probe, in which the inspiriting and testing coils arranged across could find out the delamination in a 2mm CFRP plate, the correlative parameters are the frequency in the 100kHz to 600kHz, magnitude of lift-off at 0.1mm and a proper phase.[9]

The Developing Tendency of NDT for Composites

The diversification of NDT Methods

Compared with metallic materials and structures, the properties of inhomogeneous, anisotropic and special manufacturing process of composite materials and structures, especially with the development of new-style and low cost composites, will make NDT show its diversified characteristics. With the diversification of NDT Methods, the tendency of the intercross and combination of some NDT methods will become evident. For example, Lamb waves could be excitated by laser, Lamb waves could achieve high speed inspection in the way of one-side-testing with air-couple.

Although the developing trend of NDT for composites presents the the property of diversification, the conventional ultrasonic C-scan in the type of pulse-echo and through-transmission will still maintain the dominant status at the area of manufacture. Because ultrasonic multi-layer C-scan, ultrasonic velocity C-scan and ICT have the capacity of identifying microdefects, these techniques will play important roles in the progress of material research. Aiming at complex and inhomgeneous composite components, it is possible that ultrasonic phase array will be applied successfully.

The qualitative and quantitative evaluation

Along with the rapid development of digital instrument and powerful softwares for image processing or analyzing, more abundant and accurate information of the objects in testing could be gained. By means of effective controls to interferential signals and correct identification to the proper parameters of interesting signals, such as frequency spectrum, velocity, magnitude and phase, it will be easier to confirm the character of defects. By means of the powerful function of advanced image analyzing and calculating software, the smaller difference will be caught, so the more accurate results about defect size, position and so on could be measured easily. By means of 3-D imaging technology, the real appearance of the defects could be more clearly and directly revealed.

The standardization of NDT techniques

Classifying and comparing all NDT standards, it could be easily found out that the amounts of NDT standards for the composite materials and structures is far less than that for metallic materials and structures. For airplanes, the amounts of composite materials in advanced civil and military plane is in turn 15% and 40~50%, but the amounts of NDT standards of composites is less than 5% of the total. On one hand, it is caused by the fact that the composite is a new material compared with metallic materials, and the NDT techniques for composites is still immature. On the other hand, it is caused by the character and special manufacturing process of composites. Along with time and the accumulation of experiences that NDT techniques is applied to composites, the standardization of NDT techniques for composite materials and structures would be developed widely and deeply.

The Manufacture of artificial defects

The artificial defects, according to standards and reports, are mostly simulated by Teflon film. This method is somewhat

reasonable because most composite components are fabricated into laminate structures, including skins of sandwich structures, and the defects that are the most often and the most dangerous for the application are just delamination, disbond, unbond. But this method is also somewhat unreasonable. Firstly, the effectiveness degree and typicality of artificial defects for natural defects, which made by such simple approach that places Teflon film between in layers of lamination, or between in skin and core, or between in plate and plate, is suspicious and disquisitive. In fact, Teflon film is only an inclusion foreign materials but not air in delamination, disbond or unband. Posteriorly, this way neglects and weakens the researches aiming to other defects, such as porosity, rich resin, poor resin and crack.

As well known, quantificationally simulated and manufactured defects in term of predictive designation is extremely difficult, but it is very important and nesscery for improving research level and expanding application of NDT for composite materials and structures that efficiently and accurately simulate real defects as soon as possible.

Conclusions

With the expanding appliacation, the new NDT techniques and metheds have acquired rapid development. The standardization of NDT techniques and methods will promote its extensive development and application in composites field.

The development of NDT for composite materials and structures will present a more obvious property of diversification and syntheses in the future. The ultrasonic method will still maintain dominant status in the field of NDT for composites, especially at the stage of manufacture. The characteristics of optical NDT methods, such as fast and no touch, will make them act as a more and more important role out of laboratory.

It is an important way to develop artificial defects for improving the application of NDT in composites. The superexcellent functions of computer and image tool softwares will provide a infinite assistance for correct judging and accurate measuring various defects in composite materials and structures.

References

1. Robert C.Addison: 44th International SAMPE Symposium, 44(1), 834(1999).
2 Odile Pétillon, Jean-Pierre Dupuis.: paper ID number 310, 15th WCNDT, 2000.
3. Jan O.Strycek and Hanspeter Loertscher: 44th International SAMPE Symposium, 44(1), 103(1999).
4. F.He, S.I.Rolin: Review of Progress in QNDE, 7B, 911(1988).
5. Yoseph Bar-Cohen , Ajit K.Mal,and Shyh-Shiuh Lih: Materials Evaluation, 51(11), 1285(1993).
6. A. Dillenz, D. Wu, K. Breitrück, and G. Busse: paper ID number 311, 15th WCNDT, 2000.
7. L.D.Favro, Xiaoyan Han, and R.L.Thomas: 44th International SAMPE Symposium, 44(1), 845(1999).
8. R. Pezzoni: paper ID number 732, 15th WCNDT, 2000.
9. Adriana Savin, R.Grimberg, S.Chifan: paper ID number 499, 15th WCNDT, 2000.

Proceedings of 7th Japan International SAMPE
Symposium & Exhibition, Nov. 13-16, 2001

Nondestructive Inspection for Metal Matrix Composite

Nobuhiro Higuchi#, Mitsuyoshi Uematsu#, Akira Kohno#, Takeshi Yamada#,

Yukio Kawachi# and Shinichi Yamamoto #

#: Research Institute of Advanced Material Gas-Generator,
1-13-4 Kitaohtsuka, Toshima-ku, Tokyo, 170-0004, Japan
E-mail: nobuhiro_higuchi@nasw.mhi.co.jp

Abstract

Several X-ray inspection systems have been tested for detect ability of fibers in metal matrix composites (MMC), since the location of fibers in MMC is important to assure the integrity of MMC components.

Continuous SiC fiber reinforced Ti matrix composites were inspected by ordinary X-ray system, micro-focus X-ray system, X-ray CT (Computerized Tomography) system and micro-focus X-ray CT system. Ordinary X-ray system and micro-focus X-ray system could detect two-dimensional images of fibers. Resolution of both systems was determined by using a monolayer MMC. Both systems resolved each fiber. X-ray CT and micro-focus X-ray CT could detect three-dimensional images of fibers. Resolution of both systems was determined by using a multi layer MMC. Micro-focus X-ray CT system resolved each fiber, but Ordinary X-ray CT system detected only a whole image of fibers. The capabilities and the differences between each system for MMC quality assurance are also discussed.

Key Words: MMC, Non Destructive Inspection, X-ray, CT

Introduction

MMC are under development for aerospace structural application, because of their high specific strength and stiffness. In Research Institute of Advanced Material Gas-Generator, Continuous fiber reinforced titanium matrix composites are developed for a turbine rotor and blade. [1], [2] Since the rotor and blade are rotating components, the location of fibers in a component is very important to keep the rotor balance and structural strength.

Experimental Procedure and Results

Three types of specimens, monolayer test specimen (Fig.1), multilayer test specimen (Fig.2) and mini multilayer test specimen (Fig.3) were used in this study.

Monolayer test specimen was utilized to determine the resolution of x-ray radiography system and micro focus X-ray radiography system. Single fiber images can be observed in this specimen without fiber overlap.

Multilayer test specimen was utilized to study the actual component image. The effect of fiber overlap can be observed in this specimen.

Mini multilayer test specimen was used only for micro focus X-ray CT system.

This specimen was utilized for the same purpose as Multilayer test specimen.

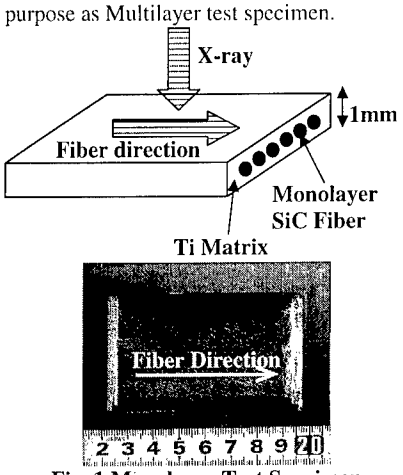

Fig. 1 Monolayer Test Specimen

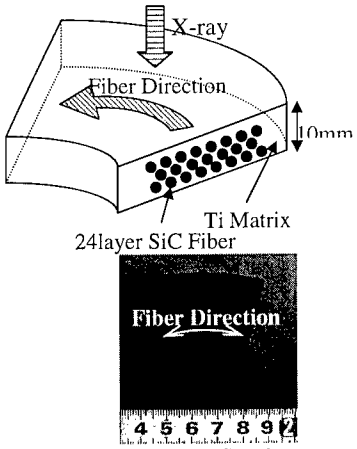

Fig. 2 Multilayer Test Specimen

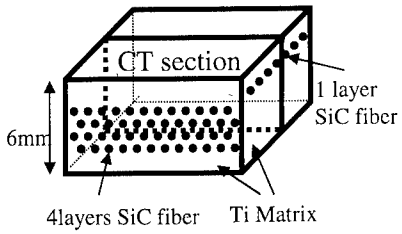

Fig.3 Mini Multilayer Test Specimen

X-ray Radiography

Ordinary X-ray radiography system was utilized for monolayer and multilayer specimen. Ordinary X-ray tube and ordinary film were used.

Monolayer specimen was used to determine the resolution of this method. Fig.4 shows the separate image of each fibers.

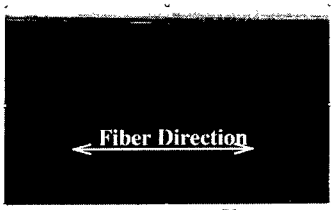

Fig.4 Monolayer image by X-ray Radiography

Multilayer specimen was used to study the difference between fiber contained area and no fiber area. Fig.5 shows the clear contrast of each area. Fig.4 and Fig.5 show the positive image of film. (high density area is black, low density area is white)

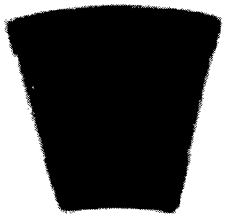

Fig.5 Multilayer image by X-ray Radiography

Micro Focus X-ray Radiography

Fig.6 shows the principle of Micro Focus X-ray system. It shows that the system can obtain magnified images of target with small penumbra($\angle U_1 > \angle U_2$).

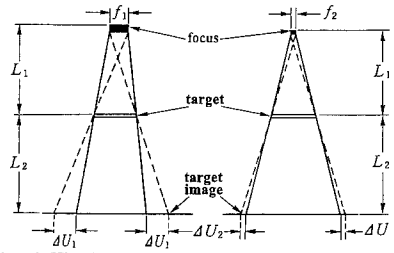

Fig. 6 The Principle of Micro Focus X-ray Radiography [4]

Fig.7 shows the image obtained by the Micro Focus X-ray Radiography system. More detail image of fibers can be seen, compared with Fig.4. Fig.8 is magnification image in the same view. Even fiber breaking point image can be seen in Fig 8.
Fig.7 and Fig.8 show the positive image of film. (high density area is black, low density area is white)

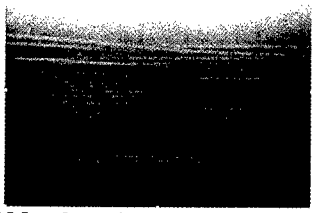

Fig.7 Monolayer image by Micro Focus X-ray Radiography

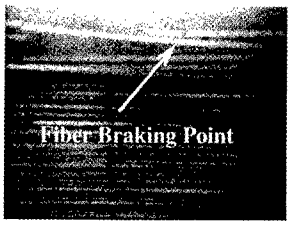

Fig.8 Monolayer magnification image by Micro Focus X-ray Radiography

X-ray CT (Computed Tomography)
CT systems can obtain the sectional image of components. Fig.9 shows the evolution of CT scan geometries.

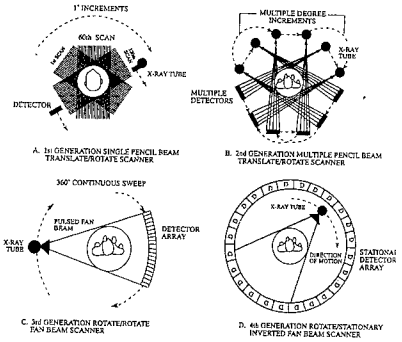

Fig. 9 Four Sketches Illustrating the Evolution of CT scan Geometries. [3]

The third generation equipment was utilized in this study. The whole image of fibers in Ti matrix can be detected for longitudinal and horizontal section.
Fig.10 shows the negative image of film. (high density area is white, low density area is black)

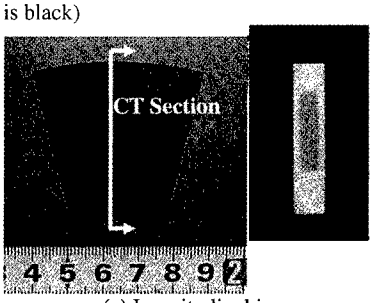

(a) Longitudinal image

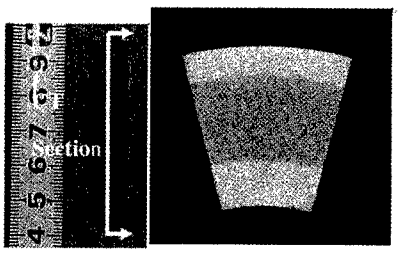

(b) Horizontal image

Fig.10 Multilayer section image by X-ray CT

Micro Focus X-ray CT

Fig.11 and Fig.12 show the cross sectional image of the Mini Multilayer Specimen. The separate image of each fiber can be seen in Fig.11 and Fig.12.

Fig.11 and Fig.12 show the negative image of film. (high density area is white, low density area is black)

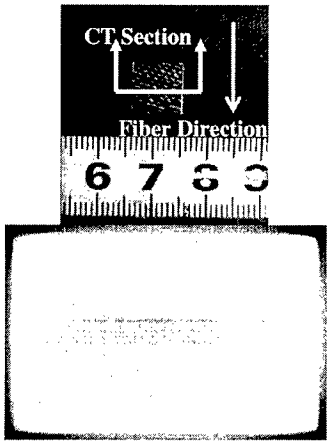

Fig.11 Multilayer section image by micro focus X-ray CT

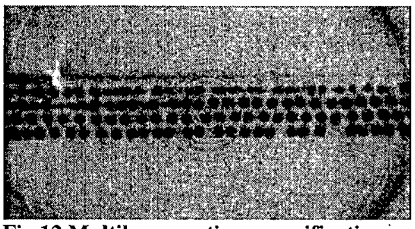

Fig.12 Multilayer section magnification image by micro focus X-ray CT

Discussion

Both the ordinary X-ray system and the micro focus X-ray system can observe the separate image of each fiber for monolayer test specimen. This result denotes that both systems have enough resolution to detect fibers in MMC. Since the whole image of fibers is detectable by these X-ray systems, the fiber location in actual component can be detected.

Three dimensional images were obtained by X-ray CT system and micro focus X-ray CT system. Ordinary X-ray CT system can detect whole fibers image, but it is difficult to get a separate image of each fibers. The micro focus X-ray CT system can detect each fiber location image, but the system can only be used for small specimen.

Conclusions

Experimental results of several X-ray methods for MMC are presented.

X-ray system and X-ray CT system can be utilized in usual inspection to detect whole fibers image to determine the location of fibers. The micro focus X-ray systems and the micro focus X-ray CT system can detect more detail image of the fibers, but it is limited to small specimen.

A good fibers location detect ability was achieved by combining these X-ray methods.

Acknowledgment

The authors wish to thank Dr. Ikeda, Mr. Mizuta (JFCC) and Mr. Shibaike (Mitsubishi Heavy Industry Takasago R&D).

References

1. T. Yamada, T. Tsuzuku, Y. Kawachi, and K. Yasuhira: Materials and Manufacturing Processes, 15(3), 347 (2000).
2. T. Yamada, A. Fukushima, C. Fujiwara, M. Hirota, Y. Kawachi and S. Yamamoto: Proc. of 7th Japan SAMPE Tech. Conf., (2001).
3. ASTM E 1441-97
4. The Japanese Society for Non-Destructive Inspection (eds.): *"New Non-Destructive Inspection handbook"*, THE NIKKAN KOGYO SHIMBUN, Tokyo, 1992 (in Japanese)

Proceedings of 7th Japan International SAMPE
Symposium & Exhibition, Nov. 13-16, 2001

Correlation Between Damage and Electrical Resistance Change in Composites with Carbon Particle and Carbon Fiber

Dong-Yeul Song, Yusuke Hirata and Nobuo Takeda

Graduate School of Frontier Sciences, The University of Tokyo c/o Komaba Open Laboratory (KOL), The University of Tokyo, 4-6-1 Komaba, Meguro-ku,
Tokyo 153-8904, Japan
E-mail:song@compmat.rcast.u-tokyo.ac.jp

Abstract

Damage and electrical resistance change in carbon particle dispersed plastic (CPDP) and carbon fiber reinforced plastic (CFRP) composites were investigated under static tension and fatigue tests. For CPDP, the electrical resistance almost linearly increased with increasing strain during loading, and the residual electrical resistance was observed even after removing load. The value of the residual electrical resistance was dependent on the maximum strain under the applied stress. Moreover, the relationship between the volume fraction of carbon particle and the electrical resistivity of CPDP was investigated in relation to the percolation theory. The electrical resistance change under applied loading could be estimated approximately using a simple theoretical model. Similarly, the relationship between the cumulative damage behavior and the electrical resistance change for CFRP was also characterized under fatigue loading.

Key Words: Carbon Particle, Carbon Fiber, Damage, Electrical Resistance.

Introduction

The electrical resistance method is expected to be effective for foreseeing damage and preventing fatal fracture of composite material structures. Recently, the relationship between mechanical parameters and the changes in electrical resistance of CFRP composite has been experimentally demonstrated [1-3]. Moreover, the damage detection utilizing the percolation structure of conductive particle instead of carbon fiber has been made[4], but this study was limited to the qualitative evaluation, and there exist few studies on the mechanical damage and electrical resistance change during fatigue of CFRP. In this study, the relationship between mechanical behavior and the change of electrical resistance for CPDP composite was evaluated using both experimental and theoretical methods. Moreover, the relationship between the cumulative damage behavior and the electrical resistance change for CFRP was characterized under fatigue loading.

Experimental Procedure

The materials used for CPDP were the conducting carbon particle of average size 5μm and an insulting epoxy matrix (Epikote 828). Specimens were prepared by injecting the mixture of carbon particles and epoxy resin with a given proportion into the mold of dumbbell shape. The electrodes for measuring electrical resistance were attached on the opposite surfaces, which were first polished to remove the insulating matrix surface layer, within the gage length of specimen using silver paste. The size of CPDP specimen was $105 \times 10 \times 1 mm^3$. Tensile tests were conducted at the crosshead speed

of 0.5mm/min. A constant current of 0.1μA was applied on the specimen, and the changes in electrical resistance under loading and unloading were measured simultaneously with stress and strain. Microscopic deformation at specimen surfaces was observed using a polarization microscope under loading. CFRP laminate specimens for fatigue test were prepared using T700S/2500 prepreg. Stacking sequence was $[\pm 25/\pm 25/90]_s$. The size of specimen was $190 \times 25 \times 1.2mm^3$. Copper sheet of 100$\mu$m was inserted between each GFRP tab and the specimen to introduce input current and to measure the resistance. Electrical contact between the carbon fibers and the copper sheet was made with silver paste. Fatigue tests were performed using a servo-hydraulic testing machine. The tests were performed in tension-tension loading at a loading frequency of 5Hz and stress ratio of R=0.1(minimun stress/maximum stress). The stress amplitude ratio (maximum stress/static ultimate strength) was 0.4 (about 280MPa). A constant current of 1mA was introduced into the ends of CFRP specimen. At each cyclic interval the specimen was unloaded and the growth of edge delamination was inspected by soft X-radiography.

Results

Static Tensile Test Result of CPDP

Figure 1 shows the electrical resistance change/strain and stress/strain curves for CPDP with 10vol.% carbon particle. The change in electrical resistance exhibited nearly linear behavior up to the final failure of specimen with increasing strain. Especially, CPDP indicated the change in electrical resistance from a considerably small strain level compared to the case of CFRP showing electrical resistance change mainly due to the fracture of carbon fibers [1-3]. This is the reason why the percolation structure formed with carbon particles shows the sensitive response (i.e., the change of conduction path) against applied loading. Figure 2 shows the electrical resistance change/strain curve for CPDP with 15vol.% carbon particle obtained from repeated loading and unloading test. It was seen that the change in electrical resistance was left after unloading at a relatively small 0.2% strain and increases with increasing strain. This means that the CPDP has the

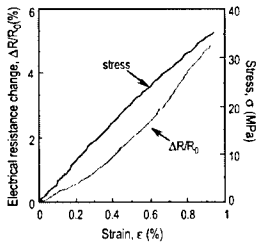

Fig.1 Relations of $\Delta R/R_0$ *vs.* ε and σ *vs.* ε for CPDP with 10 vol.% Carbon Particle

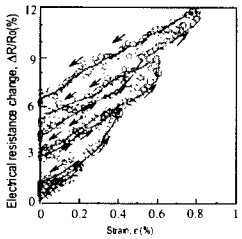

Fig. 2 Relations of $\Delta R/R_0$ *vs.* ε for CPDP with 15 vol.% Carbon Particle

ability to memorize the maximum strain applied in the past as a residual electrical resistance. This change in electrical resistance under applied load is considered to be caused by the rearrangement of carbon particles with percolation structure due to the micro-deformation and cracking of the matrix. Figure 3 shows a polarization micrograph of the surface of the CPDP specimen with 0.1vol.% carbon particle.

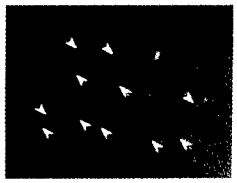

Fig. 3 Polarization Micrograph of Specimen with 0.1 vol.% Carbon Particle

The plastic deformation of matrix surrounding carbon particles was clearly observed as indicated by arrows in this figure. Thus, the existence of residual electrical resistance as described above is considered to be attributed to this plastic deformation of matrix, leading to the change of geometrical arrangement of car

bon particles from its initial state (i.e., the change of conduction path).

Relationship Between Volume Fraction of Carbon Particle and Resistivity of CPDP

The property of the composite system composed of conductive carbon particle dispersed in insulting polymer are explained as percolation phenomena i.e., when the amount of carbon particles is sufficiently high, the composite transforms from an insulator to a conductor as the result of continuous contacts between carbon particles (i.e., percolation) within the matrix. Generally, close to the percolation threshold, the concentration dependence of resistivity in a conductor-insulator composite has been well expressed with the percolation theory.

$$\rho(V) = A(V - V_c)^{-t} \tag{1}$$

where, V is the carbon volume fraction, V_c is the critical carbon volume fraction required to form a continuous conduction path, $\rho(V)$ is the resistivity at the carbon volume fraction, and A and t are the constants. According to the literature [5, 6], t was found to exist between 1.65 and 2.0 for three dimensional systems. Figure 4 shows the variation of resistivity with volume fraction of 5μm carbon particles. It is seen that the resistivity decrease abruptly when the carbon volume fraction exceeds a critical value. This suggests that the percolation theory can hold for the experimental results. The constants

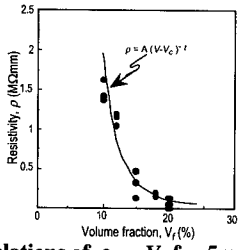

Fig. 4 Relations of ρ *vs.* V_f for 5 μm Carbon Particle

in Eq. 1 were obtained using the least square fit to the experimental data. The obtained values are V_c= 0.065, t= 1.9, A = 0.003 MΩ mm. The curve calculated with these values is also plotted in Fig.4, showing a good agreement with experiments.

Approximate Analysis of Electrical Resistance Change Under Applied Load

The change of electrical resistance of CPDP with tensile loading is developed using Eq. 1. Here, the critical volume fraction, V_c, as a first approximation, was assumed to change linearly with applied stress. Moreover, in the case of conductive particle-polymer composite the average number of contacts per particle changes linearly with stress, and was known to be inversely proportional to the critical volume fraction [7, 8]. Thus, the critical volume fraction with stress can be expressed as a simple form as follows:

$$V_c(\sigma) = \frac{V_c(0)}{1 - \alpha\,\sigma} \tag{2}$$

where, $V_c(0)$ was 0.065, the critical volume fraction when the applied stress was absent. This value was obtained from the relationship between the resistivity and the volume fraction described in Fig. 4. α is a constant. Then, substituting Eq. 2 into Eq. 1, the resistivity and its change of CPDP under applied stress were finally determined from Eqs. 3 and 4. Figure 5 shows a comparison between the analysis and

$$\rho = A\,[V - \frac{V_c(0)}{1 - \alpha\,\sigma}]^{-t} \tag{3}$$

$$\frac{\Delta\rho}{\rho_0} \approx \frac{\Delta R}{R_0} = \left[\frac{V - \dfrac{V_c(0)}{1 - \alpha\,\sigma}}{V - V_c(0)}\right]^{-t} - 1$$

$$= \left[\frac{V - \dfrac{V_c(0)}{1 - \alpha\,E\,\varepsilon}}{V - V_c(0)}\right]^{-t} - 1 \tag{4}$$

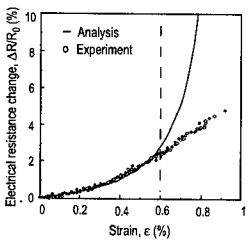

Fig. 5 Comparison Between Analysis and Experimental Results

experimental results for the CPDP of 5μm carbon particle. Here, the constant α was obtained by fitting Eq. 4 to the experimental result and its value was 0.008. The predicted result agreed well with the experimental result below 0.6% strain near the failure of material, where damage and electrical resistance greatly changed. It can be therefore said that the electrical resistance change under applied loading is evaluated approximately using the percolation equation and an appropriate model for the critical volume fraction of carbon particle as a function of the stress (or strain).

Fatigue Test Results of CFRP

Figure 6 shows the change in strain and electrical resistance of CFRP specimens ($[\pm 25/\pm 25/90]_s$) during the constant-stress fatigue loading together with the appearances of the evoution of edge delamination. It is shown that the change in electrical resistance takes place at the early stage of cycles, and increases gradually as the number of cycles increases. This resistance change due to cumulative fatigue damage was observed to be greater than during static testing by a factor of about 10 (i.e., the resistance change until the ultimate failure was about 0.035 of the original during static testing, and 0.225 of the original during fatigue). Generally, the electrical resistance change in the CFRP laminates is known to be caused by the breakage of carbon fibers or by the damage in the perpendicular direction of fiber, because electrical contact is possible between neighboring carbon fibers. In this case, the progressive increasing of resistance change in the $[\pm 25/\pm 25/90]_s$ specimen with the number of fatigue cycles are caused by the stable growth of edge delamination occurring at the 25/90 interface, that is, the contacts break between layers and the area avaliable for current flow decreases.

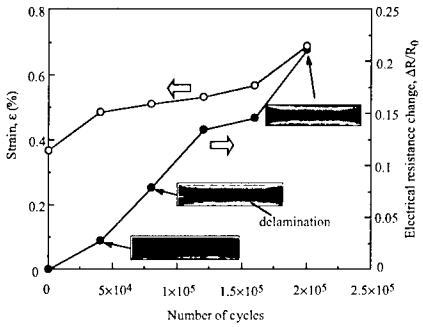

Fig. 6 Change in Strain and Electrical Resistance of CFRP Specimen during Fatigue Loading together with Appearances of Delamination Evoution

Conclusions

Mechanical damage behavior and electrical resistance change in CPDP and CFRP composites were characterized under static tension and fatigue tests. For CPDP, the electrical resistance almost linearly increased with increasing strain during loading, and the residual electrical resistance was observed even after removing load. The value of the residual electrical resistanc was dependent on the maximum strain under the applied stress.These results suggest that estimation of the maximum strain (damage state) is possible by measuring electrical resistance of composites. The residual resistance was found to be due to the plastic deformation of matrix remaining after removing loading. Moreover, the relation between the volume fraction of carbon particle and the electrical resistivity of CPDP was well expressed by the percolation equation. The electrical resistance change of CPDP under applied loading could be estimated approximately using a simple theoretical model. Furthermore, the relationship between the cumulative edge delamination behavior and the electrical resistance change for CFRP laminates was characterized under fatigue loading.

References

1. O. Ceysson et al:Scripta Mater. 34(8), 1273 (1996).
2. N. Muto et al:J. Am. Ceram. Soc. 76(4), 875 (1993).
3. K. Schulte et al:Proc. ICCM, 349 (1995).
4. M. Takada et al:J. Japan Soc. Comp. Mater. 25, 225 (1999).
5. B. Abeles et al:Phys. Rev. Lett. 35, 247 (1975).
6. F. Carmona et al:J. Appl. Phys. 61-7, 2550 (1987).
7. J. Gurland:Trans. Metall. Soc. AIME. 236, 642 (1966).
8. S. M. Aharoni:J. Appl. Phys. 43, 2463 (1972).

Proceedings of 7th Japan International SAMPE
Symposium & Exhibition, Nov. 13-16, 2001

Electric Impedance Change Method for Monitoring of Sandwich Plate Damage

Akira Todoroki[1], Saburo Murase[2], Yoshinobu Shimamura[1] and Hideo Kobayashi[1]

1: Tokyo Institute of Technology
2: Graduate student of Tokyo Institute of Technology
2-12-1 O-okayama, Meguro-ku, Tokyo,152-8552, JAPAN
E-mail: atodorok@ginza.mes.titech.ac.jp

Abstract

Debondings of sandwich plates between a skin plate of graphite/ epoxy laminated composites and core is one of the most significant damages. A new technique for detections of the debondings of the sandwich plates is proposed in the present study. The present study employs an electric impedance change method for the detections of debondings. For most of the sandwich plate, however, electric current cannot flow from skin plate to core materials. In the present study, accumulated local damage in the skin plate is monitored with the impedance change method and initiation of the debonding is estimated using the damage limit of the skin plate. In order to investigate the relationship between the damage of the skin plate and electric impedance change, tension tests of cross-ply graphite/epoxy laminates are performed measuring the electric impedance change, and an indentation test of a sandwich plate composed of graphite/epoxy skin panels and urethane form core are conducted. As a result, the applicability of the electric impedance method for detections of debondings has been experimentally shown.

Key Words: Sandwich plate, Electric impedance, Smart structure, Composites

Introduction

Sandwich plates composed of graphite/epoxy skin plates and lightweight core are widely applied in aerospace structures. In the sandwich plates, debonding between the skin plate and core created by indentation such as tool drop are significant damage that causes stiffness degradation. Since the debondings are usually very difficult to detect by visual inspection, a new technique for detection of debondings is required

An electrical resistance change method has been applied successfully to monitor a delamination crack of laminated plates [1-3]. For the method, direct electric current is charged into the laminate, and electric resistance changes of the segments between multiple electrodes are measured using a conventional strain amplifier. For the sandwich plate, however, electric current charged into the skin plate does not flow into the core not only by the thick adhesive layer but electric insulator core such as form core.

In the present paper, therefore, alternating current is employed to measure the electric impedance change of the skin plate to detect the small damage such as

matrix cracking. Before the debonding initiation, accumulated matrix cracks exits by the indentation loading. By measuring the locally accumulated matrix cracks, possibility of existence of debonding can be estimated.

In order to investigate the applicability of the method, two kinds of experiments are performed here. The first test is to know the applicability of electric impedance change method for matrix crack detection using a rectangular tension test specimen of cross-ply laminate, and the second test is to measure the limit of accumulated matrix cracks using the indentation loading of a sandwich plate specimen.

Schema of Detection Method of Debonding of the Sandwich Structure

Urethane form and aluminum honeycomb are widely applied as core materials of sandwich plates in aerospace structures. These core materials are usually bonded by thick adhesive layer that is complete electric insulator. Most of the form core materials are insulator too.

In graphite/epoxy laminates, interface debonding between fiber and matrix, matrix crack are created with local out-of-plane indentation, and those damages are produced before a debonding between skin and core. The accumulated damage in the skin plate of graphite/epoxy laminates brings the electric impedance change. Therefore, it is possible to detect the debonding between skin and core by the measurement of the electric impedance change of the skin plate of graphite/epoxy. With the relationship between the detected accumulated damages of graphite/epoxy skin plate and the debonding of sandwich plate, debonding of sandwich plate can be detected Figure 1 shows the schematic illustration of damage in a graphite/epoxy skin plates with debonding.

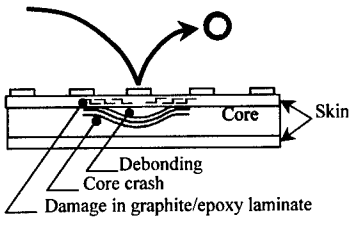

Fig.1 Schematic illustration of damage in graphite/epoxy skin plate after debonding

Experimental Methods

Cross-ply Laminates

Graphite/epoxy laminates were fabricated from a unidirectional graphite/epoxy prepreg (Q1111-2500) manufactured by Toho Tenax. The stacking sequence of the graphite/epoxy laminates is $[0_2/90]s$. Before curing, cupper foils are mounted on the surface layer, and co-cured. The cupper foils is used as electrodes for measurements the electric impedance change of the laminate. The electric impedance is measured four prove method. After curing, the laminate was cut to rectangular specimens of 210mm ×12.5mm ×1.3mm as shown Figure 2.

For the measurement of electric impedance change, a LCR meter 3522 produced by Hioki Co. was used with alternating current of 10mA at 1kHz.

A mechanical testing system was used for tension loading in the longitudinal direction, with displacement rate of 0.2 mm/min. The measurement of electric

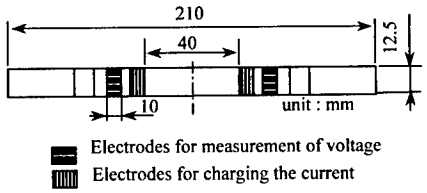

Fig.2 Sample for tensile test

impedance is conducted both on loading and after unloading at each applied stress case.

Urethane Form Core Sandwich plate

A sandwich plate composed of skin plates of graphite/epoxy and urethane form core was produced. Stacking procedure of graphite/epoxy skin plate and process of electrodes of cupper foil are the same as the case of the cross-ply laminates described in previous chapter. The stacking sequence for graphite/epoxy skin plate is [0/±45/90]s, that is quasi-isotropic laminates. The thickness of urethane form core is 8.8 mm.

Graphite/epoxy skin laminates and urethane form core are bonded together with conventional epoxy type adhesive cured at normal temperature. After bonding of the skin plates and core, the sandwich plate were cut to beam type specimens of 100mm ×15mm shown as Figure 3.

The debonding of the beam type sandwich plate specimen was created by an indentation test. The sandwich plate was set on the solid floor, and indentation loading is performed in the middle of the beam type specimen. A debonding is created just below the indented place. The indentation test was conducted using the same testing machine as described before.

With the loading, the graphite/epoxy skin plate deforms locally at the loading point. The deformation of the skin plate causes plastic deformation of the core materials. When the loading is removed, deformed core is detached from the skin plate, and the debonding is created.

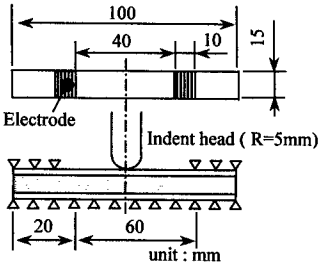

Fig.3 Testing method for indentation test

Result and Discussion

Cross-ply Laminates

Figure 4 shows the stress-displacement diagram of cross-ply laminates. The elastic deformation region is observed until approximately 50% of rupture stress. Nonlinearity is observed after the elastic deformation region. Nonlinearity is occured owing to matrix cracks and micro debondings between fibers and matrix.

Figure 5 shows the result of electric resistance measured both on loading and after unloading at each applied stress case. The electric resistance is calculated as the real part of measured electric impedance. Since the imaginary part of electric impedance small, the effect is neglected here.

In the initial elastic deformation region, the electric resistance change increases. Decrease of electric resistance is

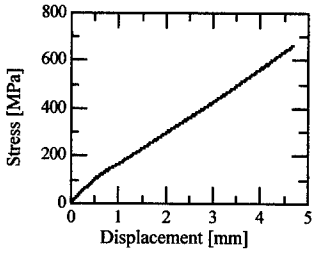

Fig.4 Stress-Displacement Diagram

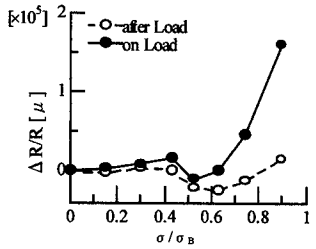

Fig.5 Electric resistance change during tensile test

observed at about 50% of rupture stress. After that, the electric resistance increases significantly just before the rupture.

The electric resistance change in the elastic deformation region coincides with the reports by many researchers [4,5]. They have proposed the application technique of CFRP composite as strain sensors.

The decrease of the electric resistance change has been reported by Chung [6]. The mechanism is our future work.

Urethane Form Core Sandwich plate

Figure 6 show the load-displacement diagram and the electric resistance change-displacement diagram. The initiation of debonding in figure 6 was observed with visual inspection. After unloading, the residual electric resistance is observed.

Urethane form core is an insulator, and the debonding between skin and urethane form core could not affect the electric resistance change. The electric resistance change is caused by accumulated damages graphite/epoxy laminates. Residual electric resistance change is also observed after un loading.

Conclusion

(1) The technique for detection of debonding between skin and core of sandwich structure with measurements of the electric impedance change of the skin plate of graphite/epoxy laminates is proposed.

(2) The electrical resistance change is observed both on loading and after unloading while tensile test of graphite/epoxy cross-ply laminates.

(3) The electrical resistance change is monitored while indentation test of sandwich plate composed of graphite/epoxy skin plate and urethane form core.

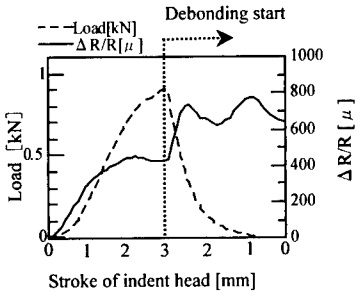

Fig.6 Electric resistance change during indentation test

Reference

1. Kazumasa Moriya and Takashi Endo: Journal of JSASS, 36(410),139(1988)
2.Yuki Tanaka and Akira Todoroki and Yoshinobu Shimamura: Trans.Jpn.Soc. Mech.Eng,, 65(640),2432(1999)
3.Yuki Tanaka and Akira Todoroki and Yoshinobu Shimamura and Hideo Kobayashi: Trans.Jpn.Soc.Mech.Eng, 67(658),1002(2001)
4.P.E.Irvong and C Thiagarajan: Smart Mater.Struct,7,456(1998)
5.N.Muto,H.Yanagida,M.Miyayama,T,Nakatsuji,M.Sugita and Y.Ohtsuka: Journal of JSCM, 18(4),144(1992)
6. Shoukai Wang and D.D.L Chung:Polymer Composites,21(1),13(2000)

Proceedings of 7th Japan International SAMPE
Symposium & Exhibition, Nov. 13-16, 2001

Ballistic Impact Behavior and Properties of Structural Ceramic Materials

Hideaki Kasano and Osamu Hasegawa

Research Center for Advanced Technology, Takushoku University
815-1 Tate-machi, Hachioji City, Tokyo 193-0985, Japan
E-mail: hkasano@ms.takushoku-u.ac.jp

Abstract

Ballistic impact tests are conducted on the structural ceramic materials of silicon carbide (SiC) and zirconia (ZrO_2) using an impact test system developed by incorporating a digital imaging system with a gas gun type impact testing machine. The digital imaging system allows visualization of the projectile's motion and the ballistic impact behavior of the target materials during testing. The present tests focus exclusively on the impact perforation and so the perforation characteristics of these materials are evaluated. The ballistic limit velocity and the residual velocity of the projectile after perforation are also estimated or predicted with the help of the analytical modeling, which is found to be very successful.

Key Words: Ballistic Impact Test, Impact Perforation Characteristics, Ultra-high Speed Photography, Analytical Modeling, Structural Ceramic Materials.

Introduction

Ceramic materials have attracted great interest for the structural applications requiring superior performance at high temperatures due to their high stiffness, low density, and high heat-resistance. However, since the monolithic ceramics are very susceptible to impact loads due to their brittleness [1], [2], their application is severely limited. Therefore, in order to reduce the brittleness and enhance the impact toughness [3], the continuous fiber reinforced ceramic composites (CFCCs) are being developed [4]. The potential applications of these ceramics and their composites are advanced gas turbine engine components including combustion liners, turbine blades, and discs, where the impact resistance against foreign objects such as carbon particles is critical to their structural integrity [5]. In the present paper, the authors are aiming at evaluating the impact perforation characteristics of the monolithic ceramic plates of silicon carbide SiC and zirconia ZrO_2 at room temperature. For this purpose, an impact test system is first developed by incorporating a digital imaging system with a gas gun type impact testing machine and then, by using this system, impact perforation

tests are performed. A projectile's motion and the ballistic impact behavior of the target plate during testing are visualized in the form of four consecutive images. Analytical modeling is also made using the conservation laws of momentum and/or energy [6], [7], which, together with the test results, leads to simple semi-empirical expressions for estimating/predicting the perforation characteristics of these materials.

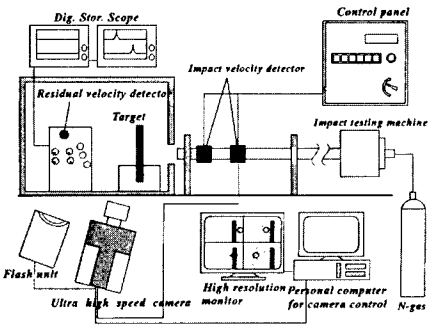

Fig.1 Impact Test System

Development of Impact Test System

Impact test system developed here is shown schematically in Fig.1 [7]. The impact machine is capable of firing a steel ball projectile of 5 mm in diameter and 0.51 g by weight at a maximum impact velocity of 330 m/s. The digital imaging system (IMACON 468) consists of an ultra-high speed camera unit, high-resolution monitor, and a personal computer for system control and data analysis. The ultra-high speed camera provides four consecutive images and they are displayed on the high-resolution monitor. The digital imaging system allows the visualization of the projectile's motion and the dynamic behavior of the target plate.

Ballistic Impact Tests

Two kinds of structural ceramics of SiC and ZrO_2 in the form of 80 mm × 50 mm rectangular plates with the thickness of 1.5 mm are chosen as the target materials in the ballistic impact tests. Only the lower edges of the target plates are clamped in the fixture and the plates are impacted normally by the steel ball projectile. The impact velocity of the projectile is measured by the velocity detector, while the corresponding residual velocity after impact perforation is determined here from the two consecutive images. The impact velocity ranges between 110 and 220 m/s. The projectile's motion and the impact behavior of the target plate are also displayed on the monitor, which are stored and/or processed in the personal computer for data analysis.

Analytical Modeling

When a steel ball projectile impinging on and passing through a target plate, a residual velocity V_R and a ballistic limit velocity V_b of the projectile are considered two major parameters that characterize the impact perforation of the target plate by the projectile. In this case, two analytical models **A** and **B** are presented for estimating the ballistic limit velocity and predicting the residual velocity [6], [7], and they formally give the same

expressions:

$$V_b = \sqrt{V_i^2 - V_R^2/\alpha^2} \qquad (1)$$

$$V_R = \alpha\sqrt{V_i^2 - V_b^2} \qquad (2)$$

where the mass coefficient α is given by

$$\alpha = \left(\frac{M}{M+m}\right)^{1/2} \qquad \alpha = \frac{M}{M+m} \qquad (3)$$

for model **A** and **B**, where M and m denote the projectile's mass and the total mass of the fragments, respectively.

Once some pairs of V_i and V_R together with α are obtained from the impact tests, the ballistic limit velocity V_b is estimated from Eq.(1) and then, by substituting it into Eq.(2), the residual velocity is predicted as a function of the impact velocity.

Results and Discussions

Figure 2 shows the residual velocity as a function of the impact velocity for SiC and ZrO_2 plates, where the filled circles represent the experimental results and the solid lines give the predictions from Eq.(2). In both plates, with an increasing impact velocity, the residual velocity increases quickly nearby the ballistic limit velocity and then it tends to increase almost linearly. The ballistic limit velocities estimated from Eq.(1) are 98.3 m/s for SiC and 82.6 m/s for ZrO_2, where, for the latter case, the data available in the estimation are limited to those close to the ballistic limit velocity. Comparison of the predictions for the residual velocities with the

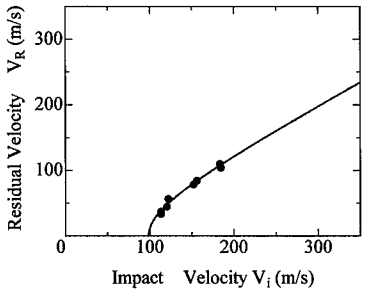

(a) SiC Plate

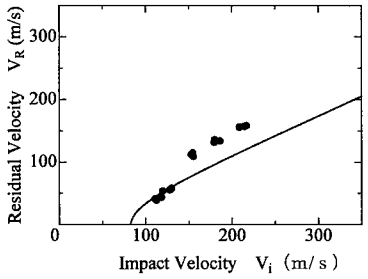

(b) ZrO_2 Plate

Fig.2 Residual Velocity vs. Impact Velocity

experimental results shows a fairly good agreement except for the case of ZrO_2 at higher impact velocities.

Figure 3 shows the relationships between the total energy lost in the perforation process and the impact velocity. The energy is found to be almost constant and the average values are 2.51 J for SiC and 1.85 J for ZrO_2.

Figure 4 shows the ultra-high speed photographs of the perforation process given by four consecutive images. From these, we find that a part of the target plates scatters in fragments with

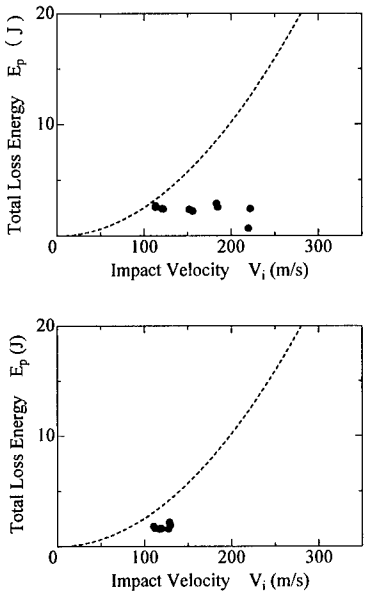

Fig.3 Loss Energy vs. Impact Velocity (upper: SiC, lower: ZrO_2)

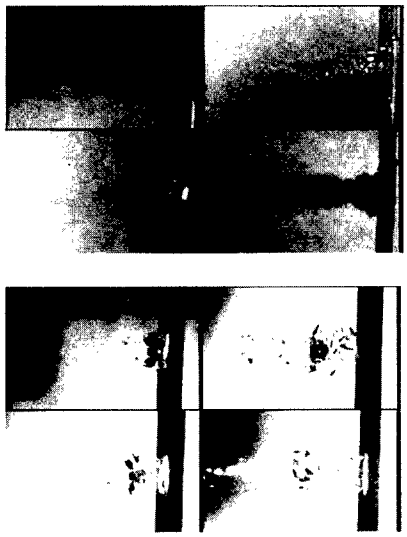

Fig.4 Ultra-high Speed Photographs ($V_i \fallingdotseq 215$m/s; upper: SiC, lower: ZrO_2)

small and large pieces, where, in general, the smaller pieces run ahead of the projectile and the larger behind that.

Conclusions

An impact test system developed here was proven to be a powerful means to the end of our study. Combination of the ballistic impact test data and the analytical modeling was successful in estimating/predicting the perforation characteristics of the silicon carbide and zirconia monolithic ceramic materials

Acknowledgements *--- The authors are very grateful to Mr. N.Yoshida for his assistance with the experimental work and data acquisition.*

References

1. J.M. Wimmer and I. Bransky, American Ceramic Society Bulletin, 56,(6), 522 (1977).
2. B.M. Liaw, A.S. Kobayashi, and A. F. Emery, Journal of American Ceramic Society, 67(8), 544(1984).
3. C.H. Hsueh and D. Hui, Composites Engineering, 5, 10 (1995).
4. T. Ishikawa et al., Science, 282, 1295 (1998).
5. Report on 300kW Class Ceramic Gas Turbine, NEDO and CGT R&D Association (1999).
6. H. Kasano and K. Abe, Proceedings of ICCM-11, Vol.II , 522(1997).
7. H.Kasano, T.Okubo, and O.Hasegawa, Int. J. Mat. & Prod. Tech., 16(1/2/3), 165(2001).

Proceedings of 7th Japan International SAMPE
Symposium & Exhibition, Nov. 13-16, 2001

Acoustic Emission Analysis of Corrosion Resistance of Glass Fiber/Vinylester Composites under Acid Environment

Machiko Mizoguchi[1], Hiroyuki Hamada[1], Tohru Morii[2] and Yoshimichi Fujii[3]

1. Division of Fibro Science, Graduate School, Kyoto Institute of Technology
Matsugasaki, Sakyo-ku, Kyoto 606-8585, JAPAN
E-mail: hhamada@ipc.kit.ac.jp
2. Department of Materials Science & Engineering, Shonan Institute of Technology
1-1-25 Tsujido-Nishikaigan, Fujisawa, Kanagawa 251-8511, JAPAN
E-mail: morii@mate.shonan-it.ac.jp
3. Seikow Chemical Engineering and Machinery, Ltd.
3-1-16 Shioe, Amagasaki, Hyogo 661-0976, JAPAN
E-mail: yfuji@gold.ocn.ne.jp

Abstract

This study dealt with the acoustic emission properties of glass fiber woven fabric reinforced vinylester composites, which were different in the chemical composition of glass fiber, under acid environment. Static tensile tests with monitoring AE were performed for the specimens subjected to the creep testing in air and in acid environment. Static tensile strength of virgin E-glass fiber composite was higher than C-glass fiber composite, while the creep lifetime of E-glass fiber composite in acid environment was extremely shorter than C-glass fiber composite. The residual strength of E-glass fiber composite sustained after creep stressing to half of the creep lifetime, however, it was significantly reduced after creep stressing to about 70% of lifetime. It was clarified through the AE monitoring that the catastrophic damage accumulated in the E-glass fiber composite after such creep stressing, and such damage reduced the residual strength. This result suggested that E-glass fiber composite showed the unexpected creep rupture.

Key Words: Acoustic Emission, Kaiser Effect, Creep, Residual Strength

Introduction

Glass fiber reinforced plastics (GFRP) have been widely used as the structural materials (chemical tanks/vessels, pipes, etc.) under severe environments such as acid and alkaline environment. In general, E-glass fiber has been used as a reinforcement of GFRP for these applications. However, E-glass fiber is not stable under acid environment, and corrosion of the fiber occurs significantly. Such degradation induces catastrophic failure of GFRP structures under acid environment, and it is unfavorable phenomenon for actual application. From this reason, application of acid resistant glass fiber (e.g. C-glass and ECR-glass fiber) is

strongly demanded as the reinforcement of FRP structure under acid environment[1]. However, the data for C-glass fiber reinforced plastics are very poor. In addition, it is important to know the strength degradation mechanism of such composites under acid environment in order to improve the corrosion resistance of composites.

From this background, this study discusses the strength degradation mechanism of E-glass fiber and C-glass fiber plain woven fabric reinforced vinylester composites under creep stressing in acid environment through the acoustic emission analyses.

Experimental Procedure

Materials used were plain woven glass fabric as reinforcement and vinylester resin as matrix. In order to discuss the influence of fiber on creep behavior, E-glass fiber and C-glass fiber were adopted as the fiber of woven fabrics. By stacking 12 plies of the same fiber fabrics, two kinds of laminates were fabricated by hand lay-up method.

In order to discuss the influence of fiber type on the creep lifetime, creep test was performed in acid environment (5% HNO_3) by applying the constant stress at various stress level, and the period to final failure was measured.

In order to discuss the residual strength after creep in acid environment, static tensile test was performed for the specimens where the creep stress (pre-stress) was applied in acid environment (5% HNO_3) prior to the static tensile test. Static tensile test was performed at a constant crosshead speed of 1mm/min in air. In static tensile test, acoustic emission (AE) from the specimen was also monitored simultaneously in order to discuss the influence of creep stress on fracture mechanism in static tensile test. AE was detected by 7600 series AE instrument (NF Corp., Japan). AE transducer with the resonant frequency of 140kHz was attached to the specimen, and AE was monitored with the total gain of 60dB and the threshold of 100mV.

Experimental Results and Discussion

Table 1 summarizes the static tensile strength of each virgin specimen. The tensile strength of E-glass fiber is generally higher than that of C-glass fiber. Corresponding this fact, the tensile strength of E-glass fiber composite was 35% higher than that of

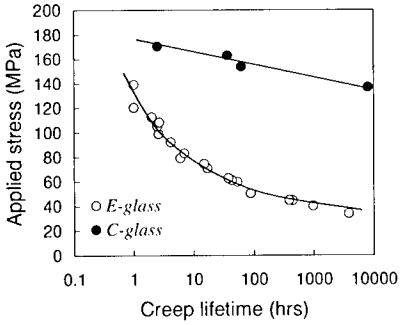

Fig.1 Creep lifetime in 5% HNO_3 solution.

Table 1 Static tensile strengths for the virgin and the pre-stressed specimens.

	Tensile Strength	Residual strength		
		Creep stressed at		
	Virgin	100 MPa, 22 hours in air	100 MPa, 1 hour in acid	100 MPa, 2 hours in acid
E-glass fiber composite	270 MPa	249 MPa	255 MPa	199 MPa
C-glass fiber composite	208 MPa	216 MPa	212 MPa	217 MPa

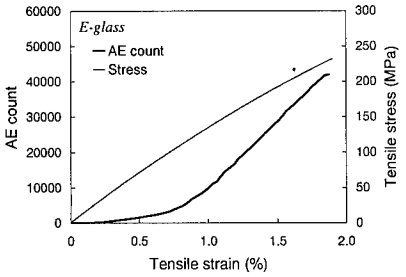

Fig.2 Stress-strain curve and AE evolution for virgin E-glass specimen.

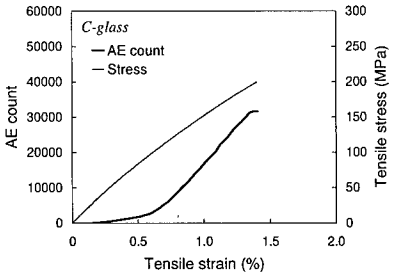

Fig.3 Stress-strain curve and AE evolution for virgin C-glass specimen.

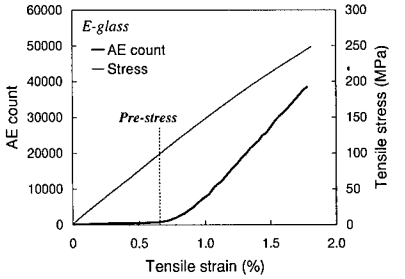

Fig.4 Stress-strain curve and AE evolution for E-glass specimen subjected to 100MPa creep stressed for 1 hour.

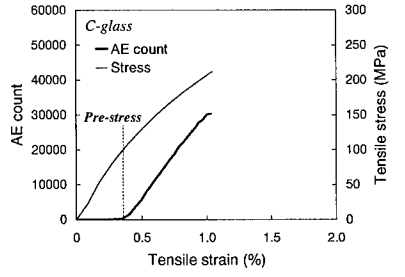

Fig.5 Stress-strain curve and AE evolution for C-glass specimen subjected to 100MPa creep-stressed for 1 hour.

C-glass fiber composite. Fig.1 shows the creep lifetime at various stress level in 5% HNO_3 solution. Creep stress level significantly affected the creep lifetime of E-glass fiber composite. In 120MPa creep stress level for E-glass fiber composite, which was almost half of the ultimate strength in static test in air, the lifetime was merely 1hr. It is well known that E-glass fiber is extremely corroded in acid environment[2], and the results shown in Fig.1 corresponded such phenomenon. On the contrary, C-glass fiber composite showed excellent creep property even in acid environment. Figs.2 and 3 shows the stress-strain curves and the AE evolution during the static tensile tests for virgin specimens. The AE counts gradually increased with increasing the applied stress at low stress level, and AE activity was stable above about 100MPa.

In order to clarify the creep rupture mechanism, static tensile tests were performed after applying the creep stress under various test conditions. As a first attempt, the creep stress of 100MPa was applied for 1 hour, which was about 40% period of creep lifetime in E-glass fiber composite. Figs.4 and 5 shows the stress-strain curves and the AE count evolution during the static tensile tests for the specimens subjected to creep stress of 100MPa for 1 hour in acid environment. Both in E-glass fiber and C-glass fiber composites, the strength reduction never occurred as summarized in Table 1, and AE never detected below the applied stress of 100MPa. This meant that the Kaiser effect still existed from the viewpoint of AE even after the creep stressing in acid solution

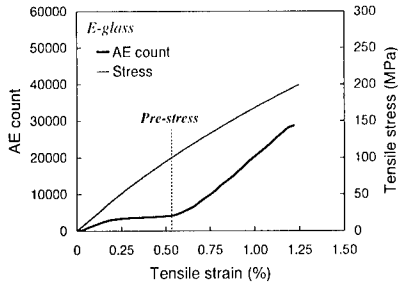

Fig.6 Stress-strain curve and AE evolution for E-glass specimen subjected to 100MPa creep-stressed for 2 hours.

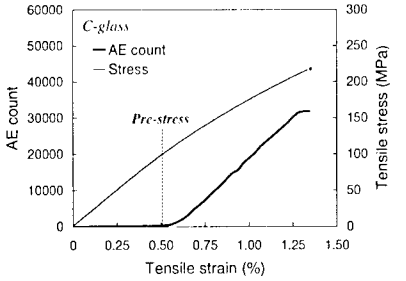

Fig.7 Stress-strain curve and AE evolution for C-glass specimen subjected to 100MPa creep-stressed for 2 hours.

in both specimens. Therefore serious damage never occurred during the creep stressing in these specimens, and the creep stress did not influence the static strength. However, the static strength in E-glass fiber composite decreased as summarized in Table 1 when the creep stress of 100MPa was applied for 2 hours in acid solution, which was about 80% period of creep lifetime. Figs.6 and 7 show the stress-strain curves and the AE count evolution during the static tensile tests for the specimens subjected to creep stress of 100MPa for 1 hour in acid environment. In C-glass fiber composite, the Kaiser effect still existed because of the low applied creep stress against the creep life-time. Therefore the serious damage never occurred during creep stressing in C-glass fiber composite. On the other hand, the AE had already detected below applied stress of 100MPa in static test for E-glass fiber composite, and it suggested serious damages had been already accumulated during the creep stressing from 1 hour to 2 hours. Such damages reduced the static strength for E-glass fiber composite. This result suggested that serious damage occurred after a certain period of creep stressing, and it might be related to the accumulation of the stored strain energy and the time for chemical reaction of glass with acid. In E-glass fiber composite, the creep rupture occurred only in the final process under creep stressing, and such process might lead the unexpected failure of E-glass fiber composite structure in acid environment.

Conclusions

This study dealt with the acoustic emission properties of glass fiber woven fabric reinforced vinylester composites, which were different in the chemical composition of glass fiber, under acid environment. Static tensile tests with monitoring AE were performed for the specimens subjected to the creep testing in air and in acid environment. The residual strength of E-glass fiber composite sustained after creep stressing to half of the creep lifetime, however, it was significantly reduced after creep stressing to about 70% of lifetime. It was clarified through the AE monitoring that the catastrophic damage accumulated in the E-glass fiber composite after such creep stressing, and such damage reduced the residual strength. This result suggested that E-glass fiber composite showed the unexpected creep rupture.

References

1. D. Santrach and R. Matzeg: Polymers & Polymer Composites, 1(6), 451(1993).
2. Q. Qiu and M. Kumosa, Composites Science & Technology, 57(5), 497(1997).

Proceedings of 7th Japan International SAMPE
Symposium & Exhibition, Nov. 13-16, 2001

On the Detection of Fatigue Damage in CFRP By Measuring Poisson's Ratio

Shun-ichi Bandoh#,Masaru Zako, Tsutomu Shiino, Tessei Kurashiki and Kenji Matsumura
#1.Kawasaki cyoh, Kakamigaha City,Gigu Prif.,504-08730,Japan
E-mail:bandoh_syunniti@khi.co.jp

Abstract

Many fatigue damage detection system for CFRP composite structures has been developed recently, but they were not successful. In this paper, a new fatigue damage detection method by measuring Poisson's ratio change is described. The phenomena that Poisson's ratio change is more sensitive than stiffness change was discovered by a simple FEM analysis. Then more precise FEM analysis has been carried out and confirmed the phenomena And, Poisson's ratio change on 0/90 and quasi-isotropic CFRP laminates were calculated.

From the static strength test results, damages such as transverse cracks could not be detected by Poisson's ratio change, because of the non-linearity of the longitudinal stiffness of CFRP laminates. However, in case of fatigue tests, it was observed that a liner relation exists between the transverse crack density and Poisson's ratio change, such as 0.5 cracks/mm transverse crack density came to 3-5 % Poisson's ratio change. This system would be useful not only for damage detection of coupon tests, but also for a health monitoring system of actual aircraft structures in the future.

Key Words: Transverse crack, Fatigue, damage detection, Poisson's ratio

1. Introduction

Many fatigue damage detection system for CFRP composite structures has been developed recently, but they were not successful.

Transverse cracks does not directly cause the structural failure, but it has been considered to be one of the failure modes in the aircraft design with a very conservative design guide. As a result, it gives the lowest design allowable (strain) and makes the structure heavier and reduces the merits of composite material over metal structures.

In this paper, a new fatigue damage detection method by measuring the change of Poisson's ratio is described. This system would be useful not only for damage detection of coupon tests, but also for a health monitoring system of actual aircraft structures.

2.Principal Theory

The phenomena that Poisson's ratio change is more sensitive than stiffness change has been discovered by FEM analysis. The elastic properties of 90 degree layers, such as E_T, G_{TZ} and ν_{TZ} shown in Table.1,were reduced by a factor of 1/100 to simulate the mechanical behavior after damage in an orthotropic laminate. The FEM model is shown in Fig.1 Then the analytical results, shown in Fig.2, suggested that Poisson's ratio reduction was more sensitive than tensile modulus change. So, the transverse cracks could be detected by measuring Poisson's ratio.

Table.1 Elastic properties of the FEM model

E_L	130(GPa)	E_T	7.1(GPa)	E_Z	7.1(GPa)
G_{LT}	3.3(GPa)	G_{TZ}	2.8(GPa)	G_{ZL}	3.3(GPa)
ν_{LT}	0.314	ν_{TZ}	0.017	ν_{ZL}	0.2569

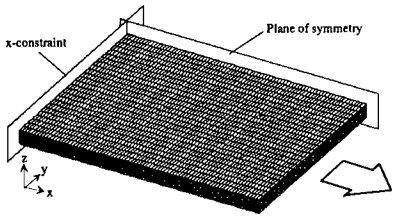

Fig.1 FEM model

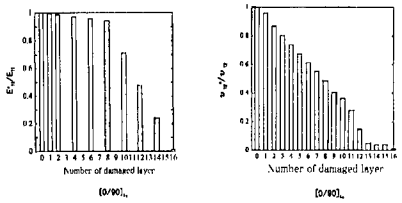

a) Stiffness changing b) Poison's ratio changing

Fig.2 Poisson's ratio and stiffness changing vs. the number of transverse cracking plies

3.Static test

To proof the phenomena, static tensile test was carried out. Fig.3 shows the test specimen and Fig.4 shows the test apparatus of transverse crack test

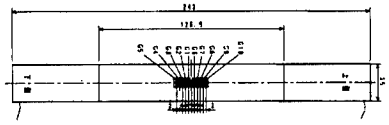

Fig.3 Test specimen

Material used for the specimen was Toho-Rayon 350 F cure epoxy CFRP pre-preg UD tape, QU135-197A (UT-500 fiber). The ply orientation was (0/90/0/90)s.

Fig.4 Test apparatus of transverse crack test

Fig.5 is one of the stress-strain charts obtained from the static tests

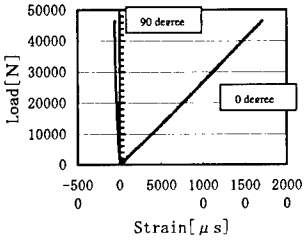

Fig.5 Experimental result of the Stress and strain relation in static test

Fig 6 shows the test results. As the transverse cracking density increases, Poisson's ratio was gradually decreased. From the static strength test results, the damages such as transverse cracks could not be detected by Poisson's ratio change, because we can recognize that Poisson's ratio in the region which transverse cracks does not occur is changed.

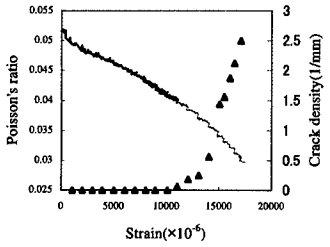

Fig.6 Relation between crack density versus Poisson's ratio

4. Fatigue test

Fatigue test was conducted for orthotropic laminates. The test specimen and the test apparatus was the same used for the static test.

As a result of the fatigue test, it was observed that a liner relation existed between the transverse crack density and Poisson's ratio change. As shown in Fig.7, 0.5(1/mm) transverse crack density comes to 4 % Poisson's ratio change.

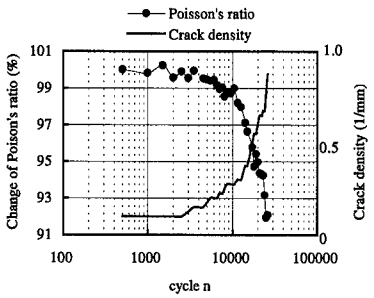

Fig.7 Test result of the fatigue testing

5.Analysis

Precise FEM analysis has been carried out to confirm the phenomena suggested in chapter 2. Fig.8 shows the microscopic observation of the transverse cracks on the test specimen.

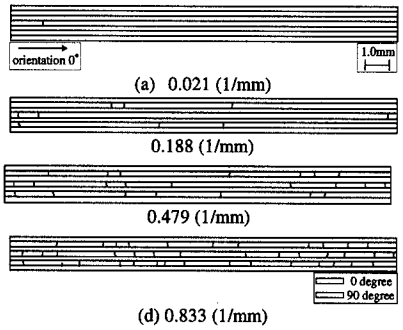

Fig.8 Observations of crack distribution

Those cracks were modeled in the FEM mesh as shown in Fig.9. Then the Poisson's ratio change on an orthotropic CFRP laminate was calculated

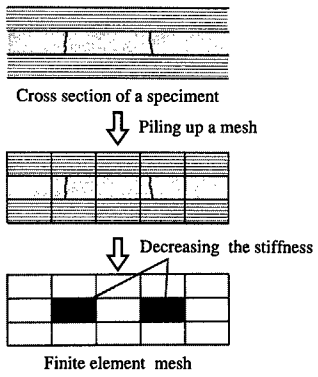

Fig.9 The process of making FEM model mesh considering transverse cracks

By FEM analysis, as shown in Fig.10, the effect of crack density on the change of Poisson's ratio for an orthotropic laminate was obtained.

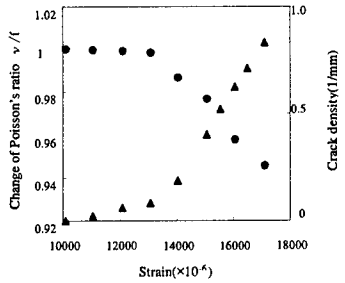

Fig.10 Effect of a crack density on Poisson's ratio for an orthotropic laminate

6.Comparison with Analysis and test results

The fatigue test results in Fig.7 and the analytical results in Fig.10 were compared in Fig. 11. From Fig.11, it was confirmed that the relation between the Poisson's ratio versus crack density was linier in both results. However, test results and analytical results were not agreed well. The reason of the difference is due to the improper assumption that elastic properties of damaged layers were reduced by a factor of 1/100 and non-linier effect of composite materials.

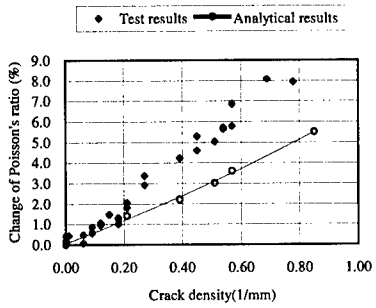

Fig.11 Comparison between the test result and the analytical result

7. Conclusion

1)Numerical results of Poisson's ratio agree with experimental ones.
2)The new fatigue damage detection method of CFRP by measuring the change of Poisson's ratio is proposed.
3)The phenomena can be used not only for damage detection of coupon tests but for a health monitoring system of actual aircraft structures using optical fiber strain censer.
4)Further testing will be necessary to apply it to actual structures.

References

1) N. Takeda and S. Ogihara, Composites Part A, 29A (1998), 1545-1552
2) N. Takeda and S. Ogihara, Proc.11th int. Conf. Compos. Mater.,Vol.5 (1997), V562V570.

Proceedings of 7th Japan International SAMPE
Symposium & Exhibition, Nov. 13-16, 2001

Adaptive Vibration Control of Composite Beams Using Neural Network Controller

I. Lee*, S.-M. Yang, J.-H. Han**, and S.-H. Youn***

Department of Aerospace Engineering,
Korea Advanced Institute of Science and Technology,
373-1, Kusong-dong, Yusong-gu, Taejon, South Korea.
* E-mail: inlee@asdl.kaist.ac.kr
** Currently ETRI, *** Currently KARI

Abstract

Experimental studies on the adaptive vibration control of composite beams with a piezoelectric actuator have been performed using neural network controller. A digital signal processor (DSP) based hardware for the real-time adaptive vibration control experiment was prepared. The proposed neural network controller has good vibration suppression performance and robustness with respect to the system parameter variations. In addition, a new feedback controller consisting of modal filter and modal neuro-controller was proposed for the real-time adaptive multi-modal vibration control of the composite beam.

Key Words: Composite Structure, Adaptive Vibration Control, Neural Network, Piezoelectric Actuator.

Introduction

Composite materials have been widely used in many advanced structural applications such as modern aircraft structures in the past several decades. Generally, these lightweight composite structures are prone to excessive vibration, which might degrade system performances and sometimes yield structural failure. Therefore, there have been active research efforts on the structural vibration suppression using passive and/or active control method. Recently, Piezoelectric sensors and actuators have attracted attention in the active vibration control [1,2].

In the real service life, environmental loads can sometimes cause local structural failure, and hence result in changes in dynamic characteristics of structures [3]. In addition, structural systems having time-varying characteristics without permanent structural damages can be easily found. When dynamic characteristics of structures are varying, vibration control using conventional linear time invariant control algorithm may result in inefficient vibration suppression, or even amplify structural vibration until structural failure occurs.

In this paper, neuro-adaptive feedback control has been presented to suppress vibrations of composite structures. The real-time implementation of the adaptive controller was performed using a DSP. Finally, a real-time adaptive multi-modal vibration control using modal filter and modal neuro-controller is introduced.

Neuro-Controller Basics

Neural Networks

Neural network is a mathematical model, which is artificially embodied by imitating

recognition or knowledge-acquiring process of human beings. The neural network used in this study consists of three layers; one input layer, one hidden layer, and one output layer. Tangent sigmoid transfer function was used for the hidden layer, and linear transfer function was used for the output layer. The output error E(**w**,**b**) to be minimized by adjusting weights and biases is defined as

$$E = \frac{1}{2}\sum_{k}(d_k - O_k)^2, \qquad (1)$$

where k, d_k, and O_k represent the index of output layer neurons, the desired output, and the output of neural network, respectively. The error back-propagation learning algorithm is applied with the momentum method and the adaptive learning rate method in order to improve convergence characteristics and the convergent speed [4].

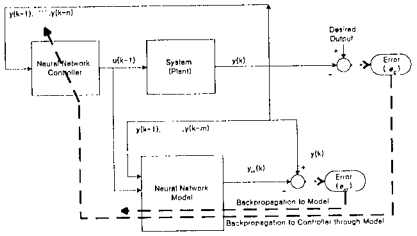

Fig.1 Overall architecture for NNC with NNM.

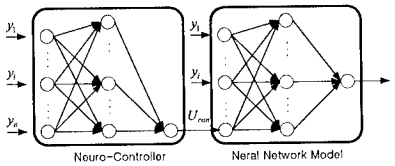

Fig.2 Connection of NNM and NNC.

Neuro-Controller

Among several control methodologies, the indirect model reference adaptive controller has been used in this study. The control system consists of the neuro-identification model (NNM) and the neuro-controller (NNC), and overall architecture of the controller is shown in Fig.1. The role of the NNM for the plant is to obtain mathematical representation of the real plant. The weights and biases of the NNM are adjusted so that the output of the NNM should be the same as that of the plant.

After completing the forward modeling, the tuning for weights and biases of the NNC is performed. Because the desired output value of the NNC is not explicitly given, this value should be calculated by the error backpropagation through the NNM, as shown in Fig.2.

Real-time adaptive vibration control

Experimental setup

In this section, the real-time adaptive vibration control experiment has been performed. Fig.3 and Table 1 show the configurations of three composite specimens prepared for the experiment. Specimens 1 and 2 were used for the single-mode vibration control experiment and specimens 1 and 3 were used for the multi-mode control experiment.

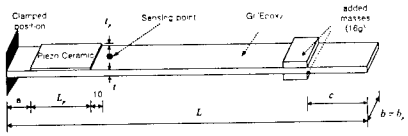

Fig.3 Geometry of the composite beam.

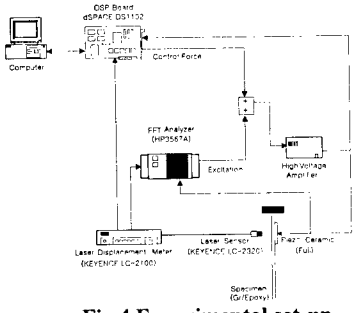

Fig.4 Experimental set-up.

Table 1 Dimensions and configurations of the composite beams

Specimen No.	1	2	3
Stacking sequence (Gr/Epoxy)	$[0/90]_s$		
Dimensions of host structure $L\times b\times t\,(mm^3)$	$300\times20\times0.425$		
Dimensions of piezo ceramic $L_p\times b_p\times t_p\,(mm^3)$	$50\times20\times0.2$		
Actuator location a (mm)	20		
Added masses location c (mm)	0	0	35
Delamination size (mm)	0	50	0
Thickness of adhesive (mm)	0.04		

The overall real-time experimental set-up for the neuro-adaptive vibration control is shown in Fig.4. The control algorithm is implemented using a DSP board (dSPACE DS1102). DS1102 uses TMS320C DSP chip of Texas Instrument as a base processor, and is equipped with 4 A/D and 4 D/A converters. The external disturbance is generated from the source channel of the FFT analyzer, and the laser displacement sensor is used to measure the displacement signal.

Single Mode Control Results

Fig.5 (a) and (b) show the changes of the frequency response functions of specimens **1** and **2** due to the application of the control, respectiely. These frequency responses were obtained by applying random external disturbance (maximum magnitude: 8V, frequency range: 0-3.16 Hz). We can see around 15~20 dB vibration reduction of the first mode for both specimens.

Fig.6 shows control results when the delamination occurs suddenly during control. It is difficult to make delamination abruptly during the experiment. Therefore, in the course of the control of the specimen **1**, the weights and biases of the NNC and NNM were saved. Then the specimen was replaced with specimen **2** and the saved weights and biases of NNC and NNM were used as the initial values of weights and biases for the next control experiment. External disturbance were applied continuously as

$$u = 5\times\sin(\omega_1 t)\ \text{(V)}. \qquad (2)$$

The magnitude of the sensor signal was reduced to about 5% of the uncontrolled magnitude. Despite the sudden change of the system, the vibration was efficiently suppressed. These results show that the present neuro-controller has effective control performance in real-time experiment even though the system is much changed abruptly.

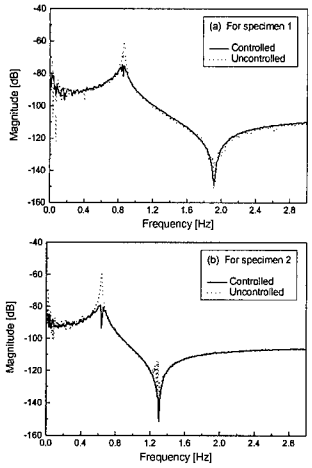

Fig.5 Vibration control results.

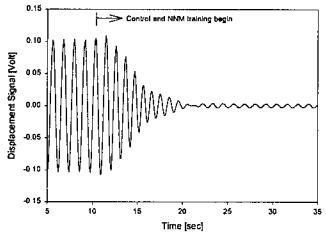

Fig.6 Adaptive vibration-control results when 50% delamination occurs under persistent disturbance.

Multi-Mode Control Results

For the adaptive multi-modal vibration control using neuro-controller, adaptive notch filter is used to separate vibration signals into modal vibration signals. Fig.7 shows the

procedure of adaptive notch filter and modal NNC's. Using recursive least square method and Bairstow method, the natural frequencies of specimens were estimated in real-time [5]. Two NNC's are connected to the corresponding modal signals so as to generate proper modal control forces. Note that a NNC without such modal filtering requires too much computation for the real-time multi-modal vibration control.

Fig.8 shows the control results when location of the added masses changes suddenly during control. The change of added mass location was emulated as described in the previous section. External disturbance were applied continuously as

$$u = 5\sin(\omega_1 t) + 20\sin(\omega_2 t) \ (\mathbf{V}). \qquad (3)$$

Fig.8 (a) shows the time history measured by the laser displacement sensor and Fig.8 (b) and Fig.8 (c) show the modal vibration signals from the modal filters.

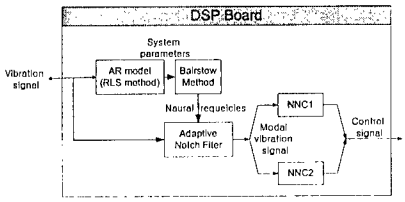

Fig.7 Block diagram for adaptive multi-modal vibration control.

Conclusions

Neuro-adaptive vibration controls of composite beams subject to sudden system parameter variations have been experimentally investigated. Significant vibration reductions have been observed using the proposed single mode neuro-controller. In addition, a new feedback controller consisting of modal filter and modal neuro-controller was proposed for the real-time adaptive multi-modal vibration control of the composite beam.

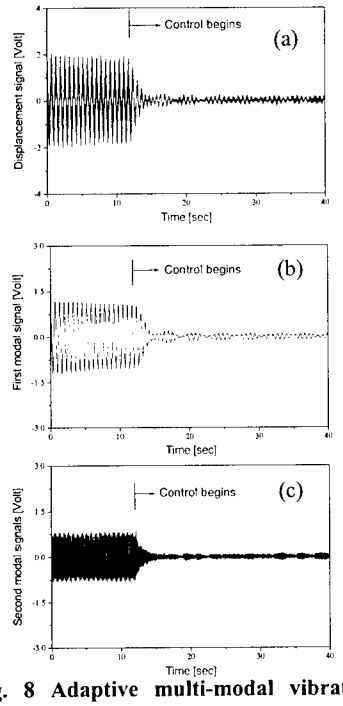

Fig. 8 Adaptive multi-modal vibration control results.

Acknowledgement

This study has been supported by a grant (Subject No. 2000-N-NL-01-C-250) from the National Research Program of the Ministry of Science and Technology, Korea.

References

1. T. Bailey and J. E. Hubbard Jr.: Journal of Guidance, Control, and Dynamics, 8 (5), 605 (1985).
2. J.-H. Han, K.-H. Rew and I. Lee: Smart Materials and Structures, 6 (5), 549 (1997).
3. I. E. Grady and E. H. Meyn: Proc. Of the AIAA SDM Conference, 1411 (1989).
4. J. M. Zuranda: "*Introduction to Artificial Neural Systems*," West Publishing Company, St. Paul, MN, 1992, pp.211-213.
5. K.-H. Rew, J.-H. Han, and I. Lee: Key Engineering Materials, 183(1), 1201 (2000).

Proceedings of 7th Japan International SAMPE
Symposium & Exhibition, Nov. 13-16, 2001

Delamination Detection Using Curvature Vibration Modes

Hisao Fukunaga#, Ning Hu#, Masaki Kameyama# and Fu-Kuo Chang##

#: Department of Aeronautics and Space Engineering, Tohoku University
Aramaki 01, Aoba-ku, Sendai 980-8579, JAPAN
E-mail: fukunaga@ssl.mech.tohoku.ac.jp
##: Department of Aeronautics and Astronautics, Stanford University
Stanford, California 94305, USA

Abstract

The present paper shows a delamination detection method based on the low-degree vibration modes. The vibration characteristics of laminated composite beams and plates have been analyzed by using a higher-order FEM model. The effect of delamination on natural frequencies, vibration modes, curvature mode shapes and the response of piezoelectric sensors has been studied in detail for providing the valuable information on delamination identification.

Key Words: Delamination, Vibration.

Introduction

Delamination is one of the most common damage due to impact. Many researches have been done to determine the changes in dynamic response of composite materials caused by delamination, and also to identify the delamination using dynamic response [1]. Curvature mode shapes in a low-degree natural vibration give useful information to detect delamination [2][3].

The present paper studies the effect of delamination on the low-degree vibration characteristics, especially on curvature mode shapes, numerically by using a higher-order FEM model [4][5]. The validation of the present numerical results is examined by the comparison with the existing experimental and analytical results [6][7]. It is shown that we can detect delamination by using the curvature mode shapes and also the response of piezoelectric sensors.

Numerical Analysis Method by FEM

We first consider a cantilevered beam with a delamination as shown Fig.1. In order to analyze the vibration of delaminated composite laminates with moderate thickness, a FEM model based on a simple higher-order plate theory is used [4], which can satisfy the free conditions of transverse shear strains on the top and bottom surfaces of plates. Displacement continuity conditions at the delamination front are implemented using the present FEM model. The FEM model also incorporates the effect of piezoelectric sensors in the vibration analysis [5].

The laminate considered in the present paper consists of T300/943 graphite/epoxy composites and the material constants of lamina are: E_{11}=134 GPa, E_{22}= 10.3 GPa, G_{12}= G_{13}= 5.00 GPa, G_{23}= 3.28 GPa, ν_{12}= 0.33 and ρ=1.48×10^3 kg/m^3. The variation of natural vibration frequencies, vibration modes and curvature mode shapes caused by delamination is analyzed by the present finite element model for the two

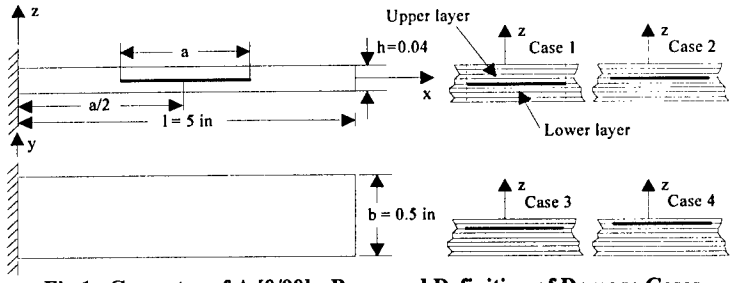

Fig.1 Geometry of A $[0/90]_{2s}$ Beam and Definition of Damage Cases

cases of a cantilevered beam and a clamped plate with an embedded delamination.

Numerical Results

Cantilevered Beam with A Delamination

We consider a cross-ply beam of eight plies $[0/90]_{2s}$ shown in Fig.1. The dimensions are 127 ×12.7×1.02 mm (5×0.5×0.04 in). Lengthwise delamination locations are at the middle of beams and the lengths of delamination and beam are denoted by "a" and "l", respectively. For the different positions of delamination along the thickness direction, four cases, Cases 1-4, are defined as shown in Fig.1.

Fig.2 shows the comparison of the present numerical results and the existing results [6][7] for the fundamental natural frequencies where the present finite element model uses the so-called "constrained model" that there are strong springs between the node pairs on two delaminated layers. In this case, the upper and lower delaminated layers vibrate together without opening modes. From this figure, it can be found that good agreement was obtained between the present method and those in [6][7]. It is seen that the natural frequencies decrease with the delamination length.

The variation of the natural vibration modes due to delamination is shown in Fig. 3 for Case 4 with 25.4 mm delamination (a/l=0.2). The natural vibration mode is normalized using the modal deflection at the free edge. The variation of the natural

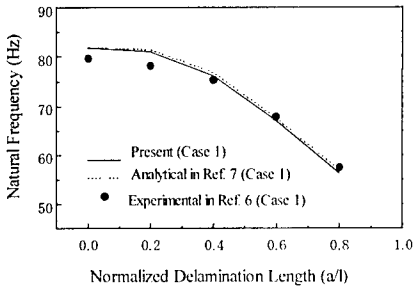

(a) Case 1

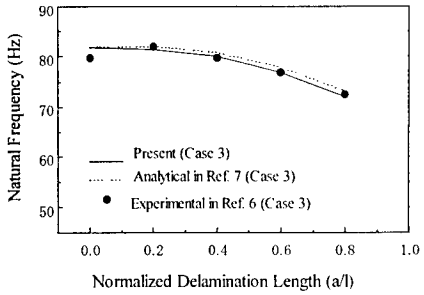

(b) Case 3

Fig.2 First Natural Frequencies for Various Delamination Length

vibration mode with and without delamination is so small that we cannot detect delamination from the information of natural vibration modes.

Next we examine the curvature mode

shapes. When the delamination of 25.4 mm(1 in) length (a/l=0.2) is located at the different interfaces, the curvatures of the first and third bending modes along the x-axis direction are shown in the Fig.4. The curvatures are normalized using the curvature at the fixed end. In these figures, it can be seen that the curvature changes most significantly for Case 1, i.e., the mid-plane delamination. As the delamination leaves from the mid-plane to the upper surface of beam, the change of curvature becomes smaller. This means that the delamination reduces the stiffness of laminates most significantly when it is located at mid-plane. It can also be found that the change of curvature for the third mode becomes more significant as compared with that for the first mode. Even for Cases 3 and 4, the sudden change of curvature for the third mode becomes more obvious as shown in Fig.4.

As curvature mode shapes are similar to strain distributions on the surface of the beam, we will examine the response of PVDF piezoelectric sensors [8]. The material properties of PVDF sensors are $E_{11} = E_{22} = 2.0$ GPa, $G_{12} = G_{13} = G_{23} = 0.8$ GPa, $\nu_{12} = 0.25$, $t = 0.003$ in (thickness), $\rho = 1.3 \times 10^3$ kg/m^3, $d_{31} = -154$ pm/V, $d_{32} = 0.0$ pm/V. Delamination locations are at the middle plane of the beam along the thickness direction (Case 1). The length of the delamination is set to be 25.4 mm (1 in), i.e., 1/5 of the total length of the beam. The beam is divided into 20 elements as shown in Fig.5. A sensor has the size of one finite element in Fig.5 and the number of sensors is 20. Then, there are four sensors within a delamination area. Fig.6 shows the response of piezoelectric sensors at the top surface layer for the third mode. It is seen that the delamination can be detected clearly.

Clamped Plate with A Delamination

A square plate with clamped boundary conditions on four edges as shown in Fig.7 is considered. The dimensions of the plate of eight plies $[0/90]_{2s}$ are $127 \times 127 \times 1.02$ mm ($5 \times 5 \times 0.04$ in). A square

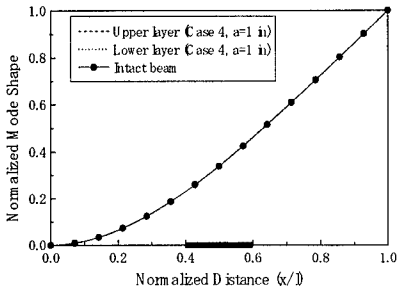

Fig.3 Comparison of First Natural Vibration Mode for Intact and Delaminated Beams (a/l=0.2)

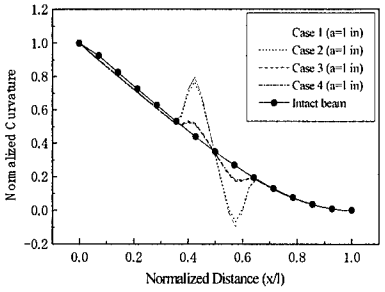

(a) First mode

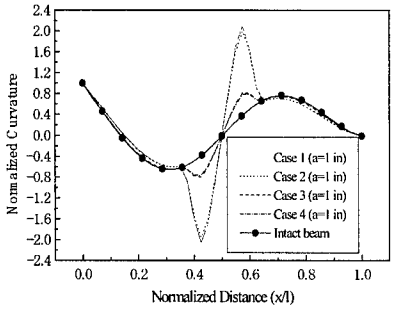

(b) Third mode

Fig.4 Curvature Mode Variation for Various Delamination Cases

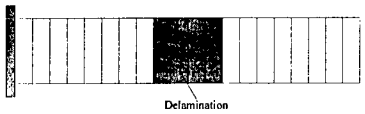

Fig.5 Delamination Location and FEM Mesh

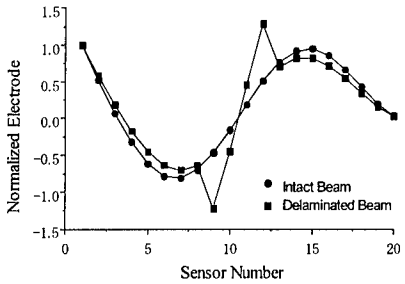

Fig.6 Response of Piezoelectric Sensors for the Third Mode

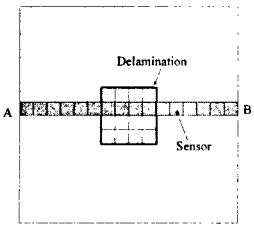

Fig.7 Delamination Location and FEM Mesh for Clamped Plate

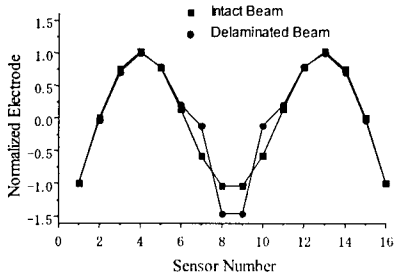

Fig.8 Response of Piezoelectric Sensors for the Third Mode in A Clamped Plate

embedded delamination is located at the center of plate and on the mid-plane of plate along the thickness direction. Now we examine the response of PVDF piezoelectric sensors. The 16×16 mesh division with the 9-node element shown in Fig.7 is used. Within the delamination area, there are 16 sensors of equal size. The response of piezoelectric sensors for the third mode along A-B line is shown in Fig.8. It is shown that the delamination can be detected clearly when we use the response of piezoelectric sensors for the third vibration mode.

Conclusions

The influences of delamination on the curvature mode shapes and the piezoelectric sensor responses for a cantilevered beam and a clamped plate have been studied. It was found that there are obvious sudden changes in the curvature mode shapes and thus in the piezoelectric sensor responses if the delamination size is relatively large. These results indicate that the piezoelectric sensors can detect delamination if sensors with the size smaller than the delamination area are used.

References

1. Y. Zou, L. Tong, and G. P. Steven: J. Sound Vib., 230(2): 357 (2000).
2. A. K. Pandey, M. Biswas, and M. M. Samman: J. Sound Vib., 145(2): 321 (1991).
3. C. P. Ratcliffe and W. J. Bagaria: AIAA J., 36(6), 1074 (1998).
4. H. Fukunaga, N. Hu and G. X. Ren: Int. J. Solids Struct., in press (2001).
5. H. Fukunaga, N. Hu and F. K. Chang: Int. J. Solids Struct., in press (2002).
6. M. H. H. Shen and J. E. Grady: AIAA J., 30(5): 1361 (1992).
7. H. Luo and S. Hanagud: Int. J. Solids Struct., 37(10): 1501 (2000).
8. H. Fukunaga and N. Hu: Proc. 3 rd Int. Workshop on Health Monitoring., in press (2001).

Proceedings of 7th Japan International SAMPE
Symposium & Exhibition, Nov. 13-16, 2001

Strain Sensor Output-based Health Monitoring of CFRP Structures by Using Localized Flexibility Method

Yoshio Aoki#, O-IL Byon (Goichi Ben)##

 # Department Precision Machinery Engineering, College of Sciences and Technology, Nihon University, 7-24-1 Narashino-dai, Funabashi, Chiba, 274-8501 Japan
yaoki@eme.cst.nihon-u.ac.jp
Department of Mechanical Engineering, College of Industrial Technology, Nihon University, 1-2-1 Izumi-cho, Narashino, Chiba, 275-8575 Japan

Abstract

This paper presents modal-based structural damage detection. Specifically, we focus on localized flexibility properties that can be deduced from the experimentally determined global eigenvalues and their modes. We describe the underlying damage detection theory that can be viewed a generalized flexibility formulation in element strain-basis. The localized flexibilities are applied to the damage detection of CFRP laminates having interior damage. The results show that the damage locations indicated as the change of flexibility are identified with high confidence.

Key words: CFRP, Damage Detection, Localized Flexibility, Inverse Analysis

Introduction

CFRP laminated composites have a very favorable strength and a stiffness-to-weight ratio among engineering materials and these make their aerospace applications highly desirable and weight savings translate directly into higher performance. A major concern in using these composites is their vulnerability to impulsive loadings by space debris, pebbles and dusts. This is because crack or damage caused inter-laminar delaminations or fiber-matrix debonding in the laminated composites, although not visible on the surface, significantly reduces their strength and/or stiffness. A rational method for detecting the damage location and the damage mechanisms in composites can therefore facilitate a wider acceptance of composites by practicing engineers. To this end, several damage detection methods have been proposed, which include ultrasonic crack detection, wave propagation and scattering, modal testing, among others [1],[2]. We have applied the localized flexibility method to damage identification in CFRP laminated beam [3].

The objective of the present paper is to offer a modal-based damage detection technique by relying on vibrations test data. We describe the underlying damage detection theory that can be viewed a generalized flexibility formulation in element strain-basis. The localized flexibilities are applied to the damage detection of CFRP laminates having interior damage. The numerical predictions are compared with the experimental results, which indicates that the localized flexibility changes yield both accurate identification of damage location and the damage levels.

Localized Flexibility Formulation

Global Flexibility Matrix

The discrete energy functional Π for a linear damped structure can be expressed as

$$\Pi(u_g) = u_g^T(\tfrac{1}{2}K_g u_g - f_g^D), \quad K_g = L^T K L$$
$$K = \begin{bmatrix} K^1 & & \\ & K^2 & \\ & & K^{n_s} \end{bmatrix}, \quad f_g^D = f_g - M_g\ddot{u}_g - C_g\dot{u}_g \tag{1}$$

where u_g is the displacement vector of the assembled global structure; f_g^D is d'Alambert's force vector that consists of the applied force vector f_g, the resisting inertia force $M_g\ddot{u}_g$, and the dissipating force $C_g\dot{u}_g$. K_g, C_g and M_g are the assembled stiffness, damping and mass matrix of the structure, respectively. K is the block diagonal collection of unassembled partitioned substructural stiffness matrices K^S (s=1~n). L is the Boolean assembly matrix that relates the assembled global displacement to the substructural ones. The superscript '$\cdot$' designates time differentiation, and the subscript 'g' designates 'an assembled global structure' to distinguish from 'unassembled partitioned substructures'. The discrete damped, time-invariant linear equations of motion for vibrating structures can be obtained from the stationary value of the preceding discrete energy functional, viz., $\delta\Pi = 0$:

$$M_g\ddot{u}_g + C_g\dot{u}_g + K_g u_g = f_g. \tag{2}$$

The input-output relation, referred to as the Frequency Response Function (FRF), is obtained by substituting a harmonic form of the input-output vectors as

$$\begin{bmatrix} u_g \\ f_g \end{bmatrix} = e^{j\omega t}\begin{bmatrix} \bar{u}_g \\ \bar{f}_g \end{bmatrix} \tag{3}$$

and solving for the frequency-domain output $\bar{u}_g$:

$$\bar{u}_g = H_g(\omega)\bar{f}_g, \tag{4}$$
$$H_g(\omega) = (K_g + j\omega C_g - \omega^2 M_g)^{-1}$$

where $H_g(\omega)$ will be called the 'global' FRF matrix and becomes to the global flexibility matrix F_g ($=K_g^{-1}$) in the quasi-static limit ($\omega \to 0$). This matrix can also be obtained in terms of the eigen modes matrix Φ and eigen values matrix Λ as

$$F_g = \Phi\Lambda^{-1}\Phi^T, \Phi^T M_g \Phi = I, \Phi^T K_g \Phi = \Lambda \tag{5}$$

Strain-Basis Flexibility Equation

In order to maintain the kinematical compatibility along the partitioned interfaces, the displacement vector of the partitioned substructures u must satisfy the following relation:

$$u - Lu_g = 0 \tag{6}$$

where u are the collections of all the substructural displacements. Let us assume that the strain output s can be related to the substructural displacement u according to

$$s = Du = DLu_g \tag{7}$$

where D is the discrete strain-displacement relation matrix that can be derived in various ways, e.g., by relying on the finite element shape functions. By introducing a Lagrange multiplier vector λ_s to enforce the kinematic compatibility condition Eq.(6), the system energy functional expressed in terms of the global nodal variables given in Eq.(1) is transformed into the two-variable functional:

$$\Pi(s, \lambda_s) = s^T(\tfrac{1}{2}K_s s - f_s) - \lambda_s^T B_s^T(s - DLu_g) \tag{8}$$
$$K = D^T K_s D.$$

A simple expression is obtained if the constraint operator B_s is chosen as a nullspace of DL, viz.,

$$B_s^T(DL) = 0 \tag{9}$$

So that the stationary condition $\delta\Pi = 0$ of Eq.(8) yields

$$DLF_g L^T D^T = P_s^T F_s P_s \tag{10}$$
$$F_s = K_s^{-1}, \quad P_s = I - B_s[B_s^T F_s B_s]^{-1} B_s^T F_s$$

where F_s is the strain-basis substructural flexibility which can be used not only for localized damage detection but more importantly for identifying damage mechanisms.

Applications to Damage Detection in Continuum CFRP Composites

Analytical Demonstration

In order to demonstrate the validity of the damage detection methods outlined in the preceding section, a quasi-isotropic CFRP laminated beam having width of 15mm, length of 180mm and 2mm thickness and fixed at both ends was chosen as an example (see Fig.1). The beam was divided into 9 same-size plate elements in the Finite Element Method (FEM) and the bending rigidity of the center(5th) element was assumed to be 85% of other elements due to the damage. For offering the relative performance of this method, the global flexibility F_g was adopted as an inverse of the global stiffness matrix that was obtained from the corresponding FEM analysis. A homotopy iterative procedure [4] was then used to obtain the strain-basis flexibility F_s in Eq.(10). The homotopy iteration procedure involved

$$\begin{aligned} F_{s,k+1} &= F_{s,k} + \beta E(r_{s,k+1}), \\ r_{s,k+1} &= (DLF_g L^T D^T - P_s^T F_s P_s)_{,k}, \\ P_s &= I - B_s[B_s^T F_s B_s]^{-1} B_s^T F_s \end{aligned} \tag{11}$$

where β was an iteration parameter and E extracted the non-zero attributes of the assumed strain-basis flexibilities from r_s. For damage detection we employed the following rigidity ratio δ^{ns}:

$$\delta^{ns} = diag(F^{ns}_{healthy} / F^{ns}_{damage}) = diag(K^{ns}_{damage} / K^{ns}_{healthy}) \tag{12}$$

where the superscript (ns) designated the substructural component or degree of freedom. Fig.2 shows that the damage indication based on the strain-basis flexibilities not only correctly detected the damaged 5th element but also computed correctly the rigidity ratio of 85%. Next, the effects of the damage location for the same CFRP laminated beam were investigated by varying the rigidity in the 2nd, 3rd and 5th elements via the strain based flexibility method shown in Fig.3. In the case of Fig.2, we used the full eigenvalues and their modes for calculating the global flexibility matrix. On the other hand,

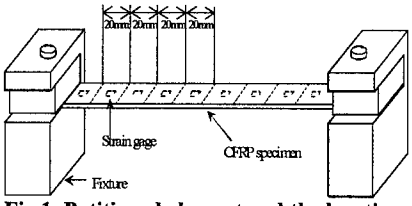

Fig.1. Patitioned element and the location of strain gage

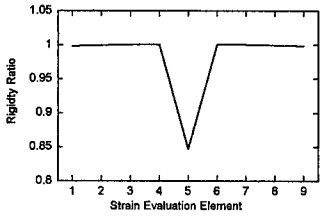

Fig.2. Damage detection based on strain flexibility

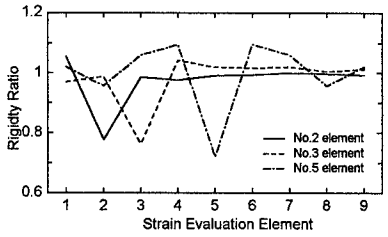

Fig.3. Analytical damage detection based on strain flexibility for various damage locations

the global flexibility matrix in Fig.3 was determined by the first three eigenvalues and their modes. Fig.3 shows that the rigidity ratio of the damaged elements was different somewhat from 0.85 for all three cases but their locations were correctly determined.

Application to Experimental Data

We carried out the damage detection by use of experimental strain data of the CFRP quasi-isotropic laminates. The strain data measured at each center of the nine elements on the beam specimens as shown in Fig.1. The impactor dropped to the center of the specimens (element 5) from 200mm height and this impact energy was 1.16J. This height was not over one to produce the failure of the specimen. The damaged area of the specimen after impact measured by a ultrasonic detection method and determined as 90.2mm^2. This area less than that of element 5. The strain data measured at the center of each element on the bottom face of specimen as shown in Fig.1. The beam then subjected to modal tests with impact hammer excitations. The FRFs were obtained by a single input and multi-output analyzer and the strains at the nine locations were measured in order to obtain the first three eigenvalues and eigenmodes. Table 1 shows the calculated and measured first three natural frequencies of the none-damaged and the damaged CFRP specimens. For the none-damaged specimen, the experimental results agreed with the FEM ones. All of the natural frequencies of damaged specimens decreased to none-damaged ones and the first value was most influenced among the three. Using the experimentally determined three global strain modes and their eigenvalues, rigidity ratios indicated as the flexibility changes were computed and they are shown in Fig4. By comparing the ultrasonic detection result with the present result, the damage location was correctly determined for the impact energy of 1.16J. Furthermore, the bending rigidity of the element 5 was supposed to be 60% of undamaged specimen.

CONCLUSIONS

The main features of the present study are summarized as follows:

(1) The damage detection, namely, the estimation of global flexibility matrix of CFRP quasi-isotropic laminates has been carried out by use of analytically or experimentally determined the first three eigenvalues and their modes. The results accurately capture the location of damage.

(2) In the case of using the impact loading to the CFRP specimen, the strain-basis flexibility method demonstrates that the rigidity of damage location is assigned to some value.

References

1. S. W. Doebling: Damage Identification and Health Monitoring of Structural and Mechanical System from Changes in Their Vibration characteristics: A Literature Survey, Report No.LA-12767-MS, (1996).
2. K. C. Park, G. W. Reich and K. F. Alvin: "Structural Health Monitoring, Current Status and Perspectives", Technomic Pub. ,1997, pp.125.
3. O. I. Byon, Y. Aoki et al: Proc. 12th Int. Conf. on Composite Materials, 375(1999).
4. S. L. Richter and E. G. Collins Jr.: Proc. Conf. on Decision and Control, 331(1989).

Table 1 Natural frequencies of CFRP laminates

Specimen	Natural Frequencies [Hz]		
	1st	2nd	3rd
Non-damage (FEM)	411.2	1128	2200
Non-damage (Exp.)	404.8	1091	2102
Damaged (Exp.)	390.0	1086	2083

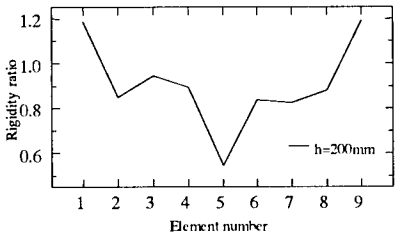

Fig.4. Experimental damage detection based on strain flexibility for the damaged specimen

Proceedings of 7th Japan International SAMPE
Symposium & Exhibition, Nov. 13-16, 2001

Delaminated Area Identification of Composite Laminated Beams Based On Resonance and Anti-resonance Frequency Change

Takaomi Inada[1], Yoshinobu Shimamura[2], Akira Todoroki[2] and Hideo Kobayashi[2]

1: Graduate school of Tokyo Institute of Technology,
O-okayama2-12-1, Meguro-ku, Tokyo, 152-8552, JAPAN
2: Department of Mechanical Sciences and Engineering,
Tokyo Institute of Technology
E-mail: tinada@ginza.mes.titech.ac.jp

Abstract

Identification of the location and size of delamination is important for structural health monitoring. In the present study, a delamination identification method using resonance and anti-resonance frequency changes is proposed. Resonance frequencies and anti-resonance frequencies of the structures are changed depending on the location and size of delamination. Since the resonance and anti-resonance frequencies are specified easily from the frequency response function, the present identification method is low cost and applicable to any structures. The present method was applied to delamination identification of graphite/epoxy clamped-clamped beams.

Key Words: Delamination identification, Resonance frequency, Anti-resonance frequency

Introduction

Recently, composite laminated structures have been applied to many structures of vehicles. Since interlaminar strength of composite laminated structure is relatively low, internal damage, such as delamination, can be easily induced in service. In order to assess integrity of the damaged structures, it is necessary to identify the size and location of the damage nondestructively.

The present study proposes a delamination identification method using resonance and anti-resonance frequency changes. For simplicity, delamination is modeled as stiffness degradation of the damaged part. In order to examine effectiveness of the present method, damage identification of a graphite/epoxy clamped-clamped beam was conducted in analysis. As a result, it is shown that there are good agreements between actual and predicted damage locations and sizes.

Damage Identification Method Using Resonance and Anti-resonance Frequency Changes

Many researchers have investigated damage identification methods using the resonance frequency changes [1-4]. However, the resonance frequency change method alone may not be sufficient for unique identification of damage location because of its symmetric properties [4]. For example, in symmetric structures like a clamped-clamped

beam, the appearance of the resonance frequency change as a function of damage location is symmetric. In this case, two candidates for damage location are obtained from the resonance frequency changes, but it is impossible to select the correct one.

In the present study, a two-stage damage identification method using resonance and anti-resonance frequency changes is proposed. The damaged domain is first identified from the anti-resonance frequency changes, and damage location and size are identified from the resonance frequency changes to the next. In order to examine effectiveness of the present method, damage identification of a clamped-clamped beam is conducted in analysis.

Damaged Domain Identification Using Anti-resonance Frequency Change

Damaged domain identification means identifying the domain in which damage is supposed to exist. In order to identify the damaged domain in a structure, anti-resonance frequency changes from an intact state is used.

Fig.1 shows a clamped-clamped composite beam with damage. The beam is 1.45mm thick, 20mm wide and 300mm long. ANSYS, a general-purpose finite element code, was used to analyze frequency response changes of the beam with damage. The stacking sequence of the beam is $[0_2/90_2]_S$, and damage is modeled as stiffness degradation of elements. Table1 shows material properties of uni-directional graphite/epoxy ply used in the analyses, where subscript 1 means the direction parallel to the fiber and subscript 2 and 3 means the direction perpendicular to the fiber. In order to model damage, the longitudinal modulus E_1 of the ply of the damaged elements is reduced to $0.8E_1$. This equals about 20% degradation of the flexural modulus of $[0_2/90_2]_S$ laminate.

The beam is divided into two spanwise domains as shown in Fig.1. Domain A is defined by $0<x/L<0.5$, and Domain B is defined by $0.5\leq x/L<1$. Existence of damage between actuating point and measuring point is detectable by anti-resonance frequency changes from an intact state. In order to use this characteristics of anti-resonance frequency changes for damaged domain identification, we set the actuating point as $x/L=0.05$ and the measuring point as $x/L=0.45$. Since the boundary of the domains corresponds to nodal point of the second flexural mode, its peak and the corresponding dip are undetectable on the frequency response measured at $x/L=0.5$. For this reason the measuring point is displaced from $x/L=0.5$ to $x/L=0.45$.

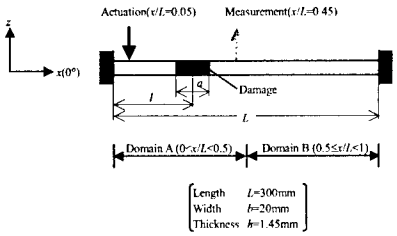

Fig.1 Clamped-clamped composite beam with damage

Table 1 Material properties of unidirectional graphite/epoxy ply

Longitudinal modulus E_1	91.5GPa
Transverse modulus $E_2(=E_3)$	8.5GPa
Longitudinal shear modulus $G_{12}(=G_{13})$	4.3GPa
Transverse shear modulus G_{23}	3.15GPa
Major Poisson's ratio $\nu_{12}(=\nu_{13})$	0.31
Transverse Poisson's ratio ν_{23}	0.35
Density ρ	1466 kg/m^3

In order to use the anti-resonance frequency changes for damaged domain identification, we use a non-dimensional parameter D as follows.

$$D_{ij}=\frac{\Delta f_{A,ij}}{\left|\Delta f_{R,i}\right|+\left|\Delta f_{R,j}\right|}\times 100 \quad (i\geq 1,\ j=i+1) \quad (1)$$

where $\Delta f_{R,i}$ and $\Delta f_{R,j}$ mean the resonance

freqnency changes of the *i*th and the *j*th mode respectively. $\Delta f_{A,ij}$ means the anti-resonance frequnecy change observed between the *i*th and the *j*th resonance peaks on the frequency response diagram. Fig.2 shows damaged domain identification example based on parameter *D*. In Fig.2, case I and case II show the results when damage is located in domain A, and case III shows the result when damage is located in domain B. Since the anti-resonance frequencies may decrease on case I, we set a threshold line of decrement as shown in Fig.2 with a dashed line. When at least one of the parameter D_{ij} is larger than the threshold , the damaged domain is identified as Domain A. When at least one of them is smaller than the line, the damaged domain is identified as Domain B.

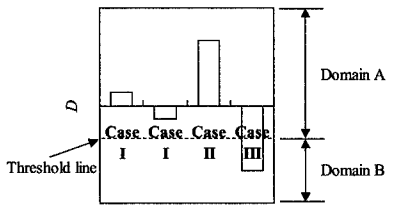

Fig.2 Damaged domain identification example based on parameter *D*

Damage Identification Using Resonance Frequency Changes

Fig.3 shows relations between damage location and the first three resonance frequencies of the flexural modes at a constant damage size (a/L=0.12) of the clamped-clamped beam (shown in Fig.1). We can see from Fig.3 that the resonance frequency changes as a function of damage location are symmetric to the center of the beam. For this reason, two candidates for damage location can be obtained from the resonance frequency changes, but it is impossible to select the correct one. In this study, we can obtain a unique damage location, since damage location and size are identified after the damaged domain identification.

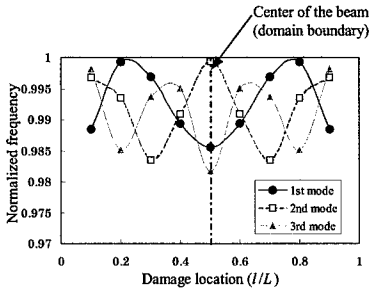

Fig.3 Resonance frequency changes of the clamped-clamped beam with damage (a/L=0.12)

We use response surfaces for damage identification. Namely, response surfaces are used to obtain the approximate expressions of relation between damage parameters and the first three resonance frequencies of the flexural modes. Since the resonance frequency changes are symmetric to the domain boundary as shown in Fig.3, we make only the response surfaces for damage identification for Domain A. For simplicity, we use polynomial response surfaces. For example, the quadratic polynomial response surface of three variables is expressed as follows.

$$y = \beta_0 + \beta_1 x_1 + \beta_2 x_2 + \beta_3 x_3 + \beta_4 x_1^2 + \beta_5 x_2^2 + \beta_6 x_3^2 + \beta_7 x_1 x_2 + \beta_8 x_2 x_3 + \beta_9 x_3 x_1 \quad (2)$$

where y is damage location or size, and x_i(i=1,2,3) is the resonance frequency of each flexural mode. In order to obtain good approximate results, cubic polynomial expressions are adopted in practical. We make response surfaces of the damage location and size respectively from 39 data sets. Adjusted coefficients of decision of the response surfaces are $R^2_{adj,location}$=0.63 and $R^2_{adj,size}$=0.83 respectively.

Damage Identification Results

In order to examine effectiveness of the present method, damage identification of a clamped-clamped beam is conducted based on analytical data. The damaged domain is identified first from the anti-resonance frequency changes, and the damage location and size are identified from the resonance frequency changes to the next.

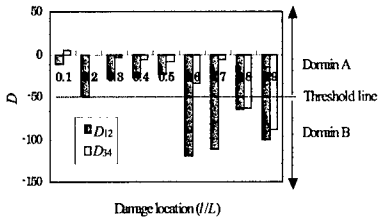

Fig.4 Damaged domain identification results of the clamped-clamped beam (a/L=0.1)

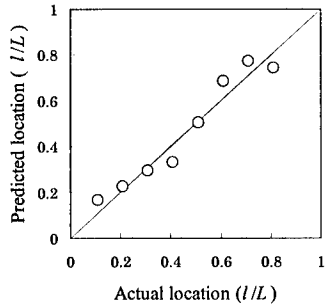

Fig.5 Comparison between actual and predicted damage locations (a/L=0.1)

Fig.4 shows damaged domain identification results of the clamped-clamped beam based on parameter D at normalized damage size is a/L=0.1. In the figure, the vertical axis is the value of parameter D, and the horizontal axis is damage location normalized by the beam length. We used two anti-resonance frequency changes for damaged domain identification. One is D_{12} and the other is D_{34}. By setting the appropriate threshold as shown in Fig.4, we can identify the damaged domain correctly. Based on the results of FEM analyses, we set the threshold as -50.

Fig.5 shows comparison between actual and predicted damage locations. For simplicity, we show only the case that the normalized damage size is a/L=0.1. Though a few data sets were not considered in the response surface of damage location, the identified values are well agreed to the actual ones. Though it is not shown in the paper, we can also identify the damage sizes precisely. The mean identification error of the damage sizes is about 7%. The damage identification results based on analytical data clearly show effectiveness of the present damage identification method using resonance and anti-resonance frequency changes.

Conclusions

This study describes the damage identification method using resonance and anti-resonance frequency changes. In order to examine effectiveness of the present method, damage identification of a clamped-clamped beam was conducted. As a result, it is shown that the damage identification method using resonance and anti-resonance frequency changes is effective in identifying damage locations and sizes.

References

1. A. S. Islam and K. C. Crag: Smart. Mater. Struct., 3, 318(1994)
2.A. C. Okafor, K. Chandrasekhara and Y. P. Jiang: Smart. Mater. Struct., 5, 338(1996).
3. X. H. Jian, H. S. Tzou, C. J. Lissenden and L. S. Penn: J. Composite Materials, 31(4), 345(1997)
4. Y. Zou, L. Tong and G. P. Steven: J. Sound & Vibration, 230(2), 357(2000)

Proceedings of 7th Japan International SAMPE
Symposium & Exhibition, Nov. 13-16, 2001

An Analytical Study of Thermal Conductivity Affecting Thermoelastic Stress Measurement of Laminate Composites

Sunao Sugimoto #, Robert E. Rowlands *, Takashi Ishikawa #

Advanced Composite Evaluation Technology Center, National Aerospace Laboratory
6-13-1 Ohsawa, Mitaka, Tokyo 181-0015, JAPAN
E-mail: sugimoto@nal.go.jp

* Department of Mechanical Engineering, University of Wisconsin, Madison, Wisconsin, USA

Abstract

Thermoelastic stress measurement is a useful nondestructive evaluation technique that can be in-situ applied. In order to apply it quantitatively to composite laminates, thermal conduction from inner layer and in-plane conduction of surface layer affecting thermoelastic stress measurement was examined in this paper. The reason of this heat conduction can be ascribed to the fact that each layer generates different levels of heat by the thermoelastic effect. Two-dimensional finite element analysis was conducted here to evaluate this heat conduction effect. Consequently, it was clarified that thermoelastic stress measurement could be quantitatively applied to conventional stacking sequences of laminate composites. It was also obtained that thermoelastic stress measurement data must be carefully dealt with if the surface layer generates relatively low heat thermoelastically.

Key Words: thermoelastic stress measurement, thermal conduction, FEA, stress concentration

Introduction

A solid body shows thermoelastic temperature change caused by load under adiabatic condition, similarly in mechanism but to much less extent than gaseous body. By utilizing this phenomenon, thermoelastic stress measurement technique was established. This technique provides the sum of principle stress changes in the surface of isotropic solid body through a temperature measurement corresponding to a load change by using infrared thermo-camera. A cyclic load is required for an accumulation of data to improve S/N ratio in temperature change data. The thermoelastic stress measurement takes only reversible stress amplitude in principle. So, effect of viscoelasticity and internal friction are not taken into account in measuring temperature data.

In the case of CFRP laminates, however, thermal conduction from inner layer (out-of-plane) and in-plane conduction occur, affecting thermoelastic stress measurement because each layer shows different generated heat by thermoelastic effect or because stress concentration

generates more heat. So, this thermal conduction should be examined to make sure the meaning of measured data. Two-dimensional finite element analysis was conducted here to evaluate this heat conduction effect and numerical results were compared with experimental results.

Finite Element Models

Finite element code ANSYS was used in this paper to examine a heat conduction effect from inner layer to the surface of CFRP laminates. Heat convection on the surface was also calculated in some cases. Two dimensional 8-node heat transfer element was used. Two types of the problems are assumed: One case is a no-hole model shown in Figure 1. This figure shows a normal section to the loading direction in the smooth specimen without a hole. The other case is a model with a circular hole, shown in Figure 2. The smooth model was a half of an actual section and the hole model was taken to a quarter of the whole section due to the symmetry derived from adiabatic conditions.

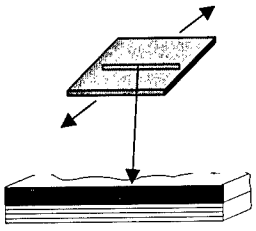

Figure 1 FEA model for smooth laminate plate.

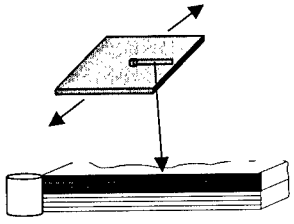

Figure 2 FEA model for laminate plate with a circular hole.

Calculation procedures for smooth laminate models

Two stacking sequences A: $(45/-45/0/90)_s$ and B: $(0/90/45/-45)_s$ were considered and compared with experimental results [3]. The calculation procedure is as follows:

(1) Nominal stresses were calculated with a uniform strain in the lamina and elastic constants of the whole laminates.
(2) A stress in each layer was calculated from nominal stresses using the classical lamination theory.
(3) Stresses in each layer were converted to stresses in fiber and transverse directions.
(4) A generated heat amplitude in each layer was obtained.
(5) These amplitudes were used as thermal input settings in FEA and the shape of generated heat in each layer was assumed as a sinusoidal function.
(6) A temperature distribution in a surface node was obtained after enough time to achieve periodically stable state.

Three boundary conditions were assumed as follows:

(a) With no conduction between layers and no convection on the surface (boundary condition #2 in Figure 3).
(b) With conduction between layers and no convection on the surface (boundary condition #3).
(c) With conduction between layers and convection on the surface (boundary condition #4).

Calculation procedures for circular hole models

In order to focus in-plane heat conduction under some stress concentration, laminate composite model with a circular hole was considered. The FEA results were compared with a theoretical result. The calculation procedure is as follows:

(1) Nominal stresses in the far field point from the circle were calculated with a

uniform strain and elastic constants of the whole laminates.

(2) A stress distribution shape of a homogeneous isotropic plate with a hole was assumed and multiplied by the nominal remote stress for determining specific stress levels.

(3) Stresses at each node were calculated from the above stress distribution and by using the classical lamination theory.

(4) Stresses in each layer were converted to stresses in the fiber and transverse directions.

(5) A generated heat amplitude in each layer at each node was obtained.

(6) These amplitudes were used as thermal input settings in FEA and the shape of generated heat in each layer was assumed as a sinusoidal function.

(7) A temperature distribution in a surface node was obtained after enough time to achieve periodically stable state.

Boundary conditions were the same as smooth laminate models.

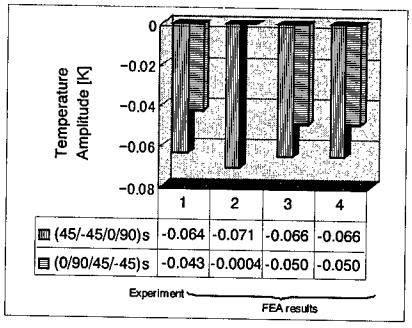

Figure 3 Comparison of temperature amplitudes in the surface of laminate composites, A: (45/-45/0/90)s and B: (0/90/45/-45)s, with FEA and experimental results.

1: experiment
2: with no heat conduction between layers and no convection on the surface
3: with heat conduction between layers and no convection on the surface
4: with heat conduction between layers and convection on the surface

Results of Finite Element Analysis

Smooth laminate models

Temperature histories at surface nodes were obtained by the procedure mentioned above. The experimental and FEA results with three boundary conditions are shown in Figure 3 for laminates A and B. In the results of laminate A with a 45 surface layer, boundary condition #2 (no heat conduction and convection considered) provides a little higher temperature amplitude than the experimental value. Conditions #3 and #4 provide very similar results to the experiment. In the laminate B with 0 surface layer, condition #2 gives, however, almost null amplitude and quite different from the experimental value. Conditions #3 and #4 lead to similar results to the experiment. The later case (laminate B) shows a typical example of an effect of heat conduction between layers. The reason of this effect is considered that a 0 surface layer generates much less heat than inner layers of 90, 45 and –45 directions. In the case of a 45 surface layer, the generated heat there is close to the average of generated heat in all layers. Hence, even no heat conduction condition provides a reasonable result in the case of laminate A. The heat convection at the laminate surface was also examined with a boundary condition #4 and the result is shown in Figure 3. There was no significant difference between #3 and #4. So, heat convection on the surface can be negligible in the present thermoelastic stress analysis.

If we check time histories in temperature change, there is no phase shift between histories of the surface temperature and load for condition #2. However, a phase shift can be observed for conditions #3 and #4. Heat conduction can be ascribed to one of the

main source of the phase shift appearing in actual measurements.

Circular hole models

In the same way of smooth laminate model, calculations for circular hole models were conducted in laminate A case. Two loading frequencies, 5 and 20 Hz, were assumed. The temperature amplitude distributions at the surface along the center line perpendicular to the load are calculated. From the calculated results, the in-plane heat conduction affects very little to temperature amplitude distribution at remote points from the hole edge. The temperature amplitude in FEA, however, leads to slightly lower amplitude than the theoretical result at a hole edge. This fact is considered as an effect of in-plane heat conduction. The temperature amplitudes by FEA for 5 and 20 Hz and the theoretical results at the circle edge of the calculated line are detailedly compared in Figure 4. This reduction of stress concentration depends on the frequency and higher frequency makes it closer to theoretical value. The temperature amplitude with 5 and 20 Hz are 83 and 90 % of theoretical, respectively. A thermoelastic stress measurement result must be carefully examined at a stress concentration region.

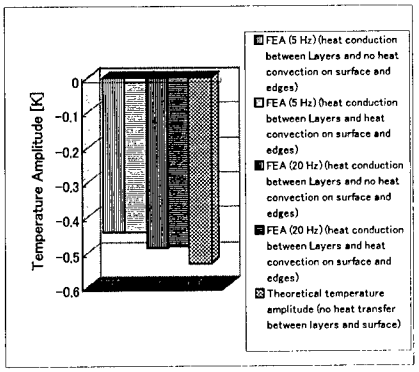

Figure 4 Comparison of temperature amplitudes at the hole edge on the surface between FEA results of 5, 20 Hz and the theoretical result.

Conclusions

The thermoelastic stress measurement can be applied to quantitative stress measurement for composite laminates with a 45 layer surface of common stacking sequence in the aerospace composite structures. In such a laminate, heat conduction from inner layers can be almost neglected. The heat convection effect on the surface is found to be negligibly small. On the other hand, it was uncovered that thermal conduction must be considered for 0 surface laminates where very low heat is generated thermoelastically. Another important finding is that the phase shift between load and temperature histories is mainly caused by the heat conduction.

It is also clarified that in-plane heat conduction effect is not significant in the remote region from stress concentration for laminates with a circular hole. It should be noted that FEA data at the hole edge is less than the no heat conduction solutions where as adiabatic condition is considered. If a sharp stress concentration exists, it is suggested that the calculated stress amplitude at the highest concentration will be relaxed by considering heat conduction. These conclusions suggest a possible application of thermoelastic stress analysis to quantitative measurement for multi-directional laminate composites.

References

1) Kazuro Kageyama: Journal of Material Science, 26, 1(1989), pp16-21 (in Japanese).
2) Sunao Sugimoto, Takashi Ishikawa: Journal of the Japan Society for Composite Materials, 23, 1, (1997), pp7-14 (in Japanese).
3) Sunao Sugimoto and Takashi Ishikawa: Proceedings of the 7th J-US Conference on Composite Materials, (1995.6), pp327-334.

Proceedings of 7th Japan International SAMPE
Symposium & Exhibition, Nov. 13-16, 2001

The Effect Of Bundle Size On Tow Impregnation During Liquid Molding Processes

Maureen E. Foley*, Suresh G. Advani*, Steven H. McKnight# and John W. Gillespie Jr.*,
*Center for Composite Materials, University of Delaware, Newark, DE 19702
#Army Research Laboratory, Aberdeen Proving Ground, MD 21005
Email: foleyme@ccm.udel.edu

Abstract

Low cost high fiber count (24 to 360K) carbon fiber tows and high areal weight glass fabrics increase the affordability of liquid molded composite structures. This paper explores the effect of bundle size on the tow impregnation during liquid molding processes. Resin and fiber wetting properties, fiber tow count and fiber volume fraction play an important role on the resin infiltration behavior within a single fiber tow. A dynamic microflow model based on Darcy's Law assumes that the infiltration of the resin is driven through capillary pressure within the tow. The model indicates that the infiltration time is ten times longer for a 60K carbon fiber tow than a 6K carbon fiber tow.

Keywords: Microflow, Tow Impregnation

Introduction

Many large-scale composite structures such as bridge decks, ship hulls, buses and train cars are fabricated using Vacuum Assisted Resin Transfer Molding (VARTM) processes. During the 1990's, the demand for low cost carbon fibers has increased for commercial applications in sporting goods, infrastructure and automotive industries. Fiber suppliers have responded to this need by offering large count tows produced from lower cost precursors. A comparison of the cross-sectional dimensions of 6K to 360K tows is shown in Figure 1A. There has also been a trend in the glass preform industry to increase the areal weight of 2-D fabrics and the renewal of interest in 3-D woven glass fabrics such as 3Weave™ by 3Tex (see Figure 1B), which have tightly packed glass rovings. The time for complete infiltration of these large fiber count carbon tows and glass rovings is expected to increase with tow size and may require optimization of the VARTM process to achieve low void content composites. A dynamic infiltration model, developed for VARTM processes, will predict the resin infiltration into a tow versus time.

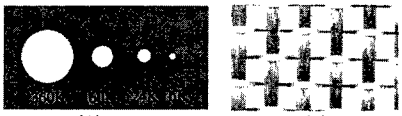

(A) (B)

Fig. 1 (A) Relative Tow Cross-Sectional Area (B) Photograph of Glass Fabric (3Weave™ by 3Tex)

Theorectical Approach

There have been many papers published on the flow in dual-scale porous media in the past 10 years due to the increase in affordability of RTM and VARTM processing. Some have focused on the difference between the intratow and intertow flow [1-2], while other have focused solely

on the flow through aligned fiber beds (intratow) [3-6]. The importance of capillary forces in the flow front were highlighted in References [7-9]. The influence of bundle or yarn size on tow impregnation, considered in this paper, has been limited in the focus of papers in the literature.

Infiltration

When high fiber count tows or rovings are in a unidirectional fabric, or woven into a 2- or 3-D fabric, there tends to be a channel of air between each tow prior to resin infiltration. The tows are assumed to be circular in cross-section (radius r_o) consisting of many circular fibers (radius r_f) arranged in a hexagonal pattern separated by a distance 2d throughout the infiltration process (Fig.2). During VARTM processing, the resin is assumed to first encapsulate the fiber tow (macroflow) and then flow radially into the tow and wet the fibers (microflow). One can assume that the tow will infiltrate at the same rate along the entire circumference of the tow (i.e. axisymmetric). A quarter-cross-section of the tow during infiltration is shown in Fig. 3. The initial tow radius is marked r_o, whereas the infiltration radius is r_i.

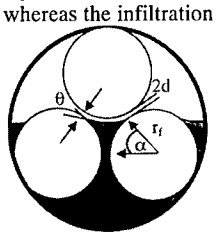

Fig. 2 Schematic of Meniscus between Three Fibers

On the microscale, the infiltration of the fiber tow is governed by the wetting of the fiber by the resin. The extent of wetting can be defined with the wetting contact angle, θ, measured from the tangent to the fiber at the fiber/resin contact as shown in Fig. 2. A directional body angle, α, also shown in Fig. 2, can be defined as the angle, which describes the location of the meniscus between two fibers as measured from the horizontal [10].

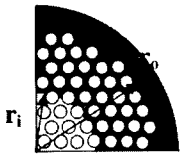

Fig. 3 Diagram of Resin Infiltration Inside the Fiber Tow

As the resin meniscus moves through the fibers within the tow, it is driven through thermodynamic considerations of the surface tensions of the fiber and matrix through capillary pressure. If the capillary pressure goes to zero or the meniscus becomes flat the driving force is zero and the flow will stop. The variation in capillary pressure can be expressed as a function of fiber radius, fiber spacing, contact angle, resin surface tension, γ_{LV}, and directional body angle as shown in equation (1) [10].

$$P_{capillary} = \frac{-\gamma_{LV}\cos(\theta+\alpha)}{r_f\,(1-\cos\alpha)+d} \qquad (1)$$

Dynamic Microflow Model

A transverse infiltration model of resin into a fiber tow has been developed to determine the time required to completely infiltrate the fiber tow. The model based on Darcy's Law, Equation (2), expressed in cylindrical coordinate system, will allow one to determine the rate of transverse infiltration of the fiber tow, $\dot{r}_i$. In equation (2), K_p is the transverse permeability, η is the Newtonian viscosity, and P is the pressure on the advancing resin meniscus. Assuming that there is no entrapped air within the tow, the pressure used is the capillary pressure of the meniscus.

$$\dot{r}_i = \frac{-K_p}{\eta(1-v_f)}\frac{\partial P}{\partial r} \qquad (2)$$

If we assume that the infiltration takes place from r_o to r_i , with a constant capillary pressure, then the infiltration time, Δt, can be calculated using the following equation.

$$\Delta t = \eta(1 - v_f)r_o^2 \left(\frac{-2\ln\left(\frac{r_i}{r_0}\right)\left(\frac{r_i}{r_0}\right)^2 + \left(\frac{r_i}{r_0}\right)^2 - 1}{4K_p P_{cap}} \right) \quad (3)$$

The infiltration is therefore a function of the fiber volume fraction, tow count, transverse permeability, capillary pressure and the viscosity of the resin. The infiltration will be complete once the infiltration front reaches the center of the tow ($r_i = r_f/r_o$).

Results

Microflow Model Inputs

The dynamic microflow model, developed in the previous section, was applied to a carbon fiber reinforced vinyl ester composite system to see if the increase in carbon fiber tow count would substantially change the infiltration time of the tow. The tow counts of 60K, 24K and 6K were chosen with fiber volume fractions of 0.8 and 0.5 for investigation. The Derakane 411-C-50 vinyl ester resin was determined to exhibit Newtonian behavior in the range of shear rates encountered in VARTM with an average viscosity of 100 cps. The resin surface tension of 35.4 dyne/cm and an average contact angle of 30° were also assumed [11]. The permeability was calculated using a lubrication approximation developed by Bruschke [12].

Capillary Pressure

The capillary pressure, Equation (1), can be expressed in graphical form as a function of directional body angle, α, and contact angle, θ, as shown in Fig. 4. The maximum capillary pressure occurs when the meniscus is located at the centerline between the two adjacent fibers (α=0°). The capillary pressure is of the same magnitude as the vacuum pressure (101 kPa) in the VARTM process. A lower contact angle is preferred for increased capillary pressure. As can be seen in Fig. 4, the peak capillary pressure for a contact angle of 5° is almost twice that of the 45° contact angle.

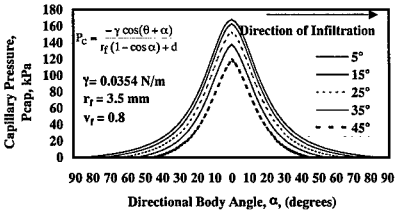

Fig. 4 Capillary Pressure Results

Dynamic Microflow Model

Assuming that there is no entrapped gas in the fiber tow prior to infiltration, one can use equation (3), with an average capillary pressure, to determine the infiltration ratio as a function of time. The infiltration time versus infiltration ratio is shown in Fig. 5. When r_i/r_o is equal to 1, the tow is empty, when r_i/r_o approaches zero, the tow is considered full. As the fiber volume fraction increases, the average fiber to fiber spacing decreases which causes a seven times increase in the capillary pressure term (4.7 to 31.2 kPa) and a significant decrease in the permeability (2.21×10^{-13} to 3.41×10^{-15} m^2). The several orders of magnitude decrease in permeability causes the infiltration time needed to meet a typical 1% void requirement to increase from 16.0 to 55.6 seconds for a 60K circular tow. The infiltration time, to reach a 1% void requirement, for a 60K tow is ten times greater than the 6K tow: (16.0 and 1.6 seconds) at the 50% fiber volume fraction and (55.6 and 5.6 seconds) at the 80% fiber volume fraction. This ten times difference in infiltration time was expected since the infiltration time equation (3) is contains a square of the tow radius term which is

directly related to the number of fibers in a tow, N, by equation (4). For two tows of equal fiber type and volume fraction, one predicts that their infiltration time is directly scaled with their tow count.

$$r_o^2 = r_f^2 v_f N \qquad (4)$$

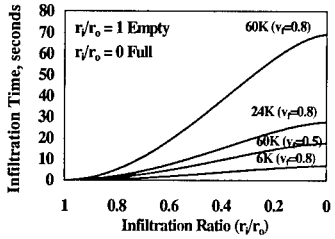

Fig. 5 Dynamic Model Results

The dynamic model results indicate that the effect of the fiber volume fraction within the tow and the tow count have a significant effect on the minimum infiltration time. In actual composites, after the arrival of the macroflow to the vent, additional infiltration time is warranted to ensure that the tows have been completely wetted through the microflow process. This additional processing time can be minimized by maximizing the capillary pressure and minimizing the entrapped air within the fiber preform.

Conclusions

The effect of carbon fiber tow count on the microflow behavior within a single tow in liquid molding processes was investigated. The dynamic microflow model, developed in this paper, assumed that the infiltration was driven solely by capillary pressure. The capillary pressure can be increased by decreasing the fiber/resin contact angle as well as increasing the resin surface tension. The model shows that the fiber volume fraction within the tow and the tow count have a significant effect on the infiltration time. The infiltration time is directly related to the tow count. As the tow count is increased from 6K to 60K, the infiltration time will increase 10 times.

Acknowledgement

Prepared in collaboration with the U.S. Army Research Laboratory Weapons and Materials Research Directorate through participation in the Materials Center of Excellence Program in Composite Materials Research under Cooperative Agreement DAAD10-01-2-0001.

References

1. R.S. Parnas, and F.R. Phelan, Frederick R. Jr.: SAMPE Quarterly, 22(2), 53 (1991).
2. C. Binetruy, B. Hilaire, and J. Pabiot: Composites Science and Technology, 57, 587 (1997).
3. T.A.K. Sadiq, S.G. Advani, and R.S. Parnas: International Journal of Multiphase Flow, 21[5], 755 (1995).
4. J. Summerscales:, Composites Manufacturing, 4[1], 27 (1993).
5. B.T. Astrom, R.B. Pipes, and S.G. Advani: Journal of Composite Materials, 26[9], 1351(1992).
6. T.D. Papathanasiou: Composites Science and Technology, 56, 1055 (1996).
7. W.-B. Young: Journal of Composite Materials, 30(11), 1191(1996).
8. C. Binetruy, B. Hilaire, and J. Pabiot: Journal of Composite Materials, 32[3], 223 (1998).
9. E. Bayramli and R.L. Powell: Journal of Composite Materials, 26[10], 1427 (1992).
10. E. Bayramli, and R.L. Powell: Journal of Colloid and Interface Science, 138[2], 346 (1990).
11. D.A. Steenkamer, S.H. McKnight, D.J. Wilkins, V.M. Karbhari, V.M.: Journal of Materials Science, 30, 3207(1995).
12. M.V. Bruschke, *"A Predictive Model For Permeability And Non-Isothermal Flow Of Viscous And Shear-Thinning Fluids In Anisotropic Fibrous Media"*, Ph.D. Dissertation, University of Delaware, 1992

Proceedings of 7th Japan International SAMPE
Symposium & Exhibition, Nov. 13-16, 2001

Effect of Orthotropic Electric Resistance on Delamination Detection With Electric Resistance Change Method

Akira TODOROKI*, Miho TANAKA**, Yoshinobu SHIMAMURA*, Hideo KOBAYASHI*

* Tokyo Institute of Technology, Department of Mechanical Sciences and Engineering, 2-12-1, O-okayama, Meguro-ku, Tokyo 152-8552, Japan
E-mail: atodorok@ginza.mes.titech.ac.jp
** Graduate student of Tokyo Institute of Technology

Abstract

An electric resistance change method is successfully applied to the delamination detections of CFRP laminates. In the present study, orthotropic electric resistances of CFRP laminates of three volume fractions of carbon fiber are measured experimentally. That reveals significant change of orthotropic electric resistances due to the small change of the volume fraction. The effect of the orthotropic electric resistance change on electric resistance measurements for delamination detection is investigated using FEM analyses. For the analyses, beam type specimens of cross ply laminates are employed. Results obtained are followings. (1) Electric resistances of thickness direction and transverse direction change significantly due to the small change of fiber volume fraction. (2)The mechanism of delamination detection with electric resistance change method was elucidated. (3) Electrodes should be mounted on fiber direction.

Key Words: Electrical properties, Delamination, Smart structure, FEM.

Introduction

Composite laminates have low delamination resistance, and that causes delamination by slight out-of-plane impacts. Since the delaminations are usually invisible or difficult to detect by visual inspections, automatic systems for delamination identifications in-service are desired. Recently, an electric resistance change method is employed to identify the internal damages of CFRP laminates [1]-[3]. Since this method adopts reinforcement carbon fiber itself as sensors for damage detections, this method does not cause reduction of static strength or fatigue strength, and applicable to existing structures. Moreover, the electric resistance change method does not cause increase weight.

In the present research, a relationship between fiber volume fraction and the orthotropic electric conductance are experimentally measured. The effects of orthotropic electric conductance are investigated and the effect of electric current charging direction is also investigated using the conductance measured by the experiments.

Experimental measurement

In order to investigate a relationship between the fiber volume fraction and electric conductance, unidirectional laminates of three types of carbon fiber volume fraction were fabricated. The material employed here is Q-111 2500: unidirectional carbon fiber/epoxy prepreg

produced by Toho Rayon Co., LTD. The conductance of longitudinal, transverse and thickness direction was experimentally measured using the different small size specimens. In order to measure the electric resistance of the specimen, silver paste is painted as electrodes. The results of the measurement are shown in Table.1.

Table 1 Fiber volume fraction V_f and Electric conductance σ

V_f	σ_0(S/m)	σ_{90}/σ_0	σ_t/σ_0
0.40	3700	1.8×10^{-4}	1.6×10^{-5}
0.47	4600	1.1×10^{-3}	2.2×10^{-4}
0.62	5500	3.7×10^{-2}	3.8×10^{-3}

Measured values of electric conductance of σ_t and σ_{90} are significantly smaller than σ_0, but they are not zero. Since carbon fiber is not straight but a wavy configuration in practical composites, fiber contact exists in the transverse and thickness direction. Besides, σ_t is smaller than σ_{90}, due to a resin rich interlamina. Since the fiber contacts depend on the fiber volume fraction, the value of σ_t and σ_{90} vary significantly by the slight change of the fiber volume fraction.

Effect of orthotropic electric conductance

Computational method and model

FEM analyses are employed for investigations of the effect of the orthotropic electric conductance using the experimental results of conductance. An adopted five-electrode-beam specimen was analyzed as shown in Fig.1. Two types of stacking sequences are computed here; [0/90]s and [90/0]s. Thickness of a ply is fixed to 0.5mm. Electrodes are mounted on the surface of the laminates, in order to investigate the effect of delamination creation and matrix crack. FEM analyses of two types of damages were performed as shown in Fig.1 and Fig.2 respectively. FEM analyses are performed using a commercially available FEM tool named ANSYS. Four-node-rectangular elements are adopted for the analysis, and the size of the each element is approximately 0.125mm. By using the auto mesh generation system of ANSYS, the specimen model is divided into approximately 19200 elements of the 2-dimentional elements. In order to analyse electric current density and electric resistance change, direct current of 30mA is charged from the electrode A to electrode B and electrode B is fixed to 0V.

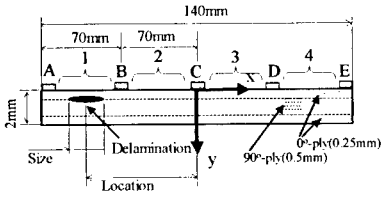

Fig.1 Specimen with delamination [0/90]s

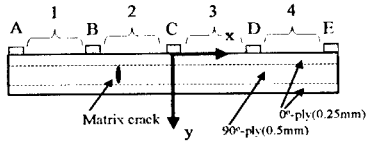

Fig.2 Specimen with matrix crack [0/90]s

Result of internal voltage contour

The internal voltage contour of an orthotropic material is shown in Fig.3. The abscissa is the location between the electrode A(-70mm) and B(0mm). The ordinate is the location of the thickness direction of the specimen.

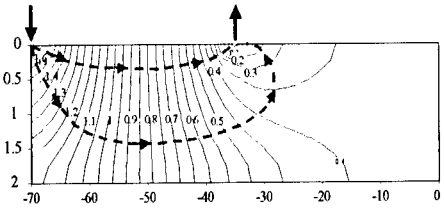

Fig.3 Internal voltage contour [0/90]s

In the case of orthotropic material, the current mainly flows into the 0-ply of the top

surface of the specimen. The electric current in the thickness direction flows gradually as shown Fig.3. When a delamination exists between the top 0-ply and 90-ply, the current into the thickness direction is disturbed by the delamination. That causes electric resistance change observed at the segment.

Electric current density

The electric current density of x-direction outside the charged segment is computed. Delamination locates between x=-57.5mm and x=-47.5mm at the interlamina between the upper 0°ply and the middle 90°ply (the size is 10mm). Current is injected from electrode A to B. The electric current density of x-direction at x=-20mm outside the segment is shown in Fig.4.

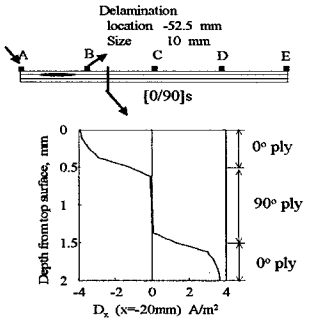

Fig.4 Electric current density

The abscissa is the electric current density of x-direction (D_x) and the ordinate is the location of thickness direction. Negative electric current density exists in the top 0°ply, and the positive electric current exists in the bottom 0°ply as shown in Fig.4. This implies that the circular electric current exists outside the charged segment. For this circulation, the electric voltage distribution due to the delamination is observed outside the charged segment. This causes the electric resistance change in the segment adjascent to the segment where a delamination exists.

Effect of charging direction

In order to investigate the effect of charging direction, two types of stacking sequence, [0/90]s and [90/0]s, are adopted and the electric voltage distribution is computed respectively. Delamination locates between x=-57.5mm and x=-47.5mm at the interlamina between the upper 0°ply and the middle 90°ply (the size is 10mm). Three sets of conductance measured by the experiments are employed. The current is charged from the electrode A to the electrode B. Surface voltage of [0/90]s and [90/0]s between the electrode A and B is showed in Fig.6 and Fig.7 respectively. The abscissa is the location of the longitudinal direction and the ordinate is the electric voltage distribution. Electrode A corresponds to x=-70mm, and electrode B corresponds to x=-35mm in these figures.

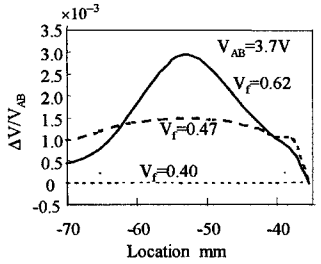

Fig.6 ΔV/V of the [0/90]s

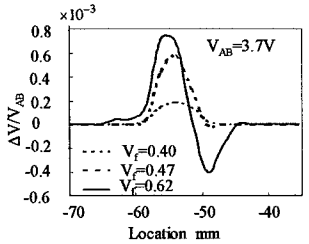

Fig.7 D_x of the [90/0]s

The voltage change at the electrode A means an existence of electric resistance change between the segment. As shown in Fig.6,

electric resistance changes can be observed for the laminates of [0/90]s except for the case of V_f=0.40. On the other hand, electric resistance changes can not be observed for the laminates of [90/0]s because no voltage change is observed at the electrode A as shown in the Fig.7. The result reveals that we should charge electric current to the fiber direction.

Results of electric resistance change

Effects of damages of delamination and matrix crack on the electric resistance measurements are investigated. Delamination locates between x=-26mm and x=-18mm and the size is 8mm. Matrix crack locates at x=-22mm. In the case of [0/90]s, matrix crack locates in the middle 90°ply. In the case of [90/0]s, matrix crack locates in the surface 0°ply.

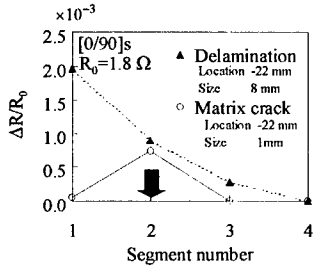

Fig.8 ΔR/R of [0/90]s

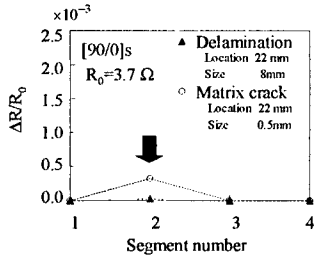

Fig.9 ΔR/R of [0/90]s

The electric resistance change due to the delamination and the matrix crack are shown in the Fig.8 and Fig.9. The abscissa is the segment number and the ordinate is the ΔR/R. The delamination and the matrix crack locate in the segment 2. For the laminate of [0/90]s, the ΔR/R due to the delamination is observed in several segment and the ΔR/R due to the matrix crack is observed only in the segment 2. For the laminate of [0/90]s, on the other hand, the ΔR/R due to the delamination is not observed and the ΔR/R due to the matrix crack is observed in the segment 2. This indicates that for the laminate of [90/0]s only the matrix crack is detected and the delamination can not be detected.

Conclusions

(1) The relationship between fiber volume fraction and electric conductance is experimentally measured. σ 90 and σ_t are significantly smaller than σ_0, and they vary depend on the fiber volume fraction. (2) The strong orthotropic electric resistace makes gradual electric current in the thickness direction, for the laminate of [0/90]s. The current in the thickness direction detects the delamination existence. (3) The electrode should be mounted on the fiber direction.

References

1.Todoroki A., Suzuki H., Kobayashi H., Nakamura H., and Shimamura Y., Transactions of the Japan Society of Mechanical Engineers Series A.; 64(622); 1654(1998), (in Japanese).

2. Todoroki A. and Suzuki H., Applied Mechanics and Engineering; 5(1); 283(2000).

3. Todoroki A. Tanaka Y., and Shimamura Y., Structural Health Monitoring 2000, edited by F.Kchang, Technomic.; 308(1999).

4. Todoroki A. Tanaka Y., and Shimamura Y., Special Technical Publication-2, JSMS, 139(2001).

Proceedings of 7th Japan International SAMPE
Symposium & Exhibition, Nov. 13-16, 2001

Damage Detection of Bolted Composite Laminates Using Electric Potential Method

Yoshinobu Shimamura[1], Sayaka Mukai[2], Akira Todoroki[1], Hideo Kobayashi[1]

1: Department of Mechano-Aerospace Engineering, Tokyo Institute of Technology
2: Graduate School, Tokyo Institute of Technology
2-12-1 O-okayama, Meguro-ku, Tokyo 152-8552, JAPAN
E-mail: yshimamu@ginza.mes.titech.ac.jp

Abstract

Mechanically fastened joints are widely used for composite structures. Damage in bolted joints occurs by bearing load, but it is difficult to detect the damage because the damaged area is hidden by lapping. In order to detect the damage, the electric potential method is applied experimentally to bolted joints and the damage propagation is observed by visual and ultrasonic inspections. As a result, it is shown that the damage of bolted joints of composite structures is detectable by the method.

Key Words: Composites, Bolted joint, Damage detection, Electric potential method

Introduction

Mechanically fastened joints are widely used for composite structures. Damage in bolted joints occurs by bearing load. It is difficult to detect the damage using conventional damaged inspection methods, such as ultrasonic and X-ray inspection, because the damage area is hidden by lapping.

In order to detect the damage, the electric potential method [1,2] is applied experimentally to bolted joints. The electric potential method is to detect damage by measuring the electric potential change of a structure before and after damage initiation. Carbon fiber reinforced composites have anisotropy of electric resistance. Damage away from electrodes may cause in the electric potential change because of anisotropy.

In this study, the electric potential change is measured during the tensile test, and the damage propagation is observed by visual and ultrasonic inspections. As a result, it is shown that the damage of bolted joints of composite structures is detectable by the method.

Specimens

Prepregs of Toho rayon co. (Q1111 2500) were laminated. The laminate was cured with electrodes at 130℃ for 1.5 hours. Then specimens as shown in Fig.1 were cut out. A bolt hole is located at one end and GFRP tabs were glued at the other end. Stacking sequence is $[0_2/\pm 45]_S$.

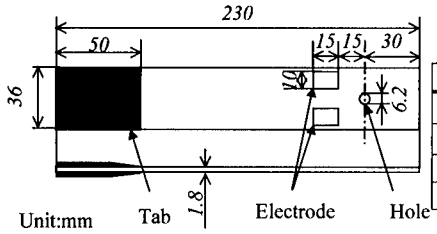

Fig.1 Specimen Configuration

Table 1 Specimens

Specimen #	
# 1	Before the knee point (A)
# 2	After the knee point (B)
# 3	After enough load drop (C)
# 4	

Experiments

Instrumental configuration is shown in Fig.2. Tensile tests at cross-head speed of 0.4mm/min were carried out. During tensile tests, applied load was held and unloaded to observe the state of damage and measure the resistance change, and re-loaded. Since the resistance change is very minute, it is amplified using a bridge circuit and a signal conditioner.

Four specimens are prepared, and tensile tests of specimen # 1 and 2 are stopped at before and after the knee point respectively. Specimen # 3 and 4 are stopped after enough load drop (Table 1). After stopping tensile test the damage propagation is observed by ultrasonic inspection (made by Hitachi construction machinery) and a microscope.

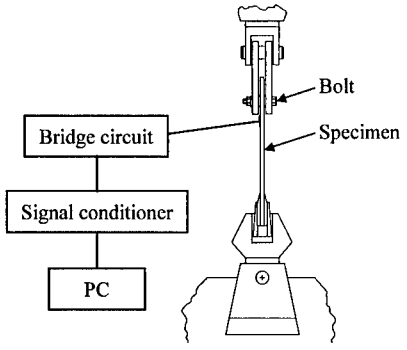

Fig.2 Instrumental Configuration

Results

The Electric Resistance Change

A typical load-displacement relationship is shown in Fig.3. Vertical axis represents load and horizontal axis represents displacement.

Load increases linearly up to the knee point. Meanwhile, the electric resistant change is almost zero although it shows slight decrease. The electric resistant change increases suddenly at the knee point. After the knee point, the electric resistant change continues to increase steadily.

As a result, the electric resistance change is induced by the damage that occurs around the knee point.

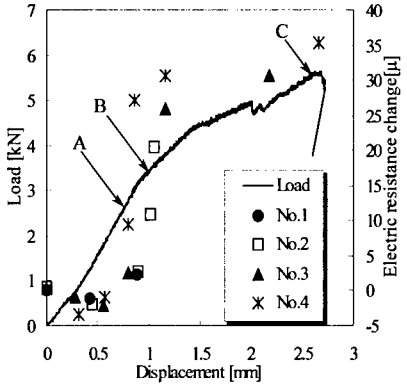

Fig.3 Electric Resistance Change

Damage Propagation

The state of damage at point A, B and C is observed by ultrasonic inspection and a microscope. Observed area is shown in Fig.4 as a gray square.

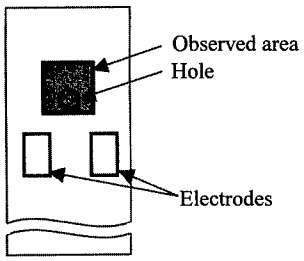

Fig.4 Observed Area

Before the knee point (point A), damage is hardly seen by visual and ultrasonic inspection as shown in Fig.5.

After the knee point (point B), the rim of the bolt hole that is adjacent to a pin deforms laterally. Fiber brakeage occurs in 0° layer at the stress concentration part (around the bolt hole) and matrix cracks propagate as shown in Fig.6.

After the load drop (point C), damage propagates to the loading direction and lateral deformation progresses farther as shown in Fig.7.

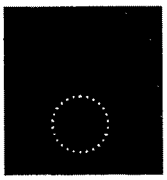

Fig.5 Damage Propagation (Point A)

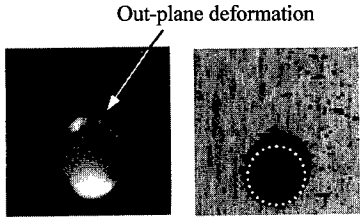

(a)Photograph (b) Surface Echo

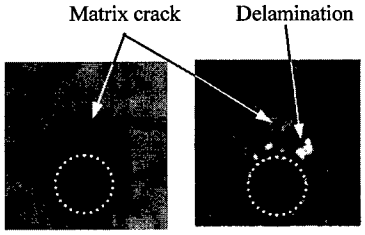

(c)Back Echo (d) Internal Echo

Fig.6 Damage Propagation (Point B)

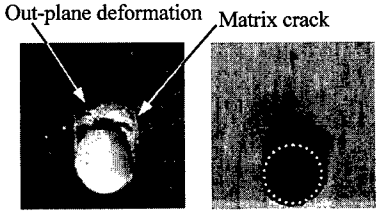

(a)Photograph (b) Surface Echo

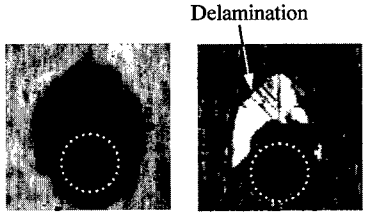

(c) Back Echo (d) Internal Echo

Fig.7 Damage Propagation (Point C)

Discussion

The electric resistant change increases rapidly by damage initiation. Then the electric resistant change increases slightly although the damage propagates to wide area.

The electric current is passed inside fiber to longitudinal direction and between fibers due to fiber contact to transverse and thickness directions. Though it is supposed that there are many routes of the electric current, the electric resistant change might be dominated by the electric current that is passed at damaged area and that is shown by a thick arrow in Fig.8. The electric current at the rim of the bolt hole is passed fiber contact from -45° lamina to 45° lamina. The rapid electric resistant change is caused by cracks that propagate at the interlayer between 45° lamina and -45° lamina. The progress of bearing damage causes the steady electric resistant change because it hardly affects the electric current pass.

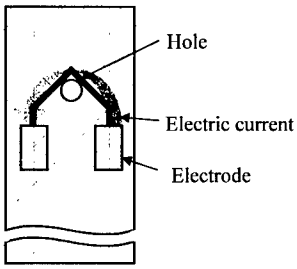

Fig.8 Electric Current of $[0_2/\pm 45]_s$

Conclusions

A Damage detection method of bolted joints using the electric potential method was experimentally investigated. As a result, it is shown that the damage of bolted joints of composite structures is detectable by the method.

References

1. A. Todoroki and H. Suzuki: Applied Mechanics and Engineering, 5(1), 283 (2000).
2. A. Todoroki, Y. Tanaka and Y. Shimamura: Materials Science Research International, JSMS, 139 (2001).

Proceedings of 7th Japan International SAMPE
Symposium & Exhibition, Nov. 13-16, 2001

Effect of Embedded SMA Foil on Mechanical Properties of CFRP Laminates

Akira Kobayashi*, Shinji Ogihara*, Yasuo Shirai** and Nobuo Takeda***

*Department of Mechanical Engineering, Science University of Tokyo,
2641 Yamasaki, Noda, Chiba 278-8510, JAPAN
**Graduate Student, Science University of Tokyo,
2641 Yamasaki, Noda, Chiba 278-8510, JAPAN
E-mail: j7500630@ed.noda.sut.ac.jp
***The University of Tokyo
4-6-1 Komaba, Mugoro-ku, Tokyo 153-8904, JAPAN

Abstract

Recently attempts are made to develop a smart material by combining composite laminates with embedded shape memory allys (SMA). In the present study, a stress analysis of a CFRP laminate with embedded SMA foil is conducted. A symmetric cross-ply laminate with embedded SMA foil is considered. Thermal residual stress is calculated which will be useful in discussion of damage development under mechanical loading which follows.

Introduction

Fiber reinforced plastic is often used as a multidirectional laminate and the thermal residual stresses arise when it is used at the temperature which is different from the curing temperature due the difference in the thermal expansion coefficient of each layer. It is known that thermal residual stresses induce matrix cracks.

On the other hand, some attempts are made to embed SMA in composite laminate in order to suppress damage initiation by using the shape memory effect of SMA [1]. However, analytical modeling of effect of SMA on the mechanical properties of composite laminates including stress analysis is not well established.

In the present paper, stress analysis procedure of composite laminates with embedded SMA foil is described. As an example, thermal residual stresses in each layer of CFRP [0/90/SMA/90/0] laminate is shown. This analytical procedure will be a basis for the laminate design using SMA.

Analysis

Analysis of SMA

Transformation of SMA is controlled by free energy as a driving force. Research in transformation kinetics has been done and various analytical models are proposed. In the present study, an analytical model which was developed by Kobayashi [1] by extending Brinson model [2] is used.

For completeness, Brinson model is briefly reviewed in the following. The stress-strain-temperature relation is expressed by the following equation.

$$d\sigma = D(\varepsilon,\xi,T)d\varepsilon + \Omega(\varepsilon,\xi,T)d\xi + \Theta(\varepsilon,\xi,T)dT \quad (1)$$

$$\Omega = -\varepsilon_L D(\varepsilon,\xi,T) \quad (2)$$

$$\Theta = -\alpha D(\varepsilon,\xi,T) \quad (3)$$

$$\xi = \Xi(\sigma,T) \quad (4)$$

and where

σ is stress tensor, ε is strain, T is

temperature, ξ is martensite variant volume fraction, D is elasticity tensor, Θ is heat elasticity tensor, Ω is metamorphosis tensor, ε_L is maximum metamorphosis strain.

Martensite variant volume fraction depends on the current values of stress tensor σ, temperature T. Brinson proposes dividing martensite variant volume fraction which is an internal condition variable into two, that is,

$$\xi = \xi_S + \xi_T \tag{5}$$

where

ξ_S is stress induced martensite variant volume fraction, ξ_T is temperature induced martensite variant volume fraction.

In the present study, an SMA which has R (Rhombohedral) variant condition under a certain stress and temperature condition is considered. Kobayashi [1] extended Brinson's model [2] to consider the R variant metamorphosis. In Kobayashi model, eq.(5) is modified as

$$\xi = \xi^M + \xi^R \tag{6}$$

$$\xi^M = \xi_S^M + \xi_T^M \tag{7}$$

$$\xi^R = \xi_S^R + \xi_T^R \tag{8}$$

and where superscripts R and M denote R variant and martensite variant, respectively. Because ξ_S and ξ_T are functions of both stress and temperature, it can be shown that

$$d\xi_S^M = \frac{\partial \xi_S^M}{\partial \sigma} d\sigma + \frac{\partial \xi_S^M}{\partial T} dT \tag{9}$$

$$d\xi_S^R = \frac{\partial \xi_S^R}{\partial \sigma} d\sigma + \frac{\partial \xi_S^R}{\partial T} dT \tag{10}$$

Finally, we have an incremental constitutive equation as follows:

$$d\sigma = \frac{1}{1 + \varepsilon_L^M D(\xi) \frac{\partial \xi_S^M}{\partial \sigma} + \varepsilon_L^R D(\xi) \frac{\partial \xi_S^R}{\partial \sigma}} \times \left[D(\xi) d\varepsilon - \left\{ D(\xi) \varepsilon_L^M \frac{\partial \xi_S^M}{\partial T} + D(\xi) \varepsilon_L^R \frac{\partial \xi_S^R}{\partial T} + \alpha(\xi) D(\xi) \right\} dT \right] \tag{11}$$

where

$$D(\xi) = \xi^R D_R + \xi^M D_M + \xi^A D_A \tag{12}$$

$$\alpha(\xi) = \xi^R \alpha_R + \xi^M D_M + \xi^A \alpha_A \tag{13}$$

$$\xi^R + \xi^M + \xi^A = 1 \tag{14}$$

$$\xi^R = \xi_S^R + \xi_T^R \tag{15}$$

$$\xi^M = \xi_S^M + \xi_T^M = \xi_S^M \tag{16}$$

and where superscript A denote austenite variant.

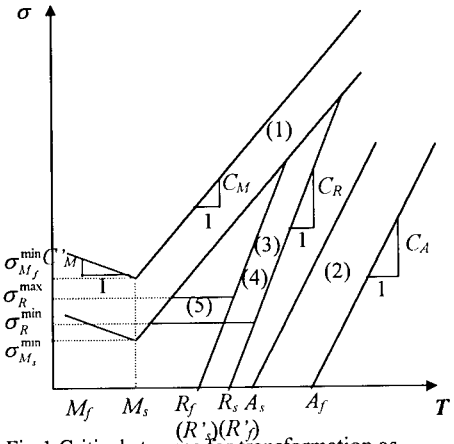

Fig.1 Critical stresses for transformation as function of temperature

Stress analysis of composite laminate with embedded SMA foil

Consider a symmetric cross-ply laminate with embedded SMA foil as shown in Fig.2. It is assumed that all the layers are perfectly bonded, thus the strains of all the layers are the same as that of the laminate. For simplicity, one-dimensional analysis is conducted.

Fig.2 Laminate configuration considered

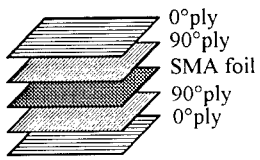

CFRP[0/90/SMA/90/0]

Stress change in each layer can be expressed as

$$d\sigma_1 = E_1(d\varepsilon - \alpha_1 dT) \quad (17)$$

$$d\sigma_2 = E_2(d\varepsilon - \alpha_2 dT) \quad (18)$$

$$d\sigma_3 = E_3(d\varepsilon - \alpha_3 dT) + d\sigma_R \quad (19)$$

where σ is stress, E is Young's modulus, $d\varepsilon$ is strain change, α is thermal expansion coefficient, dT is temperature change and $d\sigma_R$ is recovery stress in SMA. Subscripts 1, 2 and 3 denote 0° layer, 90° layer and SMA layer, respectively.

If we consider only temperature change (external force is zero), it follows that from equilibrium,

$$d\sigma_1 t_1 + d\sigma_2 t_2 + d\sigma_3 t_3 = 0 \quad (20)$$

which results in

$$d\varepsilon = \frac{(\alpha_1 E_1 t_1 + \alpha_2 E_2 t_2 + \alpha_3 E_3 t_3)dT - d\sigma_R t_3}{E_1 t_1 + E_2 t_2 + E_3 t_3} \quad (21)$$

By substituting eq.(21) into (19), it follows that

$$d\sigma_3 = \frac{(\alpha_1 - \alpha_3)E_1 t_1 + (\alpha_2 - \alpha_3)E_2 t_2}{E_1 t_1 + E_2 t_2 + E_3 t_3} dT + \frac{E_1 t_1 + E_2 t_2}{E_1 t_1 + E_2 t_2 + E_3 t_3} d\sigma_R = XdT + Yd\sigma_R \quad (22)$$

where

$$X = \frac{(\alpha_1 - \alpha_3)E_1 t_1 + (\alpha_2 - \alpha_3)E_2 t_2}{E_1 t_1 + E_2 t_2 + E_3 t_3} \quad (23)$$

$$Y = \frac{E_1 t_1 + E_2 t_2}{E_1 t_1 + E_2 t_2 + E_3 t_3} \quad (24)$$

Now, we rewrite eq.(11) as

$$d\sigma_3 = A\{D(\xi)d\varepsilon - BdT\} \quad (25)$$

where

$$A = \frac{1}{1 + \varepsilon_L^M D(\xi)\frac{\partial \xi_S^M}{\partial \sigma} + \varepsilon_L^R D(\xi)\frac{\partial \xi_S^R}{\partial \sigma}} \quad (26)$$

$$B = D(\xi)\varepsilon_L^M \frac{\partial \xi_S^M}{\partial T} + D(\xi)\varepsilon_L^R \frac{\partial \xi_S^R}{\partial T} + \alpha(\xi)D(\xi) \quad (27)$$

By substituting eq.(20) into (25), it follows that

$$d\sigma_3 = \left\{AD(\xi)\frac{\alpha_1 E_1 t_1 + \alpha_2 E_2 t_2 + \alpha_3 E_3 t_3}{E_1 t_1 + E_2 t_2 + E_3 t_3} - AB\right\}dT - AD(\xi)\frac{t_3}{E_1 t_1 + E_2 t_2 + E_3 t_3} d\sigma_R = ZdT - Wd\sigma_R \quad (28)$$

where

$$Z = AD(\xi)\frac{\alpha_1 E_1 t_1 + \alpha_2 E_2 t_2 + \alpha_3 E_3 t_3}{E_1 t_1 + E_2 t_2 + E_3 t_3} - AB \quad (29)$$

$$W = AD(\xi)\frac{t_3}{E_1 t_1 + E_2 t_2 + E_3 t_3} \quad (30)$$

By equating eqs.(21) and (28), we obtain

$$d\sigma_R = \frac{Z - X}{W + Y} dT \quad (31)$$

Finally we have

$$d\sigma_1 = \frac{(\alpha_2 - \alpha_1)E_2 t_2 + (\alpha_3 - \alpha_1)E_3 t_3}{E_1 t_1 + E_2 t_2 + E_3 t_3} dT + \frac{E_1 t_3}{E_1 t_1 + E_2 t_2 + E_3 t_3} d\sigma_R \quad (32)$$

$$d\sigma_2 = \frac{(\alpha_1 - \alpha_2)E_1 t_2 + (\alpha_3 - \alpha_2)E_3 t_3}{E_1 t_1 + E_2 t_2 + E_3 t_3} dT + \frac{E_2 t_3}{E_1 t_1 + E_2 t_2 + E_3 t_3} d\sigma_R \quad (33)$$

$$d\sigma_3 = \frac{(\alpha_1 - \alpha_3)E_1 t_1 + (\alpha_2 - \alpha_3)E_2 t_2}{E_1 t_1 + E_2 t_2 + E_3 t_3} dT + \frac{E_1 t_1 + E_2 t_2}{E_1 t_1 + E_2 t_2 + E_3 t_3} d\sigma_R \quad (34)$$

Now, we can determine the thermal residual stress in each layer of CFRP cross-ply laminates with embedded SMA foil.

Results and discussion

An example of thermal residual stresses in a CFRP cross-ply laminate with embedded SMA foil is shown here. The material properties used and the condition considered are as follows

SMA

Young's modulus [GPa]

E_M: 15.0, E_A: 50.0, E_R: 15.0

Thermal expansion coefficient [/°C]

α_M: 10.0×10^{-6}, α_A: 10.0×10^{-6}, α_R: 10.0×10^{-6}

Transformation maximum strain

ε_L^M : 0.050, ε_L^R : 0.0060

Transformation start point [°C]

M_s: -1.7, A_s: 47.9, R_s: 49.7

Transformation finish point [°C]

M_f: -28.0, A_f: 61.5, R_f: 38.3

Metamorphosis line inclination [MPa/°C]

C_M: 3.57, C_A: 6.02, C_R: 18.0

Thickness: 40 [μm]

CFRP (T700H/2500)

Young' Modulus (0° ply): 113[GPa]

Young' Modulus (90° ply): 8.39[GPa]

Thickness: 180 [μm]

Cure temperature: 130°C

Table 2 shows the thermal residual stress in each ply in both laminates with and without SMA foil at 25°C when cooled from 130°C. It is seen that the compressive thermal stress in 0° ply is lower in laminates with SMA foil. The tensile thermal residual stress in 90 ° ply is higher in laminates with SMA foil. This analysis can also be used in a stress analysis under mechanical loading.

Table 2 Thermal residual stress in each ply of CFRP laminates with and without SMA foil at at 25°C when cooled from 130°C.

	Stress [MPa] (Without SMA)	Stress [MPa] (With SMA)
0° ply	-22.1	-6.38
90° ply	22.1	23.3
SMA		-152

Conclusions

In the present study, a stress analysis of a CFRP laminate with embedded SMA foil is described. Symmetric cross-ply laminates with and without embedded SMA foil are considered. Thermal residual stress which arises when cooled from the curing temperature is calculated. This analysis will be useful in discussion of damage development under mechanical loading which follows.

Reference

1. M.Kobayashi: Suppression effect of microscopic damage in CFRP laminates by embedding SMA foil, Master thesis, The University of Tokyo (2001)
2. L.C.Brinson: One-dimensional constitutive behavior of shape memory alloys: thermomechanical derivation with non-constant material functions and redefined martensite internal variable, Journal of Intelligent Material Systems and Structures, 4, 229-242 (1993)

Proceedings of 7th Japan International SAMPE
Symposium & Exhibition, Nov. 13-16, 2001

Mechanical properties of SMA Fiber/Epoxy Composite

Akira Kobayashi#, Shinji Ogihara#, Tsuyoshi Uehara## and Nobuo Takeda###
#: Department of Mechanical Engineering, Science University of Tokyo, 2641 Yamasaki, Noda, Chiba 278-8510, Japan
##Graduate Student, Science University of Tokyo, 2641 Yamasaki, Noda, Chiba 278-8510, Japan
###The University of Tokyo, 4-6-1 Komaba, Meguro, Tokyo 153-8904, Japan
E-Mail: ogihara@rs.noda.sut.ac.jp

Abstract

Recently, many investigations on intelligent materials which can sense the change of the environment and can control its properties. One of the most promising candidates of constituent materials used in intelligent composite systems is shape memory alloys (SMA). In the present study, SMA fiber reinforced epoxy composites are fabricated and its mechanical properties are investigated. The effect of SMA surface treatment on the fiber/matrix interfacial fracture toughness is discussed through a single fiber pull-out test. Tensile tests are performed to discuss the effect of SMA recovery stress, fiber surface treatment and heat treatment on the mechanical properties of SMA fiber/epoxy composites.

Key words: Shape Memory Alloy, Interface, Single Fiber Pull-out Test

Introduction

SMA shows shape memory effect and superelastic behavior which is attractive when used in intelligent composite materials. Many studies have been conducted on fundamental mechanical properties of SMA [1] and its use in smart materials [2]. A composite material which is made of reinforcing SMA fibers and matrix metals or plastics are expected to be intelligent materials.

In the present study, we fabricate composite system which uses SMA fiber as a reinforcing fiber and epoxy matrix. If the SMA fiber is used with prestrain and heat treatment is performed after composite fabrication, it is expected that compressive stress arises in the matrix and the composite exhibit higher strength than that without prestained fibers. We also performed single fiber pull-out tests on SMA fiber/epoxy composite to measure the fiber/matrix interfacial fracture toughness. The effect of fiber surface treatment (acid cleaning) on the interfacial fracture toughness is evaluated experimentally.

Experimental procedure

Materials

A Ti-Ni SMA fiber is used as the reinforcement of the composite system. The fiber diameter is about 50μm. The Austenite start point (As) is about 100°C. A bisphenol A type epoxy (Epikote815) and triethylene hardener are used.

The resin is cured at 50°C for thirty minutes and at 80°C for eighty minutes.

Tensile tests on SMA fibers

A tensile test is conducted to study the mechanical properties of the SMA fiber. Furthermore, a loading-unloading followed by heating procedure is performed to obtain the relation between the total strain, the residual strain, the recovery strain and the recovery stress.

A single fiber pull out test

A single fiber pull-out test is conducted to measure the fiber/matrix interfacial fracture toughness. We prepare cylindrical specimens which have an embedded single SMA fiber in the epoxy resin. The cylindrical specimen has a diameter of 6mm and length of 12mm. We used surface treated fibers and untreated fibers. In surface treated fiber, the fibers are cleaned with nitric-acid of 60% concentration for four hours after cleaned with alcohol. We called the fiber which is cleaned only with alcohol "untreated fiber". The surface treatments of the fibers are summarized in Table 1. We measure the interfacial debonding length by using an optical microscope as a function of applied load. Nairn's analysis is used to obtain the energy release rate [3, 4].

Table 1 Surface treatment of SMA Wire

	60% nitric acid	Alcohol
Acid-cleaned fiber	○	○
Untreated fiber	×	○

Tensile test

We prepared composite specimens with embedded SMA fibers of 4% prestrain. The specimens are 100mm long, 10mm wide and 0.5mm thick.

We tested following specimens, that is,

1. Epoxy, 2. Epoxy (heat treatment),
3. SMA/Epoxy, 4. SMA/Epoxy(heat treatment)
5. Prestrained SMA/Epoxy,
6. Prestrained SMA/Epoxy (heat treatment)
7. Prestrained and acid-cleaned SMA/Epoxy
8. Prestrained and acid-cleaned SMA/Epoxy (heat treatment)

where, the volume fraction of composite specimens (3~8) is about 10%. The heat treated specimens are stored in a chamber at 120°C before testing.

Results and discussions

Mechanical properties and shape memory effect of SMA fiber

Mechanical properties of SMA fiber obtained by a tensile test are shown in Table 2.

Table 2 Mechanical properties of SMA fiber

	SMA
Young's modulus [GPa]	48.0
Tensile strength [GPa]	1.40
Fracture strain [%]	48.1

Table 3 shows the relation between the total strain, the residual strain, the recovery strain and the recovery stress. Definition of the strains are shown in Fig.1. It is found that the highest recovery stress is obtained when the total stain is 8%. But in that case, the permanent strain is not zero.

Table 3 Relation between total strain, residual strain, recovery strain and recovery stress

	Total strain [%]				
	2	4	6	8	10
Residual strain [%]	1.30	3.06	4.99	6.66	7.82
Recovery strain [%]	1.30	3.06	4.14	4.17	4.25
Recovery stress [MPa]	432	549	565	654	492

We choose total strain of 4% as the prestrain of

SMA fiber used in composites, because this is the highest total strain among the permanent strain becomes zero.

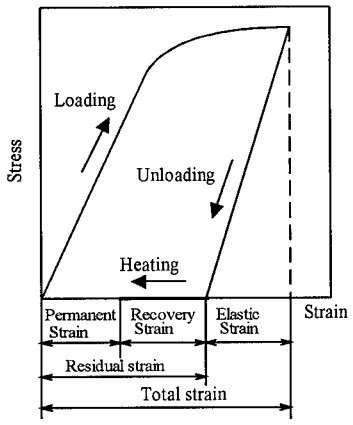

Fig.1 Definition of strains

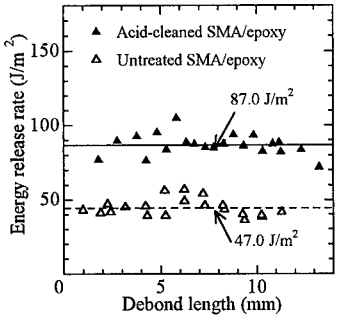

Fig.2 Crack-resistance curves for microbond specimens with acid or untreated SMA fiber

Assessment of fiber/epoxy interface by the single fiber pull out test

Fig.2 shows the interfacial fracture toughness as a function of debonding length obtained from the single fiber pull-out test for the acid-cleaned SMA fiber and untreated SMA fiber. It is found that the fracture toughness is independent on the debonding length. It is also found that the fracture toughness is higher in acid-cleaned SMA fiber than in untreated SMA fiber, which implies that the acid cleaning enhances the adhesion between the SMA fiber and the epoxy matrix.

Mechanical properties of SMA fiber/epoxy composite

Fig.3 shows the load-displacement curves of the specimens obtained by the tensile test. We can see difference in stress-strain behavior. The maximum load of each specimen is the fracture point of epoxy matrix. SMA fiber in specimens except for the prestrained and acid-cleaned SMA fiber with heat treatment does not break at the fracture point of epoxy matrix which results in the load capability after the first maximum load. The specimens with embedded prestrained and acid-cleaned SMA fiber with heat treatment have the tendency to fail at the matrix fracture point which may be due to the high interfacial strength.

Fig.4 shows the stress-strain curves of the specimens before the matrix fracture. The SMA/epoxy composites show higher Young's modulus and tensile stress at epoxy fracture, which shows the effectiveness of the SMA fibers as composite reinforcement. It is found that the strength in SMA/epoxy with acid-cleaned SMA fiber shows higher stress at epoxy fracture than that with untreated SMA fiber. This shows the effectiveness of enhancement of interfacial strength by the acid cleaning. It is seen that only the heat treatment on SMA/epoxy with untreated SMA fibers increases composite stress at epoxy fracture. This may be due to the after cure effect on the epoxy, which results in both the enhancement of epoxy strength and SMA/epoxy interfacial strength. The highest composite stress at epoxy fracture is obtained in SMA/epoxy with prestained and acid-cleaned SMA fiber with heat treatment.

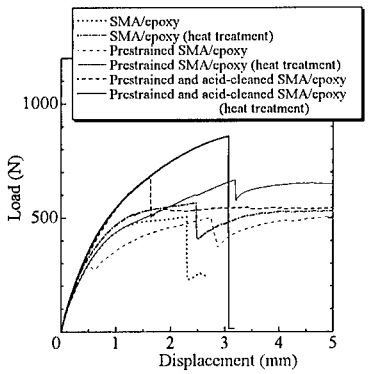

Fig.3 Load-displacement curves of the specimens

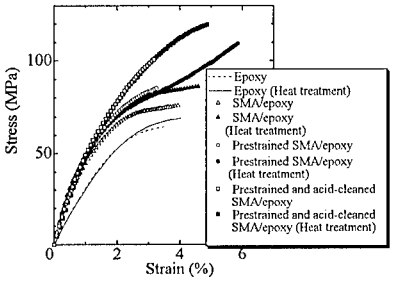

Fig.4 Stress-strain curves of the specimens

In this specimen not only the enhancement effect of epoxy and interfacial strength by heat treatment and of interfacial strength by acid cleaning, but also the effect of recovery stress by SMA fibers are valid. From these experimental results, it is found that SMA fibers can be used as composite reinforcement and that there is a possibility that SMA recovery stress can be utilized in composite strength enhancement.

Conclusion

In the present study, we fabricate the composites with embedded SMA fibers in the epoxy resin. The mechanical properties of SMA fibers and its composites and interfacial properties of SMA/epoxy are studied. From the single fiber pull-out test, the interfacial fracture toughness of SMA fiber/epoxy is measured. It is found that the interfacial fracture toughness increases by performing acid clean to the SMA fiber. It is also found that the specimens with embedded prestrained and acid-cleaned SMA fibers with heat treatment exhibits highest stress at the epoxy fractrure due to the combined effects of the recovery stress of SMA fiber, after-cure effect of epoxy resin (enhancement of both epoxy and interfacial strength). From these experimental results, it is concluded that SMA fibers can be used as composite reinforcement and that there is a possibility that SMA recovery stress can be utilized in composite strength enhancement.

Reference

1. L.C.Brinson; One-Dimensional Constitutive Behavior of Shape Memory Alloys: Thermomechanical Derivation with Non-Constant Materials Functions and Redefined Martensite Internal Variable, Journal of Intelligent Materials system and Structures, Vol.4, pp229-242 (1993)

2. A.Kobayashi, S.Ogihara, H.Yoshinari, N.Takeda; Damage Development in Composite Laminates With Embedded SMA Wires, Proceedings of the 6th Japan SAMPE International Symopium, Vol.1, pp65-68 (1999)

3. B.Miller, P.Muri, L.Rebenfield; A Microbond Method for Determination of the Shear Strength of a Fiber/Resin, Composites Science and Technology, 28, pp.17-32 (1987)

4. C.-.Liu, J.A Nairn; Analytical and Experimental Methods for a Fracture Mechanics Interpretation of the Microbond Test Including the Effect of the Friction and Thermal Stresses, International Journal of Adhesion & Adhesive,19, pp.59-70 (1999)

Proceedings of 7th Japan International SAMPE
Symposium & Exhibition, Nov. 13-16, 2001

Development of a high power shape memory materials using hydrogen storage alloy dispersed in polymer

Byungsuk KIM[1], Hiromasa YABE[1], Haru-Hisa UCHIDA[2] and Yoshitake NISHI[1]

[1]: Department of Materials Science, Tokai University
1117 Kitakaname, Hiratsuka, Kanagawa, 259-1292 JAPAN
E-mail: am026429@keyaki.cc.u-tokai.ac.jp
[2]: Department of Human Development, Tokai University
1117 Kitakaname, Hiratsuka, Kanagawa, 259-1292 JAPAN
E-mail: hhuchida@keyaki.cc.u-tokai.ac.jp

Abstract

New type of shape memory materials using volume expansion of hydrogen storage alloy was developed. The material was constructed with two kinds of silicone rubbers, like a bi-metal, defined "hydrogen storage alloy powder dispersed bi-polymer". One of silicon rubber was hydrogen storage alloy powder dispersed silicon rubber (A), and another one was pure silicon rubber (B). This bi-polymer showed shape change induced by hydrogen pressure change. The shape memory effect of hydrogen storage alloy powder dispersed bi-polymer was applicable for medical catheter.

Key Words: Actuator, Hydrogen storage alloy, Shape memory effect (SME).

Introduction

Present days, many medical doctors in a urine pipe have expected to develop soft catheter, which move variable direction. Shape memory materials can be one of the reliable actuator for medical catheter. Many shape memory materials were operated by temperature change [1-7]. However it is difficult to apply for medical catheter because large thermal changes often destroy cellular tissues. Therefore, new shape memory materials have been expected to operate without temperature change. If a catheter is operated by gas pressure near atmospheric pressure without temperature change, it can be applicable. Therefore, the shape memory bi-polymer for medical catheter has been developed. It is made of hydrogen storage alloy powder dispersed silicone rubber. A silicone rubber is soft material for human body and hydrogen transport material. In this study, $LaNi_3Co_2$ hydrogen storage alloy has been proposed. The plateau pressure of $LaNi_3Co_2$ hydrogen storage alloy is 0.5 bar at 313 K [8]. $LaNi_3Co_2$ volume expansion by formation of hydrogenation is 20.5 % [9]. Furthermore, $LaNi_3Co_2$ alloy also shows that high resistant to pulverization by hydrogen absorption and desorption cycles [10]. The temperature and pressure conditions of the $LaNi_3Co_2$ alloy are safety for human body.

Experimental

$LaNi_3Co_2$ hydrogen storage alloy were produced by arc furnace (ACM-DS01 DIAVAC Ltd.). Table1 shows conditions of arc melting. Arc melting was performed four times for alloying. Annealing were performed to homogenize the alloy. Annealing conditions are summarized in Table 2.

Table 1 Condition of arc melting.

Total gas pressure	1.6×10^{-3} Pa
Ar gas partial pressure	6×10^{3} Pa
Number of arc melting	4 times

Table 2 Condition of annealing.

Heat treatment temperature	866.5 ± 14.2 K
Heat treatment times	5.4×10^{3} s
Total gas pressure	2.0×10^{-3} Pa

The block sample was crushed, until grain sizes became 1-2 mm. Using H_2 (7N purity) sample was pulverized by several hydrogen sorption cycles. The chemical composition of hydrogen storage alloy powder was analyzed by energy dispersion X-ray spectroscopy (EDS: JSM-6301F, JEOL Ltd. Tokyo). Hydrogen storage alloy obtained was $LaNi_{3.3}Co_{2.1}$. Hydrogen storage alloy powder dispersed bi-polymer was suggested, as the bi-polymer material which constructed with two kinds of silicone rubbers, like a bi-metal. One of them was hydrogen storage alloy powder dispersed rubber (A), and another was pure silicone rubber (B). $LaNi_{3.3}Co_{2.1}$ hydrogen storage alloy powder (grain size:#25-40 μm, 0.684 g) was mixed and dispersed into pure silicone rubber (HJ-125 Semendine Ltd, 0.065 g). The sample size of the composite material was $30\times5\times1$ mm^3 (length×width×thickness). Pure silicone rubber (B) was supporting materials to bend the composite material. The composite material (A) and pure silicone rubber (B) were connected spontaneously. In those way the bi-polymer was prepared (See Fig. 1.).

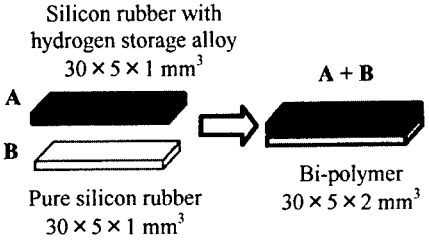

Fig.1 Schematic diagram of bi-polymer sample preparation

Using the reaction bed made of SUS316, shape memory bi-polymer was activated. The activation of hydrogen storage alloy, was performed under H_2 (7 N purity) pressure at about 50 bar. Activation was performed by the hydrogen absorption for 10 minutes and subsequently evacuated for 10 minutes. The number of the performance was 30 times. Hydrogen storage shape memory effect of an activated bi-polymer was observed in reaction bed made of glass (See Fig.2). After evacuation for 10 minutes, shape memory effect at different hydrogen pressures was monitored by a video recorder [1-5].

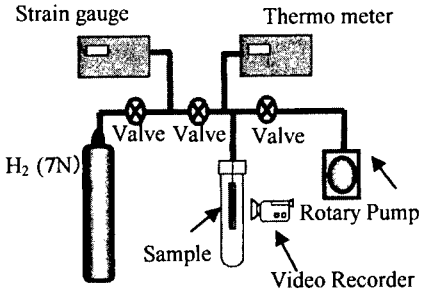

Fig.2 Schematic diagram of shape change observation system.

The measurement of the shape displacement of the bi-polymer sample was defined, as shown in Fig.3. Figure 3 shows schematic diagram of method for shape memory effect. Here the Y and X are dimensional changes vertical and parallel to the bi-polymer rod length, respectively.

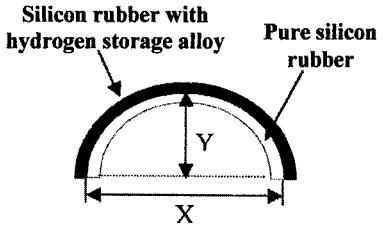

Fig.3 Schematic diagram of method for shape displacement.

Results and discussion

Figure 4 shows photograph of the shape of hydrogen storage alloy powder dispersed bi-polymer after the evacuation for 600 s at 309.5±0.5 K (See Fig.4.A). Shape of bi-polymer became straight by evacuation in reaction bed. Figure. 4 B shows the photograph of the bi-polymer shape after hydrogen absorption for 600 s at 309.5±0.5 K. The applied hydrogen pressure observed the large shape changes.

Figure 5 shows change in the shape displacement (Y/X) of the bi-polymer against hydrogen pressure in reaction bed at 309.05±0.5 K. In this figure, white squares (□) show shape displacement of bi-polymer after the evacuated for 600 s at 309.5±0.5 K, and black circle (●) shows shape displacement of bi-polymer after hydrogen absorption for 600 s at 309.5±0.5 K. The large shape changes were observed from 1 to 2 bar. Shape memory displacement became small above 2 bar. The
shape displacement (Y/X) of bi-polymer approached 0.07 above 2.5 bar.

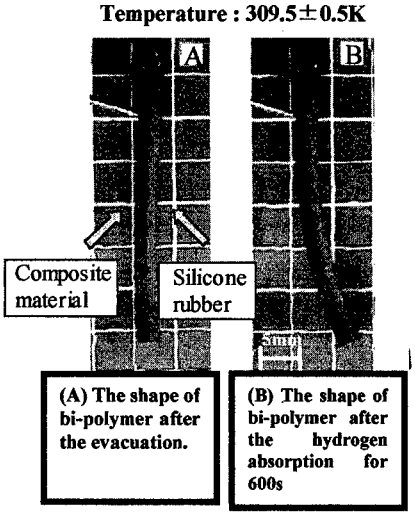

Fig.4 Relationship between changes in different hydrogen pressure against shape displacement of the bi-polymer (Y/X).

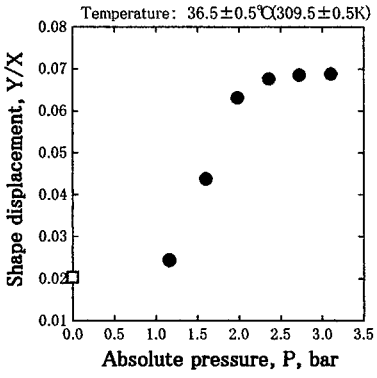

Fig.5 Optical photographs of bi-polymer shape by the evacuation (A) and the bi-polymer shape by the hydrogen absorption (B).

Figure 6 shows schematic diagram of the expanded bending displacement of shape memory bi-polymer. Shape of bi-polymer becomes straight, as it was evacuated. Since the composite material (A) was expanded by the volume expansion by the hydrogenation storage of the $LaNi_3Co_2$ alloy powder, shape of bi-polymer becomes a large bending displacement. Therefore, we succeed in development of medical shape memory bi-polymer material at 309.5±0.5 K and 1-2 bar of human body condition. We are developing medical catheter for the urine pipe.

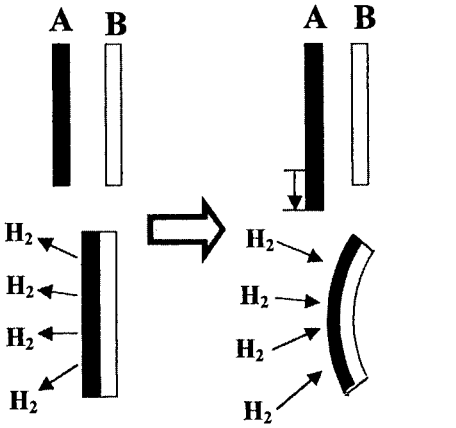

Fig.6 Schematic diagram of the mechanism for shape change by the H_2 absorption and desorption.

Conclusion

The purpose of this research was to develop a shape memory bi-polymer. It was made of $LaNi_{3.3}Co_{2.1}$ hydrogen storage alloy powder dispersed silicone rubber. The bi-polymer was safety for human body. The shape memory effect of bi-polymer was examined on the condition of human body (309.5 ± 0.5 K and 1-2 bar). Bi-polymer showed reversible shape memory effect by hydrogen absorption and desorption. It is especially that the large shape displacement was observed from 1 to 2 bar. Therefore, we succeed to develop medical shape memory bi-polymer.

References

1. T. Nakamura, T. Matsumura, K. Tajima, Y. Miyazawa and Y. Nishi, Adv. Sci, 11(1), 34 (1999).
2. M. Tetsuka, H. Yabe and Y. Nishi, J.Adv. Sci, 12(1), 38 (2000).
3. T. Matsumura, K. Takashina. and Y. Nishi, Pro.9th Int. Mat. Sym, 16 (20009).
4. T. Matsumura, T. Nakamura, H.Ishii, K. Tajima, Y. Miyazawa and Y. Nishi, Proc.44th Int. SAMPE Sym, 1961 (1999).
5. K.Takashina, H.Yabe, K.Oguri,Y. Miyazawa and Yoshitake Nishi, Appl. Ele. and Mech, in press
6. Y. Miyagawa, N.Suketomo, T.Morishita, Y. Nishi and E.Yajima, Scr. Met, 19(11), 1273 (1985).
7. N. Hagiwara, H. Yabe, K. Oguri, T. Asaka, T. Suzuki and Y. Nishi, J. Appl. Ele. and Mech, in press
8. H. H. van Mal, K. H. J. Buschow and F. A. Kuijper, J. Less-Common Met. 32.289 (1973)
9. J.J.G.Willems and K.H.J Buschow, Phi. J. Res, 39(1), 54 (1984)
10. J.JG. Wilems, K.H.J. Buschow, J. Less-Common Met. 129(5), 13 (1987).

Proceedings of 7th Japan International SAMPE
Symposium & Exhibition, Nov. 13-16, 2001

Damage Progress Behavior in CFRP Laminates under Thermal Cycle Loading

Akira Kobayashi#, Shinji Ogihara#, Takamoto Ishiguro## and Nobuo Takeda###

#: Department of Mechanical Engineering, Science University of Tokyo, 2641 Yamasaki, Noda, Chiba 278-8510, JAPAN
##: Graduate Student, Science University of Tokyo, 2641 Yamasaki, Noda, Chiba 278-8510, JAPAN
###: The University of Tokyo, 4-6-1 Komaba, Meguro-ku, Tokyo 153-8904, JAPAN
E-mail: ogihara@rs.noda.sut.ac.jp

Abstract

Considering the space environment, it is important to study the effects of thermal cycling on the mechanical properties of composite materials. It is known that composite laminates subjected to thermal cycling suffer from matrix cracking. In the present study, thermal cycling induced matrix cracking in CFRP laminates is investigated experimentally. Two kinds of carbon/epoxy systems, T800H/3631 and T300/2500, are used. Laminate configurations are $(0/90)_s$ and $(90/0)_s$ for both material systems. The specimens are thermally cycled between -196°C and 100°C. Thermal cycling tests are performed up to 1000 cycles. The polished edge surfaces of specimens are examined by the replica technique to measure the matrix crack density as a function of the number of thermal cycles. To investigate the change in matrix cracking properties due to thermal cycling, tensile tests on thermally-cycled specimens are performed.

Key Words: Thermal cycles, Matrix crack, CFRP.

Introduction

Carbon fiber reinforced plastics (CFRP) are used in the field of space applications because they have high specific strength, high specific modulus and low thermal expansion coefficients. Considering the space environment, it is important to study the effects of thermal cycling on the mechanical properties of CFRP. As CFRP is often used in the form of multidirectional laminates, thermal stress arises in plies due to the difference in the thermal expansion coefficients between the plies. It is known that the thermal residual stress often causes matrix cracking.

McManus et al. [1] studied thermal cycling induced matrix cracking in CFRP laminates. They suggested a method to predict matrix cracking behavior under thermal cycling. Brown and Hyer [2] investigated the effects of long term thermal cycling on microcracking behavior in composite materials. Henaff-Gardin et al. [3] analyzed the doubly periodic matrix cracking in cross-ply laminates and applied their analysis to discussion of matrix cracking under thermal cycling.

However, matrix cracking in laminated composites under thermal cycling is not fully understood, because only the matrix crack density is measured as a function of the number of thermal cycles in the previous studies [1-3]. The purpose of the present study is to discuss the effects of thermal cycles on the change in the critical energy release rate and the critical stress for matrix cracking. As the first step, the change in the critical values at room temperature is measured as a function of the number of thermal cycles.

In the present study, thermal cycling tests are performed on CFRP cross-ply laminates first. After thermal cycling tests, tensile tests are conducted at room temperature. The variational mechanics [4, 5] is used to evaluate the critical energy release rate and the critical stress for matrix cracking.

Experimental Procedure

Materials

Two kinds of carbon/epoxy systems, T800H/3631 and T300/2500, are used. Laminate configurations are $(0/90)_s$ and $(90/0)_s$ for both material systems. T800H and T300 are high strength carbon fibers. 3631 and 2500 are epoxy resins. The specimen size is 100mm long, 10mm wide, 0.51mm thick in T800H/3631 and 0.60mm thick in T300/2500. In the present study, a ply whose fibers are aligned in the specimen longitudinal direction is called 0° ply. The edge surfaces of the specimens are polished for detection of matrix cracks by the replica technique.

Thermal cycling tests

In the present study, a thermal cycling test apparatus is developed. The specimens are thermally cycled between -196°C and 100°C. In the high temperature chamber, a heating coil is used. The low temperature chamber is filled with liquid nitrogen. The specimens are placed in the high temperature chamber for two minutes and in the low temperature chamber for one minute. Thermal cycling tests are performed up to 1000 cycles. During the thermal cycling tests, the polished edge surfaces of specimens are examined by the replica technique periodically. The replica films are observed by using an optical microscope. The matrix crack density is measured as a function of the number of thermal cycles. The matrix crack density is defined as the number of matrix cracks per unit specimen length.

Tensile tests

To discuss the effects of thermal cycles on matrix cracking under tension, tensile tests after thermal cycles are performed. The specimen with thermal cycles (200, 400, 600, 800 and 1000 cycles) and without thermal cycling are used. Tensile tests are conducted at a cross-head speed of 0.5mm/min at room temperature. During the tensile test, the edge surfaces of the specimens are also examined by the replica technique periodically. The matrix crack density is measured as a function of the laminate strain.

Result and Discussion

In all the laminates, matrix cracking in 90° ply is observed during thermal cycling. Figure 1 shows the experimental results of the matrix crack density as a function of the number of thermal cycles. The matrix crack density is defined as the number of cracks per unit specimen length. The matrix crack density is measured at every 50 thermal cycles in T800H/3631, while 200 cycles in T300/2500. In both material systems, the number of thermal cycles at the first matrix cracking in $(0/90)_s$ and $(90/0)_s$ are similar. However, the increasing rate of matrix crack density is higher in $(0/90)_s$ than in $(90/0)_s$.

It is assumed that the material mechanical properties are temperature-independent. The stress-free temperature is assumed to be equal to the curing temperature for each material system. Because the total thickness of 0° and 90° are the same, the thermal residual stress in $(0/90)_s$ and in $(90/0)_s$ are equal. This corresponds to the experimental result that the number of thermal cycles at the first matrix cracking in $(0/90)_s$ and $(90/0)_s$ are similar.

Figure 2 shows the maximum thermal stress between the matrix cracks as a function of the matrix crack density at -196°C. It is assumed that the material mechanical properties do not change due to thermal cycling. It is found that the maximum thermal stress is higher in $(0/90)_s$ than in $(90/0)_s$. This explains qualitatively the experimental result that the increasing rate of the matrix crack density is higher in $(0/90)_s$ than in $(90/0)_s$.

Figures 3 shows an example of the matrix crack density as a function of the laminate strain under tensile loading after thermal cycling and the analytical prediction. It is seen that matrix cracking behavior is different for different number of thermal cycles. As for the experimental result after 1000 thermal cycling, matrix cracks are observed even when the laminate strain is zero, because the matrix cracks occur due to thermal cycling. The variational mechanics is used for the prediction using both the energy and stress criteria. The critical energy release rate and the critical stress are chosen to fit the experimental results. The critical values chosen are listed in Table 1 and Table 2. It is seen that the critical values decrease as the number of thermal cycles increases. In both material systems, the same values for the critical energy release rate and the critical stress are obtained from $(0/90)_s$ and $(90/0)_s$ in the specimens without thermal cycles. It is found that the decreasing rate of the critical values is higher in $(0/90)_s$ than in $(90/0)_s$. This may be because the thermal residual stress is higher in $(0/90)_s$ than in $(90/0)_s$ at the same matrix crack density (Fig.2). Because the critical values are affected by the matrix and the fiber/matrix interfacial properties, it is considered that the thermal residual stress cycles due to thermal cycles affects the critical values.

To predict the matrix cracking behavior due to thermal cycles precisely, we have to investigate the change in the critical values for matrix cracking at the lowest temperature during the thermal cycles. However, the change may be a function of thermal stress range due to thermal cycles. The thermal stress range is a function of both temperature range and laminate configuration. Without thermal cycles, the critical values for matrix cracking can be regarded as material constants in the sense that they are independent of laminate configuration. However, the critical values may change due to laminate configuration with thermal cycles.

Conclusion

Thermal cycling tests are performed on CFRP cross-ply laminates. Matrix cracking behavior under thermal cycling are examined by the replica technique. To discuss the effect of thermal cycles on matrix cracking under tension, tensile tests after thermal cycles are performed. The effect of thermal cycles on matrix cracking under tension can be evaluated by the change in the critical energy release rate and the critical stress. However, it should be noted the change is different for different laminate configurations.

References

1. H.L.McManus, D.E.Bowles and S.S.Tompkins: Journal of Reinforced Plastics and Composites, 15(2), 124 (1996).

2. T.L.Brown and M.W.Hyer: Proc. of 11th

Technical Conference, The American Society for Composites, 476 (1996).
3. C.Henaff-Gardin, M.C.Lafarie-Frenot and D.Gamby: Composite Structures, 36, 131 (1996).
4. J.A.Nairn: Journal of Composite Materials, 23, 1106 (1989).
5. J.A.Nairn and S.Hu: Engineering Fracture Mechanics, 41(2), 203 (1992).

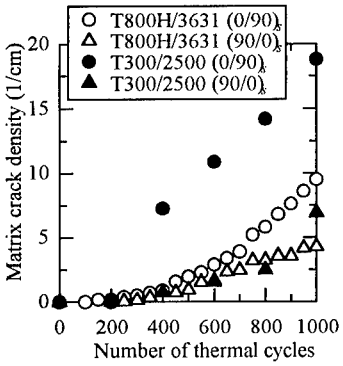

Fig.1 Matrix crack density as a function of the number of thermal cycles

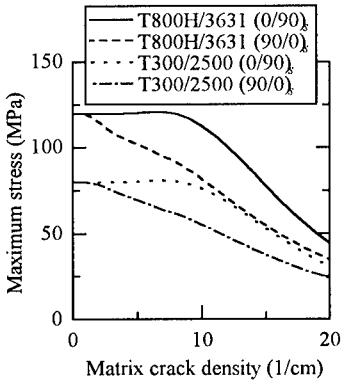

Fig.2 The maximum thermal stress associated with 90° ply cracking as a function of matrix crack density at -196°C

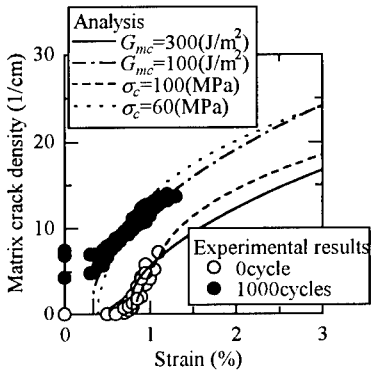

Fig.3 Matrix crack density as a function of strain in T300/2500 (90/0)$_s$ laminates

Table 1 The critical energy release rate and the critical stress in T800H/3631 laminates

	T800H/3631 (0/90)$_s$		T800H/3631 (90/0)$_s$	
	G_{mc} (J/m^2)	σ_c (MPa)	G_{mc} (J/m^2)	σ_c (MPa)
0cycle	550	150	550	150
200cycles	500	140	500	140
400cycles	475	135	475	135
600cycles	450	135	450	130
800cycles	325	115	375	125
1000cycles	250	100	275	105

Table 2 The critical energy release rate and the critical stress in T300/2500 laminates

	T300/2500 (0/90)$_s$		T300/2500 (90/0)$_s$	
	G_{mc} (J/m^2)	σ_c (MPa)	G_{mc} (J/m^2)	σ_c (MPa)
0cycle	300	100	300	100
200cycles	200	85	200	85
400cycles	125	60	175	80
600cycles	75	45	150	75
800cycles	75	45	125	70
1000cycles	50	35	100	60

Proceedings of 7th Japan International SAMPE
Symposium & Exhibition, Nov. 13-16, 2001

Evaluation Method for Initial Micro Fracture Behavior in Woven Fabric Composites

Tadayoshi Shimizu#, Toshiko Osada#, Asami Nakai#, and Hiroyuki Hamada#

#: Kyoto Institute of Technology
Matsugasaki, Sakyo-ku, Kyoto 606-8585, JAPAN
E-mail: b5330033@ipc.kit.ac.jp

Abstract

Evaluation method for initial fracture behavior of textile composite was considered in this study. Knee point found on the stress-strain curve of tensile test was used to quantitative evaluation of initial micro fracture.

Acryl silane treated woven fabric and vinylester resin was used, and one ply composites were fabricated for tensile test. Knee point was determined by various method from the stress-strain curve. Knee point can be determined quantitatively by least squares method.

Key Words: Initial Micro Fracture, Knee Point, Woven Fabric Composite.

Introduction

It has been clarified that micro fracture behaviors occurred in woven fabric composite are debonding between fiber and matrix at interface, delamination at fiber crossing part, transverse crack, filament fracture, and so on. These micro fractures contribute to macro fracture behavior of composites. Thus the initial fracture behavior is important to understand the mechanical properties of composites.

A characteristic property of woven fabric composites is a knee point on the stress-strain curve. Knee point appeared at the elastic limit, and it is considered that some fracture have occurred. Initial micro fracture of woven fabric composites was confirmed to be transverse cracks[1]. Thus, it is supposed that onset of initial fracture is agreed with knee point. Therefore, knee point found on the stress-strain curve of tensile test is considered to be used for quantitative evaluation of initial fracture. Here, it is important to evaluate the knee point with accuracy.

In this study, evaluation method of knee point was considered. The micro fracture behavior in textile composite was investigated by tensile test and in-situ observation. In order to identify the knee point, various evaluation method of knee point on the stress-strain curve was conducted.

Evaluation method

Tangent line on stress-strain curve

Generally, knee point on stress-strain curve can be determined by drawing the tangent line. We asked some students to determine the knee point. Figure 1 shows knee points identified by some students. There are personal errors as shown in Fig.1.

Image analysis

As previous study, transverse crack could be observed with a scattering of light from the cracking part of the specimen[2,3].

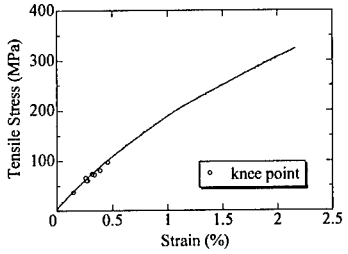

Fig.1 Knee point identified by some students.

To determine its appearance, the image processing was carried out as follows; in order to detect the transverse crack clearly, edge detection was at first executed along to the tensile direction. Second, the brightness of the picture was transformed to the binary image. Finally, the number of white pixels was counted. A series of image analysis was carried out for the picture at every 2 seconds of the tensile test. The point of initial micro fracture was determined as the beginning of the increase in number of white pixels.

Figure 2 shows typical stress-time curve and relationship between increase ratio of white pixels and time. Here, time corresponds to strain. Initial micro fracture behavior can be determined clearly with the increase ratio. Initial fracture stress is 29.2MPa. However, this image analysis method cannot be applied to thick or lightproof composites. Therefore, new evaluation method of initial fracture is required.

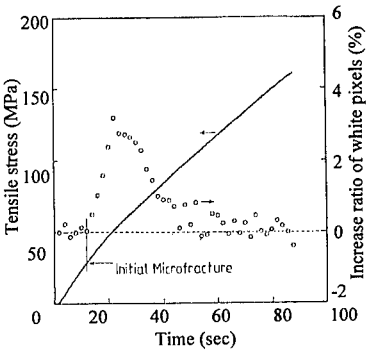

Fig.2 Results of image analysis.

Method of elastic modulus evaluation

In order to determine the knee point, changes in tensile modulus was considered. Tensile modulus is defined as a gradient of stress versus strain; tangent modulus, secant modulus and chord modulus have been used. Secant modulus is defined as the slope from origin to a certain point. If knee point clearly exists, distinct decrease will appear on secant modulus-strain curve as shown in Fig. 3.

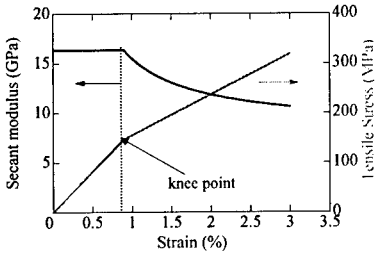

Fig.3 Secant modulus and stress-strain curve.

Least squares method

Knee point can be determined by using least square method. Knee point was identified by following procedure;

1. Linear relationship between stress and strain was calculated by least square method from the first to a certain point. The correlation coefficient for the data and least square line was calculated until the highest value was obtained. Here, initial linear region can be determined.
2. Linear relationship between stress and strain was calculated by least square method on the determined linear region.
3. The point that the residual error between experimental and calculated data became positive was defined as knee point.

Experiment

Materials

Materials used in this study were plain glass woven fabrics (WE18W: Nitto Boseki Co., Ltd., Japan) as reinforcement with 0.4 wt% silane coupling agent and vinyl ester resin (R-806; Showa Highpolymer Co., Ltd., Japan) as the matrix resin. The room temperature catalyst used was 0.7 phr methylethylketoneperoxide (MEKPO).

Tensile testing

One-ply composite was fabricated by hand lay-up technique, and tensile testing was performed to know the onset and growth of transverse cracks. During the tensile tests, the testing machine was periodically stopped and unloaded to 0, and observation of transverse cracks in fiber bundles using optical microscopy was performed.

Results and Discussion

Stress-strain curve of the composites is shown in Fig.4, and Fig.5 shows the fracture aspect by optical microscopic observation. Transverse cracks appeared at 1.0% strain in weft fiber bundles, and the number of the cracks increased, and the crack was enlarged with increasing the strain.

Figure 6 shows stress-strain curve and secant modulus-strain curve. As shown in Fig.6, secant modulus changes gradually, method of elastic modulus evaluation was not suitable for evaluation method of knee point.

Figure 7 shows results of least square method for evaluation of the initial fracture stress and strain. Initial fracture stress and strain are 104MPa and 0.5% respectively. Strain at which transverse crack observed was different from initial fracture strain. This is considered that cracks were closed when the load was removed for observation.

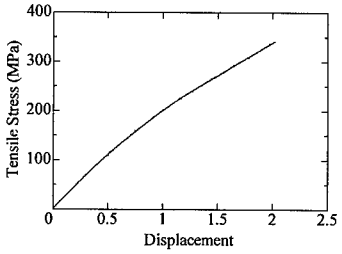

Fig.4 Stress-strain curve.

Considering the sample described in Fig.2, the initial fracture strain at knee point with least square method and strain at which the transverse crack appears are well agreed. Namely, this method is able to determine the knee point on the stress-strain curves quantitatively. Thus, this evaluation method to evaluate the initial fracture with knee point stress and strain is useful method.

Conclusion

In this study, evaluation method of initial fracture of textile composite was considered. Initial fracture in woven fabric composites is transverse crack inside of fiber bundles. Initial fracture stress and strain were evaluated by knee point on stress-strain curve with least square method.

References

1. A.Nakai, H.Hamda, N.Takeda, Proceedings of he 9th US-Japan Conference on Composite Materials, pp 753-760, (2000)
2. H. Ichihashi, H. Hamada, N.Ikuta, and Z. Maekawa, Transactions of the Society of Fiber Science and Technology, Vol.49, pp.169-175, (1993)
3. H. Hamada, Z. Maekawa, T. Morii, T. Tanimoto, and A. Yokoyama, Composite Materials : Testing and Design, ASTM STP 1274, Vol.12, pp.88-102, (1996)

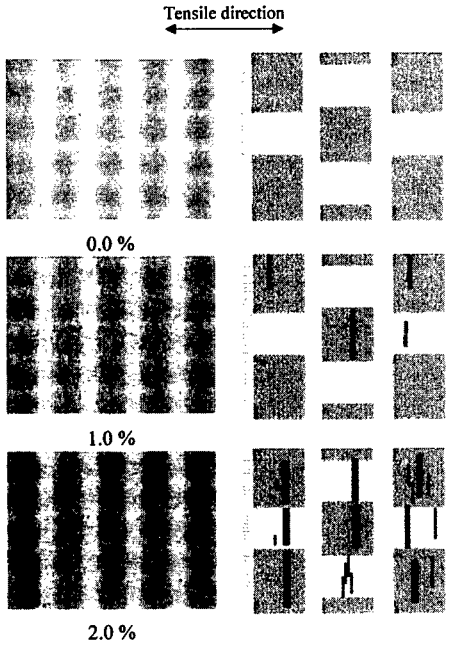

Fig.5 Fracture process of woven fabric composites.

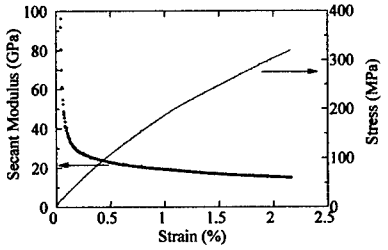

Fig.6 Secant modulus and stress-strain curve.

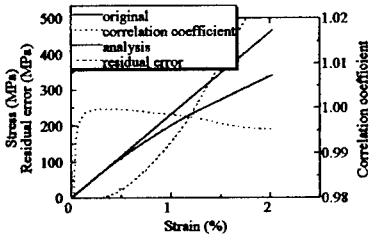

Fig.7 Results of least squares method.

Proceedings of 7th Japan International SAMPE
Symposium & Exhibition, Nov. 13-16, 2001

COLLISION FATIGUE LIFE EXTENSION OF PZT IRRADIATED BY SHEET ELECTRON BEAM

Kentaroh Takashina, Kazuya OGURI, Akira TONEGAWA and Yoshitake Nishi

Department of Materials Science, Tokai University
1117 Kitakaname, Hiratsuka, Kanagawa, 259-1292 JAPAN
E-mail: am026429@keyaki.cc.u-tokai.ac.jp

Abstract

In order to extend collision fatigue life of PZT, the sheet electron beam irradiation has been performed. The irradiation extended fatigue life and enhanced the Weibull coefficient, which indicated statistic distribution of fracture.

Key Words: PZT, Fatigue limit, Collision

Introduction

PZT is typical piezoelectric materials [1-4]. It can be usually applied forever under fatigue limit. When it is utilized over fatigue limit, fatigue life on fracture is determined. Origin of fatigue fracture often generates on surface. In order to control crack generation and growth, atom diffusion and stress relaxation near crack tips are important factors to enhance the ductility. To modify the various properties at lower temperature, materials have been often treated by electron beam (EB) irradiation [5-7]. In the present study, electron beam (EB) irradiation of high electrical potential (170 kV) was used to migrate atoms at crack tips and crystal grain boundary. Such atom migration probably dulls the edge of sharp crack tips and relaxes the stress concentration at a temperature lower than that required in conventional heat-treating. This study showed that sharp crack reduction and relaxation could be accomplished by using sheet electron beam irradiation without applying heat. Therefore the purpose of the present work is to extend collision fatigue life of PZT treated by sheet electron beam irradiation. Electron beam treatment, is a new concept to extend collision fatigue life used without accompanying heat, and has broad potential applications in the fields of engineering.

Experimental Procedure

$Pb_{0.55}\ Zr_{0.24}\ Ti_{0.21}\ O_X$ (PZT) samples were prepared by sintering under high pressure. The chemical composition and structure change were confirmed by means of EDS (energy dispersive X-ray spectrometer; HORIBA EMAX-5770W) and X-ray diffraction. The fatigue test was performed by collision between PZT cylindrical sample (2.5 mm ϕ $\times$5 mm height) and steal ball (10 mm ϕ,5.4 g) until the sample was fractured (See Figure 1). The collision energy (E_C) was controlled by the height (h). The crack was observed by means of scanning electron microscopy (SEM) and optical profile project.

The sheet electron beam irradiation was homogeneously performed using an electron-curtain processor (ELECT

OROCURTAIN PROCESSOR Type CB175/15/180L, Energy Science Inc. Woburn, MA)[5-7]. Figure 2 shows the schematic drawing of sheet electron curtain processor. The acceleration potential and the irradiating current densities were 170 kV and 8.9 $\times$ 10^{-3}mA/cm^2, respectively. The EB treatment was applied intermittently (i.e., not continuously). The conveyer speed was 10 m/min. Irradiation time was kept constant at 0.23 s in order to control the temperature in each of the four samples. The temperature of the sample was below 323 K just after the EB irradiation. The integrated irradiation time was 12.96Mrad 0.69 s. Here, the total amount of absorbed dose value was converted by the absorbed dose of the distillation water. Although the other EB treatments were usually in vacuum, the irradiated specimen was kept under protective nitrogen at atmospheric pressure in the apparatus. The oxygen concentration was less than 400 PPM in this atmosphere.

(1) PZT
(2) Polyester resin
(3) Electrode (Ni)
(4) Lead
(5) Oscilloscope
(6) Steel stick

$$E_p = mgh = E_c^i$$

E_p : Potential energy (J)
E_c^i: Ideal collision energy (J)
m : Weight of steel stick (kg)
g : Gravity (m/s^2)
h : Height (m)

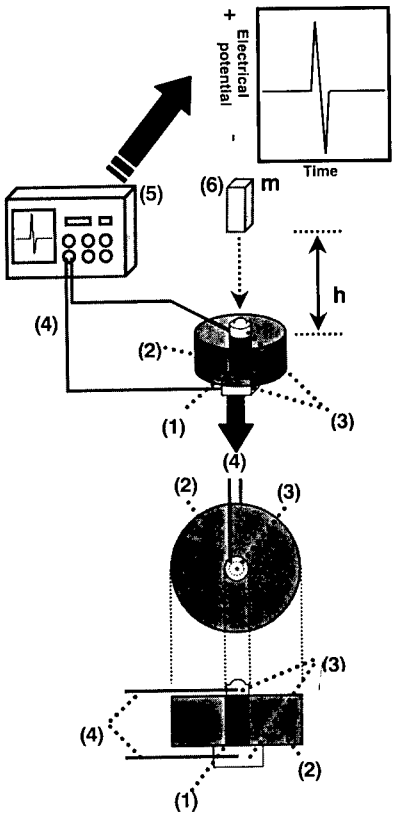

Fig.1 Collision fatigue test. Controlling fall height of steel stick varies collision energy (Ec).

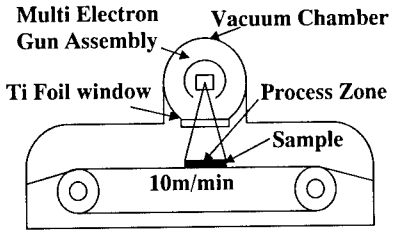

Fig.2 Schematic drawing sheet electron curtain processor. Samples are irradiated by electron beam under nitrogen atmosphere.

Results and Discussion

Fine cracks were observed on PZT sample surface after collision fatigue fracture, as shown in Figure 3 with the SEM cross-section micro-graph of PZT sample before collision fatigue test.

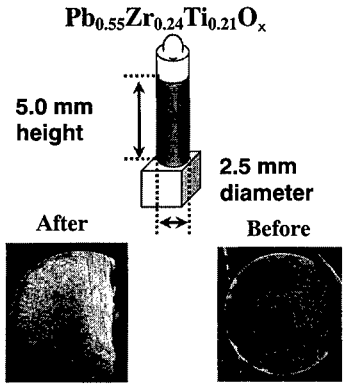

Fig.3 SEM micro-graph cross-section of PZT samples before collision fatigue test and after fatigue fracture.

Figure 4 shows change in fracture ratio against collision fatigue number at different collision number. The fracture ratio (R_f) is expressed by a following equation.

$$R_f = N_f / N_t \qquad (1)$$

Here, N_f and N_t are fractured and total number of PZT samples at different collision numbers. Offset number (R_f=0) and midpoint (R_f=0.5) of fracture were 64 and 22 for PZT samples before EB treatment. To extend the collision fatigue life, electron beam (EB) irradiation of high electrical potential (170 kV) was used to dull the edge of sharp crack tips and to relax the stress concentration. Offset number (R_f=0) and midpoint (R_f=0.5) of fracture were 233 and 55 for samples treated by EB irradiation of 4.32Mrad. The EB treatment extends the collision fatigue life, which is approximately 4 times longer than that before EB treatment.

Figure 5 shows change in the R_f against ideal collision energy on the collision test of the PZT samples with and without EB irradiation. The EB irradiation enhanced the ideal collision energy (E_c^i) at different R_f values. Namely, it enlarges the fracture toughness for PZT.

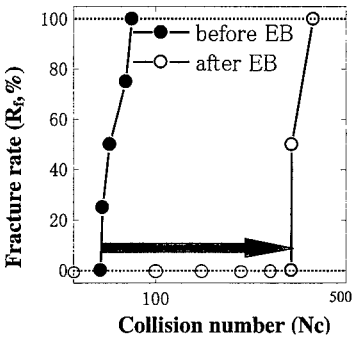

Fig. 4 Change in fracture ratio against collision fatigue number.

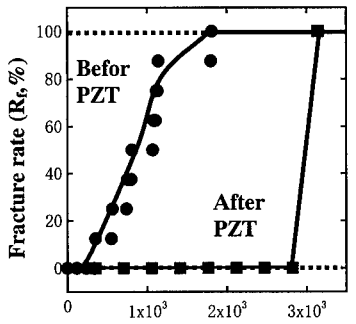

Fig.5 Change in the R_f against ideal collision energy on the collision test of the PZT samples with and without EB irradiation.

The fracture probability (P) depends on risk of rupture [8]. If the risk is assumed to be (E_c^i/E_c^o), it is expressed by a following equation.

$$P = 1 - \exp [- (E_c^i/E_c^o)^m] \qquad (2)$$

E_c^i is experimentally obtained fracture stress. When P is equal to 0.966, an expectant fracture energy (E_c^o) can be obtained.

By using Median Rank method broadly applied (Ref.9), integrated fracture probability (P) is expressed by a following equation.

$$P = (I - 0.3) / (n + 0.4) \qquad (3)$$

Here, n and I are total sample number and fractured order of each sample, respectively. A Weibull coefficient (m) indicated statistic distribution of fracture stress. If the ideal collision energy is related to the fracture stress, linear regression curve is shown in Figure 6 can be obtained of PZT samples before and after EB irradiation. The irradiation enhanced the Weibull coefficient, as shown in Figure 6 Therefore, we concluded that the EB irradiation decreased the statistics distribution of fracture toughness.

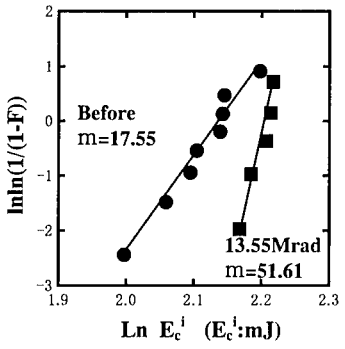

Fig.6 Linear regression curve of PZT samples before and after EB irradiation. The irradiation enhanced the Weibull coefficient.

Conclusions

To extend the collision fatigue life, electron beam (EB) irradiation of high electrical potential (170 kV) was used to dull the edge of sharp crack tips and to relax the stress concentration for PZT. The EB irradiation extended the fatigue life for PZT. The EB irradiation also enlarged the fracture toughness and decreased the statistics distribution of fracture toughness.

Acknowledgement

Authors would like to thank President IWASAKI of IWASAKI Denki Group Ltd.

References

1.K.Uchino, S. Nomura, L.E. Cross, R. E. Newnham and S. J. Jang, J. Mater. Sci. 16 (1981) 569.

2. S. Nomura and K.Uchino, Ferroelectrics, 50 (1983) 197.

3. K.Uchino, American Ceramics Society, 65 (1986) 647.

4. R. Kondoh and Y. Nishi, Bridging the Centuries with SAMPE's Materials and Processes Technology, (ISBN 0-938994-86-7) [45th SAMPE Symposium May 21-25, 2000 Edited by S. Loud, V. Karbhari, D.O.Adams, A.B. Strong, (Society for the Advancement of Material and Process Engineering, Covina, CA91722, USA)] 45, (2000) 179.

5. Y. Nishi, S. Takagi, K. Yasuda and K. Itoh,J. Appl. Phys., 70, 367 (1991).

6. Y. Nishi, H. Izumi, J. Kawano, K. Oguri, Y. Kawaguchi, M. Ogata, A. Tonegawa, K. Takayama, T. Kawai and M. Ochi, J. Mater. Sci. 32, 3637 -3639 (1997)

7. K.Oguri, K.Fujita, M.Takahashi, Y.Omori, A.Tonegawa, N.Honda, M.Ochi, K.Takayama, and Y.Nishi, J. Mater. Res. 13, 3368 (1998).

8. S.W.Freiman, GLASS: SCIENCE AND TECHNOLOGY: Vol.5 Elasticity and Strength in Glasses (Ed. By D.R. Uhlmann and N.J. Krill, Academic Press, 5,1980) pp63-65.

Proceedings of 7th Japan International SAMPE
Symposium & Exhibition, Nov. 13-16, 2001

Machinability of Heat Treated Silicon Powder Compacts

Kanyatip TANTIKOM*; Kuljira SUJIROTE**; and Sawai DANCHAIVICHIT*

*Department of Metallurgical Engineering, Chulalongkorn University, Bangkok, Thailand;
**National Metal and Materials Technology Center, Bangkok, Thailand
E-mail: kuljiras@mtec.or.th

Abstract

One major problem and limitation of processing complex-shaped ceramic components is machining. From the machining cost and ease of process points of view, reaction-bonded silicon nitride (RBSN) largely benefits from its ability to form near-net-shape product. One way to determine the machinability of heat-treated silicon powder compact is to manifest speed/feed diagrams of lathe turn and drill operations. The turned samples were characterised by measuring surface roughness average (Ra) and the drilled samples were characterised by measuring chipping edge area. These two measurements when plotted against a factor so-called material removal rate / rotational speed (MRR/V) were considered sufficient to indicate machinability of the powder compacts.

Key Words: Machining, Machinability, Powder compact.

Introduction

By reaction with nitrogen, a very loosely packed silicon powder formed a coherent monolithic silicon nitride replica of the original shape of appreciable strength. [1] The reaction is accompanied by a 22% volume expansion that occurs in void space of the powder compact. In other words, this is a near-net shape process that lends itself to the formation of complex shapes without the shrinkage and expensive machining.[2] Consequently an insight into machinability of heat-treated silicon powder compact is of primary significance.

Studies on machinability of ceramics have been concentrated on each stages; i.e. green compact or sintered products. The studies on green compact [3] related initial defect size to handleablility and resistance to clamping and chipping damage. While researchers [4],[5] tend to relate machinablity of sintered surface with factors relating hardness and toughness of the samples. However, the aim of this study focused between the two extremes; i.e the machinability of pre-sintered compacts.

A few parameters; i.e. material removal rate (MRR) together with feed and speed of machining operation, were utilised and correlated with finished surface characteristics. The MRR has been defined as the uncut area multiplied by the rate at which the tool is moved perpendicular to the uncut area. [6] For turning operation, the area removed is an annular ring of outside diameter D and inside diameter D_1 (Figure 1). The uncut area is $\pi(D^2-D_1^2)/4$. The specimen was rotated at N revolutions per minute, while the tool was fed at f_r units (millimeters per revolution) Therefore, the material removal rate is:

$$MRR = \frac{\pi(D^2-D_1^2)}{4} \cdot f_r \cdot N \qquad (1)$$

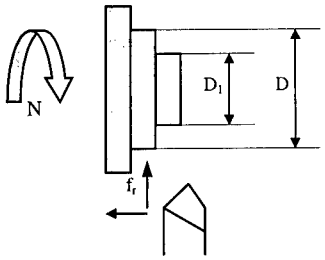

Fig.1 Schematic of specimen during turning operation

For drilling, a drill of diameter D is rotated at N revolutions per minute and fed at f_r (unit distance per revolution). The uncut area is the area covered by the drill, or $\pi D^2/4$,while the feed rate perpendicular to the area is $f_r \cdot N$. Therefore, the material removal rate for drilling is :

$$MRR = \pi D^2/4 \cdot f_r \cdot N \qquad (2)$$

The cutting speeds (m/min) can be converted to rotational speed as follows:

$$V = \pi DN \qquad (3)$$

These machining parameters; i.e. speed,feed and MRR/V were correlated with surface roughness average (Ra) of turned surface and edge chipping area of drilled surface.

Experiment Procedure

Silicon metal with average size 25 microns was selected in this experiment. Table 1 shows the chemical composition of silicon metal. The silicon powder mixed with 2 wt% polyvinyl alcohol (PVA) binder was compacted into cylindrical shape of 50 mm diameter and 17.5 mm height. The green compact were heated at 150°C/hr to 500°C then heated at 200°C/hr to 1200°C and held for 10 hrs in argon.

The machining was performed on a Plant-Sliven CU 500M lathe using high-speed steel cutting tool. The cutter speed and feed rate were varied from 250, 315, 400 and 500 rpm and 7.41, 8.55, 10.10 and 12.35 mm/min, respectively. The top surface of a sample was turned to provide a reference plane for accurate measure of depth of cut. Steps were then turned at the designed feed and speed with a 2 mm depth of cut as shown in Figure 1. The surface roughness average (Ra) of turned suface was measured by using a surface profiler Dektak^3 ST (Veeco) and a Mitutoyo surftest 201.

The perforation was performed on an ERLO (SIEMENS) machine using 3 mm diameter hardened steel bit. The drilling conditions consisted of the cutting speed of 288, 480, 685 and 1150 rpm and the feed rate of 0.08, 0.16, 0.24 and 0.35 m/min. The chipping edge area were measured using an Olympus optical microscope connected with an image analysis Omnimet 4 program.

Table 1 Chemical composition of silicon metal

Silicon metal	Element (% by wt.)				
	Si	Al	Ca	Fe	W
	99.11	0.14	0.47	0.17	0.10

Results and discussion

Observation of the machined surface by naked eyes revealed that high-speed, low cutting tool feed rate was preferable for fine smooth surface. Figure 2 compares typical 'smooth' and 'rippled' surfaces of the turned samples. It can be seen that the feature on the 'smooth' surface was dominated by inter-agglomerate fracture. While the failure on 'rippled' surface which consisted of smooth part and uneven part was exacerbated by crack propagation and linking among inter-agglomerate flaws at high feed rate.

The dependence of surface roughness average (Ra) on feed and speed varied from approximately 3 to 6 microns (Figure 3). The surface roughness average seemed to be more sensitive to speed than feed rate. Nevertheless, it should be noted that the Ra of 3.5 microns was rather favourable when compared with the Ra of green alumina compact of 7.1 microns, measured under the best cutting conditions.[7]

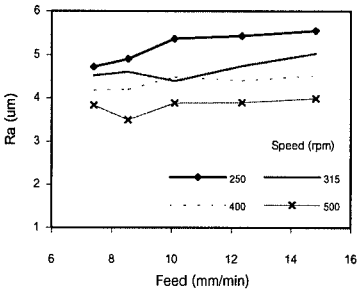

Fig 3. Speed/feed diagram of silicon compact of turning operation

500 rpm,7.41 mm/min

250 rpm,12.35 mm/min

Fig.2 SEM image of typical (a) 'smooth' and (b) 'rippled' surfaces.

Observations of samples drilled at various feed and speed under optical microscope (Figure 4) exhibit small edge chipping. A plot of measured chipping edge area in drilling against MRR/V indicates linear correlation, similar to that of Ra in turning against MRR/V (Figure 5). The slope of the plots suggest that drilling is far more sensitive to the factor MRR/V than turning operation. This is obviously caused by stress concentration at edge. The x-intercept in drilling operation provides a sufficient guideline for appropriate material removal rate.

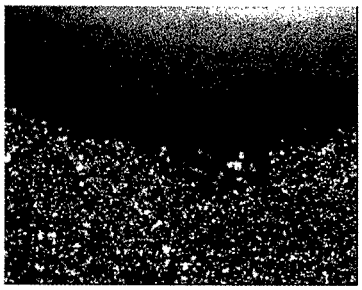

685 rpm, 0.08 m/min

Fig 4. Optical Microscope image of drilled surface

Mechanism of the material removal for both turning and drilling operations could be explained by Griffith's theory of unstable crack propagation and by the weakest link theory of Weibull. Elastic strain energy is stored in front of the cutting tip before propagation occurs. Once cracks start to propagate they tend to travel further to dissipate stored energy before linking to form a chip. Inter-agglomerate boundaries provide suitable interlinking defects.

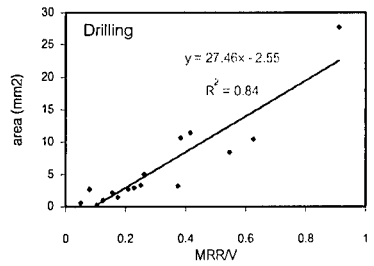

(a)

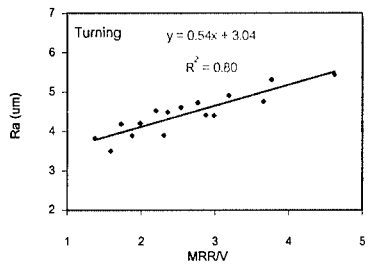

(b)

Fig 5. (a) The plot of measured-chipping edge area in drilling against MRR/V (b) the plot of Ra in turning againt MRR/V

Conclusions

Pre-sintered silicon powder compact can be machined by turning and drilling operations. At high-speed, low cutting tool feed rate was preferable for fine smooth surface and small edge chipping area. Drilling operation was more sensitive to the factor MRR/V than the turning because of stress concentration at edge. The x–intercept indicate that the drilling factor (MRR/V) should be less than 0.2 for an acceptable drilled hole, while the factor MRR/V was less influentially in turning operation.

References

[1] Popper, P. and Ruddelsden, S.N. 'The preparation, properties, and structure of silicon nitride' : Trans. Br. Ceram. Soc. 60, 603-26, (1961).

[2] Riley, F. L. 'Silicon nitride and related materials ' : J. Am. Cer. Soc. 83 (2) , (2000).

[3] Song, J. H. & Evans,J. R. G. [1997] 'On the machinability of ceramic compacts' : J. Eu. Cer. Soc. 17, 1665-73 (1997).

[4] Birkby,I.; Dransfield, G.P.; McColagan, P.; Song, J.H.; Evans, J.R.G. 'Factors affecting the machniability of fine ceramic powder compacts' : Brit. Cer. Trans. 93(5),183-86.

[5] Hockin H.K. Xu and Said Jahanmir 'Effect of Microstructure on abrasive machining of advance ceramics' : Ceram. Eng. Sci. Proc., 16(1), 295-314 (1995).

[6] Cohen, P.H. : ASM handbook Vol.16 , Machining ,13-18 (1996).

[7] Sentoku, E.; Tanaka, H.; & Kawabata, H. 'On the machinability of alumina – molding pieces (1st part) - Cutting conditions and roughness of finished surface :Powder Met. 43(4), 493-97, (1996).

Proceedings of 7th Japan International SAMPE
Symposium & Exhibition, Nov. 13-16, 2001

Tensile Strength of Carbon Fiber With Different Diameter

Ai Hamasaki[1], Yasuo Kogo[2], and Tetsuya Morimoto[3]

1: Graduate student (Corresponding Author),
Science University of Tokyo
2641, Yamazaki, Noda, Chiba 278-8510, JAPAN
E-mail: j8201631@ed.noda.sut.ac.jp
2: Science University of Tokyo
3: Advanced Composite Evaluation Technology Center,
National Aerospace Laboratory
6-13-1 Ohsawa, Mitaka, Tokyo 181-0015, JAPAN

Abstract

Localization in critical flaw distribution was studied for the accurate Weibull scaling of carbon fiber tensile strength.

Weibull scaling is known to give fracture probability of good agreement with experimental results when ideal scaling factor is selected. The factor represents probability of containing a critical flaw, which usually increase with the volume. Thus, volume has been expected as Weibull scaling factor for many brittle materials. However, on the case of carbon fiber, it is expected that surface flaw is dominant factor as the manufacturing process, handling, and so on damage the surface. In this case, the surface area appears to be ideal Weibull scaling factor of carbon fiber tensile strength.

In this work, the surface area was compared with the volume as the scaling factor of IM600 carbon fiber tensile strength. The experimental results showed that the Weibull scaling agreed better with tensile test data when volume was selected as the scaling factor. However, surface area was found less accurate as the scaling factor. Therefore, the critical flaws were supposed to be distributed in the fiber volume and thus, fiber volume is concluded ideal factor for Weibull scaling.

Key Words: Carbon fiber, Weibull distribution,

Introduction

Strength of advanced carbon fiber reinforced composites (CFRP) is dependent on the performance of reinforcement fibers. Thus, the accurate scaling of carbon fiber strength is essential for the strength characterization of CFRP. The tensile strength of brittle materials such as carbon fibers has defined as the crack-growth load from critical flaws that are distributed throughout the volume. Thus, the strength is scaled with Weibull model that describes probability of an imaginary unit scale such as volume or surface area containing the weakest flaw. Volume has been usually expected appropriate for Weibull scaling. However, it is supposed on carbon fibers that the surface area is also an important factor as localization of critical flaws is expected on the surface due to the damage in manufacturing process, handling, and so on.

Thus, surface area and volume were compared as single-modal Weibull scaling factors to derive information of critical flaw distribution.

Single-modal Weibull model is given as follows [1].

$$P = 1 - \exp\left[-\frac{V}{V_0}\left(\frac{\sigma}{\sigma_s}\right)^m\right] \quad (1)$$

Where, 'P' is the probability of a fiber having a tensile strength less than or equal to 'σ'. 'V_0' is an imaginary unit of volume. 'm' and 'σ_s' is the Weibull shape and scale parameters, respectively. The parameters are determined through Weibull plotting of '{-ln[lnP]} – lnσ' manner. In the plotting, a cumulative probability of fracture 'P_i' is approximately determined for *i*th result in a set of n samples as follows [2].

$$P_i = \frac{i}{n+1} \quad (2)$$

Experimental

Materials

The carbon fiber used in this work was IM600-6k (TOHO RAYON, Co., Ltd.), which possesses the properties in Table 1.

Table 1, Properties

Tensile strength	Elastic modulus	Strain	Diameter	Density
5690MPa	285GPa	2.0%	5μm	1.8g/cm^3

Diameter measurements

Diameter distribution along tensile test sample is detrimental to the data reliability. Thus, diameter was measured along the gauge on each fiber beforehand the tensile test.

Sample fiber was measured in the diameter with laser micrometer LSM-500 (Mitutoyo MTI Corp) within error of ±0.1μm, in the step of 1.0±0.1 mm along gauge length as depicted in Fig.1.

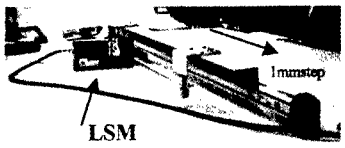

Fig. 1, measurement setup

Fiber cross-section shape analyses

LSM measures fiber diameter as the projection of laser beam. Fiber cross-section shape was thus observed to see if it is circular within acceptable error. Scanning electron microscope (SEM; HITACHI S-2150) was used in the analyses. Bundle of fibers was embedded in epoxy resin and then polished giving the samples of SEM analyses.

Tensile tests

Uniform diameter sections of D=5.0μm and D=6.0μm were prepared as tensile test samples. The gauge length was decided with the volume condition of V=2.5 $\times 10^{-13}$m^3, in order to asses if volume is suitable for the Weibull scaling of the fiber.

Paper holder was used to attach the fibers as depicted in Fig.2. Then the frame parts were cut after the clamping to the tensile test machine (SHIMADZU Ez-test, Shimadzu Corp.) leaving the fiber alone. The tensile tests were conducted under the crosshead speed condition of 1mm/min.

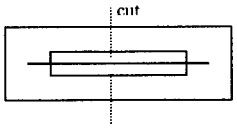

Fig. 2:Tensile test sample

Results and Discussions

Variation in fiber diameter

Each fiber exhibited variation within ± 0.5μm along the gauge as is shown in Fig. 3. However, the diameter was found distributing between fibers at a bundle from 3.5μm to 6.5μm. Thus, each fiber was approximated uniform in the diameter of mean value along the gauge.

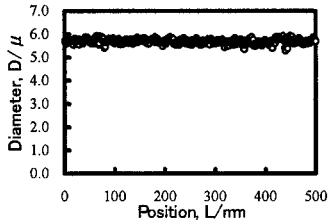

Fig. 3, Distribution of diameter Along gauge

Fiber cross-section shape

Cross-section of fibers was observed with SEM as is shown in Fig. 4. It was found that fiber cross-section shape was close to circular. Assuming the shape elliptic, the short and long axes were measured giving the mean ratio R=0.97 while 1% measurement error gives R=0.98 for the case of circular cross section. Thus, the cross section was regarded close to circular and was approximated pure circle in the following analyses.

Fig. 4, cross-section of the fiber

Tensile test and Weibull scaling

Fiber sections of 5μm and 6μm in the diameters were selected as the tensile samples in order to estimate the location of critical flaws. The tensile strength was scaled in single-modal Weibull manner as depicted in Fig. 5 resulted in the parameters of table 2. Each correlation coefficient was 0.99.

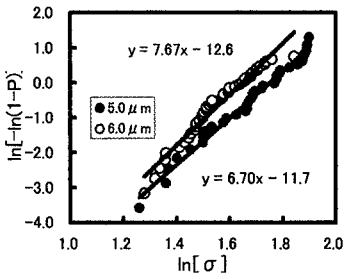

Fig. 5, Weibull plot

Table 2, Weibull parameters

Diameter	5mm	6mm
Sample Numbers	36	41
Surface area	$2.0\times10^{-7}m^2$	$1.7\times10^{-7}m^2$
m	6.7	7.7
σ_s	5.8GPa	5.1GPa
σ_{mean}	6.1GPa	5.3GPa

Each cumulative probability distribution is shown in Fig. 6.

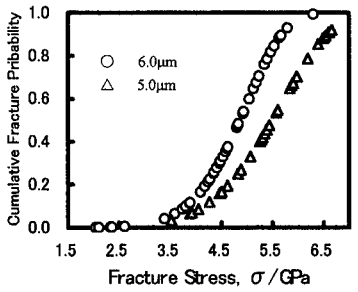

Fig. 6, Cumulative probability distribution

If critical flaws were distributed uniformly in fiber volume, the curves were expected show good agreement. However, no agreement was observed for the curves in Fig.6.

Then, surface area scaling factor was used to predict fracture probability distributions of imaginary D=5μm samples, with the Weibull parameters of D=6μm samples. As volume condition of V=2.5 $\times 10^{-13}m^3$ was set for both samples, imaginary D=5μm samples have less surface area than D=6μm samples. The solid line in Fig.7 thus appears over the D=6μm data points. However, real data points of D=5μm appear below the D=6μm data points. Therefore, surface flaws were estimated less sensitive for the final fracture than flaws inside the fiber volume.

Similarly, cross section area was applied as the scaling factor to assess if onion structure of carbon fiber causes tubular critical flaws. The result is shown as dashed line in Fig. 7. This result shows better consistency with the experimental results than the prediction in surface flaw assumption.

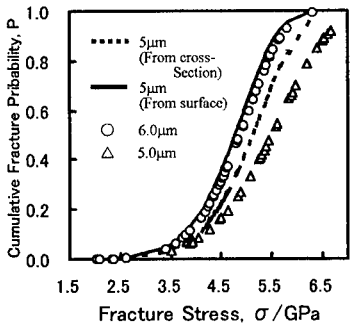

Fig. 7, Comparison of strength prediction by the size parameter

Therefore, surface flaws are estimated less sensitive than internal flaws while the distribution is not uniform in the volume. What is more, fiber diameter appeared as an important factor on the distribution of critical flaw. Thus, improvement in the tensile strength is expected by controlling the diameter in fiber production process.

Conclusions

The tensile strength of IM 600 carbon fiber has been scaled both for the surface area and the volume in single-modal Weibull manner, in order to estimate the effect of diameter on the location of critical flaws. Each sample fiber has been thus measured in the diameter along the gauge beforehand the tensile test.

It is concluded with this work as follows.

(1) Each IM 600 carbon fiber possesses uniform diameter along the gauge. However, the diameters distribute between fibers.
(2) It is estimated on the fiber fracture that the flaws are less sensitive on the surface than inside the volume.
(3) Fiber diameter is an important factor on the distribution of critical flaw. Thus, improvement in the tensile strength is expected by controlling the diameter in production process.

Acknowledgment

This experiment was done at National Space Development Agency of JAPAN (NASDA). Author thanks Mr. Morimoto for his guidance.

References

1. W.Weibull : Journal of Applied Mechanics, 293(Sep, 1951)
2. Sybrand van der Zwang : Journal of Testing and Evaluation, 17(5), 292(Sep, 1989)

Proceedings of 7th Japan International SAMPE
Symposium & Exhibition, Nov. 13-16, 2001

Eccentric Compression Bending Test for CFRP Pipe

Hiroshi Fukuda, Osamu Watanabe, Masaaki Itabashi and Atsushi Wada

Department of Materials Science and Technology, Science University of Tokyo
2641 Yamazaki, Noda, Chiba 278-8510,JAPAN
E-mail:j8200645@ed.noda.sut.ac.jp (O.W.)

ABSTRACT

This paper reports a new test method to evaluate bending strength of composite pipes. In the past, we proposed a compression bending test method to get more reliable bending strength data not only of flat CFRP coupons but also of slender CFRP pipes than conventional three- or four-point bending test. In the present paper, this eccentric compression bending test method is successfully applied to CFRP pipes whose diameter is large.

INTRODUCTION

It is well known that the bending strength of CFRP coupon is strongly affected by the stress concentration due to a hard loading device. The works of Whitney[1] and Cui and Wisnom[2] are some examples to have dealt with this stress concentration.

To compensate for this undesirable effect, the authors have hitherto demonstrated and proposed a compression bending test method[3-6] which is based on Euler buckling of a column. If we measure only the applied load and the crosshead movement during the buckling process of the column, we can calculate both the bending strength and the bending modulus applying the elastica[7].

The above undesirable effect of loading device used for 3- or 4-point bending will be more serious for CFRP pipes; in most cases the pipe will be crushed by the loading nose rather than a bending failure. Then, as a second step, we tried to apply this compression bending test to several kinds of CFRP pipes[8]. Again it was demonstrated that the bending strength by means of the compression bending was larger than that measured by the 3-point bending.

During a series of test of Ref.[8], another difficulty took place. That is, if the diameter of the pipe is large, the Euler buckling has least likely occurred. Then, as a successive work, we tried a bending by means of eccentric compression as shown in Fig.1.

In the present paper, the results of the eccentric compression bending will be shown.

PRINCIPLE OF ECCENTRIC COMPRESSION BENDING

In the case of eccentric compression bending of Fig.1, the bending moment of an arbitrary point is[9]

$$M_x = P(e + \delta - y) \tag{1}$$

and the maximum bending moment at the center of the pipe is

$$M_{\max} = P(e + \delta) \tag{2}$$

Then the maximum bending stress is

$$\sigma_{\max} = \frac{M_{\max}}{Z} \tag{3}$$

where Z is the section modulus of the pipe. If the axial compressive stress should be taken into account,

$$\sigma_{\max} = \frac{M_{\max}}{Z} + \frac{P}{A} \tag{4}$$

is the maximum stress, where A is the cross sectional area of the pipe. Equation (4) can be understood as the maximum compressive stress at failure.

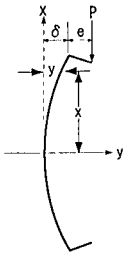

Fig. 1 Eccentric compression bending.

SPECIMEN AND TEST PROCEDURE

Test Specimen

All specimens tested here are CFRP pipes where carbon prepregs with longitudinal direction (thickness: 0.10mm) and transverse direction (thickness: 0.02mm) are wound on a cylindrical mandrel as is schematically shown in Fig.2. Two kinds of pipes were used for this test. They are, Type A: two plies of this prepreg, and the thickness is about 0.25mm; Type B: four plies of this prepreg which means the wall thickness is double, ca.0.50mm. The inner diameter of every pipe was fixed to 15mm against the previous work of 3, 5, 15mm diameters[8], because this test was mainly focused on relatively large-diameter pipes.

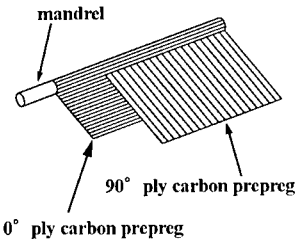

Fig. 2 Fabrication of CFRP pipe.

Eccentric Compression Bending Test

Figure 3 is a schematic view of the device for the eccentric compression bending. To realize compressive load plus bending moment at the ends of specimen, we designed and machined special fixtures. Most of eccentric compression bending tests were performed at the crosshead speed of 5mm/min. Tests were performed under the specimen length of 500, 600 or 700mm and the arm length (eccentricity) of 10, 20, 30, 40 or 50mm. At least 5 specimens were tested at each condition. In the experiment, the applied load was measured with a load cell attached to an Instron-type testing machine and the midspan deflection was measured with a displacement transducer. These data were saved in a personal computer at every 1s.

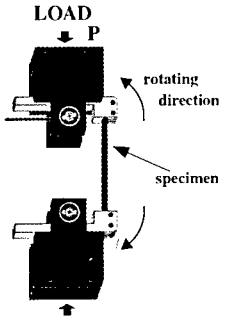

Fig. 3 Schematic view for eccentric compression bending.

RESULTS AND DISCUSSION

Type A specimens

Figure 4 shows the relation between the failure stress and the eccentricity where the failure stress is calculated by eq.(4). Each symbol indicates the average and each vertical range shows the standard deviation.

According to Fig. 4, the failure stress tends to decrease with increasing the eccentricity. This result is more or less strange because the bending strength should be the same regardless the arm length, e, is changed.

To make clear the above strange result, we observed the failure pattern. All of Type A specimens exhibited longitudinal splitting and load-bearing capacity decreased. They did not

separated into two pieces. As was described in "Test specimen," the number of fibers in longitudinal direction is 5 times of that in the transverse (hoop) direction. The failure mechanism of generating splitting may be understood as follows: Under the bending moment, a flattening of the cross section takes place; due to this flattening, carbon fibers in the hoop direction breaks; finally longitudinal splitting occurs.

If the above assumption is acceptable, the evaluation should be done using eq.(3), instead of eq.(4) and Fig.5 is the recalculation taking into account the bending moment only, eq.(3). Comparing to Fig.4, data of Fig.5 are rather uniform. By the way, the conventional 3-point bending was almost impossible for Type A specimen, that is, at very small load (stress), the splitting occurred.

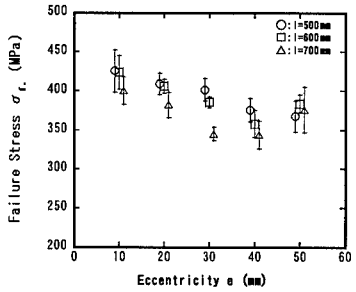

Fig. 4 Failure stress vs. eccentricity. (Type A)

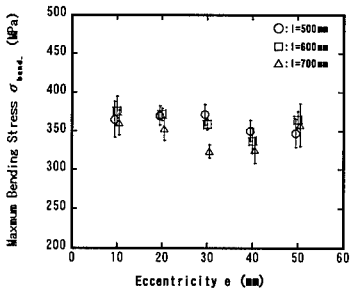

Fig. 5 Maximum bending stress vs. eccentricity. (Type A)

Type B specimen

In this case, the failure pattern seems to be a bending failure. Although we could not identify the point of failure initiation (compression side or tension side), it separated into two pieces. Due to minor problem of the attachment, we could not obtain reliable data of L=600mm and 700mm. Figure 6 is the result of L=500mm where the failure stress is calculated by eq.(4). Apparent effect of the eccentricity on the failure stress was not observed and eq.(4) might be able to be used as a measure to evaluate the bending strength.

Comparing Fig.4 or Fig.5 with Fig.6, the failure stress of Type B specimens (Fig.6) is much higher than that of Type A specimens despite that the same prepregs were used. This may be another proof that the failure pattern of Type A specimens is not a bending failure in the sense of "strength of materials."

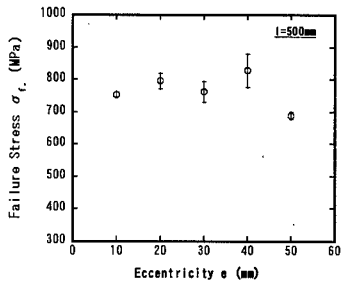

Fig. 6 Failure stress vs. eccentricity. (Type B)

This compression bending, even eccentric compression bending, inevitably includes compressive stress in addition to bending stress. If the ratio of the compressive stress to the bending stress is large, it is no more called a bending test. Figure 7 shows the most severe case of thicker specimen (Type B) and shorter length (l=500mm) where $\sigma_{comp.}$ is calculated by P/A. When the specimen length is large (l=600, 700mm) or when the wall thickness is thin (Type A), the ratio decreases compraring to

Fig.7. Thus it may be concluded that the present eccentric compression bending test is acceptable from practical view point.

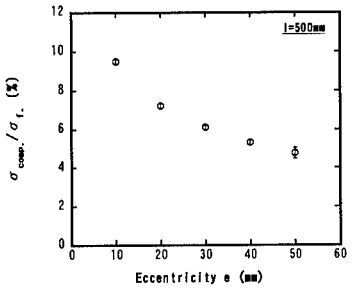

Fig. 7 Ratio of compressive stress to bending stress. (Type B)

CONCLUSIONS

An eccentric compression bending, a revised version of the compression bending, was tried against CFRP pipes. For thin-wall pipes, it was rather difficult to generate bending failure whereas fairly good results were obtained for thicker-wall pipes.

REFERENCES

1. Whitney, J. M., "Elasticity analysis of orthotropic beams under concentrated loads," Composites Sci. Tech., Vol.22, 1985, pp.167-184.
2. Cui, W.-C. and M. R. Wisnom, "Contact finite element analysis of three- and four-point short-beam bending of unidirectional composites," Composites Sci. Tech, Vol.45, 1992, pp.323-354.
3. Fukuda, H., "A new bending test method of advanced composites," Experimental Mechanics, Vol.29, 1989, pp.330-335.
4. Fukuda, H., "Compression bending test method for advanced composites," J. Japan Soc. Aero. Space Sci., Vol.41, 1993, pp.482-487(in Japanese).
5. Fukuda, H., H. Katoh and H. Uesugi, "A modified procedure to measure bending strength and modulus of advanced composites by means of compression bending," J. Composite Mater., Vol.29, 1995, pp.195-207.
6. Fukuda, H. and M. Itabashi, "Simplified compression bending test method for advanced composites," Composites, Part A, Vol.30, 1999, pp.249-256.
7. Timoshenko, S. P. and J. M. Gere, "Theory of Elastic Stability," 2nd ed., McGraw-Hill, 1961, pp.76-82.
8. Fukuda, H., T. Watanabe and M. Itabashi, "Compression bending test method for CFRP pipe," Proc. 2nd Asian-Australasiar Conf. on composite Mater. (ACCM-2000), 2000, pp.1187-1192.
9. Timoshenko, S., "Strength of Materials, Part I," 3rd ed., Van Nostrand Reinhold, 1955,p.259

Proceedings of 7th Japan International SAMPE
Symposium & Exhibition, Nov. 13-16, 2001

Effect of Cyclic Loading on the Monotonic Tensile Behavior of a 3-D Woven Si-Ti-C-O fiber / Si-Ti-C-O Matrix Composite

Takashi Gomyou*, Shijie Zhu**, Yasuo Ochi*, Toshio Ogasawara*** and Takashi Ishikawa***

*Department of Mechanical Engineering and Intelligent Systems,
University of Electro-Communications
1-5-1, Chofugaoka, Chofu-shi, Tokyo, 182-8585, Japan
**Institute of Industrial Science, University of Tokyo
4-6-1, Komaba, Meguro-ku, Tokyo, 153-8505, Japan
***Advanced Composite Evaluation Technology Center,
National Aerospace Laboratory of Japan
6-13-1, Ohsawa, Mitaka-shi, Tokyo, 181-0015, Japan
E-mail: ogasat@nal.go.jp

Abstract

Fatigue behavior of an orthogonal 3-Dimentional woven Si-Ti-C-O fiber reinforced Si-Ti-C-O matrix composite was investigated at room temperature in air. Monotonic tension and tensile fatigue tests were conducted. As a result, the ultimate tensile strength increased with a loading rate. The fatigue life of the composite seems to be time-dependent. The damages during fatigue tests were evaluated by the reduction of Young's modulus, which was almost time-dependent. The residual strength of the fatigued specimen was investigated and the result was discussed.

Key Words: Ceramic Matrix Composite, Stress Corrosion Cracking, Fatigue

Introduction

Ceramic Matrix Composite (CMC) is regarded as one of the most promising candidate materials for high temperature components in some aerospace applications such as after burner, combustion and even turbine blades of turbine engines. The research on CMC has been a hot topic, because of its high fracture toughness and thermal resistance. From the fracture modeling demonstrated by Curtin [1] [2], and Evans [3], it is known that not only the fiber and matrix strengths but also the fiber/matrix interface sliding stress strongly affect the composite strength. But more must be known before CMCs were widely accepted, especially about the fatigue properties and mechanism, because they were not studied well. Moreover, the influence of stress corrosion cracking (SCC) was not studied sufficiently. In this study, monotonic tension and tensile fatigue tests were conducted on Si-Ti-C-O fiber / Si-Ti-C-O matrix composite, and the effect of SCC on the mechanical properties was investigated.

Experimental Procedure

The composite used in this study was processed by polymer impregnation and pyrolysis (PIP) of Si-Ti-C-O matrix into an orthogonal 3-D woven Si-Ti-C-O Tyranno™ Lox-M fiber preform. Before the pyrolysis, the preform was heat treated in CO

atmosphere (TM-S6) to decrease the interface sliding stress between the fiber and the matrix. The composite contained about 40vol% Si-Ti-C-O fibers (in x, y, and z directions being 19.6,19.6, and 2.6vol% respectively) and about 10vol% of porosity. The average diameter of Si-Ti-C-O fiber was 8.5μm, and each bundle consisted of 1600 fibers. Both of monotonic tension and fatigue tests were conducted with the loading direction of y-axis. The surfaces of the specimens were polished before the tests to observe the initiation and the propagation of matrix cracks.

The monotonic tensile tests were conducted with a loading rate ranged from 0.02 to 10MPa/s under load control to investigate the effect of SCC on strength of the composite. The fatigue tests were conducted with a sinusoidal waveform under load control with a load ratio of 0.1, frequency of 0.2 and 20Hz. The specimen fatigued at the maximum stress of 260MPa for 10^5 cycles with a frequency of 0.2Hz was interrupt and then the residual strength was measured. All the mechanical tests were performed on a servo-hydraulic testing system (Model 8501, Instron, USA) at room temperature(25℃) in air (humidity: 40%). To measure the strain, two strain gages (gage length: 5mm) and a clip gage type extensometer (Instron 2620-602) were used. The initiation and propagation of matrix cracks during the tests were observed by replica method. After the fracture, the specimens were examined by using optical microscopy (OM) and scanning microscopy (SEM).

Result and Discussion

Monotonic tension

The stress-strain curves of monotonic tensile tests are shown in Fig.1. The matrix crack densities are shown in Fig. 2 as a function of applied stress. When the stress is up to 100MPa, Fig. 1 shows linear behavior because of no matrix cracks were formed. The composite is elastic in this stress range. Then the stress-strain curve shows nonlinear behavior when stress increases from 100 to 250MPa, because of the initiation and propagation of matrix crack in the 0° and 90° fiber bundles. The stress / strain curves show linear behavior again above 250MPa, because matrix crack densities are saturated and the 0° fibers primarily bear the load. Detailed description regarding non-linear stress / strain behavior of the composite was reported elsewhere [4].

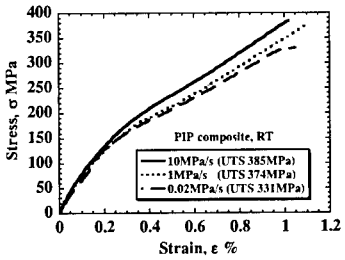

Fig. 1 Stress-strain curve of monotonic tensile tests on the SiC/SiC composite.

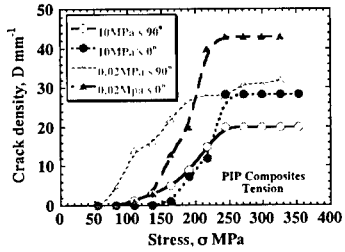

Fig. 2 Crack density for each stress level during monotonic tensile test on the SiC/SiC composite.

The ultimate tensile strength increases with a loading rate. In the case of monolithic ceramics and glasses, it is known that the strength decreases by the slow crack growth (SCG) due to SCC. The crack propagation rate due to SCC is generally expressed by a following equation.

$$da/dt = CK_I^n \qquad (1)$$

where a: crack length, t: time, K_I: stress intensity factor, C and n: material and environmental dependent constants. Stress intensity factor is known to be expressed by a following equation.

$$K_I = Y\sigma\sqrt{\pi a} \qquad (2)$$

Therefore, it is known that the relationship between the loading rate $\dot{\sigma}$ and the parameter of crack propagation "n" can be expressed by a following equation [5].

$$\log\sigma_f = (1/n+1)\log\dot{\sigma} + (1/n+1)\log B(n+1)\sigma_{inert}^{n-2} \quad (3)$$

where $B = 2/(n-2)AY^2K^{n-2}\pi$

σ_f: strength, σ_{inert}: inert strength. The relationship between the loading rate and the strength is shown in Fig. 3. The estimated parameter "n" is 39 for the composite.

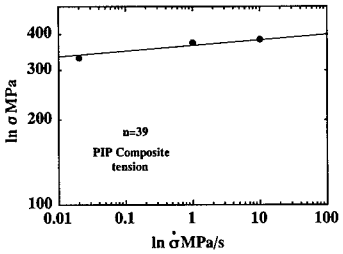

Fig. 3 Relationship between strength and the loading rate curve.

Fatigue

The maximum stress versus number of cycles to failure curves are shown in Fig. 4. The fatigue life at 20Hz is slightly longer than that at 0.2Hz. Based on SCC model, *equivalent time* can be defined for the number of cycles as follows [5].

$$t_{eq} = gN \quad (4)$$

$$g = \int_0^{2\pi/\omega} \left[h(\varpi t)\right]^n dt \quad (5)$$

$$h(\varpi t) = (1+R) + (1-R)\sin(\varpi t)/2 \quad (6)$$

where R : stress ratio ω : angular frequency. Equivalent time corresponds to the time under constant load σ_{max}. The stress versus equivalent time to failure curves are shown in Fig. 5. The fatigue lifetimes in 20Hz seem to be smaller than these in 0.2Hz. The experimental result suggests that the fatigue behavior of the composite is influenced by both SCC and cyclic damages.

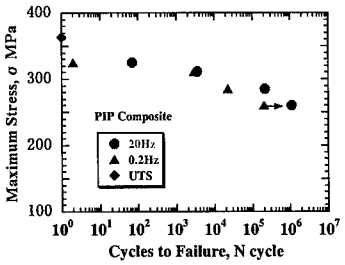

Fig. 4 S-N curves of SiC/SiC composite.

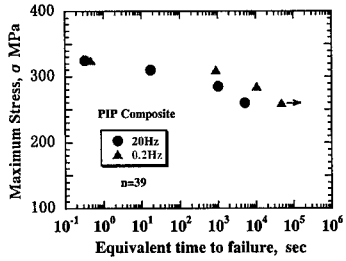

Fig. 5 Maximum stress versus equivalent time to failure curves of the SiC/SiC composite.

Normalized Young's modulus as a function of equivalent time is shown in Fig. 6. They were calculated from the slope of the hysteresis loops. The modulus deceases significantly in the first cycle because of the matrix crack propagation. The reduction of modulus does not depend on number of cycle but equivalent time. This demonstrates that a time-dependent mechanism mainly affects the microscopic damages. It is known that SCC is the main damage mechanism for SiC ceramics under tensile stress. The present results suggest that microscopic damages are strongly influenced by SCC mechanism.

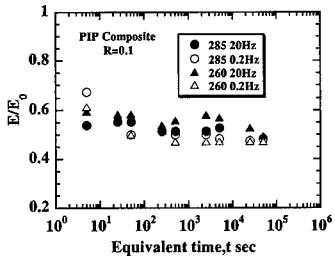

Fig. 6 Reduction of Young's modulus with time of the SiC/SiC composite during fatigue.

Residual strength

The specimen used for pre-fatigue test was fatigued at a maximum stress of 260MPa for the equivalent time of 4×10^4 sec (10^5 cycles). The stress-strain curves for the original specimen and fatigued specimen are shown in Fig. 7. The initial Young's modulus of the pre-fatigued specimen is lower than that of the original specimen due to the fatigue damages. However, the ultimate tensile strength of pre-fatigued specimen is the almost same as that of the original specimen. The similar experimental results were reported by Holmes et al. [6].

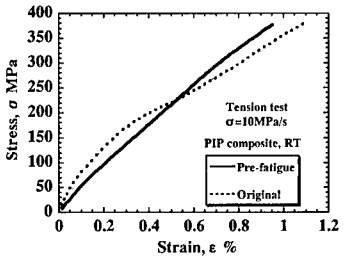

Fig. 7 Stress-strain curves of the original and pre-fatigue specimens.

The fatigued specimen must be influenced by SCC, but the residual strength did not decrease. Therefore, based on SCC model, strength reduction of the composite was estimated by eq. (8). From the equation (1), (2) and (3), the following equations are obtained [7].

$$t^{n+1} = 2(n+1)[a_i^{-((n/2)-1)} - a^{-((n/2)-1)}]/A(n-2)(Y\sigma_{max}\sqrt{\pi}) \quad (7)$$

$$\sigma/\sigma_i = \left[1-\sigma_{max}^n t/\sigma_i^{n-2}B\right]^{1/n-2} \quad (8)$$

where a_i: initial crack length, σ: strength, σ_i: initial strength, σ_{max}: maximum stress of loading, a :crack length. The normalized strength is shown in Fig. 8 as a function of equivalent time. It is understood that the tensile strength of the fatigued specimen (260MPa, 4×10^4sec) hardly decrease. Therefore the strength degradation was not observed in fatigued specimen.

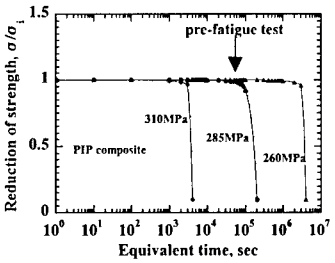

Fig. 8 The estimated strength reduction due to SCC as a function of equivalent time.

Conclusions

Fatigue behavior of an orthogonal 3-D woven Si-Ti-C-O fiber reinforced Si-Ti-C-O matrix composite was investigated at room temperature in air. The following conclusions were made:

1. The composite strength increased with a loading rate, because of the effect of SCC.
2. Although the fatigue life of the composite is mainly time-dependent, the effect of cyclic loading on fatigue life was also observed.

References

1. W. A. Curtin: J. Am. Ceram. Soc., 76 (9), 2300 (1993)
2. W. A. Curtin: J. Am. Ceram. Soc., 77 (4), 1075 (1994)
3. A. G. Evans, F. W. Zok, and R. M. Mcmeeking: Acta Metall. mater. 43 (3), 859 (1995)
4. T. Ogasawara et al.: J. Am. Ceram. Soc. 84 (7), 1565 (2001)
5. T. Ogasawara et al.: Trans. of the JASME. 59 (5), 1256 (1993)
6. J. W. Holmes, et al.: J. Am. Ceram. Society 83 (6), 1469 (2000)
7. M. Ichikawa: Trans. JASME. 57 (3), 28 (1991)

Proceedings of 7th Japan International SAMPE
Symposium & Exhibition, Nov. 13-16, 2001

Damping capacity of Ti-Ni and Ti-Ni-Cu alloys produced by lamination process

N.Urahashi, M.Sasaki*, D.Imai*, Y.Kogo, K.Hishitani and N.Igata

Department of Materials Science and Technology, Science University of Tokyo
2641 Yamazaki, Noda 278-8510, Japan
E-mail : j8201610@ed.noda.sut.ac.jp

* Nippon Metal Industry Co., Ltd.
1-30 Ohyama, Sagamihara Kanagawa 229, Japan

Abstract

Recently, the vibration and the noise problem of machines attract attention in our living and especially in the precision machine industries, the demand for higher damping materials with higher strength has increased. On these materials, Ti-Ni and Ti-Ni-Cu alloys are the most attractive alloys. However, there is difficulty in its workability. Therefore, in this study, the alloys were made from Ti/Ni or Ti/Ni-Cu laminated materials by the solid diffusion method. The highest damping was obtained in Ti-40Ni-10Cu (at%) and δ =0.1 at 250K and the ultimate tensile strength was 650 MPa.

Key words: Internal friction, High damping, TiNi , TiNiCu , Martensitic transformation

Introduction

Recently, the vibration and the noise problem of machines attract attention in our living and especially in the precision machine industries, the demand for higher damping materials with higher strength has increased.

The TiNi and TiNiCu alloys have good characteristics with respect to high damping capacity and high strength. However, there is difficulty in their workability. Therefore, we made TiNi and TiNiCu alloys from laminated materials by the solid diffusion method.

In this paper, the processing of TiNi and TiNiCu alloys from Ti/Ni and Ti/Ni-Cu laminated materials by the solid diffusion method and the effects of the composition, and annealing time on the internal friction are reported.

Experimental

Material procedure

Square titanium sheets with thickness of 0.2 mm and nickel sheets with thickness of 0.10 to 0.15 mm or nickel-copper sheets with thickness of 0.13mm were used in this process. These were cleaned before assembly, and then stacked about 180 layers in TiNi, or 181 layers in TiNiCu. The stack was put into steel box and evacuated. After hot rolling, the surface steel was eliminated

and cold rolled.

The rolled plate was next cut into small plates and again sealed in the stainless steel case. The case was pumped down to a pressure of 5.0 Pa, and then annealed at 1163K for 1.8 to 860ks for homogenizing and subsequently quenched in water.

The compositions of the samples were controlled by changing the thickness and stack number of Ti and Ni sheets in TiNi, by changing the composition of Ni-Cu sheets in TiNiCu. Table1 shows the results of chemical analysis of samples.

Table.1 Results of chemical analysis of samples

Sample No.	T1	T2
Chemical analysis(at%)	Ti-46.1Ni	Ti-48.5Ni
TN	N1	N2
Ti-50Ni	Ti-52.6Ni	Ti-54.4Ni
TNC1		TNC2
Ti-40.1Ni-10.1Cu		Ti-46.0Ni-5.3Cu
TNC3		
Ti-47.7Ni-2.0Cu		

Measurements

Measurements of the temperature dependence of the damping capacity (here after internal friction) and Young's Modulus were carried out using the transverse vibration method (ULVAC IFT-1500Y). The size of specimen was 120 x 10 x 0.6 mm^3 and the frequency was 100 to 150 Hz at room temperature. After austenitizing at 400K and cooling to 150K, internal friction was measured on heating to 400K at the rate of 2K/min. The strain amplitude was 7 x 10^{-6}. The tensile testing, SEM(scanning electron microscopy) and DSC(differential scanning calorimetry) were performed to interprete the results. TEM(transmission electron microscopy) was also used to identify the nanostructure.

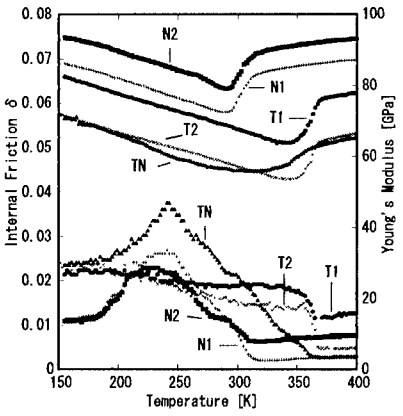

Fig.1 The temperature dependence of internal friction and Young's modulus of T1, T2, TN, N1 and N2

Results and discussion

Internal friction and Young's modulus

Effect of composition

Fig.1 shows the temperature dependence of the internal friction and Young's modulus of T_1, T_2, TN, N_1 and N_2 samples annealed at

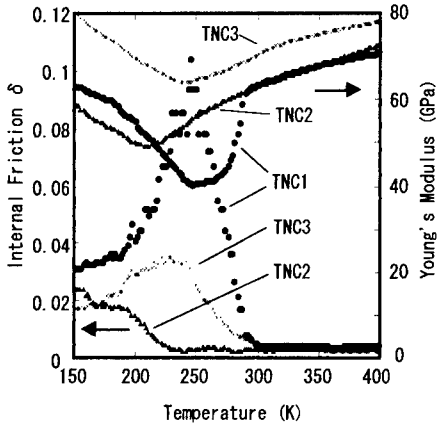

Fig.2 The temperature dependence of internal friction and Young's modulus of TNC1, TNC2 and TNC3

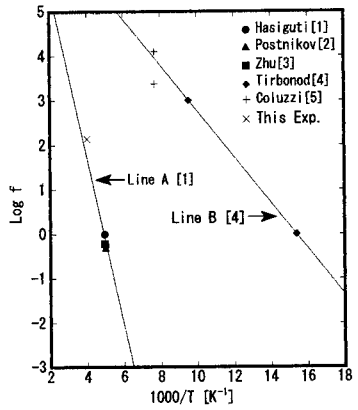

Fig.3 Arrhenius plot from the present data and the former data

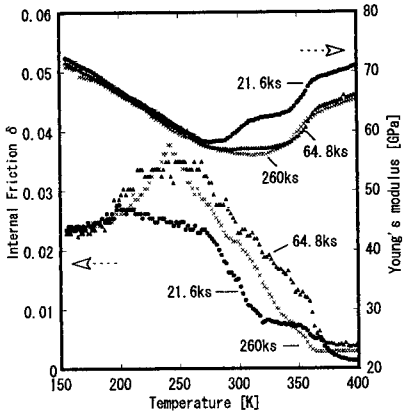

Fig.4 The temperature dependence of the internal friction and Young's modulus of TN for 21.6, 64.8 and 260ks

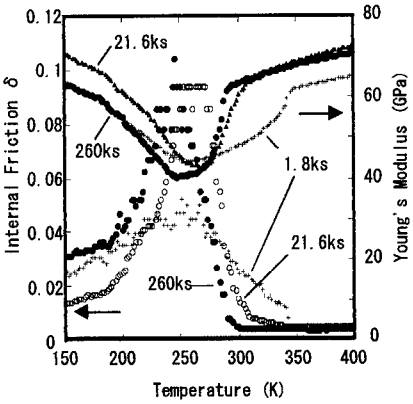

Fig.5 The temperature of dependence of the internal friction and Young's modulus of TNC1 for 1.8, 21.6 and 260ks

1163K for 260ks on the heating measurement. In Ti-rich T_1 and T_2, the rapid decrease in the internal friction corresponding to the minimum Young's modulus was observed at around 320K. In TN sample, the decrease in the internal friction corresponding to the broad minimum of Young's modulus was observed in the temperature range from 250 to 350K. A large internal friction peak was observed at around 250K. In Ni-rich N_1 and N_2, the decrease in the internal friction corresponding to the Young's modulus minimum was observed at around 290K. All those changes are due to phase change of martensite to austenite. Besides of those phenomena, a large internal friction peak was observed at around 230K in TN, N_1 and N_2.

Fig.2 shows the temperature dependence of the internal friction and Young's modulus of TNC1 TNC2 and TNC3 samples annealed at 1163K for 260ks on the heating measurement. In TNC1, TNC2 and TNC3, the minimum of Young's modulus and the maximum of internal friction were observed at 250K, 150k and 250k respectively. The deviation of the temperature of the maximum internal friction in TNC2 came from the Ni content. As for the background internal friction below the transformation temperature, it can be attributed to the motion of twin boundary in martensite. Since it is not dependent on temperature, it is considered to be due to hysteresis of twin boundary. The higher background damping in TNC alloys, would be due to B19 phase in TNC in which twin boundary is more mobile. Fig.3 shows Arrhenius plot for the

relaxation peaks of the previous results and the present data. Line A, B were plotted from the present data and the former data [1] ~ [5]. These peaks in Fig.1 and Fig.2 corresponded to Line A which were found at higher temperature than Line B, and this shows that the mechanism is not Bordoni peak but dislocation-point defect interaction peak [6] when dislocations are contained.

Since dislocations were observed in those samples, the observed relaxation peak may be due to an interaction between point defects and dislocations. In T_1 and T_2 in Fig.1 the peak was not observed. In this case the pinning of dislocations due to fine Ti_2Ni are considered.

Effect of annealing time

Fig.4 shows the temperature dependence of the internal friction and Young's modulus of the TN sample annealed at 1163K for 21.6, 64.8ks(shorter time annealing) and 260ks(longer time annealing). In shorter time annealing, Ti-rich and Ni-rich regions coexisted. Therefore background decreased and peak height decreased. However in longer time annealing, background and peak height increased due to homogenization. Fig.5 shows the results on TNC1. The similar results as Fig.4 were obtained. Finally the highest damping δ =0.1 was obtained at 250K. The strength was 650 MPa.

Conclusion

In this study, the processing method of the TiNi and TiNiCu alloys from the Ti/Ni and Ti/Ni-Cu laminated materials by the solid diffusion method was established, and the effect of composition and annealing time on the internal friction and tensile strength were investigated. The results are as follows.

(1) In TiNi, the TN sample showed the maximum damping capacity. And in TiNiCu, the TNC1 sample showed a higher damping capacity. These peak mechanisms might be due to an interaction between dislocations and point defects. And the background damping would be, due to hysteretic motion of twin boundary in martensite.

(2) In the sample of short annealing time, a high damping capacity was shown in the wide temperature range. It might be due to the coexistence of the Ti-rich and Ni-rich areas or the Ti-rich and Ni-Cu-rich areas.

(3) The highest damping δ =0.1 was obtained at 250K. The strength was 650 MPa.

Acknowledgments

The authors acknowledg the financial support from the Japan Society for the Promotion of Science Research and Development of New high Damping Material Based on Atomistic Design Project.

References

[1] R. R. Hasiguti, K. Iwasaki, J. Apple. Phys., 59 (1968) 2182.

[2] V. S. Postnikov, V. S. Lebedinsky, V. A. Yevsyokov, I. M. Sharskakov, M. S. Pesin, Fiz. Met. Metallov, 29 (1970) 34.

[3] J. S. Zhu, R. Schaller and W. Benoit, Physics letter A, 141 (3, 4) (1989) 177-180.

[4] B. Tirbond, S. Koshimizu, J. de Phys., 42 (1981) C5-1043.

[5] B. Coluzzi, A. Biscarini, R. Campanella, G. Mazzolai, L. Trotta, A. Tuissi and F. M. Mazzolai, Acta mater. 47 (1999) 1965

[6]R.R.Hasiguti, N.Igata and G.Kamoshita, Acta Met., 10, p.442(1962).

Proceedings of 7th Japan International SAMPE
Symposium & Exhibition, Nov. 13-16, 2001

Development of Pultrusion Techniques of Phenol Foam Composite

Goichi Ben+, Akiko Shoji*, Tomohiko Takimoto*,
and Yoshio Aoki++

*Graduate student of Nihon University
7-24-1 Narashinodai Funabashi-shi,274-8501,JAPAN
E-mail : shoji@pme-sv.eme.cst.nihon-u.ac.jp

+College of Industrial Technology, Nihon University
++College of Science and Technology, Nihon University

Abstract

Phenol resin has originally advantages of heat proof, flame proof and less smoke during burning and these advantages are suitable properties in the construction field.

In this paper, we present a development of pultrusion technique of phenol foam composite materials using phenol resin foam as matrix and roving glass fibers as a reinforcement in order to apply this composite to materials in the field of construction. In the case of molding phenol foam composites, it is important to control the foaming time by a use of thermal support. Next, this paper also shows mechanical strengths of the phenol foam composite comparing with those of woods. As a result, the phenol foam composite shows a possibility of use in the field of construction like natural woods.

Key Words: Phenol Resin Foam, Plutrusion
Glass fiber, compressive strength

Introduction

Phenol foam composites using phenol resin foam as a matrix and roving glass fibers as a reinforcement exhibit further weight saving, shock absorption, high insulation and flame proof. The phenol resin has originally advantages of heat proof flame proof and less smoke during burning. These advantages are suitable for applying to materials in the field of construction. Furthermore, this composite may also apply to the fields of space structures because of the inflatable function.

In order to mold phenol foam composites, a plutrusion technique, which can produce composites having the same cross section and optional length, is very useful because the volume and arrangement of fibers in the cross section of composite can be almost kept constant. We developed the system of pultrusion facilities as shown in **Fig.1**. In a general way of pultrusion forming, glass fibers pulled from roving rack are immersed in resin bath before

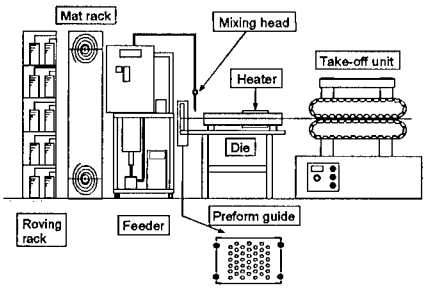

Fig.1 Plutrusion Facilities

introducing to a iron die, or they are sprayed by the pressured resin in the interior of die.

In the matrix of resin foam type, we could not use both ways stated above and we developed an original feeder machine to mold phenol foam composite materials. This feeder machine could store and pump up phenol resin containing a foaming agent, di-chloromethane, and a curing agent separately. This machine mixed them at a certain rate in the inside of mixing head just before feeding to glass fibers.

If the phenol resin containing the foaming agent was mixed with the curing agent, the temperature of resin increased owing to chemical reaction. When the raise of temperature was over 39.8°c of a boiling point in di-chloromethane, the foaming started and the phenol resin continuously became hard. In order to mold the phenol foam composite by the pultrusion method, roving glass fibers should be sufficiently immersed in the phenol resin before the start of foaming. Therefore, it is important control the time before foaming and then the time during foaming affects on a pulling velocity in the plutrusion forming. Thus, an experimental research is required to know the condition of forming process and to investigate proper quantities of phenol resin and the foaming and curing agents. Furthermore, the relations of their quantities to an expansion ratio, the proper velocity of pulling out and a compressive strength of composites should be made clear.

Experiments and Results

Foaming

After the curing agent was added to 100 g of the phenol resin including the foaming agent in a beaker, two kinds of times before and during foaming were examined under the initial circumferential temperatures. The expansion volume ratio before and after expansion in the beaker was also measured.

Table 1 shows the experimental results under three kinds of initial circumferential temperature. The lower initial temperature was, the slower process of foaming started. Furthermore, the lower initial temperature was, the smaller expansion volume ratio was obtained. Especially in the case of 15°c initial temperature, the expansion ratio dropped down. This reason is that the temperature of resin influences on the diffusion velocity of foaming gas and that the lower initial temperature reduces a growth velocity of bubbles in the phenol resin.

Table 1 Results of Foaming times and Expansion Ratio

Initial Temperature [°C]	Foaming Start Time [sec]	Foaming Time [sec]	Expansion Ratio
15	212.5	137.4	13.3
20	109.4	90.6	17.4
25	58.3	91.7	17.9

In order to mold the phenol foam composite by the plutrusion technique, it needs a longer pot life for the sufficient immersion. The pot life means a period from

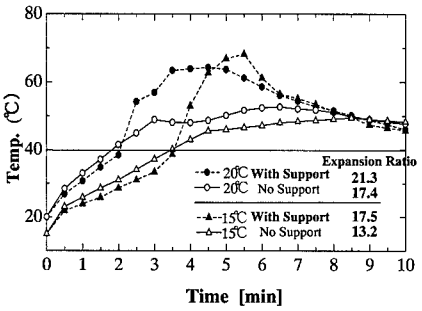

Fig.2 Temperature Change vs. Time under Thermal Support (60°c)

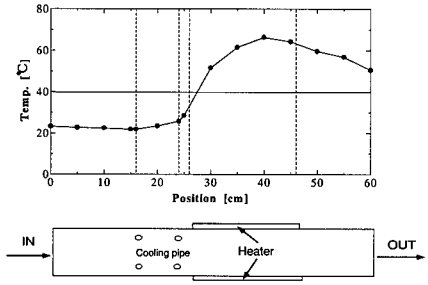

Fig.3 Thermal Distribution of Die

mixing of the phenol resin with the curing agent to the start of foaming. When the temperature of resin reached at 39.8°c owing to the chemical reaction, the foaming stated. Therefore, the lower initial temperature of phenol resin could extend the pot life, but the expansion volume ratio decreased. In order to examine the relation of environmental temperature to the expansion volume ratio, we warmed the phenol resin in the beaker under two temperatures. When the resin temperature reached at 39.8°c, the beaker was soaked in the hot water of 40°c or 60°c.

Fig 2 shows the thermal sift of phenol resin during foaming under the 60°c thermal support. Under the 60°c thermal support, the temperature of phenol resin increased immediately just after start foaming, and also expansion ratio increased.

Plutrusion

When the temperature variation based on the experimental result in the beaker **(Fig.2)** is realized in the interior of die, the enough time to immerse the glass fibers to resin and the temperature to ensure the proper expansion ratio can be obtained in the plutrusion forming. For realizing this temperature variation, heaters to warm up the die to 60°c were installed at the latter part of the die and the former part of die was cooled by four water pipes. In **Fig.3**, the temperature in the interior of the die is shown. The designed die could be divided into the two parts for the immersion and foaming.

In order to decide a velocity of plutrusion, the results of **Fig.2** was compared with that of **Fig.3** and the velocity pulling out the glass fibers was decided to 10[cm/min]. The constant volume of resin Q supplied by the feeder was calculated by the following equation.

$$Q = V_m \; A \; v \; / x \qquad (1)$$

In which, V_m :matrix volume fraction, A: cross section area of composite, v: pulling out velocity, x : expansion ratio

In the trial forming of plutrusion, the phenol resin was supplied 60g/min and the volume fraction of glass fibers was 6% in the phenol foam composite. The used glass fiber was a bulky roving type because it was easier to be immersed in the phenol resin than other types. Furthermore, a continuous strand mat glass fiber was also used.

Compression test

Two types of test specimens were formed to evaluate their compressive

strengths. Type1 used the bulky roving glass fibers only. Type2 employed both of bulky roving glass fiber and continuous strand mat glass fibers and this mat glass fibers were set to the above and the below surfaces of phenol foam composite. The volume fraction was kept the same value of 6%. The width, height and length of specimen were 52mm, 32mm, and 100mm.

The results of compression test are shown in **Table2**. The type1 was stronger than the type2 because the density of type 1 was larger than that of type 2. The phenol resin in of type 1 was not fully expanded in the die owing to being much bulky roving glasses than those in the type 2 and the continuous strand mat glass fibers did not give so effect on the compressive strength. Consequently, a relation of the density to the compressive strength in the phenol foam composite should be further investigated. Next, the strength of phenol foam glass fiber composites was lower than natural woods as shown in **Table3**. However, the strength will be improved by an arrangement and a volume of glass fibers.

Table 2 Results of Compression Test

test pieces	density (g/cm3)	compressive strength (MPa)	specific strength (cm)	specific Young's modulus (cm)
type1	0.493	13.01	269	30700
type2	0.452	10.56	238	32700

Table 3 Strength of Various Woods

	density (g/cm3)	compressive strength	specific strength (cm)
Artificial Wood	0.4	14.7	375
cedar	0.33	27.44	848
hinoki	0.41	39.2	976

Conclusions

Plutrusion techniques to form phenol foam glass fiber composite materials could be exhibited by taking account of a proper control of the temperature distribution in the interior of die. This temperature distribution depended on the division of die into the two parts for the immersion of glass fibers in phenol resin and foaming of phenol resin.

Next, a type of bulky roving among various types of roving glass fibers was employed because it was easier to be immersed in the phenol resin than other types.

Furthermore, the phenol foam composite strength had almost the same compressive strength as artificial woods but it was smaller than that of natural woods. In order to increase the compressive strength of phenol foam composite, the volume fraction of fibers should be increased and then the relations of strength to the fiber volume and the expansion rate must be investigated in future.

Acknowledgment

Authors would like to express their thanks to Vantec Co. for giving useful advices about a plutrusion technique and Showa Kobunsi Co. for offering test materials.

References

1. Nobuyuki Ozawa: *"Plutrusion techniques"*, Advanced Techniques of Molding, sigma publication. 345~352(1999)
2. Hiroshi Abe *"happouseikei"*, Advanced Techniques of Molding, sigma publication. 213~264(1999)

Author Index

Author	Page	Session	Author	Page	Session
Abbott, R.	141	B	Davies, I.J.	577	I
Abe, S.	193	B	Davies, I.J.	737	K
Abe, S.	817	M	Drechsler, K.	227	C
Advani, S.G	923	O	Dreher, G.	201	B
Akimune, Y.	123	A	El-Tantawy, F.	555	H
Akiyama, K.	107	A	El-Tantawy, F.	797	L
Aly-Hassan, M.S.	605	I	Endo, I.	259	C
Amano, O.	303	D	Endo, Y.	233	C
Amaoka, K.	145	B	Felli, F.	661	J
Ando, S.	463	G	Foley, M.E.	923	O
Aoi, T.	617	I	Fujii, R.	669	J
Aoki, T.	283	D	Fujii, Y.	713	K
Aoki, T.	593	I	Fujii, Y.	765	K
Aoki, Y.	837	M	Fujii, Y.	895	N
Aoki, Y.	911	N	Fujimaki, T.	111	A
Aoki, Y.	979	O	Fujita, T.	185	B
Arai, S.	585	I	Fujitsu, R.	709	K
Araki, O.	423	F	Fujiwara, C.	337	D
Araki, Y.	407	F	Fujiwara, C.	625	J
Araya, K.	149	B	Fujiwara, C.	629	J
Araya, K.	157	B	Fukuda, H.	593	I
Arimitsu, Y.	745	K	Fukuda, H.	967	O
Asagumo, R.	245	C	Fukuda, T.	79	A
Asai, T.	439	G	Fukuda, T.	91	A
Asai, T.	443	G	Fukuda, T.	99	A
Asanuma, H.	119	A	Fukui, T.	733	K
Asanuma, H.	649	J	Fukui, Y.	681	J
Asanuma, H.	N/A	J	Fukumori, K.	427	F
Asanuma, H.	N/A	O	Fukumoto, K.	423	F
Asari, K.	N/A	C	Fukunaga, H.	637	J
Ashizawa, M.	129	B	Fukunaga, H.	907	N
Aso, Y.	419	F	Fukushima, A.	337	D
Bandoh, S.	245	C	Fukushima, A.	629	J
Bandoh, S.	899	N	Funaki, I.	333	D
Bansemir, H.	201	B	Furuta, M.	423	F
Beckwith, S.W.	5	P	Gemma, K.	677	J
Belov, E.	689	K	Gillespie Jr., J.W.	923	O
Byon, O.-I. (Ben G.)	911	N	Gomyou, T.	971	O
Byon, O.-I. (Ben G.)	979	O	Gosse, J.	33	P
Cantoni, S.	275	D	Goto, A.	471	G
Caponero, M.A.	661	J	Goto, A.	757	K
Chang, F.-K.	907	N	Goto, K.	333	D
Chang, J.C.I.	1	P	Goto, K.	483	G
Chonabayashi, S.	633	J	Goto, K.	589	I
Chou, I.	363	E	Goto, K.	605	I
Chou, T.-W.	745	K	Goto, K.	757	K
Curtin, W.A.	67	A	Gotoh, S.	721	K
Dai, J.	379	E	Guedra-Degeorges, D.	227	C
Danchaivichit, S.	959	O	Ha, S.-K.	33	P
Davies, I.J.	565	I	Hagiwara, N.	665	J

Hahn, S.	825	M	Hirota, M.	629	J
Hakoda, G.	119	A	Hishitani, K.	975	O
Hakoda, G.	649	J	Hogami, T.	569	I
Hakoda, G.	N/A	J	Hogg, P.	N/A	K
Hakotani, M.	539	H	Honda, Y.	233	C
Hald, H.	325	D	Horizono, H.	263	C
Hamada, H.	99	A	Hosoda, S.	673	J
Hamada, H.	399	F	Hosokawa, K.	463	G
Hamada, H.	403	F	Hu, N.	907	N
Hamada, H.	701	K	Huang, X.	559	I
Hamada, H.	705	K	Huysmans, G.	717	K
Hamada, H.	737	K	Hyakutake, H.	543	H
Hamada, H.	761	K	Hyodo, S.	861	M
Hamada, H.	765	K	Ichikawa, T.	853	M
Hamada, H.	773	K	Igata, N.	975	O
Hamada, H.	777	K	Igawa, H.	321	D
Hamada, H.	793	L	Ihara, H.	511	H
Hamada, H.	805	L	Iio, S.	157	B
Hamada, H.	895	N	Ikegami, Y.	443	G
Hamada, H.	951	O	Ikoma, N.	375	E
Hamasaki, A.	963	O	Ikoma, N.	411	F
Han, J.-H.	903	N	Imagawa, K.	295	D
Hanada, M.	701	K	Imagawa, K.	299	D
Hanatani, S.	407	F	Imai, D.	975	O
Hanzawa, S.	601	I	Imai, T.	641	J
Harada, A.	145	B	Imaizumi, H.	645	J
Harada, A.	181	B	Inada, T.	915	N
Hasegawa, O.	891	N	Inai, R.	399	F
Hatakeyama, T.	237	C	Inoda, M.	733	K
Hatta, H.	589	I	Inose, K.	367	E
Hatta, H.	593	I	Inoue, M.	657	J
Hatta, H.	597	I	Inoue, N.	685	J
Hatta, H.	605	I	Inoue, S.	447	G
Hatta, H.	609	I	Inoue, S.	451	G
Hatta, H.	617	I	Inoue, T.	145	B
Hattori, T.	251	C	Inoue, T.	633	J
Hattori, T.	267	C	Inoue, T.	737	K
Hayakawa, K.	645	J	Ishida, T.	721	K
Hayashi, K.	677	J	Ishiguro, T.	947	O
Hayashi, S.	295	D	Ishii, H.	829	M
Hayashi, S.	515	H	Ishii, T.	119	A
Hayashi, Y.	279	D	Ishii, T.	701	K
Henne, R.	325	D	Ishikawa, G.	527	H
Higuchi, N.	879	N	Ishikawa, M.	801	L
Higuchi, Y.	805	L	Ishikawa, N.	375	E
Hihara, L.H.	621	J	Ishikawa, T.	275	D
Hinrichsen, J.	23	P	Ishikawa, T.	279	D
Hirahara, M.	193	B	Ishikawa, T.	507	H
Hirai, T.	869	M	Ishikawa, T.	565	I
Hirano, K.	241	C	Ishikawa, T.	569	I
Hirata, Y.	883	N	Ishikawa, T.	573	I
Hiroe, T.	237	C	Ishikawa, T.	577	I
Hirosaki, N.	123	A	Ishikawa, T.	581	I
Hirose, Y.	149	B	Ishikawa, T.	845	M
Hirose, Y.	157	B	Ishikawa, T.	919	N
Hirose, Y.	165	B	Ishikawa, T.	971	O
Hirose, Y.	185	B	Ishizawa, J.	295	D
Hirota, M.	337	D	Ishizawa, J.	299	D
Hirota, M.	625	J	Itabashi, M.	967	O

Ito, A.	483	G	Kimura, A.	613	I
Ito, M.	407	F	Kimura, K.	29	P
Ito, T.	149	B	Kimura, K.	865	M
Ito, T.	263	C	Kimura, K.	N/A	O
Ito, Y.	133	B	Kimura, T.	363	E
Iwahori, Y.	697	K	Kimura, T.	367	E
Iwamoto, M.	51	A	Kiriyama, H.	189	B
Iwasa, M.	267	C	Kishi, H.	259	C
Iwasaki, A.	71	A	Kishimoto, S.	115	A
Iwasawa, S.	697	K	Kitade, S.	79	A
Jinishi, T.	197	B	Kiuchi, N.	527	H
Kabashima, S.	307	D	Kiuchi, N.	531	H
Kageyama, K.	817	M	Ko, H.N.	601	I
Kajii, S.	569	I	Kobashi, M.	653	J
Kajita, Y.	375	E	Kobayashi, A.	935	O
Kamada, G.	539	H	Kobayashi, A.	939	O
Kamada, K.	363	E	Kobayashi, A.	947	O
Kamada, K.	367	E	Kobayashi, A.S.	535	H
Kamada, K.	555	H	Kobayashi, H.	49	A
Kamata, Y.	303	D	Kobayashi, H.	71	A
Kameyama, M.	907	N	Kobayashi, H.	809	M
Kamiharako, A.	387	E	Kobayashi, H.	887	N
Kamii, H.	633	J	Kobayashi, H.	915	N
Kamita, T.	223	C	Kobayashi, H.	927	O
Kamita, T.	317	D	Kobayashi, H.	931	O
Kamita, T.	321	D	Kobayashi, N.	785	L
Kamiyama, T.	145	B	Kobayashi, S.	531	H
Kamiyama, T.	219	C	Kobayashi, S.	769	K
Kamiyama, T.	233	C	Kobayashi, S.	813	M
Kanai, M.	817	M	Kobayashi, Y.	169	B
Kanatani, Y.	169	B	Kobayashi, Y.	N/A	L
Kanetake, N.	653	J	Kobiki, A.	781	L
Kasano, H.	891	N	Kogo, Y.	597	I
Katagiri, T.	609	I	Kogo, Y.	609	I
Katayama, T.	539	H	Kogo, Y.	617	I
Kato, M.	415	F	Kogo, Y.	963	O
Kato, T.	817	M	Kogo, Y.	975	O
Katoh, H.	519	H	Kohashi, M.	849	M
Katsuki, F.	391	E	Kohno, A.	879	N
Katsumata, H.	29	P	Kojima, K.	307	D
Kawachi, Y.	337	D	Komaki, H.	395	E
Kawachi, Y.	629	J	Komiyama, H.	9	P
Kawachi, Y.	879	N	Konnai, H.	419	F
Kawada, H.	781	L	Kono, A.	625	J
Kawada, H.	785	L	Koo, J.-H.	55	A
Kawaguchi, H.	645	J	Kosaka, T.	91	A
Kawai, M.	841	M	Kosaka, T.	99	A
Kawai, M.	849	M	Koshikiya, Y.	785	L
Kawai, S.	459	G	Kosugi, K.	157	B
Kawamoto, T.	455	G	Kosugi, K.	237	C
Kawazoe, Y.	499	G	Koyama, Y.	765	K
Kawazoe, Y.	503	G	Kubo, F.	865	M
Kemmochi, K.	371	E	Kubo, H.	407	F
Kihara, T.	527	H	Kubomura, K.	287	D
Kikukawa, H.	137	B	Kumazawa, H.	283	D
Kikukawa, H.	145	B	Kunimine, T.	677	J
Kikukawa, H.	207	B	Kuninaka, H.	333	D
Kim, B.	943	O	Kuraishi, A.	33	P
Kim, T.D.	271	D	Kuraishi, A.	211	B

Kurashiki, T.	899	N
Kurata, Y.	91	A
Kurimoto, H.	99	A
Kurokawa, T.	383	E
Kuwazuru, O.	729	K
Lee, G.C.	N/A	J
Lee, I.	903	N
Lee, J.H.	N/A	J
Lee, T.-M.	173	B
Lomov, S.	689	K
Machida, T.	753	K
Maeda, T.	395	E
Maekawa, M.	423	F
Maekawa, Z.	169	B
Maekawa, Z.	467	G
Maekawa, Z.	475	G
Maekawa, Z.	491	G
Maekawa, Z.	495	G
Maekawa, Z.	757	K
Maekawa, Z.	833	M
Marais, C.	519	H
Maruyama, D.	597	I
Maruyama, K.	353	E
Maruyama, K.	387	E
Maruyama, K.	391	E
Maruyama, S.	181	B
Masuda, I.	307	D
Masugi, K.	177	B
Masuko, Y.	841	M
Masuko, Y.	849	M
Matoba, M.	161	B
Matsubara, T.	495	G
Matsuda, K.	681	J
Matsui, J.	169	B
Matsumoto, K.	487	G
Matsumoto, N.	487	G
Matsumoto, T.	527	H
Matsumoto, T.	531	H
Matsumura, K.	899	N
Matsunaga, K.	569	I
Matsuo, K.	123	A
Matsuoka, S.	291	D
Matsushita, M.	427	F
Matsuyama, A.	423	F
McKnight, S.H.	923	O
Mitani, K.	515	H
Miura, S.	423	F
Miwa, N.	295	D
Miyagawa, H.	91	A
Miyagawa, K.	507	H
Miyagawa, K.	605	I
Miyagawa, K.	813	M
Miyaji, C.	451	G
Miyano, Y.	215	B
Miyatani, S.	63	A
Miyazaki, E.	605	I
Miyazawa, Y.	103	A
Miyoshi, N.	259	C
Mizoguchi, K.	801	L
Mizoguchi, M.	761	K
Mizoguchi, M.	765	K
Mizoguchi, M.	805	L
Mizoguchi, M.	895	N
Mizuno, H.	263	C
Mizuno, H.	299	D
Mizusaki, Y.	185	B
Mizutani, A.	613	I
Mizutani, T.	95	A
Mmmerling, S.	201	B
Moon, D.	N/A	C
Mori, T.	349	D
Morii, T.	789	L
Morii, T.	895	N
Morimoto, T.	275	D
Morimoto, T.	279	D
Morimoto, T.	963	O
Morino, Y.	275	D
Morino, Y.	279	D
Morino, Y.	329	D
Motogi, S.	79	A
Motoike, M.	161	B
Mukai, S.	931	O
Murase, S.	887	N
Murayama, H.	321	D
Mutsuyoshi, H.	391	E
Nagano, H.	345	D
Naganuma, T.	197	B
Nagao, Y.	233	C
Nagasaka, Y.	345	D
Naka, T.	91	A
Nakada, M.	215	B
Nakai, A.	99	A
Nakai, A.	701	K
Nakai, A.	713	K
Nakai, A.	721	K
Nakai, A.	733	K
Nakai, A.	737	K
Nakai, A.	749	K
Nakai, A.	757	K
Nakai, A.	761	K
Nakai, A.	769	K
Nakai, A.	773	K
Nakai, A.	777	K
Nakai, A.	793	L
Nakai, A.	951	O
Nakamura, H.	233	C
Nakamura, H.	291	D
Nakamura, K.	193	B
Nakamura, M.	153	B
Nakamura, T.	645	J
Nakamura, Y.	349	D
Nakano, K.	601	I
Nakata, M.	165	B
Nakatani, T.	399	F
Nakaya, K.	781	L
Nakayama, Y.	245	C
Nakazaki, K.	609	I
Naruse, T.	251	C

Natsume, N.	259	C	Ohie, T.	801	L
Nguyen, M.-Q.	173	B	Ohkawa, T.	749	K
Ni, Q.-Q.	51	A	Ohki, T.	51	A
Ni, Q.-Q.	833	M	Ohnabe, H.	555	H
Niitsu, M.	223	C	Ohnishi, A.	345	D
Niitsu, M.	317	D	Ohnishi, A.	349	D
Nishi, K.	539	H	Ohno, H.	535	H
Nishi, Y.	103	A	Ohsaka, N.	51	A
Nishi, Y.	107	A	Ohsawa, I.	817	M
Nishi, Y.	613	I	Ohsawa, Y.	573	I
Nishi, Y.	665	J	Ohtani, A.	737	K
Nishi, Y.	669	J	Ohuchi, A.	801	L
Nishi, Y.	677	J	Oishi, R.	55	A
Nishi, Y.	685	J	Okabe, T.	67	A
Nishi, Y.	943	O	Okabe, T.	75	A
Nishi, Y.	955	O	Okabe, T.	821	M
Nishihata, M.	677	J	Okabe, Y.	83	A
Nishikawa, S.	375	E	Okabe, Y.	87	A
Nishimoto, Y.	375	E	Okabe, Y.	95	A
Nishino, K.	585	I	Okada, M.	753	K
Nishino, Y.	411	F	Okai, T.	753	K
Nishitani, M.	149	B	Okamoto, A.	349	D
Nishiwaki, K.	223	C	Okamoto, H.	427	F
Nishiwaki, T.	431	G	Okazaki, T.	725	K
Nishiwaki, T.	435	G	Okazaki, T.	857	M
Nishiwaki, T.	439	G	Okita, T.	427	F
Nishiwaki, T.	471	G	Olson, N.	559	I
Nishiwaki, T.	475	G	Onita, T.	491	G
Nishiwaki, T.	491	G	Onoda, H.	511	H
Nishiwaki, T.	495	G	Onoda, J.	341	D
Nishiwaki, T.	701	K	Osada, T.	99	A
Nishiyabu, K.	693	K	Osada, T.	219	C
Nishiyabu, K.	709	K	Osada, T.	733	K
Nishiyama, K.	333	D	Osada, T.	761	K
Niu, H.	383	E	Osada, T.	769	K
Noda, J.	821	M	Osada, T.	773	K
Nunogaki, M.	657	J	Osada, T.	793	L
Nunome, H.	439	G	Osada, T.	951	O
Nunome, H.	443	G	Osaka, K.	91	A
Ochi, A.	349	D	Osaka, K.	99	A
Ochi, M.	161	B	Osawa, T.	237	C
Ochi, Y.	573	I	Oshima, A.	511	H
Ochi, Y.	971	O	Ota, M.	311	D
Ogasawara, T.	507	H	Otani, A.	713	K
Ogasawara, T.	565	I	Otani, A.	721	K
Ogasawara, T.	573	I	Otani, H.	459	G
Ogasawara, T.	577	I	Otsuka, S.	427	F
Ogasawara, T.	581	I	Owaki, M.	423	F
Ogasawara, T.	971	O	Ozaki, T.	825	M
Ogi, K.	547	H	Ozaki, T.	829	M
Ogihara, S.	777	K	Ozaki, Y.	479	G
Ogihara, S.	935	O	Ozawa, H.	507	H
Ogihara, S.	939	O	Ozawa, T.	307	D
Ogihara, S.	947	O	Ozawa, Y.	523	H
Oguri, K.	613	I	Pandita, S.D.	717	K
Oguri, K.	669	J	Paolozzi, A.	35	A
Oguri, K.	955	O	Paolozzi, A.	661	J
Ohashi, S.	161	B	Park, D.S.	N/A	J
Ohgi, Y.	451	G	Park, J.-B.	67	A

Park, Y.C.	N/A	J	Shimizu, T.	805	L
Parnas, R.	689	K	Shimizu, T.	951	O
Petitjean, B.	43	A	Shimizu, Y.	333	D
Pflug, J.	255	C	Shimoda, T.	275	D
Pipes, R.B.	17	P	Shimoda, T.	279	D
Prodromou, A.	689	K	Shimokawa, T.	519	H
Reifsnider, K.	559	I	Shimomura, T.	387	E
Rowlands, R.E.	919	N	Shinagawa, M.	511	H
Saito, H.	399	F	Shinbo, T.	387	E
Saito, K.	299	D	Shinohara, M.	539	H
Saito, N.	153	B	Shinya, N.	115	A
Saitou, K.	447	G	Shiomi, T.	475	G
Saitou, K.	451	G	Shirai, Y.	935	O
Sakakibara, K.	705	K	Shiraishi, T.	547	H
Sakamoto, K.	383	E	Shiraishi, T.	581	I
Sakamoto, R.	551	H	Shoji, A.	979	O
Sakanashi, T.	157	B	Soeda, Y.	263	C
Sakata, T.	459	G	Sohda, Y.	395	E
Sakata, T.	463	G	Someya, Y.	263	C
Sakurai, S.	443	G	Song, D.-Y.	883	N
Sana, T.	149	B	Suemasu, H.	837	M
Sanders, R.	447	G	Sugahara, T.	455	G
Saniger, J.	43	A	Suganuma, K.	657	J
Sasaki, G.	637	J	Sugimoto, S.	919	N
Sasaki, M.	975	O	Sugiyama, T.	123	A
Sasaki, S.	311	D	Sugizaki, K.	361	E
Sato, A.	129	B	Sujirote, K.	959	O
Sato, E.	341	D	Sun, Y.-S.	741	K
Sato, M.	569	I	Sunamoto, T.	685	J
Sato, M.	757	K	Susuki, I.	283	D
Sato, N.	423	F	Suzuki, N.	197	B
Sato, N.	427	F	Suzuki, S.	479	G
Sato, T.	589	I	Suzuki, S.	813	M
Sato, Y.	379	E	Suzuki, T.	665	J
Schm?cker, M.	325	D	Suzuki, T. M.	423	F
Schneider, H.	325	D	Suzuki, Y.	427	F
Scott, M.L.	173	B	Tachikawa, S.	349	D
Seino, S.	789	L	Taguchi, M.	483	G
Sekine, N.	215	B	Taguchi, M.	507	H
Seko, H.	307	D	Takada, S.	307	D
Senbokuya, Y.	287	D	Takagi, M.	641	J
Senbokuya, Y.	291	D	Takahashi, H.	633	J
Shibata, A.	165	B	Takahashi, S.	745	K
Shibata, T.	303	D	Takai, S.	451	G
Shigematsu, I.	153	B	Takano, M.	307	D
Shigenari, Y.	507	H	Takano, N.	709	K
Shigenari, Y.	813	M	Takano, N.	725	K
Shiino, T.	899	N	Takano, N.	857	M
Shimakawa, Y.	349	D	Takano, N.	865	M
Shimamura, Y.	49	A	Takano, S.	407	F
Shimamura, Y.	63	A	Takashina, K.	955	O
Shimamura, Y.	71	A	Takatsubo, J.	75	A
Shimamura, Y.	809	M	Takayanagi, H.	371	E
Shimamura, Y.	887	N	Takeda, N.	67	A
Shimamura, Y.	915	N	Takeda, N.	83	A
Shimamura, Y.	927	O	Takeda, N.	87	A
Shimamura, Y.	931	O	Takeda, N.	95	A
Shimizu, M.	821	M	Takeda, N.	821	M
Shimizu, T.	773	K	Takeda, N.	883	N

Takeda, N.	935	O
Takeda, N.	939	O
Takeda, N.	947	O
Takeda, S.	83	A
Takekusa, T.	531	H
Takemura, S.	535	H
Taki, T.	185	B
Takimoto, T.	979	O
Takizawa, N.	181	B
Tamai, S.	233	C
Tamura, H.	233	C
Tamura, H.	237	C
Tanaka, A.	189	B
Tanaka, A.	813	M
Tanaka, M.	927	O
Tanaka, N.	87	A
Tanaka, S.	645	J
Tanaka, Y.	49	A
Tanaka, Y.	427	F
Tanatsugu, N.	589	I
Taniguchi, N.	435	G
Tanimoto, T.	47	A
Tanimoto, Y.	467	G
Tantikom, K.	959	O
Tateishi, M.	403	F
Tenney, D.R.	17	P
Tetsuka, M.	669	J
Todoroki, A.	49	A
Todoroki, A.	63	A
Todoroki, A.	71	A
Todoroki, A.	809	M
Todoroki, A.	887	N
Todoroki, A.	915	N
Todoroki, A.	927	O
Todoroki, A.	931	O
Toi, Y.	145	B
Tojo, M.	299	D
Toki, K.	333	D
Tokubuchi, K.	411	F
Tokunaga, T.	547	H
Tonegawa, A.	613	I
Tonegawa, A.	669	J
Tonegawa, A.	955	O
Toriyama, T.	103	A
Toriyama, T.	613	I
Toyama, N.	55	A
Tsai, S.W.	33	P
Tsai, S.W.	211	B
Tsai, S.W.	215	B
Tsubouchi, K.	395	E
Tsuda, H.	75	A
Tsuda, H.	371	E
Tsunoda, H.	287	D
Tsunoda, H.	291	D
Tuttle, M.E.	N/A	H
Uchida, H.	669	J
Uchida, H.	943	O
Uchida, S.	685	J
Ueda, T.	353	E
Ueda, T.	379	E
Ueda, T.	713	K
Uehara, T.	939	O
Uematsu, M.	879	N
Ullmann, T.	325	D
Umezaki, E.	853	M
Uno, N.	367	E
Uozumi, T.	697	K
Urabe, K.	75	A
Urabe, K.	371	E
Urahashi, N.	975	O
Usuki, A.	415	F
Uzawa, K.	223	C
Uzawa, K.	317	D
Vandepitte, D.	255	C
Verpoest, I.	255	C
Verpoest, I.	689	K
Verpoest, I.	717	K
Wada, A.	967	O
Wakabayashi, K.	515	H
Wakayama, S.	531	H
Wakayama, S.	585	I
Wakayama, S.	605	I
Wakayama, S.	813	M
Wang, B.	55	A
Watanabe, A.	287	D
Watanabe, A.	303	D
Watanabe, N.	581	I
Watanabe, O.	967	O
Watanabe, T.	511	H
Watanabe, Y.	673	J
Watanabe, Y.	681	J
Watanabe, Y.	869	M
Wittig, D.-I.J.	741	K
Wu, Z.-S.	383	E
Xia, M.	67	A
Xia, M.	371	E
Xiao, Y.	845	M
Xie, J.	833	M
Xie, R.-J.	123	A
Xu, K.	873	N
Yabe, H.	107	A
Yabe, H.	665	J
Yabe, H.	685	J
Yabe, H.	943	O
Yahata, A.	137	B
Yahata, A.	161	B
Yamada, T.	337	D
Yamada, T.	625	J
Yamada, T.	629	J
Yamada, T.	879	N
Yamada, Y.	423	F
Yamagishi, K.	79	A
Yamagiwa, K.	681	J
Yamaguchi, Y.	9	P
Yamamoto, A.	801	L
Yamamoto, N.	367	E
Yamamoto, S.	337	D
Yamamoto, S.	629	J

Yamamoto, S.	653	J
Yamamoto, S.	861	M
Yamamoto, S.	879	N
Yamamoto, T.	185	B
Yamamoto, T.	543	H
Yamamoto, T.	697	K
Yamamura, Y.	809	M
Yang, S.-M.	903	N
Yokota, R.	507	H
Yokota, T.	311	D
Yokoyama, A.	399	F
Yokoyama, A.	403	F
Yokoyama, A.	705	K
Yokoyama, A.	869	M
Yokozeki, T.	279	D
Yoshida, H.	311	D
Yoshida, M.	637	J
Yoshikawa, J.	295	D
Yoshikawa, J.	299	D
Yoshikawa, N.	729	K
Yoshimatsu, K.	753	K
Yoshimura, A.	67	A
Yoshimura, T.	219	C
Yoshimura, T.	245	C
Yoshinaka, T.	329	D
Yoshino, K.	551	H
Yoshino, Y.	165	B
Youn, S.-H.	903	N
Zako, M.	487	G
Zako, M.	709	K
Zako, M.	725	K
Zako, M.	857	M
Zako, M.	865	M
Zako, M.	899	N
Zhen, L.	641	J
Zhu, S.	573	I
Zhu, S.	971	O